

AD-A169 867

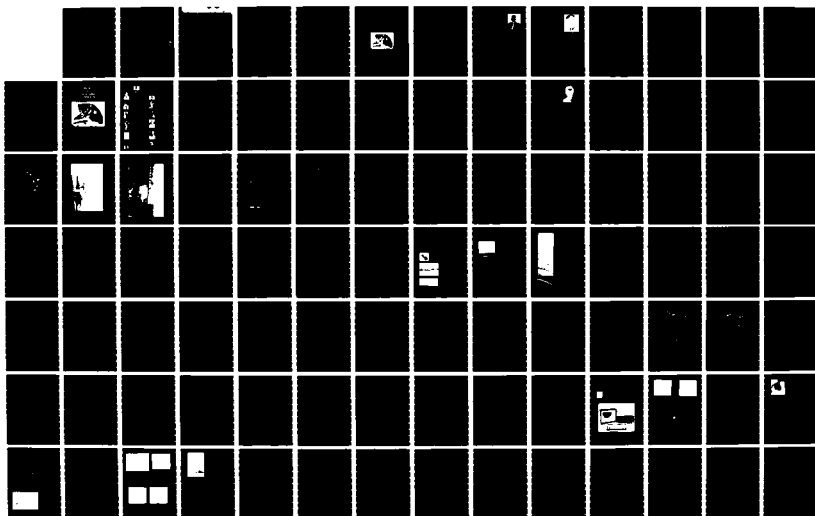
INTERNATIONAL AEROSPACE AND GROUND CONFERENCE ON
LIGHTNING AND STATIC ELE. (U) NATIONAL INTERAGENCY
COORDINATION GROUP JUN 84

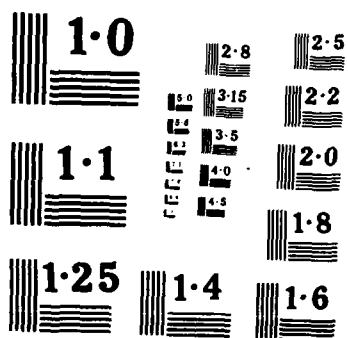
1/6

UNCLASSIFIED

F/G 20/3

NL





AD-A169 867

DTIC ACCESSION NUMBER

LEVEL

1984 PHOTOGRAPH THIS SHEET
INTERNATIONAL AEROSPACE
AND GROUND CONFERENCE ON
LIGHTNING AND STATIC
ELECTRICITY

INVENTORY

1

THE KEY TO LIGHTNING TECHNOLOGY

DOCUMENT IDENTIFICATION

DISTRIBUTION STATEMENT A

Approved for public release;
Distribution Unlimited

DISTRIBUTION STATEMENT

ACCESSION FOR

NTIS GRA&I ☒

DTIC TAB ☐

UNANNOUNCED ☐

JUSTIFICATION

BY *per Form 50*

DISTRIBUTION /

AVAILABILITY CODES

DIST

AVAIL AND/OR SPECIAL

A-1

DISTRIBUTION STAMP

DTIC
ELECTE
JUL 02 1986
S D D

DATE ACCESSIONED

DATE RETURNED

86 7 1 062

DATE RECEIVED IN DTIC

REGISTERED OR CERTIFIED NO.

PHOTOGRAPH THIS SHEET AND RETURN TO DTIC-DDAC

1984 NATIONAL INTERAGENCY COORDINATION GROUP

AD-A 169 867

UNCLASSIFIED

SECURITY CLASSIFICATION OF THIS PAGE

REPORT DOCUMENTATION PAGE

1a REPORT SECURITY CLASSIFICATION UNCLASSIFIED			1b RESTRICTIVE MARKINGS N/A		
2a SECURITY CLASSIFICATION AUTHORITY N/A			3 DISTRIBUTION AVAILABILITY OF REPORT Approved for public release; distribution unlimited		
2b DECLASSIFICATION/DOWNGRADING SCHEDULE N/A					
4 PERFORMING ORGANIZATION REPORT NUMBER(S) N/A			5 MONITORING ORGANIZATION REPORT NUMBER(S) RADC-TR-85-273		
6a NAME OF PERFORMING ORGANIZATION Measurement Concepts Corporation		6b OFFICE SYMBOL (If applicable)		7a NAME OF MONITORING ORGANIZATION Rome Air Development Center (IRDA)	
6c ADDRESS (City, State, and ZIP Code) 1721 Black River Blvd Rome NY 13440			7b ADDRESS (City, State, and ZIP Code) Griffiss AFB NY 13441-5700		
8a NAME OF FUNDING/SPONSORING ORGANIZATION Rome Air Development Center		8b OFFICE SYMBOL (If applicable) IRDA		9 PROCUREMENT INSTRUMENT IDENTIFICATION NUMBER F30600-85-C-0029	
8c ADDRESS (City, State, and ZIP Code) Griffiss AFB NY 13441-5700			10 SOURCE OF FUNDING NUMBERS		
			PROGRAM ELEMENT NO 61102F	PROJECT NO LDPE	TASK NO 08
			WORK UNIT ACCESSION NO C5		
11 TITLE (Include Security Classification) C³I TERADATA STUDY					
12 PERSONAL AUTHOR(S) John Decker					
13a TYPE OF REPORT Final		13b TIME COVERED FROM TO		14 DATE OF REPORT (Year, Month, Day) March 1986	
				15 PAGE COUNT 238	
16 SUPPLEMENTARY NOTATION This effort was funded totally by the Laboratory Directors' Fund					
17 COSATI CODES			18 SUBJECT TERMS (Continue on reverse if necessary and identify by block number)		
FIELD	GROUP	SUB GROUP			
15	04	2.4	Database Machine		
09	02	6.1	Data Management		
			Relational Database		
19 ABSTRACT (Continue on reverse if necessary and identify by block number) The DBC1012 is an excellent choice for new C ³ I systems. It has far more capability than current mainframe DBMS for most C ³ I applications. The DBC1012 can provide continuous 24-hour 365 day year operation using two or more host processors. It has excellent integrity support and good concurrency control and deadlock detection and resolution. The DBC1012 is a very complex black box with security in hardware, which makes security assessment difficult. Security tools are good but probably not sufficient for multi-compartment operation. 15 significant digits floating point calculations can be performed inside the DBM. The Teradata 1012 has an excellent foreign file capability, good facilities to browse data, and good tools for structured queries to support looking for patterns or trends in data. The DBC1012 would be very difficult to embed in a tightly coupled information system, and most current C ³ I systems are tightly coupled. The Teradata DBC1012 is a unique architecture of multiple processors, direct access storage (over)					
20 DISTRIBUTION AVAILABILITY OF ABSTRACT <input checked="" type="checkbox"/> UNCLASSIFIED UNLIMITED <input type="checkbox"/> SAME AS REPORT <input type="checkbox"/> OTHER			21 ABSTRACT AVAILABILITY STATEMENT UNCLASSIFIED		
22a NAME OF RESPONSIBLE INDIVIDUAL Patricia M. Langendorf			22b ADDRESS (City, State, and ZIP Code) RADC (IRDA)		

DD FORM 1473, 84 MAR

83 APR 1984 EDITION, GPO

AUGUST 1984 EDITION, GPO

1. AVAILABILITY STATEMENT
UNCLASSIFIED

UNCLASSIFIED

devices and software forming a parallel Multiple Instruction Multiple Datastream (MIMD) computer. The modular design can accommodate up to 1024 processors and support a theoretical data storage capacity of one trillion bytes.

The DBC operates as a dedicated backend attached to one or more host computers. At present only IBM computers are supported. However, plans to attach to VAX have been announced. The same DBC1012 is intended to be capable of interfacing both IBM and VAX machines at the same time, thus providing an intriguing capability to access the same database using computers with truly different capabilities. Plans to interface the IBM PC have also been announced.

The DBC1012 employs a relational data model with records evenly distributed across disk units to provide parallel asynchronous processing. Access is supported by the TERadata QQuery Language (TEQUEL), a high-level non-procedural dialect of SQL. Modes of operation range from interactive database query in TEQUEL to invocation by applications programs executing on the host. The DBC1012 should be accessible by any language resident on the host.

The system is constructed of off-the-shelf extremely reliable hardware and is assessed to be highly reliable and maintainable. It is redundant in both hardware and software with non-stop operation and non-step repair under most failure events. The DBC1012 capacity statistics are up to 32,000 databases, 32,000 tables per database, 256 columns per table, 30,000 records (rows) per table and 30,000 bytes per field. Each disk can hold 300 megabytes plus overhead. Efforts are under way to reduce this overhead. Analysis indicates virtually no loss in parallelism for primary key activities as the system grows and the next release plans the same capability for secondary key activities.

Human factors are excellent, with particularly desirable support to data administration. It is easy to specify input validation criteria, restructure and expand machine configuration. "Create data base" privileges can be granted and controlled. Extensive reports are available covering network processor and storage utilization, user activities and privileges, and database and table ownership hierarchies.

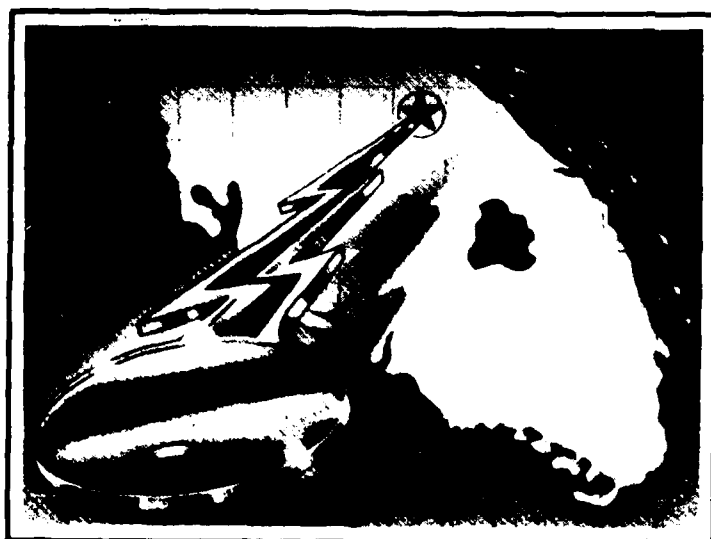
The only identified limitations of any significance are lack of a rollforward capability, which is announced for late 85 in software and announced without date in hardware, and lack of a capability to name indexes, which is an annoyance but should not limit usage.

UNCLASSIFIED

**INTERNATIONAL AEROSPACE and
GROUND CONFERENCE
on
LIGHTNING and STATIC
ELECTRICITY**

1984

TECHNICAL PAPERS



THE KEY TO LIGHTNING TECHNOLOGY

June 26-28, 1984

Orlando, Florida, U.S.A.

The 1984 International Aerospace and Ground Conference on Lightning and Static Electricity is sponsored by the National Interagency Coordination Group (NICG) in concert with the Florida Institute of Technology, and in association with the Institute of Electrical and Electronic Engineers, SAE-AE4 committee, the United Kingdom Civil Aviation Authority, the United Kingdom Royal Aircraft Establishment, Farnborough, and Culham Laboratory.

APPRECIATION

The NICG Conference Committee expresses its appreciation to the U.S. Naval Air Development Center, Warminster, Pennsylvania and to ORI, Inc. for their assistance and support in making this conference possible and in the preparation and printing of these technical papers.



CHAIRMAN'S MESSAGE

Welcome to the 1984 International Aerospace and Ground Conference on Lightning and Static Electricity. This year's theme, "Key to Lightning Technology", has as its goal the "unlocking" of the lightning and static electricity closet and the opening of the door to greater understanding of phenomenology and hardening techniques for Aerospace and Ground Systems. The conference will consist of three days of meetings and discussions intended to broaden our knowledge of theory and practical application in the areas of lightning and static electricity. There have been many portals to knowledge opened in the past but there are still more to be unlocked in the future. Hopefully our "Key to Lightning Technology" theme will identify and unlatch some of these closed doors.

The technical program consists of sixty papers to be presented during parallel sessions. This select program offers a large foundation supporting many technical arenas. Topically, we are encompassing sixteen major subjects that include many diversified areas of concern. This wide base will interest all attendees who wish to broaden their knowledge and understanding of lightning and static electricity. The conference shows a fine international representation and includes studies from outside the United States as well as from all regions within.

The technical program has been organized to offer something to both the new engineer as well as the established research scientist. It provides all of us the opportunity to learn new concepts, exchange ideas, discuss new and controversial ideas and have informal discussions and conversations with colleagues. I would like to express my appreciation and thanks to the many talented people who have worked so hard to make this a successful conference. This includes the conference speakers, session chairpersons and organizers, advisors, and last but certainly not least, the Conference steering committee and all their staff.

J.J. Fisher
Conference Chairman

KEYNOTE SPEAKER
COMMODORE W.J. Finneran



Commodore William J. Finneran graduated from Michigan State University in 1952 with a baccalaureate degree in Mechanical Engineering, after which he entered Naval Officer Candidate School where he was commissioned an Ensign in September 1952 and later attended Naval Postgraduate School where he earned a Masters degree in engineering from Princeton University.

Following assignment as Assistant Aeronautical Engineering officer in the Overhaul and Repair Department at Naval Air Station, Pensacola, he entered flight training and was designated a Naval Aviator in June 1957.

Other tours of duty have included assignment as Catapult and Arresting Gear Officer on the Staff of Commander Naval Air Force, U.S. Pacific Fleet; Assistant Maintenance and Quality Control Officer with Attack Squadron ONE NINE SIX, flying Skyraider aircraft; and Engineering Officer at the Naval Plant Representative Office, Columbus, Ohio.

Commodore Finneran served on the staff of Commander, Naval Air Systems Command as Assistant Project Manager for Research, Development, Test and Evaluation in the F-14 aircraft program. He also served as Aircraft Material and Engineering Officer on the staff of Commander Naval Air Force, U.S. Atlantic Fleet, and then as Assistant Chief of Staff for Material Readiness with Commander Task Force Seven Seven, U.S. Seventh Fleet. On 23 June 1977, Commodore Finneran assumed command of Naval Air Rework Facility, Naval Air Station, Jacksonville, Florida, one of the Navy's six industrial activities performing depot level maintenance on aircraft, engines and components. He later served as Executive Director of the Systems and Engineering Group, Naval Air Systems Command Headquarters, Washington, D.C. In May 1980, Commodore Finneran reported to Commander Naval Air Force, U.S. Atlantic Fleet as the Assistant Chief of Staff for Material.

Commodore Finneran assumed his current assignment as Assistant Commander for Systems and Engineering at the Naval Air Systems Command on 25 August 1982.

KEYNOTE ADDRESS

COMMODORE William J. Finneran

INTRODUCTION

I am genuinely sincere when I say that I am proud to stand before this prestigious group and talk to you about a subject of utmost interest to Naval Aviation: The Lightning and Static Electricity Phenomena. I can tell you I am here to learn for there is very little I can contribute to the incredible store of knowledge already assembled in this room. However, I can offer you the Navy's position on the necessity of countering the effects of lightning and static electricity. And, most likely, the Navy position is also that of the other agencies represented here who are co-sponsors of this, "The 1984 International Aerospace and Ground Conference on Lightning and Static Electricity."

ADDRESS

Ladies and Gentlemen, the Navy is currently involved in the design of the next generation fighter airplane. This aircraft will achieve superior performance by blending advanced materials, wings, engines, cockpit and avionic system designs into an aerodynamically agile, versatile, low profile airframe. From this description you can tell this aircraft will be sleek, light, and for the most part, automatic. To achieve these characteristics we will rely on the use of composite materials, digital fly-by-wire advanced techniques, and very high speed integrated circuit technology. The point I want to make is that the Navy and I, in particular, want to know what obstacles we will encounter from the effects of lightning and static electricity on this fighter pilot's dream craft.

As the Assistant Commander for Systems and Engineering at the Naval Air Systems Command, one of my priorities is to ensure that the fleet is provided with all-weather aircraft that are mechanically sound and capable of performing missions in their intended operational environment.

For many years the Navy seriously considered the effects that lightning had on aircraft as being minor. Few aircraft were lost due to lightning and the damage lightning imparted never had much impact on overall fleet operations. Why? Because, for the most part, aircraft were made of metal which provided a direct path for currents associated with a lightning strike and, because, most of our flying was in a training environment. That is, we insisted on attaining flight hours under an optimum safety and low risk combination. The rule was, if there were lightning and thunder bumpers in the area, flight operations were cancelled and we waited for a better day. In combat that rule is out, and there are few cancellations due to weather. In Vietnam, many a sortie returned to the ship with the mission aborted due to system failure caused by lightning, static electricity and other electromagnetic phenomena. Yellow sheets abounded with gripes that "ground checked OK" when maintainers troubleshot the suspected problem area. The problem was there, but the cause and correction were virtual mysteries.

Today there is growing concern in the Navy regarding the performance degradation by Electromagnetic Environmental Effects (E³) which, of course, include lightning and static electricity. Major changes in aircraft design have given birth to serious questions as to the possible safety and operational reliability of new systems under all-weather conditions. The changes from the earlier all-aluminum skin, through the use of stainless steel and titanium, and now the growing science of composite material utilization have developed aircraft which, although approaching the light-weight characteristics we desire, have become open windows to electromagnetic intrusion. During similar achievements in electronics development we have progressed from the relatively insensitive vacuum tube technology to the present-day miniaturized, micro-chip system which can be destroyed by extremely small power levels of energy. The use of these increasingly sensitive, very complex, semiconductor electronic systems has caused us to take a long, hard look at system upsets caused by environmental effects.

To emphasize my point, let me tell you of an incident which is recorded in our Safety Center Lightning Data Base, and which got the attention of a junior pilot and crew.

The newly designated aviator took off in marginal weather on his last leg of a cross-country training flight in an S-3A aircraft. As he proceeded enroute, weather deteriorated and he found himself flying through thunderstorms. As St. Elmo's fire danced upon and about his wind screen his world turned into one of torment. The instrument panel lit up and essentially told him:

- His RPM was dropping rapidly.
- His hydraulic system was about to fail.
- His navigation instruments were unreliable.
- His landing gear were down and locked.
- And his wings were ready to fold.

To add to his situation, his radios failed, his landing hook actually came down and his bomb bay doors opened. You can imagine that this young aviator's heart skipped a few beats but, as he flew out of the storm, all systems returned to normal and he landed safely.

Investigation of the incident determined that the newly designed wind screen of the S-3A was made of plastic with high carbon content and was susceptible to cracking under electrical charging stress. These cracks provided a point of entry and the static electricity created by the storm entered the wiring of the aircraft through the rain removal system on the wind screen. This caused proximity switches to do their intended job at this very unintentional time. Hence, the scramble of unusual activity in the cockpit. Let me hasten to tell you, this problem has been corrected by replacing the wind screen at a high cost, by putting filter pin connectors in the aircraft wiring system and inserting other lightning suppression techniques developed by some of the people in this very audience. WE DON'T NEED INCIDENTS LIKE THIS!

In our quest to provide the fleet with stable all-weather aircraft, we use a number of criteria for the evaluation of lightning protection. Generally, these are: safety-of-flight, mission survivability, fleet reliability, and maintenance economics. In evaluating the lightning protection for each part of a system or part of the airframe, the factors included in each of these general areas must be considered individually, although one or more factors usually predominate for each type aircraft and mission. SAFETY-of-FLIGHT requires no explanation. MISSION SURVIVABILITY of a modern platform must be considered carefully in terms of the new materials. As I mentioned previously, even low amplitude strikes could cause disablement of offensive or defensive electronic systems and cause mission essential equipment to be useless as well as make the vehicle vulnerable to enemy weapon systems. For example, mere thunderstorm cross transients can damage receiver front ends without the strike contacting the aircraft. FLEET RELIABILITY must be considered in terms of the fact that the same low amplitude strikes can produce intermittent failures in electronic systems and, therefore, reduce the mean time between failure (MTBF) criteria of otherwise reliable systems. Last, but not least, MAINTENANCE ECONOMICS. The motto of every squadron commander is "Keep 'em flying." The Navy can ill-afford chronic system failures and the accompanied loss of maintenance dollars, flight hours, and training which affect overall combat readiness.

Simply stated, our management philosophy for protection from lightning and static electricity problems is most economically and efficiently introduced in early design stages where it can often be provided with almost no weight and cost penalties. To accomplish this, we are making attempts to develop handbooks, standards and specifications to assist aircraft designers and other manufacturers to produce more reliable products: we have designated a point of contact in AIR-5161 to be responsible for electronic upset caused by lightning and static electricity. We have requested that the Navy Safety Center collect and analyze data related to lightning accidents and incidents: and, we have urged our program managers to be more alert to contractual matters to ensure Navy E³ interests are realized during the acquisition process.

I must admit, during the past few years the Navy has made great strides in characterizing lightning protection properties by:

- Developing a design guide for lightning protection of advanced aircraft fuel systems; this program will develop the engineering and qualification test techniques, and define reasonable safety margins that aircraft designers can use to evaluate risk factors and make necessary trade-offs.
- Establishing an approved Navy Training Program which will train our personnel as to the impact of system upset by environmental effects.
- Coordinating with the Atmospheric Electricity Hazards Protection Program (AEHP): An Air Force R & D program for advanced aircraft that addresses the electromagnetic environment resulting from aircraft interaction with atmospheric electricity.

- Supporting the National Interagency Coordinating Group for Lightning and Atmospheric Hazards to look into lightning static electricity matters. In fact, the chairman of this year's conference, Mr. Joe Fisher, is AIR-5161 of my staff.

And finally

- Sharing information with other governmental agencies at these conferences (Armed Forces, FAA, NASA, NOAA, DOT, and others).

CLOSING

In closing let me say, your hard work and dedication in efforts to study, understand and explain these phenomena are exemplary. Your collective contributions to this environmental science provide priceless assistance to our Navy's goals. Whatever applications can be directed to military aviation concerns will surely benefit international commercial aviation objectives as well. As I look over this vast and talented audience, I feel confident the pilot of the future will get his dream aircraft. Be assured, I speak for the Navy when I say that without your expertise and scientific know-how the phenomena of lightning and static electricity cannot be characterized and a very necessary program cannot be established to avoid and counter undesired effects.

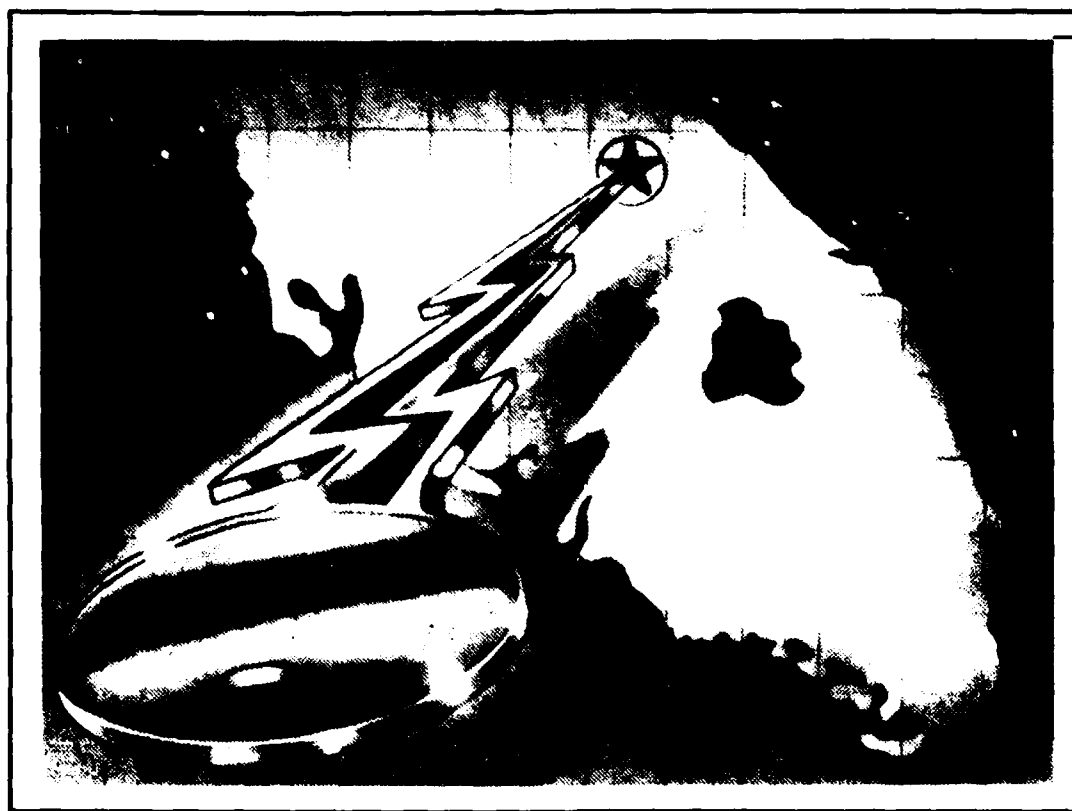
Ladies and Gentlemen, as you look around, you will recognize many of the world's leading authorities on the phenomena of lightning and static electricity, aircraft and aerospace flight environments, and ground systems. They are here with us today to share their views and knowledge of these subjects. So the task is before you.

Finally, I want to sincerely thank the participating companies and those of you who have submitted papers in support of this effort.

Thank you for the invitation, the trip has already been most beneficial.

The NICG does not assume responsibility for reprint of papers that are copyrighted in other documents. This responsibility lies solely with the author(s).

THE KEY TO LIGHTNING TECHNOLOGY



**NICG CONFERENCE
STEERING COMMITTEE
and
TECHNICAL PAPERS**

NICG CONFERENCE STEERING COMMITTEE



Chairman
J.J. Fisher
U.S. Naval Air Systems Command



Vice Chairman/Simulation
L.C. Walko
U.S. Air Force
Flight Dynamics Laboratory



Government Coordinator
W.T. Walker
U.S. Naval Air Development Center



Aircraft/Aerospace
F.L. Pitts
NASA Langley Research Center



European Coordinator
G.A.M. Odam
U.K. Royal Aircraft Establishment



Meteorology
D. MacGorman
NOAA National Severe Storms Laboratory



Conference Coordinator
W. McKerchar
Northwest Engineering Services Inc.



Helicopters
D.L. Albright
U.S. Army Aviation Systems Command



International Liaison
G. DuBro
U.S. Air Force
Flight Dynamics Laboratory



Phenomenology
Dr. A. Revay
Florida Institute of Technology



Special Advisor
N.O. Rasch
FAA Technical Center



Ground & Ship Systems
J. Foster
U.S. Naval Air Engineering Center



Special Advisor
M. Glynn
FAA Technical Center

CONTENTS

Session 1: Opening Session

Welcome: Nickolus O. Rasch, Conference Chairman 1983
FAA Technical Center, Atlantic City, N.J.

Introduction: Joseph J. Fisher, Conference Chairman 1984
U.S. Naval Air Systems Command
Washington, D.C.

Key Note Speaker: Commodore William J. Finneran
Asst. Commander for Systems & Engineering
U.S. Naval Air Systems Command
Washington, D.C.

1985 Lightning Conference Chairman
Dr. Joseph Taillet
Office National d'Etudes et de Recherches Aerospatiales, France

Session 2: Plenary

The Key to Lightning Technology
Dr. Martin A. Uman, University of Florida 1-1
Recent Advances in Lightning Protection Derived from Basic Research

Session 3A: Triggered Lightning & Corona
Chairman: R. Fowler, Norman, OK

Theoretical and Experimental Determination of Field, Charge and Current on an Aircraft Hit by Natural or Triggered Lightning 2-1
Dr. H. W. Kasemir (Colorado Scientific Research Corporation)
Comparison Between Long Air-Gap Breakdowns, Gliding Surface Discharges and Lightning Leaders 3-1
J. L. Boulay and S. Larigaldie (ONERA, France)
Bipolar Corona and Aircraft Triggered Discharges 4-1
Dr. J. A. Bicknell and B. M. Humood (University of Manchester, Institute of Science and Technology)

Session 3B: Lightning Locators

Chairman: Dr. L. W. Parker, Lee W. Parker, Inc., Concord, MA

- Federal Lightning Detection Systems Improve Agency Operations, but are Inefficiently Located and Lack Coordination to Form a National Network** 5-1
J. S. Bunting (U. S. Department of Commerce)
- Theoretical and Operational Evaluation of Time-of-Arrival (TOA) Lightning Position and Tracking System (LPATS)** 6-1
Dr. R. B. Bent and W. Highlands (Atlantic Scientific Corporation) and W. A. Lyons (R*SCAN Corporation)
- A Systematic Method for Correcting Site Errors in a Network of Magnetic Direction-Finders** 7-1
W. L. Hiscox, E. P. Krider, A. E. Pifer and Dr. M. A. Uman (Lightning Location and Protection, Inc.)

Session 4A: Triggered Lightning and Corona

Chairman: Dr. J. Taillet, Directeur Scientifique de la Physique Generale

- Rocket-Triggered Lightning—A Comparison with Natural Lightning** 8-1
R. Richmond (Flight Dynamics Laboratory)
- Prediction of Electric-Field Concentration Factors by Computer Modeling** 9-1
L. W. Parker (Lee W. Parker, Inc.) and Dr. H. W. Kasemir (Colorado Scientific Research Corporation)
- The Mathematics of Interaction Between a Conductive Cylinder on Earth and a Moving Line and Charge Due to Lightning** 10-1
Abdul Rashid (TRW)

Session 4B: Detection and Protection

Chairman: Dr. R. Bent, Melbourne, FL

- Automation of Surface Thunderstorm Observations** 11-1
M. W. Maier (Lightning Location and Protection, Inc.)
- Shuttle Transportation System (STS) Lightning Protection and Measuring System (LPMS)** 12-1
W. Jafferis (NASA Kennedy Space Center), Lt. K. Kerr (U.S. Air Force) and H. Tang (Planning Research Corporation)

Session 5A: Indirect Effects on Systems

Chairman: Mr. W. Cooley, Boeing Company, Seattle, WA

- Progress of the Atmospheric Electricity Hazards Protection Program** 13-1
R. C. Beavin, J. R. Lippert and Lt. J. E. LaVoie (Wright Aeronautical Laboratories)
- Upset Susceptibility Study Employing Circuit Analysis and Digital Simulation Software** 14-1
V. A. Carreno (NASA Langley Research Center)
- Data and Results of a Laboratory Investigation of Microprocessor Upset Caused by Simulated Lightning Induced Analog Transients** 15-1
C. M. Belcastro (NASA Langley Research Center)
- Laboratory Evaluation of Lightning Induced Transients in Aircraft Electrical Wiring** 16-1
J. C. Alliot (Office National d'Etudes et de Recherches Aerospatiales de France)

Session 5B: Ground Systems Protection
Chairman: Mr. G. Huddleston, Georgia Institute of Technology, Atlanta, GA

- Lightning Research—A User's Lament** 17-1
C. N. Golub (Eastern Space and Missile Center)
- Grounding and Bonding Requirements of Military C-E Facilities for Protection Against Lightning** 18-1
W. L. Keller (Electronics Engineering Group, Scott AFB)
- AC Power Line Protection for the IEEE 587 Class B Environment** 19-1
O. M. Clark and W. E. Roehr (General Semiconductor Industries)

Session 6A: Aircraft Systems
Chairman: Mr. G. Weinstock, McDonnell-Douglas, St. Louis, MO

- The Risk Factor in Aircraft Lightning Protection** 20-1
J. C. Corbin (Aeronautical Systems Division, Wright-Patterson AFB)
- Lightning Interaction with Commercial Air Carrier Type Aircraft** 21-1
N. O. Rasch and M. S. Glynn (Flight Safety Research Center)

Session 6B: Lightning Characterization
Chairwoman: Dr. B. Melander, Boeing Company, Seattle, WA

- The Amplitude Spectra of Lightning Radiation Fields in the Interval from 1 to 20 MHz** 22-1
E. P. Krider and C. D. Weidman (Institute of Atmospheric Physics)
- Characterization of Fast Rise Time Electromagnetic Pulses Recorded in Airborne Measurements During Florida Thunderstorms** 23-1
B. P. Kuhlman and Dr. P. L. Rustan (Wright Aeronautical Laboratory) and J. S. Reazer (Technology Scientific Services)
- Analysis of Lightning Current Measurements** 24-1
Dr. P. L. Rustan (Wright Aeronautical Laboratory) and P. R. Axup (Air Force Institute of Technology)

Session 7A: Aircraft Systems
Chairman: Mr. H. Knoller, Lockheed California Co., Northridge, CA

- Protection of Aircraft Against Static Electricity and Charge Accumulation Effects** 25-1
J. P. Simi (Les Cables de Lyon)
- Technical Study of a Lightning Data Logger** 26-1
S. S. Bernstein (Dayton T. Brown, Inc.) and V. Tukiendorf (U.S. Naval Air Engineering Center)
- Transient Spark-Arc Hotspot Surface Heating on Metallic and Reinforced-Composite Skins** 27-1
Dr. T. S. Lee and W. Y. Su (Department of Electrical Engineering, University of Minnesota)

Session 7B: Thunderstorm Studies
Chairman: Dr. A. J. Illingworth, UMIST, Manchester, England

- Surface Electrostatic Field and Meteorological Conditions in the Period of Winter Thunderstorms** 28-1
Y. Goto, F. Naito, K. Narita and M. Naito (Dept. of Electrical Engineering, Tohoku University)
- Cosmic Rays, Solar Activity, Magnetic Coupling and Lightning Incidence** 29-1
J. T. A. Ely (Space Sciences Division, University of Washington)

Session 8A: Fuel Ignition Hazards
Chairman: Mr. G. A. M. Odam, Royal Aircraft Establishment, Farnborough, UK

- Lightning Test of a CFC Aircraft Wing Tank Skin** 30-1
K. G. Lovstrand, B. Olsson, B. Wahlgren and L. Anderson (SAAB-SCANIA AB)
- Rear Surface Temperature Measurement of Aircraft Materials Subjected to Zone 2A Lightning Strikes** 31-1
E. H. Schulte (McDonnell Aircraft Co.) and W. T. Walker (U. S. Naval Air Development Center)
- Combined Mechanical-Electrical Ignition Hazards to Carbon Reinforced Composite Fuel Tanks** 32-1
J. D. Robb (Lightning & Transients Research Institute) and T. S. Lee (University of Minnesota)

Session 8B: Lightning Stroke Measurement
Chairman: Dr. P. L. Rustan, AFWAL/FIESL, Wright Patterson AFB, OH

- Measurement of Lightning Stroke Current in Winter Season at Maki, Japan** 33-1
K. Narita and Y. Goto (Dept. of Electrical Engineering, Tohoku University) and R. Funayama (Tohoku Electrical Power Company)
- Effects of Tower Characteristics on Lightning Arc Current Measurements** 34-1
Dr. B. G. Melander (Boeing Military Airplane Company)
- On the Estimation of the Lightning Return Stroke Current** 35-1
Z. Ichiro, T. Nakai and T. Takeuti (Research Institute of Atmospherics, Nagoya University)

Session 9A: Analysis Techniques
Chairman: Prof. K. Demerest, Lafayette College, Easton, PA

- On Bounding the Excitation of Wiring Behind an Aperture in a Shield from Lightning Induced Fields** 36-1
C. D. Taylor (Dept. of Electrical Engineering, Mississippi State University)
- A Time-Domain Representation of Surface and Transfer Impedances Useful for Analysis of Advanced Composite Aircraft** 37-1
P. M. McKenna, T. H. Rudolph and R. A. Perala (Electro Magnetic Applications, Inc.)
- Transient Response and Protection of Multiconductor Transmission Lines** 38-1
Prof. Dr. J. L. ter Haseborg and Prof. Dr. H. Trinks (Technical University Hamburg-Harburg)

Session 9B: Impulse Generators & Measurements
Chairman: Mr. L. Walko, AFWAL/FIESL, Wright-Patterson AFB, OH

- A New Impulse Generator for Impulses with Short Rise-Times** 39-1
Dr. E. Gockenbach, Dr. M. Modrusan and O. Frey (Emile Haefley & Co. Ltd.)
- Lightning Simulator Circuit Parameters and Performance for Severe-Threat High-Action-Integral Testing** 40-1
R. A. White (Sandia National Laboratory)
- Estimation of Standard Deviation of Disruptive Voltage on Air Gaps Under Lightning Overvoltages by Modified Up-and-Down Method** 41-1
P. Mourente, N. Santiago and C. Portela (Federal University of Rio de Janeiro)

Session 10A: Analysis Techniques
Chairman: Dr. T. Trost, Texas Tech University, Lubbock, TX

- Comparison of Methods for Measuring the Characteristic Impedance of Transmission Lines** 42-1
L. O. Hoeft and J. Hofstra (The BDM Corporation)
- Analysis of the Effects of Cable Parameters on Figures of Merit Such as "EMP Response"** 43-1
D. Bernstein (ITT) and L. O. Hoeft, A. Linder and J. Hofstra (The BDM Corporation)
- Measured Transfer Impedance and Non-Metallic Conduits Covered with Tinned Copper and SnCuFe Braids** 44-1
J. E. Merrill (Glenair, Inc.) and L. O. Hoeft and J. Hofstra (The BDM Corporation)

Session 10B: Impulse Generators & Measurements
Chairman: Mr. B. J. C. Burrows, Culham Laboratory Ukala, England

- The Use of a Distributed Peaking Capacitor and a Marx Generator for Increasing Current Rise Rates and the Electric Field for Lightning Simulation** 45-1
R. A. Perala, T. H. Rudolph and P. M. McKenna (Electro Magnetic Applications, Inc.) and J. D. Robb (Lightning & Transients Research Institute)
- UV Laser Triggering of Crowbars Used in the Sandia Lightning Simulator** 46-1
Dr. M. J. Landry and W. P. Brigham (Sandia National Laboratory)

Session 11A: Charging Mechanisms
Chairman: Mr. E. P. Krider, University of Arizona, Tucson, AZ

- Frictional Electrification of Ice & Snow** 47-1
H. Shio (Department of Physics, Hokkaido University)
- Modeling Lightning Generation Mechanisms** 48-1
J. S. Nisbet (Ionosphere Research Laboratory, The Pennsylvania State University)
- Static Charging of Different Metals by Ice Crystals** 49-1
A. J. Illingworth, J. M. Caranti and S. J. Marsh (Department of Physics, The University of Manchester Institute of Science and Technology)

Session 11B: Aircraft & Aerospace Testing
Chairman: Mr. J. Lippert, AFWAL/FIEA, Wright-Patterson AFB, OH

- Pershing II System Lightning Test** 50-1
Dr. G. R. Edlin and L. Riley (U. S. Army Missile Command) and J. D. Robb
(Lightning & Transients Research Institute)
- Electrical Safety Evaluation of a Helicopter Static Charge Grounding Wand** 51-1
J. L. Dawson (U. S. Naval Air Test Center)
- Lightning Induced Transient Protection for Commercial Airplanes Using
Frequency-Domain Analysis and Low-Level Test Methods** 52-1
D. A. East (Boeing Military Airplane Co.)

Session 12A: Materials
Chairman: Mr. J. Corbin, ASD/ENACE, Wright-Patterson AFB, OH

- Corrosion Properties of Second Generation Conductive Materials** 53-1
E. A. Groshart (Boeing Aerospace Co.)
- Measured Transfer Impedance of a Large Graphite-Epoxy Composite Tube
with Current Diverters** 54-1
L. O. Hoeft, V. A. Gieri and J. S. Hofstra (The BDM Corporation)
- Nickel Coated Graphite and Kevlar Fabrics as Part of Composites for
Lightning Strike Protection of Aircrafts** 55-1
Dr. Dahm and Dr. Ebneth (Bayer AG)

Session 12B: Lightning vs NEMP
Chairman: Dr. G. Bechtold, Naval Surface Weapons Center, Silver Spring, MD

- A Comparison of Lightning and Nuclear Electromagnetic Pulse Response
of a Helicopter** 56-1
R. A. Perala and C. C. Easterbrook (Electro Magnetic Applications, Inc.)
- A Comparison of Lightning and Nuclear Electromagnetic Pulse Response
of Tactical Shelters** 57-1
R. A. Perala, T. H. Rudolph and P. M. McKenna (Electro Magnetic Applications, Inc.)

Biography

DR. MARTIN A. UMAN



Martin A. Uman received the B.S.E. degree in electrical engineering in 1959 from Princeton University, where he was elected to Phi Beta Kappa. After receiving his Ph.D. from Princeton University in 1961, he took a post as Associate Professor of Electrical Engineering at the University of Arizona where he became interested in lightning research, particularly in lightning spectroscopy. In 1965, Dr. Uman moved to the Westinghouse Research Laboratories in Pittsburgh where he continued his lightning research and, in addition, studied the electrical, optical, and acoustic properties of long laboratory sparks. He has been Professor of Electrical Engineering at the University of Florida since January, 1972, where his primary research interest has been in the electromagnetic radiation produced by lightning. Dr. Uman is the author of three books--Lightning, Understanding Lightning, and Introduction to Plasma Physics--and approximately 75 journal articles, and was Associate Editor of the Journal of Geophysical Research from 1981 to 1983. He is a member of the International Commission on Atmospheric Electricity, the American Meteorological Society, the American Geophysical Union, and the IEEE.

In 1975 Dr. Uman and Dr. E. P. Krider, a Professor of Atmospheric Sciences at the University of Arizona, formed Lightning Location and Protection, Inc. (LLP), a company which specializes in consulting on unusual lightning problems and manufacturing lightning detection equipment. Dr. Uman served as president of LLP from 1976 until 1983 and is currently vice-president. Lightning locating equipment manufactured by LLP presently covers over 3/4 of the United States and Canada and is used in Mexico, Norway, Sweden, South Africa, Australia, Hong Kong, Japan, and the People's Republic of China.

APPLICATION OF ADVANCES IN LIGHTNING RESEARCH TO LIGHTNING PROTECTION

Martin A. Uman
Department of Electrical Engineering
University of Florida, Gainesville, FL 32611

ABSTRACT

The results of recent lightning research have already found important application in lightning protection. We discuss two areas of application: (1) detection of lightning as a basis for warning and taking of protective action, and (2) characterization of the waveshapes of lightning electric and magnetic fields and of currents so as to specify adequately the threat to systems struck directly or illuminated by the fields of nearby lightning.

I. INTRODUCTION

SOME SIGNIFICANT ADVANCES have been made in the last decade in lightning protection. These advances have been a result of progress in two general areas of lightning research: (1) lightning phenomenology, including the technology for determining real-time strike locations, and (2) lightning physics, particularly the characteristics of return stroke currents and electromagnetic fields.

(1) By phenomenology, we mean those characteristics of thunderstorms that are associated with numbers of lightning events, as opposed to the physical properties of the individual events. A phenomenological parameter of particular interest is the average lightning flash density, that is, the number of lightnings per square kilometer per year (other units are possible) as a function of location. This parameter represents the starting point for almost all lightning protection designs (for example, the lightning overvoltage protection of utility power lines) because the number of lightning failures per year for which a system is designed is directly proportional to the number of ground flashes per unit area per year. Real-time identification of phenomenological parameters such as total number of lightning events per storm and the lightning flashing rate is now possible with commercial detection equipment developed by recent research. This equipment also makes possible real-time decisions on utility system repair and repair preparation, early warning and detection of lightning-caused forest fires, and a variety of other warning functions in situations that allow protective action to be taken, such as launches at the NASA Kennedy Space Center.

(2) When an object (e.g., aircraft, building, power line, or person) is struck directly by lightning or is exposed to the intense electromagnetic fields of a nearby flash, the potentially-deleterious currents and voltages that appear in the object are determined by the physical characteristics of the lightning currents and fields and by the electrical characteristics of the object that is struck. For example, it is thought that, to a first approximation, the voltages that are induced in electronics within an airborne metal aircraft that is struck by lightning are indirectly initiated by the fastest part of the current rate-of-rise. This fast change in current induces resonant oscillations on the metallic exterior of the aircraft that are then coupled inside the aircraft via apertures such as windows in the conducting metal skin. Lightning protection is currently of considerable concern for the latest generation of military and commercial aircraft that operate with low-voltage computer circuits and

have lightweight epoxy surfaces (potential apertures) replacing the more-conventional conducting metal.

In the following three sections, we will examine in more detail the recent and widespread use of lightning detection techniques for protection (Section II); those properties of lightning that cause damage, the mechanisms of lightning damage, and new methods of protection (Section III); and some remaining questions that research can answer to facilitate additional improvements in lightning protection (Section IV).

II. APPLICATIONS OF NEW LIGHTNING DETECTION TECHNIQUES TO PROTECTION

In 1983 the Electric Power Research Institute (EPRI), the research arm of the United States power utilities, funded a long-term study of lightning flash density in the United States for the purpose of making possible better lightning protection design for power lines. The EPRI research is being carried out using lightning locating technology recently developed through basic research [1]*. For the initial part of the study a network of automatic lightning Direction Finding (DF) stations called the East Coast Network operated by State University of New York at Albany (SUNYA) [2] is being used. Future flash density studies can be expected to involve additional portions of the United States and perhaps Canada. Since 1976, over 3/4 of the area of the United States and Canada has been covered by automatic lightning DF stations and this equipment is also operating in Australia, Norway, Sweden, Mexico, South Africa, Japan, Hong Kong, and the People's Republic of China. A paper discussing the DF lightning location technique is found in these proceedings. During the last few years, a multiple-station locating system operating on a time-of-arrival principle developed following the research of Proctor [3] has been introduced commercially (see paper in these proceedings) and several single-station lightning locating systems using physical principles for ranging determined from recent lightning research have been marketed.

The primary user of lightning location data in the United States at present is the Bureau of Land Management (BLM). The BLM and the Forest Services of most Canadian Provinces utilize the time and location of lightning storms to determine when and where to look for forest fires. Early detection of these fires results in considerable savings in natural resources and in the cost of fighting the fires. BLM data are also disseminated in real time to all National Weather Service Offices in the western region via AFOS, to the

*Numbers in brackets designate References at end of paper

National Severe Storms Forecast Center in Kansas City, to Vandenburg Air Force Base, and to Nellis Air Force Base. Data from the SUNYA East Coast Network are presently being displayed in real time at the FAA Washington Air Route Traffic Control Center (ARTCC) in Leesburg, Va., the National Weather Service Forecast Office in Albany, N.Y., and Langley Air Force Base in Hampton, Va.

In addition to applications-oriented research, operational forest fire management, and Weather Service storm warning, the newly-developed lightning locating equipment is used to warn of the approach of storms in a variety of practical applications where protective action can be taken. Examples range from power utility companies (e.g., Tampa Electric Company, China Power of Hong Kong) to missile launches (e.g., Kennedy Space Center, Vandenburg AFB) to sensitive military installation (e.g., Buckley Air National Guard Base, Colorado, Cudjoe Key AF Station, Florida). In addition, lightning maps from these lightning locating systems are becoming widely shown on TV weather shows, as they are more meaningful to most viewers than the more conventional radar displays. An example of a one-day lightning map from the Tampa Electric Company [4] is shown in Fig. 1.

III. AMELIORATION OF LIGHTNING DAMAGE

A. MECHANISMS OF LIGHTNING DAMAGE - The amount and type of lightning damage is caused both by the characteristics of the lightning discharge and by the properties of the object being struck. The physical characteristics of lightning of most interest are the currents and electromagnetic fields, particularly those from the return stroke since these are usually the largest and hence protection against them will probably protect against the currents and fields from other lightning processes.

Four properties of the return stroke current can be considered important in producing damage: (i) the peak current, (ii) the maximum rate-of-change of current, (iii) the integral of the current, i.e., the charge transferred, and (iv) the integral of the current squared, the so-called action integral. Let us briefly examine each of these properties and the type of damage they can produce.

(i) For objects that present a resistive impedance, such as a ground rod driven into the earth, a long power line, or a tree, the peak voltage on the object will be proportional to the peak current. For example, a 50,000 Ampere current injected into a 400 Ohm power line produces a line voltage of 20,000,000 Volts ($V = IZ$). Such large voltages lead to electrical discharges from the struck object to the ground through the air or through insulating materials. Such flashovers can, for example, short-circuit the power system or kill people that are standing

close to the object that is struck. An example of discharges across the ground caused by the high voltage on a struck golf-course green marker is shown in Fig. 2. The magnetic forces produced by return-stroke peak currents are large and can crush metal tubes and pull wires from walls.

(ii) For objects that have an inductive impedance, such as wires in an electronic system, the peak voltage will be proportional to the maximum rate-of-change of the lightning current ($V = L di/dt$). For example, if 1 m of wire has an inductance L of 10^{-7} Henries and $di/dt = 10^{10}$ Amperes/sec, 1000 V is generated across the wire. Voltages of this level can be very harmful to solid state circuitry.

(iii) The heating or burn through of metal sheets such as airplane wings or metal roofs is, to first approximation, proportional to the lightning charge transferred (average current times time). Generally, large charge transfers are due to long duration (tenths of a second to seconds) lightning currents in the 100 to 1000 Ampere range rather than by the peak currents which have a relatively short duration. An example of a hole burned in an aircraft skin by lightning is shown in Fig. 3 [5] and some information on hole size vs. charge transferred is given in Fig. 4 [6]. A typical lightning transfers 20 to 30 Coulombs and extreme lightnings hundreds of Coulombs but, fortunately, the lightning does not often stay attached to one place on an aircraft for the duration of that transfer.

(iv) The heating of many objects and the explosion of insulators is, to first approximation, due to the value of the action integral, the integral of the square of the current over time. In the case of wires, the action integral represents the heat that is generated by the resistive impedance of the wire. Some data on wire temperature rise for typical lightning action integrals is given in Fig. 5 [6]. About 1 percent of negative strokes to ground have action integrals exceeding 10^6 . About 5 percent of positive strokes exceeds 10^7 . In the case of a tree, this heat vaporizes the internal moisture of the wood and the resultant steam pressure causes an explosive fracture.

Two properties of the electromagnetic fields are sufficient to describe most of the important damage effects: (i) the peak value of the field and (ii) the maximum rate-of-rise to this peak.

(i) For certain types of antennas or metal exposed to the lightning field, the peak voltage on the metal is proportional to the peak field. These antennas are commonly referred to as capacitively coupled.

(ii) For other antennas, such as a loop of wire in an electronic circuit or an underground communication cable, the peak voltage is proportional to the maximum rate-of-change of the field.

B. NEW RESULTS ON LIGHTNING CHARACTERISTICS - A major step forward has been taken recently in identifying the maximum rates-of-change of currents and fields from measurements of the fields. These rates-of-change are a factor of ten times larger than was believed to be the case a decade ago.

In general, the shape of the electric field radiated by a lightning return stroke depends on whether it is the first return stroke in a flash, a normal subsequent return stroke preceded by a dart leader, or a subsequent return stroke that is preceded by a dart-stepped leader. First stroke fields begin with a relatively slow "front" that rises for 2 to 8 μ s to about half of the peak field amplitude. This front is followed by a fast transition to peak. It is this fast transition that is of primary interest. Subsequent strokes produce fields that have fast transitions very similar to first strokes, but fronts that last only 0.5 to 1 μ s and that rise to only about 20% of the peak field amplitude. A reproduction of the fast field transition produced by a first return stroke, and a histogram of measured 10 to 90% fast transition risetimes are given in Fig. 6 [7]. Note that the mean risetime is only 90 ns with a standard deviation of 40 ns. The field measurements discussed above have been made by Weidman and Krider [8],[9] for lightning fields which propagated over salt water and hence which did not suffer the high frequency degradation characteristic of propagation over land.

If we assume that the initial, fast-rising fields that are produced by return strokes can be described by a transmission-line model in which a current pulse associated with return-stroke front breakdown propagates upward [10],[11], then the maximum rate of change of the channel current is related to the maximum field derivative through the relation:

$$\frac{dI(t)}{dt} = \frac{2\pi D \epsilon_0 c^2}{v} \frac{dE(t+D/c)}{dt}$$

where D is the distance to the discharge, v is the upward velocity of the current pulse, and where the ground has been assumed to be flat and perfectly conducting. This relation also assumes that the measured field is produced by a single current pulse propagating in a single channel.

Figure 7 shows a cumulative distribution of the maximum dI/dt values that have been computed for return strokes using the above equation (7). The values are plotted for a velocity of 10^8 m/s, and the dashed lines show velocities of 0.6×10^8 m/s and 1.4×10^8 m/s. Figure 7 also shows the maximum current derivatives that have been measured during lightning strikes to instrumented towers by Berger in Switzerland and Garbagnati in Italy. The maximum dI/dt data derived from the fields and shown in Fig. 7 are

considerably larger than those measured on towers. The reasons for this significant discrepancy are yet to be determined.

Lightning to ground lowering positive charge and containing positive return strokes has been recently identified [12]. The characterization of this type of lightning is of considerable importance from a protection point-of-view. Positive lightning apparently produces very large peak currents, charge transfers, and action integrals, much larger than the usual negative lightning. The Japanese report that their power systems are disrupted by a large fraction of the positive lightning strikes whereas only a small fraction of the negative lightning has this effect [13].

C. PROTECTION TECHNIQUES - There are two general types of lightning protection: (i) diversion and shielding and (ii) limiting of currents and voltages.

(i) On a residential or commercial building, for example, the diversion of lightning currents to ground via a standard system of lightning rods, down leads, and grounds is sufficient to protect the building structure itself and to decrease by imperfect shielding potentially harmful effects to electronic equipment inside.

(ii) More complete protection of electronic equipment must include limiting of currents and voltages induced by the direct strike to the structure or by traveling waves into the structure on electric power, communication, or other wires connected to the outside world. The design of the current and voltage limiting system is obviously dependent on an understanding of the waveshapes of the deleterious signals that are to be controlled; and this in turn requires a knowledge of the lightning characteristics and how the properties of the system under consideration change these characteristics. Once such a determination is made, three general types of current and voltage limiting devices can be used for electronic or power systems: (1) voltage crowbar devices which reduce the voltage difference effectively to zero and short circuit the current to ground (the carbon block and gas tube arrestors used by the telephone company are good examples of crowbar devices), (2) voltage clamps such as recently-developed solid-state Metal Oxide Varistors (MOV's) or Zener diodes which do not allow the voltage to exceed a given value, and (3) electrical filters which reflect or absorb the higher and generally more damaging frequencies in the lightning transient. Frequently, all three of these forms of protection are used together in a coordinated way.

In recent years, a systematic approach has been developed that allows an almost perfect lightning protection system to be designed for most structures. This new technique is called "topological shielding"

and it utilizes both types of protection discussed above but in a coordinated way [14]. The technique consists of nesting shields and of "grounding" each shield to the one enclosing it. All incoming wires are connected to the outside of each successive shield by a transient protective device, and therefore, at each successively inner shield, the voltage and power levels to be protected against are reduced. In Fig. 8, we illustrate the principles of topological shielding. In the top picture, the equivalent circuit is shown for the grounding of a building associated with a communications tower. The middle picture shows an external view of the building after topological shielding, and the lower picture a schematic of the topological shielding technique.

IV. FUTURE RESEARCH NEEDED FOR IMPROVEMENTS IN PROTECTION

The detailed physics of how lightning strikes a structure, powerline, or aircraft is still poorly understood. The approaching lightning leader is not aware of the object to be struck until it is perhaps a few tens to hundreds of meters away. At that time, upward-moving sparks leave the object to be eventually struck and also leave nearby objects. One of these sparks connects to the incoming leader and thus determines the strike point. When this process is better understood through basic research, we should be able to determine with higher probability what will and what will not be struck and to provide better lightning protection accordingly. For example, the positioning of overhead ground wire above transmission lines should be able to be optimized.

More information is needed about the character of lightning currents, particularly those in processes other than return strokes. Is there, for example, an upper limit on the maximum rate-of-change of current? What are the characteristics of currents in cloud flashes? We need more data on positive lightning so as to be able to characterize all aspects of it in a statistical way so that it can be taken account of properly in protection design.

Much work needs to be done on the interaction of lightning currents and fields with aircraft. For example, how are aircraft resonances affected by channel attachment? Field experiments are in progress, and accurate computer models are now becoming available with which to study these problems even in the presence of non-linear discharge properties.

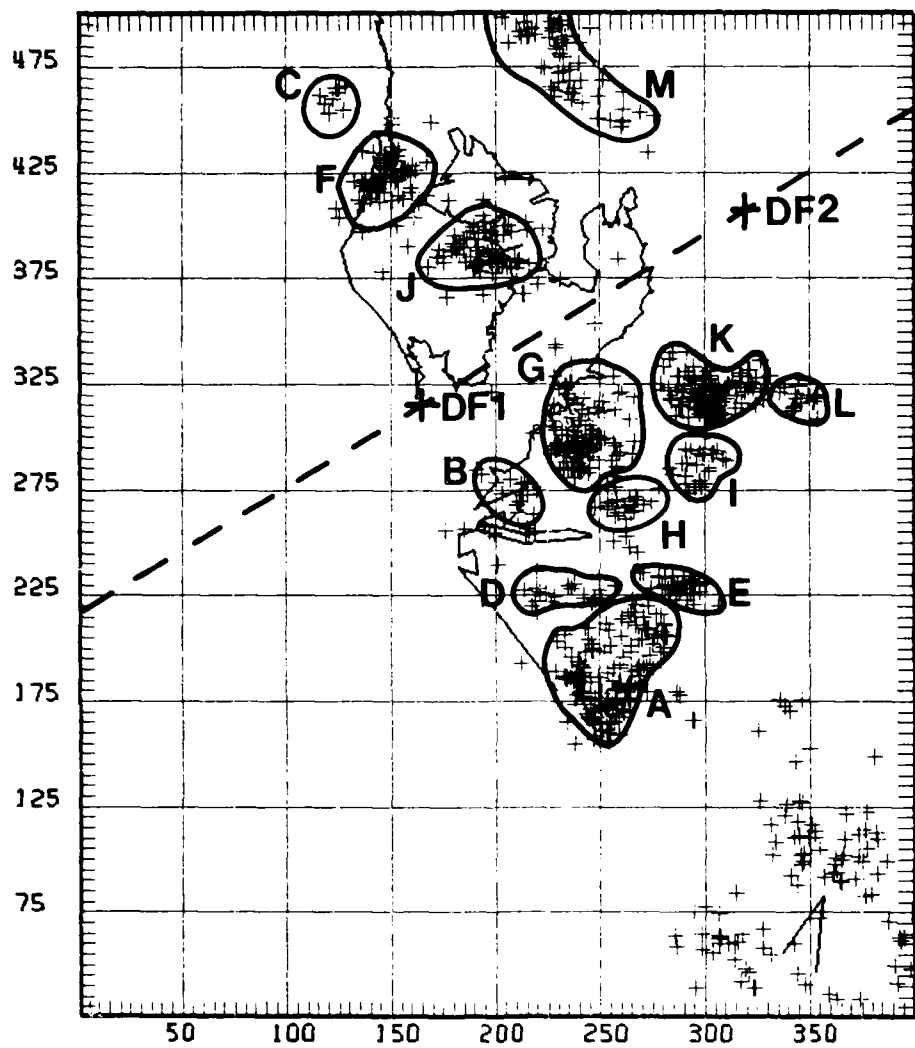
V. CONCLUSIONS

Basic research over the last decade has made possible improvements in lightning protection. As with all research, new

discoveries raise new questions. With the present interest in lightning among scientists, partly due to recent successes and partly to the important unsolved practical problems, we can expect continued progress in lightning protection during the next decade.

REFERENCES

1. E.P. Krider, R.C. Noggle, A.E. Pifer, and D.L. Vance, "Lightning Direction-Finding Systems for Forest Fire Detection." *Bull. Am. Meteorological Soc.*, 61, 980-986, 1980.
2. R.E. Orville, R.W. Henderson, and L.F. Bosart, "An East Coast Lightning Detection Network." *Bull. Am. Meteorol. Soc.*, 64, 1029-1037, 1983.
3. D.E. Proctor, "A Hyperbolic System for Obtaining VHF Radio Pictures of Lightning." *J. Geophys. Res.*, 76, 1478-1489, 1971.
4. D.W. Peckham, M.A. Uman, C.E. Wilcox, Jr., "Lightning Phenomenology in the Tampa Bay Area." *J. Geophys. Res.*, to be published 1984.
5. M.A. Uman, "Understanding Lightning." BEK, Pittsburgh, Pa., 1971.
6. F.A. Fisher and J.A. Plumer, "Lightning Protection of Aircraft." NASA Reference Publication 1008, October 1977.
7. C.D. Weidman, The Submicrosecond Structure of Lightning Radiation Fields, Ph.D. Thesis, University of Arizona, 1982.
8. C.D. Weidman and E.P. Krider, "The Fine Structure of Lightning Return Stroke Waveforms." *J. Geophys. Res.*, 83, 6239-6247, 1978.
9. C.D. Weidman and E.P. Krider, "Submicrosecond Risetimes in Lightning Return Stroke Fields." *Geophys. Res. Lett.*, 7, 955-958, 1980.
10. Y.T. Lin, M.A. Uman, and R.B. Standler, "Lightning Return Stroke Models." *J. Geophys. Res.*, 85, 1571-1583, 1980.
11. M.A. Uman and E.P. Krider, "A Review of Natural Lightning: Experimental Data and Modeling." *IEEE Trans. on EMC*, EMC-24, 79-112, 1982.
12. W.H. Beasley, M.A. Uman, D.M. Jordan, and C. Ganesh, "Positive Cloud to Ground Lightning Return Strokes." *J. Geophys. Res.*, 88, 8475-8482, 1983.
13. K. Nakahori, T. Egawa, and H. Mitani, "Characteristics of Winter Lightning Currents in Hokuriku District." *IEEE Trans. PAS-101*, 4407-4412, 1982.
14. E.F. Vance, "Electromagnetic Interference Control." *IEEE Trans. EMC*, EMC-22, 319-328, 1980.



AUGUST 8, 1979 13:00 TO 16:00 (EDST)

Fig. 1 - A map of the cloud-to-ground lightning strikes in the Tampa Bay area for August 8, 1979. Individual storms have been circled. The two DF locations in the Tampa Electric Company's lightning location system are identified. Map scale is in thousands of feet



Fig. 2 - Lightning damage caused by a direct strike to a golf course green (photo courtesy of Weatherwise, cover photo, Vol. 30, June 1977, see also, Krider, E.P., On Lightning Damage to a Golf Course Green, Weatherwise, 30, 111, June 1977)



Fig. 3 - A lightning hole burned in the wing tip of a Boeing 707 [5]

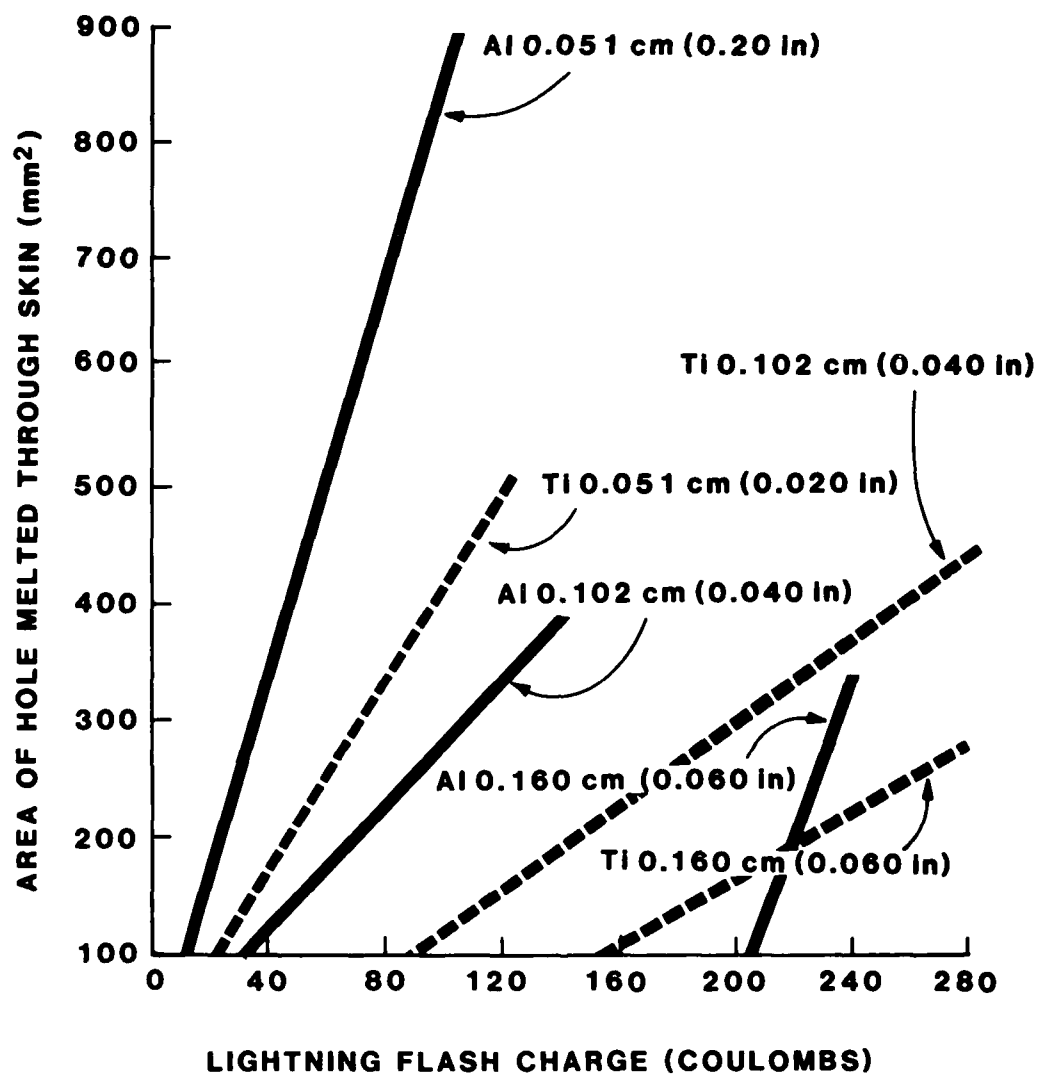


Fig. 4 - Area of holes melted through aluminum and titanium of various thicknesses by lightning charge [6]

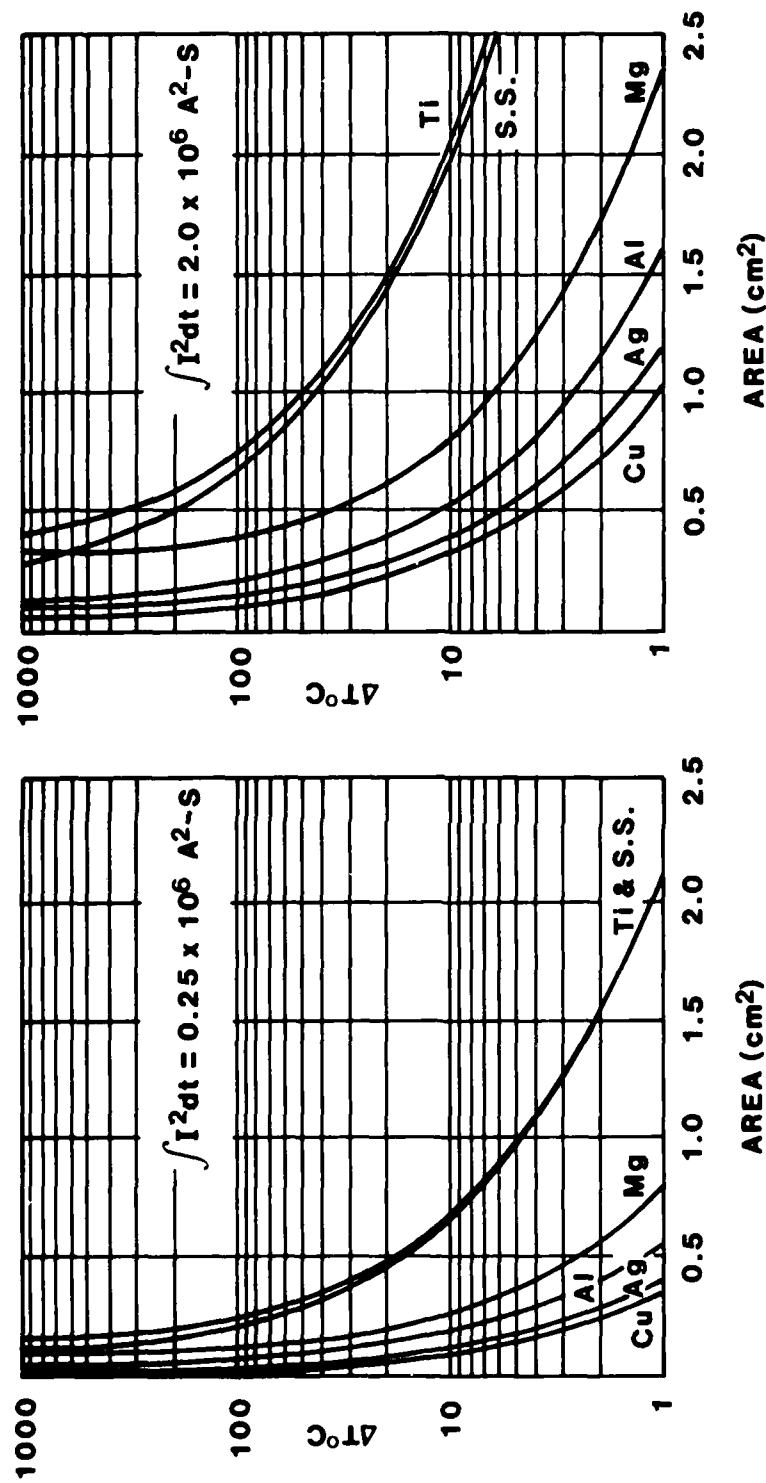


Fig. 5 - Temperature rise in various types of wires of various cross-sectional areas for two values of action integral [6]

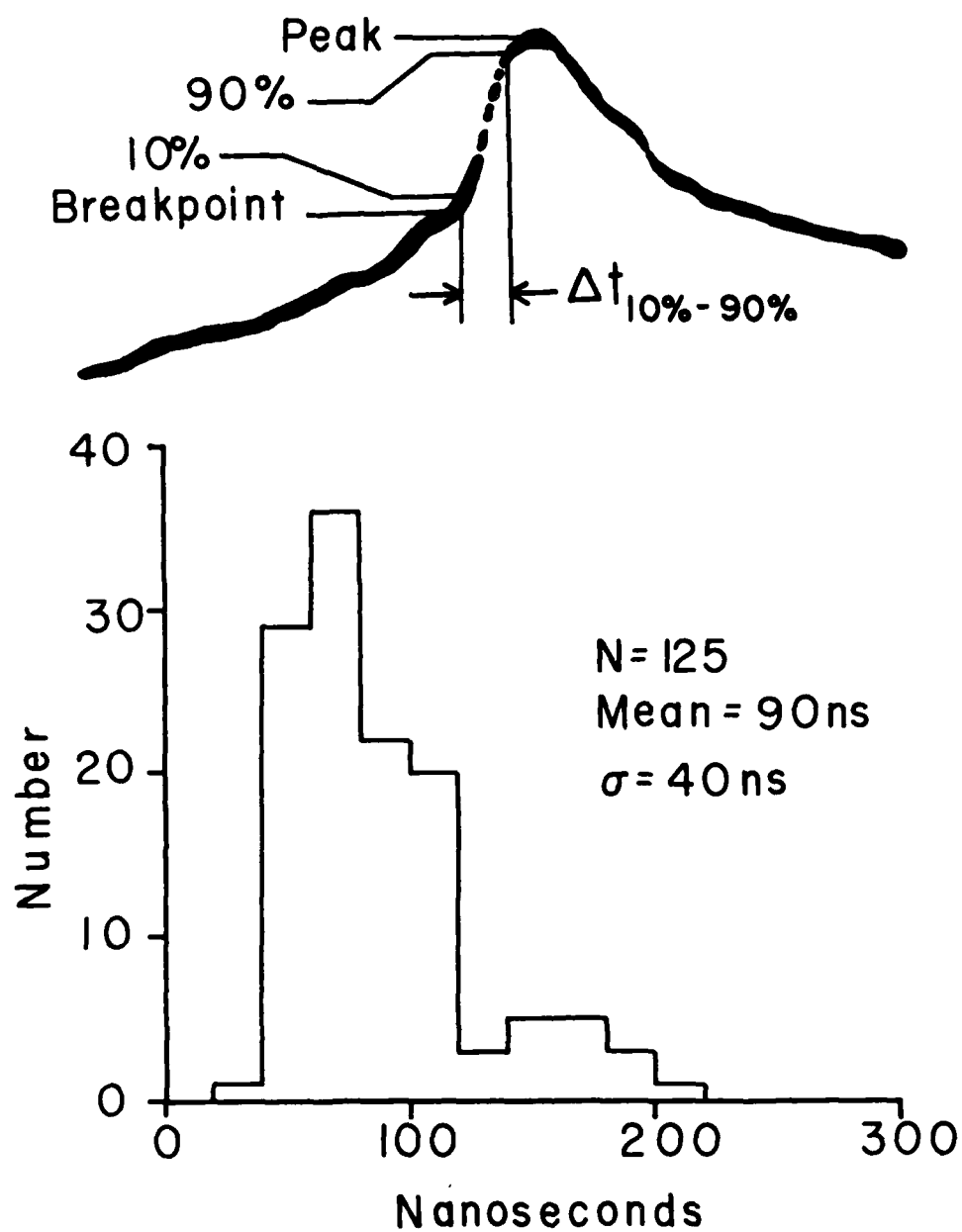


Fig. 6 - A histogram of the 10 to 90% rise of the fast transition in first return stroke electric fields [7]

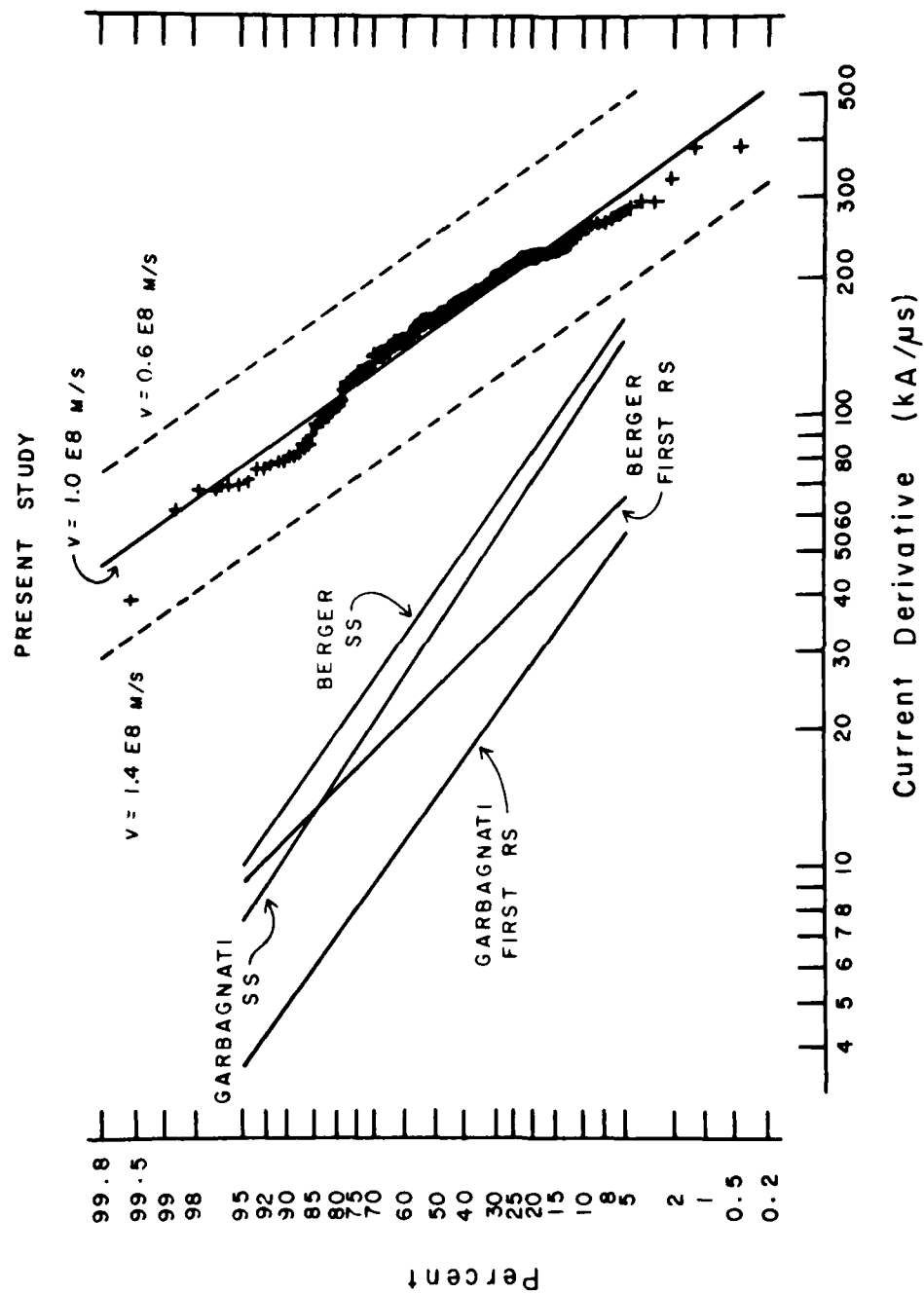
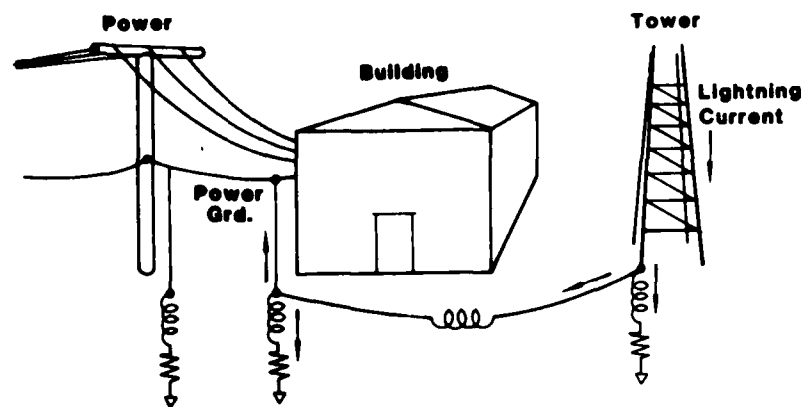
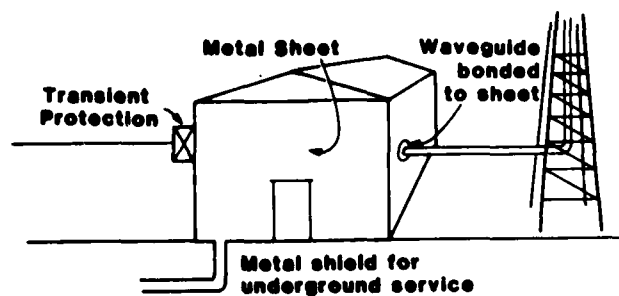


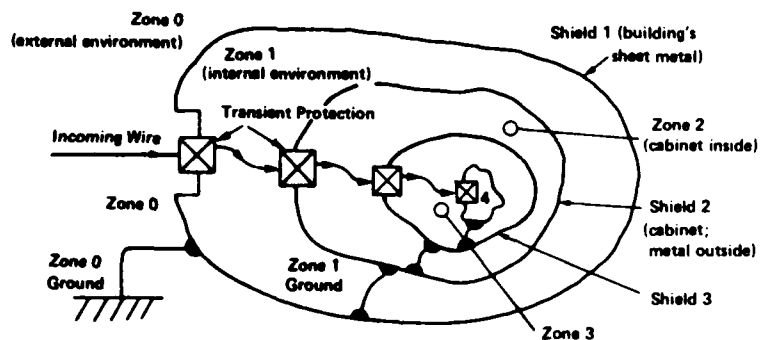
Fig. 7 - Cumulative distribution of the maximum rate-of-change of current during lightning returns strokes derived from electric field measurements and direct current measurements at towers (7)



a



b



c

Fig. 8 - A diagram illustrating the principles of topological shielding [14]

Theoretical and experimental determination of field, charge and current on an aircraft hit by natural or triggered lightning.

Heinz W. Kasemir
Colorado Scientific Research Corporation
Berthoud, Colorado, USA

Abstract

There are two types of lightning causing damage to aircraft or malfunction of instruments, namely natural and triggered lightning. They differ from each other in the initiation, the placement of the aircraft in the channel, the range of intensity and duration of the current, the frequency of occurrence, the area and type of cloud in which they are produced, etc.. Effective warning against lightning danger, hardening or immunisation of the aircraft against lightning strike, laboratory simulation of lightning for research and test purpose depend on the type of lightning we are dealing with. So far we have only the observation of pilots to differentiate between triggered and natural lightning. We will explore here the possibility to identify the type of lightning by instruments. For this purpose we have to determine the characteristic features in the field, charge, and current records obtained at an aircraft during a natural and a triggered lightning strike. These features are deduced first from theoretical calculations of these parameters. Knowing now what to look for, published data are analysed with the objective to determine if the aircraft was struck by natural or triggered lightning discharges.

THEORETICAL AND EXPERIMENTAL DETERMINATION OF FIELD, CHARGE, AND CURRENT ON AN AIRCRAFT HIT BY NATURAL OR TRIGGERED LIGHTNING.

Heinz W. Kasemir

Colorado Scientific Research Corporation
Berthoud, Colorado 80513

1. INTRODUCTION

We discuss in this paper the difference in the flight records of electric parameters for the case that a.) the aircraft triggered the lightning discharge and b.) the aircraft was hit by a natural lightning. The electric parameters are the three components of the thunderstorm gradient G_X , G_Y , G_Z , the gradient G_Q produced by the aircraft charge and the current I flowing through the aircraft. All parameters are functions of time and their time records are shown in a qualitative way in 24 pictures with a time window of about three seconds. About one second in the middle of the trace, marked by "L" and framed by two vertical lines, covers the events during the life time of the strike. There is space left before and after the lightning area to show the events of about one second before and after the lightning discharge.

The construction of these pictures is based on the electrostatic lightning theory, Kasemir(1) 1960. The application of this theory to the triggered lightning has been discussed by the author on the previous Conference on Lightning and Static Electricity Kasemir (2) 1983. Since flight records of the parameters specified above in the frequency range of 0 to about 1 kHz or more could not be found in the literature, the following discussion should be considered only as a theoretical prediction. We will devote first a few remarks to the problem what is, can, or should be measured so that the data can be physically interpreted. This would provide together with the theory a solid base for the study of the remaining unsolved problems.

2. PROBLEMS OF MEASUREMENTS AND DEFINITIONS

2.1 Frequency range.

Records of the thunderstorm gradient and the aircraft charge in the frequency range from 0 to about 10 kHz

appear best to identify the major components of a cloud and a ground discharge, and to connect them with the thunderstorm field. Field mills are used to measure electric fields from an aircraft. However their frequency range is from 0 to 10 Hz. This is not enough for the present purpose and the frequency range should be extended to at least 1 kHz but better to 10 kHz. L. Smith (3) 1954 has suggested a method how this frequency extension can be achieved.

2.2 Field or Gradient Components.

Different sign conventions are used in physics and atmospheric electricity for the field E and the dielectric displacement $D = \epsilon E$. If ϕ is the potential function of the thunderstorm and if q is the surface charge density on the aircraft we have in

Physics	Atmospheric Electricity
---------	-------------------------

$G = \text{grad } \phi$	$G = \text{grad } \phi$ (1)
$E = -G$	$E = G$ (2)
$D = \epsilon E = -\epsilon G$	$D = \epsilon E = \epsilon G$ (3)
$q = D = \epsilon E = -\epsilon G$	$q = -D = -\epsilon E = -\epsilon G$ (4)

We see that the definition of G in (1) is the same in physics and atmospheric electricity and using G in (4) instead of E or D the definition of q is also the same in both fields. We will use here as much as possible the parameters G and q to avoid confusion introduced by the different sign convention in E and D . When, however, E and D is used, it will be in accordance with the physical sign convention.

The replacement of D by q has the additional advantage that at the metallic surface of the sensor or antenna the expression "surface charge density q " conveys a better physical picture of the phenomena than the expression "dielectric displacement D ". q also unites all the different sensors or instruments appearing under different names such as field mill, D -dot sensor, fast or slow

antenna, etc. All measure the surface charge density integrated over the exposed area in one way or another.

The antenna or sensor is in all cases a capacitive coupler between the source and the first stage amplifier. The attributes "differentiating, slow, fast, etc." are not the properties of the sensor or antenna but of the first stage amplifier. This makes it relatively easy to adapt the measurement-s to any desired frequency range or band width by changing or modifying the first stage amplifier. It will not be necessary to change the antenna or the sensor.

The surface charge density q on each sensor is composed of contributions from each of the parameters GX, GY, GZ, GQ . Each of these parameters has its own scalefactor a, b, c, d , also called field concentration factors.

$$q = aGX + bGY + cGZ + dGQ \quad (5)$$

Therefore the output of one sensor is a composite of all parameters and an analysis of the data of one or even two or three sensors in term of the specified parameters is not possible without making restrictive assumptions, which have to be justified.

Rudolph and Perala (4) 1982 have given an extensive analysis of theoretical and experimental records of the D-dot sensor in the higher frequency range of about 5 kHz to 20 MHz. The parameter D-dot is generally better known under the name "Maxwell's Displacement Current". At the sensor it will convert into the complete Maxwell current, i.e. including the conduction current. There is an interesting parallelism in the discussion of the physical aspects during the approach of a leader to the aircraft given here later on and in the contract report of Rudolph and Perala. However the main emphasis in Rudolph and Perala's analysis is placed on the high frequency part of Maxwell's displacement current which will not be discussed in this paper.

Usually it requires four sensors and an accurate determination of the sixteen scalefactors to be able to solve the four linear equations of type (5) and to separate the GX, GY, GZ , and GQ . The difficult part here is not the mathematical calculation but the determination of the scalefactors. However there is a good chance that this can be done in an effective way with a computer model of the aircraft.

3. THUNDERSTORM GRADIENTS GX, GY, GZ .

The Cartesian coordinate system x, y, z has its zero point at the center

of the aircraft with positive x to the right, positive y forward, and positive z upward. The lightning will be triggered and grow in the direction of the maximum gradient and it is from this direction that the aircraft will be struck. It will simplify the discussion if we assume that the gradient is in the z direction (upper to lower fuselage) and that the x and y gradient components are zero. If the maximum gradient is in the y direction, then the strike will be triggered in or will hit from the y direction and correspondingly for the x direction. For these cases we have only to replace the label "GZ" in Fig. 1 by "GY" or "GX" to obtain the corresponding pictures for GY and GX . If the direction of the gradient has a x, y , and z component then we have to use vector addition to obtain the vector gradient.

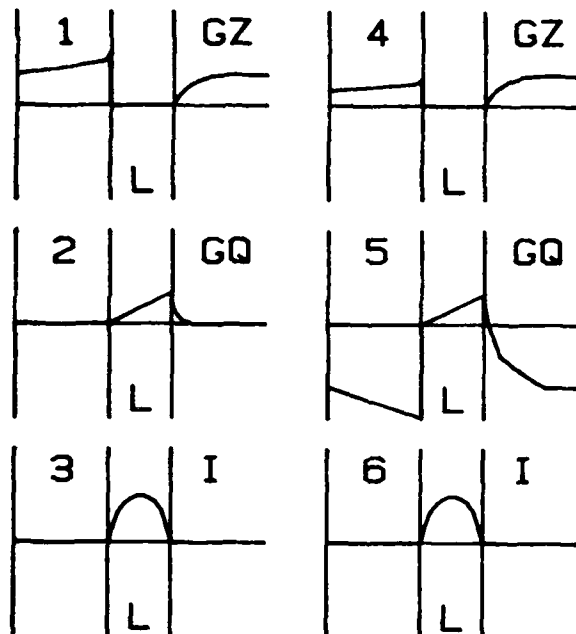
Fig.1 contains 24 pictures identified by numbers 1 to 24 and arranged in 4 columns and 6 rows. The first three rows show the pictures for a cloud discharge the last three rows are for a ground discharge. In each set of three rows the upper row displays GZ , the middle row GQ , and the lower row I . The first two columns contain the pictures for a triggered lightning and the last two columns those of a natural lightning. Hereby is the first column of a set of two for an aircraft not charged by precipitation and the second column for the aircraft charged by precipitation. The picture with the number n is referred to as Pic.n.

Pic.1 shows a GZ record that can be expected in case a cloud discharge has been triggered and no precipitation charging of the aircraft has occurred. Before the discharge is triggered the gradient increases until the trigger value of the gradient is reached. As soon as the channel develops in the $+z$ and $-z$ direction the Gz component is more and more screened with the growth of the channel. In Pic.1 this is shown as a drop to zero, but the zero value should be taken only as an indication of a reduction of the GZ components and should leave room to explain features introduced by other effects. For instance, the definition of the scalefactors is based on a homogenous external field. This assumption is not valid any more if a lightning channel is close or attached to the aircraft. We will now have mutual influence between the GZ and GQ channel. These and other interferences and deviations from the simple electrostatic model need further study. We cover this point with the general statement that all predicted curves inside the area "L" are open to corrections due

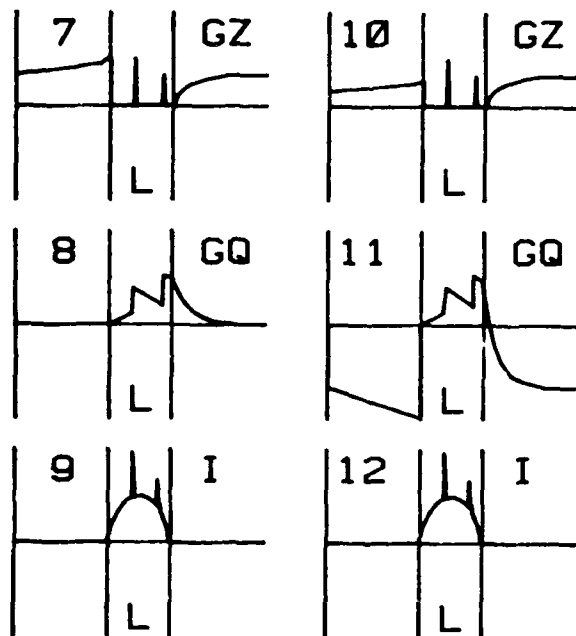
TRIGGERED LIGHTNING

No precip. charge Precip. charge

Cloud Discharge



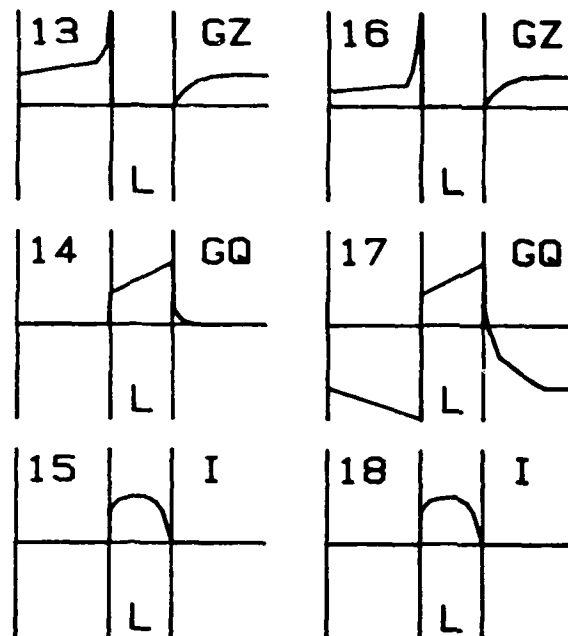
Ground Discharge



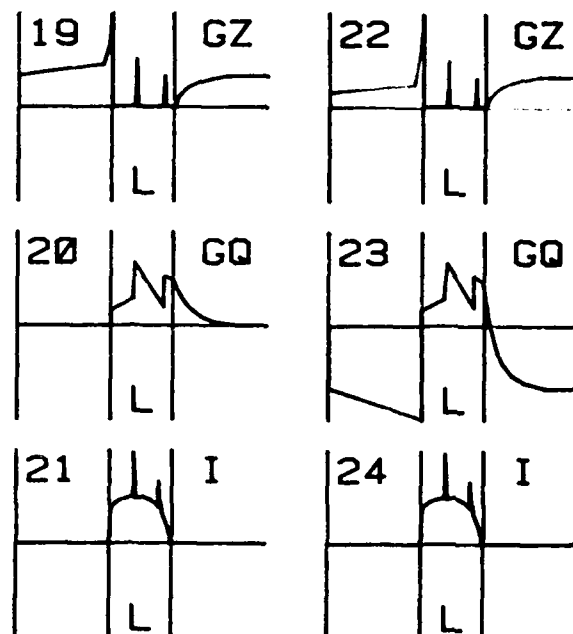
NATURAL LIGHTNING

No precip. charge Precip. charge

Cloud Discharge



Ground Discharge



GZ Z-component of thunderstorm gradient
GQ aircraft charge gradient
I lightning current flowing through aircraft

Fig. 1

to inputs outside the electrostatic assumptions.

We may however draw one general important conclusion from the screening effect of the channel. We see from (5) that with the assumption $G_X=G_Y=G_Z=0$ the q sensor output depends only on one parameter namely G_Q . This provides a situation, where a physical interpretation of the data of only one sensor is possible. If more sensor outputs are available and all traces show the same polarity and the same time dependence, then we are on fairly good ground with our assumption, that we are dealing with the charge on the aircraft. The aircraft can be charged either positive or negative but not both at the same time. If in addition the scale factors are properly determined and we divide each sensor output by its scale factor and obtain so numerical agreement between all sensor outputs, this should furnish sufficient evidence that our assumption is correct.

If however two sensor outputs show a different sign or the numerical values are not equal, this will be an indication of the influence of other effects.

The reduction of the gradient (or field) by a high tower or pole at the foot of the tower is well known under the name "inside the cone of protection". This reduction can easily be measured even in a fair weather field. If we replace the ground plane by the mirror image of the tower at the ground, we have a fair replica of the situation of a cloud discharge triggered by aircraft. This replica would even be more complete if a lightning discharge is triggered by the tower. Less similar is the case when the tower or the aircraft is struck by a lightning discharge, as we will see later on.

Pic.13 shows the G_Z trace of the aircraft struck by a cloud discharge. This trace is identical with that shown in Pic.1 with one important difference, namely the sharp gradient increase just before the lightning makes contact with the aircraft. The approaching lightning tip generates in front of it a high field concentration of the thunderstorm field which will affect the gradient record even at a distance of a hundred or of several hundred meters. If we assume an average velocity of 100 to 1000 km/s of a stepped leader, Uman (5) 1969, then the rise of the gradient should begin in the order of milliseconds before contact is made. The gradient in the last millisecond would reach values above the breakdown value and probably exceed the dynamic range of the field mills. In any case, there would be an unmistakable

strong pulse just before contact of a lightning strike. Such a pulse will not be a feature of the G_Z trace of a triggered discharge.

To complete the discussion of the G_Z records of a cloud discharge we turn now to Pic.4 and 16 which show the influence of precipitation charge on the aircraft. The gradient G_Z in Pic.4 before the lightning is triggered is low compared to Pic.1. This should indicate that part of the high gradient required at the aircraft surface to trigger the discharge is due to aircraft charge caused by precipitation. Therefore in Pic.5 corresponding to Pic.4 the gradient G_Q is high, whereas in Pic.2, which corresponds to Pic.1, the gradient G_Q is zero.

In Pic.5 G_Q is negative but in Pic.4 G_Z is positive. This does not mean that G_Z is reduced but that G_Z produces on the aircraft induction charges of opposite polarity so that regardless of the polarity of G_Q there is always one half of the aircraft surface where the gradient is increased. Then the breakdown value can be reached with the support of precipitation charging, whereas without precipitation charging the thunderstorm gradient alone may not be strong enough to produce the breakdown value.

It is common practice to take the breakdown field at the aircraft as an indicator that a lightning discharge will be triggered. This, however, would be an erroneous assumption. Reaching breakdown value on one part of the aircraft indicates only that corona discharge will start at this point. Therefore we may call this field or gradient value the corona onset field or gradient. There is still a gap in our knowledge under what conditions a corona discharge can be turned into a triggered lightning discharge.

The last G_Z record to discuss in this series is given in Pic.16 which shows the G_Z trace of a charged aircraft struck by a cloud discharge. The charge on the aircraft will not be able either to attract nor to deflect the cloud discharge. The approaching lightning tip will still produce the sharp gradient rise starting a few milliseconds before contact.

Pic.7, 10, 19, and 22 show G_Z records which can be expected if the aircraft either triggers (Pic.7 and 10) or is struck (Pic.19 and 22) by a ground discharge. The trace before the discharge is triggered or the aircraft is struck and the trace after the discharge is the same as that of the corresponding cloud discharge given in Pic.1, 4, 13, and 16 with the possible exception that the

polarity may be reversed. There is again the sharp (negative) increase of GZ just before the discharge strikes the aircraft in Pic.19 and 22 which indicates that this was not a triggered lightning but a lightning strike.

In all Figures 7,10,19, and 22 there are two sharp spikes in the "L" area indicating the passing of two return strokes. There is a large voltage difference between the return stroke channel extending from the ground to the tip and having approximately ground potential and the remaining leader stroke extending from the tip to the end of the leader stroke in the cloud still having its original cloud potential of the order of -100 MV. This is indicated by the bright spot at the tip of the return stroke. If the tip length is about 100m, along the tip exist an average field of 1 MV/m. This strong field is necessary to produce ionization to raise the tip channel from the low conductivity of the leader channel to the high conductivity of the return stroke channel. If the velocity of the return stroke is of the order of 100000 to 1000000 km/s (Uman (5) 1969) there is only a time period of 10 to 100ns to accomplish the ionization. In such a time period the tip would also pass through the aircraft and would then produce a gradient pulse of 1 MV/m going up and down in 10 to 100 ns. This pulse should be detectable by a D or D-dot sensor with a high frequency response even considering that the high conductivity of the aircraft will reduce its amplitude to a large degree. Such a fast pulse may excite resonance in the aircraft body. The current will rise in this time like a ramp function from the low level of the leader stroke to the higher level of the return stroke and decay at the end of the return stroke. There is a difference of 3 powers of 10 between the time periods of the current and the gradient pulse.

4. THE LIGHTNING CURRENT.

Pic.3 and 6 show the lightning current of a triggered cloud discharge without and with precipitation charging of the aircraft. The current input of precipitation charge is in the order of mA and will be negligible against the 10 to 100 A of a cloud discharge. Therefore both figures show the same trace. The current will rise from zero to a maximum and then drop off to zero again. Ripples from a stepping process or even K-changes, which would show up as little spikes in the current flow, are not reproduced in the pictures.

Pic.15 and 18 show the current through an aircraft struck by a cloud

discharge. The I trace is almost the same as in the triggered lightning case (Pic.3 and 6) with one exception. The current starts here not from zero but jumps up to the value of the current already flowing in the lightning channel as soon as contact is made.

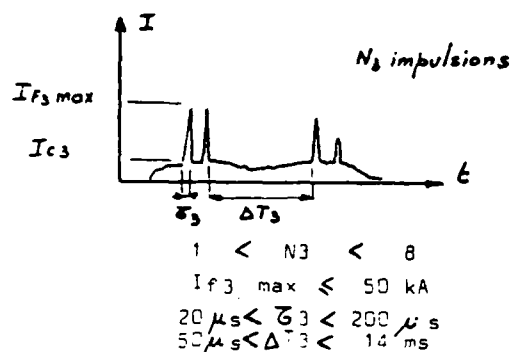
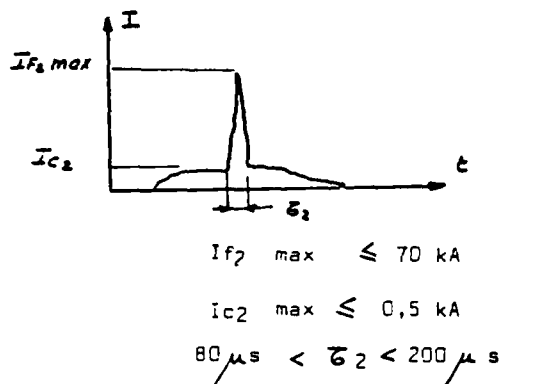
The same distinguishing feature can be seen in Pic.9, and 12 of the triggered ground discharge compared to Pic. 21, and 24 of the strike by a ground discharge. In the first case the current has a smooth rise from zero and in the second case the current jumps to the current value of the hitting lightning discharge at the time of contact.

THE SUDDEN INCREASE IN THE MEASURED PARAMETER, CURRENT AS WELL AS GRADIENT AT THE TIME OF CONTACT IS THE EARMARK OF A LIGHTNING STRIKE. WE WILL SEE LATER THAT THE SAME FEATURE CAN BE EASILY RECOGNIZED IN THE GQ TRACE. THE TRIGGERED LIGHTNING HAS NOT THIS CHARACTERISTIC PULSE IN THE GZ TRACE NOR THE STEP-LIKE INCREASE IN THE GQ AND I TRACE AT TRIGGER TIME.

The differences between the cloud and ground discharge traces are the spikes produced by the return stroke. We know this already from numerous field records on the ground. However, measured from an aircraft which is a part of the channel, the return stroke doesn't register in the GZ record as a step but as a spike, which should even be much shorter than the current spike, as discussed above. The current spike has another feature worth mentioning. It doesn't reverse the current flow of the leader stroke. The "return stroke" current doesn't return but flows in the same direction as the leader stroke current. The name "return stroke" fits only the optical phenomena for which it was originally coined.

Fig.2 shows two composite sketches of current traces measured from a French Transall aircraft during a research project of the Centre D'ESSAIS Aeronautique De Toulouse (6) 1979. The upper picture is based on three records and the lower picture on four. The maximum current peak of 70 kA in the upper and of 50 kA in the lower picture combined with the characteristic spikes of the right duration in the range of 20 to 200 microseconds identify these traces as ground discharge currents with one or four return strokes respectively. Since these are hand drawn graphs and it is not clear how accurate the beginning of the lightning current is represented, we can only say that there is a hint that the upper picture may be an example of a triggered discharge and the lower picture that of a lightning strike to the

aircraft. Unmistakable, however, is the fact that the return stroke current is of the same direction as the leader current.



Ground discharge trough Transall aircraft
Upper Pic. 1 ret.str., lower Pic. 4 ret.Str.

Fig.2 (Centre D'Essais Aero.(6) 1979)

5. THE GRADIENT GQ OF THE AIRCRAFT CHARGE

In case the aircraft is not connected to the lightning channel but charged by precipitation the charge density on a given point on the aircraft is not too difficult to calculate theoretically. This problem can be solved - as mentioned before - by using a computer model of the aircraft. However, if the aircraft has triggered a lightning or is struck by a lightning and is consequently a part of the lightning channel the problem to determine the charge density on a specified surface point by theoretical calculation requires a two step approach.

Our first problem here is to determine the charge density at the lightning channel itself and specifically at the place which will be occupied by the aircraft. Fig.3 (Kasemir (1) 1960) shows in Fig.3a the thunderstorm model of Simpson and Wilson. This is composed of three

spheres arranged vertically on top of each other. Each sphere is filled with space charge, alternating in sign, as shown in Fig.3a. The three spheres represent the main space charge volumes in the storm. The key to the determination of the charge distribution on a lightning channel is the potential function ϕ of the thunderstorm. The curve ϕ in Fig.3b,c,d shows the potential function as a function of altitude z (vertical axis) in the center line of the storm for $x=y=0$. The horizontal axis shows the values of ϕ or with a possible zero shift the values of the charge per unit length ql on the lightning channel. ql is approximately proportional to the charge density q on the lightning channel. We will assume later on, that this proportionality can be extended to the aircraft when it becomes a part of the lightning channel.

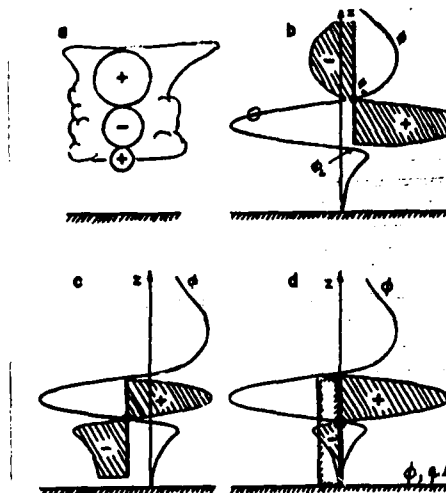


Fig. 3. Charge distribution: (a) in the thunderstorm model of Simpson Wilson; (b) on an intra-cloud stroke; (c) on a leader stroke of a cloud to ground discharge; (d) on the ground discharge after completion of the main stroke.

Potential function ϕ , horizontal axis
Charge per unit length ql , horizontal axis
Altitude z , vertical axis

Fig.3 (Kasemir (1) 1960)

In Fig.3b a cloud discharge is represented by a thick vertical line slightly to the right of the z axis. The point where it crosses the potential line is marked by a black circle. This can be the point where the cloud discharge originated or the point where the aircraft triggered the cloud discharge. The cloud discharge originating or the aircraft flying at this altitude would have assumed automatically the potential

ϕ_L of the storm at this point. Since the lightning channel as well as the airplane can be treated as conductors the whole lightning channel and all points on the airplane surface have the potential value of ϕ_L .

We define here the concept of the "bridged potential" ϕ_B (translation of the German word "überbrücktes Potential")

$$\phi_B = \phi - \phi_L \quad (6)$$

ϕ_B and ϕ are functions of z whereas ϕ_L is a constant. ϕ_L provides here a new reference potential or zero shift for the potential function ϕ_B , however ϕ_B as defined in (6) is not in any physical sense a potential discontinuity. The relation with the charge per unit length q_l and the charge density q is given by

$$q_l = -k_l \phi_B, \quad q = -k \phi_B \quad (7)$$

The factors k_l and k are based on the electrostatic lightning theory and can be calculated analytically. k_l is a true constant, i.e. independent of z , for a homogeneous thunderstorm field and has the value of about 25 pF/m. It depends only on the long and small axis of a spheroid, which represents the lightning channel in the theoretical calculation. For the inhomogeneous field of a thunderstorm k_l depends weakly on z . However for our purpose here the approximation by using the constant value also for an inhomogeneous thunderstorm field is sufficiently accurate.

The charge per unit length q_l is shown in Fig.3b as the mirror image of the potential function, mirrored on the vertical line representing the lightning channel. The hatched area shows the negative net charge on the upper part and the positive net charge on the lower part of the channel. Since these net charges are equal in amount but of opposite polarity the net charge of the whole channel is zero. The reason for the rule "net charge zero for leader and cloud discharges" is that these discharges can not pick up charges from the cloud. This has been discussed in detail by Kasemir (2) 1983.

We interrupt here the discussion of Fig.3 to draw an important conclusion for Pic.2,5,14, and 16. The charge per unit length q_l and consequently the charge density on the lightning channel and the aircraft is zero at the point of origin (marked by the black circle in Fig.3b.) Equations (6) and (7) lead to the same result since at this point $\phi = \phi_L$ and according to equation (6) $\phi_B = 0$.

If the lightning growth in such a manner that this condition remains during the lifetime of the discharge the airplane will not receive any charge from the lightning discharge. Add to this the fact that - as discussed above - the aircraft is also screened by the discharge from the thunderstorm field the aircraft experiences from a triggered cloud discharge only the weak current of few amperes. All field mills should record zero or very low values.

This result fits very well with the pilots' observation that the corona hiss in the communication gear stops immediately with the start of the triggered lightning - in the pilots' terminology this is called the "electrostatic discharge"- and that these electrostatic discharges cause no or only little damage to the aircraft.

Coming back to the topic of this paper to determine the characteristic features of a triggered and a strike by a lightning discharge we may conclude that a triggered lightning always starts with charge zero on the aircraft. This can be seen in Pic.2,5,8 and 11. The increase of the charge during the lifetime of the discharge will be explained in the next paragraph. The drop of the charge to zero of an aircraft charged previously by precipitation as shown in Pic.5 and 11 is only a guess. It is based on the assumption that any previous charge on the aircraft will be absorbed into the lightning channel and that the final charge distribution is dictated by the lightning discharge. With regard to the lightning-hit the aircraft will assume the charge of the channel tip at the time of contact.

Let's assume that in Fig.3b the aircraft is placed below the point of the lightning origin. The lightning channel coming down from above will have at its tip positive induction charge. As soon as contact is made the aircraft will receive positive charge from the channel. From then on the aircraft charge is determined by the channel charge at this altitude. If the aircraft was flying above the point of the lightning origin the events will be the same only that in this case the aircraft will be charged negative. Pic. 14,17,20 and 23 show the cases when the aircraft was charged positive by the lightning discharge. The modification introduced by a previous precipitation charge is the same as discussed for the case of the triggered lightning discharge, i.e. the previous aircraft charge will be absorbed by the lightning channel.

The explanation why the aircraft charge or the charge distribution on the

lightning channel can change during the lifetime of the discharge. Physically this can be explained by the fact that the lightning channel will not grow with the same speed at the upper and the lower tip of the channel. There are several reasons for this: 1) Positive breakdown of the air ahead of the lower tip will not occur with the same speed as the negative breakdown ahead of the upper tip. 2) The field at the upper and the lower tip are not the same. 3) The extent of the region ahead of the tip where the breakdown value is reached or surpassed is not the same at the upper and lower tip. 4) The growth of the lower tip is stopped because the tip approaches an area which has the same potential value as the lightning channel. The field ahead of the tip would drop to zero and the ionization of the air for the growth of lightning channel would stop. The result of this uneven growth is that the lightning channel changes its potential ϕ_L and with it the charge distribution on the channel.

All this is based on the electrostatic lightning theory. It would take too much space to discuss it here in more detail. From equation (6) it is obvious that a change of ϕ_L will result in a change of ϕ_B , and from equation (7) that a change of ϕ_B will result in a change of q_l and q . This possibility is indicated by the increase in GQ shown in all GQ picture of Fig.1. The general conclusion is that a change of GQ can be expected but not necessarily in the ramp like shape or polarity shown in the pictures.

Fig.3c. shows the charge distribution of the first leader stroke shortly before ground contact is made. The leader stroke may be triggered or may hit an aircraft flying through the lower part of or below the storm. With the exception of the reverse polarity the leader would have a similar effect on the GQ records as that explained for the case of a cloud discharge.

The last feature to be discussed is the signature of the return stroke. Fig.3c and d show the charge distribution on the channel shortly before and after the return stroke. This is another example of the influence of the lightning potential ϕ_L on the charge distribution on the channel with the additional variation that the net charge zero rule of the leader and cloud discharge is replaced by the condition $\phi_L=0$ after ground contact is made. Equation (6) and (7) still hold but with $\phi_L=0$.

$$\phi_B = \phi \quad (6a)$$

$$q_l = -k_l \phi; \quad q = -k \phi \quad (7a)$$

The mirror rule for the construction of the new charge distribution on the lightning channel remains valid, but note that the lightning channel is displaced from the position on the left of the vertical axis z in Fig.3c to the position of the z axis itself in Fig.3d. This does not indicate a movement of the channel in space but a change in the potential value let's say from $\phi_L = -70\text{MV}$ before ground contact to $\phi_L = 0\text{V}$ after ground contact.

We see from Fig.3d that compared to Fig.3c the positive charge area has increased and the negative charge area has shrunk, indicating that the lightning channel has lost negative charge to the ground. This is in agreement with the fact stated quite often in the literature that the ground discharge brings negative charge to earth. However the mechanism suggested here is quite different from that of discharging the leader to ground.

Along the whole channel the charge per unit length q_l and with it the charge density q has increased due to the return stroke. This causes the sudden increase in the GQ traces in Pic.8,11 and Pic.20 and 23. This step-like increase is the same for the triggered and the natural ground discharge. After the first leader stroke there will be no difference between a triggered and a natural lightning strike and the general assumption that a triggered lightning (electrostatic discharge) is relative harmless cannot be extended to the triggered ground discharge.

6. SUMMARY AND CONCLUSIONS.

Assuming that the gradient components G_X , G_Y , G_Z and the gradient GQ caused by the aircraft charge can be separated and recorded in the frequency range of 0 to 10 kHz there are certain characteristic features in the records which will differentiate the triggered lightning from the strike of a natural lightning. These distinguishing features are centered at the time of contact by a lightning strike or at the time of triggering the lightning discharge.

The contact is marked by a sharp increase in the G_X , G_Y , G_Z record, starting a few ms before contact. The GQ record should also show a step-like increase at the time of contact.

In case of a triggered lightning the G-components should show only a smooth drop of the thunderstorm value to

zero or a very low value and the GQ trace should show a smooth drop to zero if the aircraft was charged by precipitation previously. If the GQ trace was previously zero, then it would remain zero at the time of triggering.

Since no records have been found in the frequency range and with the separation of parameters the characteristic features mentioned above should be considered as a theoretical prediction.

The physical rationale of these features have been discussed in detail in this paper. Suggestions have been made how and what to measure so that the data can be analysed with a physical point of view in mind. The deductions and conclusions are based on the electrostatic lightning theory which enables us to make not only qualitative but also quantitative predictions.

REFERENCES:

1. H.W. Kasemir, "A Contribution to the Electrostatic Theory of a Lightning Discharge," JGR, 65, #7, 1873-1878, 1960
2. H.W. Kasemir, "Static Discharge and Triggered Lightning," Lightning and Static Electricity Conference, 24-1, 1983
3. L.G. Smith, "An Electric Field Meter with extended Frequency Range," Rev.Sci.Instr. 25, 510-513, 1954
4. T.Rudolph, R.Perala, "Interpretation Methodology of In-Flight Data," Electro Magnetic Applications, Inc. 1982
5. M.A. Uman, "Lightning," McGraw Book Company 1979
6. Centre D'Essais Aeronautique De Toulouse "Measure Des Caracteristiques De La Foudre En Altitude," Essais No. 76/650000, 1979.

COMPARISON BETWEEN LONG AIR-GAP BREAKDOWNS,
GLIDING SURFACE DISCHARGES
AND LIGHTNING LEADERS

by J.L. Boulay and S. Larigaldie
Office National d'Etudes et de Recherches Aéronautiques
BP 72, 92322 Châtillon Cédex, FRANCE

ABSTRACT

Many authors have already compared the main properties of long air-gap discharges and lightning leaders, such as the current waveform, propagation velocity, electronic temperature, electromagnetic radiation; some of these properties are similar, others are different.

We propose, in this paper, a general comparison of the behavior of long air-gap discharges, lightning leaders and surface discharges during their propagation.

A detailed experimental and theoretical analysis of gliding surface discharges is presently being conducted at ONERA to contribute to better understanding of the propagating conditions of lightning leaders. The experimental setup guides and controls the phenomenon precisely and makes it possible to measure the intrinsic properties of the surface discharges: velocity, channel electrical field, current, temperature and electron density.

A physical model of the gliding discharge is proposed including the different zones of the discharge: successively, the streamer, the transition, the thermalization and leader zones. A first interpretation of the VHF-UHF radiation associated with the propagation is given.

A comparison is made between such a discharge, a long air-gap discharge and lightning leader, in the case of negative polarity. Extrapolation to the data obtained on two different lightning flashes is proposed by using interferometric locations of VHF-UHF radiation sources.

INTRODUCTION

Until now, the studies of the interactions between aircraft and lightning flashes have mainly been concerned with the effects of the current wave associated with the return-stroke. Under these conditions, the phenomena involved are expressed by low frequency models that do not include the structural resonances. In modern aircraft, though, the use of composite materials, transparent to electromagnetic radiation, and integrated circuits with high input impedance calls for a more detailed examination of the effects of the

electromagnetic radiation from lightning, in particular as concerns the vulnerability of fly-by-wire techniques [1]*.

Recent data on the spectrum of lightning electromagnetic emissions bring out the existence of pulses with very short rise times (10^{-8} to 10^{-7} s) indicating excitation frequencies in the same domain as the resonance modes of an aircraft structure (from a few megahertz to several tens of megahertz) [2, 3, 4]. The analysis of these data indicates that the spectrum of electromagnetic radiation due to the lightning encompasses the spectrum associated with the Nuclear Electromagnetic Pulse (NEMP) [5].

The problem of the interaction between the electromagnetic radiation from lightning and an aircraft structure is extremely complex because the physical processes involved in the different phases of the lightning flash are themselves very different and are not completely known at the present time. If the radiation is to be appropriately modeled and simulated in a program qualifying aeronautical equipment or testing the vulnerability of a complete aircraft structure, it is important that the principal characteristics of this radiation be approximated as best possible. The tests are carried out with high-voltage impulse generators [6, 7], which are supposed to simulate the various lightning discharge phenomena: preliminary breakdown, leaders, return-stroke, subsequent stroke, etc.

It is presently felt that the main sources of VHF-UHF radiation from a lightning flash are related to sudden modifications in the properties of the plasma forming the discharge arc, in particular during the stepped-leader phase preceding the return-stroke. The transition currents and the propagation speeds of the arc discontinuities are thus determinant parameters in evaluating the characteristics of the radiation.

Our purpose is to present the essential aspects of several typical discharges, on the phenomenological level. Using the analyses of breakdowns in long air-gaps at atmospheric pressure, we first compare the properties of these breakdowns with data obtained at ONERA [8] for high-current surface discharges. We then attempt to extrapolate these data

Research supported by DRET (Direction des Recherches, Etudes et Techniques de la Délégation Générale pour l'Armement).

*Numbers in brackets designate References at end of paper.

with recent measurements [9, 10] carried out on actual lightning flashes, in the radiation and localization domain of the emission sources.

To limit the field of analysis, we will restrict ourselves to negative polarity "precursor" discharges, which are the ones most frequently encountered in lightning and correspond to the most intense electromagnetic emission phase in the lightning flashes.

REVIEW OF THE PROPERTIES OF LABORATORY-PRODUCED LONG ARCS

The properties of long arcs and lightning have already been compared [11], in particular for the return stroke [12], where it is observed that the channel temperature (approximately 30,000 K) and the electron density ($n \sim 10^{18} \text{ cm}^{-3}$) are nearly identical for both processes. Yet the phenomena precursor to these two types of discharge, before the return wave is set up, has undergone little analysis.

Much experimental research has been going on over the past few years, in particular at Les Renardières [13, 14], to characterize the electrical discharges through long air-gaps. We will restrict ourselves to recalling cases of negative polarity breakdowns for impulse voltages with very short rise times, to approximate as best possible the phenomena associated with lightning flashes [15, 16].

The results discussed here are from tests carried out in air-gaps D greater than 1 m. The data is taken from references [14] and [16]. Two breakdown developments were discovered:

FIRST TYPE OF PROPAGATION - For a rise time $\tau = 2 \mu\text{s}$ and a 1 m gap, the image converter discharge propagation recording can be represented roughly as in (Fig. 1a). An initial corona discharge appears at time T_i . After a dark zone, a negative leader A^* is established on the electrode simultaneously with a space stem D, linked to leader A by positive streamers C. We also observe negative streamers E going from the space stem to the plane. A space stem model has been proposed by Hutzler [14], who shows that the space stem is a plasma resulting from a negative streamer with a positive space charge that cannot be totally neutralized by the available electrons. This stem appears in the most advanced zone of the initial negative corona. The discharge then develops nearly continuously. When the first branch of the negative streamer reaches the plane (T_f), we observe a significant increase in the drift velocity of the stem with no change in the brightness of the discharge.

* The notation T_i , T_f , etc., and A, D, C, etc., are taken from references [14] and [16].

Not until the stem arrives in the neighborhood of the plane (T_f) does an ascending leader develop. The velocities of the positive and negative leaders then suddenly increase, until they join. The discharge channel becomes highly luminous and the gap breakdown occurs.

During the propagation, the channel lights up periodically. The light emitted from the stem remains small. These processes are accompanied by current pulses of 1 to 5 A on the HV electrode and do not cause any abrupt increase in the discharge. The mean propagation speed is $5 \times 10^5 \text{ ms}^{-1}$. It reaches 10^6 ms^{-1} when the negative streamer approaches the plane. In comparison, the velocity of the negative leader remains very low and approximately constant, at $2 \times 10^4 \text{ ms}^{-1}$. Assuming that the space charge between the electrode and the stem is uniformly distributed along the discharge, we show experimentally that the linear density is in the neighborhood of $20 \mu\text{Cm}^{-1}$ [14].

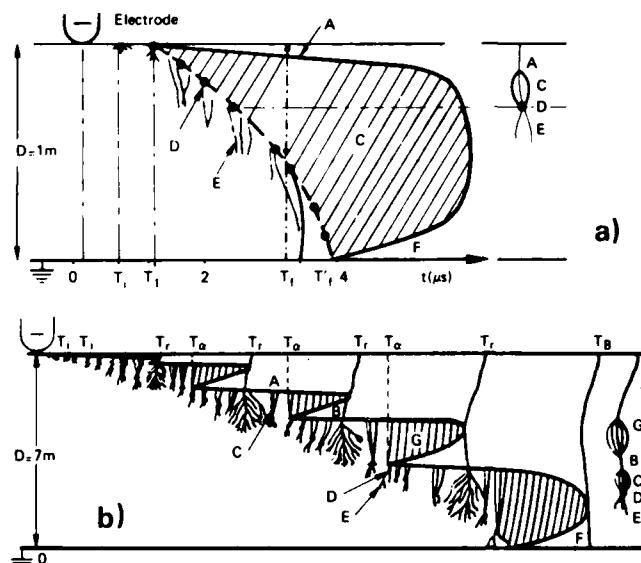


Fig. 1 - Negative discharge developments in long air gap. From [14].

a) Negative discharge - $t = 2 \mu\text{s}$.
b) Negative discharge - $t = 60 \mu\text{s}$.

SECOND TYPE OF PROPAGATION (Fig. 1b) - For longer gaps (4 and 7 m), a much more complex discharge structure is observed. In addition to the previously mentioned zones, a space leader B separates the negative leader A from the positive streamers in stem D. A zone of positive streamers G also appears between B and A. Besides the appearance of the space leader, this type of propagation is characterized by intense reilluminations of the channel at times T_r , when the negative leader and space leader join. The negative

leader then suddenly increases by the length of the space leader. A very extensive zone of streamers is established in the head of the discharge, immediately followed by the creation of a new stem, thus initiating a new progression process up to the final jump, if the field is sufficient. It should also be noted that, for very short rise times, several space leaders may appear simultaneously and in series along the discharge channel.

According to [14], the propagation speeds reach :

- negative leader : 10^4 ms^{-1} for currents on the order of 1 A,
- the system including the space stem and the associated positive and negative streamers propagates like a "bidirectional discharge" over a fictitious electrode having a mean drift velocity of 10^5 ms^{-1} . On the other hand, the actual speed of the positive streamers reaches some 10^6 ms^{-1} , and that of the negative streamers at the discharge head reaches 10^7 ms^{-1} at joining times t_r ,
- the space leader extends during its phases of continuous development at a velocity of $3 \times 10^4 \text{ ms}^{-1}$ toward the electrode and 10^4 ms^{-1} toward the plane. Note that the length of this leader over a 7 m gap can reach 1.5 m.

When the channel reilluminates, the linear density of the charges associated with the negative leader is $150 \mu\text{Cm}^{-1}$. According to the same authors [14], we can estimate that the axial field in the streamers is between 8 and 10 kV cm^{-1} , and between 3 and 5 kV cm^{-1} in the leader phases.

For the two types of propagation discussed, where the mean speed of advance of the negative leader is on the order of 10^4 ms^{-1} , the essential difference resides in a space leader establishing or not establishing a junction between the stem and negative leader.

In the first case, the electric field distribution in the gap makes it possible for the streamers to develop over great distances. The weak reillumination of the stem, defining a local alteration in the plasma, only comes from a contact between the positive streamers and the negative leader, which does not change the electrical configuration of the medium.

In the second case, the streamer-leader transition from the stem can propagate. A path of conduction is thus established between stem and negative leader that gives rise to very significant changes in the electric field at the head of the discharge, and thus the appearance of an essentially discontinuous propagation.

SURFACE DISCHARGE CHARACTERISTICS

PRELIMINARY REMARKS - These discharges

over walls of insulating material lend themselves, better than breakdowns over long air gaps, to a detailed analysis of the propagation process insofar as they are perfectly controlled in space and time.

We can recall Toepler's remarks [17] based on photographs of discharges obtained by applying an impulse voltage V_0 to an electrode placed in contact with a thin insulating surface placed on a second flat plane metal electrode kept at ground potential. As soon as V_0 goes beyond a few kV, a discharge appears around the electrode. The luminous path shows negative polarity sectors due to the progression of the streamers (Fig. 2). The radial extent ℓ of the discharge is proportional to V_0 , or:

$$\ell (\text{cm}) = \frac{V_0 (\text{kV})}{k},$$

where k is 11.2 kV/cm and is constant regardless of the dielectric plate thickness.

If V_0 exceeds a threshold V_s , which depends on the thickness and permittivity of the insulator, the discharge changes: very bright spark channels appear along the lines separating the sectors and new primary discharges are established before the channels, when the channels have crossed the previously formed discharge zone. We thus have a progression phenomenon analogous to the one observed in long breakdowns, i.e. with the formation of a stem and leader, at L for example, extending toward the negative leader while the negative streamer moves away. At the moment of junction with the negative leader at L' , the negative leader propagates over the entire length of the primary discharge up to L , where the process begins again. The velocity of the negative leader is very low here, which gives the appearance of a very discontinuous propagation.

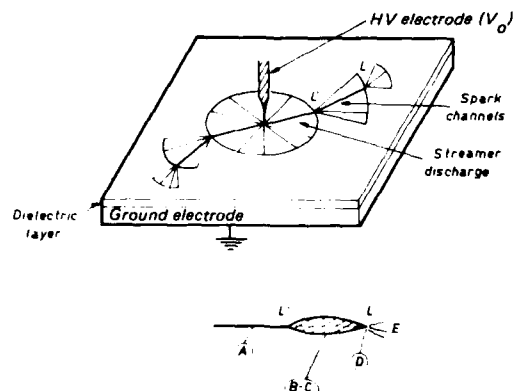


Fig. 2 - Surface discharge propagation
From Toepler [17].

As V_0 increases, the overall appearance of the discharge changes as shown in the photos in Fig. 3, taken at ONERA. In fig. 3a, where the dV_0/dt term is on the order of $5 \times 10^7 \text{ kVs}^{-1}$, we see that the sectors of the primary discharge broaden, indicating that the negative leader, which has become conductive and is increasing velocity, has propagated inside the discharge before the discharge reaches its critical size ℓ_s . When

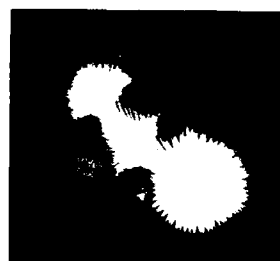
$$\frac{dV_0}{dt} = 10^8 \text{ kVs}^{-1}$$

as in fig. 3b, the discontinuity between the primary zones begins to blur, leading to a nearly continuous process when

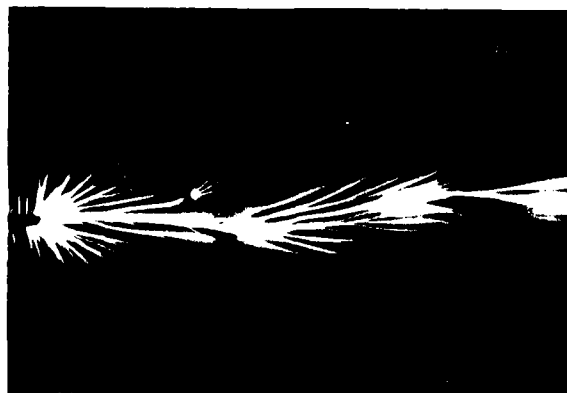
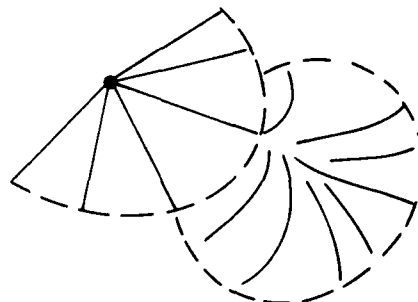
$$\frac{dV_0}{dt} > 10^8 \text{ kVs}^{-1},$$

which shows that the negative leader propagates without interruption, with a negative streamer zone at its head (Fig. 3c).

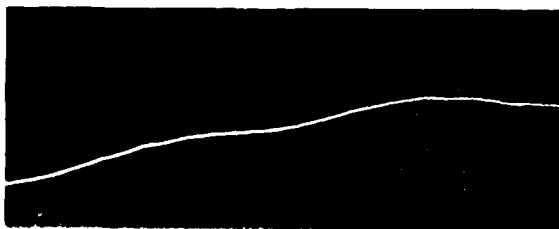
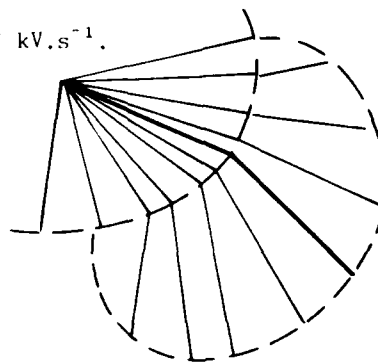
The stem, positive streamer and space leader phases have thus come together to form a "transition gap" which moves at the same speed as the negative leader. This condition supposes that a large and continuous current ($> 10 \text{ A}$) is set up in the discharge channel. The breakdown structure is brought out in the following experiment [8]: one surface of the dielectric is charged with the corona effect by an external power supply with a potential V that can be adjusted from 0 to 130 kV. The other side of the dielectric has a counterelectrode at ground level. This may cover the entire surface, giving a ramified discharge that tends to neutralize all of the deposited charges, or may simply be a metal strip giving a nearly linear discharge that is easier to analyze. The discharges are triggered by an excitation electrode on the dielectric surface which is in floating potential mode at first, during the dielectric charging process, and in then instantly raised to the reference potential by a vacuum spark gap.



$$a) \frac{dV_0}{dt} = 5.10^7 \text{ kV.s}^{-1}.$$



$$b) \frac{dV_0}{dt} = 5.10^8 \text{ kV.s}^{-1}.$$



$$c) \frac{dV_0}{dt} > 10^8 \text{ kV.s}^{-1}.$$

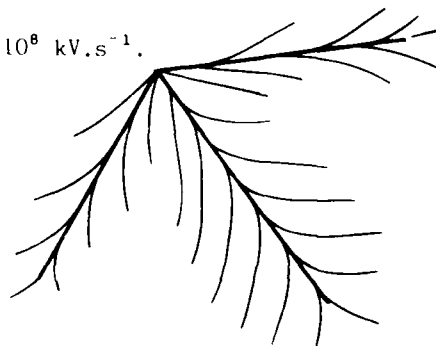
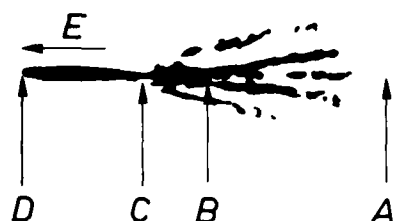


Fig. 3 Different configurations of surface discharges.

In guided mode, the photograph (Fig. 4) on the image converter with a very short exposure time (approximately 10 ns) shows in the first analysis that the discharge consists of a first zone, with streamers spread out, then a second zone corresponding to a complex transition phase where the electric field remains high but the electron density becomes very high. The last zone includes two phases: a gas thermalization phase and an expansion phase connected to the excitation electrode.



a)



b)

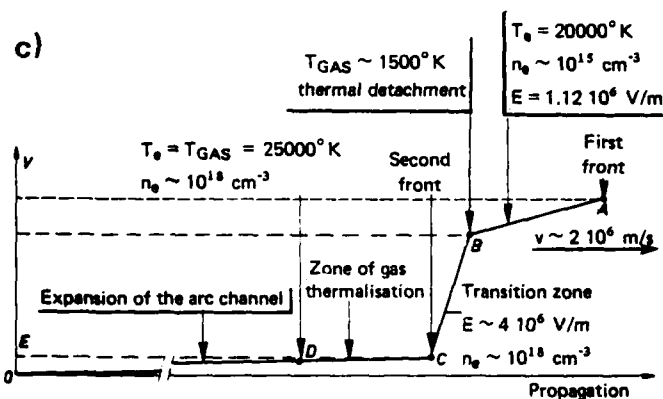


Fig. 4 - Structure of an high current surface discharge.

This scheme clearly shows that, under these propagation conditions, the various plasma transition phenomena such as the stem and space leader are concentrated in the same phase, appearing as soon as the gas temperature reaches 1500 K (thermal detachment).

The discharge current waveforms as a function of V are graphed in Fig. 5. We see a current rise time on the order of 10 ns.

The first approximation of its peak value is a quadratic function of the voltage V . For the discharge to propagate quasi-continuously, it will be seen that the current I at A must reach 10 to 20 A. These values are not attained in long air-gap breakdowns. At point B, the discharge has reached the end of the dielectric plate.

Measured by optical fibers placed along the discharge path, the propagation velocities v follow a linear law as a function of V and go from 0.5 to $3 \times 10^6 \text{ ms}^{-1}$ under these experimental conditions. Using the discharge current variation law as a function of the applied voltage V , we can calculate the linear impedance of the arc channel, as well as the mean electric field as a function of the current. The channel impedance is greater than $4000 \Omega \text{ m}^{-1}$ for currents less than 10 A, and tends toward $100 \Omega \text{ m}^{-1}$ when $I = 100$ A. For currents going from 10 to 100 A, the mean electric field varies proportionally, from 20 to 60 kV m^{-1} .

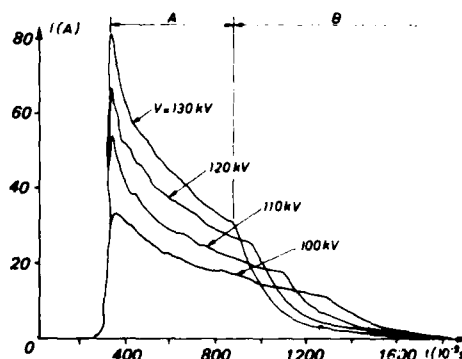


Fig. 5 - Current waveforms of surface discharges.

The relation between the experiments carried out with long air-gaps and the high-current breakdowns carried out at ONERA can be analyzed by looking at the results obtained without guiding the spark. Fig. 6a is a photograph of a branching discharge in negative polarity. The discharge contains many channels which, in certain cases, exhibit right-angle path variations. Even if the channel continues roughly along the same path, many quasi-orthogonal branches can be seen along the main channel, giving rise to very bright secondary channels. Fig. 6b is an enlargement showing that these branches are superimposed on the striations of the primary discharge head, and that consequently the process can occur only after the passage of this primary discharge. This process starts at a point near the middle of the radial extension of the striations. One part goes toward the outside, following a maximum electric field line, and then becomes a lateral branch. The other part is directed perpendicularly to the main channel and is more diffuse in appearance, broadening slightly before it

intercepts the main channel. This phenomenon is perfectly consistent with the data obtained from point-plane discharges at Les Renardières.



Fig. 6 - Comparison between surface discharges and long air-air sparks.

We again find in the scheme (6c) the propagation phases shown in fig. 1b.

These surface discharge analyses thus bring out the relation between the very low-current propagation where no leader appears, the propagation due to leader junctions in a predischARGE zone, and the continuous high-current propagation where the transition from a non-ionized medium to a dense plasma ($n_e \sim 10^{18} \text{ cm}^{-3}$) occurs generally at the same speed as the discharge transition.

Complementary laboratory experiments have also shown that the V-UHF electromagnetic radiation of the discharges is related to the appearance or disappearance of these transition zones. This process gives off characteristic pulses with a rise time of 10^{-8} s. An electromagnetic radiation model based on Rompe and Weizel's theory of air channel ionization [18, 19 and 4] confirms the pulse shapes recorded under laboratory conditions and under actual lightning flash conditions. We will use these radiation sources associated with lightning flashes in attempting to explain certain processes brought out during the phases preceding the return stroke.

LIGHTNING FLASH PRECURSOR PHASE - It is accepted that the phase prior to the establishment of a return stroke, for a ground flash, involves the advance of a stepped-leader luminous process progressing from the cloud to the ground in average steps of 50 m at a propagation speed going from 1 to $8 \times 10 \text{ ms}^{-1}$. The characteristic time between two successive propagations is typically on the order of 50 μs [20, 21]. We know that these easily observable stepped-leaders are highly ionized channels where the temperature of the neutral gases reaches 25,000 K, identical to the arc channels of surface sparks [22]. The charge densities and currents associated with these stepped-leaders have till now been analyzed by interpreting the measurements of the electric field taken on the ground.

More recently, stepped-leaders have been analyzed experimentally using electromagnetic techniques, sometimes in association with conventional optical or electrical measurements, taken on the ground. Three large categories of electromagnetic techniques have been used:

- wide band electromagnetic measurements,
- spectrum analysis measurements of the radiation,
- interferometric measurements to localize the sources of emission.

The first remark to be made concerns the wide band electromagnetic measurements. Many experiments have shown electromagnetic field pulses with a very short rise time going from several nanoseconds [2, 4] to

several tens of nanoseconds [3]. The very fact that these very short rise time exist raises the problem of the physical processes associated with stepped-leader propagation, since they assume that discharge currents are established that vary in the same characteristic times.

An interesting step forward was made with the data on the interferometric localization of the electromagnetic sources, published by Hayenga [23] in 1981 and by Richard [9] in 1983. We will examine two cases of precursors observed during a test program run by ONERA in 1981.

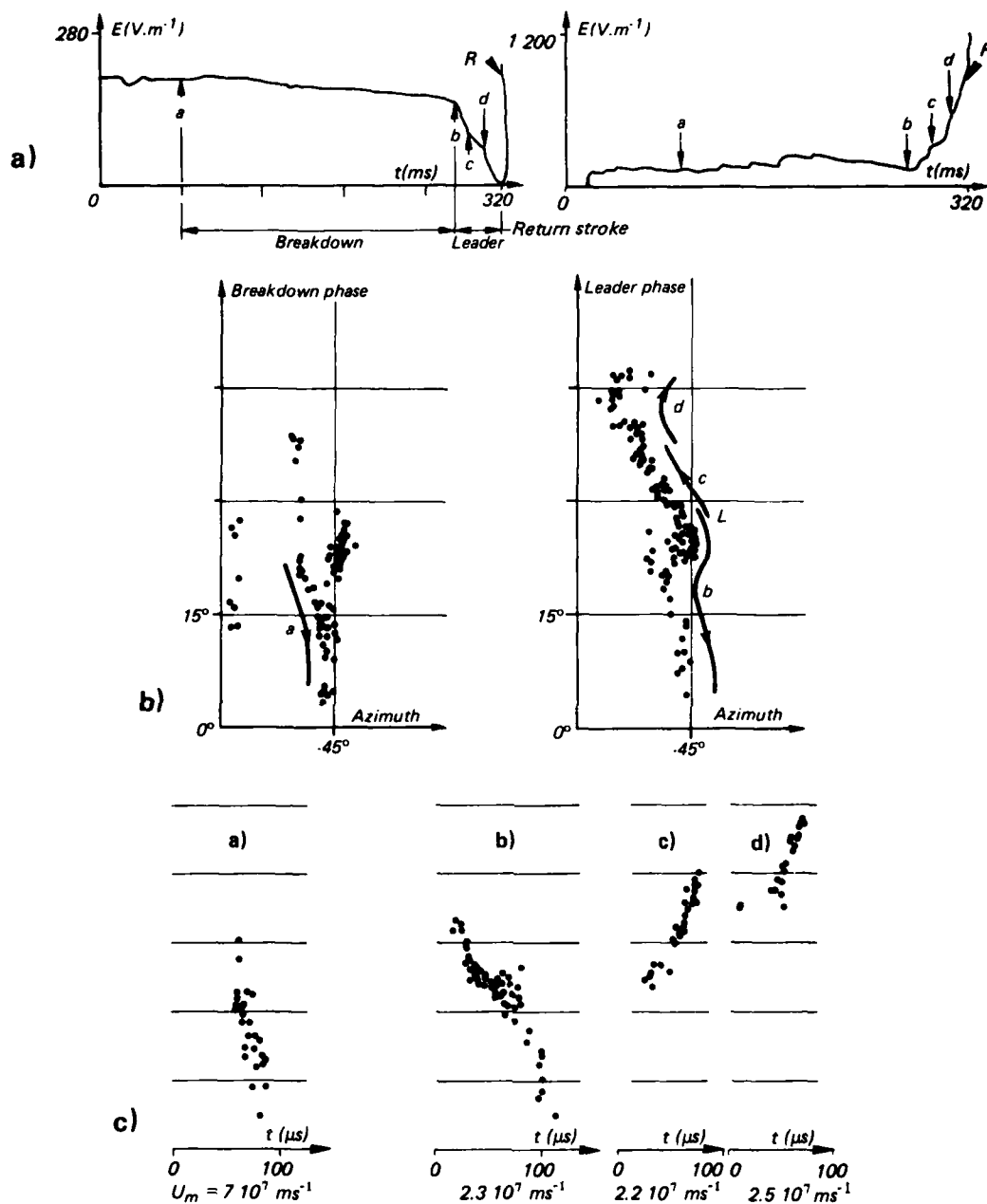


Fig. 7 - Cloud-to-ground lightning flash - VHF sources locations - Example 1.

- a) E-field at ground
- b) VHF sources locations
- c) VHF sources velocities

The first case is illustrated by the measurement data shown in fig. 7. Here we show first of all the variations in the electric field on the ground, recorded at two measuring stations (the system included a total of ten stations). These recordings clearly show an initial breakdown phase (I) corresponding to a rather slow variation in the field, followed by a characteristic phase (II) where the electric field varies more quickly, up to the point where the return stroke is established (III).

In this time interval, lasting some 320 ms, only four very short electromagnetic emission zones can be seen, at times a, b, c and d. The paths of the electromagnetic sources associated with these various zones are given in fig. 7b. The first path, which seems to initiate the entire flash, is directed toward the ground and, as the "streak" mode representation of the process shows, the propagation speed reaches $7 \times 10^7 \text{ ms}^{-1}$. We see that, although the propagation process seems to reach the ground, no ascending leader-type phenomenon or return-stroke occurs in the following 100 ms, which shows that the ionization produced remains very low and that few charges have moved downward. The second path (phase b) follows the same zone, reaches the ground and produces no ascending process either. The third path starts at roughly the same point in space but goes toward the top of the cloud. The fourth path starts at the arrival point of the propagation (c) and also goes upward. The average velocities associated with these three propagations are identical, in the neighborhood of $2.3 \times 10^7 \text{ ms}^{-1}$. Let us note that the following return-stroke emits practically no VHF signal.

With the method initially proposed by Kriebhel [24], we used the ten electric field measurements ΔE_i corresponding to zones a, b, c and d (Fig. 7) to reconstruct the displacements of the corresponding charges. The following remarks can be made concerning the results:

- the ΔE_i data do not express the advance of the electrical charge toward the ground,
- they can only be expressed by dipole charge models,
- these dipoles have a horizontal structure, corresponding to the motion of the negative charges toward the point L from a zone roughly at the same altitude and some 10 km away. These negative charges are then neutralized in the return-stroke.

The propagation processes call for the following comments:

- on the 10^{-4} s scale, the propagation of the emission sources appears to be continuous and with a roughly constant velocity, except for path (b), where two high-velocity displacement phases ($7 \times 10^7 \text{ ms}^{-1}$) are

separated by an intermediate velocity zone (approximately 10^7 ms^{-1}),

- on the 10^{-6} s scale, the electromagnetic radiation is emitted discontinuously. For times less than 10^{-6} s, the interferometric system used cannot detect the number or duration of the elementary pulses.

The second example is a cloud-to-ground flash illustrated in fig. 8. Curve 8a shows the classical variation of the electric field on the ground during a precursor phenomenon leading to a first return-stroke. This evolution lasts some 10 ms. Fig. 8b shows the distribution of the electromagnetic sources detected during the same period. The sources can be observed propagating toward the ground and reaching it in 2 ms without any detectable effect of an ascending leader. After this phase, the source localizations do not show any clear organization. While the return-stroke is being established, the few and small sources of emission are located along the discharge channel. By expanding the time scale in the first phases of the precursor, we observe (Fig. 8c) a very pronounced arrangement of the localization points, giving an image of propagation steps at intervals between 20 and 100 μs .

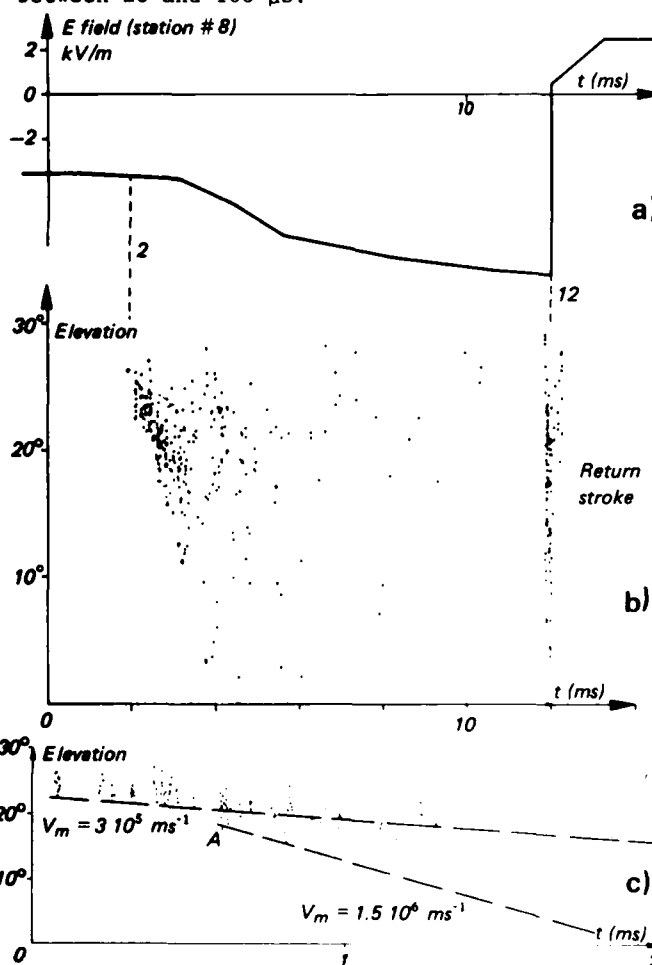


Fig. 8 - Cloud-to-ground lightning flash - VHF sources locations - Example 2.

These jumps progress downward at a rate on the order of $3 \times 10^5 \text{ ms}^{-1}$. It is not possible to define the space distribution rather seems to be random. Starting at point A (Fig. 8c), we see these sources moving downward much more quickly, at $1.5 \times 10^6 \text{ ms}^{-1}$ until the time of probable contact with the ground. During this phase, the altitude distribution of the sources no longer seems to be organized along vertical paths, but seems to fill the ground-cloud space in a random fashion, until the return-stroke is established.

Let us note, finally, that we observe no characteristic electromagnetic emission process associated with the stepped-leader leading to this same return-stroke.

Not enough electric field measurements on the ground are yet available for this example to evaluate the motion of electrical charges between the cloud and the ground with sufficient precision.

DISCUSSION AND CONCLUSION

At the present time we have only a very limited number of lightning flashes available as observed with the 300 MHz electromagnetic source interferometer system. Thus the processes discussed here cannot be taken to be of general value. We will propose only preliminary schemes explaining the current observations, based on data obtained from long air gap breakdowns and from surface discharges.

We have shown that three types of discharge propagation may appear in non-ionized air, depending on the distribution and values of the electrical field existing in the breakdown space.

- a) The first type corresponds to the low-speed displacement (10^4 ms^{-1}) of a negative leader with a predischage zone in front of it, consisting of a space stem associated with positive and negative streamers. The plasma characterizing the stem may periodically undergo electron density transitions at the instants the positive streamers and negative leader come into contact, but these transitions remain very local and do not create a real conductive junction between the stem and the negative leader. The displacement velocity of the negative streamer at the head of the discharge can reach some 10^7 ms^{-1} , depending on the electric field strength.
- b) The second type of propagation is associated with a higher-speed negative leader (10^5 ms^{-1}) that can carry currents reaching 10 A. The predischage zone includes transition phases that grow enough to link the negative leader with the space stem electrically at certain times. The leader then moves in steps (stepped-leader).
- c) The third type is the one where the leader has a propagation speed reaching some 10^6 ms^{-1} and may carry currents greater

than 20 A. The predischage zone, including a phase of negative streamers and a transition zone, moves at the head at the same speed as the leader. Under these conditions, the propagation is continuous.

We propose the following hypotheses:

- for a type a) propagation, the negative streamer may develop over large distances (1 to 2 km) in the precursor phase of a lightning flash;
- each location defined by the interferometer corresponds to the creation of a transition zone where the plasma locally reaches a density of 10^{18} cm^{-3} . If several transition zones are created within a micro-second (the system time resolution), the calculated localization point is the source barycenter.

Assuming these hypotheses, the events shown in figures 7 and 8 can be analyzed as follows:

Event A (Fig. 7) - The localization points of the sources at 300 MHz follow consistent paths. The "streak" mode recordings indicate an ordered propagation of a transition zone of small extent (space stem). The negative leader starts from a spot L in space where negative charges from faraway sites (10 km), roughly at the same altitude as L, have accumulated. These horizontal displacements have often been observed [23]. The head streamers move at speeds greater than 10^7 ms^{-1} . These streamers are associated with very small charge displacements. The junctions between the head streamers and negative leader do not occur, which confirms the fact that, at ground level, no ascending positive leader can develop after the two ground propagations (Fig. 7).

Electromagnetically, the stepped-leader does not appear prior to the return stroke. This can be explained by the existence of a quasi-continuous leader propagation in mode c, which emits practically no electromagnetic radiation.

Event B (Fig. 8) - During the first milliseconds of discharge development, the $3 \times 10^5 \text{ ms}^{-1}$ propagation speed and the organization of the electromagnetic sources along the nearly vertical paths indicate the establishment of a stepped-leader. We observe junctions between the head negative streamers and a negative leader (not detected here) having probably a rather low velocity. The location points of the 300 MHz sources seems to indicate that the junctions are made by several space leaders in series, as the long air gap breakdowns show [14]. We note that the stepped-leader progression dies down at point 1 (Fig. 8c), giving rise to a faster propagation ($1.5 \times 10^6 \text{ ms}^{-1}$) analogous to the one observed during event B. For the same reasons as at point A, the probable contact of the head streamer with the ground does not lead to the establishment of an ascending leader. The final stepped-leader

before the return-stroke is not observed, and must progress quasi-continuously by process c.

This process c, typical of a high-current surface discharge, probably corresponds to the propagation of a dart-leader characteristic of a continuous progression with propagation speeds reaching 10^7 ms^{-1} . By analogy, the leader preceding the return-stroke of the two observed events probably has more dart-leader properties than conventional stepped-leader properties.

These phenomena, observed during the establishment of an initial lightning flash return-stroke, must be gone into in greater depth using a 3-D interferometric system simultaneously with an accurate device analyzing the electric field on the ground and the optical equipment needed for observing the progression of a stepped-leader.

REFERENCES

1. R.A. Perala, T. Rodolph and F. Eriksen, "Electromagnetic interaction of lightning with aircraft". IEEE Transactions on Electromagnetic Compatibility, Vol. EMC 24, n° 2, May 1982.
2. C.E. Baum, E.L. Breen, J.P. O'Neill, C.B. Moore and D.L. Hall, "Measurement of electromagnetic properties of lightning with 10 nanosecond resolution". Proc. Lightning Tech. NASA Conf. 2128, FAA RD 80 30, April 1980.
3. C.D. Weidman and E.P. Krider, "Sub-microsecond rise times in lightning radiation fields". Proc. Lightning Tech. NASA Conf. 2128, FAA RD 80 30, April 1980.
4. G. Labaune, A. Delannoy, P. Richard and P. Laroche, "Hypothèses sur les mécanismes du rayonnement VHF6UHF de l'éclair". 2ème Col. National sur la Compatibilité Electromagnétique, Trégastel, 1-3 juin 1983, TP ONERA n° 1983-45.
5. M. Uman, M. Master, E.P. Krider, "A comparaison of lightning electromagnetic fields with the nuclear electromagnetic pulse in the frequency range 10^4 - 10^7 Hz". IEEE Transactions on Electromagnetic Compatibility Vol. EMC 24, n° 4, Nov. 1982.
6. W. Butters, D.W. Clifford, K.P. Murphy, K.S. Zeisel and B.P. Kuhlman, "Assessment of lightning test techniques". Proc. Int. Aerospace Conf. on Lightning and Static Electricity, Oxford, March 1982.
7. D.W. Clifford and K.S. Zeisel, "Evaluation of lightning induced transients in aircraft using high voltage shock excitation techniques". IEEE Int. Symp. on Electromagnetic Compatibility, San Diego, Oct. 1979.
8. S. Larigaldie, G. Labaune and J.P. Moreau, "Lightning leader laboratory simulation by means of rectilinear surface discharges". J. Appl. Phys., vol. 52, n° 12, pp. 7112-7120, Dec. 1981.
9. P. Richard, A. Delannoy, G. Labaune and P. Laroche, "VHF interferometric imaging of lightning". Int. Conf. on Lightning and Static Electricity, Fort-Worth, June 1983.
10. P. Laroche et al, "A contribution to the analysis of triggered lightning: first results obtained during the TRIP 82 experiment". Int. Conf. on Lightning and Static Electricity, Fort-Worth, June 1983.
11. M.A. Uman, "Comparison of lightning and a long laboratory spark". Proc. of the IEEE, Vol. 59, n° 4, April 1971, pp. 457-466.
12. R.E. Orville, M.A. Uman and A.M. Sletten, "Temperature and electron density in long air sparks". J. Appl. Phys., Vol. 38, Feb. 1967, pp. 895-896.
13. Les Renardières Group, "Positive discharges in long air gaps - 1975 results and conclusions". Electra, n° 53, July 1977.
14. Les Renardières Group, "Negative discharges in long air gaps at Les Renardières". Electra, n° 74, Jan. 1981.
15. R.T. Waters, "Spark breakdown in non uniform fields" in Electrical breakdown of Gases, Edited by J.M. Meek and J.D. Graggs, John Wiley and Sons Ltd, 1978.
16. G. Baldo, "Spark-over characteristics of long gaps" in Electrical breakdown and discharges in gases. Fundamental processes and breakdown. Edited by E.E. Kunhardt and L.H. Luessen, NATO ASI Series, vol. 89a, 1983.
17. M. Toepler, Ann. Phys., n° 12, 13, 1906.
18. R. Rompe and W. Weisel, Ann. Phys., n° 1-6, 285, 1947.
19. G. Labaune and S. Larigaldie, "Relations between nanosecond spark breakdown, high current leader propagation and electromagnetic radiation from lightning". To be published in J. Appl. Phys.
20. R.H. Golde, "Lightning Vol. 1 - Physics of Lightning", Academic Press, 1977.
21. M.A. Uman, "Lightning", Advanced Physics Monograph Series, Mc Graw-Hill Book Company, 1969.
22. M.C. Bordage and G. Hartman, "Spectroscopic measurements on discharges along a dielectric surface". J. Appl. Phys., Vol. 53, n° 12, Dec. 1982.
23. C.D. Hayenga and J.W. Warwick, "Two dimensional interferometric positions of VHF lightning sources", J.G.R., Vol. 86, n° C8, pp. 7451-7462, 1981.
24. P.R. Krehbiel, M. Brook and R.A. McCrory, "An analysis of the charge structure of lightning discharges to ground", J.G.R., Vol. 84, pp. 2432-2456, 1979.

BIPOLAR CORONA AND AIRCRAFT TRIGGERED DISCHARGES

J. A. Ricknell and B. M. Humood
Department of Physics
University of Manchester Institute of Science and Technology
P. O. Box 88, Manchester M 60 1QD,
United Kingdom

ABSTRACT

Recent experimental evidence suggests that aircraft may trigger a lightning stroke when flying in an electrically active environment. The mechanism of this type of breakdown is likely to be different in a number of respects from that commonly associated with long gap breakdown. This is largely due to the distribution and availability of energy: in a thunderstorm the energy density is low but the volumes are large.

The bipolar corona, which must inevitably occur from aircraft in a space charge field consists of the usual negative corona with characteristic Trichel pulses together with positive corona. In the fields commonly encountered, the negative corona remains localised. The positive corona may adopt either a streamer or a glow mode and it is the streamers, which have a relatively low propagation field (~ 4 kV/cm at atmospheric pressure), that most probably make the field energy available to a potential discharge. By contrast, the glow mode remains localised, exhibits a significantly lower current and thus requires larger fields for breakdown. Thus if this glow mode could be stabilised a measure of corona shielding would be obtained. As an illustration, some observations of bipolar corona made using cylindrical conductors are reported.

INTRODUCTION

AIRCRAFT DISCHARGES can be classified into two major groups depending upon the predominant cause of the discharge. These causes are principally:

- (1) Aircraft charging e.g. p-static
- (2) Enhancement of the space charge field.

Here a discharge refers to any event involving ionisation of the surrounding medium from low current corona to high current arcs. Obviously these causes are not mutually exclusive. Under most relevant operating conditions, the aircraft will encounter space charge fields as well as being subjected to some charging process. However, the type of discharge observed and its evolutionary prospects will depend very much upon cause.

If charging is primarily responsible then the aircraft is left with a net charge which although small raises the aircraft to a high potential because of its small capacitance. This high potential leads to corona, either from purpose-designed static wicks or other extremities, and thus the dispersal of the accumulated charge. The corona is monopolar - depending only upon the sign of the charge - and the total stored energy is small.

It has been argued that because this stored energy is so small, aircraft can never trigger high current discharges and so, ultimately, a lightning stroke. Provided the aircraft is flying in a region where the space charge or ambient field is negligible then this is a realistic assessment. With increasing field the characteristics of any discharge will change as the aircraft charging becomes relatively unimportant. The corona, for example, will become bipolar and, should the field be sufficient, the positive corona streamers in particular may develop well away from the aircraft at a velocity 10^5 ms^{-1} . The available energy, which is stored in the large scale electric field, is much increased and is further enhanced as the propagation distance rises. Bicknell and Shelton (1) have suggested that a minimum propagation distance exists beyond which sufficient energy is provided to promote the sharp increase in streamer channel conductivity required before high current discharges are possible. Kasemir (2) has discussed the energetics of static discharges and the possibility of triggered lightning whilst Gerlach et al (3) have elegantly demonstrated the actual triggering of lightning by an F106.

Following an analysis of pilot strike records Clifford (4) reports that a strike is apparently either a slow or, a relatively rare, fast event; the slow event is characterised by a building-up of local discharges before a breakdown. One evident interpretation is that the fast strike is caused by a stroke originating elsewhere in the cloud whilst the slow event is the development of aircraft corona as outlined above. Should this be an accurate interpretation then there exists the possibility of modifying the corona so as to prevent or inhibit the transition to an arc. This possibility arises because of the dual nature of positive

corona which may exist in the glow or streamer mode. The glow mode, unlike the streamer, does not propagate in an ambient field, generates a lower current and so requires larger fields for breakdown. Thus the maintenance of the glow at aircraft surfaces would provide a measure of corona shielding against the more prevalent discharge reported by Clifford. Some of the factors which determine the mode are reported here. They represent part of a wider study of corona from isolated conductors.

EXPERIMENTAL ARRANGEMENT

Conductors are supported on quartz rods in a uniform field established between plane electrodes of 0.45m diameter with a maximum separation of 0.13m; this separation is limited by the dimensions of a GRP chamber enclosing the electrodes which allows gas and pressure variations to be made. A 120kV source supplies the gap through a 12M charging resistor; the corona current is measured across a small resistor in series with the low tension electrode. Photomultipliers monitor the corona optical output from both conductor extremities. In addition to monitoring the frequency variation, the photomultiplier output allows the transition from glow to streamer mode to be identified; in the presence of a glow the negative Trichel pulses are regular but display marked frequency and amplitude modulation at streamer onset.

GLOW-STREAMER MODES

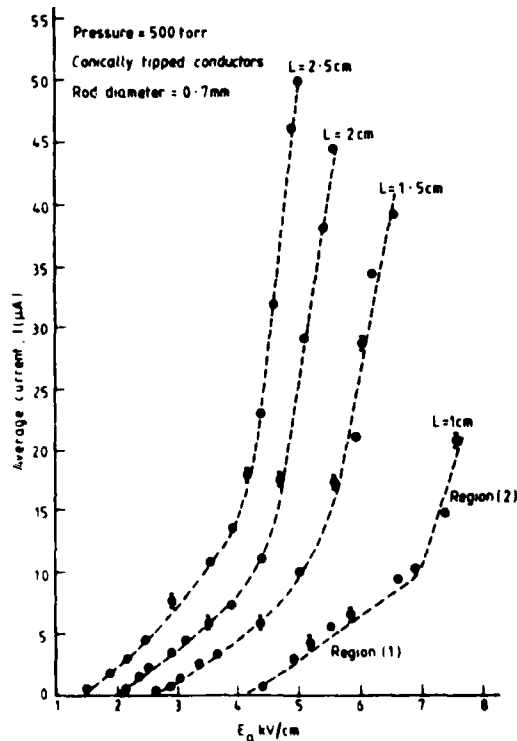


Fig 1

Some results obtained using cylindrical rods are presented here as an illustration of the phenomena. The rods have a length L (10-24mm) and diameter D (0.35-1.00mm) terminated either with hemispherical (H) or conical (C) ends with a half angle of 15° ; they may be symmetric (H-H or C-C) or asymmetric (H-C).

The corona current generated by a C-C conductor is shown as a function of ambient field and length in fig (1). For all lengths, at this particular diameter, a glow-streamer transition occurs which coincides with the sharp increase in the current. Not all conductors exhibit this mode switching. Short H-H conductors for example display only the streamer between corona onset and breakdown. Mode diagrams, such as that shown schematically in Fig (2), are useful for anticipating the expected mode

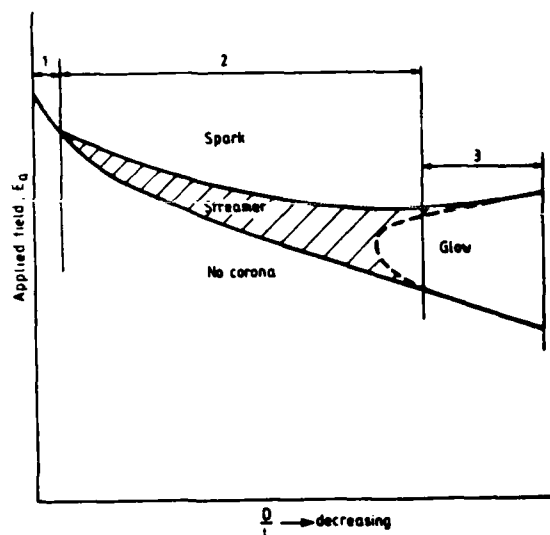


Fig. 2

The lower curve represents the corona onset whilst the upper curve is the breakdown time. With $D/L = 1$ (e.g. spheres) then the corona onset field is large enough to give immediate breakdown (section 1). With the appearance of a glow the breakdown field often increases (section 3). This is probably attributable to the significantly lower current observed during a corona glow as compared with that provided by streamers. For this particularly class of conductor, the average corona current increases linearly with the function $E_a(E_a - E_0)/p$ for an air pressure p in the range 300 p 760 torr; E_0 is the corona onset field (Fig.3).

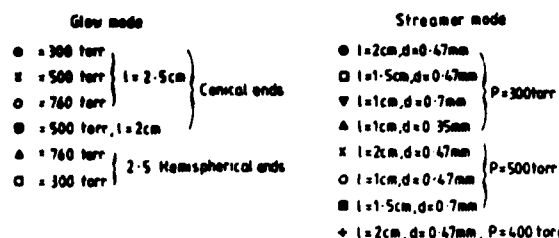


Fig 3

This illustrates clearly the sharp increase in current to be expected when switching from glow to streamer mode.

The behaviour of the asymmetric conductors emphasises, the possibility of increased protection if the glow mode is maintained. Fig. (4) provides a summary of the modes obtained for the given conductor parameters. The negative corona for all conductors consists of Trichel pulses - regular in the presence of the glow mode but modulated should streamers occur. The two asymmetric conductors (2 and 3) both exhibit the same onset field but conductor (2), which maintains a positive glow, requires a field of over 5kV/cm for breakdown whilst conductor (3), because of the streamer mode, leads to breakdown of the same gap at 3.8kV cm.

Rod diameter = 0.7 mm
 Conductor length = 1.5 cm
 Applied field, $E_0 = 3.5 \text{ kV/cm}$
 Pressure = 300 torr

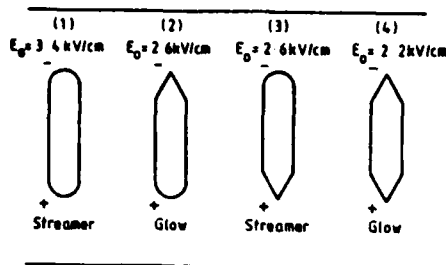


Fig 4

CONCLUSION

If aircraft triggered discharges are to occur then the energy required must be supplied from that stored in the space charge field surrounding the aircraft. Since the energy density is low, some mechanism for tapping the energy from large volumes is required. Given their unusually low propagation fields, positive corona streamers are the most likely mechanism. The positive corona may occur in two forms; the glow mode and the streamer mode. In the glow mode, the current is significantly lower and more diffuse than in the streamer mode so that larger fields are required for breakdown. If the aircraft corona can be maintained in the glow mode then a measure of corona shielding may be achieved. A study of simple cylindrical conductors indicates that geometrical factors, such as aspect ratio, can affect the observed mode; other possible factors are being investigated.

REFERENCES

1. J.A. Bicknell and R. W. Shelton, Section 7.23. Seventh International Conference in Atmospheric Electricity, Albany, New York, 1984
2. H.W. Kasemir, Section 24.1. 8th International Aerospace and Ground Conference, Fort Worth, 1983.
3. J. Gerlach, V. Masur and B. Fisher, *ibid.* Section 90.1
4. D.W. Clifford, AGARD Lecture Series No. 110, NATO, 1980

FEDERAL LIGHTNING DETECTION SYSTEMS IMPROVE
AGENCY OPERATIONS, BUT ARE INEFFICIENTLY LOCATED,
AND LACK COORDINATION TO FORM A NATIONAL NETWORK

J.S. Bunting
Office of Inspector General, Office of Audits
Denver Regional Office, 1020 15th Street, Suite 2241
Denver, Colorado 80202

ABSTRACT

Existing and planning lightning detection systems by Federal agencies could provide double or even triple coverage in some geographic areas, while other areas with more frequent thunderstorms have no coverage. Duplication of equipment and operating costs is possible since each agency operates its lightning detection system independently. Opportunities exist to coordinate the testing of equipment, siting of lightning detection systems, sharing of equipment and exchanging of lightning information. Benefits derived from a national network include expanded geographic coverage and increased efficiency of lightning detection systems for Federal agencies having operational or research requirements for lightning information.

LIGHTNING DETECTION SYSTEMS ASSIST AGENCY OPERATIONS

SEVERAL FEDERAL AGENCIES are using or plan to use lightning detection systems to improve their operations. (1)* Lightning detection systems assist forest fire fighting, aircraft refueling, munitions handling, space shuttle launches and weather forecasting. In addition, commercial users of lightning detection systems provide lightning information for electrical power-line repairs, television weather forecasts, and outdoor recreational activities. Actual or anticipated improvements in the efficiency and economy of agency operations are responsible for the increase in the use of lightning detection systems, even though the systems are not 100 percent accurate.

FIGHTING FOREST FIRES - The Department of the Interior, Bureau of Land Management (BLM) operates a lightning detection system covering 900 million acres to fight forest fires on public lands in 11 Western States and Alaska. (2) Despite Smokey the Bear, lightning starts about 10,000 forest fires a year in the United States. The lightning fire hazard is especially serious in remote areas due to greater difficulty of early detection and fire fighting. Meteorological satellites and weather radars identify systems and precipitation, but not lightning. Since some clouds produce lightning but very little precipitation, the assistance of a lightning detection system to locate lightning directly is a valuable tool.

The BLM uses its lightning detection system, in operation since 1976, to identify areas where lightning is occurring, it sends fire detection aircraft and sometimes even fire fighting crews directly to those areas. The cost of detecting and controlling lightning-caused fires has been reduced. Earlier warnings from lightning detection systems locate forest fires earlier and reduce fire fighting costs. According to reports, weather forecasters find the lightning detection system useful for regions out of weather radar range. The location, direction, and development of thunderstorms can be used to forecast hazards and to improve interpretations of weather radar displays. Lightning detection systems record 70 to 90 percent of cloud-to-ground lightning. (3) They occasionally mistake something else for lightning, and sometimes give an erroneous location for the lightning strike. Overall, the BLM fire management and fire weather personnel have found the lightning detection systems to be a valuable tool for locating lightning.

* Numbers in parentheses are References at the end of the paper.

ASSISTING NAVAL OPERATIONS - The Department of the Navy (Navy) operates a lightning detection system at the Naval Air Station and Naval Oceanography Command Detachment at Cecil Field, near Jacksonville, Fla. The Navy is planning to expand to a lightning detection network covering the east coast, gulf coast, Mississippi River and part of the west coast. The Naval Oceanography Command has the responsibility to forecast thunderstorm activity, to predict the direction and movement of thunderstorms, and to provide early warnings of thunderstorm activity to local Navy commands. The specific requirement for accurate data has significantly increased in recent years. New Naval and Marine Corps weapons systems that employ electro-explosive detonating devices are extremely sensitive to nearby lightning strikes. Aircraft and shipboard fueling operations are seriously hampered or curtailed during periods of thunderstorm activity. Large computer centers are also particularly vulnerable to power surges caused by lightning coming from thunderstorms. Precise knowledge of thunderstorm activity within the surrounding area, including the past movement of these systems, is invaluable in predicting future thunderstorm movements.

A high false-alarm rate and too many "after-the-fact" or late warnings were the main reasons for examining the capabilities of lightning detection systems. With equipment designed to detect lightning coming from a thunderstorm, the false-alarm rate could be significantly reduced, past history of thunderstorms would be better known, and forecasts could be more accurate. By reducing the false-alarm rate, savings in personnel hours could be realized by securing thunderstorm-dependent operations only when absolutely required. In addition, with the same equipment, fewer "after-the-fact" warnings should occur.

Tests conducted for a 6-month period by the Navy on a commercially available lightning detection system were very encouraging.

- No false alarm thunderstorm warnings were issued after installation of the lightning detection system.

- All thunderstorm warnings provided at least 20 minutes lead time.

- One false lightning stroke per half hour was observed during heavy thunderstorm activity. The false lightning stroke could be easily recognized and discarded since it appeared randomly.

- Only one failure of the lightning detection system occurred in six months. Lightning struck a telephone modem.

An additional benefit of the lightning detection system was its apparent ability to detect severe thunderstorm cells that

could cause wind and hail damage. Procurement of lightning detection systems by the Navy is expected to begin in late spring or summer, 1983.

PROTECTING SPACE SHUTTLES - NASA uses lightning detection systems to improve the safety of space shuttle launches and for severe thunderstorm research, including a lightning mapper from space. Apollo 12, with a crew on board and a mission to land on the moon was struck by lightning shortly after lift-off on November 14, 1969. To protect future space shuttle launches, a lightning detection system was installed in 1972 at Kennedy Space Center.(4) Having timely and accurate lightning information can avert a possible catastrophe by postponing a launch when the hazard is too great. Knowing the lightning hazard has passed or is insignificant can save \$5 million in costs needed to reschedule a launch. Since 1979, NASA has conducted research on the feasibility of mapping lightning from space by using a sensor on a geostationary satellite.(5) Lightning detection systems used in severe thunderstorms research could provide "ground truth" for a satellite mapper as well as valuable information on lightning in the interim. NASA operates lightning detection systems at Kennedy Space Center, Fla.; Langley Research Center, Va.; Goddard Space Center, Md.; and Wallops Island Flight Center, Va. Also, NASA has installed a lightning detection system at Marshall Space Flight Center, Huntsville, Ala.

These three Federal agencies -- BLM, the Navy and NASA -- are cited as examples of agencies with operational requirements for lightning detection systems. Each of the three has or expects to improve the effectiveness of the agency by increasing the efficiency and economy of their operations. Other Federal agencies are using or funding lightning detection systems, too. The U.S. Air Force uses lightning detection systems in Florida and Colorado to assess lightning hazard to refueling aircraft and to anticipate commercial power failures. The Department of Energy has funded a lightning detection system for Tampa Electric Company to study the effect of lightning on electric power distribution lines. (6) NASA and the NSF have funded weather research at the State University of New York at Albany using lightning detection systems.(7) NOAA uses lightning detection systems in weather research at Norman, Okla.,(8) and Boulder, Colo. The FAA uses a lightning detection system in thunderstorm avoidance along the Gulf of Mexico and adjacent southern states.(9) Although some of the lightning detection systems are used in research, these systems can operate year-round to meet other Feder-

al agencies' requirements. At least eight Federal agencies have operational requirements or research uses for lightning detection systems. As so many Federal agencies independently use lightning detection systems, the need for coordination increases to avoid potential duplication of equipment and operating costs.

NWS NEEDS TO COORDINATE THE GEOGRAPHIC COVERAGE OF FEDERAL LIGHTNING DETECTION SYSTEMS

Existing and planned lightning detection systems operated or funded by Federal agencies could provide double or even triple coverage in some geographic areas, while other areas with more frequent thunderstorms have no coverage (See Figs. A-1, 2,3). Duplication of equipment and operating costs already exists, and much more is possible since each agency independently operates its lightning detection system. In 1963, Office of Management and Budget (OMB) Circular A-62 assigned the responsibility for coordination of Federal meteorological services, such as lightning detection systems, to the U.S. Department of Commerce.(10)

Costing \$50,000 to \$70,000 for equipment and more for communications, a lightning detection system covers a maximum area of 250 miles. As many as 10 planned systems have substantial overlapping coverage. In addition, as many as five systems could be used to provide coverage where none is planned now. Figs. A-1,2,3 show areas with potential double or triple coverage of lightning detection systems and areas with no coverage. Analysis of these figures highlights the following.

- West Texas, with 70 thunderstorms a year, would have no coverage. Areas of the Middle Atlantic States, with 40 thunderstorms a year, could have triple coverage.

- Most of North Dakota, South Dakota, Minnesota, Nebraska, and Kansas with 30 to 70 thunderstorms a year, would have no coverage. California, with 5 to 20 thunderstorms a year, could have double coverage.

- Eastern Ohio, eastern Kentucky and western West Virginia with 50 to 70 thunderstorms a year, would have no coverage. Most of New England, with 20 to 30 thunderstorms a year, could have double coverage.

The lack of coordination in planning lightning detection system locations and the meteorologically inconsistent placement of lightning detection systems are evident.

Within the U.S. Department of Commerce, NWS has responsibility for coordinating Federal meteorological services.(11) The failure to coordinate geographic cover-

age of Federal lightning detection systems has resulted in overlapping coverage in low thunderstorm frequency areas, omission of coverage in some high thunderstorm frequency areas, and meteorologically inconsistent geographic coverage.

NEED TO FORM A NATIONAL NETWORK OF FEDERAL LIGHTNING DETECTION SYSTEMS

Potential exists for a national network of Federal lightning detection systems to eliminate double or triple coverage in some geographic areas, to provide coverage in areas where none is planned now, and to increase the efficiency of Federal lightning detection systems. Areas of interagency cooperation include testing, siting, sharing equipment and operating costs, and exchanging data. Network equipment costs should be no more than costs for existing and planned lightning detection systems. However, communication costs may be higher than for existing lightning detection systems as Federal agencies seek to link up with a national network, rather than procure additional lightning detection systems.

To assure all agencies of the accuracy and reliability of lightning detection systems, a side-by-side operational test should be conducted by an impartial interagency organization with appropriate technical expertise. Two major manufacturers of lightning detection systems have already stated a willingness to cooperate with a side-by-side operational test. The Department of the Interior, Bureau of Mines conducted a side-by-side operational testing of lightning detection systems, but had available equipment from only one of the two commercial manufacturers and research equipment.(12) Performance features tested were mean warning time, number of false alarm, failure to alarm, valid alarms and mean time to clear. Agencies could add other performance features to future tests.

SHARING SITES AND EQUIPMENT HAS ALREADY BEGUN - Interagency cooperation in siting lightning detection systems has already started and needs to increase. BLM and USFS have cooperated in lightning detection system siting for fire fighting in 11 Western States. NASA and NSF have funded the State University of New York (SUNY) at Albany for research with a lightning detection system. NASA has integrated lightning detection systems at Dahlgren and Wallops Flight Center, Va., into the east coast network operated by SUNY. The U.S. Department of Commerce, Environmental Research Laboratories in Boulder, Colo., and the U.S. Air Force share lightning detection data and operate separately purchased equipment as one system. Weather Service

Office at Jacksonville, Fla., aided the Naval Oceanography Command by providing a location for one lightning detection antenna for a northeast Florida system. The Navy recognizes that planned lightning detection systems for the east coast, gulf coast, Mississippi River Valley and west coast require cooperation with other Federal agencies for location of some lightning detection antennas and master stations for the total system planned.

Sharing or pooling of equipment to form and operate a larger, more efficient lightning detection system is another example of interagency cooperation. A few combined systems have included two agencies: BLM - USFS in 11 Western States and the Environmental Research Laboratories - the Air Force in Colorado. The NASA-SUNY system along the east coast also include participation by NSF.

Sharing or pooling of equipment is important to avoid duplication of expensive lightning detection systems. One manufacturer estimates 1981 procurement costs of less than \$1.5 million in addition to systems already purchased from the manufacturer, to provide a national network of lightning detection systems. The estimate does not include integrating other companies' equipment into the national network. In addition, communications and operations costs would be substantial. BLM estimates over \$500,000 in year-round communications and operations cost for an 11 state system. Savings in procurement costs of equipment or accessories are one time savings. However, communication costs are substantial and recur over the life of the lightning detection system. Reducing communication and operating costs by combining two overlapping systems into a larger more efficient system could save an amount equal to the equipment and operating cost.

COORDINATING COVERAGE AND EXCHANGING DATA IS NEEDED - Providing lightning detection system coverage for areas without any planned coverage could complement other NWS programs to reduce deaths from flash floods and lightning. Events provided dramatic evidence of the heavy death toll and property damage from flash floods and lightning, especially in the Northern Great Plains states, where there is no coverage.

-- South Dakota's Black Hills, on the fringe of a lightning detection system, were struck by a series of thunderstorms with extremely heavy rains in June 1972. Catastrophic flash flooding developed along a two-block-wide, 12-mile-long stretch of Rapid Creek that flows through Rapid City. Two hundred and thirty seven people died and more than \$100 million in property damage was recorded.(13)

-- Minnesota's border with North Da-

kota and South Dakota experienced six flash floods in a five-year period from 1973 - 1977.(14)

-- Nebraska and Kansas had among the highest frequency of lightning incidents (deaths, injuries and property damage) per million people from 1968 - 1977, surpassed only by three other states.

To increase the efficiency of existing lightning detection systems and to assure effective use of lightning detection systems procured by Federal agencies in the future, sharing or pooling of equipment is imperative.

Opportunities exist to expand data sharing from lightning detection systems. Examples of expanded use of lightning detection systems which could potentially increase the efficiency of operations are the following:

-- The Navy's use of lightning detection systems to increase safety of shipboard and aircraft refueling by reducing false alarms and late warnings could benefit the Air Force, Army, and Coast Guard. The FAA might find lightning data useful for terminal forecasts.

-- BLM - USFS lightning detection systems in 11 Western States could provide the Navy with lightning data, at least while the Navy awaits procurement of its own system, and perhaps permanently.

-- The east coast network operated by SUNY at Albany and supported by NASA could provide lightning data to the Forest Service, and possibly to BLM, to improve forest fire fighting in New England and Middle Atlantic States. The Forest Service has national forests in these states but no lightning detection system east of the Mississippi River.

- BLM - USFS system and the Navy's planned system could provide a wider area of ground truth for a future satellite lightning mapper for NASA. Regional, seasonal, and diurnal variations in lightning could be observed over a larger area. In addition, public utilities seeking lightning data to increase the efficiency of repair crews and minimize risk could use information from an expanded or national lightning detection network. Existing and planned lightning detection systems operated or funded by Federal agencies could form the basis for a national lightning detection network.

CONCLUSIONS

1. At least eight Federal agencies have operational requirements or research uses for lightning detection systems.

2. Interagency cooperation needs to be expanded in the areas of testing, siting and sharing of lightning detection systems.

3. Failure to coordinate geographic

coverage of Federal lightning detection systems has resulted in overlapping coverage in low thunderstorm frequency areas and omission of coverage in some high thunderstorm frequency areas, resulting meteorologically inconsistent geographic coverage.

4. Potential exists for a national network to increase the efficiency of existing and planned Federal lightning detection systems.

RECOMMENDATIONS

To improve the economy and efficiency of Federal lightning detection systems, the Office of Inspector General, Office of Audits, recommended that the Assistant Administrator for Weather Services in cooperation with the Federal Coordinator for Meteorological Services and Supporting Research:

1, request Federal agencies to provide plans of existing and future lightning detection systems including geographic coverage, testing needs, siting locations, and equipment specifications;

2, assist Federal agencies seeking lightning information by providing for interagency testing of lightning detection systems, expanding the cooperation in siting lightning detection systems and sharing equipment, and encouraging exchange of lightning information rather than procurement of lightning detection systems additional to those already planned or in operation;

3, coordinate the geographic coverage of lightning detection systems operated or funded by Federal agencies to eliminate multiple coverage in some geographic areas and to provide coverage in geographic areas where none is planned; and

4, form a national network of lightning detection systems with intercommunications capability.

The National Weather Service and the Federal Coordinator for Meteorological Services and Supporting Research have agreed with the recommendations. Currently, a national plan to coordinate lightning data is being developed.

ACKNOWLEDGEMENTS

I would like to thank Becky Purvis for her time and patience in preparing this paper. Special thanks should also go to Dr. Wilfred K. Klemperer, Division of Scientific Systems, Bureau of Land Management and Hugh Christian, Marshall Space Flight Center, National Aeronautics and Space Administration. Additional credit is due to E.P. Krider and Michael Maier for data reproduced on Fig. A-1, Dr. Rodney Bent for material contained in Fig. A-2, and the Commander, Naval Oceanography Command for information supplied in Fig. A-3.

REFERENCES

1. "Thunderstorm Killers -- Flash Floods and Lightning, Need to Improve Severe Weather Forecasting", U.S. Department of Commerce, Office of Inspector General, Denver Regional Office, September 1983.
2. E.P. Krider, R.C. Noggle, A.E. Pifer and D.L. Vance, "Lightning Direction Finding System for Forest Fire Detection", Bull. Am. Meteor. Soc., 61, No. 9, September 1980.
3. R.C. Noggle, E.P. Krider, D.L. Vance and K.B. Barker, "A Lightning Direction-Finding System for Forest Fire Detection", 4th National Conference of Fire and Forest Meteorology, St. Louis, Missouri, Nov. 16-18, 1976.
4. "Lightning Jolts NASA to Guard Shuttle", Science Digest, December 1982.
5. L.S. Christensen, W. Frost, and W.A. Vaughan, "Proceedings: Workshop on the Need for Lightning Observations from Space", NASA CP-2095, Washington, D.C., July 1979.
6. B. Fischer and E.P. Krider, "'On-Line' Lightning Maps Lead Crews to 'Trouble'", Electrical World, May 1982.
7. R.E. Orville, R.W. Henderson and L.F. Boscert, "An East Coast Lightning Detection Network", Bull. Am. Meteor. Soc., 64, No. 9, September 1983.
8. D. Rust, W.R. Taylor, D.R. MacGorman, S.J. Goodman, R.T. Arnold, V. Mazur, "Storm Electricity Research in Oklahoma -- An Overview", 8th International Aerospace and Ground Conference on Lightning and Static Electricity, Fort Worth, Texas, June 21-23, 1983.
9. "The Federal Plan for Meteorological Services and Supporting Research", U.S. Department of Commerce, National Oceanic and Atmospheric Administration, Washington, D.C., March 1982.
10. "Policies and Procedures for the Coordination of Federal Meteorological Services", Office of Management and Budget, Circular No. A-62, November 1963.
11. "National Oceanic and Atmospheric Administration", U.S. Department of Commerce, Department Organization Order 25-58, November 23, 1982.
12. R.L. Johnson, D.E. Janota, and J.E. Hays, "An Operational Comparison of Lightning Warning Systems", J. Appl. Meteor., 21, 703-707, May 1982.
13. E. Kessler, (ed.) "Thunderstorms: A Social, Scientific, & Technological Documentary", Vol. 1, Washington, D.C.: U.S. Government Printing Office, 1981.
14. R.S. Maddox, C.F. Chappell, and L.R. Hoxit, "Synoptic and Mesoalpha Scale Aspects of Flash Flood Events", Bull. Am. Meteor. Soc., 63, 1155-1164, July 1982.
15. M.J. Changery, "National Thunderstorm Frequencies for the Contiguous United States", U.S. Nuclear Regulatory Commission, NUREG/CR-2252, November 1981.
16. R.C. Binford, L.G. Byerly, E.P. Krider, M.W. Maier, A.E. Pifer and M.A. Uman, "Wideband Magnetic Detection Finder Networks for Locating Cloud-to-Ground Lightning", 8th International Aerospace and Ground Conference on Lightning and Static Electricity, Fort Worth, Texas, June 21-23, 1983.

Figs. A-1 thru A-3

THUNDERSTORM FREQUENCY IN THE UNITED STATES AND COVERAGE BY LIGHTNING DETECTION SYSTEMS

A map of annual thunderstorm occurrences with overlays of existing lightning detection systems for the two primary manufacturers and the Navy's planned lightning detection system are presented on the following pages. The need for coordination in locating Federal lightning detection systems is graphically evident by comparing these three figures. The map has three overlays and a composite.

-- A base map of the 48 contiguous United States showing the annual frequency of thunderstorm occurrence.(15)

-- Fig. A-1 shows the coverage provided by existing Federal and private lightning detection systems using Lightning Location Protection equipment. (Obtained from LLP Inc).(16)

-- Fig. A-2 shows the coverage provided by existing Federal and private lightning detection systems using Atlantic Scientific Corporation equipment. (Obtained from ASC).

-- Fig. A-3 shows a planned Navy lightning detection system. (Obtained from the Naval Oceanography Command).

The map and overlays have two qualifications.

-- A few privately operated lightning detection systems appear on the overlays: Detroit Edison company in the Michigan area (red), Atlantic Scientific Corporation in the Florida peninsula (green) and Tampa Electric Company on the Gulf Coast of Florida (red). Tampa Electric Company received Department of Energy funding for installation of its lightning detection system. In addition to these three, TV stations are operating lightning detection systems in Colo., Ga., and Wis.

-- Fig. A-1 gives the illusion of coordination and integrated lightning detection systems where they may not exist. For example, in Colorado the U.S. Air Force and the DDC Environmental Research Laboratories operate one integrated system.

However, some of the same area is also covered by the BLM. There is no connection between the two systems. In Florida, areas covered by the lightning detection systems of Tampa Electric, Kennedy Space Center and the U.S. Air Force overlap. No connection exists between Tampa Electric and the two Federal agencies to exchange lightning information.

Geographic coverage indicated on the map is accurate although small variations may exist for individual systems.

Table A-1
PRESENT USERS AND LOCATIONS OF LIGHTNING DETECTION SYSTEMS IN THE UNITED STATES

LIGHTNING LOCATION AND PROTECTION, INC. (Fig. A-1) - Department of Agriculture, U.S. Forest Service, Northern Forest Fire Laboratory, Missoula, Montana.

Department of Commerce, NOAA, National Severe Storms Laboratory, Norman, Oklahoma; Prototype Regional Observing and Forecasting System, Boulder, Colorado.

Department of the Interior, Bureau of Land Management, Boise, Idaho.

National Aeronautics and Space Administration: Goddard Space Center, Maryland; Kennedy Space Center, Florida; Langley Research Center, Virginia; Marshall Space Flight Center, Huntsville, Alabama; Wallops Island Flight Center, Virginia.

Detroit Edison Company, Detroit, Michigan; Sandia Laboratories, Albuquerque, New Mexico; Tampa Electric Company, Tampa, Florida.

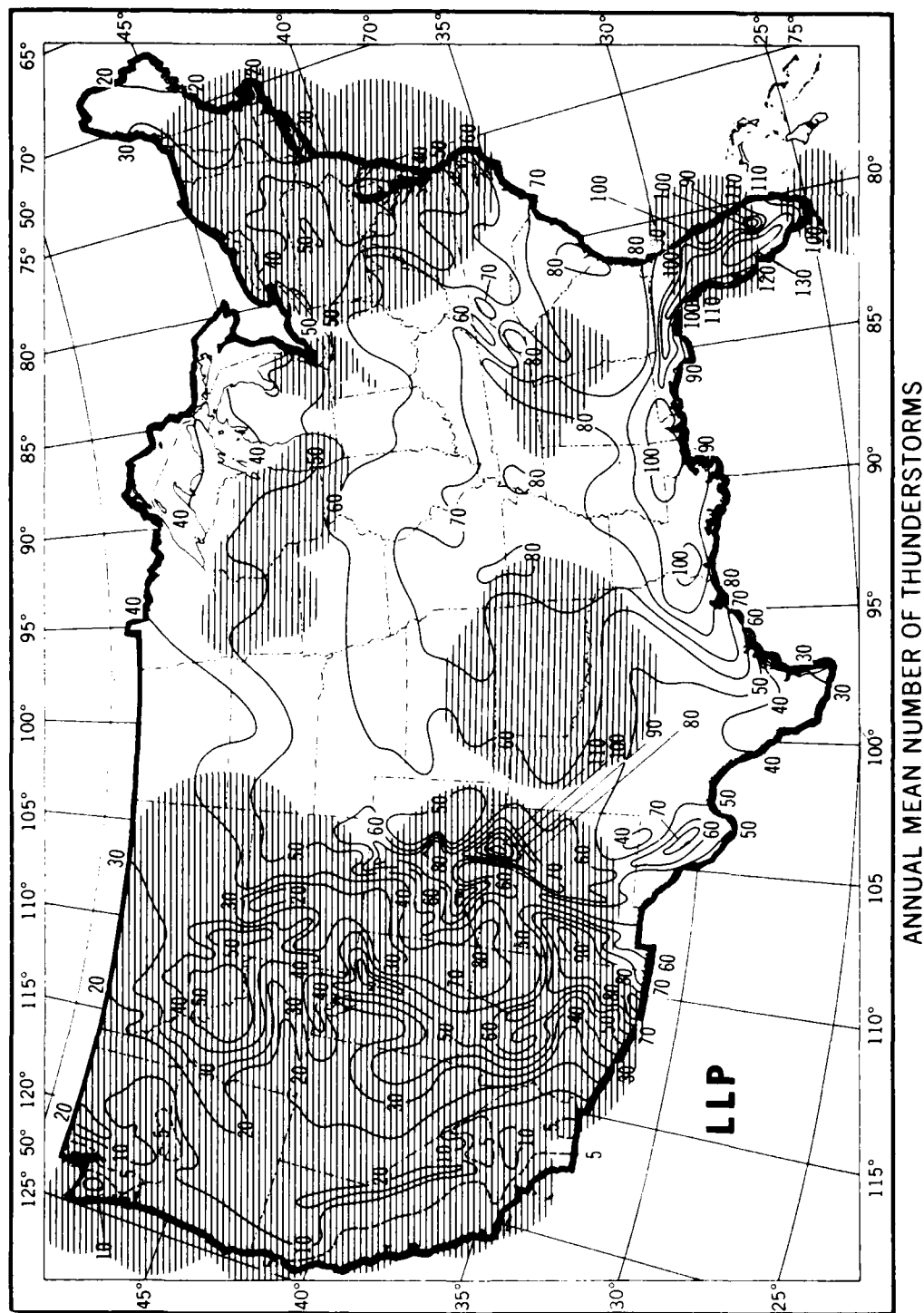
Alaska Department of Natural Resources, Fairbanks, Alaska; California Department of Forestry, Sacramento, California; State University of New York, Albany, New York.

ATLANTIC SCIENTIFIC CORPORATION (Fig. A-2) - Department of Defense, Naval Service Weapons Center, Dahlgren, Virginia.

Department of Transportation, Federal Aviation Administration, New Orleans.

Atlantic Scientific Corporation, Melbourne, Florida.

NAVY (Fig. A-3) - Naval Air Station, Cecil Field, Florida; Naval Oceanography Command, Bay St. Louis, Mississippi.



ANNUAL MEAN NUMBER OF THUNDERSTORMS

Fig. A-1 -- Federal agencies using LLP lightning detection systems

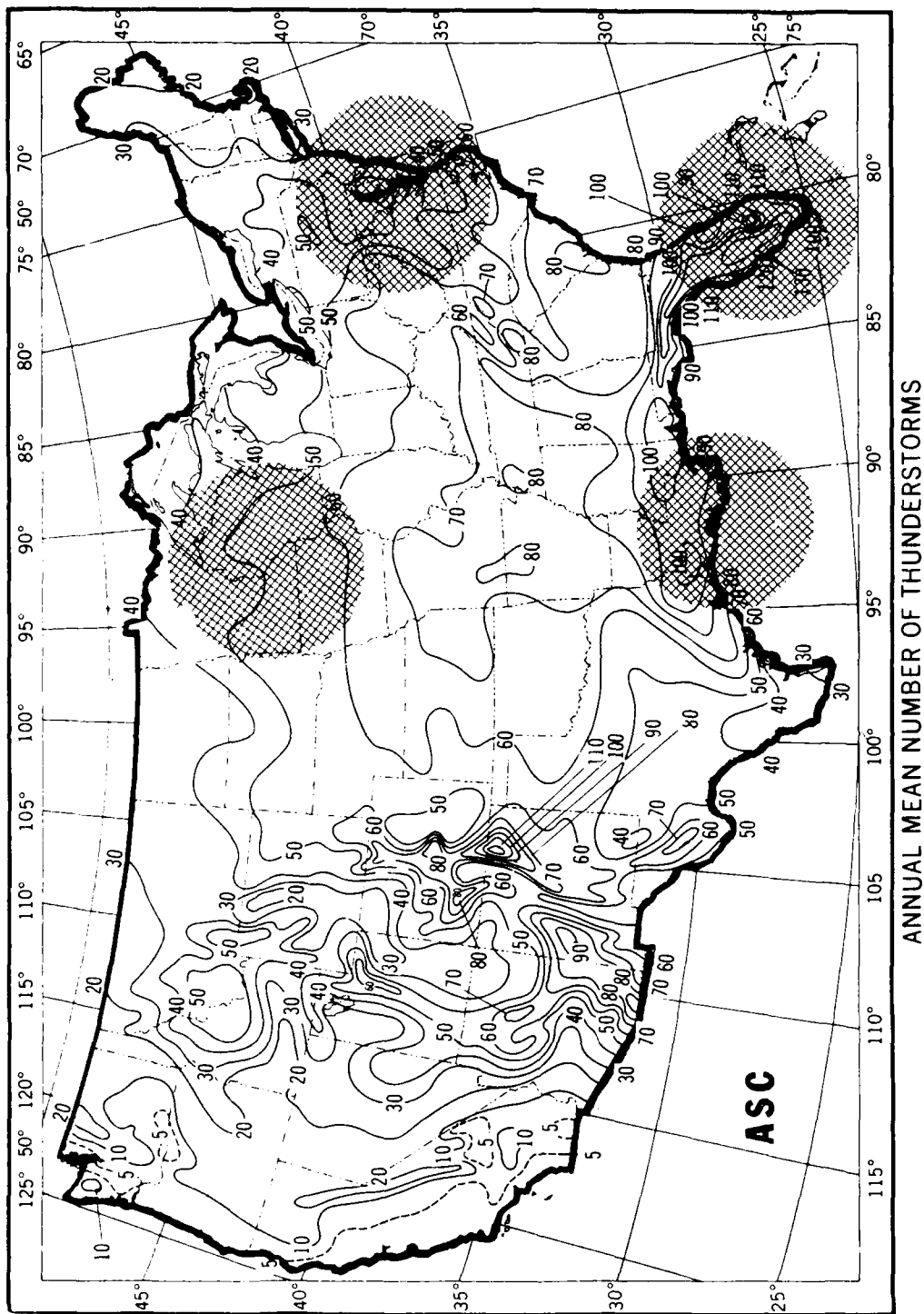


Fig. A-2 -- Federal agencies using ASC lightning detection systems

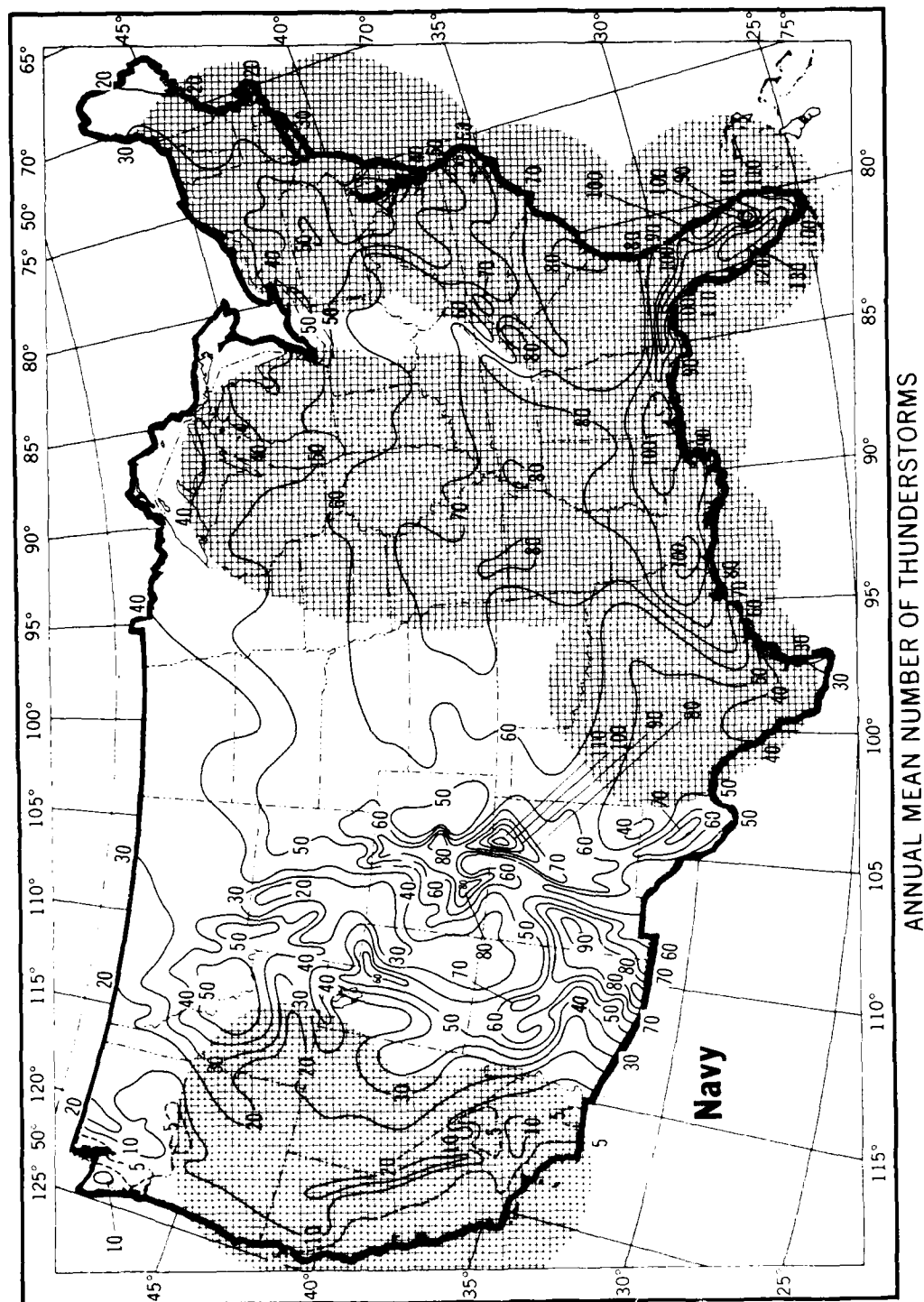


Fig. A-3 -- Proposed Navy network of lightning detection systems

THEORETICAL AND OPERATIONAL EVALUATION OF A TIME-OF-ARRIVAL (TOA)
LIGHTNING POSITION AND TRACKING SYSTEM (LPATS)

R.B. Bent and W.F. Highlands
Atlantic Scientific Corporation, Melbourne, FL 32901
W.A. Lyons
R*SCAN Corporation, Minneapolis, MN 55415

ABSTRACT

There are two satisfactory approaches for operationally locating cloud to ground (CG) lightning strikes: magnetic direction finding (MDF) and time-of-arrival (TOA). MDF systems have been widely used over the past decade. Recent technological breakthroughs now allow the real-time detection and location of lightning ground strokes over a wide area with high positional accuracy. LPATS -- Lightning Position and Tracking System -- utilizes a time-of-arrival (TOA) technique and specifically avoids the use of magnetic direction finding technology. Computer simulations of total system performance under worst case conditions predict locational accuracy of better than 750 m within the polygon inscribed by the 4 to 6 antennas (over a quarter million square miles). Theoretical estimates of the impact of a 2000 m mountain range on the propagation of LORAN-C signals and lightning wave forms introduce worst case location errors on the order of 30 to 300 m. The effect of air temperature variation on LORAN-C signal TOA is also found to be negligible. Techniques to filter out local noise, ionospheric reflections, and in-cloud discharge are described. Calculations show that local perturbations introduced by a 20 km long power line within 30 m lead to locational errors of a mere several meters.

LPATS networks now cover parts of more than 16 states. Field experience gathered since the spring of 1982 suggests that the predicted locational accuracies are being achieved. CG strikes are frequently intercompared with WSR-57 radar echoes and GOES infrared cloud images. This reveals a high degree of internal data coherence and phenomenological consistency. Strike rates of 2000-5000 hour⁻¹ are often observed over the Florida peninsula. A very slow fall-off of detection efficiency with range is indicated by the MN-WI network, which routinely tracks active thunderstorm clusters as far away as Omaha (500 km from the network's center). Initial estimates suggest upward of 85% detection within the antenna polygon, down to 50% at 400 km range. The shape of the detection efficiency curve will be determined by tracking isolated cells by 2 or 3 overlapping LPATS networks. Initial experiments show very high correlations between cells tracked at distances of 160 and 350 nm from two network centroids.

INTRODUCTION

FOR THE OPERATIONAL LOCATION of lightning cloud-to-ground (CG) strikes, there are essentially two approaches: magnetic direction finding (MDF) (Krider, et al, 1976) and time-of-arrival (TOA). MDF systems have been in use for almost a decade. As noted by Pierce (in Golde, 1977), "All techniques for locating the origin of atmospherics are subject to errors. There are three main categories of errors: Those associated with signal variability at the source; those introduced by fluctuations in the propagation characteristics, and those of localized (e.g. topographical influences on direction finding), or instrumental, origin. The relative importance of the categories differs according to the techniques involved. The multistation time-of-arrival (TOA) method is undoubtedly the most accurate way of fixing individual sources. It is also the most costly. Expenses are substantial in installation (elaborate equipment, at least three stations needed), maintenance (accurate timing required), and data processing (complicated geometry)."

Also, Pierce (1982) stated that "a time-of-arrival (TOA) method is by far the most accurate way of fixing the source of an individual sferic. It is also, understandably, the most elaborate and expensive. TOA systems are much less subject to errors than are crossed-looped techniques. Polarization errors are effectively nonexistent; site errors are very small. However, if the potential accuracy of a TOA system is to be realized and confusion between separate atmospherics is to be avoided, interstation timing of approximately 10 microseconds is required. This implies the installation of accurate time standards at each station." Since these assessments were written, the dramatic revolution in microelectronics has resulted in the availability of low cost receivers for easily available timing signals (such as LORAN-C). A four station prototype TOA network was designed by Atlantic Scientific Corporation (ASC) and established in Florida in the spring of 1982. It has been in continuous operation ever since, and is now part of a commercial system (LPATS --Lightning Position and Tracking System).

LPATS now covers part of at least 16 states, serving numerous military, utility, industrial, and broadcasting clients. The initial design criteria called for locational accuracies of at least a mile within the area enclosed by the polygon inscribing the antennas. An effective range of at least 250 km was anticipated. Earlier papers by Bent, et al (1983) and Lyons and Bent (1983) have described the basic system and presented initial examples of its output. This paper summarizes in greater detail the characteristics

of a functioning TOA system and presents additional evidence that the technique works well within its design expectations.

PRINCIPLE OF OPERATION

The TOA system depends on monitoring the accurate time an event occurs at remote sites, and performing spherical hyperbolic geometry in order to determine its point of origin (Hughs and Gallenberger, 1974). Because electromagnetic waves travel approximately 30 m in 100 nanoseconds, then if the time of arrival is monitored to some 100 nanoseconds accuracy, we would anticipate a location accuracy on the order of 30 m.

In order to accomplish the ground stroke detection, the system employs a plurality (at least three and preferably four to six) of geographically separated lightning stroke monitors. Each station consists of a lightning stroke detector and a timing signal generator that is synchronized to within a few hundred nanoseconds with the output of the timing signal generator at each others' respective location. The timing signal can be received from several available sources, including any one of the presently available LORAN-C generators as well as several other ground and satellite based transmitters. It can also be generated from within the LPATS network to each of its receivers by radio link.

The LPATS remote lightning monitor is really two receivers combined. One detects the occurrence and time of a lightning ground stroke and the other receiver listens to the timing source to establish time clock synchronization with the other receivers in the same network. The antenna system used is a combination of a standard vertical whip, plus a horizontal 18" plate mounted on a common mast. The whip is used for timing reception and the plate senses the lightning signals. The antenna system requires no special orientation and may be installed near the ground or at any convenient elevation even in the vicinity of metal structures. The two antennas are electrically independent and are separately connected with coaxial feedline cables to their respective receivers.

Each of the ground stroke detection stations is further connected via a dedicated communication link to a central analyser (CA) facility as shown in Fig. 1. The CA may be located at one of the detection stations if desired. Each of the stations is synchronized with the others by receipt of the timing signal from the selected source. As a result, the only significant error is the propagation delay differential for each listening station. Since each individual differential is fixed and known, it is compensated at the CA during the course of determining the location of the ground stroke.

When a ground stroke occurs, the electromagnetic pulse emitted is detected by each listening station which records the time of detection of the ground stroke by sampling an internal synchronized clock at that particular station. In effect, each listening station records the time that the stroke was detected relative to the standard timing cycle emitted by the selected source. This "time byte" data is then transmitted over the communication link from the detection station of interest to the CA.

At the CA, after compensating the received time byte for relative time signal propagation delay, a calculation of the stroke location is carried out. With four listening stations, the algorithm for determining the location of the ground stroke is reduced to a set of linear equations. For a three station solution, the CA solves the complex explicit non-iterative equations necessary for stroke location and outputs the data in latitude and longitude. The solutions are obtained through spherical hyperbolic geometry; two received times indicate a hyperbola on which the storm lies and the third station provides a second and third hyperbola that intersect the first at the strike point.

The LPATS contains ASC custom built microprocessor cards, each performing different high speed functions at the same time. One of these cards has been developed to allow extremely fast hardware trigonometrical calculations, as a software approach would not allow the multiple return stroke location ability that LPATS has.

The digital circuitry employed in the LPATS system is designed to accomplish the required mathematical routines at extremely high speeds to accurately locate virtually all CG lightning strokes sensed. Separate high performance circuits have been specifically designed by and for ASC to execute required functions. This approach minimizes the number of required components and thereby increases reliability. The reduced number of components allows the equipment to be contained on three to five boards in one small chassis, depending on options selected. The system allows several microprocessors to be operating in the same chassis performing different functions. Thus, we are able to monitor and locate the individual strokes in a multiple lightning flash occurring only 15 milliseconds apart.

With an LPATS system of four antennas, only three of which are required to accurately locate a stroke position, there is a great level of redundancy. LPATS is now accommodating up to 6 antennas and with this arrangement, there are 20 combinations of three antennas for stroke location, and therefore 19 solutions are redundant.

Built-in test features are an integral part of LPATS. For example, every few minutes a lightning-like pulse is injected at the front end of each receiver and the total receiver performance is verified and information reported to the central unit. This procedure tests everything in the remote receiver except the whip antennas used for reception of the lightning and LORAN data. Built-in tests also continuously monitor the telephone lines for any change in conditions and report the same on the video screen. Failures at the circuit card level are automatically diagnosed.

VIDEO INFORMATION SYSTEM

The LPATS Video Information System (VIS) is a microprocessor based system which accepts lightning positional information, stores this data (in multiples of 3000 strokes), and allows it to be displayed either in real-time or as a time dependent replay (Fig. 2). Information is received from the CA over standard telephone lines using dial-up or dedicated service. CG strikes are plotted on a high resolution color monitor and can be routed to hard copy peripherals. LPATS has the capability of being interfaced to the majority of computers. The VIS unit is configured with an RS-232 output port. This port contains stroke information in ASCII format arranged in latitude, longitude, polarity, and time for each stroke. LPATS can also generate broadcast-quality NTSC video to drive a television monitor or tape recorder. A variable display zoom is incorporated to allow magnification of any selected area. By positioning a cursor over the desired area and entering the required magnification, the map data base is then recalculated and this area is displayed on the viewing monitor. As the map is expanded, additional graphics are added, such as city names, roads, and other user defined boundaries. Cursor placement also displays the stroke time and the range and azimuth of a stroke relative to a selected location.

A CG discharge is displayed as a color dot on the CRT screen. Black and white photographs of the color monitor's capabilities are shown in Figure 3a, b. A replay mode is incorporated to allow pre-programmed time increments of data to be color time coded on the monitor. This provides the user a visual determination of storm speed and direction. A high speed time lapse feature is also available to further display storm movement.

PROPAGATION OF LORAN-C TIMING SIGNAL

In the U.S.A., the LPATS timing pulse is generated by a single LORAN-C navigational transmitter. The "timing" pulses are transmitted at a frequency of 100 KHz within a very narrow spectrum. It is well known

that LORAN-C provides an excellent medium for the dissemination of precise time and frequency on a continuous basis. The stability of the ground wave from a single transmitter provides a sub-microsecond precision capability (Potts and Weider, 1972). It should be noted that the accuracy of the entire LORAN-C system is on the order of 1 microsecond. However, LPATS only uses a single station signal and therefore achieves much better timing accuracy. For 100 kw of peak radiated power, useful signals to 2600 km are reported (Dickenson, 1959) over seawater paths. Over land paths with average conductivity (0.005 mhos/m), the ranges are about 350 km shorter. Good signal processing techniques can improve these distances.

In order to evaluate the temperature correlated LORAN-C propagation delays, we will note the results of a paper by Mungall, et al (1981). A measurement program was carried out during two full winter periods and one intervening summer, from September, 1979, to April, 1981, in order to measure both the amplitude of the propagation-delay variations, and also their reproductibility from one year to the next along two LORAN-C signal paths of 310 km and 655 km in eastern North America. The outside air temperature at Ottawa was noted daily at the time of the LORAN-C TOA measurements.

These results conclusively show that, even over two widely separated and differing propagation paths, the relative time differences at any one time are likely to fluctuate by only a few hundred nanoseconds. Such a number by itself is likely to provide typical lightning TOA location errors of only a small fraction of a mile close to the LPATS network. The errors are also likely to be further reduced by the fact that in general the LPATS timing receivers are synchronized by monitoring only one common LORAN-C transmitter. The propagation paths from this one transmitter to the LPATS network receivers are in general likely to be over similar terrain and temperature paths and not be comparable to the above experimental example. Hence, the timing discrepancies will be smaller.

The possibility that certain LORAN-C transmitter to LPATS receiver paths will pass over or around mountainous terrain exists, making the arrival time of the "first" ground wave delayed somewhat from that obtained on a smooth, spherical earth. Such an error will be constant and calculable, hence allowing corrections to be provided. It can be shown theoretically, however, that these errors are also likely to be extremely small.

Referring to Fig. 4, we see that there is a path difference between a wave passing over the mountain and a theoretical wave passing along the surface of the spherical earth between A and B. The maximum path difference will be the difference between a wave passing

over the mountains and one along the surface of a spherical earth. There is a possibility of a shorter path around the mountains, but we will only consider the maximum distance possible, namely over the mountains, where diffraction at peaks and ridges permits such propagation paths. For simplicity in the calculations, we will assume that the propagation over the mountains follows a parabolic path. Table 1 shows the result of calculating the extra path length over mountains ranging in relief up to 3700 meters.

On average the distance between transmitter and receiver is greater than 370 km, implying path differences less than 206 m, or less than 685 nanoseconds. Such a difference is extremely small, but because of the fixed situation a correction can be applied, if desired.

The only waveform distortion will be caused by multiple wavefront arrivals and the phase distortion will be the algebraic sum at a given time. The transmitted spectrum is so narrow that the filtering due to propagation is unlikely to change the waveforms. The wavelength of the LORAN-C propagated wave is 3000 m, again implying minimal propagation effects.

On another note, it has been stated by some that LORAN-C is not a highly accurate navigation system. We recognize that this is a true and factual statement. However, LPATS does not use LORAN-C for navigation. LPATS' use of LORAN-C is for timing synchronization only, and only one station is used as opposed to three in navigation. The LORAN-C master and secondary transmissions contain tightly controlled, highly stable timing reference signals traceable to the National Bureau of Standards. Accuracies better than 50 nanoseconds are achieved by choosing the proper portion of the transmitted LORAN-C signal. This is as stated by the Coast Guard in USCG publication M16562, "Specifications of the LORAN-C signal". This accuracy is continuously overseen and stringently controlled by USCG monitoring stations.

GROUND STROKE DETECTION

The most frequent mode of a lightning strike is to bring negative charge to ground. LPATS was initially designed to detect only these negative charges. Recent modifications to the system now provide the ability to detect and flag situations when positive charge is brought to the ground. The LPATS equipment monitors the electric field radiated from the discharge in a broadband spectrum of bandwidth 2 kHz to 500 kHz (3db). This will accurately monitor risetimes of 700 nanoseconds. It can be shown that the typical return stroke has risetimes varying from less than 0.5 microseconds to over 4 microseconds with close lightning being the faster and distant lightning slower. The fall time

of the lightning waveform is also significant and indicates the low frequency components. This averages around 30-40 microseconds to half-peak. In order to select a lightning return stroke waveform for acceptance by the equipment, it is necessary to perform waveform interrogation looking indirectly for these particular waveform shapes.

The LPATS design uses a matched filter technique with the filter designed around the expected return stroke waveform. Variances in that waveform for all anticipated return stroke shapes are allowed, but anything not resembling such a waveform is rejected. For instance, a sharp rise and fall time from a lightning leader would be immediately rejected. Upon acceptance by the equipment that the waveform was close to the matched filter design, the time of the initial peak, which was recorded to an accuracy of a few hundred nanoseconds, is forwarded to the CA. This time has occurred when the lightning was generally within 100 m of the ground. Matched filters also have the ability to analyze signatures deep into the background noise, hence providing a much better waveform retrieval than a regular receiver.

At times, waveforms from nearby storms contain signatures that closely resemble ground discharges, but they have actually occurred within the cloud. These signatures are usually weaker in magnitude and have also different patterns prior to the false "return stroke". In order to eliminate these erroneous values, the LPATS receiver examines the data prior to the recorded return stroke. In cloud strokes, the data in this time period is quite different from that prior to actual return strokes, thus allowing elimination of cloud stroke data resembling these strokes. Furthermore, the receivers close to a storm are not permitted to play a part in the location of the nearby activity.

In summary, the false effects of similar waveforms in cloud discharges are eliminated due to the fact that in general the energy is small and will not propagate adequately to the distant receivers as well as the stated fact that the signatures prior to the false "return stroke" are different and are rejected by LPATS. There is a possibility that some large distant discharges may cause saturation of the receiver, but this provides only a small error in the peak amplitude detection time of the signature. The equipment will read the time at the instant the unit saturates, which, for such a stroke, will occur only a few hundred nanoseconds prior to the actual peak.

PROPAGATION OF THE LIGHTNING WAVEFORM

In considering lightning waveform propagation, we must investigate waveform distortion as well as geometrical changes in the

path length due to rough terrain. The geometrical changes are similar to those discussed dealing with the LORAN-C propagation. We can also assume the propagation distance is, in general, greater than 180 km where the baseline between sites is greater than 180 km, and bearing in mind that the most distant three receivers are the ones used in the spherical hyperbolic calculations. Here again geometrical propagation errors are likely to be less than 690 nanoseconds. In the case where lightning occurs in the center of a network of four stations 185 km apart, the propagation distance is 131 km. In the unlikely event that a mountain ridge two miles high was intercepted in this short path distance, the geometrical error would only be 293 meters or 955 nanoseconds.

The most troublesome error is the distortion due to propagation of a broadband lightning electric field waveform. The closer one is to a lightning stroke, the greater the high frequency component. We can also assume that over flat land with average ground conductivity (5×10^{-3} mhos/m) the risetime of a typical lightning return stroke propagating 200 km is delayed by some 0.7 to 2.6 microseconds (Uman, et al, 1976). On average, a delay in risetime of 1 microsecond occurs between a site only some 15 to 25 km from the discharge and one some 215 to 225 km distant.

Because a typical LPATS system will only use data monitored from distances greater than 160 km, we can assume that in similar terrain to Florida we can expect average waveform distortion of the risetime of less than 1 microsecond. Considering the time of peak instead of risetimes, there is a possibility of a further delay of 1/4 to 1/2 microsecond. Once more, however, because LPATS only monitors distant lightning, these peak arrival time errors are likely to be small.

IONOSPHERIC REFLECTION EFFECTS

The LPATS receivers are designed to detect and eliminate the effects of ionospheric reflections. In order to achieve this objective, the receivers each have two thresholds and in-built logic to detect certain phenomena. Let us examine such reflected waveforms as displayed in Fig. 5. The ground wave with its associated high frequency components is evident, as are the smoother ionospheric reflections. It is shown that the ionospheric reflections are of similar peak value as the ground wave.

Our experience is that for distances less than 650 km, the peak of the ground wave is rarely less than 0.5 times the peak ionospheric reflection, and it occurs some 200 microseconds earlier. With the two thresholds in the LPATS receiver, we are able to analyze waveform slopes between threshold

crossings as well as the time between peaks. Such analysis helps with in-cloud stroke detection and can also lead to the elimination of the ionospheric reflections. For the few that pass the tests, the time of peak detection for all three recording receivers is unlikely to be an acceptable value for a mathematical solution. The mathematics tends to give complex solutions for bad data because each required time difference involves two received times. Furthermore, these data must have timing differences between sites less than the short time it takes for light to travel between them.

NOISE REJECTION

There is always a possibility of local noise interference in both the lightning stroke and timing receivers. For this reason, notch filters have been built into the equipment to eliminate these effects. A broadcast station tunable notch filter with more than 30 db attenuation has been built into the unit that has negligible effect on the broadband lightning waveform.

Two more tunable notch frequencies are available in the 15 kHz to 60 kHz band and two in the 60 kHz to 150 kHz band. These are necessary at many sites to reject the effects of powerful low frequency transmitters. All these filters have attenuation greater than 30 db.

In the 50-60 Hz region, adequate rejection is applied, although at these frequencies, the effects of the noise on the detection of a lightning stroke peak is negligible.

OTHER ERROR SOURCES

Site errors, which are a well understood major problem in magnetic field detection systems (Darvenizia and Uman, 1983), are negligible in the TOA system. Here one is only interested in detecting the arrival time of the initial return stroke peak of a received broadband lightning waveform. Any obstructions, reflections, or re-radiation have only a negligible effect on the monitored peak time. We have already discussed above the small errors that are the result of the insertion of large obstacles such as mountain ranges in the path. When we consider obstacles or reflectors that are close to the receiving site, the errors are significantly smaller or they have no effect on the initial peak arrival time.

There is also a small possibility that site errors may be evident in the arrival time of a received timing pulse. Considering the LORAN-C transmissions, one can refer to technical publications on the effect of nearby conductors on the phase of the received signal. Olsen, et al, (1982) discuss the scattering of LORAN-C navigation signals by a powerline. Applying Olsen's equations to a

situation where an LPATS receiver is placed 100 m from a 60 km long powerline, then a worst case error of 23 nanoseconds or 7 m is possible. Clearly these errors are not worth considering.

Another potential occasional source of error is the "baseline error". A baseline error could affect the accuracy of LPATS locating a stroke position. If a storm occurs along a baseline of two antennas, the storm position may not be accurately calculated using that baseline. With the four antennas utilized by LPATS and only three reported detections required to accurately position a lightning stroke, this situation rarely occurs.

EFFICIENCY AND LOCATIONAL ACCURACY

Lightning data are difficult to evaluate due to the lack of objective measurements and criteria, although a few limited attempts have been reported (Johnson, et al, 1982). At the current time, testing for internal data coherence and phenomenological consistency is the main tool for LPATS evaluation studies. Obviously it is occasionally possible to monitor a single storm by eye and compare the visual count with the recorded data. The near-field detection efficiency can then be initially estimated.

Visual observances at Melbourne and Tampa taken during thunderstorm occurrences and compared to data sensed by the LPATS for the same time period indicates a high degree of correlation; around 85%. Similarly, observations by trained weather observers at the Naval Air Station at Meridian, Mississippi have been compared with VIS data from the East Gulf network by NAS Pensacola meteorological personnel. They have confirmed a very high degree of stroke detection for that system.

In addition to the visual sightings, data from three separate networks with receivers up to 1300 km apart have been compared. On one occasion, a thunderstorm was located near Kansas City, KS. Several lightning flashes were reported by three separate LPATS networks (Florida, East Gulf, and Upper Midwest). This comparison suggests a significant degree of stroke detection efficiency. Obviously, when activity is closer to the antenna network, higher stroke detection efficiency is present. This is borne out by the following examples.

On November 1, 1983, a thunderstorm was occurring near Cape Canaveral, Florida. Fig. 6 shows the data printout from the CA. Notice that LPATS detected 14 strokes in one flash using stations over 275 km distant. This again suggests the fact that LPATS does indeed possess a very high inherent detection efficiency.

Another approach is to monitor a storm close to one network by that network and also by a distant network. On February 3, 1984, a thunderstorm was occurring near latitude 26° north and longitude 85° west. This lightning activity was detected by the Florida and the East Gulf networks. Fig. 7 is a GOES visible KB8 image at 1330 EST showing a large area of convective cloudiness. Radar summaries (Fig. 8) in fact only indicate heavy rain showers, but not thunderstorms. Maximum radar tops were 6200 m. The Ruskin, FL radar, 305 km to the west of this convective cluster was therefore unable to determine the presence of thunderstorms. Fig. 9 depicts the location of the network antennas and the distance of the station from the center of each network. Fig. 10 is a photograph of the VIS display of that storm for a 30 minute period (11:07 to 11:37 EST). During this period, the Florida network positioned a total of 1003 strokes, a moderately vigorous output for a single cluster of convective clouds.

During this time period, the East Gulf network was detecting lightning discharges from the same storm. Fig. 11 compares the lightning stroke position data from each network over a very short subset of this time (roughly 2.5 minutes). The storm was located 680 km and 385 km from the Florida and Pensacola networks respectively.

Close inspection of Fig. 11 shows an extremely tight clustering of the plotted positions. It should be further noted that near 26.0°N and 84.9°W a number of multiple stroke flashes occurred. These multiple strokes show a high degree of coincidence from both networks. Similarly, near 26.1°N and 84.5°W a flash with 3 strokes was recorded (in the same position) by the Florida network. The East Gulf network located these slightly southeast of where the Florida network indicated. If the Florida network plotted position is used as the true position then the mean error of the network for this stroke is about 7-8 km. Literature published by ASC indicates that at this very large distance, stroke positions were anticipated to be in error by a larger amount than is indicated in Fig. 11. Considering the distance involved, LPATS may have actually surpassed the theoretically predicted locational accuracies (see below).

In the 2.5 minute period presented, the LPATS network almost 700 km distant located 61% as many CG strikes as did the network centered about 400 km to the northeast. It would appear reasonable to assume a relatively slow fall-off of detection efficiency (DE) with range. Nothing to date has been observed that is inconsistent with the estimate that there is a 50% DE as far out as 400 km. It is in fact common to observe cells

with as high a strike density on the edge of the display as near the network center. Other comparisons from two networks have provided similar results.

As for the determination of CG locational accuracy, it is possible to arrive at a theoretical estimate. We know that the timing errors of the system, including propagation and site errors are significantly less than 1 microsecond. This timing error is much smaller than obtained in determining the time of peak of the return stroke waveform which is our dominant concern. Because all lightning location is performed from distant receivers some 130 to 650 km away, the waveforms will have lost a great deal of their high frequency components. Analysis of the data shown by Uman, et al (1976) indicates that the waveform initial peak time is likely to be monitored to an accuracy on the order of 1 microsecond between the receiving sites. In order to investigate the accuracy of the system on a theoretical basis, we therefore will anticipate errors of 2 microseconds as a worst case situation. A computer program was written to simulate lightning TOA data in a 40×40 matrix around any pre-determined network of four stations. In each of these 1600 blocks the timing from a theoretical flash to each receiver was distorted by a random number less than or equal to the anticipated errors. The mean error in the known theoretical lightning strike position was then calculated for fifty iterations within each block and the data plotted. These calculations were performed by the same spherical hyperbolic geometry used in LPATS, with the exception that the timing errors added to each path should be greater than those actually occurring due to timing and propagation errors. As an example of the theoretically calculated accuracy of the system, we can quote the errors obtained in locating lightning from three Florida stations (Melbourne, Ft. Lauderdale, and Naples). The errors in locating a lightning flash at the center of the Florida Peninsula some 140 km from each of these stations are as follows: mean error 97 m, maximum error 411 m, and standard deviation 76 m. At Cross City, FL, which is some 560 km from the Ft. Lauderdale receiver, the errors are as follows: mean error 2.3 km, maximum error 6.8 km, and standard deviation 1.8 km. This is probably better convective storm locational accuracy than obtainable by high powered meteorological radar.

There are various indirect indications that the observed CG strokes are consistent with the above estimates. Inspection of the position of strokes within a given flash rarely shows differences of more than a few hundredths of a degree latitude. In the case of 14 strokes with one flash, (Fig. 6), LPATS initially located the CG at 80.46°W , 28.94°N .

The average variation in successive stroke locations is less than $.01^\circ$ latitude (under 1100 meters), with a maximum variability of $.02^\circ$ longitude. It is also observed on the LPATS VIS display that "cells" of CG strikes do not tend to "smear" or become dispersive at large ranges (over 400 km). Fig. 12a is the full VIS display showing several clusters of strikes southeast of Miami (about 2000 EST, 25 October 1983). A VIS zoom display (Fig. 12b) shows that even at a range of 410 km, the CG strikes (about 471 in 90 minutes) are tightly bunched.

CASE STUDIES

Ongoing studies comparing LPATS, GOES, and radar data continue to reveal a high degree of phenomenological and meteorological consistency. This is especially evident when viewed in the animation mode, using CREAS technology (Lyons and Henz, 1978).

On 9 December 1983 from 0650 EST through 1420 EST, a significant amount of lightning activity in the Key West area appeared on the LPATS VIS monitor. This storm was unusual for both its duration and anticyclonic trajectory. During this time period, 2,548 flashes were reported for an average of 5.6 per minute, a rather routine storm. However, it should be noted this storm was located over 400 km from the centroid of the Florida network. Fig. 13 shows the LPATS VIS display of the storm CG activity. Fig. 14 is a GOES visible KB image sector at 1030 EST, at about the time the cell was just south of Key West. An active convective turret can be seen very close to the region of CG strikes.

Observation at the Naval Oceanography Command Detachment at Key West provides the following record of events for the thunderstorm. At 0500 EST, the storm was well south of the Keys. The observations for that hour show distant lightning southeast through southwest, verifying thunderstorm activity in the area, as LPATS began plotting lightning strokes as the cell crossed to the southern edge of the data display region. At 0800 EST, cumulonimbus clouds (Cb) were observed to the south. This condition was also evident at 0900 EST. At 1000 EST, cloud-to-water (CW) lightning was observed occurring to the south. The thunderstorm officially began at 1033 EST accompanied by occasional and then frequent CC, IC, CW, and CG flashes. Heavy thunder and rain showers were observed beginning at 1210 EST and continuing until 1222 EST. At 1333 EST, the last thunder was heard with Cbs persisting both south through southwest and northwest through northeast. All clouds were observed to be moving northwest.

Fig. 15 is a plot of the positions of the maximum cloud tops as observed and reported by the National Weather Service radar site at Key West. It is interesting to compare the radar path traveled by this thunderstorm to the LPATS display. The axis of CG strikes paralleled closely the radar top track. As is often observed with CG strikes, the largest amount of lightning occurred on the leading edge of the storm. This is borne out by the flash times indicated on the LPATS occurring 10-20 minutes earlier than the arrival of the maximum cloud tops.

The conventional meteorological data obtained for this storm correlated extremely well with the lightning data obtained from the LPATS.

CONCLUSIONS

The TOA technique is theoretically the optimal method for lightning location if a highly accurate timing source were available. LPATS, using LORAN-C as its timing source (in the U.S.), has a theoretical design locational accuracy of about 100 m near the network center, and of about 2300 m more than 400 km distant. It was anticipated that a significant number of CG strikes would be detected at ranges of 400 km and beyond. Since becoming operational in 1982, several LPATS networks have produced data which appear to be entirely consistent with the system design predictions. In general, the LPATS technology is apparently producing CG location data within 1 km accuracy and with detection efficiencies of at least 85% within the polygon inscribed by the 4 to 6 antennas of a network. A useful range of greater than 500 km has been achieved. Future indirect assessments of system performance will also be accompanied by increasingly rigorous direct data evaluations and intercomparisons with other locating technologies. The TOA approach appears to be remarkably insensitive to interference and disturbances. Antennas are not significantly affected by buried cables or other metallic structures (Smith-Rose, 1923; Horner, 1954), nor by local heavy precipitation which apparently interferes with MDF-type systems (Proctor, personal communication).

ACKNOWLEDGEMENTS

The author would like to thank Midwest Communications, Inc. for providing some of the GOES satellite imagery utilized by this report.

REFERENCES

1. Bent, R.B., P.W. Casper, T.H. Scheffler, and R. Leep, 1983: A Unique Time of Arrival Technique for Accurately Locating Lightning Over Large Areas. Reprints, Fifth Symposium on Meteorological Observations and Instrumentation, Toronto, Amer. Meteor. Soc., 505-511.
2. Darvenizia, M., and M.U. Uman, 1983: Research Into Lightning Protection of Distribution Systems II - Results from Florida Field Work, 1978 and 1979. IEEE, 83 SM454-6.
3. Dickenson, W.T., 1959: "Engineering Evaluation of the LORAN-C Navigation System", Jansky and Bailey, Inc., ASTIA Doc AD 229744 (NTIS).
4. Golde, R.H., 1977: Lightning, Vol. 1 and 2. Academic Press, London.
5. Horner, F., 1954: Influence of Buried Conductors on Bearings, Wireless Engineer, 30, p. 186, 191.
6. Hughes, H.G., and R.J. Gallenberger, 1974: Propagation of Extremely Low-Frequency (ELF) Atmospherics Over a Mixed Day-Night Path. J. Atm. Terr. Phys., 36, 1643-1661.
7. Johnson, R.L., D.E. Janota, and J.E. Hay, 1982: An Operational Comparison of Lightning Warning Systems. J. Appl. Meteor., 21, 703-707.
8. Krider, E.P., R.C. Noggle, and M.A. Uman, 1976: A Gated, Wideband Magnetic Direction Finder for Lightning Return Strokes. J. Appl. Meteor., 15, 301-306.
9. Lyons, W.A., and R.B. Bent, 1983: Evaluation of the Time-of-Arrival (TOA) Technique for Real-Time Ground Strike Measurements Using the Lightning Position and Tracking System (LPATS), Preprint, 13th Conf. on Severe Local Storm, AMS, Tulsa.
10. Lyons, W.A., and J.F. Henz, 1978: CREAS and SWAT: Innovative Uses of Radar, Spotter Networks and the Media to Nowcast Local Flash Floods. Reprints, Conf. on Flash Floods: Hydrometeorological Aspects, Los Angeles, AMS, 64-69.
11. Maier, M.S., R.C. Binford, L.G. Byerly, E.P. Krider, A.E. Piter, and M.A. Uman, 1983: Locating Cloud-To-Ground Lightning with Wideband Magnetic Direction Finders. Reprints, 5th Symp. on Meteorological Observations and Instrumentation, AMS, Toronto, 497-504.
12. Mungall, A.G., C.C. Costain, W.A. Ekkolm, 1981: Influence of Temperature-Correlated LORAN-C Propagation Delays. Metrologia, 17, 91-96.
13. Olsen, R.G., and A. Aburwein, 1982: LORAN-C Positioning Errors Caused by Scattering from Wires Above the Earth. IEEE, Transactions on Electromagnetic Compatibility, November.
14. Pierce, E.T., 1982: Spherics and Other Electrical Techniques for Storm Investigations. In, Thunderstorms: A Social, Scientific, and Technological Documentary, Vol. 3, E. Kessler, Ed, USDOC, NOAA, U.S. Gov. Printing Office, 135-148.
15. Potts, C.E., and B. Weider, 1972: Precise Time and Frequency Dissemination via the LORAN-C System. Proceedings, IEEE, 60, 530-539, May.
16. Smith-Rose, R.L., 1923: J. Inst. Elec. Engrs., 61, pp. 149-156.
17. Uman, M.A., C.E. Swanberg, J.A. Tiller, Y.T. Lin, 1976: Effects of 200 km Propagation on Lightning Return Stroke Electric Fields. Radio Science, 11, 985-990.

TABLE 1

EXTRA PROPAGATION TIME REQUIRED
FOR LORAN-C SIGNAL TO TRAVEL OVER MOUNTAINS OF VARIOUS HEIGHTS

<u>Distance between transmitter & receiver</u>	<u>Height of mountains</u>	<u>Extra propagation time</u>
74 km	1850 m	399 nanoseconds
74 km	3700 m	1492 nanoseconds
185 km	1850 m	249 nanoseconds
185 km	3700 m	770 nanoseconds
370 km	3700 m	685 nanoseconds

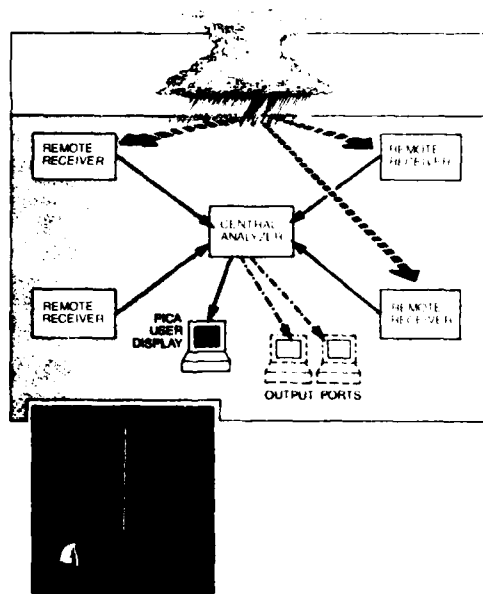


Fig. 1 - Schematic of a typical 4-station LPATS network, with the receiver antennas shown in the inset

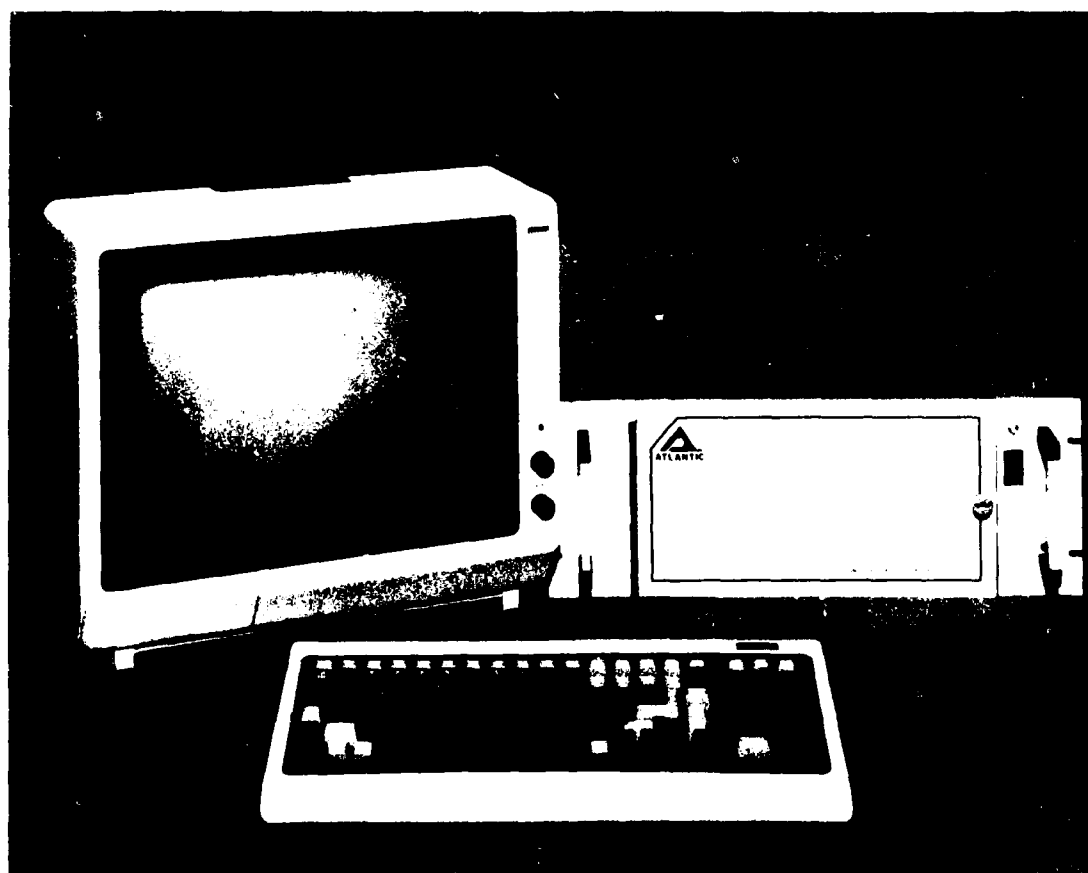


Fig. 2 - The LPATS Video Information System (VIS)

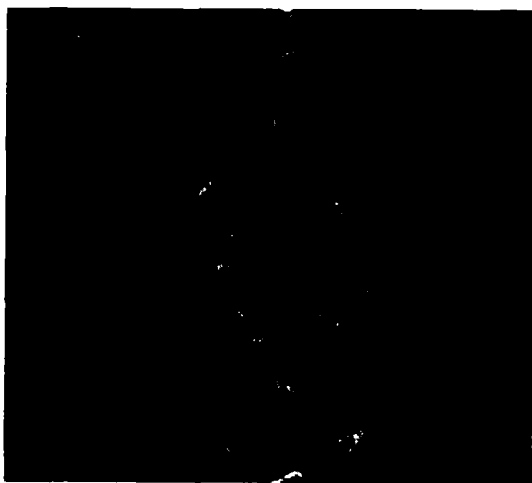


Fig. 3 - (a) A typical LPATS VIS display showing 3000 strikes associated with a squall line moving across northern Florida

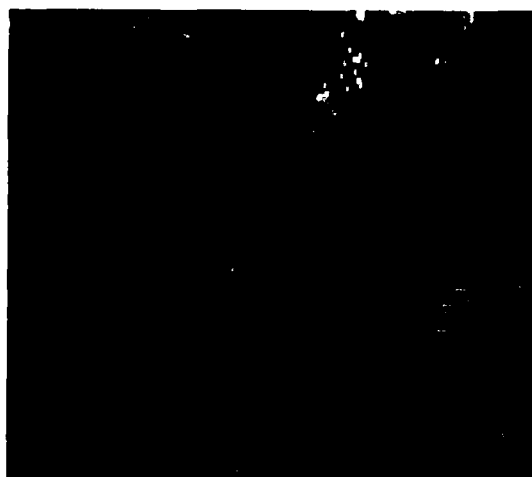


Fig. 3 - (b) A dynamic zoom onto the area west of Tampa Bay. The original image is color coded in 10 minute time increments



Fig. 4 - Differing paths between a LORAN-C transmitter (A) and receiver (B) for mountainous and flat terrain

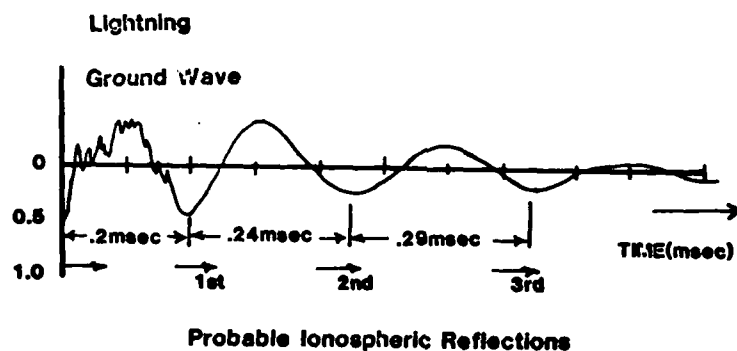


Fig. 5 - Lightning CG ground wave and probably 1st, 2nd, and higher ionospheric reflections of magnetic radiation from a distant lightning return stroke

```

2477 0000 0000 0000 +### +### +### +### +### +### 10:11:49
2478 0000 0000 0000 +### +### +### +### +### +### 10:11:51
2479 0000 0000 0000 +### +### +### +### +### +### 10:11:51
QUAD 1
CB0.46 X 028.94 Y 003.00 R
20000 6FCB 0000 735F +### +### +### +### +### +### 10:11:51
2482 7774 7A7C 7D0B -05DF -063B -0373 -005C +026C +02C8 10:11:51
QUAD 1
XS 81 NEG
QUAD 3
CB0.45 X 028.95 Y 003.01 R
AADS ABE1 AEEB B178 -05DE -0639 -0372 -005B +026C +02C7 10:11:51

QUAD 1
XS 81 NEG
QUAD 3
CB0.46 X 028.94 Y 003.00 R
CEAR CF77 B280 B50F -05DE -063B -0373 -005D +026B +02C8 10:11:51
QUAD 1
XS 81 NEG
QUAD 3
CB0.45 X 028.95 Y 003.02 R
6472 65CF 6B67 6B66 -05DF -063B -0373 -005C +026C +02C8 10:11:52
QUAD 1
XS 81 NEG
QUAD 3
CB0.45 X 028.95 Y 003.01 R
CB21 C92E CC35 CEC5 -05DF -063A -0373 -005B +026C +02C7 10:11:52
QUAD 1
XS 81 NEG
QUAD 3
CB0.46 X 028.94 Y 003.00 R
ACE1 A144 A44C A6DB -05DF -063B -0373 -005C +026C +02C8 10:11:52
QUAD 1
XS 81 NEG
QUAD 3
CB0.45 X 028.95 Y 003.01 R
ZBA6 ZCR2 ZFR9 Z249 -05DE -0639 -0372 -005B +026C +02C7 10:11:52
QUAD 1
XS 81 NEG
QUAD 3
CB0.46 X 028.94 Y 003.00 R
CEAR CF77 B280 B50F -05DE -063B -0373 -005D +026B +02C8 10:11:52
QUAD 1
XS 81 NEG
QUAD 3
CB0.45 X 028.95 Y 003.01 R
5507 5810 6A7E 60DE -05DE -0639 -0372 -005B +026C +02C7 10:11:52
QUAD 1
XS 81 NEG
QUAD 3
CB0.46 X 028.94 Y 003.00 R
6655 666C 6DFC 65E0 -063B -0374 -005B +026C +02C7 10:11:52
QUAD 1
XS 81 NEG
QUAD 3
CB0.46 X 028.94 Y 003.00 R
2922 48 8071 8379 86C6 -05DF -063B -0373 -005C +026C +02C8 10:11:52
QUAD 1
XS 81 NEG
QUAD 3
CB0.45 X 028.95 Y 003.01 R
9E0A A112 A3A1 -05DF -063B -0373 -005C +026C +02C8 10:11:53
QUAD 1
XS 81 NEG
QUAD 3
CB0.45 X 028.95 Y 003.01 R
C778 C8A7 C8B0 CEEF -05DE -063B -0373 -005B +026B +02C8 10:11:53
QUAD 1
XS 81 NEG
QUAD 3
CB0.45 X 028.95 Y 003.02 R
2495 0080 0000 0000 +### +### +### +### +### +### 10:11:53
2496 0000 0000 0000 +### +### +### +### +### +### 10:11:53
2497 0000 0000 0000 +### +### +### +### +### +### 10:11:53

```

Fig. 6 - Sample of CA printer output from the Florida network showing 14 strokes within a given flash (1 November 1983, 1011:51-53 EST, at 28.95°N, 80.45°W)



Fig. 7 - GOES visible image, KB8 sector, 1230 EST, 3 February 1984

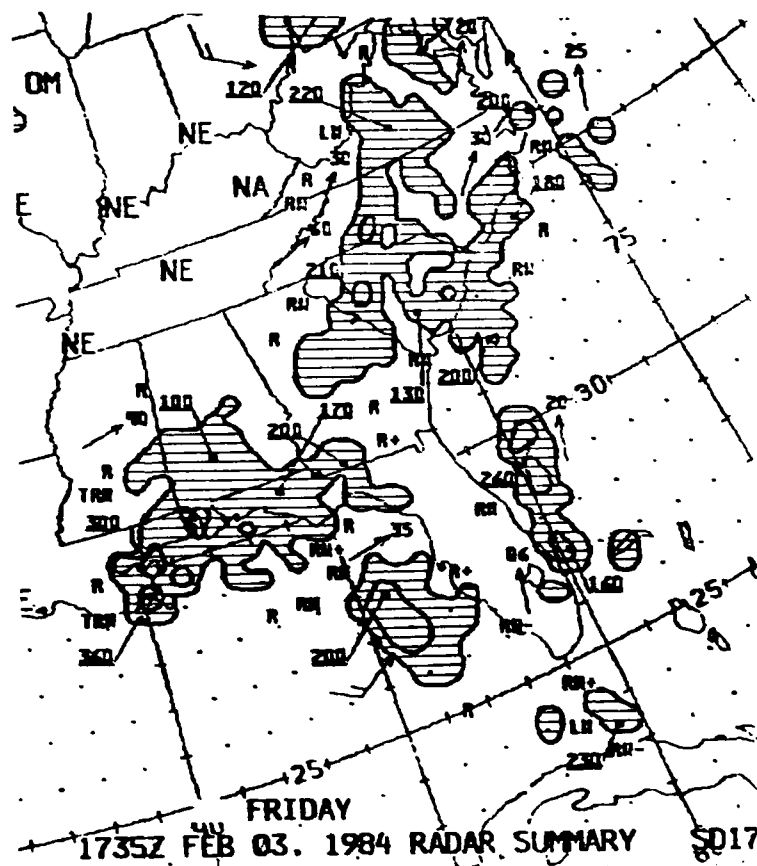


Fig. 8 - Hourly MDR radar summary, 1235 EST, 3 February 1984

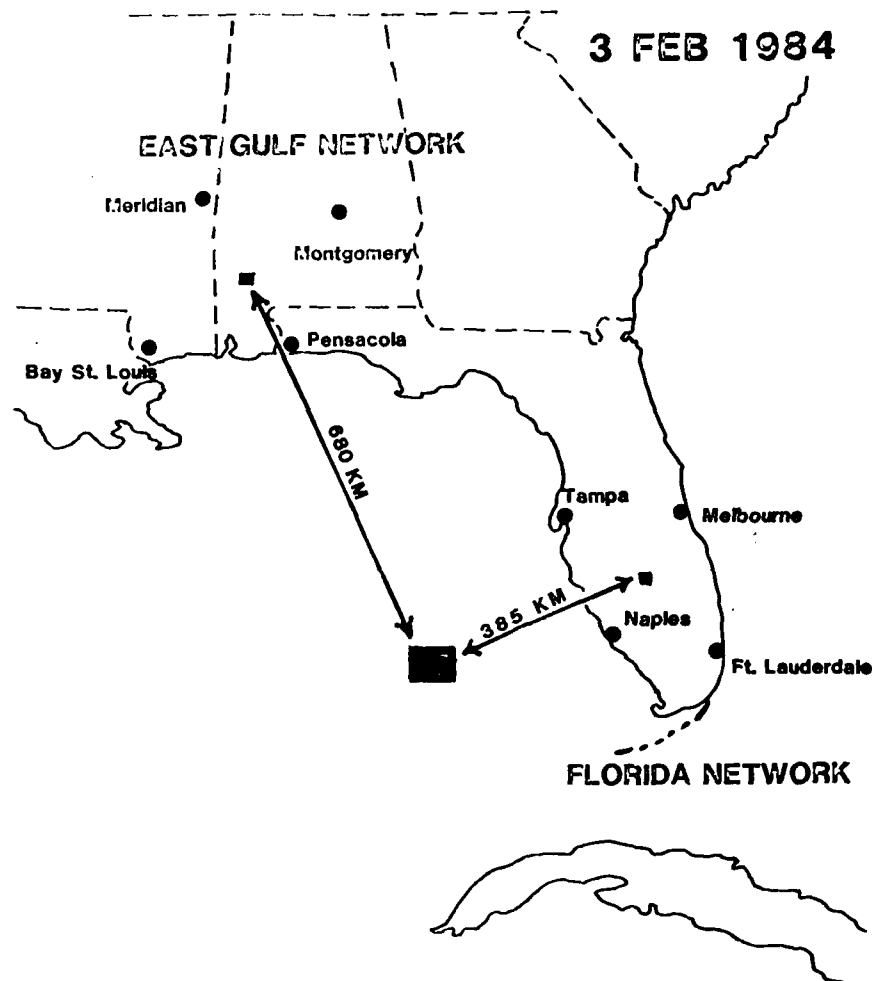


Fig. 9 - The East Gulf and Florida LPATS network configuration, and the area of CG activity monitored by both on 3 February 1984



Fig. 10 - VIS display showing CG strikes from convective cluster in the Gulf of Mexico southwest of Tampa, 1137 EST, 3 February 1984. In the prior 30 minutes, 1003 strokes were plotted in the portion of the cluster. The straight edge on the left border represents the western edge of the data field for the Florida network.

3 FEBRUARY 1984

EAST GULF NETWORK 2 mins 36 secs 32 Strikes

FLORIDA NETWORK 2 mins 30 secs 52 Strikes

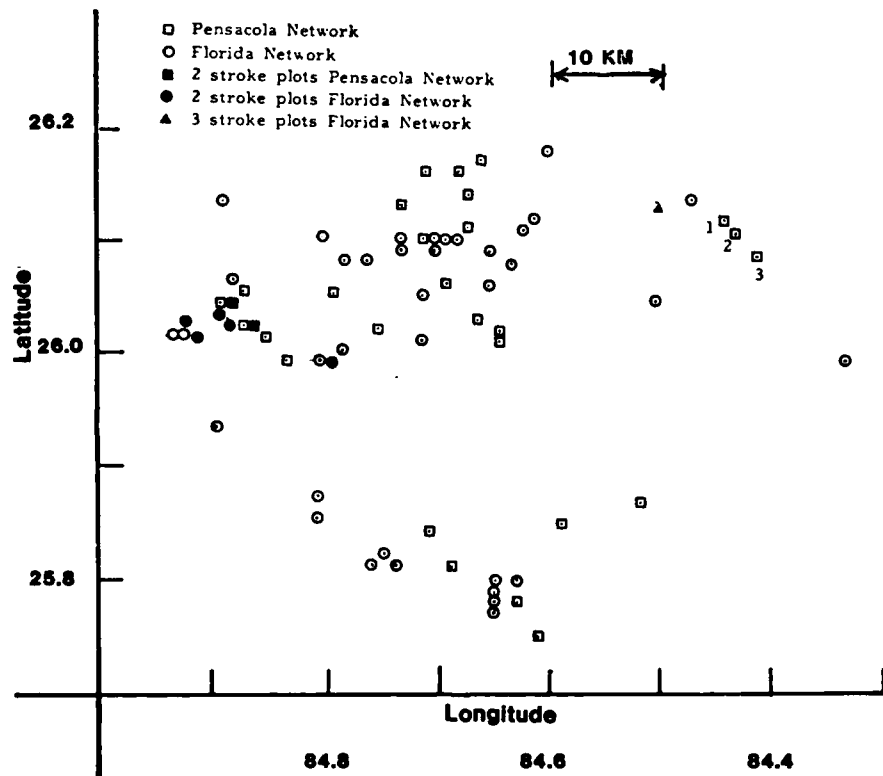


Fig. 11 - CG plots over a 2.5 minute period ending 1137 EST, 3 February 1984, from the Florida and East Gulf LPATS network

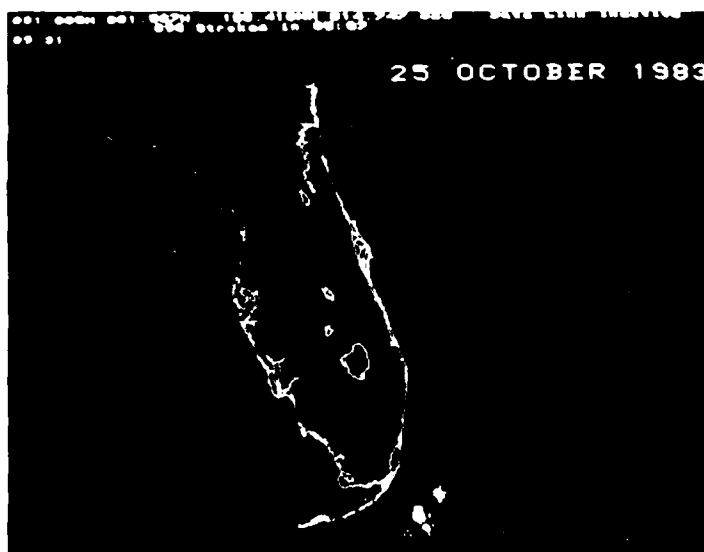


Fig. 12 - (a) VIS display showing weak clusters of convection southeast of Miami at 2135 EST, 25 October 1983. In the past 5 hours, 7 minutes, 896 strikes were noted.



Figure 12 - (b) A dynamic zoom into one of the clusters, with 471 strikes in 90 minutes, shows a tight packing of strikes. Time tags show a very slow northerly drift to the storm.

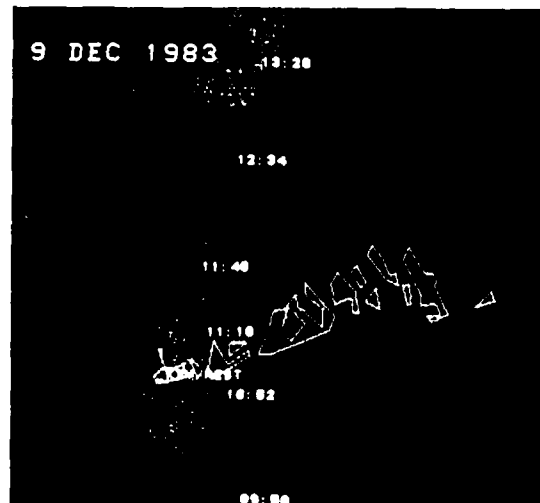


Fig. 13 - VIS display of CG strikes from 0650 to 1420 EST, 9 December 1983

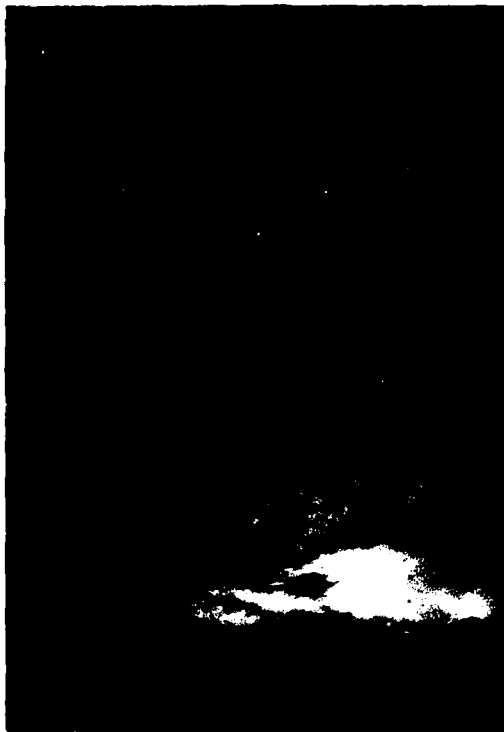
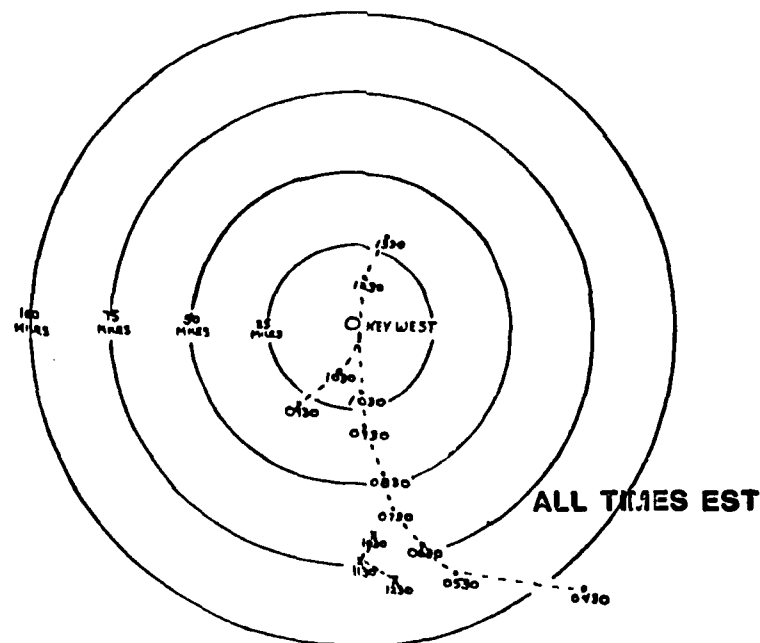


Fig. 14 - GOES visible image, KB8 sector, 1030
EST, 9 December 1983

NWS RADAR KEY WEST 9 DEC 83



MAXIMUM REPORTED TOPS

Fig. 15 - The plot of the maximum radar echo tops
at hourly intervals (0430-1330 EST, 9
December 1983) as observed by the NWS
WSR-57 radar at Key West, FL

A SYSTEMATIC METHOD FOR IDENTIFYING AND CORRECTING "SITE ERRORS"
IN A NETWORK OF MAGNETIC DIRECTION FINDERS

by

W. L. Hiscox, E. P. Krider*, A. E. Pifer**, and M. A. Uman***
Lightning Location and Protection, Inc.
1001 S. Euclid Avenue
Tucson, Arizona 85719

ABSTRACT

Extensive networks of lightning direction finders (DFs) are now operating throughout the United States, Canada, and many other countries. A small but important fraction of these installations exhibit systematic angle errors that are a function of angle, or so called "site errors," that have been known and understood since the earliest days of radio. In this paper, we describe a least-squares optimization procedure for determining an optimum lightning location if a number of DFs measure both lightning directions and signal amplitudes at the same time and if there are random errors in these measurements. We also describe a generalization of this procedure that can be used to identify and correct any systematic errors, such as a site error, that might be present at each DF site.

*Also, Institute of Atmospheric Physics, University of Arizona, Tucson, AZ

**Also, Department of Physics, University of Arizona, Tucson, AZ

***Also, Department of Electrical Engineering, University of Florida, Gainesville, FL

INTRODUCTION

EXTENSIVE NETWORKS of magnetic direction finders (DFs) are now operating throughout the United States, Canada, and many other countries to determine the location, movement, and intensity of thunderstorms; to facilitate the early detection of lightning-caused fires; to warn of impending lightning hazards; to determine whether electric power outages are lightning-caused; and for basic research and other applications [1,2,3]*. A small but important fraction of these DF stations exhibit systematic angle errors that are a function of angle or so-called "site errors." The causes of site errors have been known and understood since the earliest days of radio [4,5] and today radio direction-finders are routinely equipped with secondary correcting coils and other compensating techniques [5,6]. In this paper, we will describe a non-linear least-squares optimization procedure that can be used to determine an optimum lightning location if a number of DFs measure both lightning directions and signal amplitudes at the same time. We will also describe a generalization of this procedure that can be used to identify the presence of site errors in a network of magnetic direction finders and, if they are present, to derive a correction factor. These techniques take advantage of an inherent redundancy in the lightning data that are provided by the DF systems manufactured by Lightning Location and Protection, Inc. (LLP). The techniques are general, however, and may be applied to the problem of locating other transient sources of electromagnetic radiation with DF stations.

LIGHTNING LOCATING SYSTEM

The lightning locating system that is manufactured by Lightning Location and Protection, Inc. (LLP) [2,7] consists of 2 or more gated, wideband magnetic DF stations [1,8] that are separated by tens to hundreds of kilometers and that transmit lightning direction and signal amplitude data to a central position analyzing (PA) computer. When the position analyzer receives 2 or more simultaneous inputs from the remote DF sites, it computes the location of the lightning source either by triangulation of the DF angle vectors or by using an appropriate combination of these directions and the ratios of the signal amplitudes.

DIRECTION FINDER - The LLP direction finder senses the electromagnetic fields that are radiated by lightning on two orthogonal magnetic-loop antennas and on a flat-plate electric antenna. The bandwidths of the antenna systems are wide (approximately 1 kHz to 1 MHz) so that the shapes and polarities of the lightning field waveforms are preserved. The voltage produced by the electronics associated with each magnetic loop is proportional to the lightning magnetic field multiplied by the cosine of the angle between the plane of the loop and the direction of the incoming field. Therefore, the direction to the

lightning source can be determined from the ratio of the signals on the two orthogonal loops, a standard technique in radio direction finding [4,5].

In order to optimize accuracy and to reduce background noise, the DF electronics are designed to respond to only those field shapes that are characteristic of return strokes in cloud-to-ground flashes. The DF electronics require the incident field to have a risetime, width, and subsidiary peak structure that is characteristic of a return stroke. The electric field is used to determine the lightning polarity (most flashes lower negative charge to ground) and the overshoot of this field following the initial peak must not exceed a preset fraction of the first peak. The risetime and bipolar shape requirements also serve to eliminate very distant (> 400 km) lightning because the effects of propagation increase the field risetimes and because distant ionospheric reflections are often large and inverted with respect to the initial ground wave.

When a return stroke field is detected, the magnetic direction is determined just at the time that the radiation field reaches its initial peak. At this time, the majority of the stroke current is still within about 200 m of the ground, and therefore, any errors in magnetic direction due to horizontal channel sections and branch currents are minimized [8,9], and errors due to ionospheric reflections [10] are eliminated. Also, by sampling at this time, the direction vector points toward the ground contact point rather than some elevated portion of the channel. A microcomputer subsystem built into each DF digitizes and stores the signals for up to 14 return strokes in each flash to ground, computes the direction to each stroke, and stores the results in a buffer memory for subsequent transmission to the position analyzer.

POSITION ANALYZER - The LLP position analyzer (PA) is a preprogrammed microcomputer system that automatically accepts lightning angle and signal amplitude data from a network of DFs, calculates the lightning locations, and provides outputs for local and remote displays in real-time. The direction finders transmit lightning information to the position analyzer via dedicated voice-grade data circuits, either land lines or VHF/UHF radio links. Each DF sends the lightning angle, first stroke signal amplitude, flash polarity, number of return strokes, and the time interval between the first stroke and the DF data transmission. When the DF data are received at the position analyzer, the absolute time that the flash occurred is calculated by subtracting the DF processing interval from the time the data are received at the PA. When the position analyzer receives two or more DF inputs within a specified coincidence interval, it computes the lightning location. Prior to computing this location, the PA can, if necessary, search a table of correction factors that are applied to the incoming DF data. These correction factors include a multiplier to normalize the absolute gain of each DF, an angle rotation to

*Numbers in [] are references.

correct for improperly aligned antennas, and a "site error" correction if it should be necessary to apply an angle correction that is itself a function of angle.

LLP LIGHTNING LOCATIONS

When 2 or more DFs detect a lightning, the position analyzer computes and maps the lightning location in real-time. If just 2 DF stations have detected the flash, the location is computed either by triangulation of the DF angle vectors, or if the lightning has occurred close to the baseline connecting the two DF stations, then the position is computed using a combination of both angle and signal amplitude data. This latter method assumes that the ratio of the signal amplitudes is proportional to the inverse ratio of the ranges from each station to the lightning source. All locations are computed using spherical geometry, and the computer algorithms have 32-bit floating point precision.

If more than 2 DF stations detect the lightning, then the position analyzer has redundant data available to determine source location. For example, if 3 DFs have responded, the PA can use 3 independent pairs of angle vectors for triangulation and 3 independent ratios of signal amplitudes. The LLP position analyzer can output all the angle intersections for each lightning on command, but, in practice, the operator is usually interested in the most probable location.

The statistics of DF fixing in the presence of random measurement errors have been discussed in detail by Stansfield [11] and others. The results of this work show that the most probable source location (given just direction measurements and not signal amplitudes) is very close to the intersection of the vectors from the two closest DF sites unless the source is close to the baseline connecting these sites. Therefore, in its standard mode of operation, the LLP position analyzer tests the DF signal amplitudes to determine the two closest stations, i.e. the stations with the two largest signal amplitudes, and then computes the most probable location by triangulation of just these vectors. If the lightning is close to the baseline connecting these stations, then the more distant of the two DFs is dropped and the first and third DFs are used to derive a location by triangulation. Basically, this procedure provides a highly accurate estimate of the most probable location with minimal processing time.

OPTIMUM LOCATIONS - We have just seen that when there are more than two simultaneous DF inputs, the LLP position analyzer outputs a lightning location that is very close to the most probable location if the DF direction data contain random errors. All angle intersections are available on command and, of course, the patterns of these intersections can be used to test the DFs for mutual consistency and to evaluate the overall location accuracy.

Another question, however, is where is the

optimum source location when both direction and signal amplitude measurements are available. We have investigated this question using both computer simulated data and data on natural lightning. First we will describe a method of determining this location, and then we will show how a generalization of this procedure can be used to identify and correct any systematic errors that might be present at any (or all) DF sites.

Given N simultaneous measurements of lightning directions, θ_i , and signal amplitudes, S_i , at the direction finders ($i = 1, \dots, N$), we will define the optimum source location, say a latitude, L_a , and a longitude, L_o , and a source strength, S_o , to be the three parameters that minimize the weighted sum of the squares of the residual errors. That is, the optimum location and source amplitude minimize a chi-square function of the form:

$$\chi^2 = \sum_{i=1}^N \left(\frac{\theta_i - \theta_{oi}}{\sigma_i} \right)^2 + \sum_{i=1}^N \left(\frac{S_i - S_{oi}}{\sigma_{oi}} \right)^2 \quad (1)$$

where θ_i and S_i are the measured angles and signals, θ_{oi} is the direction from the optimum location to the i th DF site, $S_{oi} = S_o/R_i$, where R_i is the great circle distance from the optimum location to the i th DF site, and where σ_i and σ_{oi} are the standard deviations of the angle and signal error distributions.

The basic procedure is to start with an estimate of the unknown parameters, L_a , L_o , and S_o and then search for new values of these quantities that make the χ^2 a minimum. A number of search procedures have been developed for minimizing non-linear functions like Equation (1) [12,13], and most methods work best if the number of measurements is large compared to the number of unknowns. An important point to note is that when a minimum χ^2 is found, its numerical value can be used to determine how well the result agrees with the measurements. For example, if the value of χ^2 is close to the degrees of freedom, i.e. the number of measurements minus the number of unknowns, then the parameters are likely to be accurate solutions. If it is not, then there may be systematic errors in the DF data that need to be corrected before it is possible to obtain an optimum solution.

EXAMPLES OF OPTIMUM SOLUTIONS - Before we discuss systematic errors, it will be helpful to illustrate an application of our optimum location algorithm using a computer simulation of the measurement errors that have been found on natural lightning. We will assume that there are just 3 DF stations and that the random error in each direction measurement is described by the error distribution shown in Fig. 1. This distribution has been obtained from measurements on natural lightning and is probably a "worst case" for the actual random errors in an LLP DF system.

To start, we select a particular source location and then calculate the exact angles and signal amplitudes that the DFs would measure in an ideal case. Next, we add random errors to the ideal directions and signals, and then

we recompute and plot the new lightning location. We then repeat this procedure for 100 simulated lightnings at each of several source locations, and the results are shown in Fig. 2. Here, the DF site locations are indicated by crosses in each plot, and it is clear that any lightning that occurs in the center of the network is favorably located for accuracy. A highly magnified view of the boxed central cluster is shown in the upper left portion of each map.

Figures 2a, b, and c show the patterns of lightning positions produced by our simulated measurement errors at 5 source locations. The reader should note that the right-most patterns in each plot are 2 or more baseline distances from the network and that at these ranges the effects of small errors are greatly magnified. In Fig. 2a, each point has been computed using the standard LLP algorithm and thus represents a good estimate of most probable location according to the theory of Stansfield [11]. In Fig. 2b, each point is an optimum location that has been computed using our least-squares optimization procedure assuming that the signal errors are normally distributed with a standard deviation that is 8% of the mean. In Fig. 2c, the points are again optimum locations, but the signal errors have a standard deviation that is only 1% of the mean. Note that the pattern of optimum locations (Fig. 2b and 2c) has significantly less scatter than the most probable locations in Fig. 2a.

SYSTEMATIC ERRORS

If the values of χ^2 are large at the optimum location (i.e. if the minimum χ^2 in the space of the unknown parameters is large relative to the number of degrees of freedom), then the residual errors are large. If such errors persist on several different flashes in the same region, and if there is a spatial pattern to the amplitudes of the minimum χ^2 , then there are probably systematic errors in the DF measurements. The most common systematic error occurs when the DF antennas are not properly aligned North/South and East/West, but the antenna alignment is relatively easy to check. The next most common type is the "site error" and until now these have been difficult to identify and correct.

The most common cause of site errors at VLF and LF frequencies is the presence of large metallic objects near the DF antennas, e.g. overhead power lines, fences, buried pipes, etc. Such objects can scatter (or absorb and re-radiate) the incoming fields and thereby effectively alter the gain of one DF antenna loop relative to the other. In this situation, there will be a systematic error in the lightning direction (and the signal amplitude) that is a function of angle, and the resulting error curve will be a 2-cycle sinusoid of unknown amplitude and phase. If there is more than one source of error at a given DF site, then there will be a superposition of several 2-cycle error curves,

each with an unknown amplitude and phase, but the result will still be a 2-cycle sinusoid. At VLF and LF frequencies, almost all causes of site errors are constant with time. (NOTE: The LLP DF antennas operate with a very wide bandwidth and, therefore, this system is not as sensitive to local resonances as many tuned-frequency DF systems.)

DETERMINATION OF ERROR CURVES - The procedure we have developed to identify and correct site errors is basically a generalization of the least-squares minimization procedure that we have used to determine the optimum lightning locations. The method takes advantage of an inherent redundancy that is contained in the angle and signal amplitude data that are provided by LLP DF systems, and also utilizes a basic symmetry that is contained in the error curves.

First, we select a small sample of lightning flashes that are uniformly distributed over the geographical area covered by the DF network. For each lightning, we compute an optimum latitude, longitude, and source strength and the associated minimum of χ^2 (Eqn. 1). We then sum these minimum chi-square values to form a new quantity that we call the "canonical chi-square" for the network, χ_C^2 .

$$\chi_C^2 = \sum_{i=1}^{NL} \chi_j^2 \quad (2)$$

where NL is the number of lightnings in the sample (typically 200 to 300) and χ_j^2 is the minimum χ^2 for the jth flash.

Next, we allow the measured DF angles (and signal amplitudes) to be altered by an error function that itself can be a function of angle. In the simplest case, the error function at DF site i might have the form:

$$E_i = A_i \sin(2\theta_i + \delta_i) \quad (3)$$

where θ_i is the lightning direction, A_i is the maximum error amplitude, and δ_i is the phase of the error. This function has just two unknown parameters, A_i and δ_i , and, of course, more complicated functions can be used if necessary. Our final step then is to search for those values of the error parameters (the A s and δ s) that make the canonical chi-square a minimum. Once these parameters have been found, then an appropriate correction can be applied to all incoming DF data in the position analyzer.

The error corrections that are derived with this procedure can be tested by requiring that the minimum χ^2 values on individual flashes be consistent with the values expected for just random errors. The entire set of DF corrections can also be tested by selecting different samples of lightning flashes and then verifying that the values of the canonical chi-squares are consistent with just random errors.

AN EXAMPLE OF THE METHOD - To illustrate the correction procedure, we will use computer simulated data and the same DF network that has been plotted in Fig. 2. We begin with a uniform population of lightning flashes, add random errors to the ideal angles and signals, and

compute the optimum lightning positions. The results of this procedure are shown in Fig. 3a. Next, we add large site errors to each DF site and recompute the optimum locations. The results of this are shown in Fig. 3b. The angle errors that we have added to each DF to produce Fig. 3b are shown as the solid curves in Fig. 4.

Finally, we implement our error correcting algorithm using the raw data in Fig. 3b, and we obtain the error correction curves shown as dotted lines in Fig. 4. Fig. 3c shows the final lightning locations after the site corrections have been applied. Note that the pattern in Fig. 3c is very close to the original pattern we started with in Fig. 3a.

SUMMARY

In conclusion, we now have a systematic method for determining an optimum lightning location if there are both angle and signal amplitude measurements at a number of DF sites. We also have a new method that can be used to identify and correct any systematic errors that might be present at any (or all) DF sites. These procedures have been tested on natural lightning, and we expect to publish detailed results in the scientific literature in the near future.

REFERENCES

1. E.P. Krider, R.C. Noggle, A.E. Pifer, and D.L. Vance, "Lightning Direction-Finding Systems for Forest Fire Detection", *Bull. Am. Met. Soc.*, 61, 980-986, 1980.
2. R.C. Binford, L.G. Byerley, E.P. Krider, M.W. Maier, A.E. Pifer, and M.A. Uman, "Wideband Magnetic Direction Finder Networks for Locating Cloud-to-Ground Lightning", 8th Int. Aerospace and Ground Conf. on Lightning & Static Electricity, Ft. Worth, TX, June 21-23, 1983.
3. R.E. Orville, R.W. Henderson, and L.F. Bosart, "An East Coast Lightning Detection Network," *Bull. Am. Met. Soc.*, 64, 1029-1037, 1983.
4. R.L. Smith-Rose, "A Study of Radio Direction Finding", Radio Research Board Special Report No. 5, H. M. Stationery Office (Great Britain), 1929.
5. R. Keen, "Wireless Direction Finding", (3rd Ed.), Iliffe & Sons Ltd., London, 1938.
6. P.J.D. Gething, "Radio Direction Finding", Peter Peregrinus Ltd., London, 1978.
7. E.P. Krider, A.E. Pifer, and M.A. Uman, "An Automatic Locating System for Cloud-to-Ground Lightning", Lightning Technology, Proc. of technical symposium held at NASA Langley Research Center, Hampton, VA, April 22-24, 1980, NASA CP-2128, FAA-RD-80-30.
8. E.P. Krider, R.C. Noggle, and M.A. Uman, "A Gated Wideband Magnetic Direction Finder for Lightning Return Strokes", *J. Appl. Meteor.*, 15, 301-306, 1976.
9. B.D. Herrman, M.A. Uman, R.D. Brantley, and

E.P. Krider, "Test of the Principle of Operation of a Wideband Magnetic Direction Finder for Lightning Return Strokes", *J. Appl. Meteor.*, 15, 402-405, 1976.

10. F. Horner, "Very-low-frequency Propagation and Direction-Finding", *Proc. IEEE*, 104B, 73-80, 1957.
11. R.G. Stansfield, "Statistical Theory of D. F. Fixing", *J. IEE*, Part IIA, 762-770, 1947.
12. L.C.W. Dixon, "Nonlinear Optimization", English Universities Press, Ltd., London, pp. 214, 1972.
13. D.M. Himmelblau, "Applied Nonlinear Programming", McGraw-Hill, New York, pp. 498, 1972.

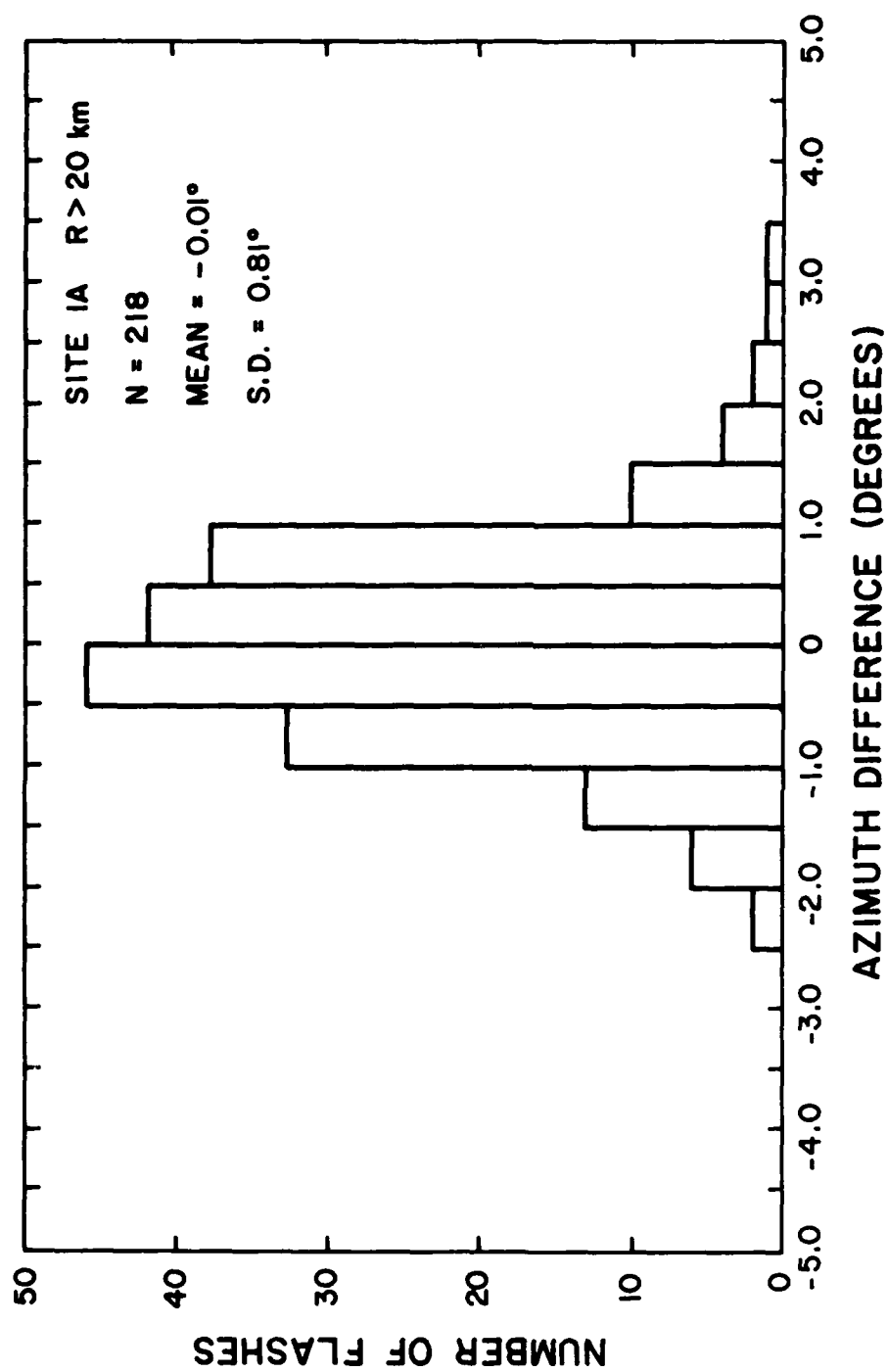


Fig. 1 - Random error distribution, measured from natural lightning, used to describe the error on direction measurements

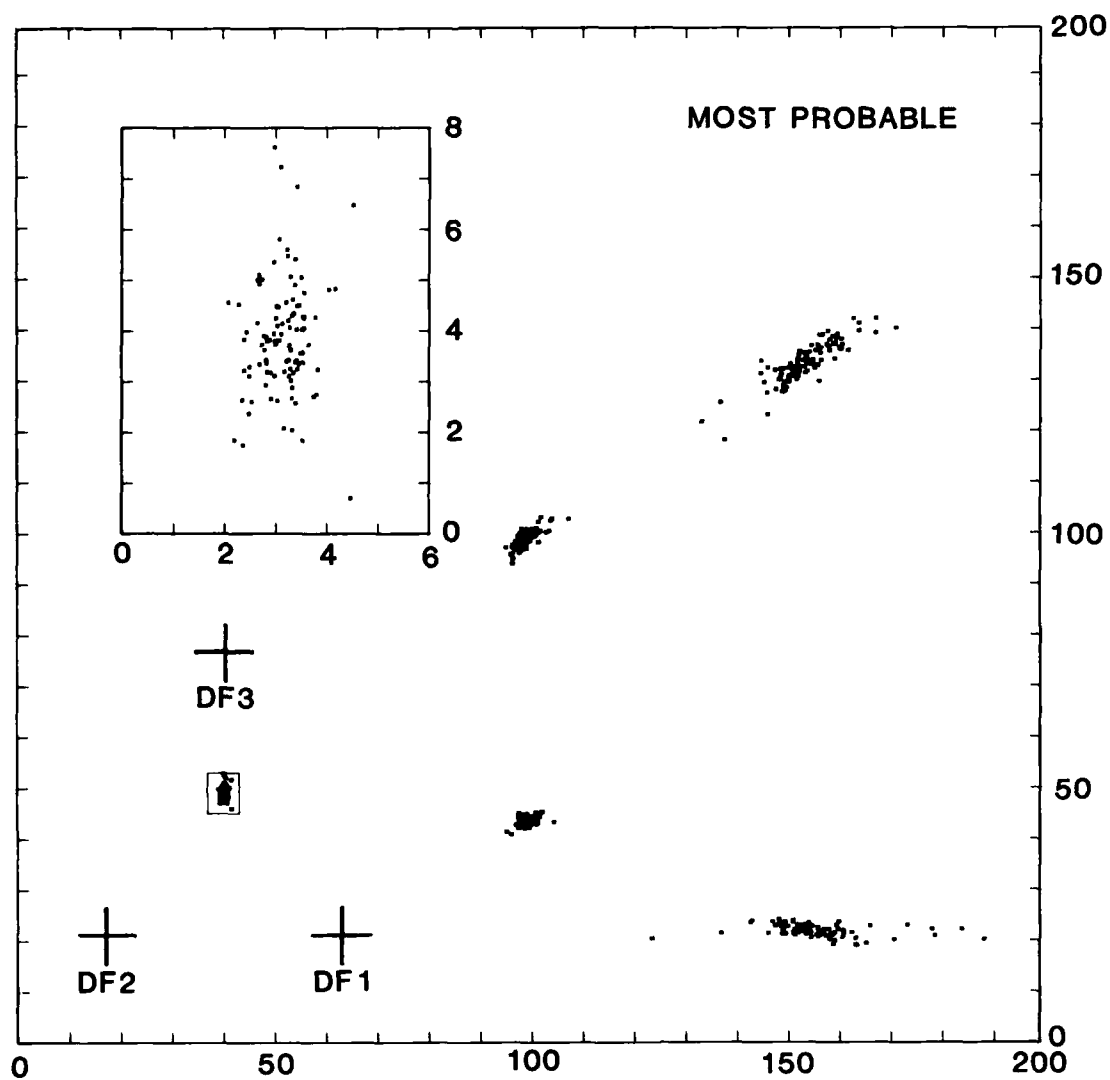


Fig. 2 (a) - The pattern of lightning positions produced by simulated measurement errors at 5 source locations. This group contains 100 positions and shows the most probable locations

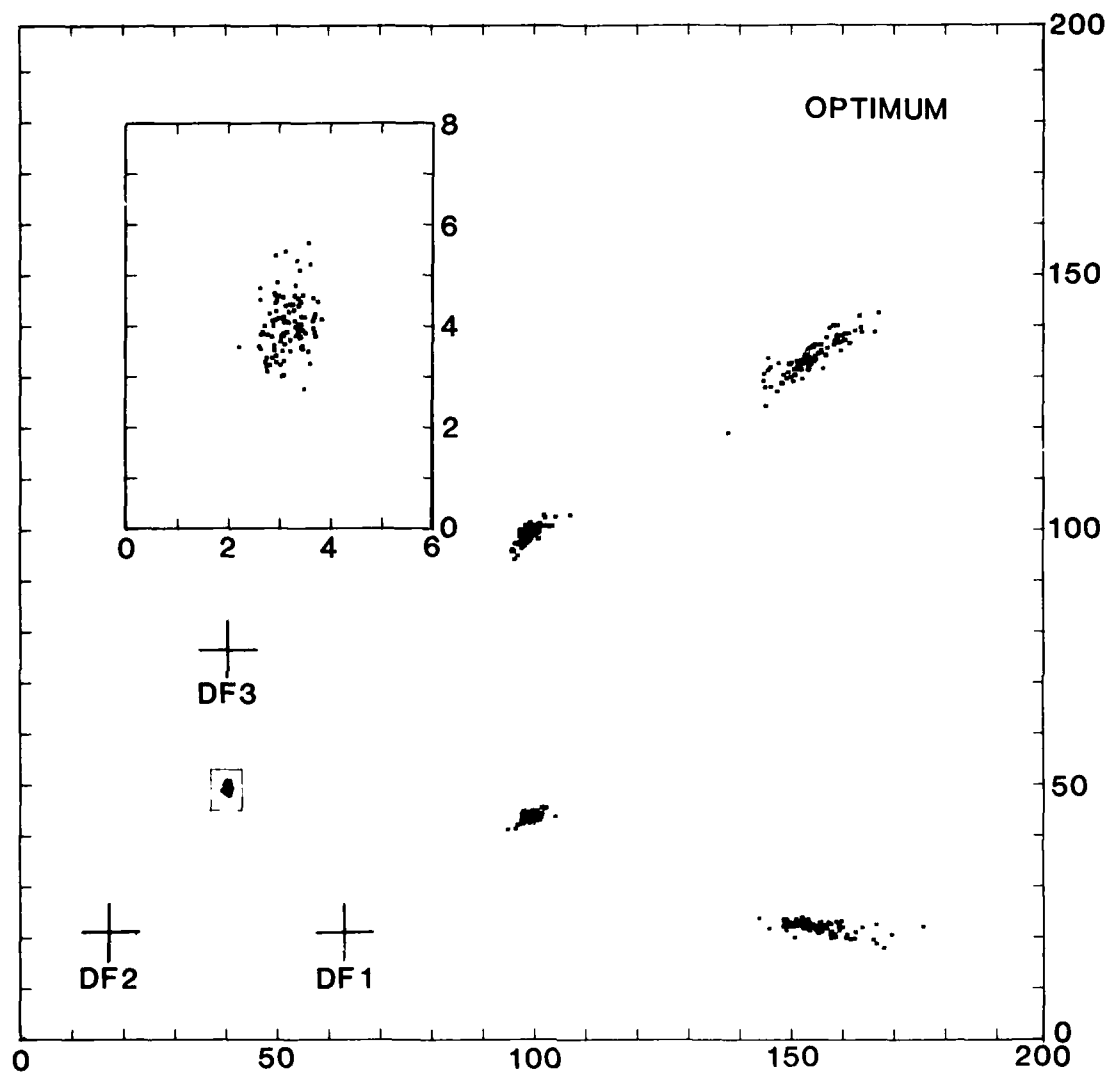


Fig. 2 (b) - The pattern of lightning positions produced by simulated measurement errors at 5 source locations. This group contains 100 positions and shows the optimum locations with signal errors normally distributed and with a standard deviation that is 8% of the mean.

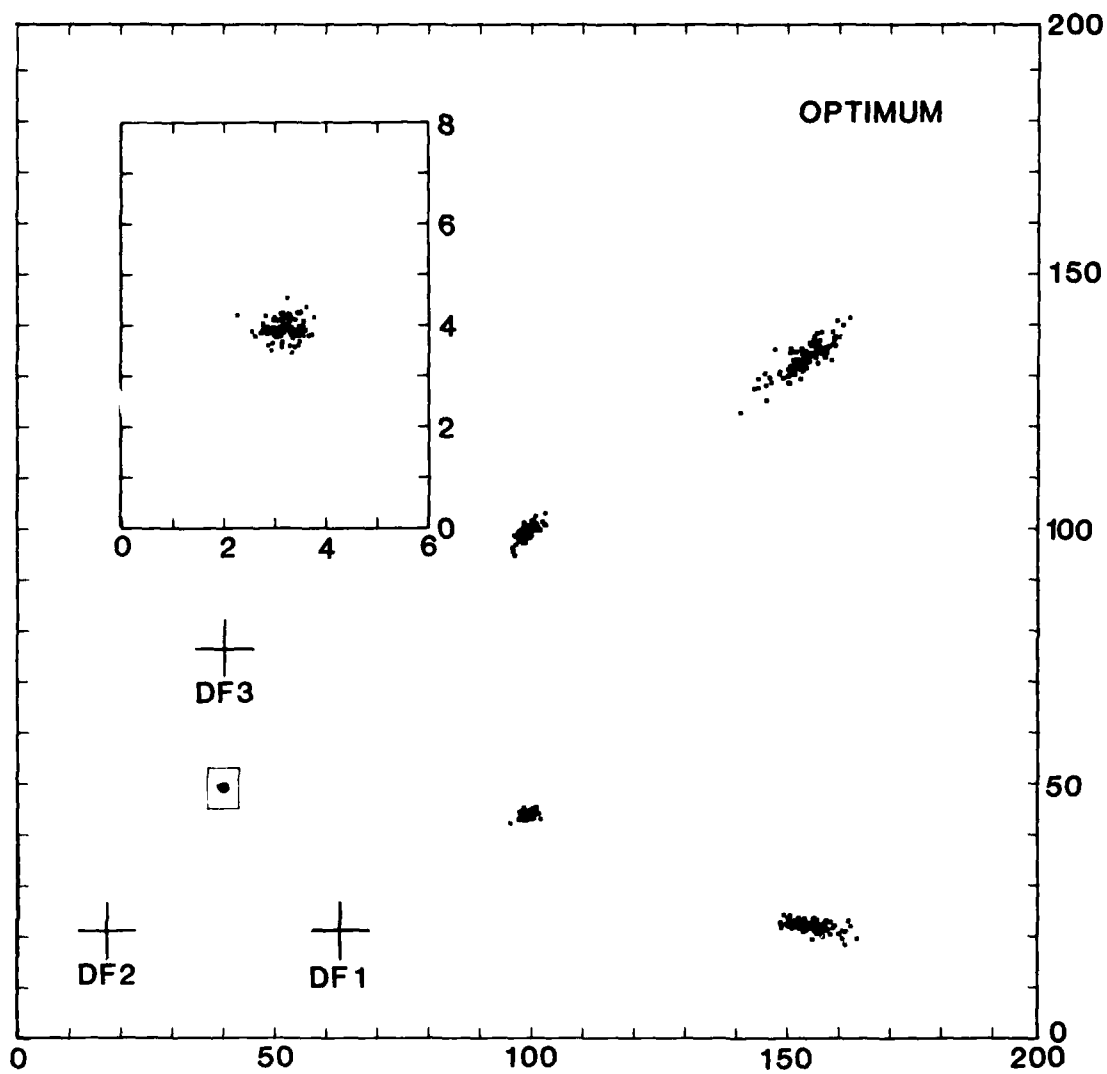


Fig. 2 (c) - The pattern of lightning positions produced by simulated measurement errors at 5 source locations. This group contains 100 positions and shows optimum locations with a normal signal error and a standard deviation that is 1% of the mean.

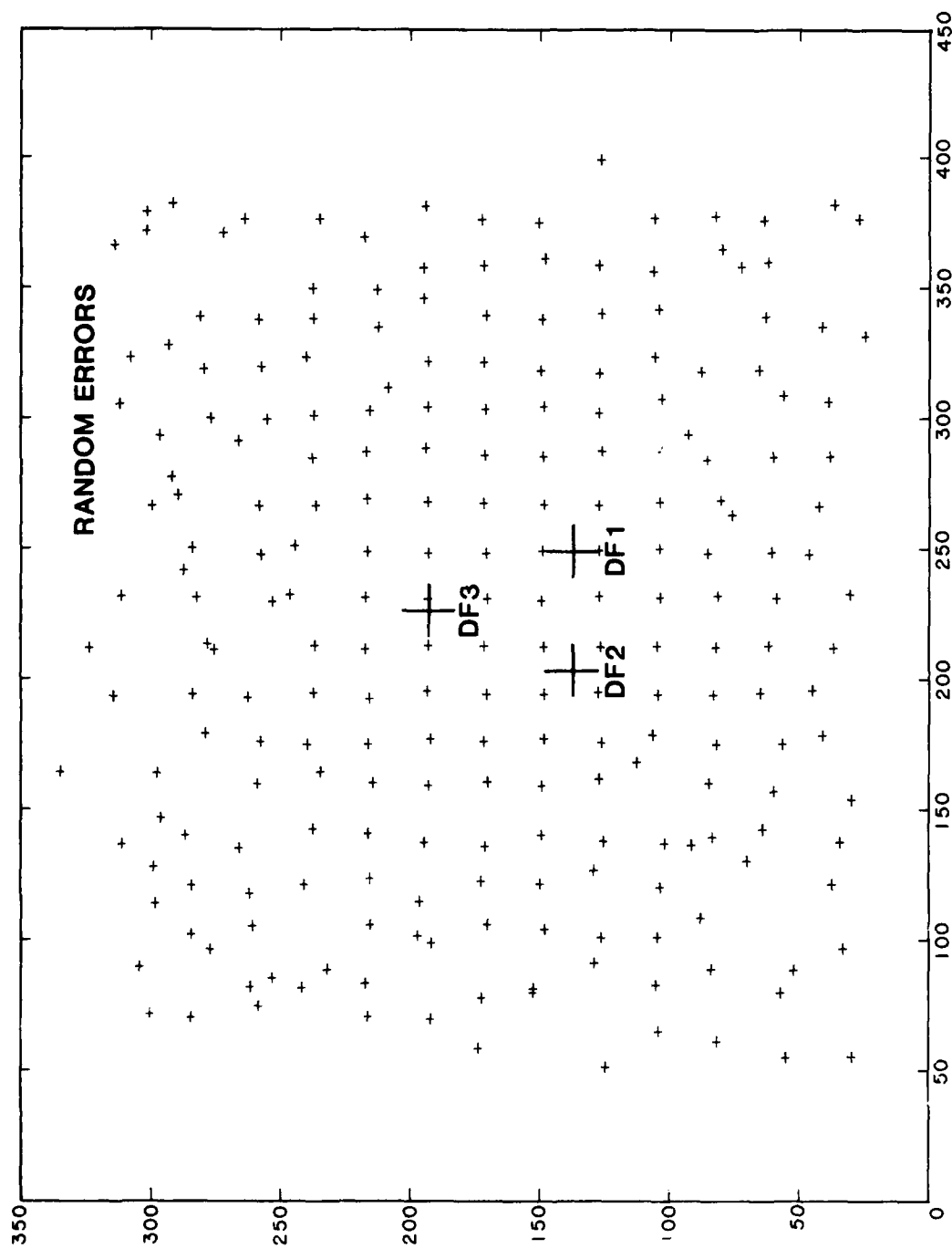


Fig. 3 (a) - The optimum locations of computer simulated lightning flashes with just random errors.

AD-A169 867

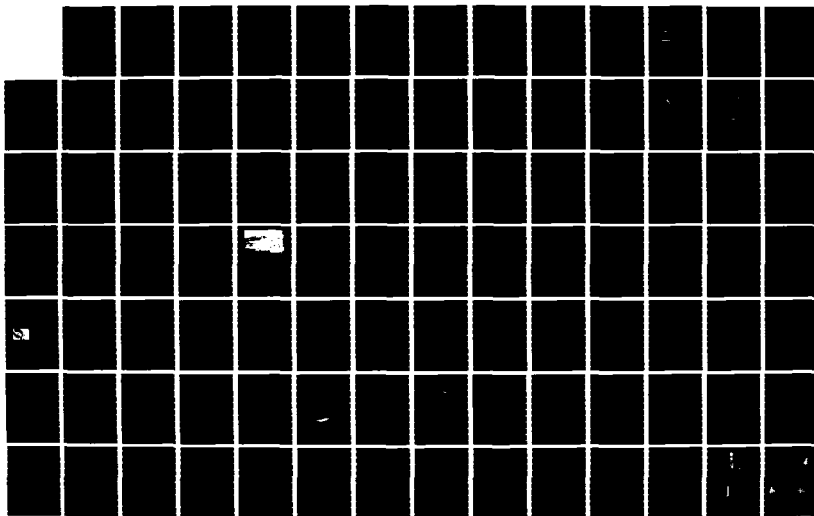
INTERNATIONAL AEROSPACE AND GROUND CONFERENCE ON
LIGHTNING AND STATIC ELE. (U) NATIONAL INTERAGENCY
COORDINATION GROUP JUN 84

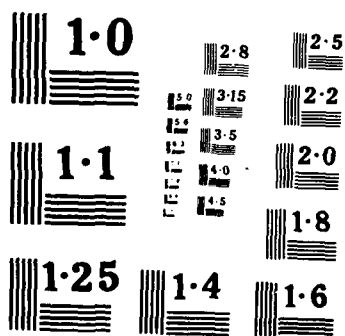
2/6

UNCLASSIFIED

F/G 20/3

NL





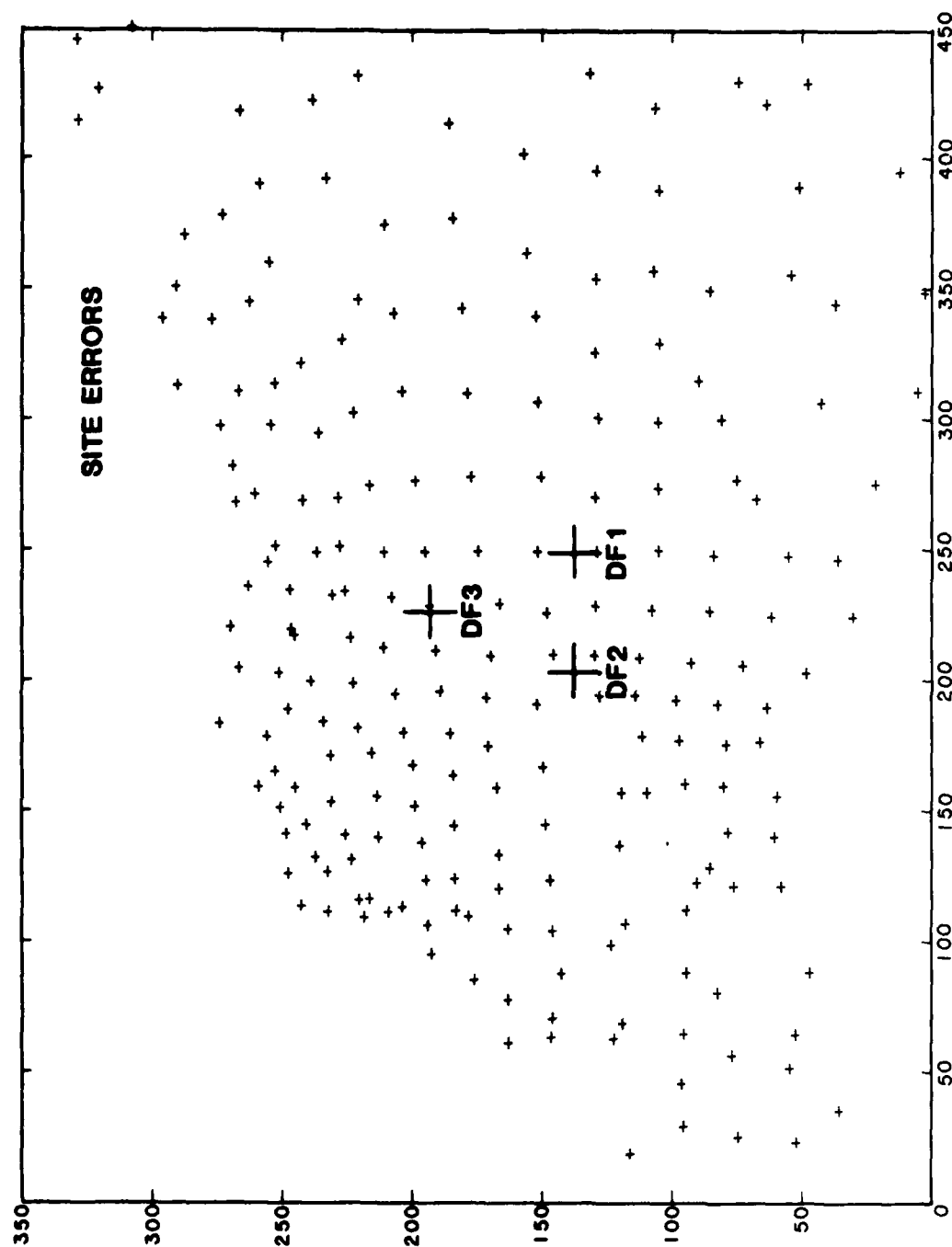


Fig. 3 (b) - The optimum locations of computer simulated lightning flashes with random errors plus large site errors at each DF.

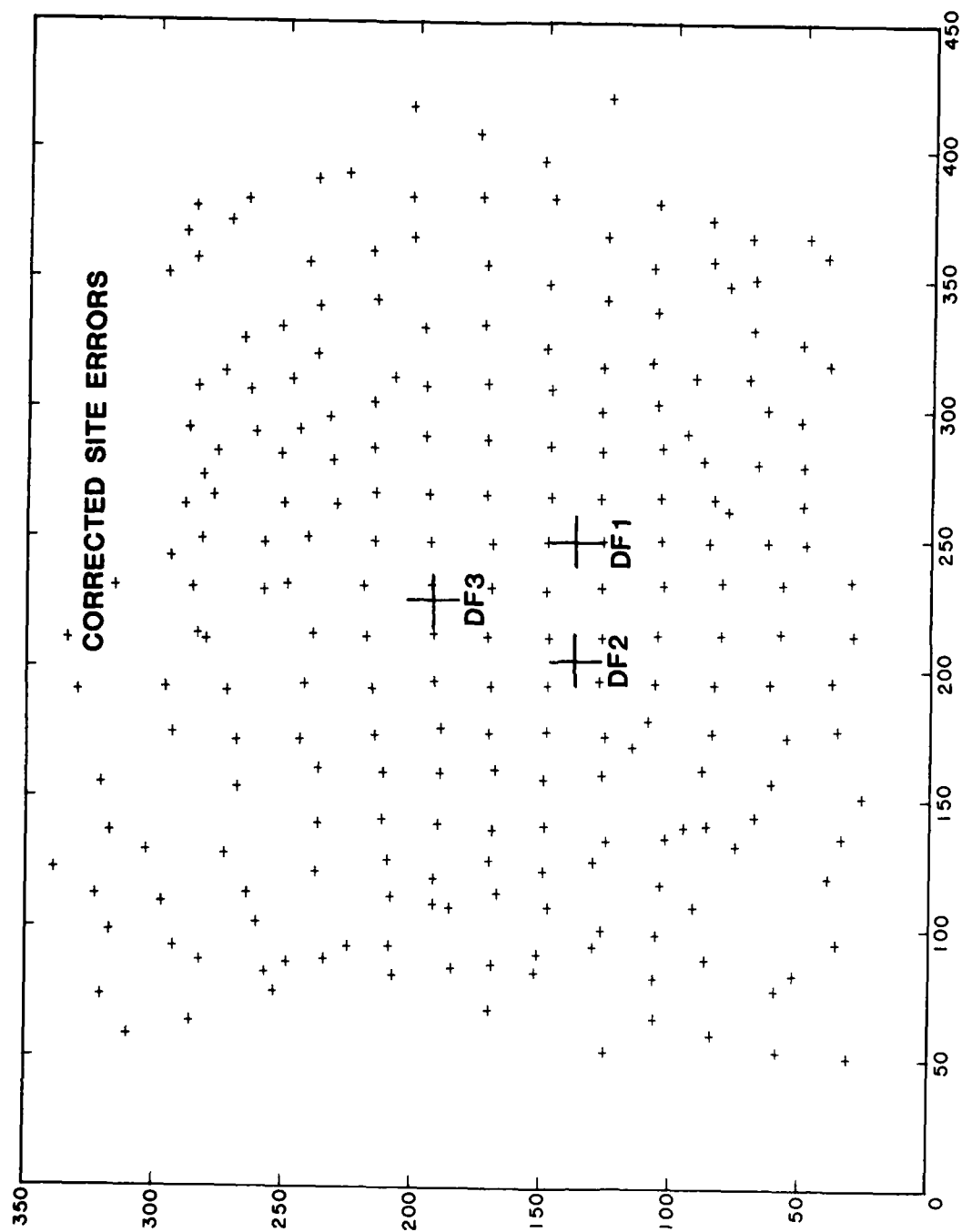


Fig. 3 (c) - The optimum locations of computer simulated lightning flashes with the same as (b) but after the site errors have been corrected.

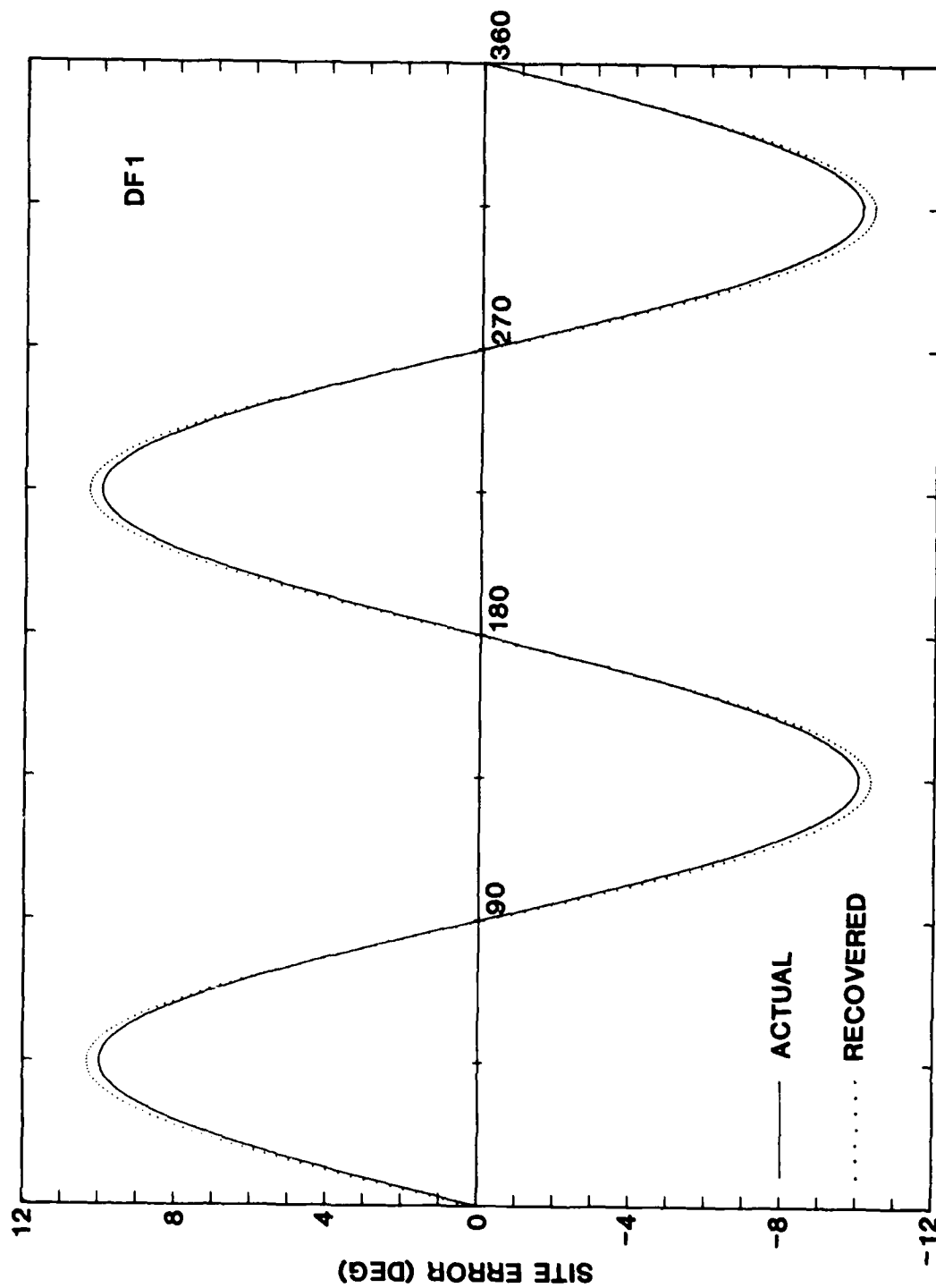


Fig. 4 (a) (b) (c) - The systematic errors that have been applied to each DF in Fig. 3 (solid curves) and the errors that have been recovered by the correction algorithm for each of these DFs (dotted curves).

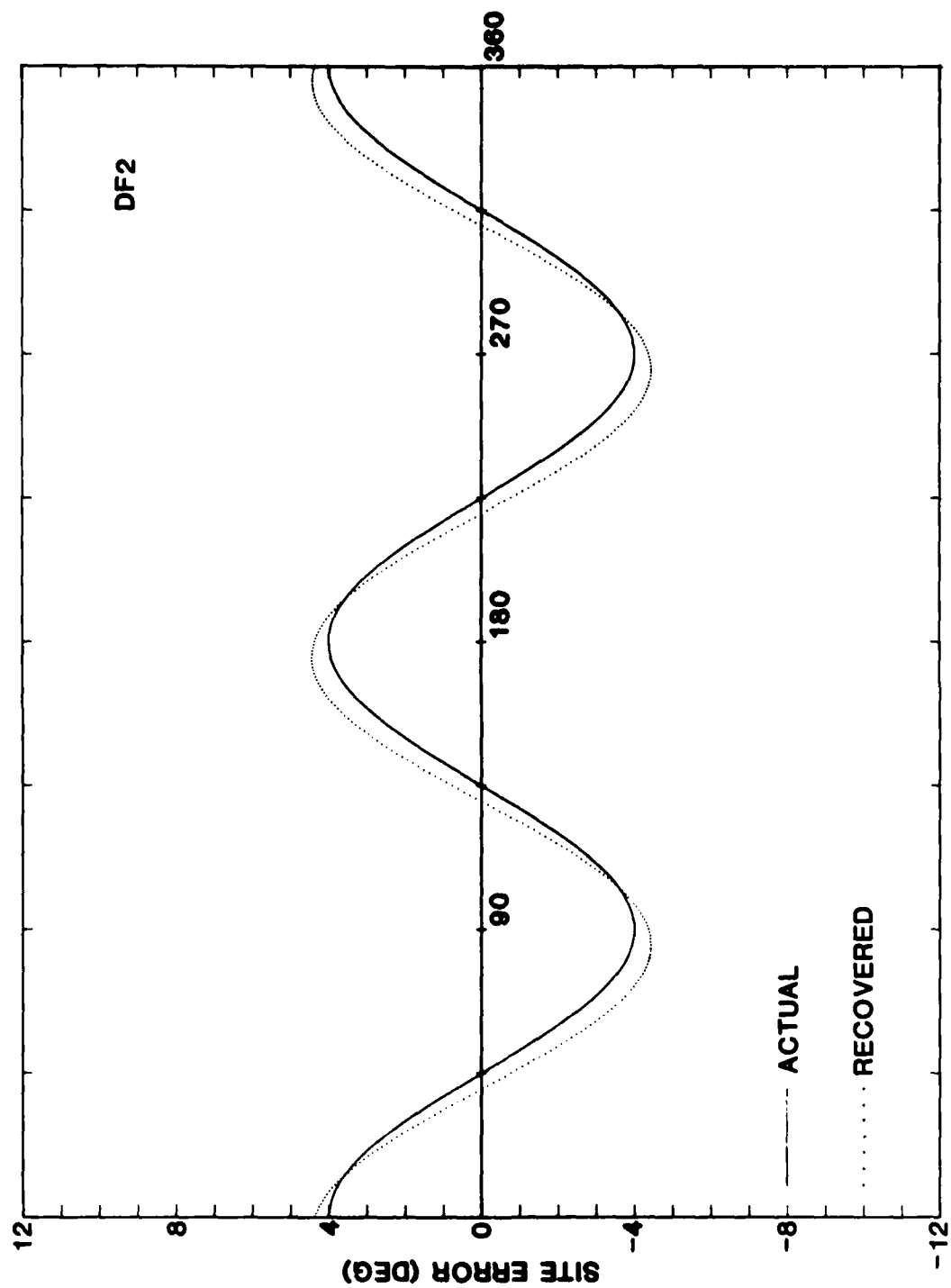


Fig. 4 (b)

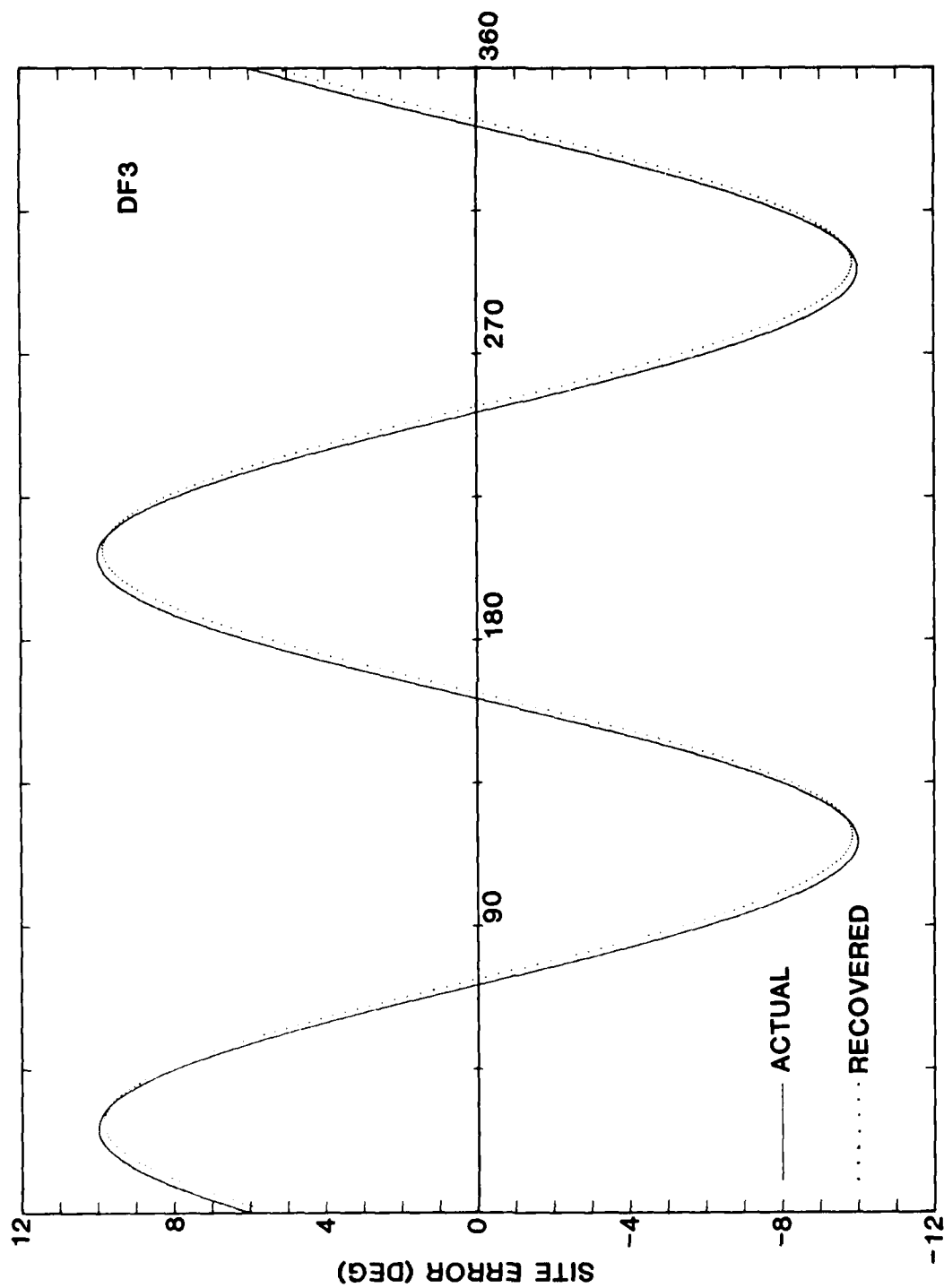


Fig. 4 (c)

ROCKET TRIGGERED LIGHTNING: A COMPARISON WITH NATURAL FLASHES

Richard D. Richmond
Atmospheric Electricity Hazards Group
AFWAL/FIESL
Wright Patterson AFB, Ohio

ABSTRACT

The Rocket-Triggered Lightning Investigation (RTLII) is a program conducted by the Flight Dynamics Laboratory at Wright Patterson AFB with the cooperation of the French research organizations ONERA and CENG. The purpose of this paper is to discuss some of the similarities that have been observed between the electromagnetic characteristics of triggered lightning and those of natural flashes. The electromagnetic waveforms of the 1983 triggered flashes were recorded at an instrumentation trailer located approximately 600 meters from the triggering site. These waveforms are compared with waveforms recorded for natural flashes and with the characteristics of natural lightning that have been reported by other researchers. These two types of lightning are shown to be very similar in such important characteristic properties as peak currents, risetimes and the number of strokes per flash.

INTRODUCTION

ONE OF THE TASKS of the Atmospheric Electricity Hazards Group (AEH) of the Air Force Wright Aeronautical Laboratories (AFWL) at Wright Patterson AFB is the characterization of the threat presented to aircraft by lightning. For this characterization, a large amount of data is needed to define the electromagnetic fields generated by lightning flashes. In 1983, the AEH Group continued an experiment to determine if the data collected from lightning that had been artificially triggered by a wire-towing rocket was suitable for this characterization. This experiment has been a joint program between the AEH group and the French Government organization, Office National D'Etudes et de Recherches Aerospatiales (ONERA). For the 1983 experiment, the location was moved from the original site at Langmuir Laboratory, near Socorro, New Mexico (1)*, to Valkaria Airport, south of Melbourne, Florida.

The addition, in 1983, of a nearby ground station equipped with instrumentation for measuring the radiated electromagnetic fields from both triggered and nearby natural lightning made it possible to directly compare the characteristics of these two types of lightning. Simultaneous electric and magnetic field waveforms were analysed for two of these triggered flashes and compared with natural flashes reported by other researchers as well as those natural flashes recorded during this experiment and with model predictions for nearby lightning. For triggered flashes, the electric and magnetic fields measured at the ground station were also compared with the channel current measured at the ground by a resistive shunt.

EXPERIMENT

THE EXPERIMENTAL SITE, Valkaria Airport, is approximately 15 kilometers south of Melbourne, Florida. The launch site was at the southern portion of the airport and consisted of a 20 meter tall tripod supporting the Lightning Strike Object (LSO). The LSO and the sensors that were installed on it were described by Schubert and Richmond (1). The rocket launchers were located on the ground around the base of the tripod. The resistive shunt for measuring the current in the lightning channel was installed on the ground beneath the LSO. This shunt had a bandwidth of from DC to nearly 100 MHz. Fiber optics transmitted the current data to analog recorders and to wide band instrumentation. Two trailers that were parked 50 meters from the tripod housed the instrumentation associated with the launch site and the LSO. Two high speed (1000 frames/sec) movie cameras were located 100 meters from the scaffold. These cameras were positioned 90 degrees from each other with respect to the scaffold. The general

layout of the site is illustrated in Fig. 1. The results of this portion of the experiment will be reported in subsequent papers.

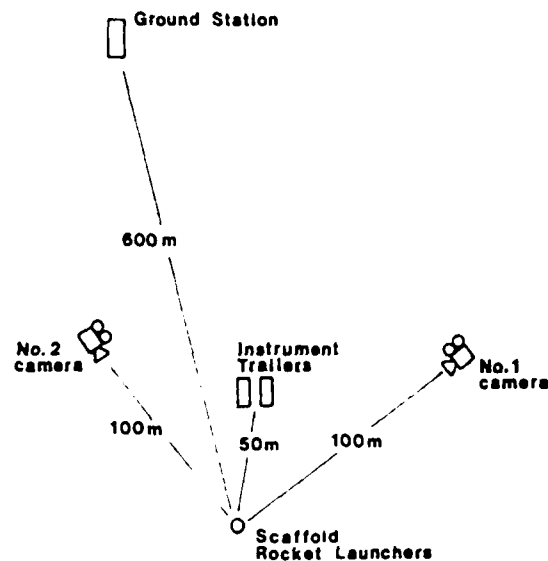


Fig. 1 - Launch site detail

THE GROUND STATION TRAILER was parked at the center of the airport and approximately 600 meters from the launch site (see map, Fig.2). To measure the magnetic fields, two crossed loops were mounted on the roof of the trailer. One loop was pointed directly at the launch site and the other was at a right angle to the first. The equivalent area of these loops was 0.1 m^2 with a frequency response of over 5 MHz (2). The loop outputs were electronically integrated and recorded on an analog tape recorder with a bandwidth of 400 Hz to 2 MHz.

TWO CAPACITIVE ANTENNAS for measuring electric fields were also mounted on the roof of the trailer. These were circular plates with areas of 0.05 m^2 and 0.20 m^2 respectively. The integrators and amplifiers provided four decade steps of electric field range from $\pm 140 \text{ v/m}$ to $\pm 140000 \text{ v/m}$. By recording these four outputs on several different channels of the recorder, a bandwidth of DC to 2 MHz was obtained. Also located at the ground site was a thunder microphone that was used to determine the range to natural lightning using the time of arrival of the thunder.

*Numbers in parentheses designate References at end of paper

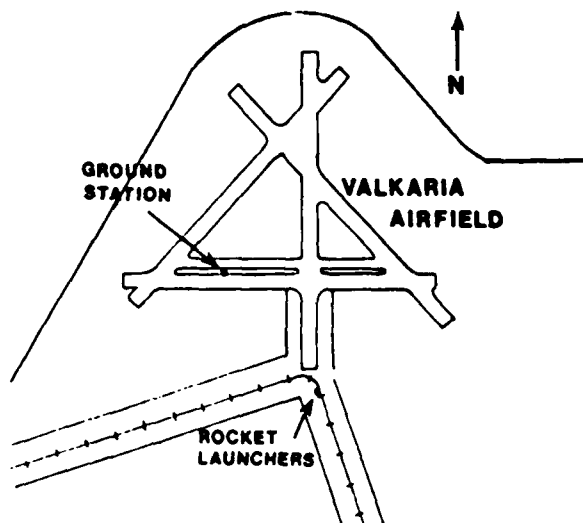


Fig. 2 - Map of Valkaria Airport

NATURAL FLASH CHARACTERISTICS

FLASH DURATION AND NUMBER OF STROKES - Kitagawa, et al (3) reported flash durations for two types of multiple stroke cloud to ground flashes. Discrete flashes were defined as those for which the stroke luminosity decayed abruptly. Hybrid flashes were those in which one or more of the strokes had continuing current associated with them. For discrete flashes, the average flash duration was reported as 438 msec, with the longest being 1699 msec. These flashes contained an average of 7 strokes with 22 the maximum reported. For hybrid flashes, the average duration was 646 msec and the maximum duration was 1928 msec. The average number of strokes for hybrid flashes was reported as 7 with a maximum of 26. These multiple stroke flashes constituted about 90% of the flashes reported.

Using a streak camera array, Kitterman (4) reported that 44% of the cloud to ground flashes recorded were of these two types. The average duration for discrete flashes (27% of the flashes) was 262 msec with the maximum being 1180 msec. The average number of strokes was 4 with a maximum of 11. For hybrid flashes (17% of the flashes), the durations averaged 442 msec with a maximum of 1050 msec. These flashes contained an average of 5 strokes per flash with a maximum of 11. Brantley, et al (5) reported average cloud to ground flash durations for the Kennedy Space Center area of 220 msec and a maximum of 1100 msec. The average number of strokes reported for these flashes was 3 with a maximum of 12.

CURRENT AMPLITUDES - From the graph of peak currents derived by Uman, et al (6) it appears that 50% of their return strokes had peak currents of less than 35 kiloamps (KA). This compares well with the mean of 23 KA computed by Lin (2), with the measured tower average of 28 KA reported by Eriksson (8) and with the 30 KA for first strokes and 12 KA for subsequent strokes from Berger (9).

RISETIMES - Uman, et al (6) reported zero to peak risetimes of 0.5 microseconds (usec) and indicated that system response time limitations were such that the risetimes could have been faster. Lin, et al (10) reported average risetimes of 1.5 usec with a standard deviation of 0.5 usec for strokes measured at Kennedy Space Center. The 10-90% risetimes for the fast portion of subsequent return strokes taken from airborne measurements and reported by Rustan, et al (11) were 0.435 usec. Again measuring the fast transition portion of the stroke, Weidman and Krider (12) reported a mean risetime of 0.09 usec.

RETURN STROKE WAVESHAPES - Several papers (Lin, et al (10); Lin, et al (7); Uman, et al (13)) report waveshapes for flashes that occurred within 2 km of the measuring sites. These waveforms were generally similar to those shown in Fig. 3.

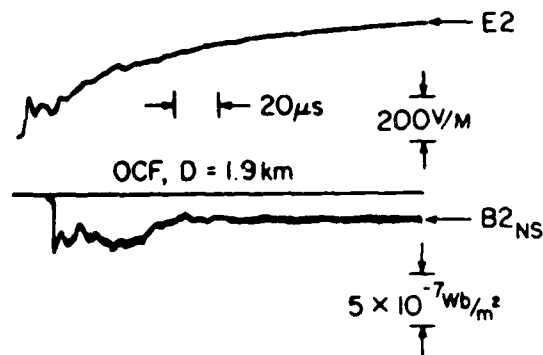


Fig. 3 - Second return stroke fields at 1.9 km (from Lin)

Although the RTL instrumentation was normally recording only during rocket launches, at least one natural cloud to ground flash was recorded. This flash, 83N025, occurred on 11 August. It struck the airport approximately 300 meters south of the ground station, this location was confirmed when the resulting fire interrupted operations for over an hour while firemen were putting the flames out. Figure 4 shows the electric and magnetic field waveshapes for the second return stroke of this flash. The waveshapes in Figs 3 and 4 are similar to those predicted by Masters, et al (4), Fig. 5.

GENERALIZED FLASH PARAMETERS - The above data for natural lightning flashes is summarized in Table 1. Based on this data and the preceding discussion, the following description of a natural lightning flash can be suggested as a general criteria against which rocket-triggered lightning could be compared. This would be a multistroke flash with 3-5 return strokes and an overall duration of 400 to 500 msec. Long continuing currents would occur between subsequent strokes at least 50% of the time. The risetimes for subsequent return strokes would be 0.5 usec, and stroke peak currents would average 30 KA. The subsequent stroke waveshapes for the near-field electric and magnetic fields should be similar to those shown in Fig. 5. Although a generalized description, the criteria are sufficient for this discussion.

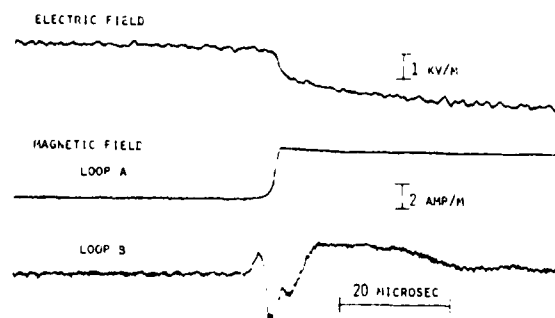


Fig. 4 - Second return stroke fields at 300 meters (Flash 83N025)

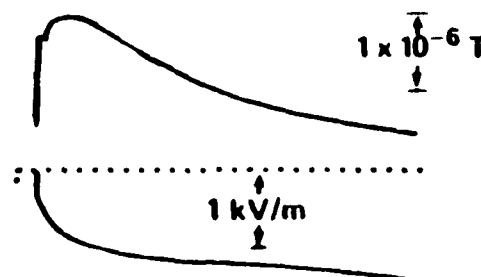


Fig. 5 - Predicted subsequent return stroke fields at 1 km (from Masters)

Table 1 - Natural Lightning Characteristics

Source	Duration (msec)		Strokes/Flash	
	aver.	max	aver.	max
<u>Kitagawa</u>				
Hybrid	646	1928	7	26
Discrete	438	1699	7	22
<u>Kitterman</u>				
Hybrid	442	1050	5	11
Discrete	262	1180	4	11
<u>Brantley</u>	220	1100	3	12

	Current Amplitude (kA)		Risetimes (usec)		Measuring Procedure
	1st R.S.	Sub R.S.	1st R.S.	Sub R.S.	
Uman	50	38	1.2	0.4	10-90
Lin	45	30	1.5	0.4	10-90
Rustan			1.0	0.8	10-90
"			0.7	0.4	Fast-Portion
Weidman			0.09		Fast-Portion
Eriksson	41	25*			
Berger	30	12			

* Reported as average for all negative flashes

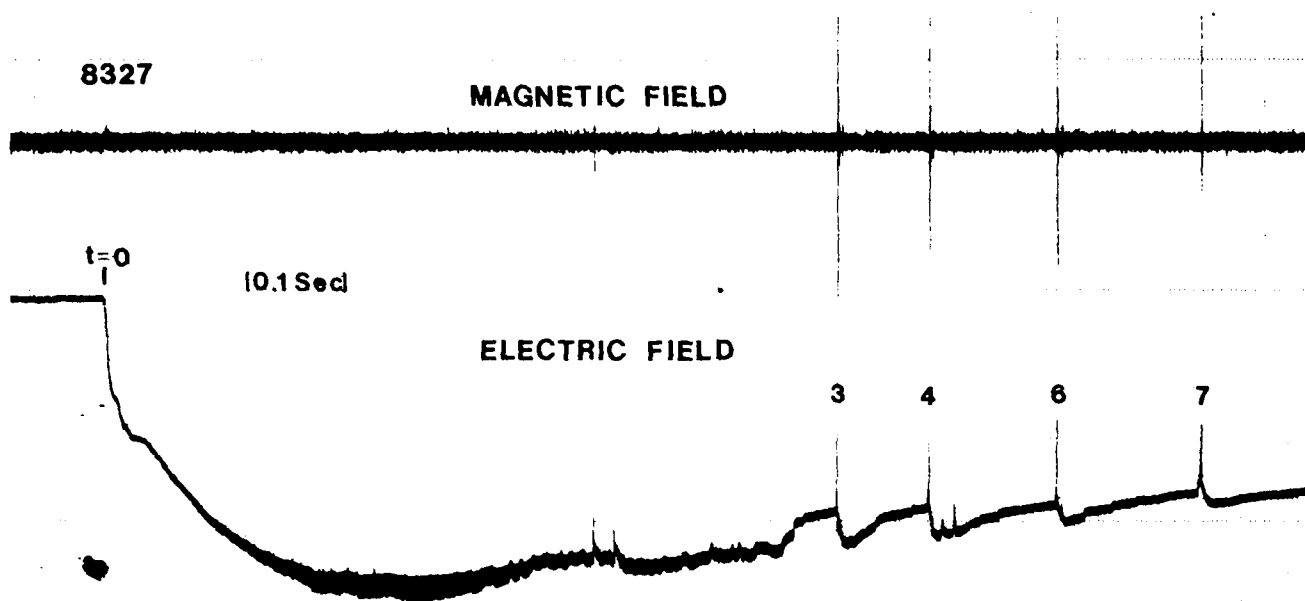


Fig. 6 - Fields for Triggered Flash 8327 at 600 meters

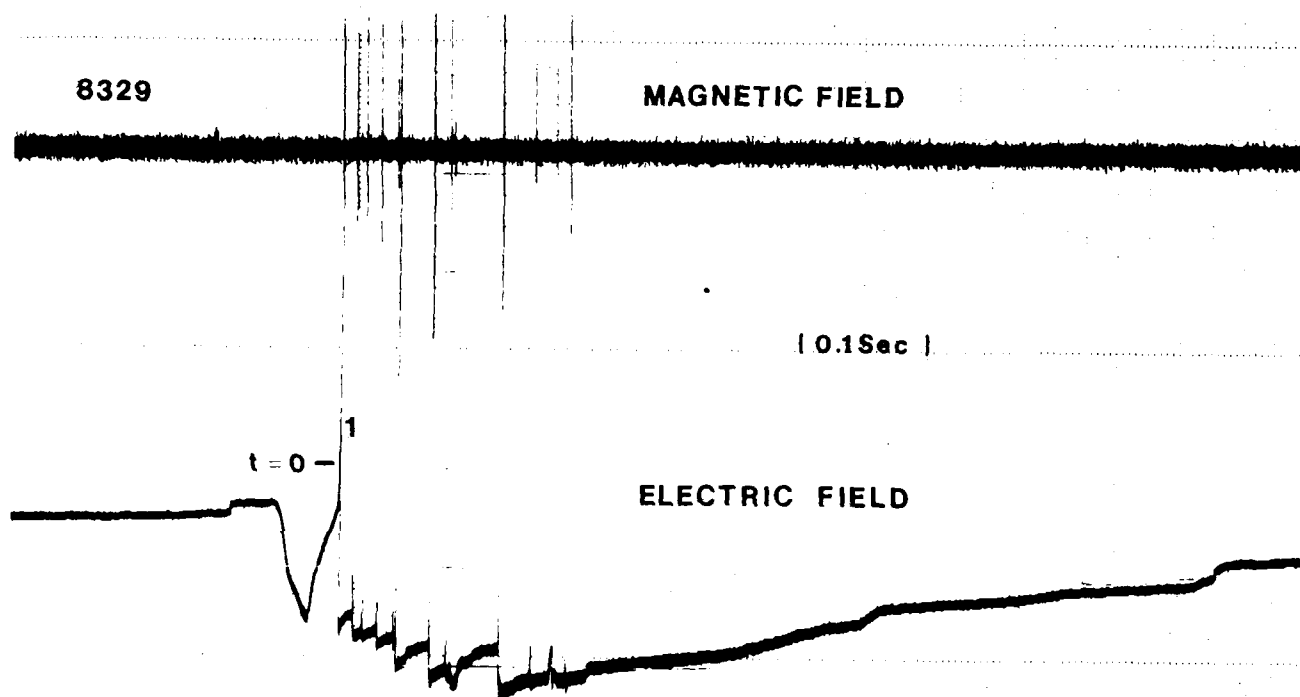


Fig. 7 - Fields for Triggered Flash 8329 at 600 meters

TRIGGERED FLASH DESCRIPTION:

LIGHTNING IS TRIGGERED by a grounded wire rising rapidly in the high electric field associated with a thunderstorm. When the enhanced field at the upper tip of the wire reaches some breakdown threshold, upward leaders begin to propagate toward the clouds (15). Once these leaders begin, current in the wire increases rapidly. The wire usually vaporizes when the current is between 10 and 50 amps. When field conditions are suitable, the leader continues to propagate upward until it connects with a downward propagating leader from the cloud and a stroke is initiated. LaRoche, et al (15) define two types of triggered flashes. The first type is considered a classical trigger. In this flash, current in the ionized path left by the vaporized wire continues to increase to those levels associated with continuing currents (100 to 1000 Amps). There may be several individual strokes in this type of flash with continuous current after the strokes. The second type of trigger, known as an anomalous flash, differs from the first in that the current in the wire stops abruptly after the wire vaporizes. After a pause of several milliseconds, a downward leader follows the ionized path. One or more return strokes will then follow. These strokes may or may not be followed by continuing currents.

The grounded end of the wire is attached to the shunt located on the ground below the LSO. When a flash is triggered, the lightning following the wire path strikes near to and even directly onto the LSO and travels through the shunt.

DURING THE PERIOD from 29 July to 14 August 1983, 33 rockets were launched with a total of 18 successful triggers. The data for this report were obtained from two of the four flashes that were triggered on 14 August (flash no's. 8327,8329). In addition to the ground station data, high speed movies and resistive shunt current data were also obtained for these flashes.

FLASH 8327 was a classical flash as described by LaRoche, et al (15). The time correlated magnetic and electric fields for the entire flash are presented in Fig. 6. Time $t=0$ represents the wire vaporizing and the beginning of continuing current in the channel. This time also corresponds to the appearance of a visible glow in the channel on the high speed movies. Current continued to flow in the channel for approximately 745 milliseconds (msec). This time was arbitrarily determined as the time when approximately 50% of the channel had gone non-luminous on the film. The entire event lasted for 1230 msec using the same criteria. For a total of eight pulses that were separately identifiable from the electric field record for this flash, four (numbered 3,4,6,7 in Fig.6) were distinct enough to be considered subsequent return strokes.

FLASH 8329 was of the type labeled as anomalous by LaRoche (15). The electric and magnetic fields for this entire event are shown in Fig. 7. During this flash, there were 11 separate return strokes with the channel going dark between each of these strokes. This flash lasted only 185 msec. In addition to the lack of continuing current, another significant difference in this flash was that the wire vaporized 25 msec before the initiation of the first return stroke.

Because the channel for these two flashes terminated at the shunt, current data is available for each of these entire events. The logarithmically compressed current waveshapes obtained from the shunt are shown in Fig. 8. The physical characteristics of these two types of flashes, as described above, can be seen in this diagram.

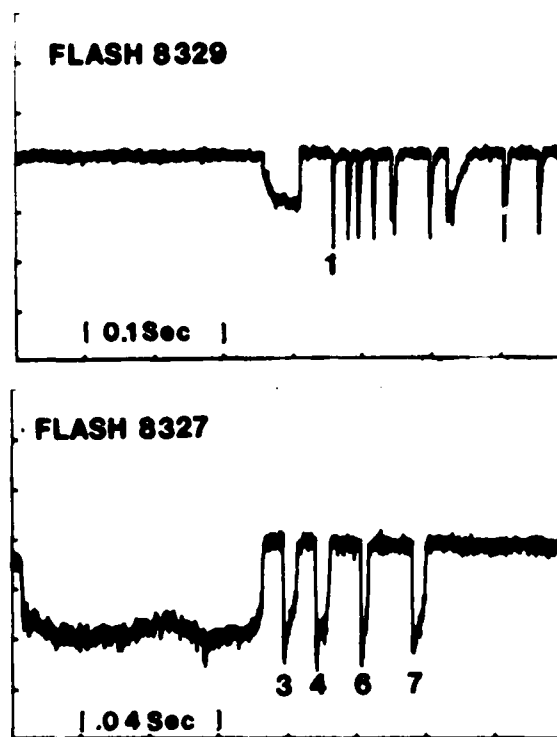


Fig. 8 - Shunt output for Triggered Flashes 8327 and 8329

COMPARISONS: NATURAL VS TRIGGERED FLASHES

THE MOST OBVIOUS DIFFERENCE between triggered and natural flashes is the absence of a first return stroke in a triggered flash. For a natural flash, the first return stroke is normally preceded by a stepped leader. For triggered lightning, even for flashes such as 8329 in which the wire vaporized some time before the initiation of the return stroke, the ionized path left by the wire creates conditions similar to a subsequent stroke. Also, for natural lightning, the first return stroke usually has a higher peak current than the subsequent strokes. However, comparing the wide spread of currents reported for natural strokes with the representative currents measured for triggered strokes (Table 2) indicates that this may not be an important difference. The flash durations and the number of return strokes/event for the flashes triggered in '83 are listed in Table 2. Of the flashes recorded by the high speed cameras, all but flash 8329 had continuing currents through at least a portion of the event. Although several of the durations listed in Table 2 are longer than that of the model proposed in the above section, all of the times and number of strokes are well within the bounds reported for natural flashes.

Table 2 - Triggered Lightning Duration and Number of Return Strokes (1983 Shunt Data)

Launch#	Duration (msec)	#Return Strokes
01	650	9
02	480	1
03	370	2
05	600	2
07	1055	2
11	855	6
14	870	2
17	940	6
20	1000	1
22	1000	1
23	1280	4
24	1160	5
27	1230	6
28	700	1
29	250	11

LOOKING AT THE CHARACTERISTICS OF THE INDIVIDUAL STROKES, the correlated electric and magnetic fields for some of the strokes in flashes 8327 and 8329 are given in Figs 9 and 10. When compared with the electric fields for natural flashes shown in Fig 3 and the calibrated fields of Fig 5, the wave shapes for these triggered flashes can be seen to be very similar. Even the radiation field peak that has been reported as difficult to identify by Tiller, et al (16) is readily apparent in some of these strokes. Table 3 lists the 10-90% peak risetimes, peak electric fields and the current measured by the shunt for the strokes in flashes 8327 and 8329. The natural wave shapes reported by Lin (10), Lin (7) and Uman (13) and the calculations reported by Masters (4) indicate that the peak amplitude for subsequent stroke about 1 Km away should be between 200 and 500 v/m. As shown in Table 3, these values compare well with the peak measured for the triggered flashes.

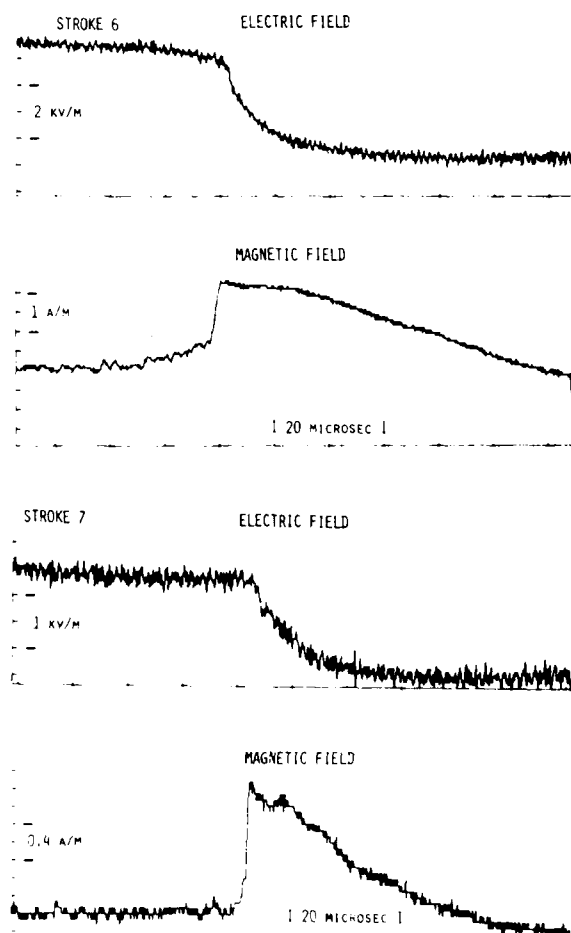


Fig. 9 - E and H fields for two return strokes of Flash 8327

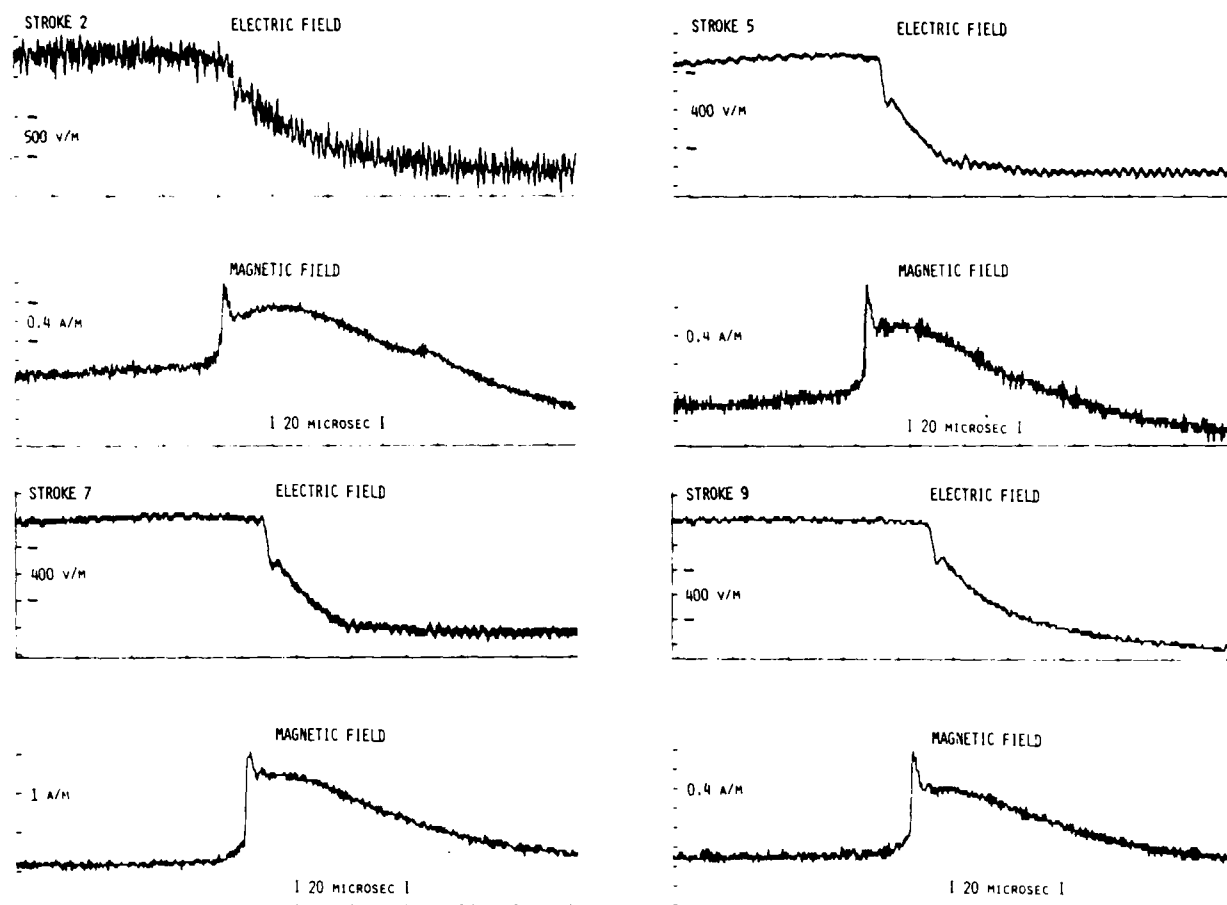


Fig. 10 - E and H fields for four return strokes of Flash 8329
Electric fields from FM cards (500 khz B.W.)

Table 3 - Triggered Lightning Characteristics

Flash	Stroke	Electric Field		Magnetic Field		Shunt Current (kA)
		Risetime (μsec)	Peak (V/m)	Risetime (μsec)	Peak (A/m)	
8327	3			0.8		24.5
	4	0.4	500	0.8		15.7
	6	0.8		1.0		23
	7	0.4	600	0.6	1.3	9.8
8329	1					45
	2	0.4	500	0.4	1.1	10.5
	3	0.4		0.5	1.4	6.6
	4	0.2	900	0.2	1.2	7.4
	5	0.3	250	0.3	0.8	3.5
	6	0.4	600	0.6		32
	7	0.6	350	0.4	1.5	3.7
	8	1.2				26
	9	0.8			1.1	7
	10					2.8
	11	0.4	175	0.6	1.7	6.6

THE MAGNETIC FIELDS MEASURED for the triggered flashes are also listed in Table 3. Again, the peak amplitudes for these strokes are similar to those reported for natural flashes. Although none of the references reported magnetic field amplitudes for flashes measured from the same distance as in this experiment, the triggered flash amplitudes are within a factor of 2 of those reported or predicted for natural strokes. Weidman and Krider (17) reported a slow first front that for subsequent return strokes had amplitudes of approximately 20% of the peak amplitudes. Although it is difficult to determine the actual duration of this slow front from the data in Figures 9 and 10, the proportions of these fronts to the peaks are similar to those of Weidman and Krider.

CONCLUSIONS

BECAUSE OF THE WIDE VARIANCE in the characteristics of the first return stroke in natural flashes, the lack of this stroke in triggered lightning should not detract from the suitability of combining data from triggered lightning with natural lightning data. The other characteristics of natural flashes, such as current level and number of strokes, are well represented by the flashes triggered during this experiment. This apparent similarity of triggered lightning to natural flashes is especially important because of the growing conviction that aircraft that are struck by lightning may, in fact, be triggering the flash, as suggested by D.W. Clifford and H.W. Kasemir (18). Triggered lightning, therefore, offers a method of obtaining "controlled" data about lightning phenomena and may be a potential procedure for "severe threat" testing of aerospace vehicles and systems.

REFERENCES

1. C.W. Schubert, R.D. Richmond, "The Rocket Triggered Lightning Investigation: 1981 Progress Report", AFWAL-TR-83-3031, May 1983.
2. P.H. Duncan, Jr., "Analysis of The Moebius Loop Magnetic Field Sensor", AFWAL-SSN #183, Sept 1973.
3. N. Kitagawa, M. Brook, E.J. Workman, "Continuing Currents in Cloud-to-Ground Lightning Discharges", J. Geophys. Res., 67, Feb 1962.
4. C.Gill Kitterman, "Characteristics of Lightning from Frontal System Thunderstorms", J. Geophys. Res., 83, October, 1980.
5. R.D. Brantley, J.A. Tiller, U.A. Uman, "Lightning Properties in Florida Thunderstorms from Video Tape Records", J. Geophys. Res., 80, August, 1975.
6. M.A. Uman, D.K. McLain, R.J. Fisher, E.P. Krider, "Currents in Florida Lightning Return Strokes", J. Geophys. Res., 78, June 1973.
7. Y.T. Lin, M.A. Uman, R.B. Standler, "Lightning Return Stroke Models", J. Geophys. Res., 85, March 1980.
8. A.J. Eriksson, "Lightning and Tall Structures", Trans Actions: The S.A. Institute of Electrical Engineers, August 1978.
9. K. Berger, R.B. Anderson, H. Kronigel, "Parameters of Lightning Flashes", Electra No. 41, July 1975.
10. Y.T. Lin, et al, "Characterization of Lightning Return Stroke Electric and Magnetic Fields from Simultaneous Two Station Measurements", J. Geophys. Res., 84, October 1979.
11. P. Rustan, B. Kuhlman, G. DuBro, J. Reazer, "Airborne Measurements of The Risetimes of Lightning Return Stroke Fields", Conference Proceedings, 8th International Aerospace and Ground Conference on Lightning and Static Electricity, June 1983.
12. C.D. Weidman, E.P. Krider, "Submicro-second Risetime in Lightning Radiation Fields", NASA Conference Publication 2128, FAA-RD-80-30.
13. M.A. Uman, et al, "Correlated Electric and Magnetic Fields from Lightning Return Strokes", J. Geophys. Res., 80, January 1975.
14. M.J. Master, M.A. Uman, Y.T. Lin, R.B. Standler, "Calculations of Lightning Return Stroke Electric and Magnetic Fields above Ground", J. Geophys. Res., 86, December 1981.
15. P. Laroche, P. Hubert, A. Eybert-Berard, "Triggered Flashes at Trip-81, First Results", Fall A.G.U. Meeting, F-11, Dec 1981.
16. J.A. Tiller, M.A. Uman, Y.T. Lin, R.D. Brantley, "Electric Field Statistics for Close Lightning Return Strokes Near Gainesville", Florida, J. Geophys. Res., 81, August 1976.
17. C.D. Weidman, E.P. Krider, "The Fine Structure of Lightning Return Stroke Waveforms", J. Geophys. Res., 83, December 1978.
18. D.W. Clifford, H.W. Kasemir, "Triggered Lightning", IEEE Transactions on Electromagnetic Compatibility, Special Issue on Lightning and Its Interaction with Aircraft, May 1982.

PREDICTED AIRCRAFT FIELD CONCENTRATION FACTORS AND THEIR RELATION TO TRIGGERED LIGHTNING

Lee W. Parker
Lee W. Parker, Inc.
252 Lexington Road
Concord, Mass. 01742

and

Heinz W. Kasemir
Colorado Scientific Research Corporation
1604 S. County Road 15
Berthoud, CO 80513

ABSTRACT

A 3-D computer model (PESTAT code) has been developed for predicting geometric field concentration factors (FCF's) on the surfaces of an aircraft that could trigger lightning upon entering the field of a strongly-electrified cloud. The present computational approach has the practical advantage that it provides a quick survey of FCF's and therefore a simple assessment of the danger to the aircraft. The FCF's and the measured ambient field vector are key parameters that would be used by a warning system for triggered strikes.

Application to a C-130 aircraft geometry yields theoretical FCF's ranging up to about 180, depending on the direction of the cloud field relative to the aircraft. The relation of the predicted FCF's and the associated critical fields to corona onset and triggered strikes is discussed. The common method of assessing triggered-lightning danger using only FCF's and a nominal value for the breakdown field is questionable, because the criterion being used leads to the critical field for corona onset. As opposed to this, the lightning danger depends on a different criterion for the critical ambient field, namely, that field which turns corona discharge into a full-grown lightning discharge.

1. INTRODUCTION

IT IS INCREASINGLY EVIDENT, from the collected data on aircraft lightning accidents, pilot reports, and theoretical considerations, that most of the lightning strikes to aircraft are triggered, i.e., initiated by the aircraft itself, as opposed to accidental hits by natural lightning (see Kasemir, this conference, and Refs. 1-3).^{*} (These triggered strikes are usually not recognized as such, and are often called "electrostatic discharges.") Hence, in assessments of lightning danger to aircraft, the emphasis should be shifted from the study of conventional lightning warning devices, that are based on detecting the presence or absence of natural lightning, to the study of warning systems that can assess the danger of a triggered discharge.

A triggered strike can occur in highly electrified clouds that do not necessarily produce natural lightning. The probability of this type of strike becomes high when the aircraft enters a high-field region. This occurs because the electric field intensity at the aircraft extremities (wing-tips, nose, tail structure, etc.) is locally enhanced over its ambient value. The enhancement is due to the nature of the surface charge distribution on the aircraft, induced by the external field. It does not depend on the presence of any intrinsic charge on the aircraft, such as "P-static" charge (the net intrinsic charge can be zero). When the enhancement at one or more points on the surface is such that the breakdown-field value is exceeded, corona discharge begins and a strike may be initiated. The enhancement multiplication factor for local field intensity is called the "field concentration factor" (FCF).

It is desirable to have a capability for predicting field concentration factors (FCF's) for any given aircraft geometry. A computer code has been developed for this purpose (PESTAT, for "Parker ElectroSTATics"). Section 2 presents our approach, based on (a) the numerical representation of the aircraft by a collection of quadrilateral or triangular surface "elements," or "patches," and on (b) the solution of a set of simultaneous equations for the surface charge densities on the surface elements. The simultaneous equations represent a discrete approximation to an integral equation that is equivalent to the Laplace equation for the electrostatic field.

Section 3 presents some preliminary numerical solutions for a C-130 Hercules aircraft. The computed field concentration factors (FCF's) range up to about 200, depending on the direction of the external field, with the highest values occurring as expected at the wing-tips, nose and tail extremities. From the FCF's, we derive critical "trigger-field" profiles (projections of surface in 3-D space defining

critical ambient field intensity as a function of direction) such that breakdown occurs somewhere on the aircraft. In Sec. 4 we discuss these results and the relation between corona onset and triggered strikes. We also emphasize the gaps and inconsistencies in our knowledge, and the difficulty of relating electrostatic theory to triggered lightning. The theory must include plasma physics.

Appendices A and B provide auxiliary analytical data as follows. Appendix A presents the computer algorithm used by the PESTAT code to evaluate the potential due to the charge of a quadrilateral planar surface area. Appendix B provides and applies analytical formulas for the fields at and near the tips of ellipsoids, that can be used as simple analytical models to calculate field concentrations (for aircraft wings, for example).

The magnitude and direction of the ambient electric field, and the geometric field-concentration factors of the aircraft, are key parameters that would be used by a warning system for triggered strikes. The present computational approach has the practical advantage that it provides a quick survey of concentration factors, and therefore a simple assessment of the danger to the aircraft.

2. COMPUTER MODEL

The computer model of the aircraft is constructed of quadrilateral surface elements or patches (with occasional triangles representing degenerate quadrilaterals). (See Fig. 1.)

One may solve Laplace's equation for the electric potential V in 3 dimensions, namely,

$$\frac{\partial^2 V}{\partial x^2} + \frac{\partial^2 V}{\partial y^2} + \frac{\partial^2 V}{\partial z^2} = 0 \quad (1)$$

From this solution one may obtain the electric field vector \vec{E} at any point from the gradient of V . However, the solution depends on the boundary conditions. Far from the aircraft the electric field must approach the ambient value \vec{E}_0 . At the (conducting) aircraft surface, the induced surface charges must distribute themselves so as to cause complete cancellation of the field in the interior. That is, the field must be purely normal at every surface point, and the surface must be equipotential.

Rather than solve Eq. (1) as a differential equation, say, by finite differences or finite elements (5,6), it is more convenient for our purposes to solve instead the equivalent integral-equation form of Laplace's equation. This means that the potential V at any "field point" (point of observation) can be written as an integral of surface charge density σ over the aircraft surface, plus the "external" potential V_{ext} (that would exist there in the absence of the aircraft) due to the ambient field:

^{*}Numbers in parentheses designate References at end of paper.

$$V = \int \frac{\sigma da}{(4\pi\epsilon)R} + V_{\text{ext}} \quad (2)$$

where ϵ is the permittivity, da is the element of surface area, and R is the distance between the field point and the surface point on da where σ is defined. We do not know σ in advance, but may solve for it by equating V (as given by Eq. (2), at every point on the surface) to the aircraft body potential V_b . Another condition is that the integral of σ itself gives the total (i.e. net) charge Q . Thus, σ satisfies the integral equation:

$$\int \frac{\sigma da}{R} - (4\pi\epsilon)V_b = -(4\pi\epsilon)V_{\text{ext}} \quad (3)$$

subject to the condition:

$$\int \sigma da = Q \quad (4)$$

In the problem of interest here, σ and V_b are an unknown function and constant, while V_{ext} and the total charge Q are considered as given. In the case where $Q=0$, the σ function is sometimes referred to as the "influence charge."

In our model these relations are approximated by dividing the aircraft surface into small quadrilateral patches with constant values of σ on the individual patches, and performing the required geometric integrations over all patches (Appendix A). There results a system of simultaneous equations for the values of the σ 's, defined to be at the centroids of the patches. Thus, Eqs. (3) and (4) are replaced by the $N+1$ simultaneous algebraic equations:

$$\sum_{j=1}^N A_{ij}\sigma_j - (4\pi\epsilon)V_b = -(4\pi\epsilon)V_{i,\text{ext}} \quad (5)$$

(where $i = 1, 2, \dots, N$)

and

$$\sum_{j=1}^N (\text{Area})_j \sigma_j = Q \quad (6)$$

where the subscript j is the index for the j -th patch and its σ , and runs from 1 to N where N is the total number of patches. The symbol $(\text{Area})_j$ denotes the area of the j -th patch, σ_j denotes the value of σ on the j -th patch, and A_{ij} denotes a geometrically-determined matrix element representing the potential at the i -th patch centroid due to unit charge density on the j -th patch. The symbol $V_{i,\text{ext}}$ denotes the value of the external potential at the i -th patch. The unknowns are comprised of the N values of σ_j plus the "body" potential V_b , i.e., $N+1$ unknowns. The method for evaluating the matrix elements (A_{ij}) is given in Appendix A.

When the voltage V_b is given and the charge Q is unknown, Q replaces V_b as an unknown so that one now solves for the σ 's and Q . Equations (5) and (6) can easily be generalized to

include multiple bodies with arbitrarily assigned voltages or charges.

Solving for the σ 's and V_b (or σ 's and Q) completes the computational task. The solution can be obtained numerically either by direct inversion or by relaxation techniques. Our computer code PESTAT implements these procedures (next section).

The procedure for evaluating a matrix element giving the potential at a "field point" P due to a patch arbitrarily located with unit charge density on it is given in Appendix A, using an original analysis that applies to any polygon. Our formulation was developed independently of the formulation for triangular patches published earlier by Rao et al (7). Of course, one can also assume simple point charges, as Shaeffer has done (8). Shaeffer's paper gives a good description of the method (he calls it a "moment method" approach) and shows how to include external fields. (Rao et al do not consider external fields.) However, the point-charge method gives poor results close to the surface, and hence, although simple, is not satisfactory for FCF calculations. We believe that the present method is superior to others available. Its power is demonstrated by results of the type discussed below.

VALIDATION OF PESTAT - An important result discussed in the next section is the field concentration factor (FCF) of about 200 produced at the wing-tips of a C-130 aircraft by a horizontal field aligned with the wing. To assess the accuracy of PESTAT in its prediction of this rather large factor, a series of numerical calculations were made for ellipsoids, whose field concentration factors can be calculated analytically (Appendix B). In particular, the large FCF of about 200 is also analytically predicted at the tip of an ellipsoid modeling the wing of a C-130 aircraft. Good agreement was obtained, provided a sufficiently large number of patches was used. The requirement became more severe with increasing eccentricities. For the C-130 FCF's to be discussed next (high eccentricities), the estimated error is about 10 percent (too high).

3. NUMERICAL FIELD CONCENTRATION FACTORS FOR A C-130 AIRCRAFT

A C-130 Hercules aircraft was modeled using of the order of 1000 quadrilateral patches. A general view of the computer model is shown in Fig. 1, showing this to be a reasonably realistic representation for obtaining preliminary solutions. We have omitted details such as engine pods and fuel tanks under the wing on the assumption that these relatively small structures, being somewhat distant from extremities such as wing-tips, nose, tail fins, etc., should make negligible contributions to the field concentration factors (FCF's) at the extremities. These additional small structures can be modeled, to any extent desired, but at a cost of more unknowns and greater computational expense.

Figure 2 shows 3 views of the computer model, projected onto the 3 principal planes of

the computational problem space:

- (a) the x-y plane
- (b) the y-z plane
- (c) the z-x plane

Figure 3 shows the FCF computed using the PESTAT code, plotted in polar coordinates of the x-y plane (horizontal plane = plane of Fig. 2a). The FCF varies from a maximum of about 180 in the y-direction (wing tip to wing tip) to a minimum of about 130 in the x-direction (nose-to-tail direction). The FCF profile has roughly an oval shape.

Figure 4 shows the FCF profile in the y-z plane (vertical plane containing the wing-tip-to-wing-tip line = plane of Fig. 2b). Here the FCF profile, which has a scalloped shape, varies from a maximum of about 180 in the y-direction (wing tip to wing tip) to a minimum of about 100 in the direction 30° from the vertical direction. The FCF is about 114 in the vertical direction.

Figure 5 shows the FCF profile in the z-x plane (vertical plane containing the nose-to-tail line = plane of Fig. 2c). The profile in this plane is not symmetric about the nose-to-tail or vertical directions. Instead, the profile is dumbbell-shaped, with its long axis at about 40° with respect to the x (nose-to-tail) direction. The maximum FCF is about 175. The short axis of the dumbbell represents a minimum FCF of about 60. In this direction the electric field is aimed towards the concavity of the aircraft profile where the tail meets the fuselage.

Since the numerical results probably overestimate the FCF's by about 10 percent, these results should be reduced by 10 percent. The reduction has not been applied in the following discussion. Additional numerical solutions were obtained for the case where tips of the ellipsoid modeling the C-130 wing were truncated. In the center of each flat end-face the FCF was down to about 40, increasing to about 200 at the edges.

CRITICAL FIELD - Next, we use the FCF profiles to define critical "trigger field" (E_{crit}) profiles in each of the 3 principal geometric planes (x-y, y-z, z-x). The critical field is obtained by dividing a nominal value of "breakdown" field, which we assume to be 3000 kV/m, by the FCF function in Figs. 3-5. This yields the trigger-field E_{crit} profiles shown in Figs. 6-8 for the 3 principal planes. The E_{crit} profiles can have curious forms, as shown particularly in Figs. 7 and 8. Of interest is the minimum value of E_{crit} , about 17 kV/m, which occurs along the wing-tip-to-wing-tip direction in the x-y plane (Fig. 6) and in the y-z plane (Fig. 7), and at about 40 degrees from the horizontal in the z-x plane (Fig. 8, in the direction from above the tail to below the nose). The z-x behavior is due to the influence of the tail-structure-fuselage interaction.

The significance of an E_{crit} profile is as follows. When the aircraft finds itself in an ambient (cloud) vector field having a given direction and magnitude, the surface field somewhere on the aircraft surface (e.g. at an extremity) exceeds the breakdown value 3000 kV/m

when the ambient field magnitude exceeds E_{crit} for the given direction. (The ambient field vector can be measured in flight using field mills. A field mill system can be designed to provide this type of data to the pilot on a continuous basis (1,9 for example).)

In the next section we discuss the physical significance of these E_{crit} profiles, and their relation to corona onset and triggered strikes.

4. TRIGGER FIELDS, CORONA AND STRIKES TO AIRCRAFT

The "trigger-field" profiles (E_{crit}) shown in Figs. 6-8 represent the critical ambient (electrified-cloud) fields that would induce breakdown at the aircraft extremities. These are therefore at least corona-onset fields, and represent a lower bound for the lightning-trigger field. However, in general the lightning-trigger fields are observed to be different from the fields required for the onset of corona discharge. There are gaps and inconsistencies in our knowledge that prevent our making a precise connection of corona-onset fields with those that would produce triggered strikes. Nonetheless, although our knowledge is incomplete, the results of this paper represent preliminary steps that must be taken along the path toward a complete understanding of the triggering phenomenon.

Triggered strikes to instrumented aircraft have been reported as occurring in a variety of conditions, certainly in high fields, up to 360 kV/m (10), but occasionally also in surprisingly low fields, down to 4 kV/m (11). If we were to interpret Figs. 6-8 as trigger-fields for strikes, they would imply that triggering can occur in a field as low as 17 kV/m when it is in the right direction. In addition, since the breakdown field is actually lower by a factor of about 3 (1000 kV/m) because of altitude, the predicted trigger field would be as low as 6 kV/m.

As examples of observed triggering and related corona phenomena, to which we ultimately may relate our predicted field concentration factors but which presently remain unexplained, we discuss next some pilot observations, and results of a relevant experiment.

PILOT EXPERIENCE - Pilot observations relevant to the triggering and related corona phenomenon are summarized by Clifford (3) as follows.

"Pilots generally agree that there are two distinct classes of lightning strikes to aircraft in flight. The first and most common variety usually occurs while flying in precipitation at temperatures near freezing. This type is preceded by a buildup of static noise in the communication gear, due to corona (visible at night). The buildup may continue for several seconds before the strike occurs.

The second variety occurs abruptly without warning. It is most likely to be encountered in or near ongoing thunderstorms, in contrast to the former variety which is often experienced in precipitation that has no connection with thunderstorms. Pilots tend to believe that the slow buildup type of discharge is not a true lightning

strike but rather a discharge of excess charge ('P-static') built up on the aircraft by flight through the precipitation. This non-thunderstorm type greatly outnumbers the other. Both kinds can create a brilliant flash and a boom which can be heard throughout the airplane."

We believe that in the "common" variety of discharge the pilots are experiencing a strike initiated or triggered by the aircraft upon entering a region of high electric field. The charge on the aircraft is not important for the energy budget but may be important for the triggering process (see below). This view was proposed by us earlier (1). Triggering of lightning by aircraft in high fields has also been discussed by Fitzgerald (9,10), Vonnegut (12), Pierce (13,14), Shaeffer (15), and Kasemir and Perkins (16), among others. The rare variety of strike, that occurs without warning, is an accidental hit of the airplane by a natural lightning that originates somewhere else in an ongoing thunderstorm.

In our opinion (expressed earlier in (1,2)), the role played by precipitation charging is as follows. The main electrical energy for the common (triggered) type of lightning strike is provided by the field of the electrified cloud. However, the electric charge on the aircraft due to precipitation ("P-static"), which is especially strong in the melting zone of a cloud, may contribute to the triggering of a lightning discharge by the aircraft in cases where the field concentrations at the extremities of the aircraft are not quite sufficient to initiate a lightning discharge. Therefore, the role of precipitation charging is not to provide energy for a full-grown lightning, but merely to help convert the corona discharge into long streamers which can then grow in the external cloud field into a proper lightning discharge. Evidence for the probable importance of precipitation charging is provided by pilot reports and by data obtained by Fitzgerald (10). Its role is discussed by Clifford and Kasemir (2).

The fact that pilots observe corona discharge in advance of a triggered strike is not surprising. Due to its many sharp protrusions (antennas, pitot tubes, landing gear, nuts, rivets, lightning arresters, exhaust nozzle rims, edges, corners, etc.), an aircraft always goes into corona discharge when it enters a region of sufficiently high field. Corona begins at a point as soon as the field at the tip exceeds the breakdown value. This can occur for ambient fields as low as a few kV/m, depending on how small the tip radius of curvature is (Appendix B). The corona discharge is relatively stable, and, unless the ambient field increases beyond some as yet unknown critical value, the aircraft will remain in corona discharge until the external field drops below the critical value for corona onset. Note that although corona may be produced by high fields (and precipitation charging), not all corona develops into a major discharge. The reasons for this are not clear. What is perhaps surprising is that many experiments have been performed in attempts to

deliberately provoke triggered strikes (both with instrumented aircraft and with wire-trailing aircraft and rockets), while few have succeeded (17-19). (Franklin's famous kite experiment might also fit into this category.) In most cases, copious corona discharges have been manifested, but without accompanying strikes. The occurrence of a soft hiss in the communication gear indicating the onset of corona is well known by pilots. This phenomenon is common and can become severe enough to black out communication, but an accompanying lightning strike is relatively rare.

CORONA AND TRIGGERING EXPERIMENT - In a set of relevant ground-based experiments, the effects of corona-producing points on the trigger-breakdown field of the shuttle-orbiter were investigated by Kasemir and Perkins (16). They used a scale model of the spacecraft placed between the plates of a meter-sized large plate condenser. As part of the investigation they also used a highly-polished spheroid to determine the trigger-breakdown field in the absence of, and in the presence of, corona-producing points on the spheroid. Details are given in Refs. (2) and (16), but some of the principal results are the following:

- (a) The observed trigger-breakdown field of the polished spheroid without corona-producing points was predicted accurately from the solution of Laplace's equation. Our predictions of FCF's for a C-130, shown in Figs. 6-8, are similar types of solutions.
 - (b) The trigger field was reduced (by 33 percent) due to the presence of corona points, and this reduction was only weakly dependent on the nature of the points (form, length, sharpness, etc.).
- These results suggest that:
- (a) Theoretically-calculated trigger-field profiles such as those in Figs. 6-8 might be valid lower-bound predictors for aircraft triggering of lightning.
 - (b) The likelihood of a triggered strike seems to be enhanced by the presence of corona (in addition to altitude-dependent reduction of the trigger field). Ordinarily the corona effect is not taken into account in the literature.

There is a caveat in extrapolating these experimental results to the triggering of lightning by aircraft. The gap between the plates was only about one meter. Hence the corona "plumes" or "filaments" could easily bridge the gap, and give one the impression that lightning may be triggered if the field exceeds breakdown values over a distance of the order of a meter. This may be a false impression caused by the unrealistically small scale of the experiment. In an actual triggered lightning discharge, the field may need to exceed breakdown over distances of the order of many meters. That is, the corona filaments or plumes may need to be many meters long before the external field can convert them into a full lightning discharge. The required

distance is not presently known and represents a gap in our knowledge. This gap cannot be filled by electrostatic arguments alone. In Appendix B we show analytically that, even for a large ellipsoid modeling a C-130 wing, it is difficult electrostatically to produce "super-breakdown" fields over off-tip distances of the order of several meters.

The theory must deal eventually with the conversion of energy from electrostatic into gas ionization and heating, and will involve plasma physics, but such a theory has not yet been developed (4,20).

APPENDIX A: EVALUATION OF MATRIX ELEMENTS FOR THE "PESTAT" CODE

Consider a planar quadrilateral "patch" as shown in Fig. 9, and a field point P at which the potential due to the charge on the patch is to be evaluated. We have chosen a coordinate system in which the patch lies in the x-y plane, and the field point P is on the z-axis, at a height z above the plane, as in the figure. (For arbitrarily-oriented patches, a suitable rotation is required to achieve the orientation of the figure.) Let the 4 vertices of the patch be labelled 1, 2, 3 and 4, as in the figure. Let the radial distances from P to each of the 4 vertices be labelled R_1 , R_2 , R_3 and R_4 , as in the figure. The derivation is lengthy; only results are given.

The matrix element is the sum of 4 contributions, from each of the 4 line segments of the patch. Consider the segment from Vertex 1 to Vertex 2, called Segment 1-2. Let the equation of Segment 1-2 be given (in the x-y plane) by:

$$y = A x + B \quad (A-1)$$

where A and B are determined by the x,y coordinates of Vertices 1 and 2. Let C and D be denoted by

$$C = (1 + A^2)^{1/2} \quad (A-2)$$

$$D = Ay + x \quad (A-3)$$

Then define F_1 and F_2 , associated with Vertices 1 and 2, by:

$$F_j = x_j \ln(y_j + R_j) + (B/C) \ln(CR_j + D_j) - z \tan^{-1}[(y_j D_j - AR_j^2)/zR_j] \quad (A-4)$$

where j takes on the respective values 1 and 2. Then the contribution of Segment 1-2 is:

$$(\Delta F)_{12} = F_2 - F_1 \quad (A-5)$$

Similar contributions are obtained from the remaining 3 sides, namely, $(\Delta F)_{23}$, $(\Delta F)_{34}$, and $(\Delta F)_{41}$, as we trace the patch in the clockwise direction. In the special case where the line

segment is vertical (A is infinite), its contribution vanishes (set $\Delta F=0$).

The potential at P due to the patch charge is then the sum of the ΔF 's. The matrix element A_{ij} ($= \int da/R$) is evaluated by choosing P to be the centroid of the i-th patch, and evaluating the contribution to the potential at P due to unit charge density on the j-th patch (the patch of the figure):

$$A_{ij} = (\Delta F)_{12} + (\Delta F)_{23} + (\Delta F)_{34} + (\Delta F)_{41} \quad (A-6)$$

Note that this procedure represents a line-integral formulation. The algorithm is valid for any polygon.

APPENDIX B: FIELD ENHANCEMENTS NEAR TIPS OF ELLIPSOIDS

To provide analytic insight for field enhancements or "field concentration factors" (FCF's) near the tips of elongated bodies (such as wings, fuselages, corona wires, etc.), we consider a triaxial ellipsoid as an analytically tractable model. The ellipsoid is defined geometrically by its semi-axes a, b and c, listed in order of decreasing dimension (a is the longest, c is the shortest). The ellipsoid is located in an ambient field E_0 in the direction of its long axis. The net charge is zero for present purposes. (This simplifies the analysis, which can be extended to include net charge. A charged ellipsoid will be discussed later.) We will be interested in two ratios: (1) the ratio of the tip field (E_{tip}) to the ambient field (E_0), and (2) the ratio of the field off the tip (E) to E_{tip} or to E_0 . The derivations are lengthy, and only the results are presented. The ratios may be expressed as follows:

At the tip of the ellipsoid in the direction of the long axis (x-direction), where $x=a$ at the tip, we have:

$$\frac{E_{tip}}{E_0} = \frac{a^2 \sin^3 \phi}{bc D(\phi, m)} (= FCF) \quad (B-1)$$

where:

$$\sin \phi = (1 - c^2/a^2)^{1/2} = (\text{focal radius})/a \quad (B-2)$$

$$m = (1 - b^2/a^2)/(1 - c^2/a^2) \quad (B-3)$$

and $D(\phi, m)$ is defined in terms of the Jacobi elliptic integrals of the first and second kind, $F(\phi, m)$ and $E(\phi, m)$, as:

$$D(\phi, m) = [F(\phi, m) - E(\phi, m)]/m \quad (B-4)$$

where

$$F(\phi, m) = \int_0^\phi \frac{d\theta}{(1 - m \sin^2 \theta)^{1/2}} \quad (B-5)$$

$$E(\phi, m) = \int_0^\phi d\theta (1 - m \sin^2 \theta)^{1/2} \quad (B-6)$$

(See M. Abramowitz and I. A. Stegun, "Handbook of Mathematical Functions," New York: Dover, 1965.)

Off the tip, where $x > a$, we have:

$$\frac{E}{E_{tip}} = T_1 + T_2 \text{ (off-tip field of ellipsoid)} \quad (B-7)$$

where

$$T_1 = \frac{E_0}{E_{tip}} \left[1 - \frac{D(\phi', m)}{D(\phi, m)} \right] \quad (B-8)$$

with

$$\sin \phi' = (1 - c^2/a^2)^{1/2} / (x/a) \quad (B-9)$$

and

$$T_2 = \frac{abc}{x(x^2 - a^2 + b^2)^{1/2} (x^2 - a^2 + c^2)^{1/2}} \quad (B-10)$$

At the tip, where $x=a$, we have $\phi'=\phi$, $T_1=0$, and $T_2=1$. Off the tip, as x increases from a towards infinity, T_2 falls off monotonically from unity towards zero, while T_1 rises monotonically from zero to E_0/E_{tip} , that is, a small number compared with unity in the cases of interest here. Hence, T_1 may be approximately neglected over most of the off-tip range of x of interest here.

This completes the set of exact formulas for the tip and off-tip fields, or FCF's, for ellipsoids.

Next we present some important limiting cases of these equations.

SPHEROID - An important case is that of the prolate spheroid, where $b=c$. In this case we have $m=1$, and:

$$E(\phi, 1) = \sin \phi = (1 - b^2/a^2)^{1/2} \\ = (\text{focal radius})/a \quad (B-11)$$

$$F(\phi, 1) = \int_0^\phi d\theta \sec \theta \\ = \frac{1}{2} \ln \left(\frac{1 + \sin \phi}{1 - \sin \phi} \right) \quad (B-12)$$

Then we have

$$D(\phi, 1) = \frac{1}{2} \ln \left(\frac{1 + \sin \phi}{1 - \sin \phi} \right) - \sin \phi \quad (B-13)$$

and E_{tip}/E_0 becomes:

$$\frac{E_{tip}}{E_0} = \frac{a^2 \sin^2 \phi}{b^2 Q_1} \text{ (spheroid)} \quad (B-14)$$

where

$$Q_1 = \frac{1}{2 \sin \phi} \ln \left(\frac{1 + \sin \phi}{1 - \sin \phi} \right) - 1 \quad (B-15)$$

For the off-tip field of the spheroid, we obtain:

$$\sin \phi = (1 - b^2/a^2)^{1/2} \quad (B-16)$$

$$\sin \phi' = (1 - b^2/a^2)^{1/2} / (x/a) \quad (B-17)$$

$$D(\phi, 1) = Q_1 / \sin \phi \quad (B-18)$$

$$D(\phi', 1) = Q_1' / \sin \phi' \quad (B-19)$$

where

$$Q_1' = \frac{1}{2 \sin \phi'} \ln \left(\frac{1 + \sin \phi'}{1 - \sin \phi'} \right) - 1 \quad (B-20)$$

so that

$$T_1 = \frac{E_0}{E_{tip}} \left[1 - \frac{Q_1'}{Q_1} \frac{\sin \phi}{\sin \phi'} \right] \quad (B-21)$$

(spheroid)

and

$$T_2 = \frac{ab^2}{x(x^2 - a^2 + b^2)} \text{ (spheroid)} \quad (B-22)$$

and $E/E_{tip} = T_1 + T_2$, as given by Eq. (B-7).

SLENDER ELLIPSOIDS AND SPHEROIDS - Other cases of interest are those of slim ellipsoids and spheroids (b/a and c/a small compared with unity). It can be shown that the approximation obtained from Eqs. (B-1) through (B-6) for the tip field is:

$$\frac{E_{tip}}{E_0} \approx \frac{a^2/bc}{\ln \left(\frac{4a}{b+c} \right) - 1} (= \text{FCF for ellipsoid}) \quad (B-23)$$

Neglecting T_1 , we have from Eqs. (B-7) through (B-10) for the off-tip field:

$$\frac{E}{E_{tip}} \approx T_2 \\ = \frac{abc}{x(x^2 - a^2 + b^2)^{1/2} (x^2 - a^2 + c^2)^{1/2}} \quad (B-24)$$

(ellipsoid)

For the spheroid ($b=c$), introducing the useful definition of tip radius of curvature $r = b^2/a$, we have the approximations:

$$\frac{E_{tip}}{E_0} \approx \frac{a^2/b^2}{\ln(2a/b) - 1} \quad (\text{spheroid})$$

$$= \frac{2a/r}{\ln(4a/r) - 2} (= \text{FCF for spheroid}) \quad (\text{spheroid}) \quad (\text{B-25})$$

and

$$\frac{E}{E_{tip}} \approx \frac{ab^2}{x(x^2 - a^2 + b^2)} = \frac{a^2r}{x(x^2 - a^2 + ar)} \quad (\text{B-26})$$

(spheroid) (spheroid)

FIELD OF A CORONA POINT - We now apply the formulas for a spheroid to a corona point. Consider a rod, of thickness 1.4 cm at its center, with a half-length $a = 0.5$ m, and with sharpened tips having radius of curvature $r = 10^{-4}$ m (0.1 mm). Then according to Eq. (B-25) the FCF at the tip is about 1300. Assuming 3000 kV/m is the breakdown field strength, breakdown is achieved at the tip when the ambient field $E_0 = 2.3$ kV/m. This value of E_0 , which corresponds to the quantity we call E_{crit} in the text, is the observed order of magnitude for corona-point onset fields, about 2 kV/m (L. H. Ruhnke, personal communication). Off the tip, however, the field falls rapidly from its tip value. According to Eq. (B-26), E falls from E_{tip} to $E_{tip}/3$ in a distance Δx only about 10^{-4} m from the tip. This small distance is of the order of r , the tip radius of curvature. The fall-off with distance Δx occurs so rapidly that even for extremely (and unrealistically) large ambient fields, breakdown is exceeded only within minute distances from the tip. As an example, in order to have "super-breakdown" fields (off-tip fields exceeding 3000 kV/m) at all values of x between $x = 0.50$ m (at the tip) and $x = 0.55$ m (an interval of $\Delta x = 5$ cm off the tip), the external or ambient field must exceed the unrealistic value 2.7 MV/m!

TIP FIELD: ELLIPSOID MODEL OF C-130 WING - We next model the wing of a C-130 aircraft by a triaxial ellipsoid having semiaxes a , b and $c = 20$ m, 2.4 m, and 0.36 m. Using the exact formula (B-1) we compute the FCF at the tip, due to an ambient field E_0 directed along the long axis. We obtain $\text{FCF} = E_{tip}/E_0 = 192$. The ellipsoid is sufficiently slim, however, to allow the use of the approximate formula (B-23), which yields $\text{FCF} = 196$, a slight overestimation by about 2 percent. The corresponding numerical calculation by the PESTAT code yields the field concentration factor $\text{FCF} = 210$, an overestimation by about 10 percent. (This error is not serious. It depends on the number of patches used, and can be reduced by sufficiently increasing the number of patches.)

OFF-TIP FIELD: ELLIPSOID MODEL OF C-130 WING - It is appropriate to use the approximation for E/E_{tip} given by Eq. (B-24) for the

off-tip field. Here, just as for the corona point (above), we consider the off-tip distance, Δx , the off-tip FCF given by multiplying E/E_{tip} by 196, and E_{crit} obtained by dividing 3000 kV/m by FCF. Thus, we obtain the following tabulation:

$\Delta x(\text{m})$	E/E_{tip}	$\text{FCF}=E/E_0$	E_0 ($E=3000$ kV/m)
0 m	1.00	196	15 kV/m
0.01	0.48	94	32
0.02	0.35	68	44
0.05	0.21	41	72
0.1	0.14	26	110
0.2	0.081	16	190
0.5	0.037	7.2	420
1.0	0.019	3.7	820
2.0	0.0090	1.8	1700

The first column gives the off-tip distance, the second shows the fall-off of the field relative to the tip value, the third gives the effective FCF for that position, and the fourth gives the ambient field required to produce breakdown at that position. The fall-off with distance is extremely rapid, the first factor of 2 occurring within a distance 0.01 m (approximately twice the smaller tip radius of curvature, 0.006 m); then the field falls off more slowly. From the fourth column we see that even for the largest observed ambient fields (of the order of 400 kV/m), the off-tip interval Δx in which "super-breakdown" fields occur is less than 0.5 m. To stretch the interval to 2 meters would require an unrealistic 1700-kV/m ambient field, a stringent requirement associated with the small tip radius of curvature. If we choose alternatively to increase the ellipsoid tip radius of curvature to fit the tip geometry of interest, this would reduce both the eccentricity of the ellipsoid model and the FCF at its tip. This exercise illustrates the difficulty, using electrostatic models for aircraft-size bodies, of achieving "super-breakdown" fields over off-tip intervals of several meters.

CHARGED ELLIPSOID - In estimating the effects of precipitation charge, it is useful to have available formulas for the tip and off-tip fields of a charged ellipsoid. It can be shown that the formulas are almost identical to the formulas for an uncharged ellipsoid in an ambient field E_0 . For the tip field, we obtain a good approximation by replacing E_0 in Eq. (B-23) by an "effective ambient field" V_b/a , where V_b is the body potential. The off-tip field variation is well approximated by the right-hand side of Eq. (B-24) without the first factor, a/x . Thus, rate of field fall-off is about the same as for uncharged ellipsoids. If we assume a vehicle potential $V_b = 0.1$ MV on the model ellipsoid, the field at the tip is about 1000 kV/m, i.e., somewhat under breakdown magnitude.

ACKNOWLEDGEMENTS

We wish to express our appreciation to L. H. Ruhnke (NRL) for stimulating discussions of corona and triggering problems, to E. G. Holeman for valuable assistance in the development of our PESTAT code, and to A. W. Glisson (U. Miss.) for kindly sending a Fortran listing of his STATIC code (see Rao et al), which proved helpful in validating our PESTAT code.

REFERENCES

1. L.W. Parker and H.W. Kasemir, "Airborne Warning Systems for Natural and Aircraft-Initiated Lightning," IEEE Transactions on Electromagnetic Compatibility, Vol. EMC-24, No. 2, pp. 137-158, May 1982.
2. D.W. Clifford and H.W. Kasemir, "Triggered Lightning," IEEE Transactions on Electromagnetic Compatibility, Vol. EMC-24, No. 2, pp. 112-122, May 1982.
3. D.W. Clifford, "Aircraft Mishap Experience from Atmospheric Electricity Hazards," NATO AGARD Lecture Series No. 110, Paper No. 2, June 1980.
4. L.W. Parker and H.W. Kasemir, "Breakdown Waves in Lightning Return-Stroke and Leader-Step Channels," 7th International Conference on Atmospheric Electricity, State University of New York at Albany, NY, 4-8 June 1984.
5. L.W. Parker, "Calculation of Sheath and Wake Structure About a Pillbox-Shaped Spacecraft in a Flowing Plasma," in Proceedings of the Spacecraft Charging Technology Conference, C.P. Pike and R.R. Lovell, editors, AFGL-TR-77-0051, pp. 331-366, Feb. 1977.
6. O.C. Zienkiewicz, "The Finite Element Method in Engineering Science," New York: McGraw-Hill, 1971.
7. S.M. Rao, A.W. Glisson, D.R. Wilton and B.S. Vidula, "A Simple Numerical Solution Procedure for Statics Problems Involving Arbitrary-Shaped Surfaces," IEEE Transactions on Antennas and Propagation, Vol. AP-27, No. 5, pp. 604-608, Sept. 1979.
8. J.F. Shaeffer, "Electrostatic Field Solutions for Irregular Electrodes Described by Potential or Net Charge," McDonnell Aircraft Company Report MDC A 1997, Dec. 1972.
9. D.R. Fitzgerald, "Experimental Studies of Thunderstorm Electrification," Air Force Geophysics Laboratory Report AFGL-TR-76-0128, June 1976.
10. D.R. Fitzgerald, "Probable Aircraft Triggering of Lightning Discharges in Certain Thunderstorms," Monthly Weather Review, Vol. 95, No. 12, pp. 835-842, Dec. 1967.
11. W.E. Cobb and F.J. Holitza, "A Note on Lightning Strikes to Aircraft," Monthly Weather Review, Vol. 96, No. 11, pp. 807-808, 1968.
12. B. Vonnegut, "Electrical Behavior of an Airplane in a Thunderstorm," Arthur D. Little, Inc. Report FAA-ADS-36, Feb. 1965.
13. E.T. Pierce, "Triggered Lightning and Some Unsuspected Lightning Hazards," American Association for the Advancement of Science 138th Annual Meeting, Philadelphia, PA, 1971.
14. E.T. Pierce, "Triggered Lightning and Its Application to Rockets and Aircraft," 1972 Lightning and Static Electricity Conference, AFAL-TR-72-325, Dec. 1972.
15. J.F. Shaeffer, "Aircraft Initiation of Lightning," 1972 Lightning and Static Electricity Conference, AFAL-TR-72-325, Dec. 1972.
16. H.W. Kasemir and F. Perkins, "Lightning Trigger Field of the Orbiter," Kennedy Space Center Contract CC 69694A Final Report, NOAA, Oct. 1978.
17. M.M. Newman and J.D. Robb, "Protection for Aircraft," in "Lightning," Vol. 2, R.H. Golde, editor, pp. 659-696 (esp. p. 662 ff.), New York: Academic Press, 1977.
18. P. Laroche, A. Eybert-Berard, P. Richard, P. Hubert, G. Labaune, and L. Barret, "A Contribution to the Analysis of Triggered Lightning: First Results Obtained During the TRIP 82 Experiment," Paper No. 22 in 1983 International Aerospace and Ground Conference on Lightning and Static Electricity, DOT/FAA/CT-83/25(A), Oct. 1983.
19. B.D. Fisher and J.A. Plumer, "Lightning Attachment Patterns and Flight Conditions Experienced by the NASA F-106B Airplane," Paper No. 26 in 1983 International Aerospace and Ground Conference on Lightning and Static Electricity, DOT/FAA/CT-83/25(A), Oct. 1983.
20. E. Barreto, H. Jurenka and S.I. Reynolds, "The Formation of Small Sparks," Journal of Applied Physics, Vol. 48, pp. 4510-4520, 1977.

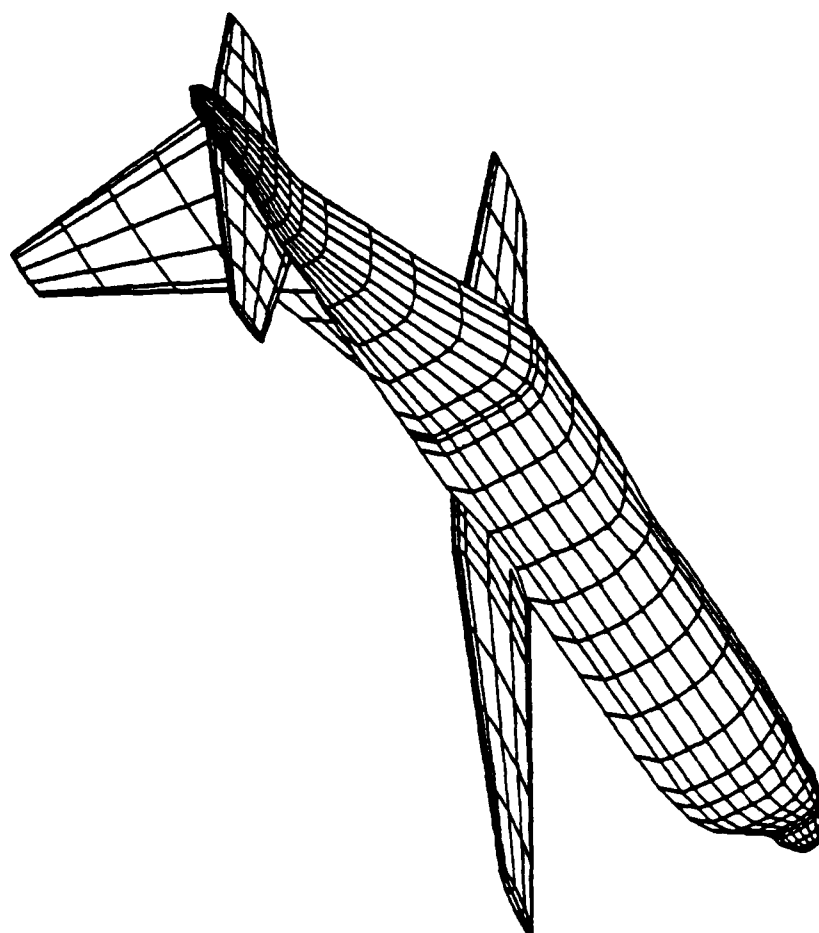
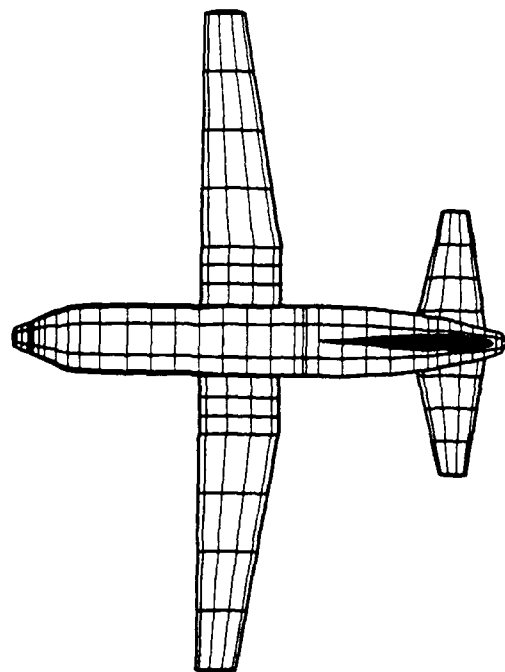


Fig. 1 - General view of a C-130 aircraft computer model using quadrilateral patches

(a)



(b)



(c)

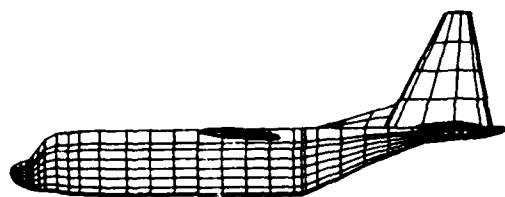


Fig. 2 - Three views of the computer model, projected onto (a) the x-y plane, (b) the y-z plane, and (c) the z-x plane (of the computational problem space)

FIELD CONCENTRATION FACTOR

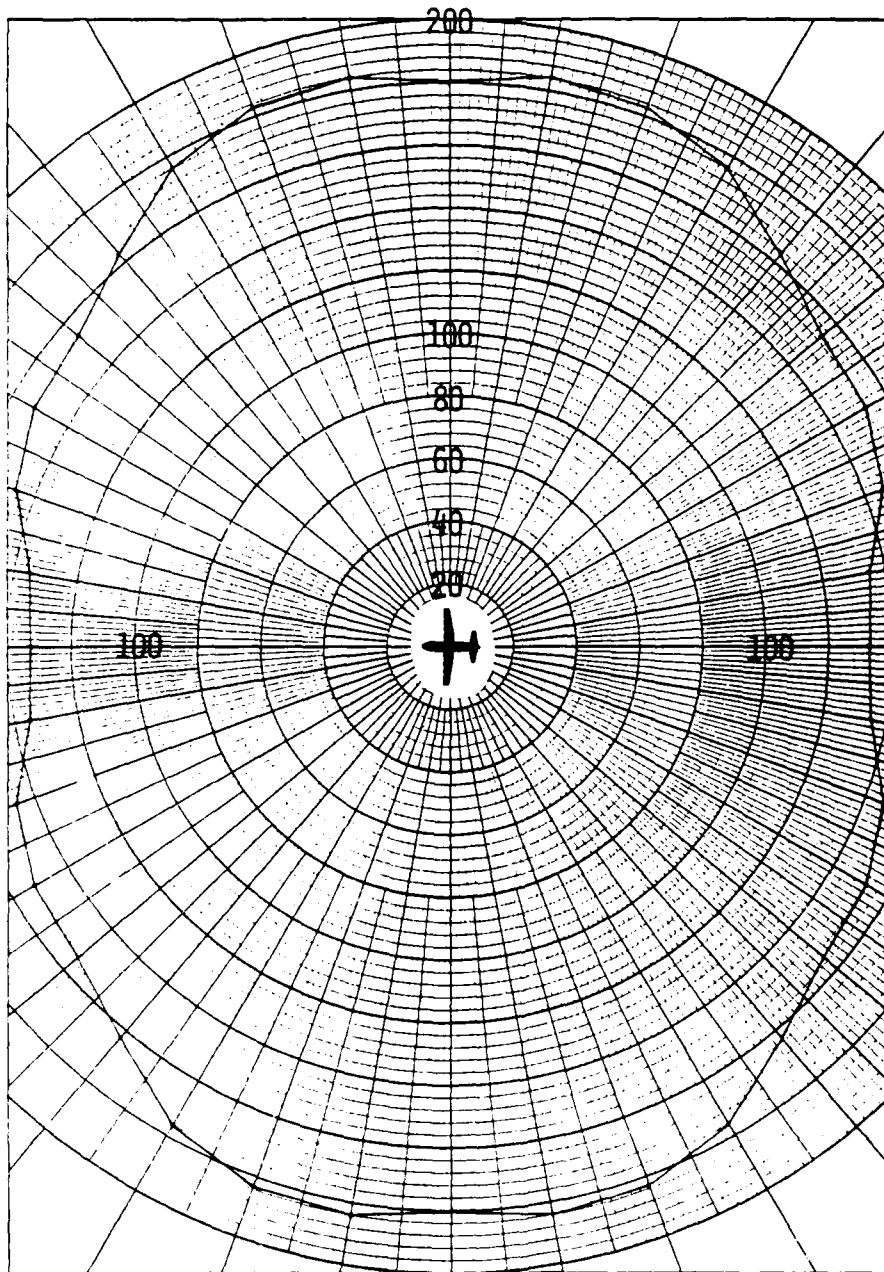


Fig. 3 - Field concentration factor (FCF) profile
in polar coordinates, in the x-y plane

FIELD CONCENTRATION FACTOR

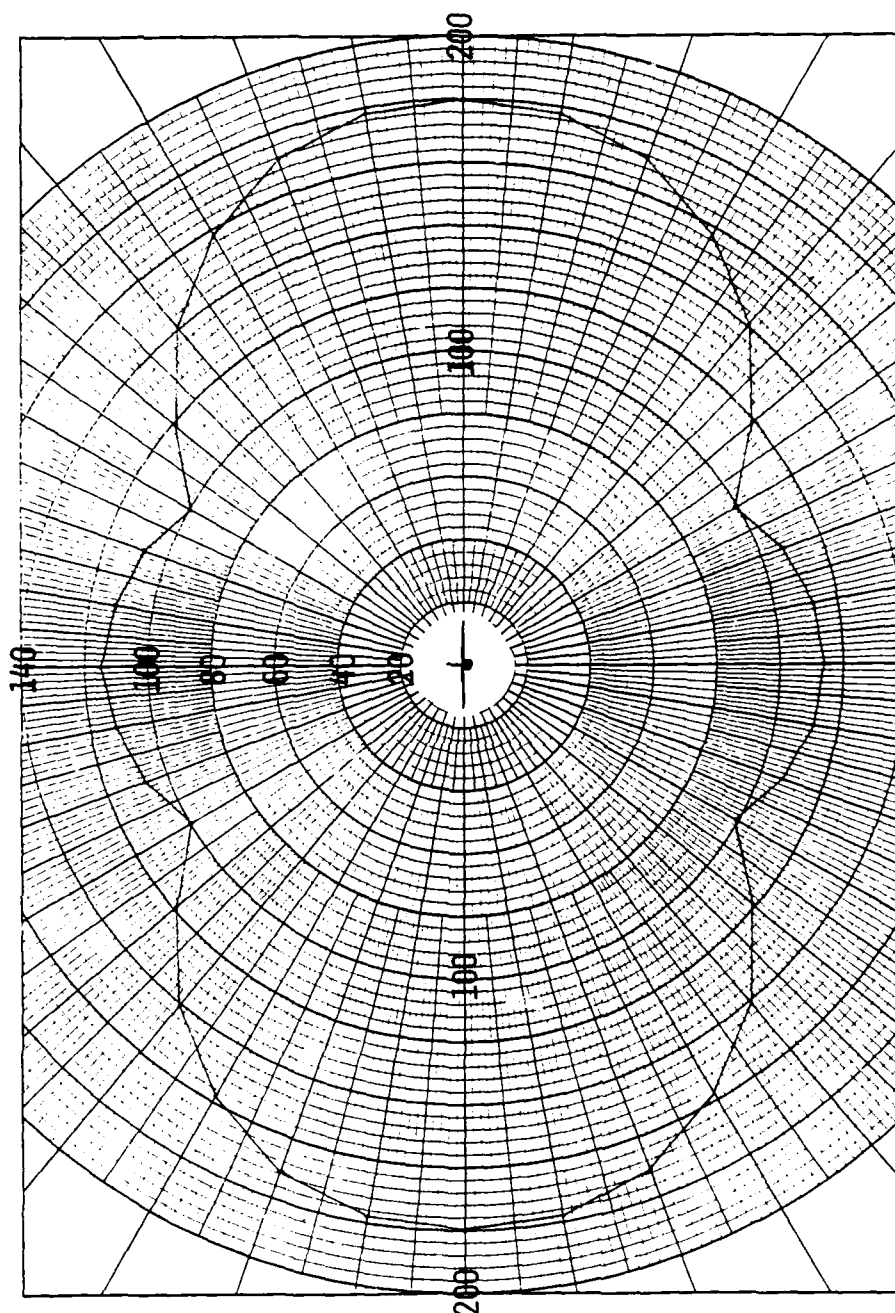


Fig. 4 - Field concentration factor (FCF) profile in polar coordinates, in the y-z plane

FIELD CONCENTRATION FACTOR

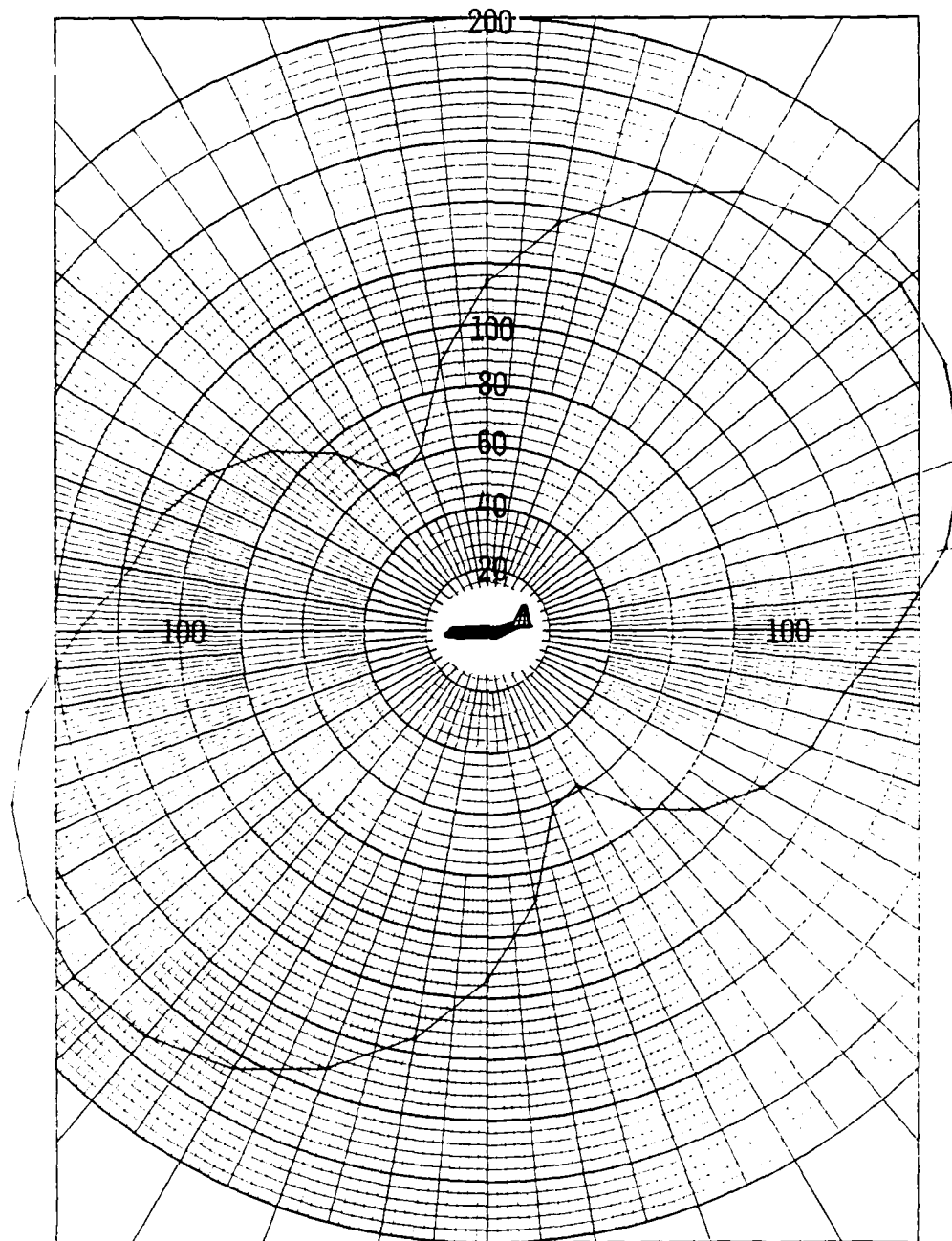


Fig. 5 - Field concentration factor (FCF) profile
in polar coordinates, in the z-x plane

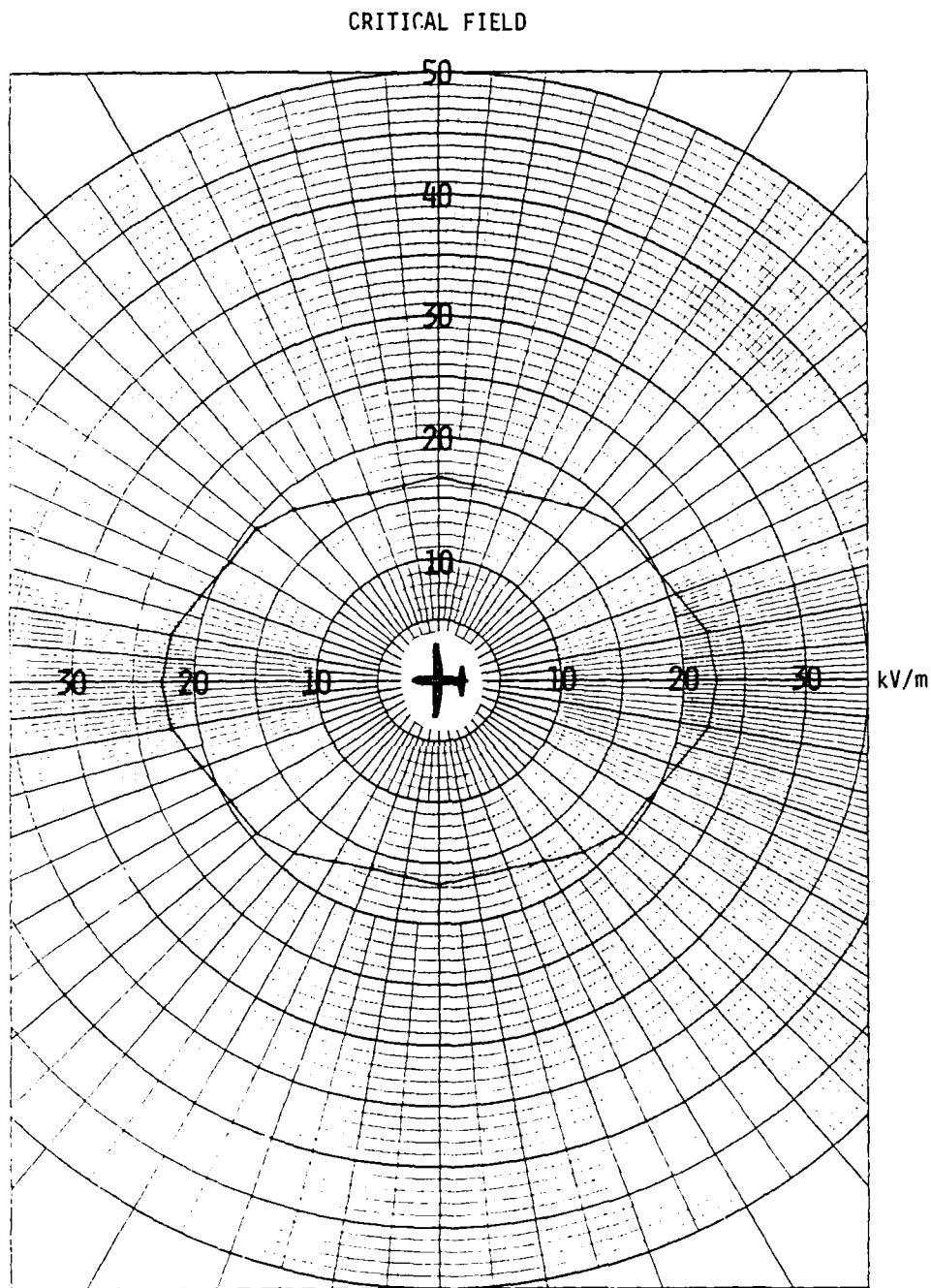


Fig. 6 - Critical field profile (in kV/m) in polar coordinates, in the x-y plane, obtained by dividing 3000 kV/m by the FCF profile of Fig. 3 (see text)

CRITICAL FIELD

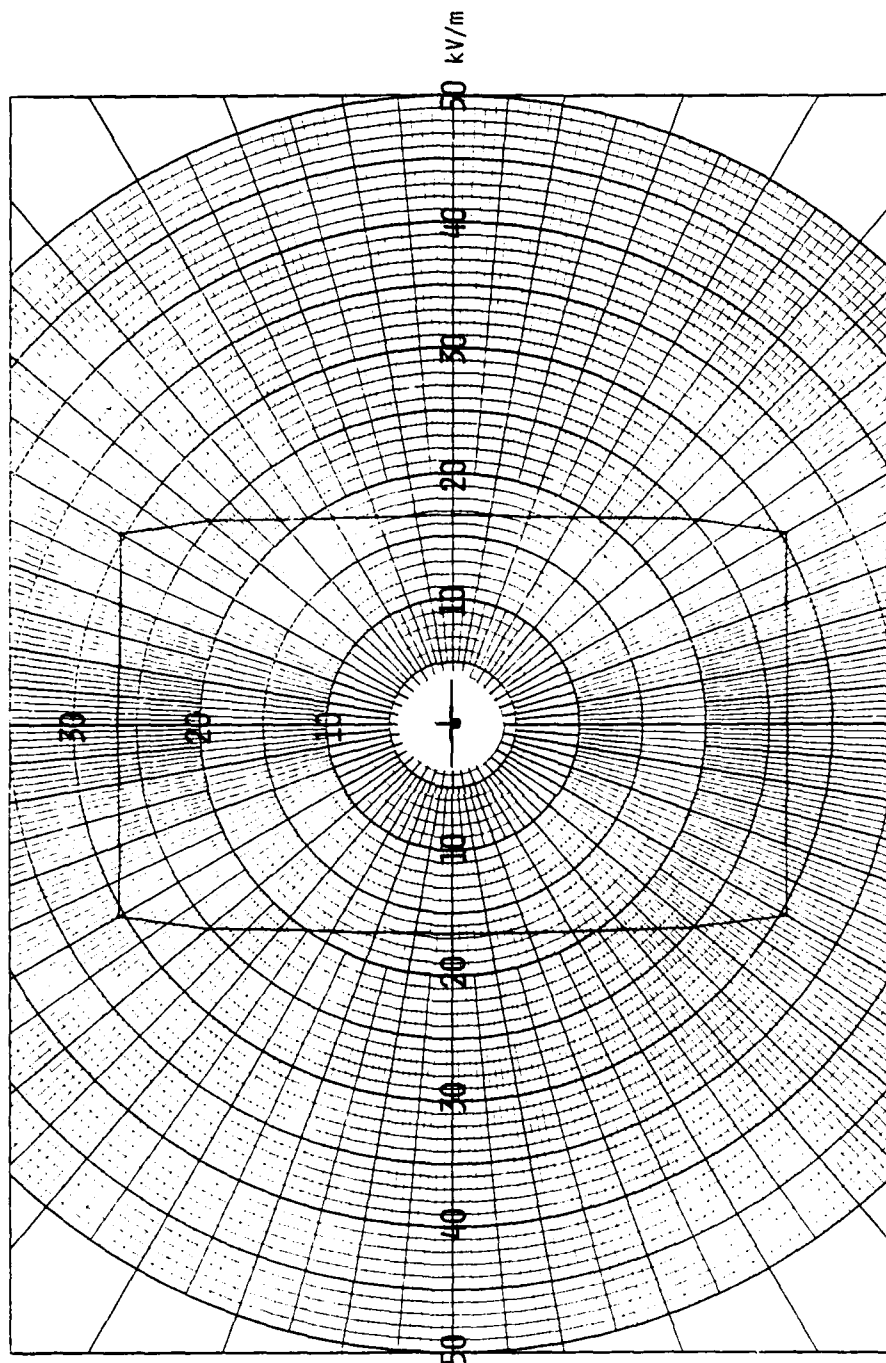


Fig. 7 - Critical field profile (in kV/m) in polar coordinates, in the y-z plane, obtained by dividing 3000 kV/m by the FCF profile of Fig. 4 (see text)

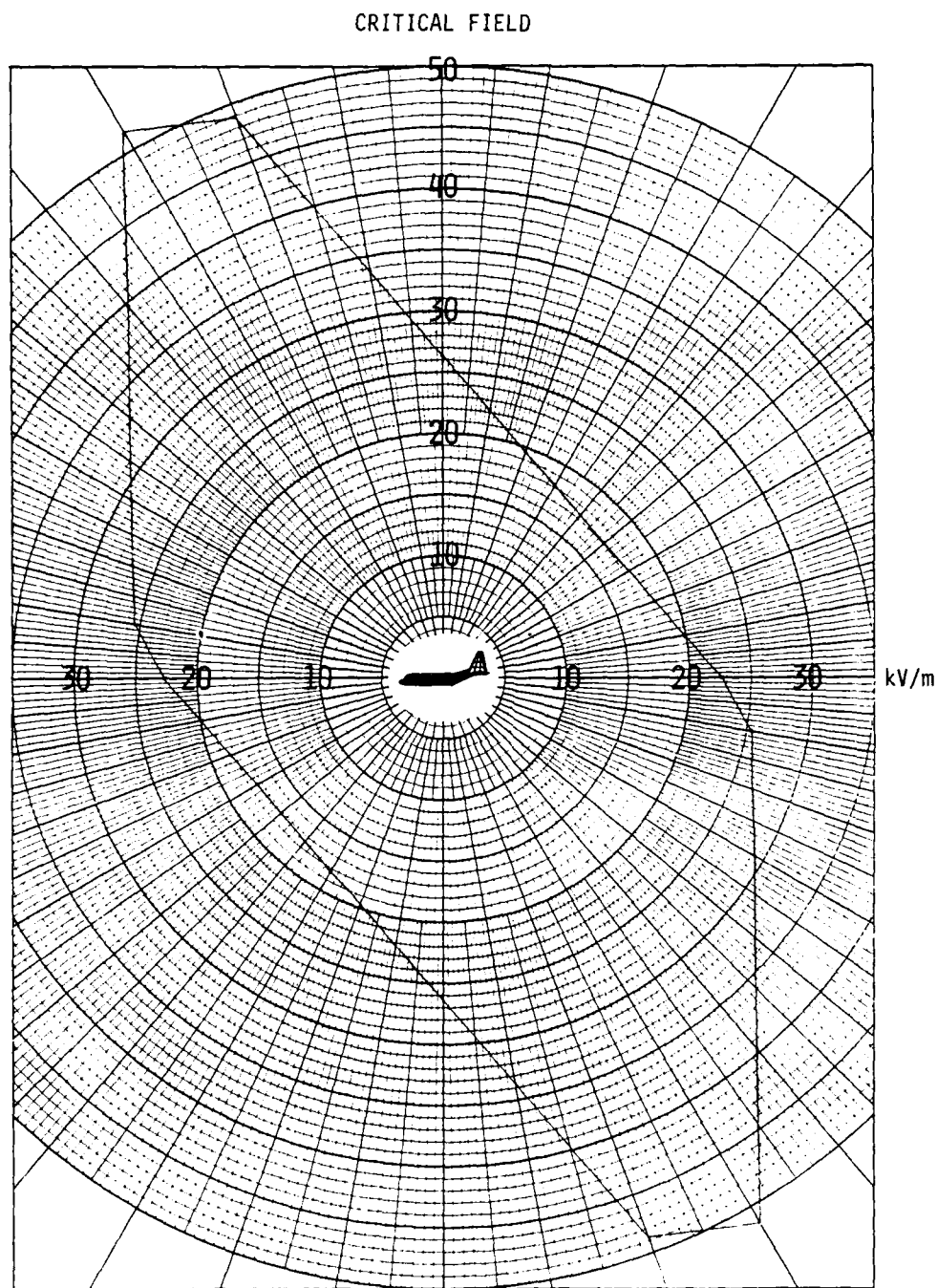


Fig. 8 - Critical field profile (in kV/m) in polar coordinates, in the z-x plane, obtained by dividing 3000 kV/m by the FCF profile of Fig. 5 (see text)

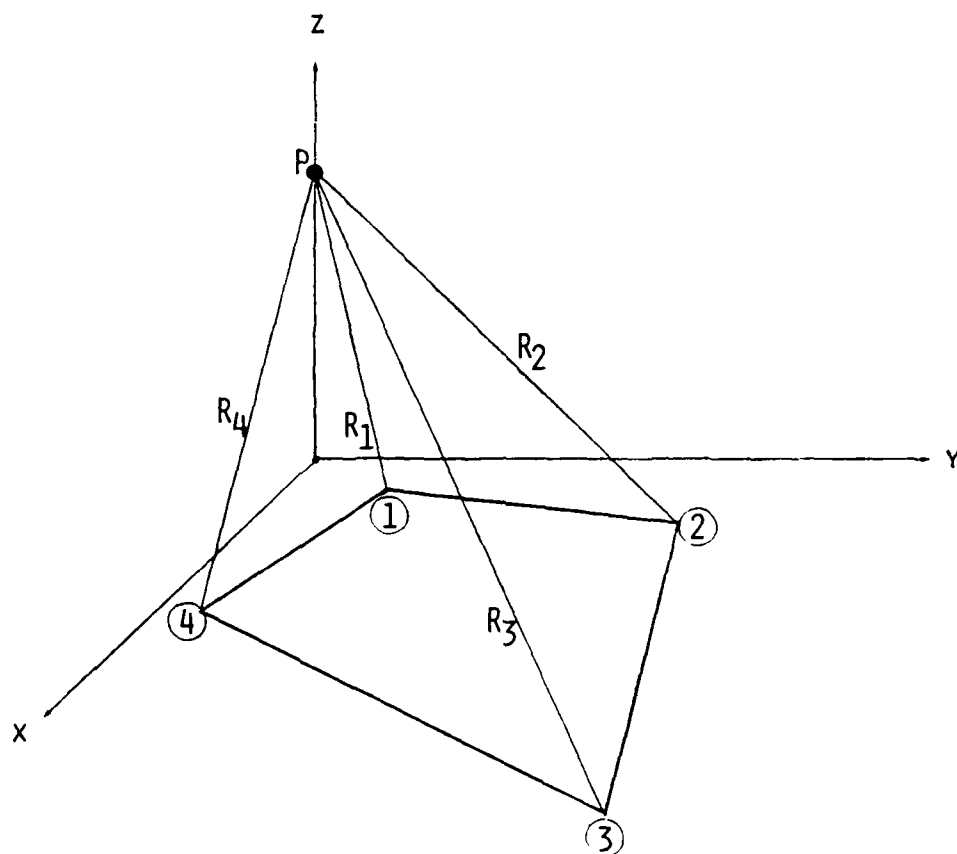


Fig. 9 - Quadrilateral patch coordinate system for computation of potential at field point P

THE MATHEMATICS OF INTERACTION BETWEEN
A CONDUCTIVE CYLINDER ON EARTH AND A
MOVING LINE AND CHARGE DUE TO LIGHTNING

by

ABUL RASHID

TRW, NORTON AFB

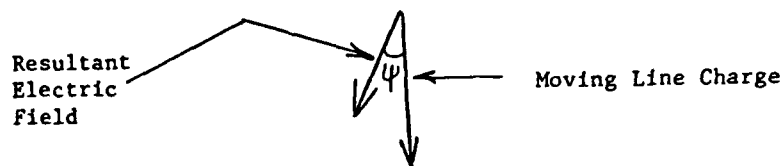
SAN BERNARDINO, CA 92409

Abstract:

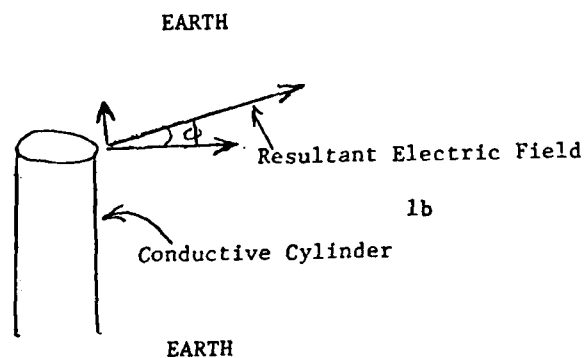
Starting from the work of Lienard and Wiechert ⁽¹⁾, Mathematical formulas for the electromagnetic fields produced by a moving line charge due to lightning are developed. It is shown that these electromagnetic fields have directive properties and the maximum electromagnetic field occurs at an angle away from the direction at which the charges are moving as illustrated in Figure 1A. These properties of the moving line charge are combined with the directive properties of the near fields produced by a conductive cylinder located on a conductive plane. The electromagnetic field produced by a conductive cylinder consists of a field parallel to the cylinder and, also, a field perpendicular to the cylinder. The perpendicular field has a maximum value at the end of the cylinder. The resultant electric field consisting of a parallel and a perpendicular field to the cylinder makes an angle to the axis of the cylinder as illustrated in Figure 1B. This angle is determined by the height of the cylinder and the frequency of excitation.

The directivities of the moving line charge and the conductive cylinder are analyzed to show the existence of a preferred path for charges to move from the cylinder to the moving line charge as illustrated in Figure 1C. It is shown that these directivity patterns determine which conductive cylinder shall be struck by lightning when such a lightning strike takes place in the presence of cylinders co-located on a flat conductive surface.

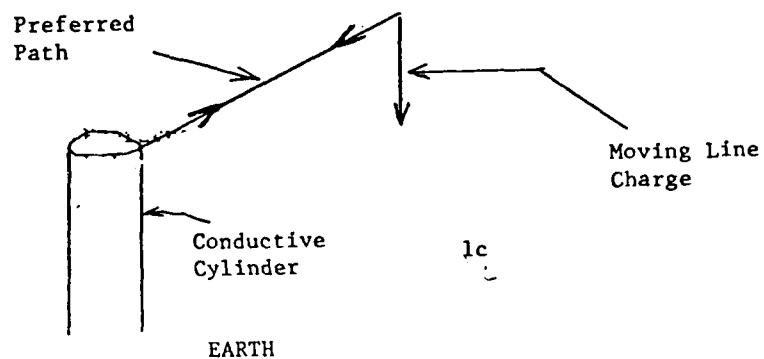
This paper was not available for incorporation into this book.



1a



1b



1c

Figure 1. Directive Properties of a moving line charge and a conductive cylinder on earth.

- (1) Classical Electricity and Magnetism by Wolfgang K. H. Panofsky and Melba Phillips, Addison - Wesley Publishing Company, Inc., Cambridge 42, Mass., March 1955, Chapter 18.

AUTOMATION OF SURFACE THUNDERSTORM OBSERVATIONS

Michael W. Maier

Lightning Location and Protection, Inc.
1001 South Euclid Avenue
Tucson, Arizona 85719

ABSTRACT

Inadequate observations and forecasts of thunderstorms have been cited as a contributing cause to many aircraft accidents in recent years. The aerospace meteorology community has long recognized the need for improved thunderstorm observations, however, thunderstorm observations which are available to flight crews of jet aircraft today have remained essentially unchanged since the time of the DC-3. Here we describe a fully automated, single station instrument system which is capable of detecting and locating thunderstorms within 100 NM of the airfield. The system operates continuously without an operator and automatically updates thunderstorm location, movement, and intensity information. Thunderstorm observations derived with this system are compared with actual surface observations at a major airport terminal. The automated thunderstorm observations are shown to be superior in content, reproducibility and timeliness to the qualitative observations of the human observer. The automated thunderstorm sensor system is designed to be compatible with the automated weather observing systems currently in the field and those under development.

This paper was not available for incorporation into this book.

SHUTTLE TRANSPORTATION SYSTEM (STS) LIGHTNING PROTECTION &
MEASURING SYSEM (LPMS)

JOINT PAPER BY WILLIAM JAFFERIS
NASA/VO (305-867-2660)
KENNEDY SPACE CENTER, FL 32899
AND
LT KEITH KERR/AF-6555 ASTG/LVT
(305-853-7201)
HARRY TANG/PRC 1217 (305-867-3407)

This paper describes the Lightning Protection and Measuring System for the Shuttle vehicle and its associated ground support equipment, which begin immediately after leaving the protection of the Vehicle Assembly Building (VAB) until the vehicle is launched. STS LPMS design evolved from the Apollo program and was improved through a Lessons Learned technique. As in the Apollo program, lightning protection consisted of good bonding, grounding, and shielding practices backed up with modeling and simulated lightning testing and validation procedures.

The measuring system consists of three major systems; (1) the Catenary Wire Lightning Instrumentation System (LWLIS), which measures lightning wave form and peak current; (2) Lightning Induced Voltage Instrumentation System (LIVIS), which measures induced voltages and current flow in the vehicle and ground support equipment; and (3) an optical system presently a three video camera system. The CWLIS measures direct lightning effects and is active at all times, and provides an alarm to the test team where lightning strikes.

The cloud to ground lightning current characteristic data collected on a continuous basis and provided to interested scientists. To date, the highest values measured have been as follows: 150 kiloamperes peak current, .35 microseconds rise time, and 28.5 kiloamperes per microsecond of current change (sensor limit). LIVIS becomes active when the orbiter is attached to the External Tank (ET)/Solid Rocket Boosters (SRB) in the VAB. All induced voltages are sensed and stored in a peak Voltmeter. The system is active from this point on through launch/post-launch. Through the use of the Launch Proessing System (LPS)/Central Data System (CDS), data can be retrieved on an archival basis to determine the time and possible cause of the event. During an adverse weather warning (possibility of thunderstorms, usually) the LPS monitors selected vehicle circuits and provides an alarm to the test team if a threshold is reached. To date, no direct/indirect lightning strikes have been greater than the induced voltages caused by normal vehicle environment.

The optical system/video completes the measuring system and is used to determine the attachment point of lightning.

All the data is collected in one report and is used to assess damage to STS vehicles/electrical and mechanical systems.

This paper will discuss three lightning events that occurred with and without a vehicle at the pad, both direct and indirect effects from nearby lightning, and strikes to the lightning mast. The discussion will include calculations/estimations of basic wave form data as measured and it's associated induced effects as measured and calculated. The following three events will be analyzed:

1. With no vehicle at Pad A
 - a) Strike to the catenary wire (measured) and associated GSE induced effect calculated vs. measured.
 - b) Assumed nearby strike to Pad A and associated GSE induced effect calculated vs. measured.
2. STS-4 vehicle at Pad A day before launch
 - a) Strike to catenary wire (measured) and associated orbiter vehicle induced effects (7 measured circuits).

This paper was not available for incorporation into this book.

PROGRESS OF THE ATMOSPHERIC ELECTRICITY HAZARDS PROTECTION PROGRAM

Jack R. Lippert, Lt Jayme E. LaVoie, and Rudy C. Beavin

Air Force Wright Aeronautical Laboratories

ABSTRACT

The two Phase AEHP Program consists of a twenty-one (21) month Phase One for Protection Definition and a thirty-three (33) month Phase Two for Effectiveness Demonstration. Results from Phase I of the Program are reported. During the AEHP Program the electromagnetic (EM) Environment resulting from aircraft (A/C) interaction with Atmospheric Electricity has been defined and its impact on electrical/electronic subsystems and equipment assessed. Computer codes have been applied to predict the impact of transients on internal wiring. These coupling predictions have been compared with experimental data for simple mock-up configurations. Trade-offs have been performed to prescribe AEHP concepts which are compatible with protection required against other EM threats; e.g., EMI, NEMP. The plan for demonstrating the effectiveness of the protection provided through ground based AE simulation is presented. This paper provides an overview of the progress to date and presents an outline of future efforts planned.

INTRODUCTION

The AEHP Advanced Development Program enjoys the application of financial and Program resources by an assembly of Military/Civilian agencies. The Flight Dynamics Laboratory of the Air Force Wright Aeronautical Laboratories (AFWAL/FI) provides the ADP office for interagency coordination and AEHP Program direction. Other Federal Military Agencies contributing to the Program include other Air Force organizations, as well as the Army, the Navy and the Defense Nuclear Agency. In addition, the Federal Aviation Administration and the National Aeronautics and Space Administration are participating in the Program, while the Boeing Military Airplane Company (BMAC) is the Prime Contractor for the Program. The National Interagency Coordinating Group (NICG) for the National AEHP Program meets annually to review the work accomplished, underway and planned by various Agencies to encourage a coordinated application of Federal resources for AEHP investigations. The National Severe Storms Laboratory of the National Oceanographic and Atmospheric Administration (NOAA/NSSL) is also a member of the NICG.

The first Phase of the AEHP Program produced design guidelines defining balanced protection concepts to provide confidence for all-weather application of advanced avionic and structural concepts in military and civilian scenarios. Balanced protection concepts which are appropriate for the uniqueness for each of four classes of A/C; e.g., Fighters, Transports/Bombers, Helicopters, and Missiles were developed. This Phase was initiated on 1 April 1982 and completed February 1984 (21 months). During Phase One of the Program the electromagnetic environments incident on A/C electrical/electronic systems were defined and appropriate protection schemes established. In order to achieve this result, the interaction of AE environments with modern A/C structure(s); e.g., advanced composite materials, high resistance metals; were determined to characterize the AE associated threat incident on advanced electrical/electronic elements; e.g., Fly-by-Wire, Power-by-Wire, et al. Appropriate hardening concepts were then evaluated experimentally to assure confident operation of flight/mission critical elements under AE threat conditions. The hardening employed includes a balanced set of: system, power and information shielding; passive/active system protection; et al. The AEHP concepts prescribed were also evaluated for their contribution to protection against other EM threats; e.g., EMI, NEMP and protection concepts against the latter are being considered for incorpor-

ation in the final AEHP schemes specified.

Phase Two is a 33 month technical investigation from March 1983 to December 1986. During that period it is planned to configure modified YUH-61 Helicopter and F-14 test beds with representative advanced electrical/electronic systems and advanced structural concepts to demonstrate the effectiveness of the balanced AEHP defined during Phase One. The test bed A/C, together with protected electrical/electronic systems representative of A/C of the 1990's will be subjected to interaction with simulated lightning flashes which will be representative of the AE threat. The results of these tests will be evaluated and appropriate adjustments made to the protection schemes employed. In addition to the demonstration of balanced protection effectiveness, techniques of qualification of protection and continued assessment of the integrity of the AEHP provided will be identified and demonstrated.

The AEHP ADP invites contributions from the aerospace technical community to improve the effectiveness of the Program and aid transition of Program results to aerospace system application. Continuing interactions will improve the quality of the AEHP Program and yield a maximum return on the Program investment.

PHASE ONE (I)

The AEHP ADP Phase I was directed toward the development/design of effective AEHP for the four classes of flight vehicles i.e., Fighters, Transports/Bombers, Cruise Missiles, Helicopters.

ATMOSPHERIC ELECTRICITY THREAT - The characterization of the atmospheric electricity threat environment imposed on flight and mission critical electrical/electronic elements aboard A/C is important for the AEHP Program. The initial definition of both lightning and precipitation static associated electrical environments for A/C has been taken from the technical record. In the case of precipitation static, the literature base has been examined, and the significant threat parameters with their range of magnitudes noted for inclusion in the atmospheric electricity threat characterization. For the lightning case, the existing tech base has been updated with results from recent airborne lightning characterization programs (F-106, C-130) as well as analyzing the impact measurement towers have had on the data collected in the past. Since the severity of lightning exhibits a probabilistic distribution, two different threat levels were determined from the statistical data base. One, a moderate threat, is what the air vehicle is normally expected to encounter and is important for mission completion and R&M

consideration. The other is as severe an encounter as to be expected throughout the vehicle life cycle and is important for catastrophic safety of flight considerations. These threats are represented by double exponential current waveforms (Figure 1).

The severe threat for the AEHP Program has a maximum rate of rise of 200 ka/ μ s with a peak current of 200kA, a fall-time to half-peak value of 50 μ s, and an action integral of 1.5×10^6 A²-sec. The moderate threat has a 20kA peak current with a maximum rate of rise of 50kA/ μ s, a fall-time to half-peak value of 50 μ s and an action integral of 1.5×10^4 A²-sec. Moderate and severe lightning flashes consist of multiple strokes with characteristics as shown in Table 1.

With the attachment of lightning flashes to A/C or the incidence of electromagnetic fields from nearby lightning events, as well as with charge accumulation resulting from precipitation static, currents and fields will be experienced at the surface of A/C. The waveform of this energy as well as the magnitude of energy transferred to elements inside the A/C will be affected by A/C geometry and material. Various computer codes have been evaluated to determine the characteristics of the threat at the circuit/element station in an A/C as the result of transfer functions and coupling effectiveness. Among codes which have been applied are WIRANT, THREDE, SRC-2D as well as PRESTO/TRAFFIC.

These codes have made possible the prediction of fields and currents to be experienced along and interior to the vehicle during lightning simulation tests with the ALCM and YG-16/mock-up test beds. These predictions were evaluated and compared to test results. Such a comparison is shown in both frequency and time domain (Figure 2a and 2b).

ELECTRONIC SUSCEPTIBILITY - The intent of the AEHP ADP is in providing effective protection concepts for flight and mission critical electronic/electrical systems of the 1990's. Table 2 indicates the technologies utilized (to be utilized) in flight and mission critical avionics systems. Preparatory to the identification of appropriate protection concepts and evaluation of their effectiveness the susceptibility of various electronic elements to upset and/or damage from electrical environments associated with Atmospheric Electricity - Aircraft interactions were established. This was accomplished by completing four tasks. First, a review of historical data was performed to determine the failure levels of the collected data (primarily EMP short pulse) and adopted these failure levels to long pulses (lightning). Second, piece-parts over-

stress testing, including TTL, ECL, CMOS & NMOS technologies, was performed to supplement the historical data and verify the failure models developed. Third, identification of present equipment damage thresholds using the results from previous equipment damage assessments, along with some new damage assessments performed under this contract were established for various classes of equipment. Finally, bench testing of new technology subsystems were conducted to evaluate system upset susceptibility.

Past testing of electronic devices provided data on electrical transient damage. The purpose of the study of historical data was to critically review and summarize all the available data, perform studies on the failure levels, and adapt these failure levels to long pulses (lightning). The major objective of the effort was to model the historical data (limited to failure pulse widths between 10ns and 10 s) using the thermal model (Wunsch-Bell). Because of the limited pulse widths of the data and the fact that newer technology IC's had not been tested a limited piece part test program was recommended to provide data for long pulse transients (up to 1ms) and new technology (LSI, CMOS NMOS).

The piece-part component tests were conducted at the AFWL Direct Drive Laboratory by the BDM Corporation. Table 3 gives a summary of the devices and failure power at varying pulse widths. Review of the data revealed that most devices show a flattening of the power to failure versus pulse width for pulses greater than about 10 microseconds. The new technology (LSI, MSI) generally showed power failure thresholds of anywhere from 1/3 to 1/10 the thresholds of the older SSI devices. What this means with respect to future trends in subsystem susceptibility to damage is (1) unless other measures are taken to harden the systems the future subsystems are likely to be softer than present subsystems by up to 10dB, and (2) since newer equipments tend to utilize digital integrated circuits which may interface directly with outside lines as opposed to older analog equipment in which most input signals come through passive devices like resistors and capacitors, there are likely to be a larger percentage of pins with low thresholds in the newer equipment.

In determining subsystem susceptibility the results from previous equipment damage assessments performed on the AEHP contract were used to identify the thresholds associated with various classes of equipment. All past and present damage analyses were performed in the frequency domain. These analyses were performed at discrete frequencies, typically 0.01, 0.1,

1, 10 and sometimes 4MHz. The pin failure predictions for thresholds of power, voltage and current for each class of equipment have been plotted on graphs as a function of frequency as illustrated in Figure 3. This allowed a lower bound to be identified as the minimum predicted failure threshold for each class of equipment. Figures 4, 5, and 6 show the resulting lower bounds for all classes of equipment for comparison. Concerning these Figures it should be noted that although the graphs show some very low voltage and current thresholds these are usually for different components.

The bench testing of three digital systems was conducted to investigate expected levels of upset for new technology subsystems. The three systems tested were the Honeywell F-16 Radar Altimeter, the Bendix ILS Receiver RIA-35A and the Hamilton Standard Propulsion Data Multiplexer. The three bench test configurations consisted of a lightning transient pulse test, a "chattering relay" test, and a ground potential test. The results of the testing is presented in Table 4.

VULNERABILITY ASSESSMENT - This experimental work obtained generic data on the susceptibility of components/subsystems in various generalized configurations when subjected to the defined lightning threat. This investigation used two different test beds (YG-16, ALCM) at two different facilities (BMAC, Sandia).

The YG-16 test bed consists of an advanced composite forward fuselage section mated to a mock-up representing the remainder of the F-16 aircraft. The forward fuselage is 78% GR/EP with some aluminum support structure. The mock-up is sheet aluminum over a wood frame in the general F-16 shape to preserve electrical lengths and resonances appropriate for the fighter aircraft. The entire test bed is supported above the ground plane by non-conducting wood bracing. A picture of the YG-16 test bed is shown in test configuration (Figure 7).

Of the two test techniques employed, The Swept Continuous Wave (Swept CW) technique injects a low level current onto the aircraft skin/structure and measures the output voltage/current at wiring/equipment stations as a function of frequency. This resulted in definition of the transfer functions in the frequency domain which may be used to determine coupling effectiveness and as an analytical tool. The other technique, pulse injection, applies a unipolar current impulse, corresponding to the moderate threat onto the aircraft with response measurements taken in the time domain. This test generated information concerning susceptibility levels and interaction mechanisms.

Testing representative wiring installations and grounding schemes of discrete circuits as well as data buss lines yielded information to characterize the induced transients and impacts due to a lightning interaction. These results directly apply toward development of protection concepts for electrical systems in a composite air vehicle. Routine wiring installation as employed in past metal airframes with structural return, cannot be tolerated in GR/EP composite primary structure. The increased resistivity of the graphite/epoxy introduces an IR drop factor to the induced transient coupling. It is conceivable to have 1000 volts drop per meter length of GR/EP structure. The IR drop would dominate the coupling mechanisms, even though the composite structure offers less shielding effectiveness than metal structure to B dot coupling as well. Protection concepts therefore are based on eliminating the IR drop coupling mode as will be discussed later.

The Air Launched Cruise Missile (ALCM) test bed is a prototype version of the production AGM-86B which has undergone skin panel(s) modification/removal and cable shield alteration to yield generic data for the general missile configuration. This test series was conducted at the Sandia Lightning Facility in Albuquerque N.M. (Figure 8). The facility subjected the ALCM to current waveforms up to the defined severe lightning threat. This severe threat coupled to a vehicle as small as the ALCM results in the strongest current density from a lightning strike anticipated for any vehicle.

Impulsing the ALCM while running on ground simulation software evaluated both damage and upset susceptibility. The internal electrical subsystems showed transient components corresponding to both aperture coupling and diffusion coupling. The transient stress testing varied the impulse current amplitude while keeping the risetime constant. This method confirmed the expected linearity of induced voltages on the test points for this configuration (Figure 9). In general, however, one must be careful in applying the linearity assumption to resistive configurations where non-linearities are more probable.

A benefit of the ALCM is that EMP simulation tests were previously performed on that weapon system and measurements of these same points for AEHP lends insight to the similarities of electromagnetic threat and protection required. Comparison of simulated severe lightning (200kA) with simulated EMP (50kV/M) effects showed higher voltages for the directly attached lightning case (Figure 10). It should be noted, however, that the baseline ALCM is a hard vehicle designed to 100v pin spec.

The information gained during this test series was of a generic nature.

PROTECTION SPECIFICATION/GUIDELINES

This effort established and evaluated practical, effective protection concepts which minimize cost, weight, power, and reliability/maintainability requirements. This trade study for life cycle cost was used to develop specifications for balanced protection for advanced (1990-95) electrical/electronic systems in advanced airframes.

Due to the near future time frame under consideration, protection concepts emphasized various shielding/grounding schemes tailored to suit the specific vehicle. One such scheme is using a conductive floor in the composite structure for power return and a shielded data bus for signal lines. Wider use of fiber optics requires further development, but as they become more economical, their advantages and their recommendation for the more distant future use is obvious. Different protection schemes were evaluated via life cycle cost (Figure 11) and comparative weights were recorded. Based on these overall inputs the multiple point grounded conducting floor option for the generic fighter offers adequate protection while having minimal maintenance requirements for near time implementation. These guidelines and recommendations were used to generate the specific protection schemes and are recorded in a design guide handbook. The AEHP handbook has recently been disseminated to industry for their review and comments. It is important that the results of this ADP are effectively communicated to aircraft and systems producers so the AEHP from the ADP may have an early introduction to the Military/Commercial aircraft fleets. Comment/suggestions from the Aerospace Community are encouraged throughout the ADP.

ELECTROMAGNETIC PROTECTION

REQUIREMENTS UNIFICATION - This task, initiated in September of 1983 and scheduled to be completed in March of 1985, is to unify requirements for AEH/NEMP/Intrasystem transient protection of electronic and electrical equipment for aircraft and air breathing missiles. Presently there is considerable uncertainty in setting levels of protection for equipment because of the increasing complexity in the system design trade-offs between installation, design and equipment specifications. The problem is compounded by overlapping EMI/NEMP requirements and the emerging need for lightning protection requirements. Qualification test procedures, MIL-STD-462 and specifications levels MIL-STD-461 will be developed which unify requirements of electromagnetic (EM) effects for the Line Replaceable Unit (LRU).

PHASE II

In Phase II the effectiveness of the AEHP Interim Design Criteria and initial AEHP concepts will be demonstrated on A/C test beds using ground-based Atmospheric Electricity Simulators. The test beds to be used will be derived from a YUH-61 Helicopter and an F-14 A/C. The basic vehicles will be extensively modified through application of advanced composite and other poorly conducting material as vehicle surface cover, as well as installation of electrical/electronic systems employing operational concepts representative of those anticipated for the 1990's. A set of special test equipment (STE) to be installed for demonstration is based on the MIL 1553 data bus with various technology sophistications LRU as readily obtainable (Figure 12). In addition, the ALCM test equipment/software will be installed and monitored during testing for functional upset. This procedure will permit the evaluation of many electrical/electronic system protection concepts, including structural aspects and local shielding as well as AEHP tolerant electrical concepts, in configurations which are representative of those which will be encountered in future A/C of the four classes being considered; i.e., Fighters, Transports/Bombers, Cruise Missiles, and Helicopters.

Phase II has only recently begun, March 1984, with active investigation being completed by October 1986 and the documentation of the AEHP Program continuing into early FY87. A product of Phase II will be finalized AEHP design concepts adjusted from the demonstration activities of Phase II. Another product from Phase II will be documentation/demonstration of procedures for initial qualification of AEHP concepts for A/C and procedures for evaluating the continuing integrity of the AFHP provided to A/C while in the operational inventory. Work is under way, both with AFWAL/FIESL and with Lightning Transients Research Incorporated (LTRI) through the AEHP Prime Contractor, BMAC to define procedures/equipment which are appropriate for demonstration of AEHP concepts and initial qualifications of System and A/C protection. FIESL, BMAC and other entities are also addressing the continuing assessment of protection integrity. Finally, during Phase II, the relationship of AEHP to protection against other electromagnetic threats; e.g., EMI, NEMP, Radar, et al; will continue to be explored. Where possible, consolidated design concepts will be documented, but where advised the need for explicit protection outside the spectrum of protection provided by AEHP will be noted.

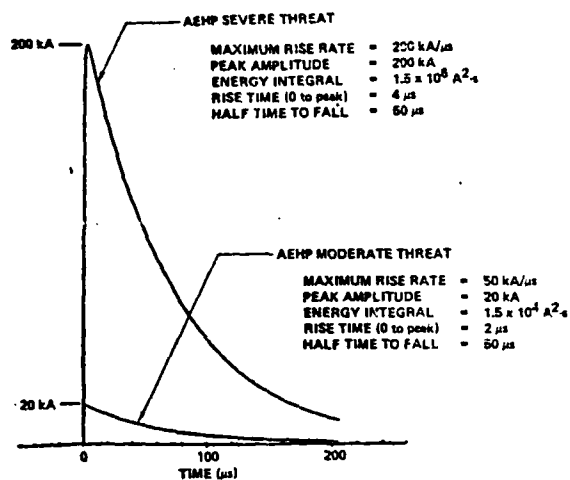


Fig. 1 - Single Stroke Threat Definition

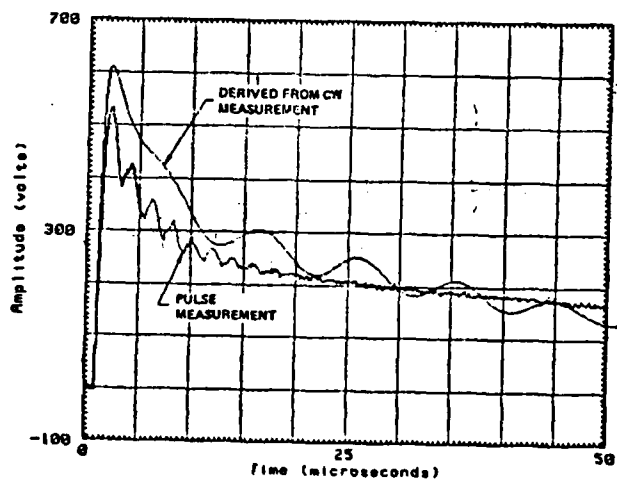


Fig. 2b - Prediction vs Measurement in Time Domain

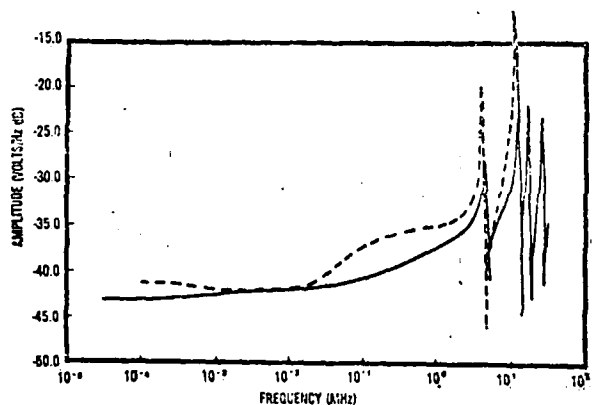


Fig. 2a - Prediction vs. Measurement in Frequency Domain

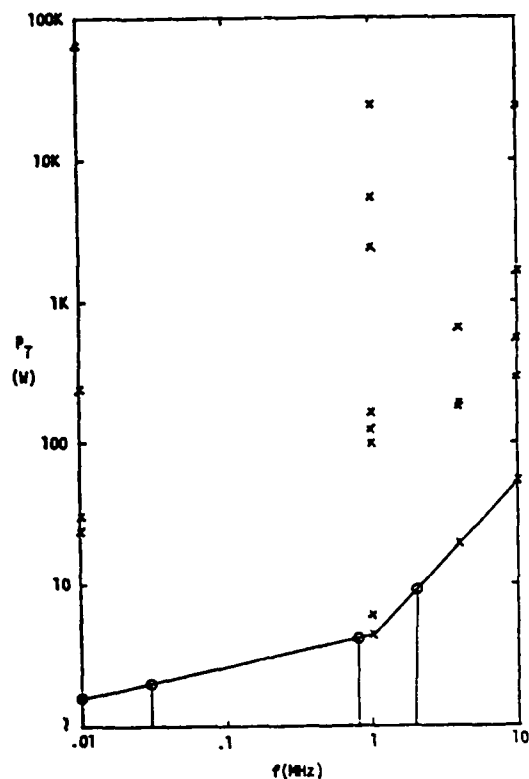


Fig. 3 - Failure Power versus Frequency for a Class of Equipment

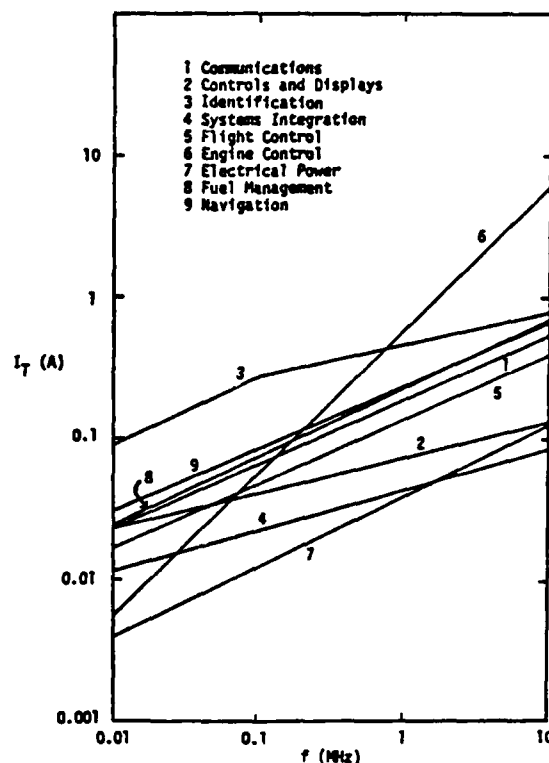


Fig. 5 - Minimum Current Damage Thresholds for Different Classes of Subsystems

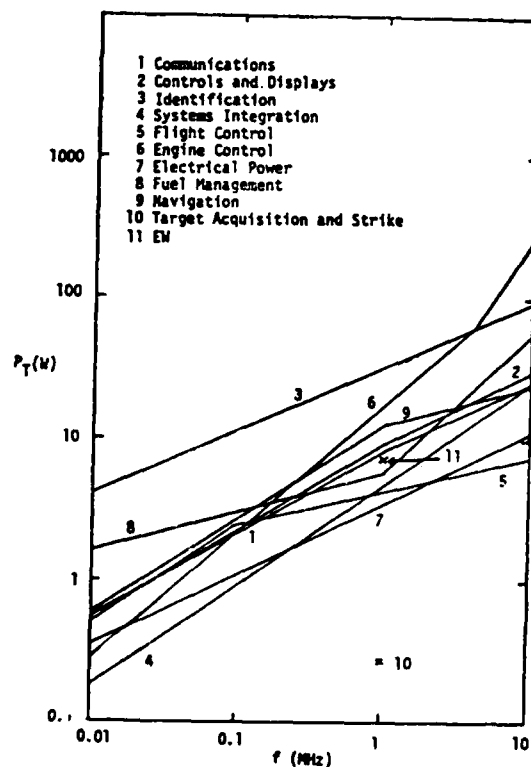


Fig. 4 - Minimum Power Damage Thresholds for Different Classes of Subsystems

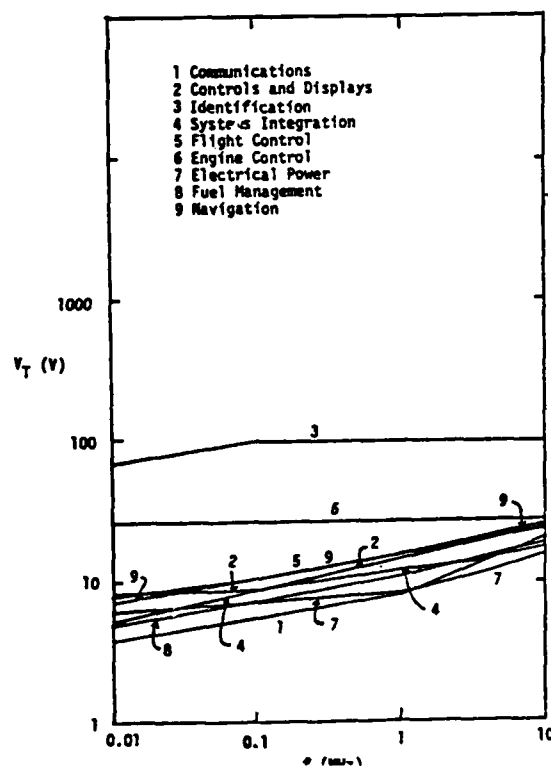


Fig. 6 - Minimum Voltage Damage Threshold for Different Classes of Subsystems

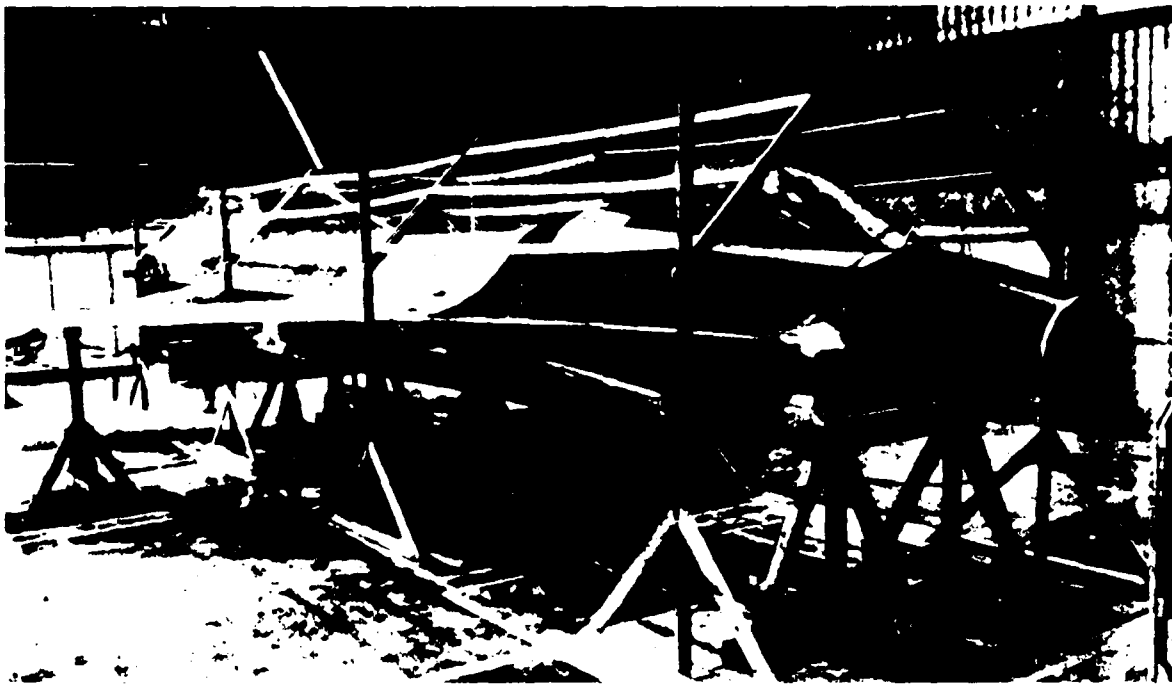


Fig. 7 - The composite YG-16 Mockup with
wire mesh return path for
quasi-co-axial configuration

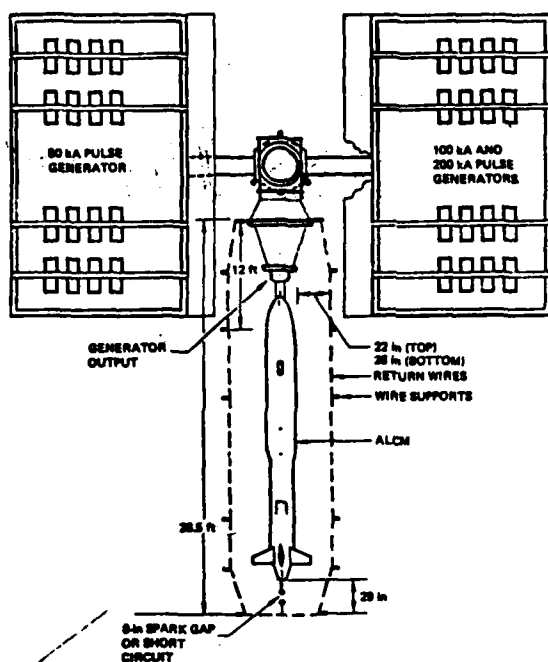


Fig. 8 - ALCM Missile and Pulse Generator Layout

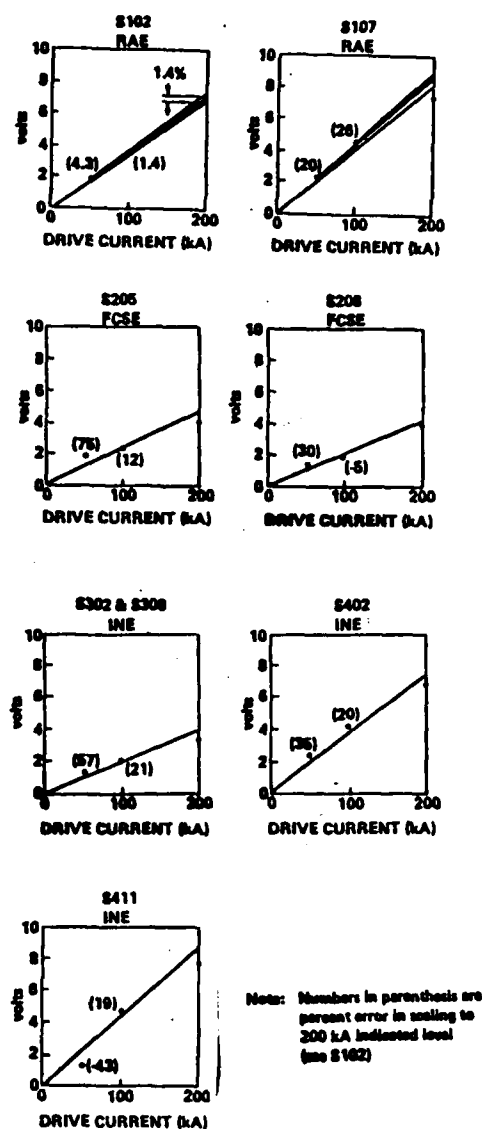


Fig. 9 - Transient Stress Test Response Linearity

SWITCH POSITION	TEST POINT	BASELINE			RACEWAY COVERS REMOVED		RACEWAY COVERS REMOVED & 2 CABLE SHIELDS ISOLATED	
		EMP 80 kA/M	AEHP (200 kA)	EMV	EMP	AEHP	EMP	AEHP
81-3	RAE-28J1-6 to chassis 28 vDC power	0.243 v (360 v)	8.9 v	TO BE ADDED	2.44 v	78 v	NO COMPARABLE CONFIGURATION	183 v
81-7	RAE-28J1-4 to chassis 28 vDC power	0.141 v (360 v)	7.3 v		*	73 v		81 v
82-6	FCSE-2J2-117 to chassis Fuel control actuator	0.377 v (100 v)	4.1 v		0.786 v	28 v		28 v
82-8	FCSS-2J2-37 to chassis Right eleven comm.	0.118 v (100 v)	4.8 v		*	18 v		18.5 v
83-2	INE-1J1-78 to chassis Ordnance alarm monitor	0.588 v (360 v)	3.3 v		*	6.2 v		86 v
83-8	INE-1J1-3 to chassis Squib enable comm.	0.213 v (100 v)	3.3 v		*	6.2 v		86 v
84-2	INE-1J5-C to chassis 28 vDC power	0.877 v (360 v)	8.8 v		*	88 v		▷
84-11	INE-1J2-63 to chassis Exhaust cover display	0.176 v (100 v)	7.7 v		0.887 v	45 v		118 v

() values are EMP pin voltage limits

*Not measured

▷ Transient monitoring equipment failure

Fig. 10 - Summary of EMP and Lightning Test Points Measurements

	CONCEPT 1	CONCEPT 2	CONCEPT 3	CONCEPT 4	
	Cable Shields	Shields & Floor	Shields & Floor w/ Insulator	Shields & Wire Type Data Bus	Shields & Fiber Optics Data Bus
ROUTE ▷	13.776	9.883	10.453	18.417	25.848
PRODUCTION ▷	68.455	52.805	54.193	72.657	96.773
OTHER ▷	3.314	2.347	2.357	1.432	2.009
SUB-TOTAL	85.545	65.035	67.003	92.506	124.629
OPERATIONS/SUPPORT	25.858	17.637	17.683	8.987	10.801
TOTAL LCC	111.403	82.672	84.686	101.493	135.430

Notes: ▷ Costs are for 500 vehicles operating 15 years beginning in 1990. Numbers represent 1983 dollars in millions.

▷ Shields with floor indicate all wires away from floor are shielded.

▷ Shields with data busses indicate all power lines and other discrete are shielded. Wire busses are also shielded.

▷ Initial Spares, Supply Administration, Ground Support Equipment

Fig. 11 - Life Cycle Cost Trade Summary for Fighter Aircraft

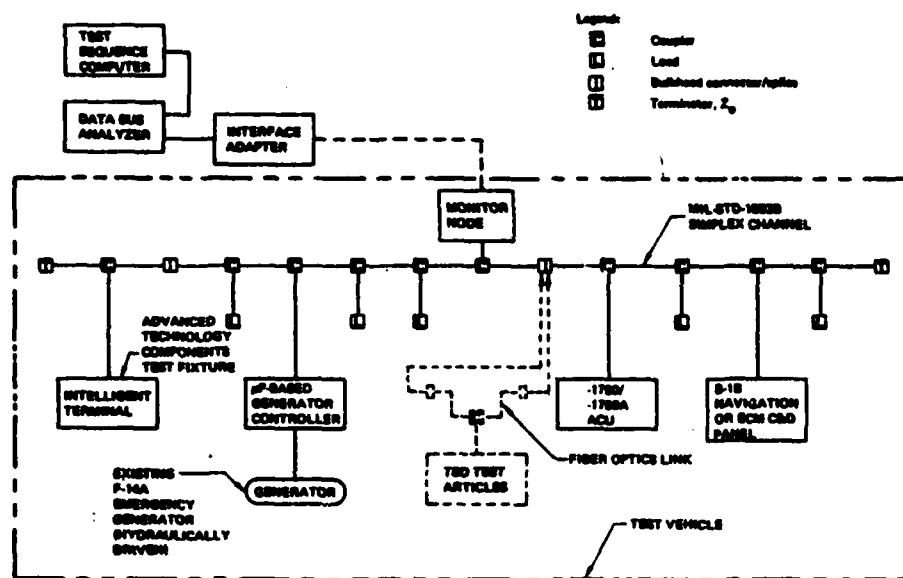


Fig. 12 - Data Buss Special Test Equipment (STE) for Phase II

Table 1 - Multi Stroke Threat Parameters

0 Duration of Transient	50 - 500 μ s
0 Inter-stroke time interval	10 - 100ms
0 Time Duration of Lightning Event	0.01 - 2 sec
0 Number of Strokes	over - 100

Table 2 - Component Technologies in Flight and Mission Critical Avionic Systems

	<u>VHSIC</u>	<u>VLSI</u>	<u>CMOS</u>	<u>GaAs</u>	<u>COLOR CRT</u>	<u>FIBER OPTICS</u>	<u>BUBBLE MEMORY</u>	<u>CCD</u>	<u>SAW</u>
1. COMMUNICATIONS	D	N	P	P		N			P
2. CONTROLS AND DISPLYAS	D	N			P			D	
3. ELECTRONIC WARFARE	D	N	P	P					
4. SYSTEM INTEGRATION	D	N	P			P	D		
5. IDENTIFICATION	D	N	P	N			D		N
6. FLIGHT CONTROL	D	N	P			N			
7. NAVIGATION	D	N	P	P	N	N			N
8. TARGET ACQUIS. AND STRIKE	D	N	P	N	N				
9. ELECTRICAL POWER		N	P		P				
10. ENGINE CONTROL	D	N	P			N			
11. FUEL MANAGEMENT	D	N	P			N			

NOTE: P - Present Technology ('80 - '85)

N - Near Future Technology ('85 - '90)

D - Distant Future Technology ('90 - '95)

Tabel 3 - Prefail (FAIL) Power Range -- Input

<u>DEVICE</u>	<u>TECHNOLOGY</u>	<u>POLARITY</u>	<u>1 μsec</u>	<u>10 μsec</u>	<u>100 μsec</u>	<u>1000 μsec</u>
SN5420J	TTL-SSI	+		2.7-3.3	2.1-2.2	1.8-2.3
MC10101L	ECL-SSI	-	15.3-16.1	4.9-7.3	4.6-5.9	4.0-4.7
MC10501L	ECL-SSI (Military)	-		4.8-5.8	4.5-6.5	
CD4011BCN	CMOS-SSI	-	31.6-36.0	9.1-10.3	5.0-6.1	5.1-5.3
MC14011BCP	CMOS-SSI	+	31.9-36.5	11.2-13.5	5.2-7.1	5.4-8.9
MC14011BAL	CMOS-SSI (Military)	+		9.3	5.3-7.8	
CD4034BE	CMOS-MSI	-		13.7-20.4	9.6-15.4	
AM270BDC	NMOS-LSI	+	Oxide failure - 35.2-41.0 Volts (max pin rating 15V)			
AM2716DC	NMOS-LSI	-	32.0-54.9	1.4-1.6	2.0-2.1	
IM66541JG	CMOS-LSI	+/-		.91-1.0	.67-.86	
2816-45	NMOS-LSI	-	Oxide failure - 29.1-32.8 Volts (max pin rating 6 V)			
D2816-4	NMOS-LSI	+		1.4(5.4)-7.3(8.5)(1)	.50(1.9)-1.4(4.4)(1)	
8748	NMOS-LSI	+	Oxide failure - 34.1-34.2 Volts (max pin rating 7 V)			
CD111DC	NMOS(CCD)-LSI	+	Oxide failure - 25.0-35.5 Volts (max pin rating 15V)			

(1) Numbers in parenthesis are failure power levels.

Table 4

Summary of Equipment Bench Test Results

Test	Interconnecting Wires	Results summary
Honeywell F-16 Radar Altimeter		
Induced spikes Induced cable Transients	All lines Unshielded Lines Shielded Lines Coaxial Lines All lines	No degradation Track and search modes. Lock up at $\pm 350V$ peak. This upset is resettable by cycling power on-off. Damage at $\pm 1400V$ peak. Track and search modes. Lock up at $\pm 400V$ peak. This upset is resettable by cycling power on-off. Damage at $\pm 1000V$ peak in self-test mode. No degradation at $1800V$ peak.
Ground Potential		Data bus lock up at $\pm 150V$ peak. This upset is resettable by cycling power on-off. Fuze blown at $\pm 500V$ peak.
Hamilton Standard Propulsion Data Multiplexer		
Induced Spikes Induced Cable Transients Ground Potential Transients	All lines All lines All lines	No degradation Unrepeatable data bus lockup at $-1400V$ peak. Otherwise, no degradation to $\pm 1800V$ peak. 28 VDC power input filter failed at $+600V$ peak. After repair the replacement filter failed at $+750V$ peak.
Bendix ILS Receiver RIA-35A		
Induced spikes Induced cable Transients	All lines Unshielded Lines Coaxial Lines Shielded lines	No degradation Damage to circuit cards at $\pm 400V$ peak. Data bus locked up at $\pm 800V$ peak and required power reset (test monitor upset). Data bus locked up at $\pm 200V$ peak (test monitor upset).
Ground Potential	All lines	Damage to circuit card at $\pm 200V$ peak. Fuze blown at $\pm 500V$ peak.

UPSET SUSCEPTIBILITY STUDY EMPLOYING CIRCUIT ANALYSIS
AND DIGITAL SIMULATION SOFTWARE

by

Victor A. Carreno*

Abstract of Paper Proposed for the
1984 International Aerospace and Ground Conference on
Lightning and Static Electricity
Session on Effects Upon Electrical/Electronic Systems
June 26-28, 1984
Orlando, Florida

This paper describes an approach to predicting the susceptibility of digital systems to signal disturbances. Electrical disturbances on a digital system's input and output lines can be induced by activities and conditions including static electricity, lightning discharge, Electromagnetic Interference (EMI) and Electromagnetic Pulsation (EMP).

The electrical signal disturbances employed for the susceptibility study were limited to nondestructive levels, i.e. the system does not sustain partial or total physical damage and reset and/or reload will bring the system to an operational status.

The front end transition from the electrical disturbances to the equivalent digital signals was accomplished by computer-aided circuit analysis. The Super-Sceptre (system for circuit evaluation of transient radiation effects) Program was used. Gate models were developed according to manufacturers performance specifications and parameters resulting from construction processes characteristic of the technology.

Digital simulation at the gate and functional level was employed to determine the impact of the abnormal signals on system performance and to study the propagation characteristics of these signals through the system architecture. Example results are included for an Intel 8080 processor configuration.

*Aero-Space Technologist, Fault Tolerant Systems Branch, Flight Control Systems Division, NASA Langley Research Center, Hampton, VA 23665, (804) 827-3681.

This paper was not available for incorporation into this book.

DATA AND RESULTS OF A LABORATORY INVESTIGATION
OF MICROPROCESSOR UPSET CAUSED BY SIMULATED
LIGHTNING-INDUCED ANALOG TRANSIENTS

by

Celeste M. Belcastro*

Abstract of Paper Proposed for the
1984 International Aerospace and Ground Conference on
Lightning and Static Electricity
Session on Effects Upon Electrical/Electronic Systems
June 26-28, 1984
Orlando, Florida

Advanced composite aircraft designs will include fault-tolerant computer-based digital control systems with high reliability requirements for adverse as well as optimum operating environments. Since aircraft penetrate intense electromagnetic fields when traversing the environment surrounding thunderstorms, these computer systems may be subjected to field-induced transient voltages and currents.

Digital system upset is one type of degradation that can occur in computer systems that are subjected to analog electrical transients. The functional error modes that occur in digital systems during upset are currently under investigation as part of a research effort whose primary goal is the development of a methodology for assessing the susceptibility/reliability of a computer system onboard an aircraft flying through a lightning environment.

This paper reports on the laboratory investigation being conducted to study upset error modes in a general purpose microprocessor and involves the random input of analog transients which model lightning-induced signals onto the interface and input/output lines of an 8080-based microprocessor from which upset error data is recorded. The program code being executed on the microprocessor during tests is designed to exercise all of the machine cycles and memory addressing techniques implemented in the 8080 central processing unit. In order to exercise all of the 8080 machine cycles, the microprocessor performs input/output operations with an intelligent peripheral device that generates interrupts and accomplishes direct memory accesses (DMA's).

A statistical analysis will be presented in which possible correlations are established between the probability of upset occurrence and transient inputs during specific processing states and operations. In addition, any possible correlations between upset error mode types and transient input points as well as various program storage mediums such as read write memory, core memory, and programmable read-only memory will also be established.

A preliminary stochastic upset susceptibility model will be presented. Probability density functions required to calculate the state transition functions for the model will be determined for the 8080 microprocessor. In addition, the susceptibility of this microprocessor to upset, once analog transients have entered the system, will be determined analytically by calculating the state probabilities of the stochastic model.

*Aero-Space Technologist, Fault Tolerant Systems Branch, Flight Control Systems Division, NASA Langley Research Center, Hampton, VA 23665, (804) 827-3681.

This paper was not available for incorporation into this book.

LABORATORY EVALUATION OF LIGHTNING INDUCED TRANSIENTS IN AIRCRAFT ELECTRICAL WIRING

by J.C. Alliot and P. Levesque
Office National d'Etudes et de Recherches Aéronautiques
BP 72, 92322 Châtillon Cédex, FRANCE

ABSTRACT

Protection of electrical and electronic systems against the atmospheric electricity hazards constituted by lightning, must be taken into special account in the design of advanced technology aircraft.

In order to bring to light the various processes of the electromagnetic fields penetration through a structure, laboratory experiments have been set up at ONERA. The purpose of this paper is to present the results obtained on a cylindrical model roughly simulating, at 1/20 scale, an aircraft fuselage. Current diffusion phenomena and direct electromagnetic couplings through apertures are analysed from the effects they induce on a test line located inside the model.

The experimental results are discussed and compared with numerical calculations.

INTRODUCTION

Lightning interaction with an aircraft flying in the vicinity of a thunderstorm cell may be separated into three main parts. First, electrical field build up in the cloud tend to increase the voltage of the floating aircraft. Rapid changes in the ambient field, produced by leader propagation or nearby strikes, cause electric charges to circulate on the structure. These circulating currents produce internal magnetic and electric fields which couple to the internal wirings.

The second process refers to stepped-leader attachment on the airframe. Charges are deposited on the structure raising its voltage rapidly to the voltage of the arc channel. At this time, breakdown strength of air limits the field that can be sustained at the surface of the airframe and profuse streaming will occur from opposite extremities of the aircraft. Thus the aircraft becomes part of the arc channel being taken by the leader. The last mechanism refers to the high magnitude current pulse flowing through the vehicle when the leader has reached its destination (ground or charge center of opposite polarity).

Research supported by DRET (Direction des Recherches, Etudes et Techniques de la Délégation Générale pour l'Armement) and ONERA.

Electromagnetic fields produced on the structure by the current pulse may excite internal wiring by diffusion and direct coupling through apertures.

For several years, ONERA is involved in lightning-aircraft electromagnetic interaction programs. The objective of this paper is to describe a laboratory research program conducted on a cylindrical structure in order to obtain more insight into energy coupling processes and to evaluate more comprehensively induced electrical transients.

EXPERIMENTAL SET UP DESCRIPTION

The cylindrical shell used in this experimental program is composed of three pieces having same length and being attached together by screws equally spaced on a circumference. Each element is made by means of an AG.5 foil whose thickness is 1 mm. The cylinder is 2.6 m long by 28 cm in diameter, with three 20 x 20 cm square apertures. Free field configuration around the cylinder has been achieved by using a coaxial return path. The circuit as a whole may be considered as a coaxial transmission line having a 50 Ω characteristic impedance. A drawing of the circuit is shown in figure 1. A double exponential current waveform, simulating a return stroke pulse, is produced by discharging a single capacitor of 75 kV through the line and a 50 Ω waveshaping resistor (Fig. 2). The resulting current waveform has a time to peak of about 40 ns and a decay to half value of about 15 μ s. The peak magnitude is 295 A. The current waveform may be approximated by the relation :

$$I(t) = I_0 (e^{-\alpha t} - e^{-\beta t}) \quad (1)$$

with : $\alpha = 4.10^4 \text{ s}^{-1}$

$$\beta = 6.5.10^7 \text{ s}^{-1}$$

$$I_0 = 300 \text{ A}$$

and its energy spectrum (Fig. 3) is given by :

$$S(\omega) = I_0^2 \frac{(\beta - \alpha)^2}{\omega^4 + (\alpha^2 + \beta^2) \omega^2 + (\alpha\beta)^2} \quad (2)$$

A photograph of the test set up is shown in figure 1.

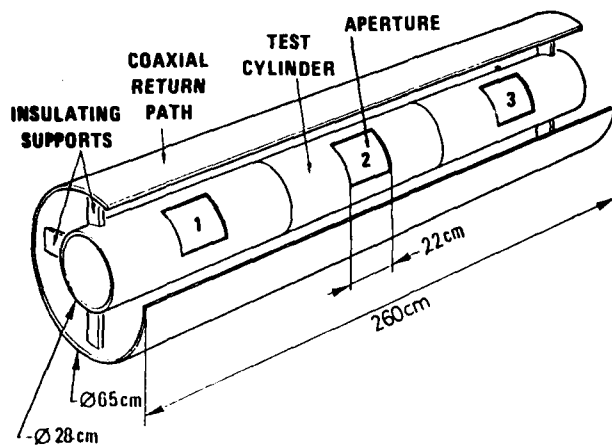


Fig. 1a - Sketch of the simulated fuselage and its coaxial return path (dimensions in cm).

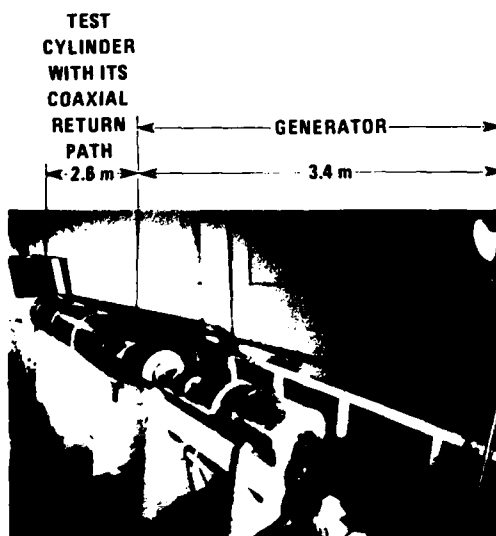


Fig. 1b - Photograph of test set up.

INSTRUMENTATION SYSTEM DESCRIPTION

Electromagnetic fields and induced signals are picked up by wideband sensors (500 Hz to 150 MHz bandwidth) and transmitted to a shielded data acquisition room by fiber optic data links (bandwidth : 1.5 kHz to 180 MHz, signal to noise ratio : 40 dB). E and H field sensors outputs are directly proportional to the field and do not need to be integrated. Analog electrical signals issued from optical data links are fed into 7912 AD TEKTRONIX transient recorders and numerical data are stored on magnetic tape using a 4052 TEKTRONIX minicomputer. Figure 4 shows a drawing of the general set up of test

*Numbers in parentheses designate References at end of the paper

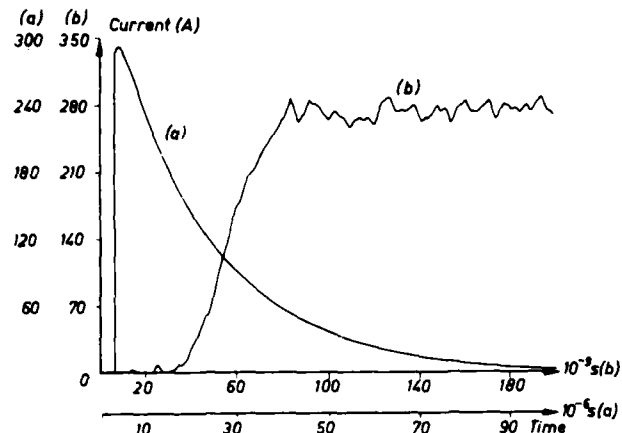


Fig. 2a - Driving current waveform.

b - Rise time evolution.

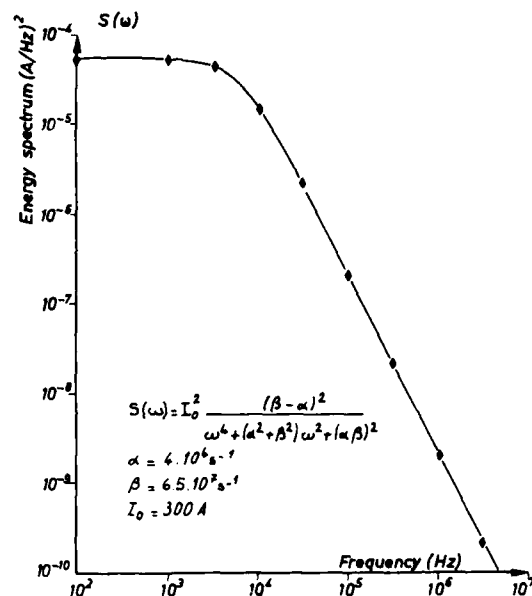


Fig. 3 - Driving current energy spectrum.

instrumentation. A more detailed description of the overall instrumentation is given in reference (1)*.

EXTERNAL ELECTROMAGNETIC FIELDS MEASUREMENTS

External electric and magnetic fields have been measured on the cylinder wall when all the openings are in short-circuit. These fields, called H_{cc} and E_{cc} , have the same temporal evolution as that of the injected current and are drawn in figure 5. Peak values of the normal electric field component is 135 kV/m and that of the magnetic field component, around the cylinder is 340 A/m. In this case the current magnitude was 290 A.

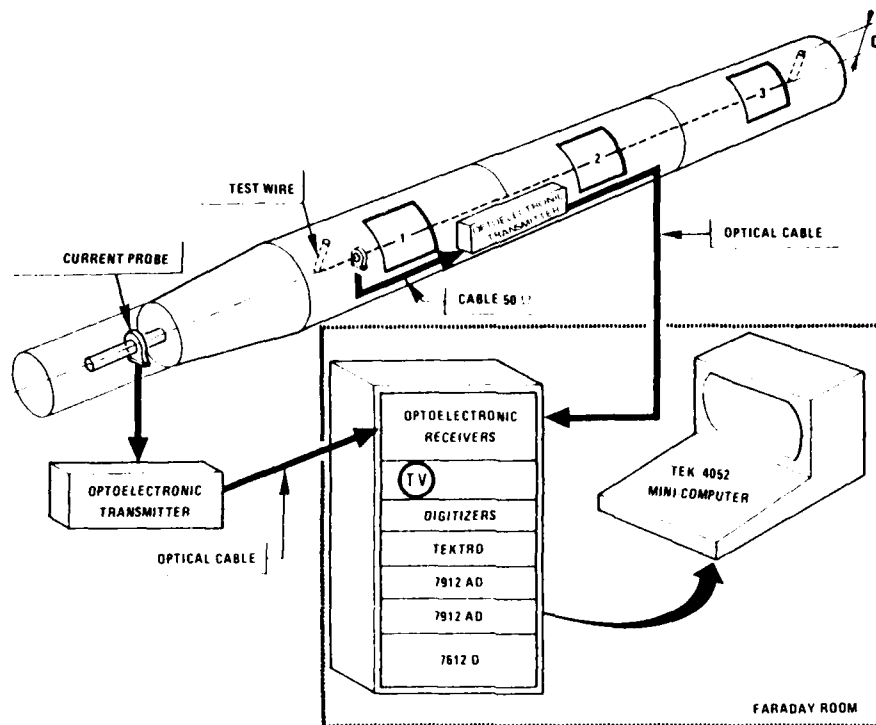


Fig. 4 - Instrumentation system.

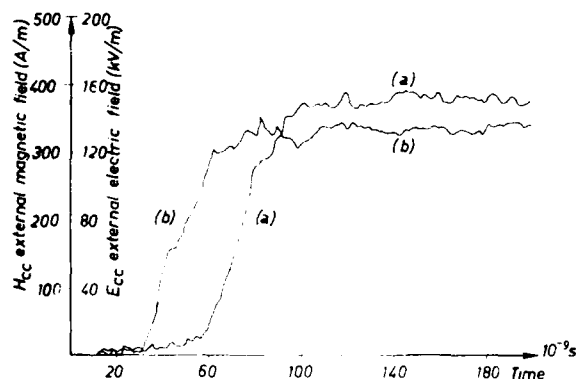


Fig. 5 - External magnetic and electric fields.

TRANSIENTS INDUCED BY DIFFUSION PROCESS

Evaluation of transient signals, induced on a transmission line located inside a structure and having all its openings in short-circuit, is obtained using transfer impedance concept(2). This function $Z_T(p)$ relates the external surface current density to the internal electric field. In the case of a cylindrical shell $Z_T(p)$ may be expressed by the relation (3) :

$$Z_T(p) = R_o \frac{\sqrt{\tau_s p}}{\text{sh} \sqrt{\tau_s p}} \quad (3)$$

where $\tau_s = \mu_0 \sigma e^2$ is the diffusion time constant, σ, e cylinder conductivity and thickness respectively, R_o cylinder D-C resistance (per unit length). When the driving current rise time is very fast, as in our case, the double exponential waveform (relation (1)) may be approximated by :

$$I(t) = I_o e^{-t/\tau} \quad (4)$$

with $I_o = 300$ A and $\tau = 1/\alpha = 25$ μ s.

For an electrically isolated straight wire extending down the length l of the cylinder and having each end connected to the internal wall, the wire short-circuit current may be expressed by the relation :

$$I_{cc}(t) = \frac{R_o l I_o}{L} \frac{\tau}{\tau - \tau_c} \left\{ \left[e^{-t/\tau} - e^{-t/\tau_c} \right] \right. \\ \left. * \sum_{n=0}^{\infty} \sqrt{\frac{\tau_s}{t}} \left[\frac{(2n+1)^2 \tau_s}{2t} - 1 \right] \right. \\ \left. \exp \left(- \frac{(2n+1)^2 \tau_s}{4t} \right) \right\} \quad (5)$$

where R, L and $\tau = L/R$ represent the circuit resistance, self inductance and time constant, respectively. * represents a convolution product.

The open circuit voltage induced on the line is given by :

$$v(t) = R_o I_o \left[e^{-t/\tau_s} \sum_{n=0}^{\infty} \sqrt{\frac{\tau_s}{\pi t^3}} \left(\frac{(2n+1)^2 \tau_s}{2t} - 1 \right) \exp \left(-\frac{(2n+1)^2 \tau_s}{4t} \right) \right] \quad (6)$$

and its temporal evolution is shown in figure 6. The curve exhibit a maximum at time $t = 7.3 \mu s$. Experimental results obtained with three wires short-circuited at each end and running along cylinder axis are shown in figure 7. Wire diameters are 0.44 mm (curve a), 1 mm (curve b) and 2 mm (curve c). Current peak values of 511, 688 and 1153 mA are obtained respectively at times $t_{MAX} = 16, 23$ and $41 \mu s$.

These experimental values are consistent with the diffusion and circuit time constants combination indicated by relation (5).

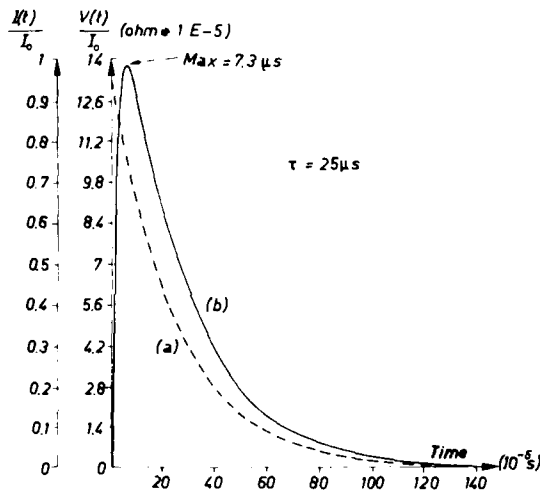


Fig. 6 - Current diffusion mechanism.
a - external current waveform.
b - voltage induced on the internal wire for $I_o = 1$ A.

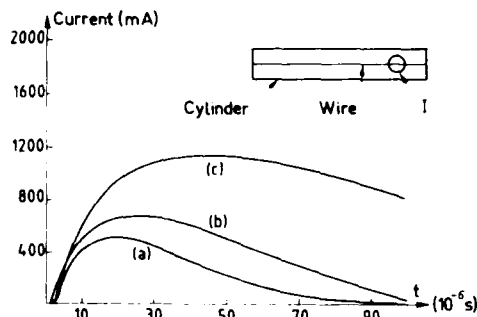


Fig. 7 - Short-circuit current flowing on the internal wire of diameter :
a) 0.44 mm,
b) 1 mm,
c) 2 mm.

For metallic shells, diffusion is usually not the most significant penetration, except that at late times, skin current redistribution effects can produce internal magnetic fields which may be of consequence. For example, if we consider a typical lightning flash having a 30 kA current peak value and connecting an aircraft to ground, a linear extrapolation of curves given in figure 7 will give a short circuit current on the wires ranging between 50 and 120 A. Furthermore, it should be pointed out that, for composite shells, diffusion can provide a larger energy penetration and having a wider spectrum.

MAGNETIC FIELD PENETRATION THROUGH A CYLINDER APERTURE

EXPERIMENTAL RESULTS - The aperture under study is located at 440 mm from one end of the cylinder and has for dimensions 200 x 200 mm. Let H_{cc} be the external magnetic field component measured near the short-circuited aperture and H_y be the internal component measured on the cylinder axis (Fig. 8). Figure 9 represents temporal variation of the H_{cc} field (curve 1) and that of the H_y component (curve 2) measured at cylinder and aperture axis intersection ; as expected the two signals exhibit the same rise time. (It should be noted that a temporal shift has been introduced between the two curves to clarify the figure).

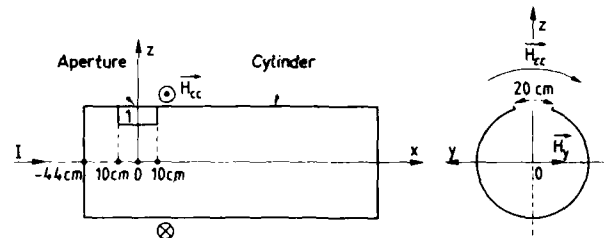


Fig. 8 - Aperture location on the cylinder.

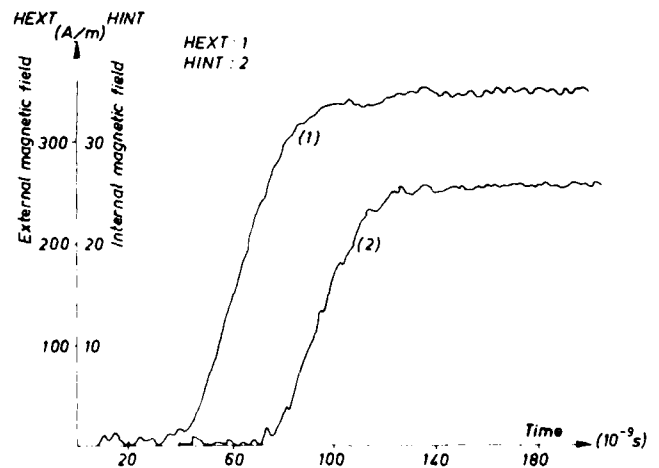


Fig. 9 - External and internal magnetic fields.

If we take H_{cc} as reference, magnetic field attenuation is of the order of 23 dB. H attenuation has also been measured in function of the distance x taken along cylinder axis and is shown in figure 10 (curve a). Taking the field obtained at cylinder and aperture axis intersection as reference, we can see that attenuation is greater than 42 dB for a distance corresponding to two times the aperture dimension.

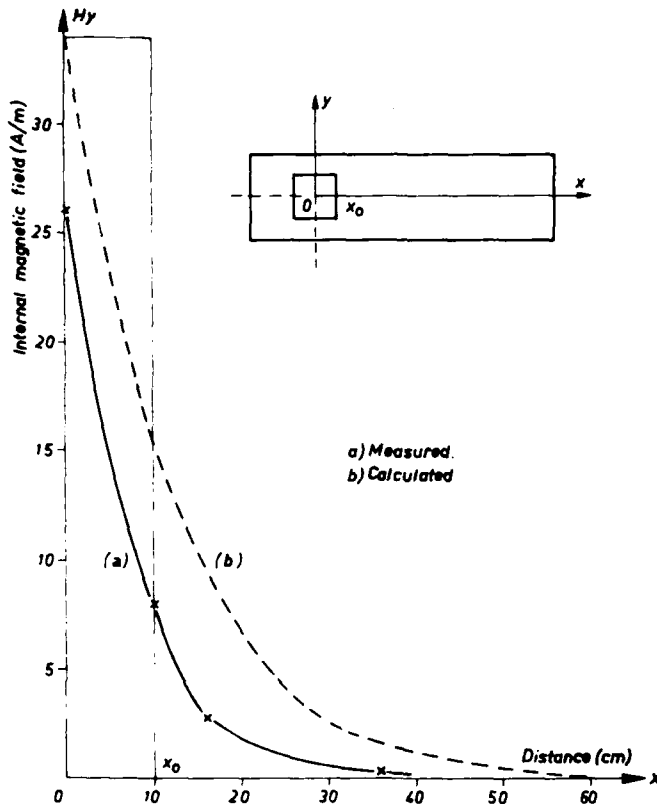


Fig. 10- Internal magnetic field attenuation in function of the distance taken on the cylinder axis.

The experimental results have been compared to those obtained by a numerical analysis.

NUMERICAL APPROACH FOR APERTURE COUPLING - Maxwell's equations derivatives can be expressed as differences of field values at neighboring spatial and temporal positions (4). The resulting equations can be used to obtain the fields at same time if the fields everywhere are known at an earlier time. Based on this method, a three dimensional finite difference computer code, called DIFFRAC(5), has been developed to calculate external surface current and charge densities on an arbitrarily shaped conductor. In this code, infinite extend of space around the object under study has been simulated by using an absorbing layer at the problem space boundary.

In order to obtain a numerical approach for experimental results described in the precedent section, magnetic field distribution inside the cylinder has been performed using DIFFRAC code. To do this, the following simplifications have been imposed (figure 11) :

- the driving field is a plane wave incident on the cylinder polarized parallel to the axis and having a Poynting vector parallel to the aperture axis,
- incident magnetic field component has the same time evolution and magnitude as that obtained in the injected current experiment described in precedent section. As a consequence aperture dimensions are small compared to the wavelength of the incident pulse,
- mutual coupling between aperture and wire has been neglected,
- the space dimensional gridding has been made using a 26 x 28 x 28 mesh. Elementary mesh size is 20 cm along cylinder axis and 4 cm in the two others directions,
- cylinder wall is perfectly conducting and has no thickness.

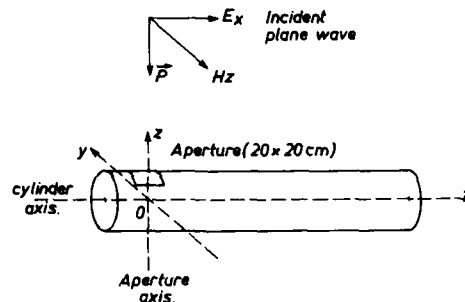


Fig. 11- Plane wave configuration.

In figure 12 we have drawn two curves corresponding to the external and internal magnetic fields variations. The first one has been calculated on the aperture axis, 2 cm above the open window and the internal component H_y has been calculated at test point O. As y in the previous section we notice a strong correlation between the time evolution of both signals. Taking the field calculated at test point A as reference, the attenuation at test point O is of the order of 20 dB. Curve b in figure 13 represents H_y component attenuation in function of distance x . This curve has the same shape as that obtained experimentally (Fig. 10) and its spatial variation law may be expressed by the relation :

$$H_y(x) = 34 e^{-k_1 x} \quad (7)$$

where $k_1 = 8.10^{-2} \text{ cm}^{-1}$ (x in cm).

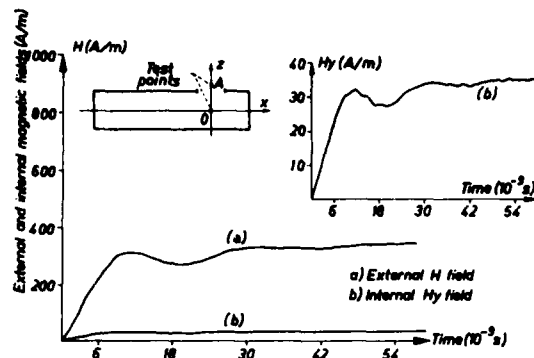


Fig. 12 - External and internal magnetic fields calculated at test points A and O respectively.

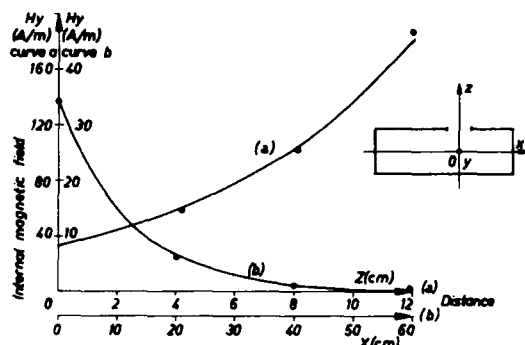


Fig. 13 - Internal magnetic field variation in function of :
- distance z (curve a),
- distance x (curve b).

In the same manner, the H_y attenuation has been calculated in function of the distance z taken along the aperture axis. This curve is called (a) in figure 13 and may be approximated by the relation :

$$H_y(z) = 34 e^{+k_2 z} \quad (8)$$

where $k_2 = 0.14 \text{ cm}^{-1}$ (z en cm).

External and internal fields temporal evolutions being identical, as shown in figure 9, H_y component may be expressed everywhere in the cylinder, by the relation :

$$H_y(x, y, z, t) = H(x, y, z)(e^{-\alpha t} - e^{-\beta t}) \quad (9)$$

This function has been integrated on the surface of a loop of length $l = 164 \text{ cm}$ and making an angle of 45° with z direction (see figure 14).

At first time ($t < 20 \mu\text{s}$) wire impedance being essentially inductive ($\omega L \gg R$), the calculated resulting short circuit current induced on the wire follows the same temporal law as that of the magnetic field and is shown in figure 14 (curve b). These calculations are in good agreement with experimental results obtained on the loop and given in figure 14 (curve a). Discrepancy is of the order of 20 %

and it will be possible to reduce this dispersion by taking a finer grid along x axis and taking into account mutual coupling between aperture and wire.

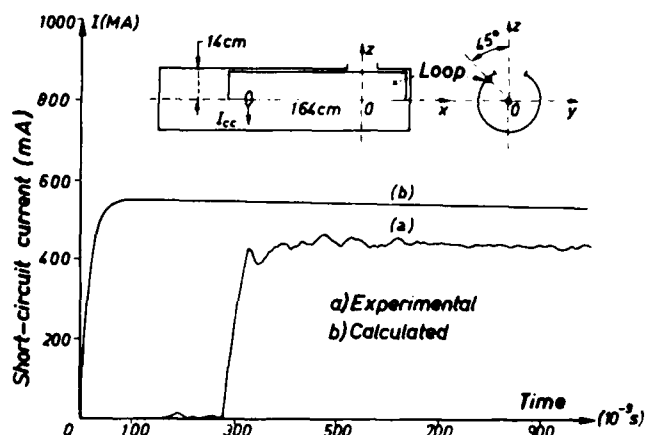


Fig. 14 - Short-circuit current induced on a loop by magnetic aperture coupling.

CONCLUSION

Lightning current flowing through a structure generate induced voltages in the internal wiring by two main mechanisms :
- current diffusion through the wall. For homogeneous conductors this mechanism generate low frequency transients which are unable to excite cable resonances. However magnitude of these transients may often be important in particular in carbon fiber structures where the diffusion time constant is very small ;

- direct flux coupling through apertures (windows, cockpit, dielectric access panels, ...). In this case induced voltages contain a very broad spectrum of energy. When they are injected into an unmatched transmission line or a resonant circuit they will often produce voltage waveforms which are very different from the exciting pulse. To determine how energy couples into electrical wirings located behind an aperture in a perfectly conducting three dimensional structure, numerical techniques can provide a realistic approach.

REFERENCES

1. J.C. Alliot and D. Gall, "Programme français d'essais en vol sur les effets électromagnétiques de la foudre". 39th Technical Meeting of the Avionics Panel of AGARD, Lisbonne (Portugal), June 16-19, 1980.
2. S.A. Schelkunoff, "The electromagnetic theory of coaxial transmission lines and cylindrical shields". Bell System Technical Journal, 13, 1934.

3. E.F. Vance, "Coupling to shielded cables". John Wiley and Sons, New-York, 1977.

4. K.S. Yee, "Numerical solution of initial boundary value problems involving Maxwell's equation". IEEE Trans. Ant. and Propag., AP 14, May 1966, p. 302-307.

5. J.P. Berenger, "Calcul de la diffraction d'une onde électromagnétique à l'aide d'une méthode aux différences finies", 2ème Colloque National sur la Compatibilité Electromagnétique, Trégastel (France), 1-3 juin 1983.

LIGHTNING RESEARCH -- A USER'S LAMENT

Cyril N. Golub
Eastern Space & Missile Center
Patrick AFB, FL 32925

ABSTRACT

Following his introduction as a Range Systems Engineer at the Eastern Test Range, Cape Canaveral, Florida, the author states that the "key to lightning technology" he is looking for is the one needed to solve problems faced by him as a result of lightning activity; these problems are presented in a composite picture of case histories found at the Cape Canaveral Air Force Station (industrial area and nine (9) active launch pads), the NASA Kennedy Space Center (industrial area and one active launch pad), and down-range sites. The various protective measures taken are enumerated and the failures of some of them are described. The situations created are often critical and usually costly. A list of problem areas needing solutions is then offered to the lightning research community as a challenge. Environmental conditions are described, including local lightning characteristics as documented in a triggered lightning experiment conducted nearby (Valkaria, FL) in the summer of 1983 (unless presented in a separate paper at the same session).

Also described are the extensive meteorological instrumentation systems in existence in the Cape Canaveral area under the author's jurisdiction, such as 34 field mill sites, a lightning location system, an extensive network of weather data gathering stations, a weather radar, an upper atmosphere sounding system, and a McIDAS-lineage data processing and display system. The area has one of the highest lightning activity in the United States. These resources are used operationally and could be made available to research agencies on a non-interference basis with launch activities. Slated for the June - September 1984 time frame is a lightning research project using an FAA CV-880 aircraft as an instrumented platform; this project is conducted jointly by the FAA, the Wright Aeronautical Lab, the Naval Research Lab, and NASA. The Eastern Space and Missile Center, Patrick AFB, FL, will provide weather/lightning data and aircraft ground support. A triggered lightning project is tentatively planned for the 1985 summer, involving the US Air Force and the French ONERA (National Office of Aerospace Engineering and Research).

The uniqueness of some of the problems and the unforgiving nature of space launch operations present a special challenge to potential contributors of solutions. The extensive resources available locally make this area a haven for lightning researchers.

This paper was not available for incorporation into this book.

**GROUNDING AND BONDING REQUIREMENTS OF MILITARY C-E FACILITIES
FOR PROTECTION AGAINST LIGHTNING**

**WARREN L. KELLER
AIR FORCE COMMUNICATIONS COMMAND, SCOTT AFB IL
(1842 ELECT ENGR GP)**

ABSTRACT

Recent inspections at military ground communications-electronics (CE) facilities have revealed a lack of consistency of the grounding aspects for both the building and the equipments. This had led to the development of a military standard (MIL-STD-188-124) titled "Grounding, Bonding and Shielding for Common Long Haul/Tactical Communications Systems" and a companion military handbook, MIL-HDBK-419, titled "Grounding, Bonding and Shielding for Electronic Equipments and Facilities". This paper outlines the technical standards and design objectives of the Standard and Handbook to ensure the optimum performance of military CE facilities and equipments. The measurement requirements and procedures for the ground system are also provided.

INTRODUCTION

MIL-STD-188-124 and MIL-HDBK-419 establish the minimum basic requirements and goals for the grounding, bonding and shielding of military ground-based telecommunications C-E equipment installations, subsystems, and facilities. The standard and handbook are mandatory in the DOD and are used in the design and engineering of new military communications systems and equipment installations including radio, satellite ground terminals, telephone central offices, microwave and data communications systems as well as C-E transportables. They are also recommended for use on existing C-E equipments and facilities, but shall not be used as the sole basis for retrofit.

The objectives of the standard and handbook are to provide for the protection of personnel, equipment, buildings and structures against the hazards posed by electrical power faults, lightning strikes and to reduce noise and electromagnetic interference caused by inadequate grounding, bonding, and shielding of communications installations.

TEXT/DESCRIPTION

THE FACILITY GROUND SYSTEM - The facility ground system consisting of the earth electrode subsystem, lightning protection subsystem, fault protection subsystem, and signal reference subsystem serves three primary functions: personnel safety, equipment and facility protection, and electrical noise reduction. It forms a direct path of known low impedance between earth and the various power and communications equipments. This effectively minimizes voltage differentials on the ground plane which exceed a value that will produce noise or interference to communication circuits. Personnel and equipment protection is afforded when, during an occurrence of an electrical ground fault, the ground system provides a path for rapid operation of protective overcurrent devices; or, during a lightning stroke, provides a low impedance path for current to earth. Personnel and equipment protection against power fault currents, static charge buildup and lightning flashover is provided both by protective ground wires and by bonding all normally non-current carrying metal objects, including structural steel support members, to the facility ground system. The ground system also provides low impedance paths between various buildings and structures of the facility, as well as between equipments within the facility, to earth in order to minimize the effects of noise currents. Since all telecommunications and electronic facilities are inherently related to earth by capacitive coupling, accidental contact, or intentional connection, ground must therefore be looked at from a total system viewpoint with various subsystems comprising the total facility ground system. Each

of the subsystems along with their standards are briefly described in the following paragraphs.

Earth Electrode Subsystem - The earth electrode subsystem consists of a network of earth electrode rods, plates, mats, or grids and their interconnecting conductors. The extensions into the building are used as the principal ground points for connection to equipment ground subsystems serving the facility. Ground potential is established by electrodes in the earth at the site or installation. The earth electrode subsystem includes the following: 1) a system of buried, driven rods interconnected with bare cable that normally forms a ring around the building; or 2) metallic pipe systems i.e., water, gas, fuel, etc., that have no insulation joints; or 3) a ground plane of horizontal buried wires. Metallic pipe systems shall, however, not be used as the sole earth electrode subsystem. Resistance to ground shall be obtained from the appropriate authority if available, or determined by testing.

Lightning Protection Subsystem - The lightning protection subsystem provides a nondestructive path to ground for lightning energy contacting or induced in facility structures. To effectively protect a building, mast, tower, or similar self-supporting objects from lightning damage, an air terminal of adequate mechanical strength and electrical conductivity to withstand the stroke impingement must be provided. An air terminal will intercept the discharge to keep it from penetrating the nonconductive outer coverings of the structure, and prevent it from passing through devices likely to be damaged or destroyed. A low-impedance path from the air terminal to earth must also be provided. These requirements are met by either 1) an integral system of air terminals, roof conductors, and down conductors securely interconnected to provide the shortest practicable path to earth; or 2) a separately mounted shielding system, such as a metal mast or wires (which act as air terminals) and down conductors bonded to the earth electrode subsystem.

Fault Protection Subsystem - The fault protection subsystem ensures that personnel are protected from shock hazard and that equipment is protected from damage or destruction resulting from faults which may develop in the electrical system. It includes deliberately engineered grounding conductors (green wire) which are provided throughout the power distribution system to afford electrical paths of sufficient capacity, so that protective devices (fuses and circuit breakers) can operate promptly. If at all possible the equipment fault protective conductors should be physically separated from signal reference grounds except at the equipotential plane. The equipment fault protection subsystem provides grounding of ventilation system ducts, conduits for signal conductors, and all other structural metallic elements as well as the cabinets or racks of equipment.

Signal Reference Subsystem - The signal reference subsystem establishes a voltage reference and minimizes noise currents in the facility so that relative voltage levels are maintained and unacceptable noise voltages do not occur on signal paths or circuits. Within a piece of equipment, the signal ground may be a bus bar or conductor that serves as a reference for some or all of the signal circuits in the equipment. Between equipments, the signal ground will be a network consisting of a number of interconnected conductors. Whether serving a collection of circuits within an equipment or serving several equipments within a facility, the signal reference network will either be a single-point or equipotential plane/multipoint depending on the equipment design, the facility and the frequencies involved. The standard for each subsystem is listed below.

EARTH ELECTRODE SUBSYSTEM (STANDARD)

General - An earth electrode subsystem shall be installed at each C-E facility to provide a low resistance path to earth for lightning and power fault currents and ensure that hazardous voltages do not occur within the facility. This subsystem shall be capable of dissipating to earth the energy of direct lightning strokes with no ensuing degradation to itself. This system shall also interconnect all driven electrodes and underground metal objects of the C-E facility. The earth electrode subsystem shall not degrade the quality of signals in the signal circuits connected to it.

Earth Resistivity Survey - The design agency shall conduct an earth resistivity survey at the site before construction is begun. The values of earth resistivities characterizing the site shall be measured and recorded. Natural features, such as rock formations and underground streams, as well as manmade features having a significant effect upon earth resistivity, shall be indicated.

Minimum Configuration - The basic earth electrode subsystem configuration shall consist of driven ground rods uniformly spaced around the facility and placed 0.6m (2 feet) to 1.8m (6 feet) outside the drip line of structures. The rods shall be interconnected with a 1/0 AWG (American Wire Gage) bare copper cable buried at least .45m (1.5 feet) below grade level. Larger size cables as well as greater burial depths shall be specified where earth and atmosphere considerations so dictate. The interconnecting cable shall be brazed or welded to each ground rod and shall close on itself to form a complete loop with the ends brazed or welded together. (See Figures 1 thru 4). Where ground wells are employed, acceptable compression type connectors may be utilized to bond the cable to the ground rod. Coverage of the earth electrode subsystem by asphalt, concrete, etc. shall be kept to a minimum in an effort to maintain the effectiveness of the subsystem.

Resistance to Earth - (DO) The resistance to earth of the earth electrode subsystem should not exceed 10 ohms.

Additional Considerations - Where 10 ohms are not obtained with the basic electrode configuration due to high soil resistivity, rock formations, or other terrain features, alternate methods for reducing the resistance to earth shall be considered.

Ground Rods - Ground rods shall be copper-clad steel, a minimum of 3m (10 feet) in length, spaced apart not more than twice the rod length, and shall not be less than 1.9cm (3/4 inch) in thickness. The thickness of the copper jacket shall not be less than 0.3 mm (0.012 inch).

Connecting Risers - Provisions shall be made for bonding the lightning down conductors, the connecting cables required by the signal reference and fault protection subsystems, as well as the equipotential plane, to the risers of the earth electrode subsystem.

Other Underground Metals - Underground metallic pipes entering the facility shall be bonded to an entrance plate and in turn to the earth electrode subsystem with a minimum length of bare 1/0 AWG copper cable whenever such connections are acceptable to both the serving suppliers and the authority having jurisdiction. (See Figures 5 and 6). The bond cable shall be welded or brazed to the earth electrode subsystem. Adequate corrosion preventive measures shall be taken. Structural pilings, tanks, and other large underground metallic masses near the periphery of the structure shall be bonded in a like manner to the earth electrode subsystem. (See Figures 7 and 8). Caution shall be used when using clamps to ground metallic gas pipes.

Resistance Checks - The resistance to earth of the electrode subsystem shall be measured only by the fall of potential technique. This shall be accomplished prior to the completion of construction of associated buildings and structures. To assure adequate performance under all climatic conditions, resistance measurements of the earth electrode subsystem to earth will be made at three month intervals for 12 months following installation. The test configuration should be recorded and repeated for each subsequent measurement. The times of such tests shall be chosen so as to demonstrate the adequacy of the earth electrode subsystem over complete ranges of local temperature and precipitation. Ground resistance measurements shall be accomplished every nine months after the initial 12 month period.

LIGHTNING PROTECTION SUBSYSTEM.

General - Lightning protection shall be provided as required for buildings and structures in accordance with the National Fire Protection Association (NFPA) No. 78, and the following:

Buildings and Structures - Lightning protection shall be provided as required for buildings and structures in accordance with the

additions and modifications specified herein and the applicable paragraphs of NFPA No. 78. This protection shall be extended to all electrical, electronic, or other elements which are a part of, or are in support of all C-E facilities. Such elements shall include, but shall not be limited to, substations (to the extent that additional protection beyond that provided by the electric utility is necessary), power poles, towers, antennas, masts, etc.

Down Conductors - Where copper-clad steel down conductors are used on structures not greater than 23m (75 feet) in height, the dc resistance of solid wires or stranded cables shall not be greater than 0.176 ohms per 305m (1000 feet). On structures greater than 23m (75 feet) in height, the dc resistance of the wire or cable shall not be greater than 0.088 ohms per 305m (1000 feet). The size of individual wires in copper-clad stranded cables shall not be less than No. 14 AWG. (In cases where mechanical and installation situations warrant, a larger (preferably No. 6 AWG copper) wire may be utilized.) The copper covering of all copper-clad steel down conductors shall be permanently and effectively welded to the steel core. The conductivity of copper-clad conductors shall not be less than 30% of a solid copper conductor of equivalent cross-sectional area. Down conductor bends shall not have a radius less than 20cm (8 in) or bends greater than 90 degrees. Any metal object within 1.8m (6 feet) of the lightning downlead shall be bonded to the down conductor (see NEC Article 250). On structures higher than 18m (60 feet) there shall be at least one additional down conductor for each additional 18m (60 feet) of height or fractions thereof, except that the interval between down conductors around the perimeters shall not be less than 15m (50 feet) nor greater than 30m (100 feet). Down conductors shall be bonded to the earth electrode subsystem.

Bonding - All bonds between elements of the lightning protection subsystems shall be made by welding or brazing or UL approved high compression clamping devices and shall have a maximum dc resistance of 1 milliohm. Welding or brazing shall be used for all bonds not readily accessible for inspection and maintenance. Soft solder shall not be used for bonding any conductor in the lightning protection subsystem.

Structural Steel - Substantial metal structural elements of buildings and towers (including overall building shield where it exists) shall be acceptable substitutes for lightning down conductors provided they are permanently bonded to each other and to the earth electrode subsystem. Bonding straps shall be employed across all structural joints.

Air Terminals (Lightning Rods) - Nonmetallic objects, extensions, or protrusions requiring protection shall have the air terminals designed and installed in accordance with requirements of NFPA No. 78, chapters 3-9 and 3-10.

Guards - Where conductive guards must be used, the guards shall be electrically bonded at each end of the enclosed lightning conductor. Each isolated section of conductive guards shall also be bonded to the lightning conductor.

Supporting Structures - Lightning protection shall be provided for radar, communications or navigational aid antenna towers, and all other similar supporting structures in accordance with the following:

Earth Electrode Subsystem. An earth electrode subsystem shall also be provided for all supporting structures. If a tower is adjacent to another structure such that the minimum distance between the tower and the structure is 6m (20 feet) or less, one earth electrode subsystem encompassing both the tower and the other structure shall be provided. For distances greater than 6m (20 feet), separate earth electrode subsystems shall be installed. Two bare 1/0 AWG copper cables shall be used by independent routes to bond the earth electrode subsystem of the tower to the earth electrode subsystem of buildings and structures that have signal, control, or power line interfaces with the tower. (See Figures 7 and 8).

Air Terminals. An air terminal shall be installed on the tower. A minimum of two conductive paths shall exist between any two air terminals and between any air terminal and the earth electrode subsystem (except for dead ends less than 5m (16 feet)).

Down Conductors. Each down conductor shall be bonded to the earth electrode subsystem of the tower. For metal towers, where the structural elements are not used as down conductors, the down conductors shall be bonded to the tower legs at the base. Down conductors connecting cables to the earth electrode subsystem shall be protected against mechanical damage. Connecting cables passing through foundations or footings shall be installed in plastic or non-metallic conduit.

WAVEGUIDE GROUNDING - As a minimum, all waveguides shall be grounded as follows:

All waveguides to the antennas shall be grounded at three points: near the antenna, at the vertical-to-horizontal transition near the base of the tower, and at the waveguide entry port.

Metallic supporting structures for waveguides shall be electrically continuous and shall be connected to the exterior earth electrode subsystem at the first and last support columns as a minimum. The wire leads shall be as direct as possible.

Waveguides shall be grounded with solid copper strap or copper wire at least equal to No. 6 AWG. Braid or fine-stranded wire shall not be used. All bends of ground conductors shall have a radius of 20cm (8 in) or greater and no bends shall be more than 90 degrees.

Waveguides shall be properly bonded to the waveguide entrance panel and the panel shall be connected by the most direct route to the earth electrode subsystem using a 1/0 stranded copper cable. For additional information see Figures 9 thru 16.

Exterior Nonstructural Metal Elements - All exterior hand rails, ladders, stairways, antenna pedestals, and antenna elements operating at ground potential shall be bonded to the lightning protection subsystem with a No. 6 AWG copper wire or larger.

Exterior Wires and Cables.

Conduit. Corrosion-protected steel conduit shall be used to completely enclose susceptible wiring (notably outdoor or underground signal wiring not otherwise protected) to shield against lightning or lightning induced currents and voltages. Such conduit shall be electrically bonded from section to section with corrosion-protected compression fittings or shall be welded or brazed at each joint. Pull boxes, junction boxes, etc. that are integral to the conduit and electrically bonded to the conduit shall be regarded as conduit. Metal manholes, where used, shall be bonded to the conduit. Nonmetallic manholes shall be bridged to provide a continuous electrical path from one section of conduit to other sections of conduit entering or leaving a manhole. The conduit shall be bonded at each end to the earth electrode subsystem of each terminating facility.

Overhead Guard Wires. Overhead guard wires shall be regarded as air terminals. Such wires shall be spaced not less than 1m (3 feet) above any signal or control circuits being protected. The minimum conductor size shall be 1/0 AWG galvanized steel. Overhead guard wires shall be grounded to the earth electrode subsystem of each terminating facility. When the distance between terminating facilities exceeds 76m (250 feet), the guard wires shall also be bonded to a ground rod at intervals not exceeding 76m (250 feet). The top of the ground rod shall not be less than 0.3m (1 foot) below grade level.

Underground Guard Wires. Buried signal, power, or control wires or cables not otherwise protected by ferrous conduit shall be protected by a bare 1/0 AWG copper guard wire embedded in the soil above and parallel to the wires, cables, or ducts. The guard wire shall be laid a minimum of 45cm (18 in) below grade level and at least 25cm (10 in) above the duct or uppermost wire or cable. Where the width of the duct or the spread of the cable run does not exceed 1m (3 feet), one guard wire centered over the duct or cable run shall be installed. Where the spread exceeds 1m (3 feet), two guard wires shall be used. They shall be spaced at least 30cm (12 in) apart and not less than 30cm (12 in) nor more than 46cm (18 in) inside the outermost wires or the edges of the duct bank. All guard wires shall be bonded at each end to the earth electrode subsystem of each terminating facility. The requirement and need

for underground guard wires shall be determined by the project engineer and the civil engineer and shall be determined on a case and location basis dependent upon the priority of the circuit and the degree of lightning anticipated.

Lightning Arrestors. Exposed and underground power lines, not otherwise protected, shall be provided with UL approved lightning arrestors at the point of entrance into the facility. The arrestors shall be installed in accordance with Article 280 of the National Electrical Code.

Security/Perimeter Fences. All security or perimeter fences shall be grounded to their own ground rods or to the earth electrode subsystem of the facility.

FAULT PROTECTION SUBSYSTEM.

General - The fault protection subsystem consists of a separate grounding conductor (green wire) to provide personnel and equipment protection against power fault currents and static charge buildup. Protection from lightning flashover shall be provided by grounding all major noncurrent-carrying metal objects, including main structural steel support members. A ground bus shall be provided in all switchboards and panelboards and a separate connecting grounding (green) wire shall be carried within the same raceway or cable with the ac power conductors. The installation shall conform with the requirements of Article 250 of the National Electrical Code.

Building Structural Steel - All main metallic structural members (except rebar) such as the building columns, wall frames, and roof trusses of steel frame buildings and other metal structures should be made electrically continuous and grounded to the facility ground system. Whenever vertical rebar is utilized to extend the facility ground system, it shall be made electrically continuous and grounded.

Pipes and Tubes - As required, all metallic piping and tubing and the supports thereof should be electrically continuous and shall be grounded to the facility ground system. See Figure 5.

Electrical Supporting Structures - Electrical supporting structures shall be electrically continuous and grounded to the facility ground system through the fault protection subsystem.

Conduit - All conduit, whether used for power distribution wiring or for signal and control wiring, shall be grounded in accordance with the following:

All joints between sections of conduit, fittings, and buses shall be treated with a conductive lubricant and firmly tightened. Gouging lock nuts shall positively penetrate all paint or other finishes.

Cover plates of conduit fittings, pull boxes, junction boxes, and outlet boxes shall be grounded by securely tightening all available screws.

Conduit brackets and hangers shall be electrically continuous to the conduit and to the metal structures to which they are attached.

Cable Trays or Raceways - The individual sections of all cable tray systems shall be bonded to each other and to the raceways which they support. All cable tray assemblies shall be connected to ground within 0.6m (2 feet) of each end of the run and at intervals not exceeding 15m (50 feet) along each run.

Wiring System Enclosures - All electrical and electronic wiring and distribution equipment enclosures, not otherwise specifically covered herein, shall be grounded. The grounding conductor shall not penetrate equipment cabinets or cases but rather shall be terminated on a ground stud peripherally welded to the metal barrier.

Metallic Power Cable Sheaths - Metallic cable sheaths on electrical power cables shall be connected to ground at both ends.

Electrical Power Systems - All electrical power distribution systems shall be grounded in accordance with the following:

AC Distribution Systems. AC power distribution systems shall have the neutral conductor grounded at the distribution transformer and to the earth electrode subsystem of the facility. The size of the ground conductor from the first service disconnect means to the earth electrode subsystem shall be as specified in Table 250-94 of the National Electrical Code. In each facility served by a common distribution transformer, the neutral shall be directly connected to the nearest point of the earth electrode subsystem. Where delta-wye system conversion is employed, the service entrance shall be a five-wire system consisting of three phase conductors, a grounded (neutral) conductor, and a grounding (green) conductor. In each facility, all power distribution neutrals shall be isolated from the C-E equipment case and the structure elements so that no ac return current flows through the equipment and fault protection subsystem or the signal reference network. The fault protection subsystem grounding (green) conductor shall be installed in accordance with the National Electrical Code for all C-E equipment. Conduit shall not be used in lieu of the separate grounding (green) wire.

Single Building with Multipower Sources. All grounded (neutral) conductors shall be grounded at the first service disconnect means of each source. For delta-wye conversions, a five-wire system shall be utilized from each source. Delta systems shall employ four-wires from the source, consisting of three phase conductors and a grounding conductor.

Multibuildings with Single Power Source. Neutral conductors from multibuildings being serviced from a single commercial power source shall be grounded at the source only. The neutral shall be isolated at the first disconnect means. A five-wire system shall be utilized from the source.

Standby AC Generators. Motor and generator frames and housings shall be grounded

in accordance with Article 250 of the National Electrical Code. The generator neutral shall be grounded directly to the earth electrode subsystem. When generators are connected in parallel, the neutrals shall be interconnected and grounded with a single ground conductor.

AC Outlets. The ground terminal of ac outlets shall be connected to the facility ground system with a copper conductor meeting the requirements of Article 250 of the National Electrical Code. The ground terminals in all receptacles on wire mold or plugmold strips shall be hard wired to the equipment ground network. Strips depending upon serrated fingers for grounding shall not be used.

Electrical Motors and Generators. The frames of motors, generators, and other types of electrical rotating machinery shall be grounded to the fault protection subsystem, according to Article 430 of the National Electrical Code.

DC Power Sources. One leg of each dc power system shall be grounded with a single connection directly to the earth electrode subsystem. The size of the grounding conductor shall be as specified by Article 250 of the National Electrical Code. Whether grounded at the source or at a load, a separate current return from load to the source shall be used to assure that no dc current flows in the fault protection or the signal reference subsystem.

Metallic Battery Racks. Metallic battery racks shall also be grounded to the facility ground system at the nearest point.

Ground Fault Circuit Interrupters. Consideration should be given that 120 volt single phase 15 and 20 ampere receptacle outlets have ground fault circuit interrupters (GFCI) for personnel protection. (See NEC Articles 210 and 215).

SIGNAL REFERENCE SUBSYSTEM.

General - A signal reference subsystem shall be installed at each facility. Signal circuits are grounded to control static charges and noise, and establish a common reference for signals between sources and loads. The desired goal is to accomplish these grounding functions in a manner that minimizes interference between equipments. Where units are distributed throughout the facility, the signal reference ground subsystem shall consist of an equipotential ground plane.

Higher Frequency Network - The higher frequency (equipotential) network provides an equal potential plane with the minimum impedance between the associated electronic components, racks, frames, etc. To the extent permitted by circuit design requirements, all reference points and planes shall be directly grounded to the chassis and the equipment case. Direct grounding shall be preferred; however, where individual circuit subassemblies must be floated at a dc potential, capacitive grounding shall be acceptable. Where mounted in a rack, cabinet or enclosure, the equipment case shall be

bonded to the rack, cabinet, or enclosure. To minimize the voltage differential between points in the higher frequency signal reference network, the dc resistance between any two points within a chassis or equipment cabinet serving as a reference for higher frequency signals shall be less than 1 milliohm (0.001 ohm). The equipotential plane shall be installed under the equipment, but for retrofit, may be installed overhead. (See Figures 7 and 8). Signal, control, and power cables should be routed in close proximity to the equipotential ground plane with the signal and control cables separated from power cables as far as practicable. The equipotential plane shall be connected to the building structure shell and earth electrode subsystem at many points.

Lower Frequency Network - A lower frequency network will be installed at facilities employing lower frequency equipments from dc to 30 kHz and in some cases to 300 kHz. The purpose of this network is to isolate lower frequency signals from all other ground networks including structural, safety, lightning and power grounds. This network prevents stray currents (primarily 60 Hz) from developing voltage potentials between points on the ground network. This lower frequency network must be connected to the earth electrode subsystem at one point only (single point) and must be configured to minimize conductor path length. A single point ground however is not viable for lower frequency equipments operating in a higher frequency environment (EMP, lightning, digital systems).

Equipment Signal Ground Terminations - Each individual unit or piece of equipment shall either be bonded to its rack or cabinet or shall have its case or chassis bonded to the nearest point of the equipotential plane. Racks and cabinets shall also be grounded to the equipotential plane with a copper strap. All equipment cases and all racks and cabinets shall have a grounding terminal provided that permits convenient and secure attachment of the ground strap.

Shield Terminations of Coaxial and Other Higher Frequency Cables - All connectors shall be of a type and design that provide a low impedance path from the signal line shield to the equipment case. If the signal circuit must be isolated from the equipment case, and if the shielding effectiveness of the case must not be degraded, a connector of a triaxial design that properly grounds the outer cable shield to the case shall be used. Shields of coaxial cables and shielded balanced transmission lines shall be terminated by peripherally grounding the shield to the equipment case. Coaxial shields and connector shells shall be grounded at junction boxes, patch panels, signal distribution boxes and other interconnection points along the signal path.

NOTE: Signal and control cables should be separated from power cables as far as practicable.

Overall Shields - Shields surrounding a cable containing individually shielded lower frequency signal lines or containing only unshielded lines shall be grounded at each end and at junction boxes, patch panels, distribution points and at other intermediate points along the cable run. Overall shields shall be grounded to cases, cabinets or conducting surfaces.

MEASUREMENT OF RESISTANCE-TO-EARTH OF ELECTRODES OR EARTH ELECTRODE SYSTEMS - The calculated resistance of a given electrode system is based on a variety of assumptions and approximations that may or may not be met in the final installation. Because of unexpected and uncontrolled conditions which may arise during construction or develop afterward, the resistance of the installed electrode must be measured to see if the design criteria are met. In an existing facility, the resistance of the electrode system must be measured to see if modifications or upgrading is necessary. The most commonly used method for measuring the resistance to earth of an earth electrode or system is the fall-of-potential method.

Fall-of-Potential Method - This technique involves the passing of a known current between the electrode under test and a current probe, C_2 , as shown in Figure 17(a). The drop in voltage between the earth electrode and the potential electrode, (P_2), located between the current electrodes is then measured; the ratio of the voltage drop to the known current gives a measure of the resistance. (By using a voltage measuring device - a null instrument or one having a high impedance - the contact resistance of the potential electrode will have no appreciable effect on the accuracy of the measurement.) Several resistance measurements taken by moving the potential probe, P_2 , from the position of the earth electrode, along a straight line to the current probe, C_2 , which is left in position. The data obtained is then plotted as resistance versus distance from the earth electrode as illustrated in Figure 17(b). This is the test method recommended for measurement of single rod or multi-rod earth electrode subsystems.

Probe Spacing - Current flow into the earth surrounding an electrode produces shells of equipotential around the electrode. A family of equipotential shells exists around both the electrode under test and the current reference probe, C_2 . The sphere of influence of these shells is proportional to the size of each respective electrode. The potential probe, P_2 , in Figure 17 provides an indication of the net voltage developed at the earth's surface by the combined effect of these two families of shells. If the electrode under test and the current reference probe are so close that their equipotential shells overlap, the surface voltage variation as measured by P_2 will vary as shown in Figure 18(a).

Since the current flowing between the electrodes is constant for each voltage measurement, the resistance curve will have the same shape as the voltage curve. For close electrode spacings, the continuously varying resistance curve does not permit an accurate determination of resistance to be made.

By locating the current reference probe, C_2 , far enough away from the electrode under test to ensure that the families of equipotential shells do not overlap, a voltage curve like that shown in Figure 18(b) will be obtained to produce the type of resistance curve shown in Figure 17.

When the distance, D , between the electrode under test and the current reference probe is very large compared to the dimensions of the earth electrode subsystem under test, the latter can be approximated as a hemisphere and interaction between the two electrodes is negligible.

Thus the true value of resistance to earth corresponds to the ratio of the measured current to the potential when x is 62 percent of the distance, D , from the electrode under test to the current probe, C_2 . It is important to remember that D is measured from the center of the electrode under test to the center of the probe and that D is large relative to the radius of the electrode under test.

Figure 19 shows an example of the data taken with the fall-of-potential method. The correct resistance of 13 ohms corresponds to the potential probe location of 27.4 meters (90 feet) which is 62 percent of the distance to the current probe.

Extensive Electrode Systems - Accuracy of earth-electrode resistance measurements is affected by the overall dimensions of the earth-electrode subsystem. Table 1 relates accuracy to the ratio of probe spacing to earth-electrode subsystem dimensions. When the earth electrode subsystem is extensive, it is frequently difficult to locate the current probe at a distance of even five times the largest dimension and measurements of resistance to earth are subject to large errors. In addition, a connection to the electrical center of the system may not be possible.

Table 1
Resistance Accuracy Versus
Probe C_2 Spacing

Accuracy	Probe Spacing
90%	5 x diagonal under test
95%	10 x diagonal under test
98%	25 x diagonal under test
99%	50 x diagonal under test

Figure 20 depicts measurement of an electrode, at point O , at the edge of a large facility. X is the distance from the electrode to the potential probe, and C_k is the distance from the electrode to the current probe. Figure 21

shows a set of resistance curves for such a facility obtained at current-probe spacings of up to 1000 feet (304 meters). Each curve corresponds to a particular distance, C_k . The potential-probe spacing is the independent variable.

On each curve the points corresponding to 62 percent of the distance to the current probe have been connected. It is evident that as the current probe location is removed further out, the resistance at the 62 percent value is decreasing. Because none of the curves in figure 21 exhibit a flat portion, even the largest spacing of current probe is evidently too small for a direct reading of the resistance. The true value of resistance can be estimated by extrapolating the connecting line to its asymptotic value.

Basic assumptions for the fall-of-potential measurements are that (1) the electrode to be measured can be approximated as a hemisphere and (2) the connection to the earth electrode is made at its electrical center. The distance from the true electrical center of the facility to the current probe (assuming the measurements are made on a radial from the electrical center) is $C_k + X$. The use of the 62 percent point on the curves of figure 21 to determine the resistance of the earth electrode should in reality correspond to a position of the potential probe that is 0.62 from the true center (D). This means that the distance, P_t , from the point of actual connection (O) to the system to the location at which the correct resistance to earth exists will be:

$$P_t = 0.62 (C_k + X) - X, = 0.62 C_k - 0.38 X$$

Where P_t = Distance of potential probe from point of connection to electrode when the measured resistance is the true value of resistance-to-earth for the electrode.

CONCLUSION

The ground systems of new CE facilities are being installed with a greater degree of uniformity and standards than those of the past. Additionally, the new grounding procedures are being implemented during rehab or upgrading of existing facilities. While comparisons between new and old ground systems are limited, the equipotential ground plane appears to be advantageous over the single point system in reducing noise between CE equipments of a system by insuring that each equipment is maintained at the same voltage potential.

Interconnecting the earth electrode subsystems of antenna towers to/with their respective transmitter/receiver buildings coupled with grounding the transmission lines at three points appears to be reducing the incidence rate of lightning entering a building via antenna transmission lines. An analysis of several damage incidents due to lightning has revealed the recommended grounding procedures were not implemented; in one case the air terminal of a

radar radome had been disconnected for maintenance purposes and had not been reconnected prior to the lightning strike. As a result the lightning passed through the radome striking the radar antenna and followed the transmission line into the equipment building.

REFERENCES

Military Standard 188-124 Grounding, Bonding and Shielding for Common Long Haul/Tactical Communications Systems

Military Handbook 419 Grounding, Bonding and Shielding for Electronic Equipments and Facilities

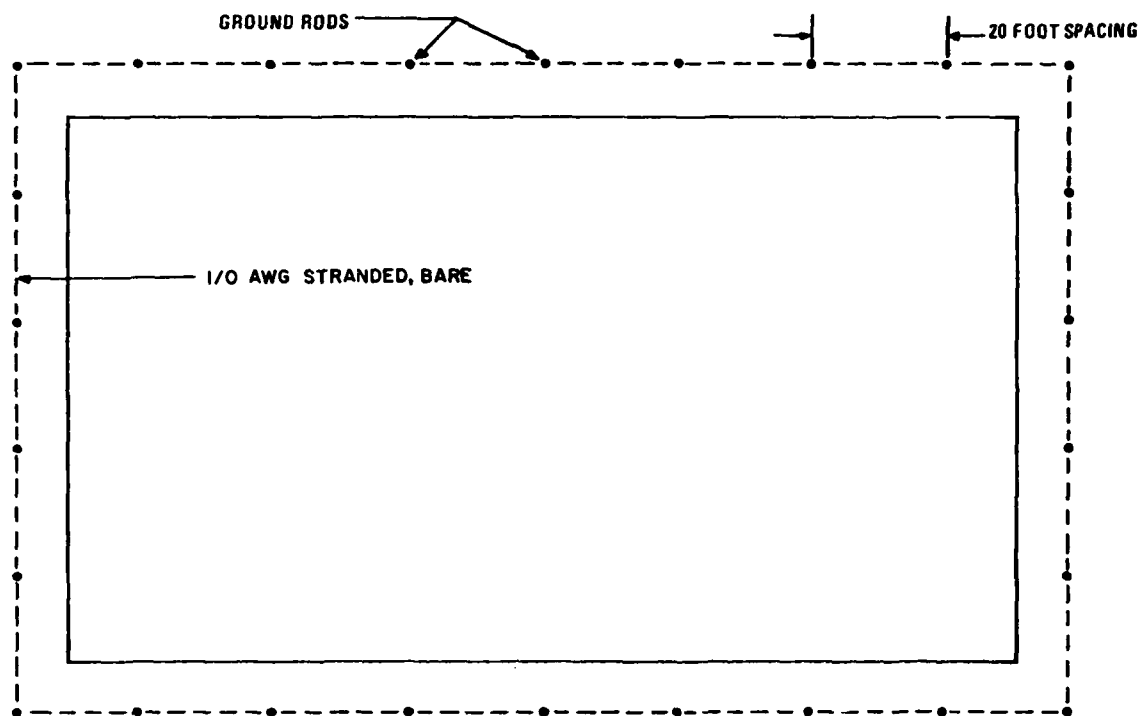


Figure .1. Minimum Earth Electrode Subsystem Configuration for Rectangular Shaped Facility

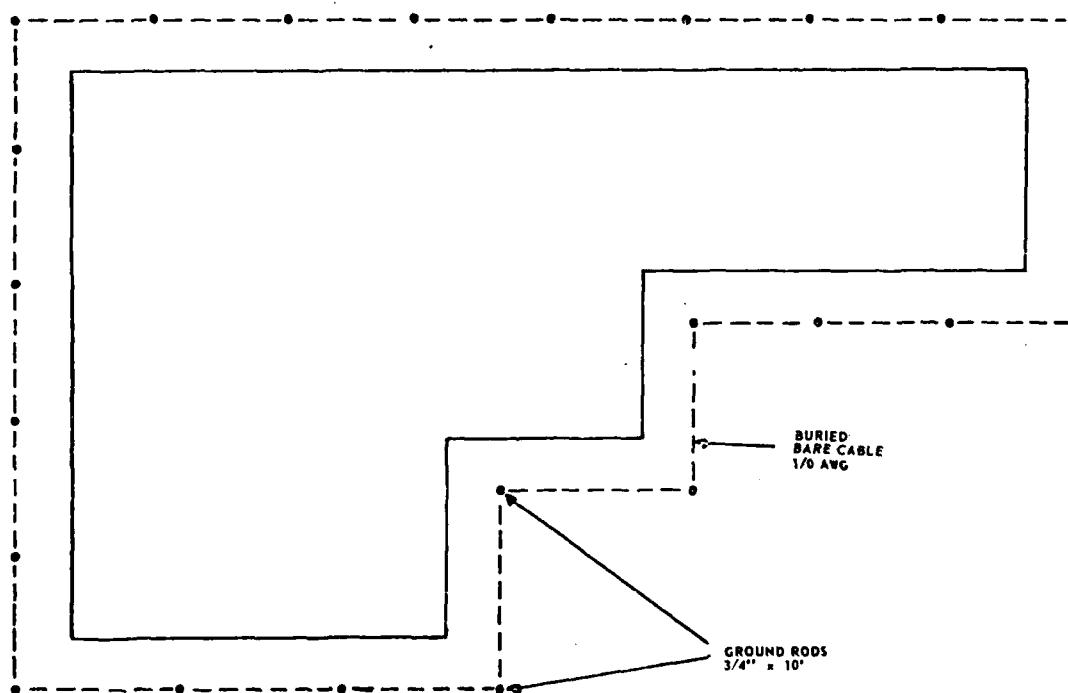


Figure 2. Electrode Configuration for Irregular Shaped Facility

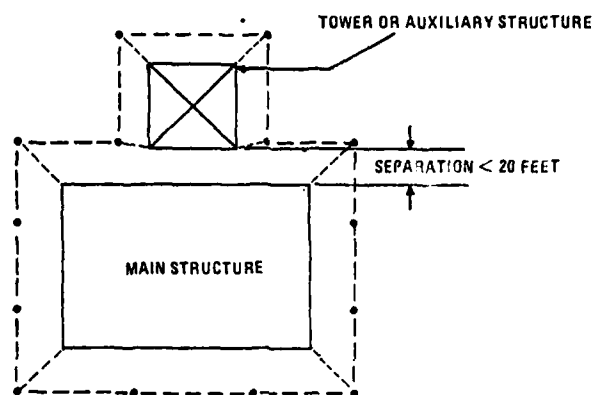


Figure 3a. Electrode Configuration for Adjacent Structures.

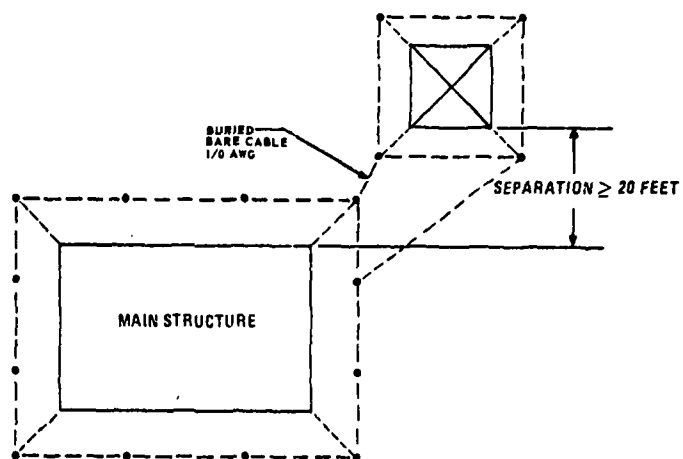


Figure 3b. Electrode Configuration for Closely Spaced Structures

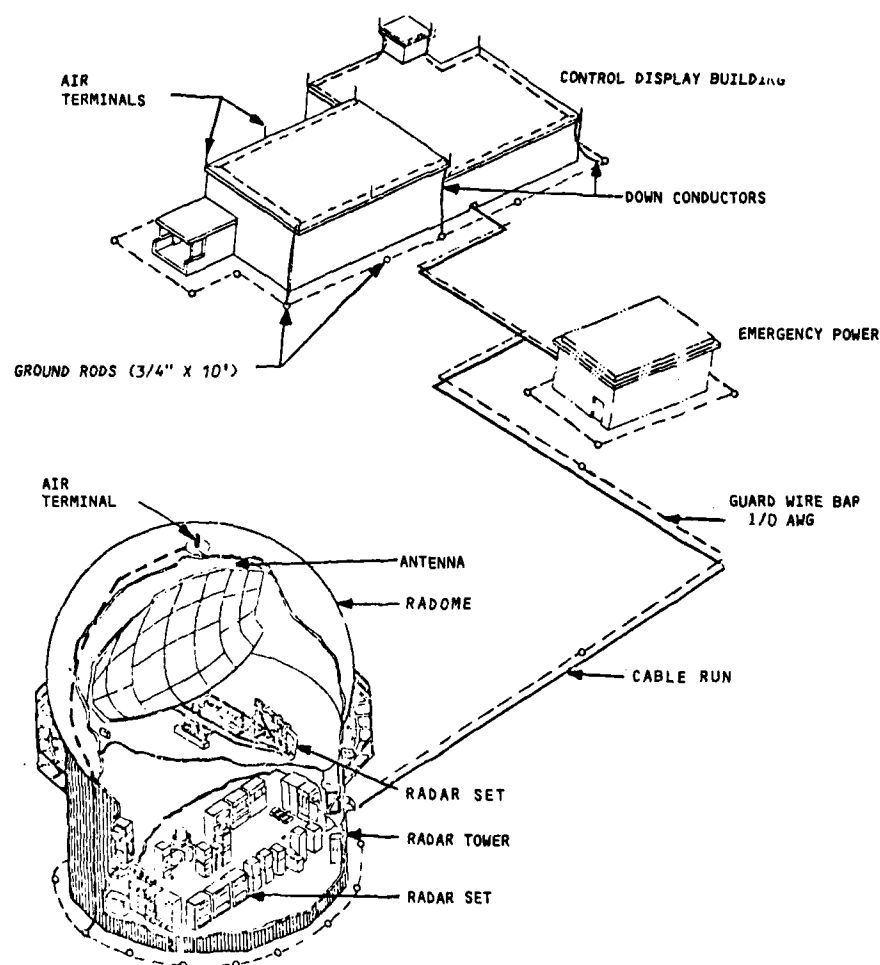


Figure 4. Grounding System for Typical Radar Installation

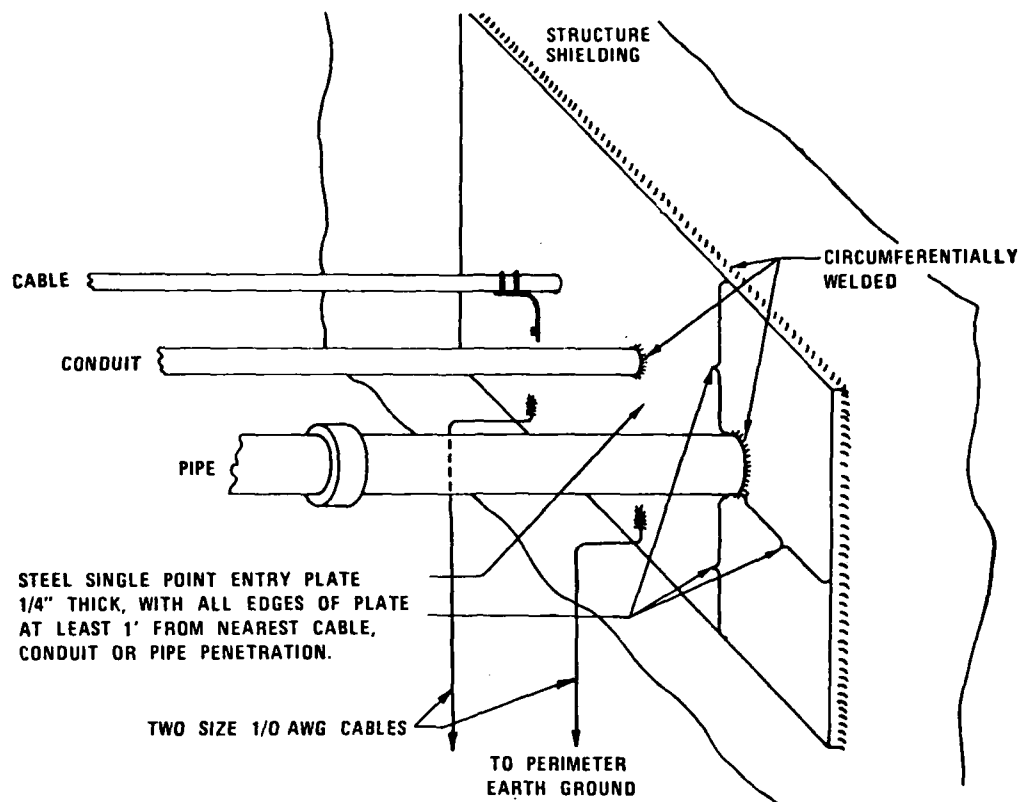


Figure 5. Typical Entry Plate Showing Rigid Cable, Conduit, and Pipe Penetrations

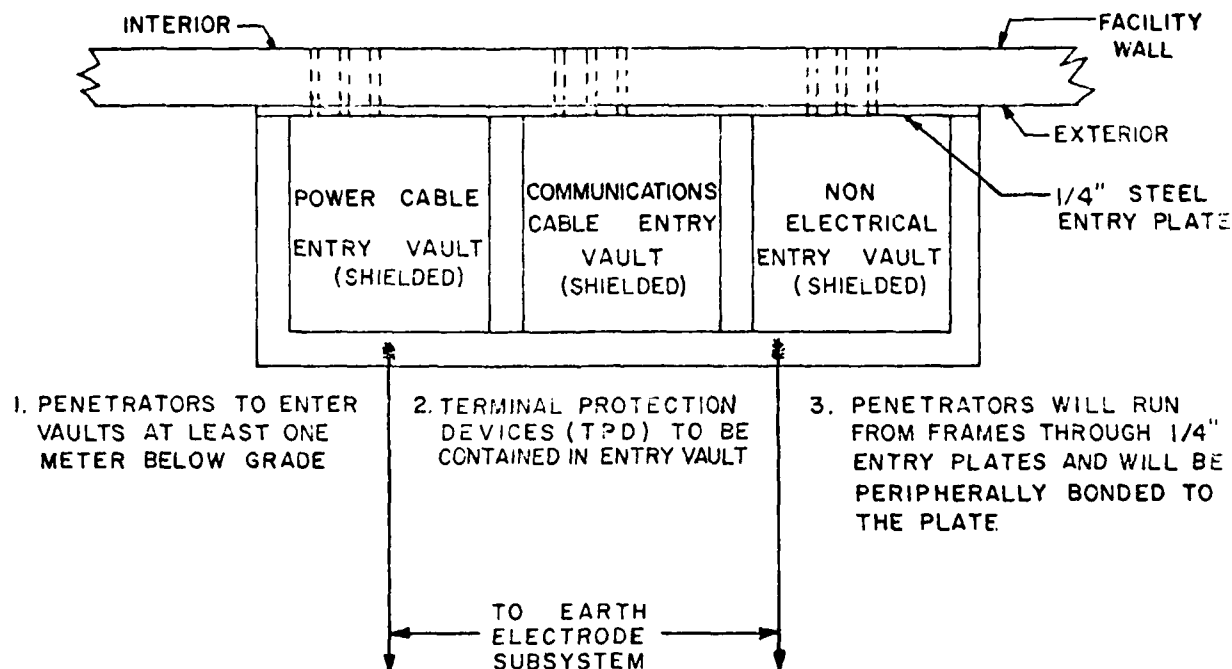


Figure 6. Typical Single Point Entry for Exterior Penetrations (Top View)

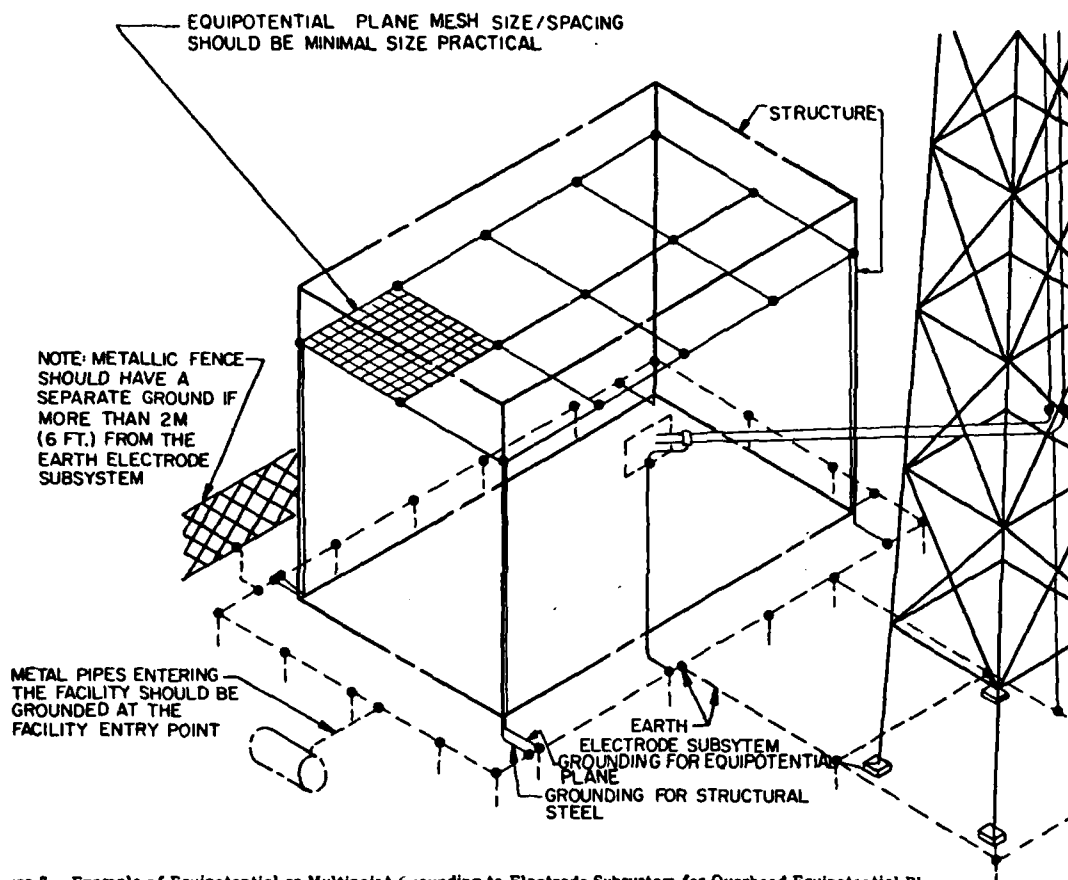


Figure 7. Example of Equipotential or Multipoint Grounding to Electrode Subsystem for Overhead Equipotential Plane

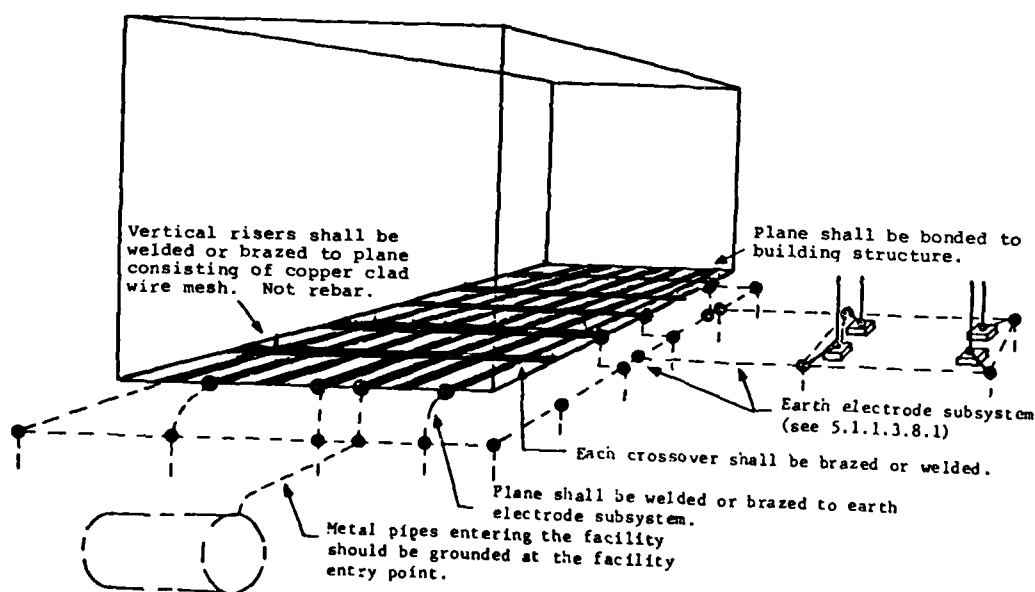


Figure 8. Example of Equipotential Plane to Earth Electrode Subsystem (for New Construction)

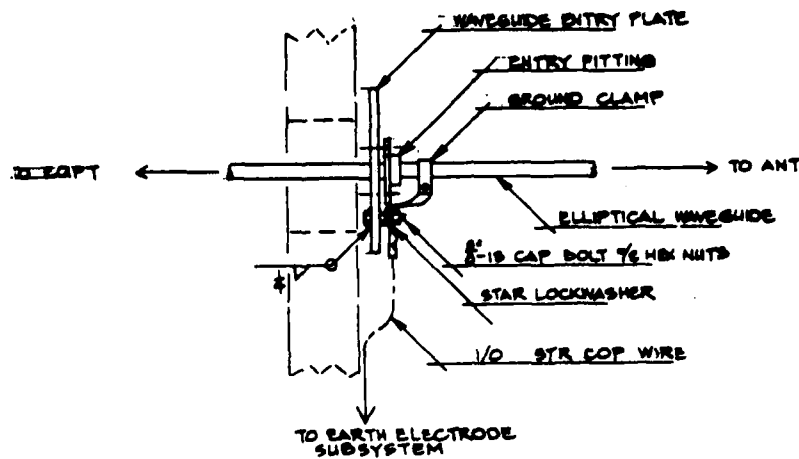


Figure 9. Waveguide Entry Plate Detail

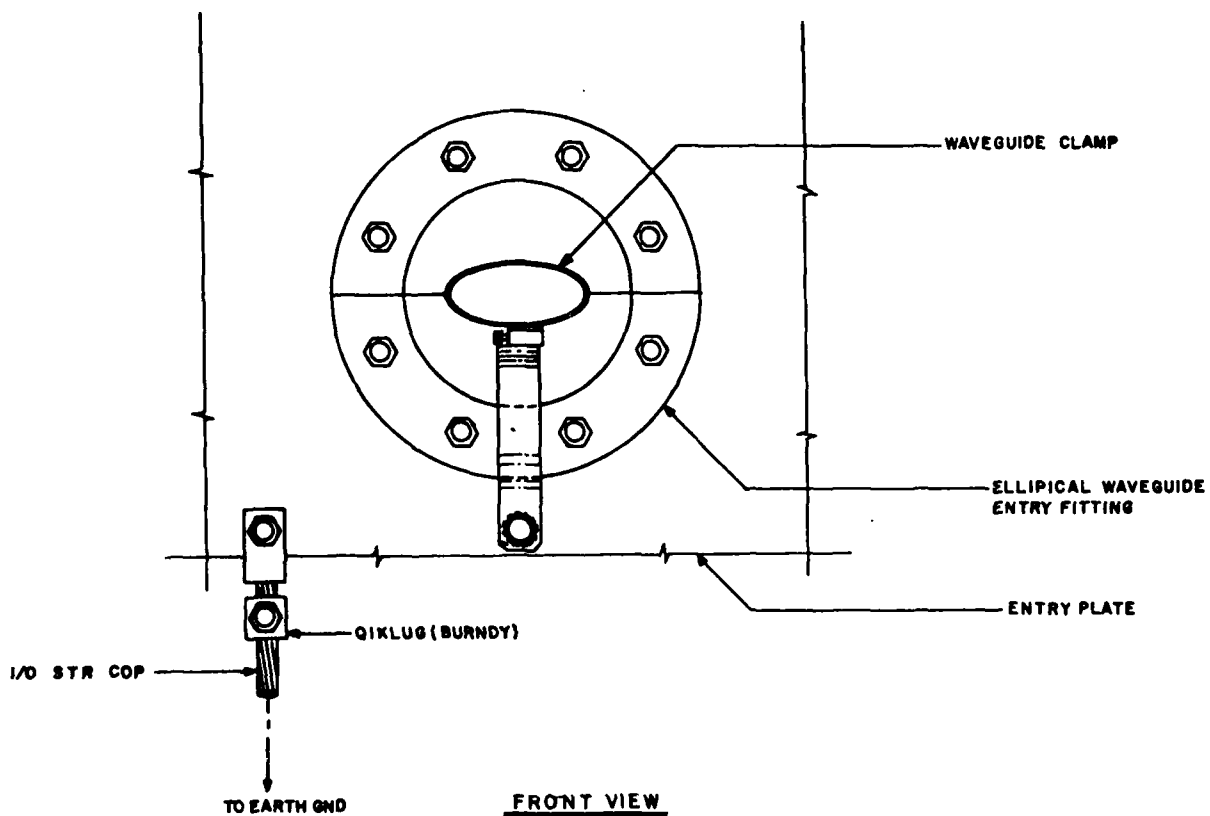


Figure 10. Grounding Detail for Elliptical Waveguide

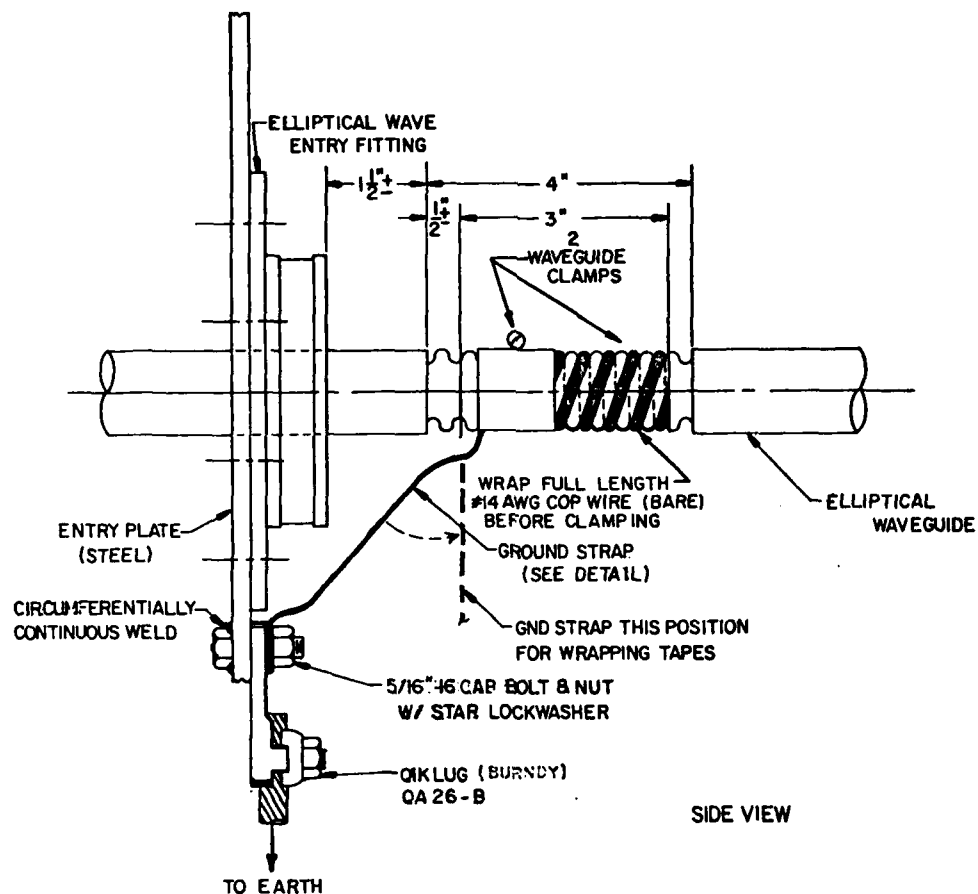


Figure 11. Grounding Details for Elliptical Waveguide

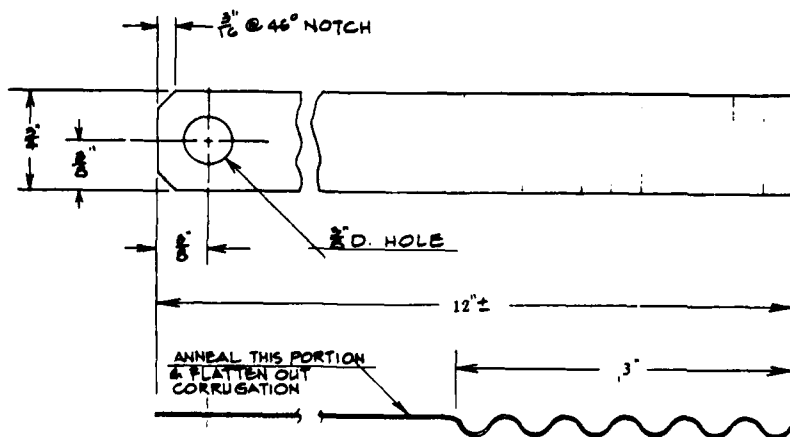


Figure 12. Ground Strap Detail for Elliptical Waveguide

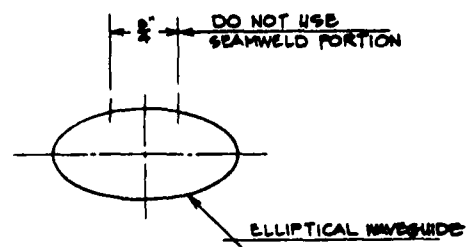


Figure 13. Strap Cutting Detail for Elliptical Waveguide

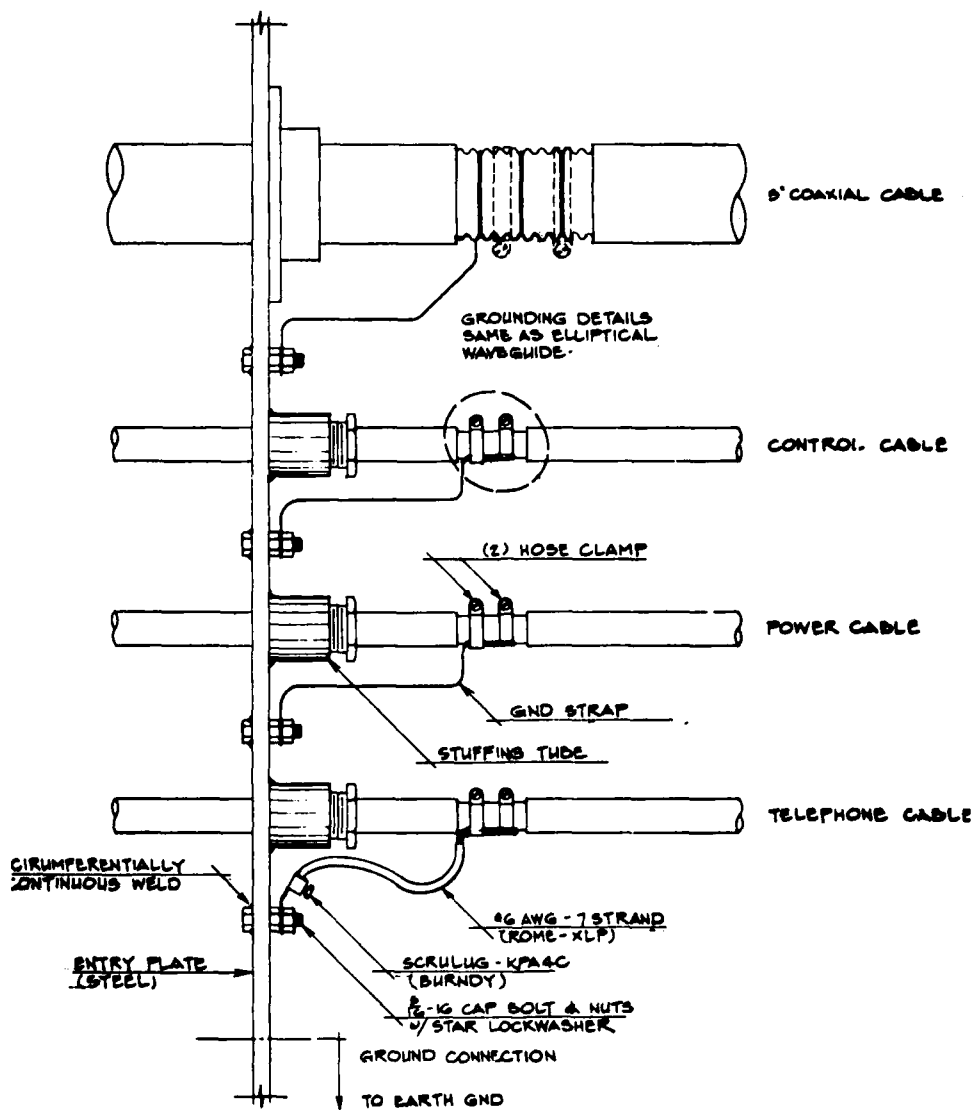


Figure 14. Typical Cable Entry Installation

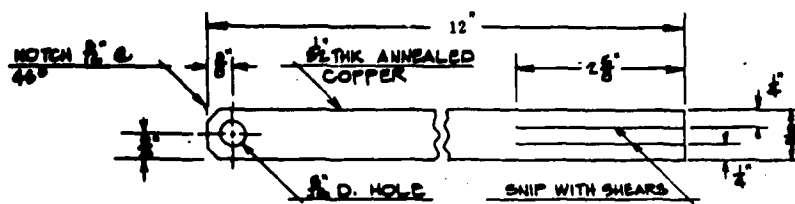


Figure 18. Ground Strap Detail

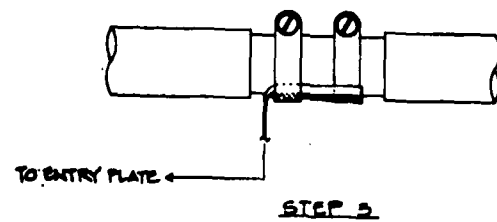
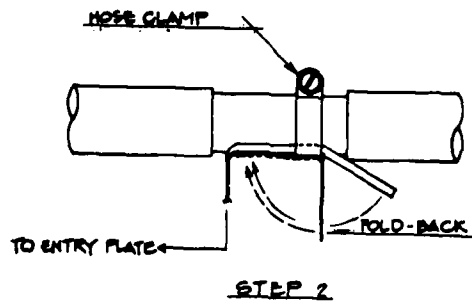
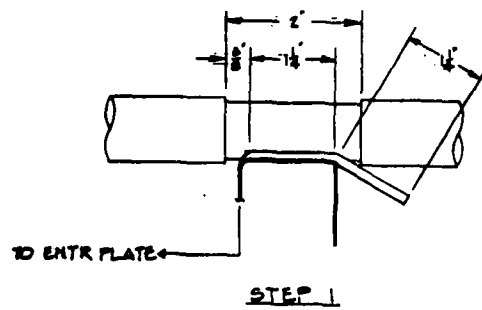


Figure 18. Grounding Steps for Cables

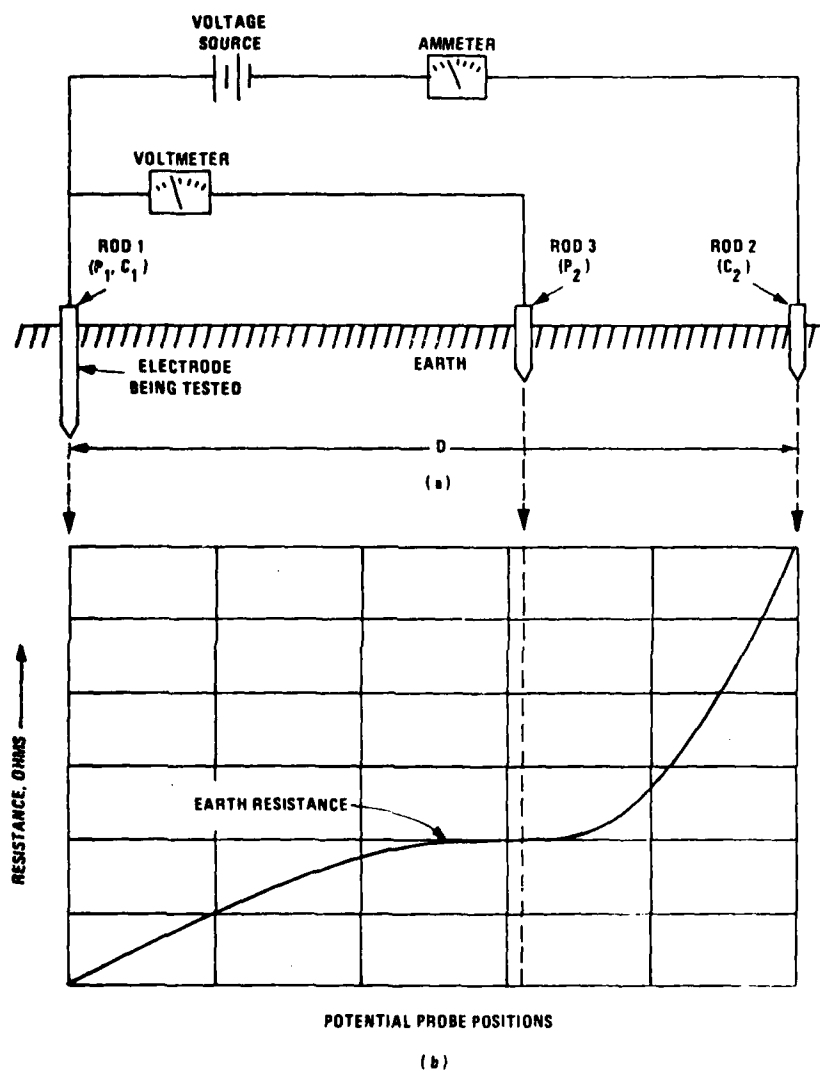


Figure 17, Fall-of-Potential Method for Measuring the Resistance of Earth Electrodes

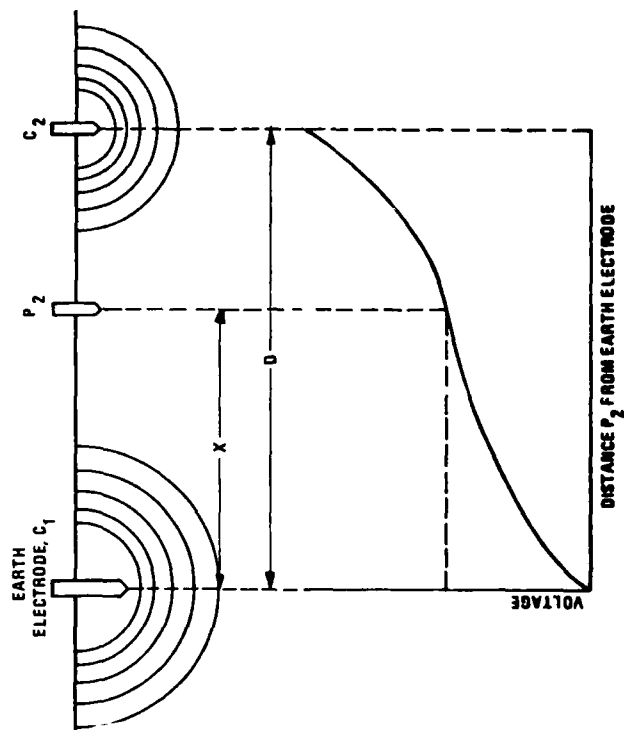
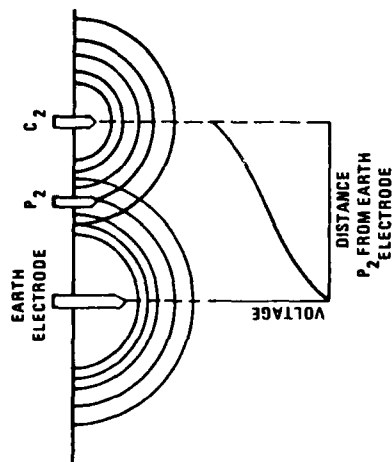


Figure 18. Effect of Electrode Spacing on Voltage Measurement

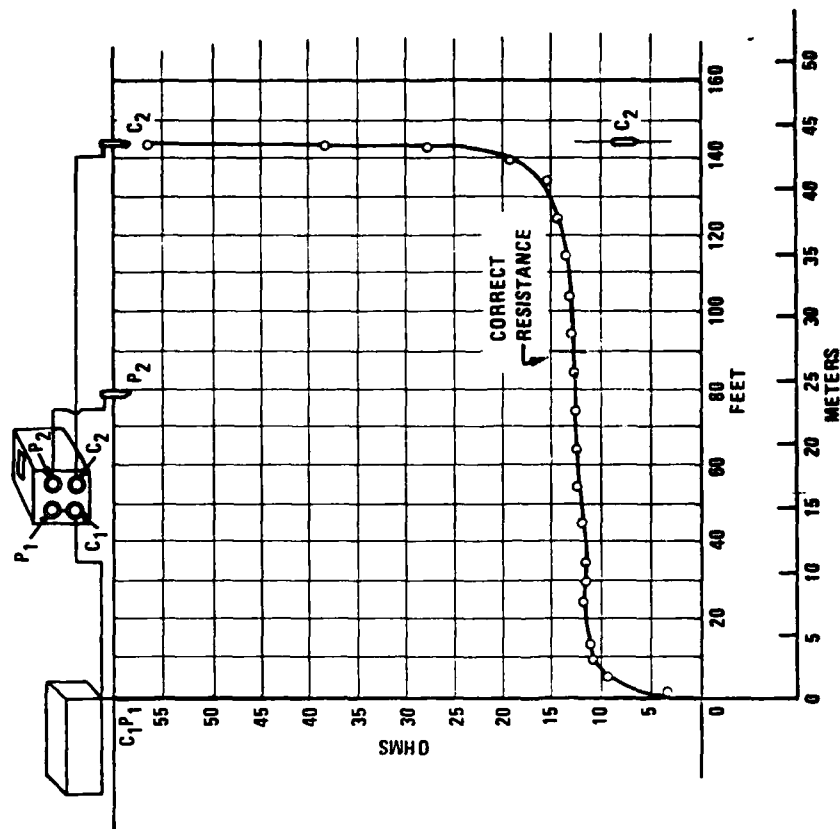


Figure 19. Resistance Variations as Function of Potential Probe Position in Fall-of-Potential Method

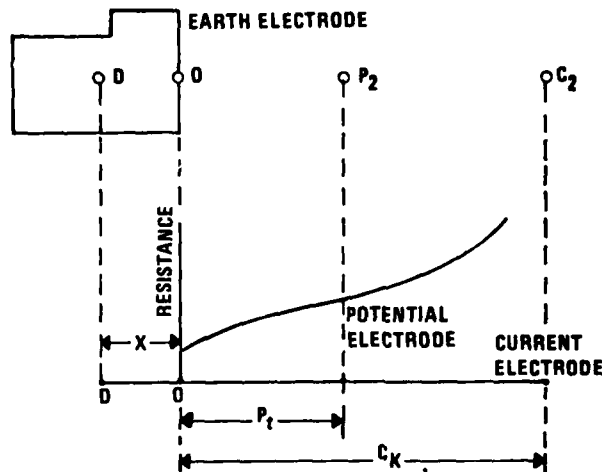


Figure 20. Earth Resistance Curve Applicable to Large Earth Electrode Systems

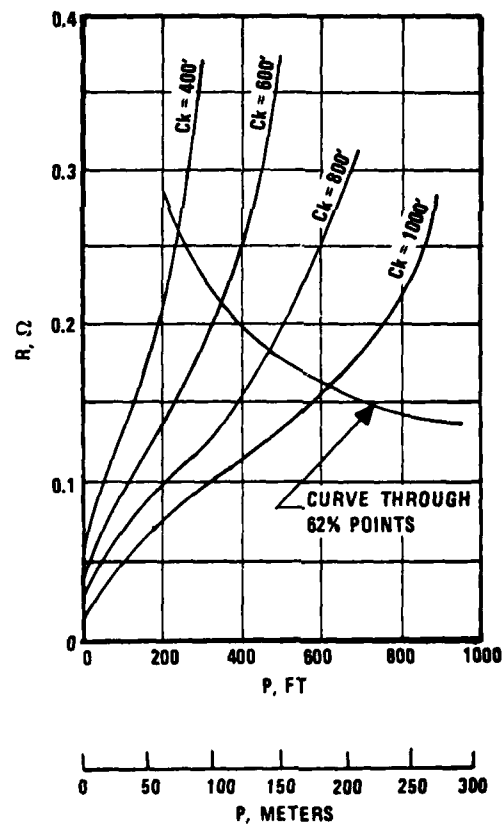


Figure 21. Earth Resistance Curves for a Large Electrode System

AC POWER LINE PROTECTION FOR AN
IEEE 587 CLASS B ENVIRONMENT

O. MELVILLE CLARK
WILLIAM E. ROEHR

GENERAL SEMICONDUCTOR INDUSTRIES, INC.
TEMPE, ARIZONA

This paper describes a unique low clamping voltage transient suppressor to protect from the 6000V peak open circuit voltage and 3000A short circuit current as defined in IEEE Standard 587 for Category B. Transients. This device, which incorporates multiple stage solid state protector components, has been specifically designed to operate under multiple exposures to maximum threat levels in this severe environment and clamp harmful voltage peaks to approximately 300V under maximum threat conditions for a 120V ac power line thus providing adequate protection to vulnerable electronic equipment. The principle of operation and test performance data will be detailed in the text of the paper.

This paper was not available for incorporation into this book.

THE RISK FACTOR IN AIRCRAFT LIGHTNING PROTECTION

John C. Corbin

Air Force Aeronautical Systems Division
Directorate of Avionics Engineering
Wright-Patterson AFB, Ohio 45433

ABSTRACT

This paper examines lightning as a threat to aircraft safety. Papers and reports on lightning-related mishaps are reviewed and synopsized. Present and future lightning protection requirements, validations, and problems are discussed. New approaches to aircraft lightning protection are advocated that offer weight, performance, and cost benefits. The paper recommends that new military and commercial lightning protection standards and specifications be tailored to allow for variations in aircraft missions, flight environment, and configurations to provide the most cost-effective protection.

INTRODUCTION

LIGHTNING IS PROBABLY the most severe uncontrolled electromagnetic environment to which aircraft are exposed [1]*. The severity of the lightning threat depends upon the probability of a flash attachment to the aircraft and the characteristics of the flash (A flash consists of one or more sequential discharges). Flash attachment can result from either natural lightning or triggered lightning. Natural lightning strikes to aircraft are relatively rare (estimated at one in a hundred) and occur abruptly without warning (without a preceding perceptible corona discharge). Triggered lightning, often confused with electrostatic discharge, is initiated by the aircraft. Triggered lightning begins with aircraft charging followed by corona discharge at aircraft extremities (Corona discharge often results in wideband noise in communication receivers and observable St. Elmo's fire at night). Coronas then transition into one or more filamentary leaders which tap the energy contained in nearby external electric fields to grow into a lightning channel. Triggered lightning may be relatively harmless to aircraft in weak field regions (e.g., no discernible pitting or structural damage, no induced malfunctions to electrical/electronic equipment), but may be devastating if the leader reaches ground or high-field regions and significant charge transfer results [2,3].

LIGHTNING-RELATED MISHAP DATA

Metal aircraft are relatively "lightning-proof" in terms of flight safety even though a few commercial and military aircraft have been lost due to lightning-related mishaps. A number of papers and reports have been written that discuss lightning-related mishaps to military, commercial, and general aircraft. A short synopsis of some of the papers and reports that have been published since 1970 follows.

Cummings [4] reviewed 340 reported lightning strikes to USAF aircraft from 1965 through June 1970. Thirty different types of aircraft and helicopters were involved. His data indicated one strike per 50,000 to 200,000 operational flight hours and an average of approximately 73 strikes per year to the fleet. Operational flight hours averaged 7-8 million for the fleet per year. Attachment point data were categorized as follows: radome 50.5%, wing tip 8.0%, wings 5.3%, vertical fin 15.1%, miscellaneous (e.g., antennas, canopy, landing gear doors, external stores, fuselage) 21.1%. Aircraft damage data were summarized as follows: none 8.9%, less than minor 88.0%, minor 0.9%, substantial 1.1%, destroyed 1.1%. Pilot injury was classified as follows: none 99.1%, minor 0%, major 0.3%, fatal or missing 0.6%.

* Numbers in brackets designate References at the end of the paper.

Auten [5] reviewed 231 reported lightning strikes or electrostatic discharges to USAF and USN jet aircraft (228 and 3, respectively) between January 1964 and August 1970. His data were categorized as to prevailing weather, types of precipitation, seasonal and time variations, altitude variations, attachment point, damage (electrical/electronic system, radome, flight controls/instruments, fuel system), damage classification (none, less than minor, minor, and destroyed), and damaged area. He did not attempt to correlate lightning strike occurrence with total flight history. His damage classification data summary was similar to that of Cummings, but his attachment point data summary differed somewhat. He also included structural damage locations with functional damage (electrical/electronic systems, flight controls/instruments) in his distribution of total aircraft damage.

Weinstock [6] analyzed lightning strikes to over seventy F-4 fighter aircraft. He enumerated attachment points to the aircraft pictorially and catalogued attachment point data under four major points of entry (nose 27%, tail 22%, wing 34%, other 17%) and fifteen damage locations or internal effects. He noted that, without the external wing tank, lightning never attached to the leading edge of the wing, but rather attached to either the nose or the wing tip. The most serious lightning incidents on the F-4 involved the electrical system. He noted that the most prevalent point of entry into the electrical system was through the heater wire in the radome pitot boom and that the navigation light wiring in the vertical fin and wing tips also provided points of entry into the electrical system.

Plumer initiated a cooperative lightning strike reporting project in 1971 in which five U.S. commercial airlines agreed to send lightning strike incident reports (completed by flight and ground crews) to him for analysis and correlation. Through October 1974, 214 strike incidents were included in a summary published in March 1975 [7]. Incidents involved lightning strikes to Boeing 707, 720, 727, 737, 747, McDonnell Douglas DC-8, DC-9, DC-10, and Lockheed L-188, L-1011 aircraft. On average, aircraft were struck most often when in a cloud, while experiencing precipitation and light turbulence, when climbing or descending at 250 knots through 10,000 to 12,000 feet, and with outside air temperature near the freezing point. Strikes occurred under many other conditions as well. The 214 incidents included 78 with no reported damage to the aircraft, 32 incidents with radome damage, 40 involving interference or damage to avionics, 27 involving static discharger damage, 3-4 involving lightning arrester failure on HF antenna systems, 6 incidents of ac generator trip-off, and no incidents of personnel injury other than momentary flash blindness. Since October 1974, approximately 600 additional reports have been received. Findings from these reports will be presented at this symposium [8].

In 1975, Plumer and Perry [9] reported on lightning strikes to U.S. and UK commercial air-

craft. UK data included 760 strikes to Viscount, Vanguard, and Britannia turboprop aircraft, and to Comet, Trident, BAC 1-11, Boeing 707, 747, and VC-10 jet aircraft from 1959 to 1974. UK data, which correlated number of lightning strikes to total flying hours for each aircraft, averaged 34 strikes per 100,000 hours. The U.S. data (214 incidents) were the same as given in [7]. The U.S. data indicated that a hole was made in either a radome or aircraft skin in 30% of the incidents, interference occurred in about 20% of all incidents, and outages occurred in about 10% of all incidents. The most commonly affected equipments were the compass, HF communications, ADF, and engine speed indicators.

Fisher and Plumer's book [10] discussed lightning strike experience to aircraft in Chapter 3. Figures included lightning strike incidents vs. altitude, flight conditions when struck, synoptic meteorological conditions when aircraft were struck, and occurrence of lightning strikes by month. Tables included incidents of reported lightning strikes to commercial aircraft (1950 to 1974) and to USAF aircraft (1965 to 1969). Reported strikes to commercial aircraft were significantly more frequent than to military aircraft.

Corn [11] presented a ten-year history of USAF lightning incidents involving aircraft and helicopters. His data showed 9 catastrophic, 7 major, and 153 minor incidents and 66 cases of damage to structure, 78 to electrical/instruments, 6 to fuel, and 19 to others. The ten-year period over which the incidents occurred was not stated. He also showed reported strikes per 100,000 operational flight hours ranging from 1.23 to 2.64 from 1969 to 1976. This strike rate is much lower than that reported by commercial aircraft which averaged about 34 strikes per 100,000 flight hours [10].

In 1977, Plumer initiated a lightning strike reporting project for general aircraft in cooperation with Flight Operations magazine. In [12], he discussed the first 40 responses from the project. He described flight and weather conditions when struck, effects of the strike to the aircraft (e.g., engine flameout, power outages, equipment damaged), and implications for protection design (zonal concepts).

Clifford [13] summarized aircraft mishap experience from atmospheric electricity hazards from previous reports and papers.

Odam and Evans [14] reported UK military aircraft lightning strike experience for a six-year period through May 1978. Over this period, the average number of incidents per year was 58. The strike rate for various aircraft ranged from 0.3 to 3.7 per 10,000 flight hours. A summary of the damage and effects caused by 346 lightning strikes during the period was presented. A more recent report [15] analyzed 295 incidents between January 1978 and September 1983 and presented data on strikes per month, number of strikes vs. outside air temperature, number of strikes vs. altitude, and a summary of damage and effects.

Lane [16] presented USN aircraft lightning strike experience from 1961 through 1980. His data included 606 incidents. He found that 98% of the strikes resulted in "limited" or no physical damage to the aircraft, but in 50 incidents electronic equipment were adversely affected, and in three cases aircraft were lost. Most likely damaged areas were nose radome (24%), wing (20%), antenna (17%), tail (17%), and fuselage (13%). Data revealed on average one strike for every 64,000 flight hours, although patrol aircraft averaged one strike for every 3,700 flight hours. The average number of strikes from 1975 through 1980 was 58 strikes per year.

Ellis [17] reported on 95 USAF lightning strike reports collected from April 1977 to August 1978.

Anderson, Kroninger, and Smith [18] reported on lightning strikes to aircraft in the Republic of South Africa from 1966 to 1981. Types of aircraft considered were Boeing 707, 727, 737, 747 and the A300 Airbus. Over the period, 132 aircraft were struck and only 8 reported damage. The ratio of strikes was 1.29 strikes per 10,000 flight. Most strikes occurred during descent (56%) or ascent (30.4%). Of 115 observations of meteorological conditions at the time of the lightning strike, 88% occurred during rain and 12% during hail or sleet.

Ziegler [19] reported more than 260 lightning strikes to aircraft of the German Federal Armed Forces from 1973 through 1982. About 80% of the strikes involved the F-104, F-4, C-160, and BR-1150 aircraft. The average number of strikes per 10,000 flight hours were 1.1, 1.2, 4.3, and 3.9, respectively, for the four aircraft. Attachment point data were presented for the F-104, F-4, and C-160 aircraft. In terms of damage, about 90% of the lightning strikes analyzed showed little or no damage except for occasionally destroyed navigation lights, static dischargers, or antennas. In the remaining 10%, considerably more damage resulted as well as failed and partially damaged electrical equipment. Even in these cases, the damaged aircraft were able to land.

Corbin [20] categorized and analyzed data from 877 USAF lightning-related mishap reports involving 56 aircraft types over a thirteen-year period (1970 through 1982). Aircraft were grouped into six general classes: attack, bomber, cargo, fighter, trainer, and helicopter. Data were tabulated under two major headings: operational conditions at the time of the lightning strike, and the effects of the strike. Operational conditions included aircraft attitude, aircraft altitude, outside air temperature, aircraft location with respect to clouds, precipitation/turbulence, and electrical activity prior to the strike. Effects of the strike included attachment point, interference/outage, effect on mission, effect on personnel, structural damage, electrical/electronic damage, and repair/replacement costs. Interference/outage occurred in 20% of the reported incidents, structural damage (usually minor) in 78% of the incidents, and

electrical/electronic damage in 8% of the incidents.

AIRCRAFT LIGHTNING PROTECTION

At a recent meeting of specialists concerned with the effects of lightning on military and commercial aircraft [21], lengthy discussions were held on lightning protection of (1) present and older aircraft (largely metallic) and (2) future aircraft (largely composite). A general consensus was reached on the following statements:

1. Present Aircraft (Largely Metallic)
 - a. Present aircraft have no fundamental lightning protection deficiencies.
 - b. Overlooked areas of lightning protection have been fixed through retrofit.
 - c. Any fuel (particularly JP-4) is a potential hazard with respect to sparking/ignition.
 - d. Metal fuel tanks can be designed and manufactured which are spark-free from lightning.
 - e. Lightning protection of radomes is not necessarily mandatory if flight safety is not involved.
 - f. The use of carbon fiber composites (CFC) in present aircraft has required considerable effort to provide sufficient/additional lightning protection.
 - g. Lightning-induced effects problems have been minimal to date. Design of fly-by-wire systems has required considerable effort to insure adequate lightning protection.
 - h. Retrofits and modifications may be an overlooked area for lightning protection.
2. Future Aircraft (Largely Composite)
 - a. Electrical bonding and grounding techniques are not adequately/sufficiently defined, measureable, quantifiable, etc.
 - b. Major R & D efforts will be required to produce lightning-safe composite integral fuel tanks.
 - c. Increased use of analysis in conjunction with testing will be required to verify induced effects protection.
 - d. Induced voltage/current levels are approaching and may exceed interface circuit failure levels in new aircraft.
 - e. Testing methods need to be revised/revamped to account for digital upset and damage mechanisms.
 - f. A number of advanced materials have not been adequately assessed as to lightning protection techniques/measures required.
 - g. Corrosion control and good electrical bonding techniques may be incompatible in future aircraft.
 - h. The impact of radar-absorbing material/structure (RAM/RAS) on lightning protection has not been addressed.
 - i. Improved performance tests and validation techniques are needed for future aircraft.
 - j. Life-cycle repair/maintenance tech-

niques need to be developed. Non-destructive tests for detection of weak links need to be developed. Cumulative effects need to be assessed.

NEW APPROACHES TO AIRCRAFT LIGHTNING PROTECTION

Odam and Evans [15] have suggested that if cloud-to-ground lightning strike parameters (which represent severe strokes) are continued to be used as a basis for design and test for all types of aircraft, there could be over-design leading to performance penalties.

Weinstock [22] has furthered this argument in stating that present lightning protection requirements for fighter aircraft are applied without consideration of mission, probability of strike occurrence, or penalties associated with protective designs. He contends that requirements may be too stringent based upon data from in-flight test programs (NASA F-106 and USAF C-130 aircraft), tabulations of strike rates per aircraft type, and an examination of strike damage records. He suggests that a revision to the method of applying lightning specifications to aircraft may be justified since unnecessarily stringent lightning protection requirements can add weight out of proportion to the lightning risk. He states that arbitrarily placing the same requirement on a fighter aircraft with built-in tolerance for battle damage and a large commercial passenger aircraft does not seem prudent or cost-effective. He presents a probabilistic approach (e.g., probabilities of occurrence, magnitude, damage) for the design of aircraft lightning protection which may avoid conventional worst-case design penalties.

Corbin and Cooley [23] have also advocated a probabilistic or statistical approach in determining the vulnerability of critical aircraft equipment to the lightning threat. Recently, Cooley [24] extended the analysis by calculating probability of equipment failure vs. lightning threat level (amperes) curves based upon lightning parameter data provided by NOAA's National Severe Storm Laboratory.

In future largely-composite aircraft with electronically-controlled flight-essential systems, lightning will become a more serious threat to aircraft safety. The application of lightning protection will have to be considered on a more rigorous risk vs. penalty basis. The references cited in this paper should provide the available data base of lightning mishap information needed for tradeoff considerations.

SUMMARY AND CONCLUSIONS

This paper has examined lightning as a threat to aircraft safety. Papers and reports on lightning-related mishaps have been reviewed and synopsized. Present and future lightning protection requirements, validations, and problems have been discussed. New approaches involving trade studies of risk vs. penalty for aircraft lightning protection have been presented and advocated

that offer weight, performance, and cost benefits. New lightning protection standards and specifications for military and commercial aircraft should be tailored for variations in aircraft missions, flight environment, and configurations to provide the most cost-effective protection.

REFERENCES

1. J. C. Corbin, "Aircraft Electromagnetic Threat Protection," Proceedings of the 1984 IEEE National Symposium on Electromagnetic Compatibility, San Antonio, Texas, April 24-26, 1984.
2. H. W. Kasemir, "Static Discharge and Triggered Lightning," Proceedings of the Eighth International Aerospace and Ground Conference on Lightning and Static Electricity, Ft. Worth, Texas, June 21-23, 1983.
3. D. W. Clifford and H. W. Kasemir, "Triggered Lightning," IEEE Transactions on Electromagnetic Compatibility, Vol EMC-24, Part I: Special Issue on Lightning and Its Interaction with Aircraft, May 1982.
4. L. E. Cummings, "A Review and Analysis of USAF Operational Lightning Problems," Air Force Avionics Laboratory Report.
5. R. K. Auten, "Analysis of USAF Jet Aircraft Experiencing Lightning Strikes," North American Rockwell, Report No. NA-71-636, July 1971.
6. G. L. Weinstock, "Lightning Protection on Advanced Fighter Aircraft," Proceedings of the 1970 Lightning and Static Electricity Conference, San Diego, California, December 9-11, 1970.
7. J. A. Plumer and B. I. Hourihan, "Data from the Airlines Lightning Strike Reporting Project, Summary Report," General Electric Company Corporate Research and Development, March 1975.
8. N. O. Rasch, M. S. Glynn, and H. Bani-lower, "Lightning Interaction with Commercial Air-Carrier Type Aircraft," Proceedings of the 1984 International Conference on Lightning and Static Electricity, Orlando, Florida, June 26-28, 1984.
9. J. A. Plumer and B. L. Perry, "An Analysis of Lightning Strikes in Airline Operation in the USA and Europe," Proceedings of the 1975 Conference on Lightning and Static Electricity, Culham Laboratory, England, April 14-17, 1975.
10. F. A. Fisher and J. A. Plumer, "Lightning Protection of Aircraft," NASA RP-1008, October 1977.
11. P. B. Corn, "Lightning Hazards Overview - Aviation Requirements and Interests," presented at the NASA/UTSI Workshop on the Need for Lightning Measurements from Space, University of Tennessee Space Institute, Tullahoma, Tennessee, February 13-15, 1979.
12. J. A. Plumer, "Lightning Effects on General Aviation Aircraft," FAA/FIT Workshop on Grounding and Lightning Technology, Report No. FAA-RD-79-6, Supplement 1A, Melbourne, Florida, March 6-8, 1979.
13. D. W. Clifford, "Aircraft Mishap Experience from Atmospheric Electricity Hazards," Proceedings: AGARD Lecture Series No. 110, Atmospheric Electricity - Aircraft Interaction, AGARD LS-110, May 1980.
14. G. A. M. Odam and R. H. Evans, "National In-Service Lightning Strike and Damage Experience; UK Experience in Relation to Proposed Design and Test Standards," UK Ministry of Defence Report.
15. G. A. M. Odam and R. H. Evans, "National In-Service Lightning Strike and Damage Experience (January 1978 - September 1983)," UK Ministry of Defence Report.
16. R. F. Lane, "United States Navy In-Service Aircraft Lightning Strike and Damage Survey," Proceedings of the 1981 IEEE International Symposium on Electromagnetic Compatibility, Boulder, Colorado, August 18-20, 1981.
17. J. E. Ellis, "Aircraft Lightning Strikes An Unavoidable Phenomena?" Flying Safety Magazine, January 1982.
18. R. B. Anderson, H. Kroninger, and M. Smith, "Lightning Strikes to Aircraft - An Analytical Study," Proceedings of the International Aerospace Conference on Lightning and Static Electricity, Oxford, England, March 23-25, 1982.
19. W. Ziegler, "Lightning Strikes to Aircraft of the German Federal Armed Forces," Proceedings of the Eighth International Aerospace and Ground Conference on Lightning and Static Electricity, Ft. Worth, Texas, June 21-23, 1983.
20. J. C. Corbin, "Lightning Interaction with USAF Aircraft," Proceedings of the Eighth International Aerospace and Ground Conference on Lightning and Static Electricity, Ft. Worth, Texas, June 21-23, 1983.
21. Combined Technical Coordination Meeting on Lightning Protection of Aircraft and SAE AE4-L Lightning Committee Meeting, Wright-Patterson Air Force Base, Ohio, October 31 - November 2, 1983.
22. G. L. Weinstock, "Probabilistic Approach to Aircraft Lightning Protection," Proceedings of the International Aerospace Conference on Lightning and Static Electricity, Oxford, England, March 23-25, 1982.
23. J. C. Corbin and W. W. Cooley, "Assessment of Aircraft Susceptibility/Vulnerability to Lightning and Development of Lightning-Protection Design," IEEE Transactions on Electromagnetic Compatibility, Vol EMC-24, Part I: Special Issue on Lightning and Its Interaction with Aircraft, May 1982.
24. W. W. Cooley, "Protection Requirements," Atmospheric Electricity Hazards Protection (AEHP) of Advanced Aircraft, Boeing Military Airplane Company, Contract F33615-82-C-3406, Sixth Quarterly Review, November 3-4, 1983.

TECHNICAL ABSTRACT

LIGHTNING INTERACTION WITH COMMERCIAL AIR CARRIER TYPE AIRCRAFT

by

Nickolus O. Rasch
Michael S. Glynn

FAA Technical Center
Aircraft and Airport Systems Technology Division
Atlantic City Airport, New Jersey 08405

and

J. Anderson Plumer
Lightning Technologies, Inc.
10 Downing Parkway
Pittsfield, Massachusetts 01201

In 1971, General Electric Company and five United States Commercial Airlines initiated a project to obtain data on lightning strikes to transport category aircraft. The purpose of the project was to obtain information on the conditions under which aircraft are most likely to receive lightning strikes in flight, and document the effects that these strikes were having upon the aircraft. For this purpose, the airlines were provided with questionnaire-type reporting forms for use by pilots and maintenance personnell in documenting lightning strike events and effects on the aircraft.

The motivation for the project stemmed from a need to obtain a better understanding of the conditions under which aircraft are struck, the places on the aircraft where strikes are most likely, and the effect of these strikes on the airframe as well as onboard electrical and avionic systems.

These data are very important to the designer of new aircraft, which incorporates increasing amounts of composite material in the airframe and solid-state avionics which are inherently more vulnerable to lightning induced effects.

Initial results from the project were published by General Electric in 1974. At that time, a total of 214 strike reports had been received. The data were found useful by designers of lightning protection for new aircraft. For example, the strike reports help clarify the locations of lightning strike zones on transport category aircraft, and alerted designers to potential lightning-induced voltage problems.

Strike reports continue to be received by General Electric, but no further data summaries were published. In 1977, the project was taken over by Lightning Technologies, Inc. By early 1984, nearly 800 lightning strike reports had been accumulated and Lightning Technologies, Inc. invited the Federal Aviation Administration Technical Center to participate in the project by computerizing each of the strike reports and correlating the data. With the data in computer memory, it would be possible to provide correlation among various reported conditions and effects.

This paper presents a summary of the strike data obtained through January 1984.

INTRODUCTION.

In 1971 General Electric Company and five U.S. Commercial Airlines initiated a project to obtain data on lightning strikes to transport category aircraft. The purpose of the project was to obtain information on the conditions under which aircraft are most likely to receive lightning strikes in flight, and document the effects that the strikes have upon the aircraft. For this purpose, the airlines were provided with questionnaire-type reporting forms for use by pilots and maintenance personnel to document lightning strike events and effects on the aircraft. A copy of the reporting form is reproduced in figure 1.

The motivation for the project stemmed from a need to obtain a better understanding of the aircraft-lightning interaction. Conditions under which aircraft are struck, places on the aircraft (i.e., zones) where strikes are most likely, and effects of these strikes on the airframe as well as on-board electrical and avionics systems. These data are very important to designers of new generation aircraft which incorporate increasing amounts of composite materials in the airframe and solid-state avionics which are inherently more vulnerable to lightning-induced effects.

Results from the project were published by General Electric in 1974 (REF. 1). At that time, a total of 214 strike reports had been received. The data were found useful by aircraft manufacturers in design lightning protection for new aircraft. For example, the strike reports helped clarify the locations of lightning strike zones on transport-category aircraft, and alerted designers to potential lightning-induced voltage problems.

Strike reports continued to be received by General Electric but no further data summaries were published. In 1977, the project was transferred from General Electric Inc. to Lightning Technologies, Inc. By early 1984, (nearly 800 lightning strike reports had been accumulated) Lightning Technologies, Inc. invited the FAA Technical Center to participate in the project by statistizing the data through the use of computers. With the data in computer memory, it was possible to provide correlations among reported conditions and effects.

Whereas, the program began with five participating airlines (American, Braniff, Continental, Eastern and United), economic factors have made it necessary for Braniff, Continental, and Eastern to cease participation. Thus, for the past 5 years, data has been furnished only by United and American. These airlines, however, provide a large geographic data base.

REPORTING OF DATA.

One side of the questionnaire form (reference figure 1) request data on the synoptic weather conditions prevalent at the time and location of the strike; effects on cockpit electrical and

avionics equipment, and effects on the crew, (such as electric shock or flash blindness). These data were provided by the flight crew. The reverse side of the questionnaire form requested data on the physical marks or damage left on the aircraft external surfaces by the strike. For example, the location and size of burned marks and melted holes were requested. This information helped to establish the places where the lightning flashes entered and exited the aircraft, and thus, was important in establishing lightning strike "zones." This information cannot normally be provided by the flight crew, who have neither the time nor equipment to perform a thorough inspection of the aircraft following a strike. Instead, this information was to be provided by the airline maintenance personnel responsible for maintaining the aircraft. Unfortunately, unless the lightning strike has caused some noticeable physical damage to the aircraft (i.e., a hole in the radome) it was not required to be "written up" by the maintenance personnel. Also, the need for quick "turn around" of the aircraft provided little time for additional inspections. Therefore, in many cases the physical damage and strike location information has not been reported.

It must be noted that these reports were not part of the airline required post-flight reports. In most of the cases, the reports were prepared by the pilots in crew domiciles sometime after the flight. Report forms were then accumulated by a cognizant individual within each airline and periodically forwarded to Lightning Technologies, Inc.

AIRCRAFT TYPE.

This paper covers lightning strike information from 10 different transport type aircraft from the aforementioned air carriers. The aircraft type included Boeing B707, B727, B737, B747, and very recently B757 and B767 aircraft. Also included were Douglas DC-8, DC-9, DC-10 and Lockheed L1011 aircraft.

REDUCTION OF DATA.

Aircraft flight conditions and synoptic weather as reported by the flight crews had been correlated as a percentage of the total number of strikes reported. Included are altitude, temperature, month of the year during which the strike occurred, the degree of precipitation, (rain, snow, hail), the extent of the turbulence, (light, moderate, heavy), electrical activity before and after the strike, and the flight conditions (climb, level flight, descent, or approach). Histograms representative of the lightning strike information for each condition are presented in figures 2 through 14. No attempt has been made to cross-correlate two or more parameters, although this capability exists now that the data are stored in computer memory.

STRIKE BY MONTH.

Figure 2 lists the lightning strikes by the month and shows that the highest incident rates

occur during the spring (March, April, and May). This has been contrary to previously reported data which indicated the highest incident period reported during the summer (June, July, and August). December continues to display the lowest reported rate.

DATA INTERPERATION.

Operational Conditions - Aircraft operational conditions at the time of the strike were categorized under the headings of aircraft attitude, aircraft altitude, outside air temperature, location, weather, and electrical activities. For ease in analyzing the data, histograms were developed and used, as this methodology clearly shows the results.

- Aircraft Attitude - The highest percentage of aircraft received lightning strikes when climbing (37 percent), with 21 percent of the strikes reported during approach (figure 3).
- Aircraft Altitude - Transport type aircraft fly barometric altitude with the altimeter set at 29.92. This references the aircraft altitude to mean-sea-level (MSL). The data indicated that 36 percent of the aircraft were struck at altitudes below 10,000 feet MSL. Eighty-seven percent of the strikes are reported at altitudes of 16,000 feet MSL or less. Lightning strikes were reported at altitudes up to 40,000 feet MSL, figure 4.

The fact that most strikes occurred when the aircraft was at altitudes of 16,000 feet or less should not be taken as an indication that lightning is less prevalent at higher altitudes. On the contrary, it is well known that thunderclouds may extend up to 60,000 feet and lightning flashes occur throughout them. Also, the NASA F106B storm hazards research aircraft has encountered frequent lightning strikes on cloud penetrations above 20,000 feet, and photographs taken of cloud tops at night from satellites, high flying aircraft (Ref. 2), and the Space Shuttle have shown indications of frequent lightning activity. The reason that commercial aircraft do not encounter many lightning strikes at the higher altitudes is because of thunderstorm avoidance procedures.

- Outside Air Temperature - Previous reports indicated that most of the lightning strikes occurred at or near the freezing level $0^{\circ}\text{C} + 5^{\circ}\text{C}$. The data clearly shows that 72 percent of the air transport lightning strikes occurred at 0° through 22° Celsius. The data is shown in figure 5. Sixty-seven percent of the report contained outside air temperature information.
- Location - Cloud - A total of 92 percent of the reports stated aircraft location with reference to clouds. Of those reported, a total of 96 percent were within the cloud, with only 3 percent reported below the clouds, reference figure 6.
- Precipitation - Within the 92 percent reporting precipitation, a total of 81 percent were

associated with rain when struck with lightning. Further breakdown is as follows; 67 percent with rain only, 6 percent rain and snow, 2 percent rain and hail, and 6 percent rain and sleet. A histogram of these results are shown in figure 7.

- Turbulence - A total of 78 percent of the reports indicated turbulence which ranged from light to heavy. This information is shown in figure 8.
- Cloud Cover - The reported lightning strike incidents appear directly related to percent of cloud cover. As the amount of cloud cover increased, the lightning strikes reported increased. This is clearly shown in figure 9. Figure 10 shows that, as the ceiling increases, the potential for a strike diminishes. No strikes were reported with a ceiling greater than 11,000 feet above ground level. The reports showed that most of the strikes occurred when the cloud tops were reported to be around 15,000 feet (figure 11).

The cloud data confirmed that aircraft lightning strikes occur either while the airplane is flying through a cloud or relatively close to one. There were no reports of strikes while aircraft were flying "in the clear" at great distances from clouds, nor reports of "bolts from the blue." It has sometimes been suggested that clear air may become sufficiently electrified to produce lightning flashes; however, there is no such evidence in this data base.

- Electrical Activity - The results show that only 40 percent of the pilots observed lightning activity either before, before and after, or after receiving a lightning strike (figure 12). Fifty percent did not observe any 'P' static effects either before or after the strike (figure 13), and only 24 percent reported observing St. Elmo Fire. St. Elmo Fire is most readily detected during periods of reduced light and might not be detected in bright sunlight or active lighting conditions.

MONTH OF THE YEAR.

As expected, many of the strike reports occurred during the spring and early summer months when thunderstorm conditions are most prevalent in the United States, however, a significant number of strikes also occurred during the winter months of December and January when thunderstorms are not as frequent. Some of these latter strikes occurred when the aircraft were flying in snow, indicating that snowstorms may become highly electrified and produce lightning. One reason for the comparatively high incidence of lightning encounter during winter months may be that avoidance of these conditions is more difficult because the conditions which produce lightning in winter storms are not as well defined or understood as those associated with summer thunderstorms. It is comparatively easy for an aircraft to identify and avoid a well-defined summer thunderstorm comprised of cumulonimbus clouds

which contain heavy rain and reach very high altitudes. On the other hand, winter storms are more often associated with nimbostratus clouds which extend over wide areas and do not have intense rain cores easily detectable by weather radar.

THE RELATIONSHIP OF STRIKES TO NUMBER OF FLIGHT HOURS.

The number of flight hours of aircraft involved in this project was not available so no correlations could be made between the strikes and the total number of hours flown by the aircraft. Airline maintenance reports involving lightning damage seem to indicate that a typical aircraft is struck approximately once every 2500 flight hours, although public statistics of this nature are rare.

EFFECTS OF THE STRIKE.

The reported effects of the lightning strike were tabulated under the following headings; attachment points, interference/outage, effects on personnel, and electrical/electronic damage.

- Attachment Points - The exact location of lightning attachment points are generally uncovered during the post-lightning strike ground inspection. Due to the size of transport type aircraft, and the complexity of locating the exact attachment points, many times the attachment points are often not located and reported.

This was evident in analyzing the data, as a total of 672 did not indicate the attachment points. Of the total 253 attachment points recorded, 28 percent were to the nose of the aircraft, with approximately 50 percent reported to the fuselage at some point. The remainder of the attachments were divided equally between the wings and tail.

- Interference/Outage - Of the total 783 reports, 87 reported outages. These outages required ground crew maintenance (either repair or replacement). The navigation systems had 30 instrument outages with only six communication systems impacted. Engine instruments had a total of 39 outages. This information is shown in figure 14.

- Effects on Personnel - Ninety-one reports stated effects on crew members. Of those reported, 80 consisted of momentary flash-blindness with only one report of electrical shock to personnel. This information is shown in figure 15.

- Electrical/Electronic Damage - From the 783 reports, only 3.1 percent (25 reports) stated any impact to the electrical/electronic systems. No engine flameouts were reported. This information is shown in figure 16.

SUMMARY AND CONCLUSIONS.

All metal transport type aircraft, when struck by lightning, will not generally sustain significant structural damage, but may encounter interference or outage of navigation, communication, or engine instruments. The reports indicated that temporary flash blindness has been the major problem for personnel.

The information gained in this report clearly shows that the aircraft manufacturers, because of increased awareness (of lightning related effects) and application of good lightning protection practices, and qualification test have designed and built all metal transport type aircraft capable of sustaining lightning strike without serious impact to the aircraft, passengers, or crew members.

The potential atmospheric electrical hazard to aircraft will challenge the designers of future generation aircraft employing advanced technology, structural materials, and critical microelectronic digital flight control systems. These designs will require close coordination between the designers, manufacturers, and FAA certification specialists to ensure that aircraft are capable of sustaining a direct lightning strike without damage to the aircraft, electronic systems, passengers, or crew.

REFERENCES.

1. "Data from the Airlines Lightning Strike Reporting Project," General Electric Company, Report GPR-75-004, dated March 1975.

2. Technical paper or report by NASA Manned Spaced Flight Center Huntsville, Alabama on U-2 photographs.

1

The purpose of this report is to gather data relating lightning strikes on mobile electronic systems to aircraft type and flying conditions. This data will be used in support of research efforts leading to the development of lightning protection systems.

Please complete and file this report (immediately following your flight, providing as much of the requested data as you can.

446 448 450 452 454 456 458 460 462 464 466 468 470 472 474 476 478 480 482 484 486 488 490 492 494 496 498 500 502 504 506 508 510 512 514 516 518 520 522 524 526 528 530 532 534 536 538 540 542 544 546 548 550 552 554 556 558 560 562 564 566 568 570 572 574 576 578 580 582 584 586 588 590 592 594 596 598 600 602 604 606 608 610 612 614 616 618 620 622 624 626 628 630 632 634 636 638 640 642 644 646 648 650 652 654 656 658 660 662 664 666 668 670 672 674 676 678 680 682 684 686 688 690 692 694 696 698 700 702 704 706 708 710 712 714 716 718 720 722 724 726 728 730 732 734 736 738 740 742 744 746 748 750 752 754 756 758 760 762 764 766 768 770 772 774 776 778 780 782 784 786 788 790 792 794 796 798 800 802 804 806 808 810 812 814 816 818 820 822 824 826 828 830 832 834 836 838 840 842 844 846 848 850 852 854 856 858 860 862 864 866 868 870 872 874 876 878 880 882 884 886 888 890 892 894 896 898 900 902 904 906 908 910 912 914 916 918 920 922 924 926 928 930 932 934 936 938 940 942 944 946 948 950 952 954 956 958 960 962 964 966 968 970 972 974 976 978 980 982 984 986 988 990 992 994 996 998 1000

THE UNIVERSITY OF CHICAGO PRESS

PAGE 1 (TO BE COMPLETED BY FLIGHT CREW)

Operational Conditions at Time of Strike

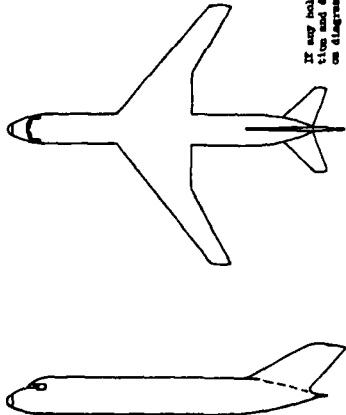
• Flight No. _____ Date _____ Time of Strike _____ Aircraft type _____
• Route _____ To _____ HSE Routing _____ Mile from _____
• Altitude _____ Ft./ Air Speed _____ Kts./
• Condition: Approach _____ Climb _____ Level Flight _____ Other _____
• Area Weather: Cloud Type _____ \$ Cover _____ Ceiling (ft.) _____ Temp at (ft.) _____ Dew Pt. (°C) _____
At time of strike aircraft was: Above Clouds _____ Within Clouds _____ Below Ceiling _____
• Experiencing: None _____ Light _____ Med. _____ Heavy _____ Turbulence _____
• Any lightning precipitation in form of: Rain _____ Sleet _____ Hail _____ Snow _____
• Were there lightning flashes in vicinity Before _____ After _____ Neither
• Were you aware of electrical activity (static) Before _____ After _____ Neither
• Was Mr. Elm's fire visible before impact Yes _____ No _____

Experiencing: (Check Which)
Interference
Outage

Compass	1-2	2	1-2	2	Any Effects on: (Check Which)
Weather Radar	1-2	2	1-2	2	AC Power System
VOR Receiver	1-2	2	1-2	2	DC Power System
ILS G/S	1-2	2	1-2	2	Flight Controls
LP AXP	1-2	2	1-2	2	Engine Fuelcock
IRS	1-2	3	1-2	2	Any Effects on Personnel, such as:
Radio Alt.	1-2	2	1-2	2	Flesh Wounds
CAS	1	2	1	2	Electric Shock
VDF QDM	1-2	3	1-2	3	
HQ QDM	1-2	2	1-2	2	
Adopt Pilot	1-2	2	1-2	2	
Other	1-2	2	1-2	2	

Additional Comments (Further Description of Effects Checked Above Such as Error Codes, Etc.) _____

PAGE 1 Completed By _____

PART II (TO BE COMPLETED BY GROUND CREW):
 Please mark strike attachment points (burn marks) on generalized aircraft sketch below. Add engine or other components, if necessary, to show attachment points.
 Indicate whether top or bottom, starboard or port, etc.


Sketch here an enlargement of the area struck (i.e., wing tip, flap, etc.). Show details such as successive pitting (severe striker) markings, etc. Fill in sketch photos if possible.

If any holes were burned through the skin, indicate location and diameter; (key to locations indicated by numbers on diagram above).

Location	Hole Diam. (In.)	Estimated Damage and Skin Material
1		
2		
3		

Describe any damage to aircraft structure or external components believed to be the result of the lightning strike.

Describe any damage to avionics or electrical components believed to have occurred as a result of the lightning strike.

PART II Completed by _____

FIGURE 1. QUESTIONNAIRE TYPE REPORTING FORM

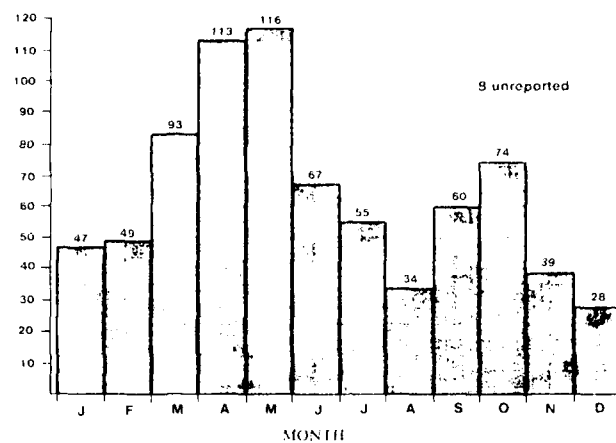


FIGURE 2. STRIKES PER MONTH

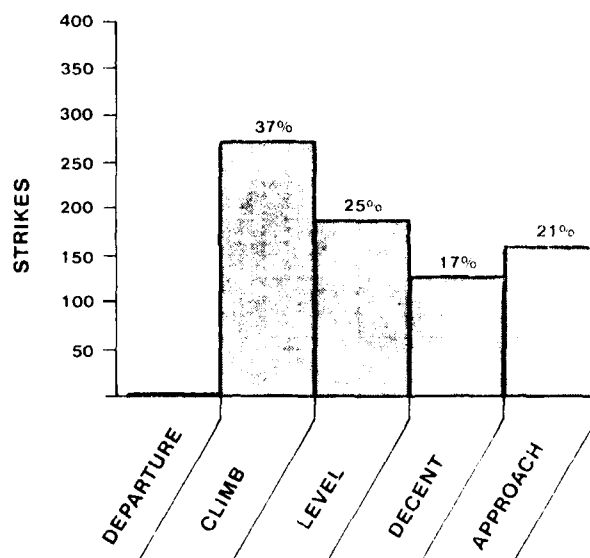


FIGURE 3. AIRCRAFT ATTITUDE

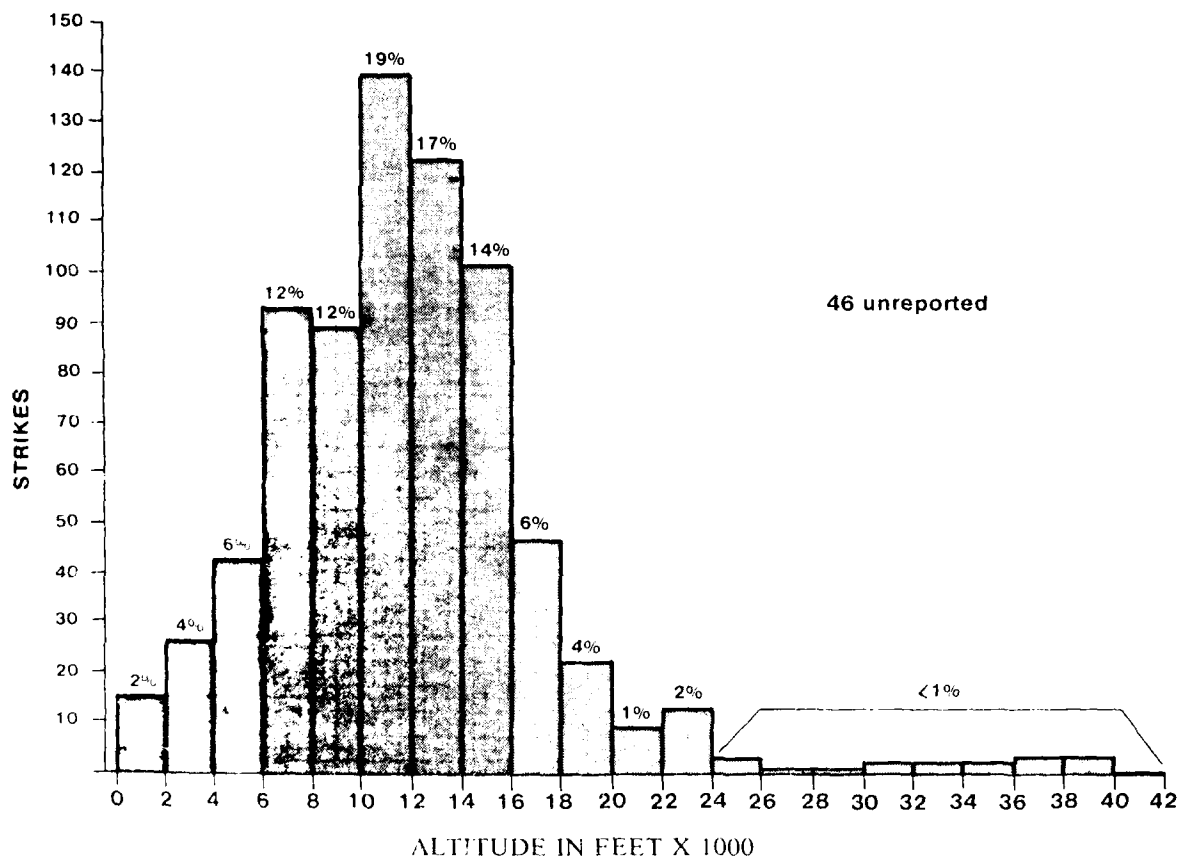


FIGURE 4. AIRCRAFT ALTITUDE

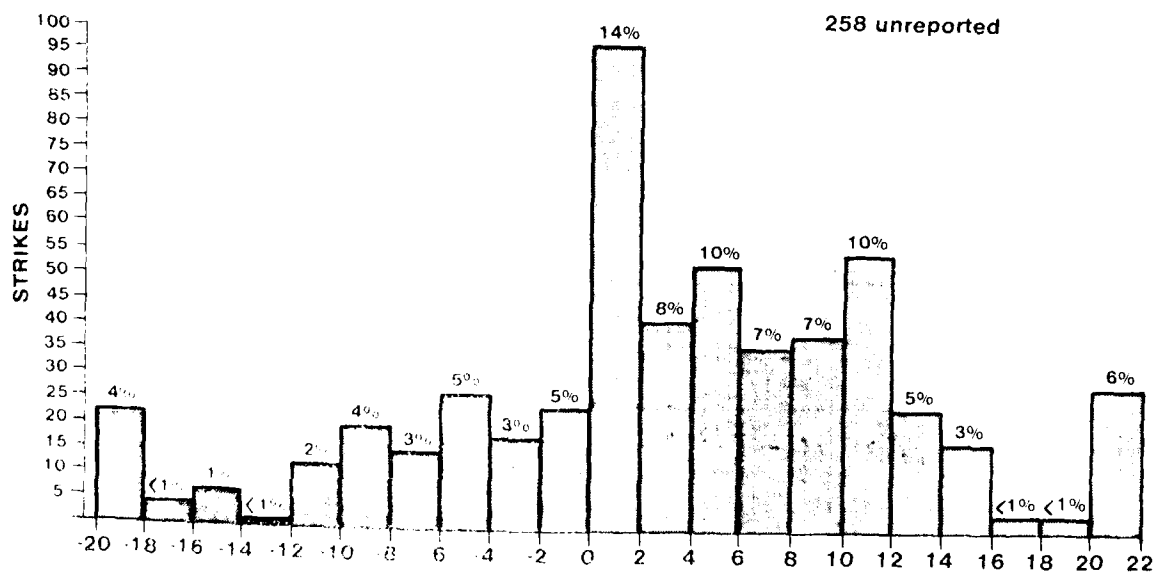


FIGURE 5. TEMPERATURE IN DEGREES (CELSIUS)

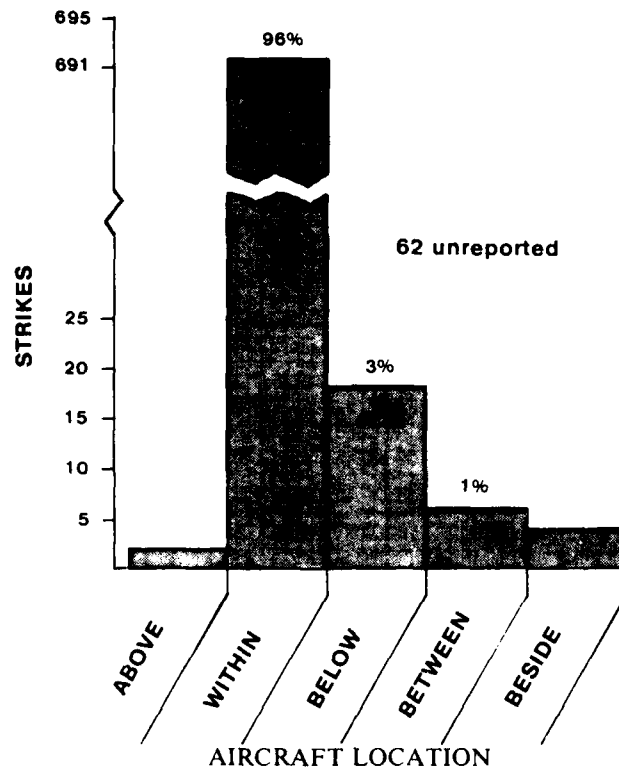


FIGURE 6. AIRCRAFT - CLOUD REFERENCE

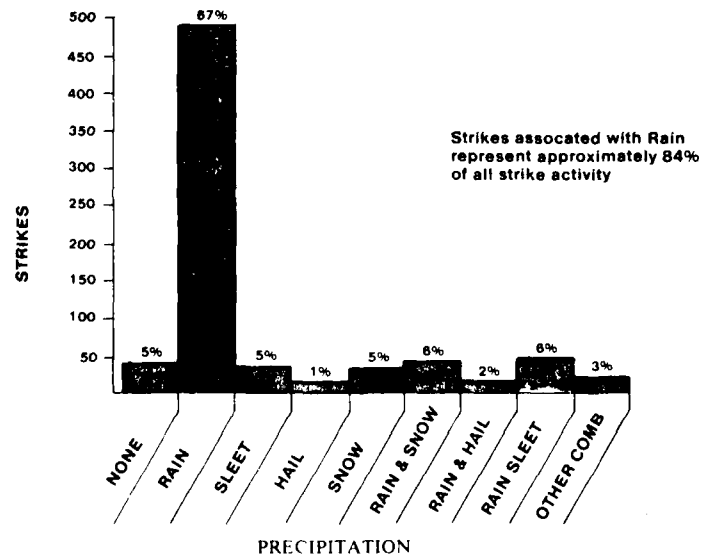
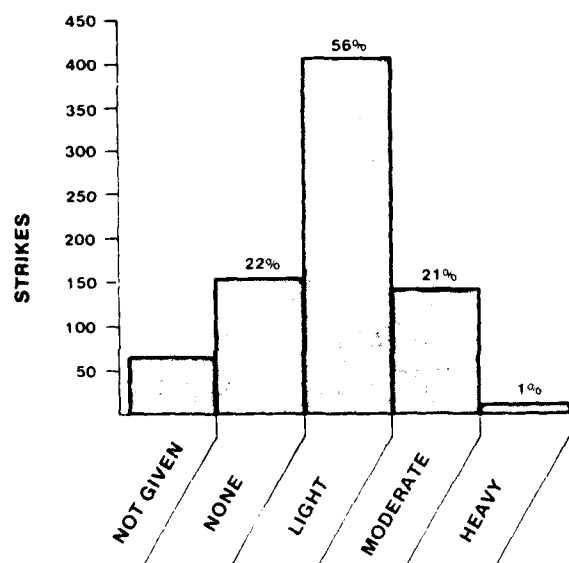


FIGURE 7. PRECIPITATION

TURBULENCE NOTED



TURBULENCE

FIGURE 8. TURBULENCE NOTED

CLOUD COVER

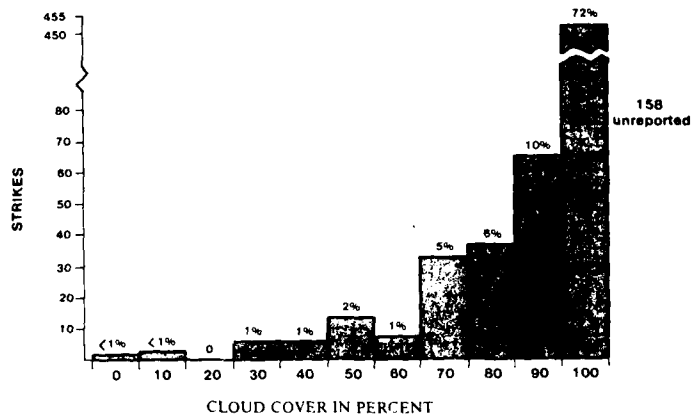


FIGURE 9. CLOUD COVER

CEILING

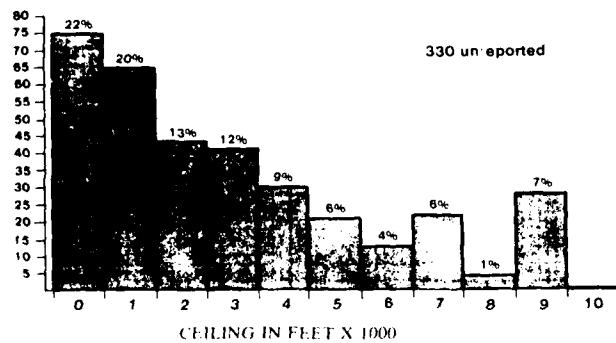


FIGURE 10. CEILING

CLOUD TOPS

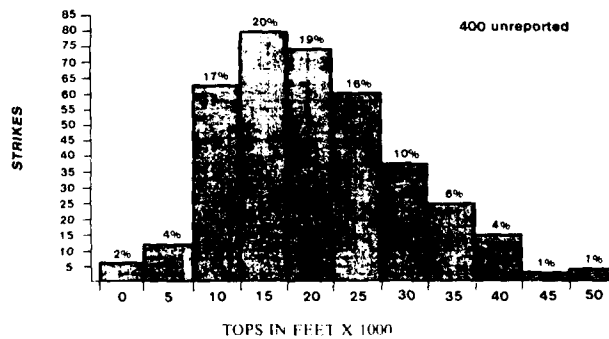


FIGURE 11. CLOUD TOPS

AD-A169 867

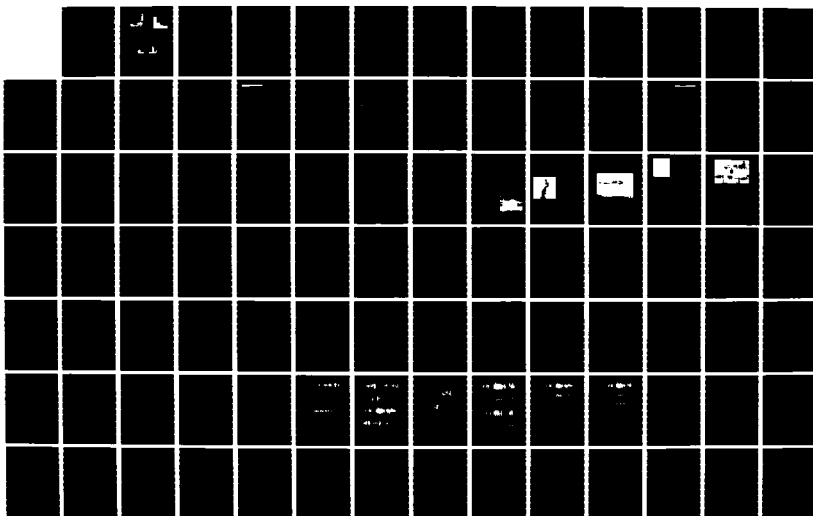
INTERNATIONAL AEROSPACE AND GROUND CONFERENCE ON
LIGHTNING AND STATIC ELE. (U) NATIONAL INTERAGENCY
COORDINATION GROUP JUN 84

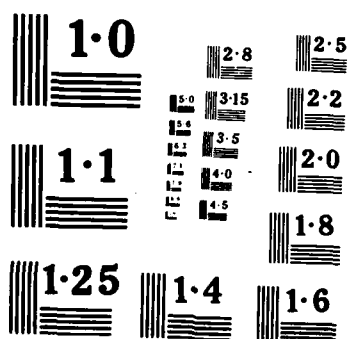
3/6

UNCLASSIFIED

F/B 28/3

NL





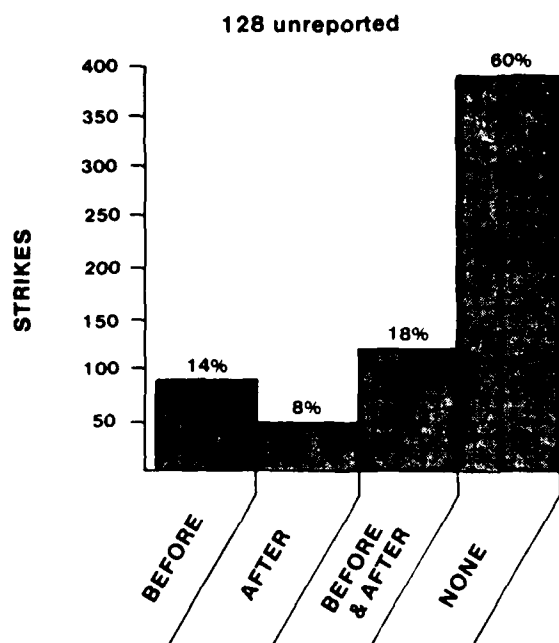


FIGURE 12. OBSERVED LIGHTNING ACTIVITIES PRIOR TO STRIKE

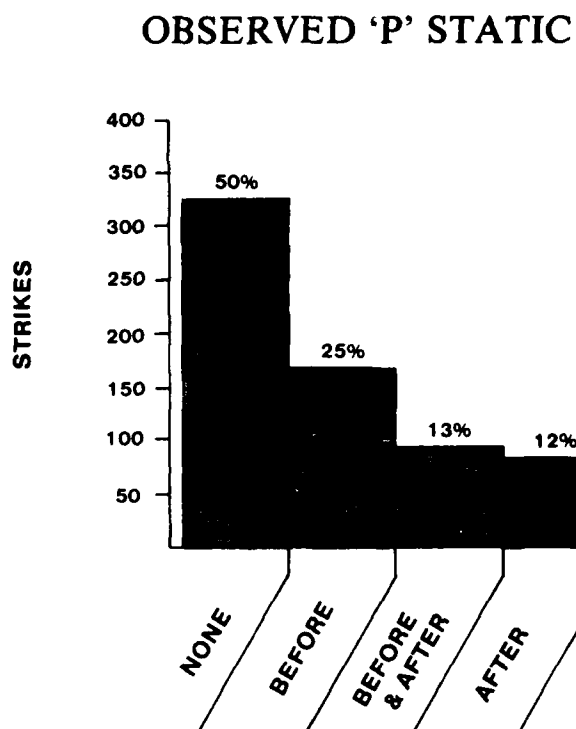


FIGURE 13. OBSERVED "P" STATIC

ELECTRONIC EQUIPMENT IMPACT DUE TO LIGHTNING STRIKES

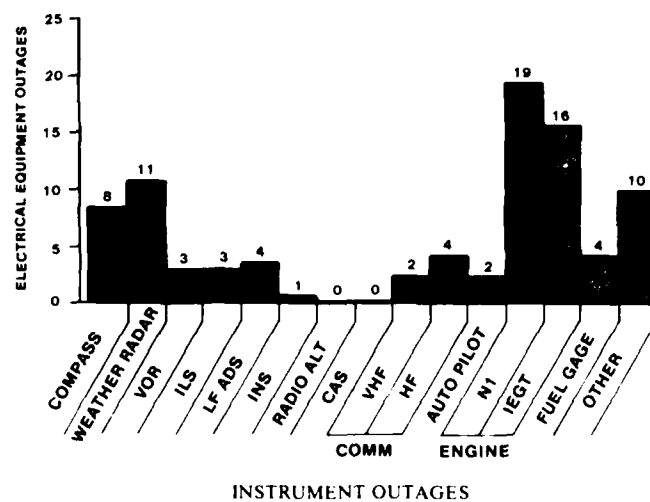


FIGURE 14. ELECTRONIC EQUIPMENT IMPACT DUE TO LIGHTNING STRIKES

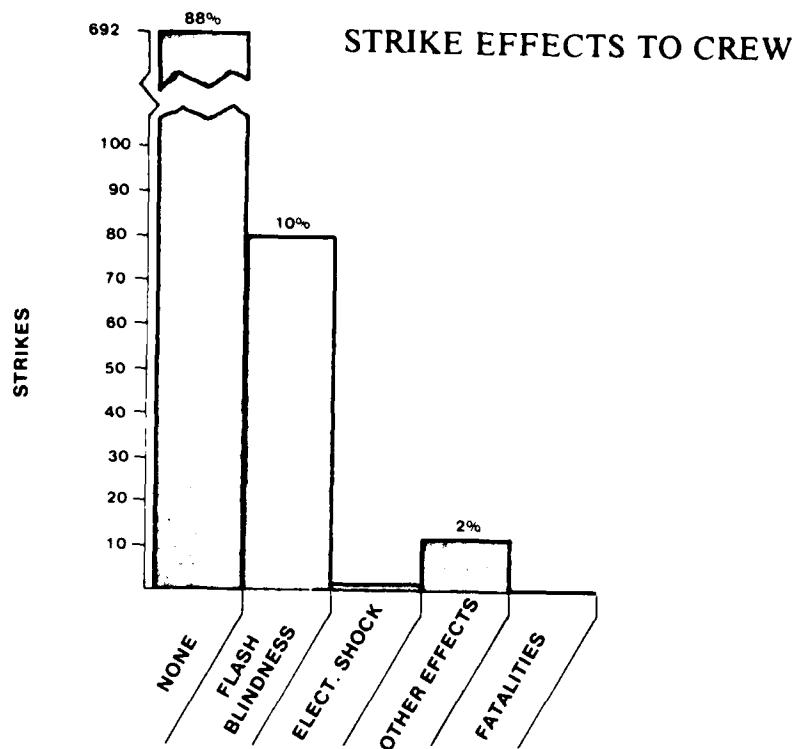


FIGURE 15. STRIKE EFFECTS TO CREW

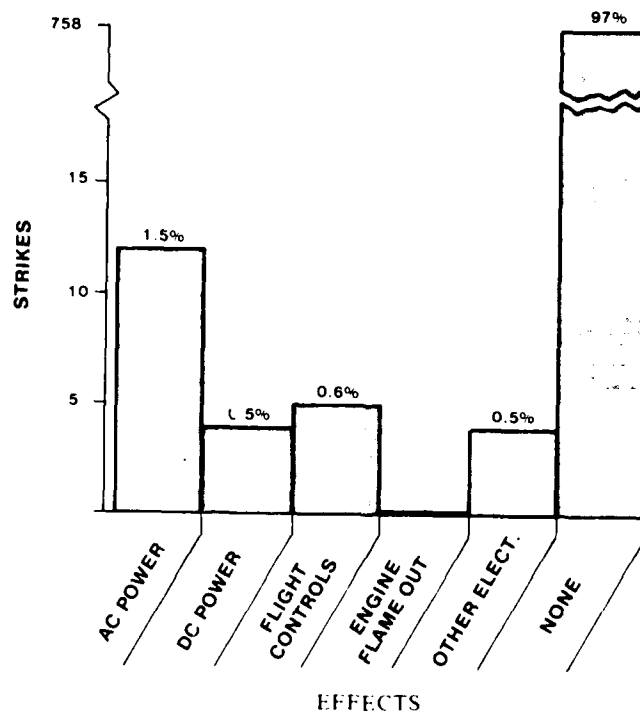


FIGURE 16. ELECTRICAL ELECTRONIC EFFECTS

THE AMPLITUDE SPECTRA OF LIGHTNING RADIATION FIELDS IN THE INTERVAL FROM 1 TO 20 MHz

E. P. Krider and C. D. Weidman†

Institute of Atmospheric Physics, University of Arizona, Tucson, Arizona

ABSTRACT

Although the interactions of lightning with aircraft and many other structures are critically dependent on the amplitudes of lightning fields in the 1 to 20 MHz frequency interval, there are relatively few absolute measurements of these spectra in the lightning literature. In this paper, we tabulate the amplitude spectra of the fast-rising components of the fields produced by return strokes, leader steps, and cloud pulses. These spectra have been derived from ground-based measurements of E and dE/dt signatures, and, in several cases, the effects of propagation over land are illustrated.

† Present Address: Centre National d'Études des Télécommunications, 22301 Lannion, FRANCE

INTRODUCTION

ELECTRIC AND MAGNETIC FIELDS produced by various lightning processes have received serious scientific study for over 200 years, but it has been only within the past decade that their detailed structure has been determined and that realistic models to describe these fields in terms of lightning currents have been developed [1]*. Recent measurements of lightning fields with submicrosecond time-resolution [2 - 8] have shown that most components of a discharge produce large changes in the field in a fraction of a microsecond, and it is now clear that these changes are at least an order of magnitude faster than was believed to be present just 10 years ago (see, for example, [9]).

It is reasonably well-known that the interactions of lightning fields and other types of EMP with aircraft, space vehicles, ships, and other systems are critically dependent on the risetimes of these fields and their spectral amplitudes in frequency intervals that contain the structure resonances [10 - 13]. Since the physical dimensions of many structures are in the range from 10 to 100 m, frequencies in the range from about 1.5 to 15 MHz (i.e., frequencies for which half of the associated wavelength equals the structure dimension) are of primary interest.

Except for the preliminary reports of Weidman et al. [8, 14], the currently available measurements of lightning amplitude spectra are limited to (1) the return stroke component, and then only for frequencies below about 300 kHz [15 - 17] and (2) spectra compiled from the outputs of narrow-band receivers [18 - 21]. The latter data have not, in general, been used to determine the spectra of individual discharge processes. Further, almost all previous measurements have been for discharges that occurred at distances of 10 km or more over land, and at these ranges frequencies above about 100 kHz can be strongly attenuated by the finitely conducting earth [16, 22-24]. In this report, we present Fourier transforms of time-domain lightning dE/dt signatures that cover the frequency interval from 1 to about 20 MHz.

DATA

The experimental apparatus that has been used to record the E and dE/dt fields and examples of the data have been given previously by Weidman and Krider [2, 4, 5, 8]. All data were obtained under conditions where the lightning locations were known and where the field propagation from the source to the recording site was entirely over salt water. Therefore, we believe that the amplitudes and shapes of the fields were not distorted by the effects of propagation below about 20 MHz. E signatures were recorded on both a slow and a

fast time scale so that the precise time that the dE/dt occurred within the E pulse could be determined. The E-field measuring system had a 10 - 90% risetime of about 40 ns, and the dE/dt system had a risetime of about 10 ns. The type of lightning process that produced a particular impulse (e.g., return stroke, leader step or a cloud pulse) was determined from the overall shape of the E signature. For specific examples of the data, the reader should see [5] and [14].

If the electric field, E, and its derivative, dE/dt, are continuous functions of time, then the Fourier transform of E, F(E), can be derived from the transform of the derivative, F(dE/dt), using the relation

$$F(E) = F(dE/dt)/(2\pi jf) \quad (1)$$

where j is $\sqrt{-1}$ and f is frequency. Since a dE/dt measurement cannot be expressed as a continuous function, the measurements are first digitized (sampled) and the discrete Fourier transform (DFT) is computed using a fast Fourier transform (FFT) algorithm. The DFT of a finite sequence of sample points, $g(t)$, is given by

$$F_d(f) = F_d(nf_0) = \Delta t \sum_{k=0}^{N-1} g(k\Delta t) e^{-2\pi jfk\Delta t} \quad (2)$$

where $0 \leq n \leq N-1$, and N is the total number of sample points. Here f_0 , the fundamental frequency, is equal to unity over the total period of the record, T_0 , and Δt (the sample interval) is equal to T_0/N . Note that $F_d(f)$ is complex and that it contains N equally spaced points (at intervals of f_0) in the frequency domain.

The discrete Fourier transform of E, $F_d(E)$, can be obtained from dE/dt records, either by integrating dE/dt and using Equation (2) or directly using

$$F_d(E) = \frac{\Delta t F_d(dE/dt)}{2j \tan(\pi f \Delta t)} - \frac{\Delta t^2}{1 - e^{-2\pi j f \Delta t}} \sum_{k=0}^{N-1} (dE/dt)_k \quad (3)$$

where $(dE/dt)_k$ indicates the value of dE/dt at $t = k\Delta t$. Note that in the limit of $\Delta t \rightarrow 0$, this expression reduces to $F_d(E) = F_d(dE/dt)/2\pi jf$, which is the same as Equation (1).

To compute a spectrum, dE/dt oscilloscope waveforms were first manually digitized using a Tektronix 4662 digitizing plotter. The number of sample points depended on the time resolution of the record and on the complexity of the waveform. Usually, 50 ns/div records were digitized using 30 to 50 sample points, and 100 ns/div records were digitized using 50 to 80 points. The FFT algorithm required that the sample points be evenly spaced in time and that the total number, N , be an integral power of 2. Evenly spaced data for the FFT calculation were generated by linearly interpolating between the

* Numbers in brackets designate References at end of paper.

manually digitized sample points. Usually 64 or 128 FFT points were computed so that the evenly spaced time interval would be about equal to the smallest sampling interval.

The E and dE/dt signatures were recorded during the summers of 1979, 1980, and 1981 in Florida, where there was an abundance of lightning and where the propagation distortion was small. For the 1979 data, the front edges of the dE/dt waveforms were elevated by the finite trigger threshold and were linearly interpolated back to zero, but the spectral amplitudes in the interval 1 to 20 MHz were not sensitive to small differences in the shape of this interpolation [14]. The differences in spectra with and without the artificial front were small, usually less than 2 dB, and never more than 5 dB. The 1980 and 1981 records were obtained using a 150 ns delay line, and these data usually began with a small, but non-zero amplitude that was not interpolated back to zero. All dE/dt records were terminated abruptly after 500 or 1000 ns, and the amplitude of the signal at the end of this interval was usually small but not exactly zero.

RESULTS

RETURN STROKES — In general, the shape of the electric field radiated by a return stroke depends on whether it is the first return stroke in a flash, a subsequent return stroke, or a subsequent return stroke that is preceded by a dart-stepped leader [2]. First stroke fields begin with a relatively slow "front" that rises for 2 to 8 μ s to about half of the peak field amplitude. This front is followed by a fast transition to peak, and it is this fast transition that is of primary interest in this report. Subsequent strokes produce fields that have fast transitions very similar to first strokes, but fronts that last only 0.5 to 1 μ s and that rise to only about 20% of the peak field amplitude.

The result of Fourier analyses of dE/dt fields radiated during the fast return stroke transition are summarized in Table 1. The spectral amplitudes are given in dB from a reference level of 1 V/m/s, and the values were computed, in most cases, by taking 20 times the logarithm (base 10) of the magnitude of $F_d(E)$ in Eq. (3). Sometimes the dE/dt waveforms were first integrated and then $F_d(E)$ was calculated using Equation (2). The reasons for using this latter method will be discussed below.

The spectral amplitudes at 2, 4, 10 and 20 MHz for first strokes that struck water 40 to 60 km NNW of the 1979 recording site and that propagated entirely over salt water are given in rows (a) and (b) of Table 1. The strokes in row (a) were located by a lightning locating system, and the field amplitudes have been range-normalized to 50 km using an inverse distance relation. The strokes in row (b) were from the same direction as data in row (a), but were not located and have not been range-

normalized. The mean spectral amplitude in row (a) is very nearly the same as row (b), which indicates that the mean range for this group was probably close to 50 km.

The data in row (c) are from first return strokes that struck within 8 to 12 km of the recording site in 1981. The locations of all flashes were determined from a lightning locating system, and the field amplitudes have all been normalized to 10 km using an inverse distance relation. The propagation path for all data in row (c) has been identified as "mostly water" because small errors in the lightning locations made it impossible to determine whether the actual strike point was to land or to water. At worst, these fields propagated over about 1 km of land and then entirely over water to the recording site. The pulse widths and peak dE/dt values for the "mostly water path" data in row (c) were essentially identical to those of fields that propagated entirely over water.

Some of the 1981 dE/dt data were recorded on a time scale of 100 ns/div, and the fundamental frequency of these records (f_0) is 1 MHz. The remaining dE/dt data were recorded on a 50 ns/div time scale, and in these cases the fundamental frequency is 2 MHz.

The strokes in rows (d), (e), and (f) in Table 1 struck water SW of the 1979 recording station at Tampa Bay. Fields from strikes in that direction had to propagate across the width of Anna Maria Island (about 1.5 to 2 km of sand) before reaching the measuring site. The three strokes in row (d) were located by the lightning locating system, and these data have been range normalized to 25 km. The data in row (e) appeared to be from the same storm, but were not detected by the lightning locating system. Note that there is essentially no difference in the mean spectral amplitudes in rows (d) and (e), so it is probably safe to assume that the data in row (e) also originated at a range of about 25 km. The subsequent strokes in row (f) were located by the lightning locating system, but the location accuracy was not good because the strikes were near the baseline and these data have not been range-normalized.

The data in Table 1 are grouped into three vertical columns. The spectral amplitudes in the left and right-most columns are based on Fourier analyses of dE/dt waveforms. The data in the center column are based on Fourier analyses of time-integrated dE/dt records. Data were placed in the left column if, at the point where the finite dE/dt record terminated, the integral of dE/dt had an amplitude that was greater than 40 percent of the peak. To reduce truncation errors, or at least to determine at what frequencies they become significant, the dE/dt data in the left column of Table 1 have been integrated and then multiplied by a windowing function $W(t)$, where

$$\begin{aligned} W(t) &= 1 & 0 < t < T_0 - 50 \text{ ns} \\ W(t) &= 0.5[1 - \cos(2\pi t/100)] & T_0 - 50 \text{ ns} < t < T_0 \end{aligned} \quad (4)$$

and T_0 is the record period. This function forces E to be zero at $t = T_0$ and smoothes the sharp edge at the end of the E record. The resulting waveform was then Fourier analyzed using Equation (2), and these spectral amplitudes are shown in the center column of Table 1. In three cases, the integral of dE/dt had returned to near zero (between 10 and 30 percent of the peak) by the end of the record, and the spectral amplitudes for these events are listed in the right column of Table 1. Clearly, the truncation errors should be smallest for these events.

The differences in the mean spectral amplitudes of the first return strokes in Table 9 are due largely to range differences. If we assume that these amplitudes are all inversely proportional to distance, then all data are in good agreement. The spectral amplitudes of the data which originated SW of the Tampa site and which propagated over 1.5 to 2 km of land are not substantially different from those of fields that propagated entirely over water.

The average, range-normalized (to 50 km) spectral amplitudes of the first return strokes in Table 1 are plotted in Figure 1. Curve (1) gives the means for the 24 first return strokes which are listed in the left column of Table 1. The means at discrete frequencies in the transform (1 MHz, 2 MHz, and at intervals of 2 MHz thereafter to 20 MHz) were simply connected together to form this curve. Curves (2) and (3) show the means for the first stroke amplitudes in the center and right columns in Table 1, respectively. Note that curve (1) decreases with frequency very nearly as $1/f$, a slope that represents a superposition of the true source spectrum plus the truncation errors. Curves (2) and (3) are similar to curve 1 to about 6 MHz, but beyond this point, curves (2) and (3) decrease more nearly as $1/f^2$. We have tried to reduce the truncation errors in curve (2), and the truncation errors in curve (3) should be smaller than those in curve (1); therefore, we think that curves (2) and (3) are the best estimate of the true spectrum of the lightning source.

The two additional curves shown in Fig. 1 in the intervals from 2 to 300 kHz and from 100 kHz to 1 MHz are the mean first return stroke spectra given by Serhan et al. [16] and by Weidman et al. [14], respectively, for 50 km. These spectral amplitudes were derived from Fourier analyses of E waveforms with total periods of 200 μ s [16] and 40 μ s [14]. Both curves are in good agreement in the interval from 100 to 300 kHz where they overlap, and the Weidman et al. data agree well with the amplitudes presented here at 1 MHz. It should be noted that Weidman et al. [14] have pointed out that because their and the Serhan et al. [16] transforms are derived from long-duration E records, they probably include components that are radiated by different physical processes and that occur over a geometrically large source. The dE/dt records, on the other hand, have a

total duration of only 500 or 1000 ns, and are, therefore, probably produced by just a single discharge channel of relatively limited spatial extent.

The spectral amplitudes of subsequent return strokes are plotted in Fig. 2. Curve (1) shows means from the left column of row (f) in Table 1, and curve (2) shows the data from the center column. Again, both spectra are nearly identical from 2 to about 6 MHz, but beyond 6 MHz, the truncation errors in the upper spectrum limit its decrease to $1/f$. The lower curve, for which truncation errors have been reduced, decreases with frequency more nearly as $1/f^2$. The mean subsequent stroke amplitudes in Figure 2 are about 5 to 8 dB higher than the mean, first return stroke amplitudes in Fig. 1, which is probably the result of uncertain subsequent stroke ranges. Again, the mean subsequent stroke spectrum of Serhan et al. [16] is shown for comparison.

LEADER STEPS AND CLOUD PULSES — The overall shapes of the fields radiated by individual steps of the stepped-leader have been discussed by references [25, 26, 5, 6, 7]. As the leader nears the ground, the amplitude of the individual step impulses increases, and occasionally such a step triggered our E or dE/dt recording system just before there was a return stroke. The maximum dE/dt occurs during the initial rise of the step waveform, and it is this portion of the waveform that is of interest in this report.

The overall shapes of the radiation fields that are produced by intracloud discharge processes have been discussed by [27, 28]. In general, the shapes of the larger pulses tend to be bipolar with several fast unipolar impulses superimposed on the initial half-cycle. These unipolar structures have fast risetimes, and the dE/dt signatures radiated during these transitions are very similar to the shapes of the signatures produced by return strokes.

Tables 2 and 3 show the amplitude spectra of the fast transitions in a limited number of leader steps and cloud pulses, respectively. These spectra were derived from dE/dt data that were obtained at the same time as the return strokes in Table 1, and, therefore, the locations of the lightning and the field propagation to the recording site should be the same in Tables 2 and 3 as for Table 1. The fields in rows (c) and (d) of Table 3 originated over water to the NE, and in this direction the field propagation was entirely over water.

The data in Tables 2 and 3 have been grouped according to the shape of the integrated dE/dt waveform. In all cases, the integral of dE/dt is positive, and there is little variation in the shape of the initial portion of the waveform. Any differences in the integrals usually appear after the first peak. For the events in the left columns of both tables, the integral of dE/dt remained large and positive for the entire duration of the record, and the final amplitude was at least 40% of the peak. Just as in the case of return strokes, any truncation of the

record will introduce errors into the frequency spectra, and therefore Fourier amplitudes of these same data after having been multiplied by the windowing function (Equation 4) are given in the second column (Column 2). Because of the windowing the truncation errors in these spectra should be less than the spectra of column (1).

Occasionally, the integral of dE/dt crossed zero or approached zero well before the end of the record. In these cases, the width of the first half cycle was narrow and the amplitude at the end of the record was of either positive or negative polarity. The spectral amplitudes for this second class of waveforms are listed in columns (3) and (4) of Tables 2 and 3, respectively. These data also have truncation errors because the final amplitudes were still between 15 and 60 percent of the initial peak. The spectral amplitudes of these bipolar data, after being multiplied by Equation (4), are given in columns (4) and (5) of Tables 2 and 3, respectively.

For cloud discharges, a third class of waveform was observed, wherein the integral of dE/dt remained positive for all but the final 50 ns of the record. The final value of the integral could be either positive or negative, but was always less than about 15% of the peak. Transforms of these data are given in Column (3) of Table 3, and here the truncation errors should be less than for either of the other two types of waveforms.

SUMMARY

We have tabulated the amplitude spectra of the fast field transitions in lightning return strokes and a limited number of leader steps and cloud pulses. The spectral amplitudes in all these processes tend to be rather similar and large. For example, the return-stroke spectrum may even exceed that of a nuclear electromagnetic pulse up to a few MHz [29]. Clearly, these lightning processes warrant further study.

ACKNOWLEDGMENT

This research has been supported in part by the Office of Naval Research, Contract N00014-81-K-0175. The final manuscript was edited by Margaret Sanderson Rae.

REFERENCES

1. M.A. Uman and E.P. Krider, "A Review of Natural Lightning: Experimental Data and Modeling", IEEE Trans. on EMC, Vol. EMC-24, pp. 79-112, 1982.
2. C.D. Weidman and E.P. Krider, "The Fine Structure of Lightning Return Stroke Wave Forms", J. Geophys. Res., Vol. 83, pp. 6239-6247, 1978.
3. R.P. Fieaux, C.H. Gary, B.P. Hutzler, A.R. Eybert-Berard, P.L. Hubert, A.C. Meesters, P.H. Perroud, J.H. Hamelin, and J.M. Person, "Research on Artificially Triggered Lightning in France", IEEE Trans. Power Apparatus and Systems, PAS-97, pp. 725-733, 1978.
4. C.D. Weidman and E.P. Krider, "Sub-microsecond Risetimes in Lightning Return Stroke Fields", Geophys. Res. Lett., Vol. 7, pp. 955-958, 1980.
5. C.D. Weidman and E.P. Krider, "Sub-microsecond Risetimes in Lightning Radiation Fields", in Proc. Lightning Technology, NASA Conf. Pub. 2128 and FAA-RD-80-30, pp. 29-38, April 1980.
6. C.E. Baum, E.L. Breen, D.L. Hall, C.B. Moore, and J.P. O'Neill, "Measurements of Electromagnetic Properties of Lightning with 10 Nanosecond Resolution", in Proc. Lightning Technology, NASA Conf. Pub. 2128 and FAA-RD-80-30, pp. 39-82, 1980.
7. C.E. Baum, E.L. Breen, F.L. Pitts, G.D. Sower, and M.E. Thomas, "The Measurement of Lightning Environmental Parameters Related to Interaction with Electronic Systems", IEEE Trans. on EMC, Vol. EMC-24 pp., 123-137, 1982.
8. E.P. Krider and C.D. Weidman, "The Submicrosecond Structure of Lightning Radiation Fields," in Proc. 8th Int. Aerospace and Ground Conf. on Lightning and Static Electricity, DOT/FAA/CT-83/25, pp. 69.1 - 69.8, Ft. Worth, TX, June 21-23, 1983.
9. R.J. Fisher and M.A. Uman, "Measured Electric Field Risetimes for First and Subsequent Lightning Return Strokes", J. Geophys. Res., 77, pp. 399-407, 1972.
10. D.W. Clifford, E.P. Krider, and M.A. Uman, "A Case for Submicrosecond Risetime Lightning Current Pulses for Use in Aircraft Induced-Coupling Studies", Int. Symp. on EMC, San Diego, Oct. 9-11, 1979.
11. F.M. Tesche, "Topological Concepts for Internal EMP Interaction", IEEE Trans. on EMC, EMC-20, 60-64, 1978.
12. C.D. Taylor, "External Interaction of the Nuclear EMP with Aircraft and Missiles", IEEE Trans. on EMC, EMC-20, 64-76, 1978.
13. C.M. Butler, Y. Rahmat-Samii, and R. Mittra, "Electromagnetic Penetration through Apertures in Conducting Surfaces", IEEE Trans. on EMC, EMC-20, pp. 82-93, 1978.
14. C.D. Weidman, E.P. Krider, and M.A. Uman, "Lightning Amplitude Spectra in the Interval from 100 kHz to 20 MHz," Geophys. Res. Lett. vol. 8, pp. 931-934, 1981.
15. W.L. Taylor, Radiation Field Characteristics of Lightning Discharges in the Band 1 kc/s to 100 kc/s, J. Res. Natl. Bur. Stand., vol. 67D, pp. 539-550, 1963.
16. G.I. Serhan, M.A. Uman, D.G. Childers, and Y.T. Lin, "The RF Spectra of First and Subsequent Lightning Return Strokes in the 1- to 20-km Range", Radio Sci., vol 15, pp. 1089-1094, 1980.
17. J. Preta, Jr., M.A. Uman, and D.G. Childers, "The Electric Field Spectrum of Lightning Return Strokes: Correction to Serhan et al. (1980)", submitted to Radio Science, October 1983.

18. A. Kimpapa, "Electromagnetic Energy Radiated From Lightning", in "Problems of Atmospheric and Space Electricity", S.C. Coroniti (ed.), Elsevier, New York, pp. 352-365, 1965.

19. L.L. Oh, "Measured and Calculated Spectral Amplitude Distribution of Lightning Sferics", IEEE Trans. Electromagnetic Compatibility, EMC-11, pp. 125-130, 1969.

20. G.N. Oetzel and E.T. Pierce, "Radio Emissions from Close Lightning", in "Planetary Electrodynamics", Vol. 1, S.C. Coroniti and J. Hughes (ed.), Gordon and Breach, New York, pp. 543-570, 1969.

21. E.T. Pierce, "Atmospherics and Radio Noise", in "Lightning: 1. Physics of Lightning", R.H. Golde (ed.), Academic Press, New York, pp. 351-384, 1977.

22. J.R. Johler, W.J. Kellar, and L.C. Walters, "Phase of the Low-Frequency Ground Wave", NBS Circular 573, June 27, 1956.

23. J.R. Wait and L.C. Walters, "Curves for Ground Wave Propagation Over Mixed Land and Sea Paths", IEEE Trans. Ant. & Prop., AP-13, pp. 904-918, 1965.

24. M.A. Uman, C.E. Swanberg, J.A. Tiller, Y.T. Lin, and E.P. Krider, "Effects of 200 km Propagation on Florida Lightning Return-Stroke Electric Fields", Radio Science, vol. 11, pp. 985-990, 1976.

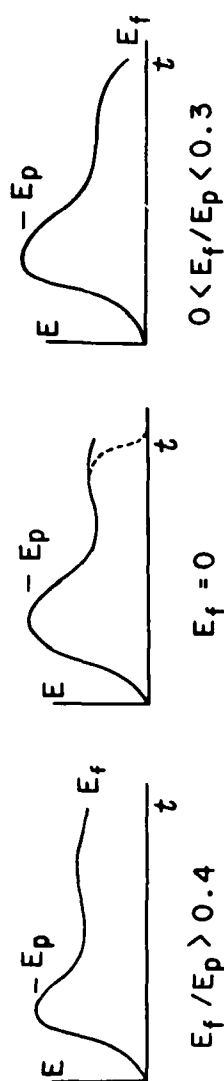
25. E.P. Krider and G.J. Radda, "Radiation Field Waveforms Produced by Lightning Stepped Leaders", J. Geophys. Res., Vol. 80, pp. 2653-2657, 1975.

26. E.P. Krider, G.J. Radda, and R.C. Noggle, "The Electric Fields Produced by Lightning Stepped Leaders", J. Geophys. Res., Vol. 82, pp. 951-960, 1977.

27. C.D. Weidman and E.P. Krider, "The Radiation Field Waveforms Produced by Intracloud Lightning Discharge Processes", J. Geophys. Res., Vol. 84, pp. 3159-3164, 1979.

28. W. Beasley, M.A. Uman, and P.L. Rustan, Jr., "Electric Fields Preceding Cloud-to-Ground Lightning Flashes", J. Geophys. Res., Vol. 87, pp. 4883-4902, 1982.

29. M.A. Uman, M.J. Master, and E.P. Krider, "A Comparison of Lightning Electromagnetic Fields with the Nuclear Electromagnetic Pulse in the Frequency Range 10^4 - 10^7 Hz", IEEE Trans. on EMC, EMC-24, pp. 410-416, 1982.



Type Location	Range Normal.	Freq. (MHz)	Number, Mean Spectral Ampl., Standard Dev.	Freq. (MHz)	Number, Mean Spectral Ampl., Standard Dev.	Freq. (MHz)	Number, Mean Spectral Ampl., Standard Dev.
(a) 1st Return Stroke 1979 40-60 km NNW Water	50 km	2 4 10 20	3, -125.0, 2.6 4, -130.2, 5.1 10, -140.7, 4.9 20, -147.4, 3.4	2 4 10 20	3, -123.7, 2.7 4, -129.4, 4.6 10, -148.2, 10.6 20, -158.0, 3.5	2 4 10 20	2, -128.5, 4.1 4, -136.6, 3.5 10, -147.4, 5.2 20, -162.2, 7.6
(b) 1st Return Stroke 1979 40-60 km NNW Water	None	2 4 10 20	8, -126.6, 5.9 4, -128.8, 4.3 10, -141.0, 4.6 20, -147.4, 5.1	2 4 10 20	8, -125.1, 5.3 4, -127.8, 3.8 10, -145.7, 6.1 20, -158.0, 5.4		
(c) 1st Return Stroke 1981 8-12 km "Mostly Water"	10 km	1 2 4 10 20	5, -103.7, 4.8 7, -107.7, 3.8 4, -122.6, 7.5 10, -125.4, 3.5 20, -132.3, 4.1	1 2 4 10 20	5, -103.3, 4.3 7, -107.5, 4.4 4, -123.0, 6.8 10, -127.2, 2.9 20, -142.2, 3.3		
(d) 1st Return Stroke 1979 20-30 km SW 1.5-2 km Land Path	25 km	2 4 10 20	3, -117.1, 3.2 4, -123.8, 2.4 10, -137.4, 1.2 20, -142.8, 1.1	2 4 10 20	3, -116.3, 3.2 4, -123.8, 2.3 10, -139.3, 2.2 20, -153.2, 1.5		
(e) 1st Return Stroke 1979 10-30 km SW 1.5-2 km Land Path	None	2 4 10 20	3, -116.9, 2.8 4, -123.6, 1.0 10, -138.6, 2.2 20, -143.6, 1.6	2 4 10 20	3, -116.0, 2.6 4, -123.7, 0.6 10, -140.4, 2.2 20, -153.7, 1.3	2 4 10 20	1, -114.0 2, -123.4 10, -142.6 20, -149.1
Rows (a)-(e) Combined Result	50 km	1 2 4 10 20	5, -117.7, 4.8 24, -124.1, 4.5 4, -131.5, 5.9 10, -141.2, 3.9 20, -147.5, 3.8	1 2 4 10 20	5, -117.3, 4.3 24, -123.1, 4.3 4, -131.2, 5.8 10, -144.7, 5.5 20, -157.8, 3.8	2 4 10 20	3, -125.7, 5.7 4, -134.2, 4.8 10, -147.8, 3.7 20, -159.8, 6.7
(f) Subsequent Stroke 1979 25-50 km SW 1.5-2 km Land Path	None	2 4 10 20	5, -118.0, 2.9 4, -123.7, 1.3 10, -134.0, 1.9 20, -139.1, 2.0	2 4 10 20	5, -117.1, 2.7 4, -123.8, 1.2 10, -136.6, 2.2 20, -150.2, 1.9		

Table 1 - Means and standard deviations of the spectral amplitudes produced by return strokes. All data are given in db relative to 1 V/m/s

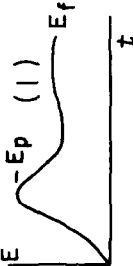

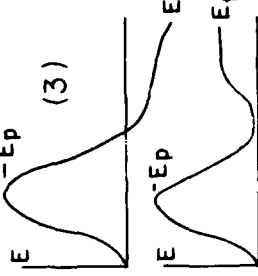
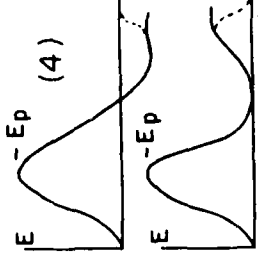
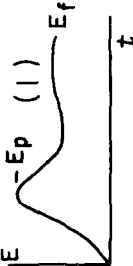

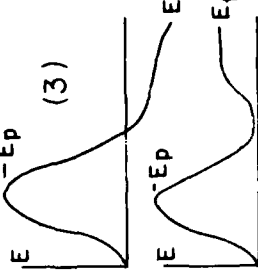
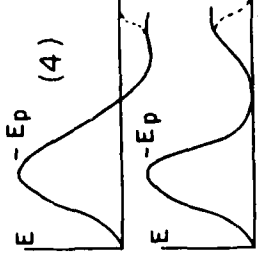
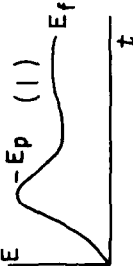

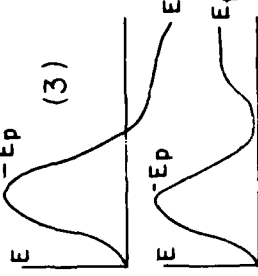
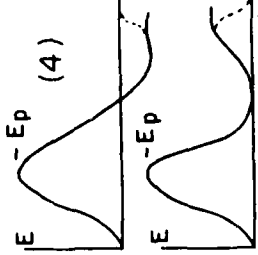
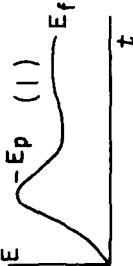

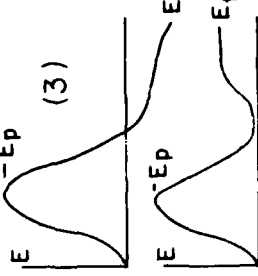
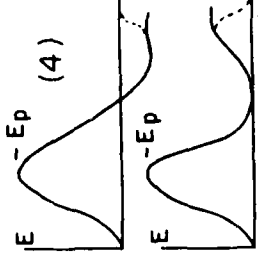
Type Location	Range Normal.	$E_f / E_p > 0.4$			$E_f = 0$			$0.15 < E_f / E_p < 0.5$			$E_f = 0$		
		Freq. (MHz)	Number, Mean Spectral Ampl., Standard Dev.		Freq. (MHz)	Number, Mean Spectral Ampl., Standard Dev.		Freq. (MHz)	Number, Mean Spectral Ampl., Standard Dev.		Freq. (MHz)	Number, Mean Spectral Ampl., Standard Dev.	
(a) Stepped Leader 1979 40-60 km NNW Water	None	2	2, -133.6, 1.4					2	2, -133.6, 1.4	2	1, -131.3	2	1, -131.3
		4	-134.3, 2.4					4	-134.3, 2.4	4	-138.8	4	-136.7
		10	-144.6, 3.3					10	-150.0, 4.4	10	-141.8	10	-145.6
		20	-152.4, 3.2					20	-163.0, 2.8	20	-155.9	20	-178.3
(b) Stepped Leader 1979 10-30 km SW 1.5-2 km Land Path	None	2	2, -122.8, 5.9					2	2, -122.8, 5.9	2	1, -120.2	2	1, -120.6
		4	-129.7, 2.1					4	-129.7, 2.1	4	-129.7	4	-131.8
		10	-139.2, 5.6					10	-142.4, 8.3	10	-144.9	10	-152.2
		20	-145.0, 5.4					20	-155.3, 5.5	20	-150.9	20	-159.8
(c) Stepped Leader 1981 11 km "Mostly water"	10 km	2	2, -131.2, 4.4					1	1, -114.9	1	1, -114.9	1	1, -115.0
		4	-135.0, 2.0					2	-115.4	2	-115.4	2	-115.6
		10	-144.9, 3.8					4	-123.7	4	-123.7	4	-123.6
		20	-151.7, 3.7					10	-147.9	10	-147.9	10	-147.3
Rows (a)-(c) Combined	50 km	2	4, -131.2, 4.4					1	1, -128.9	1	1, -128.9	1	1, -129.0
		4	-135.0, 2.0					2	-129.0	2	-129.0	2	-129.2
		10	-144.9, 3.8					4	-137.4, 1.6	4	-137.4	4	-137.4
		20	-151.7, 3.7					10	-151.5, 10.1	10	-151.5	10	-155.0
								20	-159.1, 4.7	20	-159.1	20	-173.6, 7.0

Table 2 - Means and standard deviations of the spectral amplitudes produced by leader steps near the ground

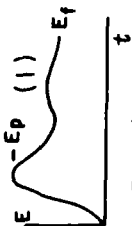

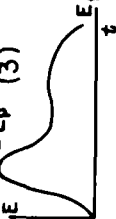
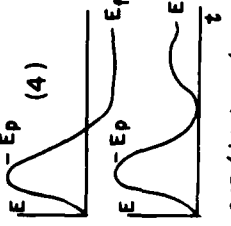
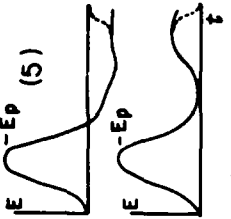
Type Location	Range Normal.																				
		Freq. (MHz)	Number, Spectral Ampl., Standard Dev.	Freq. (MHz)	Number, Spectral Ampl., Standard Dev.	Freq. (MHz)	Number, Spectral Ampl., Standard Dev.	Freq. (MHz)	Number, Spectral Ampl., Standard Dev.	Freq. (MHz)	Number, Spectral Ampl., Standard Dev.	Freq. (MHz)	Number, Spectral Ampl., Standard Dev.	Freq. (MHz)	Number, Spectral Ampl., Standard Dev.	Freq. (MHz)	Number, Spectral Ampl., Standard Dev.				
a) + Polarity 1979 40-45 km NW Water	None	2 4 10 20	3, -132.3, 1.6 -134.8, 0.9 -144.6, 0.9 -156.9, 0.6	2 4 10 20	3, -129.8, 1.8 -132.4, 1.3 -154.9, 0.6 -165.2, 1.6	2 4 10 20	2 4 10 20	2 4 10 20	2 4 10 20	2 4 10 20	2 4 10 20	2 4 10 20	2 4 10 20	2 4 10 20	2 4 10 20	2 4 10 20	2 4 10 20				
b) + Polarity 1979 17 km NW Water	None	2 4 10 20	1, -137.2 -134.3 -142.0 -149.2	2 4 10 20	1, -133.4 -132.4 -148.9 -161.6	2 4 10 20	2 4 10 20	2 4 10 20	2 4 10 20	2 4 10 20	2 4 10 20	2 4 10 20	2 4 10 20	2 4 10 20	2 4 10 20	2 4 10 20	2 4 10 20				
c) + Polarity 1979 40-50 km NE Water	None	2 4 10 20	1, -135.1 -136.3 -141.6 -149.8	2 4 10 20	1, -131.9 -133.0 -142.1 -159.8	2 4 10 20	2 4 10 20	2 4 10 20	2 4 10 20	2 4 10 20	2 4 10 20	2 4 10 20	2 4 10 20	2 4 10 20	2 4 10 20	2 4 10 20	2 4 10 20				
d) + Polarity 1979 20-40 km NE Water	None	2 4 10 20	1, -124.5 -133.6 -153.0 -167.0	2 4 10 20	1, -124.5 -133.6 -153.0 -167.0	2 4 10 20	2 4 10 20	2 4 10 20	2 4 10 20	2 4 10 20	2 4 10 20	2 4 10 20	2 4 10 20	2 4 10 20	2 4 10 20	2 4 10 20	2 4 10 20				
e) + Polarity 1979 10-30 km SW 1.5-2 km Land Path	None	2 4 10 20	3, -126.8, 3.6 -131.2, 5.8 -143.0, 6.7 -149.1, 6.6	2 4 10 20	3, -125.4, 3.8 -130.2, 5.3 -147.4, 5.9 -158.6, 6.3	2 4 10 20	2 4 10 20	2 4 10 20	2 4 10 20	2 4 10 20	2 4 10 20	2 4 10 20	2 4 10 20	2 4 10 20	2 4 10 20	2 4 10 20	2 4 10 20				
Rows (a)-(e) Combined	50 km	2 4 10 20	8, -134.0, 5.6 -136.6, 4.7 -148.0, 4.5 -154.9, 4.3	2 4 10 20	8, -132.2, 4.8 -135.0, 4.3 -153.1, 5.7 -165.0, 4.5	2 4 10 20	2 4 10 20	2 4 10 20	2 4 10 20	2 4 10 20	2 4 10 20	2 4 10 20	2 4 10 20	2 4 10 20	2 4 10 20	2 4 10 20	2 4 10 20				

Table 3 - Means and standard deviations of the spectral amplitudes produced by the fast transitions in cloud pulses

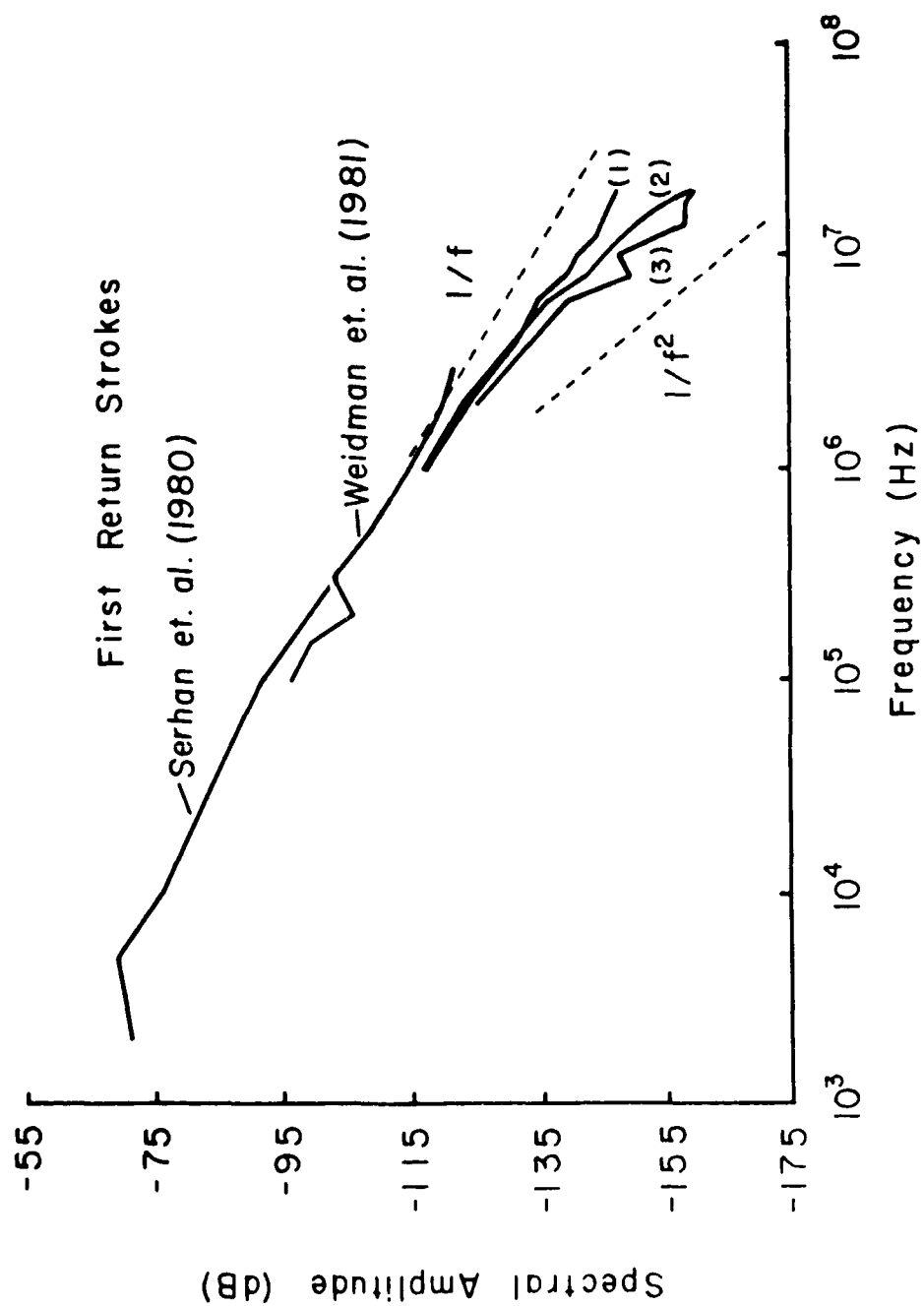


Fig. 1 - The mean amplitude spectrum of 24 first return strokes. Curves (2) and (3) are the best approximation to the true source at higher frequencies

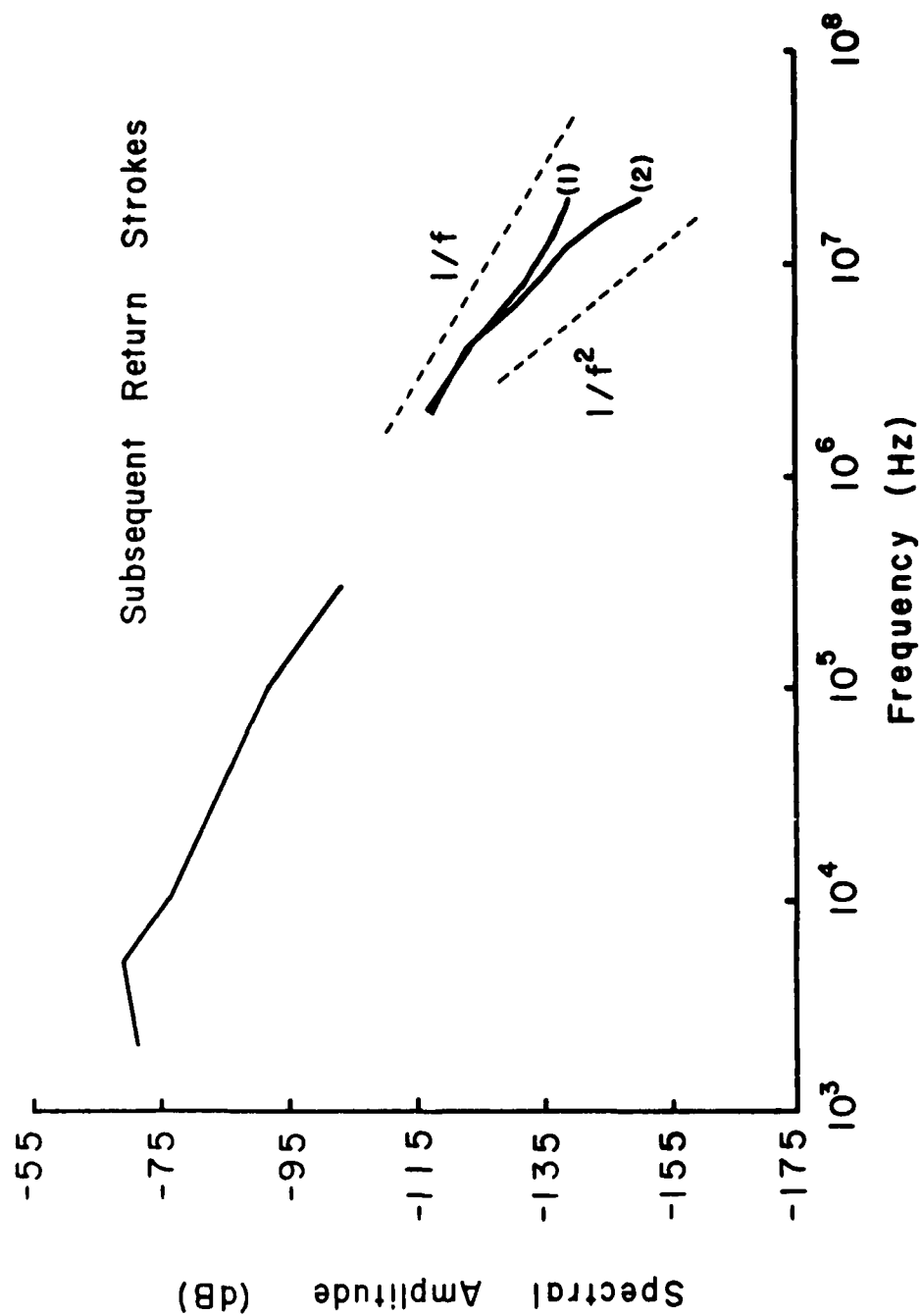


Fig. 2 - The mean amplitude spectrum of 5 subsequent return strokes. Curve (2) is the best approximation of the true source

CHARACTERIZATION OF FAST-RISETIME ELECTROMAGNETIC FIELD PULSES RECORDED IN AIRBORNE MEASUREMENTS DURING FLORIDA THUNDERSTORMS

B. P. Kuhlman
Air Force Wright Aeronautical Laboratories
Dayton, Ohio

M. J. Reazer
Technology/Scientific Services Inc.
Dayton, Ohio

ABSTRACT

A WC-130 aircraft instrumented with wideband electromagnetic field sensors was flown in south Florida thunderstorms during July and August 1981. Electric and magnetic fields on the aircraft surface were recorded continuously in analog form with 2 megahertz (MHz) bandwidth and digitally in 164 microsecond (μ s) records with 20 MHz bandwidth. Radiated magnetic field pulses occurring during intracloud flashes and prior to the first stepped leader of ground flashes were analyzed to determine risetimes, pulse widths, normalized peak amplitudes and normalized peak rates-of-change. Risetimes for all pulses ranged from 35 to 371 nanoseconds (ns), with an average of 130 ns for intracloud pulses and 116 ns for pre-leader pulses. Fifty percent pulse widths averaged 426 ns for intracloud pulses and 399 ns for pre-leader pulses. Pulse currents estimated from the magnetic fields ranged from 730 amperes (A) to 26 kiloamperes (kA), with an average of 4.6 kA.

Times between the incident pulse fields and their ground reflections were used to calculate discharge altitudes. Intracloud pulses were found to be centered around an altitude of 9 kilometers (km), while pre-leader pulses were centered around 5.5 km, slightly above the 0° Centigrade (C) isotherm. Approximately 70% of the flashes with pulses occurring below 7 km developed into ground flashes. Analysis of channel propagation patterns and velocities suggested that the discharges developed in steps of 50 to 200 meters (m) at time intervals of 1 to 93 μ s and propagated with estimated velocities of 8×10^5 to 4.7×10^7 m/s.

INTRODUCTION

Efforts have been made in recent years to characterize the fast-changing currents and electromagnetic fields associated with various phases of lightning discharges. Air Force participation in this research has arisen from the requirement to protect aerospace vehicles from damage or upset resulting from lightning strikes. Existing measurements of lightning attachments to aircraft seem to indicate that the aircraft is involved with intracloud flashes or the in-cloud portion of ground flashes (1,2), as might be expected for the altitudes at which the attachments occur. These discharges may not produce current levels as high as those for return strokes in a cloud-to-ground flash but often produce faster risetimes and comparable current rates-of-change (3,4).

We have analyzed the characteristics of impulsive discharges from in-cloud lightning processes from airborne electromagnetic field measurements. The results are pertinent in several respects. Since aircraft may be involved with the in-cloud phase of lightning flashes, knowledge of the levels produced is essential for aircraft protection. Analysis of some of the unique features of the airborne data provides insight into the physical characteristics of the discharges with application toward understanding and interpreting airborne direct strike measurements.

The measurements that were analyzed were obtained over Florida in 1981 using a National Oceanic and Atmospheric Administration (NOAA) WC-130 aircraft. This aircraft was instrumented and flown near and within thunderclouds to record radiated fields from lightning discharges, and aircraft surface currents and fields resulting from lightning attachments. A summary of the airborne radiated field measurements is given in (3), direct strike data were analyzed and reported in (1,5,6), and measurements of return stroke field risetimes and rates-of-change were reported in (5,6,7). Correlated ground-based measurements were also recorded during this program and are reported in (5,8,9).

We have confined our present analysis to the study of radiated magnetic field pulses occurring during intracloud flashes and prior to the first stepped leader of ground flashes. Leader pulses, pulses occurring later in ground flashes, and regular pulse sequences occurring during cloud or ground flashes were excluded. The characteristics derived include risetimes, pulse widths, normalized peak amplitudes and normalized peak rates-of-change as well as other general waveshape characteristics. The altitudes at which the pulses occurred were calculated, and channel propagation patterns and velocities were estimated.

SENSORS AND INSTRUMENTATION

The magnetic field near the aircraft surface was measured using a single cylindrical Moebius loop magnetic field sensor (10) mounted on the centerline of the forward upper fuselage of the WC-130 approximately seven meters from the nose of the aircraft. The loop was positioned to be sensitive to magnetic field components parallel to the fuselage axis as indicated by B_1 in Figure 1. The sensor was positioned and oriented so as to be relatively insensitive to magnetic fields associated with longitudinal wing and fuselage currents and symmetrical vertical stabilizer currents. These structures are a potential source of distortion in field measurements due to resonances that can be excited by an incident wave. Some enhancement of high frequencies is expected for broadside incidence of longitudinal magnetic fields on a long cylinder but this is not significant over the frequency range of the measurements (11,12). Therefore we assume that the measured fields are approximately equal to the incident longitudinal field components over the frequency range of interest although this remains to be verified through analytical and/or experimental means such as described in (13) and (14).

A second loop was mounted adjacent to the primary magnetic field sensor just described and oriented to respond to magnetic fields parallel to the wing axis as shown in Figure 1. Both magnetic field sensors developed a voltage proportional to the derivative of the magnetic field, with less than 1 decibel (dB) deviation, up to a frequency of 20 MHz. The two sensor outputs were compared to insure that there was no major distortion in the magnetic fields analyzed as a result of using only one component of the field.

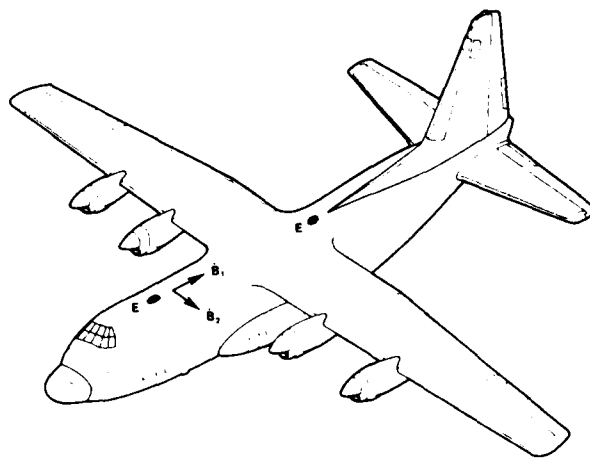


Fig. 1 - WC-130 Research aircraft showing sensor positions and axes of sensitivity for magnetic field loops

Two electric field sensors were also mounted on the upper fuselage of the aircraft. One was a flush plate dipole type (10) mounted directly ahead of the magnetic field loops as shown in Figure 1. The other was a hollow spherical dipole sensor (10) mounted even with the trailing edge of the wings. These sensors responded to the derivative of the vertical electric field with a bandwidth exceeding 45 MHz.

Signals from the two magnetic and the rear electric field sensors were transmitted over fiber optic cables to instrumentation inside the aircraft. The derivative field data were digitized using a 10-channel wide-bandwidth digital transient recorder and stored on magnetic tape. The signals were also integrated electronically and recorded on several direct record channels of a 28-channel Honeywell model 101 analog recorder. The forward electric field sensor output was integrated electronically at the sensor with a 50% decay time of about one second, transmitted through a fiber optic cable and recorded on two wideband FM channels of the analog recorder. Overall system bandwidth for the forward upper fuselage electric fields was about 0.1 Hertz to 500 kilohertz. A partial block diagram of the aircraft instrumentation is shown in Figure 2.

The digital transient recorder (DTR) sampled the data at 20 ns intervals with 8-bit amplitude resolution and provided ten simultaneous records of 8192 data points for a recording interval of 164 μ s. The recorder was triggered by pulses exceeding a preset threshold and was programmed to store a data

interval extending from 40 μ s ahead of the trigger time up to 124 μ s after the trigger time. Each time the DTR was triggered, a pulse was recorded on one channel of the analog recorder marking the location of the DTR recording interval within the overall analog record of the lightning flash.

Derivative signals were sent through low-pass filters prior to digitizing to minimize aliasing. The filters had a -3 dB cutoff frequency of 20 MHz which allowed an overall system risetime of 35 ns (10% to 90%) and a minimum pulse width of about 70 ns when the original fields were recovered by integration of the field derivatives.

Other information that was recorded included IRIG-B modulated time code, aircraft weather radar data, and aircraft heading, altitude and position. The aircraft radar and navigational information were stored digitally for subsequent processing by computer.

DATA PROCESSING

The forward upper fuselage electric field, time code and DTR trigger signal were plotted simultaneously on a strip chart from the analog tape to identify the type of lightning flash, to determine what part of the flash triggered the DTR and to determine the time of the flash so that other data could be correlated. Slowing the analog tape down and reproducing the data on a Gould ES1000 electrostatic strip chart recorder allowed an electric field bandwidth from 0.1 Hz to 40 kHz to be displayed with a time resolution of about 2 milliseconds (ms). An example of the strip chart display is shown in Figure 3.

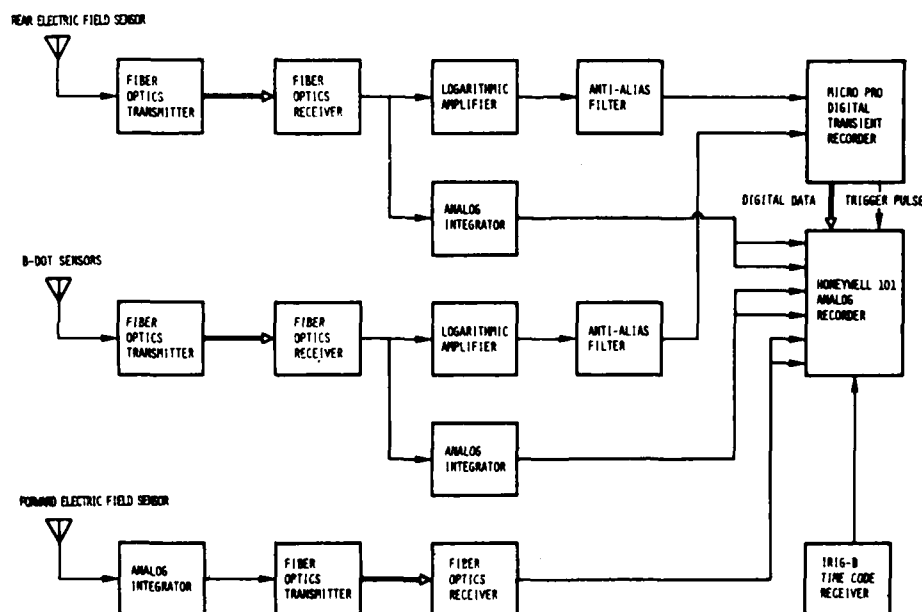


Fig. 2 - Block diagram of aircraft instrumentation

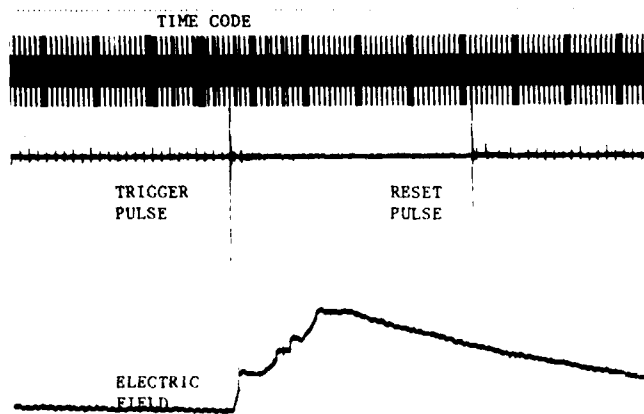


Fig. 3 - Strip chart used to identify the location of the DTR recording interval within the overall analog electric field record of the flash

Digitally recorded DTR data were read into a PDP-11 computer and stored on floppy disc for further processing. The derivative field data were scaled according to the procedures described in (5) and plotted on a Tektronix graphics terminal and hard copy. The data were also integrated numerically in the computer using a trapezoidal approximation to recover the original fields. The graphics terminal and computer were used to measure waveform parameters such as risetimes, amplitudes and pulse widths.

DTR TRIGGER LOCATIONS

Strip charts of the electric field and the DTR trigger showed that pulses were recorded throughout intracloud and ground flashes. For intracloud flashes the DTR was triggered most frequently near the beginning of the flash, occasionally before any discernible electric field change. On ground flashes the DTR was triggered most often by pulses near the beginning of the stepped leader. Fifty percent of the intracloud flashes showed a DTR acquisition within the first 60 ms of the discharge. Seventy percent of the ground flashes analyzed showed a DTR acquisition within 10 ms of the start of the leader. Some ground flashes showed a DTR acquisition before any discernible electric field change or during the period of preliminary electric field variations preceding the stepped leader (15). The strip chart resolution provided a minimum detectable field change of about 5 V/m with most flashes occurring less than 20 kilometers (km) from the aircraft. Histograms of trigger locations relative to the initial electric field change for intracloud flashes and relative to the estimated beginning of the stepped leader for ground flashes are shown in

Figures 4 and 5. The average durations of the stepped leaders and intracloud flashes were 28.6 and 390 ms, respectively.

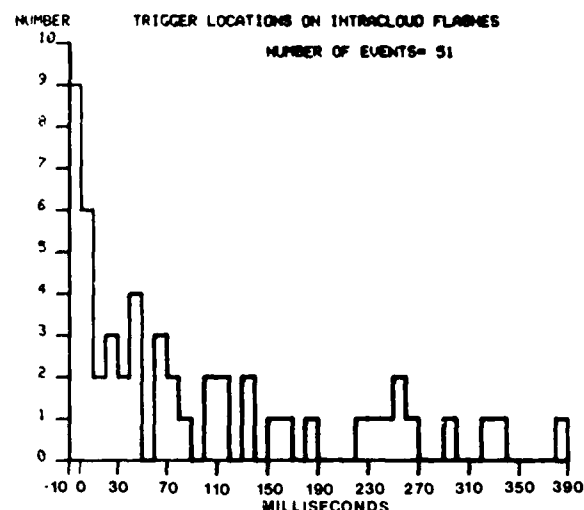


Fig. 4 - Histogram of DTR trigger times relative to the initial electric field change for intracloud flashes. Zero marks the time of the initial field change

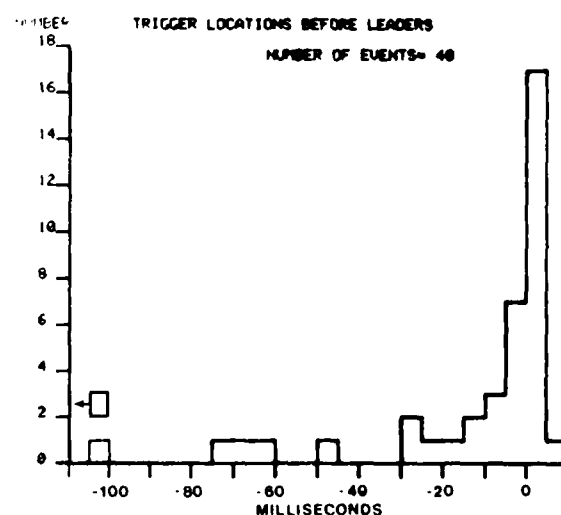


Fig. 5 - Histogram of DTR trigger times relative to the estimated beginning of the stepped leader for ground flash pulses. Zero marks the time of the beginning of the stepped leader

PULSE CHARACTERISTICS

Two hundred and eleven pulses were studied in all, 98 from 54 intracloud flashes and 113 from 42 ground flashes. Only pulses that exceeded the system noise level by a factor of two or more were included in the sample. Ninety percent of the pulses were more than 10 dB above the noise level.

Pulses occurred at intervals of 1 to 93 μ s in the 164 μ s recording periods. Waveshapes ranged from fast narrow pulses as shown in Figure 6 to wider pulses as shown in Figure 7 to more complex structures such as shown in Figure 8. The pulses typically showed an initial slow rising ramp followed by a rapid transition to peak and a somewhat slower decay through zero. In DTR records showing narrow and wide pulses the wider pulses generally had longer risetimes, larger amplitudes and slower decay rates beyond the peak. Waveshapes were found to be similar for intracloud and ground flash pulses as can be seen from Figures 6 and 7. Pulses such as those in Figure 8 occurred during both intracloud and ground flashes.

Pulses of these general types were first reported by Baum for WC-130 measurements (16) although they had not been related to a particular discharge phase. Rustan et al. presented some limited WC-130 pulse data correlated with simultaneous ground-based electric field measurements (5). More extensive intracloud pulse measurements have been reported by Weidman and Krider from

ground-based electric fields (17). Their work provided a basis for comparison with our data and suggested some further areas of investigation.

RISETIMES - Risetimes were calculated from 10% to 90% of the fast transition on the rising front of the pulse waveforms using the graphics terminal and computer for interpolation between samples. The results are plotted in the histograms of Figure 9 for intracloud pulses and Figure 10 for pre-leader pulses.

To investigate bias that might be introduced by the DTR trigger system, risetimes for pulses occurring later in the recording interval, after the pulse that triggered the recorder, were separated and analyzed. The resulting post-trigger average pulse risetimes for intracloud and ground flashes were 17.2% and 13.4% longer, showing that the trigger system favored faster pulses.

Risetimes ranged from 44 to 371 ns for intracloud pulses, with a post-trigger average risetime of 130 ns. Pre-leader pulse risetimes ranged from 35 to 293 ns, with a post-trigger average of 116 ns. Risetimes approaching 40 ns

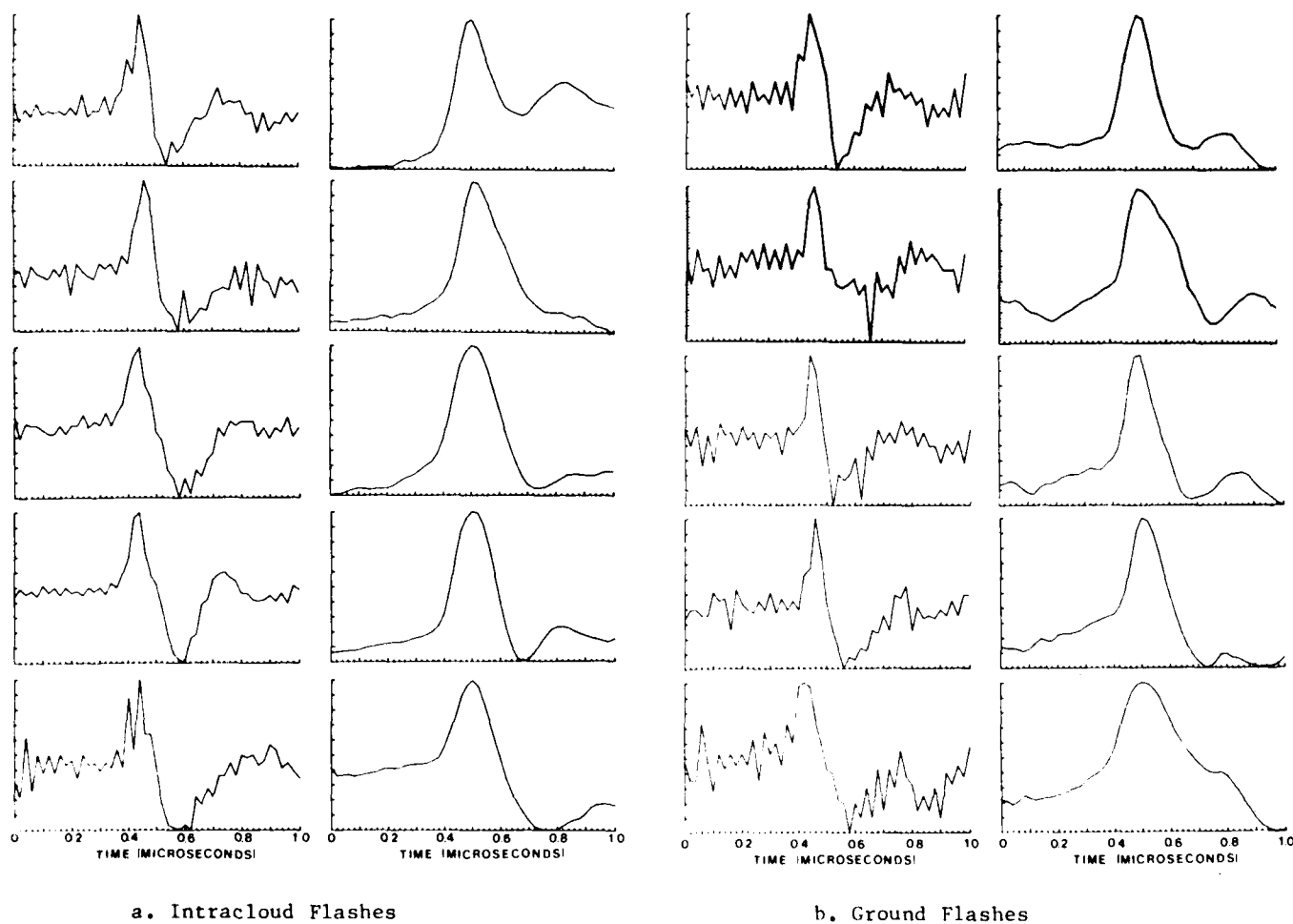


Fig. 6 - Expanded plots of narrow magnetic field pulses. The left trace shows the recorded magnetic field derivatives, the right trace shows the resulting magnetic field after integration

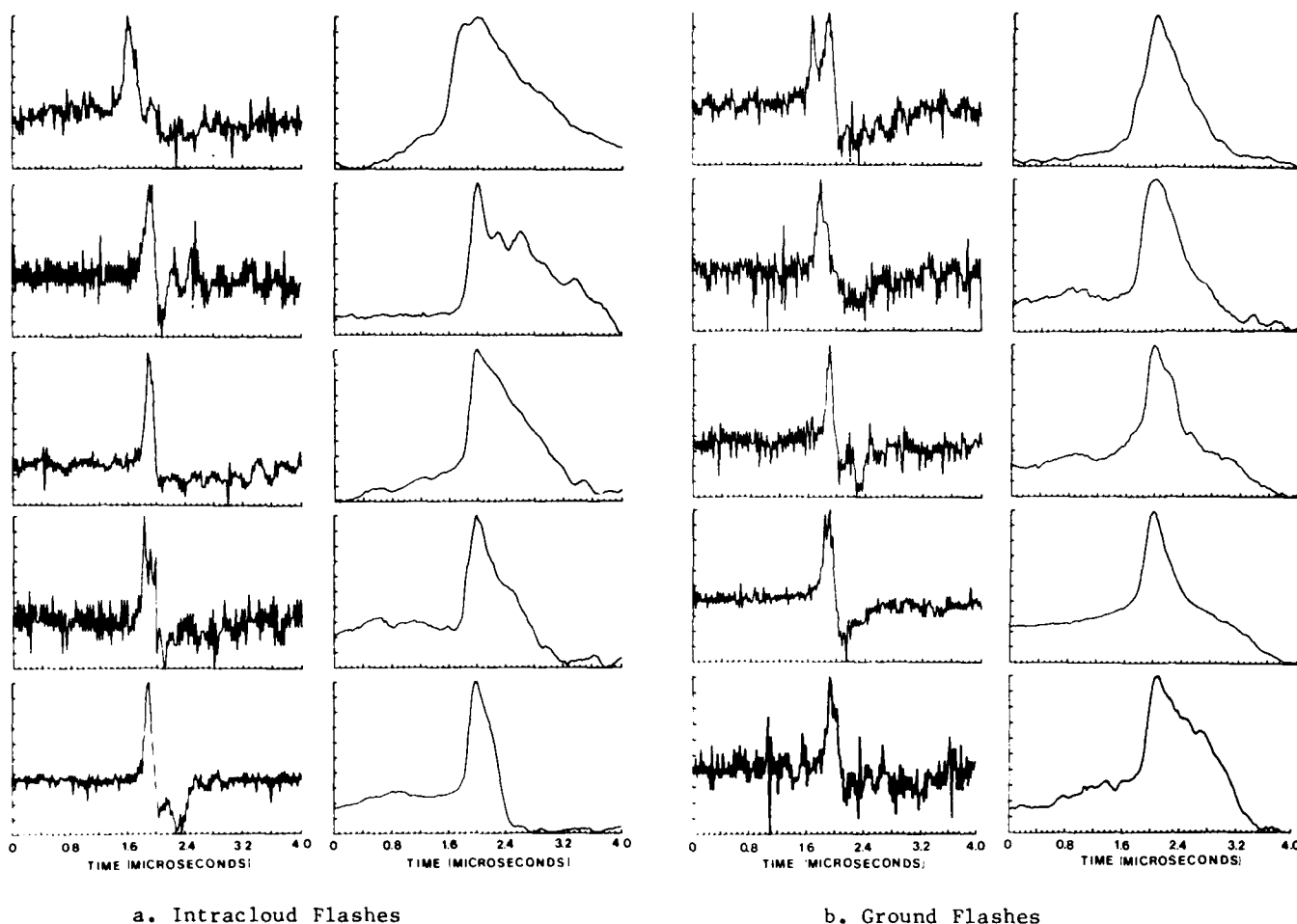


Fig. 7 - Expanded plot of wider magnetic field pulses. The left trace shows the recorded magnetic field derivative, the right trace shows the resulting magnetic field after integration

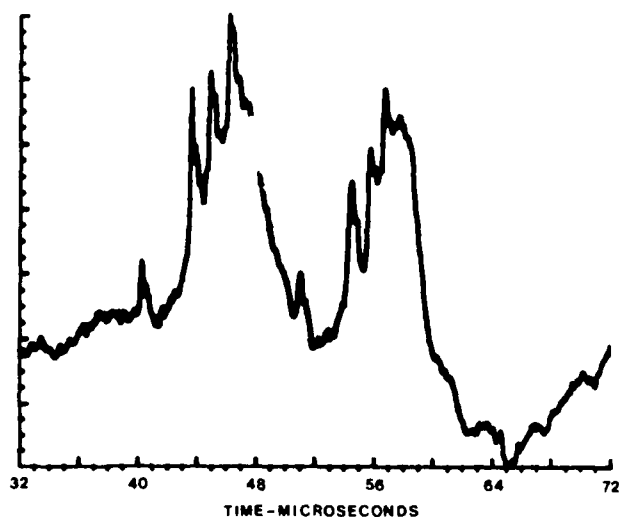


Fig. 8 - Example of intracloud pulses with a complex magnetic field structure

are limited by the anti-alias filter frequency response and the sample rate of the digital transient recorder. These risetimes are not affected by high-frequency attenuation due to ground propagation since both the source and the receiver are several kilometers above ground and less than 25 km apart.

PULSE WIDTHS - Pulse widths were measured at 50% and 10% of peak amplitude. Since some pulses were part of a more complex overall waveform they did not immediately decay to zero and therefore 10% pulse widths could not be determined. Histograms of 50% pulse widths for intracloud and ground flashes are shown in Figure 11 and histograms of 10% pulse widths are shown in Figure 12. The 50% pulse width histograms showed a peak centered around 200 ns and a gradual decline in number with increasing pulse width. The sharp drop in pulses with widths below 100 ns is probably due to the resolution limitations of the recording system. The 10% pulse width histograms showed that 36 pulses were not more than 400 ns wide at base of the pulse. Widths of slowly-varying overall pulse structures that underlie narrower pulses, as shown in Figure 8, were not

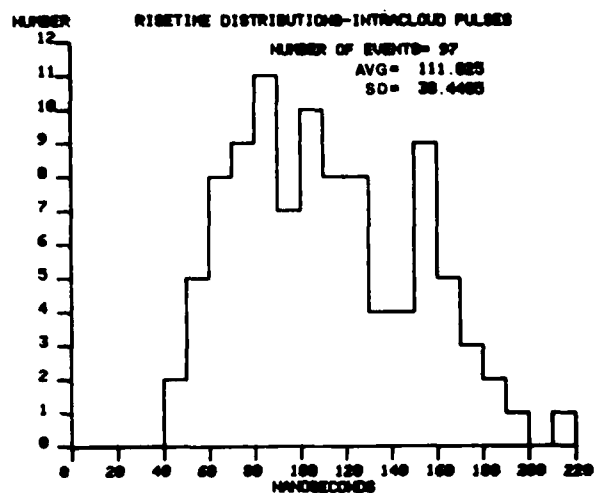


Fig. 9 - Histogram of intracloud flash pulse risetimes

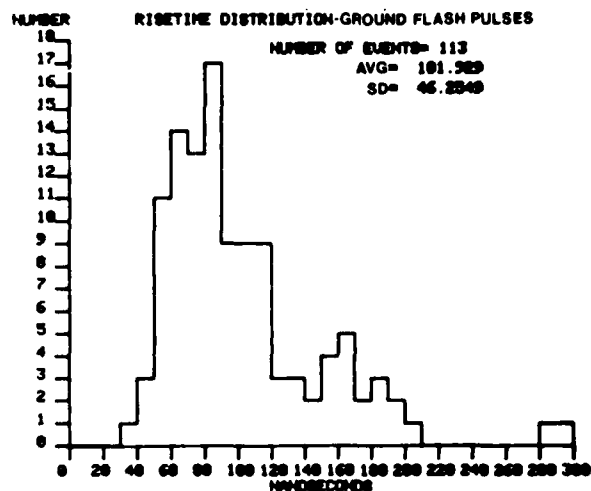


Fig. 10 - Histogram of ground flash pulse risetimes

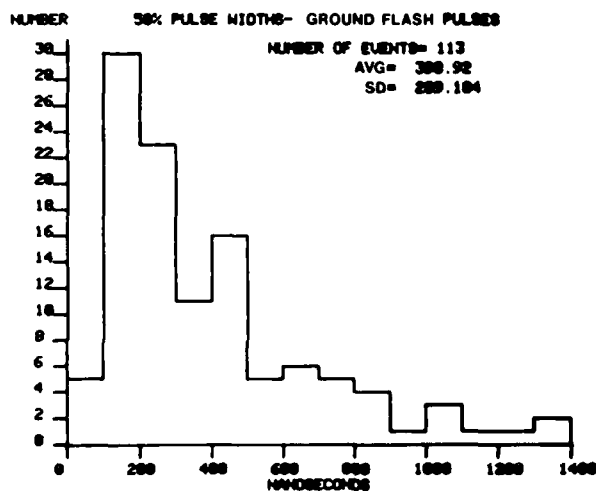
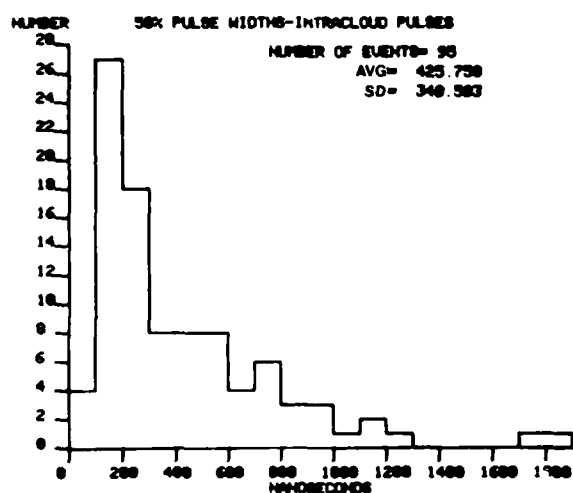


Fig. 11 - Histograms of pulse widths at 50% of peak for intracloud and ground flash pulses

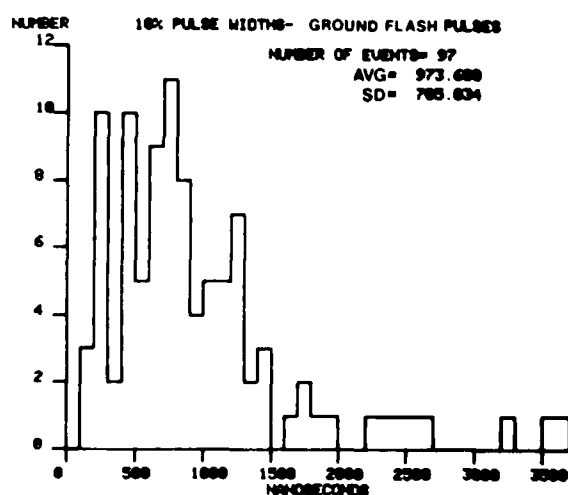
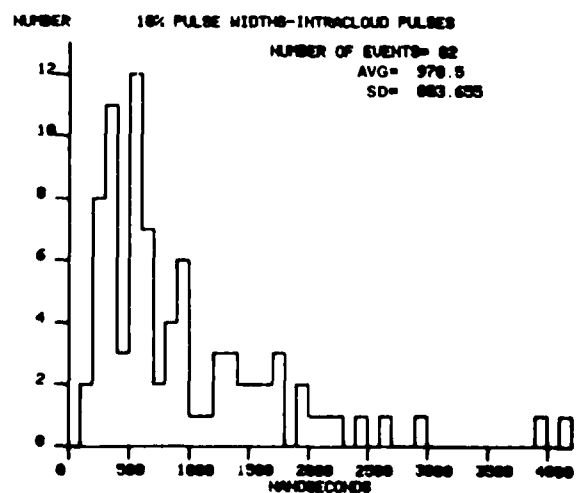


Fig. 12 - Histograms of pulse widths at 10% of peak for intracloud and ground flash pulses

determined because of the long-term accumulated errors that result from numerical integration of the derivative data.

The risetimes and 50% pulse widths are similar to those reported by Baum et al. (18) and Krider and Weidman (4) for leader pulses and return stroke fields. The initial submicrosecond structure is apparently very similar for different processes of lightning breakdown.

Most pulses tended to be bipolar regardless of pulse width with half of the pulses showing 10% or more overshoot on the decaying edge of the waveforms. As would be expected, narrow pulses decayed faster than wider pulses. Pulses narrower than 400 ns at 50% showed a peak magnetic field derivative on the decaying edge 60% to 160% as large as the rising edge magnetic field derivative.

Eighty-one percent of intracloud pulse electric field changes were negative while 91% of pre-leader pulse electric field changes were positive. Leader steps and return strokes also radiate positive field changes indicating that most pre-leader pulses produce the same direction of current flow as the leader steps that follow. Weidman and Krider (17) also observed a tendency for intracloud pulses to produce negative electric field changes and for pre-return stroke pulses to be positive.

NORMALIZED MAGNETIC FIELD AMPLITUDES AND RATES-OF-CHANGE

Since lightning fields vary with distance it is useful to normalize the levels to a specific distance so that comparisons can be made. Discharge distances and altitudes for individual pulses were estimated using radar data and the technique described in a later section. Storm locations for 31 intracloud flashes with 62 pulses and 24 ground flashes with 73 pulses were determined. Magnetic field amplitudes and rates-of-change were normalized

to a distance of 100 km assuming a straight vertical channel and an inverse distance dependence for field strength. For pulses where the discharge altitude could not be determined but distance was known, the pulse altitude was taken to be the same as that of the aircraft. Results are shown in the histograms of Figure 13 for magnetic field rates-of-change and Figure 14 for magnetic field amplitudes.

Average pre-leader pulse magnetic field derivatives were smaller than intracloud pulse derivatives by 23% and magnetic field amplitudes were smaller by an average of 18%. Averages were 11×10^3 A/m/s and 8.5×10^3 A/m/s for intracloud and pre-leader pulse derivatives and 1.4×10^{-3} A/m and 1.1×10^{-3} A/m for intracloud and pre-leader pulse magnetic field amplitudes, respectively.

For comparison, Weidman and Krider (4) have measured average values of 33 V/m/μs for 108 return strokes and 16 V/m/μs for 11 cloud pulses from ground based electric field measurements. Assuming magnetic and electric fields are related by the impedance of free space, and dividing by two to remove the contribution from the image term (19) which is present in ground fields but retarded at the aircraft location, corresponding above ground values of 44×10^3 A/m/s and 21×10^3 A/m/s are obtained. The reported ground-based measurements of return stroke electromagnetic field derivatives are about four times larger than the airborne cloud pulse measurements. Ground-based measurements of cloud pulses are about twice as high as the airborne measured values.

Average airborne measurements of pulse derivatives might be expected to be lower than the ground-based data in (4) since the aircraft was travelling between thunderstorm cells and would trigger on weak discharges when close to a storm and larger ones when the storm was

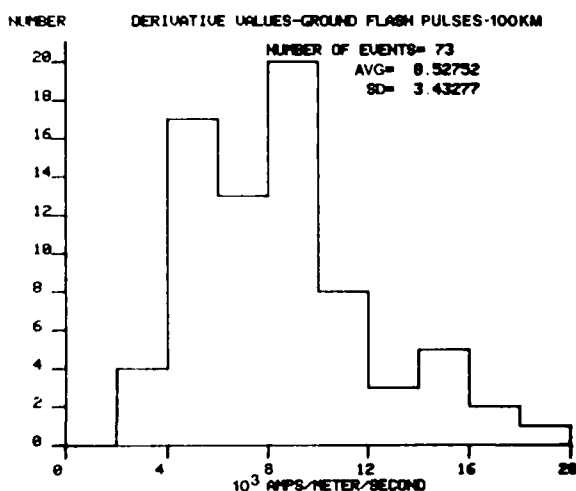
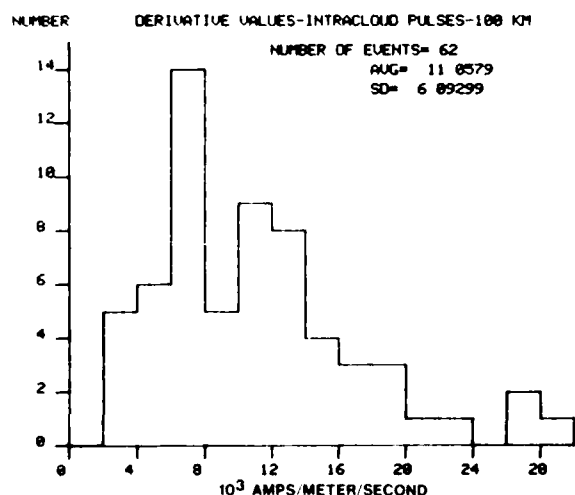


Fig. 13 - Histograms of magnetic field rates-of-change normalized to 100 km

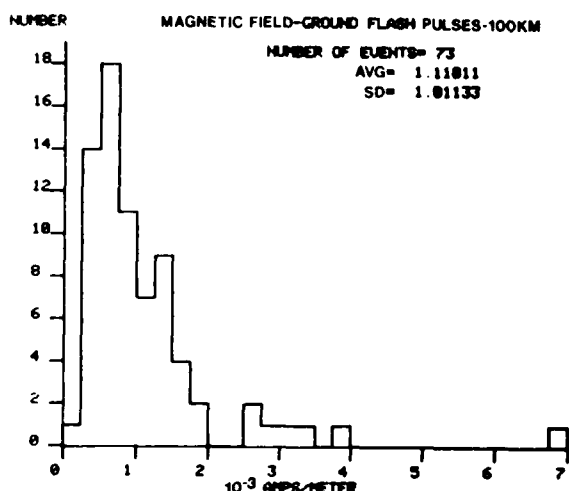
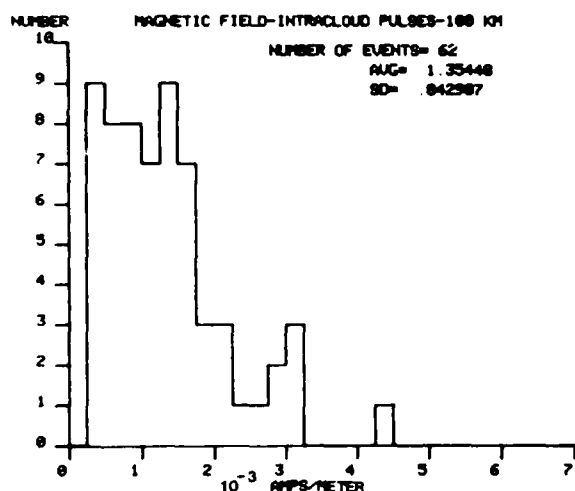


Fig. 14 - Histograms of magnetic field amplitudes normalized to 100 km

distant. Also, the DTR had a large pre-trigger recording interval which frequently contained pulses too small to trigger the recorder. These pulses were included in the statistics when they exceeded the noise level by a factor of two or more. It is significant that few pulse derivatives approached the upper levels reported in (4) for cloud discharges and return strokes. The reason for this is not known since the wide range of thunderstorm distances and trigger levels involved in the 1981 research flights should have assured the acquisition of fields from a full range of discharge amplitudes. Non-vertical channels may result in some underestimate of normalized values but the same effect would be experienced in ground measurements.

PULSE CURRENT CHARACTERISTICS - Assuming that the current pulse that generates the fields travels with a constant current profile and a constant velocity along a straight vertical channel, and deleting image terms since they are retarded by a time greater than the time to initial waveform peak, pulse currents are related to the normalized magnetic fields by:

$$I(t) = \frac{4\pi c D}{v} H(t) \quad (1)$$

with the corresponding relationship:

$$\frac{dI(t)}{dt} = \frac{4\pi c D}{v} \frac{dH(t)}{dt} \quad (2)$$

where $I(t)$ is current, D is the normalized distance, c is the speed of light, and v is the velocity of current propagation (19).

Using a current velocity of 1×10^8 m/s, an overall average current of 4.6 kA was found with a range of 730 A to 26 kA. Eighty-five

percent of the current levels were between 1 and 7.5 kA with a larger percentage of high values occurring during intracloud flashes. Current derivatives ranged from 8.6×10^9 A/s to 1.1×10^{11} A/s with an overall average of 3.7×10^{10} A/s. The highest current occurred on a pre-leader pulse while the highest current derivative occurred during an intracloud discharge.

The current levels are low compared to return strokes but they are comparable to the levels encountered by the WC-130 during two direct strikes (1) and to the levels recorded during direct strikes to other research aircraft (20,21). The current derivatives lie between return stroke levels measured during strikes to towers (22,23), and return stroke levels inferred from ground-based electric field measurements (4).

DISCHARGE LOCATIONS

For 88% of the DTR recording intervals a single reflection of the incident pulse was received at the aircraft 1.1 to 32.4 μ s later. These pulses were reflected off the ground and correspond to the image term in the electromagnetic field equations. Since the propagation distances are longer for the image, the reflection arrives at the aircraft at a later time. A distinctive example is shown in Figure 8. This group of pulses originated from a storm cell about 13 km from the aircraft during an intracloud discharge. The reflection is clearly evident beginning at about 50 μ s into the recording interval. Reflected pulses had generally the same waveshape as the initial pulse although the risetimes were slightly slower and the amplitudes reduced. Some reflections were larger than the initial pulse, some were distorted and some were undetectable, as would be expected for various channel orientations and ground conditions.

If aircraft altitude and discharge distance are known, the discharge altitude can be calculated from the difference in time of arrival of the pulse and the reflection. For an aircraft altitude H_a , and a discharge pulse at distance D and altitude H_d , the difference in time of arrival Δt is:

$$\Delta t = (\sqrt{(H_d + H_a)^2 + D^2} - \sqrt{(H_d - H_a)^2 + D^2}) / c \quad (3)$$

This equation describes a hyperbola rotated about an axis extending vertically from the ground to the aircraft as shown in Figure 15. Radar echoes from thunderstorm cells can be projected on this surface to determine a range for D in equation 3 and thus provide an estimate of lightning pulse locations. For distant flashes, low altitude pulses, or very close pulses, H_d varies little for a change in D and therefore the altitude uncertainty is small. For higher pulse altitudes the uncertainty is greater. Relative amplitudes and polarities of signals from the orthogonal magnetic field loops and the rear electric field sensor indicated quadrant and approximate direction to lightning pulses, so that storm cells could be identified on radar displays. Evidence has shown that lightning tends to occur in or near cores of high radar reflectivity (24). Therefore, distances from the aircraft to thunderstorm centers of high reflectivity were used for D in equation 1. Altitudes for 55 intracloud and 70 pre-leader pulses were calculated and plotted as shown in Figure 16.

A division is evident between the intracloud and pre-leader pulse altitudes. Intracloud pulses are centered around an altitude of about 9 km while pre-leader pulses are centered around 5.5 km, slightly above the 0°C isotherm. This type of bimodal

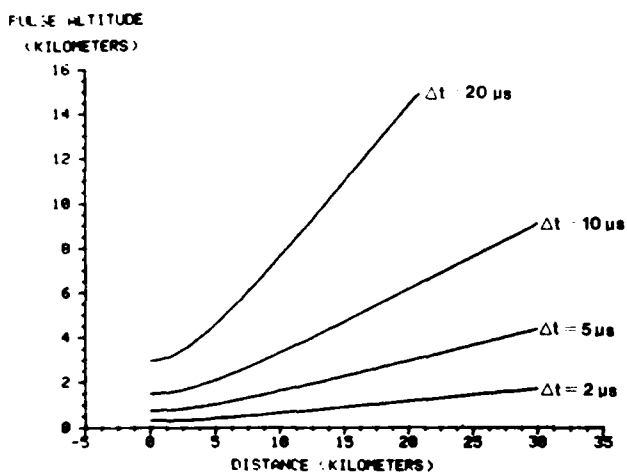


Fig. 15 - Hyperbolic curves of possible pulse altitudes and distances for an aircraft altitude of 5.2 km

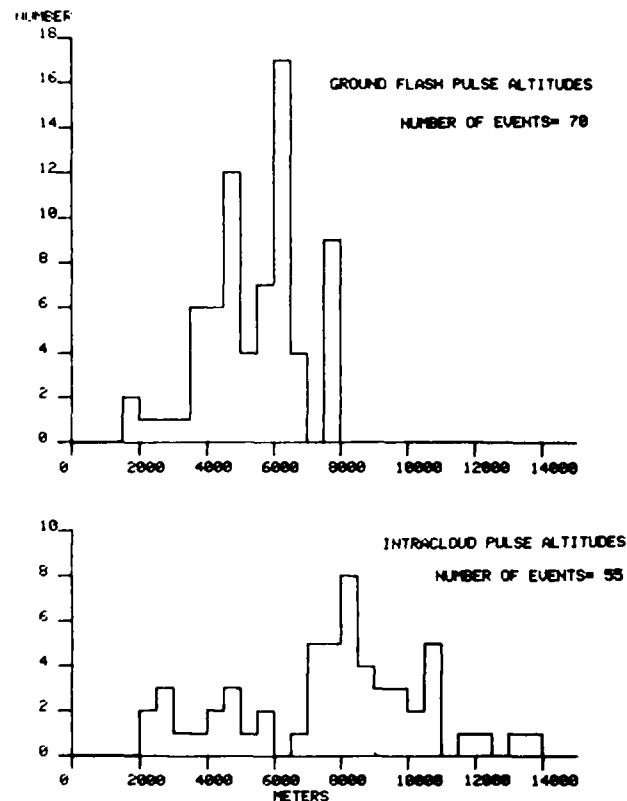


Fig. 16 - Histograms of pulse altitudes for intracloud and ground flash pulses

distribution for lightning altitudes has been found in thunderstorms in Oklahoma and Virginia (25). Since most pulses for ground flashes occurred near the beginning of the initial leader electric field change, it is probable that these discharges at altitudes of 3 to 7 km are related to the initiation of the leader. Approximately 70% of the flashes with pulses occurring below 7 km developed into ground flashes. A similar discharge pattern was found by Uman et al. (8) for VHF sources, with initial sources beginning at 7 km and propagating upwards and downwards for about 1 km before propagating towards ground.

From aircraft direct strike statistics it appears that most attachments tend to occur in the lower discharge region at altitudes of 5 km and below (26). On the other hand NASA has had success obtaining intentional strikes on a F106 research aircraft by operating in the upper discharge region (27).

A change in Δt s between pulses within a DTR recording interval corresponds to a shift in source location to adjacent hyperbolic surfaces. If successive pulses are related, this implies discharge propagation. Although the actual pulses may occur anywhere within the projection of the radar echoes on the hyperbolic surface or even outside this region and could propagate a considerable distance

with little change in Δt along the surface, some assumptions can be made regarding channel geometry to give insight into discharge propagations. The lower limit in propagation distance would be the shortest line between a given pulse location and the adjacent hyperbolic surface defined by Δt for the succeeding pulse. The maximum propagation distance over a given interval is limited by the propagation velocity.

Changes in Δt s for related sequential pulses were less than 1 μ s for the majority of 164 μ s records. This is a strong indication that the pulses were from a localized region of breakdown. Only five records showed Δt s separated by more than 1 μ s. Fourteen records showed three or more pulses with measureable reflection times and estimated distances. From this limited sample we made some observations regarding possible breakdown patterns.

Four patterns emerged from the time sequences of the pulse Δt s. Several pulse groups showed no change in Δt for successive pulses. This would imply a stationary breakdown region or as noted above it may only mean that the pulses did not depart from a given hyperbolic surface. Some records showed pulses with a given Δt followed by pulses with higher and lower Δt s. This could be interpreted as a bidirectional lengthening of the channel in a horizontal or vertical direction beginning at the initial pulse location. Other records showed a progressive decrease or increase in Δt followed by an intermediate Δt . An intermediate Δt could be caused by a change in the direction of channel propagation or by a branch from an intermediate position. The fourth pattern consisted of several stationary pulses at one position followed by breakdown several hundred meters away propagating towards the first position. There is not enough information available to resolve the ambiguities in these patterns. They do suggest several possibilities as to how breakdown may develop however.

If the channels are assumed to be vertical, most pulses are found to be separated by distances of about 50 to 200 meters. The resulting propagation rates range from 8×10^5 m/s to 4.7×10^7 m/s which are comparable to the rates found using other techniques (27,28). The assumption of a vertical channel is reasonable for most breakdown directly preceding the stepped leader but less valid for intracloud discharges. The recording system is likely to favor vertical discharges however, since the aircraft sensors responded to vertical electric fields and horizontal magnetic fields. Distant horizontal discharges would not produce strong field components in the directions required to trigger the DTR.

One interesting example highlights some of the results. The aircraft was operating 13 km from the center of a small isolated thunderstorm about 4 km across when the electric field shown in Figure 17 was recorded. The field pattern indicated a cloud-to-ground

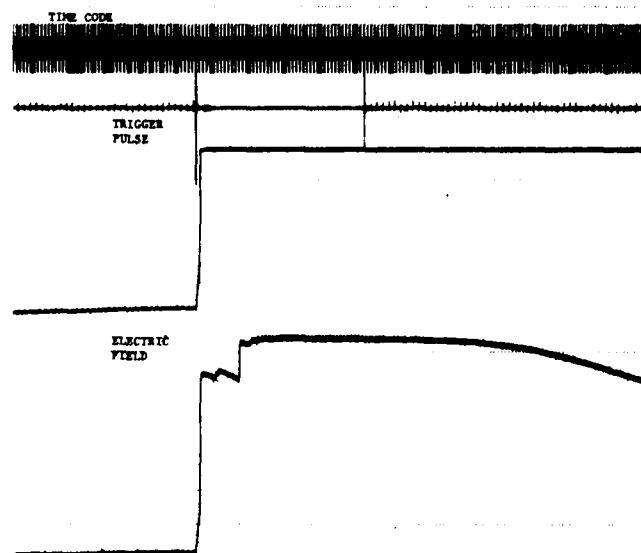


Fig. 17 - Electric field of a cloud-to-ground flash with a DTR trigger at the beginning of the stepped leader

flash with the electric field system saturating shortly after the second return stroke. An expanded plot of the DTR trigger and analog electromagnetic fields showed a DTR acquisition at the beginning of the initial leader electric field change on some large magnetic field pulses. The wide-bandwidth DTR magnetic field data is shown in Figure 18. By expanding portions of the DTR waveform it was determined that pulses 1 through 7 were initially incident and that pulses 1R through 6R were ground reflections. Equation 3 was applied to estimate pulse locations with the results used in equation 1 to infer current characteristics. The pulses at 1 in Figure 19 were on the order of 2 to 3 kA and appeared to be stationary at an altitude of 4.6 km. The large pulse at 63 μ s (number 2) initiated a downward propagation from an altitude of about 8 km that reached 7.5 km by pulse 6 in steps of 60 to 180 meters. The average downward velocity was 5.3×10^6 m/s. The large pulses at 63, 101 and 109 μ s (numbers 2, 4 and 5) indicated currents of 26 kA, 5.3 kA and 6.2 kA, respectively.

CONCLUSIONS

We have presented characteristics of discharge processes that occurred during intracloud flashes and that preceded the stepped leader of ground flashes. The discharges appeared to develop in steps of around 50 to 200 meters, at time intervals of 1 to 93 μ s, and to propagate at velocities of 8×10^5 to 5×10^7 m/s. Two regions of breakdown were found. Most intracloud discharges occurred in the upper part of thunderclouds at altitudes of 7 to 13 km. Other discharges occurred in lower cloud regions centered around

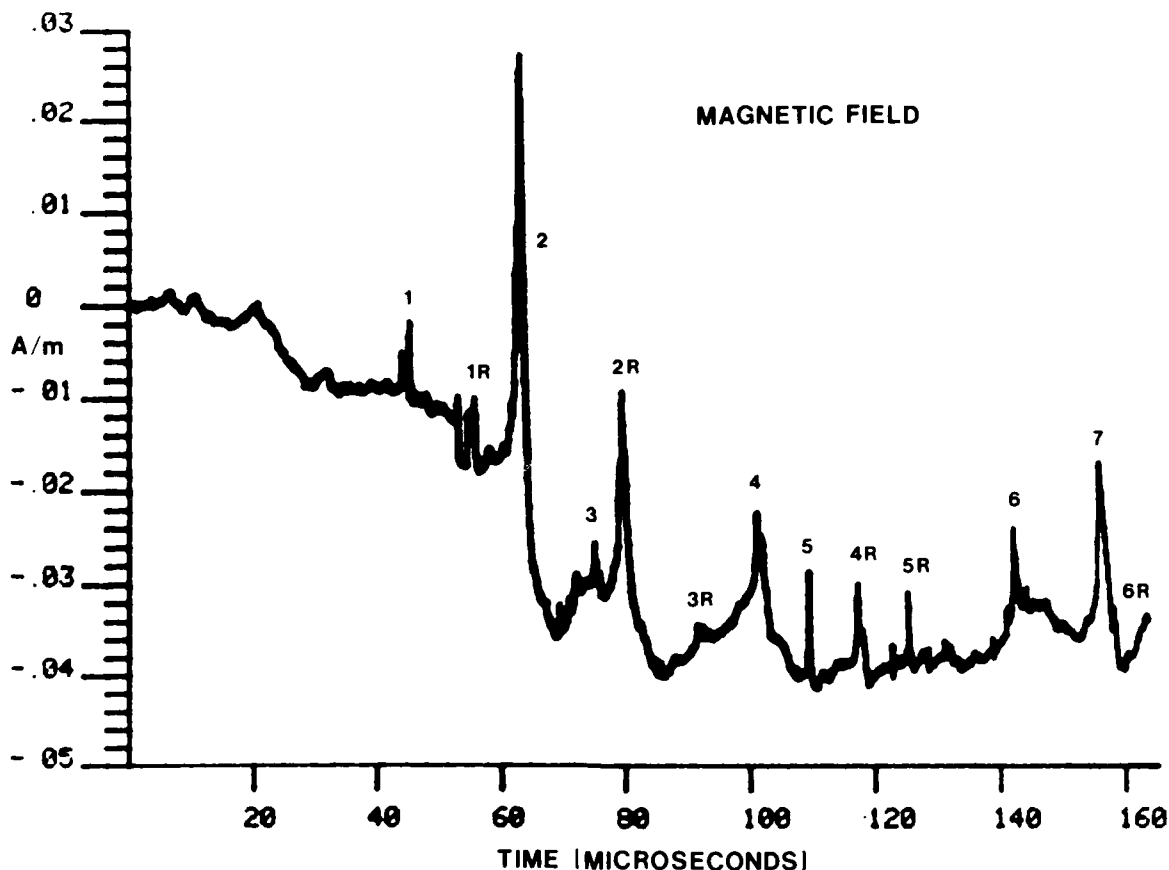


Fig. 18 - Magnetic field pulses recorded at the start of the leader for the flash shown in Figure 17

5 km. Discharges occurring below 7 km usually led to the development of a ground flash.

The discharge steps radiated bipolar magnetic field pulses with risetimes of 50 to 200 ns and pulse widths of 100 ns to 3 μ s. Currents inferred from the magnetic fields averaged 4.6 kA and current rates-of-rise averaged 3.7×10^{10} A/S. The largest current and current rate-of-change inferred were 26 kA and 1.1×10^{11} A/S.

These findings have several features in common with lightning attachments to aircraft, indicating a possible relationship. Aircraft direct strikes have been experienced in two cloud regions. Most aircraft lightning-strike incidents occur below an altitude of 5 km. Research flights seeking direct strikes have encountered lightning attachments frequently in upper areas of clouds. Measurements of direct strikes on instrumented aircraft have shown relatively moderate current levels of 30 A to 24 kA, current rates-of-change from 1.1×10^7 to 1.7×10^{11} A/S, short current risetimes and impulsive current flow (1,20,21).

A simple technique for estimating lightning discharge locations has been demonstrated using ground reflections of lightning fields in conjunction with radar data. There are uncertainties in the technique

but the results are reasonable and provide a step to step indication of discharge propagation. We hope to apply the technique to records of more complex breakdown such as regular intracloud pulse sequences and stepped leaders. Further useful data may also be found in the continuous analog field record, expanding the time interval over which locations can be determined.

REFERENCES

1. P.L. Rustan et al., "Electromagnetic Measurements of Lightning Attachment to Aircraft." Eighth International Aerospace and Ground Conference on Lightning and Static Electricity, Fort Worth, Texas, June 1983.
2. D.M. Levine and Vladislav Mazur, "Correlated Measurements of VHF Radar Signatures, RF Radiation, and Electric Field Changes from Lightning." Eighth International Aerospace and Ground Conference on Lightning and Static Electricity, Fort Worth, Texas, June 1983.
3. B.P. Kuhlman et al., "1981 WC-130 Airborne Lightning Characterization Program Data Review." USAF Technical Report, AFWAL-TR-84-3024, December 1983.

4. E.P. Krider and C.D. Weidman, "The Submicrosecond Structure of Lightning Radiation Fields." Eighth International Aerospace and Ground Conference on Lightning and Static Electricity, Fort Worth, Texas, June 1983.
5. P.L. Rustan et al., "Airborne Lightning Characterization." USAF Technical Report, AFWAL-TR-83-3013, April 1983.
6. P.L. Rustan et al., "Correlated Airborne and Ground Measurements of Lightning." Proceedings of the International Aerospace Conference on Lightning and Static Electricity, Oxford, England, March 1982.
7. P.L. Rustan et al., "Airborne Measurements of the Risetimes in Lightning Return Stroke Fields." Eighth International Aerospace and Ground Conference on Lightning and Static Electricity, Fort Worth, Texas, June 1983.
8. M.A. Uman et al., "Airborne and Ground-Based Lightning Electric and Magnetic Fields and VHF Source Locations for a Two-Stroke Ground Flash." Eighth International Aerospace and Ground Conference on Lightning and Static Electricity, Fort Worth, Texas, June 1983.
9. M.A. Uman, "Lightning Data Analysis", USAF Technical Report, AFWAL-TR-83-3116, December 1983.
10. C.E. Baum et al., "Sensors for Electromagnetic Pulse Measurements Both Inside and Away From Nuclear Source Regions." IEEE Transactions on Antennas and Propagation, Vol AP-26, No.1, January 1978.
11. C.D. Taylor, "External Interaction of the Nuclear EMP with Aircraft and Missiles." IEEE Transactions on Electromagnetic Compatibility, Vol EMC-20, No.1, February 1978.
12. B.P. Kuhlman et al., "Lightning Field Spectra Obtained From Airborne Measurements." Eighth International Aerospace and Ground Conference on Lightning and Static Electricity, Fort Worth, Texas, June 1983.
13. F.J. Eriksen et al., "Electromagnetic Coupling Modeling of the Lightning/Aircraft Interaction Event." USAF Technical Report, AFWAL-TR-81-3084, Vol III, August 1981.
14. V.V. Liepa, "Current and Charge Measurements on Scale Model EC-130 Aircraft." Final Report, Navy Contract No. N00019-77-C-0069, September 1978.
15. W. Beasley et al., "Electric Fields Preceding Cloud-to-Ground Lightning Flashes." Journal of Geophysical Research, February 1977.
16. R.K. Baum, "Airborne Lightning Characterization." Proceedings of the NASA Symposium on Lightning Technology, NASA CP2128, April 1980.
17. C.D. Weidman and E.P. Krider, "The Radiation Field Wave Forms Produced by Intracloud Lightning Discharge Processes." Journal of Geophysical Research, June 1979.
18. C.E. Baum et al., "Measurements of Electromagnetic Properties of Lightning with 10 Nanosecond Resolution", Proceedings of the NASA Symposium on Lightning Technology, NASA CP 2128, April 1980.
19. M.A. Uman et al., "The Electromagnetic Radiation from a Finite Antenna." American Journal of Physics, Vol 43, 1975.
20. B.J. Peterson and W.R. Wood, "Measurements of Lightning Strikes to Aircraft." Final Report No. DS-68-1, Federal Aviation Administration, January 1968.
21. B.G. Melander, "Lightning Data Acquisition." Final Report, NASA Contract NAS1-17446, December 1983.
22. R.B. Anderson and A.J. Eriksson, "Lightning Parameters for Engineering Applications." Electra, No. 69, 1980.
23. F. Garbagnati et al., "Parameters of Lightning Currents, Interpretation of the Results Obtained in Italy." Sixteenth Conference on Lightning Protection, Szeged, Hungary, July 1981.
24. D.R. MacGorman et al., "Some Spatial and Temporal Relationships Between Lightning and Storm Structure and Evolution." Eighth International Aerospace and Ground Conference on Lightning and Static Electricity, Fort Worth, Texas, June 1983.
25. W.D. Rust et al., "Storm Electricity Research in Oklahoma: an Overview." Eighth International Aerospace and Ground Conference on Lightning and Static Electricity, Fort Worth, Texas, June 1983.
26. F.A. Fisher and J.A. Plumer, "Lightning Protection of Aircraft." NASA RP-1008, 1977.
27. B.D. Fisher and J.A. Plumer, "Lightning Attachment Patterns and Flight Conditions Experienced by the NASA F-106B Airplane." Eighth International Aerospace and Ground Conference on Lightning and Static Electricity, Fort Worth, Texas, June 1983.
28. P.L. Rustan, "Properties of Lightning Derived From Time Series Analysis of Radiation Data, Ph.D. Dissertation, University of Florida, 1979.
29. P. Laroche et al., "A Contribution to the Analysis of Triggered Lightning: First Results Obtained During the TRIP 82 Experiment." Eighth International Aerospace and Ground Conference on Lightning and Static Electricity, Fort Worth, Texas, June 1983.

ANALYSIS OF LIGHTNING CURRENT MEASUREMENTS

P. L. Rustan

Air Force Wright Aeronautical Laboratories, AFWAL/FIESL, Ohio 45433

P. R. Axup

Air Force Institute of Technology, AFIT/ENG, Ohio 45433

The effect of towers on current measurements of lightning has been determined. Specifically, the effect of tower height, surge impedance, series resistance and footing resistance on return stroke current measurements were analyzed. Additionally, the effects of the current sensor location were determined. Currents were estimated using the double exponential return stroke model, Lin's breakdown current model, Little's lumped parameter ladder network model, and Strawe's non-linear transmission line model. The tower was modeled as a finite element transmission line. The results were then compared with three sets of data; Berger's measurements near the top of a 70 m tower, Garbagnati's measurements at the top of a 40 m tower, and Eriksson's measurements at the bottom of a 60 m tower.

The results show that the frequency response of the current in the channel and the tower height are the key parameters to determine the number of lumped elements in the transmission line model. Tower surge impedance and tower series resistance have negligible effect on current levels and rate of rise of the current. Tower footing resistance has a pronounced effect on both the current levels and the rate of rise. The results also show that the location of the current sensor has a significant effect on current level but less effect on rate of rise.

INTRODUCTION

With the increased use of non-metallic materials in the construction of aircraft skins and airframes, the protection previously provided by metal skins against lightning has been significantly reduced. Additionally, aircraft now contain more low voltage, integrated circuit equipment, both for use in the mission, and for operation of the aircraft itself. This low voltage, high speed equipment is susceptible to electromagnetic interference because electromagnetic coupling from lightning can easily generate transient voltages comparable to the signal voltages. Thus, these new aircraft designs appear to be more susceptible to damage from lightning direct attachments which can explode fuel tanks and destroy or temporarily disable flight critical avionics systems. Furthermore, these new designs are more susceptible to nearby flashes.

For these reasons, the United States Air Force (USAF) has an increased interest in understanding lightning. A well defined description of the lightning threat is needed so that aircraft can be properly designed to withstand this threat.

Current lightning threat definitions are based on return stroke tower current measurements performed primarily by Berger (1975) in Switzerland, Garbagnati (1982) in Italy, and Eriksson (1978) in South Africa. The return stroke lightning current as measured on the tower is assumed to be the same as the incident current in the channel when lightning strikes the ground. Anyone who has worked in a laboratory is familiar with the

problem of introducing error when making measurements. The tower introduces a measurement error. In this paper, the measurement error introduced by having the tower in the return stroke channel is calculated by using the following procedure:

(a) Comparison of published return-stroke lightning channels including Cianos and Pierce (1972), Lin (1978), Little (1978), and Strawe (1982); (b) Modeling the tower as a lumped element transmission line; and (c) Comparison of the results of terminating the lightning channel in a lumped transmission line (tower) versus terminating in a 100 ohms resistance (flat ground).

RETURN STROKE MODELS

Four lightning return stroke models were reviewed to consider their effects in the tower model. These models are the Cianos-Pierce version of the Bruce-Golde (1941) lightning current, the Lin's breakdown pulse current, the Little's transmission line channel, and the Strawe's non-linear transmission line.

Transmission line engineers model current as a double exponential of the form

$$I = I_0 (e^{-at} - e^{-bt}). \quad (1)$$

This waveform was used for the current in the channel with the Cianos and Pierce (1972) values of $a = 1.7 \times 10^4/\text{sec}$ and $b = 3.5 \times 10^6/\text{sec}$.

Lin (1980) modeled the return stroke current in the channel as consisting of three terms, the continuous current, the breakdown pulse, and the corona current. Only the breakdown pulse has sufficient high frequency to be used in the calculation of the peak value of the current and the rate of rise of the current. The average breakdown pulse used by Lin (1980) is shown in Figure 1. This breakdown current and the Cianos and Pierce current in equation (1) were used to make the Norton equivalent circuit of the return stroke channel as shown in Figure 2.

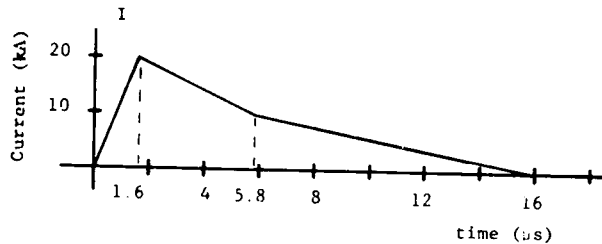


Figure 1. Lin's Breakdown Pulse Current

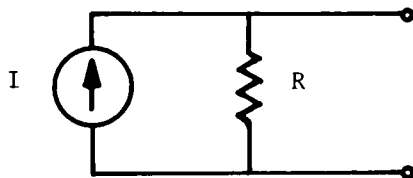


Figure 2. Norton Equivalent Circuit of the Return Stroke Channel

Little (1978) used a lumped parameter ladder network to model the lightning return stroke channel. The inductances and capacitances were chosen to meet the physical characteristics of the channel. The basic channel consisted of nine cascaded sections. With an assumed channel length of 3 km, this model has a cutoff frequency of 90 kHz. Although this model produces rates of rise that are in the top 10 percentile of measured subsequent return strokes, these rates are produced by selected circuit values; they are not due to an accurate model of the channel.

Strawe (1982) modeled the return stroke lightning current by using a transmission line with non-linear resistance elements. The version of the model used consisted of 150 sections and has a cutoff frequency near 100 MHz.

TOWER MODEL

A tower can be modeled by using circuit elements, either as a lumped element or as a transmission line. For a single lumped element model to be adequate, the transient

time needed for a pulse to propagate along the length of the tower must be small when compared with the risetime of the current pulse being measured. Towers used for lightning current measurements are about 50m in height, using a propagation velocity of .7c, the required transient time is on the order of a quarter of a microsecond. The average risetime of the fields produced by lightning return strokes has been measured from a tenth of a microsecond (Krider and Weidman, 1983) to several microseconds (Fisher and Uman, 1972). Thus, towers used to measure lightning currents cannot be properly modeled as a single lumped element and a transmission line model must be used. Figure 3 shows a four section transmission line representation of a tower.

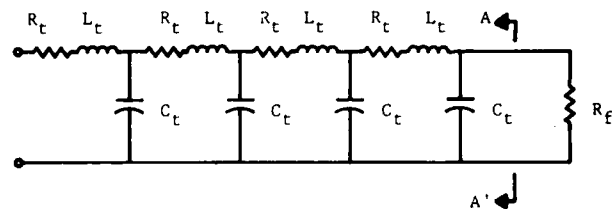


Figure 3. Transmission Line Model for Tower

Assuming no leakage conductance and negligible tower resistance, the tower surge impedance is

$$Z_t = \sqrt{L/C} \quad (2)$$

Using a typical velocity of .7c (Sargent, 1969)

$$v = \frac{.7}{\sqrt{LC}}, \quad (3)$$

where the values of L and C can be calculated for a given impedance. A surge impedance, Z_t , of 130 ohms was estimated based on the empirical equations found in the literature (Sargent, 1969). Solving (2) and (3) yields $L = 6.2 \times 10^{-7}$ H and $C = 3.7 \times 10^{-11}$ F. The number of sections needed to represent the transmission line depends primarily on the value of L and C selected and the cutoff frequency of the current in the lightning channel (Johnson, 1950). The cutoff frequency of the lightning channel was chosen as 5 MHz based on reported data (Wiedman et al, 1981) which indicates that the frequency content of lightning falls off as $1/f$ between 10^4 and 5×10^6 Hz and falls off as $1/f^2$ above 5×10^6 Hz. The number of sections per meter, n, can be calculated from equation (4), (Johnson, 1950) as,

$$\begin{aligned} n &= \pi f_c \sqrt{LC} \quad (4) \\ n &= \pi 5 \times 10^6 \sqrt{(6.2 \times 10^{-7})(3.7 \times 10^{-11})} \\ n &= .075 \end{aligned}$$

With these conditions a four section transmission line will adequately represent a tower height of 53.3 meters.

As a check of the validity of using four elements in the tower model, the sensitivity of the various parameters (peak current, maximum rate of rise, and time to peak current) were measured both at the top and at the bottom of the tower. The rate of rise at the bottom of the tower was determined to be the most sensitive parameter. Figure 4 shows a plot of the rate of rise at the bottom of the tower versus the number of sections in the tower. The model with four sections gives 94% of the rate of rise found for 10 sections. In addition to the surge impedance and the propagation velocity of the current along the tower, the tower resistance and the footing resistance of the tower must be included in the tower modeling.

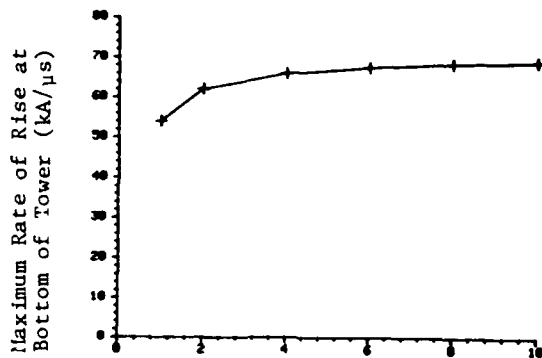


Figure 4. Sections required in the Model

All the three towers were designed to be good conductors. Assuming the conducting path to ground is only 1 cm² for a steel tower ($\rho = 1 \times 10^{-7}$ ohm meter), a tower height of 50 m has a resistance, R_t , of only 0.05 ohms. A value of one ohm was chosen as the tower resistance which corresponds to about 2×10^{-2} ohm/meter. A sensitivity analysis was performed to determine the effect of a variable tower resistance on the rate of rise of the current at the bottom of the tower. For tower resistances between .0025 and 2.5 ohms the rate of rise does not vary more than one percent.

Researchers have measured and calculated the surge impedance used for power transmission line towers (Jordan, 1934; Sargent, 1969). Sargent (1969) addressed the many analytical equations used to determine surge impedances. His work indicated that calculated values for typical towers range from 80 to 500 ohms, and measured values range from 80 to 350 ohms with a most likely value between 100 and 150 ohms. When the analytical equations of the tower surge impedance were applied to the towers used to obtain lightning currents by Berger, Garbagnati, and

Eriksson, the following values were obtained. Berger's tower surge impedance fell between 78 and 347 ohms, Garbagnati's tower surge impedance fell between 95 and 148 ohms and Eriksson's tower surge impedance fell between 283 and 345 ohms. Table 1 shows the result of a Princeton Circuit Analysis Program (PCAP) model varying the surge impedance between 30 and 500 ohms. The rate of rise of the current at the bottom of the channel, the most sensitive parameter, remains nearly constant for surge impedances between 80 and 250 ohms. An 8% variation in the rate of rise of the current at the bottom of the tower was calculated for a 500 ohms surge impedance. For the range between 78 and 345 ohms the maximum error is less than 4%. Therefore, a fixed value of $Z_t = 130$ ohms was chosen to model the tower.

Z_t Ω	Top of Tower			Bottom of Tower		
	kA	μs	kA/ μs	kA	μs	kA/ μs
30	59	3.0	55	60	3.1	64
80	59	3.0	55	60	3.1	67
130	59	3.0	54	60	3.1	67
250	58	3.1	53	60	3.1	66
500	58	3.1	51	60	3.1	62

Table 1. Varying Surge Impedance Result of a PCAP Analysis using a Little's Channel Model with a four section tower, $R_f = 10$ and $R_t = .25$.

The propagation velocity of the current along the height of the tower is expected to be between 0.7 and 0.8 times the speed of light (Sargent, 1969; Kawai, 1964). A PCAP model was used to determine the effect of 0.7 and 0.8c on the current and the rate of rise of the current at the top and at the bottom of the tower. All the parameters remain constant for both propagation velocities except the rate of rise of the current at the bottom of the tower which increased by 9% for the higher propagation velocity. A propagation velocity of 0.7c was used for the tower model.

The transmission line model of the tower must be terminated on the resistance mismatch between the tower and the earth. This termination resistance is known as the footing resistance of the tower (Lewis, 1941; Whitehead, 1942; Vainer, 1966; Gupta, 1978). Table 2 shows the results of a PCAP analysis using Little's current model, a four section transmission line model of the tower and footing resistance between 1 and 250 ohms. For lower footing resistances, the peak

current and the maximum rate of rise are lower at the top of the tower than at the bottom of the tower. For higher footing resistances, the opposite is true. The crossover occurs near 130 ohms which is the surge impedance of the tower.

R_f Ω	Top of Tower			Bottom of Tower		
	kA	μ s	kA/ μ s	kA	μ s	kA/ μ s
1	59	3.0	54	61	3.0	69
10	59	3.0	54	60	3.1	67
30	58	3.0	54	59	3.1	64
50	57	3.0	53	58	3.1	61
90	55	3.0	53	56	3.2	56
150	54	3.0	52	53	3.2	49
250	51	3.0	52	49	3.3	40

Table 2. Varying Footing Resistance
Result of a PCAP Analysis using a Little's
Channel Model with a four section tower,
 $R_t=0.25$, $Z_t=130$, and $v=2.1 \times 10^8$ m/s.

The grounding system used by Garbagnati consisted of four driven rods (1.5 to 2 meters long) and a sub-surface mesh. The impedance (measured at 100 Hz) was between 50 and 100 ohms, and slightly higher in the summer (Garbagnati, 1983). From the measured values at 100 Hz, the lower footing resistance was estimated between 4 ohms [50 ohms x 0.4 (grounding rod factor) x 0.2 (mesh factor)] and 50 ohms [100 ohms x 0.6 (grounding rod factor) x 1 (mesh factor)]. Similarly, Berger's tower grounding system consisted of a crow's foot counterpoise with a low frequency impedance of 30 ohms (Berger, 1983). Berger's tower footing resistance was calculated to be between 3 and 18 ohms. Eriksson measured the footing resistance of his tower under surge conditions to be 20 and 50 ohms (Eriksson, 1983).

The three research towers' footing resistance fall in the range from 10 to 50 ohms. Table 2 shows that over the range from 10 to 50 ohms the largest variation was 9% on the rate of rise of the current at the bottom of the tower. Therefore, to simplify the work a representative tower model was selected as standard for all three towers. The actual circuit values used for each section of the four lumped elements were $R_t=0.25$ ohm, $L_t=7.74 \times 10^{-6}$ henry, $C_t=4.58 \times 10^{-10}$ farad and the footing resistance, R_f , was 10 ohms.

TESTING THE RETURN STROKE TOWER MODEL

A Norton equivalent circuit was used to model the return stroke channel for the Cianos-Pierce's double exponential current and for the Lin's breakdown triangular current. Estimates of the return stroke channel impedance range from 200 to 1500 ohms. Since 500 ohms is the most commonly used value in the study of power line protection to a lightning discharge (Jordan, 1934; Bewley, 1951), it was used in the Norton equivalent circuit. A PCAP analysis was performed to determine the effect of terminating the Norton equivalent circuit in the four sections lumped element model in figure 3. These results were compared with those obtained by terminating the circuit with a ground resistance. The impedance the ground presents to the return stroke is not well known. Prinz (1977) used the range from 10 to 100 ohms depending on the ground conditions at the time of the strike. A termination resistance of 100 ohms was selected to be consistent with previous work (Little, 1978).

The Little and Strawe return stroke models use ladder networks and charged capacitors to simulate the channel and can be electrically connected to the transmission line representation of the tower in figure 3. These results were compared to those obtained when representing the tower by using a ground resistance. Variations of the ground resistance between 10 and 100 ohms produced less than a 2% variation in the rate of rise of the current in the channel.

Table 3 shows the actual current, the risetime and the rate of rise of the current obtained for the four return stroke models (towerless termination) when connected to a ground resistance of 100 ohms. These four models produce peak currents between 12 and 55 kA. Researchers interested in lightning protection of transmission lines over the last 30 years have primarily used the result of the AIEE Committee Report, 1950 on frequency distribution of current amplitudes.

Channel Model	At ground, R_g (100 ohms)		
	kA	μ s	kA/ μ s
Little	55	3.0	53
Strawe	12	0.35	164
Lin	17	1.6	10
Cianos-Pierce	16	1.6	53

Table 3. Towerless Termination

From the previous report, the probability of exceeding peak currents of 12, 16 and 55 kA are 60%, 50% and 7%, respectively. Since the return stroke models analyzed are based on different physical configurations, they produce a variety of currents levels.

A basic analysis of current reflection in a transmission line can provide an interpretation of the effect of the tower in the channel. The tower is a transmission line with a footing resistance less than the impedance of the transmission line. The low footing resistance produces a negative voltage reflection at the bottom of the tower, but a positive current reflection which adds to the incident current at the bottom of the tower. When the reflected wave gets back to the top of the tower, it will be reflected negatively, because the channel impedance is larger than the tower surge impedance. This negative reflection subtracts from the incident wave. Hence, after the first two reflections, the current and rate of rise are larger at the bottom of the tower than at the top.

Table 4 shows the effect of the four lightning return stroke models when a four section transmission line is introduced to model the tower effects. Regardless of the model, the peak current of the lightning channel incident to a flat ground with 100 ohms resistance is between 0.84 and 0.93 of the value obtained at the top of the tower. The ratio of the average rate of rise of the current at the top of the tower to the rate of rise of the current on the ground ranges between .71 and 1.15 for the four models tested in this work. As shown in Table 4 the effect is more pronounced at the bottom of the tower where the average values of the actual lightning current and the rate of rise incident on a flat ground with 100 ohms resistance are about 0.76 of the value measured on the tower.

Channel Model	Top of Tower		Bottom of Tower	
	Current	di/dt	Current	di/dt
Little	0.93	0.98	0.92	0.79
Lin	0.89	0.71	0.81	0.50
Cianos-Pierce	0.84	1.15	0.73	0.65
Strawe (20 sections)	0.86	1.04	0.55	0.54
Average	0.88	.97	0.76	.62
Standard Deviation	0.03	.19	0.13	.13

Table 4. Ratio of actual values to tower values

The footing resistance of the tower was chosen as 10 ohms. This is the most critical parameter in determining the effects of the tower on the current measurements. Figures 5(a) and (b) show the effect of the peak current and rate of rise as the footing resistance increases. The measurements taken on top of the tower are not as sensitive to variations on the footing resistance as the current on the bottom of the tower.

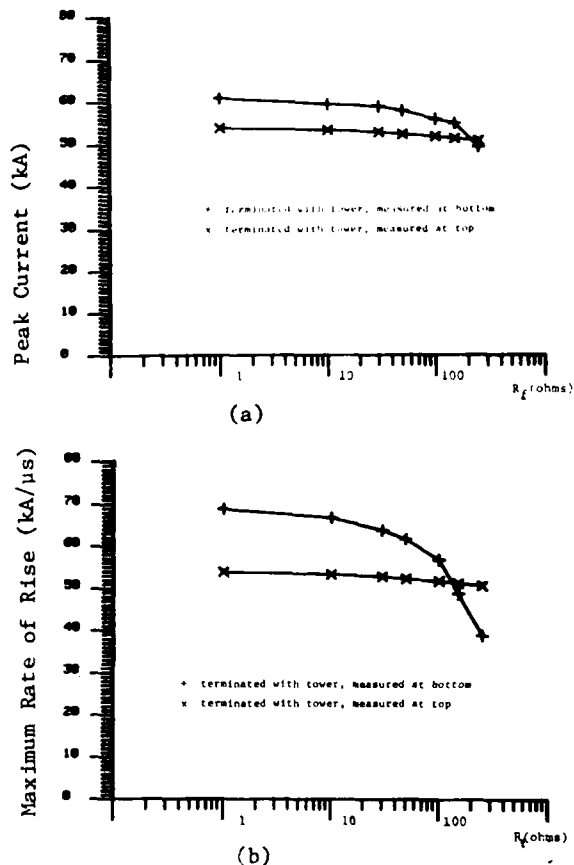


Figure 5. Analysis of a four section tower using Little's channel model $Z_t=130$ ohms, $v=0.7C$, $R_t=.25$ ohms. (a) Peak current vs footing resistance. (b) Maximum rate of rise vs footing resistance.

Table 5(a) shows the actual average values of peak current and rate of rise of the current reported by Berger, 1975; Garbagnati, 1982; and Eriksson, 1978. Table 5(b) shows the same results once the tower effects have been removed. The normalized results in Table 5(b) for Garbagnati's and Berger's measurements include the fact that their measurements were taken near the tops of their towers (Berger, 1965, 1975; Garbagnati, 1982) whereas Eriksson's measurements were made at the bottom of the tower.

Researcher	First Stroke						Subsequent Stroke					
	Peak Current			Maximum di/dt			Peak Current			Maximum di/dt		
	N	kA	σ	N	kA/ μ s	σ	N	kA	σ	N	kA/ μ s	σ
Berger (1975)	101	30	.23	92	12	.24	135	12	.25	122	40	.31
Garbagnati (1982)	42	32	.25	42	13	.36	33	17	.22	33	31	.39
Eriksson (1978)	11	41	.31	-	-	-	-	-	-	-	-	-
Amount largest exceeds smallest	37%			8%			42%			29%		

(Median Values for Negative Strokes)

- Notes:
1. N is the number of data points.
 2. σ is the standard deviation of the log of the quantity. All three researchers have found that the data fall in a log-normal distribution.
 3. Berger and Garbagnati did not provide σ . σ was calculated by assuming a log-normal distribution and calculating σ from the 5th and 50th percentiles, and averaging that with the σ from the 50th and 95th percentiles.

Table 5(a). Return Stroke Characteristics

Researcher	First Stroke						Subsequent Stroke					
	Peak Current			Maximum di/dt			Peak Current			Maximum di/dt		
	N	kA	σ	N	kA/ μ s	σ	N	kA	σ	N	kA/ μ s	σ
Berger	101	26	.23	92	14	.23	135	11	.25	122	46	.31
Garbagnati	42	28	.25	42	15	.36	33	15	.22	33	36	.38
Eriksson	11	31	.31	-	-	-	-	-	-	-	-	-
Amount largest exceeds smallest	23%			9%			50%			31%		

Berger's and Garbagnati's data normalized with the factor for the top of the tower. Eriksson's data normalized with the factor for the bottom of the tower.

Table 5(b). Normalized Return Stroke Characteristics

CONCLUDING REMARKS

A summary of the lightning current measurements performed in instrumented towers by Berger, Garbagnati and Eriksson was presented. Four return stroke models and a transmission line tower model were used to determine the effect of the tower on the current measurements. The results indicate that for Berger's and Garbagnati's data which were obtained near the top of the tower, the peak current and the rate of rise of the

current should be multiplied by 0.88 and 1.16, respectively, to exclude the tower effects. Eriksson's peak current and rate of rise of the current data which were obtained near the bottom of the tower should be multiplied by about 0.76 to exclude the tower effects. Therefore, it appears that the tower data must be scaled by these appropriate constants prior to threat analysis.

REFERENCES

1. AIEE Committee Report, "A Method for Estimating Lightning Performance of Transmission Lines," AIEE Transactions Pt III, 69, 1187-1196, 1950.
2. Berger, K. Private Communication, 25 July 1983.
3. Berger, K., et al. "Parameters of Lightning Flashes," Electra, No.41, pp. 23-37, 1975.
4. Bewley, L. V. Traveling Waves on Transmission Systems. Second edition, John Wiley & Sons, Inc., New York, 1951.
5. Bruce, C. E. R., and R. H. Golde. "The Lightning Discharge," The Journal of the Institution of Electrical Engineers, Vol. 88, Part II, No. 6, pp. 487-524, December 1941.
6. Cianos, N., and E. T. Pierce. "A Ground Lightning Environment for Engineering Usage," Stanford Research Institute, Project 1834, August 1972. DTIC No. AD907891.
7. Eriksson, A. J. Private Communication, 15 August 1983.
8. Eriksson, A. J. "Lightning and Tall Structures," Transactions: South African Institute of Electrical Engineers, Vol. 69, Pt. 8, pp. 238-252, August 1978.
9. Garbagnati, E. Private Communication, 28 July, 1983.
10. Garbagnati, E., and G. B. Lopiparo. "Lightning Parameters - Results of 10 Years of Systematic Investigation in Italy," International Aerospace Conference on Lightning and Static Electricity, 23-25 March 1982.
11. Gupta, B. P., and B. Thapar. "Impulse Impedance of Grounding Systems," IEEE PES Summer Meeting, paper A 78 563-9, 16-21 July 1978.
12. Johnson, W. C. Transmission Lines and Networks. McGraw-Hill Book Company, Inc., New York, 1950.
13. Jordan, C. A. "Lightning Computations for Transmission Lines with Overhead Ground Wires," General Electric Review, Vol. 37, pp. 130-137, March 1934, pp. 180-186, April 1934, and pp. 243-250, May 1934.
14. Kawai, M. "Studies of the Surge Response on a Transmission Line Tower," IEEE Trans. on Power App. and Systems, Vol. PAS-83, No. 1, pp. 30-34, Jan 1964.
15. Krider, E. P., and C. D. Weidman. "The Submicrosecond Structure of Lightning Radiation Fields," Int Aerospace and Ground Conference on Lightning and Static Electricity, Ft. Worth, Texas, pp. 69: 1-8, 21-23 June 1983.
16. Lewis, W. W. "Pick-up and Resistance of Counterpoise Systems," Elect. World, Vol.116, pp.1720-1721, 1766-1767, Nov 1941.
17. Lin, Y. T. "Lightning Return Stroke Models," Ph.D. dissertation, University of Florida, Gainesville, 1978.
18. Lin, Y. T., et al. "Lightning Return Stroke Models," Journal of Geophysical Research, Vol. 85, No. C3, pp. 1571-1583, 20 March 1980.
19. Little, P. F. "Transmission Line Representation of a Lightning Return Stroke," Journal of Physics D: Applied Physics, Vol 11, No. 13, pp. 1893-1910, 11 September 1978.
20. Prinz, H. "Die Blitzentladung in Vierparameterdarstellung," Bull. SEV, Vol. 68, No. 12, pp. 600-603, 18 June 1977.
21. Sargent, M. A., and M. Darveniza. "Tower Surge Impedance," IEEE Transactions on Power Apparatus and Systems, Vol. PAS-88, No. 5, pp. 680-687, May 1969.
22. Strawe, D. F., et al. "A Self-consistent Model for Return Stroke Currents and Fields," Seventh Int Aerosp and Ground Conf on Lightning and Static Electricity, Oxford, England, March 1982.
23. Vainer, A. L. "Impulse Characteristics of Grounding Systems," Elektrichestvo (U.S.S.R.), pp. 23-27, March 1966.
24. Whitehead, E.R. "Design Transmission Lines for Inherent Protection," Electric Light and Power, Vol.20, pp.32-27,78, September 1942.
25. Weidman C.C., E.P. Krider, and M.A. Uman, "Lightning Amplitude Spectra in the Interval from 100 kHz to 20 MHz," Geophysics, Res. Lett., Vol.8, pp. 931-934, 1981.

PROTECTION OF AIRCRAFT AGAINST STATIC ELECTRICITY
AND CHARGE ACCUMULATION EFFECTS

Jean Pierre Simi, Member of BNAé Working Group 58
Câbles de Lyon, Bezons, France
Michel Dill, Coordinator of BNAé Working Group 58
Centre d'Essais Aéronautique de Toulouse, Toulouse, France

ABSTRACT

This paper describes the works conducted by the French Bureau de Normalisation de l'Aéronautique (BNAé: Aeronautics Standardization Bureau).

This organization, supported by the Direction Technique des Constructions Aéronautiques (DTCA: Technical Authority for the Aeronautics Industry), a military organization, includes all the French airframe manufacturers as well as the associated equipment manufacturers.

The BNAé is organized in working groups, including working group "58", (*) specialized in problems of electromagnetic compatibility regarding aircraft, in particular interference-creating phenomena such as lightning and electrostatic charges.

In June 1984, this working group issued Recommendations RE.Aéro 702 50, discussed herein. These Recommendations concern the interference phenomena and the ways of hardening aircraft against them.

The other works conducted by the group are also discussed in the paper.

(*) Working Group "58" is connected with "Integration and Systems Dept." presided over by Mr MOUFFOCK, S.T.T.E., since its creation in 1978.

INTRODUCTION

THE USE OF MODERN TECHNOLOGY, both for airframes and for equipment, has increased the susceptibility of aircraft to atmospheric electricity, making it vital to protect them against phenomena such as lightning and static electricity.

This paper describes some of the actions undertaken in France as concerns both recommendations and research and testing in order to develop protections and improve their efficiency.

The manufacturer's representatives participating in the programs mentioned have contributed to the paper.

BNAé AND WORKING GROUP 58

The Bureau de Normalisation Aéronautique (BNAé: Aeronautics Standards Bureau) created Working Group 58 (GT58) specialized in atmospheric electricity.

This working group includes representatives from government agencies, supervisory organizations, airframe and equipment manufacturers in the aeronautics and related fields, concerned by the problems of lightning and electrostatic charges.

The group provides the opportunity to discuss these problems as they are experienced in France and has been assigned the task of reviewing and generating comments on foreign and international regulatory or standardization documents in the aeronautics field.

Another task of GT58 is to draft recommendations for the aerospace industry. Two recommendations have already been issued.

The first (RE.Aéro 702.50 - "Protection of Aircraft against the Effects of Atmospheric Electricity - Lightning and Electrostatic Charges", January 1984) is addressed in particular to design and engineering offices. It briefly describes the phenomena producing interference and details the concepts and means of protection which can be adopted. This recommendation is summarized in appendix and 50 copies of the recommendation are available for the participants in the conference.

The second recommendation (RE.Aéro 702.51, "Protection of Aircraft against the Effects of Atmospheric Electricity, Validation Tests, Project No. 3", January 1984) concerns testing. The test methods are now conventional. They are designed to verify and qualify the protection of an aircraft against the effects of lightning and static electricity.

THE TRANSALL 04 LIGHTNING PROTECTION PROGRAM

To be able to write recommendations and standards, it is necessary to know the real levels in order to suitably size the protections.

The Technical Departments of the DTCA (STTE: Technical Department for Telecommuni-

cations and Aeronautical Equipment) decided on a flight test program with the following main objectives:

- improved definition of lightning currents
- characterization of the environment to which the equipment is subjected (voltage surges, electromagnetic field, etc.)
- determination of the effect of shielding on various aeronautical materials
- study of the mechanisms generating voltage surges, etc.

The program was initiated in 1975 and the first flight tests were conducted in 1978 with the participation of the Société d'Etudes et de Fabrications des Techniques Industrielles Modernes (SEFTIM: Modern Industrial Technique Design and Manufacturing Company) and agencies of the DTCA (AIA-CF: Atelier Industriel de l'Aéronautique de Clermont-Ferrand (Industrial Aeronautics Laboratory of Clermont-Ferrand), CEV: Centre d'Essais en Vol (Flight Test Center) and CEAT). The ONERA (Office National d'Etudes et de Recherches Aérospatiales--National R&D Bureau) has participated in the tests since the 1980 campaign by conducting the wide bandwidth electromagnetic measurements and the electrostatic measurements.

Considering the particular character of the tests, it was necessary for the aircraft used as support to comply with safety requirements, to provide maximum facilities for installation of measuring equipment and to have a flight envelope suitable for lightning testing.

The choice was therefore settled on the TRANSALL C 160-04 aircraft provided for testing by the CEV and illustrated in Fig. 1.



Fig. 1 - TRANSALL 04

In addition to the parameters specific to

the aircraft (speed, angle of attack, engine rpm, altitude, etc.) measured by the CEV using conventional means, the aircraft was equipped with special instrumentation for measurement of lightning parameters such as:

- lightning current
- magnetic field
- voltage surges on equipment and aircraft power systems
- skin currents
- electrostatic measurements
- lightning sensor
- electromagnetic measurements

The general principle, tested in 1978 and finally settled on in the 1980 campaign, consists of using optical systems to transmit the essential inputs to the electronic acquisition equipment located inside a shielded frame.

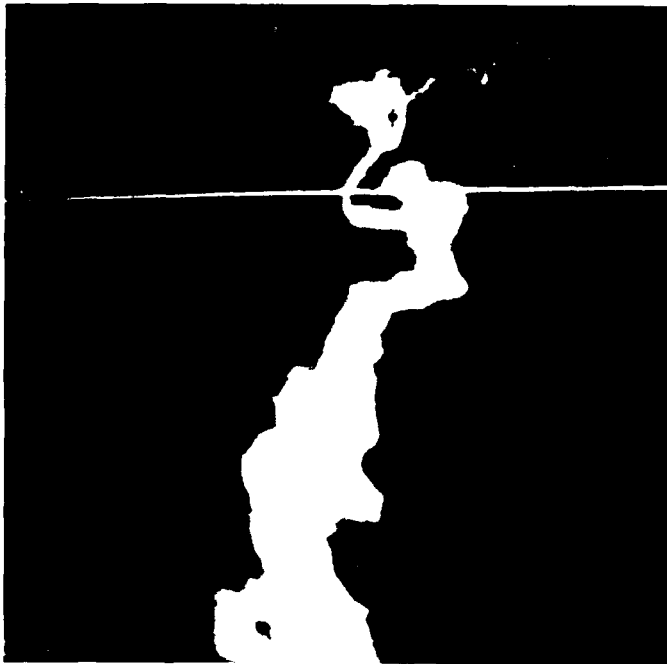


Fig. 2 - Example of video (forward rod)

Four test campaigns have already taken place. Each, with a duration of three to five months, includes a large amount of ground preparation work (integration of equipment, calibration, shock current testing) in addition to the actual flight testing.

The special equipment has undergone considerable changes during these campaigns, with the goal of optimizing the test facilities to the purpose to be accomplished and adapting the instrumentation to the constraints (bandwidth, environment, etc.) by the use of state-of-the-art equipment and by correcting any flaws observed.

During the test campaigns (19 in '78, 11 in '80 and 6 in '81), 36 lightning strikes were experienced in flight during the 47 flight hours under stormy conditions. Not all the strikes produced useful records. In some cases the acquisition was not completed, in others the levels collected were below the sensor and system sensitivities and in still others, the lightning struck the airfoil, whose span is virtually equal to the length of the aircraft.

Only a cursory analysis of the records was made, with a narrow bandwidth, thereby losing the benefit of the wide bandwidth afforded by the airborne instrumentation.

In June and July 1984, the Transall 04 is scheduled to participate in the LANDES 84 campaign including both experiments on atmospheric physics (DRET) and the normal lightning testing of the aircraft (DTCA).

Subject to favorable meteorological conditions, this campaign should provide new knowledge on aircraft lightning strikes.

BEHAVIOR OF A CARBON AIRFOIL IN LIGHTNING

Lightning tests were carried out in the framework of an evaluation program on an experimental composite carbon-resin airfoil including:

- a carbon box structure containing the kerosene
- metal moving parts on the leading edge and trailing edge
- metal stabilizers on the wing tips.

The testing on this airfoil includes the evaluation of the behavior in lightning, conducted in two stages:

1. Determination and testing of representative specimens of the various sections of airfoil.
2. Full-scale testing on a carbon wing box structure equipped with the metal parts used in flight.

The first stage of testing showed that lightning was not likely to substantially affect the mechanical strength of the structures. However, at the level of severity considered, sparking in the wing box structure is a non-negligible hazard.

The second stage of testing on one wing is designed to validate the working hypotheses and demonstrate satisfactory behavior in lightning of this carbon airfoil as concerns:

- direct effects: impact of lightning, lightning current transfer, problems of sparking, and
- indirect effects, in particular the voltages induced in the electric cables when the aircraft is struck by lightning.

The following tests are to be conducted during this second stage of testing:

- low level DC testing in continuous and pulse mode to determine the distribution of currents in the airfoil and the voltages induced in the wiring (breakdown by indirect effect)

- a sparking test by injection of high level current.

THE ALOUETTE III PROGRAM

The particular electrostatic behavior of helicopters arising from their aerodynamic structure, their capability to hover and their rotating airfoil pose problems in providing protection against the effects of the electrostatic charge by conventional means.

The STTE therefore requested the CEV, SEFTIM and the CEAT to conduct a test program as an initial approach to the phenomena and the techniques to be implemented.

The analysis being performed on the flight and ground test results is complicated by:

- the flight limits of the helicopter which made it impossible to achieve severe charge conditions
- the particularly high discharge effect of the main rotor.

These two points result in signals at levels so low that analysis is difficult.

The helicopter was not available for more complete investigations. However, on the basis of the initial results, continuation of the program appears justified after redefining

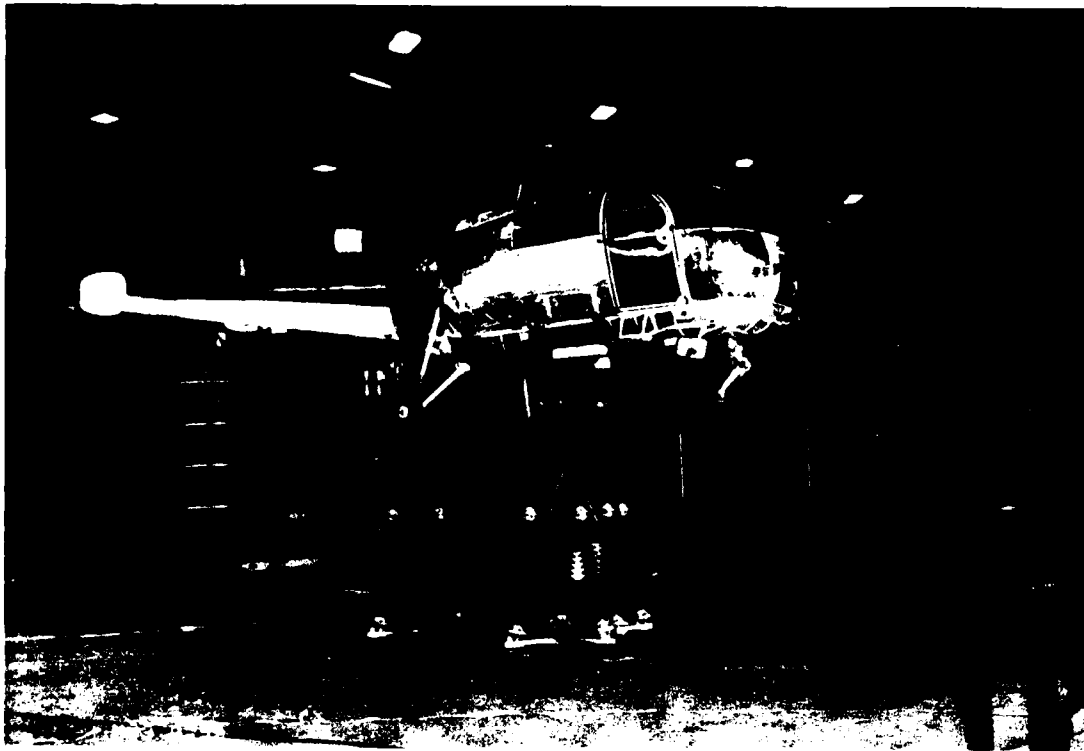


Fig. 3 - Alouette III ground testing

An Alouette III of the CEV (Fig. 3) was therefore equipped with the facilities corresponding to the problems to be investigated:

- a high voltage power supply (50 kV) which could be connected either to a discharger located in the gas jet of the turbine or to a winch thereby allowing the helicopter potential to be determined by an opposition method
- a set of six passive dischargers located on the airframe and instrumentation to measure the currents leaked off
- an instrument to measure the electromagnetic interference (radiocompass AGC)
- a radio altimeter.

the characteristics of the test and measuring equipment as well as finding a more suitable helicopter.

ANALYSIS OF THE BEHAVIOR OF PASSIVE DISCHARGERS IN THE PRESENCE OF WIND

The numerous wind tunnels tests conducted have demonstrated the effect of relative wind on operation of passive dischargers.

The tests described below were conducted in a supersonic wind tunnel on various types of commonly used passive dischargers as well as on a prototype SEFTIM discharger, illustrated in Fig. 4, whose performance it was attempted to improve by putting to use the effects due to the wind.

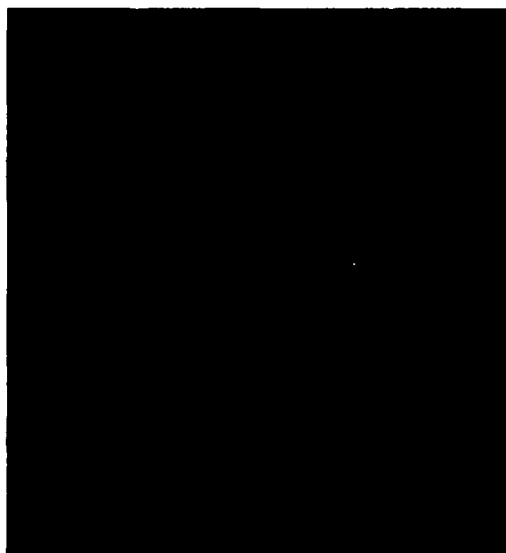


Fig. 4 - SEFTIM discharger

The discharger under test is mounted on an insulating bracket located in the airstream. A potential adjustable between 0 and 60 kV is applied to a flat metal plate perpendicular to the direction of the wind, located approximately 20 cm behind the tips of the discharger. The tests were conducted for speeds between Mach 0 and Mach 2 and the current discharge according to the potential applied and the Mach number was measured.

Table 1 shows the results obtained for a commonly used discharger (type 1) and for the prototype SEFTIM discharger (type 2).

The table shows the considerable influence of wind speed in improving the characteristics of the dischargers. This improvement is particularly noticeable on the discharger design taking this effect into account.

The protection of aircraft equipped with such specially designed dischargers is thus enhanced.

THE METEOR PROGRAM

Several earlier papers reported on the first Meteor test program, sponsored by the Engineering Agency of the DTCA and conducted by the ONERA, SNIAS, CEV and CEAT. Figure 5 shows ground testing of the Meteor.

The CEV, SEFTIM and CEAT were requested by the STTE to conduct a second program using this aircraft and the facilities with which it is already equipped to investigate two phenomena related to electric charges in aircraft, with consequences which can be crucial as regards their protection:

- electromagnetic interference generated by charges circulating in the boundary layer
- existence of heterogenous space charges.

One of the goals of the tests conducted in the framework of the Meteor program is to analyze whether charges created by triboelectric effect circulate in the boundary layers and generate electromagnetic interference on antennas located within such charged boundary layers.

Mach No.	Arcing Threshold (kV)	Type 1 Discharger				Arcing Threshold (kV)	Type 2 Discharger			
		Current Discharged (μA)					Current Discharged (μA)			
		at 10kV	at 20kV	at 30kV	at 50kV		at 10kV	at 20kV	at 30kV	at 50kV
0	13	0	0.3	1	4	13.5	0	0.45	1.3	5
0.3	11.5	0	3.8	11	28	1.6	6.5	13.5	22	50
0.5	11	0	6.5	18.5	40.5	5.2	6	19	33	77
0.7	10.5	0	6.5	13	~	1.5	13.5	28	48	~
0.9	10		3.4	22	~	3.6	6.2	21	51	~
1.041	9	0.85	10	71	~	1.2	9.8	37	133	~
1.53	7	0.09	65	~	~	< 1	41	165	~	~
1.95	2	40	~	~	~	< 1	85	~	~	~

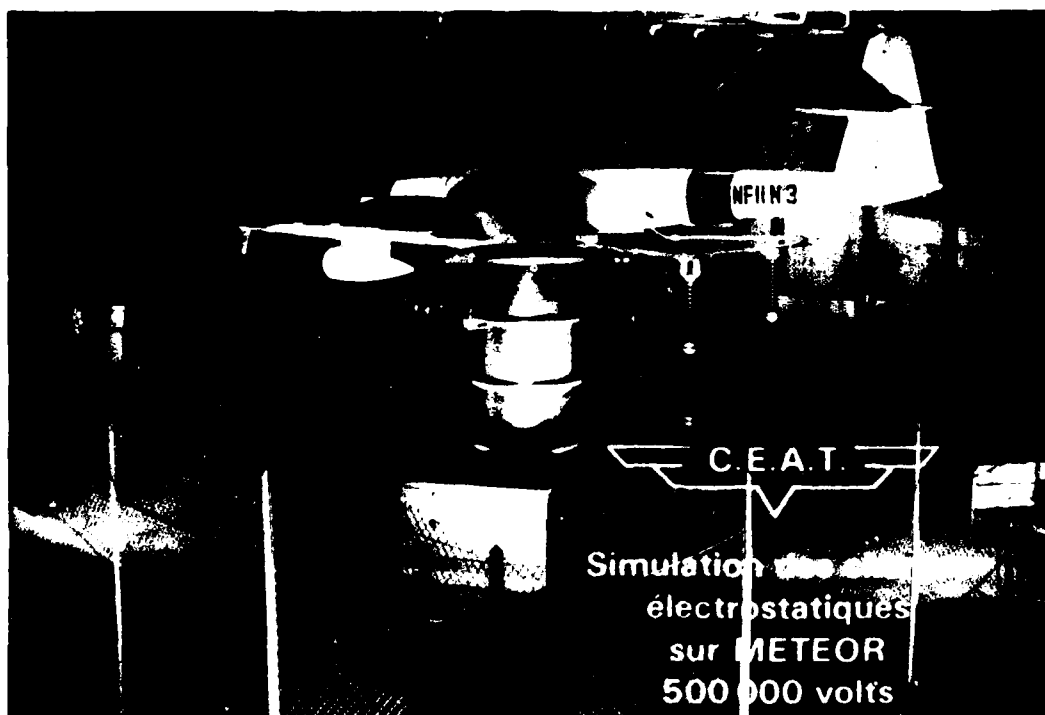


Fig. 5 - Meteor ground testing

For this investigation, two radiocompass loop antennas were installed on the Meteor aircraft, the first in the impact zone forward of the radome and the second in the sheltered zone behind the cockpit. During the tests the electromagnetic interference collected by the two antennas will be compared on two receivers tuned to the same frequency (a few hundred kHz) to investigate whether circulating charges actually exist in the boundary layers, generating electromagnetic interference. If this proves to be true, it will be necessary to conclude that existing protection is relatively insufficient in this respect.

The second investigation concerns space charges, whose existence was observed during flight testing where large amplitude variations in the amount of current discharged by two given dischargers were observed and, in the most extreme cases, the charges were observed to be of opposite polarity.

In order to analyze this phenomenon more accurately, it is planned, in the framework of the Meteor program, to record the currents discharged by the passive dischargers conventionally located on the trailing edge and also by two passive dischargers located on either side of the radome at approximately 40 cm and offset by an insulating rod to minimize the influence of the electric field created by the aircraft potential, which tends to mask the phenomenon.

APPENDIX

(Excerpt of Recommendation RE.Aéro 702 50)

0 FOREWORD

This recommendation, issued by Working Group GT58, "Lightning and Electrostatic Charges", reporting to the Branch Commission, "Aerodynes and Propulsion Systems", has benefited from the experience of representatives of:

- Government Inspection Agencies for the Aeronautic Industry
- the design and quality control departments of the main aeronautical manufacturers
- equipment manufacturers
- the airlines.

1 OBJECTIVE

This recommendation is aimed at answering the need for more efficient protection of aircraft and airborne equipment against the effects of atmospheric electricity, required due to the use of new structural materials (composites) and more sophisticated equipment, also more sensitive to electromagnetic interference.

This recommendation thus sets forth principles for the airframe, engine and equipment manufacturers, to enable them to make suitable provisions as early as in the design stage.

It also proposes an analytic approach aimed at verifying the validity of the protec-

tion implemented, specifying the types of test and recommended levels. In this respect, it supplements Recommendation RC.Aéro 542 05, which appears a minimum requirement but may prove insufficient as regards phenomena of atmospheric electricity.

The attention of the users is drawn to the fact that the means suggested may lose their efficiency with time, resulting in failure of the aircraft protection against lightning and static electricity. This recommendation sets forth principles aimed at solving maintenance problems which may be incurred with time.

Implementation of this recommendation should result in optimum protection of aircraft and airborne equipment such that:

- free flow of lightning currents is ensured by the surface finish, thereby avoiding damage to the airframe structures
- the accumulation of electrostatic charges is prevented to reduce radioelectric interference of electrostatic origin
- the characteristics and performance capabilities of the equipment and systems are preserved within specified tolerances
- more generally, all the aircraft systems are protected against the hazards of fire, explosion and damage to equipment and electric circuitry subsequent to lightning strikes and the accumulation of electrostatic charges
- the persons on board and on the ground are protected against electric shocks.

Recommendation RE.Aéro 702 51, "Validation Tests" supplements this recommendation as regards tests.

2 REFERENCE DOCUMENTS

- ISO 7137 - Aeronautics, Environmental Conditions and Test Procedures for Airborne Equipment (Ratification of Publications EUROCAE/ED-14A and RTCA/DO-160A)
- AIR 7305 - Test Conditions for Testing the Compatibility of Military Aeronautical Equipment with the Aircraft Power System
- Rec. RC.Aéro 542 05 - Grounding by Metal Plating of Aircraft
- Rec. RE.Aéro 702 51 - Protection of Aircraft Against the Effects of Atmospheric Electricity - Validation Tests
- MIL-D-9129 - Dischargers, Aircraft, Electrostatic, General Specification for
- JAR 25 - LARGE AIRCRAFT - paragraph ACJ25X899
- Culham Laboratory (Abingdon, Oxfordshire, Britain) CLM-R-212 "Designers Guide to the Installation of Electrical Wiring and Equipment in Aircraft to Minimise Lightning Effects" (1981)

TECHNICAL STUDY OF A LIGHTNING DATA LOGGER

Victor Tukiendorf, 945
Naval Air Engineering Center
Lakehurst, New Jersey 08733

and

Saul S. Bernstein
Dayton T. Brown, Inc.
Church Street
Bohemia, New York 11716

ABSTRACT

Statistical characterization of aircraft lightning strike data is vital to air safety. Successful aircraft design and test depends on the accurate specification of strike amplitude, current path, attachment points, and the variation of these parameters from strike to strike. This information is not presently available and aircraft lightning protection design and test criteria have been primarily based on laboratory reproduction of in-service structural strike damage, supported by theoretical lightning research. Modern trends in aircraft design, construction, and utilization of microelectronic avionic systems require a detailed knowledge of the interaction of the aircraft with the true lightning environment.

The intent of this study was to provide statistical characterization of lightning strike data. This was accomplished by:

1. Determining the feasibility of using the prototype lightning data logger (LDL) in a P-3 airframe.
2. Laboratory calibrating the existing prototype data logger system.
3. Selecting and calibrating sensors to be used.
4. Providing installation information, implementation method, cost analysis, and any indicated airframe modifications.

INTRODUCTION

LIGHTNING PHENOMENON - LIGHTNING IS A RANDOM PHENOMENON with characteristics that could best be described as having rapidly changing variables. Since complete knowledge of natural lightning does not exist, lightning simulation testing has been based on cloud-to-ground strike measurements.

All metal aircraft with tube-type electronics were relatively insensitive to large transients; therefore, they were not as vulnerable as present technology aircraft.

Utilization of composite materials and sensitive electronics has reduced the inherent protection provided by metal clad aircraft. Composites with weight and strength benefits offer less electromagnetic field protection.

Accurate and complete lightning strike characterization for a broad and quantitative statistical data base is required to ensure proper analysis and design for aircraft safety.

PROGRAM GOALS - The goal of this program was to evaluate the feasibility of utilizing a low cost lightning strike data logger in a P-3 aircraft. It included design, development, and calibration of a sensor system to measure electric and magnetic field to determine strike amplitude, current path, and attachment points. Integration of the lightning data logger and sensor system with the P-3 aircraft was investigated.

HARDWARE ANALYSIS

HARDWARE EVALUATION - The LDL consists of four major subsystems: Power Distribution Unit (battery backup), Front End Transient Digitizer Unit, Microprocessor-Controlled Data Logger, and sensors. Fig. 1 shows the instrumentation general block diagram for the system. The diagram indicates a system that can have many sensors (channels). The system to be used on the P-3 will have four sensors.

The first three subsystems are discussed below. The sensors are discussed separately.

The physical parameters of the subsystems are as follows:

1. Power Distribution Unit (battery backup) - 5 inch (127 mm) x 10.5 inch (266.7 mm) x 6.25 inch (168.75 mm), weight 15.5 pounds (7.03 kg).
2. Front End Transient Digitizer Unit - 6.375 inch (161.925 mm) x 15.75 inch (400.05 mm) x 8.375 inch (212.725 mm), weight 21.5 pounds (9.75 kg).
3. Data Logger - 5.25 inch (133.35 mm) x 17 inch (431.8 mm) x 9.875 inch (250.825 mm), weight 27.6 pounds (12.52 kg).

Power Distribution Unit - The LDL is powered by 400-Hz, 115-V aircraft power. The power distribution unit also contains a battery backup. Should the aircraft power fail momentarily, the battery backup takes over and guarantees continuous operation. The battery

used is a rechargeable nickel cadmium (Nicaid) type. In order to ensure operation when required, the battery must be cycled to complete discharge and fully recharged periodically. A full charge is sufficient to last for 3 months of normal flight time.

A switching power supply in the LDL converts aircraft power to the required low digital voltages. The power requirement of the system is 150 watts peak. Standby power requirement is 80 watts. Battery backup is 28 VDC at 4.0 amps peak and 3.0 amps standby for 10 amp hours.

Front End Transient Digitizer - The front end unit consists of a high speed (20 MHz) A/D converter, memory, memory control, and a serial communication interface.

The A/D converter is a multi-threshold parallel conversion type. Memory is organized into several 1024 x 8 bit segments. Each segment is interleaved to enhance memory access time. The memory controller directs the flow of data through each of 1024 address locations contained in each segment. Data can be read out of the processor via a serial fiber optic link or two-wire pair (refer to Fig. 2 and Fig. 3).

In operation, the front end continuously samples sensor output and stores this information on a RAM (Random Access Memory). The RAM is continually being updated and discarding old data. When a lightning strike of a predetermined level occurs, the data is stored in the RAM for a short time and then transmitted to the data logger for permanent storage. In this manner, pre- and post-trigger data is permanently recorded. When a strike of a predetermined level occurs, the data recorded contains information 100 microseconds before and after the triggering strike.

Microprocessor-Controlled Data Logger - The data logger is a microprocessor-oriented system, incorporating a standard format mass storage tape cassette to provide the required high capacity storage system. It has a digital display that operates in conjunction with a small key pad (on data logger front panel) that offers a quick functional checkout. The digital display has a clock that automatically is recorded as a header on the tape. The digital display will indicate triggering channel information immediately after a lightning strike.

The LDL is microprogrammable; therefore, reconfigurations in the arrangement are easily accomplished and will not necessarily require hardware changes. Each system may be tailored to fit a given flight profile. Sampling rate, dynamic range, and data storage can be programmed as required.

DATA RETRIEVAL - The original configuration of the data logger required a cassette tape reader to decode the data from the tape. For bench testing and calibration of the probes, the cassette recorder is not practical since instantaneous readout of data is

required. In order to obtain and analyze data quickly, the data logger was reorganized so that data was fed into a semiconductor memory rather than a cassette. The memory is located on an RS-232 memory buffer circuit card inserted into the data logger. This data was then transmitted via an RS-232C bus to a designated computer terminal for analysis.

SENSOR ANALYSIS

SENSOR REQUIREMENT STUDY - For this application, a sensor is a passive analog device that converts electromagnetic energy to a voltage or current.

The sensor system was required to provide the following information:

1. Time history and amplitude of lightning current.
2. Main electrical path of lightning current on the aircraft structure.
3. Electric field normal to the fuselage at one location.
4. Lightning attachment points (entry and exit points).

To obtain this information (in conjunction with data logger electronics), the following factors were taken into consideration: ease of installation, passive device requirements, sensor bandwidth, directivity, sensitivity, and simplified signal processing.

Ease of Installation - A simple method of installation was required, one that would have the least impact on the aircraft structure. Any sensor requiring modification of the airframe for mounting was deemed unsuitable. If possible, any existing struts, spars, or blade antennas may be incorporated into a sensor system in a way that would not adversely affect the airframe structure or characteristics.

Passive Device Requirements - Limited maintenance constraints require the sensor to be a passive device.

Sensor Bandwidth - The sensor bandwidth required is established by information signals processed by the front end of the data logger. Bandwidth of 10 kHz to 20 MHz is dictated by the capability of the front end digitizer unit. A linear transfer function is desired.

Directivity - Sensor directivity is not a major requirement. Isotropic antennas are not required since the metal airframe imposes boundary conditions on the fields.

Sensitivity - The sensitivity of the sensor is not a major factor since large signal levels are generated. Sensors that saturate at relatively low levels should be avoided.

Simplified Signal Processing - Signal processing can provide correction for nonlinear sensors and enhance or attenuate the signal.

SENSOR EVALUATION - The types of sensors evaluated were: off-the-shelf EMP sensors, transmission line to ground plane, blade

antenna, parallel plate-capacitive, small dipoles or rods, possible new design, and current probe.

A current probe was selected since it met all requirements listed above. The probe selected has the following specifications:

1. It has an output of 0.1 volt/amp, a maximum peak current of 5000 amps, a usable rise time of 10 nanoseconds, and an approximate low frequency 3-dB point of 240 Hz.
2. It is entirely passive and requires no external power or circuitry.
3. The accuracy is dependent only on the number of turns on the secondary coil and the value of the internal terminating resistance. The accuracy is +1%, -0% initial pulse response for all models with a high impedance load such as 1 megohm in parallel with 20 picofarads.
4. The probe is furnished with a BNC male terminal for easy integration into our sensor configuration.

SENSOR DESIGN - The current probe is the main part of the design of the three magnetic field sensors. One of the sensors is used to measure surface currents through an aircraft structure directly, the other two sensors are excited by aperture coupling techniques.

The method of using a current probe to measure structural current directly simplifies its installation since existing aircraft structure is used to measure the magnetic field. In analyzing the P-3, it was noted that an Automatic Direction Finder (ADF) sense hatch is located on the underside of the plane. This hatch is available for use as a sensor since its use will not impede any aircraft functions. Above this hatch are some cross-section wing structures. By placing the probe around one of these members, wing lightning strike information may be obtained (Fig. 4, number 3).

By this method, wing lightning strike information is obtained without having to place the sensor in the harsh and cluttered environment of the wings. The probe will be clamped around the aircraft structure and connected to the front end digitizer unit by either coaxial cable or heliax cable.

The length of wire run from the sensor to the front end must be kept as short as possible. If the length is less than 10 feet, then a coaxial cable would be acceptable. Should the length of wire run be 10 to 40 feet, a heliax cable bonded to the aircraft frame every 2 to 3 feet would be required. The cable run from the front end to the data logger should also be kept as short as possible, but it is not as critical.

The cable length from the sensor to the front end is critical. The cable to front end carries high frequency signals. Spurious noises and signal loss must be kept to a minimum; therefore, the line should be as

short as possible. While inspecting the aircraft, appropriate areas near each prospective sensor installation were noted for placement of the front ends (refer to Fig. 4).

The other two magnetic sensors will be of shorted turn current probe design. They will use aperture coupling as the method to excite the sensor. The current density (J_g), through any cross-section of an aircraft structure, will not be uniform. The waveform of J_g on primary structural elements can be approximated as the sum of the fundamental lightning current waveform and one or more high frequency response waveforms due to resonances in the aircraft structure.

The magnetic field (H_g) of the aircraft structure current will couple through apertures in the aircraft skin. If the apertures are electrically small, the internal magnetic field (H_i) will have the same waveform as the structure current (J_g). The magnitude of (H_i)/(H_g) will be less than 1. It will also be dependent on location but will be constant over the frequency range of interest. The shorted turn sensor should have a resonance that will be higher than the front end transient digitizer's frequency response (60 MHz). Then the loop itself will not generate a spurious response to J_g . The open circuit voltage in the loop will follow Faraday's law, i.e., $V = L \frac{di}{dt}$. If the inductance of the loop is greater than its resistance, the short circuit current in the loop will have the same waveform as the internal magnetic field (H_i). Therefore, by using the appropriate current probe, the lightning current waveform is obtained. The short circuit current waveform measurement is uniform over the frequency range of interest.

The pilot's skylight window is used as the aperture, and a 1/4-inch diameter copper shorting bar across the window acts as the shorted turn. The sensor (Fig. 4, number 1) is located totally inside the aircraft structure. The copper bar is placed across the skylight window with the current probe around it and electrically bonded to the airframe at each end of the bar. The current probe is then connected to the front end transient digitizer unit by a coaxial cable connection.

The third and final magnetic field sensor (Fig. 4, number 4) is identical to the pilot's skylight window sensor, except that it is located in the rear of the aircraft on the galley window. It is also aperture-coupled as its means of excitation and uses a shorting bar and a current probe for its makeup (refer to Fig. 5).

Three magnetic sensors now make up a system that is capable of detecting the electrical path of the lightning current striking the aircraft. The skylight window probe covers the front end, the galley window covers the rear section, and the ADF sense hatch probe covers the wings. Therefore, by analyzing the probes that trigger, it will then be possible

to detect the path taken by the lightning current.

The electric field probe will be located in the ADF sensor hatch. The electric field probe will be the shorted plate type (Fig. 4, number 2). The ADF hatch is made of a nonmetallic material. In the center of this material is an unused metal plate. By shorting this plate to the aircraft structure and clamping a current probe around the shorted wire, electrical field information is obtained.

CALIBRATION OF SENSORS - The calibration of the sensors is performed in a twofold program; the first on a bench level and the second is planned for a later time and is to be performed in an instrumented aircraft to provide an actual baseline. The bench level testing was performed as a combination of feasibility and calibration.

High level pulse testing must be of a level sufficient enough to trigger the instrumentation system. This will provide baseline triggering threshold data of the lightning measurement system as well as supplying high level current data.

The test setup used simulated an area of aircraft surface with an aperture of the size of the galley window cut into its metal surface. The shorting bar and current probe were placed across it and electrically bonded to the table. The metallic table top simulated the aircraft skin and structure. This setup was designed to test sensor response only and is not intended to simulate a P-3 aircraft.

Known voltage and current levels were injected into the table and the response of the sensor recorded. By analyzing the sensor response to the known input, the sensor was then calibrated.

The high test level current pulse was achieved by capacitive discharge. A bank of capacitors was charged up and then discharged to the test structure to approximate the lightning threat. With the use of a spark gap, the charge was injected on the structure. By using different charging and discharging configurations and varying basic resistance (R) and inductance (L) values of the setup, rise time and energy of the waveform being investigated were altered. The capacitor bank used generated up to 320K volts and 200K amps.

SENSOR CALIBRATION

INTRODUCTION - Laboratory calibration proved the validity of using the present LDL system with the probes chosen. The purpose of these tests was to determine the percentage of current flowing through the probe versus the total current injected on the test surface. Knowing this ratio, a baseline graph was plotted. With this baseline calibration an unknown strike amplitude can be determined.

The calibration of the test setup is obtained by knowing the strike amplitude, input attenuator setting, and current probe factor.

SENSOR CALIBRATION SETUP - Tests were carried out in a high voltage facility designed and built specifically for this program (see Fig. 6.)

The voltage output, current, rise time, and wave shape were all variable.

SENSOR CONFIGURATION - The sensor test configuration consisted of a conducting metallic surface that simulated a section of aircraft skin. The section had a 12-inch diameter opening cut into it. A copper bar was placed across the opening and electrically bonded to the metal surface at both ends. The bar was placed through the current probe prior to bonding it to the metal skin. The current probe has a transfer function (manufacturer supplied) of 0.1 volt per 1 ampere. This means that the probe output will be 0.1 volt for every 1 ampere of current that flows through the conductor.

The current probe had a BNC connector that was connected by coaxial cable to a block attenuator. The attenuator was used to lower the voltage level so as not to saturate the data logger input. The attenuator used was a flat wide band attenuator. The value of attenuation required will depend on the lightning strike current range that is desired to be investigated.

DATA RECORDING METHOD - Calibration was carried out using two modes of data recording. In addition to the tape cassette capability of the data logger, a personal computer with an RS-232C communications interface was used. The personal computer provided instantaneous readout capability.

The data logger is programmed to trigger at a level between -1 and +1 volts. This level is recorded on the cassette tape and the computer as a hexadecimal value between 0 and 255, and will vary between these values depending upon strike level (see Fig. 7.)

CALIBRATION RESULTS - Preliminary calibration tests were carried out using an oscilloscope to determine magnitude of current transfer to the probe. This was carried out as a quick "look-see" check to determine if the test setup was functioning properly.

Calibration of the sensor configuration was performed as follows: The output of the current probe was displayed on an oscilloscope. This measured the current flowing through the copper bar. The current probe converted its output to a voltage.

Current in bar (Amperes)	Total current applied (Kiloamps)
600	10.119
520	9.48
440	7.90
350	4.8

Current in bar (Amperes)	Total current applied (Kiloamps)
280	4.2
160	2.85

Plotting this data produced the sensor configuration calibration. The data showed that the sensor picked up an average of 1:15 of the total current applied (see Fig. 8.)

DATA ANALYSIS - With the previous information available, an actual data analysis from strike to waveform was then performed. The output data of the data logger is fed through the interface to the computer in hexadecimal pairs. These hexadecimal characters are also recorded on the tape cassette. Time formatting is as follows: There are 96 blocks of data for each trigger. Examples of this data are seen in Fig. 9.

Each 96 blocks represents 200 microseconds; 100 microseconds before the trigger and 100 microseconds after. Each hexadecimal pair is a 16.6 nanoseconds update. Amplitude formatting is performed by equating the hexadecimal value to the trigger level of the data logger.

Next the data is then converted to current and time, and a graph of the lightning strike may be plotted indicating current amplitude versus time (see Fig. 10.)

To determine lightning strike current amplitude on an aircraft using the previous analysis, the following data must be known:

1. Conversion factor of probe (manufacturer supplied)
2. Calibration of aircraft
3. Input attenuator setting

For example (see Fig. 11), assume the aircraft has been calibrated and proven to have a 1:15 ratio, attenuator setting is 40 dB, conversion factor is 40 dB, and data logger reads 1 volt.

With the above information we can now determine the strike amplitude.

$$dB = 20 \log \frac{V_1}{V_2}$$

where dB is the attenuator setting, V_1 = voltage entering attenuator, and V_2 = voltage at the data logger; therefore, $40 = 20 \log V/1$ and $V = 100$ volts. Since the probe conversion factor is 0.1/1 ampere, 1000 amps are flowing through the bar. The aircraft factor by calibration is 1:15; therefore, lightning strike amplitude is 1000 amps x 15 = 15,000 amps.

IMPLEMENTATION ANALYSIS

TEST BED AIRFRAME - Although any aircraft of equivalent size and mission profile may be used, the P-3C patrol aircraft has been chosen as the airframe in which the lightning statistics recording system will be installed.

The rationale for the choice of this airframe is:

1. The P-3 has been and is the most lightning struck aircraft in the naval fleet.
2. The P-3C is on patrol for long periods of time.
3. The P-3C flies at altitudes where lightning strikes occur most.
4. The P-3C airframe is large enough with capacity to accept the system with no appreciable weight or size constraints.
5. The P-3C will be capable of providing data on a greater geographical distribution scale due to the fact that it is flown in many parts of the world.

CONCLUSION

This program proved the validity of using a lightning data logger system in a P-3 airframe. The system will be relatively maintenance free and reliable.

Difficulties were encountered during the bench calibration process due to data logger hardware and RS232C software problems. Once these problems are overcome, system calibration will be straight forward and will prove extremely useful.

ACKNOWLEDGEMENT

We wish to acknowledge the assistance and guidance provided by the Boeing Aircraft Corporation during the course of this program. Boeing, the developer of this system, has provided a system and technical guidance on an as required basis throughout the program; their continued aid was a great factor in having this program come to a successful conclusion.

This program was funded by the Naval Air Engineering Center, (NAEC), Lakehurst, NJ under Contract Number N68335-81-C-4933.

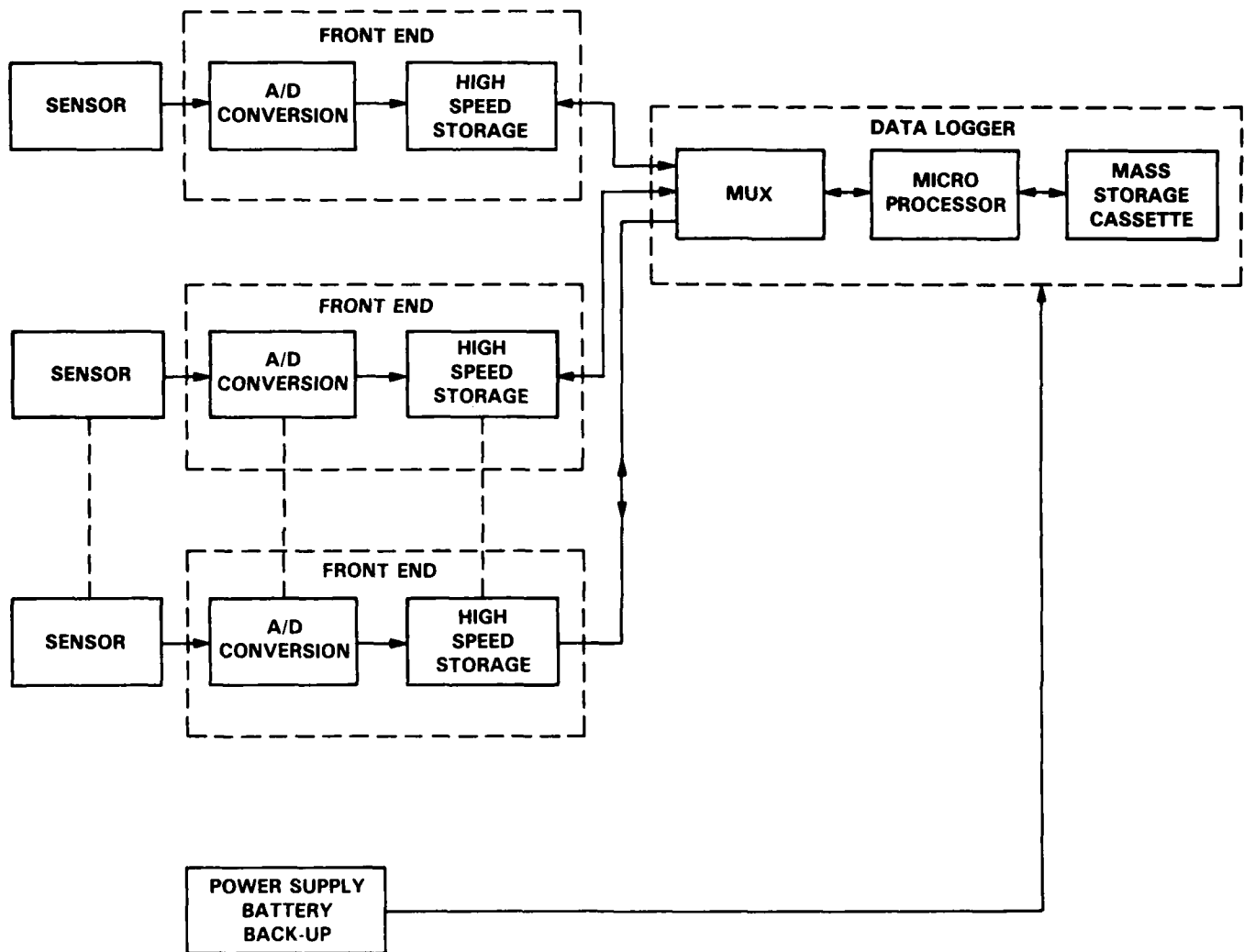


Fig. 1 - Lightning strike instrumentation general block diagram

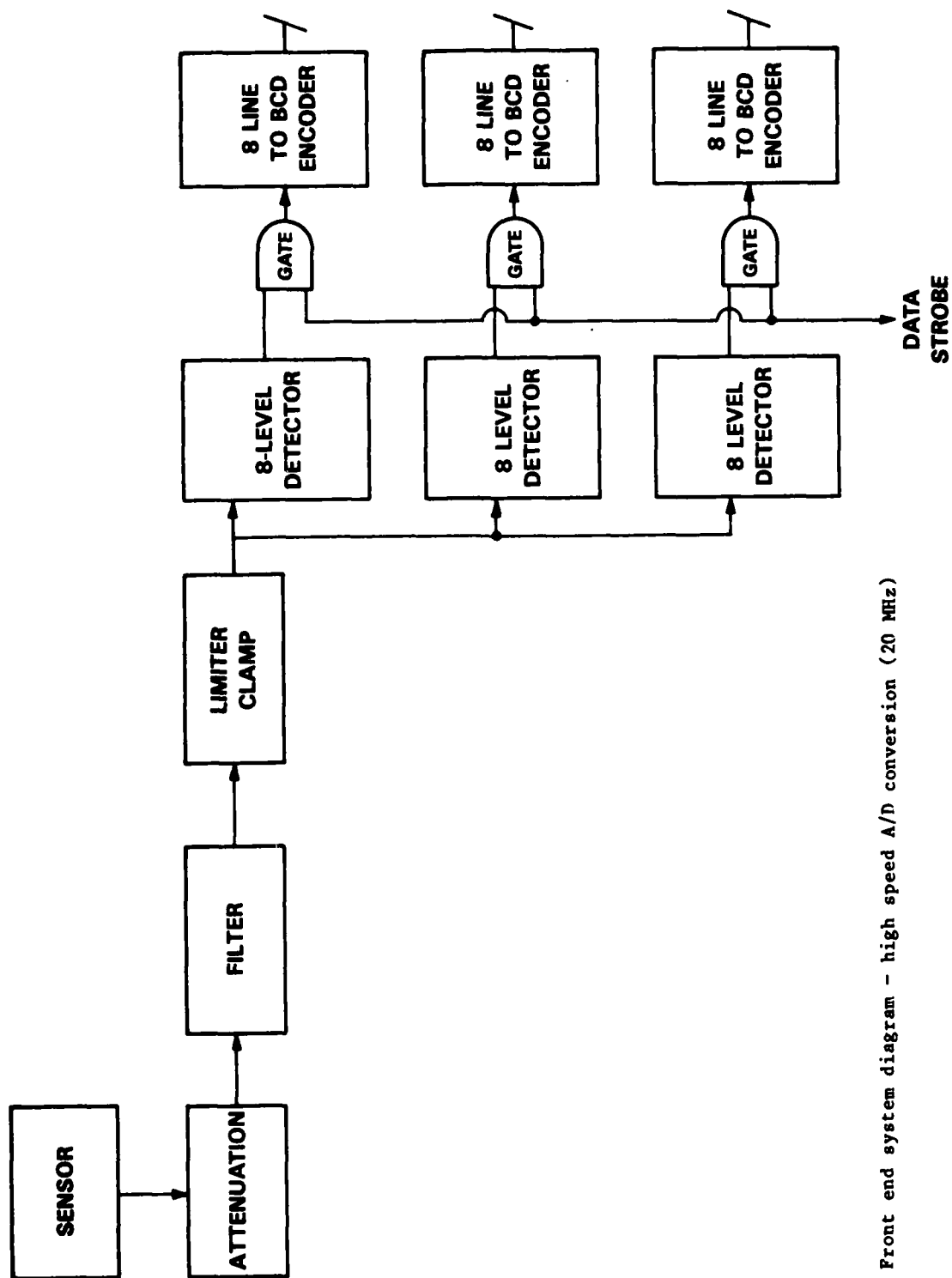


Fig. 2 - Front end system diagram - high speed A/D conversion (20 MHz)

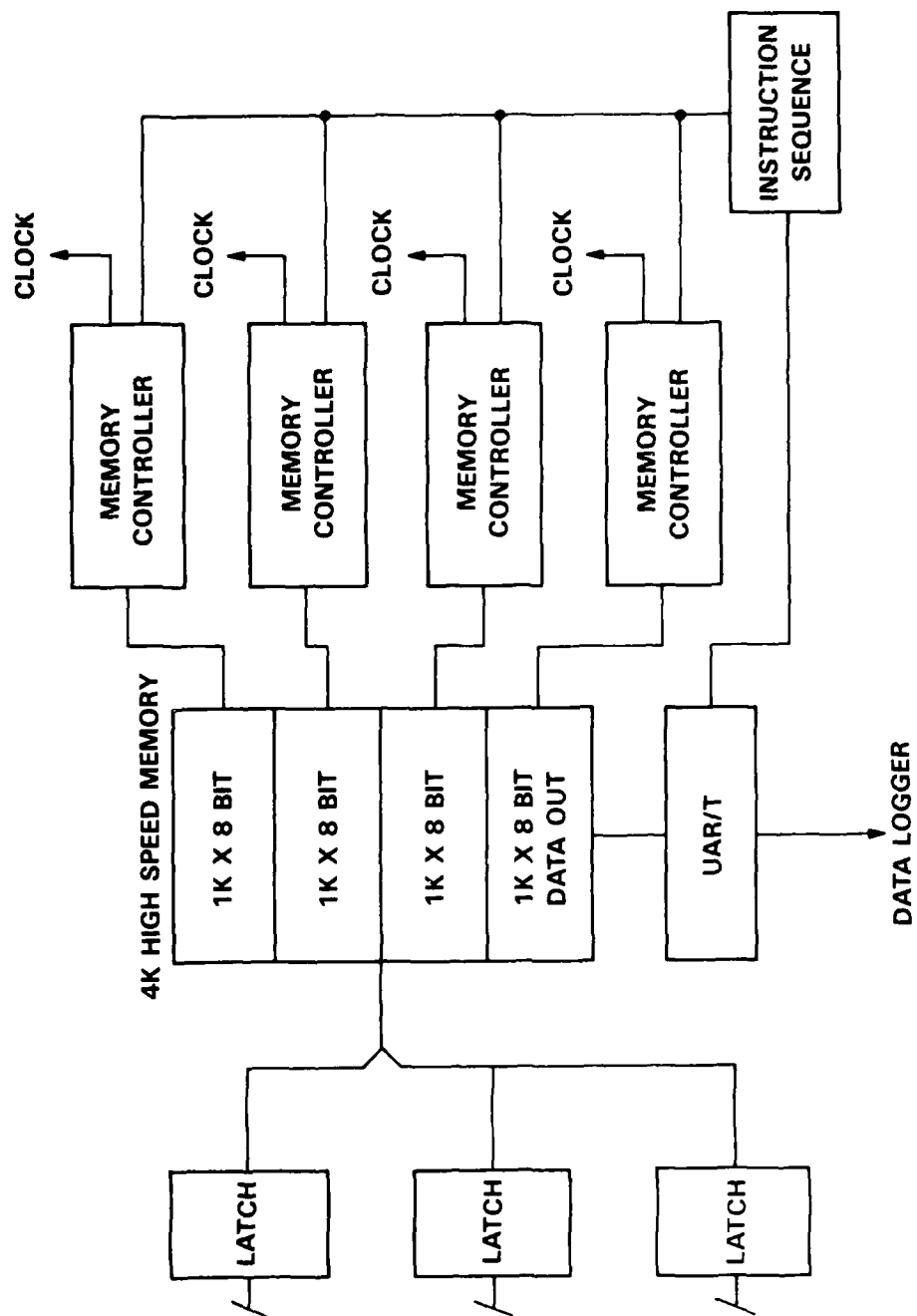


Fig. 3 - Front end system diagram - high speed memory

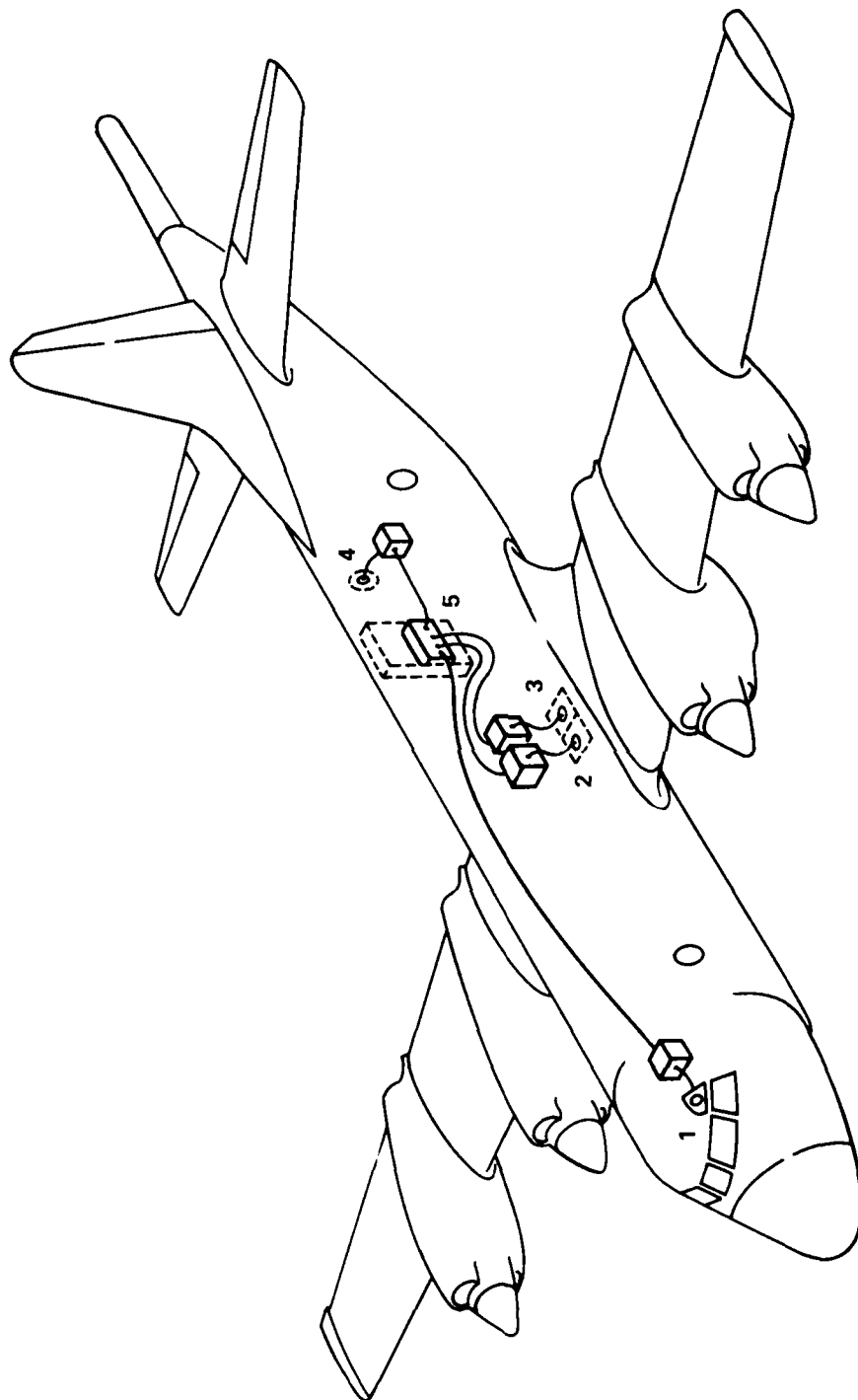


Fig. 4 - Proposed sensor configuration for data logger

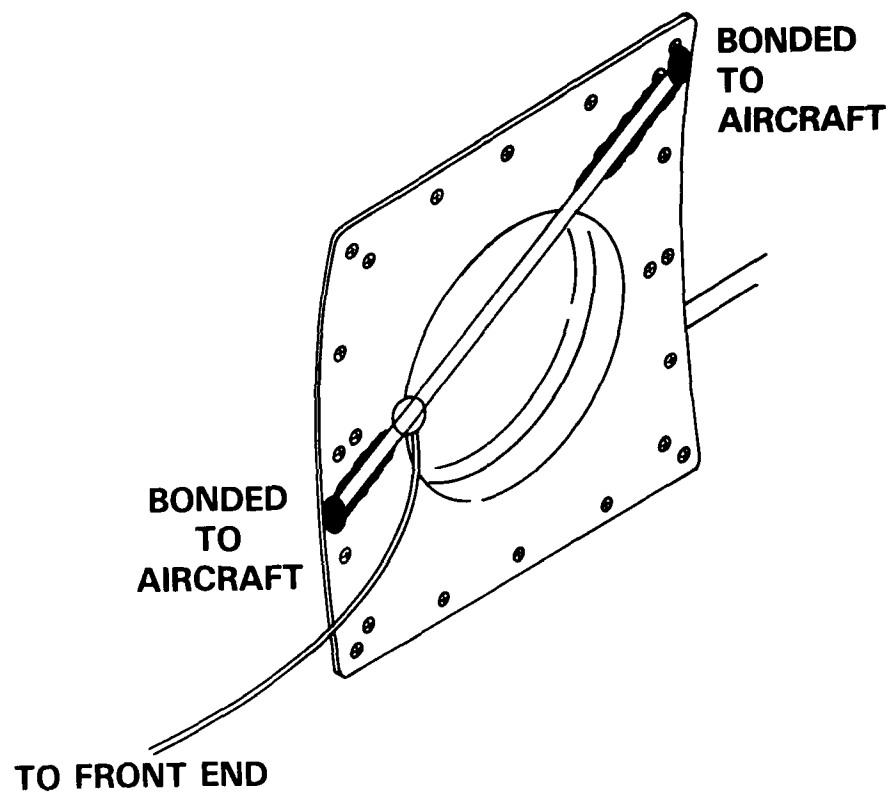


Fig. 5 - Close up view of sensor configuration

SENSOR CALIBRATION SET-UP

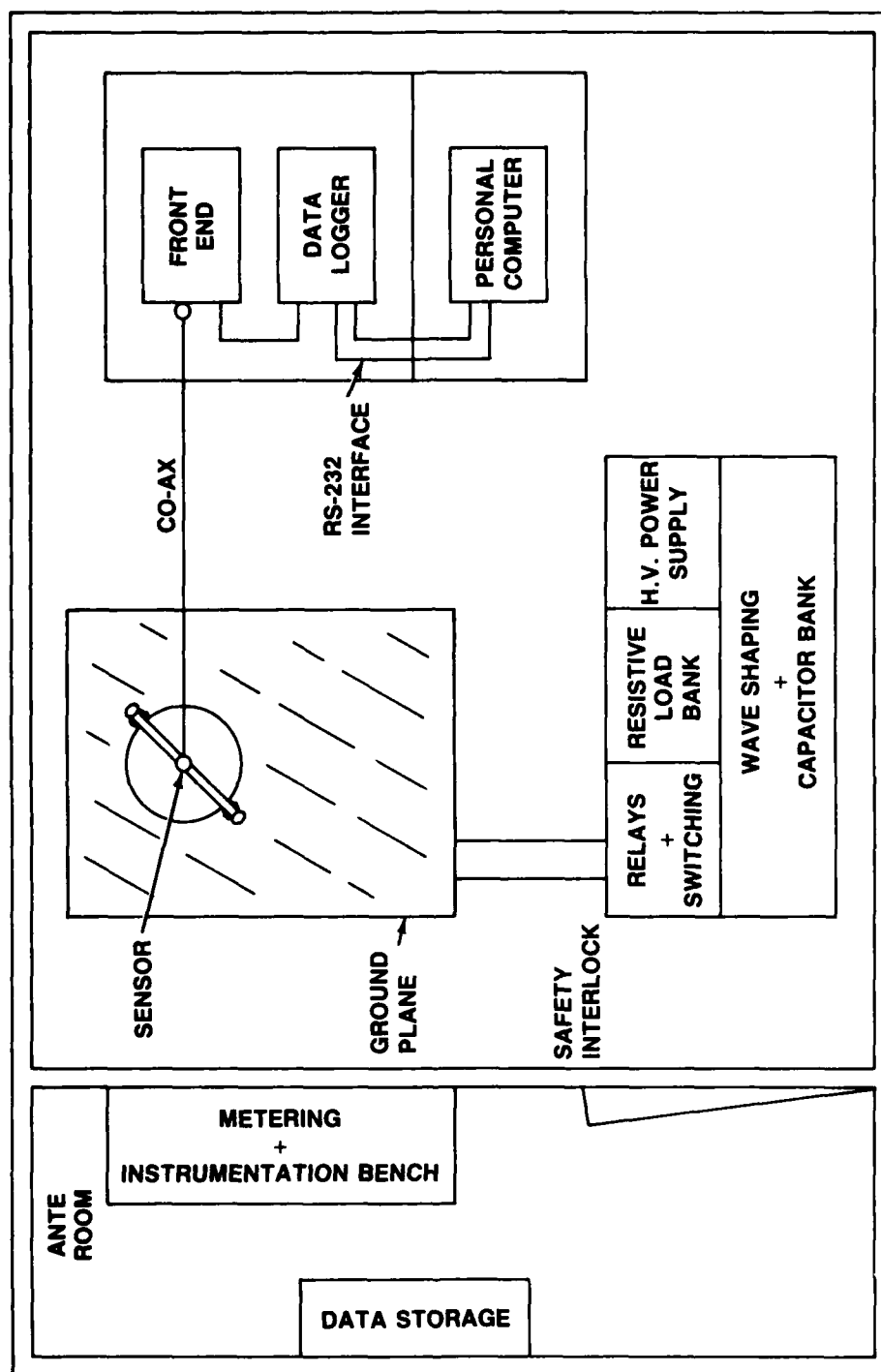


Fig. 6 - Sensor calibration setup

Trigger Levels

Hexadecimal	Decimal	Trigger Level
00	0	-1
10	16	-0.875
20	32	-0.75
30	48	-0.625
40	64	-0.50
50	80	-0.375
60	96	-0.25
70	112	-0.125
7F	127	0
90	144	.125
A0	160	.250
B0	176	.375
C0	192	.50
D0	208	.625
E0	224	.75
F0	240	.875
FF	255	+1

Fig. 7 - Trigger levels

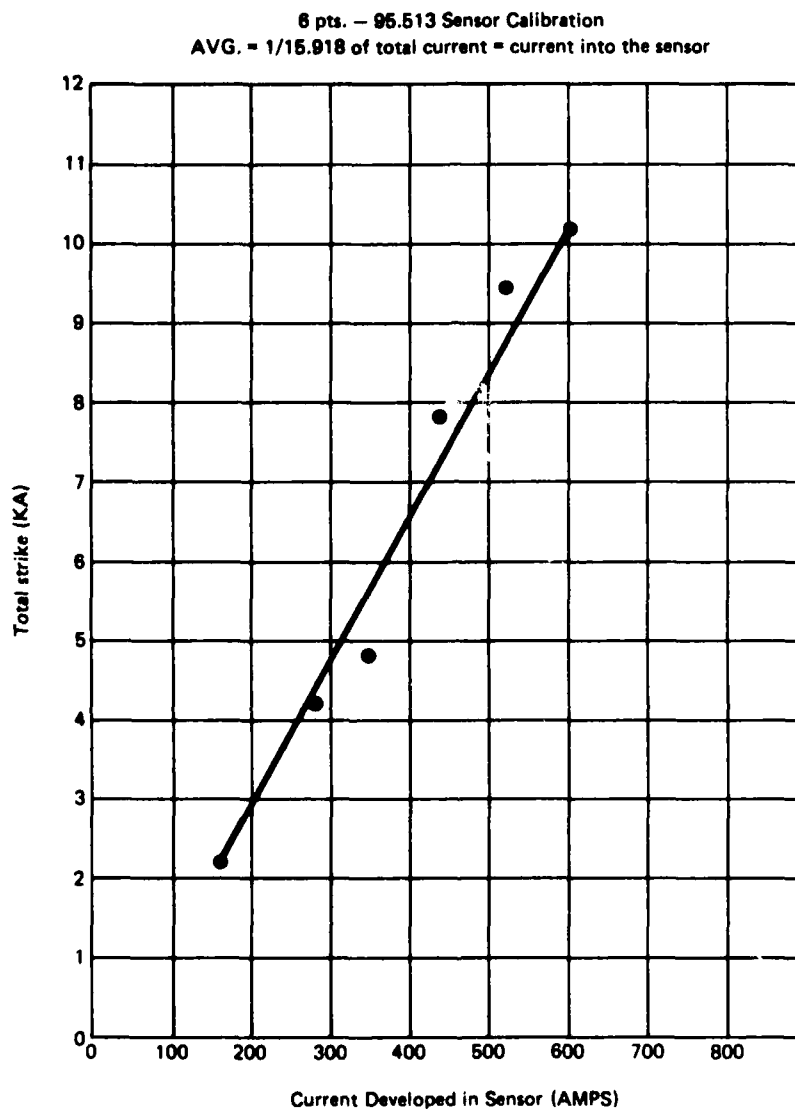
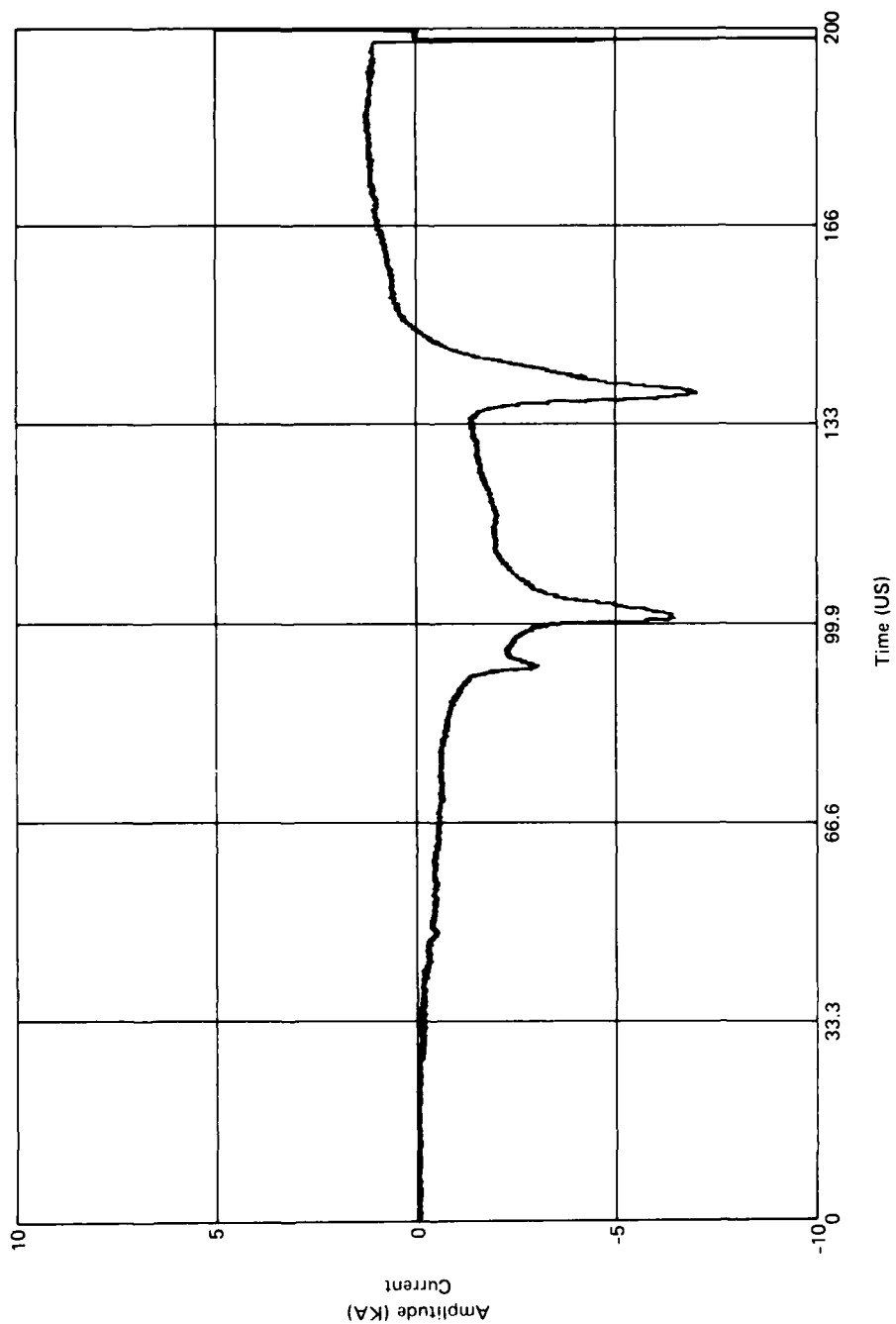


Fig. 8 - Sensor calibration graph

Fig. 9 - Data blocks



DTB.001 L:01 D:223 T:16:39:07 F:01

WARNING: Plots of more than six blocks will be desampled.

Fig. 10 - Waveform plot

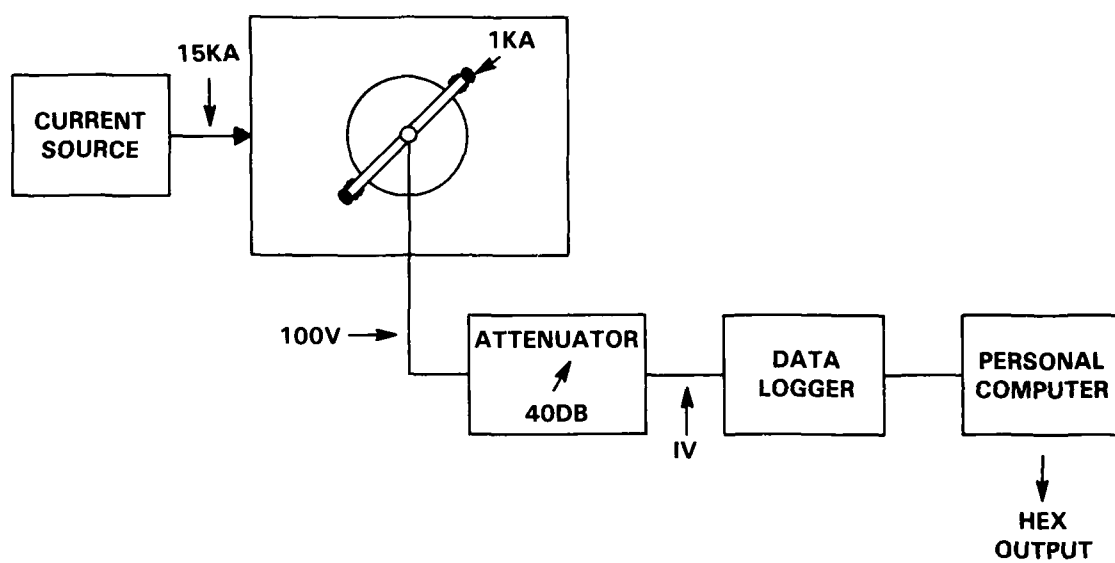


Fig. 11 - Calibration

TRANSIENT SPARK-ARC HOTSPOT SURFACE HEATING
ON METALLIC AND REINFORCED-COMPOSITE SKINS

T. S. Lee[†] and W. Y. Su

Department of Electrical Engineering, University of Minnesota, Minneapolis, Minnesota, U.S.A.

ABSTRACT

Light metals like Titanium and composite materials are being used on modern aircraft and space vehicles in place of aluminum. These new materials are far less conductive both thermally and electrically. The effect on the characteristics of lightning-induced hot spot heating of surface skin and on related hazards of fuel cell ignition is of renewed interest.

This work deals with diffusion of spark-arc heat away from the surface strike region. The treatment is through an initial-value problem, in which heat deposit is taken to be distributed in a small cylinder situated adjacent to the surface. By using the natural coordinates of cylindrical geometry, the theory establishes time-dependent temperature predictions. Of particular interest is the hot spot on the opposite side of the skin where the temperature is given through elementary functions. Comparisons between the present solution and both previous theoretical work [1] and some experimental data are performed. The results are considered to also apply in related experimental studies of pulsed-laser induced surface heating.

[†] Consultant, Lightning & Transients Research Institute, St. Paul, Minnesota, U.S.A

INTRODUCTION

EARLIER THEORETICAL INVESTIGATIONS of aircraft fuel tank hot spots [1]* caused by lightning provide some solutions for calculation of the hot spot temperatures. The solution was complex as it included terms such as error functions, which are not easily programmed with simple computers. Also, although they were useful in estimating hazards, there were some theoretical problems, such as the fact that they were carried out for rectangular geometry in order to simplify the mathematics.

*Numbers in brackets designate References at end of paper.

This paper presents a new solution in cylindrical coordinates which is simple in view of the complexities of the steps required for its solutions. The solution involves only terms such as exponentials which are easily programmable on simple computers. The new solution still utilizes a lumped heat input at the surface with no allowance for joule heating by current conduction in the material and this is most appropriate for metals.

The solution assumes an isotropic medium which makes it most useful for metal fuel tank walls but it is also of some use with carbon reinforced composites (CRC).

EQUATIONS

In Figure 1, we consider a plate made of either metallic or composite materials, with thickness b but otherwise unlimited lateral dimensions. This material is assumed to possess mass density ρ , specific heat capacity c and coefficient of thermal conduction k . Let us take a cylindrical set of coordinates with origin at the center point of one side of the plate, henceforth to be referred to as the inside surface. The z -axis is to be so oriented that the outside surface of the plate corresponds to $z = b$. The lightning stroke will be supposed to strike the outside surface at the point ($r = 0$, $z = b$) and release in its neighborhood a quantity of heat near time $t = 0$. The problem at hand is the assessment of the time-dependent temperature distribution on the inner surface of the plate, in particular the temperature at the point O , the "hot spot", which will be the most important point on the inside surface for hazard consideration.

The physical system posed above contains a characteristic time scale, say t' , which may be conveniently designated as

$$t' = \rho C b^2 / k \pi^2.$$

If the heat-release process occupies a time within a scale significantly smaller than t' , then the temporal details of that process are unimportant and the features of the subsequent energy transfer can be determined by solving an initial-value problem based on treating heat conduction as the principal physical mechanism.

Furthermore, the analysis shall be simplified by supposing that at the surfaces, no heat is lost from the plate either by conduction or by radiation to the surrounding medium and that the phenomenon has angular symmetry.

The heat-conduction equation

$$\kappa^2 \left(\frac{\partial^2 T}{\partial r^2} + \frac{1}{r} \frac{\partial T}{\partial r} + \frac{\partial^2 T}{\partial z^2} \right) - \frac{\partial T}{\partial t} = 0 \quad (1)$$

is to be solved in the region

$$\begin{aligned} 0 &\leq r < \infty \\ 0 &\leq z \leq b \end{aligned} \quad (2)$$

with the boundary conditions

$$\left(\frac{\partial T}{\partial z} \right)_{z=0} = 0 \quad (3)$$

and

$$\left(\frac{\partial T}{\partial z} \right)_{z=b} = 0.$$

In equation (1), $T(r, z, t)$ is the temperature and

$$\kappa^2 = k / \rho C$$

is the thermal diffusivity. By separation of variables with $T = R(r)Z(z)\mathcal{T}(t)$, equation (1) becomes equivalent to

$$\left(\frac{d^2}{dr^2} + \frac{1}{r} \frac{d}{dr} + \lambda^2 \right) R = 0 \quad (4)$$

$$\left(\frac{d^2}{dz^2} + \alpha^2 \right) Z = 0 \quad (5)$$

$$\left(\frac{d}{dt} + \kappa^2 (\lambda^2 + \alpha^2) \right) \mathcal{T} = 0 \quad (6)$$

in which λ and α are positive constants of inverse-length dimensions. The solution for Z from equation (5) satisfying the boundary conditions implied in (3) requires that α be allowed to assume discrete eigenvalues

$$\alpha_n = n\pi/b \quad (n=0, 1, 2, \dots)$$

alone and the corresponding eigen functions are $\cos \alpha_n z$. The solution for R following equation (4) and remaining finite everywhere has the form of $J_0(\lambda r)$, the Bessel function of the first kind of order zero. In addition, λ need not be discrete but forms a continuum instead. From equation (6), \mathcal{T} has an exponential dependence on time. In all, suitable particular solutions are of the form

$$J_0(\lambda r) \cos(\alpha_n z) \exp[-\kappa^2 (\alpha_n^2 + \lambda^2) t].$$

A general solution comprises particular solutions of this type covering all allowed values of α_n and λ . Thus,

$$T(r, z, t) = \int_0^\infty \sum_{n=0}^\infty B_n(\lambda) J_0(\lambda r) \cos(\alpha_n z) \exp[-\kappa^2 (\alpha_n^2 + \lambda^2) t] \lambda d\lambda \quad (7)$$

with the functions $B_n(\lambda)$ yet to be selected through initial conditions.

INITIAL TEMPERATURE DISTRIBUTION

Except for fortuitously simplifying initial temperature distributions, equation (7) is very difficult to use. In this work, we shall specialize in one such simple yet physically reasonable distribution. Suppose that at $t = 0$ an amount of heat Q is uniformly liberated in a small block of the plate defined by

$$\begin{aligned} b-\beta \leq z \leq b \\ 0 \leq r \leq a \end{aligned} \quad (8)$$

as illustrated in the shaded region in Figure 1. The material in this region of volume $\pi a^2 \beta$ situated on the outer surface of the plate is abruptly raised to a temperature $\theta = Q/\rho c \pi a^2 \beta$. Thus

$$T(r, z, 0) = \begin{cases} \theta & \text{in block} \\ 0 & \text{outside block} \end{cases} \quad (9)$$

By virtue of the assumptions of uniform θ in the block and the coordinate decoupling inherent in the geometry of (8), we may restate equation (9) as

$$T(r, z, 0) = \theta u(r) v(z) \quad (10)$$

where u and v are dimensionless functions defined by

$$u(r) = \begin{cases} 1 & 0 \leq r \leq a \\ 0 & a \leq r \end{cases} \quad (11)$$

$$v(z) = \begin{cases} 1 & b-\beta \leq z \leq b \\ 0 & 0 \leq z < b-\beta \end{cases} \quad (12)$$

CLOSED-FORM SOLUTIONS

From (7), we write

$$T(r, z, t) = \sum_{n=0}^{\infty} \left\{ \int_0^a B_n(\lambda) J_0(\lambda r) \exp[-(\kappa \lambda)^2 t] \lambda d\lambda \right\} \cos\left(\frac{n\pi z}{b}\right) \exp\left[-\left(\frac{n\pi \kappa}{b}\right)^2 t\right] \quad (13)$$

In response to (10) we now propose the following decoupling scheme:

$$B_n(\lambda) = A_n \theta f(\lambda) \quad (14)$$

where A_n is a dimensionless constant and $f(\lambda)$ is a function of square-length dimension leading to a companion decoupling of (13) in the form

$$T(r, z, t) = \theta \phi \psi \quad (15)$$

where two dimensionless functions

$$\phi(r, t) = \int_0^a f(\lambda) J_0(\lambda r) \exp[-(\kappa \lambda)^2 t] \lambda d\lambda \quad (16)$$

and

$$\psi(z, t) = \sum_{n=0}^{\infty} A_n \cos\left(\frac{n\pi z}{b}\right) \exp\left[-\left(\frac{n\pi \kappa}{b}\right)^2 t\right] \quad (17)$$

have been introduced. Comparison with (10)-(12) reveals that, in order to achieve the precise matching of initial conditions, it is sufficient to impose

$$\phi(r, 0) = u(r) \quad (18)$$

and

$$\psi(z, 0) = v(z) \quad (19)$$

By the standard technique of Fourier series expansion, we obtain from (12), (17) and (19)

$$A_n = \begin{cases} \beta/b & \text{if } n = 0 \\ (-1)^n \left(\frac{z}{n\pi}\right) \sin\left(\frac{n\pi \beta}{b}\right) & \text{if } n \neq 0. \end{cases} \quad (20)$$

These in turn make it possible to express (17) as

$$\psi(z, t) = \frac{\beta}{b} \left\{ 1 + 2 \sum_{n=1}^{\infty} (-1)^n \frac{\sin(n\pi \beta/b)}{(n\pi \beta/b)} \cos\left(\frac{n\pi z}{b}\right) \exp\left[-\left(\frac{n\pi \kappa}{b}\right)^2 t\right] \right\} \quad (21)$$

The selection of ϕ involves Bessel functions and is far more complicated. By (16) and (18), we have

$$u(r) = \int_0^a f(\lambda) J_0(\lambda r) \lambda d\lambda \quad (22)$$

a type of Bessel transform. Its inverse relation is

$$f(\lambda) = \int_0^a u(r) J_0(\lambda r) r dr \quad (23)$$

which by (11) becomes

$$f(\lambda) = \int_0^a J_0(\lambda r) r dr \quad (24)$$

Through the identity [2]

$$d\{x J_1(x)\}/dx = x J_0(x),$$

in which J_1 is a Bessel function of the first kind of order one, equation (24) is rendered readily integrable as

$$f(\lambda) = \frac{1}{\lambda} J_1(a\lambda) \quad (25)$$

thus reducing (16) to

$$\phi(r, t) = a \int_0^{\infty} J_0(\lambda r) J_0(\lambda a) \exp[-(\kappa \lambda)^2 t] d\lambda \quad (26)$$

Equations (15), (21) and (26) formally constitute the solution to the original initial-value problem.

SOLUTION IN SERIES FORM

Equation (26) contains products of Bessel functions in the integrand and is difficult to use. In this section, we shall endeavor to obtain a series representation for ϕ . By employing the series expansion [2] of J_1 , let us proceed as follows

$$\begin{aligned} \phi(r, t) &= a \int_0^{\infty} \left[\sum_{k=0}^{\infty} \frac{(-1)^k (a\lambda)^{2k+1}}{2^{2k+1} k! (k+1)!} \right] J_0(\lambda r) \exp[-(\kappa \lambda)^2 t] d\lambda \\ &= \sum_{k=0}^{\infty} \frac{(-1)^k a^{2k+1}}{2^{2k+1} k! (k+1)!} L_k \end{aligned} \quad (27)$$

with

$$\begin{aligned} L_k &= \int_0^{\infty} \lambda^{2k+1} J_0(\lambda r) \exp[-(\kappa \lambda)^2 t] d\lambda \\ &= \int_0^{\infty} \left[\sum_{p=0}^{\infty} \frac{(-1)^p (r\lambda)^{2p}}{2^{2p} (p!)^2} \right] \lambda^{2k+1} \exp[-(\kappa \lambda)^2 t] d\lambda \\ &= \sum_{p=0}^{\infty} \frac{(-1)^p r^{2p}}{2^{2p} (p!)^2} \int_0^{\infty} \lambda^{2(k+p)+1} \exp[-(\kappa \lambda)^2 t] d\lambda \\ &= \frac{1}{2} \sum_{p=0}^{\infty} \frac{(-1)^p (k+p)!}{(p!)^2 (\kappa^2 t)^{k+p+1}} \left(\frac{r}{2} \right)^{2p} \end{aligned}$$

where, during the evaluation, we have expanded the J_0 function [2] as well as made use of the identity of definite integral

$$\int_0^{\infty} x^m e^{-x} dx = m!$$

While equation (27) is already in a usable form as given, a more convenient form dealing with dimensionless quantities $a^2/4\kappa^2 t$ and $r^2/4\kappa^2 t$ first may be arranged as

$$\phi(r, t) = \sum_{k=0}^{\infty} \frac{(-1)^k}{k! (k+1)!} \left(\frac{a^2}{4\kappa^2 t} \right)^{k+1} M_k(r, t) \quad (28)$$

with

$$M_k(r, t) = \sum_{p=0}^{\infty} \frac{(-1)^p (k+p)!}{(p!)^2} \left(\frac{r^2}{4\kappa^2 t} \right)^p \quad (29)$$

In summary, equations (15), (21) and (28-29) establish the required solution in series form.

PROBLEMS OF SPECIAL INTEREST

A.) THIN DISK SOURCE-When the depth of initial heat deposition is insignificant compared with plate thickness, the solution takes on a simplified form. In this limit of $a/b \rightarrow 0$, we have from (15) and (21)

$$T = T' \phi(r, t) \left\{ 1 + 2 \sum_{n=1}^{\infty} (-1)^n \cos\left(\frac{n\pi z}{b}\right) \exp\left[-\left(\frac{n\pi \kappa}{b}\right)^2 t\right] \right\} \quad (30)$$

in which a normalizing temperature $T' = Q/\rho c \kappa a^2 b$ has been introduced. We note that if Q were to be uniformly distributed in the cylindrical volume having cross-sectional area πa^2 but extending over the entire thickness of the plate b , T' would be the expected initial temperature there.

B) TEMPERATURE ON THE AXIS OF SYMMETRY-The most severe heating can be expected on the central axis. By inserting $r = 0$ in (29), we have

$$M_k = k!$$

which is a constant. Therefore, equation (28) evolves as

$$\begin{aligned} \phi(0, t) &= \sum_{k=0}^{\infty} \frac{(-1)^k}{(k+1)!} \left(\frac{a^2}{4\kappa^2 t} \right)^{k+1} \\ &= 1 - \sum_{m=0}^{\infty} \frac{(-1)^m}{m!} \left(\frac{a^2}{4\kappa^2 t} \right)^m \\ &= 1 - \exp(-a^2/4\kappa^2 t) \end{aligned} \quad (31)$$

a most elementary-looking result indeed.

C) TEMPERATURES ON THE INSIDE SURFACE-The inside surface is accessible for experimental detections. Also, it is the temperature characteristics on this surface which are parameters for fuel hazard evaluations. We set $z = 0$ in (21) and achieve a simplified form for ψ , converting (15) to

$$T(r, 0, t) = T' \phi(r, t) \left\{ 1 + 2 \sum_{n=1}^{\infty} (-1)^n \frac{\sin(n\pi a/b)}{(n\pi a/b)} \exp\left[-\left(\frac{n\pi \kappa}{b}\right)^2 t\right] \right\} \quad (32)$$

where ϕ is to be provided by (28). The worst-case heating effect is felt at the center. For this "hot spot" temperature, a prediction is available by letting (31) provide ϕ , resulting in writing (32) in the form

$$T(0, 0, t) = T' \left(1 - \exp\left(-\frac{a^2}{4\kappa^2 t}\right) \right) \left\{ 1 + 2 \sum_{n=1}^{\infty} (-1)^n \frac{\sin(n\pi a/b)}{(n\pi a/b)} \exp\left[-\left(\frac{n\pi \kappa}{b}\right)^2 t\right] \right\} \quad (33)$$

SURFACE TEMPERATURE CHARACTERISTICS

Of particular interest is the hot spot temperature variation of equation (33). We present representative results through the use of universal curves in plots of T/T' versus t/t' . Typically these are bell-shaped in a semi-log plot display. In Figure 2, we have used a fixed $a/b = 0.887$ but a varying β/b according to values of 0.5, 0.31, 0.16, and 0. It is seen that as β is progressively reduced, two effects are evident. The peaking time is more and more delayed and the peak magnitude is more and more reduced, reaching normalized

values of 2.2 and 0.456, respectively, in the limit of thin-disk source. It is also seen that beyond $t/t' = 3$ the temperature quickly settles down to a set decay pattern, quite insensitive to differences in β specification. In Figure 3, we have used a fixed $\beta/b = 0.5$, but a varying a/b according to values of 1.26, 0.89, 0.63, and 0.31. It is seen that as a/b is being reduced, temperature peaking takes place earlier and earlier and the corresponding peak of the temperature profile increases relatively sharply. At very large time, i.e., beyond $t/t' = 13$, all curves converge together, irrespective of differences in a/b specification.

DISCUSSIONS

A) Presently available hot spot theory by Robb et al [1] employs a similar initial-value-problem approach but the model of initial heat deposition is in the form of a cylinder of square cross section. It should be interesting to compare predictions from the two theories using more or less comparable parameters. This we have now done by assuming for a particular material common values for the total heat input Q , thickness b , depth of heating β and the cross-sectional area of initial heating. Specifically, we use $\beta/b = 0.5$ and $a/b = 0.887$. The calculated temperature profiles based on our model of cylindrical geometry are sketched in Figure 4 as solid curves. They are the hot spot temperature and the temperature at a point $r = 1.77b$ away from the hot spot. The corresponding temperature profiles based on the square model theory are also exhibited. In dotted curves, one is for the hot spot while the other is for a point similarly displaced from the hot spot but along one of two principal axes. We observe that the two models give close predictions. For the hot spot case, the present model theory yields slightly higher value in the vicinity of the peak near $t/t' = 1.7$. For the case of the displaced location, however, the present theory predicts slightly lower values in the early phase of time and a time of peaking at $t/t' = 5.7$. The square model theory on the other hand predicts a time of peaking at $t/t' = 5.2$ for this case. It is reasonable that far away from the center, the temperature variation should be insensitive to all source details except the total heat Q . Therefore, both theories yield similar patterns in the far-field limit. In the other limit at the center, they again are seen to agree closely. It is only when the displacement is near the dimension a that perhaps some quantitative differences in features can be expected.

B) When a natural lightning stroke or a laboratory long spark strikes the surface of a metal plate, a host of phenomena occur near the strike zone. Among the ones important for hot spot considerations are surface vaporization, melting, radiation and heat conduction, for example. A purely heat diffusion theory requires knowledge on the total heat available

for conduction Q and some effective deposition volume size. Estimation of these parameters in actual test conditions encounters uncertainties.

There is some similarity between the phenomenon of pulsed-laser annealing or heating at a metal surface and that of the spark strike. In the former case, the total energy available for heating, Q , is the incident laser pulse energy minus reflected energy at the surface and other losses. It is a quantity readily calculatable. In contrast, this is not so with the latter case. There are two plausible approaches toward estimating Q for spark strike. The first is to regard the strike as an arc contact phenomenon. Thus a cathode (or anode) potential drop based on steady arc theory allows one to assess the electrical energy input at the electrode by integrating the voltage-current product over time, in effect basing surface heating on ion bombardment as its main cause. Q could then be obtained after suitably subtracting losses. The second approach is to use the pattern of melting damage as a criterion for estimating Q . In this case, volume of the pitted region on the damaged surface is measured. By assuming that the material in this volume was originally heated to exactly its melting temperature, the total amount of heat residing therein is then taken to be Q (see reference 1).

It should be recognized that the picture of a stable cathode drop is based on the space-charge effect inherent in a steady arc. In a transient arc condition, the extrapolated use of this quantity is not warranted in view of the many other accompanying physical complications.

Estimation of the amount of initially heated material based on damage examination is also difficult. For aluminum, for example, the melting temperature is only 660°C while its evaporating temperature is at around 2200°C . Thus, in between, there is a large range of temperature over which a molten metal could be in a superheated state.

For strong discharges, surface vaporization is an unavoidable observation, indicative of superheated molten material in a region immediately on and below the surface. It is then clear that subsequent heat diffusion from this region can lead to additional melting of contiguous material as time progresses until ultimately the front of thermal wave becomes insufficient to bring material up to the melting temperature. One concludes that the realistic size of the volume of initial heat deposition is probably much less than a damage examination would indicate. Secondly, the initial temperature in the deposit zone would be much higher than the melting temperature of the metal.

In experimental situations, the size of the volume of initial heat deposit must be estimated judiciously, using the visual damage volume size as an upper bound. As can be seen from the results of this work, the hot spot temperature

hinges on the size and depth of this volume. On the other hand, at a point moderately removed from the hot spot, the temperature variation can be expected to depend on Q alone, being insensitive of details of the source region. It is the measured temperature profile at an off-center point like this that can be used to come to an estimate of the parameter Q .

C) As an illustration on how to directly apply the hot spot theory to laboratory tests, we cite the data from one experiment early conducted at the LTRI using thermal couple techniques [1]. Conditions were for an aluminum plate of thickness $b = 0.318$ cm. The peak temperature was observed near 289°C at $t = 0.038$ sec. Figure 5 reproduces this hot spot temperature curve. Plotted also is a prediction based on using equation (33) with $a = 0.4$ cm, $\beta = 0.0318$ cm and $Q = 26.2$ cal. It is recognized that these parameter values have been selected within reasonable ranges to yield a prediction in gross approximation to the test data. They are not meant to be serious technical determinations.

D) In many situations involving spark arc spot heating, the input is not instantaneous but prolongs over a scale of time on the order of, or greater than, t' . Under those circumstances, the approach of initial-value problem is inadequate. It is possible, however, to regard the result in the present theory as in the form of response to impulse heating. In correspondence, the complete temperature response to a time-dependent continuous heating input would follow by the use of convolution techniques.

SUMMARY

Previously available theory of hot spot heating of a plate utilizes rectangular geometry but yields cumbersome mathematical results. The present work extends the theory to the more natural cylindrical geometry providing simple-to-use results. Intended for the study of hot spot heating by a lightning or arc stroke, the theory applies equally to studies in the related field of laser-induced heating on the surface of a plate.

REFERENCES

1. J.D. Robb, E.L. Hill, M.M. Newman, and J.R. Stahmann, "Lightning Hazards to Aircraft Fuel Tanks," National Advisory Committee for Aeronautics Technical Note 4326 (1958).
2. E.T. Whittaker and G.N. Watson, Modern Analysis, (Cambridge University Press, 1950) p. 355.

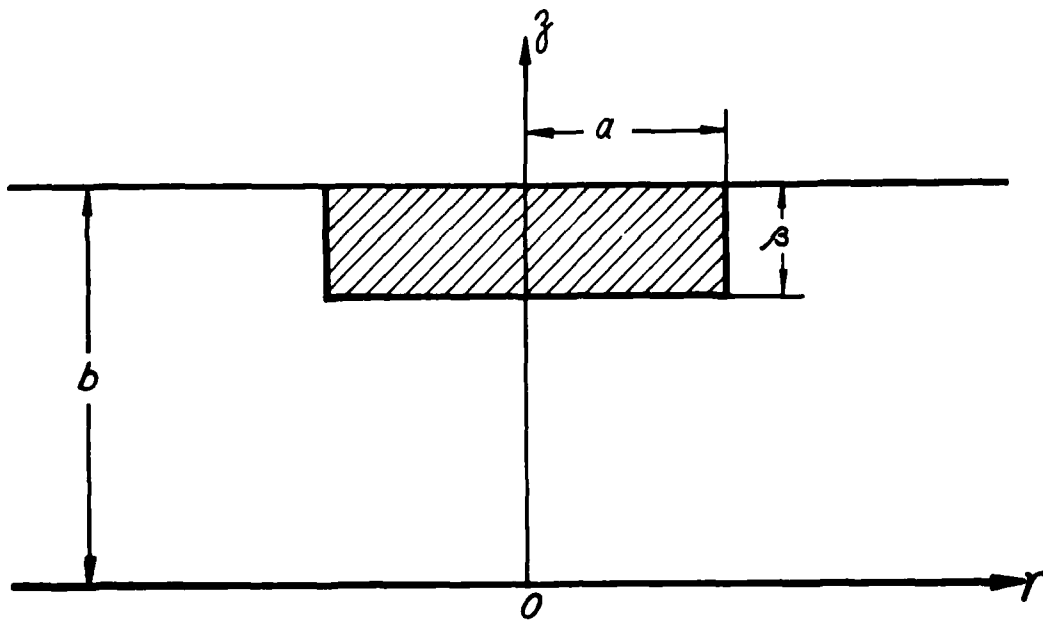


Fig. 1 - Model of initial spark heat deposition in a plate

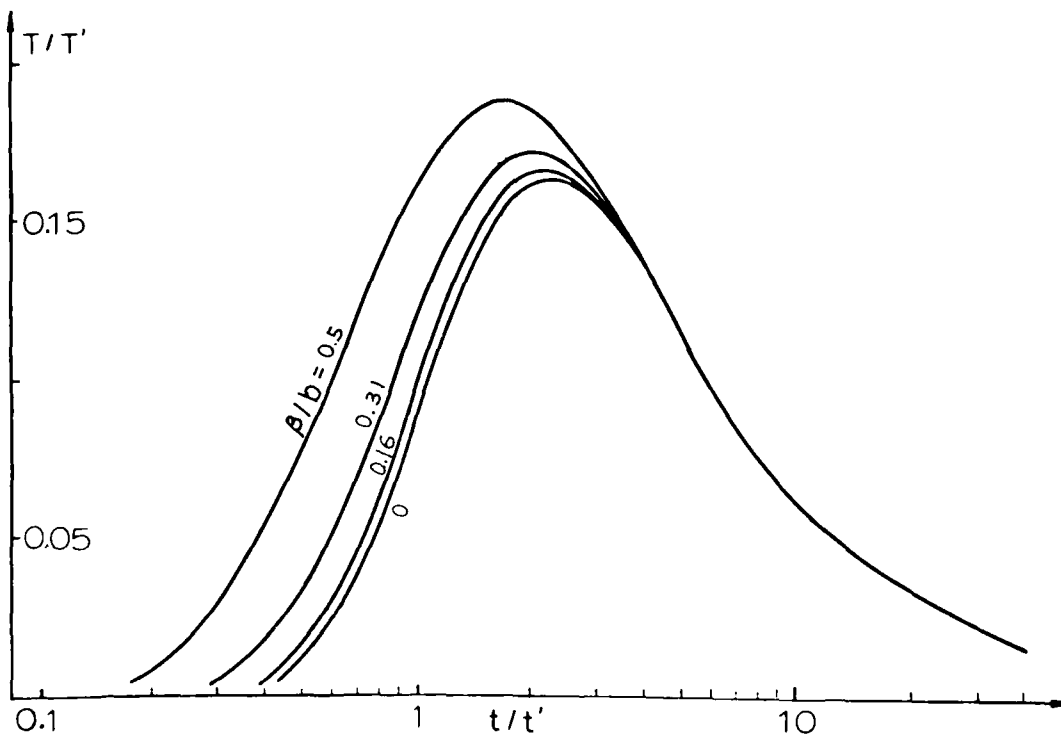


Fig. 2 - Normalized variations in hot spot temperature for $a/b = 0.887$ according to $\beta/b = 0, 0.16, 0.31$ and 0.5

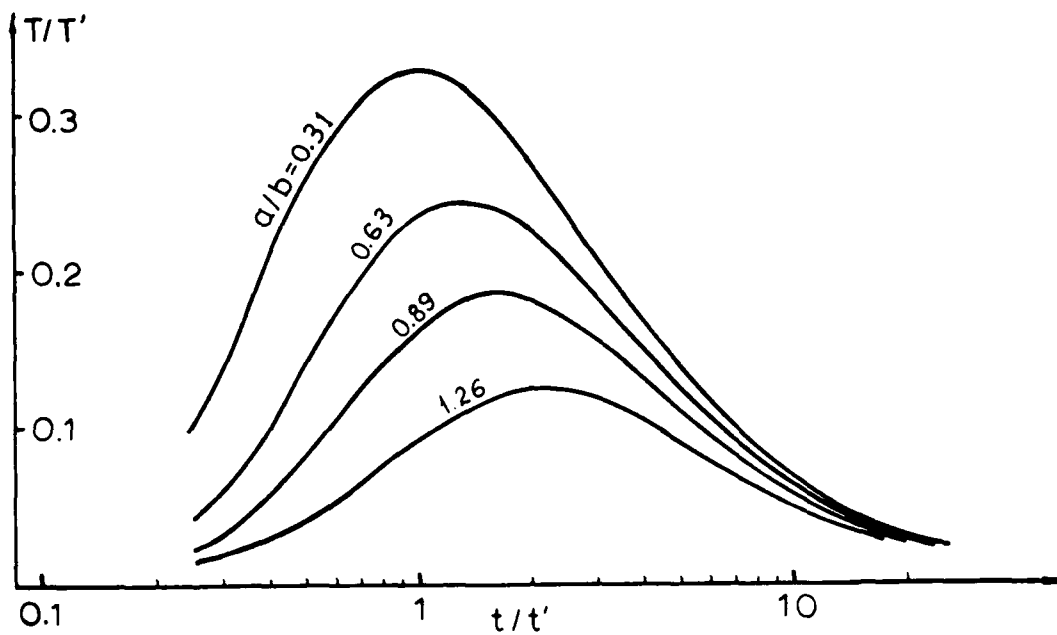


Fig. 3 - Normalized variations in hot spot temperature for $\beta/b = 0.5$ according to $a/b = 0.31, 0.63, 0.89, 1.26$

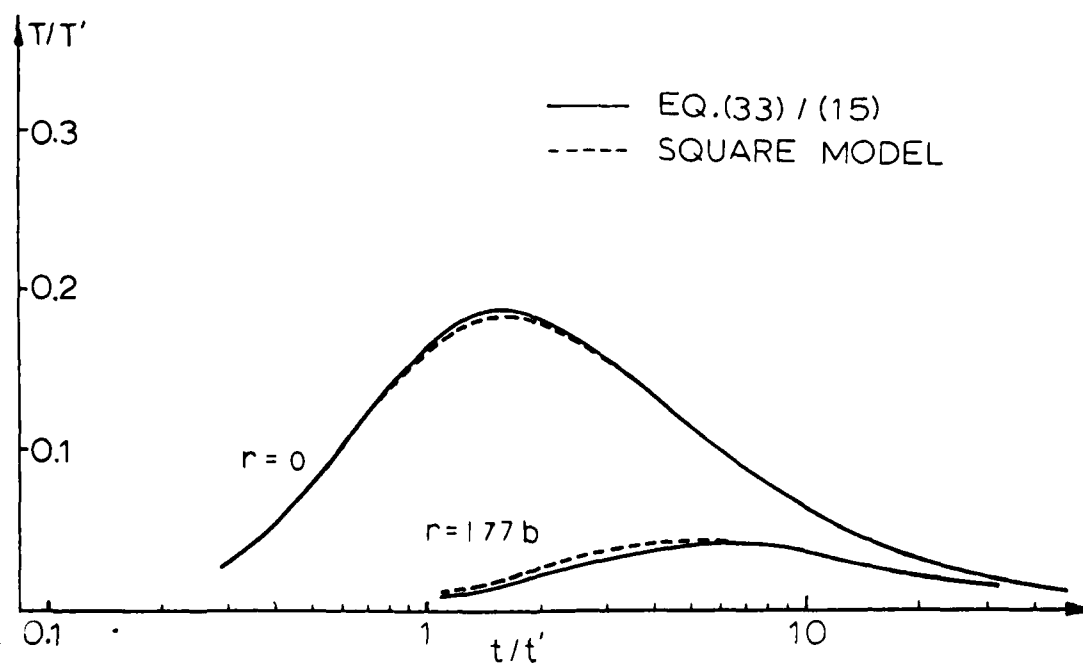


Fig. 4 - Comparison of temperature predictions at $r = 0$ and $r = 1.77b$ from cylindrical and square source model theories. Solid curves are respectively from equations (33) and (15). Dotted curves are based on theory of Reference 1

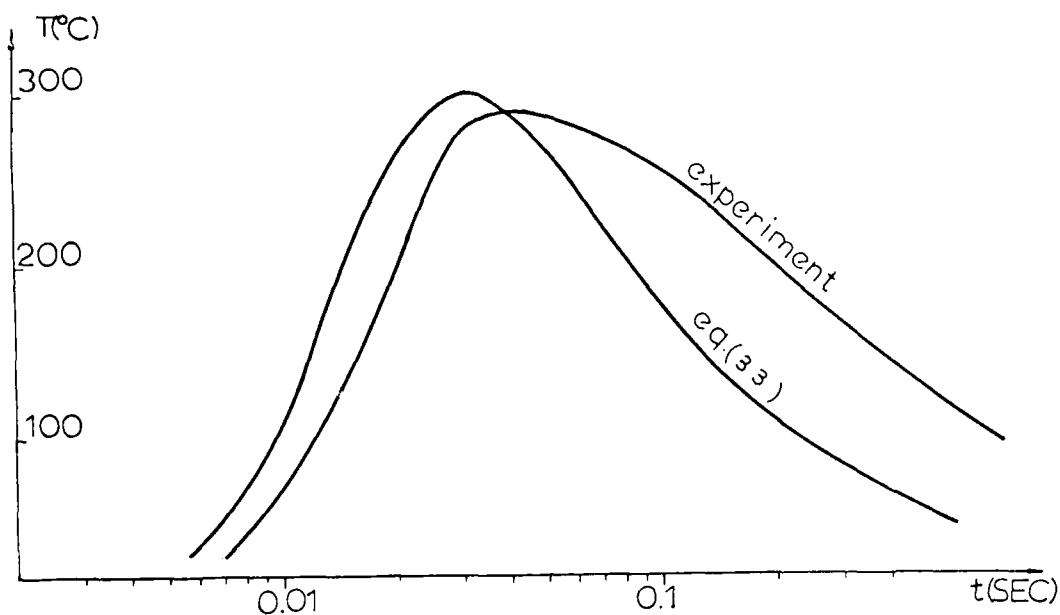


Fig. 5 - Illustrative simulation of hot spot temperature data from spark heating of an experiment on a 1/8 inch aluminum plate (Ref. 1). Parameters selected for use in equation (33) are $a = 0.4$ cm, $\beta = 0.0318$ cm and $Q = 26.2$ cal.

SURFACE ELECTROSTATIC FIELD AND METEOROLOGICAL CONDITIONS IN THE PERIOD
OF WINTER THUNDERSTORMS

Y. Goto, F. Naito, K. Narita and M. Naito

Department of Electrical Engineering, Tohoku University, Sendai 980, Japan

ABSTRACT

To clarify the winter thunderstorm characteristics, the surface electrostatic field strength has been measured by a field mill and recorded with a digital recording system at Maki(Kakumi-Hama) in Japan since the winter of 1982.

These field change data are compared with the meteorological conditions and the synoptic conditions which tend to produce storms has been analyzed in detail. Most thunderstorms which occur in districts facing the Japan Sea during the winter are air-mass storms and are produced when the temperature at 500 mb pressure level is below -20°C , it drops with a rate of more than about $10^{\circ}\text{C}/\text{day}$ and frontal surfaces of trough move east across the Japan Sea.

Moreover, spectrum analysis for the field change data in the period of thunderstorms has been done to estimate the scale of thunderclouds and convective cells with considering wind speed.

INTRODUCTION

Electric field measurements are very important to determine the quantity, distribution and movement of electric charges in thunderclouds. To identify summer thunderclouds, there are many studies of electric field measurement [1],[2],[3]. To clarify the winter thunderstorm characteristics, the surface electric field strength has been measured by a field mill at Maki in Japan since the winter of 1979 [4]. Its output has been recorded on a pen recorder. To simplify the analysis of the obtained field change data, a digital recording system controlled by a simple micro-computer board has been developed and used together since the winter of 1982.

The meteorological data at Maki have been measured by weather instruments on the observation tower where lightning currents have been measured [5],[6]. Moreover, meteorological and aerological data at Wajima and Akita could be obtained.

In this paper we describe the winter climate of the districts facing the Japan Sea and formation of thunderclouds then present examples of the electric fields produced by winter thunderstorms and meteorological conditions, examine the time development of lightning activity and finally examine the cell scales in the cloud by the spectrum analysis of field changes considering meteorological conditions.

WINTER MONSOON AND FORMATION OF THUNDERCLOUDS [7]

At the middle or end of November, a continental anticyclone begins to develop over the Asian Continent which increases in strength to foster a huge polar continental air-mass and northwesterly winds prevail throughout the winter with a peak in January. As a result, the winter of Japan is completely governed by this cold air-mass, which brings abundant snowfall and cloud, overcast weather to districts facing the Japan Sea. The first arrival of this winter monsoon is commonly at the end of November.

The monsoon winds are cut by cyclones moving from southwest to northeast over the Japan Sea reducing their strength. Then the cyclones have passed away to the northeast, the monsoon winds grow afresh, flowing into the rear side of the cyclone area.

The Siberian air-mass produced over the continent is initially very cold, dry and stable. However, on leaving the continent and passing over the Japan Sea, it is modified by the underlying water surface.

The modification of that air-mass during its passage over the Japan Sea is very important in determining the winter climate in Japan and the formation of thunderclouds.

The Tsushima warm current flowing up from

Kyushu Island and parallel to the Japan Sea coast of Honshu Island about 60-80 km distant from the shoreline is approximately 10°-12°C in winter. This current plays a fundamental role as an energy and water vapour source [8].

The rate of evaporation depends mainly upon the temperature of the evaporating surface compared with that of the air, but also upon the relative humidity of the air or its degree of saturation, and the speed of the wind. When frigid air with low humidity is advected over a relatively warm water surface, evaporation is rapid, since the vapour pressure of the cold atmosphere is always less than that over the warmer water. Moreover, under these circumstances the air is heated from below by contact with the warm water surface so that it becomes unstable.

Since the daily change in water surface temperature is small, the lower the air temperature and the higher the wind velocity, the greater is the energy and water vapour supply from the water surface.

The sensible heat supply during the period of intense outburst of the Siberian air-mass is known to have reached as much as 1000 cal/cm².day in the Japan Sea. Moreover, the latent heat is about 500 cal/cm².day. The total heat supply, which comes to 1500 cal/cm².day, exceeds the heat of the earth from the sun which is about 1440 cal/cm².day, at midday in summer.

Thus as the air-mass passes towards the Japanese Islands, inversion and turbulence in the lower layer of the Siberian air-mass intensifies the formation of cumulus at low altitudes. Moisture entering the air as water vapour and heat is widely distributed by wind and vertical air current and heighten the instability. When this combines with convergence induced by a front or other mechanism, strong cumulus convection develops and many cumulonimbus are formed.

During the cloud passage over the Japan Sea, although its bases are constant usually from 300 m to 1 km above sea, its tops increase gradually to 4-6 km in height at the coastline of Honshu Island.

INSTRUMENTATION AND DATA PROCESSING

A field mill was located on the limited space for the weather observation yard about 100 m from the coastline of the Japan Sea, about 400 m SW of the meteorological observation tower and about 13 m in altitude. It has a response time of about 0.3 sec. The mill output has been recorded on a pen recorder only in the early stage. To simplify the data analysis and to avoid the data lacks caused by troubles on recorders, a digital recording system has been developed and used together since the winter of 1982.

The system consists of a field mill, A-D converter, a digital cassette recorder and a simple micro-computer with a timer. Figure 1

shows the block diagram of the automatic digital recording system for the electrostatic field. The dynamic range of the system covers from about +53 kV/m to -53 kV/m of the electric field with a digitization accuracy of about 210 V/m.

To record the field data automatically for a long period, the field signal is sampled at 4 second intervals. It has been registered on memories of the computer with time index when their absolute value exceeds a certain threshold or their changes with time exceed a certain value. The conditions registered all of the sampled data are the absolute value exceed 10 kV/m and its time differential exceed 250 V/m.sec.. The 4 sec. sampling time constant is too slow to time-resolve individual lightning discharges, but it is more than adequate to recognize whole variation of the electrostatic field.

For processing data, digitally recorded data on magnetic tape are transferred and stored into a personal computer with a cassette data recorder. Those data can be stored on 5" or 8" floppy disk and printed out by a dot matrix printer or drawn in the analog form by X-Y plotter, moreover used for the spectrum analysis and so on. The block diagram of data processing system is shown in Figure 2.

RESULTS OF FIELD MEASUREMENT AND METEOROLOGICAL CONDITIONS

Except the electrostatic field data, the meteorological data is essential to evaluate winter thunderstorms which can be obtained at three points Wajima, Akita and Maki. Among them the data at Maki have been measured by weather instruments on the observation tower at which lightning currents have been measured simultaneously and the other include aerological data.

When the frontal surfaces of a trough move east across the Japan Sea during the winter, the aerological conditions at Wajima about 180 km WSW of Maki and Akita about 240 km NNE of Maki are similar excepting that the temperature of Akita is 2°-6°C colder than Wajima and then the temperatures of Maki and Wajima are almost same at the earth surface. So it is able to consider that the aerological conditions of Maki are same as Wajima.

The field data by the digital recording system were obtained over 260 days within about one year from Nov. 1982 to Nov. 1983. Although there were several system stops caused by program miss or surge intrusion in the early stage, the system has been operated normally as expected after some improvements. In this period, the lightning flashes to the tower were 18 times. All occurred in winter in a broad sense.

The unexpected stops on the system operation which are considered to be due to lightning surges were 3 times. This type trouble is a fatal one for the reliability of

automatic measuring and recording system. Since Dec. 1983, the improvements have been made as follows.

(1) Electrical isolation of the signal line between the mill and the recording system using an optoelectronic transmission system

(2) The automatic system restart after the power stoppage

(3) The electromagnetic shield of the system

The daily changes of the upper atmospheric temperature at 850 mb(about EL 1.5 km), 700 mb(about EL 3 km) and 500 mb(about EL 5.5 km) pressure levels over Wajima are shown in Figure 3. In the Figure, arrow heads show the time when lightning flashes strike the tower and heavy portions on the vertical axis show the periods of field records obtained by the digital recording system.

A comparison of the electric field records at Maki with aerological data at Wajima and meteorological data at Maki indicates the synoptic conditions which tend to produce thunderstorms. In winter, most thunderstorms develop at and after the frontal surface of trough moving across the Japan Sea when the temperature at 500 mb pressure level is below -20 °C, it drops with a rate of more than about 10°C/day and moderate westerly wind blow. The temperatures at the tower top of Maki(EL 270 m) drop rapidly with the rate of 2-4°C/hour when the thunderstorms attack Maki area. This drop rates depend on the wind speed and the initial air temperature before thunderstorm. The higher the initial temperature and the wind speed, the larger is the drop rate.

The wind speeds of upper atmosphere at Wajima are almost constant in the height of 0.3 km-3 km and about the same at the tower top in Maki after the time when the frontal surface of a trough moves across over Maki.

The typical examples of the electric field produced by winter thunderstorms and the temperature variations at the tower top are shown in Figure 4. Although in summer thunderstorms rarely occur, a few examples are shown in Figure 5. In winter, these fields are highly variable in both magnitude and polarity as shown in Figure 4. The fields at the ground exceed sometimes more than 20 kV/m. Several thunderstorms develop and attack the region periodically over a long period of time during one day or more. In the period there are large amplitude and abrupt changing alternations before and after the lightning flashes to the tower. These abrupt changes may represent the rapid electrical processes which occur during given intervals of ground discharges and precipitation. The time changing fields are due to moving the thundercloud charges with wind speed. Realistic examples are shown in Figure 6. Since it can be considered that the variations of field for the distance are charge distributions in the thundercloud passed over Maki area, the field changes reflect the charge center of the thundercloud.

To obtain the scales of thundercloud from the period of continuous field variation due to storm movement and wind speeds, the data have been processed with a low pass filter on the assumption that the cloud velocity is equal to the wind speed at the tower top and the wind direction is uniform.

The deduced scales are compared with the scales of clouds taken by the Geostatic Meteorological Satellite (GMS 2) "Himawari 2". The results are shown in Table 2. The reduced values from 30 km to 300 km are almost equal to the one obtained from the pictures by GMS 2.

SPECTRUM ANALYSIS OF THE FIELD DATA

To clarify the general characteristics of the slow field change, the data in the time domain when intense field is going on for each storm are analyzed to the spectrum distribution by Maximum Entropy method. And similarly the scales of thunderstorm, which is calculated from the field change considering wind speed, is analyzed to the spectrum distribution by the same method in which the each peak time is transformed into the peak distances.

Independently of time length and date for the field changes, each fundamental peak time which is the most emphatic one in these distribution is concentrated in the area between 1000 sec. and 4000 sec. and also the fundamental distance is concentrated in the area between 20 km and 50 km. It shows that the period length and scale are able to be divided into parts with both fundamental peak time and peak distance. So these fundamental peak time and peak distance seem to be equivalent to the scale of an individual lightning cell. Figure 7 and 8 indicate the spectrum distributions respectively.

We tried to compare each fundamental peak time and peak distance with temperature in the upper air at Wajima where the altitude is about 3 km on account of investigating what plays the most important role on the property of thunderstorm. Figure 9 and Figure 10 shows these comparison with lapse respectively.

In comparison, both lapse of the fundamental peak have reasonable relation with the lapse of temperature in the upper air. As the temperature decreases, the increase in both fundamental peak is recognized remarkably to some extent in the figures. It seems that the temperature in the upper tends to give an emphatic influence on each fundamental peak.

As the air temperature on the Japan Sea where Tsushima warm current flows decreases, the temperature difference between the water and above the sea surface increases relatively. That makes a lot of heat and vapour taken off from the water and occurred the unstable situation in the atmosphere. In this process the latent heat involved in the vapor is proportional to the temperature difference multiplied by the wind speed above the sea

surface. If plenty of latent heat is involved, the unstable situation will reach to higher extent in the altitude. Then the intense ascending current and large extended convection seem to occur. Because the meteorological condition is similar on the water, it seems that almost the same convection cell occurs at an equal distance.

So we made comparisons of the latent heat with each fundamental peak described above and show them in Figure 11 and 12 respectively. Both figures indicate that the latent heat has more reasonable relation with each fundamental peak.

Therefore it is considered that the scale of the convection is equivalent to the fundamental peak calculated by the spectrum analysis and depends on the air temperature and wind speed above the sea surface.

CONCLUSIONS

To clarify the characteristics of the winter thunderstorm electric field at the ground has been measured by a field mill and a digital recording system.

The obtained data of field change have been compared with the meteorological conditions and the synoptic conditions which tend to produce thunderstorm are made clear. Most winter thunderstorms which occur in districts facing the Japan Sea are air-mass storms and develop when the air temperature at 500 mb pressure level is below -20°C , it drops with a rate of more than about $10^{\circ}\text{C}/\text{day}$ and moderate wind westerly blow during the passage of trough across the Japan Sea.

When the storms attack the region the air temperature at the tower top in Maki drop rapidly with the rate of $2-4^{\circ}\text{C}/\text{hour}$.

In winter the fields are highly variable in both magnitude and polarity and its changes in wave for a long period over one day. It is considered that several thunderstorms develop and attack periodically over a long period of time during one or more.

On the assumption that thunderclouds move with wind speed field changes for the distance are thought due to the charge distributions in the cloud. From the results of the analysis horizontal distances of the charge center in the cloud are 2-15 km.

The scales of thundercloud which are deduced with the wind speed and the time length of a series field change are from 30 km to 300 km and these values are almost equal to the scales obtained by the pictures of GMS 2.

By the spectrum analysis of the field change data the scales of convection cell in clouds are from 20 km to 50 km. This sizes depend strikingly on a mount of the energy and water vapour supplied from sea surface.

In order to study more fully the winter thunderstorm further investigation of the electric fields should be continued at two points where one is Maki and the other is

Hamochi in Sado Island about 50 km W from Maki.

ACKNOWLEDGMENTS

This work was carried by the financial support for Science Research, the Education Ministry of Japan, under the Grant-in Aid of Special Research for Natural Disaster(2), Project number 58025001(1983).

We wish to express their hearty thanks to Mr. R. Funayama and his associates of Tohoku Electric Power Co., Inc. for their supports and helps in carrying out the field work. We are grateful to Mr. R. Simanuki, the head of Wajima Meteorological Observatory and Mr. S. Sumi, the head of Akita Local Meteorological Observatory who offered kindly many aerological data of each points and the associates of the weather forecast section, Sendai District Meteorological Observatory who gave kindly the copies of the cloud pictures by GMS 2.

REFERENCES

1. E.A. Jacobson and E.P. Krider, "Electrostatic Field Changes Produced by Florida Lightning", J. Atmos. Sci., 33, 103-117, 1976.
2. J.M. Livingston and E.P. Krider, "Electric Fields Produced by Florida Thunderstorms", J. Geophys. Res., 83, 385-401, 1978.
3. G.D. Freier, "A 10-Year Study of Thunderstorm Electric Fields", J. Geophys. Res., 83, 1373-1376, 1978.
4. Y. Goto, F. Naito, K. Narita and T. Sato, "The Observation of Lightning Discharges in Winter Thunderstorm at the Niigata Coast, Japan", Proc. Int. Aerospace Conf. on Lightning and Static Electricity, Oxford, A-3, 1982.
5. Y. Goto, K. Narita and F. Naito, "The digital Recording System for Lightning Currents and Some Results Obtained for Winter Thunderstorms", Res. Let. Atmospheric Electricity of Japan, 3, 27-32, 1983.
6. K. Narita, Y. Goto and R. Funayama, "Measurement of Lightning Stroke Current in Winter Season at Maki, Japan", these proceedings.
7. M.M. Yoshino, "The Winter Monsoon", The Climates of Japan, Chap. 4.(Kodansha) edited F. Fukui, 1977.
8. T. Takeuchi, M. Nakano, M. Brook, D.J. Raymond and P. Krehbiel, "The Anomalous Winter Thunderstorms of the Hokuriku Coast", J. Geophys. Res., 83, 2385-2394, 1978.

Table 1 - Comparison of thundercloud scale from pictures by GMS 2 with that deduced by field variation data

Time and date of picture	Scale from picture [km]	Scale from field data [km]
9° Feb. 6, 1983	118	90(9°-20°)
21° Feb. 6, 1983	41	40(21°-22°30')
21° Feb. 8, 1983	208	250(20°30'-2°25')
21° Feb. 9, 1983	274	180(22°- 5°)
21° Mar. 5, 1983	291	300(21°- 8°)
9° Mar. 6, 1983	33	20(9°- 9°30')
9° Mar. 7, 1983	56	55(8°30'-10°30')

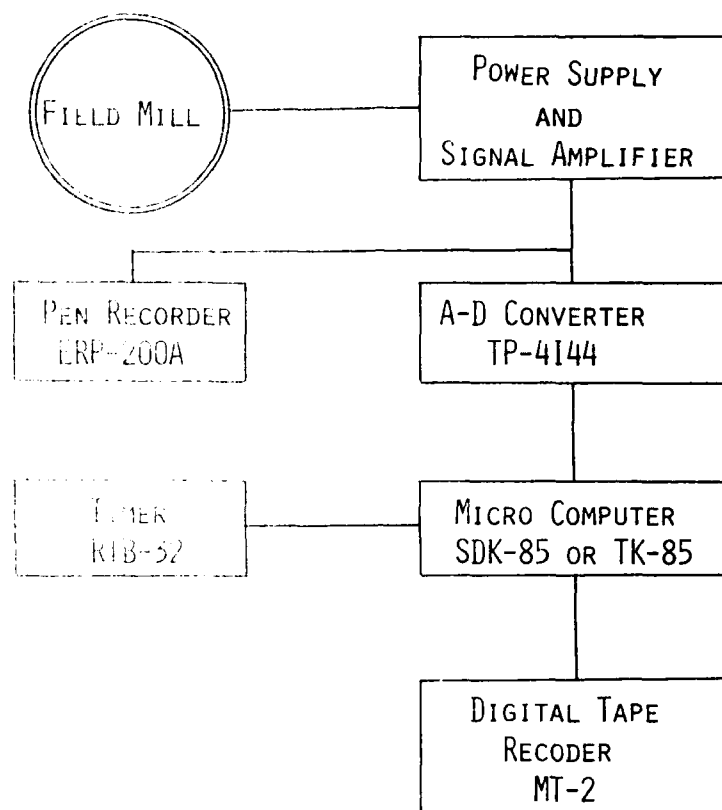


FIG. 1 - block diagram of a field mill and a digital recording system

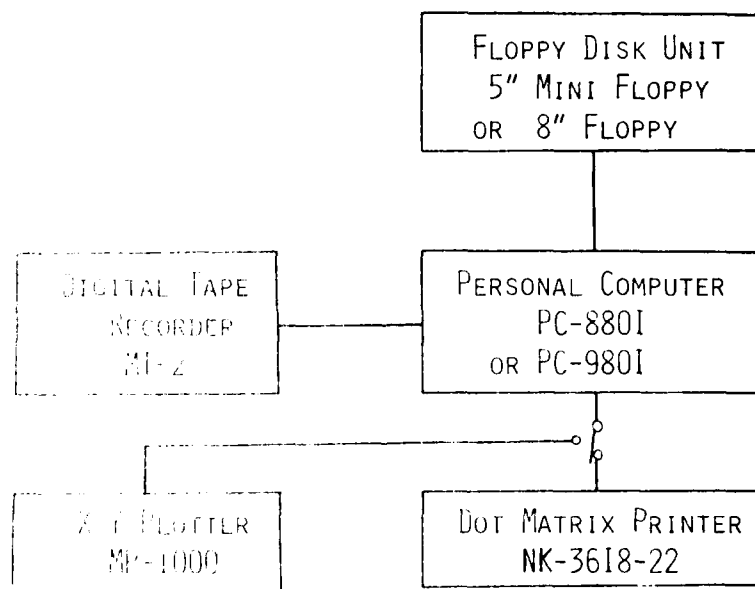


FIG. 2 - Block diagram of a data processing system

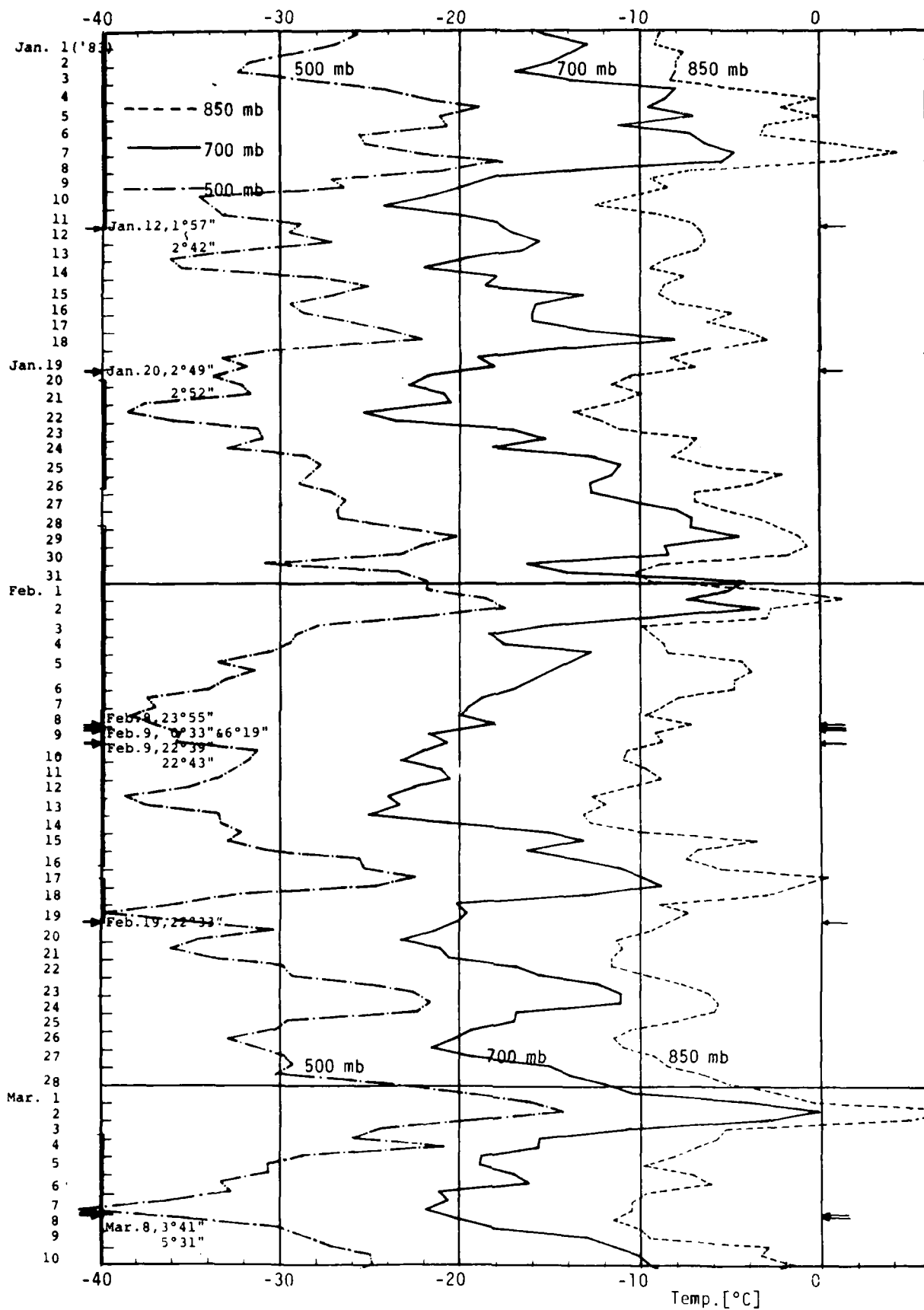
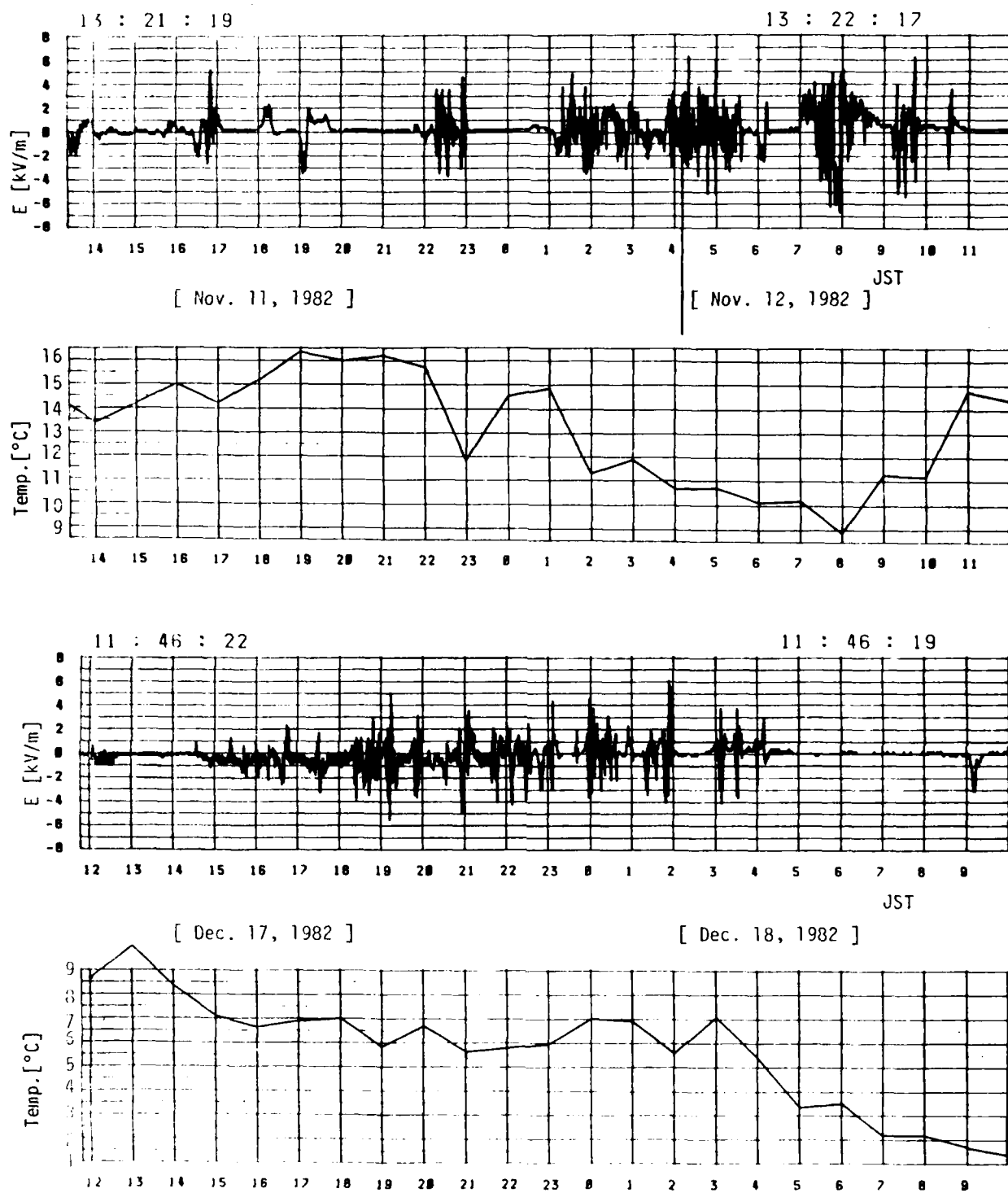
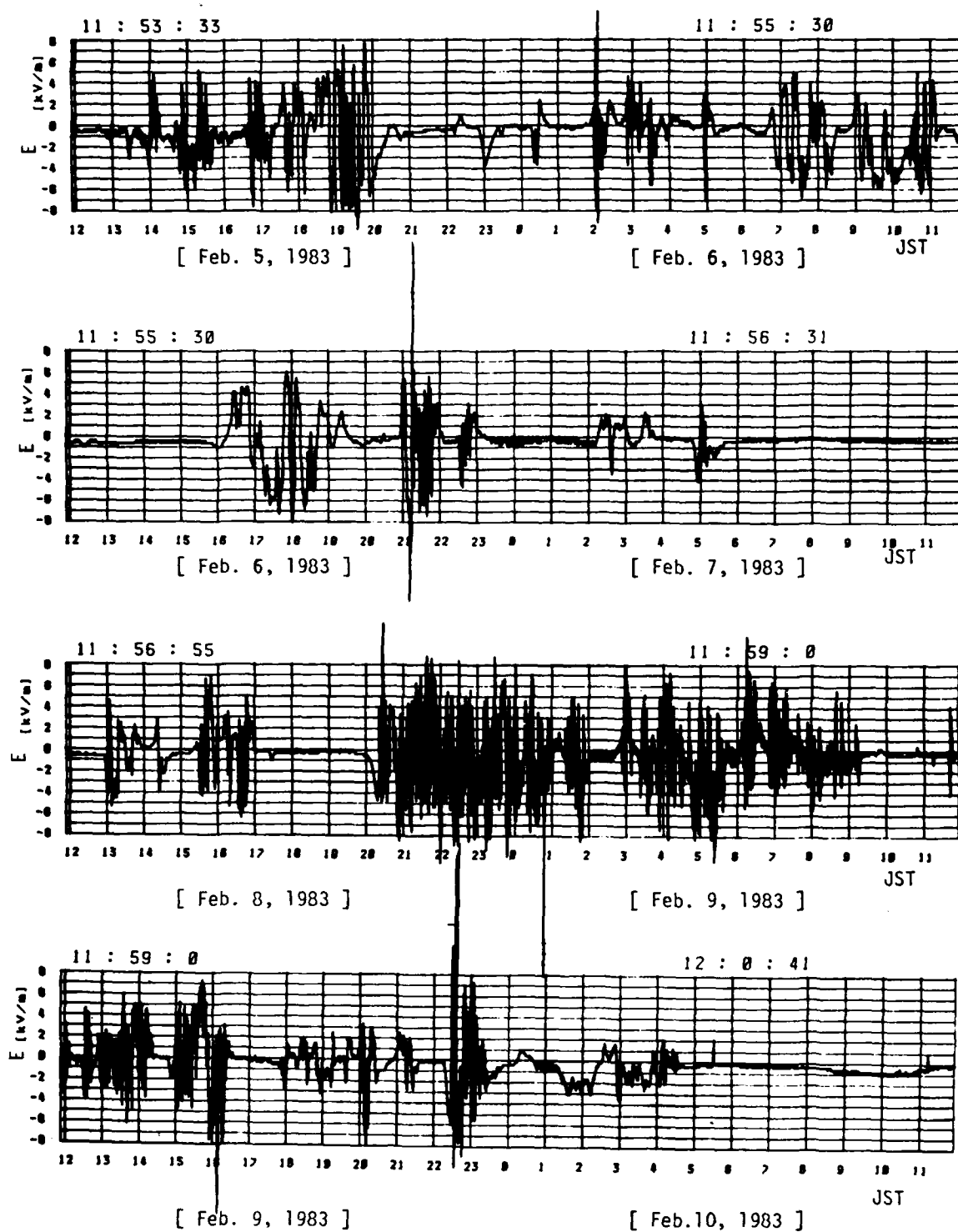


Fig. 3 - Daily changes of the upper atmospheric temperatures at Wajima



(a)

Fig. 4 - Examples of the electrostatic field data in winter
 (a) The variations of the field at the ground and the air temperature at the tower top



(b)

(b) Examples of the field change continuing for a long period over one day

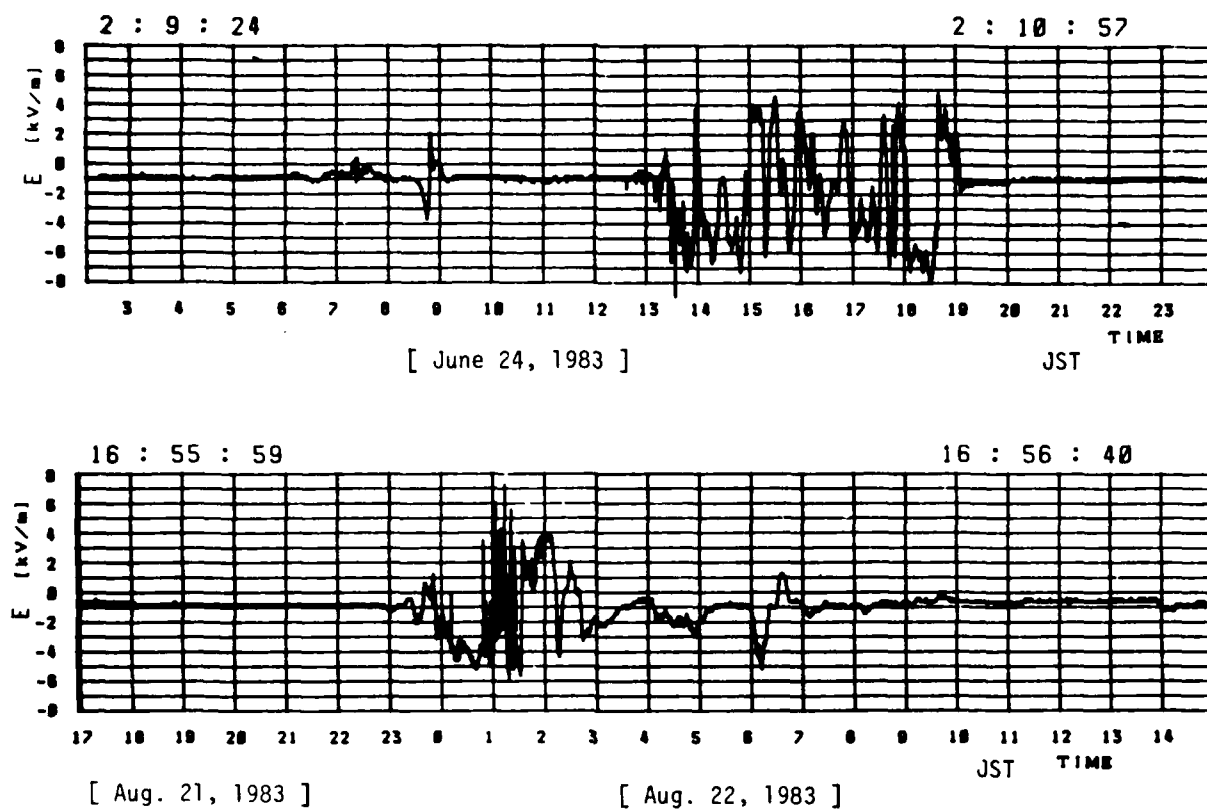


Fig. 5 - Examples of the field data in summer

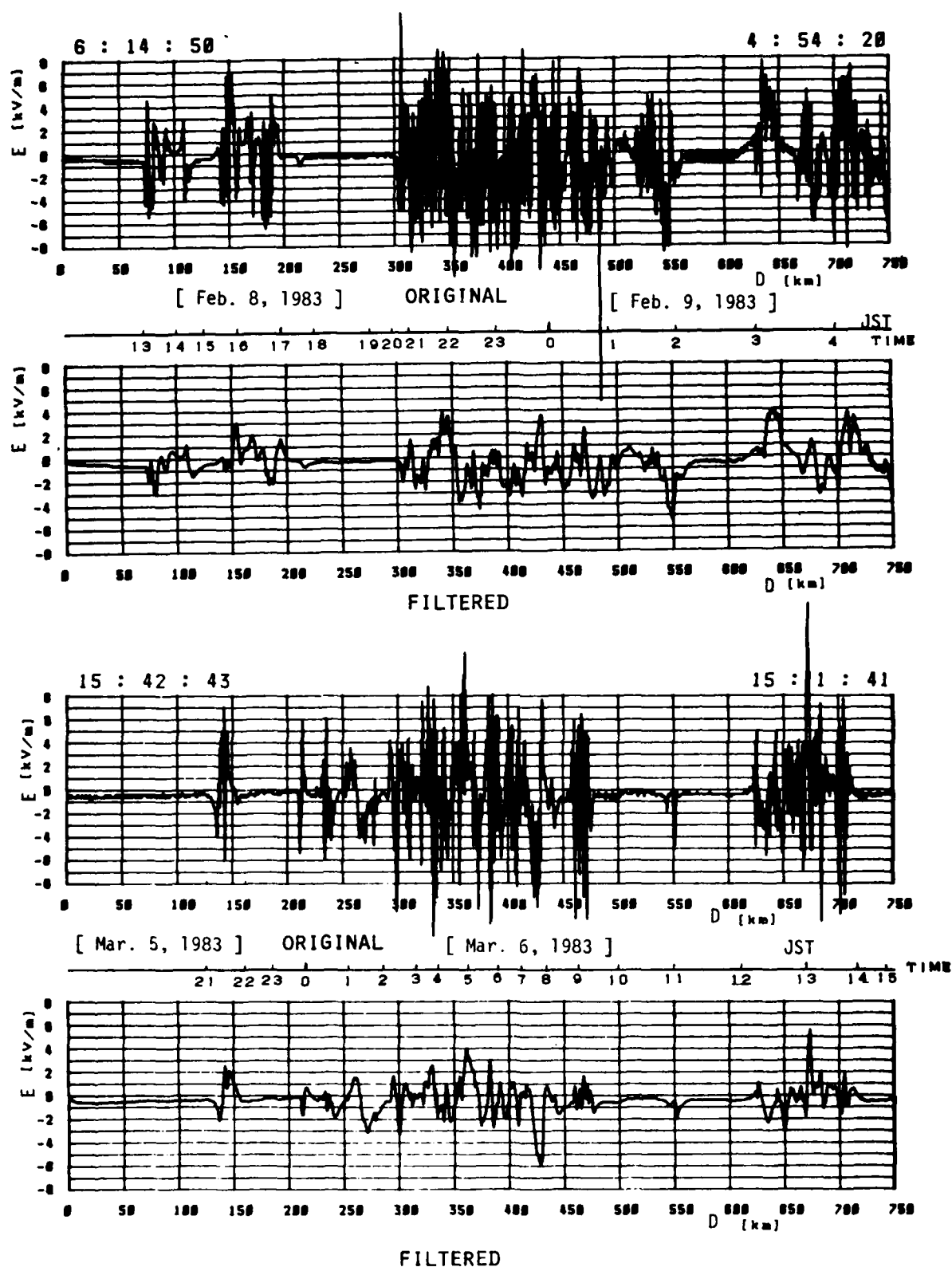


Fig. 6 - The field variations for the horizontal distance

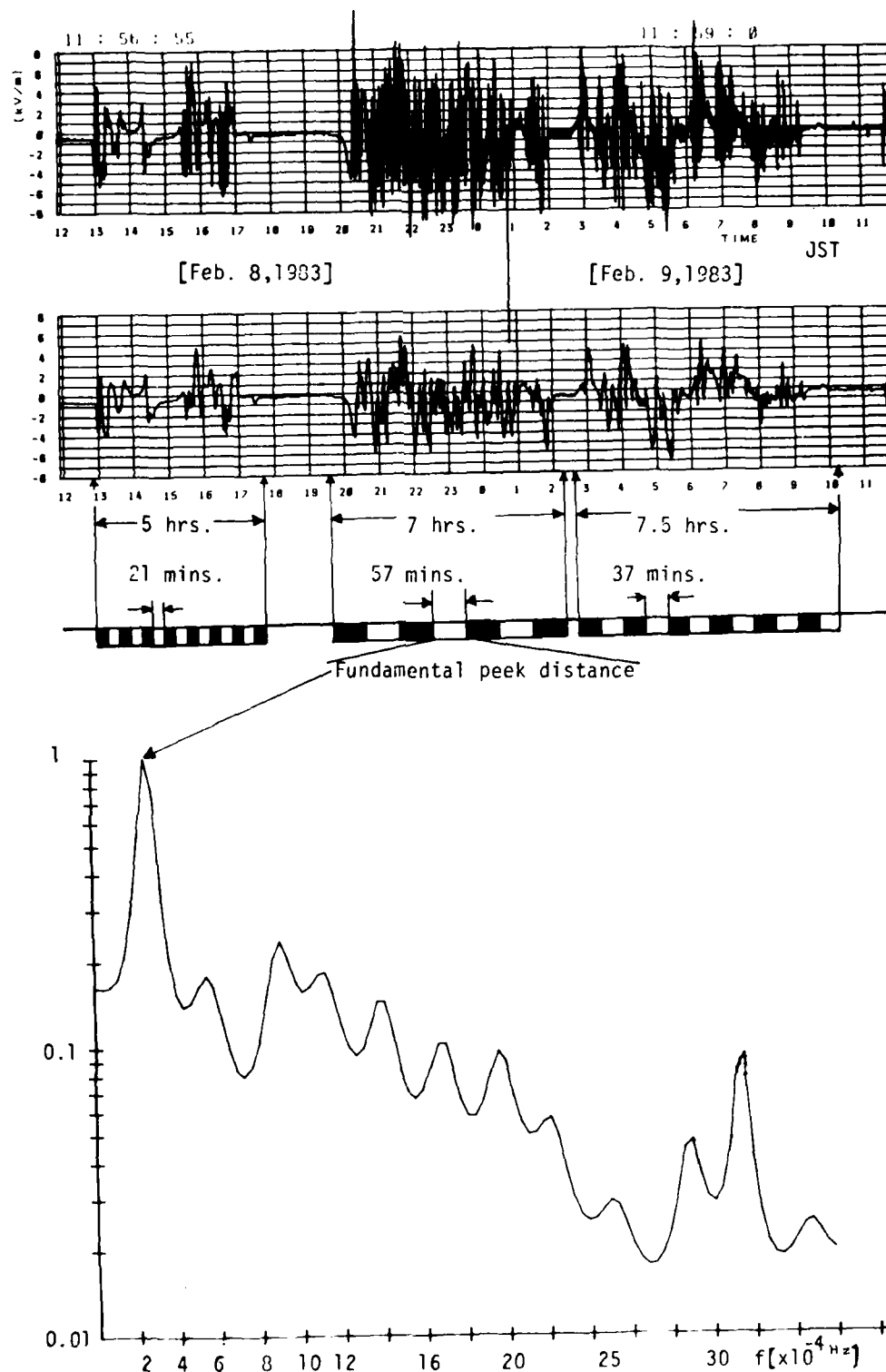


Fig. 7 - Spectrum distribution of the electric field in time domain

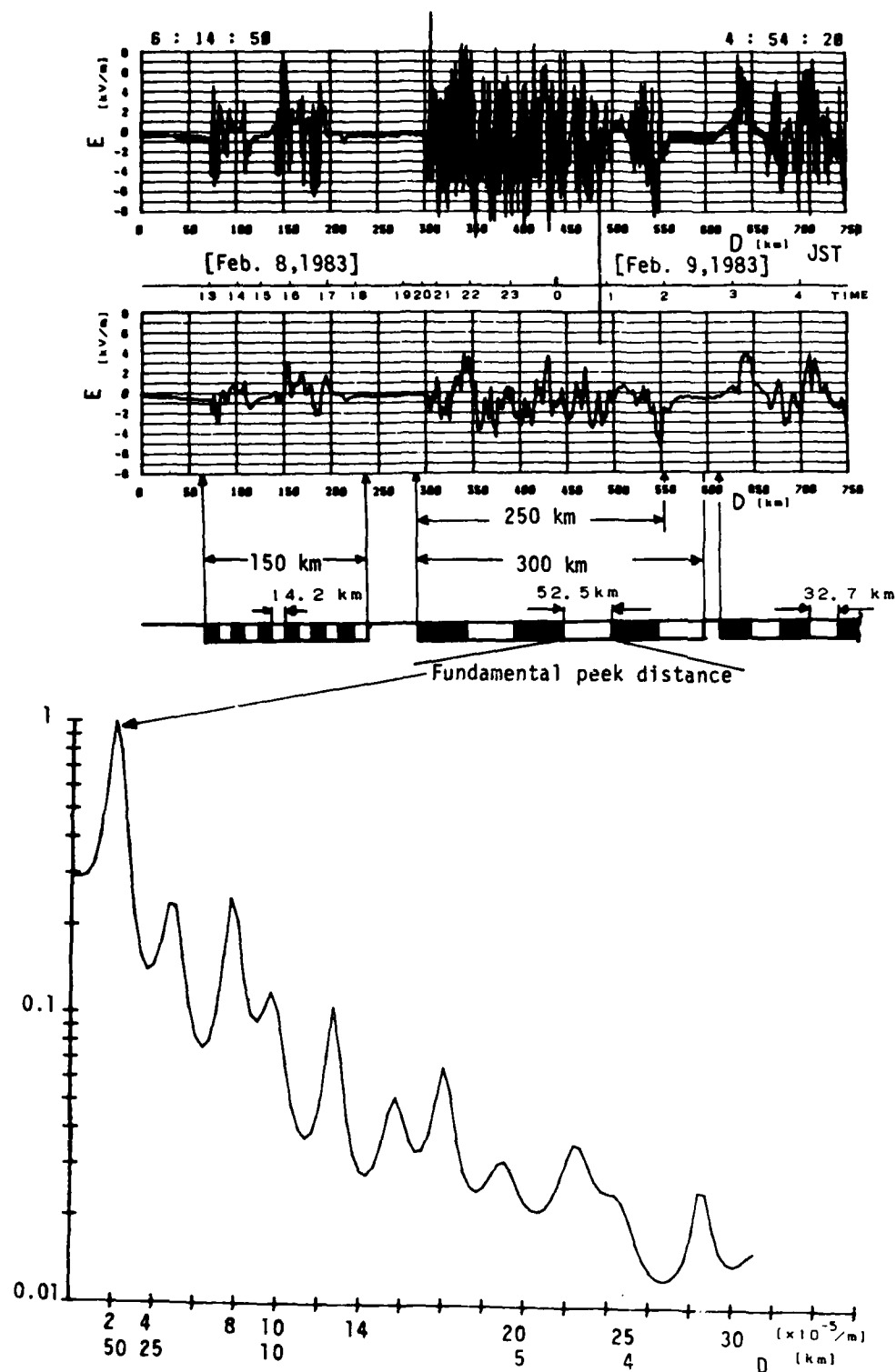


Fig. 8 - Spectrum distribution of the electric field in distance domain

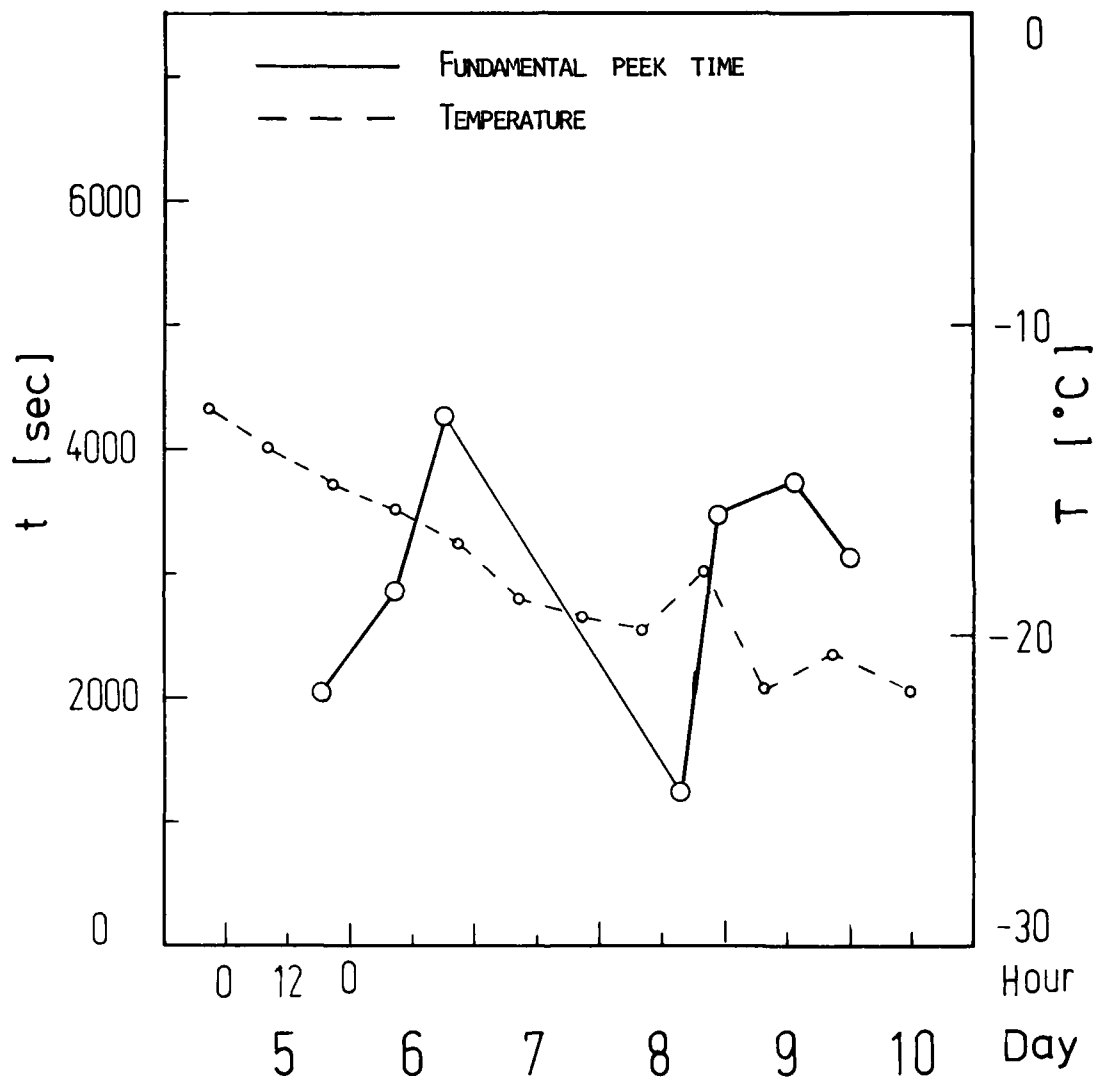


Fig. 9 - Fundamental peak time and daily change of the air temperature at Wajima

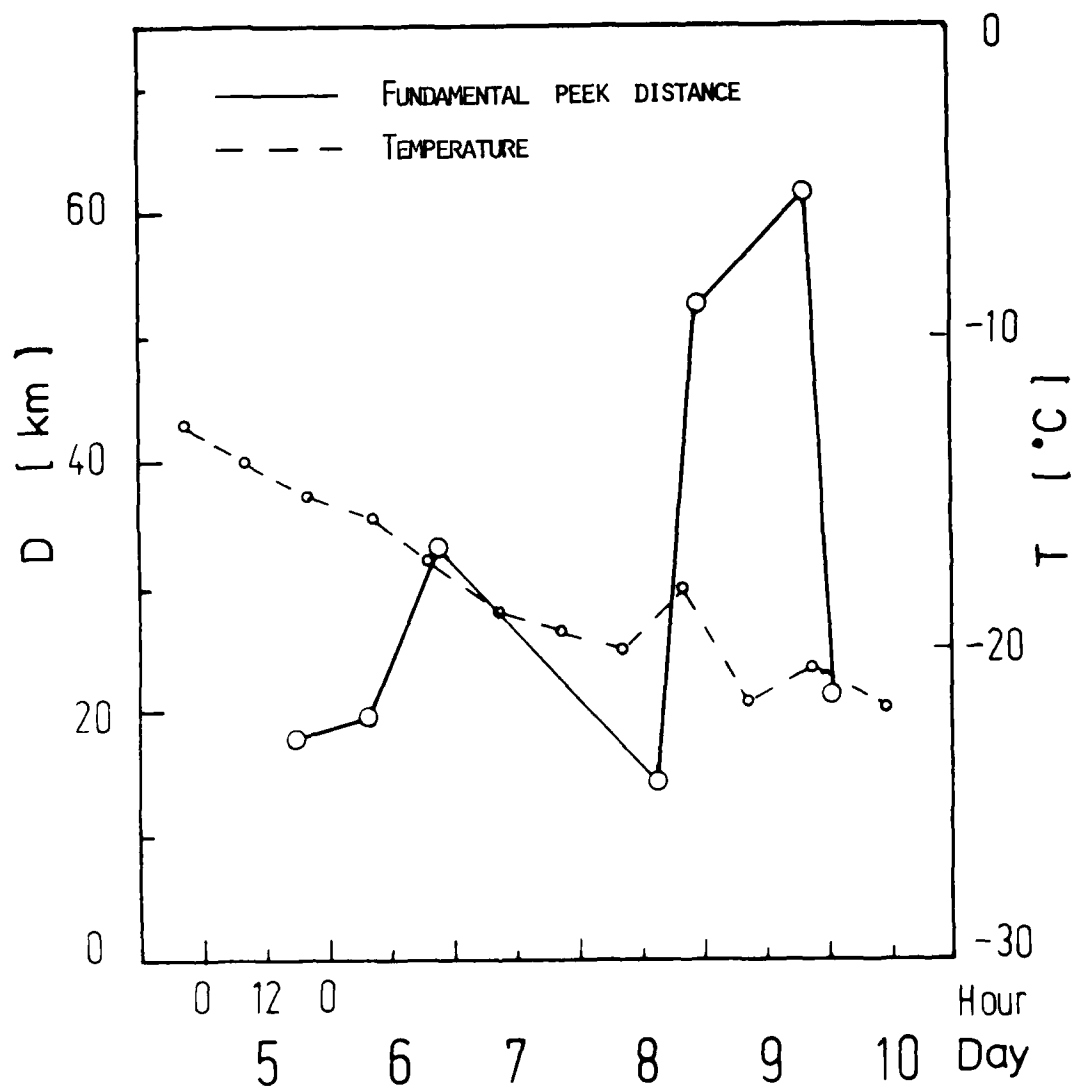


Fig. 10 - Fundamental peak distance and daily change of the air temperature at Wajima

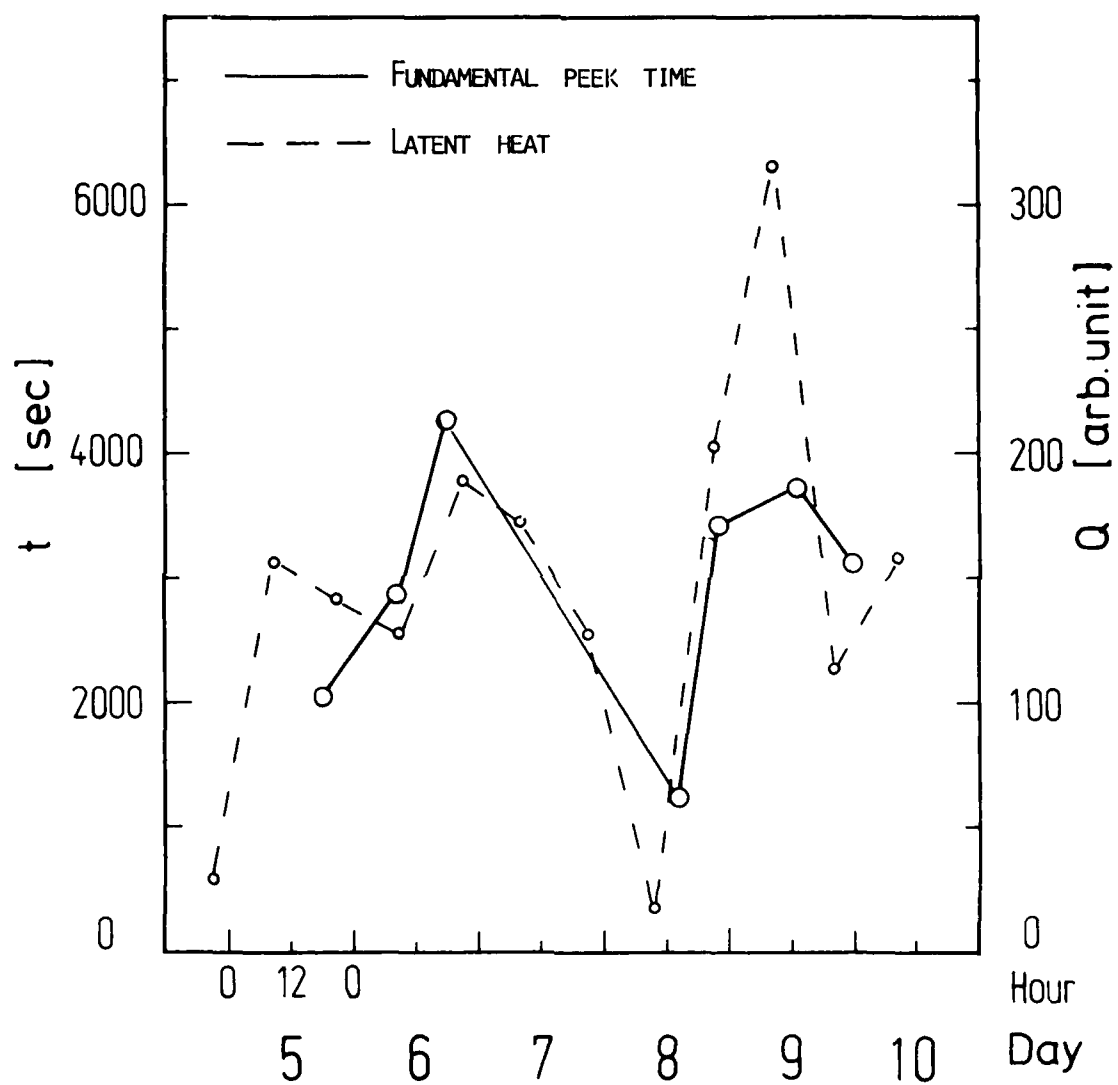


Fig. 11 - Comparison of the latent heat with the fundamental peak time

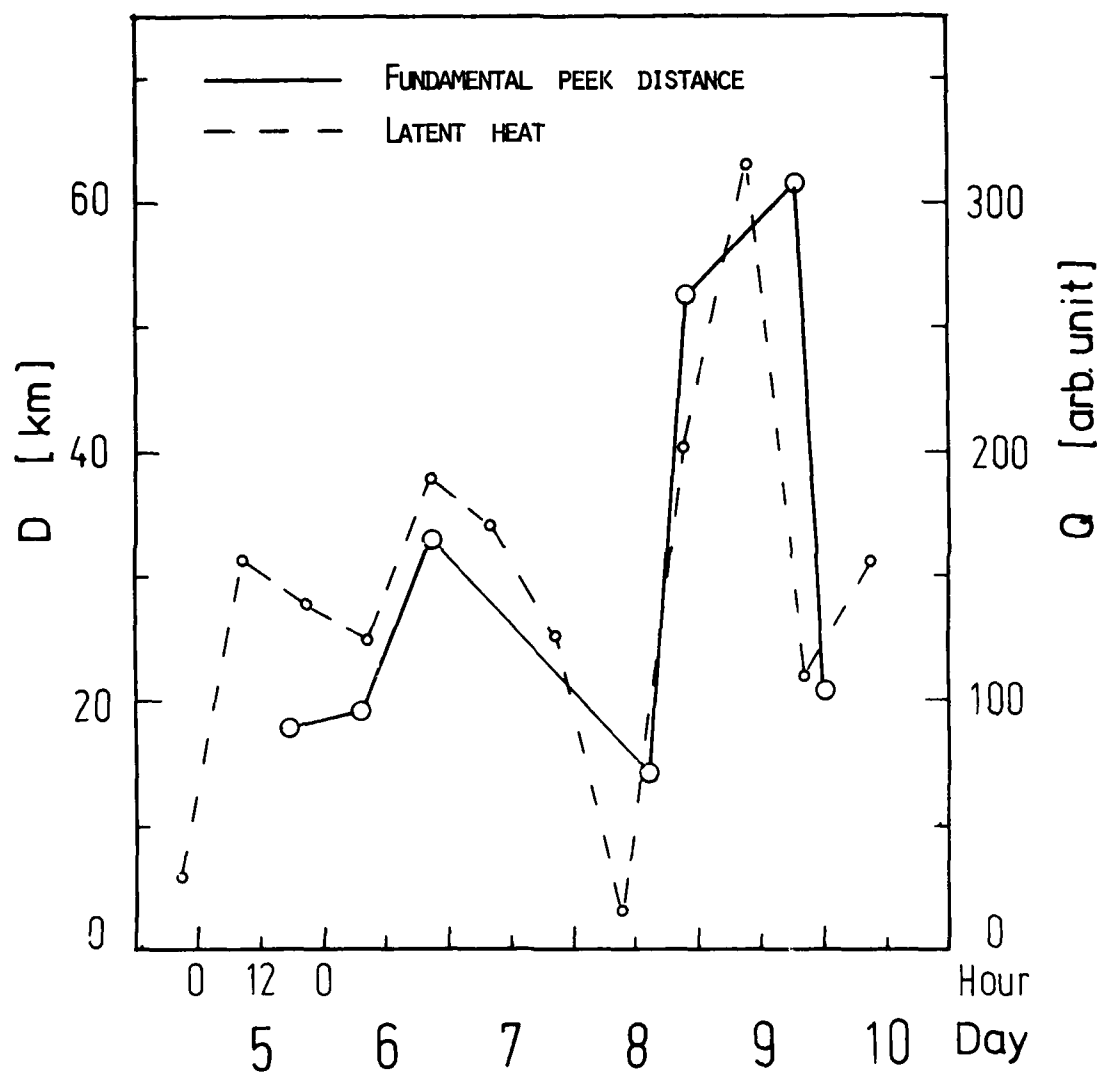


Fig. 12 - Comparison of the latent heat with the fundamental peek distance

COSMIC RAYS, SOLAR ACTIVITY, MAGNETIC COUPLING
AND
LIGHTNING INCIDENCE

J. T. A. Ely
Space Sciences Division
Geophysics Program
University of Washington
Seattle, Washington

ABSTRACT

A theoretical model is described that unifies the complex influence of several factors on spatial and temporal variation of lightning incidence. These factors include the cosmic radiation, solar activity, and coupling between geomagnetic and interplanetary (solar wind) magnetic fields. Atmospheric electrical conductivity in the 10 km region is shown to be the crucial parameter altered by these factors. The theory reconciles several large-scale studies of lightning incidence previously misinterpreted or considered contradictory. The model predicts additional strong effects on variations in lightning incidence but, possibly, only small effects on the morphology and rate of thunderstorm development.

This work was supported by the Office of Naval Research under Contract N00014-77-C-0392 and by the National Aeronautics and Space Administration under Contract NAS8-33884.

INTRODUCTION

MANY THEORIES have been advanced for each of the various aspects of thunderstorm phenomenology. Arguments have been offered both in support and in criticism of essentially all of these theories as part of the process of model evolution. Similarly, this paper describes a theoretical model and then tests its predictions against the data by showing they form a consistent set of explanations for a number of major findings previously unexplained, misinterpreted or thought to be conflicting. In view of (1) the importance of the atmospheric-electricity/solar-terrestrial research areas, (2) the limitations on funds, and (3) the cost of investigating erroneous concepts, theoretical differences must be resolved as early as possible in the program.

Lightning incidence or frequency exhibits great variation in time and space. Spatial or global lightning patterns can be seen in plots made from satellite data [1, 2, 3] and, on a different scale, in photographs made from orbit [4]. Temporal patterns of lightning incidence can be made by time records of any variable correlated with local or with global lightning such as sferics or atmospheric electrical potential gradient [5]. Many factors are involved in shaping these patterns. The standard meteorological variables including moisture content, temperature distributions, orographic lift, etc., are generally understood, at least in broad principle. However, even in these long studied areas of storm physics, establishment of details for many features, such as charge separation and transport, are still hindered by the complexity and experimental difficulties arising from the number of variables and the range of scales involved (10^{-10} to greater than 10^4 m). A less studied and less "obvious" but major determinant of lightning patterns is the distribution of ionization from somewhat below 10 km to approximately 50 km (a level called the "electrosphere"). This factor, related to the atmospheric electrical conductivity, and the processes that perturb it are the topics of interest to this paper.

In essence, the theory to be developed will show that solar activity should strongly influence lightning frequency by several processes that markedly modulate the atmospheric conductivity above thunderstorms and hence the fraction of the thunderstorm's upward (positive) current that leaks away to the electrosphere. Among the several processes are: (1) the modulation of galactic cosmic ray intensity over the 11-year solar sunspot cycle with the maxima in cosmic rays occurring

at the sunspot minima, (2) Forbush decreases in cosmic ray intensity due to "magnetized clouds" of solar plasma enveloping the earth for several days and occurring most often near the solar cycle maxima, and (3) magnetic coupling, an essentially weekly process to be discussed at length. As one example of these processes, high cosmic ray ionization above a thundercloud, common near the sunspot cycle minimum, greatly increases the storm's leakage current and therefore also increases the time required for the small remaining current to charge the cloud to striking potential. This is predicted to result in less lightning and, under certain conditions, a higher electrosphere potential during that part of the solar cycle or at any time such increases in conductivity occur. Other aspects of the model suggest: (1) altered 10 km ionization also has a major influence on weather and climate via cirrus with the effect expected to be stronger at high geomagnetic latitude, but (2) any changes in the potential do not have significant (first order) effects on either thunderstorms or climate. Hence, the model suggests upper troposphere and tropopause ionization is a much more important quantity than the more difficult to measure electrospheric potential. Thus, although the ultimate cause of variation in this upper air conductivity is solar activity, the causal chain involves a number of additional factors including atmospheric electricity, cosmic radiation, the solar cycle and two forms of magnetic coupling (one form of which is called "connection" or "merging") between the geomagnetic field (GMF) and the interplanetary magnetic field (IMF). The "connection" model has organized many observations and has made a number of predictions later confirmed experimentally [6, 7]. Before the theory is applied to interpretation of the data, a review of certain relevant aspects of these several factors will be given.

DISCUSSION

ATMOSPHERIC ELECTRICITY--It has long been known that ionization of the atmosphere in the altitude region from about a kilometer up to the electrosphere is almost entirely due to the cosmic radiation. The atmosphere can be considered the (leaky) dielectric between the two spherical capacitor shells formed by the earth's surface and the electrosphere in this simplified model. From the downward direction and the sea level value of approximately 100 volts per meter for the fair-weather atmospheric vertical electrostatic field (E), one calculates a negative charge of 450,000 coulombs resides on the earth's surface. Above the electrosphere, E is everywhere very small or zero. Thus, an equal positive shell of 450,000 coulombs must exist between sea level and 50 km. If all of this positive charge were located at 50 km (i.e. on the surface of the electrosphere), E would still be nearly 100 volts per meter just below that surface. However, it is found that E has decreased to approximately 5 volts per meter at only 10 km. (The potential of the electrosphere with respect to the ground as zero is found by a line integral of E from

Abbreviations Used:

C9	= geomagnetic activity index
EqM	= equatorial modulation
GMF	= geomagnetic field
IMF	= interplanetary magnetic field
Kp	= a geomagnetic activity index
N	= negative; P = positive
NM	= neutron monitor
NSA	= north-south asymmetry

the surface up to 50 km. It has a value that varies between about 220 and 350 KV with time of day and of year [5] and of the solar cycle.) Thus, a positive space charge of about 430,000 coulombs (i.e. 95% of the sea level surface charge) must exist in the 10 km thick atmospheric shell just above the earth's surface. Other measurements show that a positive air-earth current flows downward, is fairly constant throughout the altitude interval of interest, and is estimated to be approximately 1500 amperes for the entire earth (a few picoamperes per square meter). This current would essentially discharge the earth-electrosphere capacitor in 10 minutes if no countercurrent existed. The equilibrium is believed to be maintained by an opposite (upward flowing) positive current of 1500 amperes provided by about 1/2 ampere average from each of the earth's approximately 3000 thunderstorms.

Associated with a given thundercloud and other matter affected by its field, a number of different charge separation and transport processes exist [8, 9, 5]. Charges of both signs are liberated and transported in all directions by precipitation, convection, lightning, etc. The overall result is a positive current upward composed of both a net downward transport of negative and a net upward transport of positive charge. The upward flowing positive charge in effect divides and contributes both to charging of the upper positive (P) region and to leakage out the sides and top of the cloud along the electrostatic field lines due mainly to the dipole of the cloud and its image in the earth below. It should be noted that charge leaking upward from the top of the cloud to the electrosphere is, of course, actually falling down the potential gradient because the cloud top potential is between 10^8 and 10^9 volts above ground while the electrosphere is only approximately 3×10^5 volts. Thus, we see the 1/2 ampere (approximate) current measured above single thunderstorms indicates the effective resistance above one storm, between it and the electrosphere, is about 10^9 ohms (R_u). Also, the effective total resistance therefore between all 3000 thunderstorm generators (in parallel) and the electrosphere is of the order of 10^6 ohms. However, the 300,000 volt electrosphere potential driving a 1500 ampere leakage current through the atmosphere to earth indicates the total resistance between the electrosphere and the ground is only 200 ohms. A complete description of an equivalent circuit for even one storm would involve many components, primarily resistors and capacitors. The general scheme has been well represented in the literature [10, 11, 5]. The concern here need only focus upon two variables, the changes in R_u and the resulting division of the storm's upward flowing current into the charging and leakage components. Notice R_u is determined by the ionization between about 10 km and the electrosphere which commonly varies coherently with the more easily measured ionization at the 10 km level itself. For this and other reasons, it is often convenient simply to refer to changes in the 10 km ionization. As mentioned earlier, increases in the cosmic ray or other ionization of the region above the storm decreases R_u increasing the current leaking from

the cloud top to the electrosphere and decreasing that left to charge up the cloud's P region. Two interesting effects result from these changes: (1) the electrosphere potential may be raised by the increased current leaking to it from the top of the affected thunderstorm(s) if not simultaneously canceled by other oppositely affected storms, and (2) lightning frequency is reduced because the smaller charging currents require a longer time to reach striking potentials. To compare the relative magnitudes of these two effects, a halving of R_u above a single storm would add only one part in 3000 to the electrosphere charging current but might decrease the storm's charging current by 50% or so. One of the second order effects possible may be the increased probability of striking from the storm's N region if only the (upper) P region is weakened by the increased leakage current. In a typical case of interest to us, a large region at high latitude possibly involving 5 or 10% of the earth's thunderstorms may have charging rates altered. It was shown by E. P. Ney that atmospheric ionization above thunderstorms at, say, 30 km altitude can change by nearly 60% over a solar cycle [12]. Similar changes of order one-half are induced by other variations in cosmic rays that will be discussed. Ney also recognized that these changes might have relevance to the weather. A theory of weather influence via high latitude cirrus effects has been based on these alterations of high altitude ionization [13]. The theory being presented in this paper is also based on the same findings. A later section will show that observations of lightning incidence vary over the solar cycle by an amount to be expected on the basis of the above discussion.

COSMIC RADIATION--The galactic cosmic radiation consists of approximately 90% protons and 9% alphas (helium nuclei) and 1% nuclei with Z greater than 2. This flux has a spectrum exhibiting a broad peak from approximately 300 to 1000 Mev (i.e. 1 Gev) per nucleon and a long power law tail decreasing as approximately the third power of the energy. Two components of the galactic cosmic ray spectrum are of principal interest to this paper: the extremely variable low energy peak that contains most of the particles, and the fairly constant high energy tail. The high energy tail beyond about 10 Gev has access to, and produces atmospheric ionization at, essentially all altitudes and latitudes of the earth. The high energy flux changes very little over the solar cycle (but does exhibit a low latitude magnetic coupling effect quite different from that of the low energy flux). On the other hand, the low energy flux (below about 2 Gev per nucleon) only reaches the upper part of the atmosphere and only at high latitudes because of the geomagnetic field (GMF). For example, a 1 Gev proton can only penetrate down to approximately the 10 km altitude. Hence, the broad and variable peak is the dominant factor in determining ionization above high latitude thunderstorms and their value of R_u . These numerous cosmic ray protons that occupy the energy spectrum peak near 1 Gev have the following characteristics of relevance here: (1) as stated above, they stop at approximately 10

km; (2) they only enter the earth's atmosphere at geomagnetic latitudes above about 60° ; (3) they are strongly modulated (i.e. approximately 60%) by the solar wind changes over the solar cycle; and (4) they are essentially excluded from high latitude regions during magnetic connection of those regions to the sun. The reason for this strong effect on the 1 GeV proton flux by magnetic coupling is that the radius of curvature of such particles at approximately 10 earth radii above the magnetic poles is also equal to 10 earth radii which is also approximately the curvature change of the GMF in those regions during connection to the IMF. This is called resonant scattering. Much lower energy protons would spiral along the field lines and find their way in in spite of morphological alterations in the GMF. Much higher energy protons would still penetrate unimpeded by such merging of the fields. Thus, the "low energy" component of the cosmic radiation permits changes in solar activity to alter upper air ionization and hence lightning frequency.

THE SOLAR CYCLE AND MAGNETIC COUPLING--The solar wind consists of an essentially collisionless plasma of ionized hydrogen (protons and electrons) that sweeps out from the sun past the earth at speeds of perhaps 300 km per second during solar minimum and 600 km per second at solar maximum. Because this low density plasma is collisionless it acts as a superconductor and transports the sun's photospheric magnetic field outward from its surface, dragging it along in the plane of the ecliptic. This magnetic burden of the solar wind, the IMF, commonly points approximately away from or toward the sun. Depending upon the region of origin on the solar surface, the field transported from the sun can have different polarities, outward called positive, and inward called negative. The resulting pattern of alternating positive and negative polarity IMF regions tends to repeat itself each 27 days at the earth due to solar rotation. The alternation of IMF polarities induces two different local modulations at earth in the galactic cosmic radiation by two magnetic coupling processes. One strongly affects the low energy (about 1 GeV) flux at high geomagnetic latitudes by a process called merging or connection inducing a north-south asymmetry (NSA) in the flux. The other process produces an equatorial modulation (EqM) in the high energy (above about 5 GeV) flux reaching the atmosphere at low latitudes [14, 6].

Connection and the NSA (Description)--When the earth is in a positive sector, IMF pointing away from the sun and toward the earth, the configuration is correct for connection by an IMF flux tube to the north pole region of the GMF where flux enters the earth. In negative sectors, the topology is correct for connection only at the south pole. Connection of the IMF and GMF is analogous to that between two simple dipole magnets that connect (and attract each other) when their orientation is antiparallel (opposite) but repel, i.e. do not connect, when parallel. Similarly, for (local) cancellation, merging and connection to take place, a flux tube or bundle of the IMF must point approximately opposite to the GMF where they are

pressed together by the solar wind on the "bow" side of the earth in the GMF's equatorial plane. Because the GMF always points north at 0° latitude, a southward component of the IMF is required. Because of the several day solar wind radial transit time and because of rotational effects in the earth-sun system, the IMF arrives at earth with an azimuth approximately 45° west of the earth-sun line. Although the average direction of the IMF is along this spiral line ("toward" or "away" from the sun), instantaneous directions can vary greatly due to turbulence, etc., and, of course, during collision with the GMF. When an IMF southward flux tube cancels an equal amount of GMF flux in the bow side merging region, those flux tubes link, connecting one GMF pole to the sun.

The probability of merging appears to be greatest when the GMF direction is closest to that of the IMF, requiring less bending. When a southward IMF occurs, the oppositely directed GMF and IMF fluxes cancel in the bow side equatorial merging region, and the parent IMF flux lines entering the region from the north link or connect to the parent GMF lines also entering from the north, as stated above. This, of course, connects the sun to the earth's north magnetic pole. Because the sun is a very poor source of 1 GeV protons, and because of the "resonant scattering" of galactic cosmic ray protons in this approximate energy range by the connected flux tube, the cosmic ray intensity and upper atmospheric ionization generally decrease in northern latitudes. In a similar fashion, connection can occur between the south GMF pole and the sun in a negative IMF sector decreasing cosmic ray upper air ionization at southern latitudes. When a GMF pole is connected to the sun, the arriving 1 GeV cosmic ray flux exhibits a decrease of about 30% in the region of that pole (the flux changes are actually largest at the cusps). An increase in flux occurs at the opposite unconnected pole (which has "opened" out to the galaxy) but appeared in the satellite and neutron monitor (NM) data to be somewhat smaller in magnitude possibly due to mirroring of the arriving particles. The decrease at one pole and increase at the other are called a north-south asymmetry, occur in the low energy flux, exhibit a strong geomagnetic latitude dependence (peaking near the day side cusps at approximately 75° N and 75° S) and are not to be confused with a much studied asymmetry that occurs in many times higher energy cosmic rays measured with respect to ecliptic north and south. The NSA amplitude is large for low energy particles (and vice versa) and may decrease from solar minimum to solar maximum [14, 6].

Parallel/Antiparallel and the EqM (Description)--It was surprising to find a significant modulation in the cosmic rays reaching the atmosphere at low geomagnetic latitudes because of their high energy (approximately 16 GeV threshold for protons arriving along the local vertical) and small change in intensity over the solar cycle. The modulation may have importance both to weather via the cirrus mechanism [13] and to lightning via ionization changes. In the small amount of satellite and NM data analyzed to date, the amplitude of

EqM was found to average 30% in the 6 GeV protons arriving horizontally at the top of the atmosphere from the west but appeared to be only 1 to 2% in the Chacaltaya and Haleakala NM data for 1966 to 1968 [6]. The changes in tropopause ionization should be closer to the satellite value of EqM than to the NM values because of the lower threshold (6 GeV) of the flux sampled in orbit. Additional low latitude NM data are now being analyzed, but satellite (or balloon) measurements of low latitude cosmic rays in both positive and negative IMF sectors from solar minimum to solar maximum are needed. In the NM data, EqM weakened approaching the 1964 solar minimum [6]. More data will be analyzed. The mechanism of EqM is extremely simple and is explained in reference 6. In essence, when the IMF near the earth is approximately parallel to the equatorial GMF (i.e. north), the cut-off rigidity is increased and the arriving flux is reduced. Conversely, the flux increases when the IMF and equatorial GMF are antiparallel. The EqM and NSA peak under different conditions and times of the year and of the solar cycle. Usually NSA will have the same sign as EqM at one pole and be opposite at the other. The various factors that determine when they peak and are additive include the 23.5° tilt of the earth's spin axis with respect to ecliptic north, the 12° tilt of the GMF dipole with respect to the spin axis, the 7.25° tilt of the sun's spin axis with respect to ecliptic north, and a warping of the sun's equatorial plane current sheet involved in the Rosenberg-Coleman effect.

NSA and EqM: Seasonal, Solar Cycle and Latitude Effects--The questions of relative amplitudes and phases of the ionization perturbations due to the two principal magnetic coupling mechanisms (producing NSA and EqM) are discussed in this section. These considerations (1) determine how the effects add and subtract and (2) are of interest to changes in both lightning intensity and electro-spheric potential. The relative orientation of IMF and GMF is, of course, the ultimate variable. The dominant controlling factors are: (1) the sun's magnetic field polarity and amplitude; (2) the directions of the spin axes of sun and earth with respect to both the ecliptic plane and the earth-sun line (or to the IMF spiral direction); (3) the solar wind speed; and (4) warping of the solar equatorial current sheet. The direction variables will be considered first, followed by the solar magnetic dipole polarity, current sheet warping (the Rosenberg-Coleman effect), then wind speed and, finally, a comment on latitude effects.

As discussed above, the solar wind presses the IMF against the bow side of the GMF where the two fields can have relative orientations that range through 360°. For connection to take place, the IMF must be approximately antiparallel to the GMF (i.e. have a southward component) in the merging region. Recall that when connection takes place at one GMF pole, ionizing galactic cosmic ray flux decreases at that pole and increases at the unconnected pole producing an NSA in lightning but, possibly, almost a null effect on overall current to the electrosphere. Thus, NSA's in high latitude atmospheric ionization occur primarily when a

southward IMF encounters the earth. In contrast, low latitude atmospheric ionization is constantly affected by all relative orientations of the IMF and by the field conditions many earth radii away from the magnetopause, especially so when the IMF is most homogeneous. Of course, the maximum increase in low latitude atmospheric ionization occurs when the IMF is antiparallel and the equatorial cosmic ray cutoff is lowest, admitting the largest number of galactic cosmic rays. Thus, an antiparallel orientation (southward IMF) decreases lightning incidence at the equator (due to EqM) and at one pole (due to NSA). Recall that, due to mirroring, the increase in ionizing flux at the unconnected pole is smaller, and hence associated effects are smaller than at the connected pole, preventing a "plus-minus symmetry" in the NSA. In contrast, a parallel orientation (northward IMF) decreases ionization at all latitudes resulting in a lightning increase at both poles and the equator.

Briefly, four angles of interest are (1) the 7.25° tilt of the sun's spin axis toward the earth's 7 September position placing the earth in northern heliographic latitudes from 6 June to 6 December, and southern from 6 December to 6 June; (2) the 23.5° tilt of the earth's spin axis directly toward the sun on 21 June, away on 21 December, forward along the direction of earth's orbital motion on 21 September, and backward on 21 March; (3) the mean direction of the IMF which is along a spiral arriving at earth 45° west of the earth-sun line; and (4) the 12° tilt of the GMF dipole from the earth's spin axis which will be ignored in this discussion of seasonal (not hourly) orientation changes. On 21 December, when the GMF tilts away from the sun, the IMF would be most nearly parallel to the GMF in positive ("away") sectors if the azimuthal (spiral) component could be ignored. Similarly, on 21 March, when the GMF points backward along the orbit, positive sectors would be most nearly parallel if the radial component is ignored. In this vein, one expects maximum parallelism (due to turbulence about the average spiral field direction) to occur near 21 February for positive sectors and maximum antiparallel conditions on the same date for negative (IMF toward the sun) sectors. On 21 August, the opposites should hold, i.e. maximum parallelism for negative sectors, etc. The principles of this and of the previous paragraph can be applied to estimate the relative probability of lightning incidence fluctuations at different times of year. Clearly, connection (i.e. antiparallel orientation) is favored for positive sectors in the fall and negative sectors in the spring. Thus, one expects strong lightning incidence fluctuations that correlate with IMF sector polarity at these times. Because geomagnetic noise is strongly influenced by connection [15], geomagnetic disturbance indices should exhibit the same fall positive and spring negative modulation. This, in fact, has been observed to hold for the C9 index in data spanning the interval from 1962 to 1975, somewhat more than one sunspot cycle [16].

The solar dipole reverses polarity during years of high sunspot number, approximately two to three years after the sunspot maximum, and retains

the new polarity through the following minimum until the next post-maximum reversal [17]. During the present years of the 1986 solar minimum epoch, the southern half of the sun has a north magnetic pole. Thus, flux points out or "away" from the sun's southern hemisphere (as in positive sectors) and into or "toward" the northern half (as in negative sectors). However, in the simplest description, instead of pointing north in the equatorial plane like the GMF, the flux is dragged outward by the radially expanding highly conducting (collisionless) solar wind plasma so that the average direction of the IMF is approximately parallel to the equatorial plane pointing outward (along the spiral direction) just south of the plane and inward just north of the plane (the plane must therefore contain a current sheet). Because the earth is at south solar latitudes from 7 December to 7 June, it would be in a positive (outward flux) sector continuously for six months if the current sheet remained in the equatorial plane. However, in what is called the Rosenberg-Coleman effect, because of the so-called "baseball seam" shape of the source regions on the solar surface, the current sheet is warped, curving sinusoidally above and below the solar equatorial plane which it usually divides into four sectors. When the amplitude of warp is larger than 7.25° , the plane of the ecliptic is also (usually) divided into four sectors which rotate with the 27-day period of the sun. Frequently, low amplitude or asymmetry of warp result in only two IMF sectors [18]. Thus, approximately two to four times per month a sector boundary crosses the earth, placing it alternatively above or below the warped current sheet with corresponding changes in IMF polarity occurring within a few hours [19, p. 77; this reference is a compendium]. Because of the 7.25° tilt, the sectors are not of equal width, resulting in more time in the polarity determined by the heliographic latitude of earth when it is far from zero as in spring and fall. This result of current sheet warping combined with the heliographic latitude excursions of earth is called the Rosenberg-Coleman effect [20]. A number of annual and 11-year variations are predicted as direct results of the fact that even very small amplitude warps will move the current sheet across the earth when it is at 0° solar latitude, thereby maximizing the number of IMF sector boundary crossings in December and June. As examples, peaks are expected in December and June for both lightning frequency (as indicated by suitable sferics) and geomagnetic disturbances. Also, many 22-year variations should result according to the magnetic coupling model when the geometrical factor dominance (of positive sectors in the fall and negative in the spring) is combined with the appropriate polarities by the solar magnetic dipole reversal. An example will be given in a later section discussing Stringfellow's lightning studies.

Solar wind speed is expected to influence magnetic coupling for several reasons, most of which are enhancing. As a first example, the rate of flux merging during connection is dependent upon the rate IMF is being transported into the merging region by the solar wind. Also, for a given IMF

strength and solar wind particle density, the pressure increase due to higher solar wind speed would have at least two effects: (1) compression of the GMF with large inductive effects at earth, and (2) an increased susceptibility to connection because flux is removed from the compressed (high energy density) day side GMF by merging, consequently lowering the pressure. A third possible influence is an increasing homogeneity of the IMF we postulate may occur on the scale of about 10 GMF's (i.e. 100 earth radii) or so, even though the general trend is toward more turbulence on larger scales as solar wind increases. If this effect occurs, it would be apparent as a decrease in the IMF wavelength spectrum at frequencies of .001 Hz (and slightly below) near solar maximum when the spectral content of still lower frequencies is increasing (i.e. a steepening in spectral slope at the low wavelength end). The decrease of low frequency IMF homogeneity at solar maximum is thought to be due to magnetohydrodynamic effects (for a discussion of theory and measurements see reference 21). If the frequency spectrum in the .001 Hz interval rises less than the wind speed, the homogeneity in that scale range will increase. As solar maximum is approached, such an effect may explain the enhanced EqM and diminished NSA observed in NM data [6]. Decreased frequency of connection is expected because variation about the IMF mean position is needed to provide the close antiparallelism that favors merging. However, when connection does occur near solar maximum, the NSA effects should be larger because of the greater solar wind speed transporting the merging flux against the GMF and, possibly, the greater IMF amplitude and homogeneity. Thus, near solar maximum, NSA's may be less frequent but more intense. Such an effect has been reported in low pressure trough vorticity [19, p. 196].

At different latitudes on earth, responses may not be at all similar for a given input (such as the changes in 10 km ionization produced by the NSA and EqM effects of magnetic coupling). This possibility, as well as the subtleties of the physics, should be considered in analysis by this model (or by other methods) of the vast array of diverse phenomena shown to correlate with solar activity [19]. An excellent example is the intensification of low pressure troughs forming in the Gulf of Alaska by IMF sector boundary passage, especially when IMF polarity changes from negative to positive. This effect exhibited high statistical correlation only in the winter. The magnetic coupling model explains both the high latitude and seasonal aspects as follows: (1) in positive sectors, connection of the north GMF pole to the sun reduces the 10 km ionization permitting cirrus formation to accelerate in that altitude region thus trapping heat in the system that would otherwise have been lost by radiation [13]; (2) the winter dominance is explained by the much greater prevention of cooling afforded by high cirrus when no insolation is present and the system must radiate to a 3°K cloudless sky if the (approximately 230°K) cirrus layer does not form; and (3) the approximate equality of sector lifetime and transit time of the

system from a source region at high latitude exerts a form of resonant effect (in contrast to the low latitude situation discussed below). Because EqM does affect upper air ionization at low latitudes, sector synchronous modulation of cirrus is expected there also. However, the broad longitudinal extent and the lower average wind speeds of equatorial source regions make air mass residence time much longer than IMF sector lifetimes and prevent the quick response and resonance effects of high latitude systems. Magnetic coupling effects, of course, are still expected to appear promptly in low latitude lightning incidence which is not slowed by a dependence on rate of heat loss. Now, the lesson of this paragraph can be expressed (regarding the subtlety of these relationships in general and of latitudinal effects in particular). In spite of the seeming cancellation of cirrus modulation having two or more alterations during low latitude air mass residence time, integrated second order effects may be significant because sector widths are systematically unequal especially in the spring and fall near the maximum heliographic latitude excursions of earth. For example, during this cycle 21 minimum epoch, the broadest IMF sectors in spring will be positive (the polarity of the sun's southern hemisphere) tending to decrease ionization and therefore increase cirrus [13] (and also, incidentally, lightning, sferics, Kp, etc.). In the fall, the widest sectors will be negative. In the even numbered cycles (i.e. 20, 22, etc.), these seasonal polarity dominances will be reversed. This particular example, being a Rosenberg-Coleman effect, will of course disappear near the solstices when the earth is crossing the sun's equator and sector widths become equal.

There are other processes such as solar flares and cosmic ray Forbush decreases that can have important effects on lightning incidence. Such effects can usually be deduced by simply remembering that changes in 10 km ionization and in lightning frequency are predicted to vary inversely.

MAGNETIC COUPLING THEORY: APPLICATIONS--In addition to the diverse examples discussed above, application of the magnetic coupling model to a few important unexplained findings related to lightning are presented in this section. The model suggests lack of a consistent theory has resulted in misinterpretations that in some cases have prevented integration of valid data considered conflicting and in others have generated misconceptions regarding which variables are causal and which simply covariant. The authors cited here are, in general, not the sources of the concepts suggested to be erroneous by this paper but are merely reviewing the literature.

Lightning Correlations: 11 and 22 Year--An extensive series of studies of lightning and electrical power line faults due to lightning in Britain has shown a remarkable correlation with sunspot number. Smoothed data for lightning observations as thunderstorm days by 40 weather stations were reported by Stringfellow to exhibit a positive correlation of 0.8 for approximately 40

years spanning four solar cycles (numbers 17 through 20) [22]. Two features of this study that are most apparent in Stringfellow's Figure 1 are of considerable significance to the solar-activity/lightning-incidence question and will be considered here. These features are the 11-year correlation widely considered to be conflicting with other data, and the 22-year correlation which, to this author's knowledge, has not previously elicited extensive comment in the literature.

One of the principal reasons cited for considering the British data anomalous was the failure to detect a difference in lightning incidence due to the 11-year cycle in data from the 1965 solar minimum (OSO-2) and 1969 solar maximum (OSO-5) satellite experiments of Vorpahl, Sparrow and Ney [1]. Although those authors were well aware of the low latitude extent (within approximately 30° of the equator) of their data, the strong difference (a factor of 5 or greater depending upon altitude) in solar cycle modulation of upper atmosphere ionization between tropical and English latitudes definitively demonstrated by Ney [12] seems to have been ignored by much of the community. However, because of this latitude difference there is no disagreement between these data sets according to the magnetic coupling model.

The 22-year correlation of Stringfellow's data is extremely interesting. The annual lightning index peaks for solar cycles 17 through 20 have the following characteristics: (1) they alternate in height with 17 and 19 about the same amplitude (within 4%) and average significantly higher (about 10%) than the average of peaks 18 and 20 which also are close together in height (within 3%); and (2) the lightning index peaks in each case slightly lead the sunspot peaks (by about one year). These characteristics are predicted by the magnetic coupling model as follows. Because the solar dipole field reverses 2 to 3 years after solar sunspot maximum [17; or 19, p. 79] and because the lightning peaks occurred slightly before the sunspot peaks, the solar polarity during each peak would be the same as in the preceding minimum which were positive, negative, positive, and negative, respectively (notice following the reversal during the 1980 maximum for cycle 21, our present solar dipole polarity is negative). Thus, for example, during most of the lightning peak years associated with the sunspot maximum 19, the northern half of the sun was a magnetic north pole (which favors positive sector connection from June to December) and the southern half was a magnetic south favoring connection in negative sectors to the south pole of earth. This should considerably enhance lightning incidence in Britain (northern latitudes) in "fall" (i.e. from June to December) and in southern latitudes in "spring" (i.e. from December to June). However, because of the weakness of NSA at the unconnected pole, the decreases in "spring" in England should be much less than the increases in "fall" providing a significant net enhancement for each such year in the rising portion of the odd numbered sunspot cycles. Conversely, in the even numbered sunspot cycles, the solar dipole is

reversed and there is no "fall-positive"/"spring-negative" enhancement of connection.

Enhancement of 10 km Ionization at Low Latitudes--As discussed earlier in the description of EqM, low latitude 10 km ionization is found to change very little over the solar cycle when a sufficient number of measurements are made and averaged together for each year. For example, the increases in 10 km ionization from solar maximum to solar minimum at the equator and at 55° (north or south) geomagnetic latitudes are approximately 3% and 18%, respectively; at 30 km for the same latitudes the increases are 4% and 100%, respectively [12]. Thus, the finding of large increases in ionization lasting for a day or so at low latitude by a number of investigators was surprising. Sellars summarized these and included the remarks by W. O. Roberts regarding the importance of this anomaly and the need to explain it [23, p. 66]. As shown in this paper, EqM's of about 30% at the top of the equatorial atmosphere are explained and predicted by the magnetic coupling model and have been observed by satellite [6].

Modulation of the Electrosphere Potential--The increases and decreases in both the electrospheric potential and the fair weather electric field associated with increases and decreases in 10 km ionization have been clearly defined by Markson and others for over a decade. However, several reviewers have commented on the almost prevailing suppositions that (1) the enhanced potential and its gradient "somehow produce increased lightning" [23, p. 65], and (2) "solar effects on terrestrial meteorology occur through modulation of the global fair-weather electric field" [23, p. 75]. The magnetic coupling model shows clearly that changes in lightning and in the subject potential and its gradient occur as results of alterations in upper air ionization because of the latter's influence on the division of thunderstorm generator current between leakage and charging. Thus, changes in the field quantities are predicted to be co-results, not causes of major lightning alterations. Even in weather alteration as suggested in discussion of the cirrus mechanism below, the field quantities are predicted by the magnetic coupling model mechanisms described in this paper to exert only secondary effects.

The Cirrus Mechanism--The magnetic coupling model suggests the rate of cirrus formation is inversely influenced by 10 km ionization as follows. Any process producing enhanced 10 km ionization increases charging of water molecular aggregates because of their high capture cross-section (via inelastic collisions) decreasing recombination of the ions. The charged aggregates are then transported out of the thin cirrus region by the 5 volt/m field (before they can grow to micron size) impeding cirrus formation and enhancing cooling of the surface below [13]. As pointed out by one investigator, the common supposition is exactly the reverse of this: "Most people think" extra ionization increases nucleation and thin cirrus [24, p. 133]. Notice, in the first scenario above, the rate water molecular aggregates are transported out of the region is proportional to

both the ionization and the field strength. However, the field strength variations are much less important than the ion density variations for two reasons related to amplitude and phase. Before these are briefly discussed, it is appropriate to recall the converse mechanism predicted by the model (in which positive sector connection decreases northern latitude 10 km ionization enhancing cirrus formation and retarding heat loss from the system). This sequence is expected to be most important in sun-weather relationships. "Local" changes in tropopause ionization amplitude of approximately 30 to 100% can occur in polar regions quickly and even on a weekly basis due to IMF connection NSA's, Forbush decreases, and solar flares. Again, "local" effects such as NSA's are expected to produce only small field changes. Because of the high conductivity of the electrosphere, to obtain a 30% change in the field amplitudes, some global effect such as daily rotation through the 1800 UT thunderstorm maximum, or the modulation of cosmic ray intensity by solar activity over a sunspot cycle would be needed. Even though global effects can be impulsive as in Forbush decreases, the phases are opposite or mixed in such events: i.e. the decrease in cosmic ray ionization both diminishes the thunderstorm leakage current, opposing an increase in electrosphere potential, and decreases the clear air conductivity, slowing the fall in electrospheric potential. Anomalous situations occur in which 10 km ionization decreases and higher altitude ionization increases for obvious reasons. Although Reiter and others have shown large changes in field quantities do occur in major impulsive events, such events are much less frequent than the IMF sector effects and usually are additive to the latter. For a review of the literature and numerous considerations involved see reference 19.

Cosmic Rays and Lightning Frequency--The IMF sector synchronous modulations of cosmic rays and mechanisms to explain their involvement in atmospheric process have received attention since 1969 [6, 25]. The studies of Lethbridge [26] have shown a strong statistical correlation between cosmic ray intensity fluctuations and "thunderstorms" (lightning). Those studies found a maximum in lightning incidence approximately 3 days after the cosmic ray intensity fluctuation maximum. This finding has since been interpreted to indicate a causal relationship between the lightning maximum and the preceding cosmic ray maximum. However, most such cosmic ray maxima are related to IMF sector boundary passage. When a maximum precedes the boundary, a strong cosmic ray minimum follows it. This minimum would be in essentially exact coincidence with the lightning maximum. The magnetic coupling model explanation of lightning increases due to ionization decreases has been discussed elsewhere in this paper. That model suggests, therefore, that the demonstrated correlation described above is real, but that the cosmic ray decrease causes the lightning maximum.

Runaway Electrons--Theoretical and experimental support has in recent years reawakened interest in the suggestion made 60 years ago by

Wilson that, in the high field regions of thunderstorms, electrons might gain more energy than lost in collisions and radiation and hence accelerate for considerable distances. Kasemir has shown theoretically that sufficiently strong fields may in fact exist in association with lightning stroke "tips" [27]. Parks et al. detected x-ray bremsstrahlung of the expected character above thunderstorms [28]. It has been interpreted that such radiation increasing ionization above thunderstorms may be a regenerative process. However, as has been shown in this paper, the magnetic coupling model predicts increases in ionization above thunderstorms result in a decreased charging rate and less lightning. Hence, although the existence of runaway electrons seems reasonably established, the theory presented here suggests it is a self-limiting and hence, possibly, a rare occurrence rather than a common regenerative aspect of the storm.

Southward IMF and the Auroral Oval--The process of connection is enhanced by a southward IMF. Such merging erodes day-side IMF and has been predicted to increase flux coupled through the earth, enlarging the auroral oval. A strong correlation between size of the oval and southward field has in fact been shown by Holzworth et al. [29].

SUMMARY AND CONCLUSIONS

By means of a small number of mechanisms, the magnetic coupling model provides a self-consistent set of explanations that unify a large number of observations reported to correlate with solar activity. The successful application of this model and its mechanisms to the physical processes included as examples in this paper leads to the conclusions that:

- The magnetic coupling model may be one of the principal links between solar activity and atmospheric processes affecting weather, climate and lightning.
- The magnetic coupling model exerts its control over atmospheric and other processes primarily by modulation of the galactic cosmic radiation via IMF-GMF interactions.
- The cosmic ray variations exert their effects, in turn, by modulating the level of ionization from the upper troposphere through the tropopause.
- A wide variety of previously unexplained phenomena reported to correlate with solar activity appear tractable to analysis. This applies especially to processes of interest in weather, climate and atmospheric electricity.
- The electrospheric potential and fair weather electric field are also modulated by the cosmic ray/atmospheric ionization link. The variations in these field quantities are predicted to be only of secondary importance in comparison to the variation of ionization as mediators of solar-terrestrial effects.
- Investigation of solar-terrestrial effects is greatly simplified if, in fact, the more easily measured 10 km ionization rate proves to be the

principal independent variable within the atmosphere.

REFERENCES

1. J. G. Sparrow and E. P. Ney, "Lightning Observations by Satellite." *Nature* 232:540-1, 1971.
2. B. N. Turman, "Lightning Detection from Space," *American Scientist* 67:321-9, 1979.
3. B. N. Turman and B. C. Edgar, "Global Lightning Distributions at Dawn and Dusk." *J. Geophys. Res.* 87:1191-1206, 1982.
4. B. Vonnegut, U. H. Vaughan and M. Brook, "Thunderstorm Observations from Space Shuttle." NASA TM-82530, June 1983.
5. J. A. Chalmers, "Atmospheric Electricity," 2nd Edition. New York, N.Y.: Pergamon Press, 1967.
6. J. T. A. Ely, "Equatorial Modulation and North-South Asymmetry of Galactic Cosmic Rays Due to the Interplanetary Magnetic Field." *J. Geophys. Res.* 82:3643-8, 1977 (submitted June 26, 1969).
7. N. U. Crooker, "Dayside Merging and Cusp Geometry." *J. Geophys. Res.* 84(A3):951-9, 1979, p. 958.
8. C. B. Moore and B. Vonnegut, "The Thundercloud," in "Lightning, Volume 1, Physics of Lightning." Edited by R. H. Golde. New York, N.Y.: Academic Press, 1977.
9. J. Latham, "The Electrification of Thunderstorms." *Quarterly J. Royal Meteor. Soc.* 107: 277-98, 1981.
10. R. Markson, "Solar Modulation of Atmospheric Electrification Through Variation of the Conductivity Over Thunderstorms," in "Possible Relationships Between Solar Activity and Meteorological Phenomena," NASA SP-366, edited by W. R. Bandeen and S. P. Maran, p. 171, Supt. of Documents, Wash., D.C., 1975.
11. R. Markson and M. Muir, "Solar Wind Control of the Earth's Electrical Field." *Science* 208:979-90, 1980.
12. E. P. Ney, "Cosmic Radiation and the Weather." *Nature* 183:451-52, 1959.
13. J. T. A. Ely, "Solar Activity and Terrestrial Weather: The Magnetic Coupling Model." NASA Conference Pub. 2098, A-25-6, 1979.
14. J. T. A. Ely, "Analysis of Heavy Primary Cosmic Ray Data from the OV1-10 Satellite." Proceedings of the Midwest Cosmic Ray Conference, Louisiana State University, Baton Rouge, 1969.
15. L. Svalgaard, "Geomagnetic Activity: Dependence on Solar Wind Parameters." Chap. 9 in "Skylab Workshop on Coronal Holes," ed. E. Zirker, Colorado University Press, 1977.
16. N. R. Sheeley, J. R. Asbridge, S. J. Bame, and J. W. Harvey, "A Pictorial Comparison of IMF Polarity, Solar Wind Speed, and C9 During the Sunspot Cycle." SKYLAB/ATM Preprint, NRL, October 1976.
17. J. M. Wilcox and P. H. Scherrer, "Annual and Solar-Magnetic-Cycle Variations in the Interplanetary Magnetic Field. Standard University, Institute for Plasma Research Report 466, 1972.

18. J. T. Hoeksema, J. M. Wilcox and P. H. Scherrer, "Structure of the Heliospheric Current Sheet in the Early Portion of Sunspot Cycle 21." *J. Geophys. Res.* 87:10331-8, 1982.
19. J. R. Herman and R. A. Goldberg, "Sun, Weather, and Climate." NASA SP-426, 1978.
20. R. L. Rosenberg and P. J. Coleman, Jr., "Heliographic Latitude Dependence of the Dominant Polarity of the Interplanetary Magnetic Field." *J. Geophys. Res.* 74:5611-22, 1969.
21. P. J. Coleman, Jr., "Turbulence, Viscosity, and Dissipation in the Solar-Wind Plasma," *The Astrophys. J.* 153:371-88, 1968.
22. M. F. Stringfellow, "Lightning Incidence in Britain and the Solar Cycle." *Nature* 249:332-3, 1974.
23. B. Sellars, "Bremsstrahlung and Cosmic Ray Effects on Atmospheric Electricity." *Proceedings, ONR Workshop on Solar-Terrestrial Weather Relationship, ONRWEST Report 81-6, September 1981.*
24. T. D. Wilkerson, "Cirrus Clouds: Response to Solar Influences?" *ONRWEST Report 81-6, September 1981.*
25. J. T. A. Ely, "Solar Activity Influence on Lightning Incidence." *Proc. 25th Pacific NW AGU Mtg. Univ. of Puget Sound, 1978.*
26. M. D. Lethbridge, "Cosmic Rays and Thunderstorm Frequency." *Geophys. Res. Ltrs.* 8:521-2, 1981.
27. H. W. Kasemir, "A Contribution to the Electrostatic Theory of a Lightning Discharge." *J. Geophys. Res.* 65:1873-8, 1960.
28. G. K. Parks, R. J. Spiger, B. H. Mauk and J. Chin, "Detection of X-rays from Thunderstorm Lightning Discharge Regions." *EUS* 61(46):978-80, 1980.
29. R. H. Holzworth and C.-I. Meng, "Mathematical Representation of the Auroral Oval." *Geophys. Res. Ltrs.* 2:377-80, 1975.

LIGHTNING TEST OF A CFC AIRCRAFT WING TANK SKIN

Karl-Gunnar Lövstrand, Bengt Olsson, Bo Wahlgren and Leif Andersson

SAAB-SCANIA AB, Linköping Sweden

ABSTRACT

Lightning tests were performed on painted samples of CFC wing tank skins. The aim of the study was to find a lightning safe wing design.

The report describes four different test methods and the results obtained when testing bolted joints and the CFC skin. Photographic recordings were made of thermal sparking at fasteners. The voltage between fasteners and the CFC skin was measured for determination of electric sparking. Internal hot spot temperatures were studied with an AGA thermovision camera on skins for determination of autoignition risks. The influence on hot spots of an external high velocity air stream was studied. Ignition experiments were made using a mixture of air and ethene.

Factors governing electric ignition and "hot spot" autoignition have been related to the results found.

INTRODUCTION

CARBON FIBER COMPOSITES (CFC) are used extensively in advanced fighter aircraft structures. One concern with that is the susceptibility to lightning strikes when they are used in fuel tank skins. A lightning attachment to an unprotected CFC tank skin may produce internal sparking at fasteners and hot spots inside the tank with a temperature exceeding the autoignition temperature (AIT) of the fuel vapors.

The aim of the present study was to determine the lightning effects on different CFC wing skin designs for a wing containing JP-4 type of fuel.

The lightning tests were performed on coupon samples of CFC skins and CFC skins attached to internal CFC spars and ribs by means of metallic fasteners and anchor nuts.

TEST SAMPLES

The test samples consisted of 75 cm by 75 cm coupons of CFC panels with a thickness of 3 mm, 4.5 mm and 6.5 mm. Unprotected panels and panels covered on the outer surface with highly conducting silver paint (normally intended for EM shielding purposes) or with a flame sprayed aluminium layer were tested. The silver painted panel had a surface conductivity of about 20 S/m and the flame sprayed panel about 200 S/m.

Skin samples of 3 mm and 6.5 mm thickness were bolted to 50 mm wide CFC ribs with metallic fasteners countersunk into the skin and rivetted anchor nuts. The resistance between each fastener and the structure was 15-30 mohm when measured at a current of 5 A.

The outer bolt heads of the fasteners in 3 mm panels were treated in three different ways.

- A. Oversealed with dielectric sealant and painted with silver paint and with ordinary paint.
- B. Oversealed with dielectric sealant, painted with ordinary paint, silver paint and again with ordinary paint.
- C. Oversealed with dielectric sealant, painted with ordinary paint and covered with a 50 mm wide aluminium tape.

The 6.5 mm panels with anchor nut fasteners were only painted with the ordinary paint.

The internal anchor nuts were not oversealed in any way which represents the worst case with imperfect or lacking sealant on the fasteners.

TEST METHODS

Test testing was performed according to MIL-STD-1757 (ref 1) with the tank skin assumed to be in lightning attachment zone 2A. The action integral and the charge transferred were larger than that defined by the standard, however.

The details of the test methods have earlier been described in ref 2 and will only be described briefly below.

TEST GENERATOR AND SET UP - The coupon test samples were attached to an aluminium box. For photographic purposes, exploding gas experiments and thermovision recordings the bottom of the box could be removed. The box could be fully closed to form a shielded enclosure for voltage measurements using a battery powered oscilloscope. Four return conductors were connected from a flange on the test box to the generator.

The test generator consisted of a high current capacitor bank (30-60 uF) which could be charged up to 30 kV in parallel with a bank of car batteries forming a 300 V DC generator. The test generator could thus give a damped 20 kHz oscillatory high current pulse followed by a high charge current tail of about 260 A. High current arcs with a length of about 10 mm could be generated.

The action integral of the current and the total charge transferred in the arc exceeded that required by MIL-STD-1757 by 40-60%.

A high pressure air nozzle positioned about 150 mm from the electrode could generate a high velocity air stream (>30 m/s) tangential to the CFC skin in order to simulate the cooling effect of the airflow over an aircraft surface.

DIAGNOSTIC TECHNIQUES - Four different diagnostic methods were used at the testing: Photography, voltage measurements, explosive gas mixture and hot spot recordings.

1. Photography of the internal tank wall at fasteners.

A Polaroid camera with aperture $f = 4.7$ and 3000 ASA film was used for photographic detection of sparking at the fasteners. It had earlier been shown that this method cannot detect weak electric sparks of minimum ignition energy (ref 2 and 3). The camera was, however, in this case used for detection of thermal sparking. Such sparking often occurs in the form of burning fragments thrown out from the sparking area.

2. Voltage measurements between anchor nut and CFC skin.

As a complement to the photographic technique voltage measurements were used to indicate the possibility of electric sparking. A battery powered oscilloscope equipped with a Polaroid camera was placed on an insulating support inside the test box. The voltage induced by magnetic coupling through the CFC skin from the test generator was measured by means of a short circuit wire loop.

3. Explosive gas mixture in simulated tank compartment.

An explosive gas mixture experiment was set up to demonstrate possible ignition risks from potential sparking at fasteners, fig 1.

The gas system generated a well controlled mixture of ethene and air with an ignition energy of less than 0.15 mJ. The gas mixture was fed into a plastic bag which was attached "air tight" to the internal skin of the test sample and thus simulating a fuel tank compartment. The ignition property of the gas mixture was continuously checked during the experiment. Gas was drained through a thin pipe from the simulated tank compartment into a spherical electrode spark gap which every 10 seconds generated 1.5 mm long capacitive discharges from a capacitance of totally 9 pF. The minimum ignition energy of a mixture of ethene and air at normal pressure and temperature is 0.07 mJ. The spark gap indicated that the gas ignition energy was less than 0.15 mJ during the experiments.

A mixture of ethene and air was used because its ignition energy is comparable with that of an optimum JP-4 air mixture at a temperature elevated 100°C and a gas overpressure of about 30%. These conditions were judged to establish the worst case normally occurring in a CFC aircraft tank.

4. Hot spot temperature recordings.

The autoignition risks due to hot spot formation in CFC fuel tanks have not been investigated thoroughly before and were therefore included in the study. Recordings of the local temperature and the dynamics of the hot spots generated on the inside were made with AGA infrared sensitive thermovision cameras, type 564 and 782.

The hot spot events could thus be analysed in detail, fig 2. Maximum temperature, maximum width of isotherms and duration of hot spots above certain temperature limits were determined. The initial test sample temperature was 20°C at the experiments.

RESULTS AND DISCUSSION

PHOTOGRAPHIC RECORDINGS - The photographic diagnostics revealed that unprotected anchor nut bolts in 6.5 mm CFC skins might produce thermal sparks. The bolts in 3 mm skins protected by silver paint (protection method A and B) also produced intense thermal sparking, fig 3. The test samples protected with aluminium tape (method C) passed the testing and no significant sparking was detected at the tests.

The presence of thermal sparking was easily detected with the photographic technique. As demonstrated earlier weak electric sparking cannot always be detected with the photographic method prescribed in MIL-STD-1757. If the sensitivity is increased and at least two cameras are used in parallel coincidence criterias can be used for registrations on the film. Weak sparking can thus be distinguished from e.g. film imperfections and other disturbances. A better confidence will then be obtained with photographic diagnostics.

VOLTAGE MEASUREMENTS - The voltage drop between a fastener exposed to a simulated lightning strike and the internal CFC skin was measured for bolts through a 6.5 mm CFC skin and a CFC rib. When the test current of about 100 kA was passed through the bolt to the CFC structure a voltage drop of 440-550 V was measured. The high current resistance of the fastener was thus about 5 mohm. The recorded voltage was high enough for generation of discharges through very thin dielectric layers, across very short airgaps and also for sustaining high current arcing in airgaps. The voltage recorded did indicate that electric sparking phenomena could occur in the test samples.

EXPLOSIVE GAS MIXTURE - The explosive gas mixture experiments demonstrated that the thermal sparking which was produced at unprotected fasteners in 6.5 mm CFC panels could ignite an explosive gas mixture of ethene and air. In one out of four trials made the simulated fuel tank containing a gas mixture exploded when a lightning current was fed into an anchor nut bolt head.

The mechanism of gas ignition by thermal sparking is not fully understood. Heating of the explosive gas by the burning fragments is probably an important mechanism. Electric sparks on the other hand transfer much of the energy by ionization and production of reactive radicals. The heat transfer of thermal sparks is probably more effective if the burning fragments are stationary than if they are moving.

AD-A169 967

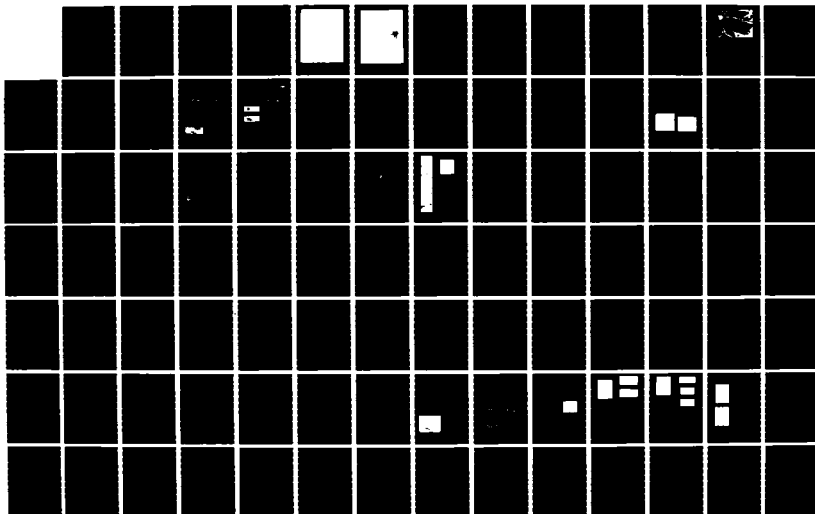
INTERNATIONAL AEROSPACE AND GROUND CONFERENCE ON
LIGHTNING AND STATIC ELE. (U) NATIONAL INTERAGENCY
COORDINATION GROUP JUN 84

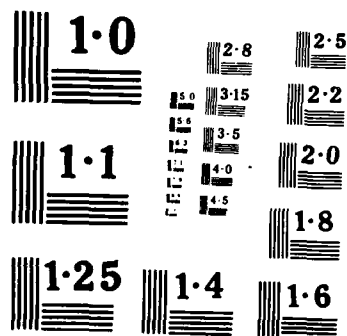
4/6

UNCLASSIFIED

F/G 20/3

NL





Any traps in the form of surfaces with low thermal conductivity which could stop the movements of burning fragments without immediately cooling them might be important. CFC surfaces, sealants, rubber and plastic components in a tank close to a sparking point may thus be of significant importance. If the heating effect dominates the ignition mechanism the AIT is also of great importance. For demonstration of ignition risks with a gas system it may be advisable to use an explosive gas mixture of the proper fuel and air. Possibly some oxygen should also be added in order to decrease the minimum ignition energy to a value representative of the most incendive mixture, for the pressure and temperature that may exist in the system. An addition of 5-10% oxygen will achieve this without affecting the AIT considerably (ref 4).

HOT SPOT RECORDINGS - The thermovision recorded temperatures are shown in figure 4 as functions of time. The figure shows how a high velocity air stream affects the time constant of the temperature decline. The maximum temperature at 4.5 mm skins was not much influenced by the air stream, whereas hot spots produced on the 3 mm unprotected skin did not reach the same high temperature when the skin was externally cooled by an air stream.

The heating of CFC is partly caused by the current action integral giving a deep lying resistive heating and partly by the charge transferred in the arc giving an arc root heating at the surface, which initially is very superficial.

The hot spot produced by a current pulse with a tail (components C and D of MIL-STD-1757) can be compared with that produced by a current pulse without a tail (component D only). The two effects contribute to comparable shares of the total heating. A tendency can be observed that the additional heat (superficial) produced by a high charge in the current tail is influenced by the air stream but that the resistive heating is not very much influenced. This indicates that the time function of the wind cooling contains two time constants when the hot spot is produced by a high current pulse followed by a current tail.

The different lightning protection schemes had rather different effectiveness. The 3 mm aluminium flame sprayed surface was only heated about 100°C above the ambient temperature. The 3 mm surface covered with silver paint on top of a primer paint was heated about 200°C above the ambient air temperature.

The surface covered with silver paint only, was heated almost 300°C above the ambient air temperature in still air, which is comparable with that of the unprotected surface. The wind effect decreased the maximum temperature of the 3 mm samples and shortened the duration of the hot spot appreciably.

Exact limits for hot spot autoignition cannot be determined from the present data on autoignition of fuels. The AIT for JP-4 is stated to be 245°C when a gas mixture is slowly heated in a small glass container (ref 5 and 6). If a gas mixture is passing slowly over a heated 4 inch steel target the AIT is about 490°C. This, however, indicates that the AIT might be affected by any geometry that prevents the gas to flow over the heated area, thus increasing the effective contact time between the gas and the heated surface (ref 7). Other authors give much higher AIT:s for metal walls heated by a lightning strike (ref 8 and 9).

Ignition experiments for determination of the conditions for autoignition of fuel vapors by hot spots on CFC skins should be performed. The influence of surface and volume geometry and orientation (horizontal versus vertical), peak temperature, width and duration of a hot spot are important parameters in such experiments.

CONCLUSIONS

The experiments showed that incendive thermal sparking will occur at fasteners which are not effectively protected from lightning attachment. Internal wall to fastener voltages high enough to sustain high current electric arcs were recorded for unprotected fasteners. High temperatures will be generated at hot spots in the tank if the skin is less than 5 mm thick. The incendivity of such hot spots is not established, but they cannot be excluded as potential ignition sources based on present knowledge about hot spot autoignition. Acceptable protection schemes for suppression of thermal sparking and hot spots were, however, found at the testing.

REFERENCES

1. MIL-STD-1757. "Lightning Protection of Aircraft".
2. B. Olsson. "Lightning Tests of Aircraft Fuel Tank Details". Int. Conf on Lightning and Static Electricity. Oxford, March 1982.

3. K.E. Crouch. "Detection of sparks in fuel system test". Int. Conf. on Lightning and Static Electricity. Oxford, March 1982.
4. B. Lewis, G. von Elbe. "Combustion, Flames and Explosions of Gases". 2nd Ed. Academic Press NY London 1961.
5. J.M. Kuchta. "Summary of Ignition Properties of Jet Fuels and Other Aircraft Combustible Fluids". AFAPL-TR-75-70.
6. K.R. Bragg et al. "Nitrogen Inerting of Aircraft Fuel Tanks". AFAL-TR-68-290 Part II. Lightning and Static Electricity Conf. Miami Fl. Dec. 1968.
7. D.G. Goodall et al. "The Ignition of Flammable Liquids by Hot Surfaces". Fire Technology, No 3, 1967, p115.
8. R.O. Brick. "A Method for Establishing Lightning Resistance/Skin Thickness Requirements for Aircraft". AFAL-TR-68-290 Part II. Lightning and Static Electricity Conf. Miami Fl. Dec. 1968.
9. F.A. Fischer et al. "Lightning Protection of Aircraft". NASA Ref. Publication 1008.

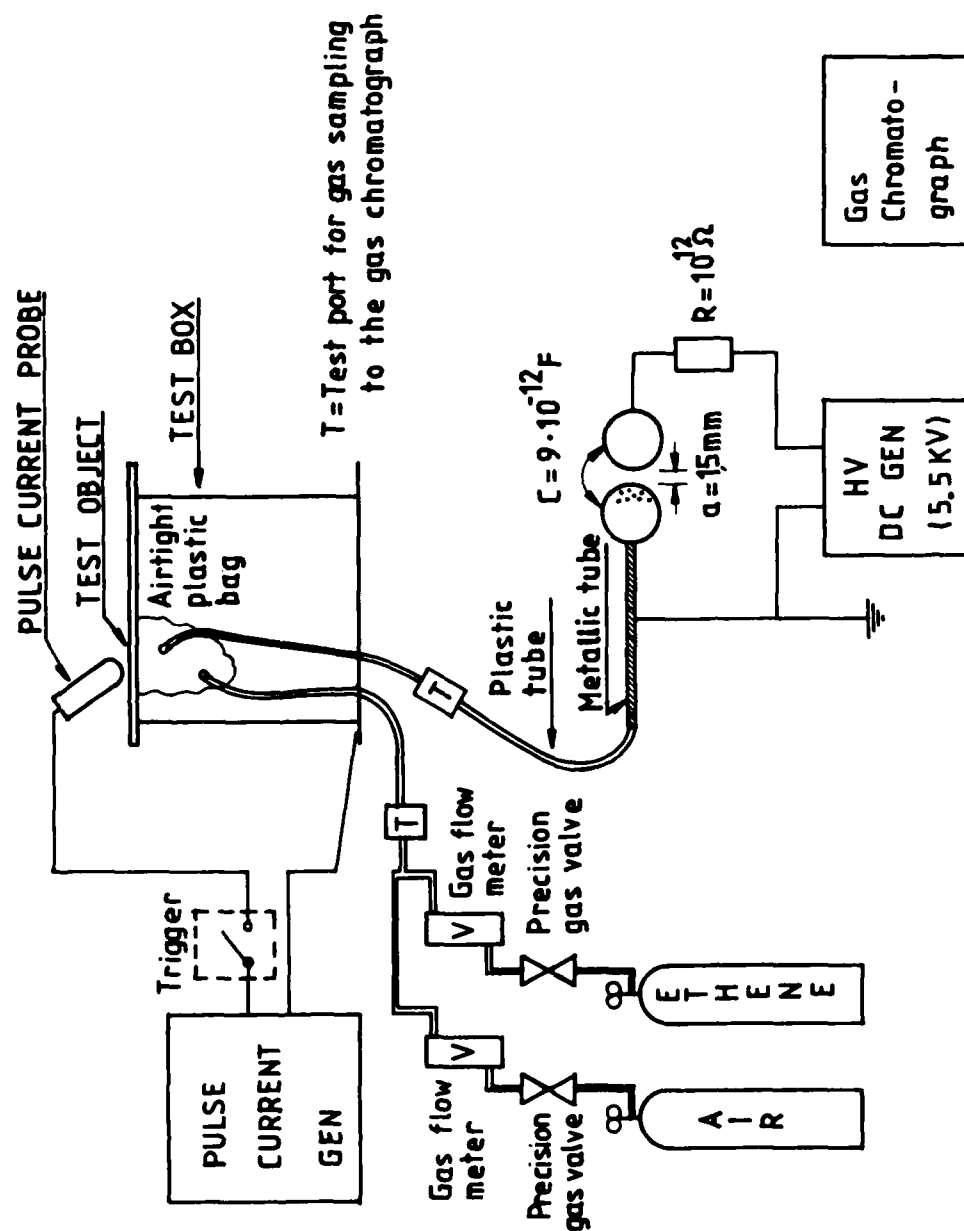


Fig 1 - Test set up for ignition experiments.

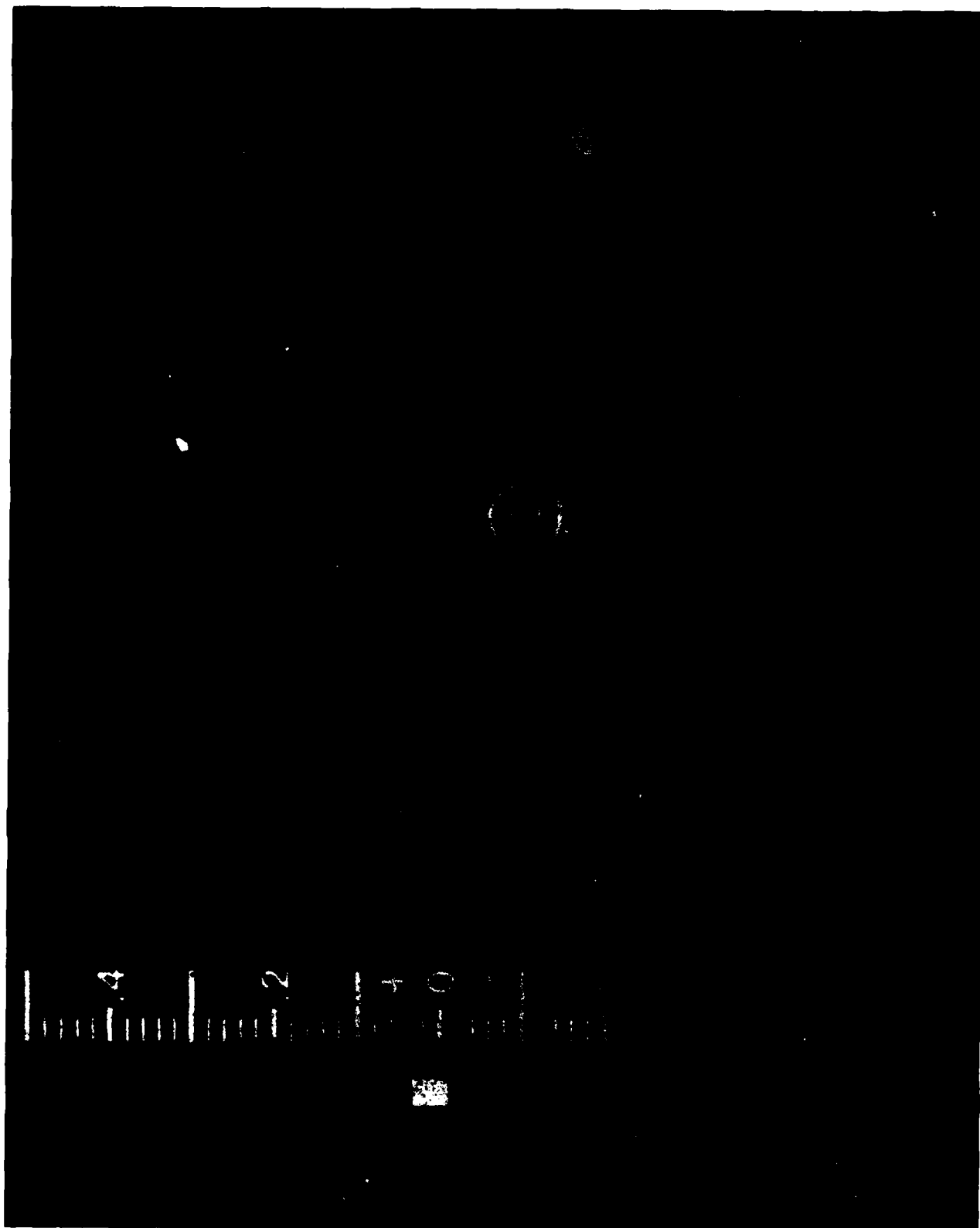


Fig 2 - Hot spot isotherms (i.t.) on 4.5 mm CFC skin recorded with AGA thermovision camera. Outer i.t. = 110°C , diameter 39 mm. Inner i.t. = 200°C .

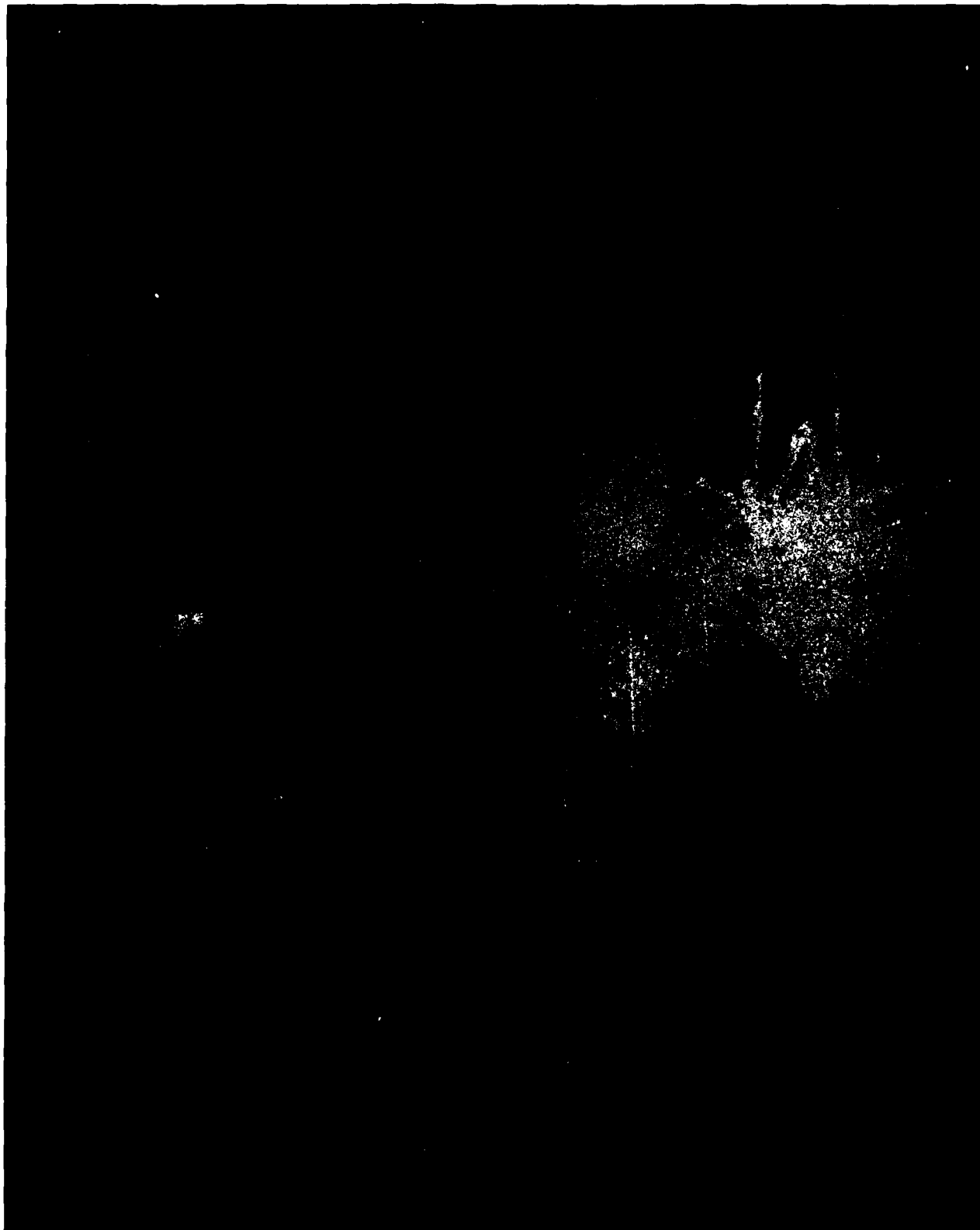


Fig 3 - Thermal sparking at anchor nuts in
CFC skin.

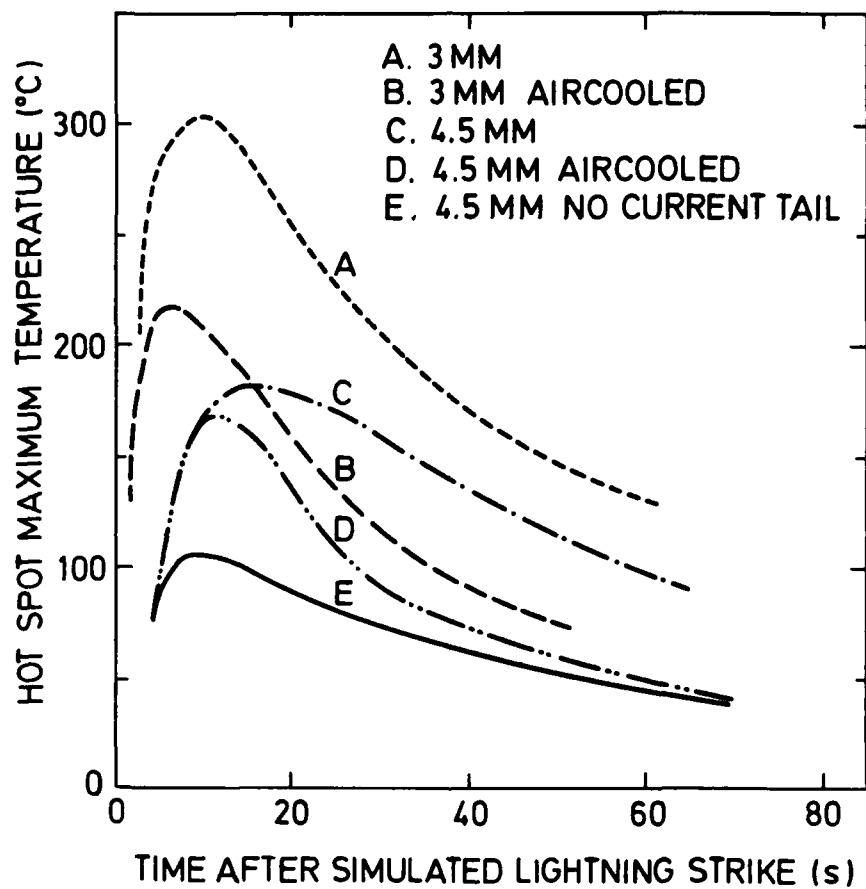


Fig 4 - Hot spot maximum temperature time functions on CFC skins for current pulse of $I = 100 \text{ kA}$, $P = 0.35 \cdot 10^6 \text{ A}^2\text{s}$ and $Q = 80^\circ\text{C}$.

**REAR SURFACE TEMPERATURE MEASUREMENT OF AIRCRAFT
MATERIALS SUBJECTED TO ZONE 2A LIGHTNING STRIKES**

E. H. Schulte

**McDonnell Aircraft Company
McDonnell Douglas Corporation
P.O. Box 516
St. Louis, Missouri 63166**

and

W. T. Walker

**Naval Air Development Center
Code 20P4
Warminster, Pennsylvania 18974**

ABSTRACT

This paper presents the results of an experimental study in which aluminum and carbon epoxy (C/E) panels, ranging in thickness from 0.060 to 0.250 inch, (0.15 to 0.64cm) were subjected to swept lightning strikes while their rear surface temperature was monitored.

Six C/E and six aluminum panels were tested. One each of the aluminum and C/E panels incorporated metal fasteners. Tests were conducted at wind speeds ranging from 65 to 170 mph (29 to 80 m/s) using the multicomponent Zone 2A current waveform specified in MIL-STD-1757A. These tests illustrated some of the similarities and differences between aluminum and C/E materials when subjected to swept stroke lightning. In general, it takes 100 times longer for the hot spot on C/E to reach maximum temperature as compared to aluminum, and the aluminum gets hotter than the C/E. Aluminum is penetrated by the continuing current (Component C of MIL-STD-1757A), and C/E is penetrated by the high-current pulse (Component D) of a lightning strike. In general, wind velocity affects the hot spot temperature in that it cools the panel and results in a lower hot spot temperature.

INTRODUCTION

Modern aircraft utilize Zone 2A areas of the wings and fuselage for fuel storage. Integral fuel tank designs contain only the aircraft skin between the lightning strike on the skin's exterior and the fuel. Design precautions are, therefore, required to prevent fuel ignition caused by a lightning strike.⁽¹⁾ Fuel ignition may result from hot spots, burn-through, or sparking inside the tank. Historically, sufficiently thick aluminum alloys of high electrical and thermal conductivities have provided adequate lightning protection. However, new composite materials such as carbon epoxy (C/E) with its high strength-to-weight ratios but lower conductivities are being required in today's high-performance aircraft. The effect of the lower conductivities of composites on the lightning formation of hot spots and other ignition mechanisms within fuel cells must be studied to determine design safety margins. These design margins must ensure that flight safety is preserved with the minimum impact to performance and mission capabilities.

In the past, numerous tests of materials have been conducted under various swept stroke and simulated swept stroke conditions in an effort to determine their resistance to lightning strikes. However, most of the past testing was not conducted utilizing the criteria specified by the new MIL-STD-1757⁽²⁾ nor was it conducted utilizing the newer composite materials. There also appears to be disagreement as to the relevance of the air flow on the melting and cooling of metal panels subjected to lightning swept stroke conditions.^(3,4)

The principal objective of these tests was to determine the effects of the lightning arc attachment to simulated generic "wet wing" skin panels in a Zone 2A area. These effects included arc dwell time, physical damage, possible internal sparking, and rear surface temperature excursions.

The tests reported herein were supported by Naval Air Development Center contract N62269-82-C-0080 and are detailed in Report NADC-83106-20.⁽⁵⁾

LIGHTNING SWEEP STROKES

When an aircraft in flight is struck by lightning, the aircraft flies through the relatively stationary arc channel which often persists for large fractions of a second. This dynamic sweeping effect results in lightning attachment to inboard sections of the aircraft (Zone 2A) which probably would not be struck directly. Zone 2A areas often are fuel containment areas, such as those in a wing, and are, therefore, subject to high current restrike attachment.

The nature of the sweeping action of the lightning arc and the damage produced by a swept stroke are usually simulated in the laboratory by using windblown arcs.^(6,7) As in aerodynamic wind tunnel testing, the aircraft surface remains stationary and the ionized arc channel moves across the skin, driven by the airstream from a wind tunnel. However, unlike wind tunnel testing where scale models can be used, lightning swept stroke testing requires full size mock-ups or actual hardware because adequate scaling factors are not available to scale physical damage.

Because natural lightning is so variable, standard lightning test current waveforms have been defined in MIL-

STD-1757A for qualification testing. For the testing of aircraft sections located within a Zone 2A swept stroke zone, the simulated lightning current waveform shown in Figure 1 is specified.

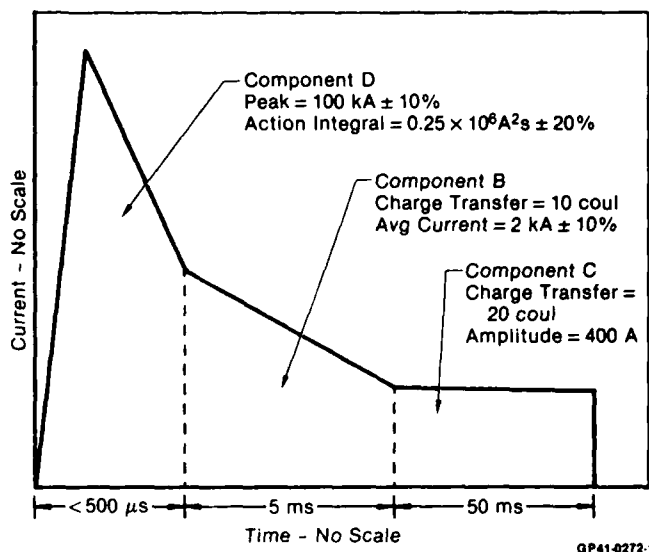


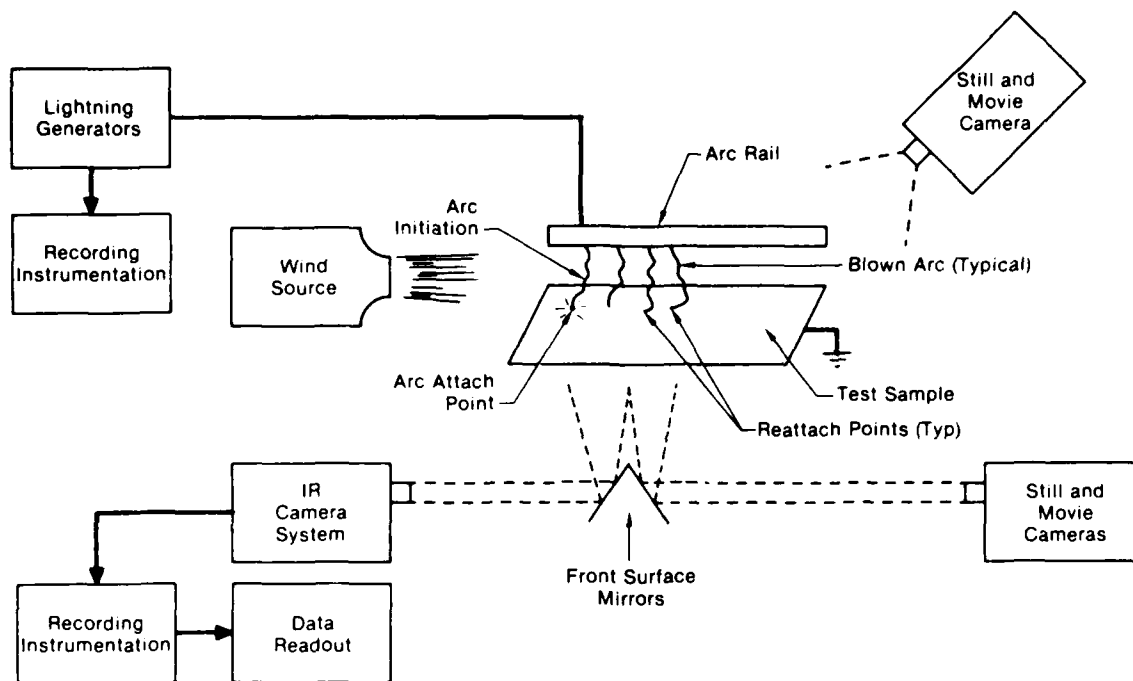
Fig. 1 MIL-STD Swept Stroke Waveform (Zone 2A)

For static tests (0 MPH air) the arc will probably remain attached at one spot for the duration (50 ms) of the lightning current. This will result in considerable energy being deposited at one location. Whereas if the arc was being blown, additional arc reattachments occur to lessen the damage at the initial attachment location. Whether the cooling effects of the air stream and the existence of additional arc reattachments are significant depends upon many factors, including the type of material being tested and the realism of the simulation.

TEST SETUP

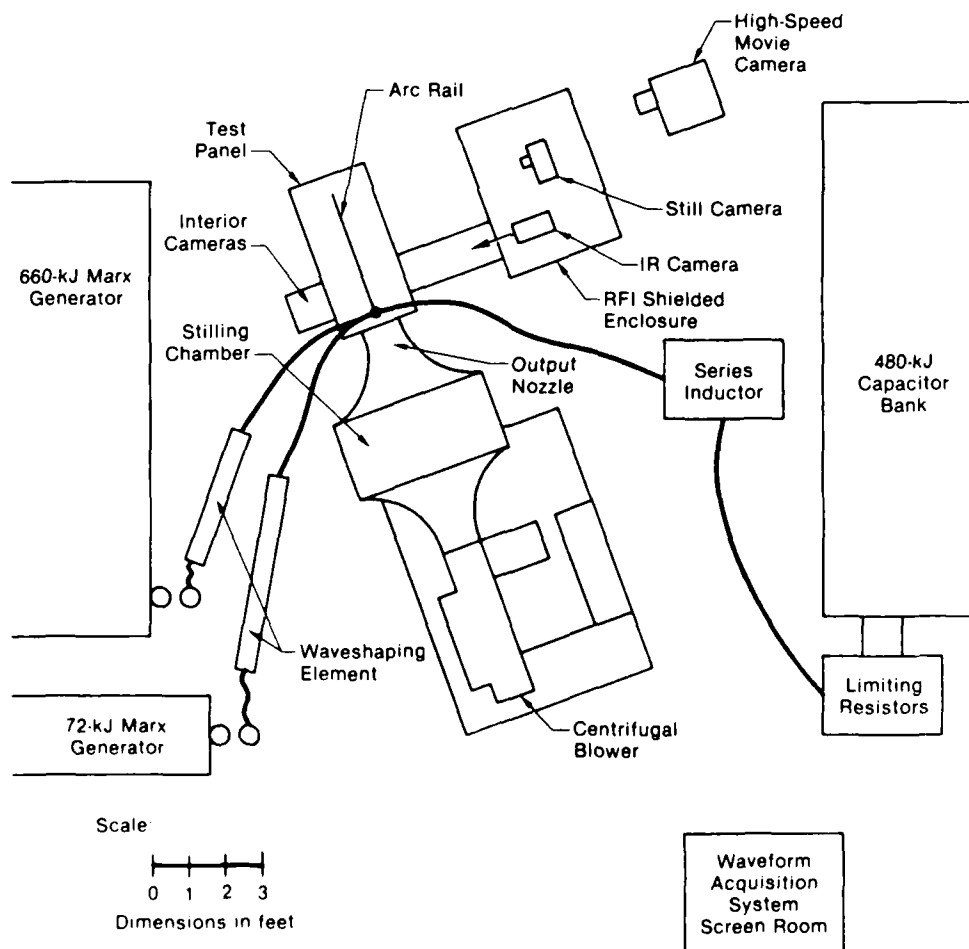
A simplified block diagram of the test setup used for these tests is shown in Figure 2 and an overhead layout of the test area is given in Figure 3. The test setup provided for a 12-inch-long simulated lightning arc to be initiated to a selected location on the test panel and then blown down the length of the panel while photographic cameras monitored the arc's progress above the test panel and infrared (IR) and photographic cameras monitored the opposite side of the panel.

The Zone 2A lightning current was (complying with MIL-STD 1757A) provided by the McDonnell Aircraft Company (MCAIR) one-megajoule lightning simulator. Additional details of this system can be obtained from References 8 and 9. Since the rate-of-rise of the high current pulse affects the damage to composites, tests were conducted with a fast rise time. The D component with an $\sim 3 \mu\text{s}$ rise time was supplied by a portion of the 660-KJ capacitor bank operating at approximately 200 KV in conjunction with the output of the 72-KJ Bank operating at 450 KV; the B component was supplied by a portion of the 480-KJ (90-KJ) capacitor bank at approximately 12 KV,



GP41-0272 2

Fig. 2 Simplified Block Diagram of Swept Stroke Test Setup



GP41-0272 3

Fig. 3 Swept Stroke Test Layout

and the C component was supplied by the remainder of the 480-KJ capacitor bank at approximately 12 KV. The various capacitor banks were connected to provide these components in a combined waveform initiated by the D component and followed by the B and C components, respectively. A typical current waveform from these tests is shown in Figure 4. The waveform is shown in its three component parts because of the vastly different amplitudes and times of the individual components. The amplitude of the C component varied as the arc was stretched, blown back, and reattached at various locations on the panel. The output of the lightning simulator was of negative polarity for these tests (i.e., the arc rail was negative with respect to the panel).

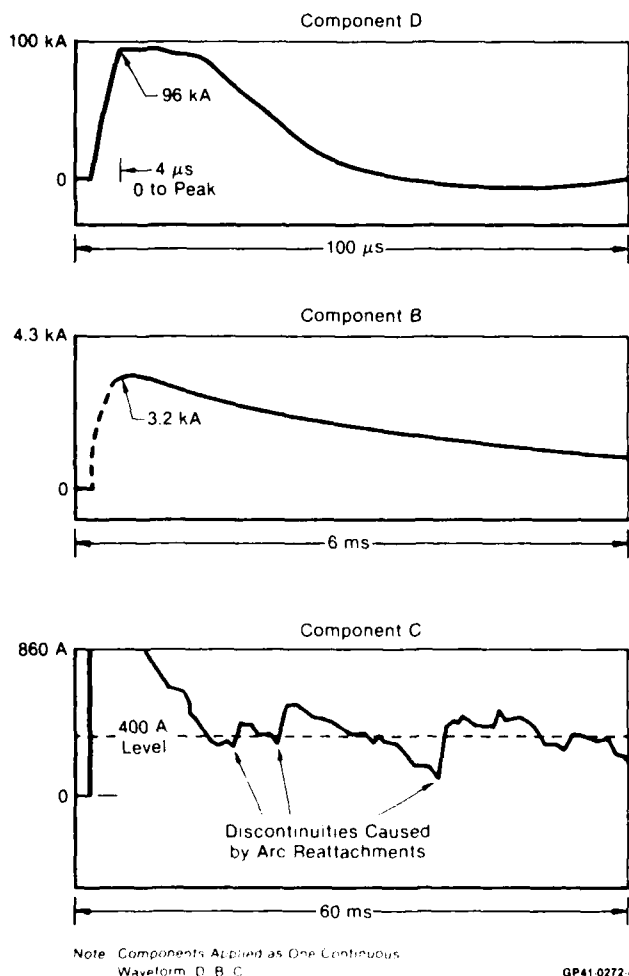


Fig. 4 Typical Lightning Current Swept Stroke Waveform (0.125 in. Thick C/E Panel With Fasteners, 65 MPH Air Velocity)

A metal arc rail, running the length of the panel, was placed 12 inches above the panel (Figure 5). A 36-gauge copper wire was attached to the rail near the wind tunnel exit and stretched to within 1-1/2 inches of the panel. The lower end of the wire was held in place by a nylon string

stretched above the panel and attached to the wire. Upon initiation of the lightning discharge, the high current would immediately vaporize the small copper wire and yield a 12-inch-long arc to the test sample which would then be extended and blown across the test sample. Dielectric tape was placed on top of the panel to force the initial attachment of the arc to the area within the field of view of the IR camera looking at the opposite side of the panel.

The wind source consisted of a large industrial blower powered by a 50-hp electric motor. An adjustable inlet vane damper on the blower was used to control the output wind velocity. The output of the blower was fed into a large screened stilling chamber and then through a 16/1 contraction ratio fiber glass nozzle (with a 12- x 12-inch outlet) to provide a laminar air flow across the test sample (Figure 2). The swept stroke tests were conducted at wind velocities of approximately 65, 105, 145, and 170 mph (29, 50, 65 and 76 m/s). Typical velocities at the nozzle exit with a panel in place are shown in Figure 6.

A test stand with a light-tight enclosure supported the test panel in the windstream. The panel was secured to the test stand by fiber glass angles on both sides of the panel, as shown in Figure 5. The ground return for the lightning current through the panel was at the downwind end of the panel.

Still cameras and high-speed movie cameras (up to 5000 fps) were utilized to photograph the lightning arc blown across the top surface of the panel and also to photograph any arcing or burn-through which occurred on the opposite side of the panel. The cameras photographing interior sparking were set up to record small amounts of the sparking (f6.3 lens opening with ASA 3000 speed film for the still camera and f2.0 lens opening with ASA 125 speed color film for the movie camera). The cameras photographing the high intensity lightning arc were adjusted to minimum settings.

For the measurement of hot spot temperatures, a non-contacting infrared camera system was selected over thermocouples and temperature-sensitive paints because it offered distinct advantages over the latter devices, as noted in Table 1.

The IR temperature measurement instrumentation consisted of a modified AGA Thermovision 780 camera and a Sabre VIII instrumentation tape recorder located in a shielded test enclosure. After a test, the magnetic tape was replayed onto a Honeywell 1858 Visicorder for data reduction. The AGA Thermovision camera was modified so that better time-temperature resolution could be obtained. By disabling the vertical sweep, a linear horizontal sweep was obtained which was scanned at a rate of 2400 sweeps/second. With the sample mounted approximately two meters from the IR camera, a field of view approximately 0.10 inch wide x 9 inches long was obtained. The IR camera viewed the underside of the panel via a silver front surface mirror. Calibration of the complete system was obtained by placing an Electro Optical Industries blackbody source at the strike location of the panel and calibrating the system for all apertures to be used during the test. Good agreement between the blackbody calibra-

TEST PROCEDURE

Each test sequence consisted of centering the desired strike area on the panel over the IR camera viewing window which was centered at the blower exit nozzle. With the arc directing wire attached to the arc rail, and with the dielectric tape on the panel, the wind source was activated and adjusted for proper velocity. The capacitor banks were then charged and discharged into the test sample.

Test shots were made at different wind velocities on each panel by displacing the panel sideways and masking previous attach points using dielectric tape to prevent preferential reattachment. Infrared camera data, current waveforms, external still photographs, and high-speed movies were taken on each test. Backside surface still photographs and movies were taken only when sparking or direct puncture were likely.

TEST SAMPLES

Tables 2 and 3 summarize the 30-inch x 54-inch (0.76m x 1.37m) flat panels utilized for this test series. Four test article parameters (material, panel thickness, surface coating, and fasteners or none) were varied.

Table 2. Test Panel Characteristics

Panel No.	Material	Nominal Thickness	Painted ⁽¹⁾	Fasteners
1	Aluminum ⁽²⁾	0.030 Inch	Yes	No
2	Aluminum	0.060 Inch	Yes	No
3	Aluminum	0.125 Inch	Yes	No
4	Aluminum	0.125 Inch	Yes	Yes
5	Aluminum	0.125 Inch	No	No
6	Aluminum	0.250 Inch	Yes	No
7	C/E (Tape) ⁽³⁾	0.060 Inch	Yes	No
8	C/E (Tape) ⁽³⁾	0.090 Inch	Yes	No
9	C/E (Tape) ⁽⁴⁾	0.125 Inch	Yes	Yes
10	C/E (Tape) ⁽⁴⁾	0.125 Inch	No	No
11	C/E (Tape) ⁽⁴⁾	0.125 Inch	Yes	No
12	C/E (Cloth) ⁽⁵⁾	0.125 Inch	Yes	No
13	C/E (Tape) ⁽⁴⁾	0.250 Inch	Yes	No

(1) Primer (1 coat): High temperature epoxy polyimide
Enamel (2 coats): Linear aliphatic polyurethane

(2) Aluminum alloy 2024

(3) Carbon epoxy tape: AS-4 fiber, 3501-6 resin, 42% resin (0.005/ply)

(4) Carbon epoxy tape: AS-4 fiber, 3501-6 resin, 35% resin (0.010/ply)

(5) Carbon epoxy cloth: T300-6K fiber, 3501-6 resin, 5 harness satin weave (0.014/ply)

GP41-0272-8

The aluminum panels were all 2024 aluminum. The composite carbon epoxy panels were fabricated in-house using aircraft material. The tapes (Ref. Table 2) were unidirectional material and the cloth was two-dimensional woven material.

Most of the test panels were made without fasteners, but one aluminum and one C/E panel included fasteners. The 0.125-inch aluminum panel was backed with a 0.125-inch x 1.25-inch-wide aluminum strip to simulate a rib attachment and used titanium fasteners which were inserted on 1-inch

Table 3. Composite Panel Layouts

Ply No.	7 (0.060 in.) 9, 10, 11 (0.125 in.)	8 (0.090 in.)	12 (0.125 in.)	13 (0.250 in.)	Rib-1 (0.100 in)
	No. of Ply (°)	No. of Ply (°)	No. of Ply (°)	No. of Ply (°)	No. of Ply (°)
1	45	45	45	45	45
2	0	0	0	0	-45
3	-45	-45	-45	-45	90
4	90	45	90	90	90
5	45	-45	0	45	90
6	-45	90	90	-45	-45
7	-45	45	-45	45	45
8	45	-45	0	0	
9	90	0	45	-45	
10	-45	-45		90	
11	0	45		45	
12	45	90		-45	
13		-45		-45	
14		45		45	
15		-45		90	
16		0		-45	
17		45		0	
18	N/A		N/A	45	N/A
19				-45	
20				45	
21				90	
22				-45	
23				0	
24				45	

Notes

1. Ply Orientation is the Fiber Direction in Tape Material and the Warp Direction of the Woven Fabric Material. 0° is in the 54-Inch Direction (the Direction of the Swept Arc).

2. Panels Were Vacuum Debulked at 6-Ply Intervals and at Completion of Lay-Up Procedures.

3. Panel Number Rib-1 Was Cut Into 8 Pieces 1.250 Inches Wide by 45.00 Inches Long.

GP41-0272-9

centers into gang channel nut plate strips running the length of the test panel. The 0.125 C/E panel was backed with 0.10-inch x 1.25-inch-wide C/E strips, and titanium fasteners were inserted on 1-inch centers into individual nut plates. No attempt was made to make these generic panels conform to the rigid aircraft specifications for fuel tank applications. No sealants or other coatings, such as might be used to seal against fuel leaks or to serve as spark suppressors, were used on the titanium fastener installations.

The panels were painted using production processes and paints. One coat of epoxy primer was applied before two top coats of an aliphatic polyurethane enamel. One 0.125-inch-thick panel of each material was left unpainted to determine the effects of the dielectric paint on swept stroke dwell times and backside temperatures. The back-sides of all metal panels were painted with a thin coat of high-temperature flat black paint to give a uniform surface emissivity needed for the infrared camera measurements. The black backside surfaces of the C/E panels were not painted.

TEST RESULTS

Sixty blown arc and two static tests were conducted using the swept stroke test setup. A summary of the test results is given in Table 4 (a complete tabulation of the data is given in Reference 5). All of the data presented in Table 4 refer only to the initial attachment of the arc by the 100-KA strike. The average penetration time refers to the delay time between the initiation of the arc and the time that the temperature rise is observed in the IR data. The average time to peak temperature is the time between the initiation of the arc and the time that the rear surface of the panel reaches its maximum temperature. Typical interpretation of the IR data is illustrated in Figure 7. The dwell time is the time that the arc remained attached at the initial attachment point. The dwell time was obtained by correlating the high-speed movie data and the lightning current test waveform. The 0.060-inch C/E panel was not tested because the 0.090-inch C/E panel was punctured.

From these test data several differences and similarities between the various materials and configurations were noted. These include: (1) vastly different hot spot time-temperature curves, (2) different damage penetration characteristics, (3) similar paint effects, (4) similar wind velocity effects, (5) dwell time similarities, (6) similar preferential arc attachment to bolts, and (7) rear surface sparking at bolts.

Hot Spot Temperature. Plots of the individual time-temperature curves are shown in Figures 8 through 15, and show that the characteristics of the aluminum panels are vastly different for similar thickness C/E panels. The aluminum heats up very quickly (on the order of 0.1 second), gets very hot, but it also cools very rapidly, and the heat is confined to a very small area. By comparison, it

takes the C/E material 100 times longer to reach a maximum temperature and it also requires a long time for the material to cool. The hot spot diameter was larger for the C/E panels than for the aluminum panels. Also included in these plots are the data for the "simulated" swept stroke (zero mph wind velocity, continuing current duration of 50 ms depositing 20 coulombs) tests on the 0.125-inch-thick panels.

The maximum hot spot temperatures were observed for the thinner panels as expected, and the time-to-peak temperature was relatively independent of wind velocity and dwell time for a given thickness of panel. The temperatures of the bolted aluminum panel were too low to be measured accurately and the sparking of the C/E bolted panel saturated the IR camera, thus no temperature data was obtained for the bolted panels.

The envelopes for all of the wind-blown arc tests are shown in Figure 16. These data clearly illustrate the different time-temperature comparisons for aluminum and C/E materials.

Penetration Characteristics. The lightning penetration characteristics of aluminum and C/E differ in their response to the individual waveform components. In general, for the aluminum panels the high peak current (D component) had only minor effects on the panels, but the continuing current (C component) caused the panel to be penetrated by melting through the panel. For example, the 0.030 aluminum panel, shown in Figure 17, was not penetrated by the D component but it was burned through during the continuing current. Whereas for the C/E panels, the high peak current caused major damage to the panels and the lower level currents only did minor additional damage to the panels. For example, the 0.090-inch C/E

Table 4. Swept Stroke Tests Data Summary

Panel Thickness and Type	Avg Penetration Time*	Avg Time to Peak Temp	Max Temp Range (°C)	Dwell Time Range** (ms)	Notes
Aluminum:					
0.25 in.	54 ms	190 ms	56-80	8-22	
0.125 in. Painted	13 ms	62 ms	98-193	3-15	
0.125 in. Unpainted	11 ms	46 ms	84-159	4-13	
0.063 in. Painted	6 ms	37 ms	496-581	14-19	Some Melting
0.032 in. Painted		(Melted Through Panel)			
0.125 in. Fasteners, Painted	(Temp Too Low, Some Sparks Noted)			5-9	Sparking
Carbon/Epoxy:					
0.25 in. Painted, Tape	3.5 s	20.7 s	65-71	8-20	
0.125 in. Unpainted, Tape	0.80 s	7.2 s	75-95	5-12	
0.125 in. Painted, Tape	0.39 s	7.9 s	98-141	4-14	Some Delamination
0.125 in. Painted, Cloth	17 ms***	6.5 s	143-161	6-17	
0.090 in. Painted, Tape		(Punctured Through Panel)			
0.125 in. Fasteners, Painted	(Excessive Sparking, Saturated IR Sys)			5-15	Sparking

*Penetration Time = Time Between the 100-kA Strike and the Interior Temperature rise

**Dwell Times for the Initial Attach Point Only

***In Some Cases the Temperature Rise Started Immediately With the 100-kA Strike

GP41-0272-10

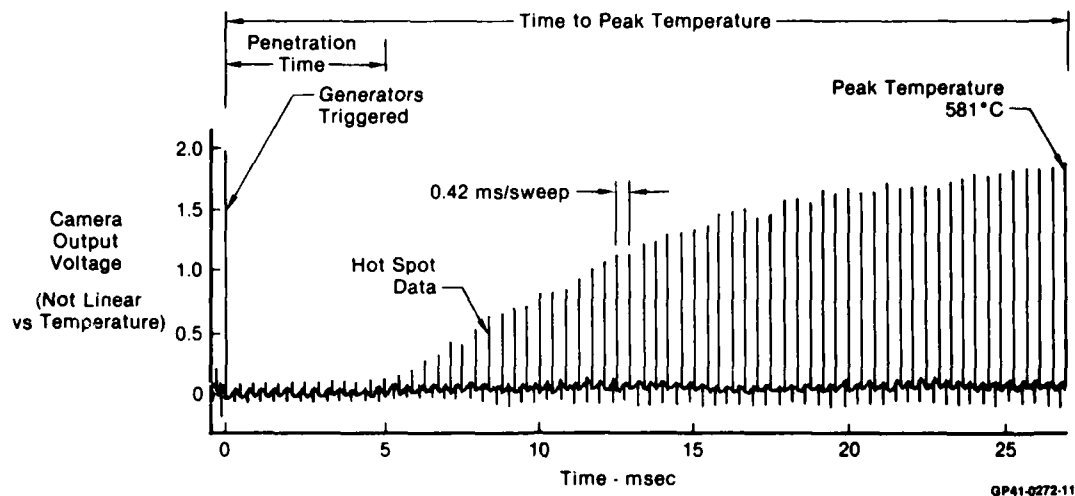


Fig. 7 IR Camera Video Output for 0.063 in. Thick Aluminum Panel

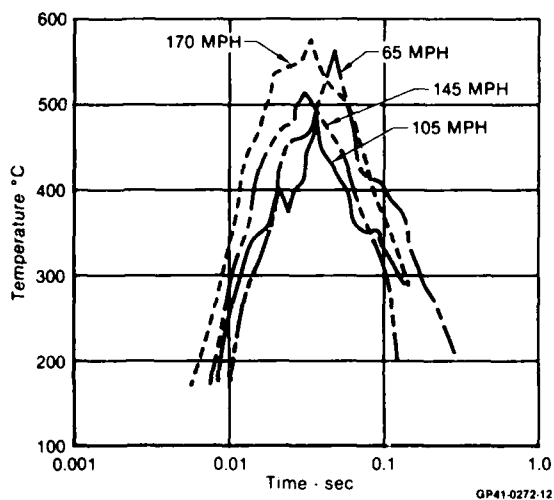


Fig. 8 Interior Hot Spot Temperature Versus Time (0.063 Inch Thick, Painted Aluminum Panel)

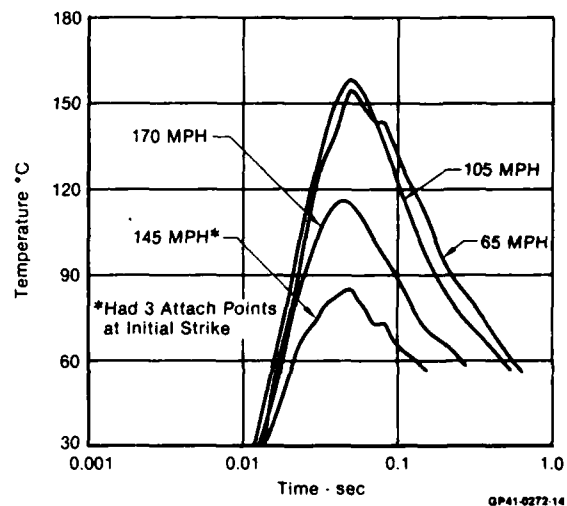


Fig. 10 Interior Hot Spot Temperature Versus Time (0.125 inch Thick, Unpainted Aluminum Panel)

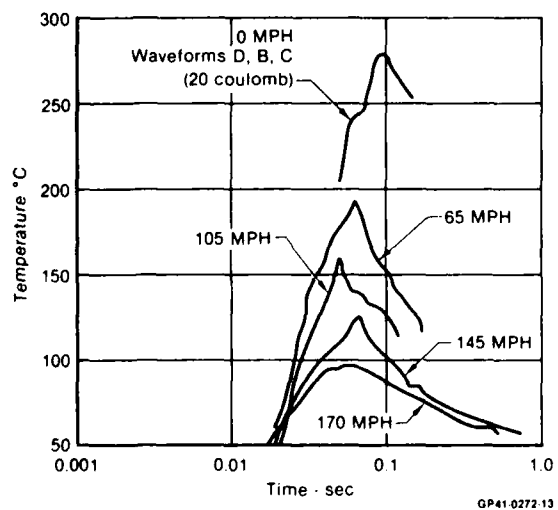


Fig. 9 Interior Hot Spot Temperature Versus Time (0.125-Inch Thick Painted Aluminum Panel)

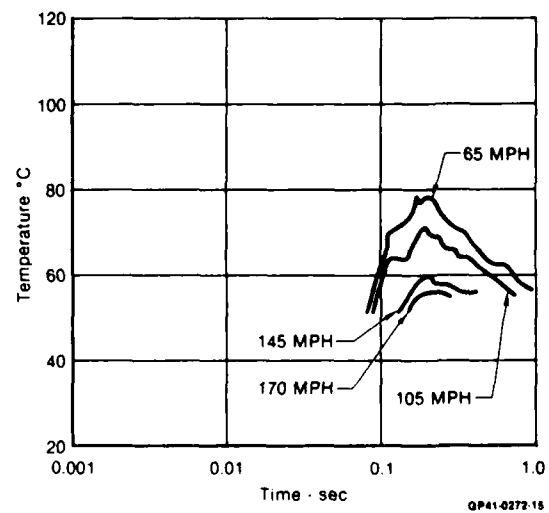


Fig. 11 Interior Hot Spot Temperature Versus Time (0.25 inch Thick, Painted Aluminum Panel)

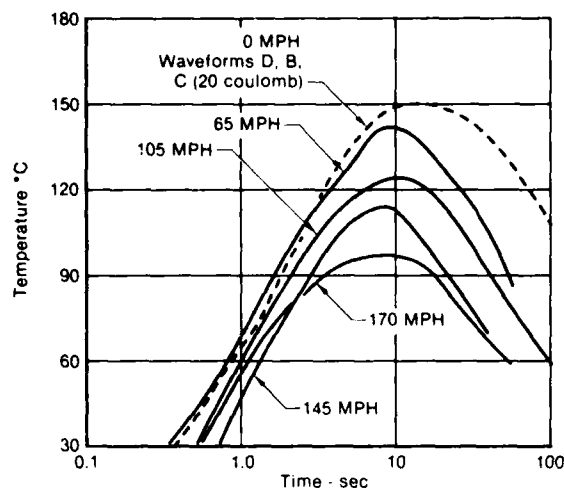


Fig. 12 Interior Hot Spot Temperature Versus Time (0.125 Inch Thick, Painted Carbon Epoxy Panel)

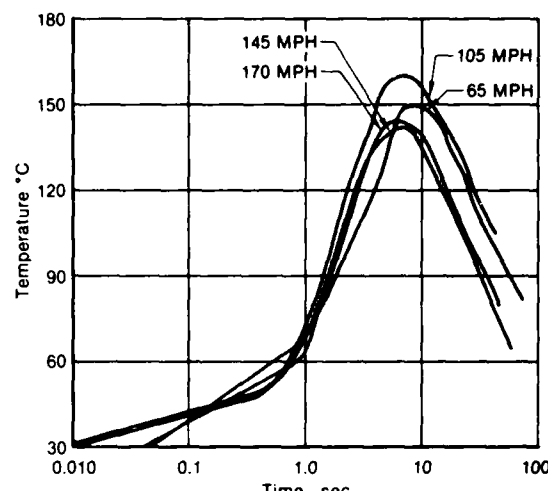


Fig. 14 Interior Hot Spot Temperature Versus Time (0.125 Inch Thick, Painted Carbon Epoxy Cloth Panel)

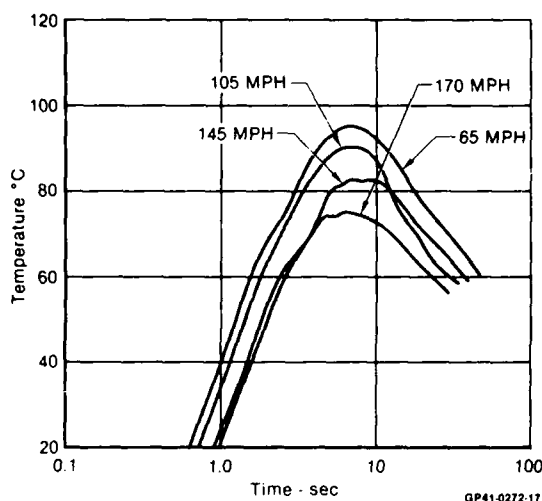


Fig. 13 Interior Hot Spot Temperature Versus Time (0.125 Inch Thick, Unpainted Carbon Epoxy Panel)

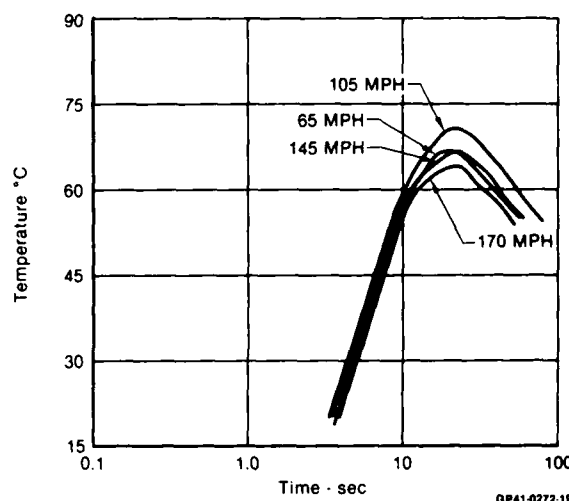


Fig. 15 Interior Hot Spot Temperature vs Time (0.25 Inch Thick, Painted C/E Panel)

panel, shown in Figure 18, was penetrated during the application of the D component, but the 0.125-inch C/E panel was not even penetrated by the D, B, and a C component lasting 50 ms.

These effects are further illustrated in the time-temperature data for the 0.125-inch-thick aluminum and C/E panels shown in Figure 9 and 12. The additional dwell time of the continuing current applied during the static test caused an increase in the aluminum hot spot temperature of approximately 90°C, for an increase of approximately 50 percent over that obtained during the 65 mph test. Whereas for the C/E panel, the increase was only 10°C which is only a seven percent increase in temperature.

Paint. Paint has a tendency to confine the arc and causes the hot spot to get hotter than a similar attachment to an unpainted panel. This can be seen by comparing the temperature data for the painted and unpainted aluminum and C/E panels, shown in Figures 9 and 10, and Figures 12 and 13.

Wind Velocity. In general, the higher the wind velocity, the lower the maximum hot spot temperature. Even on panels where the dwell time was long and the wind velocity high, the temperature was relatively low.

Dwell Time. There was a considerable scatter in the dwell time data for the various tests and no obvious differences between the dwell time for the aluminum and CE panels. Sufficient data are not available to establish dwell time vs velocity curves for the individual panels. However, when all of the data at the various speeds are averaged, the general trend of decreasing dwell time with increasing wind velocity becomes apparent, as shown in Figure 19.

Arc Reattachments. There does not appear to be an obvious correlation between wind speed and the number of reattachments down the length of an unbolted panel. The paint, however, does provide a dielectric layer which must be punctured by sufficient voltage before arc reattachment can occur. Thus, the unpainted panels, both aluminum and C/E each had approximately twice as many attach points

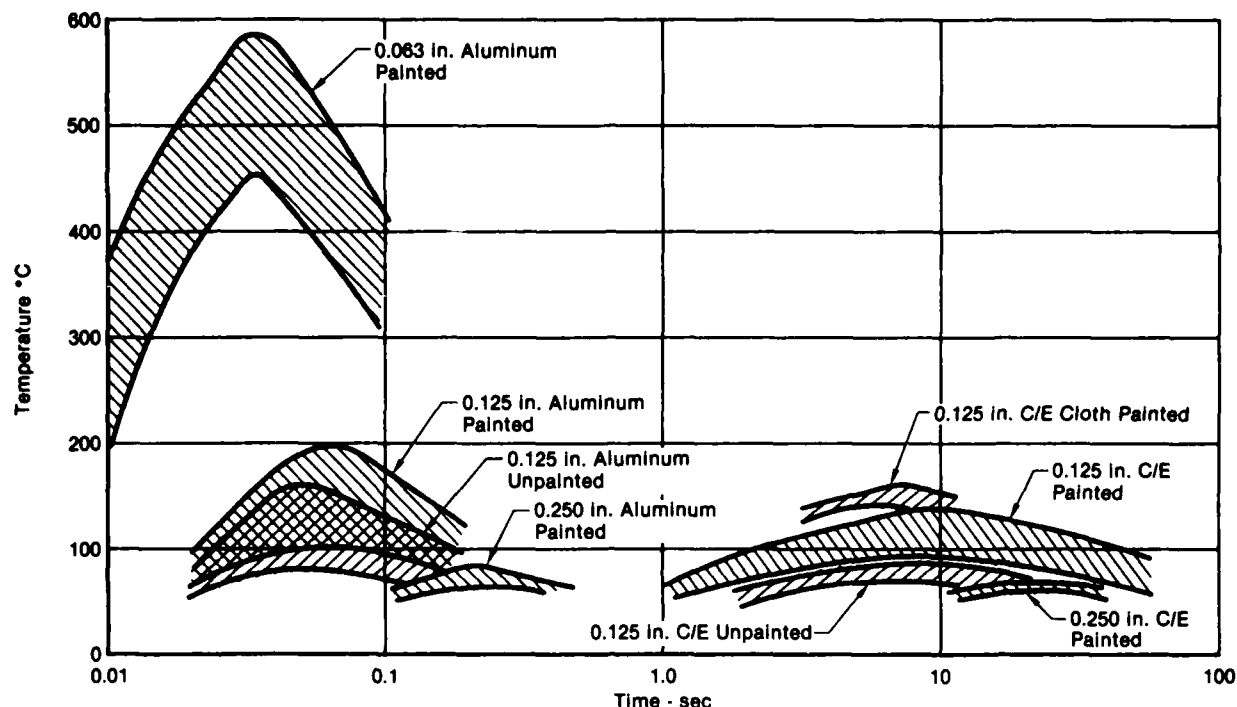
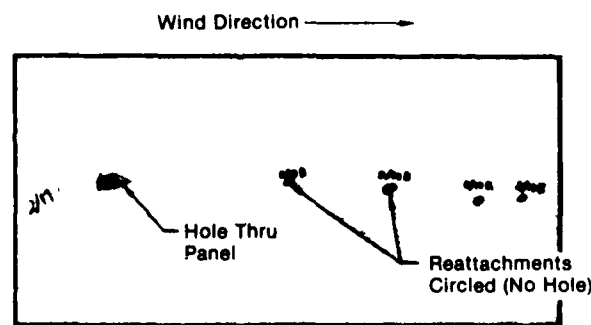


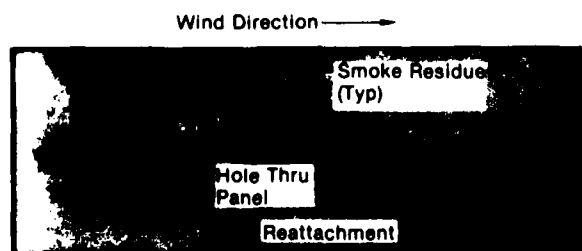
Fig. 16 Summary of Hot Spot Temperature Versus Time for Swept Stroke Tests

GP41-0272-20



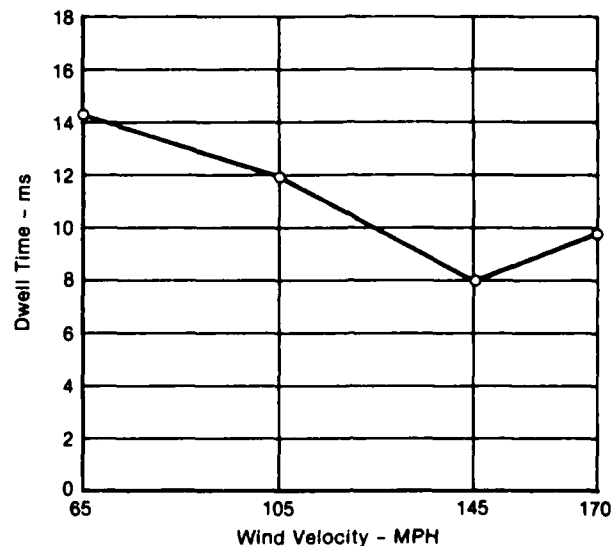
GP41-0272-21

Fig. 17 Portion of Aluminum Panel (0.030 inch) After Testing



GP41-0272-22

Fig. 18 Portion of C/E Tape Panel (0.090 inch) After Testing



GP41-0272-23

Fig. 19 Average Dwell Time of Initial Attachment for All Tested Panels Versus Wind Velocity

Fasteners. There appears to be an obvious preference of the arc to attach to fasteners as opposed to attaching to the section between fasteners even though the heads of the fasteners constitute only a small area of the panel and did not protrude above the panel surface. For example, the 0.125-inch-thick aluminum and 0.125-inch C/E panels with fasteners are shown in Figures 22 and 23. From these photos it is obvious that these small discontinuities in the panel or paint are significant as far as arc attachment is concerned. Of the 24 reattachments to the bolted

down the length of the panel as did the painted panels, as seen in Figure 20. Typical photos illustrating these effects are shown in Figure 21.

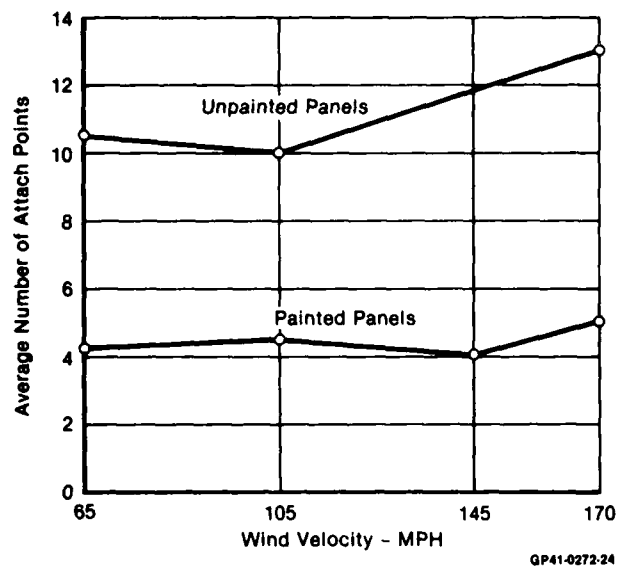
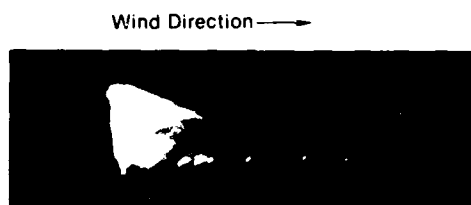
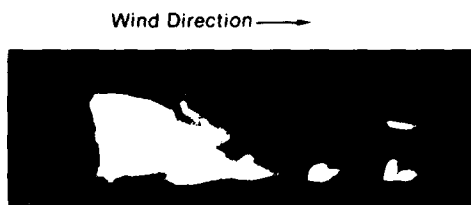


Fig. 20 Comparison of Painted and Unpainted Panels for Average Number of Attach Points



A) Unpainted 0.125 in. Thick Aluminum Panel, 170 MPH Air Velocity (11 Closely-Spaced, Discrete Attachments)



B) Painted 0.125 in. Thick C/E Panel, 65 MPH Air Velocity (Five Attachments With Some Burning Along the Carbon Fiber Direction at the Reattachments)

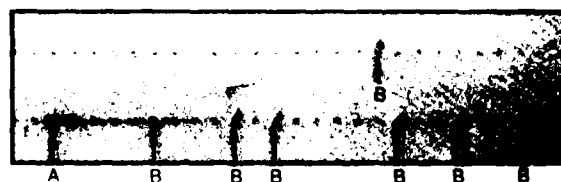
QP41-0272-25

Fig. 21 Typical Still Photographs of Blown Arc Attachments

aluminum panel, only one of these was to a location not occupied by a bolt. Similarly, of the 26 reattachments to the C/E panel, only two were to locations other than fasteners.

Sparking. Sparking on the rear of the panels without fasteners was only observed when a panel was completely punctured or burned through. The 0.125-inch tape C/E panel did exhibit some slight rear surface delamination, but the panel was not punctured and no sparking was observed.

Sparking was noted for the tests of panels with fasteners. Two of the five tests to the aluminum panel showed sparks on the photographic film and four of four tests to the C/E panel sparked.



A - Initial Arc Attachment
B - Arc Reattachments

QP41-0272-26

Fig. 22 Portion of Bolted Aluminum Panel After Testing



A - Initial Arc Attachment
B - Arc Reattachments

QP41-0272-27

Fig. 23 Portion of Carbon Epoxy Bolted Panel After Testing

DISCUSSION OF TEST RESULTS

All of these tests were conducted with the test sample temperatures initially at approximately 20°C or cooler. In order to apply the temperature curves given in Figure 16 to aircraft "wet wing" applications, the curves may have to be shifted upward by 100°C or more to account for temperature increases caused by aircraft setting in the sun and heating caused by the aircraft flying.

Most of the data showed that aerodynamic cooling of the strike area was apparent and increased with windspeed. However, a few instances did not show this phenomena. For example, the 145 mph test of the 0.125-inch-thick unpainted panel showed that its "hot spot" was cooler than the 170 mph test. After the test, it was noted that there were three initial attach points for the arc which were very close together but not close enough to be considered as one. Therefore, since each of these three areas were absorbing some of the heat energy, it is logical that the temperature of any one of them would be less because of the "sharing" of the input.

The 0.063-inch painted aluminum panel behaved differently than expected. In three of the tests of this panel, only one attach point was noted. There was no apparent reason for this behavior since the panel was tested the same as all of the others. The strike surface of this panel was melted at the attach point over a diameter of approximately a 0.15 inch and the rear surface was melted and pimpled over approximately a 0.05-inch diameter, but no hole was produced. In these instances the wind velocity had very little effect on hot spot temperature as also observed by the in-

investigators of Reference 4. Except for this one panel, the hot spots were cooled by the wind but not as much as reported in Reference 3. Since this panel exhibited rear surface melting, it was expected that the temperature measurement would have indicated a temperature 50 to 75°C higher than measured. This apparent anomaly can probably be accounted for by the fact that the melted area on the panel only covered a portion of the area seen by the IR detector at the instant the scan traversed the hot spot. In other words, the IR system "averaged" the temperature of an area larger than the hot spot and since part of this area was "cold," the indicated temperature would be less than the hottest temperature of the hot spot. Another possible explanation is that the black paint on the rear of the panel may have deteriorated at the high melting temperature of the aluminum and not remained in good thermal contact with the panel. This would then result in a lower indicated temperature.

The puncture test results of aluminum as compared to C/E were expected because similar results had been previously reported in Reference 10. However, the previous data did not make direct comparisons of identical thickness materials.

The average dwell time observed during these tests was longer than that noted during tests utilizing an enclosed wind tunnel^(3,11). For the 0.063 inch painted aluminum panel, the dwell time was generally in agreement with Reference 4 where the arc was blown off the rear edge of the test panel before extinguishing.

SUMMARY

These tests have illustrated some of the similarities and differences between aluminum and C/E materials when subjected to swept stroke lightning. In general, it takes 100 times longer for the hot spot on C/E to reach maximum temperature as compared to aluminum, and the aluminum gets hotter than the C/E. Aluminum is penetrated by the continuing current (Component C of MIL-STD-1757), and C/E is penetrated by the high-current pulse (Component D) of a lightning strike. In general, wind velocity affects the hot spot temperature in that it cools the panel and results in a lower hot spot temperature. A painted surface at the strike area results in higher hot spot temperatures. The arc dwell time for aluminum and C/E is approximately the same, and the dwell time generally decreases with increased wind velocity. In a panel with fasteners, the swept arc has a tendency to attach to the fasteners regardless of panel material.

References

1. "Protection of Aircraft Fuel Systems Against Lightning," FAA Advisory Circular 20-53, October 1967.
2. "Lightning Qualification Test Techniques for Aerospace Vehicles and Hardware," MIL-STD-1757A, July 20, 1983.
3. J. D. Robb, T. Chen: Integral Fuel Skin Material Heating from Swept Simulated Lightning Discharges IEEE Int. Symposium on EMC 1977.
4. J. A. Dobbing and A. W. Hanson, "A Swept Stroke Experiment With a Rocket Sled," In Proc. 1978 IEEE Int. Symp. Electromagn. Compat., Atlanta, GA, July 1978.
5. "Lightning Effects on Composite Material Fuel Tanks," Report No. NADC-83106-20, Naval Air Development Center, Warminster, PA, August 5, 1983.
6. D. W. Clifford, K. E. Crouch, and E. H. Schulte, "Lightning Simulation and Testing," IEEE Transactions on Electromagnetic Compatibility, Vol. EMC-24, No. 2, May 1982.
7. D. W. Clifford, "Laboratory Simulation of Swept Lightning Strokes," in Proc. Conf. Certification Aircraft Lightning Atmosp. Elec. Hazards, ONERA, Chatillon, France, Sept. 1978.
8. E. H. Schulte, "Updating the MCAIR Lightning Simulation Laboratory," in Proc. 8th International Aerospace and Ground Conference Lightning and Static Electricity, Fort Worth, Texas, June 1983.
9. E. H. Schulte and G. W. Kamerman, "A One Megajoule Lightning Simulator," FAA/Georgia Institute of Technology, Workshop on Grounding and Lightning Protection, May 1978.
10. E. H. Schulte, "Effects of Lightning Waveform Components on Graphite/Epoxy Material," Society for the Advancement of Material and Process Engineering, 23rd National Symposium, Anaheim, California, May 1978.
11. L. L. Oh and S. D. Schneider, "Lightning Strike Performance of Thin Metal Skin," 1975 Conference on Lightning and Static Electricity, Culmham Laboratory, England, April 1975.

COMBINED MECHANICAL-ELECTRICAL IGNITION HAZARDS
TO CARBON-REINFORCED COMPOSITE FUEL TANKS

J. D. Robb, Lightning & Transients Research Institute
St. Paul, MN, USA

T. S. Lee, Institute of Technology, University of Minnesota
Minneapolis, MN, USA

ABSTRACT

Lightning strikes to carbon-reinforced composite (CRC) fuel tank skins can introduce ignition hazards through a combination of effects: the mechanical separation of the fibers and the subsequent sparking across the resultant gap from ohmic drop voltages. A lightning return stroke deposits heat energy in a thin layer adjacent to the exterior free surface of a CRC skin. The resultant thermoelastic wave system marching inward is characterized by a leading shock front supported by a compression phase which in turn is followed by a rarefaction phase. Upon subsequent reflection at the interior free surface of the tank skin, the compression-supported shock wave creates a strong backward-propagated rarefaction wave. The subsequent near coincidence and interaction of the two indicated rarefaction effects lead to strong transient tensile stresses in a region distinct from but close to the interior free surface, causing local material separation. The high current densities combined with the deeper current skin depth of the CRC materials can result in ohmic drop voltages sufficient to spark across fiber separation gaps. The various phases of the hazard phenomenon are illustrated in the evaluations of the shock dynamics and the internal potential differences. The expected mechanical-electrical effects have been observed in actual lightning tests of CRC skins.

INTRODUCTION

THE INTRODUCTION of carbon-reinforced composite materials (CRC) presents new possible problems in aircraft integral fuel tanks. Lightning discharges swept over the fuel tanks surfaces can provide both shock wave damage in the inside surface to expose graphite fibers and the current penetration to cause sparking between the exposed fibers. With CRC materials, the local tensile strength between fibers will be a fraction of the strength along the fibers and therefore the shock wave magnitudes will be about comparable to the tensile strength between fibers and cracks can result. With metals, the tensile strength in any direction is well beyond the magnitudes of the shock except for thin materials and tearing of the metals from lightning strike current is not often seen.

A brief study has been carried out to evaluate the magnitudes of the problem.

BASIC MECHANISMS

A lightning return stroke deposits heat energy in a thin layer adjacent to the exterior free surface of a CRC fuel tank skin. The resultant thermoelastic wave system marching inward is characterized by a leading shock front supported by a compression phase which in turn is followed by a rarefaction phase. Upon subsequent reflection at the interior free surface of the tank skin, the compression supported shock wave creates a strong backward-propagated rarefaction wave. The subsequent near coincidence and interaction of the two indicated rarefaction effects lead to strong transient tensile stresses in a region distinct from but close to the interior free surface, causing local material separation, as illustrated in Figure 1. The high current densities combined with the deeper skin depth of the CRC materials can result in ohmic drop voltages sufficient to spark across internal fiber separation gaps. The various phases of the hazard phenomena are illustrated in the discussions of the shock dynamics and the internal potential differences.

SHOCK MECHANISMS—The shock propagation for elastic waves can be evaluated as follows. The transit time and heat diffusion time from the outer surface to the inner surface as shown in Figure 1 are:

$$\begin{aligned}\bar{t} &= b/v = \text{transit time} \\ t' &= (b/\chi)^2 = \text{thermal diffusion time through plate}\end{aligned}$$

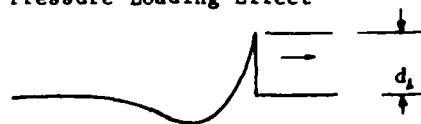
where

$$\begin{aligned}b &= \text{thickness of the skin} \\ v &= \text{velocity of the dilatational elastic wave} \\ \chi^2 &= \text{thermal diffusivity}\end{aligned}$$

Consider $t_0/\bar{t} \ll 1$ and $t_0/t' \ll 1$, where t_0 = time of current impulse duration.

The stress wave train can be considered to be approximately the superposition of two effects. These are:

a. The Pressure Loading Effect

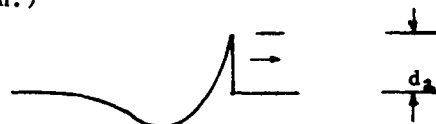


The magnitude of the stress wavefront is of the order of the external pressure pulse (100 atmospheres)

$$d_1 = P_0.$$

As an example, the stroke pressure of typically 150 atmospheres or 2250 psi would be doubled at a reflection surface to a tensile stress of about 4500 psi which is comparable to the tensile stress of the epoxy materials used to hold the graphite fibers of the CRC material together. Thus the shock pressures are of the order of magnitude required to separate the fibers at the interior surface of the skin.

b. The Thermo-elastic Effect (from heat deposition.)



This effect, thermal shock [1], is similar in waveform. The front strength is

$$\begin{aligned}d_2 &= E\alpha T/(1 - m), \\ &= 13363 \text{ psi}\end{aligned} \quad (1)$$

where T = temperature rise (est at 1500 C)

E = effective elastic bulk modulus ($\approx 10^6$)

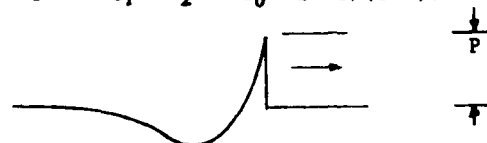
α = thermal expansion coefficient ($\approx 6 \times 10^{-6}$)

m = Poisson's ratio. ($\approx .3$).

The spacial extent of the two wavetrains are comparable in distance as they are caused by the same energy source. The thermal shock will produce a similar wave as the pressure loading and again, an enhancement of the rarefaction wave will be seen at the reflection surface as a nearly double tensile stress.

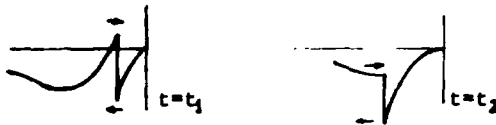
The composite pressure (based on a linear superposition) is

$$P \approx d_1 + d_2 = P_0 + E\alpha T/(1 - m).$$



The wavetrain is now sketched for two instants

of time, t_1 and $t_2(>t_1)$, following reflection at the free surface :



And the total tensile stress is:

$$\sigma = 2 [P_0 + E \alpha T / (1-m)].$$

Thus, the strength of the shock wave is the approximate sum of the two effects, the loading pressure from the arc channel and the thermo-elastic pressure from the thermal expansion of the heated outer surface layer.

c. Plate Deflection

Sections a. and b. above refer to the area in the immediate vicinity of the lightning channel. Also of interest is the "hoop stress" as a result of the skin deflection and stretching from the lightning channel impact.

Upon a concentrated stroke, the skin will be deflected substantially in the manner of a loaded thin plate. This will result in additional tensile stress on the inner surface as illustrated in Figure 2 [2].

For example, with the typical severe arc channel pressure of 150 atmospheres or 2250 psi, a deflection radius of 2 inches, a panel thickness of 0.05 inch and an elastic modulus of 50×10^6 , the tensile stress at the inner surface would be:

$$S = [3(1+m)P/(2\pi b^3)] / [\ln(r/a) + a^2/4r^2]$$

$$= 4462 \text{ psi}$$

where

- m = Poisson's ratio (.3)
- P = channel total load (2250 psi x .4 x .4)
- b = skin thickness (.05 inch)
- r = effective plate radius (2 inches)
- a = radius of channel (.02 inch)

This stress level is again of the order of the epoxy material which binds the graphite fibers together in the composite matrix.

These three effects, singly or in combination, can cause cracks in the inner skin between fibers. Numerical evaluation of these effects indicates that the tensile stress from each effect is of the order of the tensile strength of the epoxy material used to hold the graphite fibers together. The conclusion drawn is that cracking of the inner surface of a CRC material can occur along the direction of the fibers.

CURRENT DISTRIBUTION IN THE SKIN - The three-dimensional current flow in the composite material can be approximately calculated for illustration by assuming an isotropic medium and using a quasi-static configuration.

There will be a current null at the center of the inside surface as shown in Figure 3. The solution for the current flow relationships in this stagnation region may be obtained through analogy with the solution of incompressible stagnation flow following a fluid discharging from an orifice into a region of space between two impermeable parallel bound surfaces [2].

The quasi-static electric current density \vec{J} is divergence-free. In addition, because of axial symmetry with

$$\vec{J} = J_r \hat{r} + J_z \hat{z},$$

we may express it in terms of a Stoke's stream function $\psi(r,z)$ through

$$\vec{J} = \text{curl} [(\psi/r) \hat{\phi}]. \quad (2a)$$

For the stagnation region, it is known [2] that ψ is of the form

$$\psi = k z r^2, \quad (2b)$$

where k is a constant. Constant - ψ curves are hyperbolas in Figure 3. An electric potential V, likened to the "velocity potential" in fluid mechanics, is governed by the Laplace equation

$$\nabla^2 V = 0.$$

Ref. 2 also provides its solution as

$$V = k[(r^2/2) - z^2].$$

A few of these equipotential surfaces have been indicated as dotted curves in Figure 3. To determine k, we propose the following scheme: Assume that on the outer surface ($z=b$), a total current of I amperes is injected within a radius of a and that the stagnation solution applies throughout the region of the plate for $r \leq a$. Take circular contour C on the outer surface at radius $r = a$. The contour integral

$$\oint_C [(\psi/r) \hat{\phi}] \cdot d\vec{l} = [\psi(a,b)/a] 2\pi a = 2\pi k b a^2$$

is taken around C in an increasing - ϕ direction. By Stoke's theorem, this is identical to

$$\int_S \text{Curl} [(\psi/r) \hat{\phi}] \cdot d\vec{s} = \int_S \vec{J} \cdot d\vec{s} = -I,$$

where S is the disk surface (facing up) bounded by C. By equating the two, we obtain

$$k = -I/2\pi b a^2.$$

Hence, by (2a) and (2b), we arrive at the surface current density

$$J_r = (I/2\pi b a^2) r. \quad (3a)$$

The global relationship of the inner surface current density is now sketched in Figure 4. The inverse- r decay in the far field is due to the cylindrical expansion of the cross sectional area through which the current flows away uniformly. The near zone solution is that which was derived in equation (3a).

Thus,

$$\begin{aligned} \text{Far Field: } J_r &= I/2\pi b r \\ \text{Near Field: } J_r &= (I/2\pi b a^2) r. \end{aligned} \quad (3b)$$

It is seen from Figure 4 that, when these two curves are extrapolated, their intersection is at $r = a$. Thus, the interior surface current density would peak near $r = a$, which is equal to the radial dimension of the lightning arc on the outer surface, with a magnitude of the order of $I/2\pi b a$.

It is of interest to note the inner surface field strength. Here,

$$E = (1/\sigma) J_r \quad (\sigma = \text{conductivity}).$$

For small conductivity σ , the electric field E could be very large near the gauge distance, ($r=a$), which is of the order of

$$I/2\pi b a \sigma.$$

For typical severe lightning strike currents of 100,000 amperes, the inside surface field could be very great and might exceed the critical breakdown electric field for air. Inside streamering might occur for special geometries and for other materials such as boron and this streamering would not necessarily be photographed with present photographic plasma detection techniques but it could have sufficient energy to ignite flammable fuel mixtures.

These calculations used a quasistatic current distribution and an assumed isotropic material. With the much reduced conductivity in the z direction, the inside fields would be reduced and for this reason, additional work is needed with solutions for non isotropic or layered materials.

SUMMARY AND PRACTICAL IMPLICATIONS

The results of the above considerations indicated that lightning shock wave assembly could produce large tensile stresses on the internal surfaces and large electric fields which could spark across fibers exposed in any internal surface cracks.

This effect has been seen in tests of CRC materials and is illustrated in Figure 5, showing both the inner surface cracking and the sparking.

CONCLUSIONS

The combination of shock wave damage to the inner surface of thin fuel tank walls and the sparking which can be caused between exposed fibers is an effect which must be recognized in the design of lightweight CRC aircraft fuel tank skins. Of concern also is the conclusion that without external metallization of some type, the internal electric fields could exceed the critical breakdown level and cause ignition of flammable fuel mixtures with high resistivity materials or special geometries. Further work is planned to quantify these results by considering the non isotropic nature of CRC materials and electromagnetic skin effect on current penetration.

REFERENCES

1. Manson, S. S., Thermal Stress and Low-cycle Fatigue, McGraw-Hill Book Company, New York 1966, p.286
2. Eschbach, O.W., Handbook of Engineering Fundamentals, McGraw-Hill, New York, 1975, p.543
3. Batchelor, G. K., An Introduction to Fluid Dynamics, Cambridge University Press, New Rochelle, N.Y., 1970, p.78 & p.105.

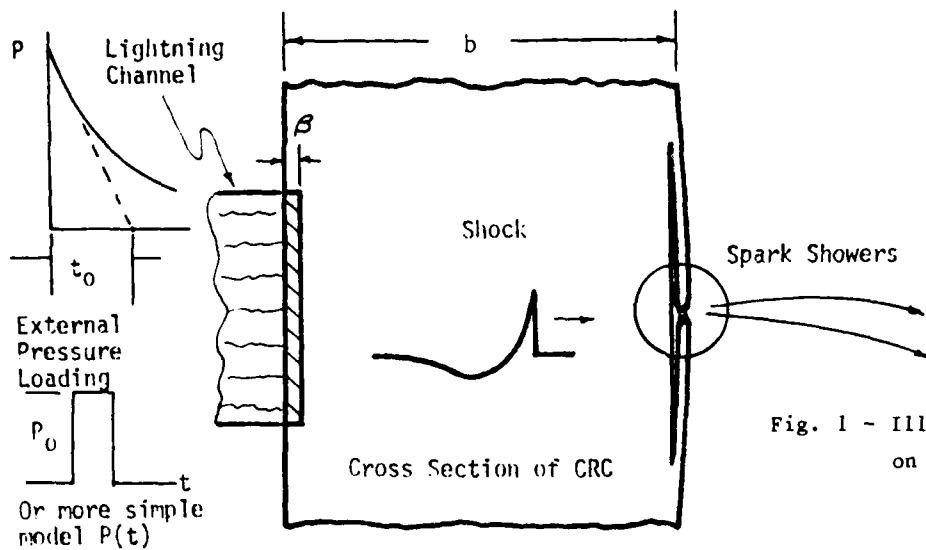


Fig. 1 - Illustration of shock effect on brittle material

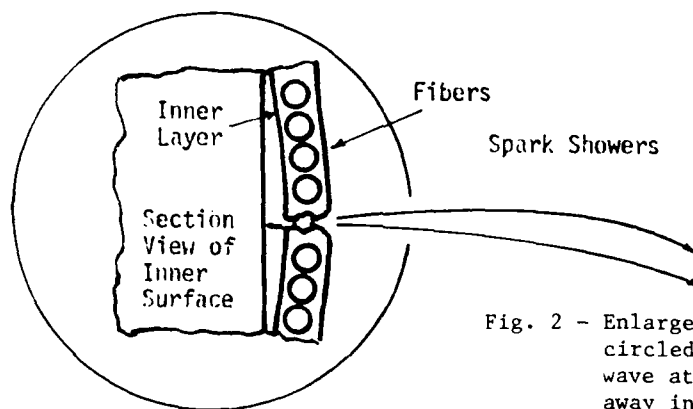


Fig. 2 - Enlarged view of failure region circled in Figure 1. Rarefaction wave at inner surface breaks away inner layer.

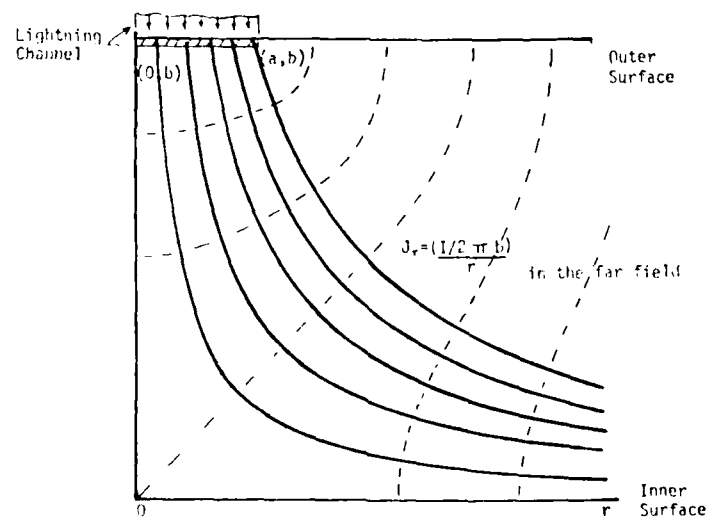


Fig. 3 - Quasi-static current flow in the stagnation region

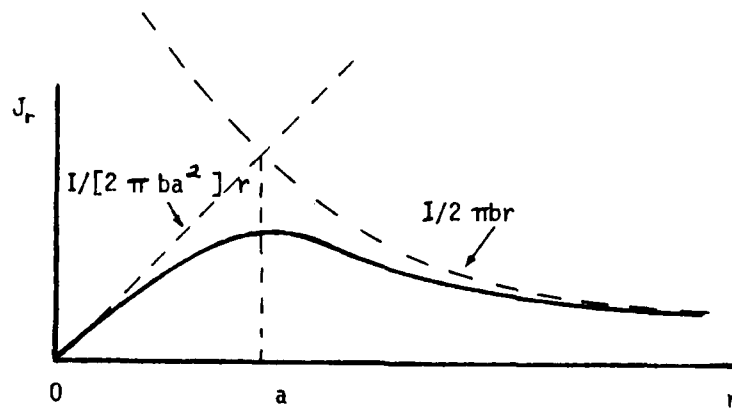


Fig. 4 - Current density variation with radius in the near zone and the far zone

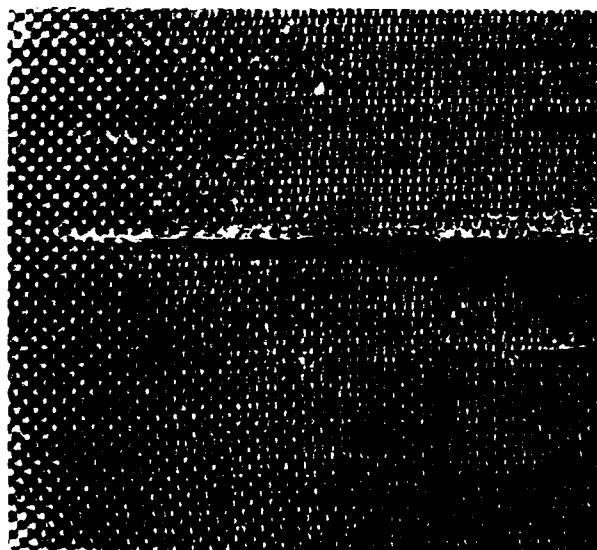


Fig. 5a - Photograph of crack on interior surface of CRC material



Fig. 5b - Photograph of sparking at interior crack in CRC material

MEASUREMENT OF LIGHTNING STROKE CURRENT IN WINTER SEASON AT MAKI, JAPAN

K. Narita, Y. Goto and R. Funayama*

Department of Electrical Engineering, Tohoku University, Sendai 980, Japan
Tel. 0222-22-1800 Ext. 4243

*General Research Center, Tohoku Electric Power Co., Inc. Sendai 980, Japan
Tel. 0222-78-0356

ABSTRACT

To measure lightning current waveforms having a long duration, a digital recording system which is controlled by a microcomputer has been developed. The lightning currents are measured by means of both a current shunt and a Rogowski coil. The current waveforms measured by this system in winter thunderstorms are tentatively classified into five types. Especially both the bipolar strokes and the strokes with these continuing currents have been observed frequently.

1. INTRODUCTION

In winter season, numerous frontal thunderstorms occur at the north west coast, Japan. For the purpose of the investigation of the lightning parameters in winter season, the lightning currents to a meteorological observation tower, which is about 150 m in height and has been elected on a hill look on Japan Sea at an altitude of 125 m about sea level, have been measured since the winter of 1976/77. This current measurement has been supported with the photograph of flashes to the tower taken by both still cameras and a video camera. The measured results using magnetic links, a magnetic tape recording device and an oscilloscope with a recording camera had been reported [1].

From the results of the lightning observation for six seasons (1976-1982), it has become clear that the majority of the flashes, which would have struck the surrounding area, were attracted to the top of the tower, hitting not only the installed lightning rods but also several other extruding portions of the tower top. In addition to the digital recording system using the coaxial type shunts for the current pickup sensors, the similar digital recording system has been developed for measuring total lightning currents to the tower. The former system consists of two coaxial shunts, a digital clock, a trigger generator, an opto-electronic transmission system, three digital transient memories, dual 8" floppy disk units and its controller using a micro-processor. The latter system consists of five Rogowski type coils, an integral unit, an opto-electronic transmission system, two digital transient recorders and a micro-computer with a digital cassette data-recorder, and it has been used for the observation since the winter of 1982.

At present, the latter system has been modified so as to measure a concurrent electric field change with a stroke to the tower.

Using the Rogowski coils for the current pickup sensors, this system has attained two important merits i.e. being both economical and reliable because of thermal destruction of the current sensors. However, the frequency range of this system is limited in both directions. This is suitable for the measurement of impulse currents but not of continuing currents.

We would like to report on the aspects of these systems and the results obtained for winter lightning currents.

2. OBSERVATION POINT AND TOWER

The lightning observation point "Maki" is located 30 km south west of Niigata along Japan Sea shore as shown on a map of Japan (Figure 1) and this point has been a same

point which had been called "Kakumi" before.

The most thunderstorms which attack Maki area are frontal storms in winter season. It is caused by the instability released through ascent of air along frontal surfaces. Consequently, the lightning stroke to the tower has not been observed yet in summer.

The meteorological observation tower is 150 m in height and has been constructed of triangular three steel pipes and steel lattice angles and supported by 12 steel wire stays (4 stays for each pole) on a hill at an altitude of 125 m above sea level. The configuration of the tower is shown in Figure 2, with the position of magnetic links. The shielding ring is installed just above the anemometer for perfect protection against the lightning and a lightning rod is added at the ring for measuring the lightning currents.

3. RECORDING SYSTEM FOR LIGHTNING CURRENT WAVEFORMS

Two measuring systems have been prepared to record the wave shape of the lightning current. The first system (system 1) utilizes five Rogowski-coils which were installed around the current paths of the tower top and this system was developed by Tohoku University. Another system (system 2), which have been used by Tohoku Electric Power Co., Inc., utilizes two coaxial current shunts which were installed below the lightning rods. Of this system, the digital recording system was manufactured by Matsushita Electric Industrial Co., Ltd (Panasonic), and the opto-electric system with the shunts was manufactured by The Fujikura Cable Works, Ltd. The schematic block diagrams of these systems are shown in Figure 3 and Figure 4.

3.1 CURRENT SHUNTS

As two lightning rods are furnished to the tower, two coaxial current shunts, having a heavy current duty, were prepared. The inner conductor of the shunt is connected to the lightning rod and the outer is terminated to the tower body. The maximum currents, its resistances and dissipation losses are 100 kA, 0.002 ohm, 10 kJ and 50 kA, 0.004 ohm, 10 kJ respectively, each response time was below 100 ns. These shunts were manufactured by Tokyo Transformer Co., Ltd.

3.2 ROGOWSKI COIL

The flashes to the tower had not only struck the lightning rods but also the other exposure portions of the tower top.

It was found that the greater part of the lightning current flowed through the tower body and the stay wires to earth and the current flowing through the down conductor was less than 10 % of the total current, therefore the lightning conductor current was neglected in this system. Two kinds of Rogowski coils which pick up the lightning current are

installed around three main steel columns and two slant poles of the tower respectively, and they are designed carefully to induce the same voltage for the same currents. To obtain the total lightning current striking the tower, those coils are connected in series. Figure 5 shows the configuration of the tower top portion and the positions of Rogowski coils.

3.3 SIGNAL TRANSMISSION SYSTEM

In the system 1, the induced voltage signal is converted to a pair of light signals for positive and negative currents with a complimentary transistor circuit which is loaded with two LEDs. The positive or negative analog signal is transmitted to the measuring room via the optical fiber cable. Transmission loss of the cable is 3.4 dB / 800 m. In the room, the light signals are inverted again into the electrical signal by two photo-diodes and operational amplifiers whose band width is from DC to 300 kHz.

The electrical signal is branched into two transient recorders and a trigger generator consisting of a window comparator circuit, which generates the trigger pulses for transient recorders.

In the system 2, the voltage signal across the shunt is converted to light signals. A LED is driven by continuous current at all times and the electrical signal is superimposed upon its bias current of LED, so the maintenance of the battery is a difficult task. The converted light signals are transmitted to the measuring room as the same way of system 1.

3.4 TRANSIENT RECORDERS AND CONTROL SYSTEM

Two kinds of transient recorders are used in the system 1. They have memory capacities of 4 kW and 8 kW, each 8 bits per word and the minimum sampling time of 50 ns and 1 μ s respectively.

When a lightning current signal exceeds the chosenthreshold level of the window comparator, a trigger pulse is generated and starts the transient recorders on a data storing. The digital data of both transient recorders are transferred to a magnetic tape by the micro-computer. The digital data recorder can record the 19 lightning events (the total record is 228 k byte).

To obtain the more precise waveforms of the lightning current, the memory of the fast transient recorder was divided to four parts (1 kW/part) and sampling time of 0.2 μ s was selected. To clarify the multi-stroke and the continuing current, the slow transient recorder was operated with sampling time of 20 μ s and the waveforms was stored into the memory from 40 ms before the trigger to 120 ms after the trigger for each lightning event.

In the system 2, three transient recorders are used. They have memory capacities of 32 kW, 32 kW and 64 kW, 8 bits per word and the minimum sampling time of 100

ns. The memories in first and second recorder are divided into five parts, therefore five strokes are stored separately in one flash. Third recorder is prepared for a multiple stroke or a continuing current. Obtained digital data are transferred to dual 8" floppy disks by the micro-computer. Two floppy disks are capable of recording 8 flashes.

3.5 IMPROVED RECORDING SYSTEM

The improved digital system of the system 1 for recording the electric field changes concurrently with the current waveforms has been developed. The electric field changes are detected by use of a slow antenna. The schematic block diagram of this new system is shown in Figure 6. For an accurate measurement of the lightning current, a new transient memory which has a memory capacity of 16 kW, 12 bits/word is prepared. Moreover the digital magnetic recording unit using a cartridge tape (ISO standard) has been introduced. This unit has a recording capacity of 20 Mbyte and a high data transfer rate (87.77 kbyte/sec). For carrying this improvement, 500 flashes are recorded in one magnetic tape.

4. LIGHTNING PEAK CURRENT BY MAGNETIC LINK

Using a magnetic link, the accurate measurement of complete current which flows to ground through the tower is a difficult work because of the complex configuration of the tower top and the many paths of current. In order to estimate the whole current flowing to the ground, 50 magnetic links are mounted on various 23 points in the tower. The peak current was estimated by a sum of the crest values of the currents flowing through the individual 14 paths of the tower. The current in each paths were determined from the reasonable current distribution in the tower from the records of magnetic links of various points in the tower.

Of the 40 flashes, 63 % were negative polarity, 28 % were positive one and remaining 10 % were too small to determine their polarities and peak values. Our measurement had started from the winter of 1976/77, however, the data by magnetic links are not many. Because that the exchange of magnetic links is a hard task on every thunderstorms, as many magnetic links are installed at various positions of the tower. Moreover, it has been revealed that the both polarity lightnings strike the tower frequently in one thunderstorm. Therefore the obtained data from magnetic links may be recorded by many lightning flashes and they show the last maximum current probably.

The consequent cumulative frequency distributions of the peak current amplitude for negative polarity and positive one are shown in Figure 7 with the other measurements [2].

5. CURRENT OSCILLOGRAM

By the use of Rogowski coils, 18 records were obtained in the period from December 1982 to November 1983. Typical oscillograms are shown in Figure 8 and 9. Of the recorded current waveforms, 67 % is a multiple stroke, and 50 % possesses a continuing current. While a bipolar stroke is 22 %. These percentages are over-counted in calculations.

Because the negative charge region (about -10°C) is lowered in its altitude, the strokes to the tower tend to be similar to an intracloud discharge [3]. It is the reason why a continuing current occurred frequently.

As shown in Figure 9, our observed current waveforms are classified into following five types;

(A) positive single-peak wave like a standard impulse

(B) negative single-peak wave like a standard impulse

(C) multi-peak irregular waveforms observed in lightning current to mountain tops by Berger (1977)

(D) negative single-peak wave with these continuing current

(E) bipolar wave [4].

The mechanism and the cause of the occurrence of the lightning currents of these five types, especially, those of type (E), recorded in winter thunderstorms, have been not sufficiently studied yet. The obtained bipolar strokes can be classified into two types. One is the case that a lightning current flows oscillatory. The other type is that the opposite polarity strokes follow after several strokes. This sample is shown in Figure 10.

6. LIGHTNING PHOTOGRAPH BY VIDEO CAMERA

The record of the new system has not been recorded by the trouble, but in the system 2, the current oscillogram had been obtained simultaneously with both a still photograph and a video image. The video recording system is operated in a NTSC mode (EIA standard), so the interval time of its frames is 1/60 ms. This video system consists of mono-chromatic ITV camera and beta format video tape-recorder (1/2" cassette magnetic tape). The total recording time is maximum 5 hours by the use of a L830 tape.

The obtained video image is shown in Figure 11 with the oscillogram. This shows multiple stroke flash having two strokes.

The recording time can be elongated to 20 hours adding the automatic cassette changer to the video recorder. Therefore the video system is useful for the lightning observation.

7. CONCLUDING REMARKS

The automatic digital recording systems

for lightning current waveforms have been developed and its aspects have been described.

The field measurement performed at the top of the high tower for winter thunderstorms, confirmed that this system was fully capable to record automatically the lightning current waveforms. The current waveforms thus obtained for winter lightnings are tentatively classified into five types.

To clarify the winter lightning characteristics, further accumulation of data in various conditions is needed. The current waveform observation by these systems made for the first time at Maki in December 1982, will be continued.

We firmly believe that the winter lightning characteristics will be made clear by the simultaneous measurement of lightning current waveforms and an electric field change. An electric field measuring system used from November 1983. However, for the trouble shooting of the system, any data have not been obtained

ACKNOWLEDGEMENTS

This work was carried out by the financial support for Science Research, the Education Ministry of Japan, under the grant-in-Aid of Special Research for Natural Disaster (2), Project number 58025001 (1983).

The authors wish to express their hearty thanks to the associates of Nuclear Power Engineering Department, Tohoku Electric Power Co., Inc. for a support. The authors also wish to thank Mr. Shimizu who took many still photographs at midnight under severe weather, Mr. Takaya for kindly help and advice.

REFERENCES

1. Y. Goto, F. Naito, K. Narita and T. Sato, "The observation of lightning discharges in winter thunderstorm at the Niigata coast, Japan", Proc. Int. Aerospace Conf. on Lightning and Static Electricity, A-3, 1982.
2. R.H. Golde, "Lightning", Academic Press, 1977.
3. M.A. Uman, "Lightning", McGraw-Hill Book Company, 1969
4. K. Berger, "Novel observations on lightning discharges: Results of research on Mount San Salvatore", J. Franklin Inst., 283, 1967

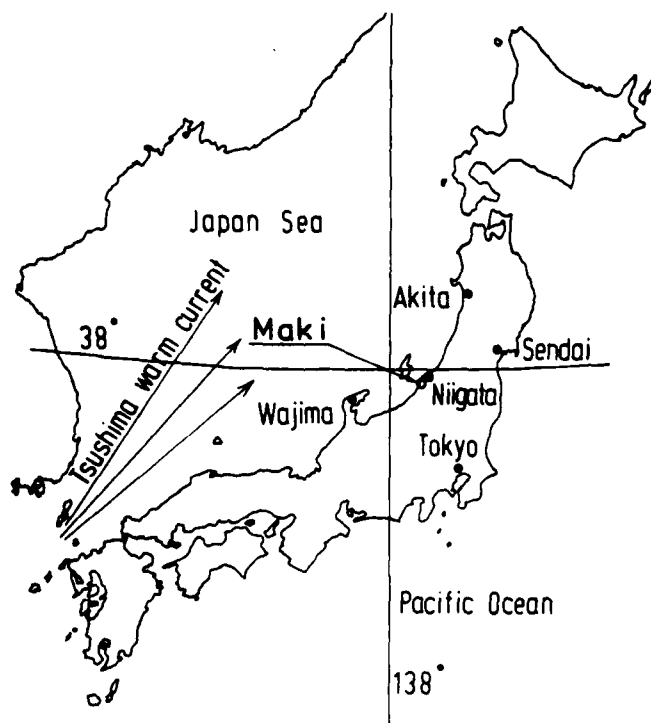


Fig. 1 - Location of observation point "Maki" on map of Japan

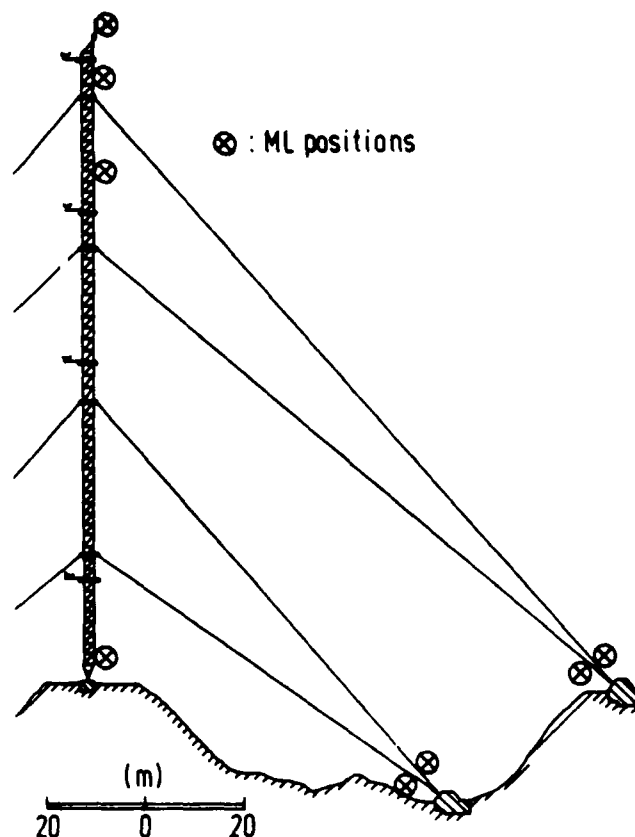


Fig. 2 - Meteorological tower and position of magnetic link

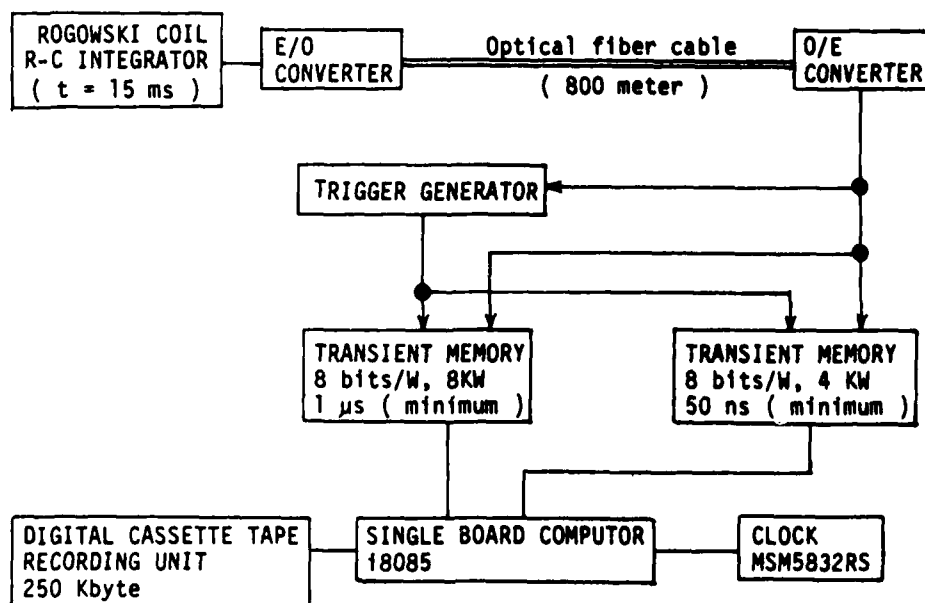


Fig. 3 - Schematic block diagram of system 1

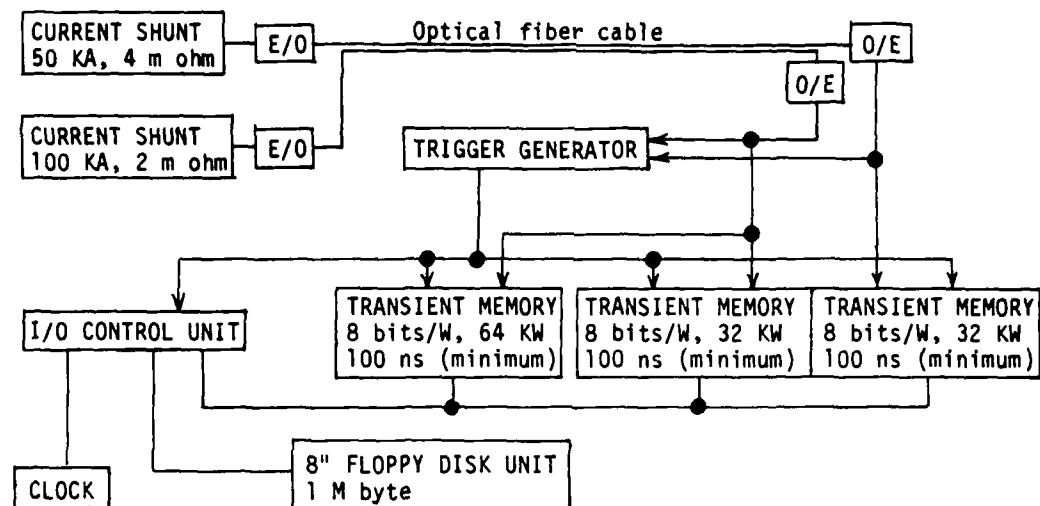


Fig. 4 - Schematic block diagram of system 2

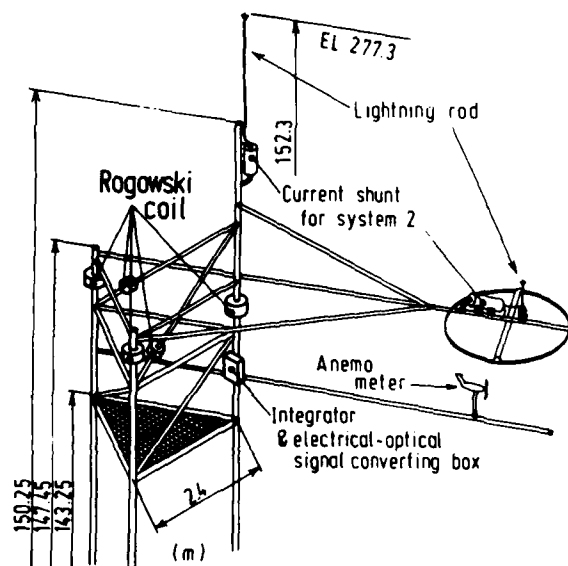


Fig. 5 - Tower top configuration and position of Rogowski coil & current shunt

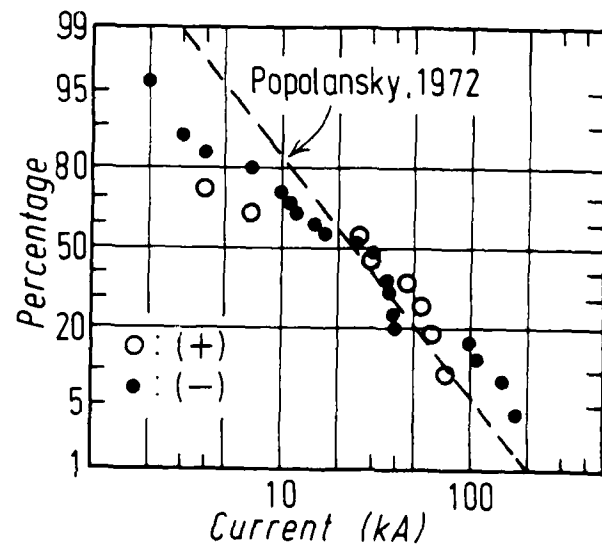


Fig. 7 - Cumulative frequency distribution of lightning peak current

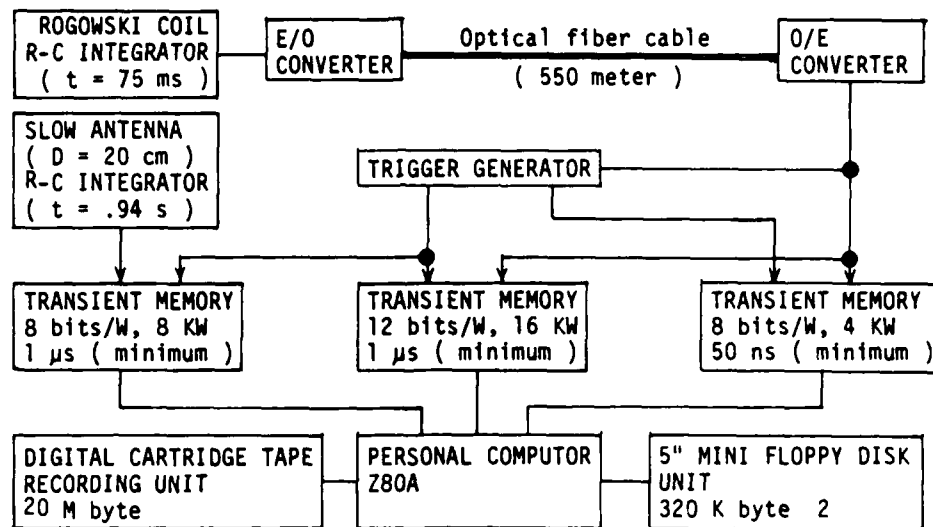


Fig. 6 - Schematic block diagram of improved system

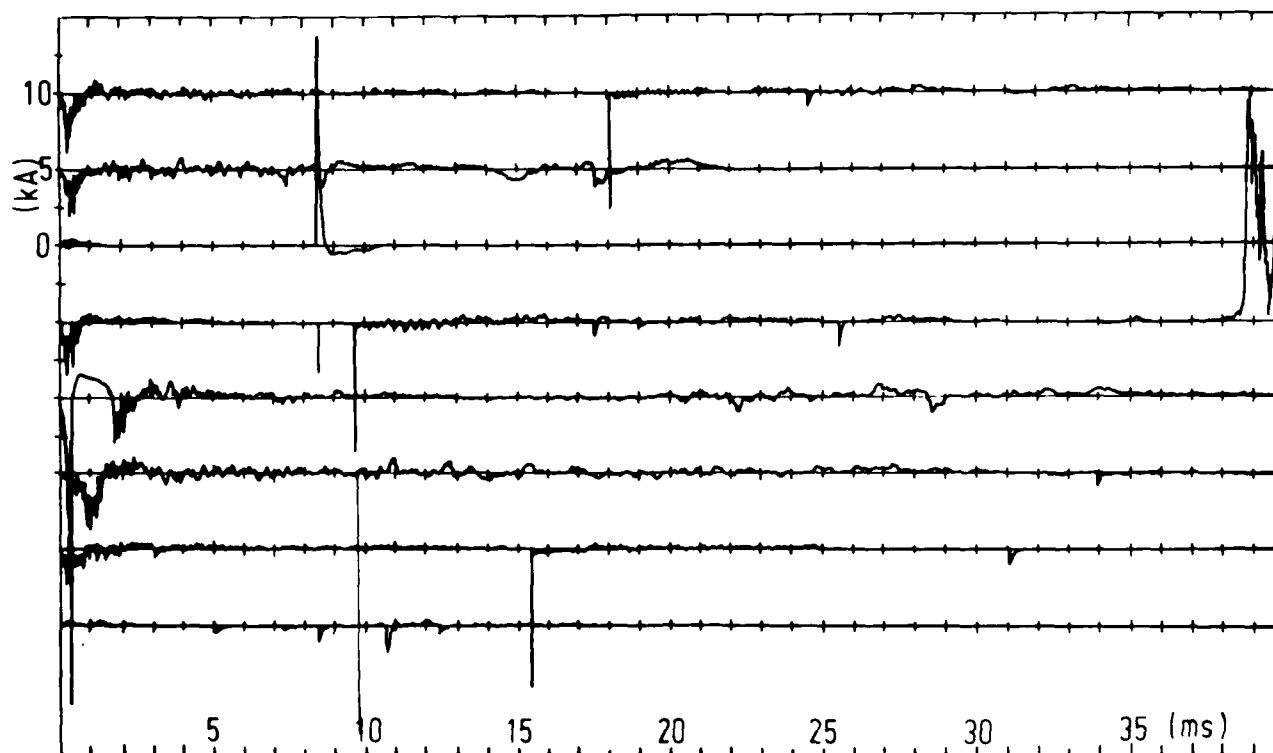


Fig. 8 - Examples of current oscillograms

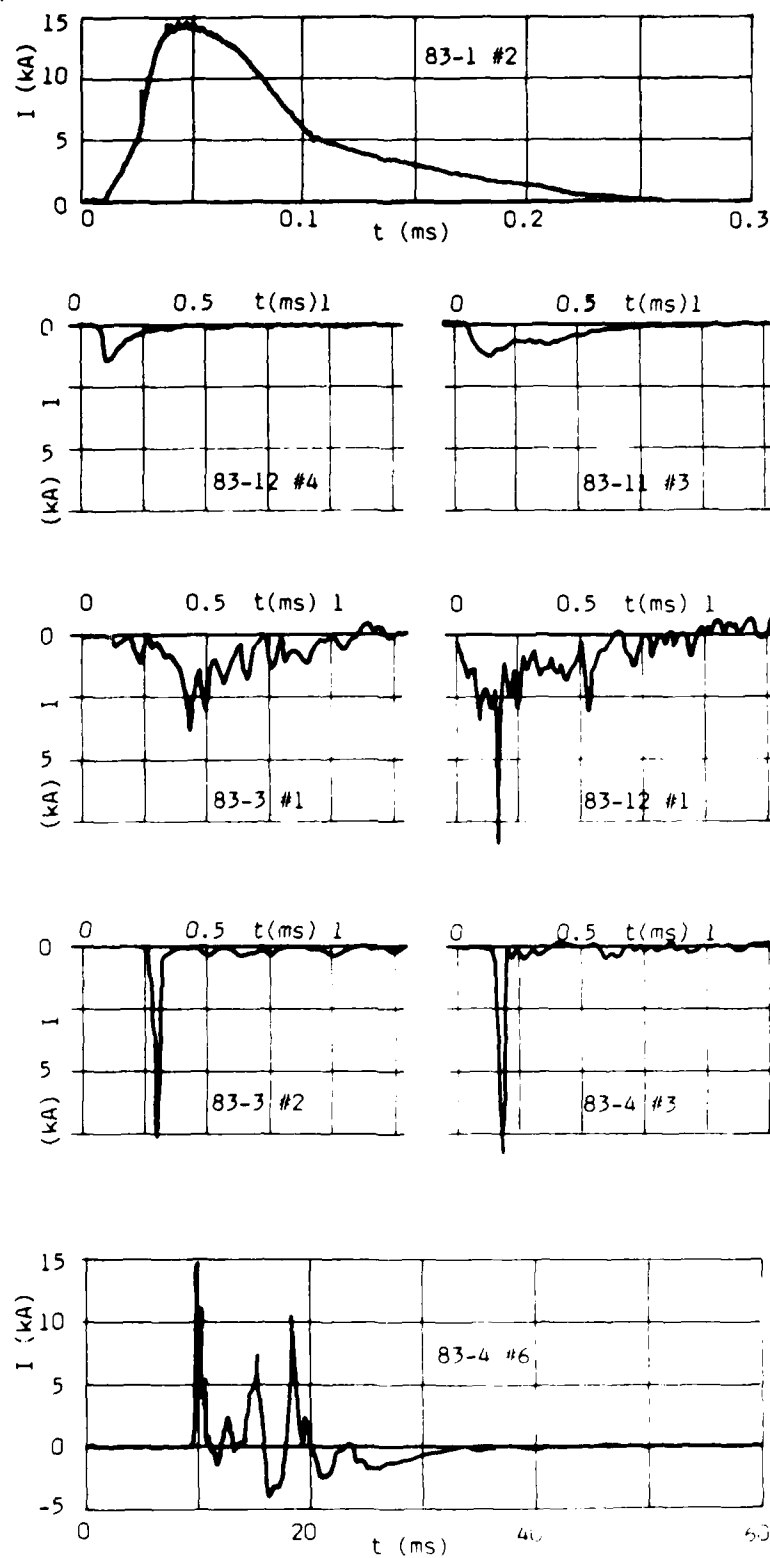


Fig. 9 - Classification of current oscillograms

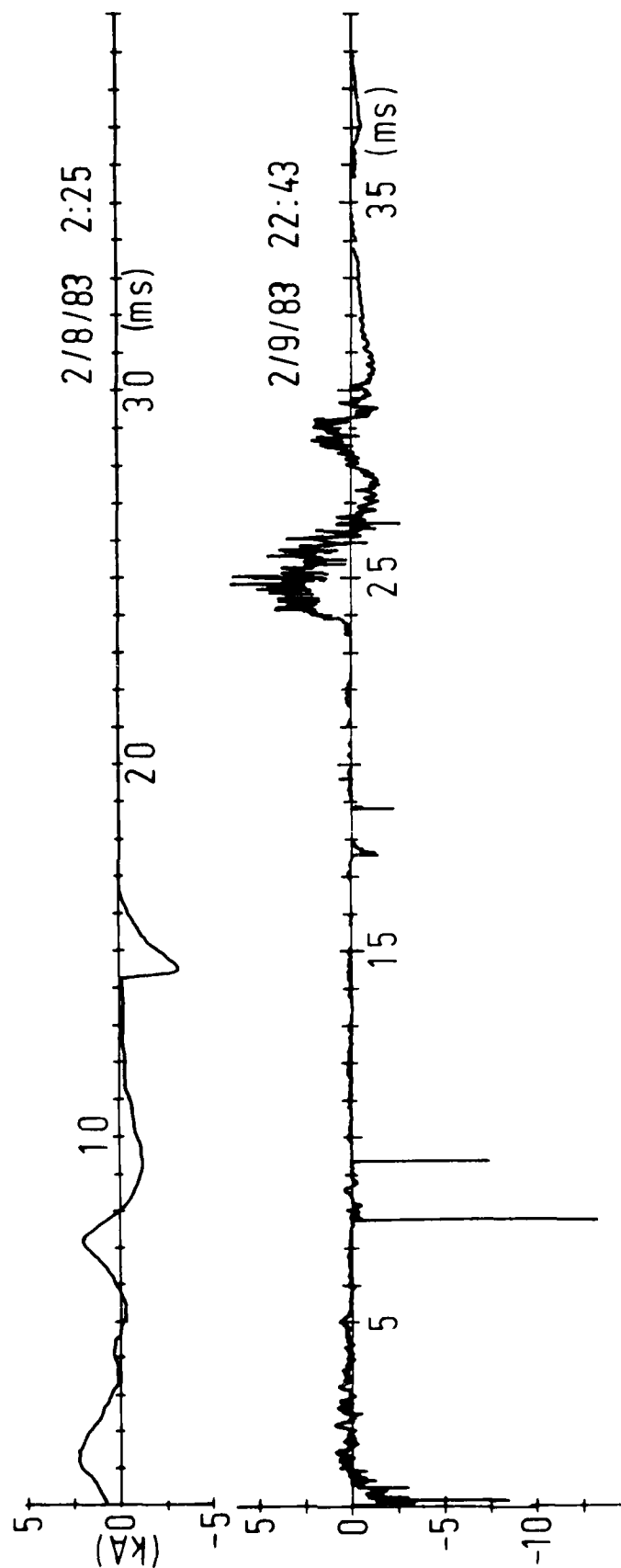
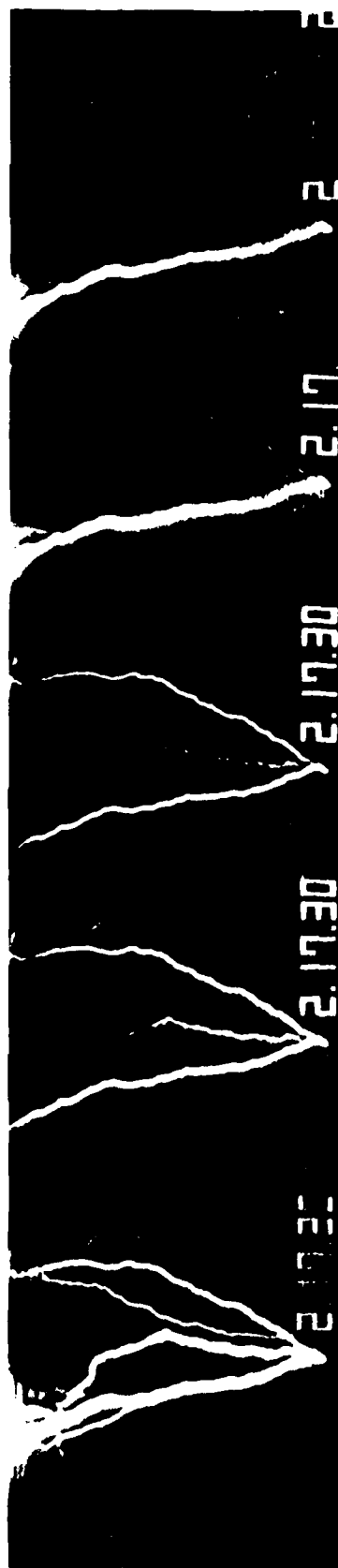
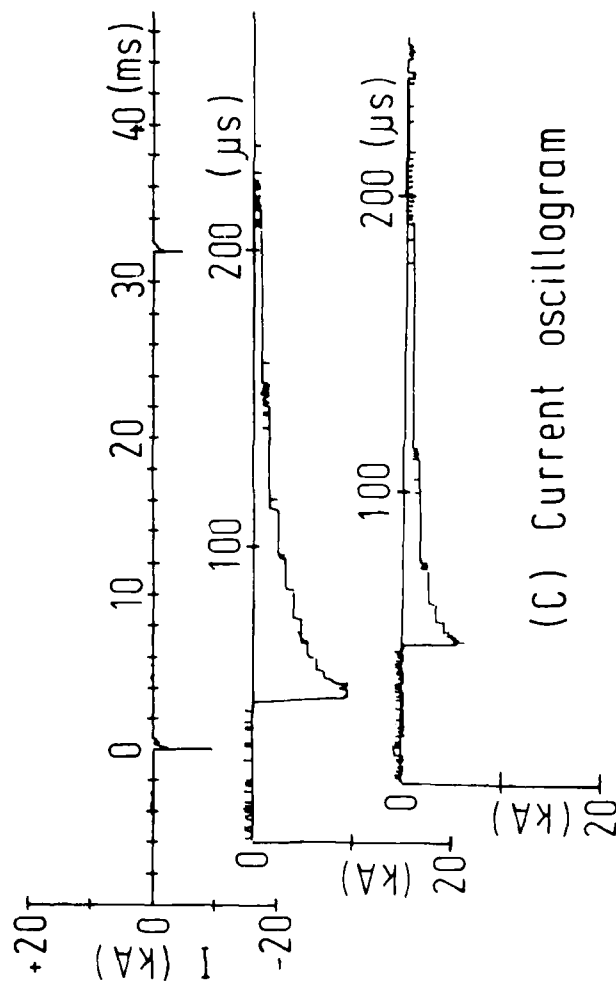


Fig. 10 - Examples of bipolar strokes

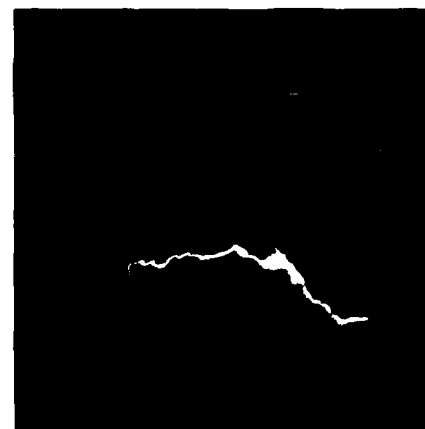


(A) Video image

time →



(C) Current oscillogram



(B) Still photograph
from another direction

Fig. 11 - Video image and its current oscillogram

EFFECTS OF TOWER CHARACTERISTICS
ON LIGHTNING ARC MEASUREMENTS

B. G. Melander

Boeing Military Company

Seattle, Washington

ABSTRACT

Most of the statistical data on lightning currents is based on tower measurements of cloud-to-ground lightning. The effect of the tower on these lightning current measurements must be considered to establish the validity of the present lightning threat levels. Recent measurements by Krider of currents inferred from distant EM field values have not agreed with the previous tower measurements. This paper calculates correction factors to be used in renormalizing the tower data to represent the true arc current. Parameter studies are done for many tower parameters as well as lightning arc parameters. Normalization factors for the tower data of Berger and Garbagnati were found to be near unity. Eriksson's data was found to be reduced by a factor of 1.56. Statistics based on these three data sets were calculated from the normalized data to produce a curve representative of the total tower data. Mean values of current amplitude and rise rate, 13 kA and 15 kA/ μ s respectively, were found to agree with previous results. The upper 1% value of 115 kA for current amplitude also agrees with previous results. The upper 1% value of 440 kA/ μ s for rise rate was found to be much larger than previous tower results, but in closer agreement with the rates inferred from distant EM field measurements.

INTRODUCTION

The statistical base for lightning characterization has been largely from measurements obtained on tall metal towers. Berger[1] in Switzerland, Garbagnati[2] in Italy and Eriksson[3] in South Africa have accumulated the most recent statistics on lightning currents from tower measurements. Berger's and Garbagnati's measurements were made on towers on adjacent mountain tops in the Alps. Eriksson's data was obtained on a tower on a high plain in South Africa.

Recent electric field measurements by Krider[4] have indicated current rise rates much larger than those previously measured by Berger and Garbagnati on towers. Concern for the accuracy of tower measurements has led to the present investigation of the effects of tower parameters on lightning measurements.

The lightning arc model used in this study was developed by Strawe[5,6] and is reviewed in the next section. A lumped element model of a transmission line type tower was connected to the lightning arc model. Peak currents and rise rates were calculated at the top and bottom of the tower for a variety of tower and lightning parameters. Normalization factors for the tower measurements were obtained and applied to Berger's, Garbagnati's and Eriksson's data.

The results of these tower effect calculations indicate that metallic tower measurements taken near the tower top as by Berger and Garbagnati are fairly accurate in giving true lightning parameters of the strikes measured. The separate question of whether the type of lightning striking towers is truly representative of natural lightning is still unanswered. The statistics seem to indicate a fairly low mean level of peak current (13 kA) and rise rate (15 kA/ μ s) but large upper 1% levels of 115 kA and 440 kA/ μ s respectively.

Organization of this paper begins with a short review of the Strawe lightning arc model. A description of the tower model used and the tower parameters follows. Lightning arc parameters are examined next. Results lead to an averaged set of normalization factors applied to the tower data. Lastly the tower data is normalized and new statistics derived via regression analysis from the combined data of all the above tower arc statistics.

STRAWE'S LIGHTNING MODEL

Strawe[5,6] has developed a model of a cloud-to-ground return stroke in which the non-linear breakdown physics is included from first principles. This model is a digital simulation of the arc processes and generates current, temperature, resistance, capacitance, and other channel parameters. These parameters are determined from the past current time history using a shock wave (Braginskii type) model of the arc channel. The model outputs peak currents, decay times, and scale heights similar to linear models. It also provides current rise times and rise rates in agreement with measured data. It indicates that the velocity of propagation of the current wave pulse declines with altitude, as observed photographically, e.g. by Idone and Orville[8], even when the line model is initially uniform in temperature and channel diameter. Most importantly, it predicts a substantial decline in current and current rise rate with altitude or distance from the discharge initiation. Decrease in current amplitude has been observed by Jordan and Uman[9] using luminosity studies.

In the calculations performed to date only the equivalent line resistance per unit length is considered non-linear and time varying. In principle, the inductance and capacitance should also be time functions. However, since these involve logarithmically and therefore slowly varying time dependent terms, they are not initially included in the model.

The resistance models developed for use are based on the spark channel model of Braginskii[10]. This relatively simple model assumes that a conducting channel has been established prior to the initiation of the spark by a prebreakdown streamer or leader process. The resultant arc radius, temperature, pressure, etc. are determined from the spark current time history. The current is assumed to heat the initially conducting arc plasma to higher temperatures and tens of atmospheres of pressure. This condition produces a hydrodynamic shock wave in the air surrounding the spark channel resulting in a rapid channel expansion. Braginskii uses the strong shock approximation to simplify the physical picture of the expansion process. This picture produces an essentially uniform electrical conductivity (determined from channel temperature and pressure) which is

nearly constant in time. The channel resistance per unit length is determined from the conductivity and the arc radius.

The channel parameters are described in terms of a deposited energy rate set by the local current time history. Hydrodynamic continuity equations predicting mass, momentum, and energy together with two equations of state relating pressure, temperature, mass density, and internal energy density were solved as a function of time. The model was developed to include the lost and reabsorbed thermal radiation from the channel, temporal variation of thermal and electrical conductivity, and low pressure momentum transfer.

Comparison with a more detailed nonlinear physics model developed by Gardner[11,12] shows excellent agreement between the two models. Time histories of core temperature and channel resistance for a short arc segment for both models are shown in Figure 1. Agreement between the two is excellent. Comparison

of Strawe's model with core temperature calculations and measurements given by Plooster [13,14], Hill [15,16], and Orville [17] agree both in magnitude and in radial dependence.

Strawe's model uses a lumped element approach to model a lightning arc. Most of the elements are chosen to be unequal to avoid resonance and reflection problems within the model. Elements used near the switch point are the shortest where the time resolution needed is the highest. Rates of change away from this point are expected to slow down and so the segment lengths increase. The shortest segment lengths used to date are 1m.

TOWER MODEL

Since Strawe's lightning model is a lumped element model, the simplest approach to implement when modeling a tower also uses lumped elements. The justification for this approach lies in the often used transmission line models for power transmission towers. A lumped element model of a transmission line works as long as the elements are sufficiently short to accommodate the highest frequency of interest. The highest frequency depends on the particular lightning model used. Higher current rise rates mean higher frequencies and shorter segments are required. Two studies were made of the number of sections versus lightning parameters on the tower. Figures 2 and 3 show the number of RLC elements versus peak current and rise rate. For a rise rate of $80 \text{ kA}/\mu\text{s}$ (Figure 2), the number of elements needed to obtain consistent results is 20 or more segments for a 50m tower. For a rise rate of $160 \text{ kA}/\mu\text{s}$ (Figure 3), the number of elements needed goes up to 50 or more. Most of the calculations performed here use the lower rise rate lightning model and a 20 element tower.

RLC parameters for a tower model need to be specified. Tower characteristics were investigated for the tower configurations of Berger, Garbagnati, and Eriksson by Axup[18] in his masters thesis. He defined ranges of values for tower resistance, surge impedance, footing resistance, and wave propagation velocity on the tower. These values are discussed in detail in a paper by Rustan[19] contained in these proceedings. Since the exact parameters of each tower are not known, a parameter study was performed using Strawe's lightning arc model as the current source. The sensitivity of the tower measurements to accurate values of the

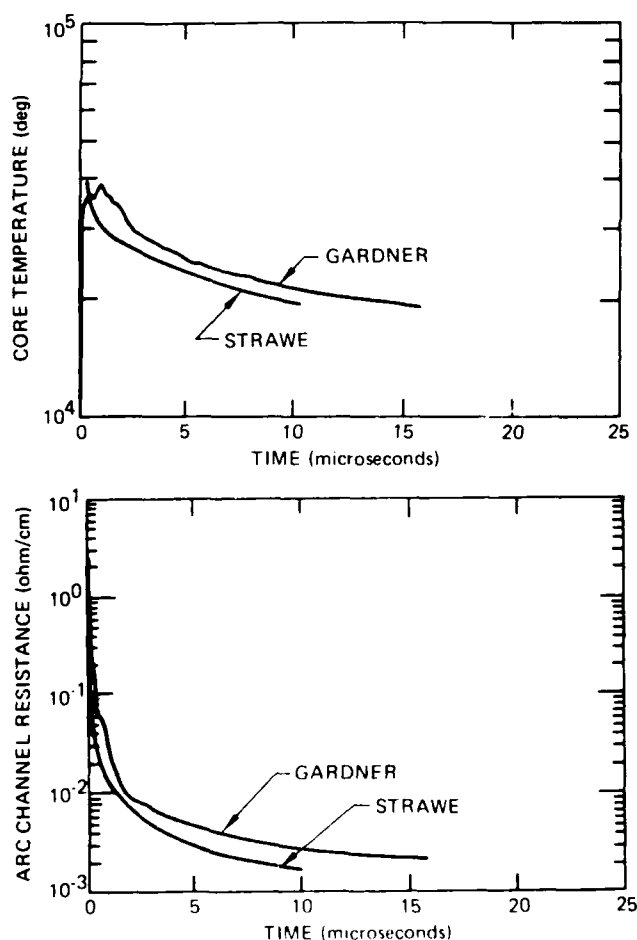


Figure 1. Comparison of Strawe's and Gardner's Lightning Arc Codes

above parameters can then be determined.

For reasonable values of tower parameters (defined in the next several sections), the results predict that tower measurements at the tower bottom give larger values of both peak current and rise rate compared to a natural strike hitting the ground. At the tower top the current amplitude measurement is also larger than natural lightning, however, the rise rate measurement is slightly less than real lightning. Since both Berger and Garbagnati made measurements near the top of their respective towers, their results should be fairly close to the actual lightning parameters of the tower strikes.

The parameters of a model tower were varied and are described below. The parameters studied were footing resistance, tower resistance, surge impedance, wave velocity, and tower height.

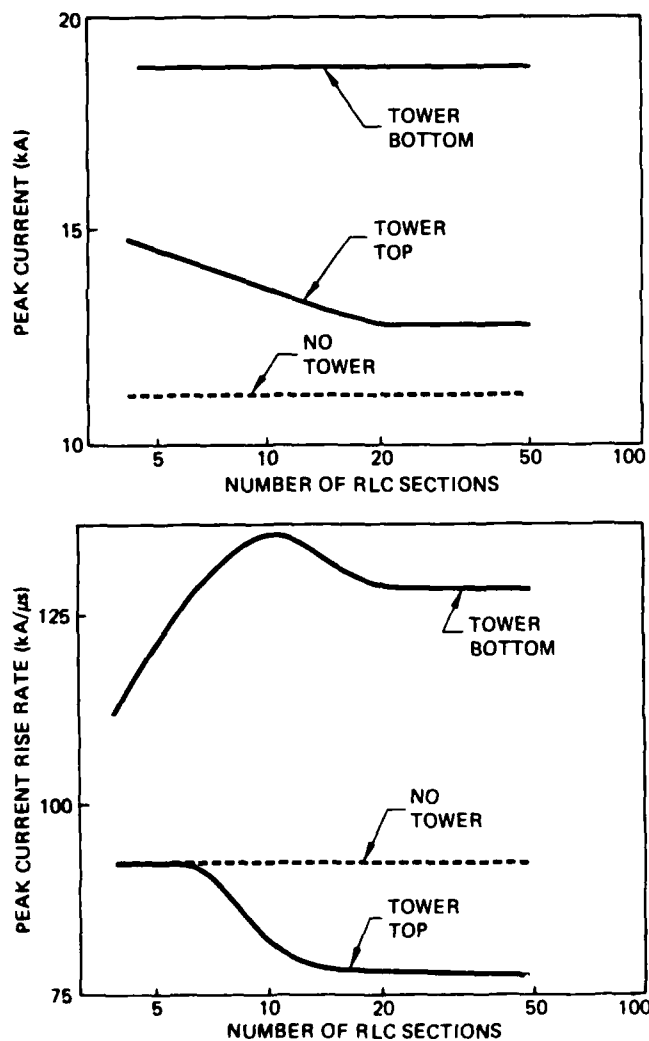


Figure 2. Current Parameters Versus Number of Tower Elements for Moderate Rise Rate

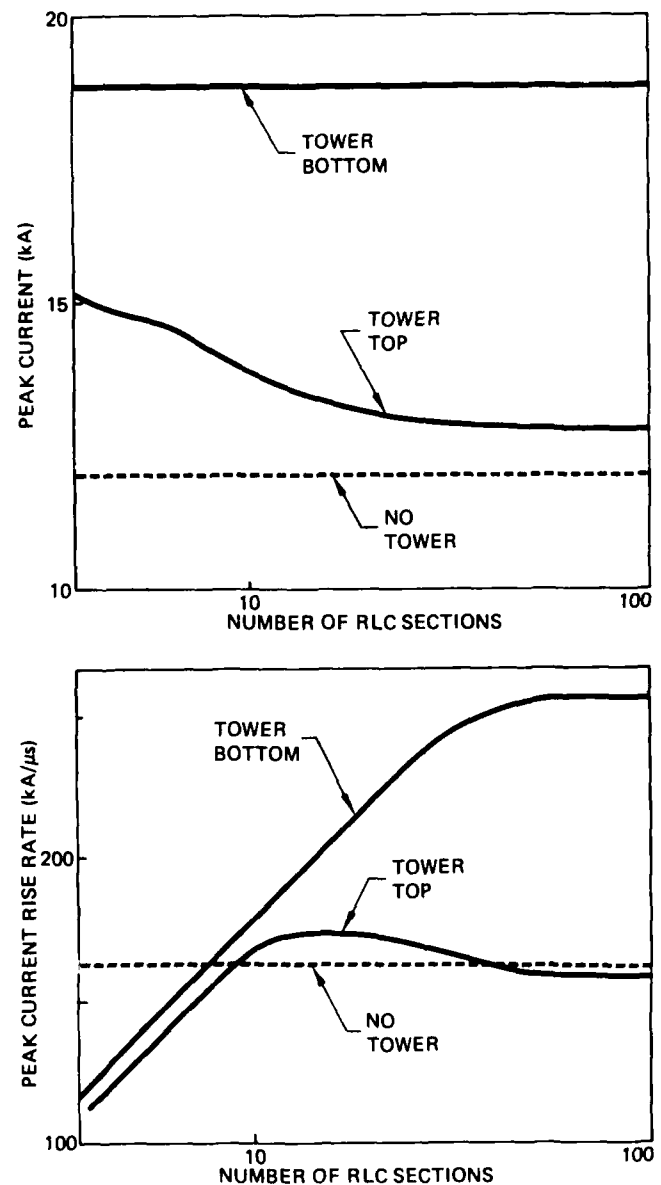


Figure 3. Current Parameters Versus Number of Tower Elements for Large Rise Rate

FOOTING RESISTANCE—Figure 4 shows the variation of peak current and rise rate with footing resistance of the tower. The grounding system of the towers as described in Axup were designed for low footing resistance. Figure 4 shows little or no change in tower current measurements at the tower top. Measurements made at the tower bottom are much more sensitive to footing resistance. Both peak current and rise rate vary dramatically for footing resistances between 10 and 100 ohms which is the expected range for a well grounded tower. The nominal value chosen for footing resistance for the remainder of this study is 30 ohms, the same chosen by Axup in his tower study.

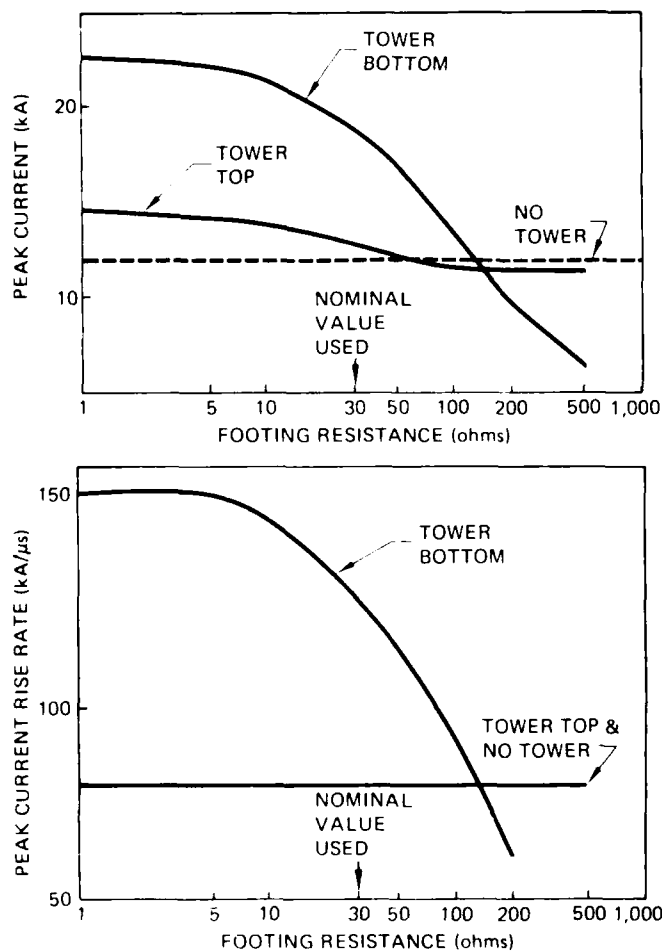


Figure 4. Current Versus Footing Resistance of Tower

TOWER RESISTANCE—Figure 5 shows current values versus tower resistance. Since all the towers were designed to be good conductors, an expected value of the total tower resistance is in the 0.1-2 ohm range[18]. The variation shown in Figure 5 shows no change in tower measurement characteristics until the tower resistance is over 10 ohms. Tower resistance should not be a critical parameter to characterize for a metal tower unless made with high resistance connections or corrosion is present. The value chosen for a standard tower in this study is 1 ohm.

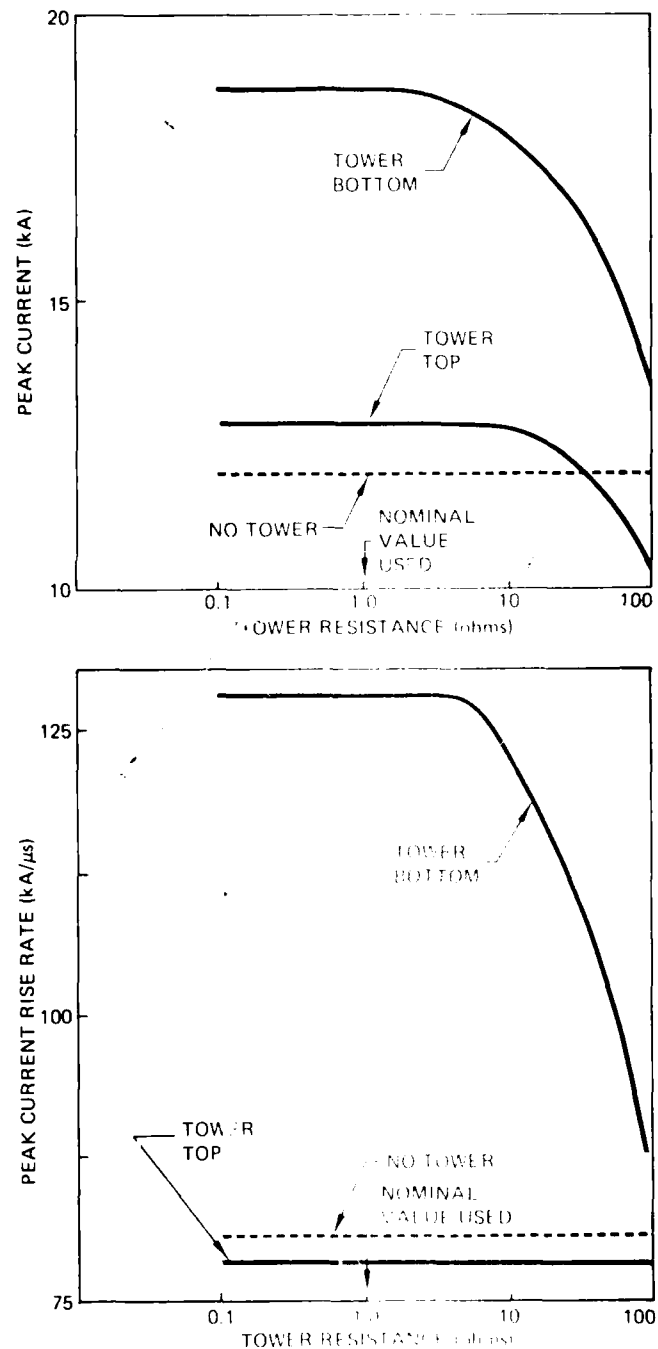


Figure 5. Current Versus Tower Resistance

SURGE IMPEDANCE—The high frequency impedance of a tower is much larger than the DC resistance due to inductive and capacitive effects. Surge impedance is given by the square root of inductance over capacitance. Typical measured and calculated tower values range from 80 to 500 ohms[18]. Figure 6 shows the sensitivity of tower measurements to surge impedance values. In the above range of values the tower current measurements vary by 25% or less. Again the bottom measurements are much more sensitive to changes in surge impedance than values obtained near the tower top. Surge impedance should be measured for a tower since the current parameters can become sensitive to very low or very high values. The nominal value chosen was 130 ohms[18].

WAVE VELOCITY—Table I shows current parameter variations to tower wave propagation velocity. Wave propagation velocity is equal to the reciprocal of the square root of tower inductance times capacitance. Little sensitivity exists to wide variations in propagation velocity. This is not considered to be a critical parameter. The value chosen for a standard was 0.7c.

TABLE I

Current parameters versus wave velocity

v/c	tower bottom		tower top	
	I _{pk} (kA)	I _{pk} (kA/μs)	I _{pk} (kA)	I _{pk} (kA/μs)
0.5	18.8	136	12.0	78
0.6	18.8	132	12.8	78
0.7	18.8	128	12.8	78
0.8	18.8	128	13.2	78
0.9	18.8	128	13.2	78

TOWER HEIGHT—Since the towers which Berger, Garbagnati, and Eriksson used were different heights, 70m, 40m, and 60m respectively, the effect of tower height on the measurements is studied. The towers were modelled with segment lengths of 2.5m (corresponding to 20 elements for a 50m tower which is the standard tower used in most of these studies). To model various tower heights, the number of elements used per tower was varied. Little variation of current parameters with tower height occurs as seen in Table II. The largest variation between a 20m tower and a 100m tower was a 10% decrease in rise rate. This assumes, however, that the surge impedance, wave velocity, tower

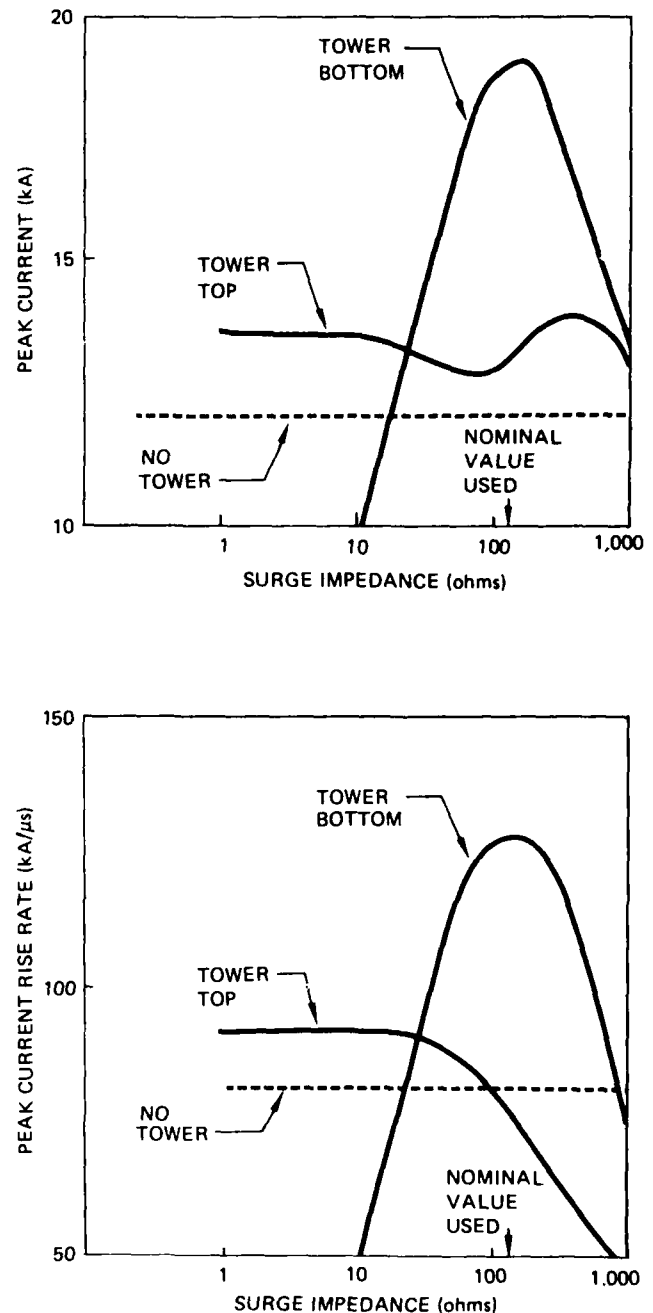


Figure 6. Current Versus Tower Surge Impedance

resistance are not varying. Since all are dependent on tower height, especially surge impedance, tower height variations may not be accurate. The results point out that while tower height itself is not an important factor, the change in surge impedance due to changes in tower height is more important. The nominal value of tower height chosen was 50m.

Table II

Current parameters versus tower height

height (m)	tower bottom		tower top	
	I _{pk} (kA)	I _{pk} (kA/μs)	I _{pk} (kA)	I _{pk} (kA/μs)
20	16.8	128	13.6	78
40	18.8	128	13.2	78
50	18.8	128	12.8	78
60	18.8	132	12.8	78
80	18.8	132	12.4	79
100	18.8	132	12.0	79

LIGHTNING PARAMETERS

The last section concerned itself with changing the tower characteristics. These studies were all performed with a standard peak current of 12 kA and a rise rate of 81 kA/μs. This section varies the lightning source characteristics. The normalization factors for high and low current and rise rate levels are determined here. The normalization factors resulting from comparison of tower results to different ground impedances struck by natural lightning is also considered.

CURRENT PARAMETERS—Straw's lightning model allows changes in the initial conditions to vary peak current and rise rate. Two different current amplitude levels with identical rise rates and two rise rate values with identical current amplitudes were examined with and without a tower present. The results are presented in Table III. The normalization factors are the ratios of values with a tower present to values without a tower. Values greater than one indicate tower measurements larger than natural lightning while values less than one indicate measurements lower than real lightning. The normalization factor does not change substantially when the current parameters are changed. Therefore, average values of the normalization constants can be calculated and used for all tower measurements.

Table III

Current parameters versus normalization factors

Normalization factors					
No tower		Tower bottom		Tower top	
I _{pk}	I _{pk}	F _i *	F _i	F _i	F _i
12.0	81	1.57	1.58	1.07	.951
12.0	164	1.57	1.56	1.07	.976
22.2	164	1.55	1.56	1.16	.951
Average		1.56	1.57	1.10	.959

* F_i = I_{pk}-with tower/I_{pk}-no tower
F_i = I_{pk}-with tower/I_{pk}-no tower

GROUND RESISTANCE—The last parameter to be examined is the ground resistance of a natural lightning strike. This study was performed with the standard peak current of 12 kA and rise rate of 81 kA/μs as used elsewhere in this paper. Table IV shows the variation of normalization factors for ground resistances ranging from 10 to 500 ohms. A ground resistance of 100 ohms was the standard used in the remainder of this study. The table shows that a factor of two change from 100 ohms results in changes of 13% or less to the normalization factors. This implies that ground resistance is not a crucial parameter when deriving normalization values for a tower unless the values are very large or small.

TABLE IV

Normalization factors versus ground resistance

Ground Resistance (ohms)	Tower bottom		Tower top	
	F _i	F _i	F _i	F _i
10	1.38	1.39	.941	.837
50	1.47	1.49	1.00	.895
100	1.57	1.58	1.07	.951
200	1.74	1.78	1.18	1.07
500	2.27	2.42	1.54	1.45

RESULTS

Using the averaged values of the normalization factors from Table III, the tower data of Berger, Garbagnati, and Eriksson are normalized. The results are shown in Figures 7-9. Berger and Garbagnati measured currents near the top of their towers. The normalization factors used from Table III for the tower top are very close to unity. Thus, both Figures 7 (Berger), and 8 (Garbagnati) show very little shift in the data due to normalization. Peak currents are normalized to slightly smaller values while rise rates are slightly increased.

Eriksson's data is effected much more by normalization since it was measured near the bottom of his tower. Normalized peak currents are shown to be substantially reduced as seen in Figure 9. His rise rate statistics were not available. However, the maximum rise rate he measured was reported to be 180 kA/ μ s in 11 events. This corresponds to the upper 9% of his data, much larger than the values measured by Berger and Garbagnati whose 9% levels are 102 kA/ μ s and 111 kA/ μ s respectively. When Eriksson's maximum rise rate is normalized using the average value in Table III for the tower bottom, the result is 115 kA/ μ s. This compares very favorably to normalized values of Berger's and Garbagnati's data for the 9% level of 107 kA/ μ s and 114 kA/ μ s.

Normalized tower data can be combined to give total statistics on tower measurements. Since the original data of Berger, Garbagnati, and Eriksson was not available for this study, their published statistics were used to create new data sets. Their number of data sets were used to select points from the log normal statistical curves. Points from 1-99% evenly spaced both in standard deviation and logarithms of current or rise rate were chosen from their cumulative percentage curves. A regression analysis was done to best fit all the normalized data. Analyses were done for first return and subsequent strokes using data from Berger and Garbagnati. Positive strokes from Berger's data also were normalized and used in cumulative statistics for all the strokes. The data from Eriksson was not classified as to stroke type and was included in the first return results.

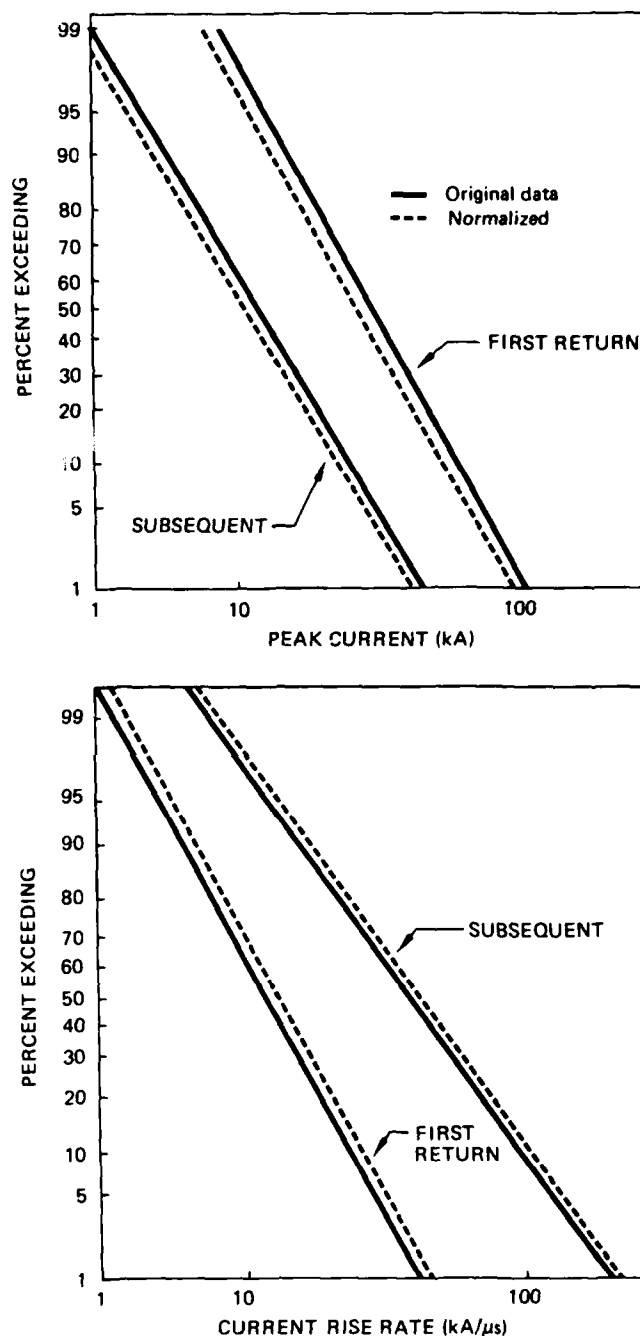


Figure 7. Berger's Tower Data--Normalized

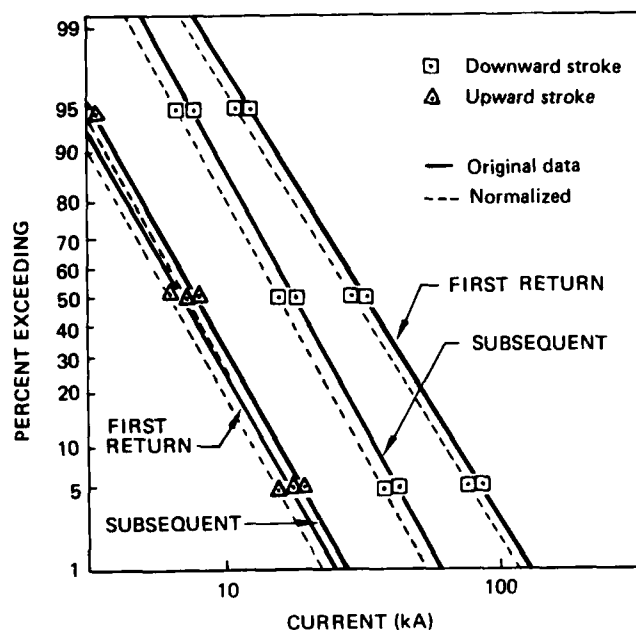


Figure 8. Garbagnati's Tower Data—Normalized

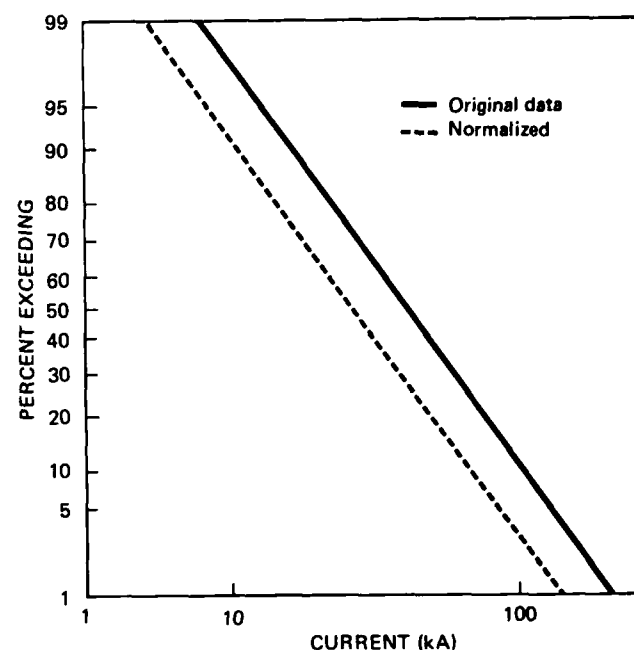
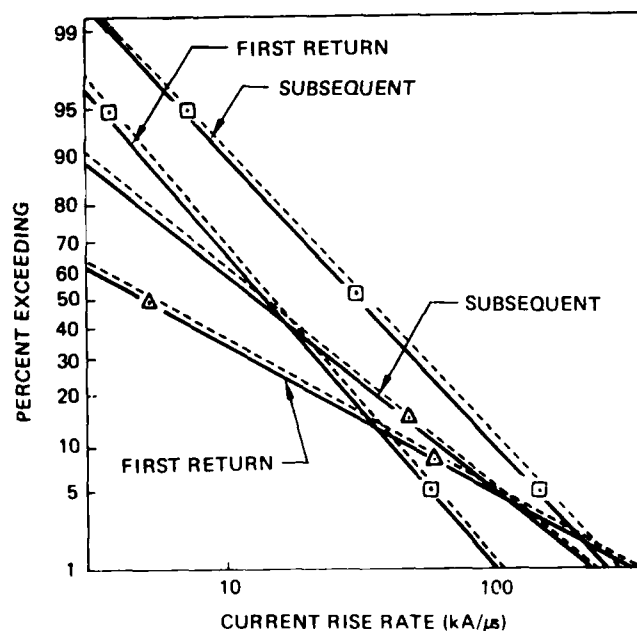


Figure 9. Eriksson's Tower Data—Normalized



Results of the regression fits to the data are shown in Figure 10. First return and subsequent strokes are shown as well as the combination of those and positive stroke data. Note the dashed lines above 100 kA for first return stroke current amplitude and above 100 kA/μs for all rise rate values. The dashed lines are to emphasize the fact that no direct current measurements were made above these levels. Table V gives a summary of the statistics including the number of data points, mean values, and standard deviations (in logarithmic units). These numbers may be expected to change if the original data becomes available for this type of analysis.

TABLE V

Cumulative statistics on normalized tower data

	95%	50%	5%	σ	N
Peak Current (kA)					
First Return	3.7	18	90	.42	215
Subsequent	3.5	9.5	26	.26	310
All	2.8	13	61	.41	551
Peak Rise Rate (kA/ μ s)					
First Return	1.0	9.7	92	.60	195
Subsequent	3.3	23	167	.52	297
All	1.4	15	167	.63	513

* σ = standard deviation and is in logarithmic units.

N = number of data points

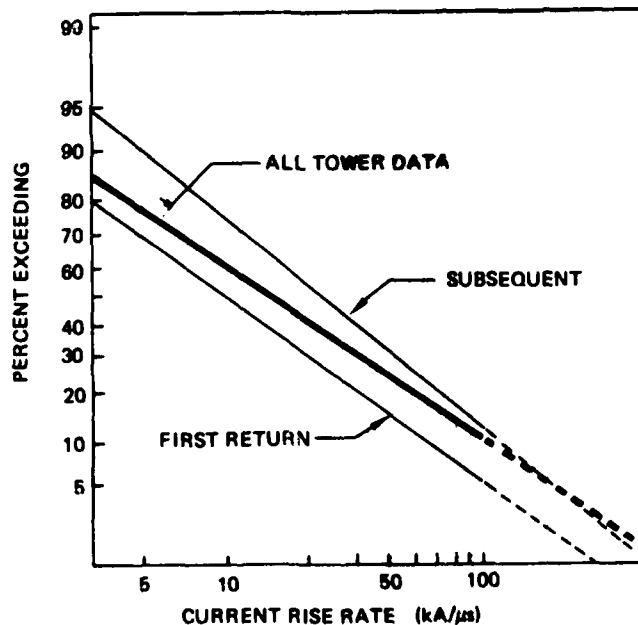
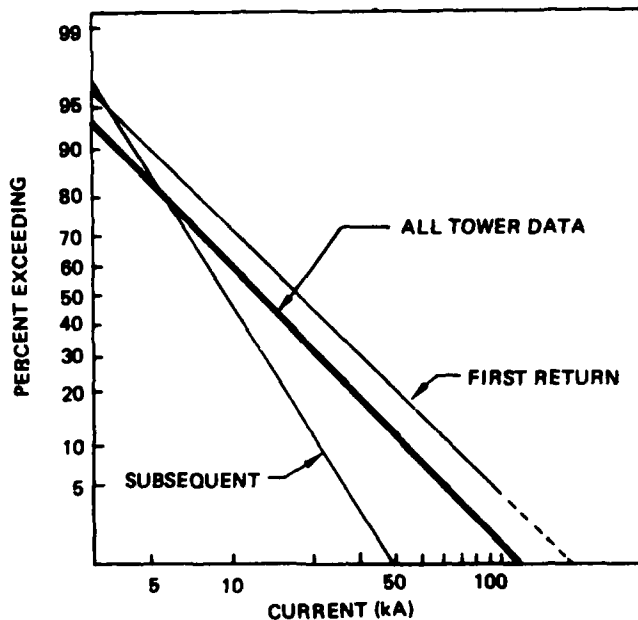


Figure 10. Regression Fit to Tower Data

The mean values of the regression fit to the tower data are almost identical to the results of Cianos and Pierce[7]. Cianos and Pierce had mean current values of 20 kA for first return strokes and 10 kA for subsequent. Their average rise rate value was 22 kA/ μ s. The upper 5% current levels are identical for first return and almost a factor of two lower than Cianos and Pierce for subsequent. Cianos and Pierce's 5% values for current amplitude are 90 kA for first return and 45 kA for subsequent. The upper 5% rise rate values are much higher than Cianos and Pierce, especially for subsequent strokes. The upper 5% value they derive is 70 kA/ μ s. While mean values agree between this study and that of Cianos and Pierce, the upper percentile rise rate values presented here are much higher. These high rise rate values agree more with results obtained by Krider [4] for upper 1% values.

SUMMARY

The effect of a lumped element tower on a non-linear basic physics type lightning model has been examined. For a well grounded, conducting tower, most tower characteristics were found to be of small importance. This includes tower resistance, wave velocity, and tower height. Footing resistance and surge impedance were the most crucial to determine for a measurement tower. However, for a low tower resistance and a surge impedance between 100-500 ohms,

measured tower values do not vary much with a change in these parameters.

The effect of the tower on lightning of different peak currents and rise rates was also studied. Little effect of lightning arc parameters was seen so the results were averaged to use for normalization purposes.

The effect of comparing tower measurements to lightning striking ground of various resistances was the last effect examined. Differences in normalization factors on the order of 10% were seen when changing ground resistance by a factor of two.

All the parameters studied suggest tower data to be fairly accurate when measured near the top of the tower. Errors of 60% or more can occur near the bottom. Measurements taken near the bottom are also more sensitive to some tower parameters such as surge impedance, footing resistance, and tower resistance.

Renormalizing the tower data made little difference in Berger's and Garbagnati's data. A large effect was seen in Eriksson's data. The large rate of rise value of 180 kA/ μ s which he reported decreased to 115 kA/ μ s after normalization. This normalized value now agrees with Berger's and Garbagnati's normalized data.

The cumulative statistics derived from all the tower data show low mean values for current (13 kA) and rise rate (15 kA/ μ s). Upper 1% values are 115 kA for current amplitude and 440 kA/ μ s for rise rate. This high 1% value of rise rate agrees with Krider's value of 400 kA/ μ s inferred from electric field measurements. However, no direct current measurements of rise rates this large have ever been measured. Krider's mean value of 150 kA/ μ s for current rise rate is also much higher than the mean obtained here.

The discrepancies between results obtained here and previous results indicate more work needs to be done to establish reliable lightning current statistics. Mean current parameters calculated in this paper agreed with results of Cianos and Pierce but disagreed with those inferred from Krider's measurements. Upper percentile values for rise rate agreed with Krider but not with Cianos and Pierce.

Further work on accumulating the existing data from tower and electric field data needs to be done. The actual tower data should be normalized and fit to a new cumulative statistical curve. Electric field data should be

incorporated into these statistics once the effect of statistical biasing by high trigger threshold setting and an unresolved factor of two in the current inferred from the fields [20] is resolved.

Many unanswered questions need resolution. Tower data needs to be further studied to understand the effect of the mountain peaks on the data. Bandwidth limitations of older data need to be examined. The effect of upward going leaders on tower data should be analyzed. Current parameters inferred from EM field measurements need verification from direct current measurements.

ACKNOWLEDGEMENTS

This study was inspired by questions arising from the Atmospheric Electricity Hazards Program (AEHP) at Boeing. I would like to thank D.G. Chapman for help with the Strawe lightning arc model. I would also like to thank P. Axup and P. Rustan for sharing their results from their own study on tower effects.

REFERENCES

1. Berger, K., et. al., "Parameters of Lightning Flashes", *Electra*, no. 41, 23-37, 1975.
2. Garbagnati, E., Lopipard, G.B., "Lightning Parameters-Results of 10 Years of Systematic Investigation in Italy", *Proceedings of International Conference on Lightning and Static Electricity*, Oxford, England, March 1982.
3. Eriksson, A.J., "Lightning and Tall Structures", *Transactions: South African Institute of Electrical Engineers*; Vol. 69, Pt. 8, 238-252; August, 1978.
4. Krider, P., Weidman, E.D., "The Submicrosecond Structure of Lightning Radiation Fields", *International Aerospace and Ground Conference on Lightning and Static Electricity*, Fort Worth, Texas, June 1983.
5. Strawe, D.F., "Lightning Source Model Development Program", Boeing Document D180-22936-1, January 1978.
6. Strawe, D.F., Geren, W.P., Chapman, D.G., "A Self-Consistent Model for Return Stroke Currents and Fields", *Seventh International Aerospace and Ground Conference on Lightning and Static Electricity*, Oxford, England, 24-26, March 1982.

7. Cianos, N., Pierce, E.T.; "A Ground Lightning Environment for Engineering Usage", Stanford Research Institute, Project 1834,
8. Idone, V., Orville, R.E., "Lightning Return Stroke Velocities in the Thunderstorm Research International Program (TRIP)", JGR, 87, 4903-4915, June 1982.
9. Jordan, D.M., Uman, M.A., "Variation in Light Intensity with Height and Time from Subsequent Lightning Return Strokes", JGR, 88, 6555-6562, August 1983.
10. Braginskii, S.I., "Theory of the Development of a Spark Channel"; Soviet Physics, JETP, 7, 1068, 1958.
11. Gardner, R.L., "A Model of the Lightning Return Stroke", PhD. Thesis, University of Colorado, 1980.
12. Frese, M.H., Gardner, R.L., "A Comparison of Calculated Lightning Channel Characteristics as Computed by a Simple Physical Solution and a Detailed Finite Difference Calculation", MRC Report to Boeing Military Company under Contract CM9221, Report No. AMRC-R-417.
13. Plooster, M.N., "Numerical Simulation of Spark Discharges in Air", Phys. Fluids, 14, 2111, 1971.
14. Plooster, M.N., "Numerical Model of the Return Stroke of the Lightning Discharge", Phys. Fluids, 14, 2124, 1971.
15. Hill, R.D., "Channel Heating in Return Stroke Lightning", JGR, 76, 637, 1971.
16. Hill, R.D., "Comments on Quantitative Analysis of a Lightning Return Stroke for Diameter and Luminosity Changes as a Function of Space and Time" by R.E. Orville, J.H. Helsdan, and W.H. Evans", JGR, 80, 1188, March 1975.
17. Orville, R.E., Helsdan, J.H., Evans, W.H.; "Quantitative Analysis of a Lightning Return Stroke for Diameter and Luminosity Changes as a Function of Space and Time"; JGR; 79: 4059-4067; September 1974.
18. Axup, P.R., "The Effects of Towers on Lightning Current Measurements", Masters Thesis, Air Force Institute of Technology; DEcember 1983.
19. Rustan, P., Paper this Conference.
20. Baum, C., Private communication.

On the Estimation of the Lightning Return Stroke Current

Zen-Ichiro Kawasaki, Yoshichika Mizutani, Taketoshi Nakai
and
Tosio Takeuti

The Research Institute of Atmospherics, Nagoya University,
3-13 Honohara, Toyokawa, Aichi, 442, JAPAN

Abstract

A method for estimating return stroke currents directly with the measured electric field intensity and magnetic flux density is developed using both transmission line model and Lin-Uman-Standler's model for return stroke currents. This method is mainly based on Variational Principle. It is confirmed by numerical experiments that the relative errors of peak values of estimated currents are at most a few percents of the original ones and we can conclude this new method is much useful for the return stroke current estimation.

Introduction

This paper describes a numerical study on an estimation method of return stroke currents directly with the measured electric field intensity and magnetic flux density due to a lightning return stroke. The current estimation problem is formulated as an inverse problem which is frequently discussed in the field of an electromagnetic wave scattering.

First we try to expand a time varying current on the lightning channel into an orthogonal series. In order to perform the series expansion we define a quantity J , a kind of energy difference between measured fields and those of calculated ones. The quantity J includes unknown expansion coefficients, which are to be determined under the condition that the energy difference should take a minimum value. With the aids of Variational Principle we can find that this minimization is realized when partial differential coefficients are zero. After a little mathematical treatment a linear equation of unknown coefficients is derived and this can be solved with a computer. Then we can get the time variation of a return stroke current.

To show the validity of this method we would apply this method to the transmission line model. In this model the current at ground level is assumed to propagate up the channel as it would go along an ideal transmission line. The electric field intensity and magnetic flux density for a given current are calculated by the equation derived by Uman et al. Then these fields obtained numerically are used to estimate the model current. For simplicity we assume that the distance, the channel length, the return stroke velocity and the attenuation constant of currents are known because we can determine these parameters by various measurements such as an optical observation etc. Though any kind of orthogonal series is available, we use the orthogonal polynomials in this paper. Furthermore the channel is assumed to be vertical. On the above conditions numerical results are given for various distances, return stroke velocities and the attenuation constants.

E and B due to Lightning Discharge

After Uman [Uman et al., 1975] the electric field intensity E and the magnetic flux density B on the ground at a distance D from a vertical channel of height H are given by

$$E(D, t) = \frac{1}{2\pi\epsilon_0} \left[\int_0^H \frac{2 - \sin^2\theta}{R^3} i(z, t - R/c) dz + \int_0^H \frac{2 - 3\sin^2\theta}{cR^2} \frac{\partial i(z, t - R/c)}{\partial t} dz \right] a_z \quad (1)$$

$$B(D, t) = \frac{\mu_0}{2\pi} \left[\int_0^H \frac{\sin\theta}{R^2} i(z, t - R/c) dz + \int_0^H \frac{\sin\theta}{cR} \frac{\partial i(z, t - R/c)}{\partial t} dz \right] a_\phi \quad (2)$$

where ϵ_0 , μ_0 and c are respectively the permittivity, the permeability and the speed of light of free space. For the time varying currents in eqs. (1) and (2) several currents models have been proposed until now. Among these models we would use the transmission line model [Uman et al., 1969] and the Lin-Uman-Standler's model [Lin et al., 1980] in this paper.

In the transmission line model the current at the ground level is assumed to propagate up the channel as it would go along an ideal transmission line. Then the current at the altitude z and time t are given by

$$i(z, t) = i(t - z/v) \quad z < H \\ = 0 \quad H < z \quad (3)$$

where v is the constant return stroke velocity.

On the other hand in Lin-Uman-Standler's model the current is composed of three separate currents components and given by

$$i(z, t) = i_b(z, t) + i_c(z, t) + i_u(z, t) \quad (4)$$

$$i_b = i(t - z/v) \quad z < H \\ = 0 \quad H < z$$

$$i_c = I_0 \left[\frac{\exp(p_1 z_m + p_1) - \exp(p_1 z + p_1)}{p_1} - \frac{\exp(p_2 z_m + p_2) - \exp(p_2 z + p_2)}{p_2} \right]$$

$$i_u = \text{constant}$$

where

$$p_1 = d(1/v + 1/c) - 1/\lambda$$

$$p_2 = \beta(1/v + 1/c) - 1/\lambda$$

$$p_3 = -d(t - t_{om} + z/c - R/c)$$

$$p_4 = -\beta(t - t_{om} + z/c - R/c)$$

$$z_m = \text{Max}[H, (t - t_{0h} + z/c - R/c) / (1/v + 1/c)]$$

Here the notation used in this paper are quite the same as used in Lin's paper. Both transmission line model and Lin-Uman-Standler's model have several unknown parameters. So to get some information about the time varying current with the measured fields a great deal of labour is usually needed such as "trial and error" described in Lin's paper. Then the purpose of this paper is to propose a direct estimation method of return stroke currents with observed E and B. The direct estimation of currents with E and B is just to solve the first kind Fredholm Integral Equations. In next section we would discuss this problem in detail.

Formulation of the Problem

Both transmission line model and Lin-Uman-Standler's model include several parameters and these parameters are usually determined by iteratively comparing the calculated and measured fields. So in this section we present a new method to estimate the return stroke currents directly with measured E and B due to a lightning return stroke. We would discuss the method to solve the Integral Equations (1) and (2) for the current and to determine the unknown time function $i(z, t)$.

First we would try to expand an unknown function $i(z, t)$ on the return stroke channel into an orthogonal series $f_j(z, t)$

$$i(z, t) = \sum_{j=1}^N A_j f_j(z, t) \quad (5)$$

where A_j is the unknown expansion coefficient to be determined. Here we define a new quantity given by the next equation

$$J = \int_0^T \left[\left(\sum_{j=1}^N A_j F_j(t) - E_{0z}(t) \right)^2 + \left(\sum_{j=1}^N A_j G_j(t) - B_{0\phi}(t) \right)^2 \right] dt \quad (6)$$

where

$$F_j(t) = \frac{1}{2\pi\epsilon_0} \left[\int_0^H \frac{2 - \sin^2\theta}{R^3} f_j(z, t - R/c) d\tau dz + \int_0^H \frac{2 - 3\sin^2\theta}{CR^2} f_j(z, t - R/c) dz - \int_0^H \frac{\sin^2\theta}{C^2 R} \frac{\partial f_j(z, t - R/c)}{\partial t} dz \right] \quad (7)$$

$$G_j(t) = \frac{1}{2} \left[\int_0^H \frac{\sin\theta}{R} f_j(z, t - R/c) dz + \int_0^H \frac{\sin\theta}{CR} \frac{\partial f_j(z, t - R/c)}{\partial t} dz \right] \quad (8)$$

The physical meaning of the quantity J is a kind of energy difference. Then the expansion coefficient A_j is to be determined as the quantity J takes the minimum value. With the aids of Variational Principle we know that this minimization is able to be realized when the partial differential coefficients on A_j are equal to zero.

$$\frac{\partial J}{\partial A_k} = 0 \quad (k=1, 2, \dots, N) \quad (9)$$

After a little mathematical treatment on equation (6) following relations are derived.

$$\sum_{j=1}^N A_j \left(\int_0^T [F_k(t) F_j(t) + G_k(t) G_j(t)] dt - \int_0^T [E_{0z}(t) F_k(t) + B_{0\phi}(t) G_k(t)] dt \right) = 0 \quad (K=1, 2, \dots, N) \quad (10)$$

If we perform the integration in eqs.(7), (8) and (10), equation (10) becomes a matrix equation (11).

$$[H]a - b = 0 \quad (11)$$

In order to perform these integrations the measured electric field E, magnetic flux density B and expansion function F(t) and G(t) may be approximated by setting

$$E_{0z}(t_c) = \sum_{j=1}^N E_{0j} \psi_j(t_c) \quad (12)$$

$$B_{0\phi}(t_c) = \sum_{j=1}^N B_{0j} \psi_j(t_c) \quad (13)$$

$$F_k(t_c) = \sum_{j=1}^N F_{kj} \psi_j(t_c) \quad (14)$$

$$G_k(t_c) = \sum_{j=1}^N G_{kj} \psi_j(t_c) \quad (15)$$

The integration is easily performed by dividing the period into N subintervals t_1 ($l=1, 2, \dots, N$) and the function being the step function determined by

$$\psi_j(t_c) = 1 \quad \text{in } \Delta t_{cj} \\ = 0 \quad \text{in } \Delta t_{ck} (j \neq k) \quad (16)$$

From the above discussion A_j can be determined by solving a linear equation (11) and the time variation of the return

stroke current can be determined with equation (5).

Numerical results and discussion

(1) Transmission line model

To show the validity of this method, numerical experiments are performed. That is, first we numerically simulate the E and B due to the lightning return stroke with the transmission line model, its current given by

$$i(z, t) = \exp(-\gamma z) [\exp(-\lambda t) - \exp(-\beta t)] \quad (17)$$

where v and γ are respectively the constant return stroke velocity and the attenuation constant of return stroke currents. Next to these numerically simulated E and B we apply the direct current estimation method and estimate the time varying current. Though any kind of orthogonal series is available for the expansion function, we choose the orthogonal polynomial.

$$i(z, t) = \exp(-\gamma z) \sum_{j=1}^N A_j (t - z/v)^{j-1} \quad (18)$$

For simplicity we assume that the distance, the channel length, the return stroke velocity and the attenuation constant of currents are known, because we can determine these parameters by various measurements such as optical observations.

A typical estimated result is shown in Fig.1 together with the original current. Here the original current, the double exponential type current, are used to calculate the example E and B. Furthermore the relative errors of the estimated peak currents for various return stroke velocity, distance and attenuation constant are shown in table 1. Both of them are quite similar. The relative error is at most a few percent and from these results we can conclude this method is useful for return stroke current estimation of the transmission line model.

(2) Lin-Uman-Standler's model

Next we should try to apply this method to Lin-Uman-Standler's model. In Lin-Uman-Standler's model the break down pulse current essentially propagates along the channel and we can easily estimate with the same procedure as described above. The uniform current is easy to determine as described in Lin's paper. So the remained problem is the estimation of corona components. Let us consider the following expansion of corona source element.

$$i_c(z, z', t) = \exp(-z'/\lambda) \sum_{j=1}^N C_j (t - t')^{j-1} \quad (19)$$

Where C_j is the unknown coefficient to be determined. After a little mathematical treatment the corona current $i(z, t)$ is derived in following form.

$$i_c(z, t) = \sum_{j=1}^N C_j \sum_{k=1}^j \left[\frac{(j-1)! (-\lambda)^k}{(k-1)! v^{k-1}} \right] \cdot \exp(-z'/\lambda) (t - z/v)^{j-k} \quad (20)$$

Then we can use eq.(11) and easily obtain the coefficients C_j . One of the estimated result is shown in Fig.2 together with the original corona current. These two currents shapes are quite the same as the results in Fig.1. In Table 2 relative errors of peak values of estimated currents for various channel lengths and distances are shown. The relative errors are also at most a few percent. We can conclude that this method is useful to the estimation of corona current too.

(3) Discussion

In section (1) and (2) we have already discussed about how to estimate the return stroke current with E and B. It is cleared up that this new method is useful for the estimation. However all used data are simulated ones, that is without noise. So we need more discussion about the case of data including some noise before conclusion. The simulated E and B added by random noises, which root mean square values are ten percent of the peak values, are used for estimation and the average of relative errors of ten times experiments is only 3.8 percent. That is, we can find even if the measured data includes some noises, we are able to estimate the return stroke current rather exactly. Then we can conclude this method is much useful for the estimation from the view point of current shapes and relative errors.

Conclusion

We proposed the new return stroke current estimation method in this paper. This method was applied to the transmission line model and Lin-Uman-Standler's model and we could obtain excellent results. We can conclude that this method should be applied to the current estimation.

References

- Y. T. Lin, M. A. Uman and R. B. Standler, "Lightning return stroke models", J.

- Geophys. Res., **85**, 1571-1583(1980)
- M. A. Uman and D. K. McLain, "Magnetic field of lightning return stroke", J. Geophys. Res., **74**, 6899-6909(1969)
- M. A. Uman, D. K. McLain and E. P. Krider, "The electromagnetic radiation from a finite antenna", Amer. J. Phys., **43**, 33-38(1975)

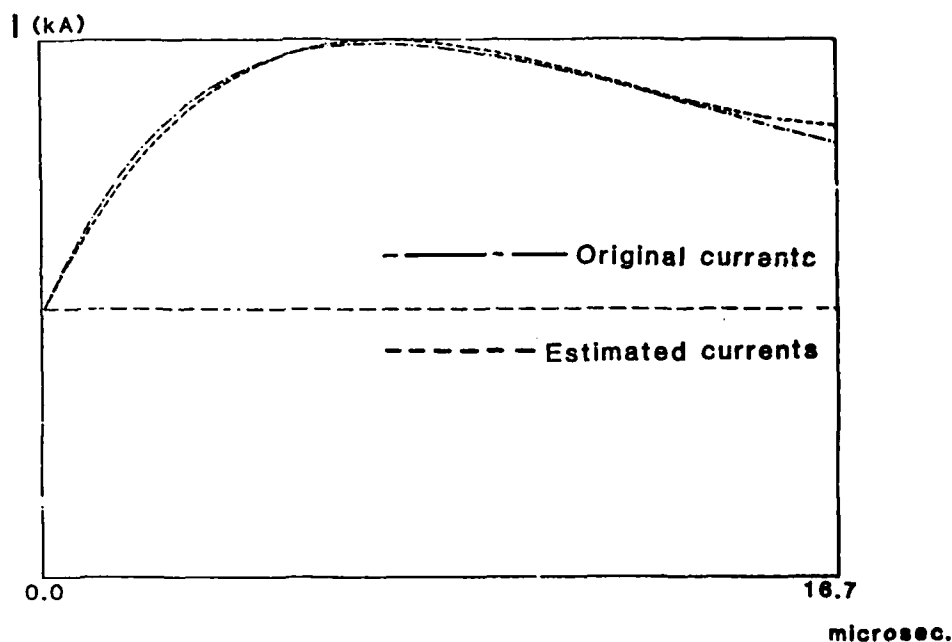


Fig.1 The typical estimated current of Transmission line model

Table 1 The Relative errors of peak values of estimated current (%)
(The case of attenuation constant =1.0)

v\D	5	10	20
.01	-0.53	-1.20	-6.27
.05	2.00	-1.20	-2.93
.10	1.20	1.47	-0.13

(the case of attenuation constant =0.0)

v\D	5	10	20
.01	-1.47	-2.00	-4.80
.05	2.67	0.00	0.13
.10	2.13	1.20	1.47

v:velocity of return stroke(km/ μ sec)
D:distance(km)

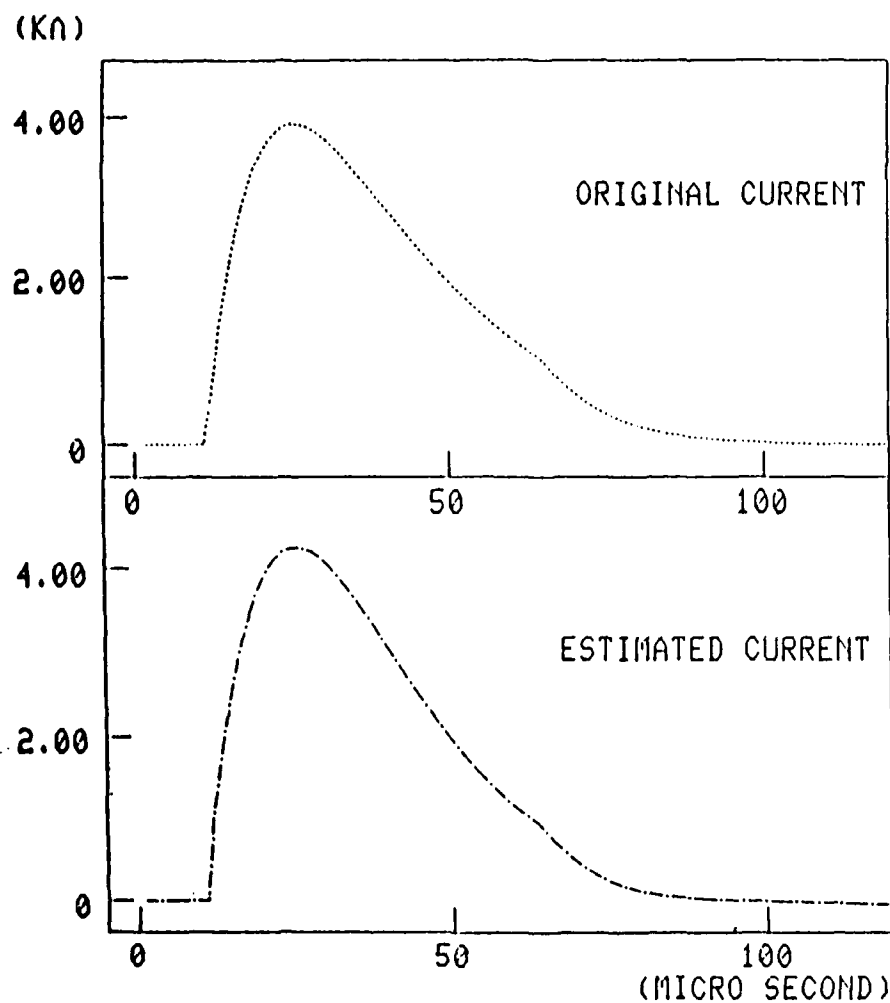


Fig.2 The typical estimated current of Lin-Uman-Standler's model
(corona current)

Table 2 Relative errors of peak values (%)

L\D	5	10	20
2	-1.7	0.4	-1.7
5	1.2	0.7	8.8
10	1.1	-0.3	0.8

L:channel length(km)
D:distance (km)

ON BOUNDING THE EXCITATION OF WIRING
BEHIND AN APERTURE IN A SHIELD
FROM LIGHTNING INDUCED FIELDS

Clayborne D. Taylor
Department of Electrical Engineering
Mississippi State University
Mississippi State, MS 39762

ABSTRACT

A terminated wire behind an aperture in a shield is considered to be illuminated by lightning induced electromagnetic fields. Coupling between the wire and the aperture is fully considered by using receiving antenna theory. Expressions are derived for the upper bounds on the termination currents and voltages. Both radiated fields and channel attachment fields are considered.

INTRODUCTION

An electromagnetic shield from lightning induced fields simply provides a barrier to the propagation of electromagnetic fields from one region to another. The diffusion of the fields through the walls of the shield has been well studied. For shields that are perforated, either deliberately or inadvertently, a substantial degradation in shielding effectiveness may occur. Normally the quantitation of the degradation can be accomplished by the consideration of three processes (assumed independent): external interaction, aperture penetration, and internal coupling. The conventional approach for treating coupling through apertures has used small aperture approximations, i.e. the aperture is required to be electrically small and the wiring behind the aperture is required to be separated from aperture a distance sufficient for the dipole field approximation to be valid. And in determining internal coupling within a shielded region, generally loading effects on the aperture from internal wiring (and termination impedances) in proximity to the aperture are ignored. However, the aperture-wiring interaction can be appreciable, and in general can not be neglected.

In this paper an analysis is developed for obtaining the excitation of terminated wiring behind aperture-perforated shields. Coupling between the aperture and the wire are included by considering the aperture to be a receiving antenna with the wire configuration providing the load impedance presented to the antenna. This load impedance is determined by using conventional transmission line theory and therefore only the TEM mode current is obtained. However, if

the wire spacing is small in terms of the wavelength and the wire length, only the TEM mode is significant.

Using the analysis, expressions are derived for the upper bounds on the termination current and voltage for a wire behind a slot-perforated screen, that is exposed to typical lightning induced fields. Both radiated fields and channel attachment fields are considered.

ANALYSIS

GENERAL CONSIDERATIONS - The configuration being considered is shown in Figure 1. Here a terminated wire behind an aperture presents an impedance load to the aperture antenna. The equivalent circuit for the receiving antenna is shown in Figure 2. Following standard receiving antenna theory

$$V_{oc}^{(s)} = \vec{h}_e^{(s)} \cdot \vec{E}^{inc} = I_{sc}^{(s)} Z_{in}^{(s)} \quad (1)$$

is the open-circuit voltage of the receiving antenna in terms of the effective height and incident electric field. Here $Z_{in}^{(s)}$ is the input impedance of the aperture antenna, and $I_{sc}^{(s)}$ is the short-circuit current. Often it is more convenient to consider the complementary antenna with effective height $h_e^{(d)}$ and input impedance $Z_{in}^{(d)}$ where

$$Z_{in}^{(s)} Z_{in}^{(d)} = \frac{1}{4} \eta_o^2 \quad (2)$$

and

$$\vec{k} \times \vec{h}_e^{(s)} = \frac{1}{2} \frac{\eta_o}{Z_{in}^{(d)}} \vec{k} h_e^{(d)} \quad (3)$$

Here η_o is the intrinsic wave impedance of free space and \vec{k} is the propagation vector of the incident plane wave [1].

Using (1)-(3) it is readily shown that

$$V_{oc}^{(s)} = \frac{\eta_o^2}{4 Z_{in}^{(d)}} I_{sc}^{(s)} \quad (4)$$

where

$$I_{sc}^{(s)} = \hat{n} \cdot (\vec{h}_e^{(d)} \times \vec{J}_s) \quad (5)$$

Here \hat{n} is the unit vector outward normal to the aperture surface and \vec{J}_s is the surface current density at the aperture that would exist if the aperture were completely sealed.

From Figure 2, the solution for I_s , the wire current at the aperture is

$$I_s = \frac{V_{oc}^{(s)}}{Z_{in}^{(s)} + Z_{11} + Z_{12}} \quad (6)$$

where Z_{11} and Z_{12} are the input impedances seen on each side of the aperture. If the wire behind the aperture extends a distance ℓ on each side of the aperture, then

$$Z_{11} = Z_{12} = Z_c \frac{Z_L \cos k\ell + jZ_c \sin k\ell}{Z_c \cos k\ell + jZ_L \sin k\ell} \quad (7)$$

where Z_L is the load impedance terminating the wire and

$$Z_c = \frac{\eta_o}{2\pi} \operatorname{arc} \cosh \left(\frac{h_w}{a_w} \right) \quad (8)$$

Here h_w is the wire height and a_w is the radius of the wire behind the aperture (see Figure 1). Note that the application of standard transmission line theory yields the load current,

$$I_L = \frac{Z_c}{Z_c \cos k\ell + jZ_L \sin k\ell} I_s \quad (9)$$

which becomes after applying (4) through (7)

$$I_L = \frac{Z_{in}^{(s)} Z_c \hat{n} \cdot (\vec{h}_e^{(d)} \times \vec{J}_s)}{(Z_{in}^{(s)} + 2Z_L) Z_c \cos(k\ell) + j(Z_{in}^{(s)} Z_L + 2Z_c^2) \sin(k\ell)} \quad (10)$$

The corresponding load voltage is obtained by using $V_L = I_L Z_L$.

If the dimensions of the aperture are small in terms of the wavelength, then the following approximations are valid for the complement of a thin slot (the narrow strip dipole):

$$h_e^{(d)} \approx \frac{h(\Omega-1)}{\Omega-0.61} \hat{z} \quad (11)$$

$$Z_{in}^{(d)} \approx \frac{\eta_o}{6\pi} (kh)^2 - j \frac{\eta_o}{2\pi} \frac{\Omega-3.39}{kh} \quad (12)$$

where

$$\Omega = 2\ell n \left(\frac{8h}{w} \right) \quad (13)$$

Here w is the slot width and $2h$ is the slot length.

Consequently using (11), (12) and (2) in (10) yields the termination currents of the wire behind an aperture for general conditions. However it is required that the aperture dimensions must be small in terms of the wavelength. For most applications this low frequency requirement is applicable. For convenience in obtaining the bounds on the termination currents certain generic conditions are considered.

$$(i) \quad Z_L = Z_c$$

When the wire behind the aperture is terminated in a resistance equal to the characteristic impedance Z_c , (10) through (12) yields

$$I_L \Big|_{\max} \approx \frac{\pi}{4} \frac{\mu_o h^2}{Z_c (\Omega-3.39)} \frac{\Omega-1}{\Omega-0.61} j\omega J_s e^{-jk\ell} \quad (14)$$

for $kh \leq .1$. Note that (14) represents the upper bound on the termination current for matched terminations. A corresponding upper bound on the load voltage is

$$V_L \Big|_{\max} = Z_L I_L \Big|_{\max} \quad (15)$$

Time domain upper bounds can be obtained from (14) and (15) via Fourier transform theory. Accordingly (14) yields,

$$I_L \Big|_{\text{peak}} \approx \frac{\pi}{4} \frac{\mu_o h^2}{Z_c (\Omega-3.39)} \frac{\Omega-1}{\Omega-0.61} \frac{d}{dt} J_s \Big|_{\text{peak}} \quad (16)$$

and (15) yields,

$$V_L \Big|_{\text{peak}} = Z_L I_L \Big|_{\text{peak}} \quad (17)$$

$$(ii) \quad Z_L = 0$$

Often the wire(s) behind an aperture is shielded. Consequently the transfer function for the shield can be used to obtain the current on the wire(s) inside the shield if the shield current is known [2]. Treating the shield as a single wire behind the aperture, the terminations become electrical shorts. Accordingly (10)-(12) yields for $kh < 0.1$ and $k\ell < 0.1$

$$V_L \Big|_{\max} \approx \left[1 + \frac{4}{\pi} \frac{Z_c (\Omega - 3.39)}{\eta_o} \frac{\ell}{h} \right]^{-1} \frac{h(\Omega - 1)}{\Omega - .61} J_s \quad (18)$$

Of course the corresponding load voltage is zero.

As before time-domain bounds can be obtained via Fourier transform theory. They are,

$$i_L \Big|_{\text{peak}} \approx \left[1 + \frac{4}{\pi} \frac{Z_c (\Omega - 3.39)}{\eta_o} \frac{\ell}{h} \right]^{-1} \frac{h(-1)}{-.61} j_s \Big|_{\text{peak}} \quad (19)$$

$$(iii) \quad Z_L = \infty$$

With open-circuit terminations, the termination currents become zero. However using $V_L = I_L Z_L$ with (10) and allowing $Z_L \rightarrow \infty$, the following load voltage expression is obtained:

$$V_L \Big|_{\max} \approx \frac{\pi}{4} \frac{\mu_o h^2}{\Omega - 3.39} \frac{\Omega - 1}{\Omega - .61} j\omega J_s \quad (20)$$

for $kh < 0.1$ and $k\ell < 0.1$.

The corresponding time-domain voltage upper bound is

$$V_L \Big|_{\text{peak}} \approx \frac{\pi}{4} \frac{\mu_o h^2}{\Omega - 3.39} \frac{\Omega - 1}{\Omega - .61} j_s \Big|_{\text{peak}}$$

LIGHTNING EXCITATION - Because natural lightning exhibits varied and discontinuous waveshape components it is not possible to make absolute and definitive statements. The general approach is to select representative current waveshapes and then to draw appropriate conclusions. As seen in the analysis of the excitation of terminated wires behind apertures, two parameters of concern are the threat level peak current and the threat rate-of-rise level for the lightning current.

According to Uman et al. [3] threat levels for the peak channel current are about 35 kA for an average first return stroke and 175 kA for a severe stroke. They also indicate that the maximum rate-of-rise can be estimated by considering one-half of the peak channel current is achieved in about 0.1 μ s.

In order to obtain the surface current density, J_s , induced by lightning additional considerations are necessary. For example, if direct attachment of the lightning channel occurs then the current density on the shield with the aperture will be directly related to the channel current [3]. However if attachment does not occur then the current density on the shield must be obtained by solving a scattering problem [4]. It is rather

obvious that the peak time-domain current will occur with direct attachment. However the rate-of-rise of the surface current is not necessarily greater for channel attachment.

REFERENCES

1. C. D. Taylor, E. Harper, C. W. Harrison, Jr., and W. A. Davis, "On Bounding the Excitation of a Terminated Wire Behind an Aperture in a Shield" accepted for publication in IEEE Transactions on Antennas and Propagation.
2. E. F. Vance, Coupling to Shielded Cables, Wiley: New York (1978).
3. M. A. Uman, M. J. Master, and E. P. Krider, "A Comparison of Lightning Electromagnetic Fields with the Nuclear Electromagnetic Pulse in the Frequency Range 10^4 - 10^7 Hz", IEEE Trans. Electromag. Compat., Vol. EMC-24, No. 4, pp. 410-416, November 1982.
4. R. A. Perala, T. Rudolph and F. Eriksen, "Electromagnetic Interaction of Lightning with Aircraft", IEEE Trans. on Electromag. Compat., Vol. EMC-24, No. 2, pp. 173-203, May 1982.

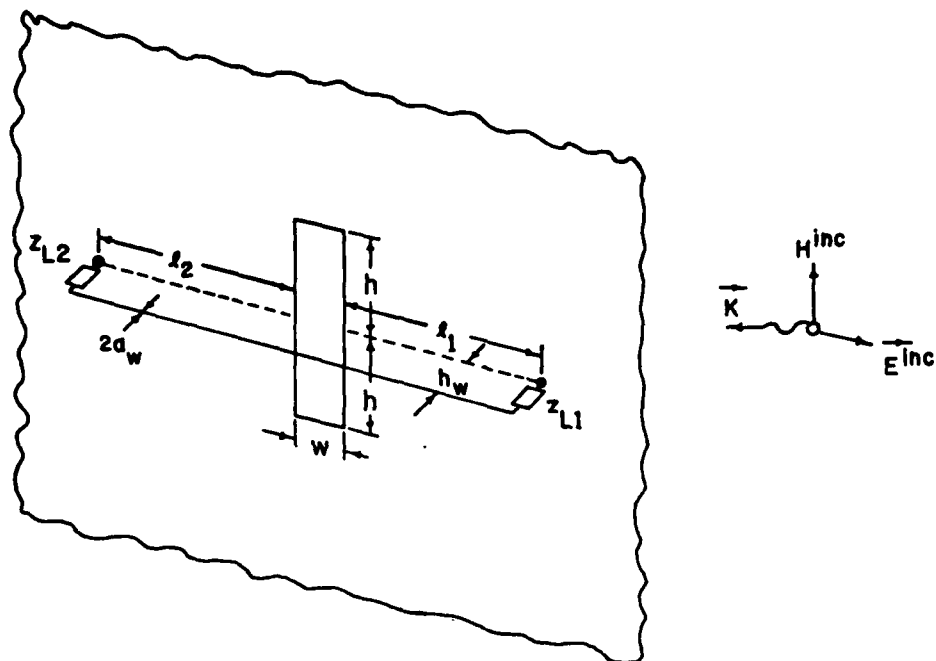


Figure 1. Terminated Wire Configuration Behind a Rectangular Aperture in a Metal Plate Shield

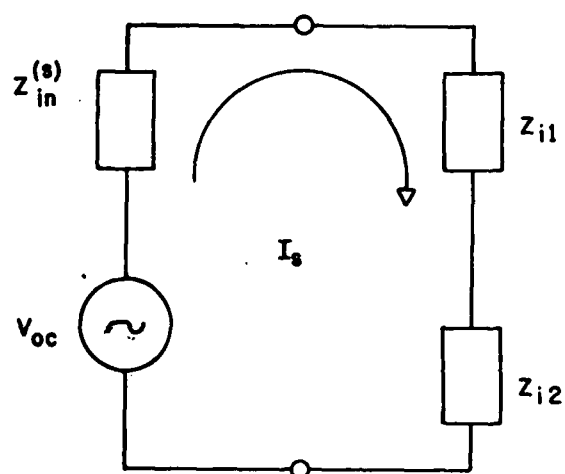


Figure 2. Equivalent Circuit for the Slot Receiving Antenna with the Load Impedance that is a Series Combination of Z_{i1} and Z_{i2}

A TIME DOMAIN REPRESENTATION OF SURFACE AND TRANSFER
IMPEDANCES USEFUL FOR ANALYSIS OF ADVANCED COMPOSITE AIRCRAFT

By

P. M. McKenna
T. H. Rudolph
R. A. Perala

Electro Magnetic Applications, Inc.
P. O. Box 26263
Denver, Colorado, 80226
(303)989-2744

ABSTRACT

Because of the proliferation of advanced composite materials in future and present aircraft, it is necessary to accurately include their effects on the electromagnetic coupling paths. An important numerical method which is used to calculate aircraft coupling response is the three-dimensional time domain finite difference solution to Maxwell's equations. The spatial resolution of such codes for typical aircraft may be on the order of 1/3 to 1/2 m, which means that modeling of thin structures such as lossy aircraft skins cannot be accurately done with conventional techniques. There is therefore a need to define and illustrate an approach whereby lossy surfaces can be treated in the time domain by defining a relationship between the surface electric and magnetic fields such that the details of the skin do not have to be directly modeled.

Lightning coupling to aircraft with graphite composite skins is complicated by the low conductivity of the composite material compared to metal. In order to properly account for the presence of composite material the external electromagnetic fields are related in the frequency domain by

$$\frac{E}{H} = Z_s = \frac{j\eta}{\tanh(jk_m d)}$$

and the internal electric field E just inside the composite skin is related to the external magnetic field H just outside the skin by

$$\frac{E}{H} = Z_T = \frac{\eta}{\sin(k_m d)}$$

where η is the material intrinsic impedance and k_m is the material propagation constant. Infinite series partial fraction expansions of these impedances are decomposed into bounded infinite sums of solutions to ordinary differential equations in the time domain. Convergence of the sums occurs with relatively few terms. Results for both external and internal coupling are presented.

INTRODUCTION

THE USE OF GRAPHITE EPOXY COMPOSITES in many current and future civilian and military aircraft significantly alters the coupling of electromagnetic fields to these aircraft. The high conductivity of metal aircraft skins shields internal conductors from external electromagnetic fields because diffusion through the skin is usually almost negligible. The only important shielding considerations below 100 MHz arise from seams, apertures, or penetrating conductors. Graphite-epoxy composite materials are about three orders of magnitude less conductive than aluminum. Because of this lower conductivity, electromagnetic field diffusion through the aircraft skin can be significant (1)*. Furthermore, the higher intrinsic impedance resistance of the graphite-epoxy composite material relative to metal will alter skin current patterns significantly when electromagnetic fields are present at high levels for durations exceeding the current redistribution time. This is the case with lightning.

Unfortunately, the spatial resolution of time domain finite difference approximation solutions to Maxwell's equations is far too coarse to be able to resolve the thickness of composite layers when the entire aircraft is contained in the problem volume. This lack of resolution precludes the treatment of composites by direct calculation of the conduction current in the composite material in the time domain. Because expressions for the surface impedance and surface transfer impedance are frequency dependent, they must be transformed to the time domain in order to obtain usable relationships between the E and H fields tangential to the surface of the composite. This paper describes an approximate technique for relating E and H fields tangential to the surface of the composite material which is appropriate for lightning coupling to aircraft. Briefly, the technique decomposes the frequency domain expressions for the impedance into an infinite sequence of partial fraction expansions which transform into an infinite sequence of analytically soluble ordinary differential equations in the time domain.

The organization of the remainder of this paper is as follows. First, a short derivation of the frequency domain expressions for the surface impedance and surface transfer impedance is presented. Second, the transformation from the frequency domain to the time domain is derived. A description of the implementation in a time dependent finite difference computer program is also described. Third, results of external and internal coupling analyses are presented and discussed for a lightning environment. Last, a summary and conclusions are presented.

*Numbers in parentheses designate References at end of paper.

DERIVATION OF THE SURFACE IMPEDANCE AND THE SURFACE TRANSFER IMPEDANCE FOR A CONDUCTING SLAB

In general the conductivity of graphite epoxy composite materials is anisotropic. However, the off-diagonal elements of the conductivity tensor are either zero or much smaller than the diagonal elements (1) and will be neglected. In addition, it will be assumed that the two diagonal elements of the conductivity tensor which are tangential to the surface of the composite material, σ_{xx} , and σ_{yy} are effectively equal because of the $0^\circ/+45^\circ/90^\circ$ layering of the composite. The conductivity normal to the surface, σ_{zz} , is much less than σ_{xx} or σ_{yy} . Thus the most effective coupling of electromagnetic fields through the composite will occur for both the E and H fields tangential to the surface of the composite. To this end, consider the situation diagrammed in Fig. 1. A composite planar slab of thickness d normal to the z-axis is illuminated by a normally incident plane wave. The surface impedance, Z_s , is the ratio of the incident plus reflected electric field at $z = 0$ to the integrated conduction current density. The surface transfer impedance, Z_T , is the ratio of the transmitted electric field at $z = d$ to the integrated conduction current density. By Fourier transforming in space and time and imposing continuity of the tangential components of E and H, it can be shown that

$$Z_s = \frac{jk_m}{\sigma} \frac{[\cosh(jk_m d) + \chi \sinh(jk_m d)]}{[\sinh(jk_m d) + \chi(\cosh(jk_m d) - 1)]} \approx \frac{jk_m}{\sigma} \coth(jk_m d) \quad (1)$$

for $\chi \ll 1$, and

$$Z_T = \frac{jk_m}{\sigma} \frac{1}{[\sinh(jk_m d) + \chi(\cosh(jk_m d) - 1)]} \approx \frac{k_m}{\sigma} \frac{1}{\sin(k_m d)} \quad (2)$$

$$\text{for } \chi \ll 1. \text{ Here } \chi = \frac{\mu_2}{\mu_0} \frac{k_0}{k_m} \quad (3)$$

$$k_0^2 = \omega^2 \mu_0 \epsilon_0 \quad (4)$$

$$k_m^2 = -j\omega\mu_2 (\sigma + j\omega\epsilon_2) \quad (5)$$

and $\sigma = \sigma_{xx} = \sigma_{yy}$.

For the frequencies of interest, (<100 MHz) and the conductivities of graphite epoxy composites (8000 mho/m - 20000 mho/m), $\chi \ll 1$. Also,

$$k_m \approx \frac{1}{\sqrt{2}} (1-j) (\omega \mu_2 \sigma)^{1/2} \quad (6)$$

so that the intrinsic impedance of the composite material, η , can be written

$$\eta = \frac{k_m}{\sigma} \approx \frac{1}{\sqrt{2}} (1-j) \left(\frac{\omega \mu_2}{\sigma} \right)^{1/2} \quad (7)$$

TRANSFORMATION TO THE TIME DOMAIN

In order to obtain time domain expressions for the relationship between the electric field and the conduction current in the composite slab, equations (1) and (2) were rewritten using the following identities

$$\coth x = \frac{1}{x} + 2x \sum_{n=1}^{\infty} \frac{1}{(n\pi)^2 + x^2} \quad (8)$$

$$\sin x = x \prod_{k=1}^{\infty} \left(1 - \frac{x^2}{k^2 \pi^2} \right) \quad (9)$$

Substituting the first expansion (8) into equation (1) and substituting the approximate form for k_m (6) yields

$$E(\omega) = \left[\frac{1}{\sigma d} + j\omega \left(\frac{2}{\sigma d} \right) \sum_{n=1}^{\infty} \frac{1}{\omega_n + j\omega} \right] J(\omega) \quad (10)$$

$$\text{where } \omega_n = \left(\frac{n\pi}{d} \right)^2 \frac{1}{\mu_2 \sigma} \quad (11)$$

Forming a decomposition of the series and transforming each term into the time domain results in an infinite sequence of ordinary differential equations in the time domain as follows

$$E^0(\omega) = \frac{1}{\sigma d} J(\omega) \quad \text{corresponds to}$$

$$E^0(t) = \frac{1}{\sigma d} J(t) \quad (12a)$$

$$E^1(\omega) = j\omega \left(\frac{2}{\sigma d} \right) \frac{1}{\omega_1 + j\omega} J(\omega) \Leftrightarrow \quad (12b)$$

$$\frac{d}{dt} E^1(t) + \omega_1 E^1(t) = \left(\frac{2}{\sigma d} \right) \frac{dJ}{dt}$$

⋮

$$E^n(\omega) = j\omega \left(\frac{2}{\sigma d} \right) \frac{1}{\omega_n + j\omega} J(\omega) \Leftrightarrow \quad (12c)$$

$$\frac{dE^n(t)}{dt} + \omega_n E^n(t) = \frac{2}{\sigma d} \left(\frac{dJ}{dt} \right)$$

The solutions of these ordinary differential equations (12) are analytic. The time domain electric field is then an infinite series of convolutions

$$E(t) = \sum_{n=0}^{\infty} E^n(t) = \frac{1}{\sigma d} \left[J(t) + 2 \sum_{n=1}^{\infty} \int_0^t dt' e^{-\omega_n(t-t')} J(t') \right] \quad (13)$$

where the initial conditions are $E^n(t=0) = 0$ ($n = 0, 1, \dots, \infty$).

Similarly, substitution of the product expansion for the $\sin(x)$ (9) in equation (2) and writing k_m as in equation (6) gives

$$E(\omega) = \frac{1}{\sigma d} \frac{J(\omega)}{\prod_{n=1}^{\infty} \left(1 + \frac{j\omega}{\omega_n} \right)} = \quad (14)$$

$$\frac{2}{\sigma d} \sum_{k=1}^{\infty} \frac{(-1)^{k+1}}{\left(1 + \frac{j\omega}{\omega_k} \right)} J(\omega)$$

$$\text{where } \omega_k = \left(\frac{k\pi}{d} \right)^2 \frac{1}{\mu_2 \sigma} \quad (15)$$

Following the same procedure that was outlined above the time domain electric field transmitted through the composite layer can be written as an infinite series of convolutions:

$$E(t) = \frac{1}{\sigma d} \left[J(t) + 2 \sum_{n=1}^{\infty} (-1)^n \int_0^t dt' e^{-\omega_n(t-t')} J(t') \right] \quad (16)$$

where once again $E^n(t=0) = 0$ ($n=1, 2, \dots, \infty$) and $J(t=0) = 0$.

Implementation of the series expansions (13) and (16) in a time dependent finite difference approximation solution requires back storage of the tangential components of the H fields in order to compute the external or internal coupling through the composite material, at least at early times. At late times both so-

lutions converge to $E(t) \sim \frac{J(t)}{\sigma d}$. Depending on the bandwidth of the calculation, and the conductivity and thickness of the composite, the series expansion for the transfer impedance (16) may converge less than 20 terms at early time. The series expansion for the surface impedance (13) requires approximately 200 terms to converge for calculations with 100 MHz bandwidths.

RESULTS

AS A DEMONSTRATION OF THE TECHNIQUE described above the results of external and internal electromagnetic coupling by lightning to a simple scattering object are presented. The problem is solved by a linear, time dependent, three dimensional, explicit finite difference approximation method (2). The spatial grid size is 1m in all three Cartesian coordinate directions. The time step is 1.75 ns. Inside the problem volume a current channel is attached to one of the 5m x 5m faces of a box with dimensions 5m x 3m x 5m. A line of zeroed E fields is attached to the opposite face to carry off the current after it has flowed across the box. The attached current has a waveform with a \sin^2 rise to peak in 1 μ s and an exponential decay with a time constant of 50 μ s. The peak current is 200,000 amperes. Two of the four 5m x 3m faces opposite each other are graphite-epoxy composite with thickness .03 in and conductivity 15,000 mho/m. The other faces of the scatterer are assumed to be perfectly conducting. For comparison, the same current was attached to a perfectly conducting scatterer with same dimensions.

In Fig. 2 the component of the tangential H field associated with the primary direction of current flow is shown. The location of the sample point is above one of the composite faces. The solid curve represents the waveform for the case of the scatterer with two composite faces. The dashed line represents the waveform for the scatterer with all faces perfectly conducting. The waveforms shown in Fig. 2 are characteristic of other locations above the composite surface. The growing difference between the waveforms with time is due to current redistribution on the scatterer to avoid the lower conductivity composite faces. This is also clear in Fig. 3. The waveforms shown are also components of the H field tangential to the surface above one of the perfectly conducting faces. The component is associated with the primary direction of current flow. The solid curve again represents the scatterer with two composite faces while the dashed curve represents the scatterer with all six faces perfectly conducting. The surface current above the perfectly conducting face is growing for the composite box because the current is gradually dividing resistively. Fig. 4 shows the waveform of the electric field diffused through the composite skin due to the current density in Fig. 2. This electric field would act as a driver for conductors located inside the composite box. For large amplitude direct lightning strikes the diffusion of electromagnetic fields through the composite skin will result in large field intensities inside the composite skin.

SUMMARY AND CONCLUSIONS

THE ELECTROMAGNETIC COUPLING of lightning to aircraft with graphite-epoxy composite skins is complicated by the frequency dependence of the impedance relations. By decomposing the approximate forms for the impedances into series expansions, each term becomes the solution of an ordinary differential equation in time. With appropriate initial conditions the solutions corresponds to convolutions which converge to the low frequency limit of a purely resistive impedance. The series expansions are easily implemented in time dependent finite difference approximation solutions of Maxwell's equations. There are two major effects of the use of graphite epoxy composite materials in lightning coupling. First, there is a resistive division of skin currents at late time away from the composite surfaces and onto the metal surfaces. Second, the lower conductivity of graphite epoxy composites relative to metals allows substantially larger diffusion of electromagnetic fields through the composite skin.

REFERENCES

1. R. A. Perala, K. M. Lee and R. B. Cook, "EMP Coupling to a Composite Aircraft," Proceedings of the IEEE 1978 International Symposium on Electromagnetic Compatibility, Atlanta, Ga., p. 233.
2. D. E. Merewether and R. Fisher, "Finite Difference Solution of Maxwell's Equation for EMP Applications," EMA 79-R-4, (Revised), Electro Magnetic Applications, Inc., P. O. Box 8482, Albuquerque, N. M. 87198, April 1980.

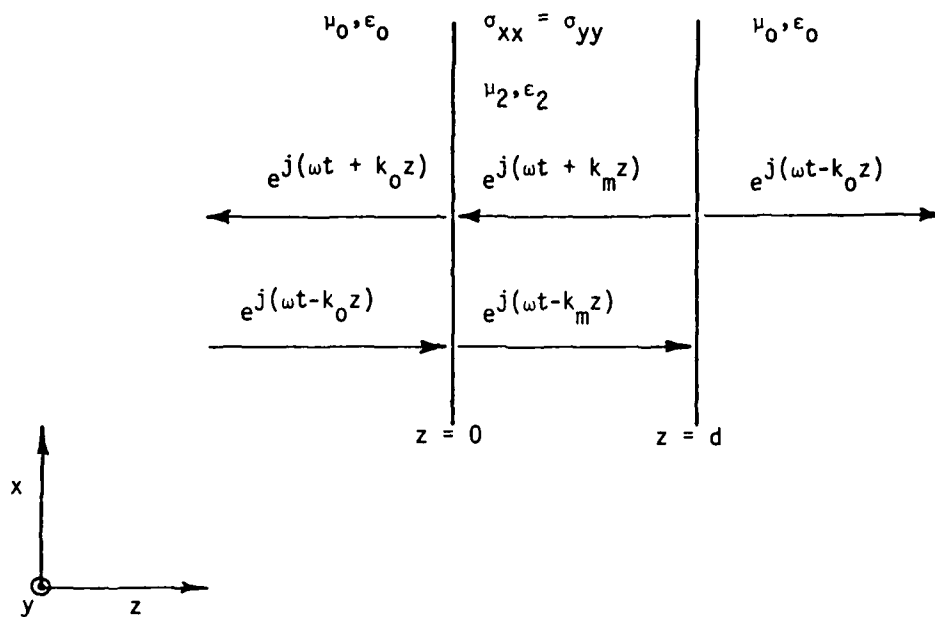


Fig. 1 - A plane wave incident on a planar composite slab of thickness d . The space and time dependence of the E and H fields is shown above the horizontal arrows.

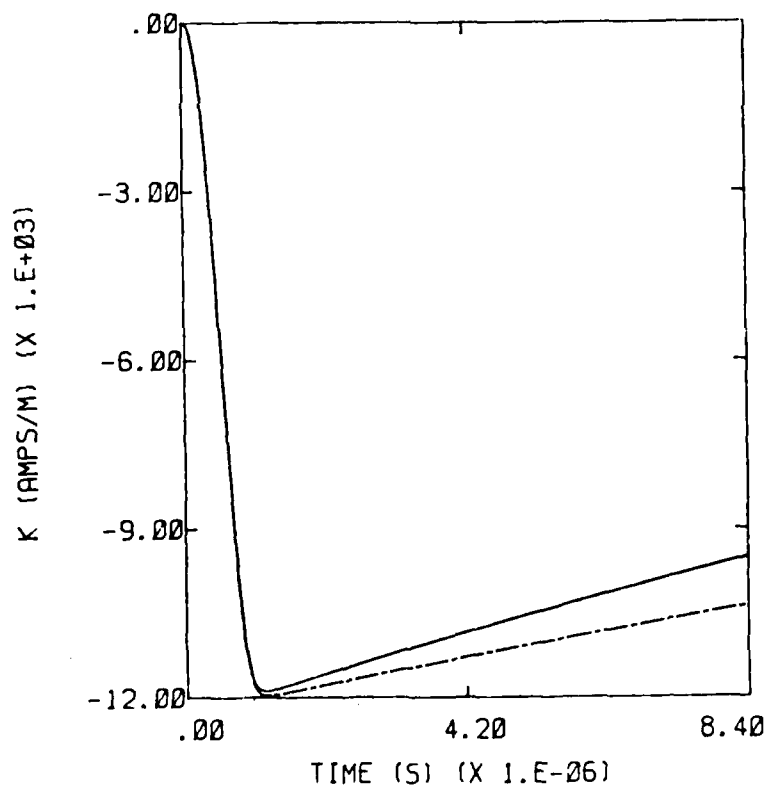


Fig. 2 - Tangential H field component (or axial surface current density) for a composite box (solid curve) and a perfectly conducting box (dashed curve) above a composite face.

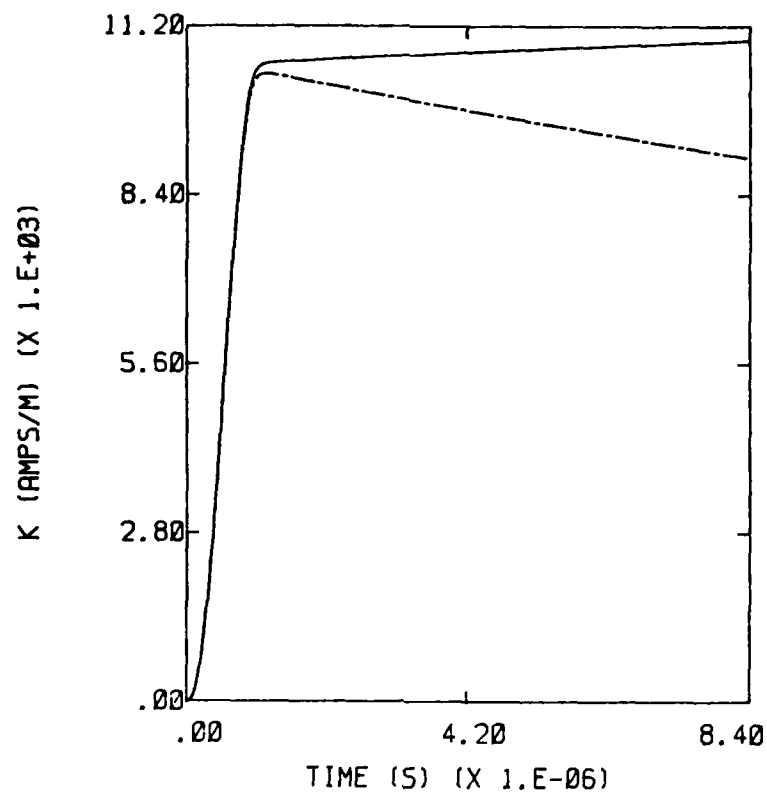


Fig. 3 - Tangential H field (or axial surface current density) component for a composite box (solid curve) and a perfectly conducting box (dashed curve) above a perfectly conducting face.

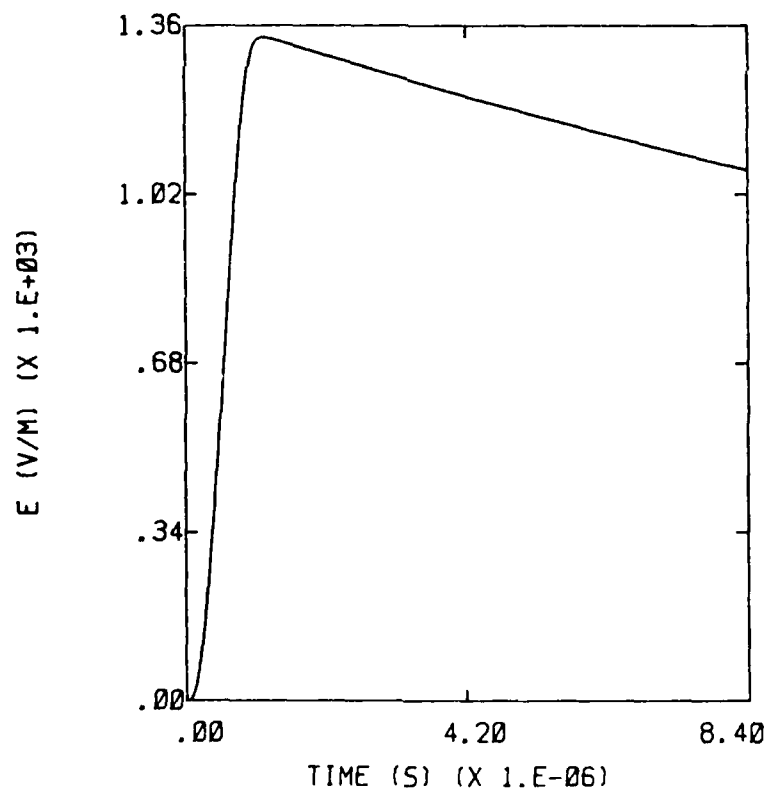


Fig. 4 - The principal component of the electric field diffused through a composite layer corresponding to the solid curve in Fig. 2.

TRANSIENT RESPONSE AND PROTECTION OF MULTICONDUCTOR
TRANSMISSION LINES

J.L. ter Haseborg and H. Trinks
Technical University Hamburg-Harburg
Hamburg, Germany

ABSTRACT

Coupling and propagation mechanisms of lightning- and EMP-induced currents on transmission lines as well as problems concerning protective measures against these currents are treated.

Starting from the transfer impedance of the cable and an arbitrarily assumed sheath current by means of the transmission line equations the propagation of these currents - e.g. caused by lightning or EMP - on the conductors of multiconductor transmission lines is computed. The computations are carried out in consideration of an equivalent circuit diagram which besides inductive and capacitive couplings contains also ohmic losses in the conductors and frequency-dependent dielectric losses in the insulation.

CONCERNING THE SHIELDING of ground systems, airborne, and ground equipment against electromagnetic interferences the shielding efficiency is reduced particularly by feeding of interfering currents through cable entries [1]*, [2]. Starting from a realistic common mode excitation for all conductors, cable entries for multiconductor transmission lines are of special interest. In order to estimate the protection efficiency by special protection circuits, the time-dependent or frequency-dependent shape respectively of the interfering currents on the transmission lines has to be known. Particularly the influence of the transmission line parameters on the propagation of the currents will be considered. A variation of the edge steepness of interfering guided pulses by the line parameters influences the response of protection circuits [1], [2].

As shown in Fig. 1 interfering currents I_s - e.g. caused by lightning or EMP - are induced primarily on the cable sheath. Dependent on the shielding efficiency of the sheath, which is described by the frequency-dependent transfer impedance, the sheath current I_s partially is coupled into the inner conductors (I_c).

TRANSFER IMPEDANCE

The coupling mechanism between sheath currents and conductor currents is described analytically by the frequency-dependent transfer impedance as defined by Kaden [3], Fig. 2. So for instance, for different braided shields Fig. 3 shows the transfer impedances Z_T as a function of frequency (solid curves) where by represents the ohmic resistance of the sheath. In order to obtain an analytical description for the propagation of the currents by means of the transmission line equations, that is not only for the inner conductors but also for the cable sheath, the cable sheath (e.g. a braided sheath) is replaced by an equivalent cage consisting of n conductors as shown in Fig. 4. By means of suitably dimensioned parameters of the cage in consideration of a constant radius r , it is possible to realize a definite transfer impedance Z_T . The dashed curve in Fig. 3 shows the frequency-dependent transfer impedance of a cage. There is a good agreement between the curves belonging to the braided shield and the curve for the cage. A comparison between the dashed and solid curves in Fig. 3 shows that the cage corresponds to a braided shield with a C_0 -value of approx. 94.5 %. The quantity C_0 represents the value for the optical coverage of the shield.

THE TRANSMISSION LINE EQUATIONS

Starting from the transmission line equations an equivalent circuit diagram is used which besides inductive and capacitive couplings considers also the line losses (ohmic losses in the conductors and frequency-dependent losses in the insulation) [4], [5]. Fig. 5 shows the equivalent circuit diagrams, Fig. 5a for a two-wire line and Fig. 5b for a multiconductor line with

* Numbers in parentheses designate References at end of paper.

n conductors. The equations (1) up to (4) represent the transmission line equations for a two-wire line in the:

time-domain:

$$\frac{\partial u}{\partial z} = - (R' + L' \frac{\partial}{\partial t}) i \quad (1)$$

$$\frac{\partial i}{\partial z} = - (G' + C' \frac{\partial}{\partial t}) u \quad (2)$$

frequency-domain:

$$\frac{dU}{dz} = - \underline{Z}' \cdot \underline{I} ; \underline{Z}' = R' + j\omega L' \quad (3)$$

$$\frac{dI}{dz} = - \underline{Y}' \cdot \underline{U} ; \underline{Y}' = G' + j\omega C' \quad (4)$$

The transition to $n+1$ conductors provides the equations in matrix notation:

$$-\frac{d[\underline{U}]}{dz} = [\underline{Z}'] \cdot [\underline{I}] \quad (5)$$

$$-\frac{d[\underline{I}]}{dz} = [\underline{Y}'] \cdot [\underline{U}] \quad (6)$$

The matrix $[\underline{Z}']$ contains the series impedances of the conductors and the mutual inductances, while the matrix $[\underline{Y}']$ contains the capacitances and the shunt conductances. The manufacturers of cables normally specify these values only for the operating frequency - e.g. $f = 800$ Hz. In this case the transmission line parameters of the complete cable (inner conductors in connection with the cable sheath consisting of the cage conductors) are computed according to the formulas shown in [6] and [7].

Concerning the transmission-line theory there is no difference between the inner conductors of the cable and the cage conductors replacing the cable shield. Starting from (5) and (6) the wave equation for the multiconductor transmission line is obtained:

$$\frac{d^2[\underline{U}]}{dz^2} = [\underline{E}] \cdot [\underline{U}] \quad (7)$$

$$\text{with } [\underline{E}] = [\underline{Z}'] \cdot [\underline{Y}'] \quad (8)$$

Equation (7) represents a coupled differential equation system. A linear transformation provides decoupled wave equations for the multiconductor transmission line:

$$[\underline{U}] = [\underline{V}] \cdot [\underline{w}] \quad (9)$$

$$\frac{d^2[\underline{w}]}{dz^2} = [\underline{v}]^{-1} \cdot [\underline{E}][\underline{v}][\underline{w}] \quad (10)$$

$$\text{whereby } [\underline{v}]^{-1} [\underline{E}] \cdot [\underline{v}] = [\underline{\Gamma}^2] \quad (11)$$

is a diagonal matrix and equation (11) represents an eigenvalue problem. The columns of the matrix $[\underline{v}]$ contain the eigenvectors of $[\underline{E}]$ and the elements of $[\underline{\Gamma}^2]$ ($[\underline{\Gamma}^2]$ is a diagonal matrix) are the eigenvalues of $[\underline{E}]$. A decoupled differential equation system is obtained:

$$\frac{d^2[\underline{w}]}{dz^2} = [\underline{\Gamma}^2][\underline{w}] \quad (12)$$

The components of $[\underline{w}]$ are designated as natural waves of the multiconductor transmission line. The root of the eigenvalue Γ^2 represents the propagation constant of the natural wave w_i . By means of various matrix operations the solution of the differential equation system is obtained:

$$[\underline{U}(z)] = [\underline{A}(z)] \cdot [\underline{U}(z=0)] - [\underline{B}(z)] \cdot [\underline{I}(z=0)] \quad (13)$$

$$[\underline{I}(z)] = -[\underline{C}(z)] \cdot [\underline{U}(z=0)] + [\underline{D}(z)] \cdot [\underline{I}(z=0)] \quad (14)$$

with

$$[\underline{A}(z)] = [\underline{v}] \cdot [\cosh \Gamma z] \cdot [\underline{v}]^{-1} \quad (15)$$

$$[\underline{B}(z)] = [\underline{v}] \cdot [\sinh \Gamma z] \cdot [\underline{\Gamma}]^{-1} \cdot [\underline{v}]^{-1} \cdot [\underline{Z}] \quad (16)$$

$$[\underline{C}(z)] = [\underline{Z}]^{-1} \cdot [\underline{v}] \cdot [\underline{\Gamma}] \cdot [\sinh \Gamma z] \cdot [\underline{v}]^{-1} \quad (17)$$

$$[\underline{D}(z)] = [\underline{Z}]^{-1} \cdot [\underline{v}] \cdot [\underline{\Gamma}] \cdot [\cosh \Gamma z] \cdot [\underline{\Gamma}]^{-1} \cdot [\underline{v}]^{-1} \cdot [\underline{Z}] \quad (18)$$

The quantity z marks the location on the line. The computations are carried out in consideration of arbitrary transmission line terminations (termination impedance matrix).

THE COMPUTATIONS

For the computations a braided-shield cable with 4 inner conductors is taken as a basis [5], [8], [9]. The braided shield is replaced by a cage consisting of 12 conductors with a transfer impedance as shown in Fig. 3 (dashed curve).

Fig. 6 depicts the complete arrangement. According to the transmission line terminations in the telephone engineering a termination of 600 Ω symmetrical is valid. The ground being a shell surrounds the cable cylindrically with the radius r , it is valid $r \gg r_c$. At the cable end the shield is connected to ground. The resistor R_g considers a finite conductivity of the ground.

Starting from the arrangement shown in Fig. 6, Fig. 7 and 8 represent the coupling and propagation of sheath currents. For these computations a definite coupling point at $z=0$ for e.g. lightning- and EMP-induced currents I_0 on the cable sheath is assumed. In Fig. 7 or Fig. 8 respectively the rise time of the sheath current

pulse at $z=0$ shows a value of approx. 10 ns or 50 ns respectively and the decay time a value of approx. 200 ns or 500 ns respectively. Referring to Fig. 6 the Fig. 7 and 8 contain the primary sheath current pulse I_0 at $z=0$ and at the locations $z_1=6m$, $z_2=12m$, $z_3=18m$, $z_4=24m$, $z_5=30m$

the current pulses I_0 on the cable sheath and the current pulses I_0^s on one of the four inner conductors. The amplitudes of the currents are normalized whereby the amplitude of the sheath current pulse I_0 ($z=0$) is the scaling factor. The coupling mechanism of the sheath current into the inner conductors essentially depends on the edge steepness of the sheath current and the frequency-dependent transfer impedance of the cable sheath. Although the difference between the edge steepnesses of the primary sheath current pulses I_0 ($z=0$) amounts only to factor 5 ($t_r=10$ ns in Fig. 7, $t_r=50$ ns in Fig. 8), an influence on the shape of the pulses coupled into the inner conductor can already be detected.

PROTECTIVE MEASURES

Protective measures against surge currents on transmission lines are shown and discussed comprehensively in [1], [2]. The protection circuits described in [1] and [2] essentially contain non-linear components. Particularly the arresters provide a response which is dependent on the edge steepness of the applying surge. Extensive measurements have shown these effects [1], [2], Fig. 9. Starting from the computation results describing the pulse shape on the conductors it is possible to determine the response of protection circuits at arbitrary locations on the transmission line.

CONCLUSIONS

The main computer program and the sub-routines are dimensioned theoretically for transmission lines with an arbitrary number of conductors. On account of limited calculating time and special numerical problems at present the computations are realized for 16 conductors. It is intended to increase this value. Additionally, the influence of the following parameters shall be investigated:

- rise and decay time of the sheath current pulse
- dielectric constant ϵ_r of the insulation
- number of the inner conductors.

Particularly theoretical and experimental investigations will be carried out concerning propagation of residual pulses which are caused by responding arresters.

The research work is executed in co-operation with the industry and other scientific establishments.

REFERENCES

1. J.L. ter Haseborg and H. Trinks, "Protection against Lightning Surge Voltages on Communication Lines and Power Lines", International Aerospace and Ground Conference on Lightning and Static Electricity, Forth Worth,

USA, June 21 - 23, 1983

2. J.L. ter Haseborg and H. Trinks, "Protection Circuits for Suppressing Surge Voltages with Edge steepnesses up to 10 kV/ns", 5th Symposium on Electromagnetic Compatibility, Zurich, March 8 - 10, 1983

3. H. Kaden, "Wirbelströme und Schirmung in der Nachrichtentechnik", Springer-Verlag, Berlin, Göttingen, Heidelberg, 1959

4. A.K. Agrawal, H.J. Price, and S.H. Gurbaxani, "Transient Response of Multiconductor Transmission Lines Excited by a Nonuniform Electromagnetic Field", IEEE Trans. Electromagn. Compat., vol. EMC-22, no. 2, May 1980

5. J.L. ter Haseborg, "Die numerische Berechnung der Leitungsparameter eines gekreuzten Linienleitersystems", Diplomarbeit Technische Universität Braunschweig, Okt. 1974

6. J.C. Clements, C.R. Paul, and A.T. Adams "Computations of the Capacitance Matrix for Systems of Dielectric-Coated Cylindrical Conductors", IEEE Trans. Electromagn. Compat., vol. EMC-17, no. 4, Nov. 1975

7. C.R. Paul, A.E. Feather, "Computations of the Transmission Line Inductance and Capacitance Matrices from the Generalized Capacitance Matrix", IEEE Trans. Electromagn. Compat., vol. EMC-18, no. 4, Nov. 1976

8. H.G. Unger, "Theorie der Leitungen", Vieweg-Verlag, Braunschweig 1967

9. A. Kolbe, "Einkopplung und Ausbreitung von transienten Strömen auf abgeschirmten Mehrfachleitungen", Studienarbeit, Hochschule der Bundeswehr Hamburg, Hamburg, Feb. 1984

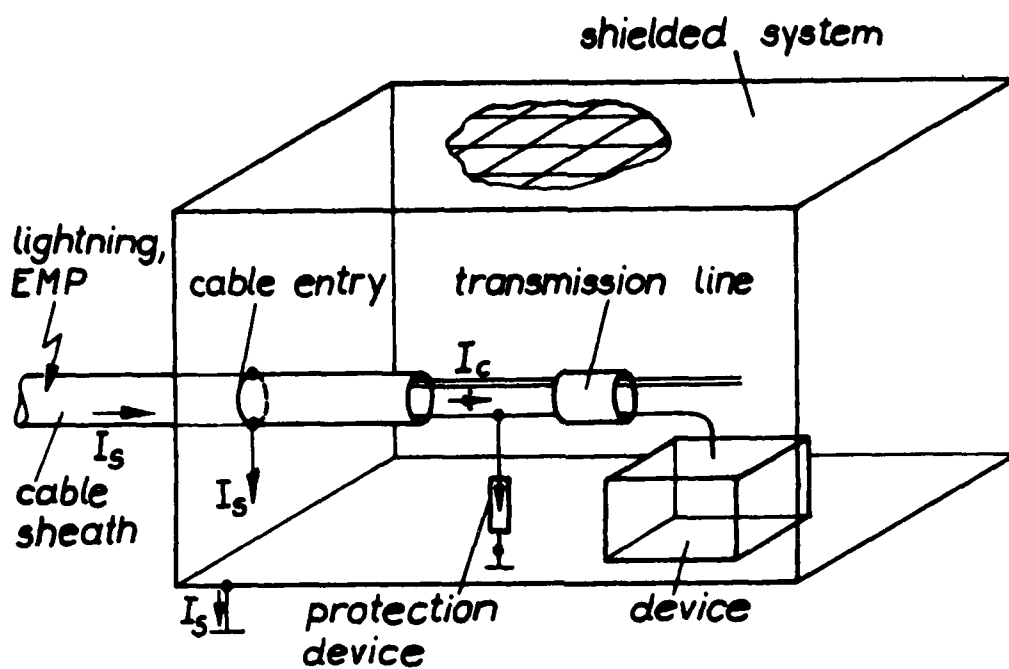


Fig. 1 - Interfering currents penetrating the shield of electronic systems via cable entries

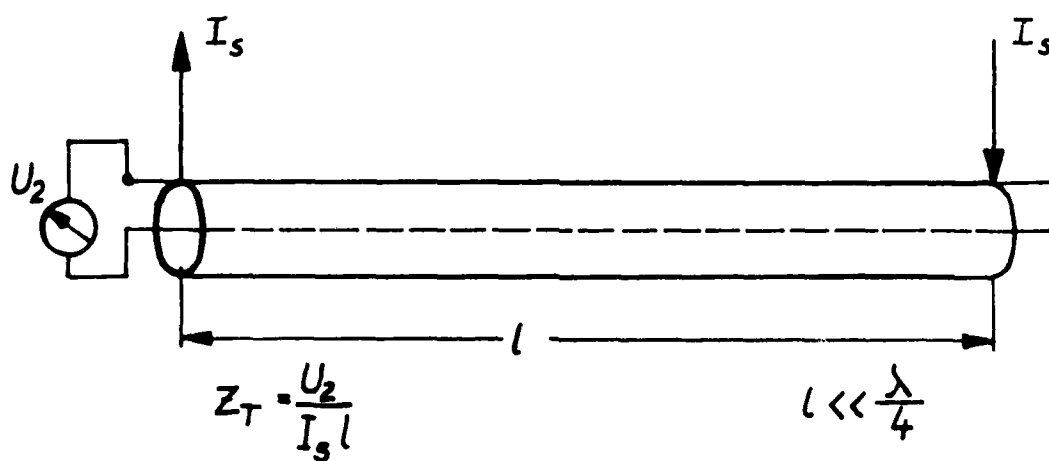


Fig. 2 - The transfer impedance of a cable according to [3]

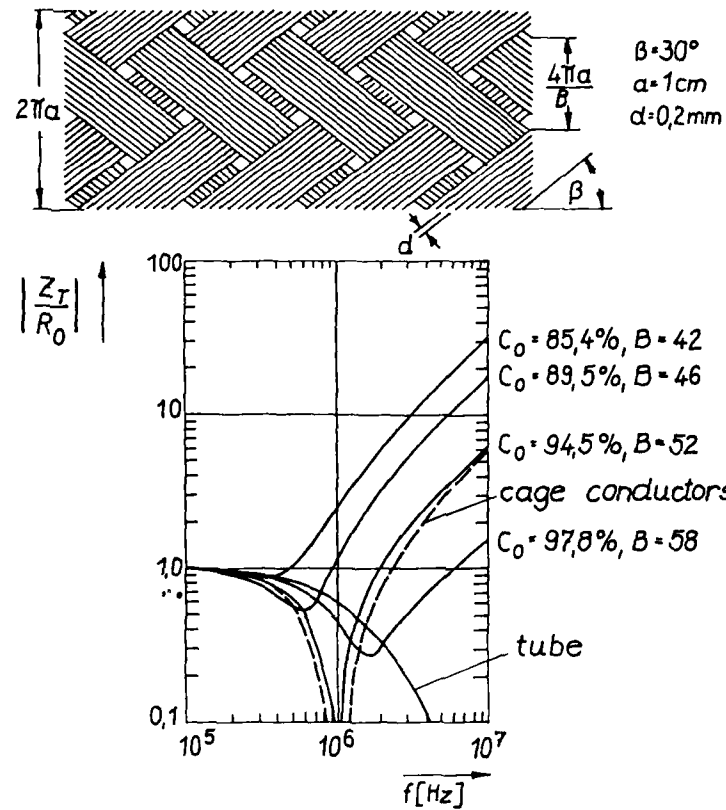


Fig. 3 - Transfer impedance of braided shields,
 C_0 : optical coverage of the shield

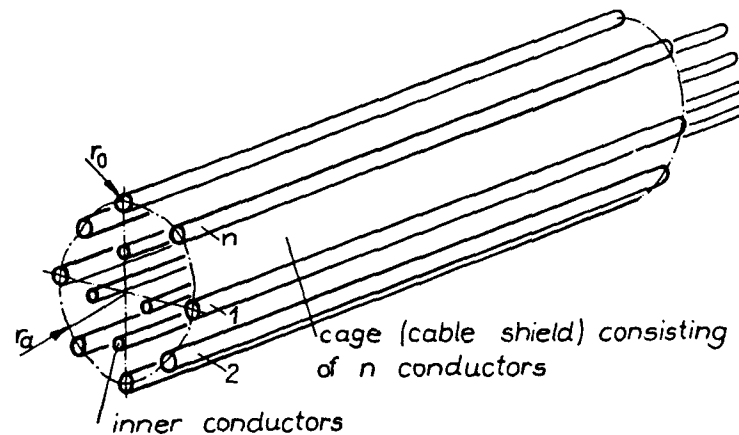


Fig. 4 - Cage conductors as equivalent cable sheath concerning the transfer impedance

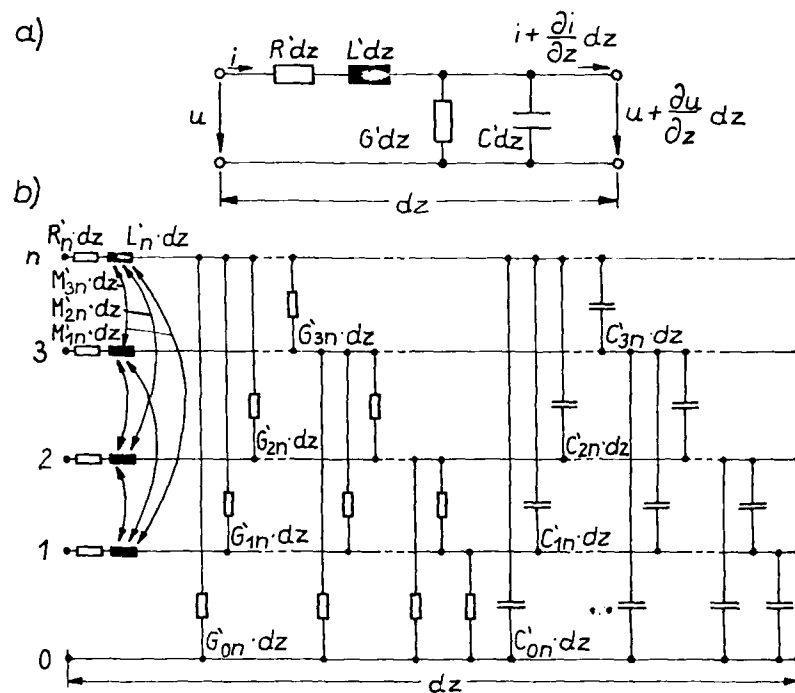


Fig. 5 - Equivalent circuit diagram for:

- a) a two-wire line
- b) a multiconductor line with n conductors

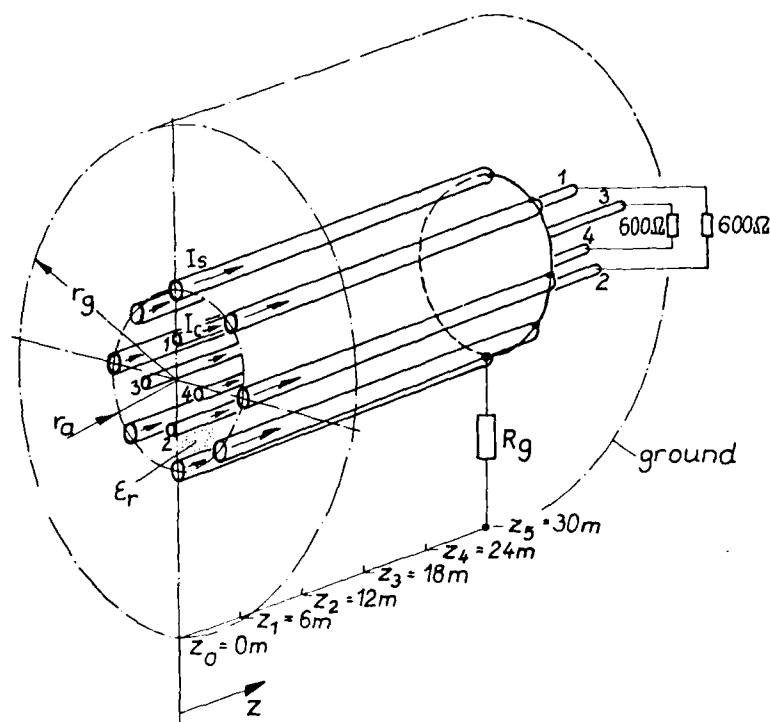


Fig. 6 - Arrangement of the cable for the computations, braided shield replaced by a cage

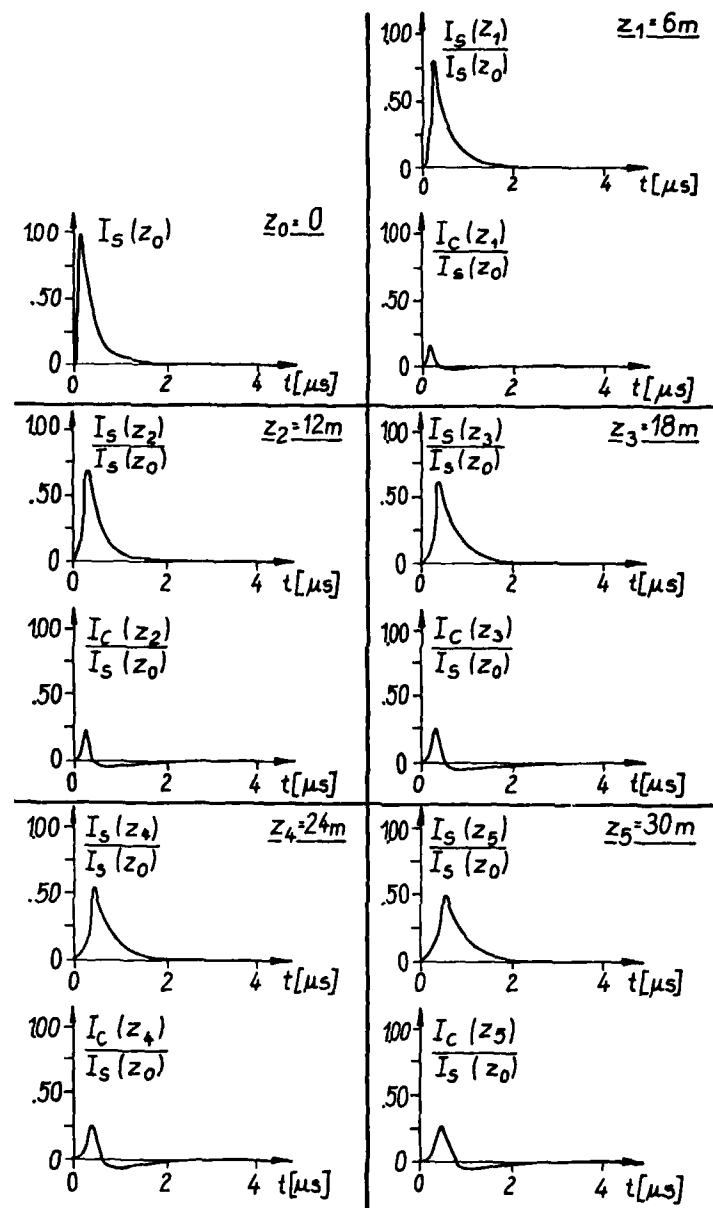


Fig. 7 - Computation results, coupling and propagation of the currents I_s and I_c on the transmission line according to Fig. 6, primary sheath current pulse $I_s(z=0)$: rise time=10 ns, decay time=200 ns

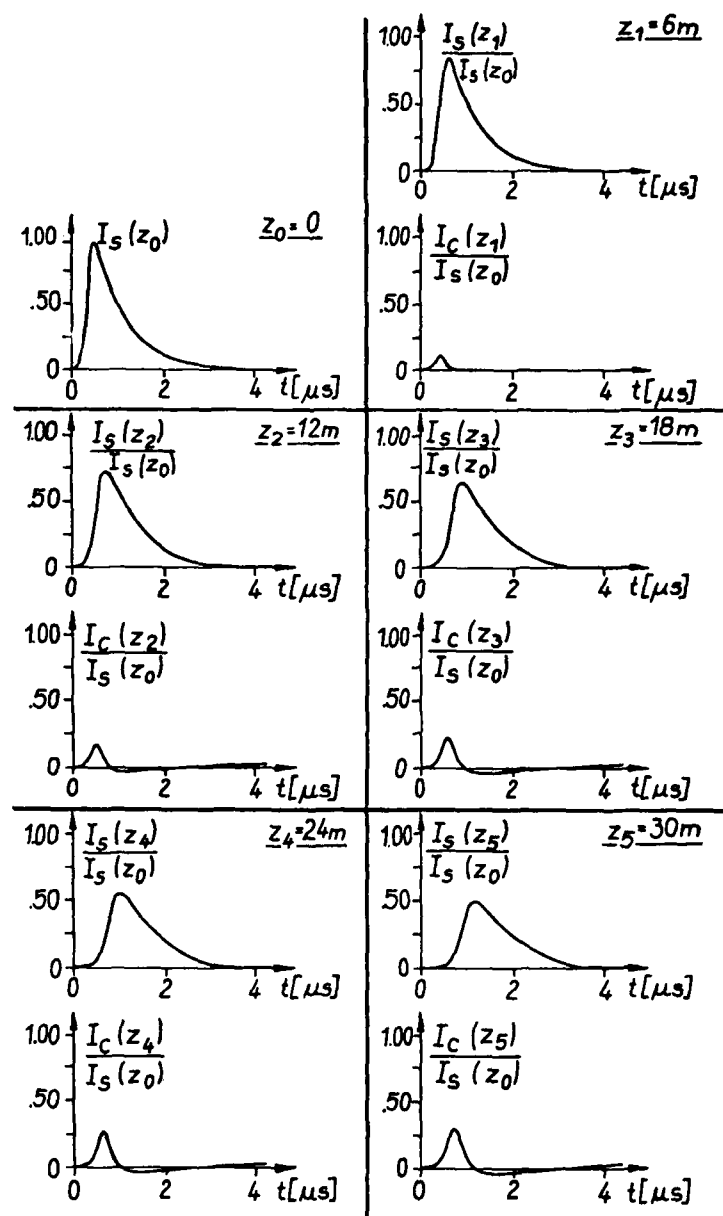


Fig. 8 - Computation results, coupling and propagation of the currents I_s and I_c on the transmission line according to Fig. 6, primary sheath current pulse $I_s(z_0=0)$: rise time=50 ns, decay time=500 ns

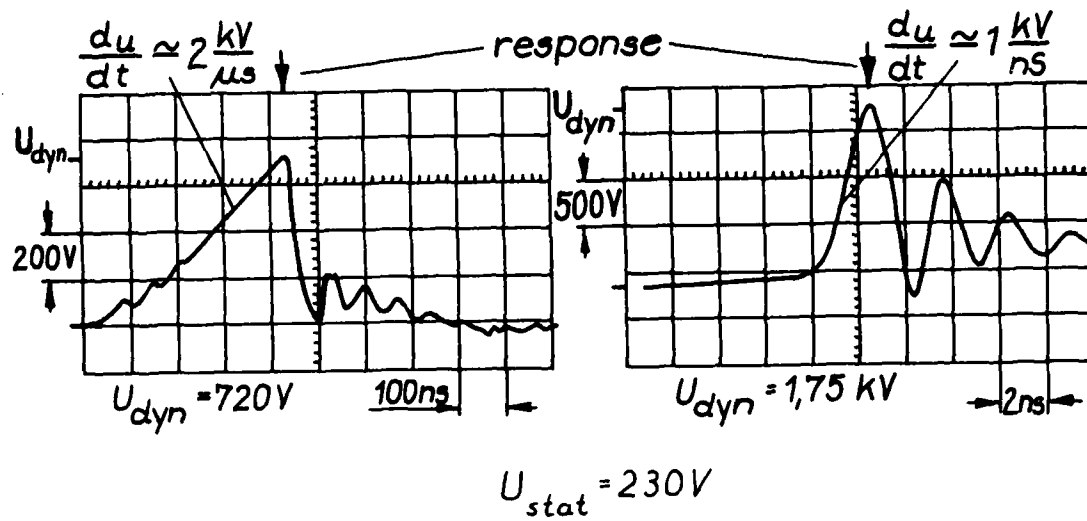


Fig. 9 - Measurement results concerning response of gas arresters dependent on the edge steepness of the applying surge on the line

A NEW IMPULSE GENERATOR FOR IMPULSES WITH SHORT RISE TIMES

M. Modrusan, E. Gockenbach, O. Frey
Emile Haefely & Co. Ltd., Basel, Switzerland

Abstract

Numerous test facilities have been designed to simulate electromagnetic pulses. The system described in this article generates a rectangular current and voltage impulses across a low-resistance load. The rise time for the current impulse with a peak of 8 kA is less than 300 ns. The voltage impulse reaches a peak of 400 kV with a rise time of less than 100 ns. The generator is composed of a cascade circuit with distributed-constant R-C-L stages. There is good correlation between actual full scale measurements and calculations and scaled down model measurements. Ancillary devices such as peaking circuits can improve current impulse rise times to about 130 ns and reduce voltage impulse rise times to below 10 ns.

Introduction

With the proliferation of electronic components in numerous electrical engineering applications, the significance of electromagnetic compatibility has increased dramatically. There are many circumstances which can influence the functional integrity of electronic components or even destroy them. Fast transient voltage changes, for example, can capacitively couple into a device and cause damaging high over-voltages in the circuitry. Excessive electric field strength can also result in the failure of electronic components. On the other hand, induced currents can cause malfunctions. Typical examples are lightning strikes, breakdowns in gas-insulated switch gear and especially NEMP. Poor grounding quality can also cause potential differences in circuits or enclosures which in turn represent a hazard to the individual components. The duration and the shape of the voltage or current impulse also has an impact on the electromagnetic behavior of components.

A number of test systems have been designed to simulate these widely varying pulse phenomena. Voltages range from several kV to several hundred kV and current generation capabilities range from several kA to several 10 kA. [1 to 6].

The voltage and current characteristics in these systems can be adjusted to meet these specific requirements of test objects. This article introduces a test system which is capable of generating a rectangular voltage or current pulse across a low-resistance load.

Description of Experimental Circuit

As mentioned, the purpose of this system is to generate a rectangular impulse. Figure 1 shows the character-

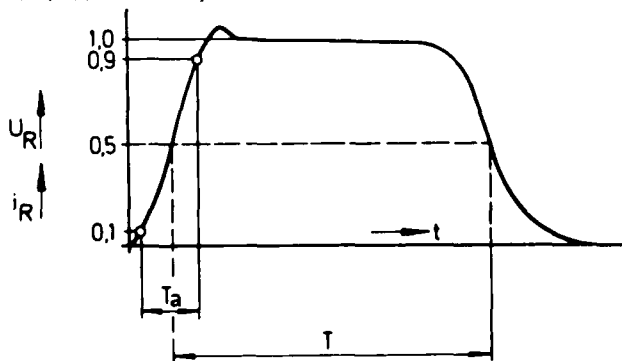


Fig. 1 - Impulse form

istics of such an impulse. The rise time T_a is defined as the time it takes for the impulse to rise from 10% to 90% of its final value. The duration of the rectangular pulse is defined as T . It is the distance between the two 50% values. Finally, the amplitude is the value to which the impulse settles after initial overshoot.

The configuration of LC elements required to generate such an impulse is shown in the equivalent circuit diagram of Fig. 2.

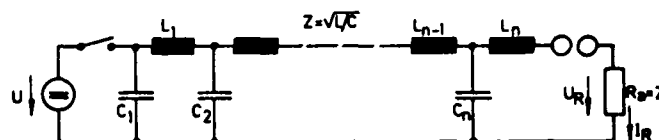


Fig. 2 - Schematic diagram of the test circuit

The capacitors are charged with parallel inductances and finally discharged to the load resistance via a spark gap; the load represents the test object. Electrically, both L and C elements can be varied to obtain the desired shape of the impulse, but for economic reasons, adjustments are made only by changing the inductances. These adjustments could be made empirically but can be optimized in advance with the aid of a specially developed program.

To enhance understanding and standardize terms for the following sections, we will develop several equations based on Figure 2. According to [7], the duration of the impulse can be represented by the equation

$$T \approx 2\sqrt{LC} \quad (1)$$

wherein L = total inductance
C = total capacitance

The termination resistance R_a must comply with the characteristic impedance

$$Z = \sqrt{L/C} \quad (2)$$

The maximum voltage and the maximum current are equated as follows:

$$U_R = U \frac{R_a}{R_a + Z} \quad (3)$$

$$I_R = \frac{U}{R_a + Z} \quad (4)$$

The shape of the impulse will only correspond to the curve shown in Figure 1 if the termination resistance R_a corresponds to the characteristic impedance Z .

If this is not the case, the voltage across the termination resistance will change every time the cycle doubles. The voltage characteristic is then represented by the equation

$$\frac{U_R}{u} = \frac{R_a (R_a - Z)^p - 1}{(R_a + Z)^p} \quad (5)$$

where $t \cong p \cdot T$ and $p = 1, 2, 3 \dots n$.

The rise time T depends on the capacitance, inductance and load. Particularly when very short rise times are involved, however, it will be necessary to consider the influence of stray capacitances and the inductance of the connection elements.

Description of Generator

A series circuit of several capacitance stages is necessary to generate voltages exceeding 50 kV across the termination resistance, i.e. voltages exceeding 100 kV in the impulse generator. According to the Marx Principle, the capacitors, i.e. the individual networks in the system, are charged in parallel and then discharged into the test object across the series spark gap. Figure 3 shows the impulse

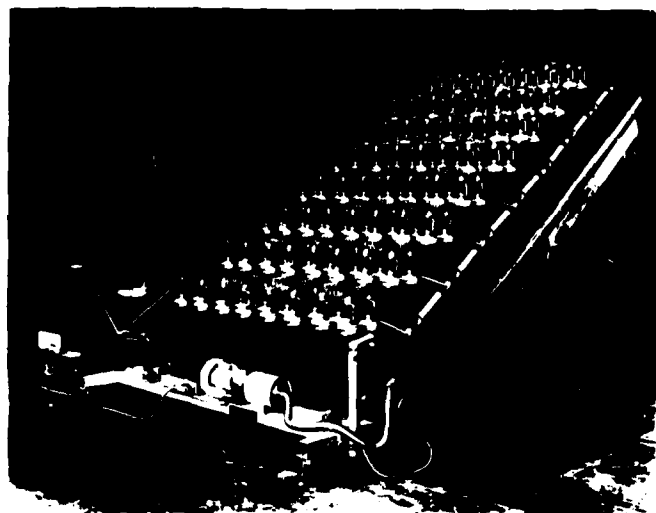


Fig. 3 - Impulse generator

generator configuration. In deviation from the circuit commonly used in impulse voltage generators, the stages consist of LC combinations with 16 elements rather than only of capacitances. Each of the 8 stages is designed for a charging voltage of 100 kVmax. so that when the generator is terminated with the characteristic impedance ($R_a = Z$), a maximum voltage of 400 kV can be obtained across the test object according to equation 3. Under identical conditions, equation 4 results in a maximum current of 8 kA.

On the left, Figure 3 shows the rectifier which is used to adjust the charging voltage via a thyristor switch. A particular type of controller known as the Trigatron is used to charge the system with a constant current; the Trigatron has adjustment features for charging voltage and charging time. This device also fires the impulse generator and allows convenient synchronization with external start signals. The delay time between the occurrence of the start signal and the occurrence of the peak impulse value is approximately 500 ns.

Figure 3 also shows the ladder configuration of the elements which was chosen for space and assembly reasons. Each step up the ladder corresponds to one network element. The switching spark gaps on the right hand side of the illustration are located at the right ends of the LC combinations. They are housed in insulating cylinders to achieve reciprocal irradiation. Further, the insulating cylinder is ventilated with filtered air in order to prevent uncontrolled discharges caused by dust particles in the air. The gap width is automatically adjusted in compliance with the charging voltage. Additionally, a check pulse device is attached to the lowermost switching spark gap to initiate correct firing or prevent possible malfunctions such as spontaneous firing or no firing via the Trigatron.

Each function of the Trigatron such as generator charging, spark gap triggering, impulse synchronization can also be manually controlled.

Description of Current and Voltage Characteristics

A certain number of elements is necessary to generate a rectangular impulse with a specified duration T . The inductances are defined by the characteristic impedance of the test object and by the duration of the impulse. The characteristic impedance of the generator is obtained from the characteristic impedances of the individual stages according to the equation

$$Z = m \cdot Z_s \quad (6)$$

wherein m = number of stages and

Z_s = characteristic impedance per stage.

For $Z = 50 \Omega$, we obtain for $m = 8$ a characteristic impedance per stage of $Z_s = 6.25 \Omega$.

Additionally, the self-inductances of the capacitors must be considered because they have the same magnitude as the inductances of the individual LC elements. They limit the steepness of the current rise, but to some extent, stray capacitances can provide compensation.

Apart from the capacitances and inductances of the individual network elements, Figure 4 also shows the stray inductances and capacitances which are attributable to the design of the impulse generator. The self-inductances of the feeder lines, voltage dividers and load resistance are also shown in the equivalent circuit diagram, because these elements partially effect the

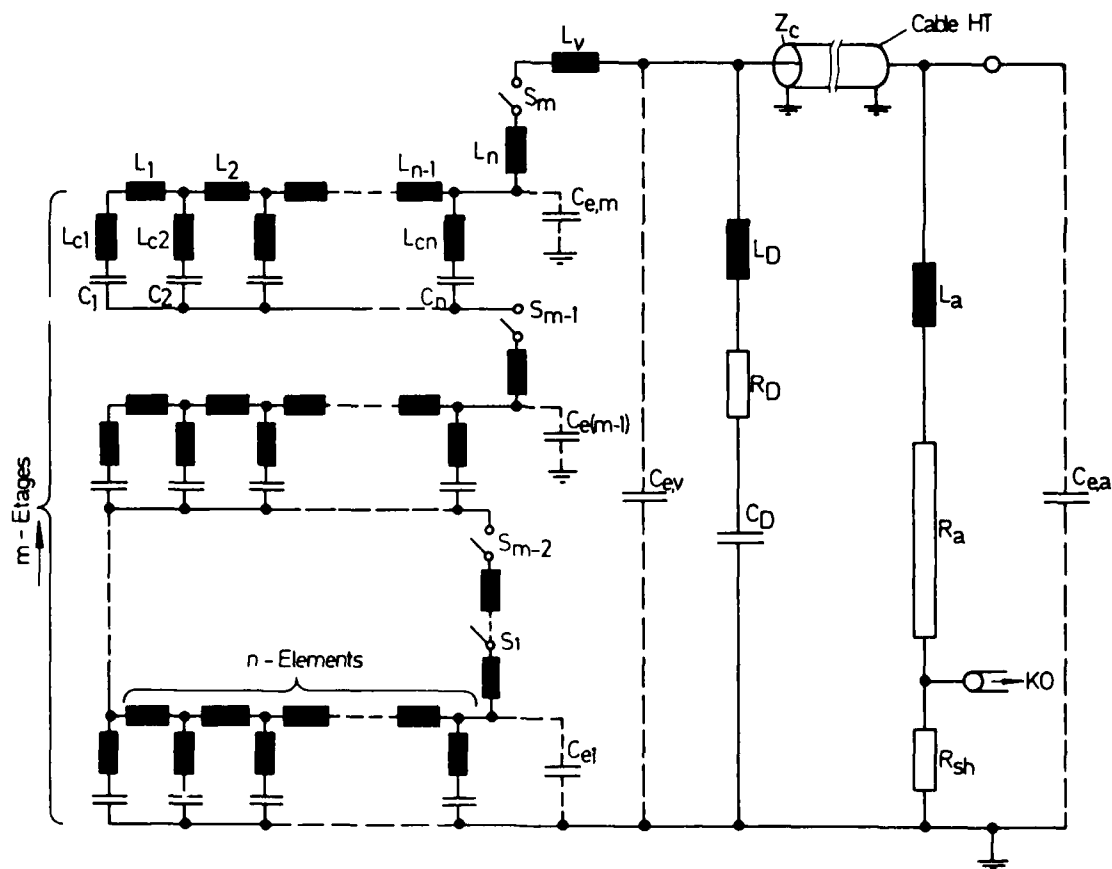


Fig. 4 - Equivalent circuit diagram

rise time and the high-frequency oscillations at the front end.

The voltage across load resistance R_a (see Figure 4) which always contains a certain inductance L_a can be calculated with the equation

$$U_R = I_R \cdot R_a + L_a (dI_R/dt) \quad (7)$$

wherein the current flowing through the load resistance is designated with I_R . At the front, the time characteristic of the voltage deviates from that of the current because of the deviations between certain elements such as stray capacitances and inductances.

The design of the impulse generator was based on a 300 ns rise time both for the current and voltage impulse. Model measurements and calculations were conducted to test this requirement. The diagram shown in Figure 4 is based on the calculations.

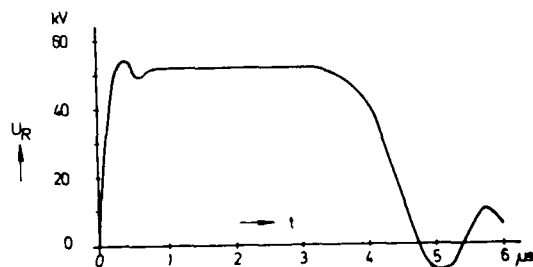


Fig. 5 - Calculated voltage impulse form with $R_a = 50$ ohm

Figure 5 shows the voltage impulse with a charging voltage of 100 kV and a load of $R_a = 50 \Omega$. This calculation was conducted without a high-voltage cable to enable a comparison with measurements later on.

To verify calculations, however, the voltage impulse under identical conditions was calculated with $R_a \rightarrow \infty$ as shown in Figure 6. As expected, the

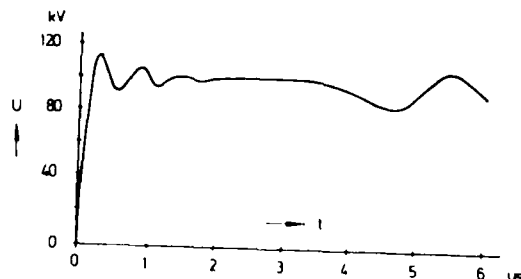


Fig. 6 - Calculated voltage impulse form with $R_a \rightarrow \infty$

voltage amplitude was twice as high as with a termination corresponding to the characteristic impedance while rise times are roughly identical.

The model measurements in calculations showed that rise times in the region of 300 ns are also possible with multi-stage distributed-constant network configurations.

Test Results

Figure 7 shows the voltage curve with a load of $R_a = 50 \Omega$ and without a load. The measurement was made without a high-voltage cable so that the results can be directly compared with calculations (Figures 5 and 6). Correlation between measurements and calculations is good. The minor deviations on the front wave result from the fact that the stray capacitances and the additional inductances in the generator

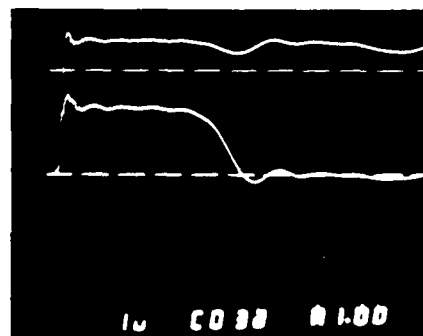


Fig. 7 - Measured voltage impulse form
top curve with $R_a \rightarrow \infty$
bottom curve with $R_a = 50$ ohm

elements were not accurately definable in the calculation. On the other hand, the inductances of the last stage after the spark gap have a greater influence on the rise time than the inductances of the load resistance so that it was possible to closely simulate the elements which determined the transient characteristics with mathematical methods.

Figure 8 shows the current and voltage oscillogram.

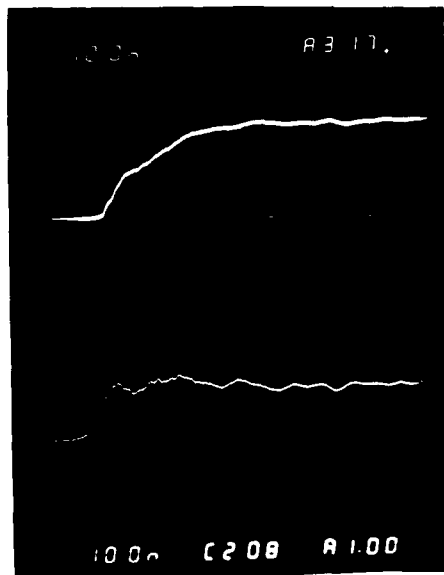


Fig. 8 - Measured voltage (bottom) and current (top) impulse form

These measurements were made without a high-voltage cable for a total charging voltage of 200 kV and a load resistance of $R_L = 50 \Omega$. By means of a damped capacitive voltage divider, with a transformation ratio 620:1 connected to the load resistor, a voltage of 100 kV was measured. The voltage rise time amounts to approximately 100 ns. The current curve peaked at 1.8 kA with a rise time of approximately 280 ns.

Given these very short rise times, correct instrumentation is crucial because it would be intolerable to have a limited bandwidth of the measuring system cause an adulteration of the curve.

As already mentioned in the introduction, recording devices were developed along with the actual test system. Figure 8 illustrates the possibility of producing current and voltage oscillograms. The rectangular unit step responses of the two measuring systems are shown in Figures 9 and 10; this allows verification of the transmission characteristics and thus a characterization of the measuring system themselves.

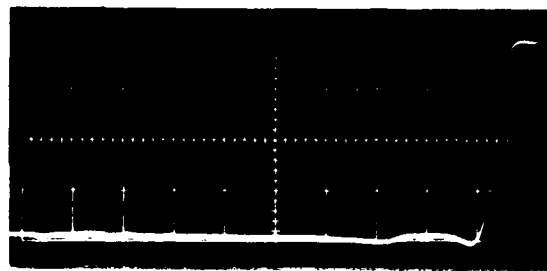


Fig. 9 - Unit step response of the shunt

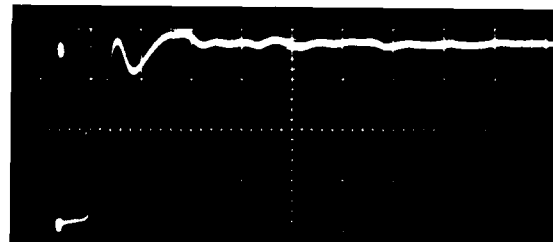


Fig. 10 - Unit step response of the voltage divider

Both measuring systems exhibit very low overshoot and very short decay times. The rise time of the applied shunt in Fig. 9 is approximately 20 ns, much smaller than the rise time of the measured signal.

The voltage divider is a damped capacitive divider with the transformation ratio of 620. According to Figure 10, its rise time is about 30 ns, again very much smaller than the rise time of the impulse.

The voltage divider is a high-resistance type which prevents any distortion of the impulse form.

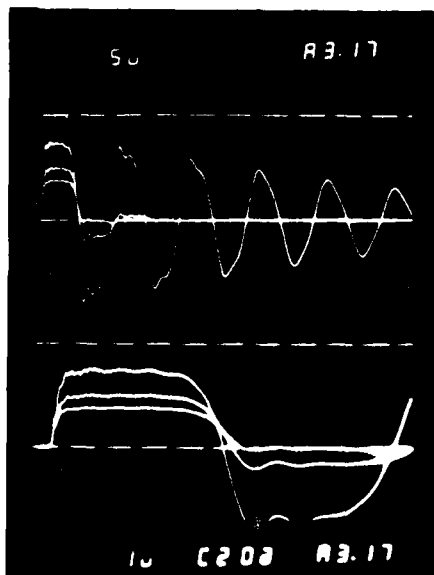


Fig. 11 - Current impulse form with $R_a = 50\Omega/25\Omega/0\Omega$

Figure 11 illustrates the current curves for various termination resistances over two time scales. Using a termination which is equivalent to the characteristic impedance ($R_a = 50 \Omega$), the characteristic corresponds to the curves already shown in Figure 7.

If the termination resistance is reduced to half the characteristic impedance, for example, the result is a higher current with less modulation. If the termination resistance is short-circuited, the current is even higher and is limited only by the characteristic impedance. The form of the current impulse then corresponds to a travelling wave which is gradually reduced to a roughly sinusoidal oscillation caused by the stray capacitances.

Under certain circumstances, it may be necessary to obtain even shorter rise times. This can be achieved with a so-called "peaking circuit". Figure 11 shows a schematic of the test circuit with an associated peaking circuit. The same diagram also shows the auxiliary circuit which forms the decay of the impulse. The peaking circuit consists of an R-L and C combination that shapes the impulse front. The element which shapes the tail or limits the impulse length is a capacitively controlled, triggered chopping spark gap [8].

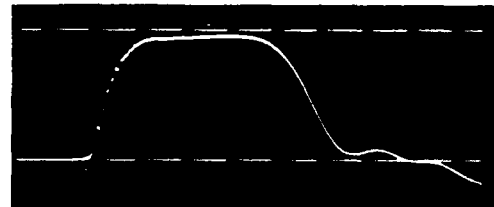


Fig. 12b - Voltage impulse form with peaking circuit



Fig. 12c - Voltage impulse form with peaking circuit and chopping spark gap

Figure 12 shows the influence of this auxiliary circuit. The tests were performed using fewer circuits with four stages and ten elements per stage.

Figure 12a shows the curve with the normal front steepness and the limited impulse length. Figure 12b shows the distinctly shorter rise time caused by the peaking circuit, and Figure 12c illustrates the result of the chopping spark gap which causes the faster decay.

A special peaking circuit makes it possible to produce impulse voltage rise times of less than 10 ns.

On the other hand, this impulse generator can also be used for rise times of up to 1.5 μ s and tail times of approximately 2 μ s by correspondingly configuring L and C elements.

Synopsis:

Electromagnetic compatibility is a key characteristic of electronic components. Numerous test systems have been developed to verify the immunity levels. The test system introduced in this article has the following parameters:

- Max. charging voltage of 800 kV to produce a 400 kV output voltage across a 50 Ω load
- Characteristic impedance = 50 Ω
- Multi-stage configuration with 1 iterative network per stage
- Max. current 8 kA through a 50 Ω load

Calculations and model measurements showed that rise times in the order of 300 ns are possible for a rectangular current impulse. The test results then showed that very good correlation was achievable between calculations and actual generator measurements. The current impulses exhibited a rise time of less than 300 ns, while voltage impulse rise times were even shorter than 100 ns.

The associated instrumentation systems have rise times of less than 30 ns and are therefore capable of detecting the very fast current and voltage transients.

The use of a so-called "peaking circuit" will further shorten the impulse front times. In experiments, current rise times of less than 130 ns and voltage impulse rise times of less than 10 ns were obtained.

By appropriately reconfiguring the circuit, the test system can also be used for slower impulses with rise times of 1.5 μ s and tail times of 2 μ s.

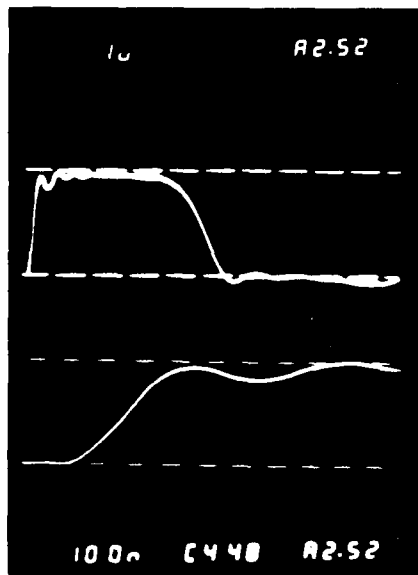


Fig. 13a - Current impulse form without peaking circuit

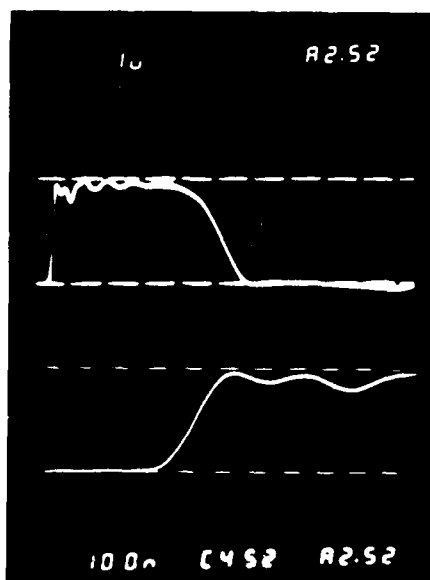


Fig. 13b - Current impulse form with peaking circuit

As already mentioned, the rise time of the voltage impulses is much shorter than that of the current impulses.

Literature

K. Feser, M. Modrusan, H. Sutter,
"Steep front impulse generators for EMP

Simulation", 3rd International Symposium on High Voltage Engineering, Milan, 1979

K. Feser, M. Modrusan, K.H. Gonschorek, H. Singer, "Mobile EMP System with High Flexibility", EMC Symposium 1981, Zürich

K. Feser, M. Lutz, "Surge Testing Requirements Analysis", Electronic Tests 1980, Benwill Publishing Corporation

O. Frey, "The Origins, the Effects and the Simulation of Transients, as well as their International Standards", Electronic Show and Convention 1982, Boston

E. Gockenbach, M. Modrusan, H. Sutter, "An impulse generator to simulate lightning effects on aircraft", 8th International Aerospace and Ground Conference on Lightning and Static Electricity 1983, Fort Worth

M. Modrusan, "Long-duration impulse current generator for arrester tests according to IEC recommendations", Bull. SEV Vol. 68 (1977), p. 1304-1309

A. Rodewald, "A new triggered multiple gap system for any kind of voltages", 1st International Symposium on High Voltage Engineering, München, 1972

M. Modrusan, "High Current Impulses for Testing Purposes", to be presented by E. and M. 1984, Vienna, Austria

LIGHTNING SIMULATOR CIRCUIT PARAMETERS AND PERFORMANCE
FOR
SEVERE-THREAT, HIGH-ACTION-INTEGRAL TESTING

Robert A. White

Sandia National Laboratories
Albuquerque, New Mexico 87185

ABSTRACT

The lightning simulator at Sandia National Laboratories (SNL) has been used to subject a number of DOE and military test items to severe levels of simulated lightning. This paper discusses some example circuits and circuit parameters related to tests made with this crowbarred Marx-generator-type simulator. Examples of fast-rising, high-peak, long-duration simulated lightning currents that have been produced into full-size test items are presented. Peak currents up to 250 kA with i - μ s rise times and action values up to greater than $6 \times 10^6 \text{ A}^2\text{S}$ have been injected into various test systems.

A DIRECT LIGHTNING STROKE is the most severe natural electromagnetic threat that a complex electrical system may experience. The consequences of system failure may be so great in some instances that even the unlikely event of worst-case environment must be evaluated. Simulated lightning testing may then be required to assure that critical systems either will not fail or will fail in an acceptably safe manner. Analysis and extrapolation of low-level test data to higher levels may sometimes be adequate. At other times, it may be important to subject the system to simulation of extreme-value lightning parameters.

The need for severe-threat lightning simulators and test philosophies related to their application has been treated in previous lightning conferences and publications. Severe-threat or worst-case lightning parameters are being considered or specified for an increasing number of systems. As more is learned of natural lightning and the potential hazards associated with it, there is increasing support for testing with the higher values of stroke energy and higher values of current rate-of-rise. Even though extreme values of parameters for natural lightning do not occur on a high-probability basis, stroke location and intensity of natural lightning are most unpredictable. Thus, for some critical systems with new or proposed technology, the hazards are great enough to justify testing with severe or worst-case stroke parameters. However, the physical size, complexity, and variability of the circuits that produce natural lightning are such that simulation of worst-case conditions is not an easy task.

Providing severe lightning threat levels to large as well as small test items is a capability of the SNL lightning simulator(1)* and is one of the main reasons it was developed. This developmental lightning simulator and some of the earlier tests made with it were described or mentioned in several papers(2)(3) presented at the 1983 International Aerospace and Ground Conference on Lightning and Static Electricity.

The continuing development of this lightning simulator and most of the tests with it are in support of defense-related programs for the Department of Energy (DOE). Its primary use has been for internal SNL test programs. However, it has also been used in several series of lightning tests made for the Navy and the Air Force. Lightning simulation tests were made in 1982 with two full-size, powered, functional aircraft (F-14A and F/A-18) for the Naval Air System Command.(4) Since then it has also been used in a series of lightning tests with the air-launched cruise missile (ALCM) made for the Air Force. Some of these

tests are described below and in other papers of this conference.

A high value of "Action-Integral" in this presentation is one that equals or exceeds those values generally considered representative of a severe natural stroke. Different references use various values for this ranging from $1.2 \times 10^6 \text{ A}^2\text{S}$ to $2 \times 10^6 \text{ A}^2\text{S}$, frequently derived from the data compiled by Cianos and Pierce.(5) "Action" as described by G. W. Anderson and F. W. Neilson (6) has long been used to represent the energy per ohm of resistance associated with any particular current waveform. It is a common term equal to $i^2 dt$, present in most specifications of natural or simulator lightning parameters and has also been defined in a lightning context as 'potential stroke energy' by Berger.(7)

Significantly higher values of action than needed to represent a severe threat have been produced with this simulator. The $10^7 \text{ A}^2\text{S}$ action-integral presented in last year's description of this simulator and the action of some of the current waveforms discussed in following sections are examples. Maximum available action from a simulator is usually greatly restricted by total load circuit resistance. Total circuit resistance, including the test item for this simulator, usually must be limited to a few ohms in order that severe-threat values of action can still be provided. However, this is not the case with natural lightning because maximum available stroke energy is often little affected by resistance of the object struck.

Natural lightning channel inductance and stored magnetic energy may be hundreds of times greater than in a typical simulator circuit. The self-inductance value of a cloud-to-ground channel might easily range up to greater than 5 millihenrys. An established peak current of 200 kA through that value of inductance would correspond to 100 megajoules of magnetic energy. Cloud-to-ground channels from the base of the cloud to earth might be expected to have a lower value of inductance since they may be less than 1 km in length. However, altitudes of charge centers likely to flash(8)(9)(10) and main stroke channels(11) are frequently greater than 2 km.

Positive strokes (frequently attributed to having the highest peak currents) also tend to occur through clear air from higher altitude from the sides of near-vertical wall portions of the thundercloud. Stroke energy available from severe natural lightning is not often discussed in recent literature. In an early summary, L. V. Bewley(9) (General Electric Co.), estimates stroke energy for more typical lightning to be of the order of 1 megajoule. If maximum resistance values for test items of interest continue to increase, they may become a significant factor in selecting required energy values for future lightning simulators.

* Numbers in parentheses designate References at the end of the paper.

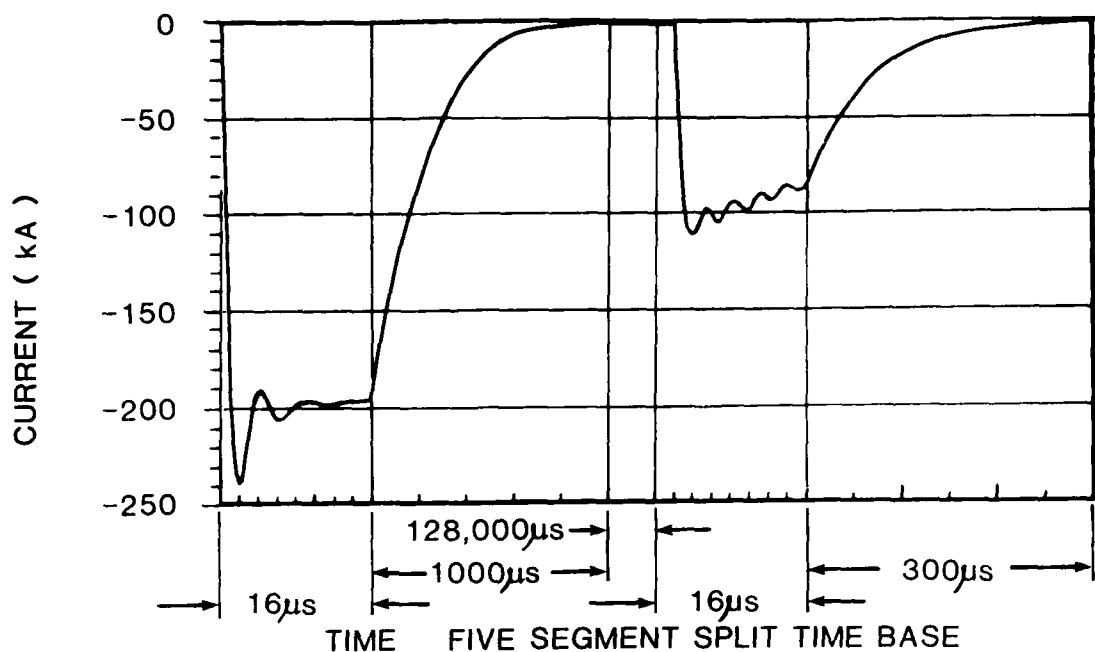


Fig. 1. Double-pulse simulated severe lightning

An advanced development program(12) being coordinated by the Air Force Wright Aeronautical Laboratories (AFWAL/FIEA) is one example of the work underway in the lightning protection area. This Atmospheric Electricity Hazards Protection (AEHP) program is a joint undertaking of USAF, USA, USN, DNA, FAA, and NASA, described elsewhere(13)(14) in this and previous conferences. Lightning protection concepts developed by the overall program are expected to minimize cost, weight, power, and reliability/maintainability requirements for advanced airframes and systems. The ALCM lightning tests made with the SNL simulator were made for AFWAL to support a portion of the AEHP program.

SIMULATOR PERFORMANCE AND CIRCUIT PARAMETERS

HIGH-CURRENT DOUBLE PULSE - Many of the tests made with this lightning simulator require double-pulse, fast-rising, high-action current pulses. The two exponentially decaying pulses have been separated in time by a selectable time interval ranging from 30 milliseconds up to as long as 1 second. One such test record is shown in Fig. 1. This record was obtained using one of the lightning facility Tektronix 7612 digitizers, which provides a split time base capability. The horizontal time base shown is divided into five separate time intervals, with each of the five having different sweep speeds. Time separation between pulses was about 128 milliseconds for this test. Time of rise for each of the pulses was 2 μ s. This test also

included continuing current in the several-hundred-ampere range between pulses and also continuing well past the second pulse.

CROWBARRED MARX SIMPLE DIAGRAM - A very simplified equivalent circuit for the crowbarred Marx generator method of generating a fast-rising high-current pulse with a long-duration exponential tail is shown in Fig. 2. The three series elements C_M , R_M , and L_M are a simplified conceptual representation of one or more Marx generators. A completely equivalent

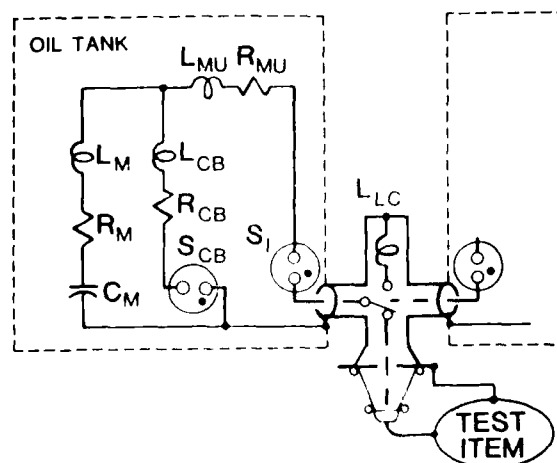


Fig. 2. Simplified circuit diagram for crowbarred Marx

circuit diagram of one Marx generator, including significant stray circuit parameters, may utilize more than 100 circuit elements. Elements S_{CB} , R_{CB} , and L_{CB} represent a simplified equivalent circuit for the crowbar switch and its associated connections. The test item is represented in this simplified circuit by L_L and R_L . Elements L_{MU} and R_{MU} represent inherent interconnection impedances along with "makeup" inductors and resistors deliberately added to the circuit to control pulse shape.

Additional descriptions of the fast-pulse Marx generators, the rotating equipment motor/generator set used for continuing current, and tests conducted with the simulator facility were presented by J. C. Bushnell(2) and the author(3) in last year's conference.

CIRCUIT PARAMETER VARIATIONS - A single set of circuit parameters is obviously not practical with this simulator. The need to answer different kinds of questions involves the use of multiple Marx generator pulse sources, selectable charge voltage, different wave-shaping components, and different load circuits. Interconnections of overall system elements can be relatively easily rearranged to provide some degree of flexibility for supporting different test conditions.

The two oil-filled Marx generator tanks and the connections used during a portion of the ALCM tests are shown in the physical layout of Fig. 3. Both simulator tanks are often used together, as required, to provide double-pulse tests; however, either simulator tank can be used alone, as is often done for single-pulse tests. Some tests are done with continuing current, and some are not. Different oil-insulated makeup inductors are used to aid in control of time to peak by compensating

for different load inductances. Energy-absorbing resistor values are changed as needed within the constraints of available materials or components. Liquid electrolyte resistors have been used with considerable success. Some successful testing used resistor assemblies made from graphite rods rather than from high-resistivity metal sometimes used in other resistors.

IMPROVEMENT IN CAPABILITIES - During the past year, a continuing need to conduct tests with the existing capability of this developmental simulator has constrained development activities. Even so, significant improvements to simulator capabilities were achieved.

Total stored energy that can be used more or less routinely in operational tests with the simulator has been increased since January 1983. The higher energy Marx generators that were installed in the north simulator tank were mentioned in the 1983 conference. At that time, they had been used very little. Since then, they have been used for many tests and are working well. Changing the crowbar switch dielectric gas from a mixture of argon, nitrogen, and SF_6 to pure SF_6 , along with other operating and design changes, has permitted the maximum charge voltage to be increased for routine operational tests. With the same two low-capacitance ($0.088 \mu F$) Marx generators in the south tank, the increased operational level of Marx voltage allowed by using pure SF_6 gas in the crowbar and using ultraviolet laser triggering has increased available stored energy in the south tank by a factor of nearly 2.

When the F-14 and F-18 Navy aircraft were tested during 1982, there was only one low-capacitance Marx generator in the north tank, which was usually constrained to operating at about 70% of full-rated charge. That one low-capacitance Marx has since been replaced by two high-capacitance Marx generators that are often operated at full-rated charge to provide a full 1.6-MV output driving voltage. Together, these two changes have resulted in about an eightfold increase in available operating stored energy in the north tank.

A block diagram of Fig. 4 shows the high-current pulse-forming portion of the simulator. Capacitance and energy values of the available connection options are summarized in Table 1. Although there has been no test requirement to do so, a peak current as high as 390 kA has been produced by firing both simulator tanks at the same time.

PARAMETER INTERRELATIONSHIPS - Peak current, time-to-peak, stored energy, maximum rate-of-rise in current, etc., are all inter-related and related to circuit parameters such as inductance, capacitance, resistance, and initial charge voltage. The basic underdamped RLC electrical discharge equations control these relationships. Total discharge loop inductance is selected to provide the desired time to peak. The time to $1/4$ period is often set around $2 \mu s$ or a full period of $8 \mu s$ and a

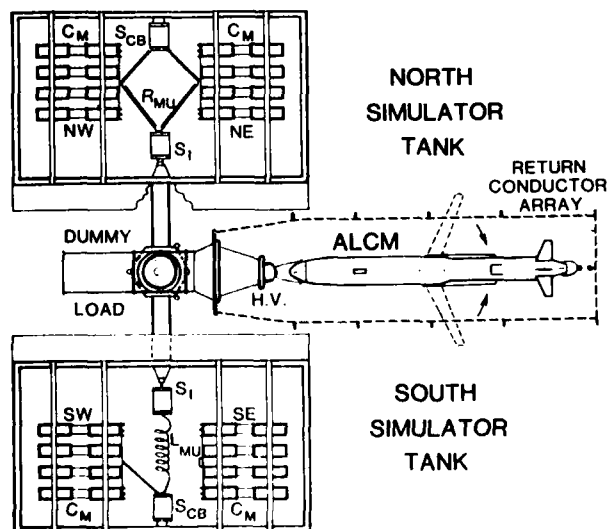


Fig. 3. Lightning simulator arrangement for ALCM tests

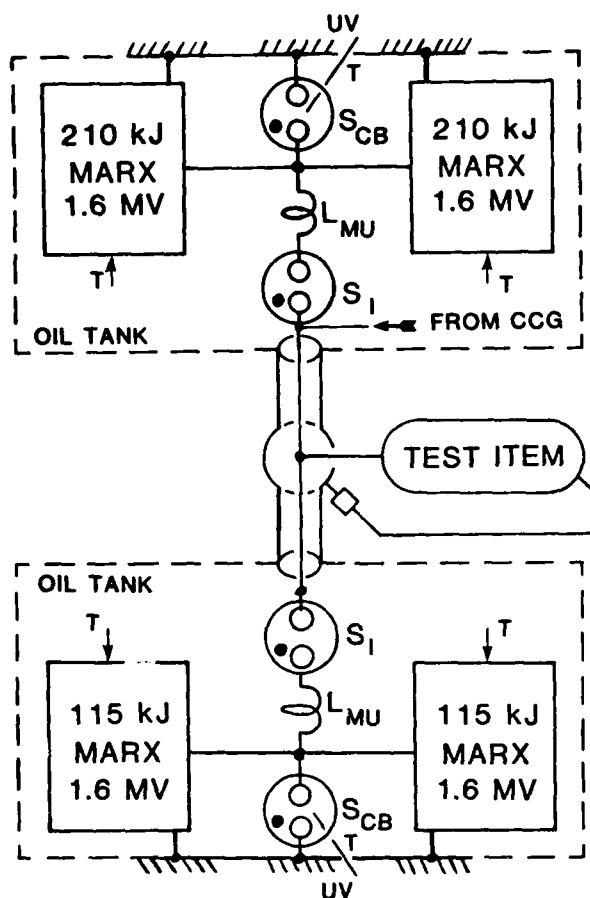


Fig. 4. Lightning simulator, double-pulse discharge circuit

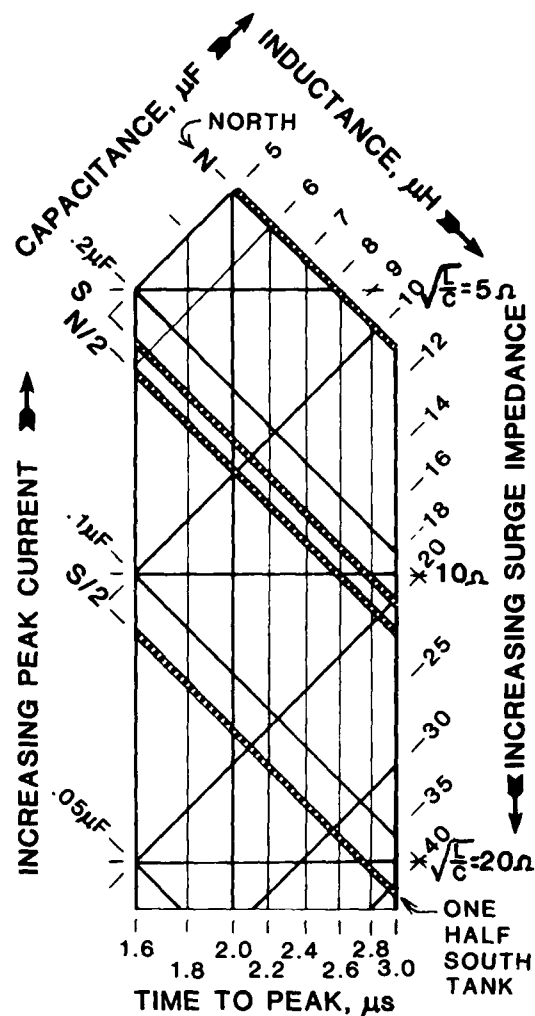


Fig. 5. Lightning simulator parameter interrelationships

Table 1

Capacitance and Energy Available
(All have been used in tests)

	Capacitance nanofarads	Voltage megavolts	Energy kilojoules)
North Tank	330.	1.6	422.
South Tank	176.	1.6	225.
One North Marx	165.	1.6	211.
One South Marx	88.	1.6	113.
Both Tanks	506.	1.6	647.

ringing frequency (without crowbar) of 125 kilohertz. Different times to peak are also used. Table 2 shows the total loop inductance needed to give an 8-μs period. Surge resistance, $\sqrt{L/C}$, values are tabulated for the same conditions. The values tabulated for maximum possible peak current are determined by Marx erection voltage, 1.6 MV, divided by surge resistance (or $V_0 \sqrt{C/L}$) for the ideal case of zero-resistance damping.

The chart in Fig. 5 shows interrelationships between time to peak, surge resistance, inductance and capacitance for the special case of zero resistance. The four heavy dotted lines on this chart are the four selectable simulator capacitances from the previous tables. This chart might be considered to be a single slice of multidimensional solid in which either resistance or voltage is varied in a direction perpendicular to the plane shown.

Table 2

Inductance and Surge Impedance
for 8-microsecond Period

Marx Cap.	Inductance for $T = 8 \mu s$	Surge Impedance $\sqrt{L/C}$	Maximum Current $I_p = V\sqrt{C/L}$
(nF)	(MH)	(ohms)	(kA)
330.	4.9	3.856	415.
176.	9.2	7.230	221.
165.	9.8	7.707	208.
088.	18.4	14.46	111.

Numerical peak current values are not shown in this chart because they are obviously related to initial voltage as well as the value of L and C shown. An estimate for peak current with zero damping can be obtained from $I_p = V_0 \sqrt{L/C}$. For instance, the chart intersection of the 0.330 μF capacitance for the north tank and a total circuit inductance of 8 microhenries nearly coincides with the 5-ohm value for surge impedance. If, for example, 1.5 MV is assumed for Marx initial erection voltage (about 94% of full charge), then that value divided by a 5-ohm surge impedance indicates that the 5-ohm horizontal line also corresponds to an undamped RLC peak current of 300 kA. For similar assumptions, the 10-ohm level would correspond to 150 kA, and the 20-ohm level would be 75 kA.

This chart is intended to give only a quick, visually aided feel for the interrelationships. Circuit resistances in the real simulator, however, are not zero (resistance is also deliberately added), and crowbar switching is normally set to occur before peak current. A different slice of this multi-dimensional parametric relationship could be examined for typical simulator parameters, including the effects resistance and selected crowbar times. This same 5-ohm surge impedance level then might be found to correspond to a peak current of about 225 kA or about 75% to 80% of the zero-resistance peak current.

Maximum or initial values of di/dt , \dot{I} , for the current pulse front, might be labeled along the increasing inductance scale for selected Marx driving voltages. Since initial $di/dt = V/L$, for a 1.6-MV driving voltage, the 8-microhenry grid line would correspond to a current rate of rise of 2×10^{11} A/s.

Peak current and time to peak produced in any given test are a function of crowbar switching time as well as of the circuit parameters and charge voltage selected.

Peak output current would be highest in the case of ideal switching at peak of the RLC

current waveform. This peak occurs at 1/4 cycle into the oscillation for the near-zero resistance RLC circuit. The time to 1/4 period, in that case, is equal to $(\pi\sqrt{LC})/2$. However, voltage applied to the crowbar switch is zero or near zero at that time. Switching at an earlier time, when voltage has decreased no more than 50% from its initial value provides more favorable conditions for triggering the crowbar switch. Switch closure at 50% of peak crowbar voltage still provides about 86% of the maximum peak current.(1)(2) As the quality of the trigger mechanism is improved, it permits the crowbar switch to be triggered at lower percentages of initial voltage values.

Energy transfer from the Marx capacitor bank to circuit inductance reaches maximum at 1/4 cycle. With a perfect zero-impedance crowbar switch, energy still stored in the Marx capacitance or inductance at switching time would be unavailable to the load. This trapped energy oscillates within the Marx/crowbar loop and is eventually dissipated by resistance in that loop. If the arc resistances in the Marx spark gaps and the crowbar spark gap are a significant portion of the total loop resistance, then corresponding energy will be dissipated in them.

Instant changeover from an RLC underdamped discharge to a perfect RL exponentially decaying discharge circuit would require an ideal crowbar switch that changed from a megavolt or higher voltage insulator to a perfect, high-current short circuit. The real physical crowbar switch and the conductors that form the crowbar leg of the circuit have finite impedance. The inductance of the crowbar circuit leg must be very small when compared to either the load circuit inductance or to the Marx generator source inductance. The same is true for resistance. Coupling from the Marx/crowbar loop to the load circuit loop occurs because the crowbar-circuit-leg impedance is greater than zero and is common to both high-current circuit loops.

The lower inductance at the Marx/crowbar loop causes it to have a shorter RLC oscillation period than the uncrowbarred RLC oscillation period for the main Marx/load loop. This 2.5- to 4- μs period crowbar oscillation shows up at early time as a superimposed overshoot oscillation at the start of the damped LR exponential decay in current. The shorter oscillation period of the crowbar is easily distinguishable from the oscillation period of the main Marx/load circuit loop, which also controls initial current rise time.

SIMULATED LIGHTNING TESTS WITH THE ALCM

The lightning simulation tests conducted at SNL with the ALCM demonstrate some of the improvement in simulator capabilities made since January 1983. The greater Marx-stored energy and higher operating voltage mentioned previously permitted faster rise times, higher

peak currents and longer duration pulses than were possible with the full-size operational aircraft tests in 1982. (The lower 2-microhenry inductance of the ALCM and its return circuit also contributed to making these results possible.)

Direct-stroke natural lightning was simulated for 29 tests made with a prototype AGM-86B missile during a 3- or 4-week period in July and August 1983. Different selected current levels were injected nose-to-tail into the missile for several different test series. Currents delivered had peak values that ranged from 50 to 250 kA and had action values ranging up to $6 \times 10^6 \text{ A}^2\text{S}$. These long-duration, high-energy pulses had steeply rising current fronts with 10% to 90% rise times on the order of 1 μs . Current rate-of-rise reached or exceeded $2 \times 10^{11} \text{ A}$ in those cases where it was required.

BMAC personnel took care of all aspects of the test related to the missile and its response characteristics. As prime contract representatives on the AEHP program for AFWAL, the Boeing engineers directed the overall test and specified the test sequence. D. B. Walen(15) provides additional description of these tests conducted as a part of Task IV of the AEHP program(14) previously referenced elsewhere in this and past conferences.

Sandia personnel were responsible for the simulator performance, operation, and maintenance. The simulator data acquisition system was used to digitize transient waveforms of currents applied to the missile and of response signals derived through BMAC missile instrumentation.

LIGHTNING CURRENTS INTO ALCM - Nominal peak current (I_0) of 50 kA, 100 kA, and the

severe-threat 200-kA level were specified for the three different test levels. An example of a digitized transient current record for each level is shown (Fig. 6) with a slow time base. The additional dotted curve is the theoretical double-exponential current pulse representing the severe threat, as specified by BMAC and AFWAL. B. G. Melander(16) at BMAC discusses the rationale concerning selection of this waveform to represent a "severe threat."

AFWAL representatives requested that the AEHP 200-kA peak current and a current minimum-rate-of-rise of $2 \times 10^{11} \text{ A}^2\text{S}$ both be provided if possible. All simulator pulse objectives of the test series were met or exceeded and the BMAC and AFWAL representatives were quite satisfied with the simulator performance.

LONG-TAIL, HIGH ACTION - The action values for the 200-kA long-duration current pulses recorded for the ALCM tests obviously exceeded the specified $1.5 \times 10^6 \text{ A}^2\text{S}$. The thick, high-conductivity, aluminum structure and skin of the missile provided a low value of damping resistance in these tests. A test item with a higher resistance would result in a more rapid drop in the L/R exponential decay of the current waveform.

At peak current during the 200-kA tests, 160 kilojoules of magnetic energy was stored in the 8 microhenrys of test-item and discharge circuit inductance. A small value of lumped resistance was added to the circuit to shorten the exponential L/R decay time and to cut down partially on the action that resulted from this high value of magnetically stored energy. Solid-rod graphite resistor assemblies were made and used in the tests to

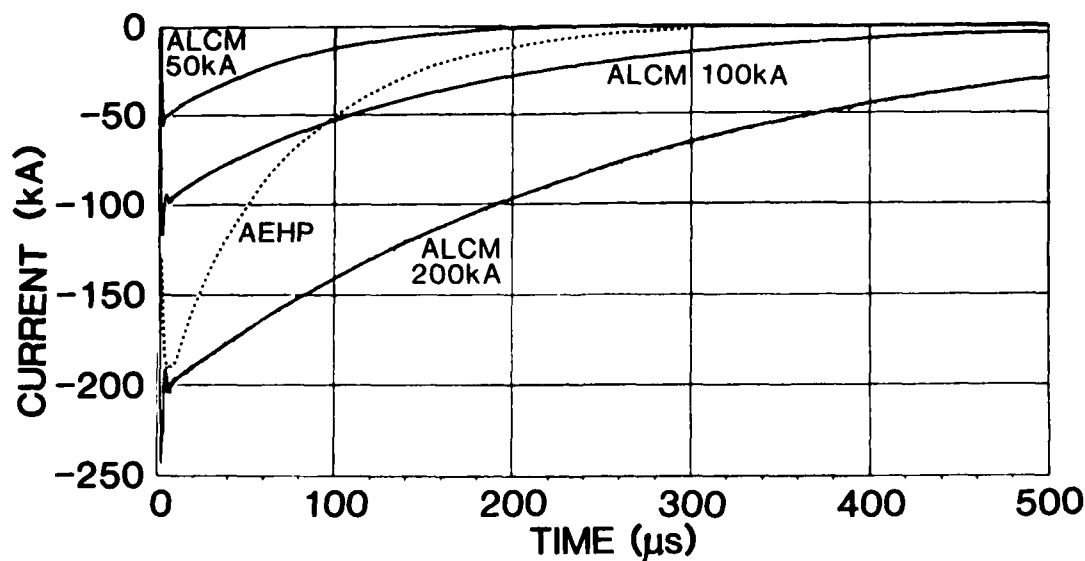


Fig. 6. Fast-rising, long-duration currents recorded in ALCM

partially reduce delivered action. However, appropriate higher value, high-energy-dissipation resistors with the needed very low inductance could not be produced in a timely manner. Fortunately, the AFWAL and BMAC test representatives were agreeable to action integrals higher than normally specified for a severe-threat pulse. Therefore, no effort was made to insert additional energy-dissipating resistance into the test circuit.

Action values for the 200-kA shots were about 4 to 6×10^6 A²S. Action values for the 100-kA shots were about 0.5 to 0.9×10^6 A²S and were appropriately less than 0.1×10^6 A²S for 50-kA shots. Necessary values of series resistance for the lower energy 50-kA pulses were much easier to provide, so there was no problem in reducing them to the considerably narrower pulse widths specified.

FAST-RISING CURRENT PULSES - The three digitized current records are shown in Fig. 7 with a fast time base. The AEHP severe-threat double-exponential pulse is again shown as a dashed trace for comparison.

These current pulses satisfied the AFWAL request for a fast rise time. The AEHP severe-threat, double-exponential reference pulse has an initial value of di/dt of 2×10^{11} A/s, but its high values of di/dt persist only for a very short duration. The 200-kA simulator pulses exceeded the requested high value of di/dt and also sustained a high level of di/dt for longer time. The derivative of current (and test-item-applied voltage waveform), for the double-exponential reference current waveform, has a rapid exponential decrease from its initial value. The cosine-like derivative of the simulator current waveform decreases quite slowly at early times. For equal values of maximum instantaneous di/dt , the average value of rising di/dt is much higher for the simulator pulse than the average value of rising di/dt for the reference, double-exponential pulse. Because a high value of di/dt is sustained, the overall time-of-rise for the simulator pulse is quite short.

Crowbar switching before the RLC underdamped current peak is reached can also contribute to reducing the time to output pulse peak current. Maximum or average values of attainable di/dt are easily estimated for the simulator by noting that initial di/dt is simply related to source driving voltage divided by total loop circuit inductance, or V/L .

Computer-aided transient circuit analysis before the tests aided in setting up the simulator and in assuring that the requisite waveforms could be achieved. A SCEPTRE-computed current waveform (computed after the tests) is shown in Fig. 8 for comparison with the 200-kA, severe-threat current waveform recorded in the ALCM tests.

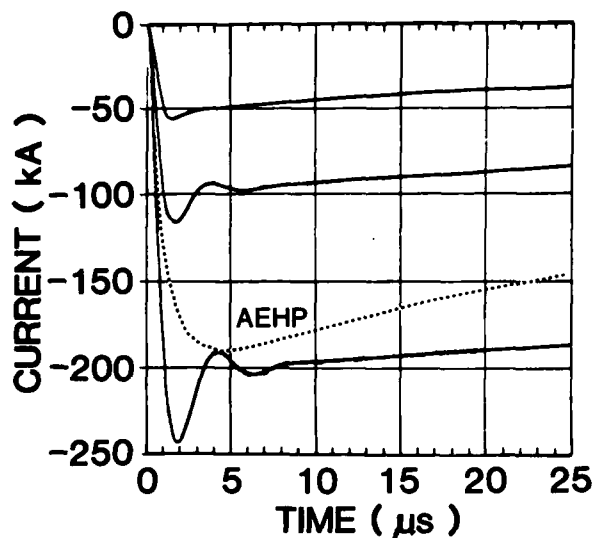


Fig. 7. Early-time portions of ALCM waveforms in Fig. 8

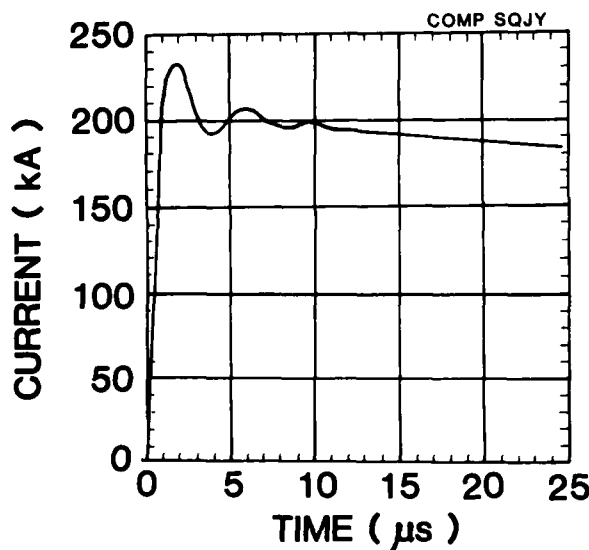


Fig. 8. Computed 200-kA current pulse

CURRENT FREQUENCY SPECTRUM - The AEHP severe-threat, double-exponential-pulse, frequency spectrum is shown (dashed line) in Fig. 9 along with the Fourier transform frequency spectrum of the same ALCM 200-kA simulator pulse (Test BZHCAA) shown in the other figures. This fast Fourier transform was made from an 8000-point digitized record of the test waveform. Spectral amplitude of the simulator pulse equaled or exceeded that for

the theoretical pulse over the entire frequency range shown.

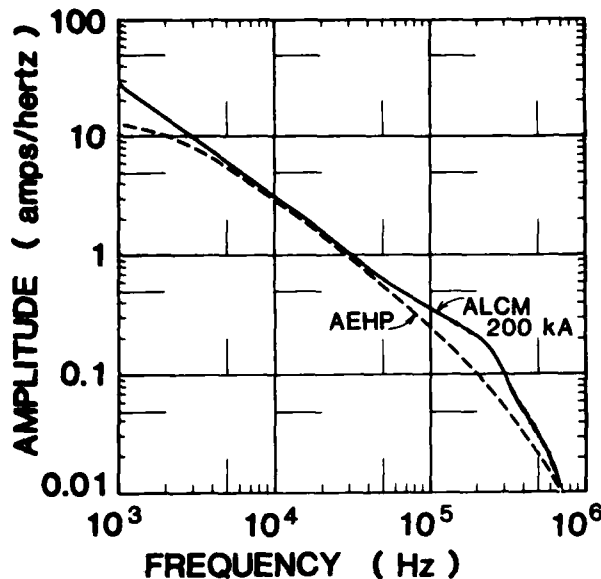


Fig. 9. Comparison of spectral content of ALCM test pulse and AEHP reference pulse

SIMULATOR VOLTAGE WAVEFORMS

MARX TERMINAL VOLTAGE - The Marx terminal voltage, also applied to the crowbar switch, consists of the downstream $L di/dt$ voltage drops along with the usually much smaller IR voltage drops. If the Marx generator were an ideal charged capacitor with zero internal inductance and resistance, and had no switch drop, then its output would be a cosine waveform. Even though the terminal voltage of the Marx generator is lowered or modified from that resulting from the discharge of an ideal capacitor by internal impedance voltage drops, it is still basically an underdamped cosine-like waveform. The crowbar switch must withhold this applied voltage until crowbar switching operation is permissible.

The overall effect is that an inductive voltage divider consisting of Marx inductance and downstream inductance connected directly across the ideal capacitance of the Marx. The inductance ratio determines how much of the ideal capacitor voltage waveform is applied to the crowbar switch. Crowbar switch voltage will be high if inductance downstream from the crowbar is a large fraction of the total series circuit inductance. It will be correspondingly low for a low-inductance load circuit.

The initial step in the simulator voltage waveform is very abrupt. Voltage rate of rise

depends on location in the circuit. Primarily limited by numerous stray capacitances and the voltage multiplication process in the Marx, dv/dt may exceed 10^{13} . Natural lightning dv/dt may be even higher, but simulator dv/dt is still so high that numerous stray capacitance resonant circuits in the local simulator/test-item environment become shock excited.

OUTPUT TERMINAL VOLTAGE - Voltages at the input to the test item are such that return circuit conductors must be adequately spaced from the test item to prevent air sparkover. Even with spacing sufficient to prevent sparkover, multiple streamers sometimes form at the high-voltage terminal. Photographic records taken during the ALCM tests show about 40 separate, diffuse, negative streamers propagating radially outward from the high-voltage terminal corona ring. Many of these streamers attained lengths on the order of 250 mm before luminescence from them became so diffuse that it was no longer recorded.

The higher amplitudes of the output voltage pulse persist only as long as current is rising. This relatively short duration of the voltage pulse makes the task of insulating for it easier than if the pulse were longer. If the amplitude of the simulator negative terminal voltage pulse is not already quite low, it drops abruptly at crowbar switch closure time. The applied negative voltage pulse width was around 1 μ s or slightly more for the ALCM tests, depending on which test series was being conducted.

COMPUTER SIMULATION OF CIRCUIT RESPONSE

The Air Force SCEPTRE(17(18) program is one of several transient-circuit analysis aids that has been used frequently at SNL. SCEPTRE was developed in the 1960s by IBM on contract to the Air Force Weapons Laboratory (AFWL) as a general transient analysis program. It has been quite valuable for computer modeling many circuit variations related to development and operation of the lightning simulator. Voltage and current waveforms at any point in the circuit along with power, energy, and action can be readily computed if values and characteristics for circuit elements are determined.

COMPUTED VOLTAGES - The voltage waveforms of Fig. 10 were computed using SCEPTRE and a more detailed circuit model than the previous basic circuit. For these waveforms, Marx series resistance, R_M , was made a higher value than would naturally occur without the addition of fixed resistance. This has resulted in more rapid damping of the oscillatory discharge. Known stray capacitances were deliberately left out of the analytical circuit for these plots in order to omit some of the high-frequency ringing that would otherwise occur at the time of step changes in voltage.

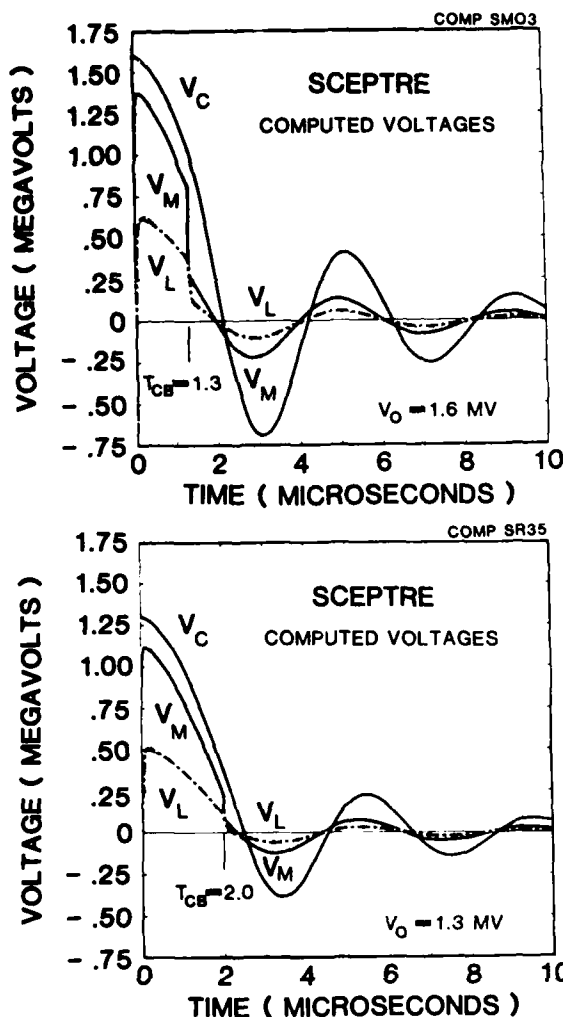


Fig. 10. Computed voltage waveforms

The total voltage across the dielectric of the Marx capacitors is shown as V_C . Due to internal impedance and switch drop, this is reduced at the output of the Marx to V_M . Marx terminal voltage, V_M , is the same as that across the crowbar switch. When crowbar switching occurs, V_M is shorted out. With a perfect short circuit, V_M would go to zero and stay there. Since Marx voltage and residual, stored, source energy are not zero at crowbar switch time, this energy continues to oscillate back and forth within the Marx/crowbar loop. Because the crowbar is not a perfect short circuit, this Marx/crowbar oscillation is coupled to the downstream circuit and shows up on the load (test item) voltage, V_L .

CIRCUIT DIAGRAM FOR COMPUTED WAVEFORMS - An example of a slightly more detailed equivalent circuit model that is often adequate for analyzing or predicting most circuit response for this simulator is shown in Fig. 11. The Marx generator is again shown in very simple form as elements C_M , L_M , and R_M , along with some shunt resistance. The make-up inductance and resistance are again shown as L_{MU} and R_{MU} . Load inductance L_L and load resistance R_L are shown at the right. L_{MU} may represent either a physical coil or a straight pipe conductor, depending on the current pulse required. Without the connecting elements from the continuing current generator, this is the kind of circuit model used for the voltage waveforms of Fig. 10.

Actual physical circuit parameters can usually be calculated from recorded waveforms of previous simulator operation. Digitized records of an oscillating discharge made without crowbar switching permit calculation of total equivalent series inductance, providing that Marx series discharge circuit capacitance is known. Records from other tests, in which various circuit elements or

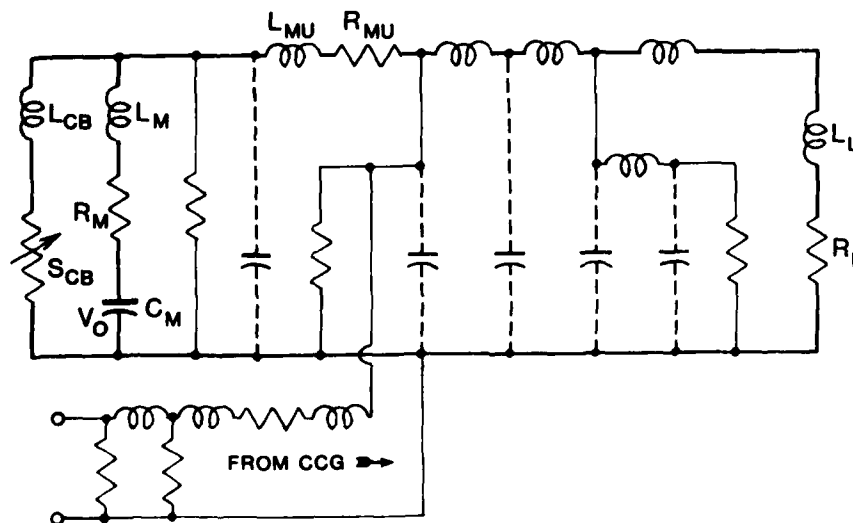


Fig. 11. Circuit model for computing performance

loads on the simulator were changed, permit determination of other elemental circuit parameter values.

When continuing current is required in a test, continuing current generator (CCG) connections from the motor/generator set are brought in through the network of isolating elements shown in the lower part of the diagram.

The computer circuit model used for two parallel Marx generators (i.e., an entire tank) can usually be about the same as for a single Marx except for the substitution of different element values. The extremely simplified Marx generator model, represented here as only three elements, is in fact a very complex circuit when its high-frequency characteristics are considered. There are many stray capacitances and stray inductances associated with each Marx generator(2) and its 32 high-energy storage capacitors and 16 each 200-kV spark gaps. Stray capacitances also exist to the walls and floor of the tank. The two halves of each Marx may not trigger and erect with absolute simultaneity. These and other factors give rise to a large number of parasitic-element, resonant circuits.

The stray capacitance of the crowbar switch itself is shock-excited into high-frequency oscillation when the Marx generator erects. The overall complex of high frequencies is superimposed onto the basic cosine (uncrowbarred) output waveform of the Marx generator and applied to the crowbar spark gap.

Physical layout of the entire discharge circuit frequently affects what is needed in the detailed equivalent circuit. Few of the discharge circuit elements are really lumped constant elements. Almost all of the physical conductors, components insulation, etc., constitute distributed parameter portions of the overall circuit. With more detailed consideration, bus bars become inductors with shunting stray capacitance (or transmission lines). Large-diameter solenoids of copper or stainless-steel tubing also have turn-to-turn and coil-to-container stray capacitances. The oil-insulated interconnecting and coaxial output conductors of the simulator often must be treated as transmission lines.

As a result, the overall circuit sometimes becomes a combination of resonant tank circuits and distributed-parameter transmission lines intermingled with the elements of the basic lumped element discharge circuit. The remaining inductive and capacitive elements of Fig. 11, located between L_{MU} and L_L , are lumped constant representations of distributed constant elements in the simulator.

OSCILLATION DAMPING RESISTORS

Current waveforms recorded with the simulator for the past few years have had the 200-kHz to 350-kHz crowbar oscillation superimposed on the pulse just after rise. This

underdamped oscillation often persisted for more than 30 μ s and was caused by oscillation in the Marx/crowbar loop. This crowbar oscillation was very nearly damped out on the previously shown ALCM 50- and 100-kA test current waveforms.

The improved oscillation damping and waveshape control evidenced in the ALCM tests is the result of new high-energy, copper sulphate solution Marx damping resistors added in series into the Marx/crowbar circuit loop. A pair of copper sulfate solution resistors was made for each Marx generator so that one could be installed in series in each of the two paralleled halves forming each Marx generator. When the Marx/crowbar loop damping resistors were made and installed in each of the Marx generators, they worked well to dampen the crowbar oscillation.

The fact that characteristic impedance or surge impedance, $\sqrt{L/C}$, is lower for the crowbar loop than it is for the load circuit loop allows selection of a compromise value of damping resistance. A suitable resistance selection rapidly damps out the crowbar loop oscillation but has only a limited effect on the output peak current attained. The Marx damping resistors can easily be left out of the simulator when superimposed oscillations on the current waveform are not considered a problem or may even be desired.

Identification of the sources of other undesirable high frequency oscillations often allows something to be done to reduce or eliminate them. If the characteristic impedance, $\sqrt{L/C}$, of the oscillation is high, it can often be damped out by a shunt resistance value that is sufficiently high that it does not have any detrimental effect on the main discharge circuit. Most of the methods available to damp oscillations are energy-absorbing and cause reductions in available output current for any given stored energy. Since charge voltage must then be increased to make up for the losses to the added damping elements, reduction in noise on a waveform often cannot be made without cost.

It is more difficult for the crowbar switch to withstand the applied voltage if a large amount of high-frequency ringing is present on the Marx output waveform. Failure of the crowbar switch to properly hold off its applied voltage short-circuits the Marx at an early time so that little energy is delivered to the intended load. Adding a fixed, liquid resistor directly across the crowbar switch has aided in improving its hold-off voltage characteristic by reducing high-frequency noise on its applied voltage waveform.

Other circuit elements can be added or changed in value to obtain beneficial effects. The initial fast-rising pulse applied to distributed constant portions of the circuit results in multiple pulse reflections that may be either beneficial or undesirable, depending on the particular overall objective. Frequently, they may show up as undesirable

superimposed steps or ripple on the output current pulse.

If the overall simulator current pulse is being delivered into low-impedance loads, the source circuit is generally quite tolerant of shunt resistive loads added to terminate or match some of the transmission line stubs or to damp out high characteristic impedance LC oscillation.

A branched transmission line is formed by the coaxial-output, oil-insulated, output conductor arrangement located between the two Marx tanks. Transmission-line reflection-induced ringing on the current waveform has been essentially eliminated by adding a shunt resistor to ground between the isolation spark gap and the output bushing in each of the two simulator tanks.

CROWBAR TIMING EFFECTS ON MARX CURRENTS

How simulator circuit response is affected by crowbar timing is shown by Fig. 12, in which SCEPTRE-computed current waveforms are shown for different crowbar timing conditions. Except for crowbar timing and charge voltage, simulator model circuit parameters were identical for both sets of plots, and for the previous plots of voltage in Fig. 10. Similar 200-A output-current, I_L , pulses were produced. Marx generator current, I_M , and crowbar switch current, I_{CB} , are shown with each of the resulting output currents. Crowbar time for the upper set of plots was 1.3 μ s and was increased to 2.0 μ s for the lower set. Marx charging voltage was decreased for the lower set of plots to provide about the same current pulse in each case. Marx erection or circuit driving voltage was 1.6 MV for the upper set and was reduced to 1.3 MV for the lower set of plots.

Improved simulator operation is indicated by the waveforms if the quality of the trigger mechanism is sufficient to make the crowbar close at times nearer zero voltage. Fig. 12 also indicates that stress likely to cause degradation and damage to the Marx generator components should be less for the later crowbar time. High-frequency oscillation of dielectric energy through the Marx capacitor is less. Reduction of high-charge and high-energy oscillation through the Marx spark gaps should reduce wear and tear on them. Voltage stress on the capacitors would also be less for the same output current. Early-time, high-frequency peak power and energy dissipation in the crowbar switch will also be less with a later crowbar time.

The crowbar switch was required, for the upper set of waveforms, to hold off a higher nominal peak voltage (voltage peak averaged through mean of parasitic high-frequency ringing). Peak voltage applied to the crowbar was 1.36 MV, with the crowbar switching occurring at 59% of peak. For the lower set of current waveforms, the crowbar was subjected to 1.22 MV and was switched at 20% of nominal

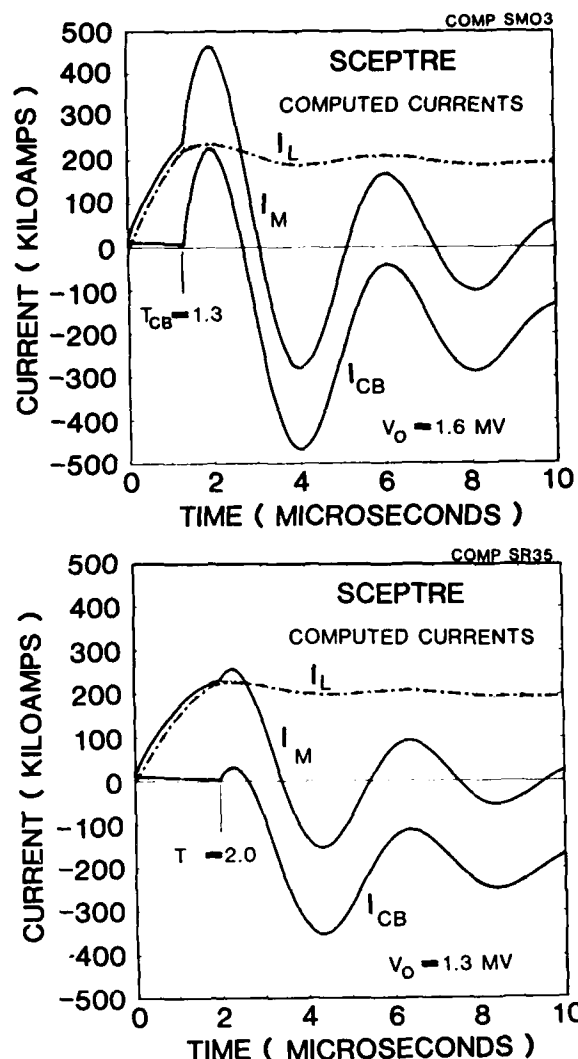


Fig. 12. Crowbar timing effect on currents within the simulator

peak voltage. It may be concluded from this that even though different crowbar timing selections may cause no more than 15% to 20% total change in output peak current, other early-time currents in the simulator may be affected more drastically, particularly those in the Marx generator.

Even though the two exponential decaying output current waveforms of Fig. 12 have basically the same initial (peak) current, charge, and action, there are differences at the pulse front that may be important. For the upper set of computed current waveforms with the earlier crowbar time, the output current, I_L , has a higher average and initial di/dt and also a shorter time of rise. The small overshoot oscillation (crowbar ring) on both is less and damps out more quickly for the case with the later crowbar. If absolute maximum values of di/dt are needed, then high-charge voltage and early-crowbar timing, as

well as minimum total circuit inductance, become important.

The analytical model circuit used for computing the waveforms of Fig. 12 had only a small amount of resistance deliberately added into the Marx/crowbar loop. Addition of even more resistance would damp out the oscillation more quickly and reduce energy dissipated in the Marx spark gaps and capacitors. The resistance selected must not be so high that the increase in charge voltage needed to maintain peak output current becomes excessive.

The question may arise, relative to this figure, as to why load current and Marx current do not exactly coincide before crowbar time. The difference is due to current flowing into equivalent shunt resistance across both the Marx and crowbar switch. A portion of this current is shown as the part of the crowbar waveform, I_{CB} , that occurs before crowbar action starts. This part of I_{CB} is due to the current into a circuit element representing the physical CuSO_4 damping resistor placed directly across the real crowbar switch. Small currents due to Marx stage isolation and charging resistors that also contribute to the difference are not shown in the figure.

Trigger characteristics of the laser-beam-triggered spark gap used in this simulator for crowbar switching are similar in many ways to the well-known characteristics of electrically triggered spark gaps. Greater trigger energy or a better trigger mechanism is required to produce good triggering when main-gap voltage is only a small fraction of operating hold-off voltage. Also, the spark gap switch is more difficult to trigger if main-gap voltage is decreasing rather than increasing or holding steady.

The ultraviolet laser provides a good triggering mechanism for the crowbar spark gaps used in this lightning simulator. M. J. Landry's description(19) of the laser-triggered crowbar spark gaps used in this simulator appears elsewhere in this conference.

SUMMARY AND CONCLUSIONS

The SNL lightning simulator is still in development, and its capabilities are being increased with time, but its present combination of simulation capabilities is believed to be unique. Double-pulse (two-stroke) high-level flashes have been provided in many tests to simulate multiple-stroke natural lightning. Tests with full-size weapon systems have achieved and exceeded the requirements for all aspects of severe-threat natural lightning simulation. Peak current, current rate-of-change, charge, action, continuing current, and high-voltage values related to severe lightning can all be furnished in a single-flash simulation using present technology. A wide range in selectable output characteristics is made possible by the modular nature of this versatile simulator. Maximum energy storage and potential stroke energy have been increased to the point where higher resistance test items can be evaluated. Important improvement in simulator operational capabilities were made during 1983, including change-over from infrared to ultraviolet laser triggering of the crowbar switches. Faster current-rise-time, higher peak current, smoother and better current pulse shape, and greater reliability have been demonstrated. A very successful test series of 17 consecutive double-pulse 200-kA/100-kA tests was made during January 1984.

ACKNOWLEDGMENT

F. W. Neilson suggested and supported many of the approaches to the improvements described as well as the basic design for the simulator. The good results with the SNL lightning simulator facility have resulted from the contributions of many people. Numerous individuals both in internal organizations at SNL and in external agencies within the U. S. Departments of Energy and Defense have cooperated and provided support. W. P. Brigham, W. B. Vandermolen, R. J. Goode, M. J. Landry, R. I. Ewing, J. C. Bushnell, J. G. Kostas, and others contributed to implementing the improvements to the simulator and its successful operation.

REFERENCES

1. F. W. Neilson, "An Extreme Lightning Test Facility." Unpublished internal report, 1977.
2. J. C. Bushnell and J. G. Kostas, "The Sandia Lightning Simulator." Addendum, 8th International Aerospace and Ground Conference on Lightning and Static Electricity, DOT/FAA/CT83/25, Fort Worth, TX, June 1983.
3. R. A. White, "Full System Tests Using the Sandia Lightning Simulator." 8th International Aerospace and Ground Conference on Lightning and Static Electricity, DOT/FAA/CT-83/25, Fort Worth, TX, June 1983.
4. Ronald I. Ewing, "Performance of the Sandia Lightning Simulator during F-14A and F/A-18 Aircraft Lightning Tests." 8th International Aerospace and Ground Conference on Lightning and Static Electricity, DOT/FAA/CT-83/25, Fort Worth, TX, June 1983.
5. N. Cianos, E. T. Pierce, "A Ground Lightning Environment for Engineering Usage," Stanford Research Institute Technical Report, No. 1, Project 1834, August 1972.
6. G. W. Anderson and F. W. Neilson, "Use of The Action Integral in Exploding Wire Studies," Vol. I, "Exploding Wires," edited by W. G. Chace and Howard K. Moore, Plenum Press Inc., 1959.
7. K. Berger, R. B. Anderson, H. Kroninger, "Parameters of Lightning Flashes," *Electra*, 89 23-37, 1975.
8. W. L. Taylor, W. D. Rust, D. R. MacGorman, and E. A. Brandes, "Lightning Activity Observed in Upper and Lower Portions of Storms and its Relationship to Storm Structure," 8th International Aerospace and Ground Conference on Lightning and Static Electricity, DOT/FAA/CT-83/25, Fort Worth, TX, June 1983.
9. L. V. Bewley, "Traveling Waves on Transmission Systems," 2nd Edition, John Wiley and Sons, 1933.
10. W. D. Rust, W. L. Taylor, and D. R. MacGorman, "Storm Electricity Research in Oklahoma: An Overview," 8th International Aerospace and Ground Conference on Lightning and Static Electricity, DOT/FAA/CT-83/25, Fort Worth, TX, June 1983.
11. L. E. Salanave, "Lightning and its Spectrum," University of Arizona Press, 1980.
12. R. C. Beavin, J. R. Lippert and Lt. J. E. Lavoie, "Atmospheric Electricity Hazards Protection Program", 8th International Aerospace and Ground Conference on Lightning and Static Electricity, DOT/FAA/CT-83/25, Fort Worth, TX, June 1983.
13. J. R. Lippert, "Vulnerability Assessment of Electrical/Electronic Subsystems and Equipment to Atmospheric Electricity", 8th International Aerospace and Ground Conference on Lightning and Static Electricity, DOT/FAA/CT-83/25, Fort Worth, TX, June 1983.
14. J. R. Lippert, J. E. LeVoie, and R. C. Beavin, "Progress of the Atmospheric Electricity Hazards Protection Program," 9th International Aerospace and Ground Conference on Lightning and Static Electricity, Orlando, FL, June 1984.
15. D. B. Walen, "High-Level Lightning Simulation Test on the AGM-86 ALCM," 9th International Aerospace and Ground Conference on Lightning and Static Electricity, Orlando, FL, June 1984.
16. B. G. Melander, "Atmospheric Electricity Threat Definition for Aircraft Lightning Protection," 8th International Aerospace and Ground Conference on Lightning and Static Electricity, DOT/FAA/CT-83/25, Fort Worth, TX, June 1983.
17. H. W. Mathers, S. R. Sedore, and J. R. Sents, "SCEPTRE Support." IBM Corp., Contract F29601-67-C-0049 for AFWL, Kirtland AFB, NM, April 1968.
18. H. W. Mathers, "SCEPTRE (System for Circuit Evaluation and Prediction of Transient Radiation Effects)." IBM Corp., included in G. W. Zobrist, "Network Computer Analysis", Boston Technical Publishers, 1969.
19. M. J. Landry and W. P. Brigham, "UV Laser Triggering and Crowbars Used in the Sandia Lightning Simulator," 9th International Aerospace and Ground Conference on Lightning and Static Electricity, Orlando, FL, June 1984.

AD-A169 867

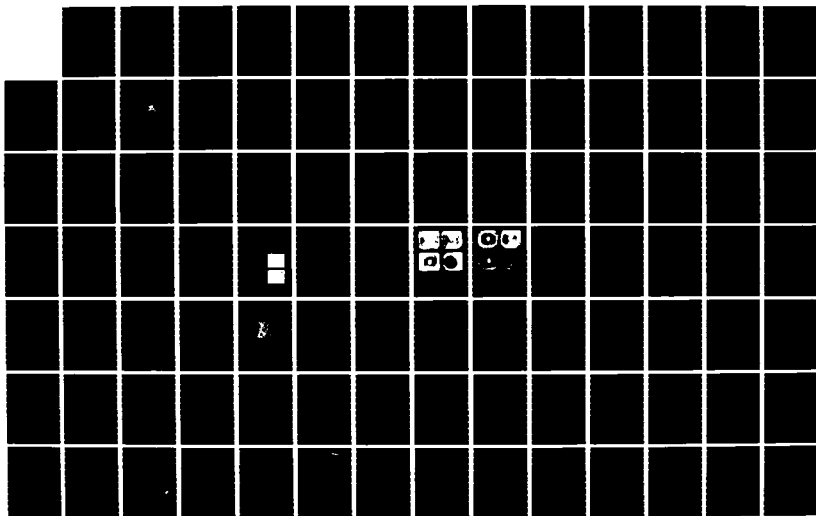
INTERNATIONAL AEROSPACE AND GROUND CONFERENCE ON
LIGHTNING AND STATIC ELE. (U) NATIONAL INTERAGENCY
COORDINATION GROUP JUN 84

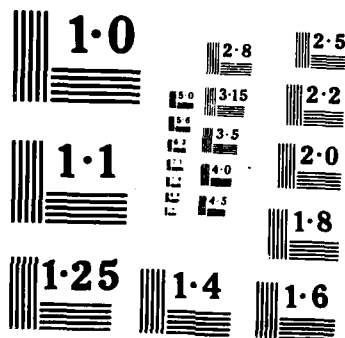
5/6

UNCLASSIFIED

F/G 28/3

NL





ESTIMATION OF STANDARD DEVIATION OF DISRUPTIVE VOLTAGE OF AIR GAPS UNDER
LIGHTNING OVERVOLTAGES BY MODIFIED UP-AND-DOWN METHOD

P. MOURENTE

COPPE/UFRJ - RIO DE JANEIRO, BRAZIL

N. SANTIAGO

COPPE/UFRJ and ELECTRA, BRAZIL

C. PORTELA

COPPE/UFRJ and PTEL, BRAZIL

ABSTRACT

Is a common practice in insulation coordination studies to model the gaps by a disruptive voltage probability distribution. This distribution is usually obtained from laboratory tests and the up-and-down method is the most used. This method is very convenient since it requires few shots and the critical flashover voltage estimate obtained is accurate. However the mean square deviation estimate is very sensitive to the voltage step chosen, resulting in incorrect values. This may lead to insulation over or underdesign.

In this paper the errors due to the voltage step used on the tests are studied and corrections suggested.

INTRODUCTION

AN ASPECT TO BE CONSIDERED in transmission line design is the insulation. The insulation is formed by several gaps in parallel. Those gaps must be coordinated in such a way to assure proper performance of the line without raising the costs.

It is usual in the insulation coordination studies to represent the gaps by a disruptive voltage probability distribution. Depending on the gap, different types of distributions can be used.

Air gaps, as conductor to tower clearances and insulator strings, may be represented by a normal distribution which is fully characterized by a mean value (\bar{U}) and a mean square deviation (σ).

For very small probabilities this assumption may be in error, and a different distribution should be considered, e. g. a Weibull distribution. However, for comparison purposes and more simple presentation, an exact normal distribution is assumed.

In order to obtain these parameters (\bar{U} and σ) laboratory tests are performed and the literature reports in this subject are common [1-3].

Two methods are most used to obtain these parameters:

- conventional interpolation;
- up-and-down method.

The conventional interpolation method gives correct estimates of both \bar{U} and σ . It permits also to check if the normal distribution fits the actual gap distribution. This method requires a large number of shots which implies in time consuming tests.

The up-and-down method requires less shots and gives a good estimate of \bar{U} ; practically equal to the one given by the conventional method. However the σ estimate differs appreciably of the estimate obtained by the conventional method.

It may be observed that σ estimated by the up-and-down method changes largely with the chosen value of the voltage step.

Thus the value of σ estimated may lead to incorrect insulation coordination. That may be an overdesign, leading to a more expensive line, or underdesign which impairs the performance of the electrical system.

In this paper a study of the errors in the estimation of σ by the up-and-down method is presented and correcting procedures suggested.

UP-AND-DOWN METHOD

The up-and-down method as prescribed in the standards [4, 5] consists in the application of a series of n voltage impulses with a given wave form. The peak value of the impulse wave is a function of the previous shot. For instance starting from an initial value U_0 the next shot will have a peak value $U_1 = U_0 - \Delta U$ if there is a discharge or $U_1 = U_0 + \Delta U$ if the gap withstands. The value of ΔU is named voltage step and usually chosen as $0.03U_0$ for lightning impulses and $0.05U_0$ for switching surges.

After the application of several shots, a minimum of twenty for lightning impulses, \bar{U} and

σ may be estimated by [4, 5]:

$$\bar{U}_e = \sum_{i=1}^n U_i / n \quad (1)$$

$$\sigma_e = \left[\sum_{i=1}^n (U_i - \bar{U}_e)^2 / (n-1) \right]^{1/2} \quad (2)$$

The correct values \bar{U} and σ shall be into the intervals given by [5]:

$$\bar{U}_e - \sigma_e t_p / \sqrt{n} \leq \bar{U} \leq \bar{U}_e + \sigma_e t_p / \sqrt{n} \quad (3)$$

$$\sigma_e \left| (n-1) / \chi^2_{1-p/2} \right|^{1/2} \leq \sigma \leq \sigma_e \left| (n-1) / \chi^2_{1-p/2} \right|^{1/2} \quad (4)$$

where t_p is the Student variable;

$$p = 1 - P_c$$

P_c probability of \bar{U} and σ be contained in the defined intervals.

It may be noted that equations (3) and (4) state that the confidence on the estimates is a function only of the number of shots and not of the voltage step chosen. That means that is expected that the value of ΔU does not influence significantly the test results.

A study of the influence of the ratio $\Delta U / \sigma$ is necessary.

EVALUATING THE INFLUENCE OF $\Delta U / \sigma$

The influence of $\Delta U / \sigma$ may be evaluated in different ways:

- numeric simulation;
- analytical study;
- laboratory tests.

NUMERIC SIMULATION - This is a fast method to check if there is any influence of $\Delta U / \sigma$ in the estimates of \bar{U} and σ . The Monte Carlo method will be used.

This simulation consists in using a pseudo-random number generating function, which presents an uniform probability density. To a given value of voltage U the flashover probability is $p(U)$, a random number r is generated, the decision if there is flashover is then taken as bellow:

$r < p(U)$ there is flashover

$r \geq p(U)$ the gap withstands

This permits a simulation of the actual test procedure.

In Tables 1, 2 and 3 the numeric simulation sequences obtained to $\Delta U = \sigma/2$, σ and 2σ are shown.

In Fig. 1 the normal distribution which was used to simulate the gap ($\bar{U} = 0$ and $\sigma = 1$) is compared against the estimated distribution (\bar{U}_e and σ_e).

It is possible to see in Fig. 1 that for values of $\Delta U < \sigma$ the estimated mean square deviation σ_e is lower than the actual value σ . The opposite being true for $\Delta U > \sigma$.

ANALYTICAL STUDY - Assume a gap characterized by a normal distribution (\bar{U} and σ). From an initial value U_0 there are two alternatives

for the next shot: the peak voltage may be $U_1 = U_0 - \Delta U$ if there is discharge or $U_1 = U_0 + \Delta U$ if the gap withstands.

Repeating the procedure described above to each one of the alternatives to U_1 , a tree of alternatives may be drawn as shown in Fig. 2.

Note that in the U_0 point the flashover probability is $p_1 = p(U_0)$. So there is a probability p_1 , to go to point $U_1 = U_0 - \Delta U$ and $(1-p_1)$ to go to $U_1 = U_0 + \Delta U$.

The total probability of each path may be found and using equations (1) and (2) to each path a pair of estimates (\bar{U}_e and σ_e) is obtained, see Fig. 2. This allows to obtain also the confidence limits.

In Table 4 and Figs. 3 and 4 the confidence limits obtained to the estimates \bar{U}_e and σ_e by the above described procedure to a tree of 15 steps and several values of $\Delta U/\sigma$.

LABORATORY TESTS - This is an expensive method which is sensitive to factors of difficult control. It is presented here just as an example and the information it provides is practically the same provided by the numeric simulation.

The tests were performed using a 20 cm rod-rod gap. The rods were made on aluminium of 2.54 cm in diameter with tips machined in shape of revolution hyperboloids. The wave shape used was the standard lightning impulse 1.2/50 (μ s).

Comparison between the estimated distributions obtained by the conventional method and the up-and-down method is presented on Fig. 5.

No correction to atmospheric conditions was applied, since it was not necessary for the purpose of comparison. Atmospheric conditions were:

temperature of 34°C;
relative humidity equal to 0.72;
atmospheric pressure of 755 mm of Hg.

IMPORTANCE OF CORRECT ESTIMATION OF σ

The up-and-down method permits a good estimation of \bar{U} , but not of σ . A simplified example may be used to emphasize the importance of a correct estimate to the mean square deviation σ .

Assume a typical 750kV transmission line in which the switching surge is the governing criteria for design.

The following assumptions have been made for evaluation purposes:

a) the overvoltage space distribution in each shot, is equivalent to an uniform overvoltage distribution in 200 towers, of equivalent overvoltage values;

b) the equivalent overvoltage value has a normal distribution with mean value 0.977 MV and mean square deviation 0.12 MV;

c) the atmospheric conditions are, in each shot, identical in the 200 towers and characterized by altitude 1000 m, ambient temperature with mean value 20°C and mean square deviation of 5°C, relative humidity with mean value 0.60 and mean square deviation 0.15;

d) temperature and humidity are supposed to be statistically independent;

e) rain is supposed to occur in 50% of the time during which humidity is over 75%;

f) the switching probability not correlated to atmospheric conditions.

A set of insulation distances has been considered in the range of 4.6 to 6.6 m.

The computation has been done according to [6].

Figure 6 shows, for illustration the probability distribution of flashover in a 5.5 m air gap considering 200 towers in parallel.

The curves were done considering the following mean square deviations of each gap: $0.03\bar{U}$, $0.05\bar{U}$ and $0.07\bar{U}$.

Identical curves were obtained for other gap distances.

Combining the overvoltage distribution with the flashover probability distribution of the line, it is shown in Fig. 7 the trip-out probability as a function of gap distance and σ of each gap.

Assuming a desired trip-out probability, under switching conditions equal to 0.001, the gap distance must be 5.5 m, considering $\sigma = 0.05\bar{U}$ for each gap.

If the transmission line were designed for $\sigma = 0.05\bar{U}$ and the actual value is $\sigma = 0.07\bar{U}$, the trip-out probability will rise from 0.001 to 0.0068.

In the other hand, if the actual value is $\sigma = 0.03\bar{U}$ an additional amount of US\$3000/km would have been spent without need.

MODIFYING THE UP-AND-DOWN METHOD

The up-and-down method is very popular in high-voltage laboratories, and permits good estimation of \bar{U} without requiring long time consuming tests. It would be convenient to correct the tendency of the method in giving incorrect estimates to σ .

Two situations may arise:

- the tests are being performed;
- the tests have been performed.

In the first case, it is possible, after a small number of shots, to evaluate \bar{U}_e and σ_e . Introducing in the vertical axis of Fig. 4 the value of $\sigma_e/\Delta U$, a new value of $\Delta U/\sigma$ will be found on the horizontal axis. Thus ΔU may be chosen in order that $\Delta U/\sigma_e$ lays between 0.95 to 1.50.

In the second case may not be possible to repeat the tests, thus it is desirable to apply a correction factor to the estimated σ_e . This will be possible if ΔU is known.

Introducing U/σ_e in Fig. 4 and drawing an horizontal line from this point, the intersection with the middle curve will give a new figure to $\Delta U/\sigma$. Thus σ'_e , a new estimate of mean square deviation, is given by:

$$\sigma'_e = \sigma_e \cdot \sigma/\Delta U \quad (5)$$

For instance, in the laboratory tests which results are shown in Fig. 5, there is a case where $\Delta U = 25.70$ kV. In this case the estimated parameters were:

$$\bar{U}_e = 212.7 \text{ kV}$$

$$\sigma_e = 13.07 \text{ kV}$$

These figures may be compared with the estimates obtained in the conventional method:

$$\bar{U}_e = 207.6 \text{ kV}$$

$$\sigma_e = 7.80 \text{ kV}$$

This comparison shows good agreement between the two estimates of \bar{U} and discrepancy on the estimates of σ .

Applying the correcting procedure $\Delta U/\sigma_e = 2.0$ is introduced in Fig. 4 and $\Delta U/\sigma = 2.92$ is obtained which leads to $\sigma'_e = 8.80 \text{ kV}$, which is far close to the 7.80 kV given by the conventional method.

CONCLUSION

The up-and-down method gives an accurate estimate of the mean value \bar{U} , if $\Delta U/\sigma$ lies between 0.3 and 3.

The estimate of the mean square deviation σ is sensitive to the voltage step used in the tests. The errors in this estimation have been shown to be inherent to the up-and-down method.

This error may be reduced using the correcting procedures described in the text.

REFERENCES

1. Y. Aihara; T. Harada; Y. Aoshima; Y. Ito - Impulse Flashover Characteristics of Long Air Gaps and Atmospheric Correction. IEEE Transactions on Power Apparatus and Systems, vol. PAS 97, n° 2, March/April 1978, pp. 342-348.
2. G. Gallet; G. Leroy; R. Lacey; I. L. Kromer - General Expression for Positive Switching Impulse Strength Valid up to Extra Long Air Gaps. IEEE Transactions on Power Apparatus and Systems, vol. PAS 96, n° 6, Nov/Dec 1975, pp. 1989-1993.
3. P. Zacke; A. Fischer; H. Boecker - Break down Phenomena of Rod-Rod Gaps Under Impulse Voltages of Opposite Polarities on Both Electrodes. IEEE Transactions on Power Apparatus and Systems, vol. 96, n° 2, March/April 1977, pp. 701-708.
4. IEC 60-2, High Voltage Test Techniques Part 2, Test Procedures, 1973.
5. ABNT-NBR-5389, High Voltage Test Techniques, Test Procedures (in portuguese), Associação Brasileira de Normas Técnicas, Nov/1981.
6. Portela C., Overvoltages and Insulation Coordination (book, in portuguese), COPPE/UFRJ, 1982.

TABLE 1 - NUMERIC SIMULATION WITH $\Delta U = 0.5 \sigma$

U	p(U)	SHOT N°																				TOTAL
		1	2	3	4	5	6	7	8	9	10	11	12	13	14	15	16	17	18	19	20	
$U_o + \Delta U$	0.69						1						1		1		1					4
U_o	0.50	1		1		0		1				0		0		0		1		1		9
$U_o - \Delta U$	0.31		0		0				1		0								0		1	6
$U_o - 2\Delta U$	0.16									0												1
$U_o = \bar{U}$		$\bar{U}_e = -0.10$																				
$\Delta U = 0.50$		$\sigma_e = 0.42$																				

TABLE 2 - NUMERIC SIMULATION WITH $\Delta U = \sigma$

U	p(U)	SHOT N°																				TOTAL
		1	2	3	4	5	6	7	8	9	10	11	12	13	14	15	16	17	18	19	20	
$U_o + \Delta U$	0.84						1						1		1		1					4
U_o	0.50	1		1		0		1				0		0		0		1		1		9
$U_o - \Delta U$	0.16		0		0				1		0								0		1	6
$U_o - 2\Delta U$	0.02									0												1
$U_o = \bar{U}$		$\bar{U}_e = -0.20$																				
$\Delta U = 1.00$		$\sigma_e = 0.83$																				

TABLE 3 - NUMERIC SIMULATION WITH $\Delta U = 2.0 \sigma$

U	p(U)	SHOT N°																				TOTAL
		1	2	3	4	5	6	7	8	9	10	11	12	13	14	15	16	17	18	19	20	
$U_o + \Delta U$	0.97		1		1										1						1	4
U_o	0.50	0		0		1		1		1		1		0		1		1		0		10
$U_o - \Delta U$	0.03						0		0		0		0				0		0			6
$U_o = \bar{U}$		$U_e = -0.20$																				
$\Delta U = 2.00$		$\sigma_e = 1.45$																				

TABLE 4 - ANALYTICAL STUDY OF THE ΔU INFLUENCE ON THE \bar{U}_e E σ_e VALUES OBTAINED BY THE UP-AND-DOWN METHOD

$\frac{\Delta U}{\sigma}$	$\frac{U_e - \bar{U}}{\sigma}$	$\frac{\sigma_{U_e}}{\sigma}$	$\frac{U_e - \sigma_{U_e} - \bar{U}}{\sigma}$	$\frac{U_e + \sigma_{U_e} - \bar{U}}{\sigma}$	$\frac{\bar{\sigma}_e}{\sigma}$	$\frac{\sigma_{\sigma_e}}{\sigma}$	$\frac{\bar{\sigma}_e - \sigma_{\sigma_e}}{\sigma}$	$\frac{\bar{\sigma}_e + \sigma_{\sigma_e}}{\sigma}$
0.1	-0.8793	0.4640	-1.3433	-0.4153	0.2637	0.0963	0.1674	0.3600
0.15	-0.6424	0.4320	-1.0744	-0.2104	0.3255	0.1335	0.1920	0.4590
0.2	-0.4916	0.4048	-0.8964	-0.0868	0.3701	0.1548	0.2153	0.5249
0.3	-0.3183	0.3721	-0.6904	0.0538	0.4411	0.1690	0.2721	0.6101
0.5	-0.1722	0.3538	-0.5260	0.1816	0.5694	0.1644	0.4050	0.7338
0.7	-0.1116	0.3552	-0.4668	0.2436	0.6950	0.1593	0.5357	0.8543
1.0	-0.0675	0.3662	-0.4337	0.2987	0.8773	0.1590	0.7183	1.0363
1.5	-0.0318	0.3911	-0.4229	0.3593	1.1666	0.1670	0.9996	1.3336
2.0	-0.0100	0.4195	-0.4295	0.4095	1.4442	0.1798	1.2644	1.6240
3.0	0.0249	0.4900	-0.4651	0.5149	1.9802	0.2390	1.7412	2.2192
5.0	0.0914	0.8930	-0.7116	0.8944	3.0192	0.4291	2.5901	3.4483
7.0	0.1581	1.2932	-1.1351	1.4513	4.0520	0.5777	3.4743	4.6297
10.0	0.2581	2.1126	-1.8545	2.3707	5.6012	0.7476	4.8536	6.3488

- Notes: 1) \bar{U} - mean value of actual normal distribution
 σ - mean square deviation of actual normal distribution
- 2) U_e - estimated mean value of each path
 σ_e - estimated mean square deviation of each path
- 3) \bar{U}_e - mean value of the U_e distribution
 σ_{U_e} - mean square deviation of the U_e distribution
- 4) $\bar{\sigma}_e$ - mean value of the σ_e distribution
 σ_{σ_e} - mean square deviation of the σ_e distribution

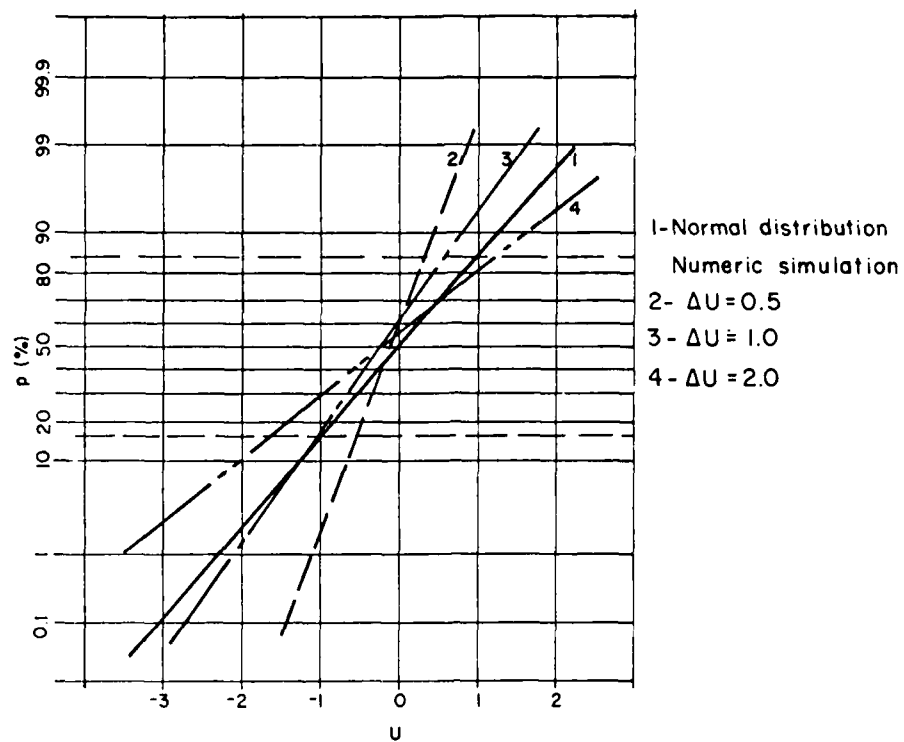


Fig. 1 - Normal distribution used to simulate the gaps

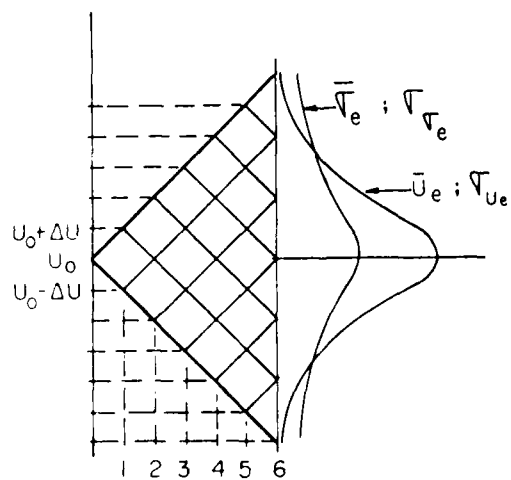


Fig. 2 - Tree of shots alternatives

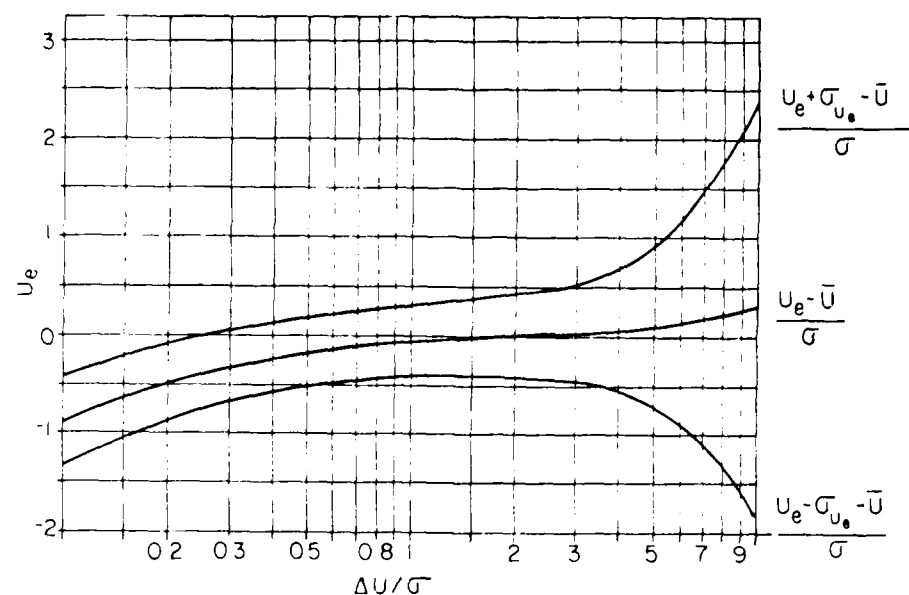


Fig. 3 - Influence of ΔU in \bar{U}_e estimation

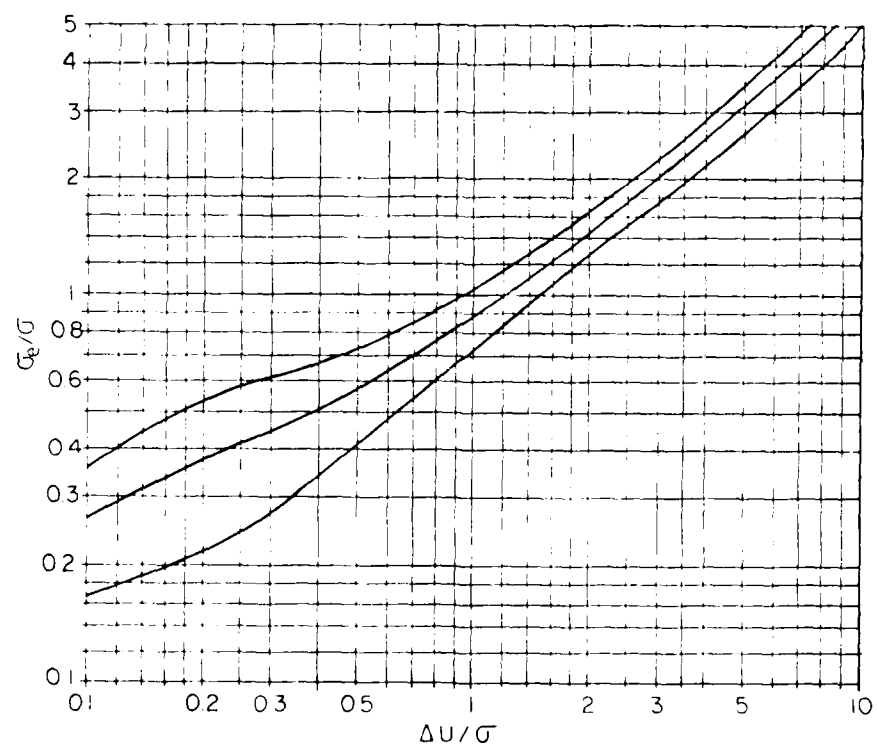


Fig. 4 - Influence of ΔU in σ_e estimation

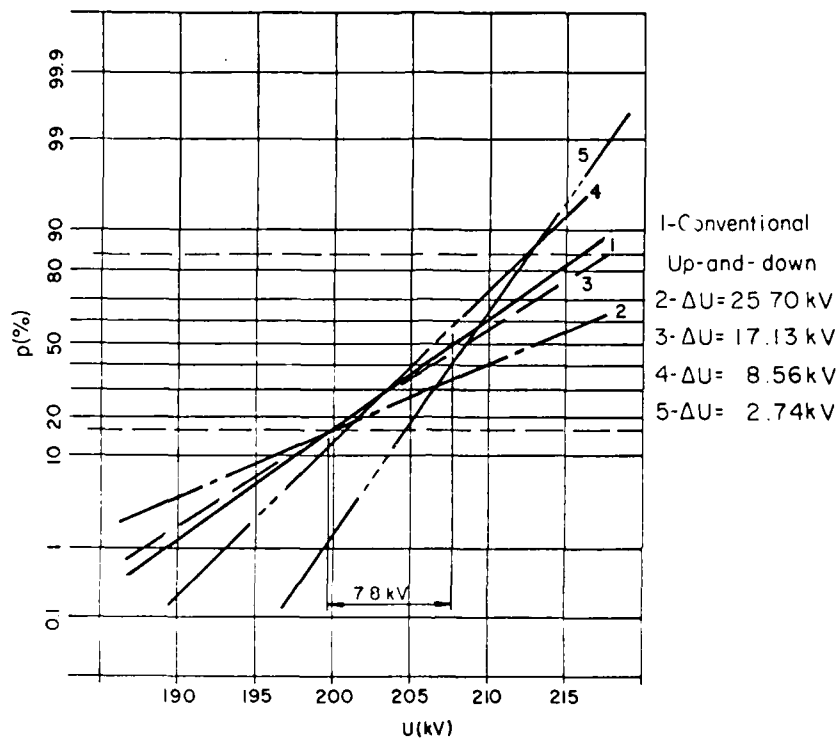


Fig. 5 - Comparison between the estimated distributions obtained by the conventional and up-and-down methods

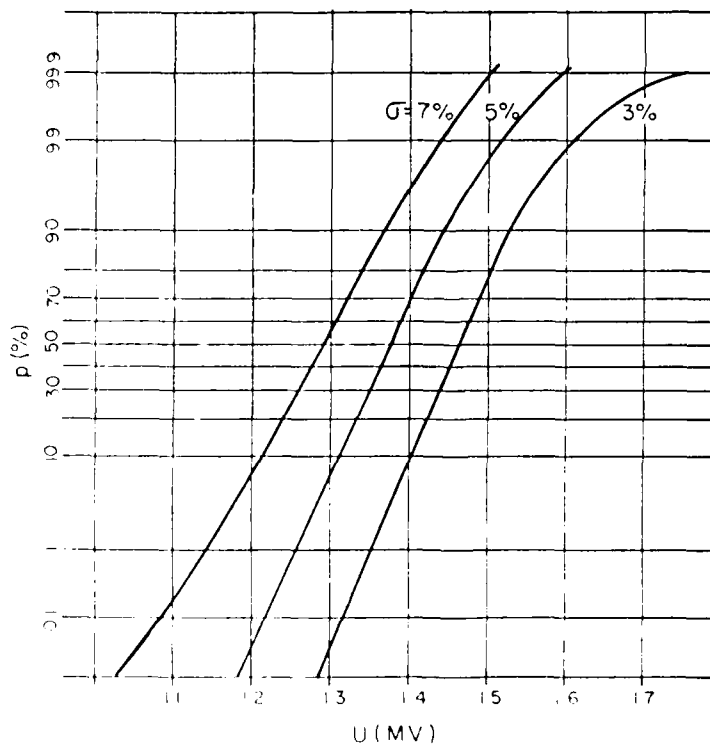


Fig. 6 - Probability distribution of flashover in a 5.5 m air-gap considering 200 towers in parallel

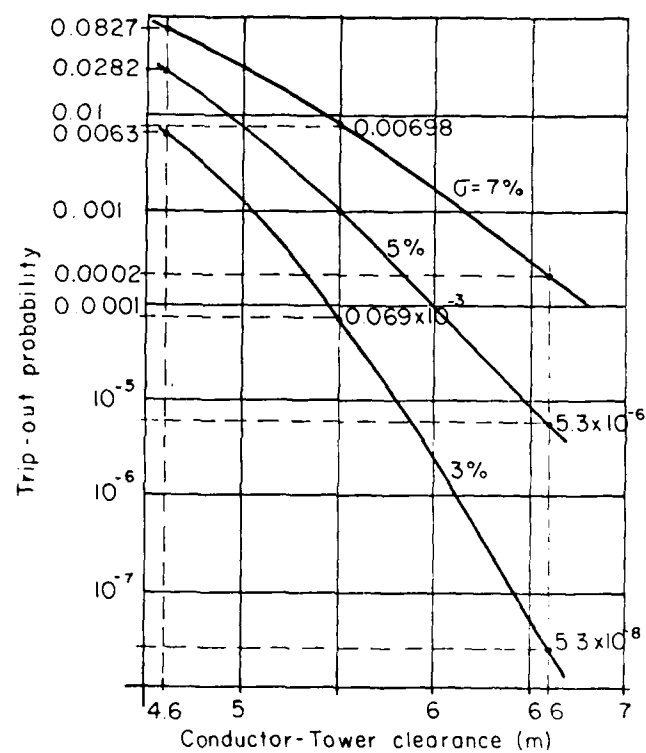


Fig. 7 - Trip-out probability as a function of gap-distance

COMPARISON OF METHODS FOR MEASURING THE CHARACTERISTIC IMPEDANCE OF TRANSMISSION LINES

L. O. Hoeft and J. Hofstra
1801 Randolph Road S.E.
The BDM Corporation, Albuquerque, New Mexico

ABSTRACT

A new method for determining the characteristic impedance of transmission lines has been developed. This method uses a computer-controlled impedance analyzer to measure the resistance, inductance, conductance, and capacitance of a cable as a function of frequency from 100 Hz to 13 MHz. It also calculates characteristic impedance, relative phase velocity, and attenuation. This method, called the impedance analyzer method, as well as the more traditional time domain reflectometry and propagation velocity (IEC 96-1) methods, were used to measure five cable samples, consisting of coaxial, two-wire and two-wire-shielded transmission lines with nominal characteristic impedance from 25 to 300 ohms. A comparison showed good agreement for characteristic impedances near 50 ohms. However, if the impedance is significantly different from 50 ohms, the uncertainties in the measurements are greater.

© 1984 IEEE

Printed with permission from 1984 IEEE National Electromagnetic Compatibility Symposium
April 24-26, San Antonio, Texas

INTRODUCTION

A KNOWLEDGE OF THE CHARACTERISTIC IMPEDANCE of transmission lines is a fundamental requirement for most lightning and EMC analysis. Because characteristic impedance is often not included in the wire specifications, the analyst or system designer frequently has difficulty obtaining this information. A good source of this information is laboratory measurements.

Two common methods for measuring characteristic impedance are time domain reflectometry and the propagation velocity method of IEC 96-1. Time domain reflectometry applies a fast risetime pulse to the transmission line and measures the voltage reflection coefficient, $\rho(t)$, which is defined as the instantaneous ratio of the reflected voltage wave, $V_2(t)$, to the incident voltage wave, $V_1(t)$, that is, the reflection coefficient $\rho(t) = V_2(t)/V_1(t)$.

The time domain reflectometer graphically displays the reflection coefficient, V_2/V_1 , on the instrument's CRT. In practice, the reflection coefficient is presented vertically on the CRT as a function of time with the middle of the screen equal to $\rho = 0$, the top of the screen equal to $\rho = 1$ and the bottom of the screen equal to $\rho = -1$. The horizontal axis of the display is directly proportional to distance or location on the line. The characteristic impedance Z_0 is calculated using the equation

$$Z_0 = Z_L ((1+\rho)/(1-\rho)), \quad (1)$$

where Z_L is the characteristic impedance of a reference line for which ρ is defined to be zero.

The International Electrotechnical Commission [1]* uses a method to determine characteristic impedance that is called the propagation or phase velocity method. This method assumes that the permittivity of the dielectric does not change with frequency. The characteristic impedance may be calculated from the velocity ratio (dimensionless) and the capacitance of the cable in (farads/meter):

$$Z_0 = \frac{1}{v_r C} \quad (2)$$

where Z_0 = characteristic impedance (ohms), v_r = velocity ratio (dimensionless), c = velocity of propagation in free space (m/s), C = capacitance (farads/m).

The specification states that the capacitance should be measured at the frequency where the velocity is measured, which is usually between 200 MHz and 400 MHz. It is usually measured, however, at much lower frequencies such as 1 MHz or 1 kHz because few capacitance bridges operate at hundreds of MHz. Fortunately, the capacitance of cables does not

change appreciably with frequency. The cable's length and resonant frequency are then used to obtain the propagation velocity ratio. In practice, the preceding equation is not used directly; instead the following method is employed.

A sample of a cable of suitable length is connected to a signal generator and a detector, the signal generator being previously calibrated for frequency. With the opposite end of the cable open or short-circuited, changing frequency will result in a periodic change of the input impedance since the impedance of the cable is a periodic function of the frequency. The frequency difference between two minima (or two maxima) depends on the electrical length of the cable, and therefore the phase velocity in the cable. The measured frequency difference, Δf , and the total capacitance, C , of the length of the test cable are used to calculate the characteristic impedance:

$$Z_0 = \frac{1}{2\Delta f C} \quad (3)$$

where Z_0 = characteristic impedance, in ohms, Δf = frequency difference, in hertz, C = capacitance of cable sample in farads.

In order to evaluate Δf with greater accuracy, the frequency difference $\Delta f'$ for n periods of variation is measured, and the single period frequency difference calculated, namely:

$$\Delta f = \frac{\Delta f'}{n} \quad (4)$$

Both of these methods measure the high frequency limit of the characteristic impedance.

With the advent of the microprocessor-controlled impedance analyzers such as the HP-4192A, another method for measuring characteristic impedance is now convenient; namely, the measurement of the resistance, inductance, conductance, and capacitance of the cable sample as a function of frequency, and the calculation of the characteristic impedance using the equation:

$$Z_0 = \sqrt{(R + j\omega L)/(G + j\omega C)} \quad (5)$$

The relative phase velocity and attenuation can also be calculated from the fundamental measurements.

DESCRIPTION OF IMPEDANCE ANALYZER METHOD

A schematic of the experimental arrangement is shown in Fig. 1. The entire measurement is controlled by the computer. After the computer requests and receives operator inputs on the cable sample and the measurement, such as length, name, units (feet or meters), calibration options, etc., it requests the impedance analyzer, via an IEEE-488 bus, to measure the circuit parameters. The auxiliary relay shorts the leads at the far end of the cable for

*Numbers in brackets designate references at end of paper.

impedance measurements, R and L, and opens them for admittance measurements, G and C. This process is repeated at five frequencies per decade for frequencies between 100 Hz and 13 MHz.

The computer then calculates the characteristic impedance, the velocity ratio, and the attenuation, prints all measured and calculated values in tabular form, and plots the data versus frequency on the computer terminal printer.

Two special test fixtures are used in making the measurements: the auxiliary relay/relay actuator and the impedance analyzer adapter. As previously mentioned, the auxiliary relay is used to open and short the leads at the far end of the cable. The relay is closed for series inductance and resistance measurements and open for parallel capacitance and conductance measurements. An alternate procedure has been used in which all of the capacitance and conductance measurements are made with the leads on the far end open. The leads are then soldered together and the resistance and inductance are measured at each of the frequencies.

A special adapter changes the four-wire measurement port on the HP-4192 impedance analyzer to a two-wire system. This fixture is mounted on the front of the HP-4192 impedance analyzer. The parasitic resistance, inductance, conductance, and capacitance of the test fixture is measured during calibration and subtracted from the measured values.

The characteristic impedance of the specimen is calculated at each frequency using

$$Z_0 = \left(\frac{(2\pi fL)^2 + R^2}{(2\pi fC)^2 + G^2} \right)^{1/4} \quad (6)$$

where Z_0 = characteristic impedance, f = frequency, L = inductance, R = resistance, C = capacitance, and G = conductance.

After the characteristic impedance is obtained, it is used to calculate the relative propagation velocity or propagation velocity ratio using the formula

$$v_r = \ell / Z_0 Cc, \quad (7)$$

where ℓ = the sample length in meters, $c = 3 \times 10^8$ m/sec, Z_0 = characteristic impedance, and C = capacitance.

The attenuation is calculated using the equation [2].

$$ATTN = \frac{8.686}{2} \left(\frac{R}{Z_0} + GZ_0 \right) \text{ dB/unit length.} \quad (8)$$

This equation was obtained from a standard handbook on cables [2]. The attenuation is presented in English or metric units depending on which units are specified for the circuit parameter measurements.

All of the final transmission line parameters are tabulated after the completion of the final frequency. These data are subsequently plotted and transferred to the thermal printer for a permanent record of the test run.

A TYPICAL MEASUREMENT

An example of the printed output from a typical cable characterization measurement is shown in Figs. 2 through 8. Fig. 2 shows that capacitance is relatively independent of frequency. The measured inductance (Fig. 3) shows some variation with frequency. Below 10 kHz, the variation is a measurement artifact due to inaccuracies in the measurement of inductance at low frequencies. At high frequencies, the inductance is expected to vary somewhat due to mutual repulsion effects. The conductance (Fig. 4) is approximately proportional to frequency as expected. At low frequencies, the resistance (Fig. 5) is the d.c. value, while for frequencies above 100 kHz, the resistance increases because of the skin effect. Fig. 6 shows the calculated relative phase velocity and Fig. 7 shows the calculated attenuation. Finally, the calculated characteristic impedance is shown in Fig. 8. It approaches the high frequency limit (where $Z_0 = (L/C)^{1/2}$) for frequencies above a few hundred kHz.

EFFECT OF LENGTH ON MEASUREMENT ACCURACY

The impedance analyzer method can be used on cables of any length; however, meaningful results can only be obtained if cables are within a certain range. If the cable is too short, the measurement is dominated by the parasitic R, L, C, and G associated with the test fixture. If the cable is too long, it no longer is electrically short at the upper end of the frequency range (13 MHz) and the measurement loses its meaning. The length of the test cable should be long compared to the end effects but still be electrically short. In order to demonstrate this effect, the cable characterization routine was used to measure the characteristic impedance of various lengths of RG-58U. This cable should have an impedance of 50 ohms. The results (Fig. 9) show that the characteristic impedance increases at high frequencies and varies erratically for cable lengths greater than 3m. This is attributed to the fact that the cable is no longer electrically short in the upper frequency range. Thus, if meaningful measurements are desired in the MHz range, the cable sample should be about 1m long.

COMPARISON OF CHARACTERISTIC IMPEDANCE MEASUREMENT METHODS

In order to establish the credibility of the characteristic impedance methods discussed in this report, and to compare their applicability, three independent techniques were used to measure the characteristic impedance of five

cable specimens. The samples measured are listed in Table 1. In general, the samples were selected to give a range of nominal characteristic impedance. All samples were cut to a 1-m length excluding hookup pigtails on each end which increased the overall length by about 1 1/2 inches. The resulting measurements are summarized in Table 2.

All three techniques for determining the characteristic impedance of a transmission line yielded acceptable results. For values close to 50 ohms, all results were in good agreement as shown in Table 2.

However, if the impedance is significantly different from 50 ohms, the uncertainties in the measurement become greater. With the TDR, variations will result in large swings of the characteristic impedance by the nature of the $\frac{1+\rho}{1-\rho}$ relationship when the reflection coefficient gets larger. This requires that the reflection coefficient be read to a higher precision to achieve the same accuracy. As an example, the change in impedance between a reflection coefficient of 0 and .1 is the difference between 50 and 61 ohms, or 11 ohms. A corresponding change in ρ between .7 and .8 produces impedances of 283 and 450 ohms, or a difference of 167 ohms. The impedance analyzer method and propagation method share similar problems at the higher impedances. The capacitance becomes very small and proportionally larger errors occur in these measurements. The propagation velocity method (IEC Standard 96-1) does have the advantage of using longer sample lengths which raises the capacitance and thus achieves a greater accuracy per unit length. This results from the fact that relatively low frequencies are used in the capacitance bridges, allowing the use of longer cables before interference from standing wave patterns produces anomalies in the measurement.

An advantage that the impedance analyzer has over the other techniques is that it requires little skill in its application and provides additional useful data (R, L, G, C, and v_r). There is a degree of calibration and technique required to implement each of the other techniques. The TDR needs to be calibrated before use, and reading the data off the display requires a certain degree of judgment and expertise. The same holds true for the capacitance bridge and network analyzer. The impedance analyzer method, however, is a "load and run" operation needing only a reasonable amount of care in sample preparation and length determination.

The impedance analyzer method also calculates the propagation velocity as a function of frequency. The accuracy of these data can be checked by comparison with published values for the dielectric constant for the known materials used in the samples. The expression relating dielectric constant to propagation velocity is

$$v_r = \frac{1}{\sqrt{\epsilon_r}} \quad (9)$$

where v_r = relative velocity, and ϵ_r = relative dielectric constant. Alternatively, $\epsilon_r = 1/v_r^2$.

Table 3 presents these data.

It can be seen that there is good agreement between the measured and listed values for the first three samples and the effective dielectric constant for polyolefin is reasonable. The dielectric constant of the TV antenna lead is less than unity, which is implausible. However, it is very close to air, which is the major component of the dielectric in this sample.

CONCLUSION

The newly developed impedance analyzer method for measuring characteristic impedance, along with time domain reflectometry and propagation velocity methods, were used to measure the characteristic impedance of five samples of widely varying impedance. All three methods of determining characteristic impedance yielded acceptable results. For values close to 50 ohms, all results were in good agreement; however, if the impedance is significantly different from 50 ohms, the uncertainties in the measurement become greater. The impedance analyzer method has the advantage of providing additional information on the frequency dependence of resistance, inductance, conductance, capacitance, attenuation, and relative phase velocity.

REFERENCES

1. "Radio-Frequency Cables - Part I: General Requirements and Measuring Methods," IEC Standard Publication 96-1A, 1976, Geneva: International Electrotechnical Commission, 1976.
2. C. A., Harper, ed., "Handbook of Wiring, Cabling, and Interconnecting for Electronics," New York: McGraw-Hill, Inc., 1972.

TABLE 1
DESCRIPTION OF TEST CABLES

1) RG 223/U	- 50 Ω double shielded silver plated coax with a solid silver plated center conductor. Polyethylene dielectric.
2) RG 174/U	- 50 Ω miniature coax with single braided shield and stranded center conductor. Polyethylene dielectric.
3) PVC Coax	- 25 Ω miniature coax with a single braided shield and stranded center conductor. Polyvinyl chloride dielectric.
4) Polyolefin Jacketed Twisted Shielded Pair	- Twisted pair measured in the differential mode with the shield floating. Polyolefin dielectric.
5) TV Antenna Lead in Cable	- Commercial 300 Ω twin lead antenna cable. Web dielectric unknown.

TABLE 3
COMPARISON OF PROPAGATION VELOCITY TO DIELECTRIC CONSTANT

Sample	v_p at 4 MHz	ϵ_r Measured	ϵ_r Listed
1) RG 223	.66	2.30	2.26
2) RG 174	.65	2.37	2.26
3) PVC Coax	.54	3.43	3.15
4) Polyolefin	.59	2.87	--
5) TV Antenna Lead	1.01	.98	--

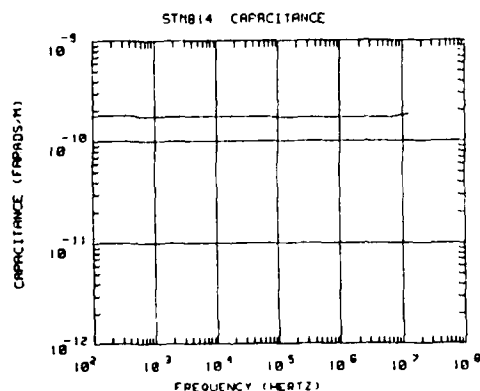


Fig. 2 - Capacitance versus frequency for a typical cable

TABLE 2
COMPARISON OF THE CHARACTERISTIC IMPEDANCE MEASURED BY THREE METHODS

SAMPLE	IMPEDANCE ANALYZER METHOD	TDR METHOD	PROPAGATION VELOCITY METHOD
1) RG 223/U	49.2 Ω	50.0 Ω	50.1 Ω
2) RG 174/U	53.1 Ω	55.3 Ω	50.7 Ω
3) PVC Coax	28.9 Ω	28.4 Ω	26.7 Ω
4) Polyolefin	54.2 Ω	50.0 Ω	52.5 Ω
5) TV Antenna Lead	385.0 Ω	283.3 Ω	445.6 Ω

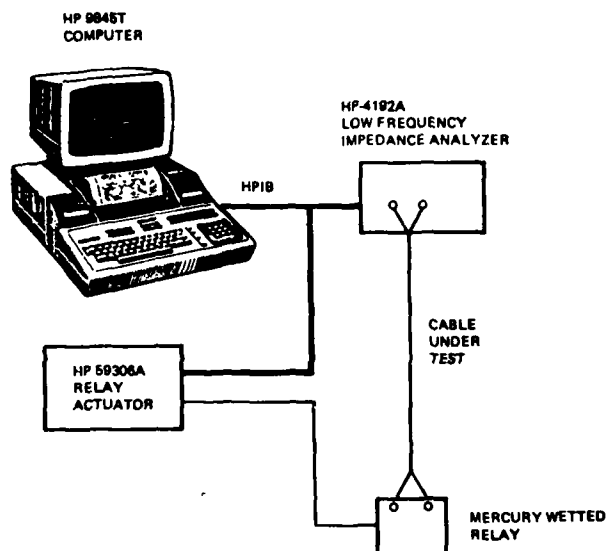


Fig. 1 - Schematic diagram of the instruments used to measure characteristic impedance by the impedance analyzer method

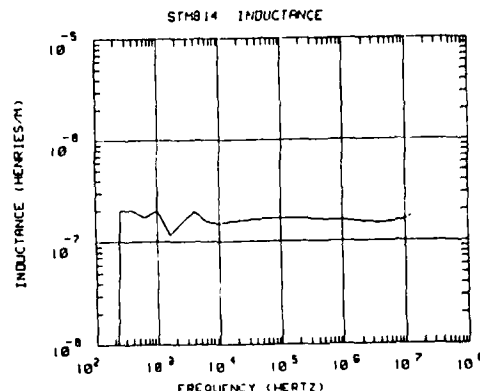


Fig. 3 - Inductance versus frequency for a typical cable

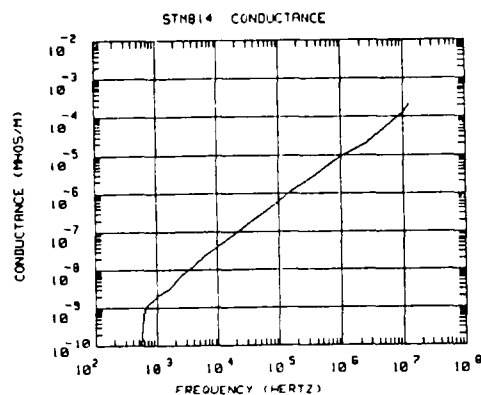


Fig. 4 - Conductance versus frequency for a typical cable

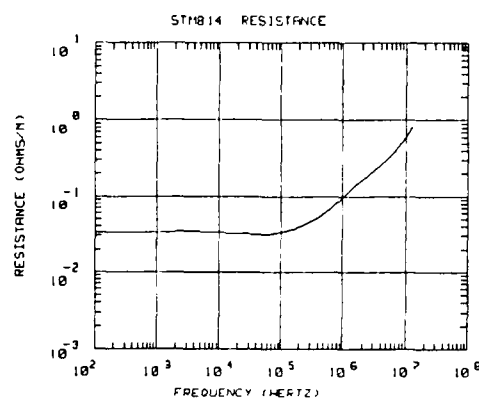


Fig. 5 - Resistance versus frequency for a typical cable

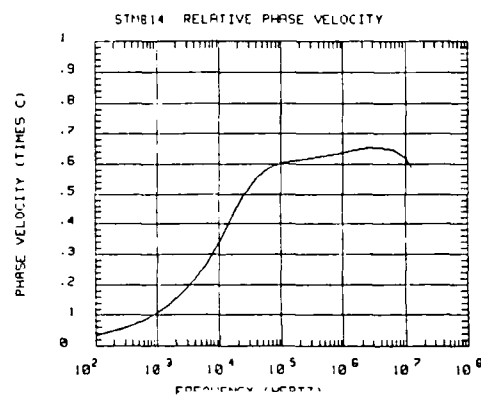


Fig. 6 - Relative phase velocity versus frequency for a typical cable

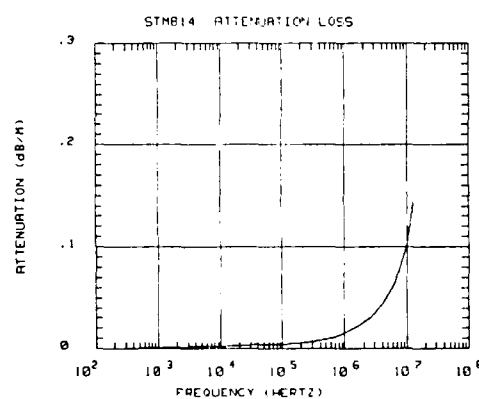


Fig. 7 - Attenuation versus frequency for a typical cable

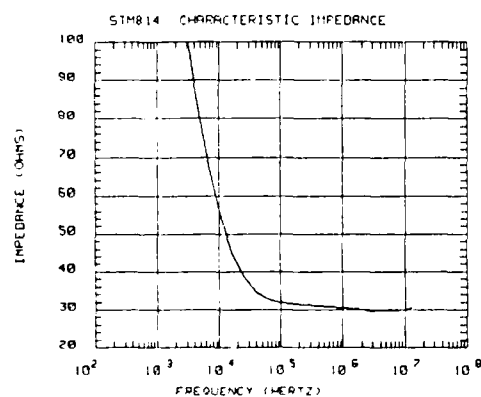


Fig. 8 - Characteristic impedance versus frequency for a typical cable

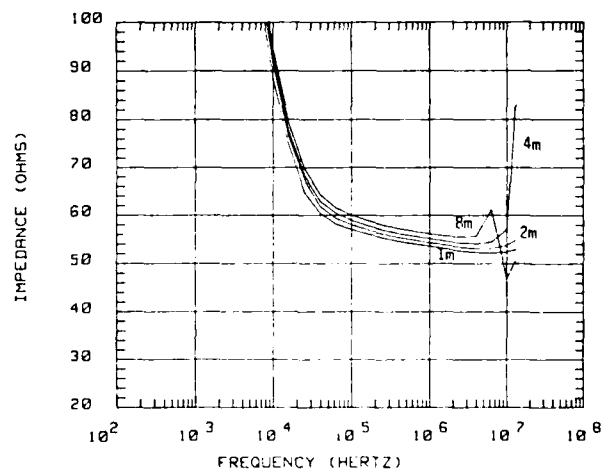


Fig. 9 - Effect of cable length on measured characteristic impedance

ANALYSIS OF THE EFFECTS OF CABLE PARAMETERS ON FIGURES
OF MERIT SUCH AS "EMP RESPONSE"

Lothar O. Hoeft, Alan Linder, and Joseph S. Hofstra
The BDM Corporation, Albuquerque, New Mexico
Dean Bernstein
ITT, Surprenant Division, Clinton, Massachusetts

ABSTRACT

An approach to specifying shielding against transients, such as lightning and EMP, is to compute a figure of merit that combines or integrates a number of factors that are important to shielding using appropriate weighting factors. One such figure of merit is the "EMP Response" that is being used to specify shielded cable. This figure of merit combines the frequency content of an EMP transient with the frequency dependence of the cable shield's transfer impedance. After integration in the frequency domain, a single number is obtained.

Cable designers normally design a cable to meet surface transfer impedance parameters, such as resistance and mutual inductance per unit length. How "EMP Response" depends on these cable parameters is not immediately obvious due to the number of variables involved in the calculation. This paper seeks to give the cable designer a sense of what is important.

A computational model, called the skin depth/long line model, was developed which allowed the "EMP Response" to be calculated for arbitrary cable shield parameters (resistance and mutual inductance). Plots of "EMP Response" versus either shield resistance or mutual inductance showed similar behavior. For resistances greater than 10 milliohms/m and mutual inductances greater than 600 to 700 picohenries/m, the "EMP Response" is always less than 60 dB and would not meet the specification. For mutual inductances below 100 picohenries/m, the "EMP Response" is relatively independent of mutual inductance. Similarly, for resistances less than 3 to 5 milliohms/m, the "EMP Response" is relatively independent of shield resistance. Thus, the cable designer should attempt to design the cable shield with resistances less than 5 milliohms/m and mutual inductances of less than 200 or 300 picohenries/m. If these conditions are met, production tolerances would not be critical; however, if the resistance or mutual inductance is outside of this range, meeting a 60 dB "EMP Response" specification is much more uncertain.

INTRODUCTION

SURFACE TRANSFER IMPEDANCE is being used increasingly in cable shielding specifications. Some specifications [1]* also include a parameter called "EMP Response." This is defined as:

EMP Response =

$$-185 - 10 \log \int_0^{4 \times 10^8} \frac{Z_t(f)^2 df}{(\alpha^2 + f^2)(\beta^2 + f^2)} \quad (\text{dB}) \quad (1)$$

where $Z_t(f)$ = surface transfer impedance at frequency f (Ω/m), $\alpha = 2.39 \times 10^5$, $\beta = 4.12 \times 10^7$, f = frequency (Hz).

The objective of this program was to show how cable parameters, such as resistance and mutual inductance, affect the "EMP Response" and to gain an insight into the question of how sensitive the "EMP Response" calculation is to manufacturing tolerances.

APPROACH

The analysis was performed in two phases. First, a series of models of increasing complexity were developed to describe the transfer impedance. These models were used to calculate the "EMP Response" in order to determine what frequency ranges were important, and how sensitive the "EMP Response" calculation was to model complexity. This was accomplished by calculating the "EMP Response" using a variety of models and plotting the results of each intermediate step (transfer impedance, integrand, integral, and "EMP Response"). Second, the models were used to determine how the "EMP Response" varies with transfer impedance parameters.

RESULTS

MODELS - Five surface transfer impedance models were used during the Phase I analysis. These were as follows:

The R_0 or Resistance Only Model - This model was the simplest model possible and assumed that the cable shield acted like a simple resistor, and did not exhibit skin depth, high frequency leakage, or long line effects.

The Simple Cable Model - The cable shield was modeled as a resistance and mutual inductance, $Z_T = R_0 + j\omega M$, where R is the d.c. resistance, M is the mutual inductance, $\omega = 2\pi f$ and f is frequency. This model neglects the skin and long line effects, but is frequently used to describe cable shields.

The Skin Effect Model - This model considers the cable shield to be a cylindrical shield with high frequency coupling. The skin effect, i.e., the lack of current diffusion, is accurately modeled. This is a good representation of the transfer impedance of braided

cable. It does not model the long line effects which become evident in the voltage response measurements for frequencies where the sample is a half-wavelength long or longer. Surface transfer impedance, as defined by MIL-C-85485, includes these long line effects. Mathematically, this model describes the surface transfer impedance by the equation:

$$Z_T = \frac{R(1+j)T_s/\delta}{\sinh((1+j)T_s/\delta)} + j\omega M \quad (2)$$

where: $R = 1/(\pi\sigma DT_s)$

$$\delta = (1/\pi f\sigma\mu)^{1/2}$$

and σ = cable shield conductance
 $= 5.8 \times 10^7$ (ohms M)⁻¹
 μ = cable shield permeability = $4\pi \times 10^{-7}$
 D = cable shield diameter = $1.234 \times 10^{-2}\text{m}$
 T_s = cable shield thickness = $1.246 \times 10^{-4}\text{m}$

Skin Depth/Long Line Model - The skin depth model was modified to account for long line effects, and thus corresponds more closely to the measured voltage response which MIL-C-85458 calls transfer impedance. This model consists of the skin effect model, #3, multiplied by a long line factor. Mathematically, this factor is given by:

$$\text{Long Line Factor} = \frac{\sin \theta}{\theta}$$

where: $\theta = \pi f l (\sqrt{\epsilon_r} + 1)/c$

and l = length of cable = 1m
 ϵ_r = relative dielectric constant of cable insulation = 3
 c = speed of light = 3×10^8 m/s

Measured Data - Actual measured transfer impedance data for a real cable sample was also used to calculate the "EMP Response."

COMPARISON OF MODELS

The "EMP Response" was calculated using each of the mathematical models, assuming cable parameters similar to the one for which measured data were available. These parameters were d.c. resistance, 3.57×10^{-3} ohms/m; mutual inductance, 2.5×10^{-11} Henries/m; shield diameter, $1.234 \times 10^{-2}\text{m}$; shield thickness, $1.246 \times 10^{-4}\text{m}$. For each of the "EMP Response" calculations, intermediate results were plotted at four stages in the computation. These four plots are shown in Figs. 1 through 4 for the measured data computation. The transfer impedance is plotted in Fig. 1. Next, the integrand (the quantity inside the integral) is plotted in Fig. 2. The integral is calculated, and the result is shown in Fig. 3. The integrand is integrated over frequency. The quantity labeled "Integral" is the definite integral up to the frequency shown

*Number in brackets designates reference at end of paper.

on the X axis. Finally, the "EMP Response" is plotted in a similar manner in Fig. 4.

Note that all the quantities in the integrand of the "EMP Response" are real numbers and are squared. Therefore, the integrand is always a positive and monotonically increasing function. Furthermore, the integral is a number less than 1; consequently, the logarithm is negative. Since the "EMP Response" is proportional to the negative logarithm of the integrand, the "EMP Response" calculation will start as a very large positive number at low frequencies and get progressively smaller as the contributions at higher frequencies are added. If the integral or the "EMP Response" is independent of frequency in a frequency range, then the transfer impedance is relatively unimportant in that frequency range. This frequency dependence of the "EMP Response" will be used to evaluate the importance of the mutual inductance for frequencies above 1 MHz.

Figs. 5 and 6 show the integrand and "EMP Response" calculated using the resistance only model. The transfer impedance is frequency independent; therefore, the integrand plot shows the frequency dependence of the denominator, $1/(\alpha^2 + f^2)(\beta^2 + f^2)$ scaled to an appropriate value by the resistance. At low frequencies the frequency is less than either α or β , and the integrand is equal to $R^2/\alpha^2\beta^2$. When the frequency exceeds α (239 kHz), the integrand decreases with frequency at the rate of 40 dB/decade or a factor of 100 per decade. When the frequency exceeds β (41.2 MHz), the integrand decreases at $1/f^4$ or 80 dB per decade (a factor of 10,000 per decade). Therefore, the high frequencies are deemphasized in calculating the "EMP Response." In fact, examination of the "EMP Response" shows little change above a few MHz, confirming that the EMP response calculation deemphasizes the high frequencies. Only the first break frequency (239 kHz) can be seen in the plots of the integral and EMP response for the simple resistance model.

Figs. 7, 8, and 9 show the "EMP Response" calculated using the simple cable model. This model used a mutual inductance of 2.5×10^{-11} H/m, corresponding to a high quality cable. This can be seen in the transfer impedance plot, where the break frequency is about 20 MHz. The only other change from the simplest case is that the plot of the integrand (Fig. 8) does not change slope significantly at 40 MHz, since the increase of the transfer impedance cancels out the effect of the β break frequency in the denominator. The final "EMP Response" (Fig. 9) is 68.015 dB as compared to 68.091 for the simple resistor model, confirming the earlier observation that the "EMP Response" deemphasizes the high frequency.

Figs. 10 and 11 show the "EMP Response" calculated using the skin effect model. The transfer impedance (Fig. 10) of this model differs from the previous one in that it now has a significant dip in the 1 to 10 MHz range. This dip makes a significant change in the

integrand, but only slightly changes the "EMP Response" (Fig. 11), increasing it (making it better) from 68.015 for the simple cable model to 68.797 for the skin depth model.

Figs. 12, 13, and 14 show the "EMP Response" calculated using the skin depth, long line model. The long line effect limits the response at high frequencies. However, the integrand (Fig. 13) is already 6 orders of magnitude down when the long line effects become evident; consequently, it does not make a significant difference. The "EMP Response" (Fig. 4) is 68.838 dB, which is essentially the same as for the skin depth model.

The "EMP Response" calculated using measured transfer impedance data from the real cable was shown in Figs. 1 through 4. Comparison of these figures with Figs. 12, 13, and 14 shows that the skin depth/long line model is a reasonable approximation of the performance expected from a real cable. If anything, the skin depth/long line model is a little conservative since its "EMP Response" was 68.838 dB compared to 69.338 dB calculated using real data. No great importance should be attached to the difference in these two numbers, since the accuracy of this analysis is probably no better than 1 dB.

The results of the model comparison are summarized in Table 1. These results show that the skin depth/long line model is a good approximation of real data and can be used to perform a more extensive parametric study of the effect of transfer impedance parameters on the "EMP Response." By looking only at the data shown in Table 1, one could conclude that only the cable shield resistance was important for calculating "EMP Response." This would be an erroneous conclusion, as will be seen later. The model comparison was performed using a high performance cable as the example. The "EMP Response" of cables with significantly more leakage at high frequencies can be significantly affected by the cable shield's mutual inductance.

EFFECT OF CABLE PARAMETERS ON "EMP RESPONSE"

The effect of cable parameters on the "EMP Response" was investigated by calculating the "EMP Response" using the skin effect/long line model for resistances between 1 and 10 milliohms/m and mutual inductances between 25 and 750 picohenries/m. The transfer impedance and the "EMP Response" are summarized in Table 2 and Figs. 15 and 16. Included in Figs. 15 and 16 are the "EMP Response" calculated using the transfer impedance measured on actual cables.

Examination of Figs. 15 and 16 shows that the model calculation accurately predicts (within 1 dB) the performance of the three measured cables. Thus, the model is credible.

Fig. 15 shows the "EMP Response" plotted against mutual inductance for several values of resistance. All of the calculations fall below the heavy solid line, which decreases at the rate of 20 dB per decade of mutual inductance.

This means that there is no way of making a cable with a high or good "EMP Response" if the mutual inductance is high. If the resistance is greater than 10 milliohms/m, the "EMP Response" will always be less than 60 dB. Consequently, the cable would not pass the specification. The shield resistance depends primarily on the number of strands in the braid, which in turn depends on the cable diameter. Cables less than 3/8 or 1/4 inch will have resistances greater than 10 milliohms/m. Therefore, there is no way for small cables to meet the specification. If the mutual inductance is less than 100 picohenries/m, the "EMP Response" is independent of mutual inductance, but primarily dependent on resistance. Thus, if the cable's resistance (an easily predicted quantity) is less than 3 to 5 milliohms/m, the braid construction would not have to be truly optimized in order to meet the specification.

Fig. 16 shows the "EMP Response" plotted as a function of resistance. Again, all the data fall below the heavy solid line, which decreases at 20 dB per decade of resistance. This means there is no way of making a cable that has high resistance so that it can meet the specification. Similarly, all cables that have mutual inductances greater than 600 to 700 picohenries/m will have "EMP Responses" of less than 60 dB and, therefore, will not meet the specification. For shield resistances of less than a few milliohms/m, the "EMP Response" is relatively independent of resistance, and the braid design is less critical.

Examining the "EMP Response" plot can show when the high frequency performance of the cable is making a significant contribution to the "EMP Response." For the cable shown in Figs. 1 through 4, the high frequency performance was so good that the "EMP Response" did not change above 1 MHz. Figs. 17 and 18 show the transfer impedance and "EMP Response" for a cable that has relatively poor high frequency performance. A decrease of the "EMP Response" above 1 MHz is clearly seen, indicating that the final "EMP Response" of 58.42 is determined primarily by the poor high frequency performance.

Examination of the parametric "EMP Response" calculations described previously shows that the high frequency contribution is insignificant if:

$$\frac{M}{R} < 2.5 \times 10^{-10} \quad (3)$$

This does not mean the cable would necessarily pass the 60 dB specification, since either the resistance may still be too high or both the resistance and mutual inductance may be too high. If the above criteria are met, one knows that in order to improve the "EMP Response" (i.e., raise it), he has to decrease the resistance.

In order to use this criterion, the mutual inductance must be measured. A simple way of obtaining this from the transfer impedance is to

find a portion of the plot at high frequencies where the transfer impedance is increasing in a straight line at 20 dB per decade. This is usually between 10 and 20 MHz. The transfer impedance and frequency is read, and the mutual inductance is obtained by the equation:

$$M = Z_T / 2\pi f \quad (4)$$

This concept can be extended further by using the above equation to restate the high frequency criterion. This becomes: "If the transfer impedance at 10 MHz exceeds 1.57 times the d.c. resistance, the "EMP Response" will be determined primarily by the high frequency performance. If the transfer impedance at 10 MHz is less than 1.57 times the d.c. resistance, the high frequency performance will have an insignificant effect on the "EMP Response."

SUMMARY

A conceptual model, called the skin depth/long line model, was developed which allowed the "EMP Response" to be calculated for arbitrary cable shield parameters (resistance and mutual inductance). Plots of "EMP Response" versus either shield resistance or mutual inductance showed similar behavior. For resistances greater than 10 milliohms/m and mutual inductances greater than 600 to 700 picohenries/m, the "EMP Response" is always less than 60 dB and would not meet the specification. For mutual inductances below 100 picohenries/m, the "EMP Response" is relatively independent of mutual inductance. Similarly, for resistances less than 3 to 5 milliohms/m, the "EMP Response" is relatively independent of shield resistance. Thus, the cable designer should attempt to design the cable shield with resistances less than 5 milliohms/m and mutual inductance of less than 200 or 300 picohenries/m. If these conditions are met, production tolerances could be relaxed. If the resistance or mutual inductance is outside of this range, meeting a 60 dB "EMP Response" specification is much more uncertain.

REFERENCE

1. "Cable, Electric, Special Purpose, Lightweight, General Specification for," PMS 400-881, September 22, 1981.

Table 1
Comparison of Cable Shield Models

Model	EMP Response
Resistance Only	68.091 dB
Simple Cable ($R + j\omega M$)	68.015 dB
Skin Effect	68.797 dB
Skin Depth/Long Line	68.838 dB
Measured Data (ITT-45)	69.338 dB

Table 2
EMP Response in dB as a Function of Cable
Shield Resistance and Mutual Inductance
Using Skin Depth/Long Line Model

Resistance (Milliohms/m)	Mutual Inductance (picohenries/m)			
	25	75	250	750
10	59.88	59.88	59.52	56.56
3.57	68.84	68.60	65.84	58.41
1	79.52	76.56	68.04	58.52

ITT-45 ACTUAL TEST DATA

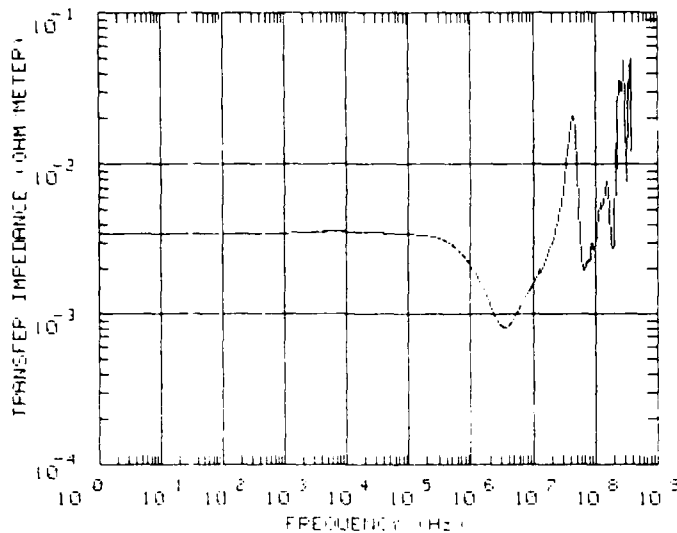


Fig. 1 - Measured transfer impedance of a sample cable

ITT-45 ACTUAL TEST DATA

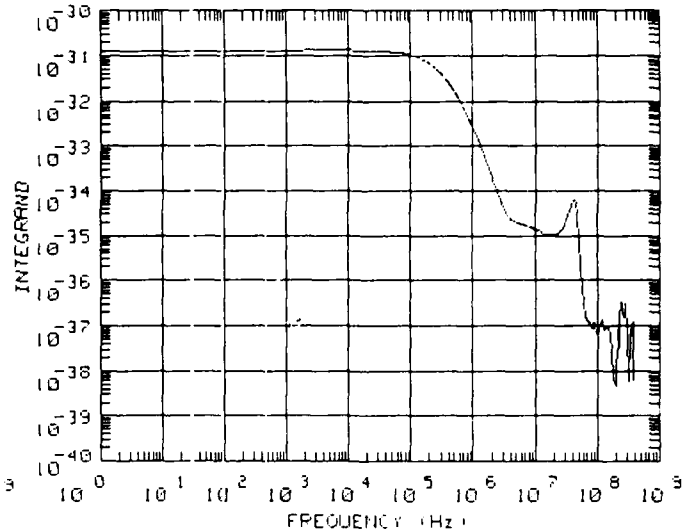


Fig. 2 - Integrand of the "EMP Response" for a sample cable using measured transfer impedance data

ITT-45 ACTUAL TEST DATA

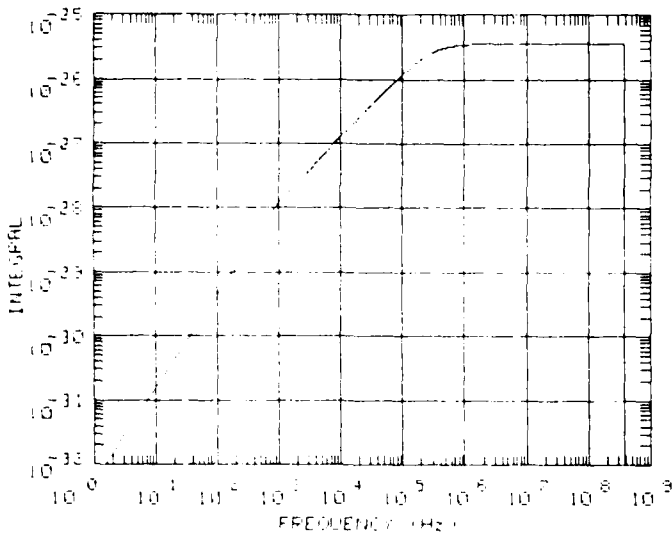


Fig. 3 - Integral of the "EMP Response" for a sample cable using measured transfer impedance data

ITT-45 ACTUAL TEST DATA

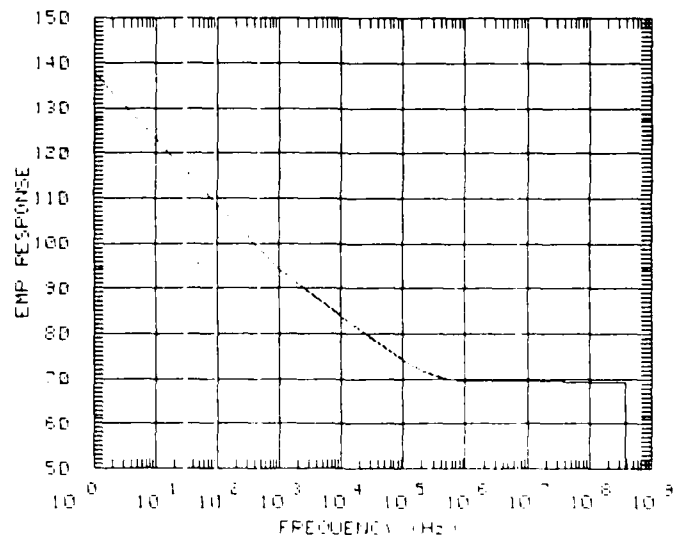


Fig. 4 - "EMP Response" for a sample cable using measured transfer impedance data

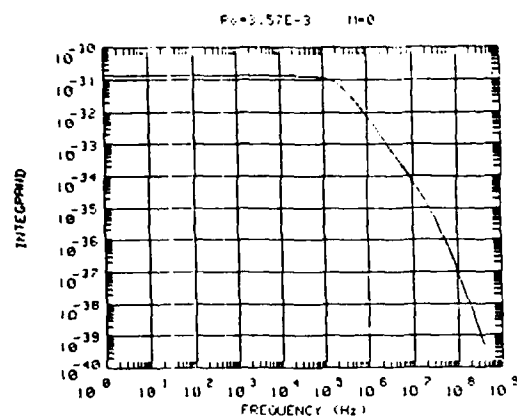


Fig. 5 - Integrand of the "EMP Response" using the resistance only model

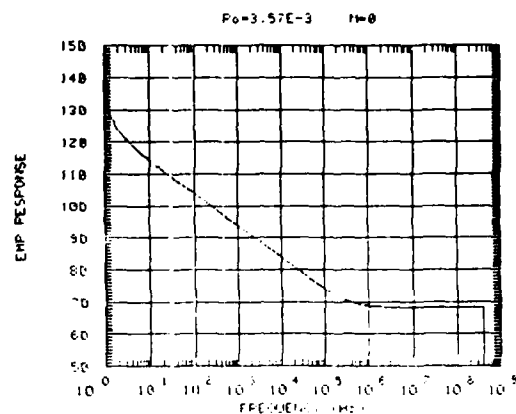


Fig. 6 - "EMP Response" calculated using the resistance only model

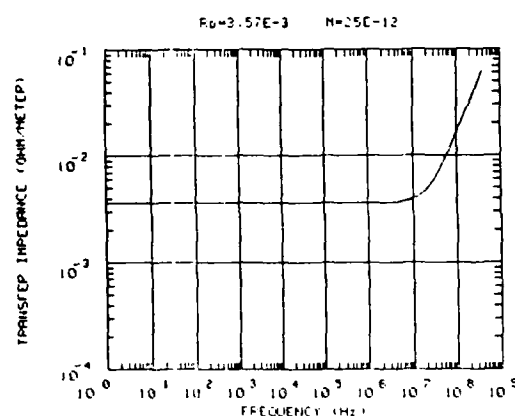


Fig. 7 - Transfer impedance of the sample cable using the sample cable model

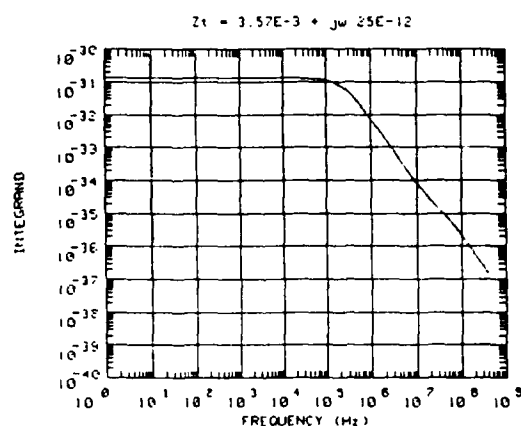


Fig. 8 - Integrand of the "EMP Response" using the simple cable model

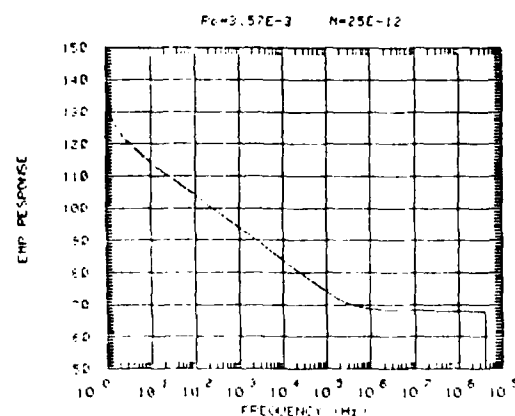


Fig. 9 - "EMP Response" calculated using the simple cable model

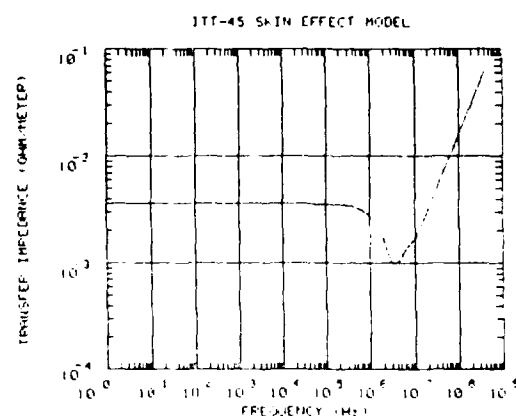


Fig. 10 - Transfer impedance for the skin effect model

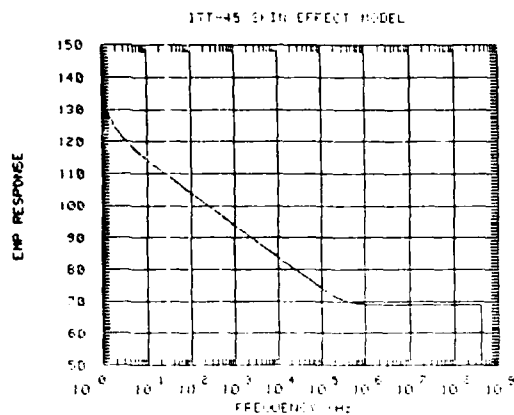


Fig. 11 - "EMP Response" calculated using the skin depth model

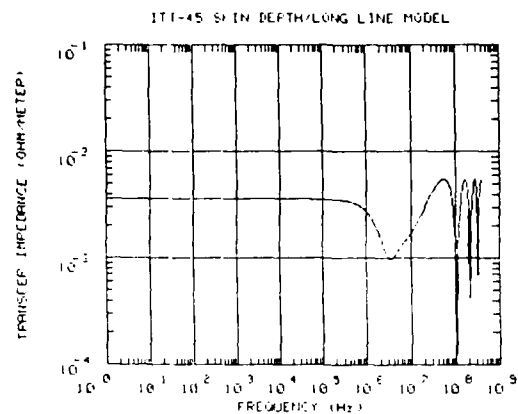


Fig. 12 - Transfer impedance for the skin depth long lines model

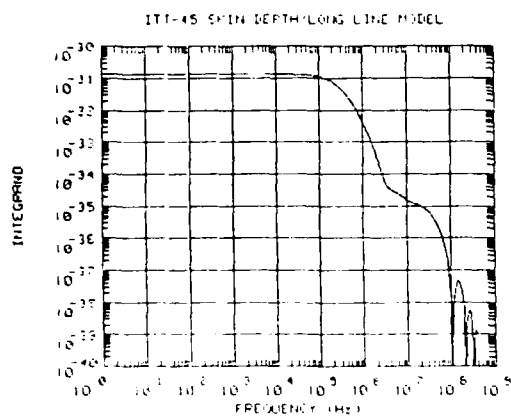


Fig. 13 - Integrand for the "EMP Response" using the skin depth long line

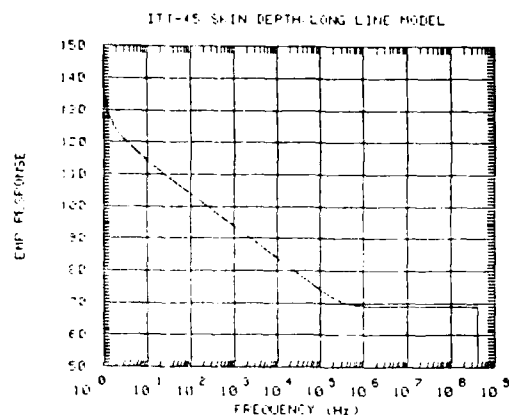


Fig. 14 - "EMP Response" calculated using the skin depth long line model

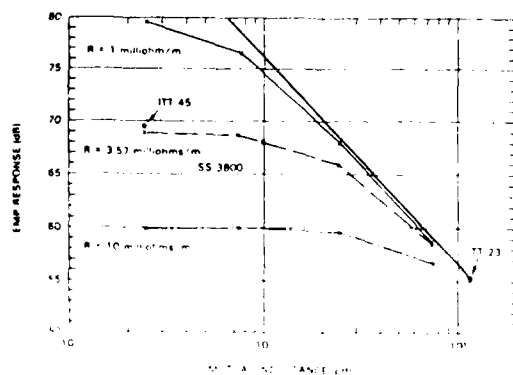


Fig. 15 - "EMP Response" as a function of mutual inductance

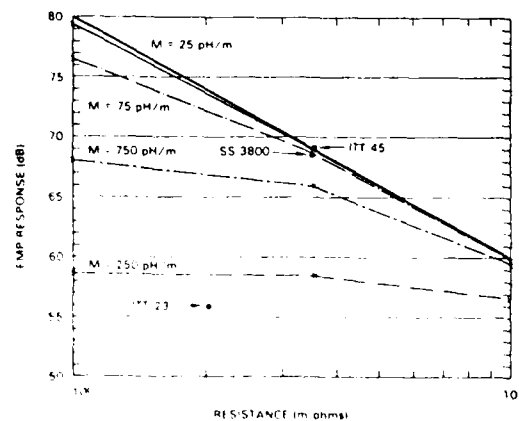


Fig. 16 - "EMP Response" as a function of resistance

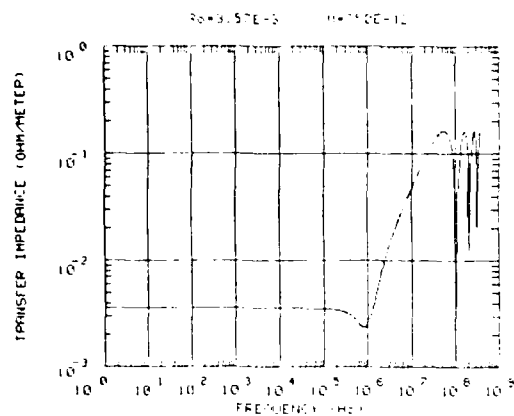


Fig. 17 - Transfer impedance of a cable that has poor high frequency

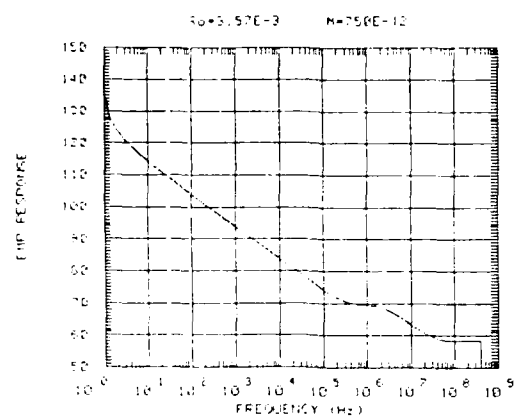


Fig. 18 - "EMP Response" for a cable that has poor high frequency performance

MEASURED TRANSFER IMPEDANCE OF METALLIC AND
NON-METALLIC CONDUITS COVERED WITH TINNED COPPER
AND SnCuFe BRAIDS

Lothar O. Hoeft and Joseph S. Hofstra
The BDM Corporation, Albuquerque, New Mexico
John E. Merrell
Glenair, Inc., Glendale, California

ABSTRACT

The surface transfer impedance of eight flexible conduits was measured over the frequency range of 1 kHz to 100 MHz, using a 1.2-meter-long quadraxial test fixture and two network analyzers controlled by a computer using the IEEE-488 bus. The samples included both brass and plastic conduits covered with various combinations of bronze, tinned copper, and SnCuFe braids. These measurements showed that the tinned copper braid significantly improved the performance of the basic brass conduit covered with bronze braid. Adding a second layer of braid further improved the performance, especially above 100 kHz. Using SnCuFe braid as the intermediate layer resulted in improved performance between 10 kHz and 200 kHz.

Similar results were obtained for plastic conduits covered with tinned copper and SnCuFe braids except that above 1 MHz these samples showed the typical mutual inductance coupling expected of braided cable rather than the very low transfer impedance, indicative of a solid shield typical of a flexible brass conduit.

© 1984 IEEE

Printed with permission from 1984 IEEE National Electromagnetic Compatibility Symposium
April 24-26, San Antonio, Texas

INTRODUCTION

FLEXIBLE CONDUIT ASSEMBLIES are being used increasingly as electromagnetic barriers to prevent coupling between circuits and the external world. They are useful for preventing external threats such as lightning, EMP, and external environments from affecting the internal circuits, as well as keeping the internal circuits from radiating as in TEMPEST and some EMC applications. Surface transfer impedance is the intrinsic property that defines the shielding properties of these flexible conduit assemblies. Unfortunately, measured transfer impedance data on these products are not plentiful, especially for some combinations of overbraid. This paper describes a program that sought to provide such data and will describe the test samples, the system used to make the measurements, system calibration, and will also present the results of the measurements.

TEST SAMPLES DESCRIPTION

The test samples were of two general types: four samples used a brass conduit/bronze braid as their innermost shielding layer, and four samples consisted of various braids attached to Kynar convoluted tubing. All conduit assemblies were 49 inches long, with a 1-inch inside diameter. They all had brass end-fitting terminations which allowed the test sample to be attached to the test fixture. The sense wire was an inner core made up of 19 conductors (#12 AWG) with suitable fillers to center the conductors with the conduit. The diameter and inner core were chosen to be representative of applications where these conduit systems could be used.

All flexible metal-core conduit assemblies had the following identical construction features and characteristics:

- 1) Brass inner core
- 2) Bronze braided shield
- 3) Standard end-fitting terminations (brass)
- 4) Inner core of 19 conductors (#12 AWG), with suitable fillers to center the conductors within the conduit.

The test samples had additional braided shields as indicated below, starting with the bronze braid:

<u>Test Sample Number</u>	<u>Description</u>
1	a) No additional braid
2	a) Tinned copper braid
3	a) SnCuFe braid b) Tinned copper braid
4	a) Tinned copper braid b) Tinned copper braid

All of the flexible plastic tubing conduit assemblies had the following construction features and characteristics:

- 1) Kynar convoluted tubing (thermally stabilized) 1.0 inch ID.
- 2) Inner core of 19 conductors (#12 AWG), with suitable fillers to center conductors within conduit.
- 3) Standard end-fitting terminations (brass).

The test samples had shields applied as noted below:

<u>Test Sample Number</u>	<u>Description</u>
11	a) External tinned copper braid
12	a) Copper foil b) External tinned copper braid
13	a) Tinned copper braid b) Tinned copper braid
14	a) Tinned copper braid b) SnCuFe braid

TEST METHODOLOGY

DESCRIPTION OF THE TEST FIXTURE AND INSTRUMENTATION - A 1.2-meter quadraxial test fixture was used to drive a uniform current along the sheath of the sample cable being tested. The advantage of this design over coaxial or triaxial arrangements, is its suitability for broad-band measurements, immunity to outside influences, and the availability of a convenient reference ground plane for the instrumentation. The quadraxial fixture was constructed using an inner and outer trough with the test sample inside the inner trough. This is electrically equivalent to three nested transmission lines. The quadraxial fixture dimensions would ideally be determined by providing an inner and outer trough (transmission line) impedance of 100 ohms each, since this maximizes power flow into and out of the 50-ohm instrumentation ports. However, a 100-ohm outer trough impedance would require a trough 3 feet wide and at 100 MHz, modes other than TEM would propagate. The outer trough dimension was chosen to be 8 inches on a side; therefore, the perimeter corresponds to a half wavelength at 185 MHz, which is above the highest frequency of interest. The impedance of the inner trough was 73.87 ohms and the outer was 72.5 ohms.

Fig. 1 shows the construction details of the measurement and termination ends of the fixture. The drive voltage was fed to the inner trough, and a 5000-ohm pickoff resistor was used for the reference port measurement. The cable shield current was directly proportional to the inner trough voltage. The fixture output was the voltage from the center conductor or sense wire of the test sample.

The test cable terminations were screwed into the brass adapter sections of the test fixture. All of the conductors were connected together to form the sense wire. These wires, in conjunction with the cable shield, formed a transmission line with an impedance of about 15 ohms. The transmission line was terminated in a 15-ohm resistor at the far end and an L-pad network at the near end, which matched the sample to the 50-ohm measurement system. The brass adaptor section was clamped to the outer trough wall at the measurement end and to the inner trough through the trough termination resistor at the termination end.

The IEEE 488 interface bus forms the nucleus for the test instrumentation as illustrated in Fig. 2.

The HP-461A amplifier was used for the low frequency portion of the test, and the IFI 5300 power amplifier was used for the high frequency part. An HP-4192A impedance analyzer was used below 13 MHz, and an HP-8505A network analyzer was used between 0.5 and 100 MHz.

MEASUREMENT PROCEDURES - The measurement sequence begins with sample preparation. All of the core wires were connected together and served as the sense wire. The brass adapters were installed on each end of the test specimen, and the assembly was placed in the test fixture. An impedance check was performed on the output port to ensure that no resistors had been broken or shorted during the installation. The inner trough termination resistance was adjusted to match its characteristic impedance calculated from the diameter of the sample. The signal source of the analyzer was connected to the fixture drive point, and the test fixture's output and reference lines were connected to the analyzer's test and reference channels, respectively. The computer then acquired the data by means of the IEEE 488 bus and reduced the data by calculating transfer impedance and shielding effectiveness.

CALIBRATION - At the beginning of this test series, the entire set up was calibrated using a solid brass pipe with a 5/8-inch outer diameter and a 0.065-inch wall thickness as a test sample. This measurement is shown in Fig. 3. The d.c. resistance of this sample was 1 milli-ohm. The measured transfer impedance matches the prediction and the d.c. resistance to well within experimental accuracy. Above 600 kHz, the noise level of the measurement system can be seen. The higher noise level of the low frequency impedance analyzer is evident in the frequency range where measurements are made with both high and low frequency network analyzers.

RESULTS

TRANSFER IMPEDANCE MEASUREMENTS - The surface transfer impedance of each of the test samples was measured using the instrumentation and procedures described previously.

Figs. 4 through 7 present the measured transfer impedance of several samples with

similar or contrasting construction features. These samples are plotted on the same graph for comparison. Fig. 4 shows the effects of adding layers of tinned copper braid. SnCuFe versus tinned copper braid is compared in Fig. 5. Figs. 6 and 7 show the results of measurements on the flexible plastic-core conduit assemblies. Fig. 6 shows the effects of adding a copper foil, and Fig. 7 compares the effects of using SnCuFe as the outer braid.

A comparison of the measured transfer impedance of samples that used a brass core (Figs. 4 and 5) shows that the measurements are very consistent below 0.5 or 1 MHz, but display some variation between the measurements made with low and high frequency network analyzers. The discrepancy between the low and high frequency network analyzers is due to the fact that the shields are so good that the analyzers are working near their noise limit. The noise level and accuracy of the HP-4192A is considerably worse than that of the HP-8505A under these conditions. Therefore, the data from the high frequency network analyzer should be used if there is any question.

D.C. RESISTANCE MEASUREMENTS - The d.c. resistance of each of the conduit systems was measured by passing 5, 10, and 20 amps from one end-fitting termination to the other and measuring the voltage across the sample with a high impedance digital voltmeter. The three measurements were typically within a few tens of micro-ohms of each other. The three measurements on each sample were averaged and normalized to the resistance per meter. These data are tabulated in Table 1.

DISCUSSION

Fig. 4 clearly demonstrates the dramatic increase in performance that results from the addition of one or two layers of tinned copper braid over the brass convoluted/bronze braid. This is consistent with earlier studies [1]*.

The comparison between tinned copper and SnCuFe as a middle braid shows that at very low frequencies (1 kHz), SnCuFe has a higher resistance than tinned copper. However, by about 10 kHz the ferromagnetic properties of SnCuFe braid become evident and produce a lower, that is, a better transfer impedance. This behavior is also evident in the flexible plastic-core assemblies (Fig. 7).

The flexible plastic-core conduit assemblies show the typical performance expected of a braided cable, that is, a frequency-independent transfer impedance below 100 kHz where the current diffusion predominates and a transfer impedance that is proportional to frequency above a few MHz where mutual inductance coupling predominates. As shown in Fig. 6, the addition of copper foil to a flexible plastic-core conduit

*Number in brackets designates reference at end of paper.

assembly improves the high frequency performance by a factor of 4 (12 dB). A second overbraid reduces the high frequency transfer impedance by about a factor of 10 (20 dB).

SUMMARY

Measurement of the surface transfer impedance of eight flexible conduit assemblies shows that:

- 1) The measured transfer impedance of the flexible metal-core conduit assemblies was consistent with their being equivalent to a solid shield.
- 2) The addition of extra layers of tinned copper overbraid significantly improved the performance of the brass conduit/bronze braid.
- 3) The use of a SnCuFe middle braid improved the performance of the assembly above 10 kHz.
- 4) The flexible plastic-core cable assembly had characteristics that were similar to a braided cable. The effect of additional layers of braid and the use of SnCuFe braid were both evident.

REFERENCE

1. J. S. Hofstra, M. A. Dinallo, and L. O. Hoeft, "Measured Transfer Impedance of Braid and Convolute Shields," Record of the 1982 IEEE International Symposium on Electromagnetic Compatibility, September 1982, IEEE 82CH1718-6.

Table 1
Measured Resistance of Samples

<u>Sample Number</u>	<u>Core</u>	<u>Braid</u>	<u>d.c. Resistance (milliohms/m)</u>	<u>Transfer Impedance at 1 kHz (milliohms/m)</u>
1	Brass	Bronze	3.68	3.77
2	Brass	Bronze/ Tinned Copper	1.246	1.24
3	Brass	Bronze/SnCuFe/ Tinned Copper	0.904	9.84
4	Brass	Bronze/ Tinned Copper/ Tinned Copper	0.707	0.746
5	Kynar	Tinned Copper	2.295	2.33
6	Kynar	Copper Foil/ Tinned Copper	1.90	1.91
7	Kynar	Tinned Copper/ Tinned Copper	1.09	1.07
8	Kynar	Tinned Copper/ SnCuFe	1.46	1.44

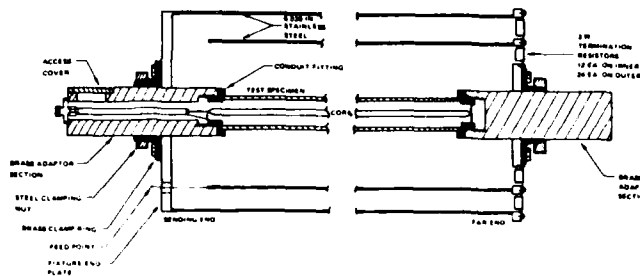


Fig. 1 - Diagrammatic view of quadraxial test fixture

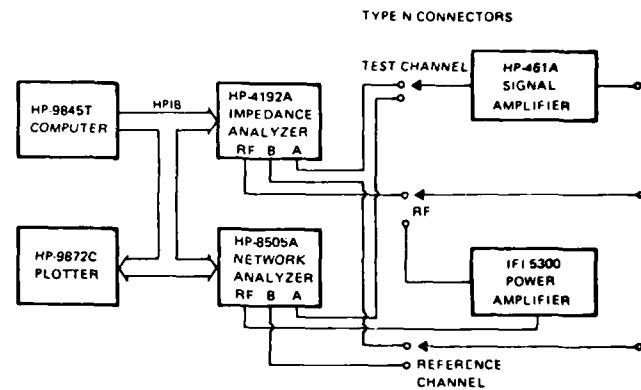


Fig. 2 - Computer-controlled data acquisition system

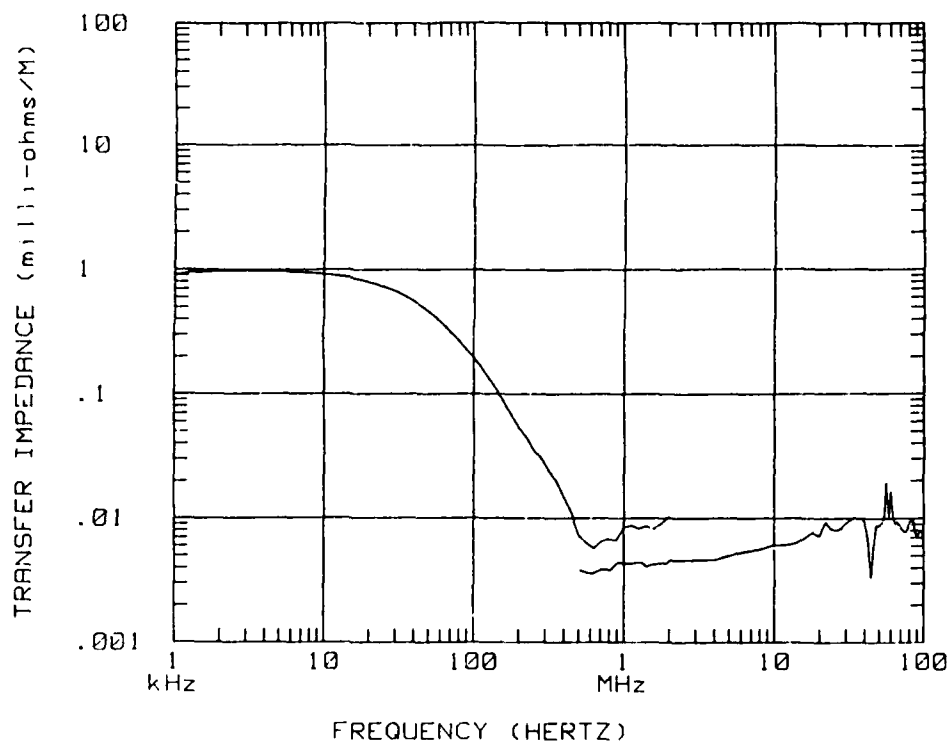


Fig. 3 - Measured surface transfer impedance of a 5/8 inch diameter brass calibration shield (D.C. resistance is 1 milliohm/meter)

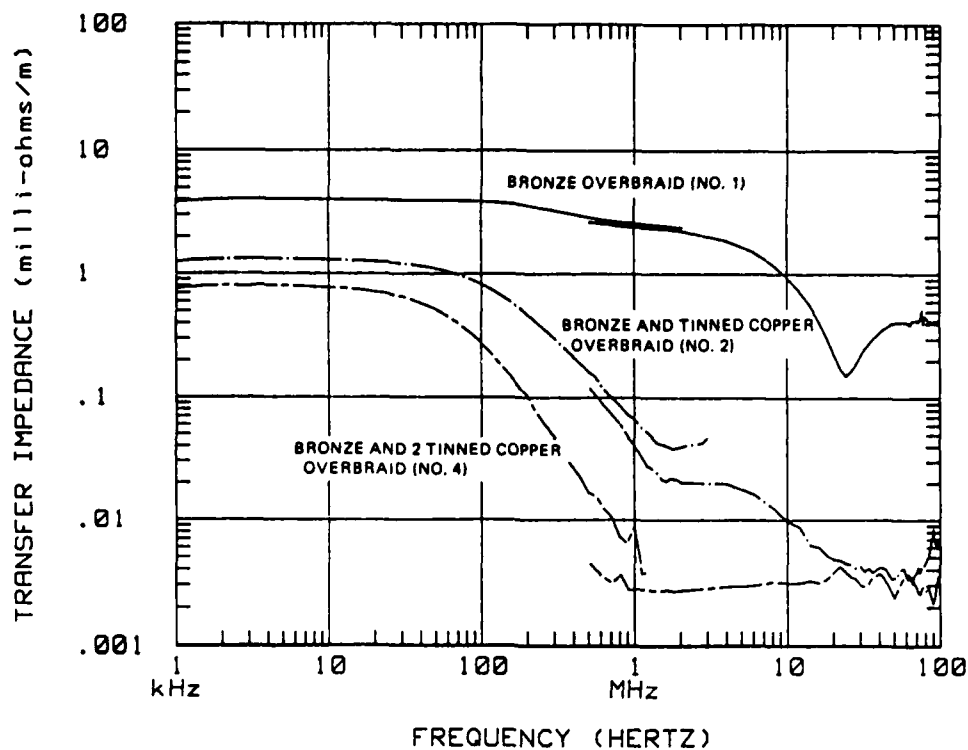


Fig. 4 - Measured transfer impedance of three flexible metal-core conduit assemblies showing the effect of adding tinned copper braids

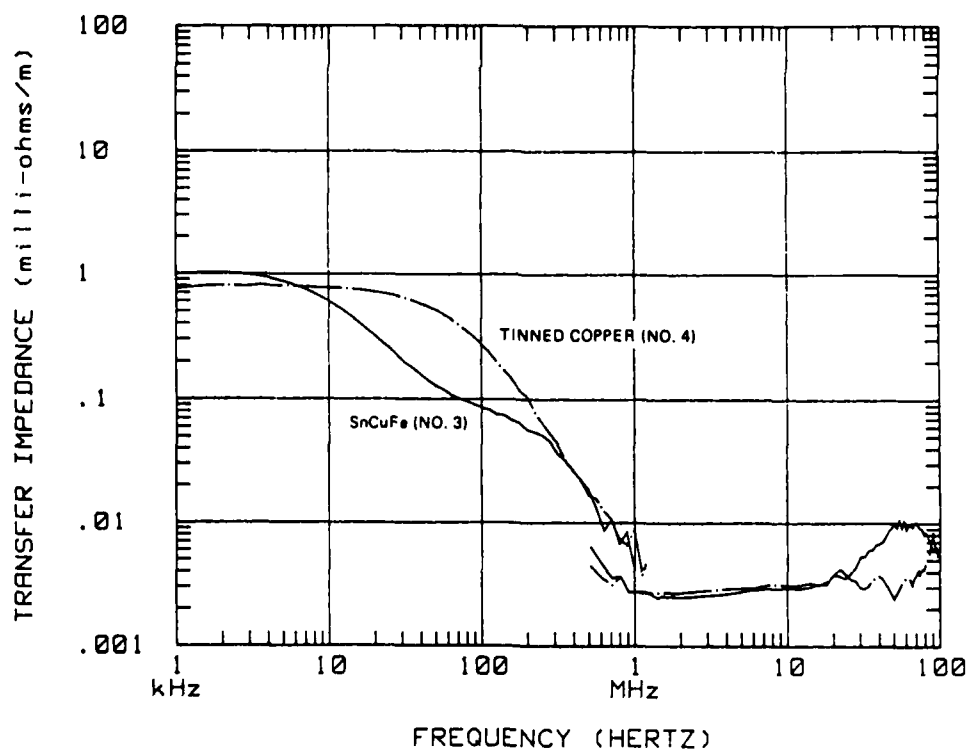


Fig. 5 - Comparison of samples with SnCuFe or tinned copper as the middle braid

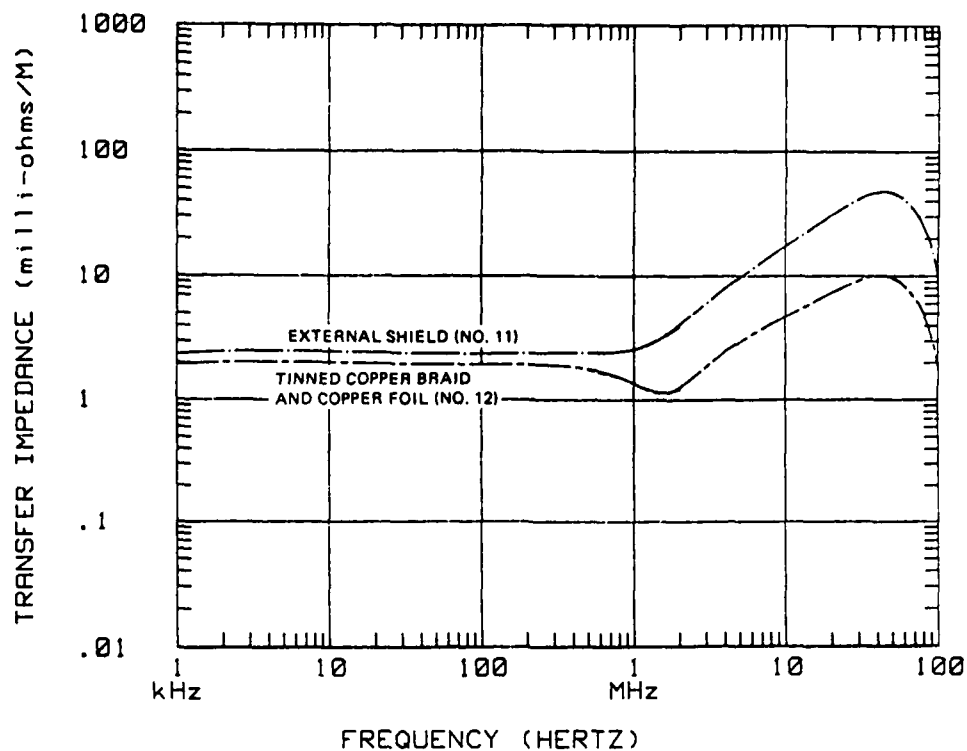


Fig. 6 - Comparison of flexible plastic-core conduit using tinned copper braids and copper foil

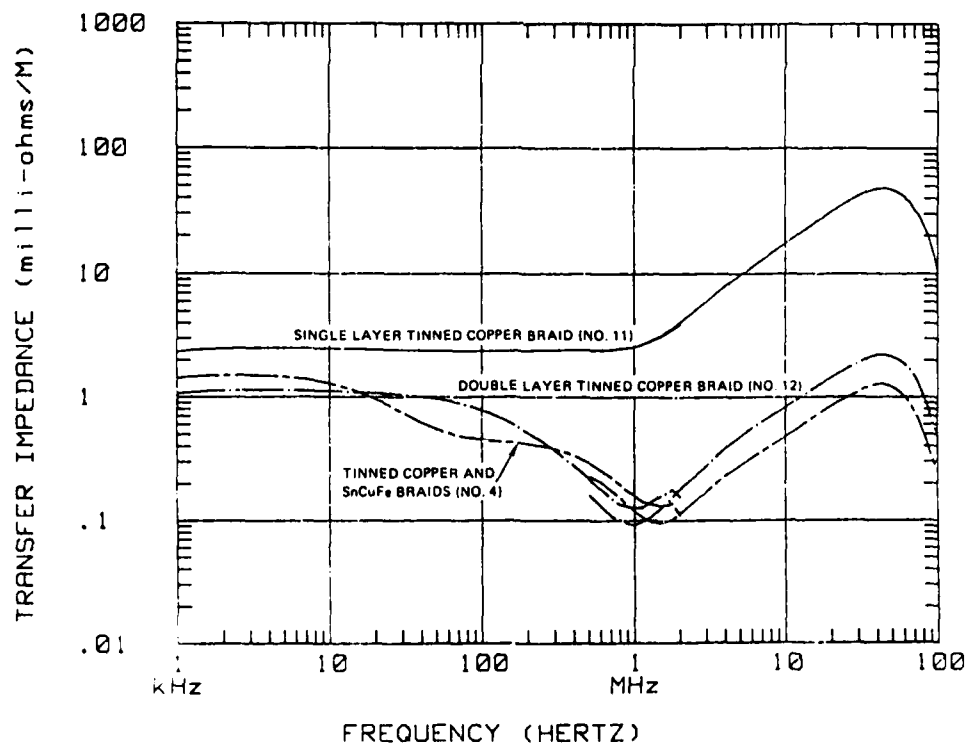


Fig. 7 - Comparison of flexible plastic-core conduit assemblies using single and double layer tinned copper and tinned copper/SnCuFe braids

THE USE OF A DISTRIBUTED PEAKING CAPACITOR
AND MARX GENERATOR FOR INCREASING CURRENT RISE RATES
AND THE ELECTRIC FIELD FOR LIGHTNING SIMULATION

R. A. Perala, T. H. Rudolph and P. M. McKenna
Electro Magnetic Applications, Inc.
P. O. Box 26263
Denver, Colorado 80226
(303) 989-2744

and

J. D. Robb
Lightning & Transients Research Institute
2531 W. Summer Street
St. Paul, Minnesota 55115
(612) 631-1221

ABSTRACT

One of the problems which has always been evident in the use of Marx generators for lightning simulation is the difficulty of obtaining fast rates of current rise and electric field excitation for the system under test. In a paper published in last year's proceedings, we discussed the use of discrete peaking capacitors for increasing the current rate of rise.

In this paper, we present numerical and experimental results pertaining to the use of a distributed peaking capacitor. This capacitor is a square plate above a ground plane. The plate is 50m x 50m square, and is 10m above the ground plane. A 1.3 MV Marx generator is placed at one edge and a large down conductor with a gap placed at another location is used to provide the current source for the system under test.

In this system, the Marx generator charges the plate, which then subsequently discharges through a gap in the down conductor to the test object. Thus, the initial rate of rise is determined from the charge on the down conductor and peaking capacitor, and is not greatly dependent upon the Marx generator.

This approach was successfully used to test the Pershing II missile system. Three dimensional finite difference numerical analysis techniques were used to theoretically model the system and results are favorably compared with those obtained experimentally. Rise rates well in excess of 2×10^{11} A/s are possible.

INTRODUCTION

A LIGHTNING TEST of the Pershing II system was conducted in September 1983. The test configuration is shown in Figure 1.

The objective of the study reported here is to define a way in which current rates of rise exceeding 10^{11} A/s can be injected into the test object. The basic concept is to use the top plate of the MICOM EMR (Missile Command Electromagnetic Radiation) facility as a distributed peaking capacitor.

The peaking capacitor is charged by a Marx generator and then discharged to the test object by arc attachment. The resulting current should have a greater rate of rise than would be possible without the peaking capacitor.

This approach is similar in concept to that which is described by Robb and Peralá in the 1983 Lightning Conference Proceedings (1)*. The principal difference between the present approach and the one described there is that the latter utilizes a discrete peaking capacitor, whereas the present approach utilizes a distributed peaking capacitor.

Some of the problem areas investigated are:

- a. The effects and importance of spurious resonances.
- b. The problems associated with the interaction of the Marx generator with the peaking capacitor.

The analysis of a three dimensional peaking capacitor with the Marx generator is accomplished by a numerical three dimensional finite difference solution of Maxwell's equations in the time domain. The Marx generator and the connecting cable are modeled as circuits or transmission lines which are integrated into the 3D code.

The objectives here are to:

1. Examine the dynamic interaction of the LTRI generator with the disk.
2. Identify the best place to attach the generator to the disk.
3. Determine the best switching conditions for the spark gap in the vertical conductor.

THREE DIMENSIONAL MODELING OF THE DISTRIBUTED PEAKING CAPACITOR

There are two main goals for the 3D numerical model. First, the model is to provide an accurate description of the dynamic interaction of the LTRI Marx generator

*Numbers in parentheses designate References at end of paper.

with the distributed peaking capacitor. Second, parameter studies are to identify candidates for the attachment point on the peaking capacitor for the LTRI Marx, the position and size for the electrode, and trigger and charging voltage conditions for the Marx/peaking capacitor combination which will give the largest peak currents and current rise rates.

The numerical model of the LTRI Marx-distributed peaking capacitor is basically a staggered grid, time dependent, three dimensional finite difference approximation (accurate to second order) to Maxwell's equations. Electric fields tangential to problem space boundary surfaces are specified by a first order radiating boundary condition (2). Further details of the numerical method are discussed in (3). The spatial grid interval is 2m in all three Cartesian coordinate directions. The time increment is 2 ns. The resulting computation bandwidth is approximately 30 MHz.

The distributed peaking capacitance is modeled as a 50m x 50m perfectly conducting ground plane. The ground plane terminates two mesh spaces from the boundary surfaces normal to the horizontal directions. A tapered feed is attached to the upper flat plate and extends to 2m above the ground plane. At this height the feed is 6m wide.

It should be noted that a perfectly conducting surface is obtained numerically by zeroing the electric fields tangential to the surface. Due to the discrete nature of finite difference methods all field variables are a volume average over a unit cell centered on the position of that field. Hence, the upper flat plate and tapered feed have a nominal thickness of 2m.

The interconnection of the Marx generator with the upper flat plate is achieved by a transmission line 10m long. Two different transmission lines have been used. All cases with the transmission line terminating at the end of the tapered feed have a non-uniform transmission line whose characteristic impedance varies smoothly with $\ln(h)$ where h is the height above the ground plane. h varies from 2m to 10m.

The expression for the characteristic impedance of each section of the transmission line is:

$$\eta = \frac{\eta_0}{\pi} \ln \left(\frac{4h}{d} \right) \quad (1)$$

where η_0 is the impedance of the free space and d is the diameter of the transmission line which is assumed to be .025m.

For other cases where the drive point is not at the end of the tapered feed, a uniform transmission line 10m above the ground plane and .025m in diameter has been used. The termination voltage for the end of the transmission line connected to the feed or flat

plate is the potential difference of that point above the ground plane as determined by the 3D model at each time step.

The Marx generator is modeled by a circuit connected to the other end of the transmission line with a 40 nF capacitance in series with a 10 μ H inductance. Initially, current through the Marx generator is zero and the Marx capacitor charge voltage is specified.

The electrode is modeled as a thin wire for all cases except for the square 2m x 2m cross section case. In all cases the electrode is charged along with the peaking capacitance by its connection to the upper flat plate, but it is disconnected from the ground plane. When the trigger voltage criterion is reached the electrode is shorted to the ground plane.

DYNAMIC INTERACTION OF THE LTRI MARX GENERATOR AND THE DISTRIBUTED PEAKING CAPACITANCE - The interaction of the LTRI Marx generator and the distributed peaking capacitance can be understood by viewing the system's interaction sequence of three steps.

First, the Marx capacitance charges the peaking capacitance. If the system were not triggered, this charging process would result in sinusoidal oscillation of charge between the two capacitors that would be slowly damped by radiation from the peaking capacitor and transmission line.

Once the potential difference across the peaking capacitance reaches the trigger condition, the electrode is shorted to the bottom ground plane.

Three distinct resonances then occur. First, the down conductor resonates in an antenna mode with a wavelength approximately equal to twice the length of the conductor. This frequency is about 14 MHz. The amplitude of these resonances are rather small compared to the overall response and are not distinguishable in the waveform of Figure 2.

The second resonance is the LC circuit oscillation of the peaking capacitor and the down conductor. This resonance is highly visible in Figure 2 and is on the order of 1 MHz.

The static capacitance of the distributed peaking capacitor (flat plate plus tapered feed) is 4.45 nF.

The third resonance is the oscillation of the total circuit inductance with the Marx capacitance. This is on the order of 100 kHz and is indicated in Figure 2.

RESULTS OF PARAMETER STUDIES - Table 1 lists the results of a parameter study designed to identify optimum choices for a realistic simulation of natural lightning peak currents and rise rates. The parameters varied were electrode size, electrode location, initial Marx charge voltage, trigger voltage, and location of the transmission line connection to the peaking capacitor. An example of the current out to 6 μ s is shown in Figure 3.

Figure 4 shows the time derivative of the current.

The location of the electrode and the transmission line attachment point are relatively unimportant in altering the peak current or rate of rise, although the peak currents and rates of rise were largest for constant conductor size and Marx and trigger voltage when the electrode position and transmission line attachment point were close to each other.

The size of the electrode influences the peak currents and rise rates. However, the ratio of peak currents does not correspond exactly to the ratio of the square roots of the electrode inductances, as might be expected if the effective impedance at early times depended only on the ratio of electrode inductance to the peaking capacitance. The reason for this is that the relative phase of the peaking capacitor discharge to the Marx capacitor discharge is also important in determining the peak current and rise rate.

The most important parameters in determining peak current and current rise rates are the initial Marx charge voltage, and, to a lesser extent, the electrode trigger voltage. Once again the dependence is complicated by the dependence of peak currents on the relative phase between peaking capacitor and Marx capacitor discharge as well as the total effective impedance of the coupled Marx and distributed peaking capacitor system through the Marx inductance, transmission line, and the long electrode. The main result is that the largest peak currents and current rise rates are achieved for Marx capacitor charge voltages of 1.6 MV and trigger voltages of approximately 2.7 MV. The largest peak currents are on the order of 117 kA with corresponding current rise rates of 5×10^{11} A/s for a 2m x 2m square electrode.

COMPARISON TO MEASURED DATA - A typical current waveform obtained during the Pershing II missile test is shown in Figure 5. This is to be compared with the calculated waveform for the same configuration shown in Figure 6. Note that the currents demonstrate a high degree of similarity, both in magnitude and form. The noise evident in the calculated waveform can be attributed to the lack of dissipation mechanisms in the model which were, of course, present in the experimental configuration.

SUMMARY AND CONCLUSIONS

The modeling results indicate the following:

1. The LTRI Marx generator and the peaking capacitor combination should be able to provide on the order of 100 kA of current at the largest charge and trigger levels.

2. Values of $\frac{\partial I}{\partial t}$ should well exceed 10^{11} A/s and one might consider reducing this with

series inductance in the down conductor so that the threat criterion is not greatly exceeded.

3. Three resonances are introduced by the test fixture and Marx generator interaction: the antenna mode of the down conductor, the LC circuit mode of the peaking capacitance and down conductor, and the slow circuit response of the Marx generator interaction with the entire test fixture.

REFERENCES

1. J. D. Robù and R. A. Perala, "Measurements with Theoretical Analysis of

a Full Scale NEMP Type Lightning Simulator for Aerospace and Ground Conference on Lightning and Static Electricity, June 21-23, 1983.

2. G. Mur, "Absorbing Boundary Conditions for the Finite Difference Approximation of the Time-Domain Electromagnetic-Field Equations, IEEE Transactions on Electromagnetic Compatibility, EMC-23, November 1981.

3. D. E. Merewether and R. Fisher, "Finite Difference Solution of Maxwell's Equation for EMP Applications," Electromagnetic Applications, Inc., Report EMA-79-R-4, April 27, 1980.

Table 1 - Summary of the Peak Current and Current Rise Rates for the Three-Dimensional Parameter Study (1)

CASE	CONDUCTOR SIZE	ELECTRODE LOCATION	TRANSMISSION LINE ATTACHMENT POINT	MARX CHARGE VOLTAGE (MV)	ELECTRODE TRIGGER VOLTAGE (MV)	INITIAL PEAK CURRENT (kA)	PEAK CURRENT (kA)	$\frac{\Delta I}{\Delta t}$ Linear (10^{10} A/s)	$\frac{\Delta I}{\Delta t}$ Peak (10^{11} A/s)
1	1"	Center	Feed	1	1	34	41	6	6
2	4"	Center	Feed	1	1	36	44	7	8
3	12"	Center	Feed	1	1	41	50	11	21
4	2 m x 2 m	Center	Feed	1	1	55	66	13	21
5	4"	Outboard End	Feed	1	1	35	40	7	8
6	4"	Throat End	Feed	1	1	38	43	8	8
7	4"	Center	Outboard End	1	1	36	42	7	8
8	4"	Center	Throat Corner	1	1	36	43	7	8
9	4"	Center	Center	1	1	39	44	8	8
10	4"	Throat End	Throat End	1	1	41	43	8	9
11	4"	Center	Feed	1	1.5	38	49	13	13
12	4"	Center	Feed	1.6	1	52	64	9	8
13	4"	Center	Feed	1.6	2	60	74	15	17
14	4"	Center	Feed	1.6	2.5	59	80	17	23
15(a)	2 m x 2 m	Center	Feed	1.6	2.7	100	117	51	59
15(b) ⁽²⁾	2 m x 2 m	Center	Feed	1.6	2.7	100	117	28	57
15(c) ⁽³⁾	2 m x 2 m	Center	Feed	1.6	2.7	85	116	35	48

(1) All cases except 15(b) and 15(c) have the transmission line as described in the text.

(2) Case 15(b) has a .1" radius transmission line 10 m long.

(3) Case 15(c) has no transmission line. The Marx generator is attached directly to the end of the tapered feed.

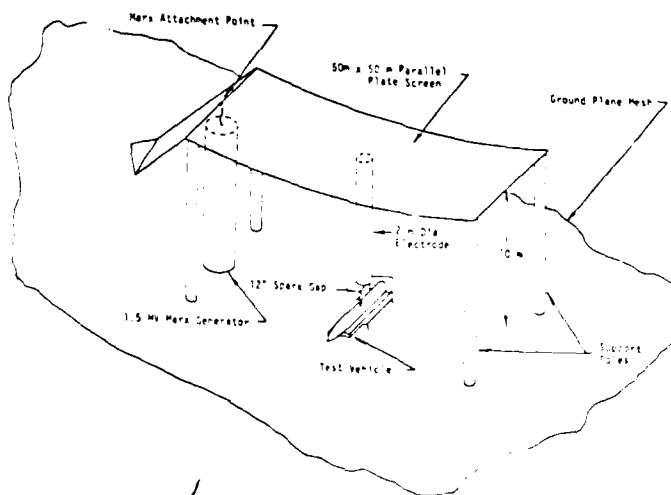


Fig. 1 - Direct strike test configuration

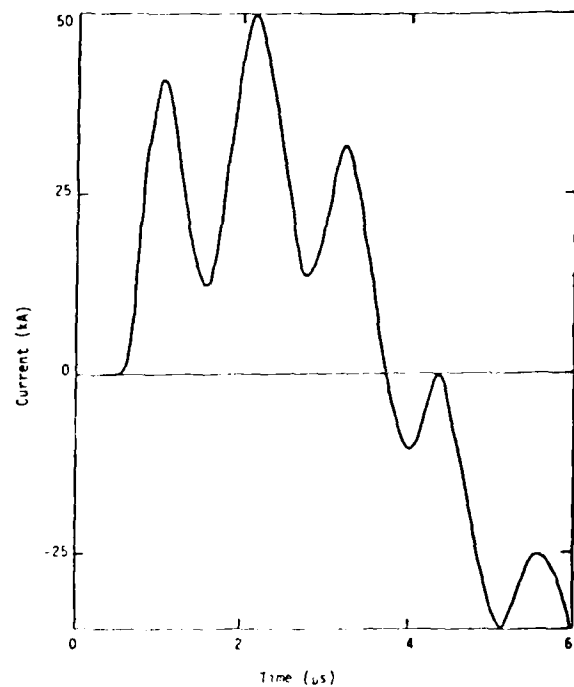


Fig. 3 - Current through a 2m x 2m electrode located at the center of the flat plate. The transmission line is attached to the end of the tapered feed. The LTRI Marx charge voltage is 1 MV. The electrode trigger voltage is 1 MV.

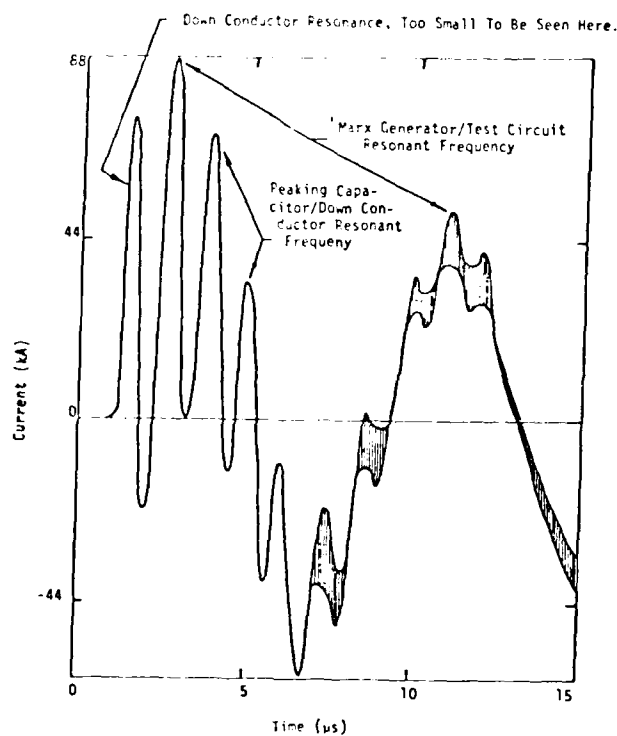


Fig. 2 - Current in a 2m x 2m electrode located at the center of the flat plate. The transmission line is attached to the end of the tapered feed section. The LTRI Marx charge voltage is 1.6 MV. The electrode trigger voltage is 2.7 MV.

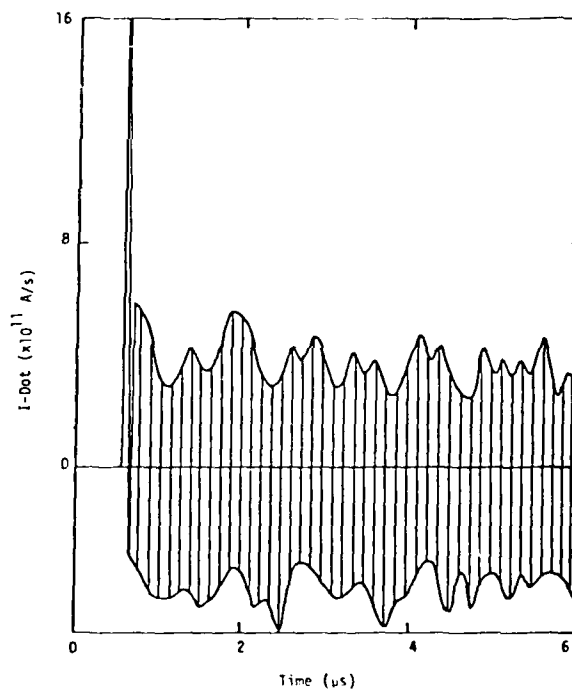


Fig. 4 - Time derivative of the current for the same case as Fig. 3.

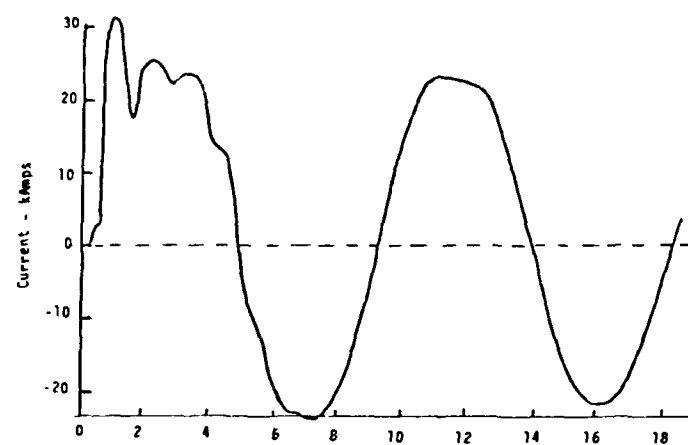


Fig. 5 - Experimental direct strike current waveform

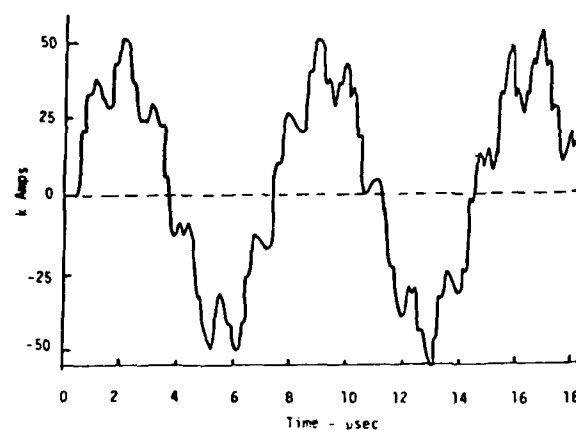


Fig. 6 - Calculated direct strike current waveform

UV LASER TRIGGERING OF CROWBARS USED IN
THE SANDIA LIGHTNING SIMULATOR

Murphy J. Landry and William P. Brigham
Sandia National Laboratories
Albuquerque, NM 87185

ABSTRACT

We have applied the techniques of IR and UV laser-triggered switching of gaps to crowbar switching two Marx generators, delivering >250 to 50 kA in small and large impedance loads. Crowbar switching delays of 0.08 to 0.28 μ s were observed if the laser radiation arrived in the crowbar gap when its voltage was $>44\%$ of its maximum applied voltage or at 23 to 68% of its self-break voltage. We have successfully triggered a 5.0 cm crowbar gap with 35 mJ of $\lambda = 249$ nm radiation when filled with 80 psig of SF_6 . Electrodes have operated with 40 coulombs of charge for 47 shots without detrimental surface damage.

INTRODUCTION

The Sandia Lightning Simulator (SLS) operation is based on the use of a crowbarred Marx generator in an RLC underdamped circuit (1,2).^{*} It is possible to use the SLS in obtaining fast-rising, long-lasting, unidirectional current pulses in full-scale operation systems (3-5). Since the initial proposal and the demonstration of the feasibility (6) of using a gas-dielectric-triggered spark-gap as a 1 MV crowbar, a significant amount of effort in developing the simulator has been given to the design and method of triggering the crowbar.

Ideally, the crowbar switch clamps or shorts-out the capacitance of the source at peak current. Once the crowbar is shorted, the RLC circuit for the rising-current pulse changes to an L/R circuit for the decaying-current pulse. The current decays in relation to the L/R time constant of the crowbar switch and load circuit. The crowbar switching technique has proven to provide fast-rising, long-duration, unidirectional current pulses more efficiently than either a double exponential overdamped circuit or a critically damped circuit.

We review the use of laser-triggered switching (LTS) techniques and the theory of SLS operation. We describe the different types of crowbar switches (i.e., electrical-, IR- and UV-triggered crowbars), the IR and UV lasers used to trigger the crowbars, and the optical alignment of the crowbar-laser system. We discuss experimental results which include: [1] the self-break voltage (SBV) characteristics of the crowbars, [2] the delay in crowbar switching as functions of percentage of maximum voltage on the crowbar (V_{CBM}) and self-break voltage of the crowbar, and [3] the condition of the electrodes under different operational conditions.

LASER-TRIGGERED SWITCHING

Much research has been done on laser trigger switching of gaps using IR, visible and UV lasers. An excellent review of IR and visible LTS is given by Guenther, et al (7) where gap breakdown was initiated by focusing the laser radiation on the target electrode. Pendleton and Guenther (8) triggered a 1.5-cm gap, which was filled with 1 atm of SF_6 , in less than 10 ns when operating close to SBV. A 5-cm lens focused the 4- to 80-MW, 10-ns, $\lambda = 694.3$ nm radiation transverse to a gap with 0 to 80 kV applied. Minimum delays were observed when the laser beam was focused on the charged cathode electrode. Guenther and Bettis (9) observed a 12-ns delay for a 1.16-cm gap with 630 Torr of air when operating at 80%

of its SBV, which was 30.7 kV. A slightly shorter delay (12 ns compared to 14 ns) was observed when the 2.5-J, 15-ns (170-MW), $\lambda = 694.3$ nm laser pulse was focused coaxially onto a charged anode target instead of a charged cathode. For a 3-cm gap with 350 psi of N_2 , the delay was about 3 ns when the laser power was 250 MW.

Bettis and Guenther (10) switched a 2-cm, high-pressure, gas-filled spark gap at up to 700 kV with 80-mJ, 6-ns FWHM, $\lambda = 1064$ nm laser pulses of 1.5 mrad divergence. The gap was filled with SF_6 or Ar- N_2 mixture at 500 to 3000 Torr pressure. In a 90%-Ar and 10%- N_2 mixture at 3000 Torr their observed delay [1] increased with decreasing percent of SBV, [2] increased with decreasing laser power, and [3] changed slope at 8 ns and 50% of SBV for stainless steel target electrodes and at ~12 ns for tungsten, brass, and aluminum target electrodes.

Strickland, et al (11) studied LTS at 575 kV. They used a 2-cm pressurized gap with 17 000 Torr of a 50%-Ar, 40%- N_2 and 10%- SF_6 mixture and irradiated with 80 mJ of 1060-nm Nd:YAG radiation, which had a 1.5-mrad divergence. At 80% of SBV a 10-ns delay was observed. Moriarty, et al (12) examined LTS at up to 3 MV with 15 000 Torr of a 50%-Ar, 40%- N_2 and 10%- SF_6 mixture using several joules of 694.3 nm radiation. They both observed (11,12) subnanosecond jitter but only at voltages close to SBV (97% and 94%, respectively). The use of an argon mixture instead of only SF_6 requires an increased pressure for the same voltage and gap spacing, or an increased gap spacing for the same voltage and pressure. The high voltage switching at high pressure poses engineering and safety concerns, while the increased electrode spacing gives the switch higher impedance.

A trigger mechanism fundamentally different from that for IR and visible switching, which utilizes the volume interaction of the laser beam with the insulating gas in the switch to form an ionized channel between the electrodes, was initially studied by Bradley and Davies (13) and Bradley (14). The presence of the 337.1 nm radiation from a N_2 laser in the N_2 -filled gap decreased the streamer closing time from 65 ns to 33 ns. Rapaport, et al (15) using a higher quality laser beam, initiated a streamer in the volume of a 0.5-cm gap with 7 mJ of 20-ns, 248-nm KrF, 75-mrad divergence radiation. A delay of about 7 ns was observed when the gap was charged to 80 kV and had 3 atms of SF_6 , which was 120% of the pressure at which spontaneous dc breakdown occurred.

Using the ionized channel between electrodes in a gap pressured with 2060 Torr of SF_6 , Woodworth, et al (16) successfully triggered a

^{*} Numbers in parenthesis designate references at the end of the paper.

1.77-cm gap, pulse-charged to 0.5 MV. A 2-ns delay was observed when the gap, operating at about 80% of SBV, was triggered with as little as 4 mJ of KrF radiation emitted from an injection-seeded oscillator-amplifier system (20 ns, $\lambda = 248$ nm). A slightly longer delay of about 2.5 ns was observed at a higher pressure of 3500 Torr and a gas mixture of 10% SF₆ and 90% N₂. Woodworth, et al (17) extended their work to an 11-cm, 2.3-MV self-breakdown-voltage gap switch similar to those used in PBFA-I (18). The increased gap length required an increase pressure of 3100 Torr of SF₆ and 27 to 127 mJ of KrF laser energy to yield delays in switch closure from 18 to 33 ns, respectively, when the gap was operated at 75% of SBV. The KrF laser used in these studies (16,17) had a divergence of 200 μ rad (full angle).

Additional work by Adams, et al (19) has resulted in the simultaneous switching of two 2.4-MV self-breakdown voltage switches within 1.7 ns when 55 mJ of KrF radiation was focused by a 90-cm focal length lens. The 11-cm gap was pressurized to 2170 Torr of SF₆. At 80% of SBV the delays of the two switches were about 25.5 and 29 ns.

A study of UV LTS of a 5-MV multistage gas switch by Adams, et al (20) resulted in superior switching by a KrF laser compared to a frequency-quadrupled Nd:Yag laser (delay of <4 ns for the KrF compared to 15 ns for the Nd:YAG). The 4.45-cm gap was pressurized with a different pressure of SF₆. The 20-ns, $\lambda = 248$ nm injection-seeded KrF and the 2 ns $\lambda = 266$ nm, frequency-quadrupled Nd:Yag laser beams had 150 and 160 μ rad beam divergence (full angle). The KrF laser had a larger beam dimension (6 mm by 20 mm) than did the Nd:Yag (7-mm dia.). The poorer Nd:YAG trigger performance may be related to the fact that the 2-ns Nd:YAG pulse was shorter than the closure time of the gap, whereas the 20-ns KrF pulse was comparable. A previous investigation (10) for laser pulses focused on the target electrode showed that the delay in LTS was controlled primarily by the laser pulse to about 50% of SBV or to a delay equivalent to the laser pulse width. This effect has not been verified for volume gap initiation with UV laser radiation.

THEORY OF OPERATION

The basic operation of the Sandia Lightning Simulator has been previously described by Bushnell and Kostas (2) and White (5). The major innovation (1) in the SLS is the use of a crowbar switch across the Marx generator to allow the switching at peak current or when the charge in the Marx capacitor has been transferred to the crowbar-load loop inductors. The basic simplified crowbarred-Marx generator circuit is shown in Fig. 1. The crowbar

circuit requires a low inductance voltage source to drive the peak current through the external load inductance. The peak current, I_0 , in the load is obtained from the first quarter cycle of an undamped RLC circuit mainly,

$$I_0 = V \sqrt{C_M / L_T}, \quad (1)$$

where $L_T = L_L + L_M + L_t$, and C_M is the capacitance of the Marx. Ideally, the crowbar is closed at zero voltage, i.e., peak current, shorting out the discharged Marx capacitors. The current in the crowbar load loop I_L then decays according to the $(L_t + L_L + L_{CB}) / (R_t + R_L)$ time constant.

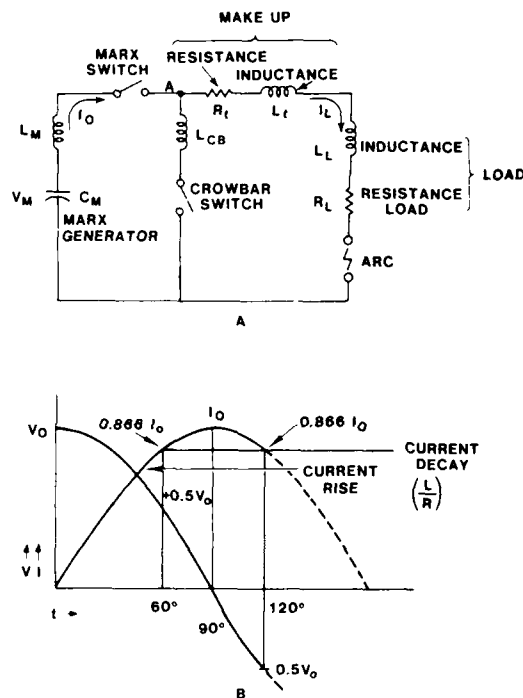


Fig. 1 - Crowbarred Marx generator circuit with voltage and current waveforms

We find it extremely important to do computer simulation of the circuit proposed for upcoming tests. We routinely run simulation plots, using the Air Force SCEPTRE program (21,22), to predict load currents before we fire the SLS into the component to be tested or even into a dummy coil representing the inductance of the component to be tested. These plots give us the voltage and current levels for some circuit components and allow us to evaluate critically the performance of these components. From these computer simulations, we can decide whether it is safe to operate the SLS at the proposed levels.

At constant load current (I_L), as the crowbar switching is delayed in time to switch at crowbar voltage of 59 to 0% of maximum voltage across the crowbar (V_{CBM}) the peak current increases by about 20% (see Figs. 2A and 2B). The increase in peak crowbar current (I_{CB}) is Marx current (I_M) trapped in the Marx-crowbar loop (Fig. 1), which is superimposed on the load-crowbar loop. We would like to minimize this peak reverse Marx current. The increase in peak crowbar current contributes little to the total charge in the crowbar because these Marx-crowbar oscillations are damped in about $10 \mu s$, at which time the amplitude of the crowbar current equals to the negative of the load current (see Figs. 2A and 2B).

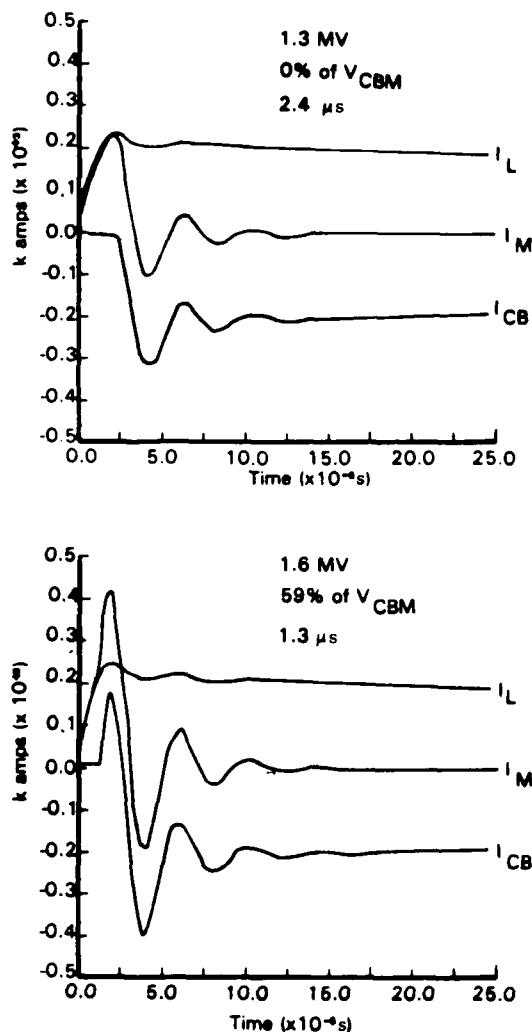


Fig. 2 - Current effects of crowbar switching at different percentage of V_{CBM}

The crowbar must [1] withstand the full open circuit Marx voltage (1.6 MV), [2] be triggerable externally at lower voltage,

preferably at zero volts, [3] have low inductance and resistance when shorted, and [4] be able to carry the full charge of the main current pulse, containing 40 coulombs, for a reasonable number of simulator shots.

The simulator is designed so that the time to the current peak is nominally $2 \mu s$. At this time, with low voltage across the Marx generator, the crowbar should be triggered. The allowable jitter in crowbar triggering is on the order of 100-300 ns. This is orders of magnitude larger than allowable for other uses of gas dielectric switches (17). As in other applications, the most desirable insulating gas in the crowbar is SF_6 , since it has higher breakdown strength (23) than many gases. To date, the crowbars in the SLS have used either pure SF_6 or a mixture of SF_6 with other gases.

TYPES OF CROWBAR SWITCHES

Electrical Triggered Switches -- The original crowbar (2) was a trigatron, which had an electrical trigger electrode mounted in one of the stainless steel electrodes. A 400-kV trigger pulse initiated the discharge which took about 100 ns to short. The gap space was about 9.2-cm long, and a pressure of 90 psig of SF_6 was used. This crowbarring scheme accomplished the design goal of a 200-kA pulse. Difficulties in obtaining reliable operations and the limited operating voltage range for a fixed gap spacing led to considering IR LTS (7) and eventually UV LTS (16,17,19,20).

IR and UV Laser-Triggered Switches -- The data presented in this paper were taken with IR and UV triggering. The crowbar switch housing used in SLS LTS is the same for IR and UV triggering. Fig. 3 shows the 44.5-cm dia. by 47-cm long housing, which is made of aluminum end plates insulated from each other

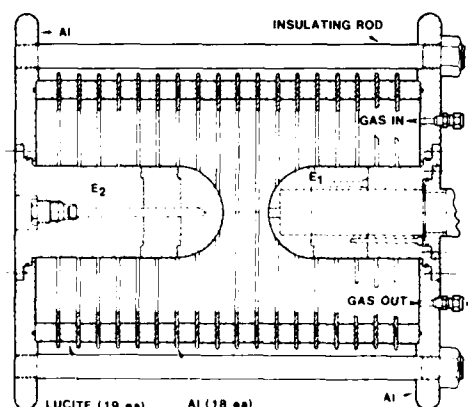


Fig. 3 - Crowbar housing used with IR and UV laser triggering

by lucite rings with aluminum spacers, providing capacitive voltage gradings. The 10.2-cm dia. electrodes are spaced 9.3 cm for IR and 5.0 cm for UV triggering. The laser beam entered the crowbar gap through a 1.1-cm hole in electrode E, which had contained the electrical trigger electrode of the trigatron. The gap spacing could be reduced for UV triggering because the insulating gas was pure SF₆ pressured at 105 psig instead of the 50%-N₂, 40%-Ar and 10%-SF₆ mixture pressured to a maximum of 250 psig for IR triggering.

For IR triggering a 15-cm focal length lens and a protective sapphire window were mounted in a cylindrical tube, which was inserted from the outside of the crowbar into electrode E₁. A second window was located at the tank wall. The lens position was adjustable so that its focal point was 0.95 cm from the charged cathode target electrode E₂ -- in an attempt to create a plasma both at the surface of electrode E₂ and in the gap between electrode E₁ and E₂.

For UV triggering, the lens was mounted as shown in Fig. 4. The focal length of the lens was increased to 50 cm so as to create a longer ionized streamer in the gap. The lens was positioned external to the crowbar. Two ports, A and B, were provided to allow purging the window with SF₆ immediately after the crowbar was triggered. The lens assembly allowed the laser light to focus just past the center of the gap toward electrode E₂. The aperture kept debris in the gap from getting to the window.

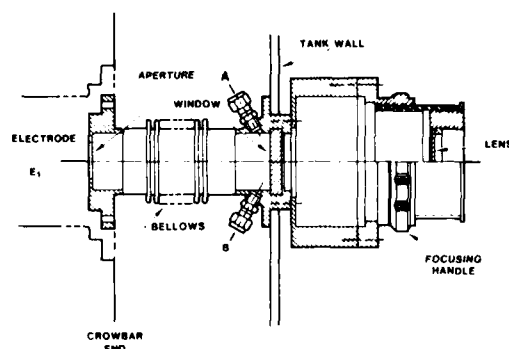


Fig. 4 - Window and lens assembly used for UV laser triggering

IR AND UV LASERS

The IR laser is a Pockels cell Q-switched Nd:glass oscillator which sometimes included an amplifier. The 20-ns, $\lambda = 1062$ nm beam had a divergence of 5-6 mrad.* The large beam

*Manufacturer specification full angle at 50% of energy.

divergence forced us to place the laser immediately outside the tank, containing the Marx generators, isolation gap, crowbar and make-up circuit (2). In either IR laser configuration, at least 3.5 J was required into the window at the tank wall to assure gap triggering. When the amplifier was used, ≥ 4 J of laser energy was provided.

The UV excimer laser is a Lambda Physik model EMG 150 or 150 ES injection-locked laser system with a 1-mm diameter apertured oscillator directed into an unstable amplifier. The $\lambda = 249$ nm, 20-ns pulse of either system had a divergence of < 200 μ rad* and beam steering of 3 mm at the focus of a 10 m lens. The measured energy at the output of these lasers was > 0.50 J (EMG 150) > 1.0 J (EMG 150 ES). Both beams were 0.96 cm by 2.54 cm. The EMG 150 had the long dimension horizontal while the EMG 150 ES had it vertical. The latter is preferred because a smaller diameter directing mirror could be used. The temporal profile of the UV pulse is shown in Fig. 5. The risetime to peak pulse energy is almost 4 ns and pulse width is about 20 ns.

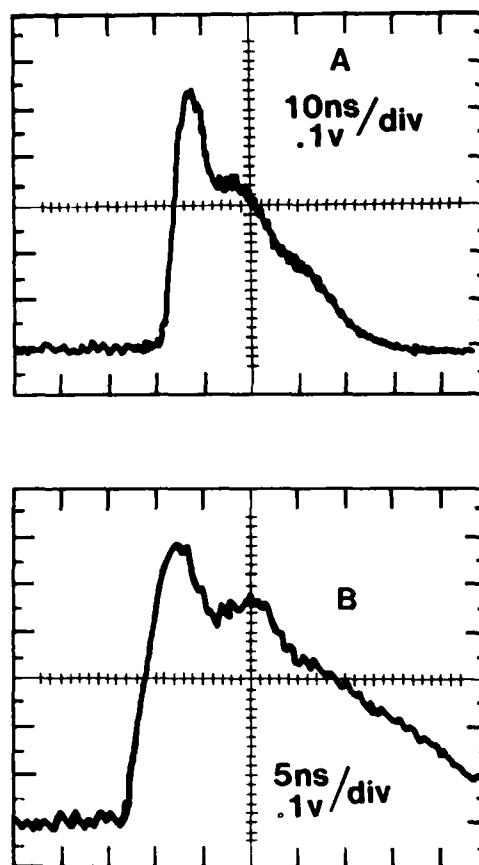


Fig. 5 - Temporal response of UV laser pulses

The IR laser oscillator and amplifier were positioned immediately outside the Marx generator tanks. The IR laser and Pockels cell power supplies and the UV laser and power supply were located in the laser room outside of the high bay area (Fig. 6) in order to avoid sympathetic triggering of the lasers by the Marx when it erects. Placing the UV laser in the laser room increased the distance from the laser source to the entrance lens of the crowbar (9.5 m for the north tank and 24.6 m for the south tank) compared to when the IR laser was used (2.0 m for the south tank and 0.5 m for the north tank). The inherent 300 μ rad beam steering of the UV laser beam could cause as much as 2.9 and 7.4 mm beam displacement at the north and south entrance lens, respectively.

this happens, we change the gas in the laser. We now change the gas about once per week in the EMG 150. In some other models of KrF lasers the gas fill may last only a few hours.

When performing tests, we operated the UV laser only in its external trigger mode. We provided three trigger pulses to the UV laser: the first trigger readied the laser, the second trigger fired the laser at the proper time so as to trigger the north crowbar (Fig. 6) at 1/2 the peak voltage of the Marx. The third trigger fired the laser at the proper time so as to trigger the south crowbar at 1/2 the peak voltage of the Marx. Normally, we switched greater than 200 kA and 100 kA in the first and second pulses, spaced >30 ms apart.

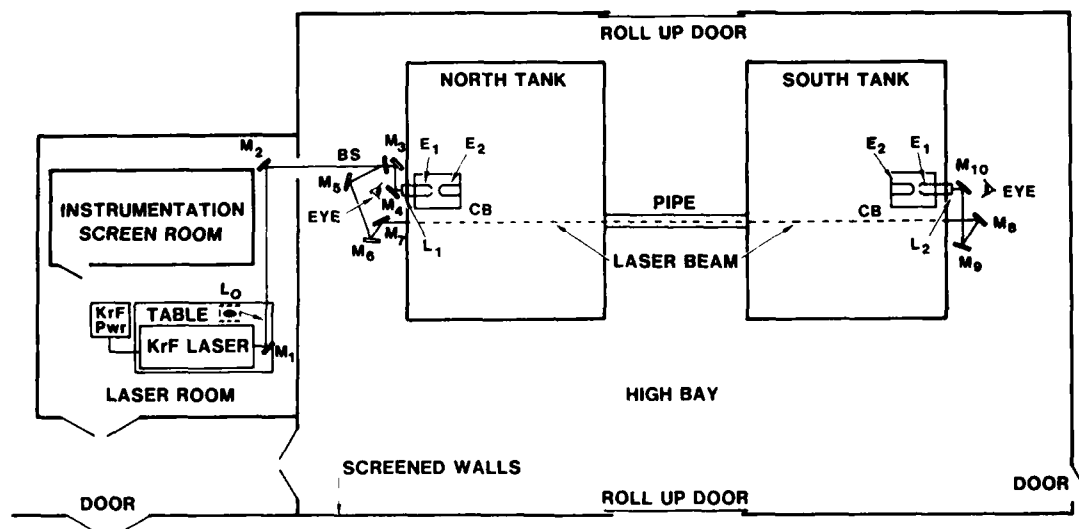


Fig. 6 - Sandia Lightning Simulator featuring the KrF (UV) laser alignment layout

The UV laser was positioned on an NRC table (no air suspension) with a laminar downflow system overhead and down-curtains over the table. The downflow has proven to be a necessity in our dusty environment. We make sure that we cover all mirrors not under the down-flow when we have a greater than 1-hour wait between test shots. We routinely blow off the windows and beamsplitters before a laser shot. We have not replaced any mirrors or beamsplitters because of dust damage since we started UV operation in April 1983.

Our criterion as to whether we have the right energy and beam profile to initiate the crowbar is to break down air with a 1 m focal length lens. The length of the air breakdown for our laser is about 1-2 cm when the laser has been freshly filled with gas and is well aligned. As the gas ages, the arc length decreases, and at times the breakdown is erratic and does not occur for every laser shot. When

When the second current pulse was produced by IR triggering, only two trigger pulses were provided to the UV laser. The third trigger pulse went to the Pockels cell of the IR laser. Similar load current pulse amplitudes were produced, but spaced from on the order of tens of milliseconds to seconds apart.

The use of a KrF UV excimer laser instead of a Nd:glass IR laser to trigger crowbars affords several advantages: [1] provides an easily available low divergence laser beam, [2] enables the use of pure SF₆ instead of mixed gas, which allows lower switch pressure and shorter gap spacing for greater safety, less switching delays and jitter operation, and [3] supplies a lower wavelength, 249 nm compared to 1062 nm, requiring low laser energy to initiate the gas breakdown with either SF₆ or the mixed gas.

OPTICAL ALIGNMENT

The IR and UV laser beam alignment to the crowbars was performed in a similar manner except for the fact that a He-Ne laser was used for the IR alignment and the UV beam itself was used for the UV alignment. For the IR alignment, the He-Ne beam was centered on a burn made on processed polaroid film positioned about 2.4 m from the oscillator output. The He-Ne beam was then directed into the center of the window at the tank wall and the center of the hole in electrode E_1 (Fig. 3) by two mirrors.

The alignment of the UV laser used the UV beam and a card or the breakdown of the air in aligning the crowbar. The UV laser beam was positioned in the center of mirrors M_1 - M_{10} , lenses L_1 and L_2 and beamsplitter BS (see Fig. 6) using a white card and a circular card with a cross (target #1) placed in front of the lenses (Fig. 3). Electrode E_2 was removed from both crowbars. A circular target, #2, made with tracing paper containing a cross in its center, replaced E_2 . Crowbar, CB, was positioned in its cradle which was secured to the tank floor. The crowbar was secured to the aperture end of the UV window and lens assembly (Fig. 4), which was secured to the tank wall, but made flexible by the bellows. With the eye looking through the back of M_4 , through lens L_1 , and the aperture (Fig. 4), one can locate the cross on target #1. The air breakdown at the focus of the lens and the cross of target #2 were centered in the aperture. The focus point was properly positioned, using M_3 and M_4 . Mirror M_3 translates the laser beam across M_4 , and M_4 tilts the beam into lens L_1 and target #2. Alignment was complete when the laser beam was in the center of target #1 and the aperture, air breakdown point and the cross on target #2 were within 1 mm. The crowbar in the south tank was aligned in a similar manner with the eye behind M_{10} looking into the crowbar with E_2 removed and target #2 in position.

EXPERIMENTAL RESULTS

The operational goals of the SLS were first accomplished using electrical triggering of the crowbar. Shortly after, electrical triggering was replaced by IR laser triggering. Continuing demands upon the SLS forced us to consider more reliable means for triggering the crowbar. Due to the emerging technology (16,17,19,20) of UV laser trigger switching of gaps, one half of the SLS was converted from IR to UV triggering. Heavy test schedules, which included Sandia-related components and the Air Launched Cruise Missile (ALCM) for the Air Force Wright Aeronautical Laboratory with Boeing Military Airplane Company directing the testing (5), delayed the complete conversion of the last half of the SLS until after the

ALCM was successfully tested in mid-August 1983.

Since the complete conversion to UV triggering, we have a sufficient number of double current pulses to dispel our concerns about crowbar-laser beam alignment in the south tank after the Marxes in the north tank erected. At times, especially if we get a discharge in the Marx tank, we have felt severe floor vibrations in the High Bay, Laser Room, and Instrumentation Screen Room (Fig. 6). The long optical path from the UV laser to the crowbar in the south tank of 24.6 m and the optical mounts positioned on pedestals have proved not to be a problem. On the contrary, the optical alignment of the UV laser-crowbar system results in more accurate laser beam positioning in the crowbar than was previously attainable with the IR laser-crowbar system.

Self-Break Voltage -- It is advisable to operate the crowbar switch at pressures higher than the self-break pressure for maximum Marx voltage (1.6 MV). On the other hand, the voltage at which the crowbar switch should be operated is low. The delay in the closure of the crowbar switch is a strong function of laser energy or power density at focus, percent of self-break voltage (SBV) at the time the laser pulse enters the crowbar, and pressure in the crowbar. Since the cosine crowbar voltage function passes through zero at the desirable crowbar-switch closure, the delay may be sufficiently long so as to inhibit switch closure, and the resultant output is an underdamped sine wave.

To determine a safe operating pressure for different Marx charge voltages, the self-breakdown threshold of the switch pressure vs. Marx charge voltage was determined. Fig. 7 shows these results for both IR and UV crowbars -- the difference being that for the IR crowbars the 50.3%- N_2 , 40.6%-Ar and 9.1%- SF_6 gas mixture was used and the gap spacing was 9.3 cm, whereas for the UV crowbars, SF_6 was used and the gap spacing was 5.0 cm. The tests were conducted by first pressurizing the crowbar to a level at which it self-breaks when the 165-nfd Marx is erected for a specific charge voltage. The procedure was repeated at slightly higher pressure (increments of 5 psig for the UV and 10 psig for the IR) until the crowbar did not self-break and the Marx rang at the output load. Self-break occurs to the right of the lines in Fig. 7. It is evident that the SF_6 has insulating characteristics superior to the mixed gas. The better insulating effect of a higher percent of SF_6 in the mixed gas is illustrated by points 1 thru 5 (Fig. 7) where the gas mixture was 50.6% N_2 , 49.3% Ar and 10.1% SF_6 compared to 50.3% N_2 , 40.6% Ar and 9.1% SF_6 for all the rest of the IR crowbar self-break data points.

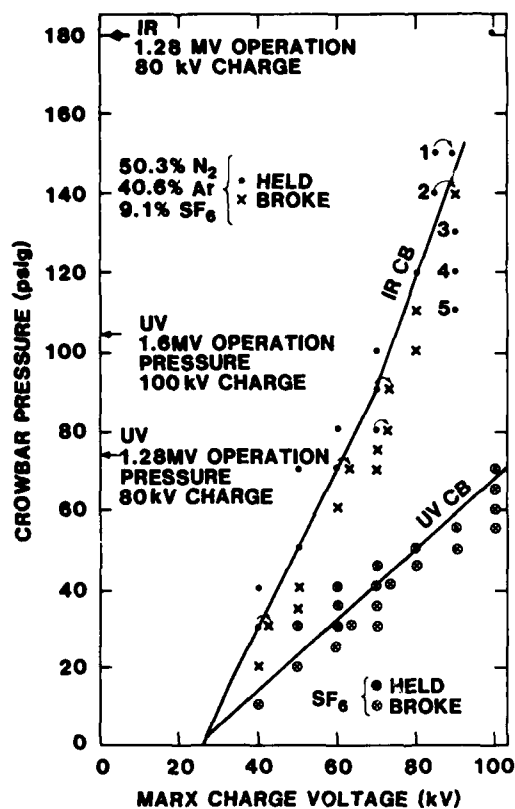


Fig. 7 - Self-break pressure of crowbars for IR and UV laser triggering relative to Marx charge voltage

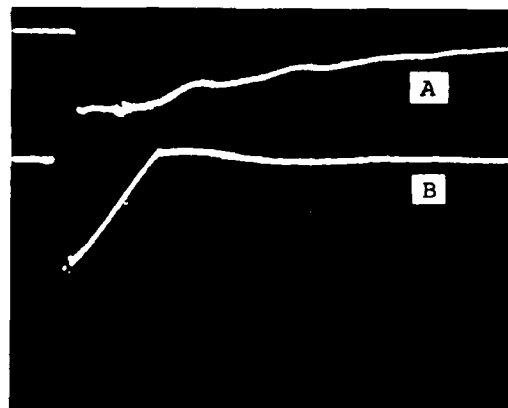
The data presented in this paper was taken with 1.5 times the pressure represented at the specific Marx charge voltage (at the line). Refined self-break measurements would better position the self-break line and allow us to reduce the operating pressure, thus reducing crowbar trigger delays if the crowbar switching characteristics are like the high-voltage gaps triggered by Woodworth, et al (16,17) and Adam, et al (19,20). Operation of the crowbars at 1.5 times the self-break pressure allows acceptable delays for switching the crowbar at a voltage level 50% of SVB.

Crowbar Delay -- The crowbars have been operated repeatedly with <200 psig of mixed gas (50.3% Ar, 40.6% N_2 and 9.1% SF_6) and <105 psig of SF_6 when triggering with 1062 nm IR and 249 nm UV radiation of >3.75 J and 160 mJ, respectively.

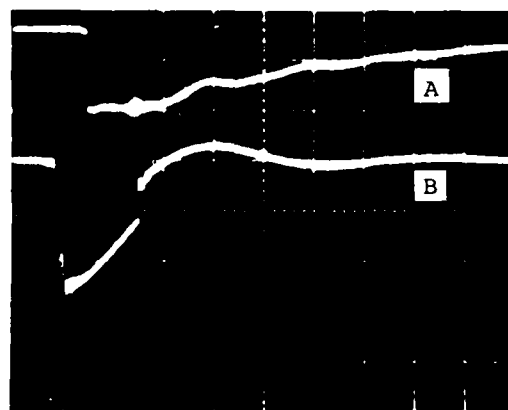
We have successfully triggered the crowbar switch after Marx erection before and after the first-zero-voltage crossing. The after-zero-crossing (positive switching) scheme was the one first tried and was used at SLS with electrical and IR-laser triggering. The present before-zero-crossing scheme (negative

switching) was initiated when the IR laser triggering of one crowbar was replaced by the UV laser.

The ideal crowbar switch is at zero volts on the crowbar. Lower average load current results with positive and negative switching because some energy is left in the Marx capacitors. The ideal crowbar switched voltage is shown in Fig. 8, trace B, which is the trace of the voltage across the crowbar monitored at point A in Fig. 1. The laser trigger occurred at 39% of $-V_{CBM}$, but the crowbar did not switch until 8% of $+V_{CBM}$ (positive switched). Presently we have the greatest reliability in crowbar switching at about 50% of V_{CBM} (negative switching) (Figs. 8B, trace B). At this level, we can still extract 86.6% of the current from the Marx (Fig. 1B) (1). The top trace, A, in Figs. 8A and 8B is the electrical trigger from the UV laser which references the UV laser pulse relative to the crowbar voltage, Trace B. The laser pulse occurs 0.94 μs after the negative-going pulse of trace A.



A



B

Fig. 8 - Laser trigger pulse and crowbar voltage waveform

Crowbars were triggered with both UV and IR radiation at different Marx voltages. The resulting time to establish the short in the crowbar relative to the time the laser trigger arrived in the crowbar (we called the delay) is plotted against the percent of maximum crowbar voltage at the time the laser trigger arrived at the crowbar gap in Fig. 9. The percentage of maximum crowbar voltage (V_{CBM}) was determined by considering the ratio D which is

$$D = (L_T + L_{CM} - L_M)/L_T, \quad (2)$$

where L_T is the Marx-load loop inductance, L_M is the Marx-crowbar loop inductance and L_{CM} is the crowbar inductance (0.5 μH). (L_T is 11.5 μH for one Marx in the north tank with the 165 nfd capacitors and 17.5 μH for one Marx in the south tank with the 88 nfd capacitors. L_M is nominally 2.4 μH per Marx.) V_{CBM} is then

$$V_{CBM} = D V_{MAX}, \quad (3)$$

where V_{MAX} is the maximum Marx voltage. The percentage of V_{CBM} is then a ratio of V_{CB}/V_{CBM} times 100, where V_{CB} is the voltage on the crowbar prior to shorting.

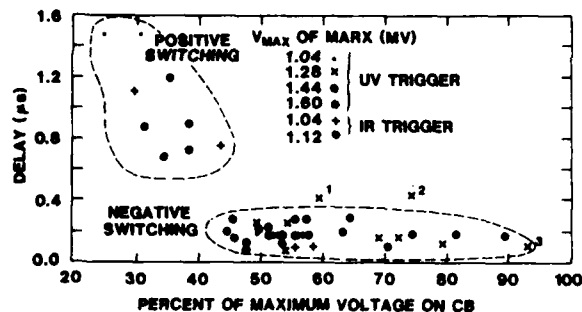


Fig. 9 - Delays in crowbar switching relative to percentage of V_{CBM} for UV and IR laser triggering

Two clusters of data points are apparent: one for negative switching and the other for positive switching. Negative switching occurred on a decreasing negative voltage across the gap while positive switching occurred on an increasing positive voltage. It appears easier to control the crowbar near zero volts during positive switching. The delays for negative switching varied from 0.08 to 0.28 μs while positive switching the delays varied from 0.68 to 1.4 μs . All the data in the cluster with negative switching resulted when the crowbar gap voltage was $>44\%$ of $-V_{CBM}$ at the time the laser radiation arrived in the gap,

while in the cluster with positive switching the crowbar gap voltage was $<44\%$ of V_{CBM} . The two smallest delays for positive switching occurred when the UV trigger arrived at the crowbar when the crowbar voltage was 39 and 35% of $-V_{CBM}$, but crowbarring did not occur until the crowbar voltage was 8 and 10% of $+V_{CBM}$ (positive switching) when V_{CBM} was 1.4 and 1.64 MV, respectively.

All the data switched with UV laser had 170 mJ of trigger energy. The data points 1, 2 and 3 in Fig. 9 were recorded with 85, 41 and 35 mJ of UV laser trigger energy into the crowbar instead of the 170 mJ normally used. At 59% of V_{CBM} (pt. 1) and 74% of V_{CBM} (pt. 2) the delay decreased with the increase in laser energy. At the higher 93% of V_{CBM} (point 3) the delay was comparable to the delays when the UV laser energy was 170 mJ or the power density was 1.04×10^{11} W/cm².

The delay plotted as a function of the percentage of crowbar self-break voltage is illustrated in Fig. 10. The percentage of self-break voltage was determined by considering the self-break pressure vs. Marx charge voltage curves of Fig. 7. The lines are extended to intersect with the value of pressure used in the crowbar. The Marx charge voltage corresponding to this pressure was multiplied by 16, the number of Marx capacitors in series, to obtain the self-break voltage (SBV). The percentage of SBV is the ratio of the voltage on the crowbar at switching to SBV $\times 100$.

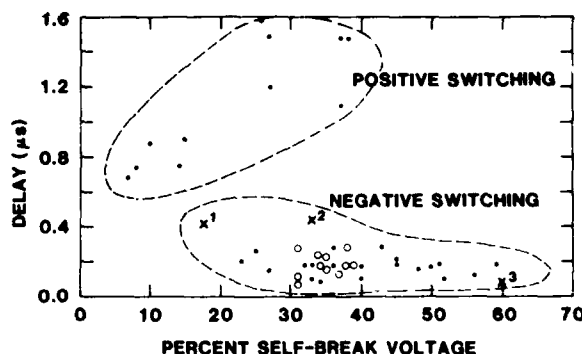


Fig. 10 - Delays in crowbar switching as a function of self-break voltage for UV and IR laser triggering

For negative switching, the crowbar switched at 23 to 68% of SBV. The trend is a decrease in delay with an increase in percent of SBV. For 27% of SBV the smallest delay of 0.15 μs occurred when the command to switch the crowbar was given at 40% of $-V_{CBM}$. Waiting until 36% of V_{CBM} the crowbar was not controlled until positive switching, and finally switched at 1.2 μs ($V_{CBM} = 1.0$ MV). For positive switching, the smallest delay of 0.68 μs occurred at 7% of SBV when V_{CBM} was +1.18 MV.

The delay increased to 1.48 μ s at 27 and 37% of SBV when V_{CBM} was +0.85 MV. For all the results with positive switching, the attempts to crowbar were made when the voltage of the gap was negative.

The 11 big open and black ties in Fig. 10 are for UV triggering the north and south Marx with ~255 kA and ~125 kA load currents, respectively. The larger delays recorded for crowbar switching the south tank over the north tank for 31 to 37% of SBV could be caused by the larger distance between L_2 and the UV laser (24.6 m) than between L_1 and the UV laser (9.5 m). We have observed that a 3-mm displacement of the laser beam quenched the crowbar action in the north tank when the laser energy was 41 mJ.

At 33% of SBV the delay decreased with increasing laser trigger energy (compare point 2 to the other points in negative switching). At the higher 60% of SBV (point 3) the delay was comparable or less than the delays when the laser trigger energy was 170 mJ. The laser energy was 85, 41 and 35 mJ for points 1, 2, and 3, respectively.

We have successfully triggered a 165-nF Marx generator charged to 1.6 MV with as little as 35 mJ of 249 nm UV laser energy or a power density of 2.2×10^{10} W/cm². Normally we used 160-170 mJ or about 1.04×10^{11} W/cm², which is about one-half the energy or power density available from the EMG 150. At this time, we do not know the relation of power density as a function of delay in switching, but we expect that the crowbar delay will decrease with increasing laser energy or power density.

Electrode Conditions -- At SLS we have had concerns about crowbarring 200-kA load currents with one crowbar. The erratic behavior of the crowbar, when switching large currents with IR triggering, was presumed to be related to electrode roughness; however, improper optical alignment, laser energy and gas purging could be responsible. Figs. 11 and 12 show the condition of two types of electrodes, stainless steel with K25* inserts of 5.0-cm diameter (Figs. 11A and 11B) and solid K25 electrodes (Figs. 11C and 11D and Figs. 12A-12D). The hole in the positive grounded electrode, through which the laser beam passed, was nominally 1.1 cm in diameter. The stainless steel electrodes with K25 inserts (Figs. 11A-11B) have many self-breaks, as is evident from the roughened surface spots located away from the center of the electrode. For electrodes which experienced only laser-controlled breakdown, these

roughened spots are missing (see Figs. 12A-12D). The roughened spots are more pronounced for the stainless steel electrodes with K25 inserts than for the solid K25 (compare Figs. 11A and 11B to 11C and 11D, which also had self-breaks). The choice of a 5.0-cm diameter K25 insert was unfortunate in that there is apparent high current or field densities out to about 5.0 cm for the solid K25 (Figs. 11C, 11D, 12A-12D). Therefore, the boundary created by the insert could have well affected crowbar performance by creating high field gradients. The stainless steel electrodes with K25 inserts of Figs. 11A and 11B and the K25 electrode of Figs. 11C and 11D were triggered by the IR laser with up to 4.0 J of energy by a 20 ns pulse (3.4×10^{11} W/cm²). For the K25 electrode in Figs. 11C and 11D, 70 of the 159 shots crowbarred 100 kA, 130 to 180 μ s pulse width current pulses with about 17 coulombs of charge; 19 shots crowbarred 50 kA, 50 μ s pulse width current pulses with about 3.4 coulombs, and 70 shots crowbarred 100 kA, about 150 μ s pulse width current pulses with about 17 coulombs of charge. The last 70 shots were triggered by about 160 mJ of UV radiation, while the rest of the shots were triggered by up to 4 J of IR radiation. The different current pulse widths were caused by the different impedance load (L_L/R_L ratio). Even at these relatively low current pulses with small charge, there is evidence of glazing and cracking on the surface of the charged cathode electrode (Fig. 11D).

The K25 electrodes photographed in Figs. 12A and 12B crowbarred 47 current pulses of >200 kA amplitude 140 to 165 μ s pulse widths, and containing between 33 to 47 coulombs of charge (depending upon the load L_L/R_L ratio). Similarly, the electrodes illustrated in Figs. 12C and 12D crowbarred 37 current pulses containing >200 kA amplitude, (<6 shots had pulse widths of 420 μ s and contained 74 coulombs of charge); the rest had 150 to 210 μ s pulse widths and contained 33 to 46 coulombs. Neither of these electrodes show any cracking. Both of these pairs of electrodes received about a third fewer shots than the pair of electrodes that exhibited the cracking, (see Fig. 11D). These two pairs of electrodes did, however, receive at least twice the charge as the pair in Fig. 11D. The electrodes of Fig. 12A and 12B were triggered by about 170 mJ or 1.04×10^{11} W/cm² of UV radiation per trigger, while those illustrated in Fig. 12C-12D were triggered by about 35 mJ or 2.2×10^{11} W/cm² of UV radiation per trigger for most of their 37 shots. We believe that both pairs of electrodes (Figs. 12A-12D) could be reused for satisfactory crowbar operation.

* K25 is 25% copper and 75% tungsten composite made by compacting and sintering tungsten powder into a porous skeleton, which is then infiltrated with molten copper.

New Developments -- Recently we at SNLA have put the Lambda Physik model EMG 150 ES KRF laser on line. With this laser emitting one-fourth of its energy into each of two



A



B



C



D

Fig. 11 - Condition of crowbar electrodes switched by IR triggering

crowbars, we have operated the entire SLS system and switched nearly 200-kA and 100-kA pulses spaced 30 ms apart. This experience has demonstrated that we have sufficient energy to operate four crowbars using the EMG 150 ES. If we could crowbar two switches in one Marx tank we could provide up to four current pulses from the two Marx tanks, two for each tank.

CONCLUSIONS

We have successfully adapted the technique of UV laser-triggered switching of crowbar

laser triggering of crowbars at small percentages of self-break voltage. The same basic crowbar switch has been used in electrical, IR and UV triggering. Two crowbars have been triggered 30 ms apart using UV and IR triggering and using UV triggering from one UV laser source. Changing from IR ($\lambda = 1062$ nm) to UV ($\lambda = 249$ nm) laser radiation triggering allowed us to reduce the crowbar from ≤ 250 psig (50.3%-N₂, 40.6%-Ar and 9.1%-SF₆ mixture) to ≤ 105 psig (SF₆) while reducing the gap from 9.5 to 5.0 cm. When we used 170 mJ or 1.04×10^{11} W/cm² of UV radiation, which was at least 2 times more energy or power

ACKNOWLEDGMENTS

We thank Roger J. Goode for supporting the laser, optics and electronic instrumentation. We acknowledge technical discussions with Robert A. White, Jim C. Bushnell, and Joe G. Kostas on many aspects of our results. We are indebted to Robert L. Hughes for the optic design of the crowbar optics. Test support by W. B. Vandermolten is greatly appreciated.

REFERENCES

1. F. W. Neilson, "An Extreme Lightning Test Facility," unpublished internal report, Sandia National Laboratories, 1977.
2. J. C. Bushnell and J. G. Kostas, "The Sandia Lightning Simulator," Eighth International Aerospace and Ground Conference on Lightning and Static Electricity, Fort Worth, TX, June 21-23, 1983, p. 64-1.
3. Robert A. White, "Full-System Testing Using the Sandia Lightning Simulator," Eighth International Aerospace and Ground Conference on Lightning and Static Electricity, Fort Worth, TX, June 21-23, 1983.
4. Ronald I. Ewing, "Performance of the Sandia Lightning Simulator During F-14A and F/A-18 Aircraft Lightning Test," Eight International Aerospace and Ground Conference on Lightning and Static Electricity, Fort Worth, TX, June 21-23, 1983, p. 73-1.
5. R. A. White, "Lightning Simulator Circuit Parameters and Performance for Severe-Threat, High-Action-Integral Testing," 1984 International Conference on Lightning and Static Electricity, Orlando, FL, June 26-28, 1984.
6. R. L. Parker, "Feasibility Studies for Crowbarring One Megavolt on the LILI Facility," Sandia Laboratories, SAND78-1700, April 1979.
7. A. H. Guenther and J. R. Bettis, "The Laser Triggering of High-Voltage Switches," J. Phys. D: Appl. Phys., 11, 1577-1613 (1978).
8. Winston K. Pendleton and Arthur H. Guenther, "Investigation of a Laser Triggered Spark Gap," Rev. of Sci. Instrum., 36, 1546-1550 (November 1965).
9. Arthur H. Guenther and Jerry R. Bettis, "Laser-Triggered Megavolt Switching," IEEE J. of Quantum Electron., QE3, 581-588 (November 1967).
10. Jerry Ray Bettis and Arthur H. Guenther, "Subnanosecond-Jitter Laser-Triggered Switching at Moderate Repetition Rates," IEEE J. of Quantum Electron., QE-6, 483-491 (August 1970).
11. D. M. Strickland, J. R. Bettis, and A. H. Guenther, "Low Power Laser-Triggered Switching at Voltage 500 kV," Rev. Sci. Instrum. 44, 1121-1122 (August 1973).
12. J. J. Moriarity and H. Milde, "Laser-Triggered Switching Study," Contract F-29601-C-0001, Ion Physics Corp. (1969).
13. L. P. Bradley and T. J. Davies, "Laser-controlled Switching," IEEE J. of Quantum Electron., QE7, 464 (September 1971).
14. L. P. Bradley, "Preionization of Streamer Propagation," J. Appl. Phys. 43, 866-890 (March 1972).
15. W. R. Rapoport, J. Goldnar and J. R. Murray, "KrF Laser-triggered SF₆ Spark Gap for Low Jitter Timing," IEEE Trans. on Plasma Science, PS-8 167 (1980).
16. J. R. Woodworth, C. A. Frost and T. A. Green, "UV Laser Triggering of High-Voltage Gas Switches," J. Appl. Phys., 53, 4734-4739, July 1982.
17. J. R. Woodworth, R. G. Adams, and C. A. Frost, "UV-Laser Triggering of 2.8-Megavolt Gas Switches," IEEE Trans. of Plasma Science, PS10, 257-261, December 1982.
18. T. H. Martin, G. W. Barr, J. B. VanDevender, R. A. White, and D. L. Johnson, "Pulsed Power Accelerators for Particle Beam Fusion," Proc. 14th Pulse Power Modulator Symposium, p. 300, June 1980.
19. R. G. Adams, D. L. Smith, and J. R. Woodworth, "Simultaneous Ultraviolet Laser Triggering of Two Multimegavolt Gas Switches," Appl. Phys. Lett., 43, 163-165 (July 1983).
20. R. G. Adams, W. B. Moore, J. R. Woodworth, M. M. Dillon, F. Morgan, K. J. Penn, "Ultraviolet Laser Triggering of a 5 Megavolt Multistage Gas Switch," Proc. 4th Pulsed Conference, Albuquerque, NM, June 1983.
21. H. W. Mathers, S. R. Sedore, and J. R. Sents, "SCEPTRE Support," IBM Corp., Contract F29601-67-C-0049 for AFWL, Kirtland AFB, NM, April 1968.
22. H. W. Mathers, "SCEPTRE (System for Circuit Evaluation and Prediction of Transient Radiation Effects)," IBM Corp., included in G. W. Sobrist, "Network Computer Analysis," Boston Technical Publisher, 1969.
23. L. G. Christophorou, D. R. James, and R. Y. Pai, "High Voltage Research (Breakdown Strengths of Gaseous and Liquid Insulators) and Environmental Effects of Dielectric Gases," Semiannual Report ORNL/TM-7624, April 1-September 30, 1980, p. 112.

FRICTIONAL ELECTRIFICATION OF ICE AND SNOW

Hisashi Shio

Department of Physics,
Hokkaido University of Education
Iwamizawa, Hokkaido, Japan

In order to understand the mechanism about many solid precipitation particles charging in the process of up-down drifting in thunderclouds, the author made investigation in to an effect of hardness on the charging of ice by rubbing between the pairs of ice cubes the following facts were obtained:

Anisotropy of Properties	Combination of Specimens with anisotropic hardness	
	Hard Surface	Soft Surface
Temperature	Cold Surface	Hot Surface
Crystallization	Surface with Prism plane	Surface with Basal plane
	Surface with Recrystallizing	Surface with Single crystal
Sign of Charge	(+)	(-)

It was concluded that the dependency of the sign of charge upon the temperature difference on the crystallographic anisotropy is explained by the difference in scratch hardness between the rubbed surfaces of the pairs of specimens. Namely, concerning the rubbing between pairs of contact surfaces of difference hardness and since the rubbed surface with the softer spot may be deformed plastically to a higher degree than that with the harder spot. As a result, the softer surface may degenerate into an abnormal layer in which an excess dislocation occurs during rubbing, and a part of this dislocation may be separated into a dislocation-jog which is charged negatively and H_3O^+ . Moreover, H_3O^+ may be moved more readily from softer surface to harder surface than the dislocation-jog owing to the mobility of H_3O^+ which is greater than that of dislocation-jog. As a result, the harder surface is positively electrified against the softer surface.

This paper was not available for incorporation into this book.

MODELING LIGHTNING GENERATION MECHANISMS

John S. Nisbet

Communications and Space Sciences Laboratory
Department of Electrical Engineering
The Pennsylvania State University
University Park, Pa 16802.

ABSTRACT

In understanding the generation of lightning it is important to be able to relate external measurements to the magnitudes of the active centers where the charge build-up is occurring.

The relations between the divergences of the current systems in a thundercloud and the build up of the active centers at which lightning strokes are initiated are discussed. Boundary layers of charge arise when currents cross conductivity gradients at the edges of clouds and between the cloud and the ground and their relation to the measurements is examined.

Divergences in current systems result from the differences in transport properties of the positive and negative charge carriers, namely the differences in charge which affect their behavior in electric and magnetic fields, in mass which affects their behavior under acceleration and in the earth's gravitational field, in mobility which affects the behavior in electric fields, in ionizability which affect their charge, and in size which affects their resistance to motion in the surrounding air. The build up of charge centers is discussed in terms of the rates of generation or destruction of charge carriers of differing transport properties and of the relative importance of the various mechanisms to their subsequent behavior in the force fields in and below the cloud.

INTRODUCTION

UNDERSTANDING THE MECHANISMS FOR GENERATING ELECTRICITY IN THUNDERCLOUDS is important for the early prediction of the dangers of lightning and is of considerable intrinsic scientific interest. Despite extensive studies over the past hundred years, there is still no consensus for the mechanisms by which a given thundercloud has been electrified.

The present paper will discuss some of the considerations affecting the buildup of the active charge centers, namely, the generation and destruction of charge carriers of different transport properties and of the relation of these to the subsequent motions and the divergences in the current systems. These will then be used to discuss the measurements necessary to determine the important physical variables affecting the generation of electrical energy in a given storm.

MAXWELL CURRENT STREAMLINES, ACTIVE CENTERS, AND SHIELDING LAYERS

The Maxwell current is the sum of the current due to physical charge transport and the displacement current and is given by,

$$\underline{J}_M = \underline{J}_P + \underline{J}_{cv} + \underline{J}_L + \underline{J}_C + \epsilon \frac{d\underline{E}}{dt} = \text{Curl } \underline{H} \quad (1)$$

where \underline{J}_M is the Maxwell current density
 \underline{J}_P is the precipitation current density
 \underline{J}_{cv} is the convection current density
 \underline{J}_L is the lightning current density
 \underline{J}_C is the conduction current density
 \underline{E} is the electric field strength
 ϵ is the permittivity
 and \underline{H} is the magnetic field density

The divergence of the Maxwell current density and the integral of its normal component over any closed surface are zero, since it is representable by the curl of a vector field.

The electric field is related to the charge Q by the Maxwell equation,

$$Q = \epsilon \int_S \underline{E} \cdot d\underline{s} \quad (2)$$

where Q is the charge bounded by the surface and $d\underline{s}$ is the incremental surface area vector. The conduction current density, \underline{J}_C , is given by

$$\underline{J}_C = \sigma \underline{E} \quad (3)$$

where σ is the conductivity, so that

$$Q = \int_S \underline{J}_C (\epsilon / \sigma) \cdot d\underline{s} \quad (4)$$

Now if $\overline{\epsilon / \sigma} = \bar{T}$ is the weighted average relaxation time constant of the atmosphere over a surface surrounding the charge Q , then integrating equation (1) over such a surface gives, with equations (2), (3), and (4),

$$-(I_P + I_{cv}) = \frac{Q}{\bar{T}} + \frac{dQ}{dt} + I_L \quad (5)$$

where all currents out of the volume are defined as positive. What are important in lightning generation are the active charge centers where the processes resulting in the electrification are operating. In these the charges, and hence the electric fields, build up until breakdown occurs. During the buildup phase with $I_L = 0$, all terms on the right side of equation (5) are of the same sign as the charge. Net driving currents into positive charge centers and out of negative charge centers are thus necessary if lightning and electrical activity are to be sustained. It is the determination of these currents that is of primary interest in understanding thunderstorm electrification mechanisms. Since the total normal Maxwell current integrated over any closed surface is zero, this implies a positive displacement current out of positive and into negative growing charge centers.

In an inactive charge center with all driving currents zero,

$$\frac{dQ}{dt} = - \frac{Q}{\bar{T}} \quad (6)$$

Such inactive centers are produced, for example, when the lighter ions left behind by the precipitation particles are convected away from the region of charge separation. Lightning strokes produce very large divergences in the current density because of their small diameters and large currents so that the resulting charge irregularities are correspondingly large. The velocities in a thundercloud are large so that these charge irregularities can be moved from their point of origin by significant distances before they recombine. The conditions which led to the original divergence in the current density may then no longer be present so that the charge center becomes inactive. Though large electric fields may be produced locally, these centers are largely irrelevant to the processes producing the storm electrification.

Measurements of the Maxwell currents external to the thundercloud can serve to discriminate the currents into each of the active centers in the cloud. Figure 1 shows the streamlines of the Maxwell currents for three ratios of the currents into the upper and lower active center of the cloud. On the ground the three can be very easily discriminated one from another by Maxwell current measurements if the current in the channel under the cloud is measured.

While the Maxwell currents provide the best measurement from which the currents into the active centers can be determined, electric field measurements may be easier to make around the cloud, and the ratio of cloud-to-ground strokes to top-to-bottom charge transfer is one of the more simple measurements to make.

Figure 2 shows the potential contours for six ratios of the current I_P below the cloud to I_C in the cloud. The model simulations are at

times when electrical breakdown was occurring at the lower charge center. It is apparent that only in the cases where I_p/I_C was either approximately zero or one are the electric fields below the lower charge center comparable in intensity to those in the cloud. In cases when the magnitude of the current into the lower active center is small, the electric fields below the cloud would be small, and cloud-to-ground strokes very difficult to produce.

The electric fields and charge distributions in a thunderstorm are, in general, very complex. When currents cross conductivity gradients, such as exist at the boundary of a cloud, dynamic charge distributions arise to maintain the Maxwell current. The normal component of the Maxwell current J_M is continuous across a conductivity gradient. In the simple static case $J_M = J_C$,

$$\int_1^2 \rho_v dx = 6 J_C (1/\sigma_2 - 1/\sigma_1) \quad (7)$$

where,

ρ_v is the charge density in the boundary layer. Though these so-called "shielding layers" greatly affect the electric fields, their influence on the the streamline pattern of the Maxwell currents is likely to be minimal as long as the voltage across them is small compared to the cloud-to-ground voltage. They do produce layers of negative charge at the cloud surface where the conduction current is outwards and layers of positive charge where the current is inwards because the conductivity is lower inside than outside the cloud. A second region where there is a conductivity gradient is at the earth's surface where a layer of shielding charge extends above the ground for a few hundred meters below the cloud. Notable among recent studies of the layer is the theoretical work of Willett [1979] and the measurements of Standler and Winn [1979], Standler [1980], Winn et al. [1983], and Chauzy and Raizonville [1983]. Figure 3 shows the relations of these boundary charge layers to the Maxwell current streamlines.

Any theory of cloud electrification must be able to explain the location and magnitudes of the upper and lower regions of current divergence in the cloud. The shielding layers around the cloud and at the conductivity gradients caused by the exchange layer and coronal ions are products of the major cloud electrification systems and are secondary to them.

THEORIES FOR ELECTRICAL GENERATION MECHANISMS

It is apparent from the considerations in Section 2 that to produce active centers at which lightning activity can be initiated requires the divergence of a current system. This in turn requires the generation or destruction of positive and negative charge

carriers of different transport properties and a force field which can cause them to be moved in a manner that will produce the divergence in the current system at the active centers.

The difference of the polarities of the positive and negative charges alone is sufficient to cause relative motion between them in electric or magnetic fields. Motion of charge carriers in magnetic fields is the major system used in the commercial generation of electricity; however, the magnetic field of the earth and the wind velocities in a thundercloud are too small to make a sensible contribution to the electric field. In cases when a current flows across a conductivity gradient, the electric field changes and a space charge layer is established. In the limiting case the sum of the potentials across all of the shielding layers in series cannot exceed the potential of the major charge center causing the Maxwell current system in the first place, so such shielding layers are not generally of primary importance.

The convection field around a thunderstorm is inwards and upwards, and so ions from the shielding layer at the ground are convected into the cloud. This has been proposed by Grenet [1947] and Vonnegut [1953] as a cloud electrification mechanism. Initially there is a divergence of the current at the front of the column that will charge the cloud as it enters it. Subsequently the rate of charging depends on the interactions of the charged particles with the cloud. If they merely recombine with charged particles of opposite sign at the top of the cloud, a conduction current will be set up that will continue the convection current, and no current divergence may result. If, however, they diffuse across a shear gradient and charge exchange with particles of different velocity, then charge buildup can occur.

The convective field around a thundercloud is complicated, and large shear gradients occur associated with gradients in particles of different masses, mobilities, and electron affinities. The interaction of the current systems and the conductivity gradients provides a source of charged ions, the wind system the energy to move them against the electric fields, and the regions of wind velocity shear the opportunity to produce the current divergences.

Precipitation mechanisms provide simultaneously for the charge separation and the current divergence. They rely on the precipitation particles being ionized with predominantly one polarity. Because these particles are heavier than the ions carrying the reversed polarity, they fall with respect to them, creating a divergence in the current in the region in which the heavy particles are ionized. If the precipitation particles fall to ground at a uniform velocity and with the same charge, then only one active charge center will result. If, however, as is more common, the velocity or the charge changes, other regions of

current divergence and consequently other active regions are produced. In particular it appears that the current carried by the precipitation in the cloud is much larger in magnitude than that below the cloud, and frequently of the reverse polarity. In this case the streamlines of the Maxwell current resemble those of Figure 1(c).

Thunderclouds contain large updrafts and downdrafts, and it is important to remember that the rate of descent of the precipitation in fixed coordinates may be very different from its rate of descent with respect to the surrounding air. The electrical energy generation rate is given by the product of the current and the voltage, i.e., it is related to the motion of the particles with respect to the earth. The mechanical work being done on the particles is dependent on the velocity with respect to the surrounding air and is greatly enhanced in the presence of updrafts.

MAGNITUDES AND MECHANISMS

Any explanation of the mechanisms of thundercloud electrification must be based on an understanding of the magnitudes of the generator currents and of the regions in which the divergences occur. Figure 4 shows the Maxwell current streamlines for the charging current, a cloud-ground discharge, and a top-bottom discharge. True Maxwell current measurements on the ground from an adequate network should provide the required information.

A lower bound for the generator currents is given by the rate of charge transport by lightning. To this must be added the conduction and convection currents out of the active centers. There remains some uncertainty about these because of the uncertainty about the conductivity in the cloud and about the relation of the wind fields to the charge density distribution. Jacobson and Krider [1976] have described the charge transfer in a number of Florida thunderstorms derived from a network of 23 field mills around the Kennedy Space Flight Center. "Medium storms usually began with discharges occurring at a rate of about 1 per minute for 10 to 20 minutes and the activity increased abruptly to about 7 discharges per minute in a five minute interval." They found that ground discharges usually neutralized 10-40 C of negative charge, in agreement with similar studies at other locations around the world.

The above figures would give lower bounds for the generator current ranging from about 0.3 to 3 A. Most of the charges were located from 6 km to 9.5 km where the time constant of the atmosphere outside the cloud is from 15 to 30 seconds based on the measurements of Kraakevik [1958a,b] and Markson et al. [1981]. Nisbet [1983] has discussed the relationship between the ratio of the time between lightning discharges to the electrical time constant at the charge height, t_g/T , and the ratio of the generator current to the minimum current that would just produce breakdown, I_G/I_0 . Using

these relations and assuming that 25% of the charge is removed by each discharge would lead to the conclusion that when the time between strokes was about 7 per minute, about 60 to 75% of the charge would flow in lightning currents, resulting in an estimated generator current of 4 to 5 A. At the lower charge rates the fraction of the charge that flows as conduction currents is much larger and the uncertainty correspondingly larger. A rough estimate based on the above figures leads to an estimate of 5 to 10 times the charge lowered by lightning or about 1.5 to 3 A. This range of from 1.5 to 5 A seems to be quite consistent with a number of model studies we have carried out in attempts to reproduce current density measurements above clouds such as those of Gish and Wait [1950] and Stergis et al. [1957], as well as the Maxwell current measurements of Krider and Musser [1982].

Without understanding the mechanism for producing the divergence of the current, much guesswork must be involved in estimating the size of the region involved. Measurements in storms commonly show charge densities of the order of 10^{-8} Cm^{-3} , and total charges associated with the storms discussed above are probably of the order of 100 C to give an estimated volume of the order of 10^{10} m^3 . Considering the sizes of the clouds involved, the volume could probably not be an order of magnitude larger than this, though it would be difficult to rule out smaller estimates. We may take as reasonable lower bounds for the required charge separation rate $0.15 \text{ to } 5 \text{ nCm}^{-3}\text{s}^{-1}$ over this volume. For accurate comparisons current density measurements coupled with in-situ sampling of the charge densities, particle distributions and wind systems are required. For comparison purposes the microphysical models of Tzur and Levin [1981] gave maximum rates of $0.6 \text{ nCm}^{-3}\text{s}^{-1}$ in warm clouds by the polarization charging of drops, and in a cold cloud model calculated maximum rates of $.07 \text{ nCm}^{-3}\text{s}^{-1}$ for the Workman-Reynolds effect and $.06 \text{ nCm}^{-3}\text{s}^{-1}$ for collisions between drops and ice.

The maximum currents producible by convection mechanisms may be estimated by multiplying maximum measured charge densities by corresponding velocities and areas. Standler and Winn [1979] have shown that the charge densities in the space charge layer under similar thunderstorms to those described by Jacobson and Krider [1976] are of the order of 1 nCm^{-3} . If we take a vertical velocity of 10 ms^{-1} over an area of 10^7 m^2 , then the current into the cloud could be as large as 0.1 A. As fair weather charge densities are considerably smaller, convection currents prior to the buildup of charge in the storm are probably at least an order of magnitude smaller than this. It does not seem that convection currents from the surface charge layer can make a major contribution to the generator current in the active phase of a storm. Similar considerations

apply to other convection current systems that have been proposed involving shielding layers of charge around the cloud.

A further problem with such mechanisms is the difficulty in producing the current density divergence necessary to build up the charge and electric field. Vonnegut et al. [1962] conducted experiments in which a space charge boundary layer of either sign could be produced below cumulus clouds. Their measurements indicated that a major portion of the convection current entering the bottom of a cloud left as a conduction current at the top and that the charge density in the cloud did not build up with time. These considerations do not, however, preclude the convection currents from playing a role in initiating electrification.

CONCLUSIONS

Understanding the temporal behavior of different types of thunderstorms is crucial to being able to make predictions about their development. The measurement of the current system on the ground and around the cloud is the key to this understanding.

It has been shown that whereas the electric field measurements are extremely sensitive to conductivity gradients and convective fields, the Maxwell current densities are continuous, divergenceless, and little affected by shielding layers at the earth. The generator current for storms where the time between lightning breakdowns is small compared with the electrical time constant of the undisturbed atmosphere at the height of the charge center can be estimated quite accurately from the charges transferred by lightning. When the times between lightning breakdowns are much longer, this procedure is much less reliable; however, they can still be calculated from Maxwell current measurements on the ground below the cloud. It is readily seen that such current measurements place serious restrictions on possible mechanisms for cloud electrification.

ACKNOWLEDGEMENTS

This research was supported by NASA under grant NSG-134-61 and by the National Science Foundation under grant ATM-8311993.

REFERENCES

- Chauzy, S. and P. Raizonville, 1983: Electrostatic Screening Below Thunderstorms Due to Coronae at Ground Level, in Proceedings in Atmospheric Electricity, edited by L. H. Ruhnke, pp. 184-188, A. Deepak Publishing, Hampton, Virginia.
- Gish, O. H., and G. R. Wait, 1950: Thunderstorms and the earth's general electrification, J. Geophys. Res., 55, 473-484.
- Grenet, G., 1947: Essai d'explication de la charge électrique des nuages d'orages, Extrait Annls. Geophys. 3, 306-307.
- Jacobson, E. A., and E. P. Krider, 1976: Electrostatic field changes produced by Florida lightning, J. Atmos. Sci., 33, 103-117.
- Kraakevik, J. H., 1958: Electrical conduction and convection currents in the troposphere, Recent Advances in Atmospheric Electricity, 75-88.
- Kraakevik, J. H., 1958: The Airborne Measurement of Atmospheric Conductivity, J. Geophys. Res., 63, 161-169.
- Krider, E. P., and J. A. Musser, 1982: Maxwell currents under thunderstorms, J. Geophys. Res., 87, 11,171-11,176.
- Markson, R., J. Sedlacek, and C. W. Fairall, 1981: Turbulent transport of electric charge in the marine atmospheric boundary layer, J. Geophys. Res., 86, 12,115-12,121.
- Nisbet, J. S., 1983: A dynamic model of thundercloud electric fields, J. Atmos. Sci. 40, 2855-2873.
- Standler, R. B., and W. P. Winn, 1979: Effects of coronae on electric fields beneath thunderclouds, Q. J. R. Met. Soc., 105, 285-302.
- Standler, R. B., 1980: Estimation of corona current beneath thunderclouds, J. Geophys. Res., 85, 4541-4544.
- Stergis, C. G., G. C. Rein, and T. Kangas, 1957: Electric field measurements above thunderstorms, J. Atmos. Terr. Phys., 11, 83-90.
- Tzur, I., and Z. Levin, 1981: Ions and precipitation charging in warm and cold clouds as simulated in one-dimensional time-dependent models, J. Atmos. Sci., 18, 2444-2461.
- Vonnegut, B., 1953: Possible mechanism for the formation of thunderstorm electricity, Bull. Am. Met. Soc. 34, 378.
- Vonnegut, B., C. B. Moore, R. G. Semonin, J. W. Bullock, D. W. Staggs, and W. E. Bradley, 1962: Effect of atmospheric space charge on initial electrification of cumulus clouds, J. Geophys. Res., 67, 3909-3922.
- Winn, W. P., R. B. Standler, C. B. Moore, C. R. Holmes, and L. G. Byerley, III, 1983: Electric structure of New Mexico thunderstorms from balloon-borne instruments, in Proceedings in Atmospheric Electricity, edited by J. Latham, pp. 285-289, A. Deepak Publishing, Hampton, Virginia.
- Willett, J. C., 1979: Fair weather electric charge transfer by convection in an unstable planetary boundary layer, J. Geophys. Res., 84, 703-718.

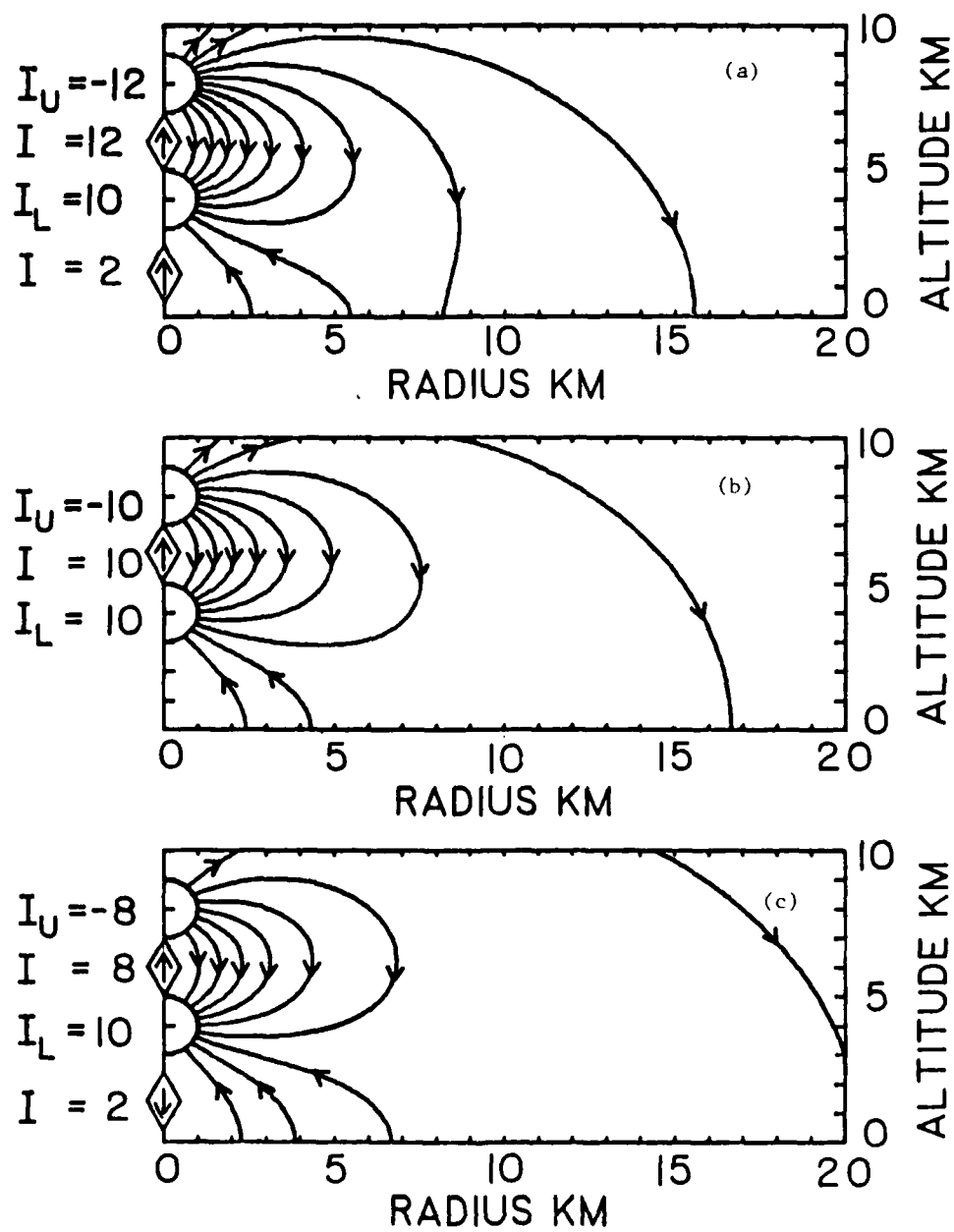


Fig. 1 - Stream lines of Maxwell currents for three ratios of currents to upper and lower charge centers

CONTOUR INTERVAL 50 MV

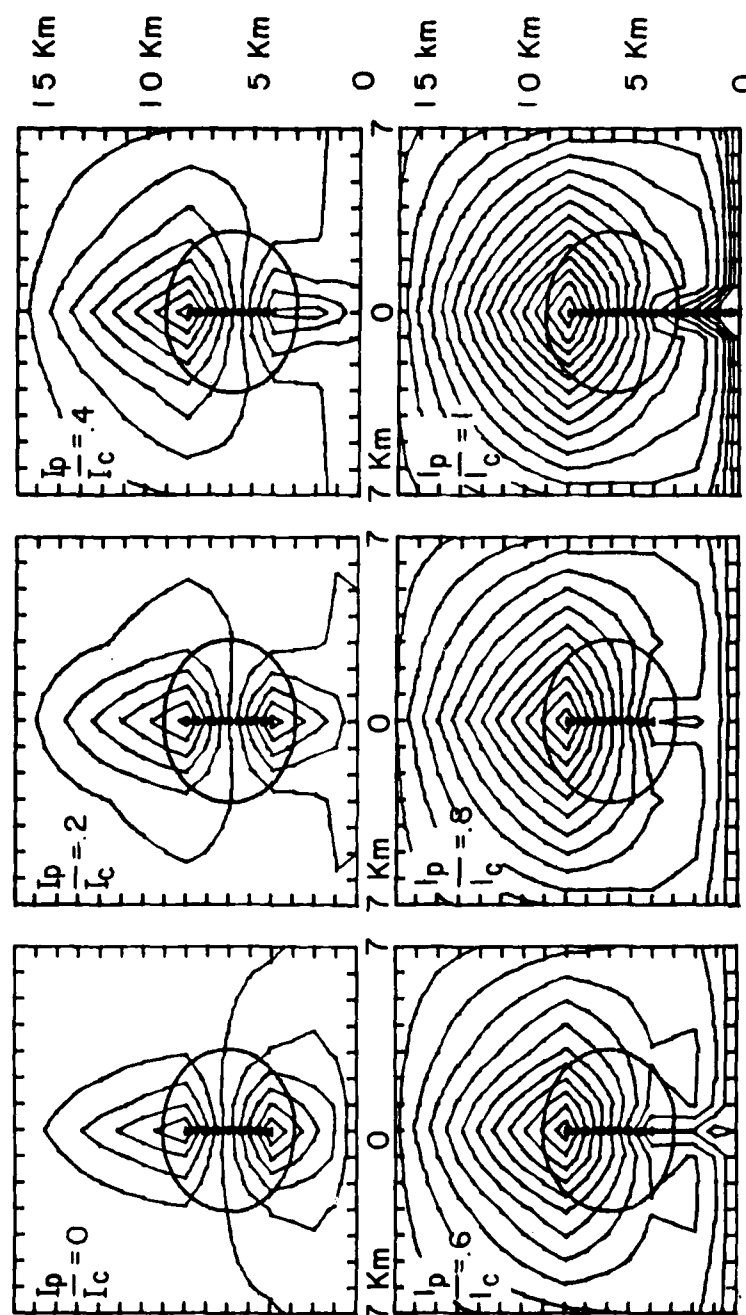


Fig. 2 - Potential contours for six ratios of current I_p below the cloud to the current I_c in the cloud

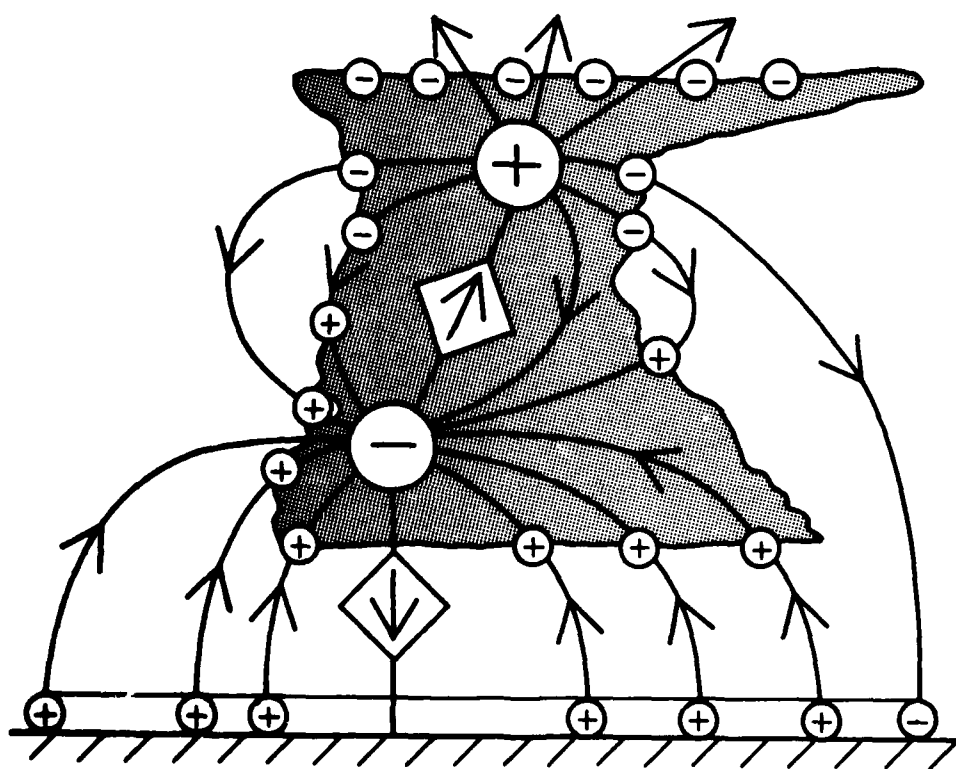


Fig. 3 - Relation of boundary charge layers to the Maxwell currents

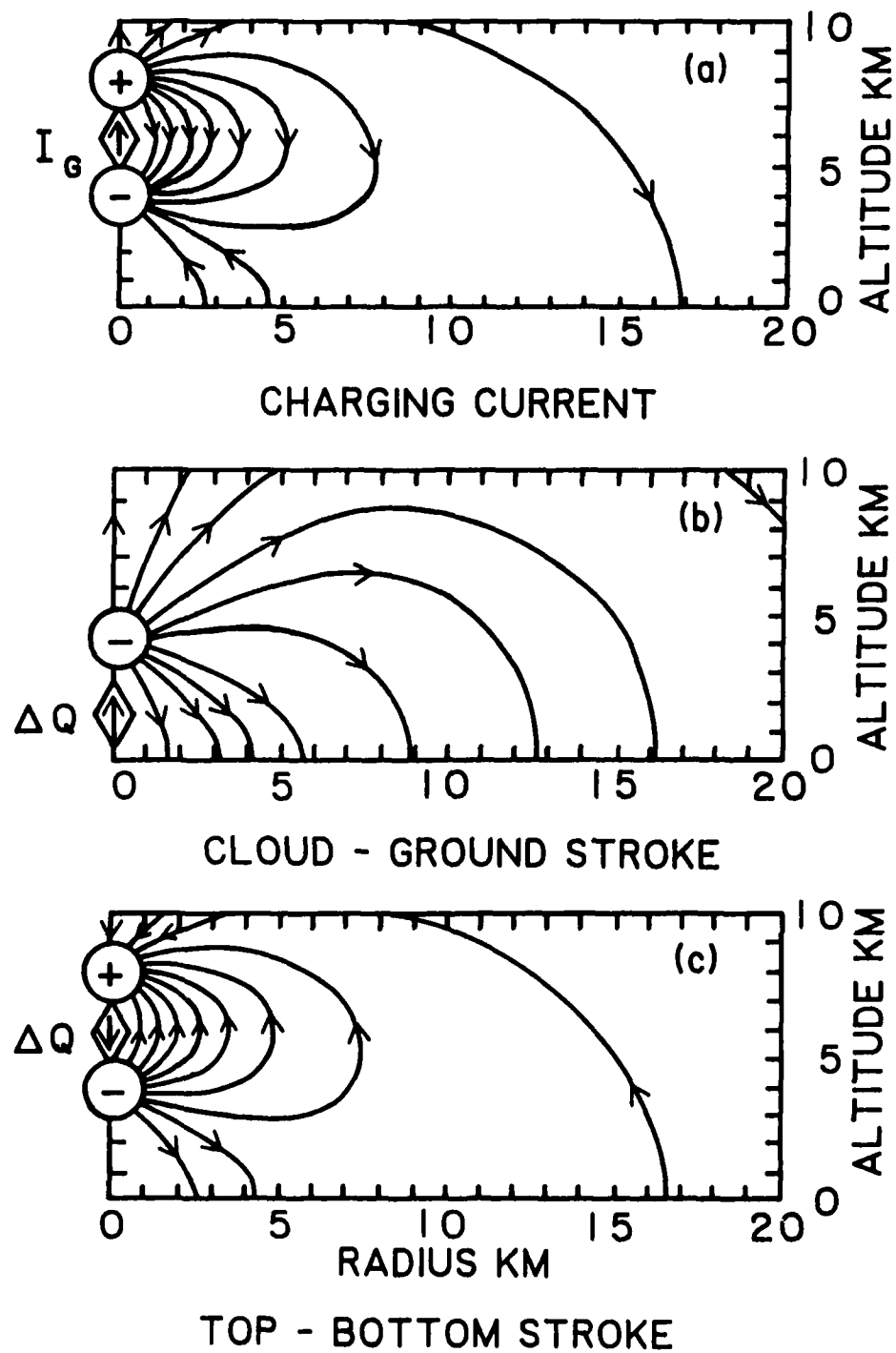


Fig. 4 - Maxwell current density streamlines for the charging current, a cloud-ground stroke, and a top-bottom stroke

STATIC CHARGING OF DIFFERENT METALS BY ICE CRYSTALS

+J. M. Caranti, *A. J. Illingworth and *S. J. Marsh

*Physics Department; UMIST, Manchester M60 1QD, England

+IMAF, Cordoba, 5000, Argentina

ABSTRACT

It is known that aircraft usually charge negatively when they fly through clouds. We report laboratory experiments which show that for speeds of up to 80ms^{-1} small ice particles charge most metal targets negatively, but that magnesium acquires a positive charge. The charge transfer was found to be proportional to the impact velocity and to the square of the size of the ice particle. It appears that the charging is controlled by the work function of the metal.

INTRODUCTION

AIRCRAFT GENERALLY ACQUIRE negative charge when they fly through clouds, as a result of the triboelectric or frictional charging occurring when water or ice particles in the cloud collide with the aircraft surface. Effort in the past has been directed towards characterising the currents expected in different meteorological conditions, and then designing an efficient method of discharging the aircraft. However, modern aircraft constructed from composite materials may have different charging properties from conventional ones, and, furthermore, any interference in modern digital control systems is potentially more hazardous than for the traditional analogue methods.

Tanner (1) has reported current densities for aircraft to be in the range $50\text{--}100\ \mu\text{A}\cdot\text{m}^{-2}$ for cirrus clouds, $100\text{--}200\ \mu\text{A}\cdot\text{m}^{-2}$ for stratocumulus, and $300\ \mu\text{A}\cdot\text{m}^{-2}$ for snow. Boulay and Laroche (2) measured the current to probes covered with conducting paint on a Meteor aircraft flying at $200\ \text{ms}^{-1}$, and confirmed these values. They estimated that the overall capturing area of the aircraft was about 8m^2 , and calculated the maximum charging current to be 3mA , which compared well with the highest discharger current recorded of over 2mA . On only one occasion, in liquid precipitation near the ground, did they record positive current. In an investigation which extended to higher speeds, Nanevich (3) also measured current in the range $100\text{--}200\ \mu\text{A}\cdot\text{m}^{-2}$, but, in addition, observed the ice crystal concentration. At mach 1.2 he estimated that each ice crystal collision transferred about 50pC , the value was slightly higher at 200ms^{-1} , but at mach 1.9 the charge per interaction was reduced by about 50%.

At an earlier conference (4) we suggested that the charging occurring when ice crystals collided with metals depended upon the work function (or contact potential) of the metal and the ice. In that laboratory study the velocities of up to 10ms^{-1} were unrealistically low, and it is not clear that the same charging mechanism should operate at higher velocities when cracking and fracturing of the ice may occur (5).

We now report the results of an experiment in which ice particles of size from 50 to $100\ \mu\text{m}$ were accelerated to speeds between 10 and $80\ \text{ms}^{-1}$ and the charge transfer measured when they collided with various metal targets. This particle size range is appropriate for crystals occurring naturally in clouds which are responsible for most precipitation static. Trinks and ter Haseborg (5) have carried out experiments with 20mm diameter ice projectiles to simulate the effect of hailstone charging. Such large particles were totally pulverised when they hit metal targets at speeds in the range 35 to $1000\ \text{ms}^{-1}$. The targets acquired negative charges of up to 10pC per interaction, but the total number of these violent collisions in a cloud should be low.

APPARATUS

Water droplets in the size range $50\text{--}200\ \mu\text{m}$ with a controllable charge (0 to $+250\text{fC}$) were produced at the rate of about 1Hz by an Abbott and Cannon (6) droplet generator on top of the cold room. Each droplet then froze slowly as it fell down a tube into the cold room and collided with a tenuous cloud of minute ice crystals, which was formed by cooling a short section of the tube. The time for the particle to pass between two induction rings placed just below the freezing section then enabled the terminal velocity of each particle to be determined, and hence the size estimated to better than $10\ \mu\text{m}$. After falling a further 45cm , sufficient for the $100\ \mu\text{m}$ particles to freeze completely and reach thermal equilibrium, the particles were accelerated to speeds of up to 80ms^{-1} by compressed air. The compressed air was introduced at the periphery of the tube between two co-axial cones with an adjustable separation of about 1mm . This symmetric conic jet served to centre and to accelerate the small ice particles. The accelerated ice particles then passed through a final induction ring before hitting the target. The target was a cylinder 4mm in diameter and was easily removable so that the charging properties of different materials could be investigated.

Separate amplifiers were placed as close as possible to both the induction rings and the target to reduce microphonic and 50Hz pick up to the equivalent of less than 2fC . The amplifier outputs were summed, recorded, and subsequently replayed and examined on a digital storage oscilloscope. Because the amplifier has a rise time of $3\ \mu\text{secs}$ but a long (100msec) decay time for any charge deposited on the target, it was possible to differentiate between the rapidly varying induced charges caused by approaching and departing charged particles, and the long 100msec exponential decay when charge was transferred to the target. Considerable information on the nature of the interaction could be derived from the shapes of the waveforms as shown in Figure 2.

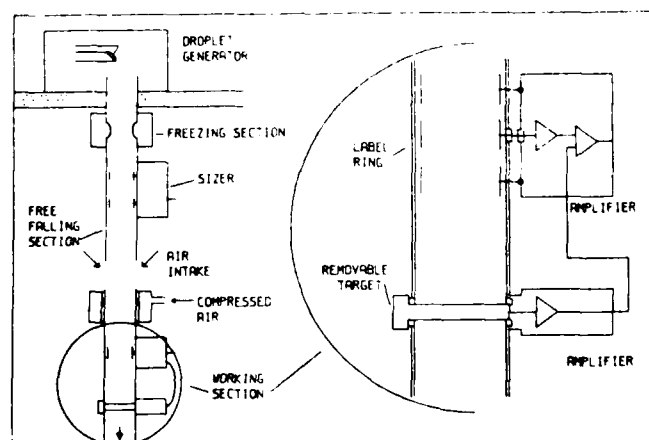


Fig.1. The apparatus for studying individual collisions of ice particles with various metal targets.

In all cases the first pulse is the passage of the particle through the induction ring with its initial label charge, q_i . The start of the second excursion of each waveform is the charge induced on the target as the particle approaches, and from the elapsed time since the passage through the induction ring the velocity of impact may be calculated. Subsequently, on actual collision a variety of waveforms are possible transferring charge q_t to the target as shown in Figure 2 and described below:

- a) If the second pulse is smaller than the first, then the particle has just missed the target, such waveforms are of great help when trying to align the apparatus. When the two pulses are equal there is ambiguity; either the particle has passed very close to the target but just missed it, or it has collided and separated but no charge has been transferred,
- b) Either the particle has hit the target and stuck to it - a 'collection'; or it has collided, donated its charge to the target, and then left carrying no charge
- c) The particle has collided with and separated from the target, transferring to the target an amount of charge (q_t) equal to a fraction of the initial charge (q_i) on the particle.
- d) Positive charge ($>q_i$) has been acquired by the target.
- e) Negative charge has been acquired by the target.
- f) as for d), but after collision the ice particle has rebounded upstream and then been accelerated and passed close to the target within 'electrostatic range' inducing the blip superposed on the exponential decay.
- g) An extreme case of f) in which the particle has rebounded upstream and then bounced a second time on the ice target and transferred additional charge during the second interaction.
- h) Initially appears to be similar to a), but the presence of the third pulse confirms that the particle has bounced upstream and then passed close to the target; this cannot be a collection but must indicate an interaction with zero charge transfer.

In examples f), g) and h) the rebounding and subsequent sensing of the particle indicate a more head-on collision, whereas the earlier waveforms will tend to reflect a more equatorial or grazing interaction. There is an equivalent set of waveforms for negative initial label charge. On occasion more complex waveforms are observed which initially appear to violate charge conservation, until it is realised that the particle must have bounced from the target to the wall where it acquired a spurious charge being sensed by the target amplifier a second time. Such pulses were rejected.

RESULTS

The experiments were carried out with ice particles made from distilled water having a conductivity of less than $1.5 \cdot 10^{-6}$ mho cm^{-1} , which is appropriate for natural ice occurring in the atmosphere. In all these studies the temperature was kept at -10°C . Most metals were found to charge negatively, but one important exception was magnesium which charged positively over the range of velocities covered in this

study. Figure 3a shows an event in which a $100\mu\text{m}$ ice particle transferred $+1200\text{fC}$ to a magnesium target. From the 1.5msec delay between the sensing of the initial charge (q_i) of 160fC and the time to hit the target 12cm below, an impact speed of 80ms^{-1} was derived. The interaction in Figure 3b is similar with the magnesium target receiving $+880\text{fC}$, but in this case the waveform is of the type shown in Figure 2f, suggesting that the small ice particle has bounced upstream and then been reaccelerated and passed close to the target. At these high speeds

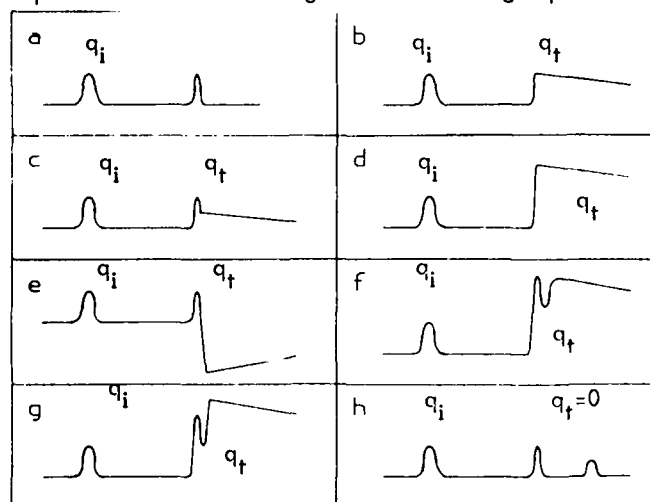


Fig.2. - A selection of the various possible waveforms from the amplifiers. For explanation see the text.

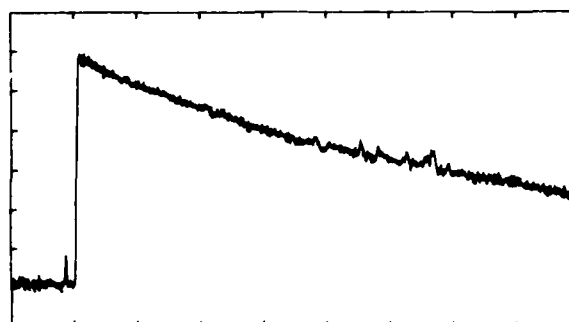


Fig.3a - Positive charging when a $100\mu\text{m}$ ice particle hits a magnesium target at 80ms^{-1} . Horiz scale 10msec per division, vert scale 200 fC per division -10°C .

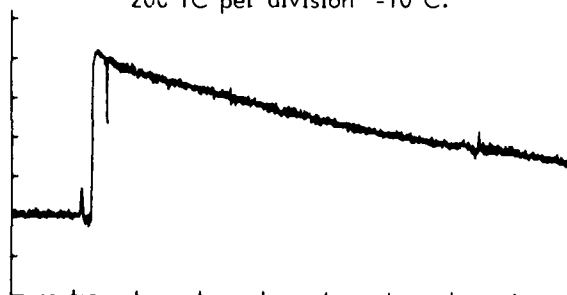


Fig.3b - Positive charging of magnesium target. Conditions and scales as for 3a.

the microphonic noise is equivalent to 30fC. Figure 4a displays the charging of a nickel target by -250fC when hit by a 100 μ m ice particle at 10ms⁻¹, and again in this example the particle bounces and subsequently passes near to the target. Typical charging of a brass target covered with polyurethane paint is shown in Figure 4b, in this case the target receives a charge of -400fC from a 60ms⁻¹ interaction, with microphonic noise now reduced to 15fC. On this expanded time scale the shape of the induced pulse as the particle approaches and leaves the target is clearly visible, and from these slopes it is possible to derive the velocities of approach and separation and to examine the mechanics of the collision in more detail.

In both Figure 3 and 4 the initial charge (q_i) is a small fraction of the total charge transferred (q_t) to the target. A series of preliminary experiments with much larger initial charges confirmed that q_i was not affecting the charge transferred to the target, and that q_i could be regarded as an identifier 'label'. It appears that in the short time available, the initial charge carried by the small ice particle is not able to migrate along the surface of the ice to the area of contact of the ice and metal, where it could affect the charge transfer. This is in accordance with our knowledge of the surface conductivity of ice (7); however, to minimise any possibility of interference the initial charge was kept to the smallest value which still allowed the particle to be identified as it passed through the induction ring, and permit definite confirmation of genuine events. Any charge transfers which were not preceded by the correct label at the correct time before contact with the target were probably due to spurious dust particles or extraneous ice particles, and were excluded from the analysis. In this way unambiguous waveforms as displayed in Figures 3 and 4 predominated, and problematic waveforms of the type shown in Figure 2 a,b,c, and h with their attendant difficulties of interpretation were avoided.

When histograms of the charge transfers for many events under a given set of conditions were plotted, they showed the same general features found for low speed ice-metal collisions reported previously (8); the distribution was skew with a tail of large transfers having magnitudes twice or three times the mean. The shapes of these histograms suggest that there is some random process in the charge transfer process itself, and that although the calculated standard deviations for the charge transfer was usually about half the mean value, the expectation value for the transfer was fairly well defined when 40 events were taken together.

Figure 5 shows a plot of the average charge transfer for ice impacting upon magnesium and nickel targets as a function of velocity. Before each run both targets were freshly polished. There was some evidence of changes in magnitude of up to 50% as the magnesium target aged, but this ageing did not affect the sign of the transfers. The trend from the Figure is quite clear, with an approximately linear increase with velocity for the positive charging of

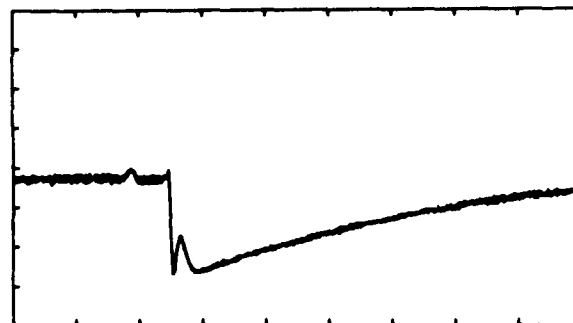


Fig.4a - Negative charging of a nickel target at 10ms⁻¹ by a 100 μ m ice particle, at -10°C. Horiz scale 20msec per division, vert 100fC per division.



Fig.4b - Negative charging of brass covered with polyurethane paint. 60ms⁻¹. Horiz scale 2msec per division, vert scale 200fC per division.

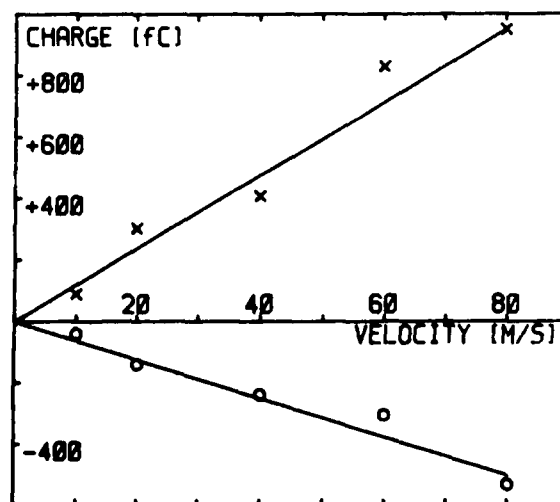


Fig.5 - The charge transferred to magnesium (X) and nickel (O) targets as a function of velocity by 100 μ m ice particles at -10°C.

the magnesium and for the negative charging of the nickel. With the compressed air available it was difficult to attain velocities of 100ms^{-1} , but from a limited amount of data the increase in charge with velocity appeared to extend to this higher speed.

In order to examine the effect of size on the charge transfer a series of experiments was performed using ice particles in the size range 75 to $220\text{ }\mu\text{m}$ and a nickel target. For some of the interactions with the largest particles positive charging was found, and these events were often accompanied by complex waveforms of which Figure 6 is a typical example. From this Figure it seems that there is bouncing and break up into three fragments which subsequently pass close to the target; one or more of the fragments may have received additional charge from a rebound off the walls of the tube. It appears that although the 45cm long free fall section of tube is long enough for complete freezing of the $100\text{ }\mu\text{m}$ particles, because of the mass increase and greater terminal velocity, the $200\text{ }\mu\text{m}$ particles are only partially frozen and so are likely to disintegrate when hitting the target.

Figure 7 displays the average charge transfer as a function of the square of the size of the ice particles for collision velocities of 10 and 60ms^{-1} . Data for sizes above $200\text{ }\mu\text{m}$ have not been included because of the fragmentation problems discussed above. For the 10ms^{-1} run with $183\text{ }\mu\text{m}$ particles about one third of the events resulted in positive charge transfer with an average value of $+3\text{fC}$, but only the two thirds which gave simple waveforms with negative charging have been included in the analysis. No positive events were observed for the other points shown on the graph. For the experiments at 60ms^{-1} the compressed air was interfering with the droplet generator and so some difficulty was experienced in keeping the droplet size constant and is responsible for the increased scatter. For both velocities, it is clear that the average charge transfer is increasing with velocity, and there is strong evidence for a square law dependence. A short experiment using $130\text{ }\mu\text{m}$ supercooled liquid droplets at 60ms^{-1} with a nickel target confirmed positive charging for non-frozen particles with an average transfer of $+120\text{fC}$.

Experiments (8) at 10ms^{-1} have shown a good correlation of charge transfer with the work function of the metal, but we have not yet completed a comprehensive study at the high speeds. However, a target of barium oxide, which has a low work function charged consistently positively at high speeds. Other materials including aluminium, carbon and silver charged negatively. When $100\text{ }\mu\text{m}$ particles at 60ms^{-1} and a target of brass covered with polyurethane paint were used, an average transfer of -670fC was measured, a teflon covered target resulted in an average value of -500fC , and a target covered with smooth ice also charged negatively but to a lesser degree.

The ice crystals occurring in the atmosphere are vapour grown and have different shape and momentum from the spherical particles used in this experiment. At the start of each experiment a cloud of minute ice crystals would form in the cooled section of the free fall tube, and this cloud would persist for a few minutes, and give rise to occasional

clearly observable charging events when the crystals hit the target. Such events were not preceded by a recognisable label and so, because of the unknown size of the ice crystal, were not included in the analysis, however, the crystals always gave the same sign of charging as the controlled ice spheres. The low work function magnesium charged positively and the nickel acquired negative charge.

CONCLUSION

The charging of metal targets by small ice particles increases linearly with velocity for speeds of up to at least 80ms^{-1} , and is approximately proportional to the square of the particle size for spheres of diameter up to $200\text{ }\mu\text{m}$. Gaskell and Illingworth (9) found a similar dependence for ice-ice collisions at much lower speeds of less than 12ms^{-1} , and observed that these results implied that the charge transfer was proportional to the contact area (A) predicted by elastic collision theory to vary as

$$A \propto v^{4/5} r^2 \quad (1)$$

where v is the velocity and r the radius of the small particle. Work on collisions below 10ms^{-1} (8) has shown that the charge transfer depends upon the work function of the metal, and if the work function (or contact potential) difference between the metal and the ice is V , then the charge transfer should be given by

$$q = CV \quad (2)$$

where C is the capacitance as the small particle separates from the target and is proportional to the contact area A in equation 1. The positive charging observed at the higher speeds in this paper by magnesium and barium oxide targets, and the negative charging for other targets with larger work functions indicate that the differences in contact potential are controlling the charge transfer at these higher speeds.

Partially frozen and liquid drops appear to charge targets positively; positive charging by splashing water drops at much lower speeds has been explained in terms of the disruption of the electric double layer (10).

The negative charging found in this study with most common metals and paint covered targets is consistent with the negative charging observed with aircraft. Direct quantitative comparison of the laboratory studies with aircraft measurement involves an assumption of the typical size and concentration of ice particles in clouds. The charge per interaction for a $100\text{ }\mu\text{m}$ particle has been found to be about -1pC at 80ms^{-1} . From our derived velocity and size dependence this would suggest that a $200\text{ }\mu\text{m}$ particle at 200ms^{-1} would charge a target by about -10pC . If the concentration was 100 per liter then the current would be about $200\text{ }\mu\text{A m}^{-2}$, in agreement with most densities reviewed in the introduction. Boulay and Laroche (2) recorded one occasion of positive charging in rain, which is compatible with our findings with liquid drops. Nanevich (3) found a charge per crystal of about -50pC at much higher velocities. It would be of interest to fly magnesium probes to see if they charged positively.

We plan to continue this work extending the interactions to higher speeds, and also to investigate the properties of other materials. At present some targets charge positively and others negatively, alloys may exist which give zero charging. Such materials would appear to minimise any static charging to aircraft.

ACKNOWLEDGEMENT

This work has been performed with the support of the Meteorological Office and the EOARD (grant AFOSR 82-0323). Travel funds were provided by NERC under grant GR/5384. We would like to thank Peter Kelly for his advice and help in the workshop.

REFERENCES

1. R.L. Tanner, et al., "Precipitation Charging and Corona-Generated Interference in Aircraft", Technical Report No. 73, Project No. 2494, Contract AF 19 (604) 3468, 1961.
2. J.L. Boulay and P. Laroche, "Aircraft Potential Variations in Flight", Eighth Lightning and Static Electrification Conference, Forth-Worth, 1983.
3. J.E. Nanevicz, "Flight-Test Studies of Static Electrification on a Supersonic Aircraft", Lightning and Static Electrification Conference, Culham, 1975.
4. J.M. Caranti, and A.J. Illingworth, "Static Charging by Collisions with Ice Particles", Lightning and Static Electrification Conference, Oxford, 1982.
5. H. Trinks, and J.L. ter Haseborg, "Electric Charging by Impact of Hailstones and Raindrops", Eighth Lightning and Static Electrification Conference, Forth Worth, 1983.
6. C.E. Abbott, and T.W. Cannon, "A Droplet Generator with Electronic Control of Size, Production Rate, and Charge", Rev. Sci. Inst. 43, 1313-7, 1972.
7. A.J. Illingworth and J.M. Caranti, "Ice Conductivity Restraints on the Inductive Theory of Thunderstorm Electrification", VIIth Int. Conf. on Atmos. Electricity, Albany, New York, 1984.
8. J.M. Caranti, A.J. Illingworth, and S.J. Marsh, "The Charging of Ice by Differences in Contact Potential", VIIth Int. Conf. on Atmos. Electricity, Albany, New York, 1984.
9. W. Gaskell, and A.J. Illingworth, "Charge Transfer Accompanying Individual Collisions Between Ice Particles and Its Role in Thunderstorm Electrification", Quart. J.R. Met. Soc., 106, 841-854, 1980.
10. Z. Levin, and P.V. Hobbs, "Splashing of Water Drops on Solid and Wetted Surfaces", Phil. Trans. Roy Soc. A, 269, 555-585, 1971.

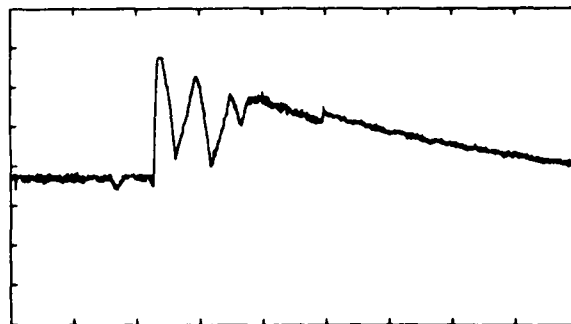


Fig.6 - Positive charging of a nickel target at 10ms^{-1} by a $183\mu\text{m}$ diameter particle. Vertical scale 100fC per division, horiz scale 20 msec per division.

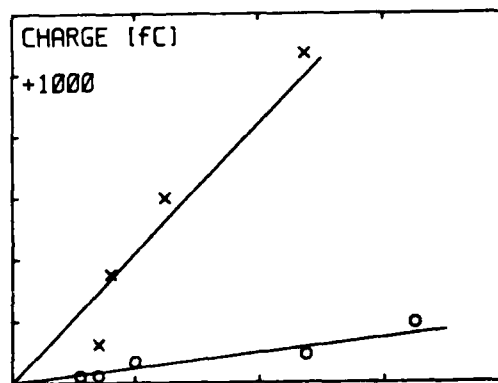


Fig.7. - The charge acquired by a nickel target as a function of the size of the ice particle $\times 60\text{ms}^{-1}$. $\circ 10\text{ms}^{-1}$. The units of the horizontal scale are $10^4 \mu\text{m}^2$.

LIGHTNING TESTS OF PERSHING II

L. H. Riley and G. R. Edlin
US Army Missile Command, Huntsville, Alabama
R. A. Perala and C. C. Easterbrook
Electro Magnetic Applications Inc., Denver, Colorado
J. D. Robb
Lightning & Transients Research Institute, St. Paul, Minnesota

ABSTRACT

Lightning tests have been carried out on the Pershing II system. The tests were performed on full scale hardware consisting of the erector launcher, tractor, a non-fueled missile, the Platoon Control Central, and the interconnecting cables. Hardware availability limitations did not allow for testing of a full platoon as it could not be deployed. This does not invalidate the results, however, in that the lightning hazard is quite localized, especially for a direct strike.

Two types of tests were accomplished: nearby lightning and direct strike. The objective of the tests was to determine if the lightning effects requirements on the missile were met. These requirements are that in no case should lightning cause a nuclear incident, and that the system should be able to operate and fulfill its mission after a nearby strike. The tests showed that these requirements are met with safety margins which exceeded 30 dB. Tests were done while the missile system was fully powered in the "hot hold" mode and also while the system was unpowered. Measurements were made of internal voltages and cable currents.

Tests were accomplished with current waveforms whose peak values of current and the current time derivative exceeded those which are commonly used to characterize natural lightning in a worst case sense. However, because the test waveshapes differed in some respects from natural lightning, some of the internal measurements were extrapolated to worst case lightning environments by computerized Fourier analysis techniques.

In addition to the system level tests, Bruceton tests to determine fire/no fire characteristics of exploding bridge wires and hot wire initiators were conducted. These were then compared to measured and extrapolated voltages in order to determine no fire margins.

LIGHTNING ENVIRONMENT AND SURVIVABILITY REQUIREMENTS

IN ORDER TO carry out a test program, the lightning parameters must be specified. Therefore, the most recently published lightning measurements and statistics were first reviewed and utilized to characterize the natural lightning environment. Since Pershing II is a tactical, ground-based system, only cloud to ground lightning data (which tend to be the most severe) have been considered. Both direct strike currents and electromagnetic fields produced by nearby strikes have been considered in the test program. It is noted that the channel current environment presented here is that obtained by direct measurements, and are not those inferred from remote electromagnetic field measurements.

The lightning parameters chosen to characterize the threat are: maximum current rise rate, peak current, and the magnetic and electric fields. The frequency domain spectra of the current and fields are also presented.

Current Rate of Rise - Measurements showing the highest rate of rise of current in the return stroke are given by Berger [1]*. Berger's data indicates a moderate threat level of 50 kA/us, exceeded 35% of the time, and a severe threat level of 200 kA/us exceeded only 1% of the time. These data are somewhat higher than the figures reported earlier by Cianos and Pierce [2]. Figure 1 shows Berger's statistical results with the threat levels indicated.

*Numbers in brackets designate References at end of paper.

Peak Current - Peak return stroke currents have been measured and statistics tabulated by Berger [1], Cianos and Pierce [2], Popolansky [3], and Garbagnati and Zopipard [4]. Good representation of measured data is given by Popolansky, and is shown in Figure 2. The moderate threat level of 20 kA peak is exceeded 60% of the time and the severe threat level of 200 kA peak is exceeded 1% of the time.

Magnetic Fields - The Pershing II is supposed to withstand a strike 10 m away without system failure. The magnetic fields for natural lightning are assumed to be given by

$$H = I/2\pi r$$

which means that severe magnetic fields of 3185 A/m and rates of change of 3.2×10^4 A/m/s can be expected.

Electric Fields - Time domain electric fields have been measured at various distances (1-200 km) from lightning channels. The electric field consists of three parts: the induction field, static field, and the radiation field, which vary inversely with distance r according to r^3 , r^2 , and r , respectively. The time rate of change is largest for the radiation field, which is the only component measured at large distances. At a distance of 100 km,

values of dE/dt range from 5×10^6 to 80×10^6 V/m/sec, with a mean of about 30×10^6 V/m/sec. Field levels on the order of 10 V/m are measured [5]. If this value is extrapolated back to 10m, we obtain maximum rates of change of 7.5×10^{11} V/m/sec. There are no known measurements at close range of the electric field; however, the coupling to the missile is mostly proportional to dE/dt , so a value of 7.5×10^{11} V/m/sec was used as that characteristic of natural lightning.

Frequency Spectra - Frequency domain data combines the rates of rise, peaks, and total energies into a single plot. Therefore, they are quite useful in characterizing the lightning threat. Figures 3 and 4 show the most recent and reliable measured spectra for return stroke currents and nearby radiated electric fields for natural lightning. The current spectrum is due to Berger [1] and the electric field spectra to Serhan et.al., [6] and Weidman et.al., [7]. The electric field data has been adjusted to a range of 15 meters from measurements taken in the range 15 to 17 km utilizing a 1/R relationship. This will cause errors at low frequencies, but will be correct at the high frequencies where coupling is most important.

THE DESIGN SPECIFICATIONS FOR LIGHTNING - Since the Pershing II (PII) system must meet design requirements for a severe threat, only the severe threat lightning parameters are given here. These parameters are obtained from [8] and were derived primarily from data reported in Cianos and Pierce [2]. The lightning strike model consists of three return strokes given by:

(1) Initial Stroke:

$$I(t) = I_0 [e^{-\alpha t} - e^{-\beta t}] + I_r [e^{-\gamma t} - e^{-\delta t}]$$

where $I_0 = 206$ kA

$$I_r = 9 \text{ kA}$$

$$\alpha = 1.7 \times 10^4 \text{ sec}^{-1}$$

$$\beta = 3.5 \times 10^6 \text{ sec}^{-1}$$

$$\gamma = 10^3 \text{ sec}^{-1}$$

$$\delta = 10^4 \text{ sec}^{-1}$$

(2) Second Stroke:

Same as the first except $I_0 = 103$ kA and the time delay is 60 milliseconds from the first stroke.

(3) Third Stroke:

$$I(t) = \frac{I_0}{2} [e^{-\alpha t} - e^{-\beta t}] + 400 (.120 t^{.5} - .500)$$

Here the intermediate current component (I) included in the first and second stroke is replaced by a 400 amp continuing current to 500 milliseconds.

The time history of this lightning current model is shown in Figure 5 and a summary of the parameters is included in Table 1.

Spectra associated with the specified return stroke current and with the nearby electric and magnetic fields are shown in Figures 6 and 7. Figure 6 is the Fourier Transform of the double exponential waveform of Figure 5. The electric field spectrum of Figure 7 was taken directly from the design environment specifications and the model utilized to generate it is unknown.

From the electric field spectrum of Figure 7, one can infer a time domain waveform whose transform matches that of Figure 7:

$$E(t) = 12.6 \times 10^3 (u(t) + e^{-1.26 \times 10^3 t} \cos(6.28 \times 10^3 t))$$

This is observed to consist of a step function of about 10 kV/m plus a damped sinusoid having a derivative of 8×10^3 V/m/sec. It is unclear how this can relate to a real environment, because the static field is surely much more than that and the radiation field (the component having the large dE/dt) surely does not have the shape of a damped sinusoid. Therefore it does not seem prudent to consider this a realistic threat environment.

THE TEST WAVEFORMS - During the lightning program two basic waveforms were utilized to simulate the electrical stress on the missile systems. A 150 kilohertz damped sinewave provided the high rate of current rise (up to 3×10 Amps/sec) and a 15 kilohertz damped sinusoid was used to meet the high current requirements (up to 250 kAmps). Figure 8 and 9 show the initial cycles of the higher frequency current waveforms. The nearby strike waveform is given in Figure 8 and the direct strike waveform in Figure 9. There is a slight difference in the two because of the differences in the down-current path. The direct strike has a higher peak current and a slightly higher rate of rise. The corresponding frequency spectra of the two current waveforms are given in Figures 10 and 11.

The high peak current waveform is shown in Figure 12 with its frequency spectrum given in Figure 13. The spectrum is typical of a damped sinusoid.

The measured electric field 15 meters from the simulated nearby strike is given in Figure 14 and its spectrum is given in Figure 15. Note that the measurement is only of the early part of the waveform, and because of that the low frequency spectrum is in error. The high frequency part is limited by the digitization interval of the manual digitization of the oscilloscope photograph.

It is of interest to compare the measured test waveforms with those generated in an analytical study [9] utilizing a 3D finite

difference method. The comparison current waveforms and spectra generated from the 3D analysis are shown in Figures 16 through 18. The computer model discussed by Perala et. al. [9] was adjusted slightly to match the actual parameters and configuration utilized in the tests. Direct comparison of the corresponding figures demonstrates a high degree of similarity, both in magnitude, and form. The only significant difference in the waveforms is the ~1 MHz spike that exists in the numerical solution for the direct strike (Figure 18). This frequency corresponds to the peaking capacitor/down conductor resonance. This resonance is not so prominent in the actual test facility waveforms.

COMPARISON OF TEST WAVEFORMS, DESIGN SPECIFICATIONS, AND NATURAL LIGHTNING - A final item to be considered is the adequacy of the tests in meeting the test requirements. This is best shown by comparing the appropriate frequency spectra.

The comparison for the current waveform is shown in Figure 19. It is noted that the test waveform significantly exceeds the specification in certain cases, and at some frequencies is less than the specifications.

A comparison of the measured electric field at 15 meters and the design specification electric field at 10 meters is shown in Figure 20. Note that the measured field is greater than the design specification at all frequencies above about 100 kHz. The low frequency content of the measured field is not shown because of the short data record length as discussed previously.

The important time domain parameters for the various lightning environments are given in Table 2. It is observed that both the peak current and the peak dI/dt for the tests exceed those for natural lightning. The dE/dt for the tests is less than for natural lightning because of the difference in peak current. If dE/dt for the test were scaled by the ratio of currents it would increase to 13.5×10^3 volt/m sec, almost double that for natural lightning.

PERSHING II SURVIVABILITY REQUIREMENTS - Pershing II has different requirements for nearby and attached lightning.

It is required to survive and operate after a nearby strike 10 m away from the missile. This means that no systems can be permanently damaged such that the missile could not perform its mission after a nearby strike.

The missile is not required to survive an attached strike; however, no nuclear incident is to result from an attached strike. Practically speaking, this means that none of the Exploding Bridge Wires are allowed to detonate, although the hot wire devices can detonate without causing an incident.

PII LIGHTNING TESTS

TEST CONFIGURATION - Two test configurations were utilized in the PII lightning

tests; one configuration for direct strike tests and one for nearby strike tests. The configuration for direct strike is shown in Figure 21. Plan views for both tests are shown in Figure 22, giving details on the location of the major components.

Measurements were made at the critical test points in the missile electronics systems.

INSTRUMENTATION - The test instrumentation was set up as shown in Figure 23. Four channels were available for each shot. One of these channels was dedicated to recording the injection current waveform.

The critical test points were measured utilizing a voltage probe consisting of a 1000 ohm resistor and a 50 coaxial line as shown in detail A of Figure 23. This arrangement gives a voltage division of 21. Each test circuit was measured and corrected for any variations in this voltage division. The three bulk cable currents in the warhead were sampled utilizing Solar Electronics Model 0741-1 current probes having a transfer impedance of 0.63 ohms and a flat frequency response over the range 10 kHz - 30 MHz.

The instrumentation rationale utilized is based upon the fact that the critical parameter for safety is the common mode voltage induced on the squib or detonator circuits. Thus, only one wire of the shielded twisted pairs were measured although the other wire was measured for several test points with little difference noted.

For the nearby strike tests, electric and magnetic field measurements were made 1 meter from the missile and at ranges of 10, 15 and 20 meters from the current channel (down electrode). The magnetic fields were measured utilizing a shorted loop with a current probe as in Figure 24(a). The electric fields were sampled with a parallel plate capacitance probe as shown in Figure 24(b). Calibration of the H-field probe is,

$$H = 44 \text{ V amp/m}$$

and for the E-field probe,

$$E = 1.54 \times 10 \text{ V}$$

where V is the output voltage of the probe.

DATA ACQUISITION - A total of 170 test shots were fired during the lightning test program. Seventy of these shots were direct strikes to the missile. The tests were grouped into 5 categories as follows:

1. Nearby Strikes
2. Direct Strikes, Low Level
3. Direct Strikes, Low Level, Low Frequency
4. Direct Strikes, High dI/dt
5. Direct Strikes, Low dI/dt, High Peak Current

Since it is most difficult to produce a single test current that has a total spectral content equal to that of natural lightning, the direct strike tests were conducted with a low frequency waveform separate from the higher frequency waveforms that produced the required rate of change of current. This is standard practice for lightning tests and meets test requirements because the points of entry that respond to the high rate of current rise do not respond to the low frequency components and vice-versa. The test program was designed to meet the natural lightning rates of rise, peak currents and total energy content by combining the various results.

EXTRAPOLATION TO THREAT LEVELS - The double exponential current waveform utilized for the design threat has a peak dI/dt of approximately 7×10^6 amp/sec. This rate is 2.3 to 2.5 times the peak rate attained during the tests. Therefore, it is of interest to try and predict the test point voltages which would occur if the vehicle were subjected to the exaggerated threat. Two test points were chosen for the analysis; one EBW circuit and one hot wire squib. These test points were chosen because they produced the highest response during the earlier tests.

The analysis procedure utilized was to compute the test current-to-circuit voltage transfer function, multiply this result by the Fourier transform of the new threat current waveform, and then compute the inverse transform of the result. The end product of this process yields the extrapolated time domain voltage at the test point, i.e.

$$H(\omega) = \frac{\int_0^{\infty} V_m(t) e^{-j\omega t} dt}{\int_0^{\infty} I_{te}(t) e^{-j\omega t} dt}$$

$$\text{and } V_p(t) = \int_0^{\infty} H(\omega) I_p(\omega) e^{j\omega t} d\omega$$

where

- V_m = time domain voltage measurement
- V_p = time domain extrapolated voltage
- I_{te} = time domain test current
- I_p = time domain (specification) current.

The original test point voltage measurements are shown in Figure 25. Figure 26 shows the frequency domain transfer function for the test point and Figure 27 gives the transfer function. The inverse transforms are shown in Figure 28.

Some words regarding the transfer functions of Figures 26 and 27 should be added. The most obvious feature is the low frequency value. One would expect that the voltages would relate to dI/dt, but it is a constant in the figures. The reasons for this are clear.

First, the amplitude digitization error is significant and limits the dynamic range of the data. Although the time domain functions were

recorded on a 7912AD digitizer, there were so many drop outs that this data was of limited value. The curves were therefore digitized manually. Because of this, the amplitude can only be resolved to within about one trace width (line width), which means that the error in amplitude resolution is a few percent, which results in a dynamic range of between 30 and 40 dB. It should also be pointed out that even for an 8 bit digitizer (256 amplitude increments if the measurement is full scale), the dynamic range is only about 48 dB. Thus, it is possible to have a DC (or low frequency) offset of 1/2 of an amplitude increment. Practically speaking, this means that the DC (or low frequency) value of the Fourier transform (which is simply the time integral) of a measured voltage or current cannot be resolved within the accuracy of the dynamic range, which is on the order of 30-40 dB. Because the DC levels of Figures 26 and 27 are between 50 dB and 20 dB below the peak values, one must not assume that they are correct.

Secondly, additional low frequency errors also occur because the record length of the measured data is limited, and the response was analytically continued to zero with a damped sinusoid. Even though the late time measurements indicated a damped sinusoidal behavior, the analytic continuation will introduce some low frequency error. Thus the extrapolated measurements cannot be expected to be accurate at late times, but they should be rather accurate for the early time portions indicated in Figure 28.

If it assumed that the extrapolated voltages are correct, one needs to determine the implication relative to lightning hardness. First, consider the EBW. The extrapolated peak voltage is 4620 volts, which according to the common mode tests would flash-over to the case. Since this circuit has a resistance of 500 Ohms to ground, the maximum flash-over current would be 9 amps. This is 42 dB below the level that could fire the device according to the tests. The extrapolated voltage on the hot wire device is 3735 volts. This voltage would also cause this device to flash-over externally. With a resistance to ground of 20 Ohms, the flash-over would produce a maximum common mode current of 186 amps. However, these units were tested to a current of 15,000 amps without detonations. The margin of safety is 38 dB even for the design specification current waveform which has a dI/dt more than a factor of 2 higher than a severe lightning stroke predicated by measurement statistics.

TESTS OF INITIATOR DEVICES

LTRI completed a series of tests on both the exploding bridge wire (EBW) and the hot wire ordnance devices. The test procedure utilized has come to be known as the "Bruceton" test, and was developed by the Explosive Research Laboratory at Bruceton, Pennsylvania [10].

Briefly, the method involves changing the stress on a specimen (electrical, mechanical or otherwise) by a finite increment after each specimen has been tested. The stress is increased if the specimen does not explode, or decreased if the specimen does explode. This test procedure insures that many tests will be made near the median stress level and is more efficient than standard methods in that a given degree of accuracy can be obtained with fewer observations.

Exploding Bridge Wire Tests - The test set-up for the differential mode EBW tests is shown in Figure 29. The circuit components were chosen to give an approximate 1×50 usec pulse to the device. The test level was varied by controlling the charge voltage on the capacitor. Since the EBW's varied somewhat in impedance, the test current steps were not equal as required for the Bruceton analysis. Therefore, the data were reorganized into equal current steps in order that a firing current analysis be done.

Common Mode Tests - The Bruceton tests discussed above were done for the differential or normal firing mode for the devices. However, the signal coupled to the devices as the result of a lightning strike would be mostly common mode. Thus, common mode tests were run on a large sample of both hot wire and EBW devices to determine, if possible, the common mode voltage and current required to fire the devices.

COMMON MODE TEST CONCLUSIONS - Since only one device from a total specimen sample of 52 was actually detonated in the common mode and pin to case tests, a Bruceton type analysis of the data was not considered to be justified. However, the common mode tests demonstrated clearly that the common mode electrical current required to fire the squibs is considerable. For the EBW's, there is at least a 60 dB margin between the flash-over current required to fire a device and the maximum common mode current likely to be coupled to the device by a direct lightning strike. Similarly there is more than a 55 dB margin between the maximum common mode test current impressed on the hot wire devices (without any detonation) and the maximum current expected to be coupled to these circuits by a nearby lightning strike. These conclusions are based upon the common mode voltages and resistances measured on the squib circuits during the PII lightning tests.

It is conceivable, on the other hand, that a severe threat, direct strike to the missile could fire one of the hot wire squibs.

During the lightning tests, measurements on several of the hot wire squib currents indicate that a differential mode current in excess of 20 amps could be attained with a full threat, direct strike of 200 kA. The observed firing of a gas bottle squib during the direct strike tests confirm this conclusion.

DISCUSSION AND CONCLUSIONS

Extrapolation of the test results to the design threat current indicates that even under this extreme lightning test environment the safety margin exceeds 30 dB for the hot wire squibs and exceeds 40 dB for the EBW's for a nearby lightning strike.

In summary, the tests of the electrically operational Pershing II (with propellant removed) showed that no firing occurred in the warhead or rocket motor igniter which is in conformance with the requirements for nuclear safety. The tests also showed that no EBW or hot wire squib ignition occurred from nearby lightning strikes (10 meters) with current rates of rise of 2×10 amperes per second, although, non-safety critical squibs (gas bottle and gas generator) ignition did occur during the direct strike tests. Analyses of the test data also indicated that firing some hot wire squibs was a possibility for high level, direct strikes. However, firing of non-critical squibs by a direct strike is acceptable within the Pershing II requirements.

The final conclusions relating to the Pershing II requirements are as follows:

1. Nuclear safety is assured for the Pershing II for all lightning threats with a safety margin of better than 40 dB.

2. The Pershing II system will remain operational following a nearby lightning strike at 10 meters with a safety margin better than 30 dB.

REFERENCES

1. Berger, K., R. B. Anderson, and H. Korninger, "Parameters of Lightning Flashes," *Electra*, 80, 23-27, 1975.
2. Cianos, N., E. T. Pierce, "A Ground Lightning Environment for Engineering Usage," Stanford Research Institute, Technical Report No. 1, Project 1843, August 1972.
3. Popolansky, F., "Frequency Distributions of Amplitudes of Lightning Currents," *Electra*, 22, pp. 139-147, 1972.
4. Garbagnati, E., G. B. Zopipard, "Lightning Parameters - Results of 10 Years of Systematic Investigation in Italy." Proceedings of International Conference on Lightning and Static Electricity, Oxford, England, March 1982.
5. Weidman, C. D. and E. P. Krider, "Submicrosecond Risetime in Lightning Radiation Fields," *Lightning Technol.*, NASA Conference Publication 2128, April 1980.
6. Serhan, G. I., M. A. Uman, D. G. Childers, and Y. T. Lin, "The RF Spectra of

First and Subsequent Return Strokes in the 1-200 km Range," *Radio Science*, 1980.

7. Weidman, C. D., E. P. Krider, and M. A. Uman, "Lightning Amplitude Spectra in the Interval from 100 kHz to 20 MHz," *Geophys. Res. Lett.*, Vol. 8, pp. 931-934, 1981.

8. "PII Lightning Analysis," Martin Marietta Analysis Report 1401000-001, May 11, 1981.

9. Perala, R. A., P. M. McKenna, C. C. Easterbrook, and T. H. Rudolph, "Implementation of a Distributed Peaking Capacitor with a Marx Generator for Increasing Lightning Test Current Rise Rates and Electric Field Excitation," *Electro Magnetic Applications*, Inc. Report EMA-83-R-40, October 1983.

10. "Statistical Analysis for a New Procedure in Sensitivity Experiments," A report submitted to the Applied Mathematics Panel, National Defense Research Committee by the Statistical Research Group, Princeton University.

Table 1
P11 Pershing Direct Strike Lightning Model [8]

Stroke Order	Return Strokes		Time Between Strokes (ms)	Intermediate Current Model †			Continuing Current
	Peak* Current (kA)	Charge (C)		Model Current, I_0 (kA)	I_1 (kA)	Charge (C)	
1	200	~ 12	60	206	9	~ 8	Final Stage†
2	100	~ 6		103	9	~ 8	
3	100	~ 6	60	103	0	0	

Totals: Charge transferred = 200 C
Duration = 0.5 s
Action integral = $1.9 \times 10^6 \text{ A}^2\text{-s}$

* The time history for all strokes is defined by Eq. (1), with $\alpha = 1.7 \times 10^4 \text{ s}^{-1}$ and $\beta = 3.5 \times 10^6 \text{ s}^{-1}$. The time to peak current is 1.5 μs for all strokes. The time to half-value is 40 μs for all strokes.

† The time history for all intermediate currents is defined by Eq. (3) with $\gamma = 10^3 \text{ s}^{-1}$ and $\delta = 10^4 \text{ s}^{-1}$.

‡ Final-stage continuing current = A; duration = 400 ms; charge transfer = 160 C.

Table 2 Comparison of Time Domain Parameters for Tests, Design Spec., and Measured Lightning

Condition	Peak Current	Peak dI/dt	Near Field dE/dt
Test High dI/dt	34 kA	$3.0 \times 10^{11} \text{ Amp/sec}$	$2.3 \times 10^{11} \text{ V/m/s}$
Test High Current	250 kA	$2.5 \times 10^{10} \text{ Amp/sec}$	n/a
Design Specification	200 kA	$7.2 \times 10^{11} \text{ Amp/sec}$	$8 \times 10^7 \text{ V/m/s}$
Measured Lightning Severe Threat	200 kA	$2.0 \times 10^{11} \text{ Amp/sec}$	$7.5 \times 10^{11} \text{ V/m/s}$

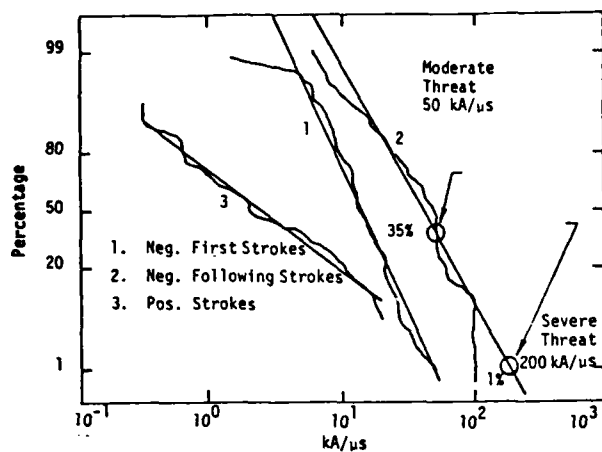


Fig. 1 - Distribution of maximum rate of current rise from Berger, et.al [1]

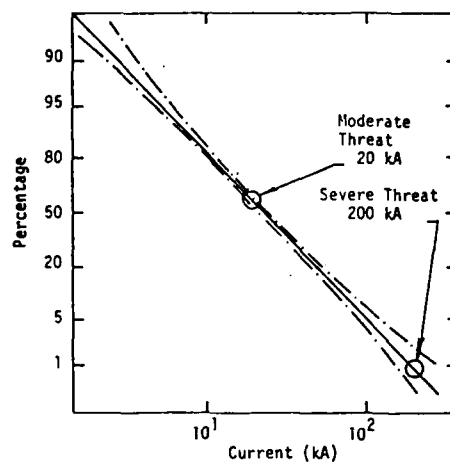


Fig. 2 - Peak lightning current statistics (Popolansky [3])

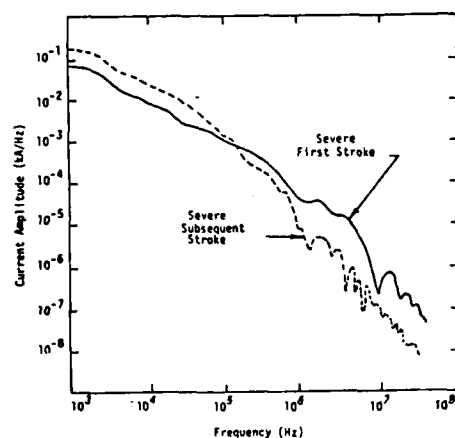


Fig. 3 - Measured frequency spectra of return stroke currents from Berger [1]

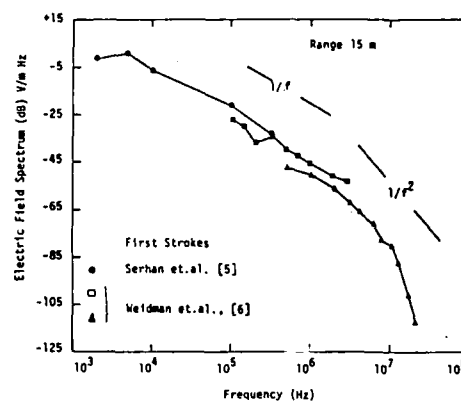


Fig. 4 - Measured frequency spectra of the radiated electric fields adjusted to 15 meters range

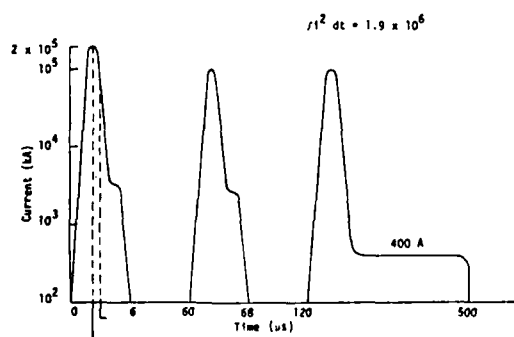


Fig. 5 - Time history of Pershing II direct strike lightning model [8]

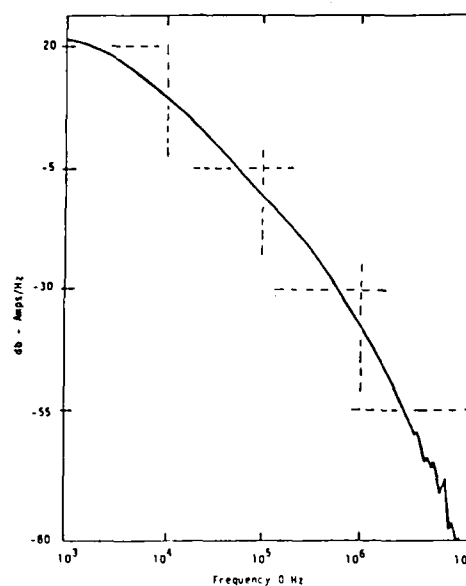


Fig. 6 - Frequency spectrum of return stroke current

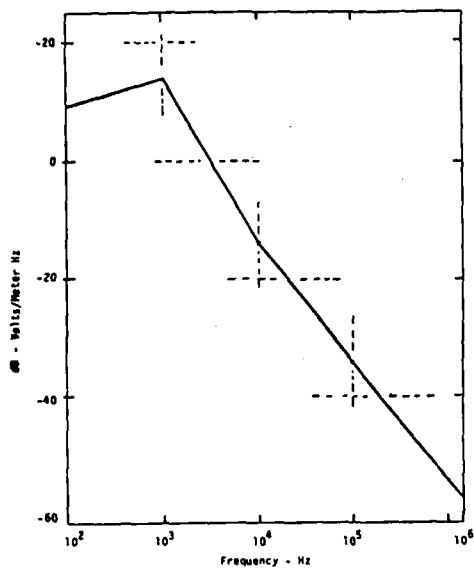


Fig. 7 - Frequency spectrum of the electric field at 10 meters from current channel [8]

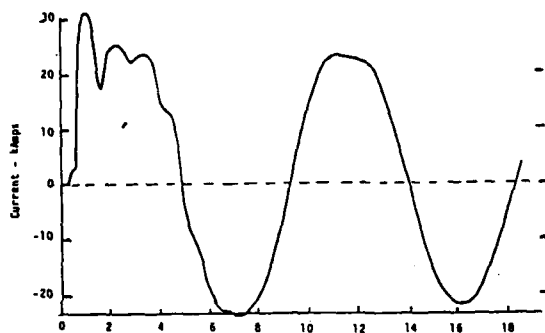


Fig. 9 - Direct strike current waveform

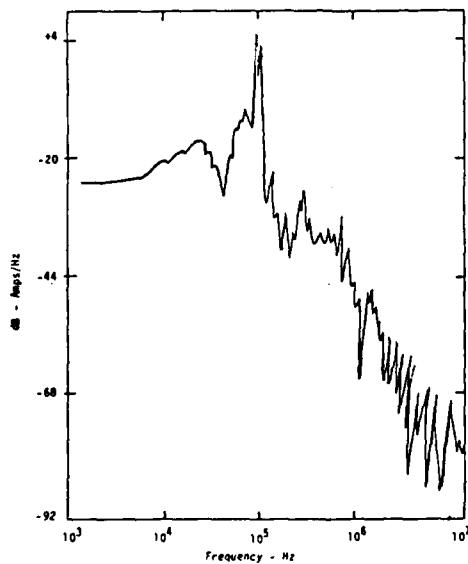


Fig. 11 - Frequency spectrum of measured direct strike current waveform

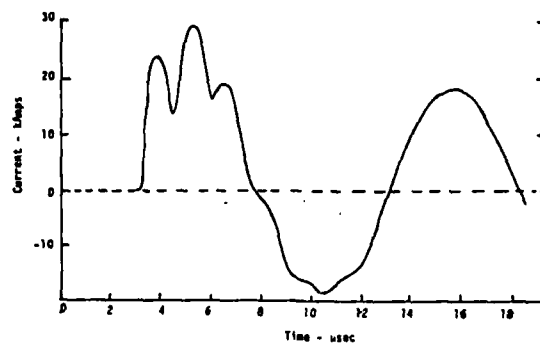


Fig. 8 - Nearby strike current waveforms

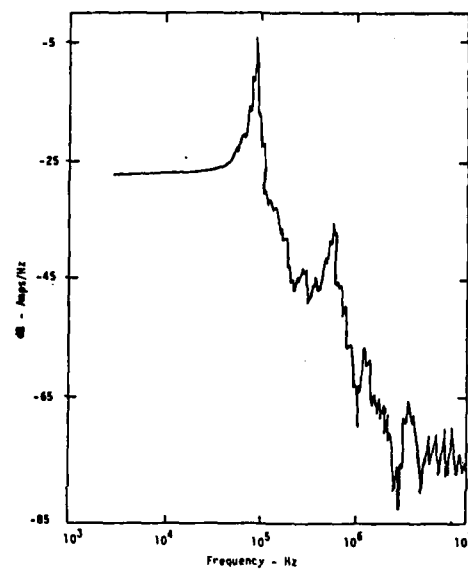


Fig. 10 - Frequency spectrum of measured nearby strike current waveform

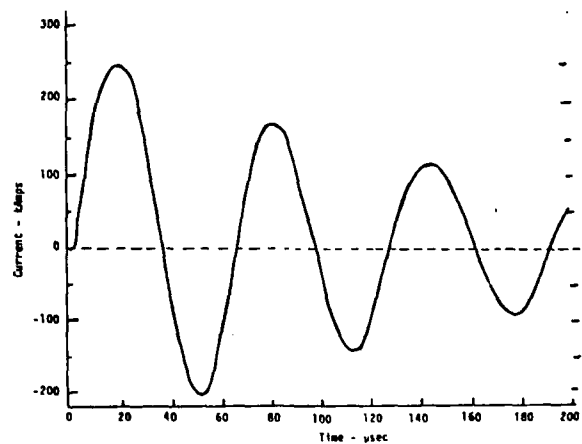


Fig. 12 - Injection current waveform for high peak current, direct strike tests

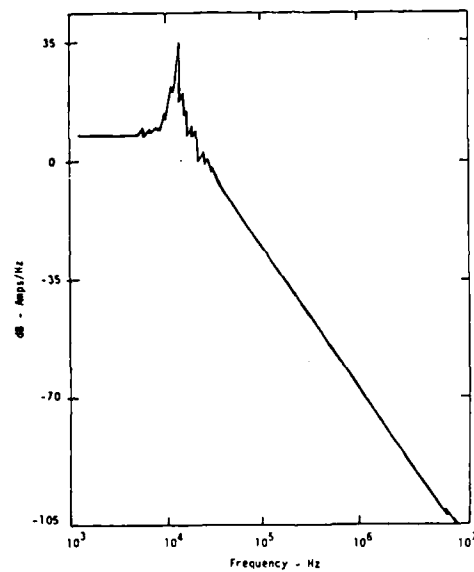


Fig. 13 - Frequency spectrum of the high current, low frequency, direct strike waveform

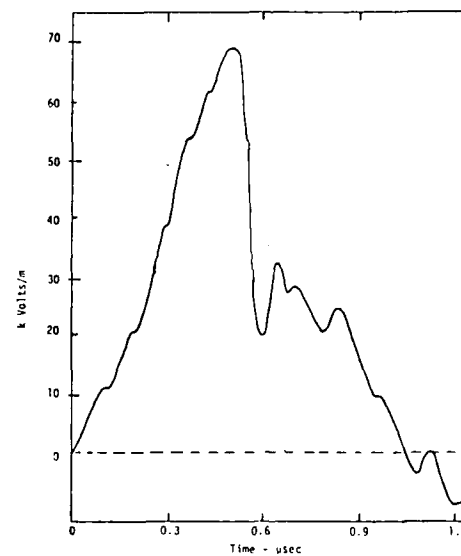


Fig. 14 - Electric field measured at 15 meters (from oscilloscope trace)

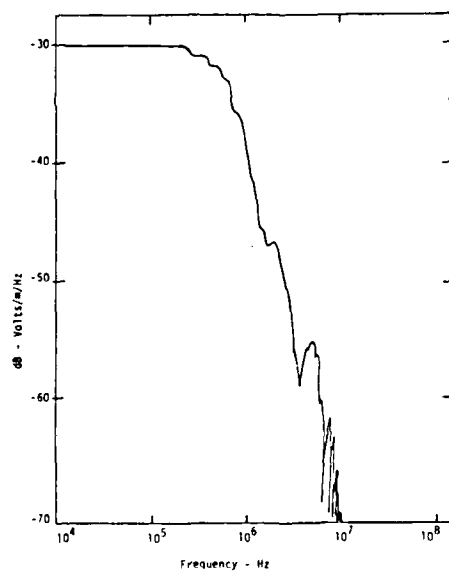


Fig. 15 - Frequency spectrum of electric field measured at 15 meters

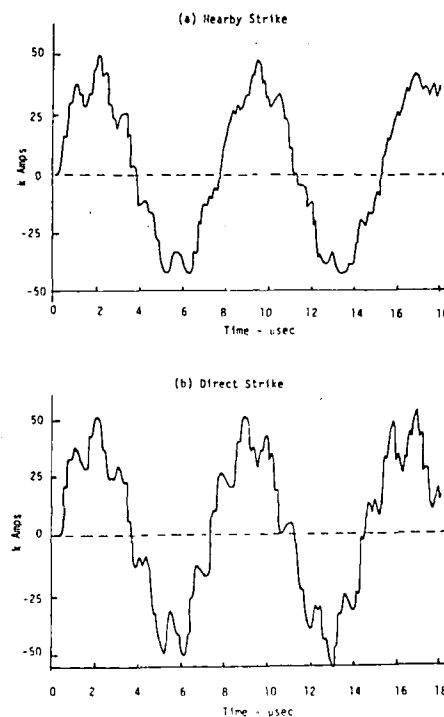


Fig. 16 - 3D modeled current waveform

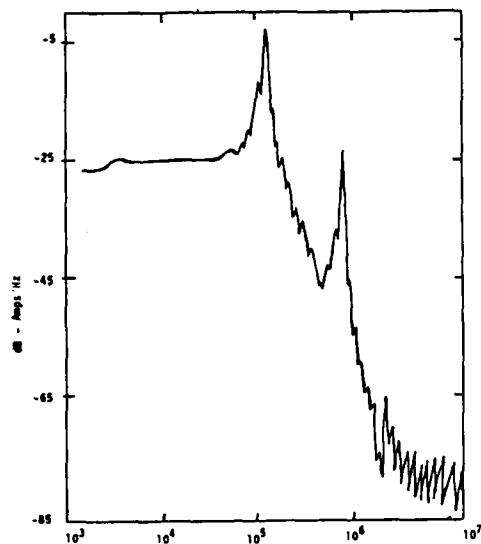


Fig. 17 - Frequency spectrum of the nearby strike current waveform generated from the 3D analysis

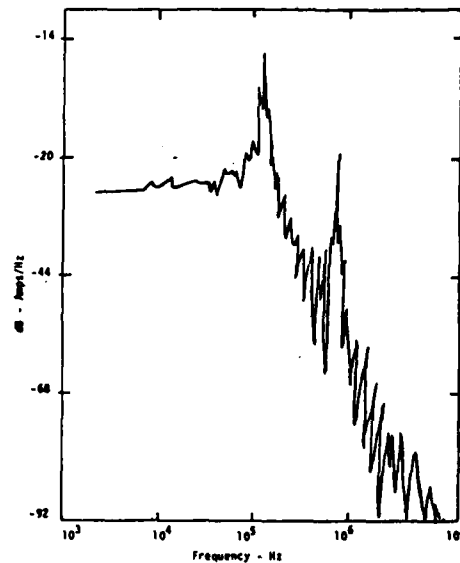


Fig. 18 - Frequency spectrum of the direct strike current waveform generated from the 3D analysis

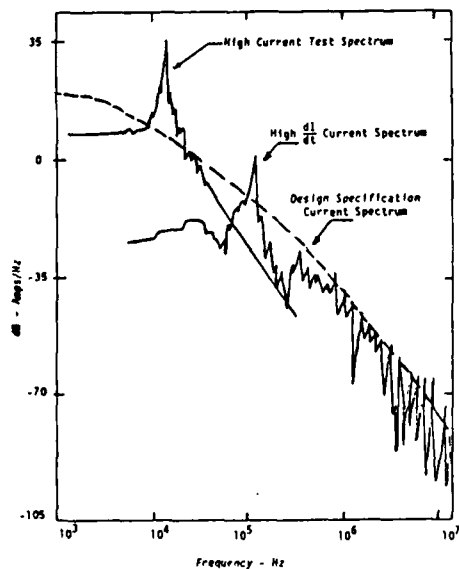


Fig. 19 - Comparison of test currents, design spec. current, and measured lightning current, frequency spectra

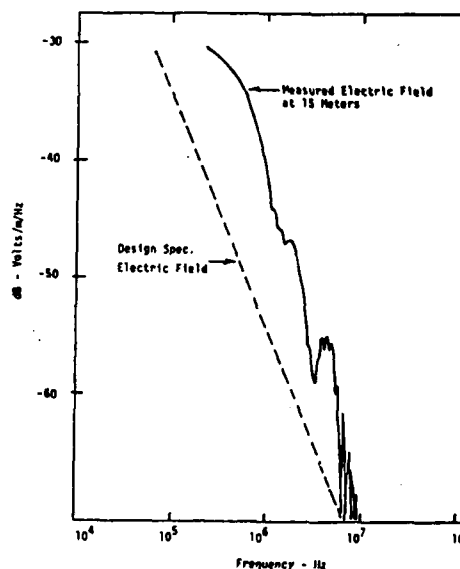


Fig. 20 - Comparison of frequency spectra for the test electric field at 15 meters and the design specification electric field at 10 meters

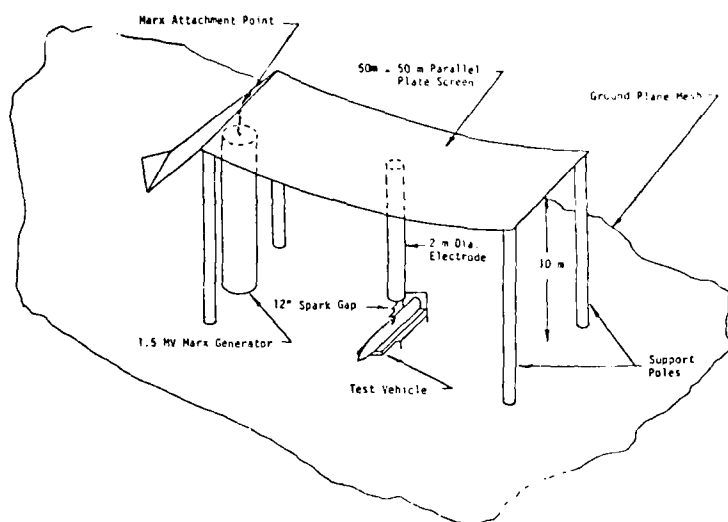
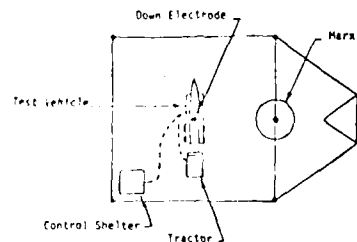
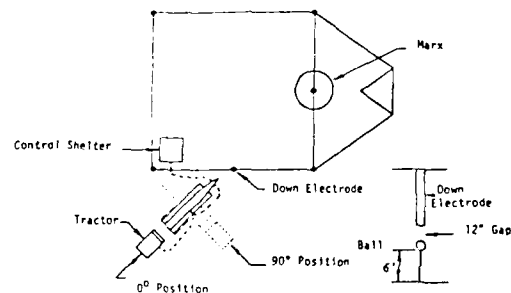


Fig. 21 - Direct strike test configuration



(a) Direct Strike Configuration



(b) Nearby Strike Configuration and Electrode Detail

Fig. 22 - Plan views - test configuration

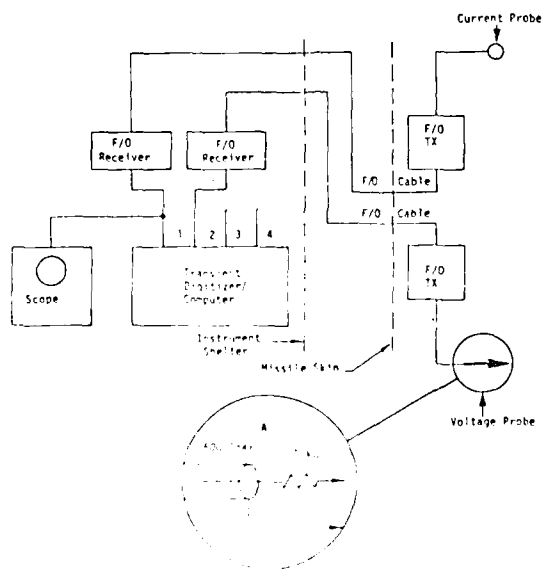
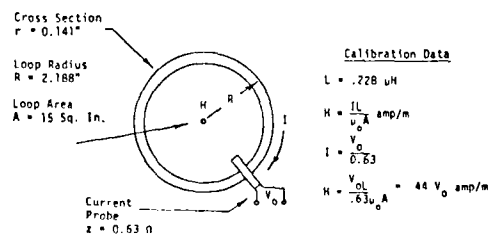
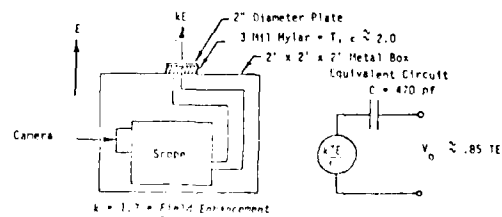


Fig. 23 - Instrumentation configuration



(a) Magnetic Field Probe



(b) Electric Field Probe

Fig. 24 - Electric and magnetic field probes

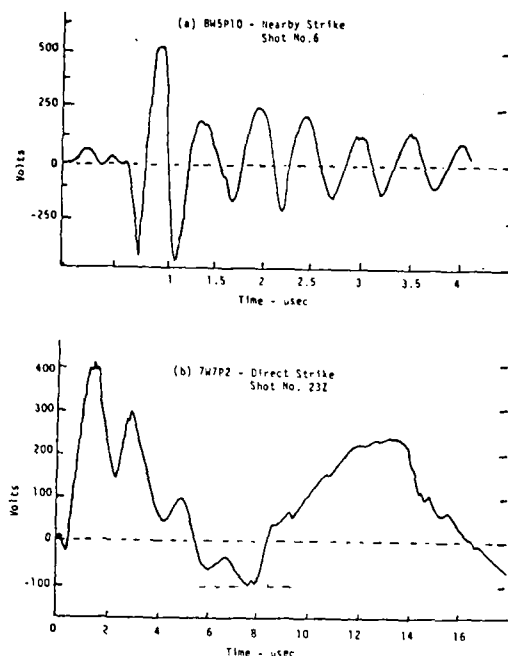


Fig. 25 - Measured voltage on two sample test points

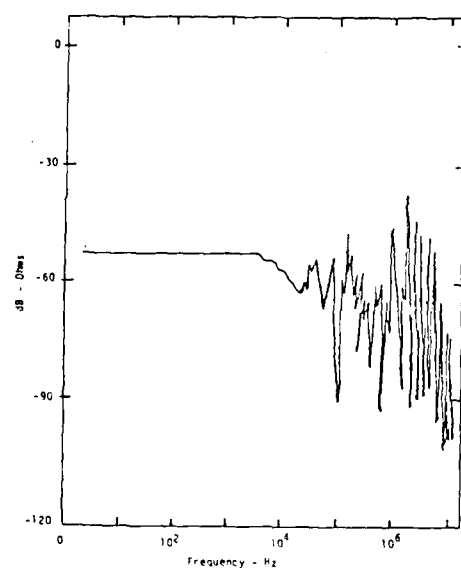


Fig. 27 - Transfer function for test point 7W7P2 - direct strike

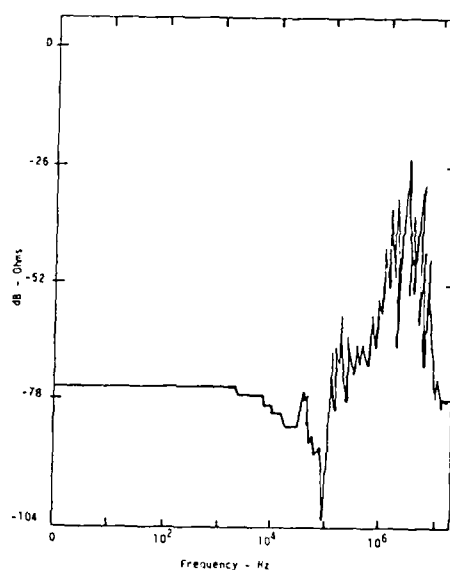


Fig. 26 - Transfer function for test point 8W5P10 - direct strike

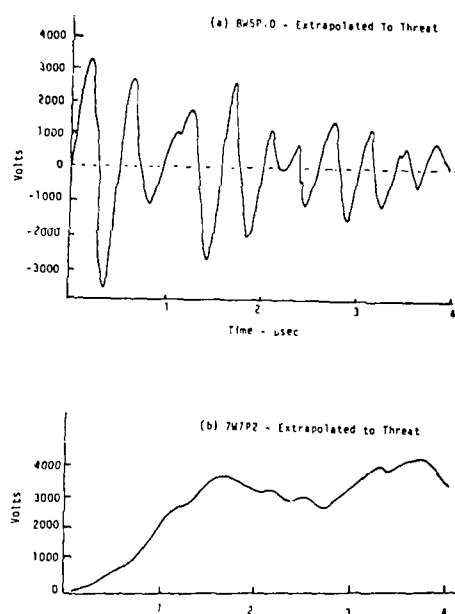


Fig. 28 - Two sample test point voltages extrapolated to the specification threat level utilizing the computed transfer functions

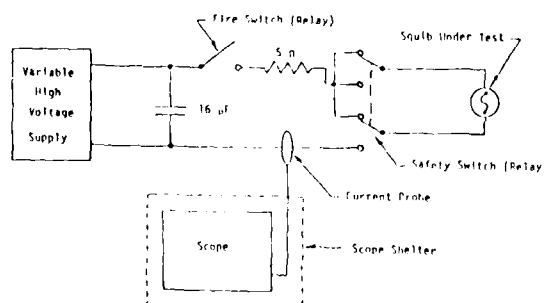


Fig. 29 - Test setup for Squib tests. High voltage supply and relays were controlled from a safe location

ELECTRICAL SAFETY EVALUATION OF A HELICOPTER
STATIC CHARGE GROUNDING WAND

J. L. Dawson
Naval Air Test Center, Patuxent River, Maryland

ABSTRACT

The Electronic Systems Branch, Electromagnetic Compatibility (EMC) Section of the Naval Air Test Center, was directed to test a Helicopter Static Charge Grounding Wand designed by the Rotary Wing Aircraft Test Directorate (RWATD) to determine its Electrostatic Discharge (ESD) capabilities and to evaluate the electrical safety aspects of the design. This particular discharging wand was designed to standardize the discharge wands currently used in the Fleet and in the Marine Corps. Presently each activity manufactures their own wands using guidelines presented by the Navy and, unfortunately, incidents arise throughout the year where ground handlers are being electrically shocked, either by improper use of their wands or through poor wand design. Several tests were employed using an ESD simulator designed to duplicate the static discharging of a large helicopter. The simulator is capable of variable capacitance with a maximum delivered voltage of 336 Kv. Tests were conducted to evaluate all phases of helicopter/ground handling crew interfacing with emphasis not placed on proper handling of the wand or use of the wand with ideal grounds (less than 100 ohms), but rather with the expected and sometimes unexpected misuses of the wand. Tests were also conducted to determine the effectiveness of a supplied grounding stake in areas of differing ground potentials (i.e., grassed sod, dry/wet sand, etc.). Test results are presented which shows that the wand, when used in the proper manner and when attached to an ideal ground, is relatively safe and adequate for discharging large helicopters. However, the design tends to be dangerous when less than ideal grounds are utilized (i.e., rusty metal, corrosion, painted surfaces, frayed ground wire, dry or wet sand, etc.). The wand is also dangerous if not used properly (i.e., improper hand placement, contact with the ground wire, non-continuous contact with the aircraft, etc.). The wand also allows arcing to occur which is a hazard to fuel and ordnance. In the process of summarizing the results presented, several possible solutions to the various problems are suggested. It is strongly recommended that whatever design is chosen for a Helicopter Static Charge Grounding Wand, that all handlers receive extensive training in its proper use and safety.

DISCUSSION

AN ELECTRICAL SAFETY evaluation was conducted on a Helicopter Static Charge Grounding Wand; depicted in Fig. 1. The wand was similar to the wand described in paragraph 3.4.2 of MIL-HDBK-274(AS) 1*. The problem in developing an appropriate evaluation, was in determining the various helicopter/ground handler interfaces, postulating the possible errors and misuses of the grounding system in each interface, simulating these anomalies in METHODS OF TEST and choosing electrical parameters which would be conducive to SAFETY. The solution evolved into a test consisting of three configurations of grounding wand applications:

- o Shipboard Verticle Replenishment - simulation of grounding to ship structures.
- o Shorebased Verticle Replenishment - simulation of grounding to static ground points and using a ground stake in varying earth mediums.
- o Handling of refueling and ordnance - special concerns for arcing.

*Numbers in brackets designate References at end of paper.

In each phase of the test, the charged helicopter was represented by an Electro Static Discharge Simulator (ESDS) represented in Fig. 2. The ESDS is a marx generator capable of delivering 336 KV at an energy level of 20 joules, which is comparative to a CH-53 Sea Stallion helicopter charged to 90 Kv and represents a lethal electric shock. The high discharge voltage was selected to maximize detection of design deficiencies linked to material breakdown. References have indicated aircraft potentials in excess of 200 Kv 2 and as high as 1 Mv 1.

The human operator (bare handed wand handler) was represented by a string of ten 68 ohm resistors connected in series (R_1) to avoid arc overs associated with single resistors. The value of 680 ohms was selected as the nearest standard value resistance of the average body resistance value presented in MIL-HDBK-274(AS) 1 and reference 3.

During the test, it became evident that meaningful quantitative measurements of voltages across the resistive load R_1 (simulated wand handler) would be distorted by noise generated within the measuring instruments by the Electromagnetic Pulse (EMP) generated by the ESDS. Various efforts to eliminate the EMP with filtering and shielding, failed. Substitute qualitative measurements using arc over observations proved to be sufficient in accomplishing a meaningful testing of the grounding system.

RESULTS AND DISCUSSION

The verticle replenishment configuration is represented in Fig. 1 and was tested as shown in Fig. 2 with R_2 initially represented by hangar ground, a value less than 10 ohms. In this configuration, the wand satisfactorily discharged the ESDS ten times with no apparent safety hazard to the operator. During the performance of this portion of the test, the following misuse anomalies were contrived (a sort of what if?):

- o The M83413-1 clamp becomes detached.
- o R_2 approaches and exceeds 10K ohm (due to attachment to painted, rusted or corroded surfaces, deterioration of the wand components or hook up to a non-standard static ground point).
- o Mishandling of the wand, with hand positions on the wand in close relation to the cargo hook, contact with the grounding cable, and noncontinuous wand contact with the helicopter.
- o Using the ground stake in varying earth mediums.
- o Use of the wand in a salt spray environment.

With the M83413-1 clamp detached (open circuited), the wand became unsafe. Arcing was observed between the ungrounded wand and R_1 (simulated wand handler) still attached to hangar ground. After examining the wand, burn holes were discovered at the point of arcing. When R_1 was relocated on the

wand (representing a different hand placement), additional discharges caused new burn throughs as shown in Fig. 3. The voltage required to burn through and cause damage to the wand as well as the operator, was 190 Kv. Once a burn through was established, hand placement above a burn through reduced the breakdown voltage to the equivalent voltage required to burn through the ground cable vinyl coating and arc the air gap between the ground cable and the operators hand. This voltage was found to be 100 Kv. Separate tests of the grounding cable, outside of the wand, showed that damage to the vinyl coating (cracks, burns, or thin spots) would cause breakdowns at voltages less than 1 Kv. Even with the clamp laying on concrete, there is still some finite resistance associated with ground and therefore affording some protection to the wand handler 2. Tests were conducted in a similar configuration as Fig. 2, except with the clamp (R_2) laying on concrete and a 0.1 inch gap placed between R_1 and hangar ground, attached first to an undamaged wand and then to an undamaged portion of the external grounding cable. The 0.1 inch gap was representative of a 3 Kv - 5 Kv spark gap (depending on ambient temperature and humidity) 3 4 and corresponds to the range of REFLEX ACTION SHOCKS (9 to 25 mJ) for a 2000 pF helicopter 1. In this configuration, arcing occurred across the 0.1 inch gap at discharges of 50 Kv and 30 Kv respectively, with no evident burn throughs to either components. The easiest way to avoid burn throughs and operator shock, is to relocate the grounding cable outside of the wand, in a manner similar to standard shepherd's crooks. The wand handler should then maintain a 6 inch separation between himself and the grounding cable (6 inches should suffice for protection up to 400 Kv 4). An alternate wand design based on a simple modification of the existing wand, appears in Fig. 5.

The test configuration of Fig. 2 was reestablished, and the value of R_2 was increased until arcing occurred to

R_1 (simulated hand contact) when the ESDS was repeatedly discharged at maximum output. With R_1 attached to the wand, arcing occurred at $R_2 = 40 \text{ K ohm}$. With R_1 attached to the grounding cable, arcing occurred at R_2 less than 100 ohms. Again, it is quite obvious that operator contact with the grounding cable during a high voltage discharge could be hazardous. Keeping both hands on the wand at all times would prevent wand handlers from accidentally grabbing the cable with the free hand.

The wand was placed in the configuration of Fig. 4 and initially set with $d_1 = d_2 = 1$ inch and moved outward until discharge arcing attached predominantly to the wand's hook. This configuration represents various hand positions on the wand in respect to the cargo hooks location. The distance at which the wand's hook received 12 out of 20 discharges, was $d_1 = d_2 = 6$ inches. At 10 inches, all attachments were to the wand. Therefore, to avoid a hazardous situation, a caution area should be designated on the wand covering the first 10 inches below the hook attachment screws.

The wand and associated ground stake (driven 2 feet deep) satisfactorily discharged the maximum output of the ESDS when both the wand and the resistive load were grounded to moist grassed sod. A similar test was performed with wet sand as the grounding medium. While performing this test, the ESDS operator continually received electrical shocks to his feet, at which time a panel of plexi-glass was employed to provide insulation for the ESDS operator. At each discharge, arcs were observed between the wand and R_1 (simulated wand handler). In the wet sand grounding medium, only discharges below 50 Kv would be relatively safe. Similarly, hazardous situations are expected when any dryer or less ionized earth mediums, such as dry clays, gravel or desert sand are used to ground the wand. Even with poor ground earth mediums, a helicopter can still reach a safe level of charge, if given at least 5 RC time constants to discharge prior

to touching the aircraft. Using the maximum resistance of 120 M ohms representing a chain laying on rocks over hard desert 2 and using a 2000 pF helicopter for example, would result in a 5 RC time of 1.2 seconds. To maximize safety, the wand handler should allow at least 3 seconds to expire after contact with the helicopter prior to indicating a safe condition.

A maximum dry air spark gap distance between two attachment points on the grounding wand was established for a maximum ESDS discharge and then expanded by 1 inch. The wand was then sprayed with tap water to simulate a wet wand. With a regular tap water spray, no arcing was observed between the two attachment points. Using a saline spray of 14 g NaCl/L of tap water (mid range of salinity spray test values 4), caused arc overs across the entire length of the wand. These tests indicate that there will be greater risks of arc overs to wand handlers in a salt spray environment. To reduce arc overs, the wand handler should wash or wipe off his wand prior to contacting a helicopter or its' cargo.

During the various tests, several long arcs were observed. These long arcs (up to several inches), will cause a potential hazard when handling fuel or ordnance. An arc length of 0.02 inches minimum is needed to ignite proper air fuel ratios 5 . The minimum energies required to ignite fuel is 0.26 mJ 5 and for ordnance, 35 mJ 1 . One possible solution would be to discharge the helicopter at a safe distance away from the fuel or ordnance and then, with a ground established, move the helicopter to the cargo. As with all other helicopter grounding situations, after initial discharge contact is made, constant grounding must be maintained to avoid additional charge build up. With large helicopters, recharging may only take a manner of seconds.

CONCLUSIONS

In summarizing the conclusions of this test, it must be remembered that the test methods were developed with

emphasis on SAFETY. Therefore, the tests as a whole represent worse case conditions. The wand handler who is issued this particular wand may never encounter the scenarios depicted by these tests. However, in the issuance of this equipment, we must ensure that the wand handler be given the safest equipment and be trained to expect, avoid, or control all of the possible hazards. With this in mind, the test results indicate that the wand handler should:

- o Ensure that the grounding clamp is attached to a low resistance ground and that the grounding wand and cable are undamaged.
- o Avoid contact with the grounding cable at all times.
- o Maintain a hand placement of at least 10 inches from the hook attachment screws.
- o Allow enough time for the helicopter to discharge to a safe level.
- o Be aware of the hazards of salt spray.
- o Maintain safe distances when handling ordnance and fuel.

RECOMMENDATION

It is recommended that the existing wand be altered as follows:

- o Remove the ground cable from within the wand and attach it externally as shown in Fig. 5.
- o Add black striping from the top of the wand to a minimum of 10 inches from the hook attachment screws forming a caution zone (see Fig. 5).

In addition, the wand handler should:

- o Maintain a 6 inch clearance between the ground cable and all personnel.
- o Employ a 3 second equilibrium time after helicopter contact before indicating a safe condition.
- o Maintain a continuous ground after initial discharge contact.
- o Keep both hands on the wand.

It is strongly recommended that whatever design is chosen for a Helicopter Static Charge Grounding Wand,

that all handlers receive extensive training in its proper use and safety.

ACKNOWLEDGEMENT

Special thanks go to Mr. C. Lee; my associate, who was quite shocked by these tests and not always by the results.

REFERENCES

1. MIL-HDBK-274(AS), "Electrical Grounding for Aircraft Safety", 1 November 1983.
2. D.G. Douglas and J.E.Nanevich, Stanford Research Insititute and B.J. Solak, Boeing Company, Vertol Division, "Passive Potential Equalization Between the Cargo Handler and a Hovering Helicopter", 1969.
3. R.H. Golde, "Lightning Protection", Chemical Publishing Company, New York, N.Y. 1974.
4. IEEE Std 4-1978, "IEEE Standard Techniques for High Voltage Testing", 1978.
5. MIL-HDBK-238, "Electromagnetic Radiation Hazards", 10 Aug 1973.

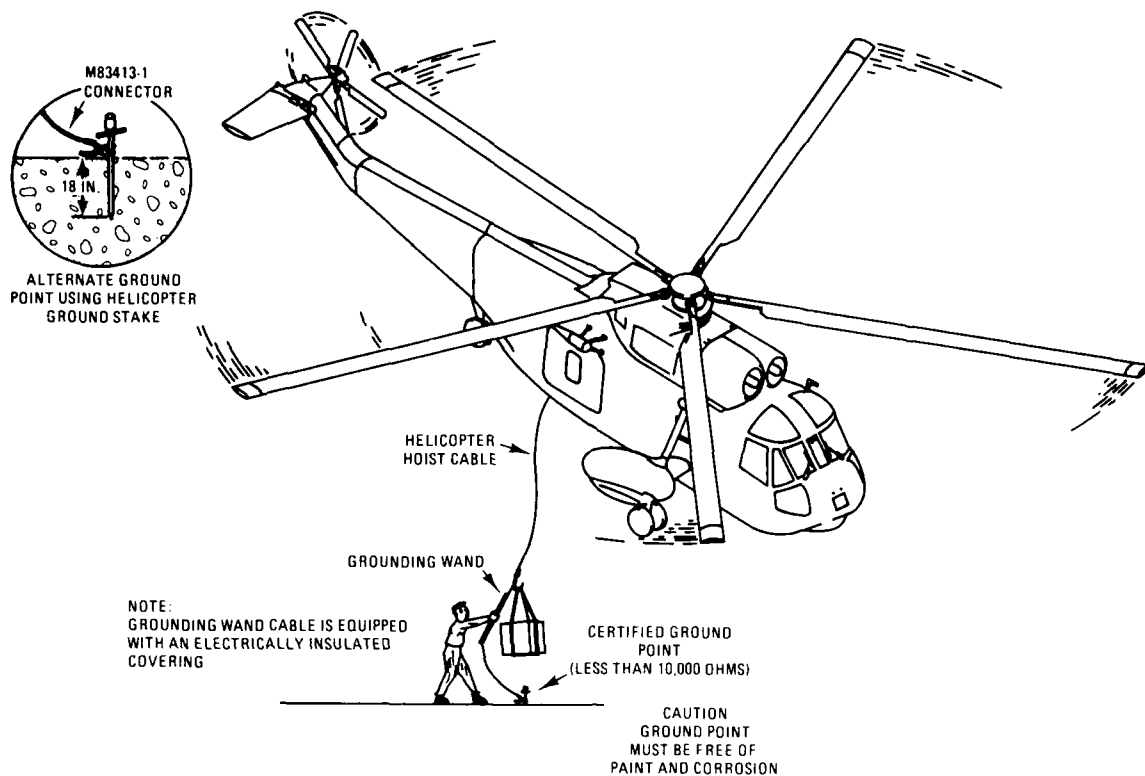


Fig. 1 - Static grounding of a hovering helicopter

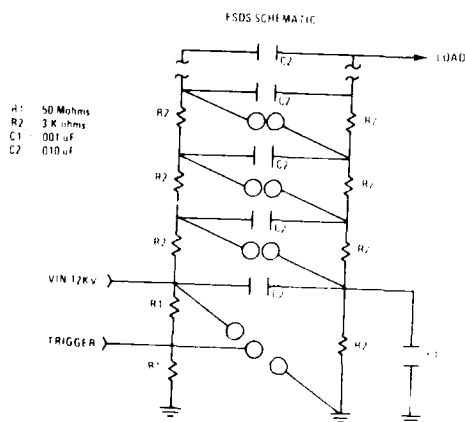
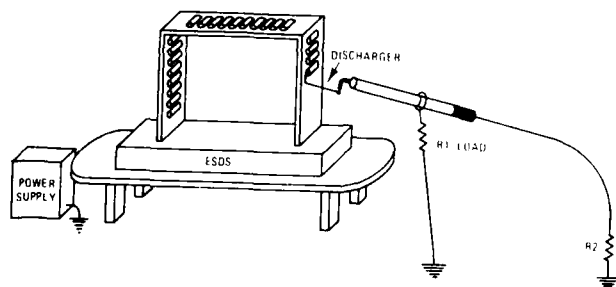


Fig. 2 - Typical ESDS setup and schematic

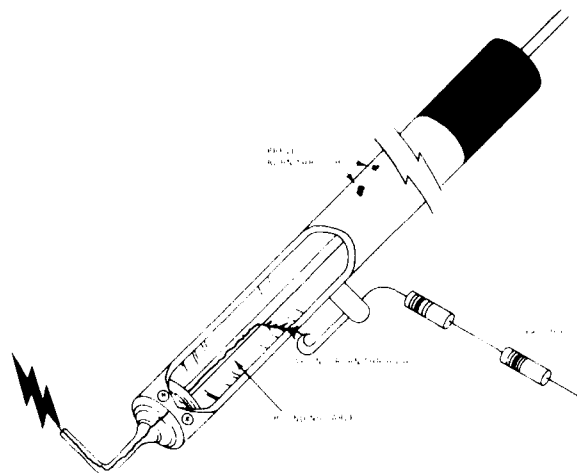


Fig. 3 - Arcing burn through of grounding wand

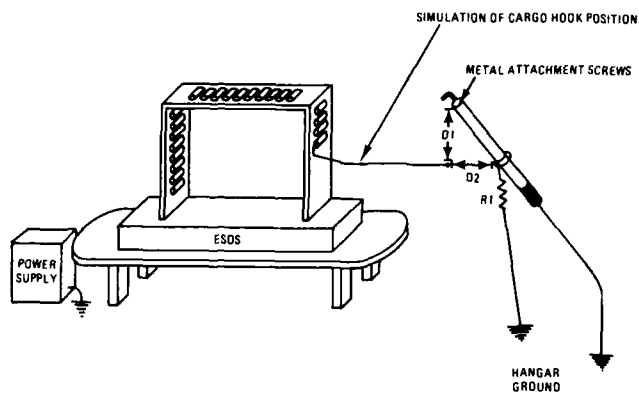


Fig. 4 - Hand position in relation to cargo hook location test

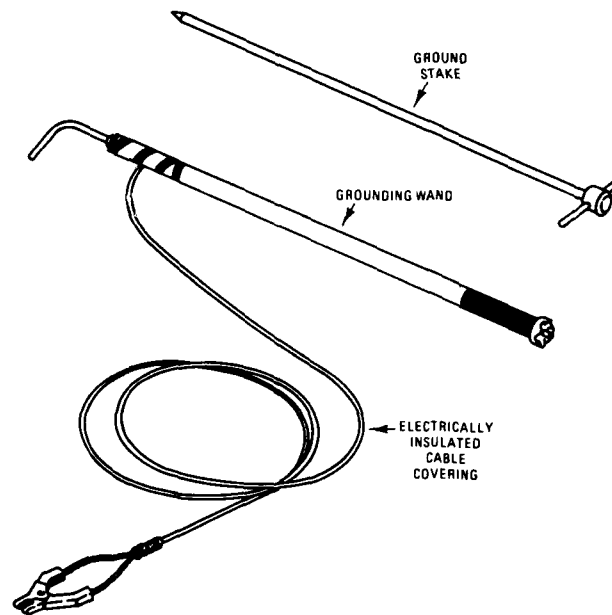


Fig. 5 - Alternate Helicopter Static Charge Grounding Wand design

LIGHTNING-INDUCED TRANSIENT PROTECTION FOR COMMERCIAL AIRCRAFT, USING FREQUENCY DOMAIN ANALYSIS AND LOW-LEVEL TEST METHODS

D. A. East
Boeing Commercial Airplane Company
P.O. Box 3707, M/S 47-31
Seattle, Washington 98124

ABSTRACT

The analysis and test methods used to design and validate the lightning protection for commercial aircraft are applied to an aluminum airplane with extensive use of composites in the secondary structure. Airplane leading edge and engine nacelle wiring is routed in areas that are covered by composite structure. The lightning-induced coupling analysis and modeling for this wiring is described. Low-level testing to develop or validate the coupling models is described. Comparison of model responses with test data is made. Using the model to extrapolate to full lightning threat levels is discussed.

INTRODUCTION

A COMPREHENSIVE EFFORT is necessary to protect commercial aircraft flight critical electrical and electronic systems from the induced effects of lightning. In this paper, an approach for developing the necessary protection is presented which uses frequency domain coupling analysis and swept-CW testing. The approach is presented through a design example where lightning protection is developed for electronic engine control electronics.

GENERAL APPROACH

An approach for designing lightning protection for commercial airplanes is outlined as follows:

1. Define lightning threat environment.
2. Define electrical and electronic equipment criticality.
3. Establish equipment qualification test waveforms and levels consistent with the expected induced transients after protection.
4. Assess the vehicle geometry and equipment wiring to determine exposure to lightning currents.
5. Perform simple calculations using the threat and vehicle geometry to establish baseline transient estimates for comparison with hardness levels of qualified equipment.
6. Recommend additional protection beyond inherent structural protection if required.
7. Construct a more detailed transient prediction model for the most critical equipment wiring. Using lab, mockup, and full-sized airplane tests, develop the model and improve the induced transient estimates. Use model to develop candidate protection methods when required.

8. Perform swept-CW lightning simulation ground tests on vehicle with the chosen protection methods implemented.
9. Update prediction model based on swept-CW test results (if required). It may be necessary to repeat items 8 and 9 if satisfactory results are not achieved with the initial chosen protection method.

For present commercial airplane protection a double-exponential lightning current threat waveform with a peak current of 200 kA and a peak current rate-of-rise of 2×10^{11} A/s is used for design and analysis purposes. A reasonable maximum equipment qualification level of 600V is used, which is a compromise between having all the protection in the equipment and having it all in the wire shielding. The testing in 7 and 8 is to develop the prediction model for making various tradeoffs to choose the optimum protection and to verify the protection effectiveness.

DESIGN EXAMPLE: ENGINE CONTROL ELECTRONICS PROTECTION

Wiring that feeds engine-mounted electronics from the flight deck or electronics bay passes under dielectric and advanced composite panels and fairings on its way along the wing leading edge through the strut and onto the engine. Accordingly, the wiring is exposed to fields from engine and wing lightning currents should lightning attach to the airplane. Initial estimates of the coupling to this wiring require the following tasks:

1. Establish the lightning attachment to the airplane that gives a current flow path that produces maximum coupling to the control wiring.
2. Identify wire routing and those portions of the routing where exposure to lightning currents will most likely occur. This is essentially locating electromagnetic apertures.
3. Calculate the open circuit voltage that the wiring will be exposed to at each aperture. Since wire runs are not straight and orderly, average heights and lengths are used. Nearby metallic hardware (ducts, spar stiffeners, control cables) reduces effective loop areas, but credit for the shielding from the hardware is ignored in the preliminary calculations.
4. From the calculations, if the sum of all the apertures is above the electronics-qualified hardness level (600V), develop possible protection methods to reduce levels to within 600V.

In a nacelle-to-opposite-wingtip attachment (Fig. 1), current will flow from the engine inlet up into and along the wing leading edge to the fuselage (Fig. 2). Significant coupling to the engine control wiring will occur (Fig. 3). The coupling to engine wiring occurring along the flow path can be broken down into segments and an equivalent aperture voltage source calculated for each segment. The engine aperture will be discussed to demonstrate the approach. To save weight the engine fan cowl (Fig. 4), which was previously constructed of aluminum, has been changed to graphite composite structure, and engine wiring is routed underneath it. The wiring is more exposed to the induced effects of lightning because the composite cowl does not provide the degree of shielding an aluminum one would. To assess the exposure of the wiring, a simple calculation is made assuming the cowl is not providing any shielding and is essentially removed (Fig. 5). The voltage on a wire installed above the fan case is:

$$V_{oc} = A \frac{\partial B}{\partial t} = \frac{\mu_0 L H}{Cir} \dot{i} \quad (1)$$

A = loop area = LH

L = wire length = 1.3m

H = wire height above fan case = .0762m

$\frac{\partial B}{\partial t}$ = derivative of the magnetic field with respect to time and proportional to the lightning current.

\dot{i} = derivative of the lightning current with respect to time

= 2×10^{11} A/s

μ_0 = permeability of free space

= $4\pi \times 10^{-7}$ H/m

Cir = circumference of the fan case

= $\pi (2.54)m$

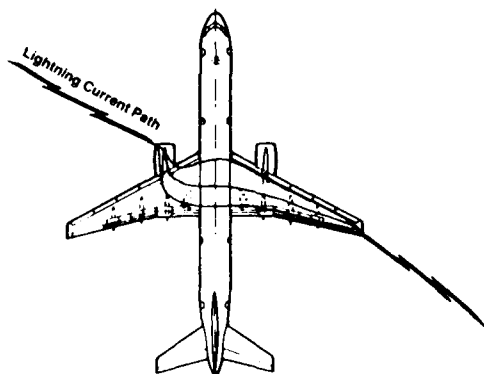


Fig. 1 - Lightning Current Flow Path for Nacelle-to-Opposite-Wingtip Strike

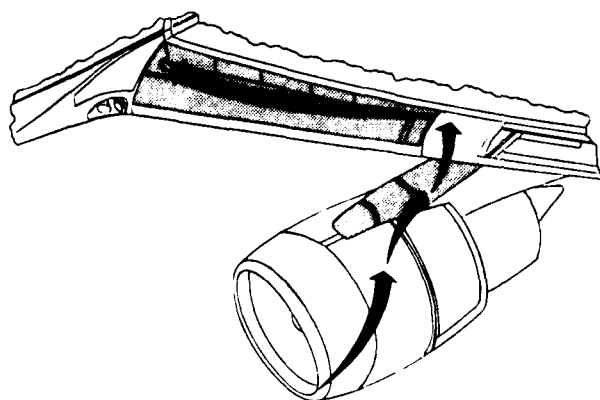


Fig. 2 - Lightning Current Flow Along Nacelle and Wing Leading Edge

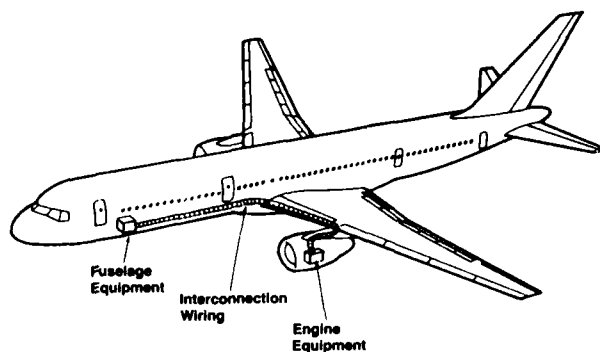


Fig. 3 - Engine to Fuselage Wire Routing

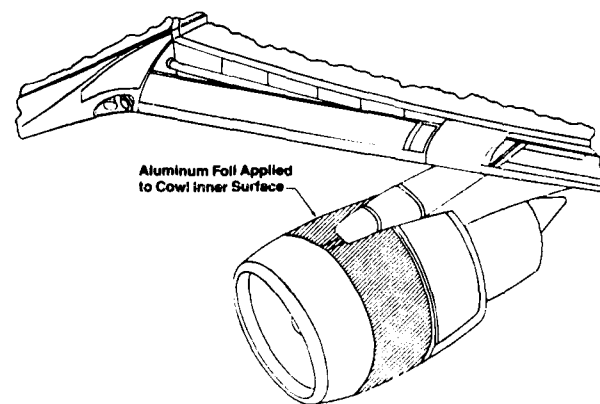


Fig. 4 - Aluminum Foil on Fan Cowl Inner Surface

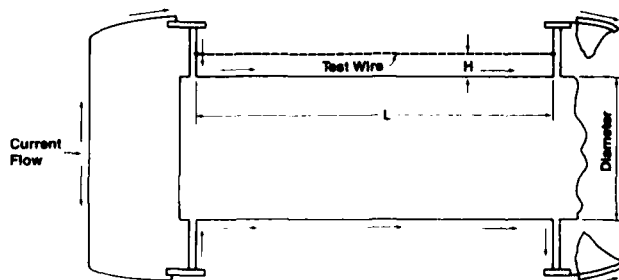


Fig. 5 - Engine Test Wire Geometry Without Cowl

The open circuit voltage is proportional to the loop area and the changing magnetic field. Using values from the geometry, the voltage is:

$$V_{oc} = \frac{(4\pi \times 10^{-7})(1.3)(.0762)}{\pi(2.54)} (2 \times 10^{11})$$

$$= 3.12 \text{ kV} \quad (2)$$

This calculation shows the voltage to be much larger than the 600V equipment qualification level, indicating the need for more protection in this area. All other apertures along the wire route are assessed in this manner to determine the total exposure voltage level. Protection methods are developed for each aperture, and trades are made based on protection effectiveness, weight, cost, reliability, maintainability, and other factors to select the optimum protection method. For the fan cowl aperture, a protection method that uses a thin aluminum foil layer applied to the inner surface of the fan cowl was chosen to shield the underlying wires. Installing metal braid over the wiring or rerouting it closer to the fan case are other protection methods. The foil was grounded around the fore and aft edges and near the strut to primary structure, providing a current path above rather than below the wires (Fig. 6). The voltage on the wiring protected by the foil was expected to be reduced considerably and to be related to the current times the resistance of the foil layer plus a contribution from any apertures created in the foil by access panels and other cowl penetrations. The accuracy of the transient estimates with and without protection installed depends on how well the physical parameter values in the equations are known. Many parameter values can only be determined by testing. To ensure the most flight critical electronics are adequately protected, a mathematical/analytical model is constructed that can be developed through testing and used to improve the transient estimates. With the model, sensitivities to parameters can be readily determined and various protection trades examined. In the frequency domain it is much easier to see the effects of changes in design details (i.e., parameters) than it is looking at a time domain response pulse. The swept-CW test method is excellent for developing this frequency domain model.

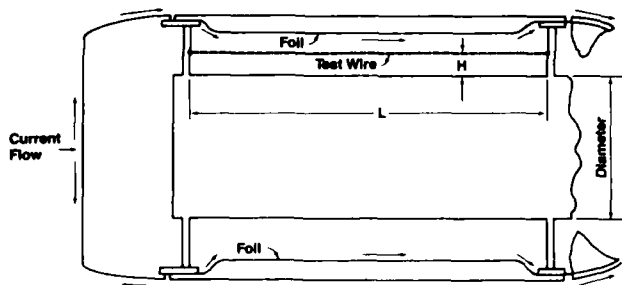


Fig. 6 - Cowl Current Flow With Foil on Fan Cowl

ANALYTICAL COMPUTER MODEL

A more detailed coupling analysis can be made using an analytical computer model constructed from a circuit

analysis code that models discrete elements and transmission lines. The airplane can be modeled as a collection of transmission lines for the various structural sections such as the wing, fuselage, and stabilizers. The wire bundles and electronics can be modeled with discrete elements for the loads, and transmission lines for the wires. Aperture sources are calculated from the airplane transmission-line model (Fig. 7) and connected into the wire bundle model to determine load responses. With this type of model the longitudinal current distribution is calculated, airframe and wire resonances are included, and sources are added with the correct phase relationships. The model also outputs responses in the frequency domain in the form of transfer functions with reference to the airframe lightning input current, which can be compared with swept-CW test data that is measured as a transfer function. The block "NAC1" represents the engine nacelle where the fan cowl aperture is located. To calculate the open circuit voltage on a wire with the cowl removed, the block "NAC1" is broken into two blocks at the approximate location of the wire. An inductor, representing the mutual inductance between the engine fan case and the wiring, is placed between the two blocks (Fig. 8). The value of the inductor "M" is related to the geometry as shown in the initial transient estimate.

$$M = \frac{\mu_0 L H}{C_{ir}} \quad (3)$$

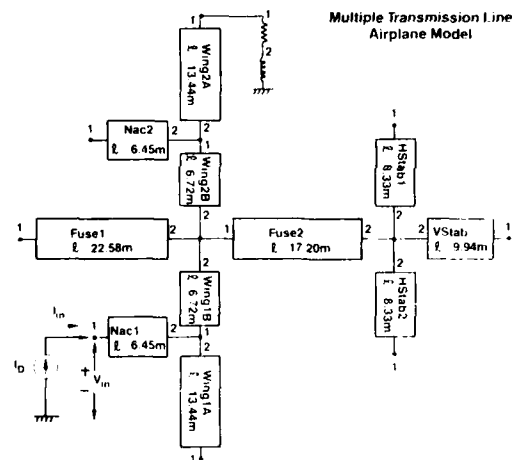


Fig. 7 - Airplane Transmission-Line Model

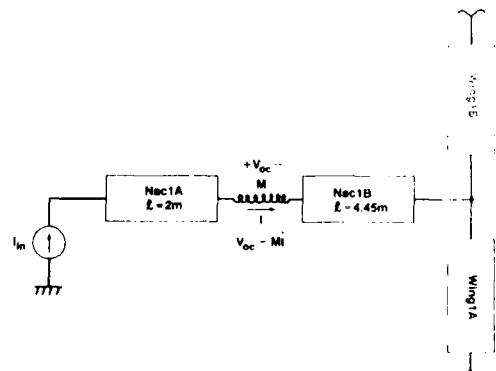


Fig. 8 - Aperture Source Calculation Using Airplane Model

The voltage across the inductor is:

$$V_{oc} = M \dot{I} \quad (4)$$

which is the relationship for the voltage on the wire. In the frequency domain this expression is

$$V_{oc} = j\omega M I$$

$$\omega = 2\pi f \quad (5)$$

If the voltage is divided by " I_{in} ," the current into the nacelle, a transfer function is formed that can be compared with swept-CW test data.

$$TF_{voc} = \frac{V_{oc}}{I_{in}} = j\omega M \frac{I}{I_{in}} \quad (6)$$

All the aperture sources can be calculated by breaking the transport transmission-line model at locations where apertures exist and inserting discrete elements which give the desired functional relationship between the current or voltage at the locations and the aperture voltage or current sources. The value of " M " from the simple calculation is 15.6 nH, which can be compared with the value obtained from the swept-CW test data.

SWEPT-CW TESTING

For the design example where coupling to engine control wiring is considered, short test probe wires were installed at locations on the engine and along the wing (Fig. 9) to measure the various aperture sources. The particular responses measured were the open circuit voltage and short circuit current on each wire divided by the current into the nacelle as a function of frequency from 1 KHz to 13 MHz. Current is injected into the nacelle, exits by the opposite wingtip, and returns to the generator through a ground screen.

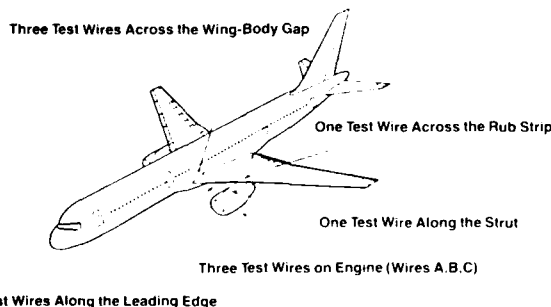


Fig. 9 - Test Wire Installation for Ground Test

In the ground test the wingtip is shorted to the ground screen. To configure the model accordingly, the wingtip is connected to ground through a small resistance and inductance (Fig. 7). The longitudinal current distribution is different during the testing than it would be for an airplane in flight being struck by lightning. The model is configured this way while being developed with test data. Once the data and model agree sufficiently, the model is reconfigured for the in-flight case (Fig. 10).

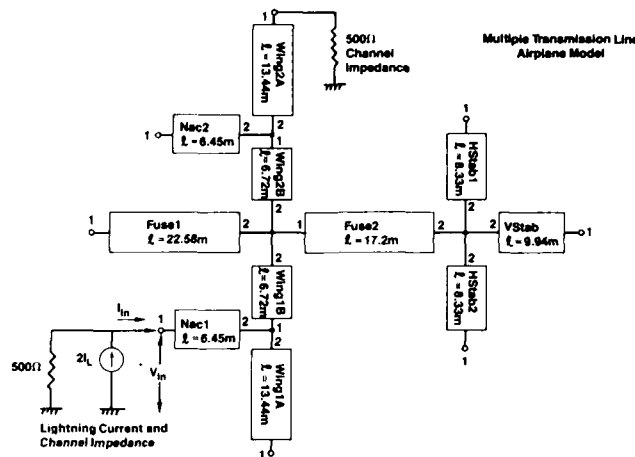


Fig. 10 - Airplane Model Configured for In-Flight Strike Calculation

The open circuit voltage swept-CW transfer function (TF_{VOC}) on the engine fan case test wire with no foil installed has the form:

$$TF_{VOC} = \frac{V_{oc}}{I_{in}} = j\omega M \frac{I}{I_{in}} \quad (7)$$

The mutual inductance can be extracted from the low frequency behavior (the frequency is below airplane structure and wire resonant frequencies) of the open circuit voltage transfer function. Below 500 KHz, $|I/I_{in}| = 1$, and the transfer function reduces to

$$TF_{VOC} = \frac{V_{oc}}{I_{in}} = j\omega M \quad (8)$$

$$\text{giving } |M| = \frac{(V_{oc}/I_{in})}{2\pi f_0} \quad (9)$$

where V_{oc}/I_{in} is obtained from the data at f_0 , where the plot is changing at a rate of 6 dB/octave of frequency. Looking at V_{oc} on the horizontal wire (Fig. 11) at 100 KHz (130 KHz sweep) $V_{oc}/I_{in} = -46.6 \text{ dB} = 4.7 \times 10^{-3}$

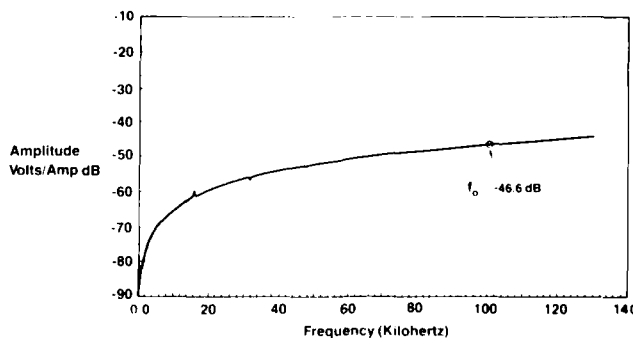


Fig. 11 - Swept-CW Data: VOC Horizontal Wire, Cowl Open (130 kHz)

giving
$$M = \frac{4.7 \times 10^{-3}}{2\pi (100 \times 10^3)} \quad (10)$$

$= 7.49 \text{ nH}$

Using this mutual inductance in the airplane model, the analytic transfer function, TF_{VOC} (Fig. 12), was calculated and should be compared to the CW data (Fig. 13).

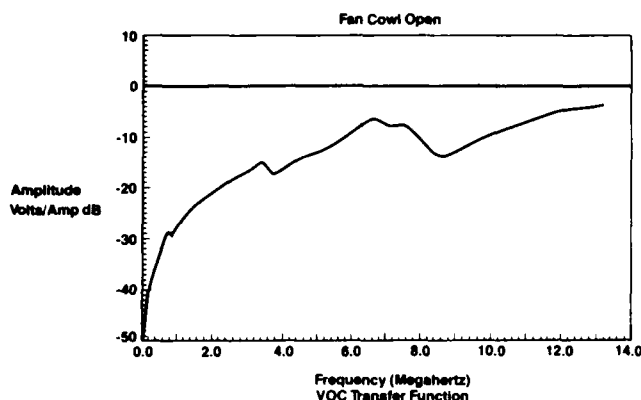


Fig. 12 – Model Transfer Function: VOC Horizontal Wire, Cowl Open

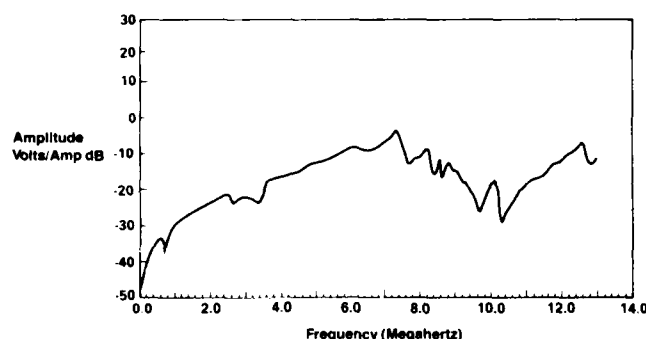


Fig. 13 – Swept-CW Data: VOC Horizontal Wire, Cowl Open (13 MHz)

The short circuit current swept-CW transfer function TF_{ISC} on engine fan case test wires with cowl removed has the following form.

$$TF_{ISC} = \frac{I_{sc}}{I_{in}} = \frac{j\omega M}{R_w + j\omega L_w} \frac{I(x)}{I_{in}} \quad (11)$$

where R_w and L_w are the wire resistance and inductance respectively.

At frequencies high enough that $\omega L_w > R_w$ (and low enough that $|I(x)/I_{in}| = 1$), the transfer function flattens out and is equal to

$$TF_{ISC} = \frac{j\omega M}{j\omega L_w} = \frac{M}{L_w} \quad (12)$$

Since M is determined from the open circuit voltage transfer function, the wire inductance L_w can be calculated as

$$L_w = \frac{M}{|TF_{ISC}|} \quad (13)$$

knowing the magnitude of TF_{ISC} over the region, the transfer function, is flat.

At a frequency below where the transfer function flattens out and the magnitude is down by 3 dB, the wire resistance and inductive reactance are equal:

$$R_w = \omega L_w \quad (14)$$

which allows determination of the wire resistance also.

For the horizontal wire on the fan case whose CW transfer function is shown (Fig. 14), the data is flat at -42 dB, giving:

$$L_w = \frac{M}{|TF_{ISC}|} = \frac{7.49 \text{ nH}}{7.943 \times 10^{-3}} = .94 \mu\text{H} \quad (15)$$

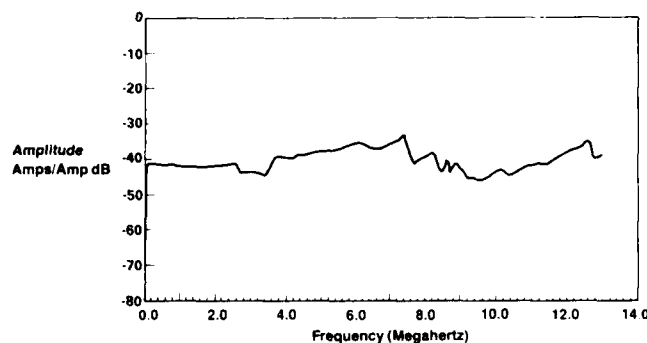


Fig. 14 – Swept-CW Data: ISC Horizontal Wire, Cowl Open

The transfer function is 3 dB down at $f = 14.5 \text{ KHz}$, giving

$$\begin{aligned} R_w &= 2\pi f L_w \\ &= (2\pi)(14.5 \text{ KHz})(.94 \mu\text{H}) \\ &= .086\Omega \end{aligned} \quad (16)$$

Using these values in the model, the transfer function (Fig. 15) was calculated.

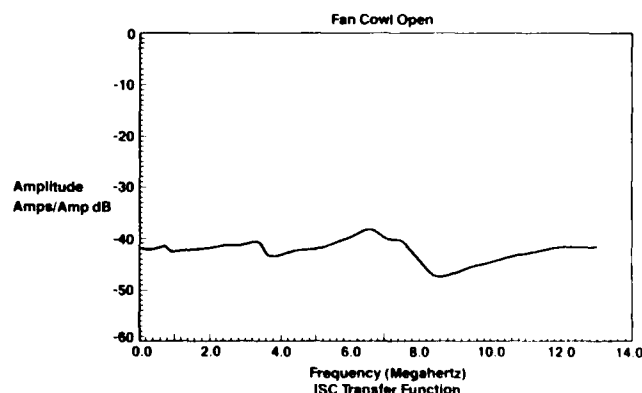


Fig. 15 – Model Transfer Function: ISC Horizontal Wire, Cowl Open

With the aluminum foil sheet installed on the cowl inner surface, the foil diverts current from flowing entirely on the fan case below the wire, reducing the fields and induced wire voltage. Current is shared as a function of impedance (fan case versus cowl) and, as such, is frequency dependent. At low frequencies all the current flows on the fan case, and at higher frequencies, where the current is being shared inductively, the cowl foil carries most of the current. As a function of frequency, the current on the case is

$$I_{\text{CASE}} = \frac{A}{A + j\omega} I_{\text{TOTAL}} \quad (17)$$

where A is the frequency at which the current on the case is reduced by 3 dB. The variable A is the ratio of the foil and joint resistance to the fan case cavity inductance and can be determined from the measured swept-CW transfer functions. The resistance of the fan cowl foil layer was much higher than a continuous 2 mil aluminum foil sheet, and most of the resistance was found to be located in the joints where the foil sections were spliced together. The measured open circuit voltage transfer function (Fig. 16) is modified from the cowl-open case by the factor $A/(A + j\omega)$ and is:

$$TF_{\text{VOC}} = j\omega M \frac{A}{A + j\omega} \quad (18)$$

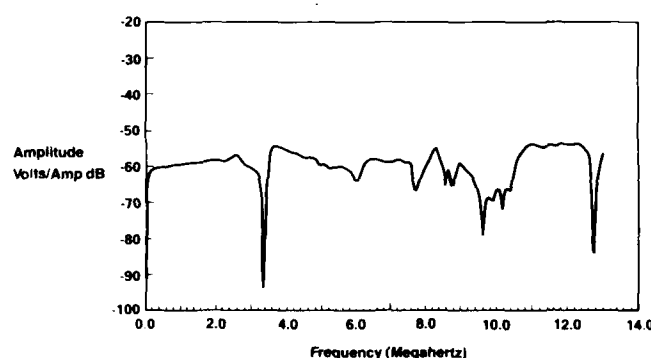


Fig. 16 – Swept-CW Data: VOC Horizontal Wire, Cowl Closed

The measured short circuit current transfer function (Fig. 17) is also modified by the same factor and is given by:

$$TF_{\text{ISC}} = \frac{j\omega MA}{(R_w + j\omega L_w)(A + j\omega)} \quad (19)$$

From the data the parameter values are:

$$\begin{aligned} M &= 7.49 \text{ nH} & , & & A &= 2\pi (21.25 \times 10^3) \\ R_w &= 100 \text{ m}\Omega & , & & L_w &= 1.5 \text{ }\mu\text{H} \end{aligned} \quad (20)$$

Model transfer functions, using the above parameters (Figs. 16 and 17), can be compared to the measured data (Figs. 18 and 19). The testing showed the mutual inductance to be approximately 6 dB lower than the calculated estimate and gave a quantitative measure of the foiled cowl shielding effectiveness, which could not be calculated. All the other

individual aperture sources are determined in a similar manner and included in the model. The overall circuit responses are obtained by running the model with the sources installed in a transmission-line model of the wire bundling and circuit loads and transforming the result to the time domain.

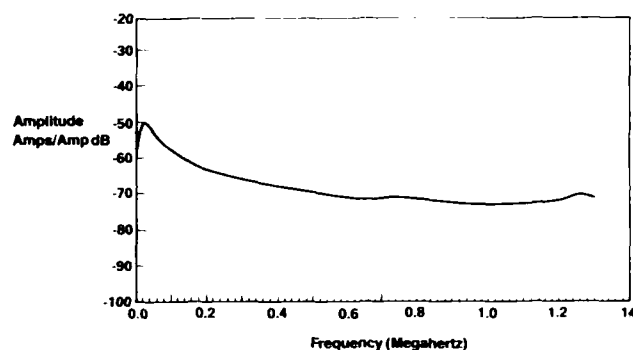


Fig. 17 – Swept-CW Data: ISC Horizontal Wire, Cowl Closed

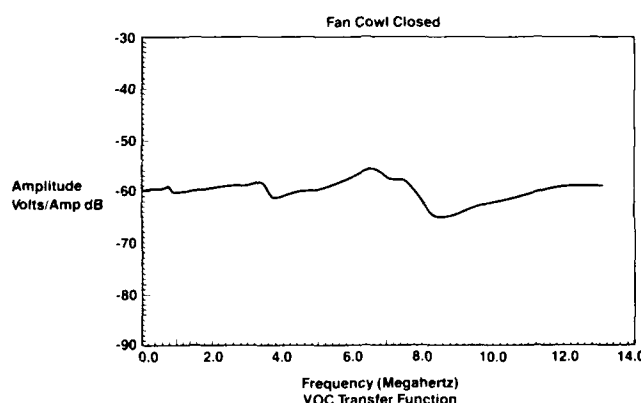


Fig. 18 – Model Transfer Function: VOC Horizontal Wire, Cowl Closed

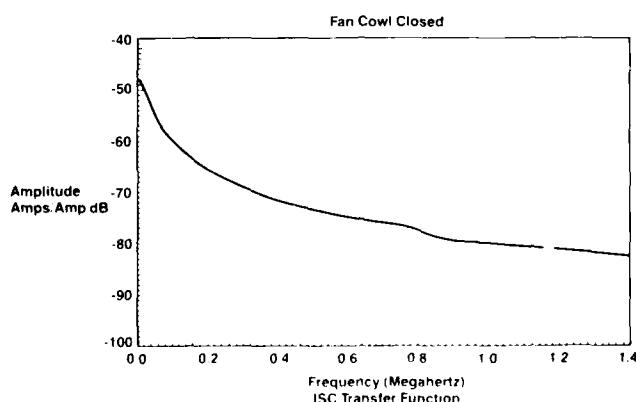


Fig. 19 – Model Transfer Function: ISC Horizontal Wire, Cowl Closed

PROTECTION ASSESSMENT FROM MODELING AND TEST RESULTS

At this point an evaluation of the protection can be made by comparing the equipment hardness levels with the transient levels obtained from the model for a full threat, in-flight lightning strike. The airplane transmission-line model will be configured as shown (Fig. 10) for the in-flight threat. Airframe resonances will change from the ground test case because the lightning channel impedance (500Ω) is much higher than the test generator and wingtip termination impedances. If the voltage is less than 600V by some chosen safety margin, the design is adequate. If the expected levels are too large, additional protection should be developed using the model to evaluate the effectiveness of available protection methods. Another ground test with the protection installed should then be done and the results extrapolated with the model to the in-flight case to confirm design acceptability.

CONCLUSION

An approach for designing induced transient protection for airplanes has been described. This approach uses frequency domain coupling models developed through swept-CW testing to predict in-flight lightning-induced transients. The significance of the modeling and swept-CW testing is that together they allow the determination of the nature and location of the wiring excitation along the airplane. The primary excitations from apertures, once determined, can be reduced through various protection methods which can be implemented and examined with the model. The improved understanding of the coupling will hopefully result in an optimum design.

CORROSION PROPERTIES OF SECOND GENERATION CONDUCTIVE MATERIALS

Earl Groshart
The Boeing Aerospace Company
P. O. Box 3999, Seattle, WA 98124

This paper will discuss the corrosion resistance and other properties of second generation conductive (EMI control) materials.

Since the introduction of the silver filled/epoxy adhesives, coatings, lubricants, gaskets and other materials was introduced for EMI control in the 60's, a new generation of materials have developed. These materials use fillers of nickel, stainless steel, carbon and aluminum and a variety of resins including acrylics, polyurethanes, latexes and alkyds.

These materials have been tested for their own corrosion resistance and their ability to prevent corrosion of a variety of substrates in a humidity and salt fog environment. DC resistance values are used as a measure of the extend of corrosion.

The galvanic effects generated between these materials and structural aluminum were studied in extremely corrosive environments, ie. salt spray.

Data for the use of these materials in design and data for their processing in manufacturing were developed and are reported in this paper.

This paper was not available for incorporation into this book.

MEASURED TRANSFER IMPEDANCE OF A LARGE GRAPHITE EPOXY
COMPOSITE TUBE WITH CURRENT DIVERTERS

L. O. Hoeft, V.A. Gieri and J. R. Hofstra

The BDM Corporation
1801 Randolph Road S.E.
Albuquerque, New Mexico 87106

ABSTRACT

The transfer impedance of a 47-inch long, 11.5-inch diameter, 0.1-inch thick graphite epoxy tube was measured in a quadraxial test fixture from 10 Hz to 100 MHz. These measurements showed that the sample behaved like a homogeneous material with a conductivity of about 2×10^4 mhos/M. Four copper tubes were fastened to the sides of the tube as current diverters. Measurement of this configuration showed that the transfer impedance began to increase at 100 Hz and reached the original value (without diverters) by about 30 kHz, suggesting that inductive current division is more important than resistive current division for frequencies above a few tens of kilohertz. Additional measurements explored the effect of joint impedance and composite-metallic conduit-braided cable structures.

©1984 IEEE

Printed with permission from 1984 IEEE National Electromagnetic Compatibility Symposium
April 24-26, San Antonio, Texas

INTRODUCTION

COMPOSITE MATERIALS are being used more frequently in advanced aerospace systems. This use led to concerns about their ability to shield against electromagnetic fields and carry large currents generated by lightning or EMP. The purpose of this study was to explore the electromagnetic properties of graphite-epoxy composite and to take an initial look at how electromagnetic energy couples through a composite-metallic conduit-braided cable structure.

After the approach is presented, the results of measurements that determined (1) the composite material properties, (2) the effect of current diverters, (3) joint fastener spacing, and (4) multiple material coupling will be presented and discussed. Finally, the results will be summarized.

APPROACH

The surface transfer impedance method was chosen as the most desirable approach for determining the electromagnetic properties of the graphite epoxy since it is: (1) very reproducible, (2) relatively easy to measure, (3) easily interpretable, and (4) corresponds to configurations frequently seen in the aerospace industry. A 49-inch long, 11.5-inch diameter, 0.1-inch thick sample of graphite epoxy was obtained and made into a 50-ohm transmission line by inserting a metal cylinder into its center. Each end of the composite tube was prepared by machining the surface and fastening 3/4 inch copper rings on the inside and outside using conductive epoxy and rivets (4-inch spacing). The ends were sealed with copper end caps which could be soldered to the tube's end rings.

A special quadraxial test fixture was built to accommodate the sample, and the surface transfer impedance was measured using procedures normally used for cable measurements [1]*. A computer-controlled data acquisition system, shown in Fig. 1, was used to make the measurements from 10 Hz to 100 MHz. The sense wire for measuring the voltage was either the metal cylinder inside the composite tube or, in the case of the composite tube-metallic conduit-braided cable combination, it was the twisted pair of the braided cable connected in common mode.

Besides measurements of the composite tube itself, several configurations were measured in which 5/8-inch O.D. copper pipes were placed on the exterior and interior surfaces of the composite tube to see how currents would flow on structures made with both composite and metal current paths.

*Numbers in brackets designate references at end of paper.

RESULTS

TRANSFER IMPEDANCE OF A COMPOSITE CYLINDER WITH AND WITHOUT CURRENT DIVERTERS - Fig. 2 shows the measured transfer impedance of the composite tube, with and without four copper current diverters. The measured transfer impedance of the composite tubing without diverters displays the classic shape expected of a solid cylindrical shield. This suggests that graphite epoxy acts like a homogeneous material. The d.c. resistance (18.4 milliohm/m) is in good agreement with the low frequency transfer impedance (17.0 milliohms/m). This resistance and the break frequency are consistent with a homogeneous material with a conductivity of 2×10^4 mhos/m.

The purpose of the second set of measurements was to determine the effect of adding current diverters in parallel with the composite tube. Four 5/8-inch copper pipes, each with a d.c. resistance of .48 milliohms/m, were soldered to the composite tubing end caps in two configurations. One configuration placed the current diverters at equally spaced intervals around the circumference of the tube. The other configuration placed the current diverters in pairs on opposite sides of the tube. This configuration was meant to correspond to cable conduits on the leading and trailing edges of a wing or cableways on a space vehicle. The results of these measurements are also shown in Fig. 2.

The addition of these current diverters to the exterior significantly lowered the low frequency transfer impedance. However, it begins to increase at 100 Hz, and by 30 kHz the effect of the diverters has disappeared. This is consistent with earlier measurements of cableways with aluminum sides and a steel top and bottom [2]. At very low frequencies, the current divides resistively. Since the parallel resistance of the four diverters is more than two orders of magnitude below that of the composite, essentially all the current flows on the diverters. The d.c. resistance of this configuration (equal spacing) was 0.23 milliohms/m, which is reasonably close to the low frequency transfer impedance (about 0.3 milliohm/m) if the finite resistance of the end cap is considered.

As the frequency increases above 100 Hz, the current starts to spread around the tube, following the path of least impedance. In this frequency range, the inductance of the tube is becoming more significant than the resistance. The current follows the path of least inductance, that is, the current tends to spread itself evenly around the circumference of the structure. The second configuration (two pairs opposite each other) has a higher inductance; therefore, the transition begins at a lower frequency than for the first configuration (four equally spaced diverters). Above 30 to 100 kHz, all configurations looked essentially the same. Thus, current diverters are not particularly effective against fast risetime transients like

AD-A169 867

INTERNATIONAL AEROSPACE AND GROUND CONFERENCE ON
LIGHTNING AND STATIC ELE. (U) NATIONAL INTERAGENCY
COORDINATION GROUP JUN 84

6/6

UNCLASSIFIED

F/G 20/3

NL





1.0



1.1



1.25



1.4



1.6



1.8



2.0



2.2



2.5



2.8



3.15



3.5



4.0



4.5

EMP or some parts of the lightning waveform. On the other hand, such transients should not produce high surface current densities since the fast risetime current is spread more or less uniformly over the structure.

EFFECT OF END CAP CONNECTIONS - A major concern in the electromagnetic design of composite structures is the performance of the joints. A complete investigation of the electromagnetic characteristics of joints in composite material was outside the scope of this study. However, the effect of joints was explored by simulating a worst case condition, namely that the composite material did not make contact and the only electrical connection was by means of fasteners (bolts, rivets, etc.). In this study the fasteners were simulated by short wires connected between the composite tube and end caps which were insulated from the tube. No current diverters were used.

The measured transfer impedances for one, three, and six connections are shown in Fig. 3. The connection spacing is 36, 12, and 6 inches for these three cases. At low frequencies, i.e., up to 100 kHz, the transfer impedance is equal to the samples' d.c. resistance. At high frequencies, above 1 MHz, the transfer impedance is proportional to both the frequency and the connection spacing. This suggests that the high frequency performance is dominated by the mutual inductance coupling due to the slots or apertures that exist between these connections. The magnetic and electric polarizability, and the corresponding mutual inductance of such slots can be calculated. The major unknown is the effective height and width of the slot, since it does not have zero depth. These measurements show that nonuniform joints, such as might be expected in practice, act like apertures and dominate the behavior of the material above 1 MHz.

TOTAL TRANSFER IMPEDANCE OF A COMPOSITE TUBE-METALLIC CONDUIT-BRAIDED CABLE SHIELDING SYSTEM - Most practical shielding situations do not usually consist of a single shield, but are composed of metallic and composite structures, conduits, and cable shields. The purpose of the third phase of this study was to investigate the total effect of such a combination. The quadraxial test fixture was used to inject a current on the outside of the composite tube. A twisted, shielded wire pair was placed at various locations and the common mode voltage was measured. The ratio of this voltage to the injected current is defined as the total transfer impedance. For the first measurement, the twisted, shielded pair ($R = 33$ milliohms/m) was placed on the outside surface of the composite tube. Next, the twisted, shielded pair was placed over a strip of 2-inch wide copper tape (resistance = 9.9 milliohms/m). Finally, the twisted, shielded pair was placed in a 5/8-inch copper pipe and placed either outside or inside the composite tube. The results are shown in Fig. 4.

The uppermost plot of Fig. 4 is the transfer impedance of the graphite epoxy tube. The second plot is that of a twisted, shielded pair on the outside of the tube. At very low frequencies (below 100 Hz), the current divides resistively, and since the resistance of the twisted, shielded pair is almost twice that of the composite tube, the current flowing on the twisted, shielded pair is one-third of that flowing on the tube. Between 100 Hz and 30 kHz, the current spreads because it is seeking the path of lowest inductance. This behavior was described earlier in this paper in the discussion of current diverters. The total transfer impedance decreases, because less and less current flows on the cable shield. Finally, the total transfer impedance increases because direct mutual inductance coupling predominates.

The third plot on Fig. 4 is the total transfer impedance for a combination where the twisted, shielded pair is placed over a strip of 2-inch wide copper tape. This plot is similar to that of the twisted, shielded pair cable alone except that the total transfer impedance is lower. This behavior is expected, since the copper tape diverts current away from the cable braid.

Finally, the bottom plot of Fig. 4 shows the total transfer impedance of the twisted, shielded pair in a 5/8-inch diameter, 0.064-inch thick copper pipe attached to the outside of the composite tube. In this case, the total transfer impedance is dominated by the very low transfer impedance of the copper pipe.

The results of the total system simulation phase of this study suggest that even high resistance portions of the structure play an important role in keeping the current off the cable shields, thereby reducing the overall electromagnetic coupling at high frequencies. In addition, the current division appears to be primarily inductive.

SUMMARY

This study demonstrated the following:

- 1) Graphite epoxy acts like a homogeneous conductor with a conductivity of 2×10^4 mho/m.
- 2) Metal current diverters lowered the transfer impedance below 100 Hz, because of resistive current division. However, the effect of such diverters essentially disappeared by 30 kHz suggesting that the current follows the path of least impedance, which in this case is the path of least inductance.
- 3) Nonuniform joints behave like apertures and dominate behavior above 1 MHz.
- 4) All parts of the structure, including those of relative high resistance, play a significant role in diverting current from the cable shields. In fact a composite tube-braided cable combination demonstrated reasonably good electromagnetic performance.

ACKNOWLEDGEMENT

The authors wish to thank Mr. Don Haggard, SKYLINE Industries, Fort Worth, Texas for his help in fabricating and preparing the graphite epoxy sample.

REFERENCES

1. J. S. Hofstra, M. A. Dinallo, L. O. Hoeft, "Measured Transfer Impedance of Braided and Convoluted Shields," 1982 IEEE International Symposium Record on Electromagnetic Compatibility, IEEE 82 CH 1716-6, September 1982.
2. J. S. Hofstra, L. O. Hoeft, "Measured Transfer Impedance at Current Reduction Ratios of a Generic Cableway," IEEE 1983 International Symposium Record on Electromagnetic Compatibility, IEEE 83 CH 1838-2.

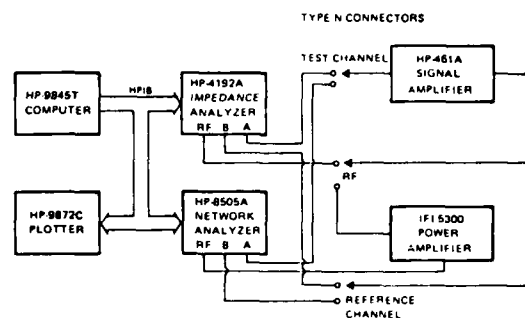


Fig. 1 - Computer-controlled data acquisition system

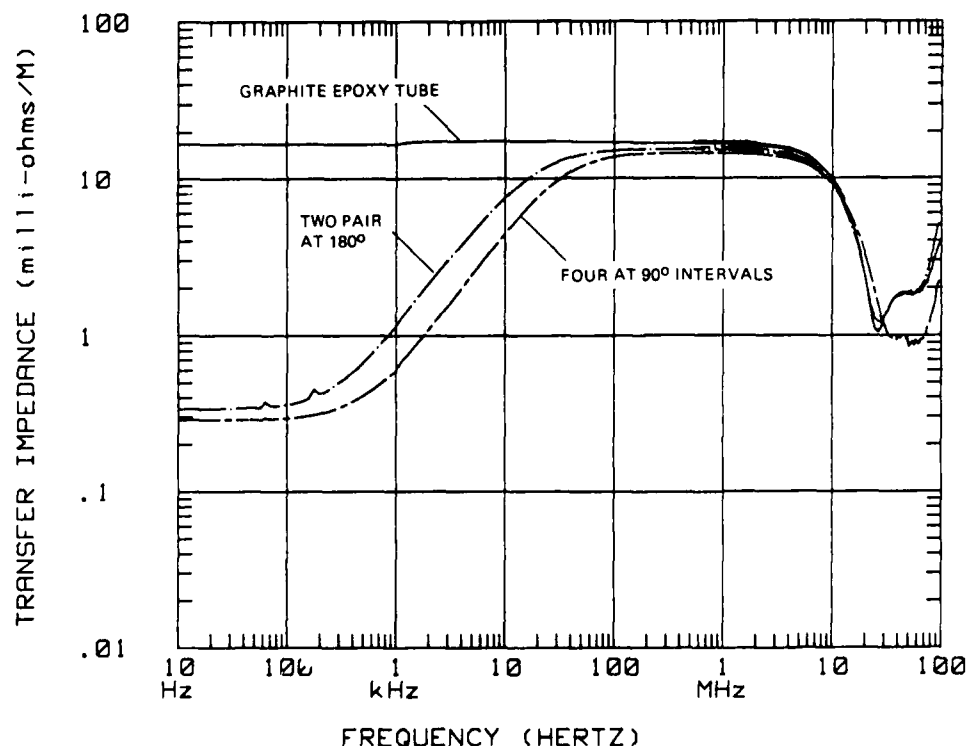


Fig. 2 - Effects of current diverter placement on the measured transfer impedance of graphite epoxy tube with current diverters

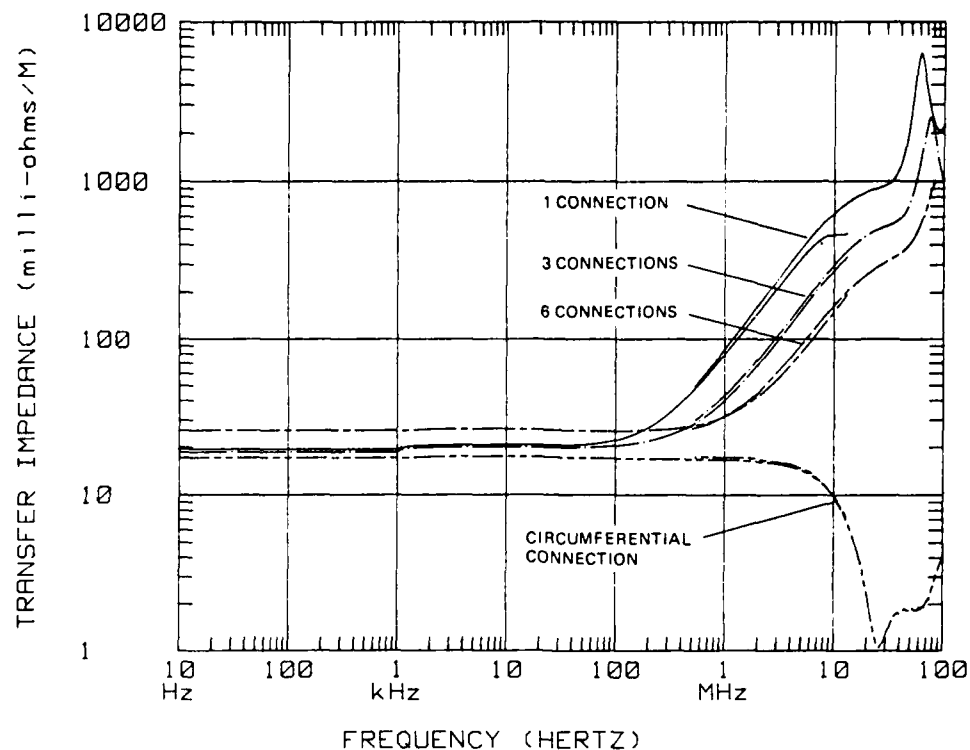


Fig. 3 - Effect of number of end cap connections on the measured transfer impedance of the graphite epoxy composite tube

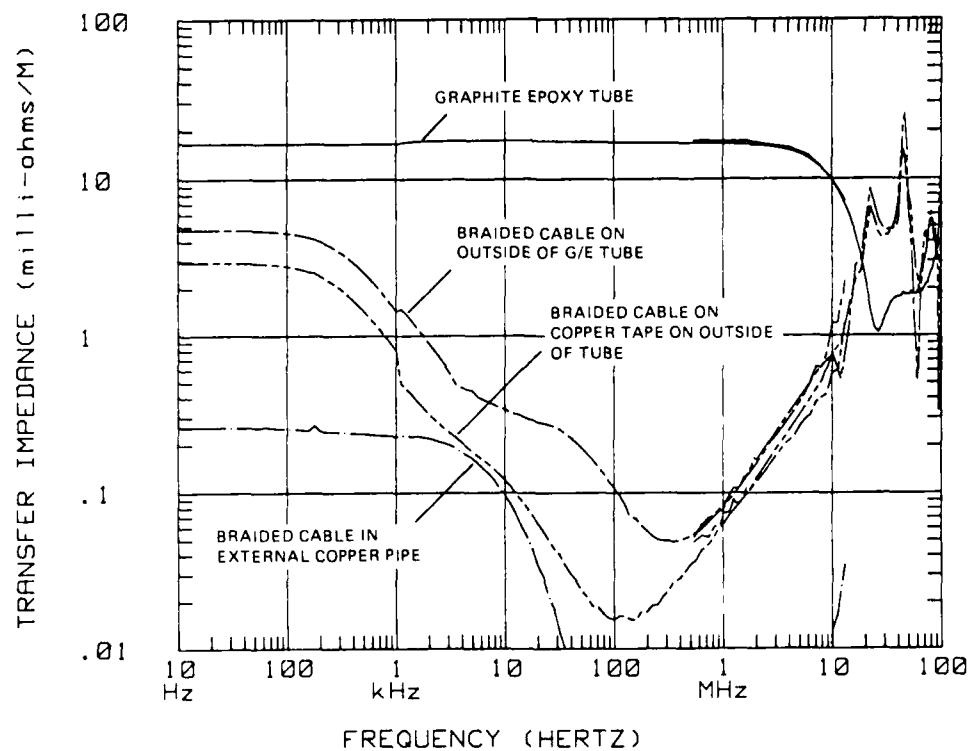


Fig. 4 - Total transfer impedance of composite tube-copper-conduit-braided-cable shielding system

NICKEL-COATED GRAPHITE AND ARAMIDE FABRICS AS PART OF COMPOSITE FOR
LIGHTNING STRIKE PROTECTION OF AIRCRAFT

Harold Ebneth Ph.D

Bayer AG Leverkusen, West-Germany
Central Research Dept. Application of New Products

ABSTRACT

Highly nickel-coated graphite and aramide fabrics will provide adequate composite structure protection from zone 2 A lightning strikes. The coating level used will depend on the damage tolerance and structural make-up of the part to be protected.

Adequate protection implies that a level of coating can be chosen, which when applied will limit the damage to a level which can be tolerated by the structure.

These highly nickel-coated fabrics show an excellent shielding effectiveness from electromagnetic waves (attenuation of 40 to 60 dB) and outstanding reflection of microwaves (loss of reflection ≤ 0.1 dB).

SUMMARY

Nickel-coated graphite fabrics with an amount of 100 to 150 g/m² will provide adequate composite structure protection from zone 2 A lightning strikes (100 kA, 0.25 10⁶ A².s and 3.6 kA, 10 coulombs). Graphite fabrics coated with nickel of more than 150 g/m² will provide protection for composite structures subject to zone 1 A lightning strikes (200 kA, 2 x 10⁶ A².s and 3.6 kA, 10 coulombs). The coating level used will depend on the damage tolerance and structural make-up of the part to be protected.

Adequate protection implies that a level of coating can be chosen, which, when applied, will limit the damage to a level which may be tolerated by the structure.

Tests on nickel-coated aramide filament fabrics like Kevlar indicate that an equivalent protection can be produced.

Both nickel-coated fabrics show an excellent shielding effectiveness in the range of 1 GHz - 96 GHz (attenuation of above 40 dB) and outstanding reflection of microwaves in the same range of frequency (loss of reflection ≤ 0.1 dB, i. e. ≥ 98 % reflection).

INTRODUCTION

Advanced composite structural materials are presently being considered for various applications on new aircraft systems. Many details were published during the 8th International Aerospace and Ground Conference on Lightning and Static Electricity, June 21 - 23, 1983, Fort Worth, Texas, USA [1]. Many of the applications expose the new materials to the effects of lightning strikes. MIL-STD-1757 "Lightning Qualification Tests Techniques for Aerospace Vehicles and Hardware", 17 June 1980 and SAE AE4L Report, "Lightning Test Waveforms and Techniques for Aerospace Vehicles and Hardware", 20 June 1978, both define aircraft lightning strike attachment zones and specify simulated lightning tests to evaluate structural system performance. Composite structural materials are frequently used in zone 1 A (wing skin, fuselage panels, gear doors, bay doors and nose cones). Zone 1 A specifies the application of simulated lightning strike components A (200 kA, 2 x 10⁶ A².s) and B (10 coulombs, 2 kA, 5 ms). Consequently, development tests which apply zone 1 A tests comprised of components A and B are quite appropriate.

LIGHTNING STRIKE PROTECTION

Bayer AG and Mobay Chemical Corporation, Penn Lincoln Parkway West, Pittsburgh, Penn. 15 205, USA, have developed a lightning protection system, Baymetex-C for composite materials which involves applying a nickel

coating to the graphite and aramide fabric. Surface plies of the treated materials are used to protect the structure.

Approximately 400 composite panels containing plies of nickel-coated fabrics were subjected to lightning tests representative of the zones 1 A and 2 A lightning environment. The pure nickel-coated graphite fabrics were also tested before being embedded in the epoxy resin.

The tests were conducted at Lightning Technologies, Inc., 10 Downing Parkway, Pittsfield, Massachusetts, 01201 and Technical University of Braunschweig, West-Germany, Institute for High-Voltage Engineering, D-3300 Braunschweig, Pockelstr. 4.

Due to the many variables inherent in the fabrication of any composite structural system, the amount of protection necessary cannot be predicted without testing representative samples of the proposed design. This will be true of any lightning protection system. The amount of nickel metal on the graphite or Kevlar fabric may therefore vary according to the intended application and the lightning strike zone.

TEST SAMPLES

The test samples, nickel-coated graphite filament yarn fabrics and panels (fibre-reinforced epoxy resin panels), consisting of three filament yarn fabrics: one glass silk fabric, one non-metallized and one nickel-coated graphite filament yarn fabric (type 3 K 70 P) on the top, tested in West Germany, (in 1981 and 1982) were prepared by Bayer AG, Leverkusen and supplied to the Technical University of Braunschweig.

The samples tested in the USA were improved and the top ply of all test panels of the protected fabric was impregnated with the same epoxy resin system as contained in the underlying plies.

All painted samples were coated with a standard aircraft coating system as follows:

- ° 0.0005 to 0.001 inches of an epoxy primer complying with Boeing Material Specification (BMS) 10 - 79 Type 2
- ° 0.0015 to 0.002 inches of a polyurethane topcoat complying with BMS 10 - 60 Type 2

TEST PROCEDURES

Tests carried out by the University of Braunschweig:

The metallized parts of the laminates were clamped in two 40 cm long metal terminals arranged on opposite sides of the square test sample. In the tests for current-carrying capacity of the laminates, one terminal was earthed and the other was connected to the impulse current generator. When coupling the impulse current via an arc, a circular impulse-current carrying electrode of 1 cm diameter was attached at a distance of 1 mm above the laminate, which was earthed via the two terminals at its edges.

The impulse current amplitudes were approx. 10, 30, 50 and 100 kA in each case. The 10 - 50 kA values were produced using the generator at the Institute's branch in Braunschweig (capacitance 12.5 μ F, charging voltages up to 60 kV). A damped oscillation was generated with a period of 45 μ s; the impulse current values given are the crest values of the first semi-oscillation. The 100 kA impulse current was produced using a larger generator at the Institute's branch in Hallendorf (77 μ F, 15 kV).

The tests in the US were conducted in accordance with MIL-STD-1757 Method T02, zone 1 A, using arc entry current injection.

The samples were subjected to components A and B, as well as to a partial zone 2 A test consisting of components D and B. Sample damage assessments were made using visual means by Lightning Technologies.

The simulated lightning current pulses were generated using RLC circuits. The capacitance bank was charged to a predetermined voltage and discharged, on a single shot basis, through inductance, resistance and the test panel. Values of capacitance, inductance, and resistance are chosen to obtain the required voltage and current waveshapes as well as to insure that the test item impedance is small compared to circuit impedance and will therefore not affect waveshapes when inserted.

The measurements were displayed and photographically recorded on Tektronix oscilloscopes. The measurement signals are relatively low compared to the applied test, and shielding of the signal cables and the oscilloscopes is fairly important. The oscilloscopes are housed in an RF shielded room and the cables routed to them are carried from the point of test to the room in metal conduits.

The current measurements were made using a 100 : 1 pulse current transformer with a 0.01 ohm burden resistor and a 0.005 ohm resistive shunt. Component A currents were measured on the current transformer, which has a 1 Hz to 100 MHz bandwidth and a current-

time IT product of greater than 64 A.s and was constructed by the General Electric Company. The resistive shunt exhibits a 10 ns response time and 1 000 joule dissipation. The shunt is manufactured by T & M Research Products, Inc.

The oscilloscopes are periodically calibrated using a crystal controlled square wave generator (Heath Kit Model IG 4505) and the internal voltage calibrator, which is checked with a Fluke Model 8020A Multimeter.

Voltage and current pulse waveshapes and amplitude measurements were made in accordance with IEEE STD 4-1978, "IEEE Standard Techniques for High Voltage Testing".

All arc entry tests were conducted using a 3/8 inch diameter steel rod electrode and with a 1 1/4 inch gap between the rounded end of the rod and the panel surface.

RESULTS

The test results in Germany for current-carrying capacity show that the resin impregnation causes a reduction in the permissible surface current density in comparison with bare metallized fabric. As discharges when carrying current must be avoided due to the associated destruction of the resin, highly metallized laminates allow an impulse current of approximately 1 kA per cm of material width. On the basis of the tests performed, no material destruction is to be expected at a current of this order.

High current levels at the strike point with arc coupling lead to irreversible damage of the resin matrix and also to partial damage of the metallized fibre inlay. Only highly metallized fabric displays no, or only negligible, damage. However, as the current intensity of a lightning charge can be very high, it must be assumed that direct lightning coupling into the laminate can lead to intolerable damage.

The outbreak of fire observed in some cases can be attributed to the impregnating epoxy resin.

Many more test panels have been tested in the US. More than 400 panels were investigated. Several metals, metal combinations, types of fabric weave and panel combinations were used.

Tests were applied to both painted and unpainted samples. In general, the size and extent of damage is related to the amount of nickel added to the fabric. The greater the weight of nickel added, the less the damage.

The blast force associated with the test subjects the panel to a mechanical shock. It appears that if the simulated lightning current has damaged some of the plies in a particular test sample design, the shock can crack or break the remaining plies. Tests performed on various sample panel sizes, cross-sections and types of layups indicate that all parameters affect this area of performance. For example, tests conducted previously on other panels of the same dimensions but with different weave and resin systems exhibited no tendency to break as did the present sample panels. Consequently, the structural protection afforded to a composite part by any protective coating or fabric must be verified on the part. Tests on other configurations can be used to make comparisons or preliminary screening decisions but cannot be depended on for final design data.

In almost every case, the unprotected sample was heavily damaged and in some instances destroyed completely.

All reported tests were conducted on painted panels. Previous experience has shown that the paint has a significant effect on the results. As can be seen from the figure, any protective system evaluation requires that the sample be coated with a paint system, preferably the one that will be applied in service.

A study of the test samples reveals that even the lowest weight of added nickel greatly improved the survivability of the panel. The determination of the weight of added nickel needed to provide protection will depend on several factors, including - but not limited to - lightning strike zone, number of plies, and damage tolerance.

It must be noted that a substantial lightning strike on any composite structure will cause some damage. Protecting the composite from all damage will require a coating which is so heavy as to negate the advantages of using the composites in the first place.

The results indicate that Baymetex[®]-C nickel coatings of 100 to 150 grams per square meter will provide adequate protection for areas subjected to zone 2 A lightning strikes (100 kA). The amount of coating utilized will be determined by part criticality and damage tolerance. Parts coated with 100 g/m² nickel coating may require maintenance or replacement prior to further flights while parts using 150 g/m² or more will require no more than cosmetic repairs.

For areas subject to zone 1 A strikes (200 kA, 0.25 10⁶ A.s and 3.6 kA, 10 coulombs) a metal coating of more than 150 grams per square meter should be used. This is a recommendation, based on observed damage to the

second ply. If the structure of the part can survive limited second ply damage, then lighter coatings with metal can be considered. In general, the weave and graphite yarn types seem to have a minimal effect on performance. It has been found, however, that a plain weave, like type 3 K 70 P (Boeing), gave the best results in the tests.

A sample with 150 g Ni/m² exhibited a surface ply damage area of about 12 inch but no second ply damage. Maybe this effect is related to the fact that the lower layer of the fabric (non-metallized graphite fabric) acts like the second ply of another fabric and tends to limit the depth of the damage.

It has also been found that the first metallized ply on the top of the composite test panel is sufficient to provide lightning strike protection. Another metallized ply underneath has almost no additional effect on the protection.

SHIELDING EFFECTIVENESS AND REFLECTION OF MICROWAVES

It has been found, that all these highly metallized fabrics and also the composites with a metallized fabric on top have excellent properties regarding shielding effectiveness and reflection of microwaves. Tests of attenuation and reflection of microwaves were conducted at Bayer AG, Leverkusen, Department of Central Research Application of New Products.

In general it has been found, that the attenuation of electromagnetic waves in the range of 30 MHz to 76 GHz is above 40 dB. All composite samples show, however, an attenuation of 60 dB and above.

$$(40 \text{ dB} = \frac{1}{10^4} = \frac{1}{10\,000} = \text{shielding of } 99.99 \%)$$

$$60 \text{ dB} = \frac{1}{10^6} = \frac{1}{1\,000\,000} = \text{shielding of } 99.9999 \%)$$

The reflection of microwaves is also excellent and therefore gives the composite a high shielding.

Even with a small amount of nickel the test panel showed a reflection of 98 % and higher, i. e. a loss of reflection of ≤ 0.1 dB in the range of 1 GHz to 76 GHz.

Values above 76 GHz and below 10 MHz are under investigation.

REFERENCES

[1] D.T. Auckland, R.F. Wallenberg, and J.A. Birken "The Effects of New Technology Trends on Aircraft Lightning Vulnerability and the Capability to Identify Technology Deficiencies", 8th International Aerospace and Ground Conference on Lightning and Static Electricity. June 21 - 23, 1983, Fort Worth, Texas, U.S.A., Modelling of Direct-Strike Lightning Coupling by a Transfer Function Technique, pages 16-1 to 16-9

Author Index

Alliot, J. C. 16
Anderson, L. 30
Axup, P. R. 24

Beavin, R. C. 13
Belcastro, C. M. 15
Bent, R. B. Dr. 6
Bernstein, D. 43
Bernstein, S. S. 26
Bicknell, J. A. Dr. 4
Boulay, J. L. 3
Brigham, W. P. 46
Bunting, J. S. 5

Caranti, J. M. 49
Carreno, V. A. 14
Clark, O. M. 19
Corbin, J. C. 20

Dawson, J. L. 51
Dill, M. 25

East, D. A. 53
Easterbrook, C. C. 50, 56
Ebneith, H. Dr. 55
Edlin, G. R. Dr. 50
Ely, J. T. A. 29

Frey, O. 39
Funayama, R. 33

Gieri, V. A. 54
Glynn, M. S. 21
Gockenbach, E. Dr. 39
Golub, C. N. 17
Goto, Y. 28, 33
Groshart, E. C. 53

Highlands, W. 6
Hiscox, W. L. 7
Hoeft, L. O. 42, 43, 44, 54
Hofstra, J. 42, 43, 44, 54
Humood, B. M. 4

Illingworth, A. J. 49

Jafferis, W. 12

Kasemir, H. W. Dr. 2, 9
Kawasaki, Z. I. 35
Keller, W. L. 18
Kerr, K. Lt. 12
Krider, E. P. 7, 22
Kuhlman, B. P. 23

Landry, M. J. Dr. 46
Larigaldie, S. 3
LaVoie, J. E. Lt. 13
Lee, T. S. Dr. 27, 32
Levesque, P. 16
Linder, A. 43
Lippert, J. R. 13
Lovstrand, K. G. 30
Lyons, W. A. 6

Maier, M. W. 11
Marsh, S. J. 49
McKenna, P. M. 37, 45, 52
Melander, B. G. Dr. 34
Merrell, J. E. 44
Mizutani, Y. 35
Modrusan, M. Dr. 39
Mourente, P. 41

Naito, F. 28
Naito, M. 28
Nakai, T. 35
Narita, K. 28, 33
Nisbet, J. S. 48

Olsson, B. 30

Parker, L. W. 9
Perala, R. A. 37, 45, 50, 56, 57
Pifer, A. E. 7
Portela, C. 41

Rasch, N. O. 21
Rashid, A. 10
Reazer, M. J. 23
Richmond, R. D. 8
Riley, L. 50
Robb, J. D. 32, 45, 50
Roehr, W. E. 19
Rudolph, T. H. 37, 45, 57
Rustan, P. L. Dr. 24

Santiago, N. 41
Schulte, E. H. 31
Shio, H. 47
Simi, J. P. 25
Su, W. Y. 27

Takeuti, T. 35
Tang, H. 12
Taylor, C. D. 36
ter Haseborg, J. L. Prof. Dr. 38
Trinks, H. Prof. Dr. 38
Tukiendorf, V. 26

Uman, M. A. 1, 7

Wahlgren, B. W. 30
Walker, W. T. 31
Weidman, C. D. 22
White, R. A. 40

END

DT/C

8-86